

AD A063851

CCC FILE COPY

0 NW

AGARD-CP-235

AGARD

ADVISORY GROUP FOR AEROSPACE RESEARCH & DEVELOPMENT

7 RUE ANCELLE 92200 NEUILLY SUR SEINE FRANCE

LEVEL

AGARD CONFERENCE PROCEEDINGS No. 235

Dynamic Stability Parameters

DDC
RECEIVED
JAN 26 1979
A

DISTRIBUTION STATEMENT A

Approved for public release
Distribution Unlimited

NORTH ATLANTIC TREATY ORGANIZATION



DISTRIBUTION AND AVAILABILITY
ON BACK COVER

NORTH ATLANTIC TREATY ORGANIZATION
ADVISORY GROUP FOR AEROSPACE RESEARCH AND DEVELOPMENT
(ORGANISATION DU TRAITE DE L'ATLANTIQUE NORD)

1
AGARD Conference Proceedings No. 235

6
DYNAMIC STABILITY
PARAMETERS.

11 May 78 12 629 p.

Papers presented and discussions held at the Fluid Dynamics Panel Symposium held in Athens, Greece,
22-24 May 1978.

45-64

THE MISSION OF AGARD

The mission of AGARD is to bring together the leading personalities of the NATO nations in the fields of science and technology relating to aerospace for the following purposes:

- Exchanging of scientific and technical information;
- Continuously stimulating advances in the aerospace sciences relevant to strengthening the common defence posture;
- Improving the co-operation among member nations in aerospace research and development;
- Providing scientific and technical advice and assistance to the North Atlantic Military Committee in the field of aerospace research and development;
- Rendering scientific and technical assistance, as requested, to other NATO bodies and to member nations in connection with research and development problems in the aerospace field;
- Providing assistance to member nations for the purpose of increasing their scientific and technical potential;
- Recommending effective ways for the member nations to use their research and development capabilities for the common benefit of the NATO community.

The highest authority within AGARD is the National Delegates Board consisting of officially appointed senior representatives from each member nation. The mission of AGARD is carried out through the Panels which are composed of experts appointed by the National Delegates, the Consultant and Exchange Programme and the Aerospace Applications Studies Programme. The results of AGARD work are reported to the member nations and the NATO Authorities through the AGARD series of publications of which this is one.

Participation in AGARD activities is by invitation only and is normally limited to citizens of the NATO nations.

The content of this publication has been reproduced directly from material supplied by AGARD or the authors.

Published November 1978

Copyright © AGARD 1978
All Rights Reserved

ISBN 92-835-0223-X



*Printed by Technical Editing and Reproduction Ltd
Harford House, 7-9 Charlotte St, London, W1P 1HD*

EXECUTIVE SUMMARY

- (1) The Symposium was organized in recognition of the strong present-day interest in dynamic stability of aerospace vehicles. The purpose of the Symposium was to discuss the specific needs for dynamic stability information, the form in which it should be presented and the various means of obtaining it.
- (2) The modern aerospace vehicle is often exposed to unsteady, irregular or asymmetrical flow fields that may have significant effects on its characteristics of motion. This is caused by the fact that the flight envelope of a present-day military aircraft or missile often encompasses flight at high angles of attack, flight at non-zero sideslip angles and the ability to perform translational maneuvers. An additional complication arises because of the geometry of a military fighter aircraft which often includes a long forebody, particularly conducive to complex flows at higher angles of attack. Such flight conditions and aircraft configurations induce flow phenomena such as flow separation, vortex shedding, vortex bursts, etc., which are highly non-linear and complex and can strongly affect both the static and the dynamic stability parameters. This is in sharp contrast with the situation that existed only a few years ago, when the aircraft were exposed primarily to relatively orderly flow at low angles of attack and zero sideslip, and when the dynamic stability problems were considered to be well under control for most flight conditions except, maybe, during some phases of the stall/spin maneuver.
- (3) One of the most important steps needed to gain a satisfactory understanding of the flight dynamics of an aircraft exposed to these complex flow fields is the establishment and the verification of a necessary mathematical model to describe its motions. The verification should be conducted by determining a complete set of stability parameters for a particular configuration, by predicting a series of extreme maneuvers, and by comparing them with the actual flight histories. Although the verification should be sought at the lowest necessary level of sophistication of the mathematical model, it is almost certain that such a model must include non-linear and time-dependent terms.
- (4) The flow phenomena mentioned under (2) are directly responsible for a number of important effects that may have a considerable impact on the stability analysis of a modern aerospace vehicle. The following should be mentioned here:
 - (a) the strong non-linear dependence of almost all stability parameters on angle of attack and, to some extent, also on angle of sideslip and rate of spin. As a result, stability derivatives can no longer be considered as constants, but must be determined as functions of nominal flight conditions. This greatly increases the number of required experiments. In more extreme cases, in the presence of significant nonlinearities or of several large aerodynamic terms in the equations of motion, the principle of linear superposition and the use of derivatives may have to be abandoned altogether;
 - (b) the significant static and dynamic cross-coupling effects that have been shown to exist between the lateral and the longitudinal degrees of freedom. This makes it necessary to consider the lateral and the longitudinal equations of motion simultaneously and not in two separate groups as often done in the past. New experimental techniques, some of which already described at the Symposium, are needed to determine the dynamic cross-coupling derivatives;
 - (c) the translational acceleration effects, such as can be encountered when the aircraft performs a plunging or a transversal oscillation. This has direct application to aircraft equipped with direct-lift or direct-sideforce controls. The translational acceleration derivatives are also necessary to separate correctly derivatives appearing in composite expressions such as result from traditional oscillatory experiments around a fixed axis.

So far, relatively little work has been done in the above-mentioned areas and an accelerated program of research is most urgently required.

- (5) Six countries reported on new developments in wind-tunnel techniques for dynamic stability testing. At present the most useful among such techniques appears to be the technique of rigidly forced oscillation, which provides a direct measurement of the quantities required, can be used in the presence of considerable static loads and can be applied for measuring direct as well as cross and cross-coupling derivatives due to both angular and translational oscillation. In addition, two countries use an indirect technique, which employs a multi-degree-of-freedom elastically forced oscillation and where the derivatives are obtained by solving an assumed set of equations of motion. Furthermore, in an effort to better simulate the aerodynamic phenomena that are associated with the spin motion of an aircraft, five countries have recently developed rotary balances, with which the rate of spin can be correctly simulated for an arbitrary combination of angles of attack and sideslip.

- (6) There was a strong feeling that although the manifestations of some high-angle-of-attack or asymmetrical flows in terms of their effects on dynamic stability parameters are becoming known, the exact nature of these flows – especially in oscillatory or unsteady situations – was still largely undefined. Also lacking is detail understanding of the configuration dependence of such flows. More research into the fluid dynamics aspects of dynamic stability effects is urgently needed.
- (7) In addition to problems indicated in paragraphs (3), (4), (5) and (6), the following areas require increased attention in the next few years:
- (a) control derivatives. This is of particular importance for control-configured vehicles;
 - (b) stability and control derivatives of aeroelastic configurations. Of special interest here is the possibility of obtaining dynamic information on aeroelastic configuration from a combination of dynamic rigid model data and static aeroelastic model data;
 - (c) wind-tunnel and support interference effects on oscillatory experiments, especially at high angles of attack, and effects of flow unsteadiness.
- (8) The Symposium was attended by about 120 people and consisted of 6 regular sessions, a workshop session for last moment contributions, and a round table discussion. Four of the regular sessions were devoted to various means of obtaining dynamic stability parameters, such as represented by wind tunnel techniques, flight test techniques and analytical techniques; this was followed by a session on motion analysis and nonlinear formulations and another one on sensitivity and simulator studies. The programme contained 8 invited and 28 contributed papers from 7 countries. Four participants availed themselves of the opportunity of presenting additional material during the workshop session.
- (9) One of the most important aspects of the Symposium was that it brought together specialists of all the four disciplines involved, that is wind tunnel and flight test experts and people who carry out fluid dynamics and flight mechanics analyses. It is, of course, only through a simultaneous use of all these disciplines that a better understanding of the flight dynamics of a modern aircraft can be achieved. Very few meetings of this nature, if any, ever take place. There was a general feeling among the participants that another such symposium in three to four years time would fulfill an equally useful role, especially in view of the unusual, complex configurations that are now being considered for the future generations of military aircraft.

AGARD FLUID DYNAMICS PANEL

CHAIRMAN: Mr J.L.Jones - M.S. 202-11
NASA Ames Research Ctr
Moffett Field
California 94035 - United States

DEPUTY CHAIRMAN: Dr. K.J.Orlik-Rückemann
National Aeronautical Establishment
National Research Council
Montreal Road
Ottawa K1A OR6 - Canada

PROGRAM COMMITTEE MEMBERS

Dr. K.J.Orlik-Rückemann (Chairman)
National Aeronautical Establishment
National Research Council of Canada
Montreal Road
Ottawa, Ontario K1A OR6 - Canada

Mr P.P.Antonatos
7400 Eagle Creek Drive
Dayton, OH 45459 - USA

M. l'Ing. de l'Armement A.Coursimault
Section "Etudes Generales"
Service Technique de l'Aéronautique
4 Avenue de la Porte d'Issy
75996 Paris Armées - France

Mr J.L.Jones - M.S. 202-11
Chief, Planning and Analysis Office
NASA Ames Research Center
Moffett Field, CA 94035 - USA

Dr. Ing. B.Laschka
Messerschmitt Bolkow-Blohm GmbH
Unternehmensbereich Flugzeuge
Postfach 80 11 60
8000 Munchen - Germany

Professor E.Mattioli
Istituto di Meccanica applicata e Macchine
Universita di Ancona
Via della Montagnola, No. 30
60100 Ancona - Italy

Dr. G.G.Pope
Head, Aerodynamics Dept
RAE - Farnborough GY 14 6 TD
Hants - U.K.

Dr. B.M.Spee
NLR
Anthony Fokkerweg 2
Amsterdam 1017 - Netherlands

Dr. I.C.Statler
(Representative of FMP)
Director, US Army Air Mobility
R and D Laboratory
Ames Directorate - Ames Research Center
Moffett Field, CA 94035 - USA

PANEL EXECUTIVE

Mr Michael C.Fischer

Mail from U.S. and Canada:
AGARD/NATO
APO New York 09777

Mail from Europe
AGARD/NATO
7 rue Ancelle
92200 Neuilly-sur-Seine

ACCESSION FOR	
DTIC	White Section <input checked="" type="checkbox"/>
DDP	Dark Section <input type="checkbox"/>
UNANNOUNCED	<input type="checkbox"/>
JUSTIFICATION	
BY	
DISTRIBUTION/AVAILABILITY CODES	
Dist.	AVAIL. ORG. OR SPECIAL
A	

CONTENTS

	Page
EXECUTIVE SUMMARY	iii
AGARD FLUID DYNAMICS PANEL OFFICERS, PROGRAM COMMITTEE AND MEETING THEME	v
	Reference
<u>SESSION I – WIND TUNNEL TECHNIQUES I</u>	
TECHNIQUES FOR DYNAMIC STABILITY TESTING IN WIND TUNNELS by K.J.Orlik-Rückemann	1
NOUVELLE TECHNIQUE D'ESSAIS SUR MAQUETTES LIBRES EN LABORATOIRE POUR LA DETERMINATION DE CARACTERISTIQUES AERODYNAMIQUES par W.Charon et R.Verbrugge	2
NEW NASA-AMES WIND TUNNEL TECHNIQUES FOR STUDYING AIRPLANE SPIN AND TWO-DIMENSIONAL UNSTEADY AERODYNAMICS by G.N.Malcolm and S.S.Davis	3
EXPERIMENTAL DETERMINATION OF DYNAMIC DERIVATIVES DUE TO ROLL AT BRITISH AEROSPACE WARTON DIVISION by A.W.Matthews	4
WIND TUNNEL TESTING OF DYNAMIC DERIVATIVES IN W. GERMANY by X.Hafer	5
ON THE TEST PROCEDURES OF THE DERIVATIVE BALANCES USED IN W. GERMANY by J.v.d.Decken, E.Schmidt and B.Schulze	6
<u>SESSION II – WIND TUNNEL TECHNIQUES II</u>	
Paper 7 cancelled	
EXPERIMENTS ON CROSS-COUPLING AND TRANSLATIONAL ACCELERATION DERIVATIVES by K.J.Orlik-Rückemann and E.S.Hanff	8
A GENERALIZED TECHNIQUE FOR MEASURING CROSS-COUPLING DERIVATIVES IN WIND TUNNELS by E.S.Hanff and K.J.Orlik-Rückemann	9
DETERMINATION DE NON-LINEARITES DE STABILITE DYNAMIQUE par X.Vaucheret	10
SOME FACTORS AFFECTING THE DYNAMIC STABILITY DERIVATIVES OF A FIGHTER-TYPE MODEL by W.Staudacher, B.Laschka, B.Schulze, P.Poisson-Quinton and M.Canu	11
AN EXPERIMENTAL STUDY OF THE HYPERSONIC DYNAMIC STABILITY OF PITCHING BLUNT CONICAL AND HYPERBALLISTIC SHAPES IN A SHORT RUNNING TIME FACILITY by R.A.East, A.M.S.Qasrawi and M.Khalid	12
UNSTEADY AERODYNAMICS OF OSCILLATING CONTAINERS AND APPLICATION TO THE PROBLEM OF DYNAMIC STABILITY OF HELICOPTER UNDERSLUNG LOADS by A.Simpson and J.W.Flower	13
<u>SESSION III – FLIGHT TESTING TECHNIQUES</u>	
AIR FORCE FLIGHT TEST CENTER EXPERIENCE IN THE IDENTIFICATION OF STABILITY AND CONTROL PARAMETERS FROM DYNAMIC FLIGHT TEST MANEUVERS by P.M.Jeglum	14

	Reference
ESTIMATION OF AERODYNAMIC CHARACTERISTICS FROM DYNAMIC FLIGHT TEST DATA by K.W.Iliff	15
AERODYNAMIC INTERACTIONS ON THE FIGHTER CCV TEST AIRCRAFT by R.A.Whitmoyer	16
IDENTIFICATION OF THE STABILITY PARAMETERS OF AN AEROELASTIC AIRPLANE by E.G.Rynaski, D.Andrisani, II, and N.Weingarten	17
NONLINEAR PARAMETER IDENTIFICATION AND ITS APPLICATION TO TRANSPORT AIRCRAFT by T.J.Galbraith and T.J.Petersen	18

SESSION IV – ANALYTICAL TECHNIQUES

A SURVEY OF ANALYTICAL AND EXPERIMENTAL TECHNIQUES TO PREDICT AIRCRAFT DYNAMIC CHARACTERISTICS AT HIGH ANGLES OF ATTACK by A.M.Skow and A.Titiriga, Jr	19
PRESENTATION OF STABILITY DERIVATIVES IN MISSILE AERODYNAMICS AND THEORETICAL METHODS FOR THEIR PREDICTION by C.P.Schneider	20
THE USE OF PANEL METHODS FOR STABILITY DERIVATIVES by R.Roos	21
AN ANALYTIC THEORY OF SUPERSONIC/HYPERSONIC STABILITY AT HIGH ANGLES OF ATTACK by W.H.Hui	22
IDENTIFICATION OF UNSTEADY EFFECTS IN LIFT BUILD UP by P.Mereau, R.Hirsch, G.Coulon and A.Rault	23
EFFECT OF FLOW SEPARATION VORTICES ON AIRCRAFT UNSTEADY AERODYNAMICS by L.E.Ericsson and J.P.Reding	24
OSCILLATORY AERODYNAMICS AND STABILITY DERIVATIVES FOR AIRFOIL SPOILER MOTIONS by R.Bernier and G.V.Parkinson	25

SESSION V – MOTION ANALYSIS AND NONLINEAR FORMULATIONS

THE ROLE OF TIME-HISTORY EFFECTS IN THE FORMULATION OF THE AERODYNAMICS OF AIRCRAFT DYNAMICS by M.Tobak and L.B.Schiff	26
MATHEMATICAL MODELS OF AIRCRAFT DYNAMICS FOR EXTREME FLIGHT CONDITIONS (THEORY AND EXPERIMENT) by H.H.B.M.Thomas and G.Edwards	27
LINEAR OR NON-LINEAR ANALYSIS METHODS – WHEN AND HOW? by J.Roskam	28
AIRCRAFT STABILITY CHARACTERISTICS AT HIGH ANGLES OF ATTACK by J.Kalviste	29
EXPRESSION DES FORCES AERODYNAMIQUES NON-LINEAIRES EN DYNAMIQUE DU VOL par M.Scherer	30
NONLINEAR OSCILLATIONS AT HIGH INCIDENCE by G.D.Padfield	31

THE DYNAMIC STABILITY IN FLIGHT OF SPINNING BLUNT BODY PROJECTILES
by P.C.Parks

32

SESSION IV – SENSITIVITY AND SIMULATOR STUDIES

RESULTS OF PILOTED SIMULATOR STUDIES OF FIGHTER AIRCRAFT AT HIGH ANGLES OF ATTACK

by J.R.Chambers, W.P.Gilbert and L.T.Nguyen

33

SENSITIVITY OF AIRCRAFT MOTION TO AERODYNAMIC CROSS-COUPLING AT HIGH ANGLES OF ATTACK

by W.H.Curry and K.J.Orlik-Rückemann

34

AIRCRAFT MOTION SENSITIVITY TO VARIATIONS IN DYNAMIC STABILITY PARAMETERS
by R.W.Butler and T.F.Langham

35

IDENTIFICATION OF KEY MANEUVER-LIMITING FACTORS IN HIGH-ANGLE-OF-ATTACK FLIGHT

by D.E.Johnston

36

WORKSHOP SESSION

GUST-VEHICLE PARAMETER IDENTIFICATION BY DYNAMIC SIMULATION IN WIND-TUNNELS

by B.Krag

W1

ROUND TABLE DISCUSSION

RTD

TECHNIQUES FOR DYNAMIC STABILITY

TESTING IN WIND TUNNELS

by

K.J. Orlik-Rückemann
 Unsteady Aerodynamics Laboratory,
 National Aeronautical Establishment,
 National Research Council of Canada,
 Ottawa, Ontario, K1A 0R6,
 Canada

SUMMARY

A systematic review is presented of the methods and techniques that are used for wind-tunnel measurements of the dynamic stability parameters (derivatives) of an aircraft. The review is illustrated by numerous examples of experimental equipment available in various aerospace laboratories in Canada, France, the United Kingdom, the United States and West Germany.

1. INTRODUCTION

The modern aerospace vehicle is exposed - much more often than in the past - to unsteady flow fields that may have significant effects on its characteristics of motion. This occurs, for example, whenever an oscillatory motion is experienced by an aircraft flying at an angle of attack that is high enough to cause flow separation or vortex shedding, or whenever two configurations flying in close proximity are exposed to some unsteady disturbance as it may happen immediately after a separation maneuver. In addition, the modern aircraft often flies in conditions causing significant flow asymmetry, such as that associated with asymmetric vortex shedding, application of direct side-force controls or presence of a small angle of sideslip. The space shuttle and the high performance military aircraft (including CCVs) are prime examples of vehicles for which these phenomena are of high interest. The unsteady flow fields involved are usually highly nonlinear and complex and result in stability characteristics that are strong functions of angle of attack and that may represent a significant aerodynamic coupling between the longitudinal and the lateral degrees of motion. A good knowledge of stability characteristics at high angles of attack is essential for a better appreciation of the entire complex of stall/spin problems and may even lead to a re-examination of the present formulation of equations of motion.

As a result of the above developments, the dynamic stability information - considered of rather lesser importance for a number of years - is again becoming an object of relatively high interest. The reason is obvious: in the past, at low angles of attack, most of the dynamic stability derivatives were relatively easy to predict analytically, exhibited as a rule only smaller variations with varying flight conditions and, therefore, had only a relatively insignificant or at least a relatively constant effect on the resulting flight characteristics of the aircraft. In many cases it was therefore satisfactory, in the flight mechanics analysis, to use a constant value of a particular dynamic stability derivative, often determined by some simple approximate method of calculation. With the advent of flight at high angles of attack at high speeds, all that has drastically changed (Fig. 1). The dynamic stability derivatives are now found to depend strongly on non-linear effects and can no longer be calculated using relatively simple linear analytical methods as in the past. Also, these derivatives are known now

FIG. 1 THE CHANGING INTEREST IN DYNAMIC DERIVATIVES - HIGH α VERSUS LOW α

	LOW α	HIGH α
FLOW	MAINLY LINEAR, OFTEN WELL-KNOWN	STRONG NON-LINEAR EFFECTS (SEPARATION, TRANSITION, VORTEX SHEDDING, ETC.)
ANALYTICAL PREDICTION OF DYNAMIC DERIVATIVES	EASY (LINEAR POTENTIAL METHODS AND VARIOUS APPROXIMATIONS OFTEN ACCEPTABLE)	DIFFICULT (HIGHLY NON-LINEAR, OFTEN SPECULATIVE, APPROXIMATIONS RISKY)
MAGNITUDE OF DYNAMIC DERIVATIVES	SMALL (\times)	SOMETIMES LARGE, VARYING SIGN (P 100%)
VARIATION OF DYNAMIC DERIVATIVES WITH α	SMALL	SOMETIMES LARGE AND RAPID
EFFECT OF DYNAMIC DERIVATIVES ON FLIGHT TRAJECTORY AND ON STABILITY AND CONTROL	INSIGNIFICANT OR AT LEAST CONSTANT AND WELL-KNOWN	MAY OFTEN BE SIGNIFICANT
INTEREST IN DYNAMIC DERIVATIVES	LOW	HIGH

to sometimes undergo very large changes, perhaps of one or even two orders of magnitude and often involving a change of sign, as a result of only a minor variation in flow conditions (such as in the angle of attack) and therefore can easily become of significant importance for the flight behaviour of the aircraft. In addition, for an aircraft rotating in a flat spin, the dynamic stability derivatives at high angles of attack may also display a nonlinear dependence on the spin rate of rotation. To underline the fact that in all these cases stability derivatives no longer can be considered

constant, a different nomenclature may be needed, and some authors have started introducing *stability parameters* instead. In this review paper, however, the term *stability derivatives* will mostly be used.

Dynamic stability information can in principle be obtained from model experiments in many different types of facilities (see e.g. Ref. 1). Here belong, for instance, tests in aeroballistic or hypervelocity ranges, out-door free-flight tests using either rocket-propelled or radio-controlled gliding models, wind-tunnel free-flight tests using freely launched or remotely controlled models, or spin-tunnel experiments. All these techniques, however, have one common disadvantage - they are not suitable for experiments at high Reynolds numbers. In addition, although some of them can be used for extraction of dynamic stability derivatives from the model motion history, this is rarely done. Thus the main use of these techniques is for visual studies of the stability characteristics and motions of the aircraft, all at low Reynolds numbers.

The best way to obtain model-scale dynamic stability information at realistic Reynolds and Mach numbers is to perform captive-model experiments in high Reynolds number wind tunnels, and the present discussion, therefore, will be mainly restricted to that type of capability. Of course, dynamic stability derivatives can also be extracted from full-scale flight tests. Since, however, the results of such tests are obtained too late to significantly affect the design of a new aircraft, the relevant techniques are not included here. However, it should be kept in mind that full-scale flight experiments are most essential for correlating the values of various dynamic stability parameters and the flight behaviour of already existing aircraft. Such correlations are badly needed for obtaining a better understanding of the relative importance of the various derivatives as well as for a realistic evaluation of the presently used methods of motion analysis, especially with regard to the high angle-of-attack stall and spin conditions.

Finally, a few words about the importance of simulating, as fully as possible, the flight Reynolds number. Such a simulation, of course, constitutes one of the standard requirements for all kinds of aerodynamic testing and may be particularly important at high angles of attack. Considerable efforts are presently being made to construct new facilities to satisfy this requirement as well as possible, despite various economical and technical constraints. However, it is not realistic to expect that any large facilities may be built specially for the purpose of dynamic testing. There is no need, therefore, to specify in this paper any desirable values of Reynolds number, other than by indicating that they should be as high as can be obtained at any particular time. It should be kept in mind, however, that after a certain amount of dynamic stability information - for several configurations and at various flow conditions - has been accumulated, it may be possible to review the situation again and perhaps to reduce the number of derivatives for which as complete as possible Reynolds number simulation is essential, thereby permitting some dynamic stability testing to be performed in smaller, less expensive, facilities.

2. DYNAMIC STABILITY DERIVATIVES

The concept of a stability derivative is of course related to the traditional form of equations of motion where the result of a small disturbance from the equilibrium flight condition is described by linear superposition of contributions caused by the change in various attitude variables and their time rates of change. The traditional stability derivatives are constants representing the rate of change of a given aerodynamic coefficient with the variable in question, at a point where the variable itself is zero. With present-day interest in flights at relatively high values of some of the displacement variables (such as α , β and the rate of spin) it is necessary to consider stability derivatives as functions of those variables and apply the proper local value of the functions for each equilibrium condition. In cases where the variations described by these functions are relatively rapid or where the disturbances are no longer very small, it may also be necessary to replace a particular constant derivative with an analytical expression defining its variation in the vicinity of the equilibrium position.

Even if we have to recognize that a stability derivative is not always a constant but may sometimes be a function of one or more displacement variables, the basic experimental methods to obtain the required information remain the same as in the past. The number of required experiments, however, becomes much larger since, instead of determining a single value, we must now obtain enough points to define a function. It follows that it is even more important now than in the past to perform these experiments in an efficient manner.

The number of necessary experiments is also much larger because many more derivatives may now be needed. While in the past the dynamic derivatives of interest were often limited to the three damping derivatives with an occasional mention of the dynamic cross derivatives, up to three times that many derivatives may be needed for a modern fighter configuration. The various categories of dynamic derivatives are indicated in Table I, together with a set of definitions of dynamic moment derivatives that follows the North American usage. A similar table can be set up for the dynamic force derivatives which, however, are often of considerably lesser interest and will, therefore, not be dwelled on here in any detail. It should be remembered, however, that some dynamic force derivatives may be quite important in special cases, such as when considering direct-sideforce or direct-lift controls or when transferring dynamic moment derivatives from one axis to another.

TABLE 1
DYNAMIC MOMENT DERIVATIVES

PURE ROTATION			TRANSLATIONAL ACCELERATION			OSCILLATION AROUND FIXED AXIS		
$C_{lp} = \frac{\partial C_L}{\partial \dot{\beta}}$	$C_{mp} = \frac{\partial C_m}{\partial \dot{\beta}}$	$C_{np} = \frac{\partial C_n}{\partial \dot{\beta}}$	$C_{la} = \frac{\partial C_L}{\partial \dot{\alpha}}$	$C_{ma} = \frac{\partial C_m}{\partial \dot{\alpha}}$	$C_{na} = \frac{\partial C_n}{\partial \dot{\alpha}}$	DAMPING DERIVATIVES	CROSS DERIVATIVES	CROSS-COUPLING DERIVATIVES
$C_{lq} = \frac{\partial C_L}{\partial \dot{q}}$	$C_{mq} = \frac{\partial C_m}{\partial \dot{q}}$	$C_{nq} = \frac{\partial C_n}{\partial \dot{q}}$	$C_{lb} = \frac{\partial C_L}{\partial \dot{\beta}}$	$C_{mb} = \frac{\partial C_m}{\partial \dot{\beta}}$	$C_{nb} = \frac{\partial C_n}{\partial \dot{\beta}}$	$C_{lp} + C_{l\dot{\beta}} \sin \alpha$	$C_{lr} - C_{l\dot{\beta}} \cos \alpha$	$C_{lq} + C_{l\dot{\alpha}}$
$C_{lr} = \frac{\partial C_L}{\partial \dot{r}}$	$C_{mr} = \frac{\partial C_m}{\partial \dot{r}}$	$C_{nr} = \frac{\partial C_n}{\partial \dot{r}}$				$C_{mq} + C_{m\dot{q}}$	$C_{np} + C_{n\dot{p}} \sin \alpha$	$C_{nr} - C_{n\dot{r}} \cos \alpha$
						$C_{nr} - C_{n\dot{r}} \cos \alpha$		$C_{mp} + C_{m\dot{p}} \sin \alpha$
								$C_{nq} + C_{n\dot{q}}$

In addition to the familiar *damping* derivatives (C_{mq} , C_{nr} and C_{lp}) and *cross* derivatives (C_{np} and C_{lr}), Table 1 contains also groups of derivatives labelled *cross-coupling* derivatives and *acceleration* derivatives. The first of those, *cross-coupling* derivatives (C_{nq} , C_{lq} , C_{mr} and C_{mp}) are a direct result of the fact that the modern aircraft often flies in conditions causing significant flow asymmetry, as indicated before. These derivatives relate the longitudinal and the lateral degrees of freedom of an aircraft, providing aerodynamic coupling that did not exist in symmetrical flow conditions which were of main interest in the past. It follows that in cases where these derivatives are of a significant order of magnitude, the traditional (and very convenient) separation of equations of motion into longitudinal and lateral groups can no longer be considered acceptable and that in such cases all these equations have to be considered simultaneously.

The last group of derivatives is labelled *acceleration* derivatives and is represented by moment derivatives due to $\dot{\alpha}$ and $\dot{\beta}$. The word acceleration refers to translational acceleration, which in the first approximation is proportional - from the aerodynamic point of view - to the time rate of change of the angular deflection in the same plane of motion. The aerodynamic reactions due to vertical acceleration, for example, are equivalent to those due to the time rate of change in the angle of attack ($\dot{\alpha}$). Similarly, the lateral acceleration is related to the time rate of change in the angle of sideslip ($\dot{\beta}$). The derivatives associated with these variables are of great interest in connection with the already mentioned applications of direct-sideforce or direct-lift controls. They may also be used to separate the purely-rotary derivatives (such as C_{mq}) from their fixed-axis oscillatory counterparts (such as $C_{mq} + C_{m\dot{\alpha}}$).

The reason why an oscillation around a fixed axis results in a *sum* of a purely-rotary derivatives (such as C_{mq}) and a translational acceleration derivative (such as $C_{m\dot{\alpha}}$) sometimes creates confusion and so a few words of explanation may be in order here.

Let us consider, as an example, the longitudinal case. For a free-flying aircraft the variations in the angle of pitch and in the angle of attack can occur independently of each other, and each gives rise to a different longitudinal distribution of the normal velocity. The distribution due to the angle-of-pitch variation (i.e. due to the pitching velocity q) varies along the chord and intersects zero at the axis of rotation, while the distribution due to the angle-of-attack variation is constant along the chord. In the case of an oscillation around a fixed axis both variations occur at the same time and even if the two variables q and α are themselves equal, their effects are different and have to be superimposed. As already indicated, the contribution due to $\dot{\alpha}$ is equivalent to one due to vertical acceleration, since $\dot{\alpha} = \dot{z}/V$.

Similarly, in the lateral case, a rolling (p) or a yawing (r) motion around a fixed axis at an angle of attack causes a simultaneous variation in the rate of change of the angle of sideslip ($\dot{\beta}$). If a system of body axes is used, the resulting composite expressions include a trigonometric function of α , such as in $C_{nr} - C_{n\dot{\beta}} \cos \alpha$ or $C_{np} + C_{n\dot{\beta}} \sin \alpha$.

3. REVIEW OF EXISTING WIND-TUNNEL CAPABILITIES FOR DYNAMIC STABILITY TESTING

It may be useful to spend a moment on examining the availability of equipment for dynamic stability testing in various countries of the world. About five years ago a review of the pertinent wind-tunnel capabilities in North America was performed by the present author (Ref. 2) and a very brief summary of this review will be presented here. The summary takes into account some of the changes that occurred in those five years and that happen to be known to the author.

It was found, on the basis of a suitable questionnaire, that 17 organizations in the USA and Canada have capabilities for dynamic stability testing and these organizations are listed in Table 2, together with their location, name of a cognizant person and an abbreviation of their name. Together these organizations operate 37 wind tunnels

TABLE 2. ORGANIZATIONS IN USA AND CANADA THAT ARE EQUIPPED FOR DYNAMIC STABILITY MEASUREMENTS IN WIND TUNNEL

ABBREV.	ORGANIZATION	LOCATION	COGNIZANT PERSON
BRL	BALLISTIC RESEARCH LABORATORIES	ABERDEEN	K. OPALKA
CAL	CALSPAN CORPORATION	BUFFALO	R.W. COTTER
CONVAIR	GD CONVAIR AEROSPACE DIVISION	SAN DIEGO	D.P. CUMMING
FLUIDDYNE	FLUIDDYNE ENGINEERING CORPORATION	MINNEAPOLIS	J. HOLDHUSEN
MIT	MIT AEROPHYSICS LABORATORY	CAMBRIDGE	C. HALDEMAN
NAE	NATIONAL AERONAUTICAL ESTABLISHMENT	OTTAWA	K.J. ORLIK-RUCKENMANN
NASA-ARC	NASA AMES RESEARCH CENTER	MOFFETT FIELD	G. MALCOLM
NASA-LRC	NASA LANGLEY RESEARCH CENTER SUBSONIC-TRANSONIC AERODYNAMICS DIV. DYNAMIC STABILITY BRANCH FLUID DYNAMICS BRANCH	HAMPTON	J.R. CHAMBERS R.A. KILGORE
NSWC	NAVAL SURFACE WEAPONS CENTER	SILVER SPRING	S.M. HASTINGS
NOTRE DAME	UNIVERSITY OF NOTRE DAME	NOTRE DAME	C.W. INGRAM
NSRDC	NAVAL SHIP R & D CENTER	WASHINGTON	S.M. GOTTLIEB
PWT	ARO, INC., PROPULSION WIND TUNNEL	TULLAHOMA	H.C. DUBOSE
SANDIA	SANDIA CORPORATION	ALBUQUERQUE	J.M. PETERSON
VAC	VOUGHT AERONAUTICS COMPANY	DALLAS	J.M. COOKSEY
VAF	ARO, INC., VON KARMAN GAS DYNAMICS FAC.	TULLAHOMA	G.E. BURT
VPI	VIRGINIA POLYTECHNIC INSTITUTE	BLACKSBURG	J.F. HARCHMAN

TABLE 3. ORGANIZATIONS OUTSIDE OF NORTH AMERICA THAT ARE EQUIPPED FOR DYNAMIC STABILITY MEASUREMENTS IN WIND TUNNEL (PARTIAL LIST)

COUNTRY	ORGANIZATION	LOCATION	COGNIZANT PERSON
BELGIUM	VON KARMAN INSTITUTE FOR FLUID DYNAMICS	RUCHE-BASIN-GRANDE	D.E. RICHMONDS
FRANCE	OFFICE NATIONAL D'ETUDES ET DE RECHERCHES AEROSPATIALES	CARTILLON	(A. ACHERON)
		RODANE	H. CANU
	INSTITUT DE MECANIQUE DES FLUIDES	LILLE	B. VERBAUMER
	INSTITUT DE MECANIQUE DES FLUIDES	MARSEILLE	J. VALENTI
ITALY	AERONAUTICA MACCHI, S.P.A.	VARESE	E. BAZZOCCHI
	UNIVERSITY OF NAPLES	NAPOLI	L. LECCE
JAPAN	NATIONAL AEROSPACE LABORATORY	TOKYO	S. TADAOKA
SWEDEN	FLYTEKNISKA FORSKNINGSTALLEN	STOCKHOLM	B. LINDBLAD
SOUTH AFRICA	NATIONAL MECH. ENG. RESEARCH INSTITUTE	PRETORIA	H.E. BEYERS
UNITED KINGDOM	AIRCRAFT RESEARCH ASSOCIATION	BEDFORD	S.C. CARTER
	ROYAL AIRCRAFT ESTABLISHMENT	BEDFORD	B.A. FAIR
	UNIVERSITY OF SOUTHAMPTON	SOUTHAMPTON	N.A. EAST
	BRITISH AIRCRAFT CORPORATION	PRESTON	P. SMITH
USSR	N.I. KHALIKIN POLYTECHNIC INSTITUTE	LENINGRAD	
W. GERMANY	DEUTSCHE FORSCHUNGS-UND VERSUCHSANSTALT FUR LUFT-UND RAUMFAHRT	OTTUMBERG	E. SCHMIDT

that are suitably equipped for dynamic experiments, and of this total there are 10 hypersonic (or hypervelocity), 9 supersonic, 11 transonic and 7 subsonic wind tunnels. Main performance data for these tunnels, including the Reynolds number information, are tabulated in Ref. 2. No corresponding survey was made at that time of the capabilities outside of North America, but it is well known that such capabilities exist in several countries, particularly in France, Japan, Sweden, the United Kingdom and West Germany. A partial list of organizations outside of North America that are equipped for wind-tunnel dynamic stability measurements is shown in Table 3.

The most important conclusion that can be drawn from Ref. 2 is that, apart from the low-speed ($M < 0.1$) capabilities at NASA Langley and some recent developments at NAE and at PWT, no wind-tunnel capabilities exist at the present time in North America for measuring dynamic stability derivatives of aircraft at angles of attack higher than 28° . It is quite possible that this conclusion is also representative of the situation in other countries of the world. On the other hand, considerations such as those presented in Ref. 3 clearly indicate that the majority, if not all, of the dynamic derivatives mentioned in Section 2 may be needed for a modern high-performance military aircraft in a Mach number range up to 0.6 at angles of attack from 20° to 90° and - to a somewhat smaller degree - also at transonic Mach numbers for angles of attack from 20° to 50° . At Mach numbers up to 0.6 and for angles of attack from 40° to 90° some derivatives should also be determined as functions of the rate of rotation in a spin, if at all possible. There is, therefore, at the present time, a considerable gap between the probable needs and the existing capabilities; this gap, however, is now being reduced by developmental efforts in several laboratories, where new high-load (= high α) oscillatory and rotary balances are being constructed and put into operation.

4. METHODS OF MEASURING DYNAMIC DERIVATIVES

In a review made several years ago (Ref. 1) of the methods of measurement of aircraft dynamic stability derivatives, the present author introduced a systematic classification of the various methods, which included both the free flight conditions and situations where the model was constrained in one or more degrees of freedom, as is most often the case during wind tunnel experiments. Subsequent categories took into account the behaviour of the model in the test section (model moving versus model fixed) and the principal quantity to be measured (reactions versus motion). All in all, sixteen wind-tunnel methods were identified, many of them containing sub-categories and most of them represented by several apparatuses, which were in actual use in 1959 (the year of the review) or at any time prior to that.

It would obviously be impractical to attempt, in the short time available, to go over this 1959 review in any detail, and even less practical to embark on some form of an expanded version of that review which should include all the developments since that time. Instead we will examine in some detail some of the more important methods and techniques that are in use today, with special emphasis on those that are adaptable to high-load (= high α or high Re) wind-tunnel testing. The old 1959 review (or its 1963 modified version, Ref. 4) still provides, however, a very useful reading for anybody thinking about developing and constructing a new apparatus in this field, since it contains a lot of information about various approaches and basic principles on which such an apparatus could be based or perhaps which, on the contrary, should not even be tried.

In Fig. 2 a list by category is presented of wind-tunnel methods which are in use today. All methods which cannot be used in a wind tunnel (such as range tests) and methods which only have historical (such as whirling arm) or conceptual (such as measurement of motion of the rolling flow around a stationary model) significance, have been omitted. Even so, the practical value of the remaining methods is somewhat uneven, with the methods employing an oscillating or rotating model being the most important, since they are best suited for measuring dynamic derivatives at realistic flight conditions (that is, with proper simulation of angles of attack and sideslip, Mach number and, if possible, also Reynolds number).

It is, of course, difficult to include all the pertinent information on a figure such as Fig. 2. "Captive model" refers to a model mechanically suspended, and magnetic

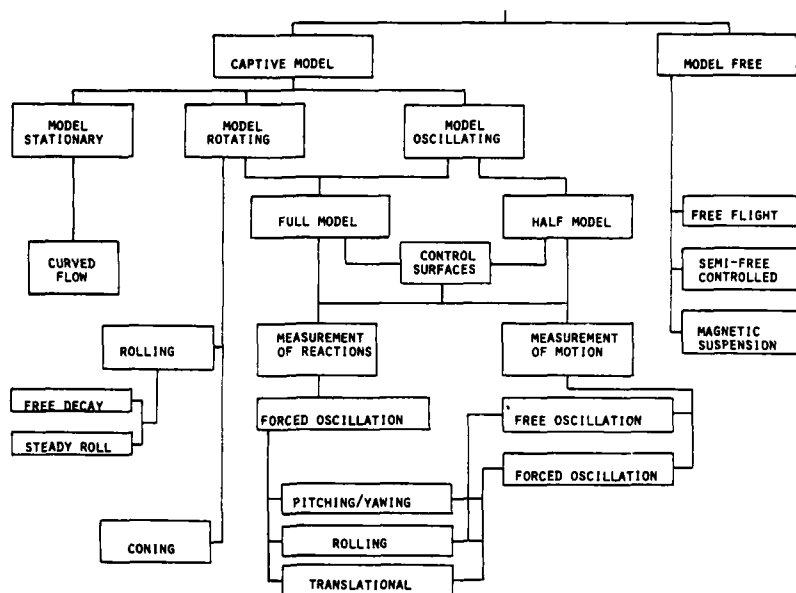


FIG. 2 WIND-TUNNEL METHODS IN USE IN 1977 FOR MEASUREMENT OF DYNAMIC CHARACTERISTICS

suspension is therefore found under "model free". Similar methods can be employed for oscillating full and half models, but the latter can, of course, only be used when both the model and the flow around it are symmetrical. In the present context this restricts the use of half model techniques to studies of pitching and plunging oscillations at not too high angles of attack (say up to 20° or so), and to studies of the oscillating control surfaces and their effects. The continuous rolling experiments can be performed using both forced and free rotation, whereas in coning and spinning the most usual measurement is that of aerodynamic reactions. Forced oscillation can be performed using either constant oscillatory torque or constant oscillatory displacement (inexorable drive), the latter very important when testing at higher angles of attack, where a large static aerodynamic moment has to be overcome. Although in most cases each block represents one particular technique or apparatus, there are cases where a single apparatus can perform, simultaneously or successively, functions indicated in two or more blocks, such as combining coning and spinning, pitching and plunging or using the same equipment for either forced or free oscillation. Finally, the techniques employing free-flying (in a wind tunnel) or magnetically suspended models are not at present suitable for dynamic testing at realistic flight conditions, while experiments using a semi-free, remotely-controlled model usually lead to qualitative (pilot opinion) or cinematographic results, even if more recently attempts have been made to employ certain derivative-extraction procedures (originally developed for flight testing) for this type of semi-free flights in a wind tunnel. More about this later.

In the subsequent sections of this paper the methods indicated in Fig. 2 will be discussed in some detail, using examples of appropriate experimental equipment that is in use today in the U.S.A, Canada, U.K. and some other countries. In describing this equipment the present author will be drawing in some cases (indicated by quotation marks) on descriptions found in the original papers, on the assumption that no one is better qualified to describe an apparatus than the original researcher. Proper references will, of course, be indicated everywhere.

This review is based on the author's notes from a 1977 lecture series at the von Kármán Institute for Fluid Dynamics (Ref. 5). However, the description of those methods and techniques that are separately discussed in this Symposium has been replaced by a short paragraph and a suitable reference each. For lack of space it was also necessary to eliminate most of the material dealing with instrumentation and data acquisition and reduction. To obtain this information the reader is referred to Ref. 5 and the original references for each technique.

5. FORCED-OSCILLATION TECHNIQUES. MEASUREMENT OF REACTIONS.

As mentioned before, this group of techniques can be further subdivided according to the type of drive. If an *electromagnetic* drive is used, the amplitude of the applied torque (or force) is usually constant and the amplitude of the displacement depends on the total damping in the system. In addition, when the oscillation is around such an axis and such an angle that a considerable aerodynamic restoring moment exists, the equilibrium position with the wind on will be different from that with the wind off. If we assume that the mechanical restoring moment $K(x - x_0)$ is zero for $x = x_0$, the wind-on restoring moment $[K(x - x_0) + kx]$ will be zero for $x = x'_0$, such that $x'_0 = x_0 K / (K + k)$, where the aerodynamic stiffness k can be obtained from local conditions, e.g. for a

pitching oscillation we have $k = (C_m)_{\text{local}}/\alpha$. In most cases where oscillation is around zero or small values of angles of attack or sideslip, the mechanical stiffness K is much larger than k and the difference between x'_0 and x_0 is small. For other cases, and especially for the important pitching oscillation around a high mean angle of attack, k may be appreciable and, unless cancelled out by some trimming device, may lead to situations where insufficient free space will be left for the model in which to oscillate (the model will be hitting a mechanical stop on one side).

The use of an inexorable drive, of the *mechanical* or *hydraulic* type, prevents all this from happening but usually results in a much more complicated and bulky apparatus. Most of the high-load apparatuses are of this type. The displacement amplitude is then kept constant and the amplitude of the applied torque or force is adjusted as needed. In this technique (also called rigidly forced oscillation) a preselected motion is imparted to the model and forces and moments between the model and the forcing part of the apparatus are measured. The model motion may be angular or translational and is usually sinusoidal, in which case the derivatives are obtained from the in-phase and quadrature components of the measured aerodynamic reactions. In principle both force and moment derivatives can be measured, and the measurement can be made in both the same degree of freedom as the imparted oscillation (resulting in damping derivatives) and in other degrees of freedom (resulting in cross and cross-coupling derivatives). This method must therefore be considered as the most general of all the methods listed in Fig. 2.

It is usually advantageous, especially for single-degree-of-freedom experiments, to operate at frequencies at or near the resonance, since this minimizes the torque or force required to sustain the oscillation and also increases the accuracy of the experiment.

5.1 NASA Langley, Full-Scale Tunnel ($M < 0.1$)

The NASA Langley forced-oscillation apparatus set-up for pitching experiments in the Full Scale Tunnel is shown in Fig. 3. With minor changes in the experimental arrangement the same apparatus can also be used for yawing or rolling experiments (Ref. 6). Force and moment derivatives due to pitching, rolling or yawing around a fixed axis can be measured at angles of attack up to 110° . The amplitude is adjustable and can be as high as $\pm 30^\circ$. A 6-component internal balance is used with on-line data reduction. The oscillatory motion is imparted to the model by means of a flywheel-driven system of pushrods and bellcranks, powered by a 3 h.p. electric motor. The frequency of oscillation (typically 0.5-1.5 Hz) is varied by changing the speed of the motor. Reference signals proportional to the sine and cosine of the flywheel rotation angle are generated by a precision sine-cosine potentiometer. By multiplying the balance signals by those reference signals and integrating, the in-phase and out-of-phase (quadrature) aerodynamic derivatives are obtained.

5.2 ONERA, Chalais-Meudon

An apparatus similar to the one above is available in the large low-speed wind tunnels S_1 and S_2 at Chalais-Meudon, near Paris. Moment derivatives due to pitching, yawing (Fig. 4) or rolling can be obtained with a 5-component moment balance at angles of attack up to 30° and angles of sideslip up to 12° in the frequency range of 1 to 2 Hz (Ref. 7).

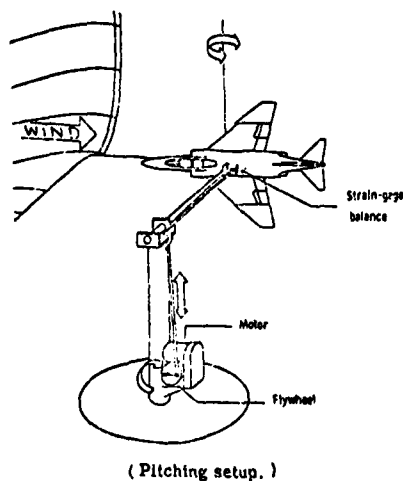


FIG. 3 FORCED-OSCILLATION APPARATUS. NASA LANGLEY FULL SCALE TUNNEL (Ref. 6)

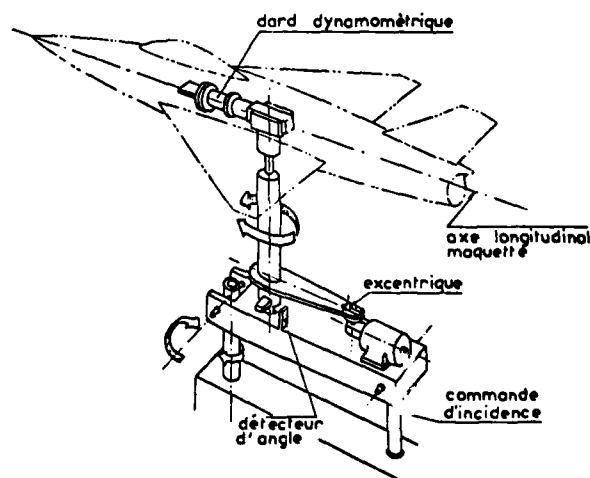


FIG. 4 FORCED OSCILLATION APPARATUS. ONERA CHALAIS-MEUDON (Ref. 7). (Yawing Setup)

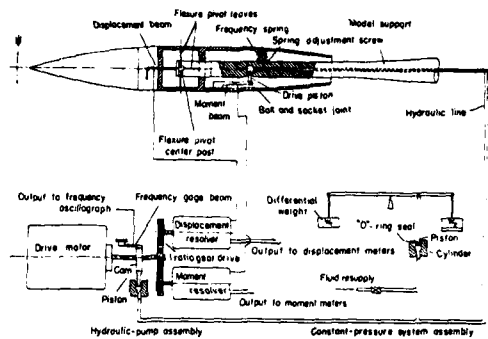


FIG. 5 FORCED-OSCILLATION PITCH/YAW APPARATUS. NASA LANGLEY HIGH SPEED TUNNELS (Ref. 9).

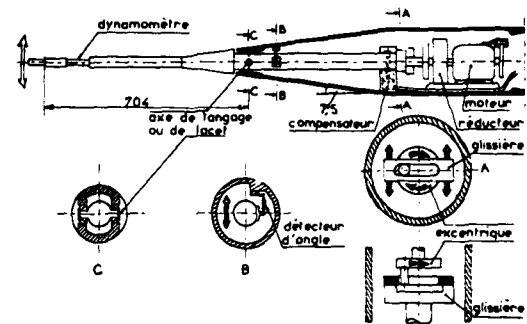


FIG. 6 FORCED OSCILLATION APPARATUS. ONERA MODANE (Ref. 7). (Pitching or Yawing Setup).

5.3 NASA Langley, High-Speed Tunnels

In Ref. 8 a forced-oscillation roll apparatus is described that is compatible with both the 7 x 10 Foot High Speed Wind Tunnel ($0.2 < M < 0.85$) and the 8-Foot Transonic Pressure Tunnel ($0.2 < M < 1.2$). A 2 h.p. variable-speed motor is used to oscillate the sting and model by means of an offset crank. A torsion spring internal to the sting is connected to the front of the strain-gauge balance section and provides a restoring torque which, together with any existing aerodynamic spring, can balance out the model inertia, when the model is oscillated at velocity resonance. A system of resolvers, filters, and damped digital voltmeters is used to separate the torque signal into in-phase and out-of-phase components. The apparatus is designed for a maximum normal force of 1000 lbs and can be used at angles of attack (or angles of sideslip) of up to 22°.

A similar principle of operation is used for the forced-oscillation pitch/yaw apparatus depicted in Fig. 5. This apparatus is described in Ref. 9 and has been used in both the abovementioned wind tunnels. More recently, the hydraulic drive shown in Fig. 5 has been replaced by a mechanical actuator.

5.4 ONERA Modane

Forced oscillation apparatuses are used in the high speed wind tunnel S_2 at Modane ($0.2 < M < 3.2$) for oscillatory experiments in pitch or yaw (Fig. 6) and in roll. An eccentric drive is used for the pitch (yaw) apparatus and a direct drive and a gear-box arrangement for the roll apparatus. A 5-component moment balance provides the pertinent static and damping information; in addition, the rolling apparatus is capable of measuring the cross derivative of the yawing moment due to rolling. Frequency range is of the order of 5 to 10 Hz.

5.5 AEDC-VKF

One of the typical VKF forced-oscillation apparatuses for measuring pitch or yaw damping is shown in Fig. 7 (Ref. 10). The apparatus "utilizes a cross-flexure pivot, an electric shaker motor, and a one-component moment beam which is instrumented with strain gages to measure the forcing moment of the shaker motor. The motor is coupled to the moment beam by means of a connecting rod and flexural linkage, which converts the translation force to a pitching moment. The system operates at small amplitudes and at oscillation frequencies from 2 to 56 Hz. The cross flexures, which are instrumented

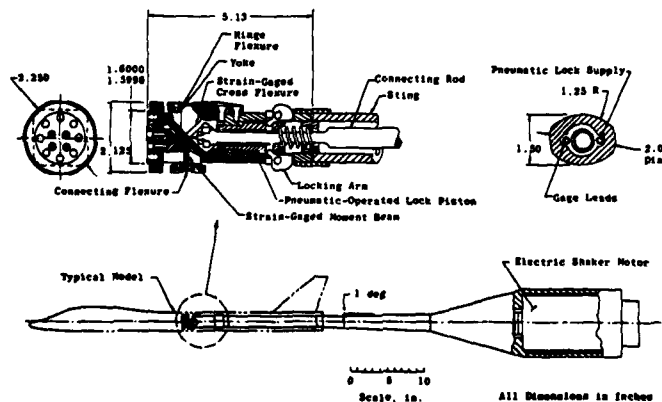


FIG. 7 FORCED-OSCILLATION PITCH OR YAW APPARATUS. AEDC-VKF (Ref. 10).

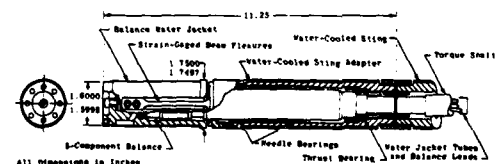


FIG. 8 FORCED OSCILLATION ROLL APPARATUS. AEDC-VKF. (Ref. 11)

with strain gages to provide a voltage proportional to the model pitch displacement, support the model loads and provide a restoring moment which cancels the inertia moment when the system is operating at the natural frequency of the model-flexure system. The motor is controlled by an electronic feedback loop which maintains constant oscillation amplitude of the model and thus provides a means of testing both dynamically stable and dynamically unstable models. The out-of-phase component of the AC voltage output of the moment beams and cross flexures provides a measure of the pitch-damping coefficient, $C_{mq} + C_{m\dot{\alpha}}$. The in-phase component is used in conjunction with an accurate frequency measuring instrument to determine the slope of the pitching-moment curve, $C_{m\dot{\alpha}}$. The apparatus is equipped with a set of interchangeable cross flexures and moment beams, to be selected according to the test requirements. It can be used in several large transonic and supersonic wind tunnels at both VKF and PWT.

A VKF forced-oscillation roll apparatus is shown in Fig. 8 (Ref. 11). It "utilizes a water-jacketed, five-component balance, twin beam flexures, roller bearings to support the loads, and electric printed-circuit drive motors. The motors are directly coupled to the balance and supply up to 120 in.-lb roll moment to oscillate the system at amplitudes up to $\pm 3^\circ$ and at frequencies from 2 to 20 Hz. The twin beam flexures mount from the stationary sting to the oscillating water jacket and provide a restoring moment which cancels the inertia moment when the system is operating at the natural frequency of the model-flexure system. The flexures are instrumented to measure the roll displacement. The entire mechanism is water-cooled to permit testing in the hypersonic tunnels. Maximum acceptable normal load is 1200 lb." The apparatus can be used to obtain dynamic derivatives $C_{lp} + C_{l\dot{\beta}} \sin \alpha$, $C_{np} + C_{n\dot{\beta}} \sin \alpha$ and $C_{yp} + C_{y\dot{\beta}} \sin \alpha$. It can be calibrated by means of a specially developed two-arm magnetic damper with which known rolling moment, yawing moment and sideforce can be applied and compared to the output data obtained using the normal data-acquisition-and-reduction procedure.

5.6 AEDC-PWT

Several forced-oscillation apparatuses are available at PWT for use in their 4-Foot and 16-Foot Transonic Tunnels and 16-Foot Supersonic Tunnel. They are designed for high loads (up to 8000 lb normal force) and are, therefore, hydraulically driven. One such apparatus is shown in Fig. 9 (Ref. 10). It was designed for testing finned bombs and missiles at high angles of attack. A cross-flexure pivot is used and the frequency can be adjusted by interchanging a cantilever spring. The damping torque and the amplitude are the quantities measured. This apparatus is at present limited to a normal force of 600 lb in the 4-Foot Transonic Tunnel but can be scaled up for use in the two 16-Foot Tunnels. A model sting cavity of 3.72 in. in diameter is required for an oscillation amplitude of $\pm 3^\circ$.

Two forced-oscillation apparatuses for use in the PWT 16-Foot Tunnels are being constructed, one for oscillation in roll and the other for oscillation in pitch/yaw. The design normal force is 4000 lb and the minimum model sting cavity is 3.25 in. It is expected that it will be possible to use both apparatuses at angles of attack up to approximately 90° . The roll apparatus will be capable of measuring both rolling and yawing moment derivatives due to rolling. The pitch/yaw apparatus will include a five component balance and will have the capability of also measuring cross and cross-coupling derivatives. Another similar set of two forced-oscillation apparatuses is being developed for a maximum normal force of 1500 lb.

5.7 DFVLR

A crankshaft-driven forced-oscillation apparatus for pitch, yaw, roll or heave is being designed for use in three different wind tunnels at DFVLR. In addition to measurements of damping derivatives, the apparatus will also be capable of obtaining some of the cross and cross-coupling derivatives. The frequency range is 0.2 to 3 Hz. This apparatus and the related test procedures are described in more detail later on in this Symposium (Refs. 12 and 13).

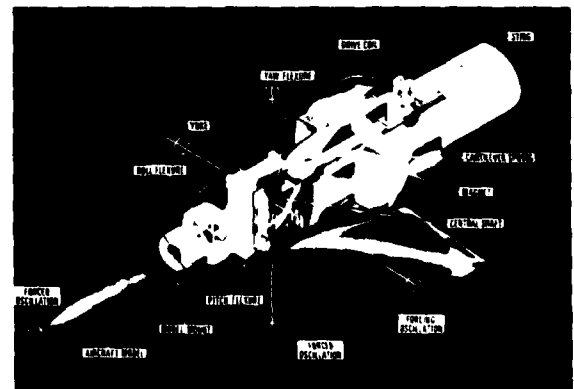
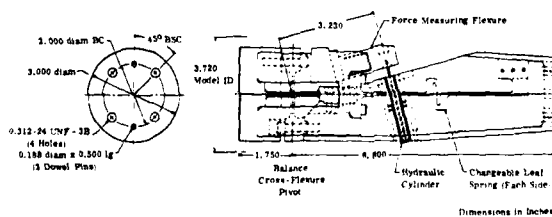


FIG. 9 FORCED OSCILLATION PITCH APPARATUS. FIG.10 FORCED OSCILLATION PITCH/YAW APPARATUS, NAE. CUT-AWAY DRAWING OF THE APPARATUS SET UP FOR PITCHING EXPERIMENTS. (Ref.14)

5.8 NAE

The first forced-oscillation apparatus capable of a direct measurement of the full complement of damping, cross and cross-coupling moment derivatives due to pitching and yawing was constructed at NAE in 1973. Since then some modifications and improvements have been incorporated; a cut-away drawing of the apparatus in its present form is shown in Fig. 10. More recently, a companion apparatus has been constructed for direct measurements of all the moment derivatives due to oscillation in roll. This apparatus is depicted in Fig. 11. Both apparatuses have capabilities of also measuring some dynamic force derivatives. The instrumentation system includes lock-in amplifiers to retain only those portions of the signals from the various bridges that are coherent with the primary oscillation. The data reduction for cross and cross-coupling derivatives is based on a direct conversion of secondary deflection vectors into the causative aerodynamic moment vectors, thereby permitting a *direct* determination of all the derivatives (as distinct from *indirect* methods where the derivatives are obtained by solving the pertinent equations of motion). A unique 3 degree-of-freedom dynamic calibrator (Fig. 12) is available to verify the fundamental aspects of the method, and to confirm the various procedures and programmes used in the day-to-day operation. The two apparatuses, the instrumentation system, the data reduction and the calibrator are all described, together with some pertinent experimental results, at a later point in this Symposium (Refs. 14 and 15). The scaling up of this equipment, to render it compatible with high-load requirements of large high-Reynolds number facilities is presently being envisaged.

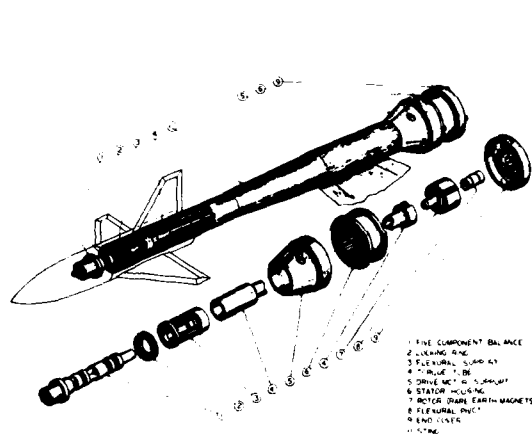


FIG. 11 FORCED OSCILLATION ROLL APPARATUS, NAE.

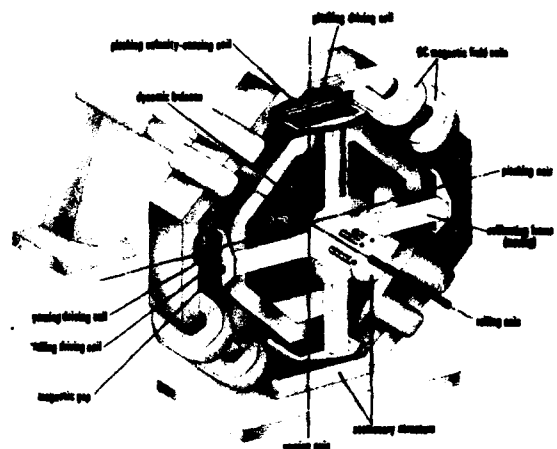


FIG. 12 NAE 3 DEGREE-OF-FREEDOM DYNAMIC CALIBRATOR. (Ref. 15)

6. FORCED-OSCILLATION TECHNIQUES. MEASUREMENT OF MOTION.

Here belong techniques where the model is suspended elastically in such a way that it can oscillate in several degrees of freedom simultaneously, although one degree of freedom is usually predominant. As the excitation frequency varies, this predominant degree of freedom changes to another. The amplitude and phase of the various motions (rather than of the various reactions, as in the preceding section), together with the information about the forcing force (or torque) and frequency, are measured and fed into a system of equations of motion, which is then solved for the unknown stability derivatives. This is then quite different from the methods of the preceding section, where the cross and cross-coupling stability derivatives were obtained directly in each degree of freedom from the measured forced reactions and the known forcing motion.

In the limiting case of a single-degree-of-freedom oscillation, the techniques in this section reduce to the "constant-amplitude torque" subgroup of the preceding section, where the direct derivatives can be obtained from the amplitude and phase of the forced motion (and the information about the forcing torque and frequency in the same degree of freedom) by means of a direct calculation rather than indirectly by solving a system of equations.

6.1 RAE-Bedford

A unique multi-degree-of-freedom forced-oscillation apparatus is in use at RAE (Ref. 16). The following description applies to a three-degree-of-freedom apparatus for tests in yaw, roll and sideslip, but the general principles are the same as those for an older apparatus for pitch and heave tests (Ref. 17). The apparatus "consists of a spring unit to provide flexibilities in yaw and roll, mounted on a sting which necessarily introduces some sideways flexibility, an electromagnetic vibration generator for exciting oscillations, and strain gauges for measuring the model motion. The system has three modes of oscillation; one is nearly a pure roll, but the yawing oscillation has its axis some distance behind the centre of the spring, and the sideslipping mode usually includes a

considerable amount of yawing motion. The test procedure is to oscillate the model at or near the natural frequency of each mode in turn. The derivatives are obtained by solving the equations of motion, using measured values of the amplitudes, frequencies, and excitation forces, together with previously determined values of the model inertias. The required aerodynamic derivatives are then obtained as the differences between wind-off and wind-on values at the same amplitude.

The spring unit consists of a forward cantilever spring, which provides most of the flexibility in yaw and roll, and a rear cantilever spring which adds to the overall sting flexibility in order to reduce the sideslip frequency to bring it nearer the yawing frequency. It also makes the rig less dependent on the characteristics of the support system which are, in practice, apt to cause difficulties.

A feature of the rig is that all the mechanical parts are mounted on a standard sting and form a self-contained unit which can easily be installed in different wind tunnels. (The equipment has been used in the 8 ft x 8 ft supersonic tunnel and the 13 ft x 9 ft low speed tunnel at RAE, Bedford, and in the 9 ft x 8 ft transonic tunnel at ARA.) The spring unit is designed so that realistic values of the frequency parameter are obtained without recourse to specially lightweight model construction.

The drive system is shown diagrammatically in Fig. 13. The electromagnetic vibration generator applies both a longitudinal force and a rolling torque to the offset arm which is rigidly attached to the model. The longitudinal force produces an internal couple between the model and the end of the sting, which is equivalent to a combined external yawing moment and side force. The system thus provides yawing-moment, rolling-moment, and side-force excitation at the same time. To excite each mode of oscillation it is merely necessary to set the oscillator to the appropriate frequency and adjust the current to give the required amplitude. The excitation will also produce a small response in the other modes, but this is allowed for in the analysis which is based on the complete equations of motion of the system."

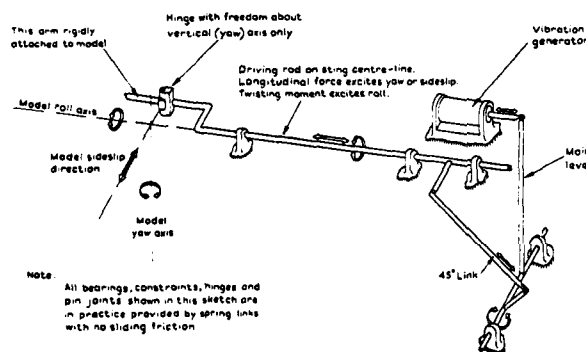


FIG. 13 FORCED-OSCILLATION 3 DOF APPARATUS. RAE-BEDFORD. DRIVE ARRANGEMENT. (Ref. 16)

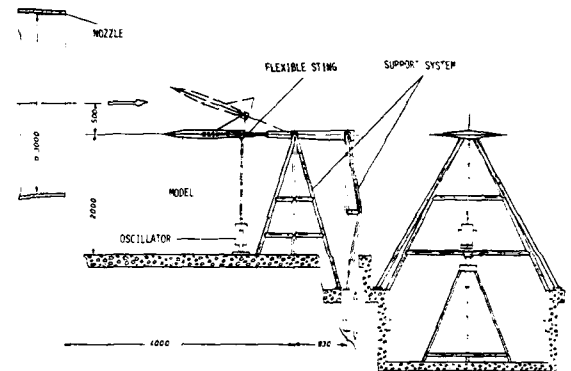


FIG. 14 FORCED-OSCILLATION 3 DOF APPARATUS. DFVLR-AVA. (Ref. 18)

6.2 DFVLR-AVA

Another multi-degree-of-freedom forced oscillation apparatus initially modelled after the aforementioned apparatus at RAE-Bedford, is used in the DFVLR-AVA low-speed, open-test-section, 3 m tunnel in Göttingen. Due to a relatively high level of pressure fluctuations in that tunnel it was necessary to employ a different, more powerful, means of model excitation, as well as to introduce variable artificial damping of the model motion. The experimental arrangement is shown in Fig. 14. The model is mounted on an elastic sting anchored to a rigid support structure but adjustable to vary the mean angle of attack. The front part of the sting consists of two cantilever springs, one after another. An electrodynamic vibrator imparts an excitation of a constant displacement amplitude to a point near the base of the model, resulting in an oscillation in one or more of the following degrees of freedom (attained in the order of increasing excitation frequency):

- rotation about a transversal axis (yawing) (when the two springs deflect in the same direction);
- transversal oscillation (in sideslip) (when the two springs deflect in opposite directions);
- rolling oscillation (when the springs are subjected to torsion).

Similarly, with the model rotated 90° on the sting, oscillation in pitch and in plunging can be obtained. Model motions, the excitation force and the frequency are measured, and the Ritz-Galerkin energy equations of model motion are used for the data reduction. The apparatus and the associated data reduction are described more fully in Refs. 12 and 13.

7. FREE-OSCILLATION TECHNIQUES

The method of free oscillation is probably the oldest and is usually considered to be the simplest of the various oscillatory techniques. Usually no complicated drive or

control system is required and the data reduction is relatively straightforward and lends itself well to automatic processing by computer. On the other hand, the method is usually limited to measurement of direct damping and stiffness derivatives and may not always be suitable for using under conditions of dynamic instability and in the presence of highly non-linear effects or large aerodynamic moments.

Basically, the method involves evaluation of a decaying oscillatory motion performed by an elastically suspended model following some initial disturbance. Elastic pivots (such as crossed flexures) or gas-bearing pivots (which contribute very little damping) are commonly used for mounting the model. The initial disturbance may take the form of (a) mechanical release from a displaced position, (b) application of a mechanical impulse, or (c) excitation at resonance and sudden interruption of the source of excitation. The first two of these methods are relatively simple to arrange but have the disadvantage of requiring large forces to obtain high initial amplitudes when the elastic stiffness of the flexure is large, and may introduce transient oscillatory effects at the beginning of the decaying oscillation. Method (c) overcomes this difficulty but requires more complicated equipment to impart to the model a constant-amplitude oscillation. This is usually done by means of electrical excitation; an alternative method involves use of pulsating air jets impinging on some suitable surface of the model.

It lies in the nature of the free-oscillation method that the results are representative of an amplitude range rather than of a discrete value of amplitude, but with modern instrumentation this amplitude range can be made very small so that the variation of results with amplitude (if any) can be obtained as conveniently as with constant-amplitude forced-oscillation methods.

7.1 NAE

A simple application of the free-oscillation method is shown in Fig. 15 (Ref. 19). The model is sting mounted with the centre of oscillation defined by a flexural pivot and the main restoring moment provided by a cantilever spring. The rather unusual combination of these two features was made possible by the use of a flexible link and two additional flexural pivots for attaching the rear of the cantilever spring to the sting. The deflection and release of the model prior to the start of oscillation is accomplished by a solenoid-actuated spring-loaded tripper that acts on a replaceable metal pad inside the model. The solenoid moves the tripper forward and keeps it inside until the model oscillation reaches its lower bound. At that time the power is turned off to retract the tripper, after which the solenoid can be activated again for the next deflection and release of the model. This cycle of operation can be repeated as many times as is necessary. Model-position information is obtained from strain gauges on the spring and on the sting.

In applications involving very small models in supersonic wind tunnels it may sometimes be very difficult to provide internal space for an excitation device. In such cases it may be possible to employ an external pulsating pneumatic jet, mounted at a certain distance upstream of the model, as shown in Fig. 16 (Ref. 20). The jet is pulsed by means of an exciter valve consisting of a short motor-driven cylindrical plug loosely fitted in a valve body with inlet and outlet ports tangential to the plug. The plug is contoured with circumferential slots to provide an approximately sinusoidal variation in open area through the valve for a constant rotational speed of the plug. The exciter is used to bring the model to the desired oscillation amplitude and is then turned off, and the resulting decaying oscillation is analyzed in the standard fashion, without any disturbing effects on the tunnel flow.

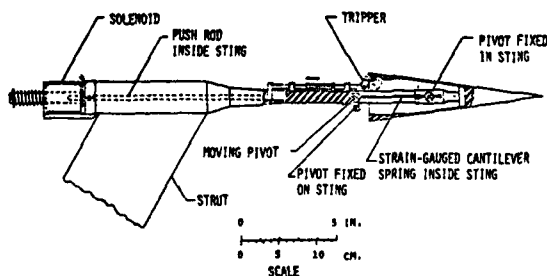


FIG. 15 FREE-OSCILLATION PITCH APPARATUS. NAE. (Ref. 19)

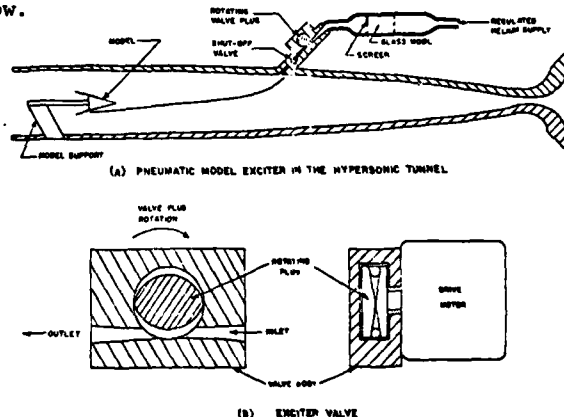


FIG. 16 EXTERNAL EXCITATION BY MEANS OF A PULSATING PNEUMATIC JET. NAE. (Ref. 20)

7.2 AEDC-VKF

An example of the use of a gas-bearing pivot is shown in Fig. 17. Such pivots, of course, have an almost negligible internal damping, which may be important for testing at hypersonic Mach numbers, where the aerodynamic damping to be measured is itself very small. As an example, the relative contribution of the typical mechanical and still-air tare damping to the total damping measured for a blunted cone at various Mach numbers is

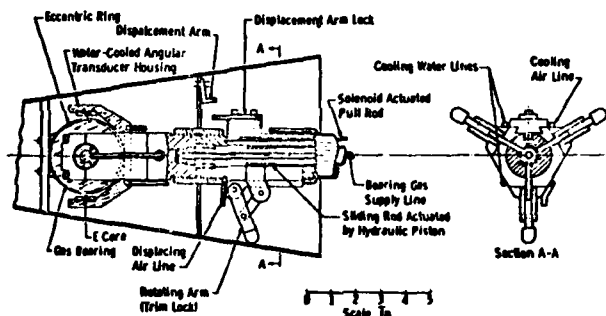


FIG. 17 LARGE AMPLITUDE FREE OSCILLATION PITCH APPARATUS USING GAS-BEARING PIVOT. AEDC-VKF. (Ref. 10)

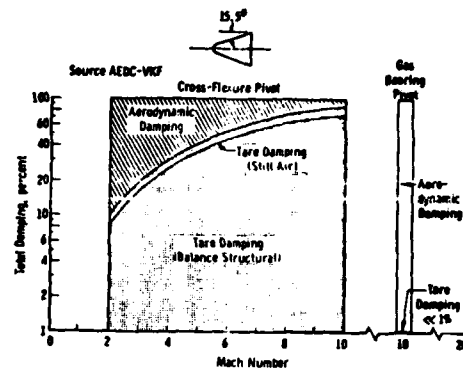


FIG. 18 CONTRIBUTION OF MECHANICAL AND STILL-AIR TARE DAMPING TO TOTAL DAMPING

shown in Fig. 18. It is obvious that as the Mach number increases extreme care must be taken to minimize the tare damping or, alternatively, to measure it with a high degree of accuracy. When using a gas-bearing pivot, such as in the apparatus shown in Fig. 17, there is no mechanical connection between the moving and the stationary parts of the mechanism; the models must therefore be statically and dynamically stable to be tested on such an apparatus. A special variable-reluctance, angular E-core transducer provides a continuous time history of the model displacement. This particular apparatus is designed for large-amplitude ($\pm 15^\circ$) oscillation, thereby making use of yet another advantage of gas-bearing pivots; a large oscillation amplitude would normally not be compatible with a cross-flexure pivot. The apparatus is water cooled to permit operation in hypersonic wind tunnels.

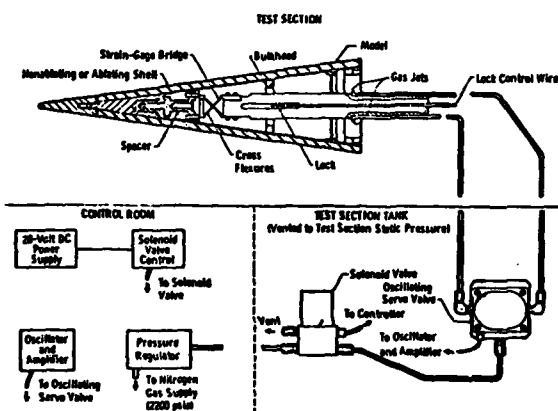


FIG. 19 FREE-OSCILLATION PITCH APPARATUS USING GAS-JET EXCITATION. AEDC-VKF. (Ref. 10)

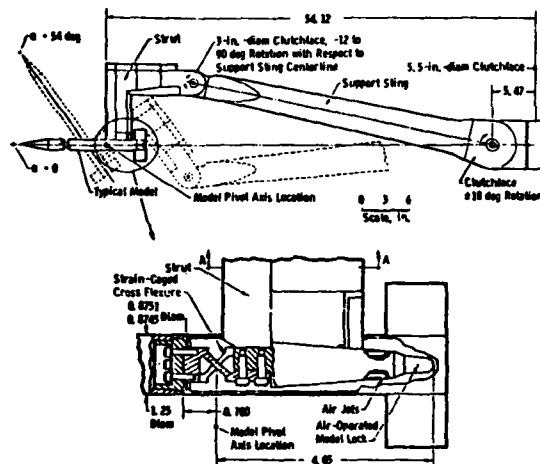


FIG. 20 HIGH ALPHA FREE-OSCILLATION PITCH APPARATUS. AEDC-VKF. (Ref. 21)

Another AEDC-VKF free-oscillation apparatus employs a system of alternative pulsating nitrogen jets (Fig. 19) to excite the model to the desired oscillation amplitude. The frequency of the pulsations can be set by an oscillating servo valve to the natural frequency of the flexure-model system.

Gas-jet excitation is also used in the VKF High-Alpha Pitch Damping Apparatus shown in Fig. 20 (Ref. 21). The apparatus utilizes a small-amplitude single-degree-of-freedom cross-flexure balance which is supported by a strut and sting that can be manually varied to provide angles of attack ranging from -15° to 90° ; at the same time, the position of the strut-sting-model system can be adjusted for minimum aerodynamic interference. A pneumatic and spring-operated locking device holds the model during injection into the tunnel or retraction from it. Several interchangeable balances with different stiffnesses are available.

Free oscillation can also be used for more than one-degree-of-freedom experiments. Such applications, however, have nothing in common with the standard free-oscillation techniques. A three-degree-of-freedom apparatus consisting of a spherical gas bearing, a three-axis variable-reluctance angular transducer, a model-release mechanism and a model-locking system is available at VKF. This apparatus allows the model to freely pitch, yaw or roll on the gas bearing. The test procedure consists of releasing the model at the desired initial conditions and of monitoring its behaviour as function of time. The aerodynamic damping coefficients are obtained by fitting the proposed solution of the 3 equations of motion to the experimental data, as in free-flight data-reduction procedures (but using only the moment equations of motion).

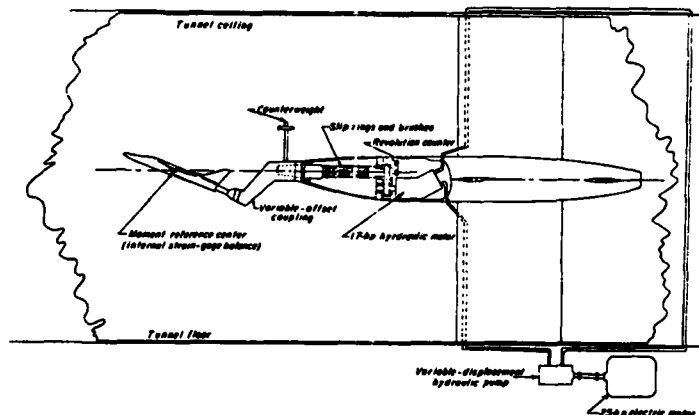
8. ROLLING TECHNIQUES

These techniques are in principle similar to the oscillatory techniques. They can be subdivided into techniques using steady roll (corresponding to forced oscillation) and free decay (corresponding to free oscillation). A few examples will be given below.

8.1 NASA-Langley

The steady-state forced-roll apparatus which can be used in NASA-Langley 7 x 10 Foot High-Speed Wind Tunnel is shown in Fig. 21. The model is mounted on a six-component strain-gauge balance of the type normally used for static tests of sting-supported models. The angle of attack can be varied by means of interchangeable couplings between the balance and the rotating sting support. The model is driven by a constant-displacement, reversible hydraulic motor located inside the main sting body. The speed of rotation is varied by controlling the fluid displacement in a hydraulic pump, which actuates the hydraulic motor. Corrections have to be applied to the data for deflection of the balance and support under load and for the centrifugal forces introduced by these deflections and by any initial displacement of the model CG from the roll axis (Ref. 22).

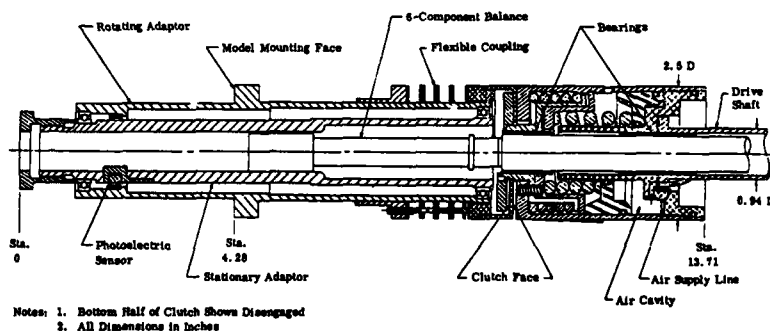
FIG. 21 STEADY-ROLL APPARATUS.
NASA-LANGLEY. (Ref. 22)



8.2 AEDC-PWT

A free-decay roll apparatus designed for experiments on short-finned missile or bomb models in the 4-Foot Transonic Wind Tunnel is shown in Fig. 22. The apparatus features a hydraulic-motor-driven sleeve mounted on ball bearings on a 6-component balance. The model is mounted on a sleeve and can be spun up to desired spin rate at which point a pneumatic-operated clutch is used to disengage the drive motor, permitting the model to rotate freely on the bearings. Spin rate and balance data are recorded during the free-spin cycle. The drive system can deliver 138 lb. in. of torque to the model at roll rates up to 5000 rpm.

FIG. 22 FREE-DECAY ROLL
APPARATUS.
AEDC-PWT. (Ref. 10)



8.3 AEDC-VKF

The free-spin (or a free-decay) roll apparatus at AEDC-VKF (Fig. 23) is intended primarily for tests on missiles at high angles of attack. A six-component balance is supported by a strut that can be manually set in 6-deg. increments to provide various prebend angles. These manual settings along with the tunnel pitch mechanism provide an angle-of-attack range from -5 to 90 deg. The balance supports an adapter with three ball bearings and the model is mounted directly to the bearings. An air-operated brake is located on the front of the adapter and is used to stop model rotation. The brake as well as a mechanical lock can be used to obtain static force coefficients at zero spin rate. Roll-damping data are obtained as the model spins up (for models with canted fins) or as the model spins down after it is spun up by high pressure air jets impinging on the fins.

The rotational speed, roll position, and roll direction are computed from the electrical pulses produced by a ring with alternating reflective and non-reflective surfaces passing three internally mounted infrared-emitting diodes and phototransistors. The mechanism is designed for spin rates up to 12,000 rpm and normal force loads of 300 lb." (Ref. 21).

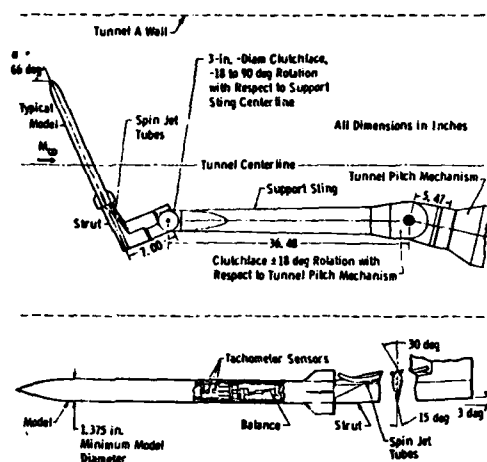


FIG. 23 FREE-SPIN HIGH ALPHA ROLL APPARATUS. AEDC-VKF (Ref. 21)



FIG. 24 ROTARY BALANCE. NASA-LANGLEY. (Ref. 24)

9. ROTARY BALANCES

In recent years there has been an increased emphasis on a better simulation of the aerodynamic phenomena that are associated with the spin motion of aircraft. Also, it was shown in Ref. 23 that to take into account the non-linear coupling effects that exist between pitch, yaw and roll, a generalized formulation of equations of motion was necessary, and that in this new formulation one of the important contributions to the total aerodynamic moment was related to the rotary or coning motion. To simulate such a motion in a wind tunnel the model, at some fixed combination of incidence and sideslip, is attached to a rotary balance, whose axis is parallel with the wind-tunnel centreline. Several such balances are now in existence, for both low-speed and high subsonic wind tunnels, including those at NASA-Langley, NASA-Ames, RAE-Bedford, BAC-Warton, DFVLR-Cologne, Aeronautica Macchi and IMF.

It should be noted that by slightly tilting the axis of a rotary balance it is possible, in principle, to superimpose an oscillatory motion in pitch or yaw on the main rotary motion. However, it is not yet known whether the accuracy involved in such an experiment would be sufficient to permit the determination of the derivatives due to pitching and yawing.

9.1 NASA Langley

The rotary balance at NASA-Langley Full Scale Tunnel (Ref. 24) is shown in Fig. 24. It is capable of providing six-component data over a range of angles of attack of 45° to 90° and in a range of nondimensional spin rate $\Omega b/2V$ of ± 0.3 , at low speeds and at a Reynolds number up to 3.3 million/m. The apparatus is designed for tests employing relatively large-scale models which can also be used for flight tests involving drop model techniques. "Thus the aerodynamic data can be measured with the rotary balance at the same value of Reynolds number as that obtained in flight tests, and the data can then be used, together with conventional static force data, as inputs to theoretical spin prediction programs for correlation with the results of flight tests."

9.2 NASA Ames

The new NASA-Ames rotary balance (Fig. 25) is designed specifically for use in the 12-Foot Pressure Tunnel and the 11-Foot Transonic Tunnel. The apparatus which is described in detail in one of the subsequent papers (Ref. 25), allows a remote change of angles of attack and sideslip, up to a combined value of 30° ; the use of bent

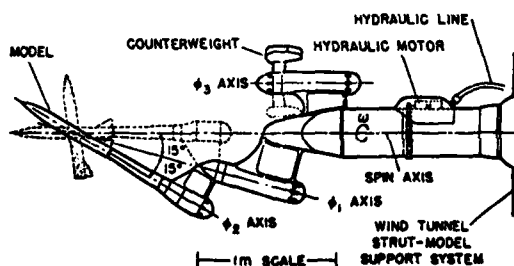


FIG. 25 ROTARY BALANCE. NASA-AMES. (Ref. 25)

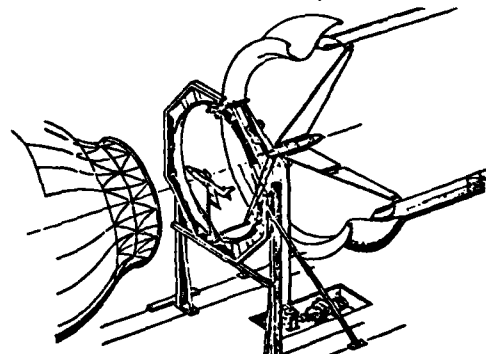


FIG. 26 ROTARY BALANCE. AERONAUTICA MACCHI. (Ref. 26)

stings and top-mounted models permits a further adjustment of the angle of attack to 100° and of the angle of sideslip to 25° . The apparatus has a spin-rate capability of 400 rpm.

9.3 Aeronautica Macchi

A new rotary balance has recently been constructed (Fig. 26) for low-speed experiments at angles of attack up to 90° . All six aerodynamic components can be measured and a finite radius of spin can be simulated. The experimental arrangement includes an unusual circular rail which serves to take up the centrifugal force acting on the model and to eliminate elastic distortion of the support arm (Ref. 26).

10. HALF-MODEL TECHNIQUES

The use of half models for static testing of symmetric configurations at symmetric flow conditions has been a recognized experimental procedure for a long time (see, for example, Ref. 27). This technique eliminates all interference problems usually associated with the presence and with the oscillation of a sting, permits the use of models larger than otherwise possible and allows for a more convenient arrangement of the test equipment (outside of the wind-tunnel wall). On the other hand, the technique has some problems of its own, such as the possible effect of the gap between the model and the tunnel wall and the effect of an interaction between the shock and the wall boundary layer. And, of course, the applications are strictly limited to symmetrical flow conditions.

10.1 NAE

Following its successful application to static experiments, the half-model technique has been used routinely at NAE for oscillatory experiments around zero or nearly-zero mean angles of attack (Ref. 28). In order to utilize it in connection with problems of flight at higher angle of attack, it became important to determine the range of angle of attack for which the condition of flow symmetry was satisfied. This was investigated partly by measuring the static side force on all models at zero yaw, to determine the highest angle of attack at which the flow over an unyawed full model was still symmetrical, and partly by conducting a flow visualization study to find the highest angle of attack at which the surface flow on full and half models still were in reasonably good agreement. On the basis of such investigations carried out on two cones and one ogive-cylinder configuration it was found (Ref. 19) that the highest angle of attack for which the above conditions were satisfied was of the order of 15° to 20° at *subsonic* and *supersonic* speeds. This was subsequently confirmed by a direct comparison of oscillatory results obtained with full and half models (Ref. 19). It is expected that for wing-body configurations where the main aerodynamic contributions come from the wing this limiting angle of attack may be even higher, due to the shielding effect of the body. However, similar comparisons conducted at *transonic* speeds (Ref. 48) have yielded somewhat less satisfactory results.

Of course, in order to obtain satisfactory results with a half-model technique, certain precautions have to be taken to ensure that the possible sources of errors are minimized. Thus the effect of tunnel-wall boundary layer can be reduced significantly by the use of a properly designed reflection plate and by the resulting removal of the half model from the main portion of the boundary layer. The effect of the gap can be minimized by making the gap between the model and reflection plate as small as possible, at the same time ensuring that the gap is still located within the outer region of the tunnel-wall boundary layer. In some cases the use of a small fence at the root of the half model may be desirable. Further details and examples of practical arrangements can be found in Refs. 19 and 29.

If carefully executed, the use of the half-model technique for subsonic and supersonic oscillatory experiments on the longitudinal stability of pointed bodies and pointed wing-body configurations at mean angles of attack up to approximately twice the nose semivertex angle appears very attractive. The technique is particularly recommended for cases where static or dynamic sting interaction may be expected to be significant or where the shape of the model afterbody is incompatible with a sting mounting. Some examples of additional possible applications will be discussed in subsequent paragraphs.

The standard NAE half-model apparatus (Ref. 30) is shown in Fig. 27. A half model (which usually is separated from the tunnel-wall boundary layer by a reflection plate - not shown) is mounted on a strain-gauged cruciform spring for pitch oscillation or a double cantilever spring for vertical-translation oscillation. The drive is provided by an electromagnetic oscillator, as shown. The apparatus can be used either for constant amplitude forced-oscillation tests or for free-oscillation tests.

One interesting application of half-model oscillatory techniques involves the determination of the dynamic interference between two (oscillating) aircraft flying in close proximity. If the entire maneuver occurs in the longitudinal plane of symmetry, with the two aircraft one above the other (as it fortunately happens to be the case in many practical situations), the half-model technique provides a relatively straightforward, practical approach. Fig. 28 shows an example of such an experimental arrangement, as applied for investigating the dynamic interference effect on the damping in pitch of the two component vehicles of the fully reusable, early version of the space

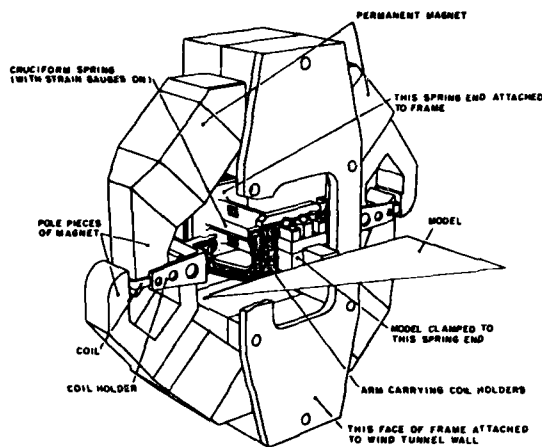


FIG. 27 HALF-MODEL OSCILLATORY APPARATUS SET-UP FOR OSCILLATION IN PITCH. NAE. (Ref. 30)

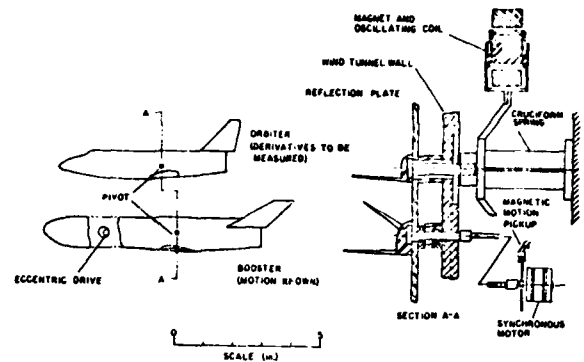


FIG. 28 HALF-MODEL EXPERIMENTAL ARRANGEMENT FOR STUDYING STATIC AND DYNAMIC INTERFERENCE EFFECTS ON THE STATIC AND DYNAMIC PITCHING MOMENT DERIVATIVES OF THE SHUTTLE ORBITER DURING THE INITIAL PHASES OF AN ABORT SEPARATION. NAE. (Ref. 31)

shuttle immediately after a hypothetical abort separation. The two half models were mounted close to a reflection plate and could perform independent oscillatory motions in pitch; the static and dynamic pitching moment derivatives of the orbiter were measured, as functions of the amplitude, frequency and (for synchronous oscillation) the phase angle of the booster (Ref. 31).

Another application of the dynamic half-model technique involves the determination of the exhaust-plume interference on the damping-in-pitch derivative of an aerospace vehicle. The half-model technique is eminently suitable for such an investigation since it eliminates entirely the undesirable reaction that would otherwise occur between an oscillating plume and the stationary sting of a full-model conventional arrangement. Fig. 29 shows a flow-visualization photograph of a half model of the launch configuration of the early fully-reusable shuttle mounted on the same dynamic half-model balance as shown before. A high-pressure nitrogen supply line was incorporated in the balance, and a pressure chamber and an exhaust nozzle was inserted in the body of the booster (Ref. 31). The shape and the size of the plume were simulated by duplicating the nozzle-exit wall angle, the initial plume-boundary angle and the ratio of the initial plume-boundary Mach number to the specific-heat ratio. It should be noted that it is one of the advantages of the half-model technique that a surface oil-flow visualization process can be used not only to show the surface flow on a model but also to give an approximate picture (modified by the wall boundary layer) of the flow around the model - in this case of the exhaust plume.



FIG. 29 HALF MODEL OF THE SHUTTLE LAUNCH CONFIGURATION WITH SIMULATED EXHAUST PLUME, MOUNTED ON THE PITCH-OSCILLATION APPARATUS (no oil was applied to the main part of the reflection plate). NAE. (Ref. 31)

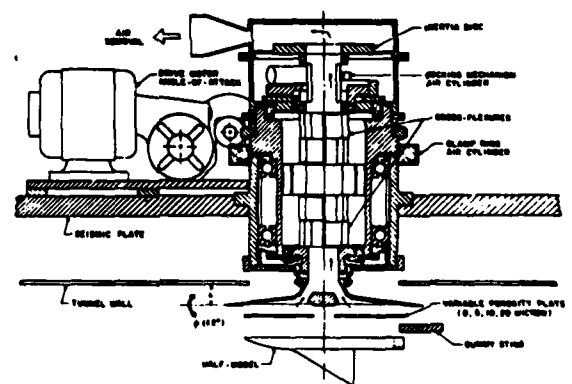


FIG. 30 FREE-OSCILLATION WALL-MOUNTED PITCH APPARATUS. AEDC-PWT. (Ref. 10)

10.2 AEDC-PWT

The PWT wall-mounted free-oscillation apparatus is shown in Fig. 30. The half model (or a full model mounted from its side) is supported by a rigid shaft which in turn is suspended within a cylinder by two sets of flexures permitting the shaft to rotate about its axis. Excitation is accomplished by an air-cylinder mechanical cocking and release mechanism. The mean angle of attack is varied by simply rotating the apparatus in the wind-tunnel wall. The apparatus is used in the PWT 1-Foot Transonic Wind Tunnel (Ref. 10).

11. ACCELERATION DERIVATIVES

At the present time no capabilities exist anywhere for routine measurement of the translational acceleration derivatives, i.e. derivatives due to α and β effects, which were discussed in Section 2. In principle the equipment discussed in Section 6 could be employed for that purpose, but so far, to the best of the present author's knowledge, the efforts to obtain this type of information with the two apparatuses described there have met with only very limited success. Some non-zero values of $C_{m\dot{\alpha}}$ and $C_{Y\dot{\beta}}$ have been obtained at DFVLR and RAE, respectively, but the results displayed a large scatter and therefore cannot be considered really meaningful. However, two apparatuses with which $\dot{\alpha}$ and $\dot{\beta}$ derivatives could be measured did exist in the past and are briefly described here, as is an exploratory apparatus for *half-model* plunging experiments and another one with which both the pitching and the plunging oscillation of *two-dimensional* wings can be studied.

11.1 Calspan

The apparatuses mentioned in Section 6 both use an indirect method of measurement, i.e. solving a system of equations for the unknown derivatives. An apparatus where the acceleration derivatives could be measured directly was developed at Calspan (Cornell) in the early 1960s (Ref. 32), for use in their 8-Foot Transonic Wind Tunnel. The system had the ability to force the model inexorably in any desired planar sinusoidal motion. For instance, for study of longitudinal dynamics, the following basic motions could be achieved:

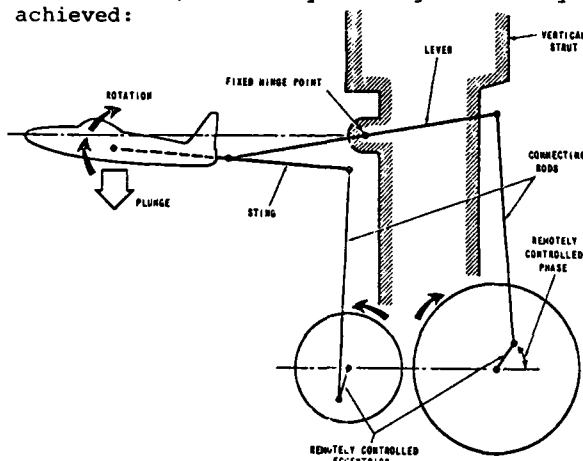


FIG. 31 FORCED-OSCILLATION 2 DOF PITCH OR YAW APPARATUS. CALSPAN. (Ref. 32)

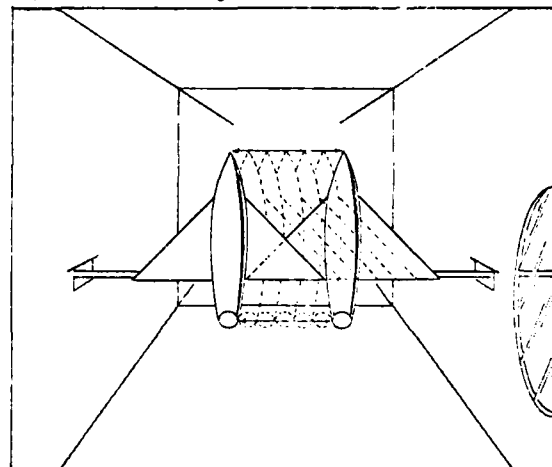


FIG. 32 LATERAL-OSCILLATION APPARATUS. NASA-LANGLEY. (VPI). (Ref. 33)

- rotary oscillation around a fixed axis (sum of q and $\dot{\alpha}$ effects),
- plunging oscillation ($\dot{\alpha}$ effects only),
- pure pitching motion (q effects only).

The pure pitching motion will be discussed in more detail in Section 12. By rotating the model 90° around the sting, the derivatives due to r , β , and the sum of these two effects could similarly be investigated. In all cases the desired motion was imparted to the model by a mechanical drive system, consisting of linkages and connecting rods, eccentrically mounted on two high-inertia flywheels (Fig. 31). The available frequency range was from 3 to 12 Hz and amplitudes up to $\pm 5^\circ$ or ± 0.5 ft and accelerations of up to 200 rad/sec^2 or 20 g's could be achieved in the rotational and translational case, respectively. The normal force capability, at the model center of gravity, was 1200 lb. Models could be installed at non-zero angles of attack, using bent stings, subject to load limitations. This apparatus has not been used for some time now and it is not known whether it can still be considered operational. It seems certain that at least the electronics part of it, including the instrumentation used for data analysis, may need updating.

11.2 NASA Langley

Lateral-acceleration (or acceleration-in-sideslip) derivatives were measured at Langley in the 1950s, using a model mounted on a transversal strut which performed an

oscillatory motion as indicated in Fig. 32. The motion was imparted to the strut by a system of pushrods eccentrically attached to a flywheel. The apparatus was used both in the free-oscillation (Ref. 33) and forced-oscillation (Ref. 34) modes of operation, in the 6 ft. x 6 ft. test section of the old NASA-Langley low-speed stability tunnel. The apparatus was employed for systematic investigations of the dynamic characteristics of wings and wing-body configurations, and good-quality, highly-consistent values of derivatives $C_{l\beta}$ and $C_{n\beta}$ were obtained. This apparatus has now been moved to the Virginia Polytechnic Institute, but it does not appear to have been used in recent years.

11.3 NAE

A recent NAE vertical-oscillation half-model apparatus is shown in Fig. 33. The apparatus constitutes a modification of the half-model pitch apparatus shown in Fig. 27, with a double-cantilever spring replacing the original cruciform spring and with a cruciform sensor added for measuring derivative $C_{m\alpha}$ in the forced-oscillation mode. The apparatus is also capable of measuring the force derivative $C_{Z\alpha}$.

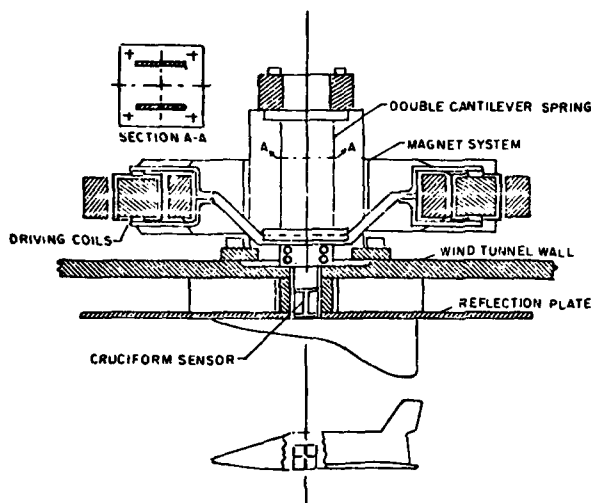


FIG. 33 VERTICAL-OSCILLATION HALF-MODEL APPARATUS. NAE.

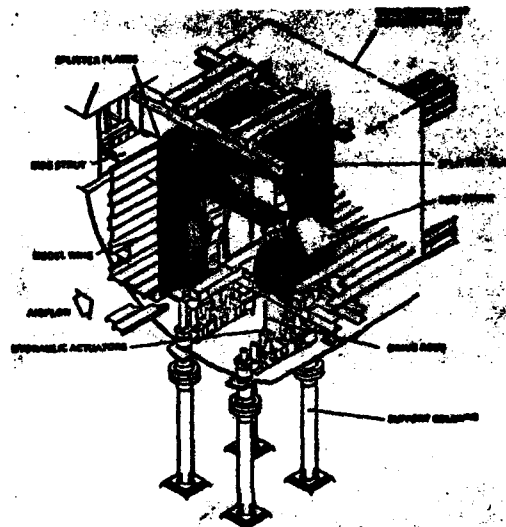


FIG. 34 TWO-DIMENSIONAL OSCILLATORY APPARATUS. NASA-AMES (Ref. 25)

11.4 NASA Ames

A large forced-oscillation apparatus (Fig. 34) for experiments on two-dimensional wings performing pitching or plunging oscillations or any combination of the two motions has been developed recently for use in the Ames 11 Foot Transonic Wind Tunnel. Although the main purpose of the apparatus is to study the unsteady pressures that result from the above motions, the integration of these pressures may be used to yield the pertinent two-dimensional stability derivatives. The apparatus is described in some detail in a later paper in this Symposium (Ref. 25).

12. PURELY-ROTARY DERIVATIVES

There are, of course, two ways of splitting the composite fixed-axis oscillatory derivatives (such as $C_{mq} + C_{m\alpha}$) into their component translational-acceleration (such as $C_{m\alpha}$) and purely-rotary (such as C_{mq}) parts. One is to measure the vertical-acceleration or lateral-acceleration derivatives (as discussed in Section 11 above) and the other to measure the pertinent purely-rotary derivatives. The latter can be determined, in principle, by any of the following techniques:

- whirling arm (no longer in use),
- curved flow,
- forced snaking motion.

12.1 VPI (Curved Flow)

A curved-flow 6 ft x 6 ft test section, originally developed at NASA Langley (Ref. 35) is now in use at the Virginia Polytechnic Institute, which in 1958 acquired the Langley stability tunnel. The curved-flow technique is based on the concept of simulating a steady curved-flight condition by using a fixed model and arranging wind-tunnel flow in such a way that it is curved in a circular path in the vicinity of the model and that it has a velocity variation normal to the streamlines in direct proportion to the local radius of curvature. This is achieved by using flexible side walls for curving the flow and by employing specially constructed vertical-wire drag screens upstream of the test section for producing the desired velocity gradient across the tunnel flow. These screens vary in mesh size across the wind tunnel, with the most dense

portion of the screens located at the inner radius of the curved test section (Fig. 35). The technique allows measuring pure-yawing (due to r only) or pure-pitching (due to q only) derivatives with a fixed model mounted on a static balance. The simulation of the steady curved flight is not exact, however, and corrections have usually to be made for the buoyancy effect caused by the static-pressure gradient normal to the streamlines (which does not exist in curved flight). In addition, there are dissimilarities in the behaviour of the model boundary layer (which on the model in a curved flow tends to move toward the center of curvature, contrary to its normal tendency in curved flight), and possible problems due to a rather high degree of turbulence behind the wire screen. Hopefully, however, in many cases these phenomena may be considered to have only a minor effect on the measurement of purely-rotary derivatives. No other technique is at present available - and operational - for that purpose.

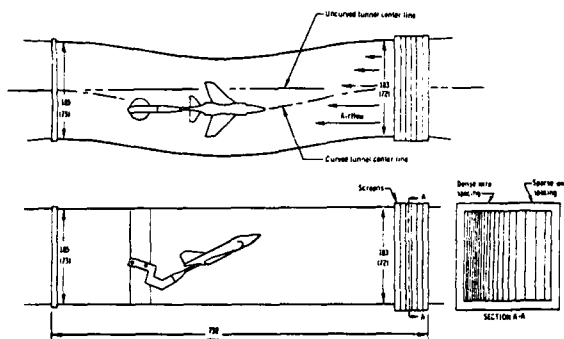


FIG. 35 CURVED-FLOW TECHNIQUE. VPI. FORMERLY AT NASA LANGLEY. (Ref. 35)

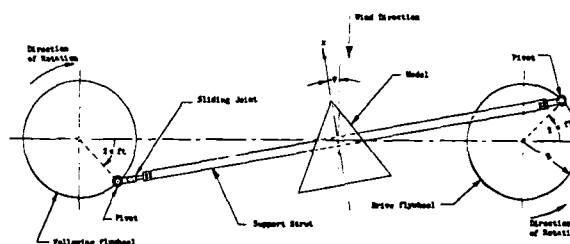


FIG. 36 SNAKING MOTION APPARATUS FOR SIMULATION OF PURE YAWING. NASA LANGLEY. (VPI). (Ref. 36)

12.2 Calspan (Snaking Motion)

As mentioned before, the Calspan apparatus described in Section 11.1 was also capable of simulating purely-rotary motion, such as pure pitching. This was achieved by generating a so-called "snaking motion" which was a particular planar combination of rotational and translational motions (in the pitch plane) such that the instantaneous angle of attack - which includes vector components generated by these two motions - remained at all times constant. If we write the instantaneous angle of attack as

$$\alpha = \alpha_0 + \theta_0 e^{i\omega t} + (\dot{z}/V_0) e^{i\omega t}$$

the above condition is satisfied if $\theta_0 = -(\dot{z}/V_0)$, i.e., if the contributions of the rotary oscillation and of the plunging oscillation are equal in amplitude but opposite in phase. This could be achieved by the mechanical arrangement shown in Fig. 31 and described in Section 11.1, from which also the remaining comments apply.

12.3 NASA Langley (Snaking Motion)

Long before the Calspan apparatus was constructed, a concept of a similar snaking motion, but generated by different mechanical means, was used at NASA Langley to simulate pure yawing motion (Ref. 36). The proper combination of the fixed-axis oscillation and the lateral oscillation was achieved by attaching the model (via a strain-gauge balance) to a transversal strut supported at the ends by counter-rotating flywheels, as shown in Fig. 36. As was the case with the equipment described in Section 11.2, this apparatus was used in the Langley stability tunnel for systematic investigations, yielding good-quality results on derivatives C_{nr} , C_{lr} and C_{Yr} . It has now been moved to the Virginia Polytechnic Institute, but to the best of the present author's knowledge has not yet been used in its new location.

A good summary of the experience obtained by NACA and NASA concerning the low-speed lateral-directional dynamic derivatives due to lateral acceleration, pure yawing and the sum of these two effects is given in Ref. 37, which also includes an extensive bibliography.

13 MODEL FREE

Two of the major problems encountered in performing captive-model dynamic-stability experiments in wind tunnels is (a) the inevitable interference associated with a mechanical model support and its vibration, and (b) the inherent inability of any mechanical support to provide simulation of the unrestrained model motion. Thus it has been recognized that a definite need exists for a wind-tunnel technique with which experiments could be performed without having to employ a mechanical model support. Four such techniques will be considered in the present section, namely, (a) techniques employing models launched into the wind-tunnel flow and performing free flight in the test section, (b) techniques employing remotely-controlled models flying in the test

section with only a flexible control-and-safety cable attached to the model, (c) techniques employing cable-suspended models, which can perform motion in five degrees of freedom (all except longitudinal translation), and (d) techniques employing magnetically suspended and magnetically actuated models. At the present time techniques (a) and (d) have only been used with relatively small models and must therefore be considered as mostly useful for exploratory experiments rather than systematic or routine dynamic-stability testing.

13.1 NAE (Free Flight)

The free-flight technique has two main variants, depending on whether the model is initially suspended mechanically (e.g. by means of a wire that is then burnt off or cut off at the beginning of experiment) in the upstream part of the test section, or whether it is launched into the test section from an initial position downstream of it (as shown diagrammatically in Fig. 37). The first variant gives a better control of the initial model attitude, whereas the second gives a longer duration of experiment, since both the upstream and the downstream travel of the model can then be utilized. In each variant of the technique two methods of data acquisition can be applied; one in which the time history of the model flight in one or two planes of motion is obtained from film taken with a high-speed movie camera; and another where this information is deduced from accelerometer data transmitted by FM telemetry. Since other data such as pressure or temperature can also be transmitted by telemetry, a combination of these two methods of data acquisition is also possible. Once the motion of the model is known, the required aerodynamic coefficients and stability derivatives can be obtained by fitting, on a computer, the recorded flight history with the solution of pertinent equations of motion, and determining the coefficients and derivatives for the best fit.

The adaptation of the free-flight technique to the NAE helium hypersonic wind tunnel is described in Ref. 38. The system uses a pneumatic launcher and polystyrene injection-molded models. The data are obtained from a high-speed movie film at a typical speed of 3000-4000 frames per second. The optical system, permitting viewing the model in two orthogonal planes on the same frame, is shown in Fig. 38.

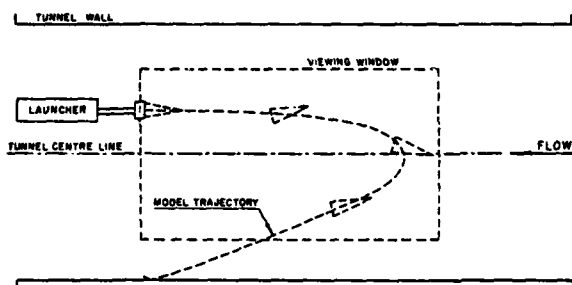


FIG. 37 FREE-FLIGHT TECHNIQUE USING LAUNCHED MODELS. NAE. (Ref. 38)

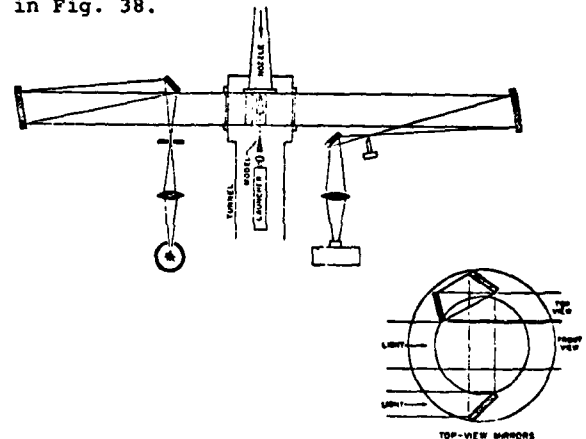


FIG. 38 FREE-FLIGHT TECHNIQUE. OPTICAL SYSTEM. NAE. (Ref. 38)

13.2 CSIR-ARU (Free Flight)

Recent developments in the launching procedures used with the free-flight technique are described in Ref. 39. The pitch-jet launch system shown in Fig. 39 permits the model to be launched at a relatively small angle relative to the launch-gun axis and then to impart to it an angular velocity immediately after release; the maximum (large) angle of attack will then be attained only when the model reaches the observation area, without affecting the trajectory too much. The model can be spun-up on a spindle before the release and the angular velocity after launch is imparted by one or two air jets mounted on the launch head. An alternative shot-put launch is also shown in Fig. 39; it provides a rail-type support instead of the spindle, with one fin (of a missile) guided in a slot along the rail, which can be set at angles from 0 to 90°.

A comprehensive summary of procedural details concerning techniques which employ free flight in wind tunnels can be found in Refs. 39 and 40.

13.3 NASA Langley (Remotely-Controlled Free Flight)

A unique free-flight testing capability exists in the NASA-Langley Full Scale Wind Tunnel. A relatively large (typically around 4 ft span) powered model can be flown without restraint in the 30 ft x 60 ft open test section of that tunnel (Ref. 41). The model is controlled by three operators who can transmit pneumatic and electric power and control signals to the model via a flexible trailing cable (Fig. 40). This flexible cable also incorporates a thin steel safety cable which is passed through a pulley above the test section and which can be used to catch the model if an uncontrollable motion or mechanical failure occurs. The entire flight cable is kept slack during the flight and is controlled by a separate safety-cable operator. Typical results may include steady

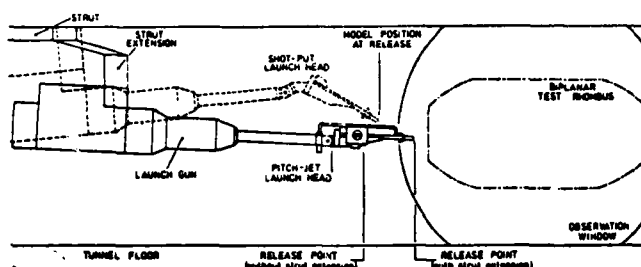


FIG. 39 FREE-FLIGHT TECHNIQUE. LAUNCHER.
CSIR-ARU. (Ref. 39)

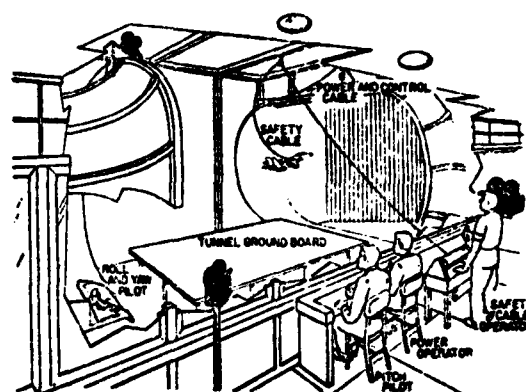


FIG. 40 REMOTELY-CONTROLLED FREE FLIGHT.
NASA LANGLEY. (Ref. 41)

flights at high angles of attack, studies of pilot control techniques at high angles of attack and evaluation of artificial rate damping. The results are mainly qualitative and consist of pilot opinion of the behaviour of the model and of cinematographic records.

13.4 NASA Langley (Cable-Mounted Semi-Free Models)

Another "free-flight" technique has been developed for the NASA Langley Transonic Dynamics Tunnel. The model is suspended in the wind tunnel by a two-cable mount system, which allows lateral and vertical translation of the model as well as angular rotations about all three axes (Ref. 42). The procedure involves measuring the response of the model to known input disturbances such as control-surface deflections or external forces applied through the suspension cables. The stability derivatives are then extracted from equations of motion for the model suspension system using procedures developed initially for flight-test measurements.

13.5 University of Virginia (Magnetic Suspension)

Dynamic testing with magnetically suspended models has now been pursued for a number of years, mainly at MIT, at the University of Southampton and the University of Virginia. Dynamic derivatives such as C_{lp} and $C_{mq} + C_{m\dot{q}}$ have been successfully measured and some work has also been performed on studies of spinning and coning bodies. An experimental arrangement used at University of Virginia in a 11 cm x 11 cm vertical subsonic wind tunnel is described in Ref. 43. A large pair of Helmholtz coils produces a uniform field to magnetize the model and a second pair of opposed coils creates a vertical gradient which opposes the weight and drag of the model. The remaining coils create horizontal gradients, which introduce side forces on the model. The test section of the wind tunnel is located inside the coils. Model position is sensed optically and a feedback control system, which drives power amplifiers supplying current to the coils, is used to keep the model centered. For the dynamic stability experiments, the model is forced periodically in a combined pitching and heaving motion. A theoretically predicted flight history is then fitted to the measured behaviour of the model by varying the stability derivatives in the analytical expressions for the best fit.

A useful review of the techniques and procedures related to the use of magnetically suspended models can be found in Ref. 44.

14. CONTROL-SURFACE OSCILLATION TECHNIQUES

So far we have dealt with dynamic-stability testing of full or half models of complete configurations. Sometimes, however, the dynamics of a component of an aircraft is also of interest. Most often this applies to a control surface such as an aileron. In principle, knowledge of two different effects may be required: (a) the hinge-moment derivatives of an oscillating surface, and (b) the derivatives of aerodynamic reactions acting on the model due to the oscillation of a control surface. The necessary tests are most conveniently performed using a half model of the aircraft configuration; the hinge moment measurements can be performed with any of the free or forced-oscillation methods mentioned before, whereas the reactions of the model itself can be measured using methods similar to those employed for cross and cross-derivative measurement.

14.1 NAE

An experimental arrangement for measuring the static and dynamic hinge-moment derivatives of a control surface on a half model of a delta-wing aircraft is shown in Fig. 41. Two small circular coils operating in ring-shaped gaps in two permanent-magnet units (mounted on the outside of the wind-tunnel wall) impart an oscillatory motion to the shaft of the control surface (Ref. 45). The method of free-oscillation with feedback excitation is used.

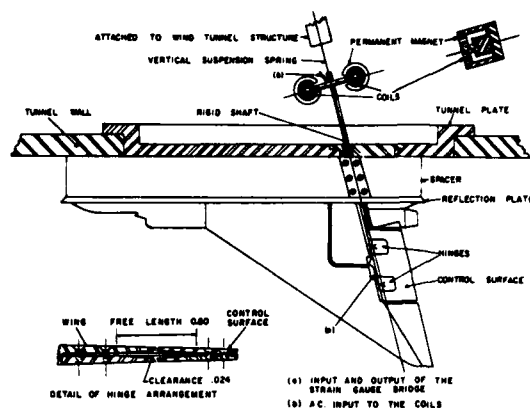


FIG. 41 CONTROL-SURFACE OSCILLATION.
NAE. (Ref. 45)

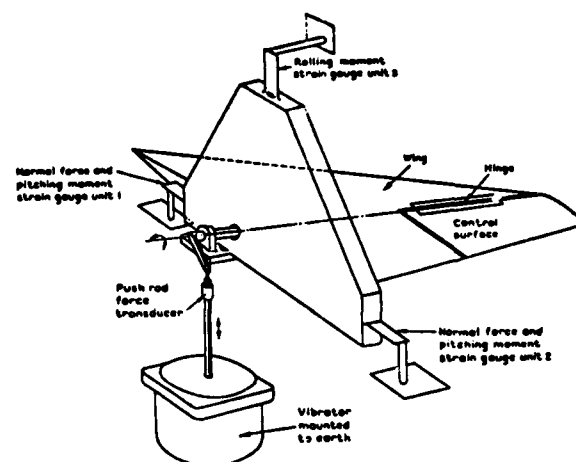


FIG. 42 CONTROL-SURFACE OSCILLATION.
RAE-BEDFORD. (Ref. 46)

14.2 RAE-Bedford

An example of an apparatus which permits simultaneous measurement of hinge-moment derivatives and wing derivatives due to control oscillation is shown in Fig. 42. The model is supported on a strain-gauge balance that measures the normal force, pitching moment and rolling moment due to control oscillation, while another strain-gauge unit measures the oscillatory hinge moment. The incidence, mean control angle, amplitude and frequency can be varied (Ref. 46). The rig is used in RAE-Bedford 3 ft x 3 ft high-speed wind tunnel.

15. CONCLUDING REMARKS

In this review the emphasis was placed on the basic principles of various methods and on the practical aspects of various techniques, as illustrated by numerous examples, descriptions and sketches of actual existing apparatuses. These examples, collectively, are not necessarily intended to constitute a complete catalogue of all the existing equipment of this type; in fact, the author is certain that there are several apparatuses in various laboratories around the world, that have not been included. The author hopes, however, that all the important *methods and techniques* that are in use today have been covered. Techniques that are not applicable to *aircraft* testing (such as Magnus balances) have been omitted.

Topics such as detail design considerations, instrumentation, data acquisition and reduction, calibration methods, static and dynamic sting interference, wind-tunnel interference, small amplitude versus large amplitude testing, frequency effects, effects of wind-tunnel flow unsteadiness, model construction, sensitivity studies, typical results - are all highly pertinent to the subject matter of this review, but could not possibly be included due to unavoidable limitations which had to be imposed on this presentation. Some of these topics are discussed in the material listed in the references, and in particular in papers of a slightly more general or summary nature, such as Refs. 1-5, 10, 24, 40 and 47. It is hoped that the present review may fulfil a useful role by serving as a guide to the astonishing variety of methods and techniques which are available for wind-tunnel investigations of the dynamic stability of aircraft.

16. REFERENCES

1. Orlik-Rückemann, K.J. Methods of Measurement of Aircraft Dynamic Stability Derivatives. NRC, Canada, LR-254, 1959.
2. Orlik-Rückemann, K.J. Survey of Needs and Capabilities for Wind Tunnel Testing of Dynamic Stability of Aircraft at High Angles of Attack. NASA CR 114583, 1973.
3. Orlik-Rückemann, K.J. Dynamic Stability Testing of Aircraft - Needs Versus Capabilities. Prog. Aerospace Sci., Vol. 16, No. 4, pp 431-447, Pergamon Press. 1975.
4. Orlik-Rückemann, K.J. Wind Tunnel Measurements of Dynamic Derivatives. Lecture Notes, University of California, Los Angeles. Second Edition, August 1963.
5. Orlik-Rückemann, K.J. Dynamic Stability Testing in Wind Tunnels. Von Kármán Institute for Fluid Dynamics. Lecture Series 99. "Aerodynamic Inputs for Problems in Aircraft Dynamics" April 1977.

6. Grafton, S.B.
Libbey, C.E. Dynamic Stability Derivatives of a Twin-Jet Fighter Model for Angles of Attack from -10° to 110° . NASA TN D-6091, January 1971.
7. Scherer, M.
Lopez, J. Progrès Réalisés dans les Techniques de Mesure des Dérivées Aérodynamiques en Soufflerie Méthode d'Oscillations Forcées. AGARD CP-17, pp 411-436, 1966.
8. Boyden, R.P. Effects of Leading-edge Vortex Flow on the Roll Damping of Slender Wings. Journal of Aircraft, Vol. 8, No. 7, 1971.
9. Braslow, A.L.
Wiley, H.G.
Lee, C.Q. A Rigidly Forced Oscillation System for Measuring Dynamic-Stability Parameters in Transonic and Supersonic Wind Tunnels. NASA TN D-1231, 1962.
10. - Dynamic-Stability Measurement Capabilities in the AEDC Wind Tunnels. AEDC/B-2, 1976.
11. Burt, G.E. Forced-Oscillation Test Mechanism for Measuring Dynamic-Stability Derivatives in Roll. J. of Aircraft, Vol. 12, No. 1, 1975.
12. Hafer, X. Wind Tunnel Testing of Dynamic Derivatives in W. Germany. AGARD FDP Symposium on Dynamic Stability Parameters, Paper 5, 1978.
13. v. d. Decken, J.
Schmidt, E.
Schulze, B. On the Test Procedures of the Derivative Balances Used in W. Germany. AGARD FDP Symposium on Dynamic Stability Parameters, Paper 6, 1978.
14. Orlik-Rückemann, K.J. Experiments on Cross-Coupling and Translational Acceleration Derivatives. AGARD FDP Symposium on Dynamic Stability Parameters, Paper 8, 1978.
15. Hanff, E.S. A Generalized Technique for Measuring Cross-Coupling Derivatives in Wind Tunnels, AGARD FDP Symposium on Dynamic Stability Parameters, Paper 9, 1978.
16. Thompson, J.S.
Fail, R.A. Oscillatory Derivative Measurements on Sting-Mounted Wind Tunnel Models at RAE, Bedford. RAE TR66197, 1966 (also AGARD CP 17).
17. Thompson, J.S.
Fail, R.A. Oscillatory-Derivative Measurements on Sting-Mounted Wind-Tunnel Models; Method of Test and Results for Pitch and Yaw on a Cambered Ogee Wing at Mach Numbers up to 2.6. ARC R & M 3355, July 1962.
18. Schmidt, E. Die AVA-Derivativwaage. DLR-Mitt, 74-32, 1974.
19. Orlik-Rückemann, K.J. Half- and Full-Model Experiments on Slender Cones at Angles of Attack. Journal of Spacecraft and Rockets, 11, No. 9, 575-580, September 1973.
20. Orlik-Rückemann, K.J.
Tanne, J.W. Use of Pneumatic Model Exciter in a Hypersonic Wind Tunnel. DME/NAE Quart. Bulletin. 1962(3)
21. Usselton, B.L.
Jenke, L.M. Test Mechanisms for Obtaining Dynamic Stability Characteristics of High Fineness Ratio Bodies at Angles of Attack up to 90 Deg. AIAA 9th Aerodynamic Testing Conference Proceedings, pp 76-90, June 1976.
22. Henderson, W.P.
Phillips, W.P.
Gainer, T.G. Rolling Stability Derivatives of a Variable-Sweep Tactical Fighter Model at Subsonic and Transonic Speeds. NASA TND-3845, 1967.
23. Tobak, M.
Schiff, L.B. Generalized Formulation of Nonlinear Pitch-Yaw-Roll Coupling. AIAA Journal, vol. 13, No. 3, pp 323-332, 1975.
24. Chambers, J.R.
Bowman, J.S. Jr. Stall/Spin Test Techniques Used by NASA. AGARD CP-199, Paper 13, 1975.
25. Malcolm, G.N.
Davis, S.S. New NASA-Ames Wind Tunnel Techniques for Studying Airplane Spin and Two-Dimensional Unsteady Aerodynamics. AGARD FDP Symposium on Dynamic Stability Parameters, Paper 3, 1978.
26. Bazzocchi, E. Stall Behaviour and Spin Estimation Method by Use of Rotating Balance Measurements. AGARD CP-199, Paper 8, 1975.
27. Van der Blik, J.A. Notes on Half Model Testing in Wind Tunnels. NRC, Aeronautical Report LR-235, 1959.
28. Orlik-Rückemann, K.J. Possible Use of Half-Model Oscillatory Techniques for the Study of Shuttle Abort Separation Dynamics. Proceedings of Space Transportation Systems Technology Symposium, Cleveland 1970, NASA TM X-52876, Vol. 1, 99-118, July 1970.
29. Orlik-Rückemann, K.J.
LaBerge, J.G. Static and Dynamic Longitudinal Stability Characteristics of a Series of Delta and Sweptback Wings at Supersonic Speeds. NRC, Aeronautical Report LR-396, January 1966.

30. Orlik-Rückemann, K.J. Measurement of Aerodynamic Damping and Stiffness Derivatives in Free Oscillation with Automatically Recycled Feedback Excitation. NRC NAE Aero Report LR-246, 1959.
31. Orlik-Rückemann, K.J.
LaBerge, J.G.
Hanff, E.S. Supersonic Dynamic Stability Experiments on the Space Shuttle. Journal of Spacecraft and Rockets, 9, No. 9, 655-660, September 1972.
32. Statler, I.C.
Tufts, O.B.
Hirtreiter, W.J. The Development and Evaluation of the CAL/AF Dynamic Wind-Tunnel Testing System. AFFDL-TR-66-153, 1967.
33. Riley, D.R.
Bird, J.D.
Fisher, L.R. Experimental Determination of the Aerodynamic Derivatives Arising from Acceleration in Sideslip for a Triangular, a Swept and an Unswept Wing. NACA RM L55A07, 1955.
34. Lichtenstein, J.H.
Williams, J.L. Effect of Frequency of Sideslipping Motion on the Lateral Stability Derivatives of a Typical Delta-Wing Airplane. NACA RM L57F07, 1957.
35. Bird, J.D.
Jaquet, B.M.
Cowan, J.W. Effect of Fuselage and Tail Surfaces on Low-Speed Yawing Characteristics of a Swept-Wing Model as Determined in Curved-Flow Test Section of Langley Stability Tunnel. NACA TN 2483, 1951 (Supersedes NACA RM L8G13, 1948).
36. Queijo, M.J.
Fletcher, H.S.
Marple, C.G.
Hughes, F.M. Preliminary Measurements of the Aerodynamic Yawing Derivatives of a Triangular, a Swept, and an Unswept Wing Performing Pure Yawing Oscillations, with a Description of the Instrumentation Employed. NACA RM L55L14, 1956.
37. Coe, P.L., Jr.
Graham, A.B.
Chambers, J.R. Summary of Information on Low-Speed Lateral-Directional Derivatives due to Rate of Change of Sideslip, β . NASA TN D-7972, 1975.
38. Lucjanek, W.W.
Adams, P.A. Development of Free-Flight Technique for NAE Helium Hypersonic Wind Tunnel. DME/NAE Quart. Bull. 1966(3).
39. Beyers, M.E. Analysis of High-Manoeuvrability Vehicles in Free Flight. Ph.D. Thesis, U. of the Witwatersrand, Johannesburg, December 1977.
40. Dayman, B., Jr. Free-Flight Testing in High-Speed Wind Tunnels. AGARDograph 113, 1966.
41. Grafton, S.B.
Chambers, J.R.
Coe, P.L., Jr. Wind-Tunnel Free-Flight Investigation of a Model of a Spin-Resistant Fighter Configuration. NASA TN D-7716, 1974.
42. Bennett, R.M.
Farmer, M.G.
Mohr, R.L.
Hall, W.E., Jr. A Wind Tunnel Technique for Determining Stability Derivatives from Cable-Mounted Aeroelastic Models. AIAA 1977 Atmospheric Flight Mechanics Conference, Paper 77-1128, 1977.
43. Bharathan, D.
Fisher, S.S. Stability Derivative Measurements with Magnetically Suspended Cone-Cylinder Models. J. of Spacecraft and Rockets, vol. 14, no. 12, pp. 719-723, December 1977.
44. Covert, E.E.
Finston, M.
Vlajinac, M.
Stephens, T. Magnetic Balance and Suspension System for Use with Wind Tunnels. Progress in Aerospace Sciences, vol. 14, pp. 27-107, Pergamon Press, 1974.
45. Orlik-Rückemann, K.J. Some Data on Elevator-Damping and Stiffness Derivatives on a Delta Wing Aircraft Model at Supersonic Speeds. NRC NAE Aero Report LR-250, 1959.
46. Wight, K.C.
Lambourne, N.C. A Control-Surface Oscillatory Derivative Rig for Use with Half-Models in High-Speed Wind Tunnels. RAE TR 75026, 1975.
47. Schueler, C.J.
Ward, L.K.
Hodapp, A.E., Jr. Techniques for Measurement of Dynamic Stability Derivatives in Ground Test Facilities. AGARDograph 121, 1967.
48. Shadow, T.O. An Investigation of the Half-Model Reflection-Plane Technique for Dynamic Stability Testing at Transonic Mach Numbers. AEDC-TR-76-165, 1976.

NOUVELLE TECHNIQUE D'ESSAIS SUR MAQUETTES LIBRES EN LABORATOIRE
POUR LA DETERMINATION DE CARACTERISTIQUES AERODYNAMIQUES

W. Charon et R. Verbrugge
Institut de Mécanique des Fluides
5, boulevard Paul Painlevé, 59000 - LILLE (France)

SOMMAIRE.-

Une méthodologie nouvelle est exposée relative à l'étude sur maquettes en vols libres en laboratoire de phénomènes liés à l'aérodynamique asservie. La technique expérimentale est notamment mise en oeuvre dans le cadre de travaux sur la régulation de portance par volets rapides sur avion de transport actuel (A.T.A.), en vue de déterminer en premier lieu les caractéristiques aérodynamiques instationnaires propres aux surfaces portantes de l'avion (aile et empennages) ainsi qu'à des mouvements rapides de gouvernes. Ces travaux ont été organisés pour constituer un support expérimental adapté à l'identification sur modèle des coefficients aérodynamiques instationnaires.

Les aspects suivants de la technique d'essais seront développés :

- Principe et méthode expérimentale. Moyens mis en oeuvre.
- Mesure et traitement de données instationnaires.
- Identification structurale des maquettes d'essais.
- Réalisation à partir de vols libres d'une première identification aérodynamique sur la base d'un modèle quasi-stationnaire, simulation et prévision des vols.
- Originalité, diversité et choix des entrées "sensibilisantes" vis-à-vis des paramètres aérodynamiques à identifier, définition d'un programme expérimental type.
- Niveau de confiance sur les résultats expérimentaux.

Des résultats d'essais seront présentés pour conclure sur les performances de la méthode, sa capacité de constituer une base de données pour l'identification de phénomènes instationnaires, sa complémentarité vis-à-vis de méthodes dynamiques en soufflerie, son champ d'application, en particulier vis-à-vis de l'étude de la stabilité dynamique à grande incidence.

1 - INTRODUCTION.-

L'Institut de Mécanique des Fluides de Lille développe depuis sa création en 1930 des méthodes expérimentales basées sur le vol libre de maquettes. Ces méthodes ont été initialement appliquées et développées pour l'étude de la vrille libre en soufflerie verticale : reconnaissance du phénomène et étude de la phase de récupération. Depuis 15 ans environ la méthode d'essais a été étendue aux maquettes catapultées en vol libre en laboratoire afin de constituer un support expérimental bien adapté à l'analyse de phénomènes instationnaires tels que la réponse de l'aérodyne aux rafales verticales ou latérales, à l'étude de l'atterrissage en air calme ou avec perturbations extérieures ou encore en vue de traiter de l'amerrissage forcé ou du crash.

Afin d'apprécier l'intérêt du développement de cette méthode expérimentale originale, nous proposons l'argumentation suivante (voir fig. 1) :

- Représentation directe des phénomènes caractéristiques du vol.
- Evolution dans un environnement bien déterminé.
- Détermination précise des caractéristiques massiques, inertielles et structurales des maquettes.
- Maîtrise des "entrées" du système.
- Adaptation à des domaines de vols particuliers (effet de sol, grandes incidences...).
- Large complémentarité vis-à-vis d'autres méthodes expérimentales.

Jusqu'à une période récente ces essais sur maquettes libres en laboratoire ne considéraient que l'étude du mouvement longitudinal et le plus souvent avec gouvernes fixes. Ces conditions de l'expérience, imposées notamment par les possibilités limitées d'une instrumentation extensive et performante des maquettes, compatible avec les contraintes imposées par les conditions de similitude de l'essai, peuvent aujourd'hui être entièrement reconsidérées. En effet un nouveau laboratoire de vol libre a récemment été mis en oeuvre, il permet l'utilisation de maquettes de grande taille (2 à 3 m. et jusqu'à 40 Kg de masse). Parallèlement une importante gamme de capteurs miniaturisés de hautes performances ainsi que des actionneurs sont désormais disponibles auxquels on peut associer des systèmes numériques de télémétrie et de télécommande apportant richesse d'informations et précision ainsi que performances du point de vue des commandes de vol. La contribution de ces moyens à l'extension des capacités de la méthode expérimentale est déterminante. Les méthodes de commandes automatiques peuvent ainsi être intégrées aux essais qui constituent alors une base expérimentale précieuse pour le développement de ces techniques.

La mise en oeuvre de ces moyens a nécessité une méthodologie nouvelle pour définir et analyser les vols : définition des moyens de trajectographie, synchronisation espace-temps, logiciels d'acquisition des données, de simulation, de restitution des variables, de validation des informations dynamiques et d'identification aérodynamique des maquettes libres.

Nous présentons ici les principaux aspects de cette nouvelle technique d'essais et son application originale à la détermination de caractéristiques aérodynamiques sur la base d'un modèle quasi-stationnaire pour le mouvement longitudinal. Une évaluation des performances de la méthode et de l'ouverture du domaine d'applications sera proposée.

Les travaux considérés ont été développés dans le cadre de l'étude de phénomènes liés à l'aérodynamique asservie (x) en étroite collaboration avec le groupe ADERSA-GERBIOS (Vélizy - France) qui présente dans le cadre de ce même Symposium une communication relative à l'identification sur la base des vols libres des effets instantanés de portance. Ils constituent une première étape pour l'étude de la régulation de portance par volets rapides pour avion de transport actuel (A.T.A.).

2 - PRINCIPE ET METHODE EXPERIMENTALE - MOYENS MIS EN OEUVRE.-

2.1 - Principe de base - Similitude physique.

Dans l'inventaire des variables à prendre en compte pour les essais en similitude sur maquettes volantes il y a lieu de considérer naturellement les caractéristiques massiques et inertielles du modèle évoluant dans le champ de pesanteur g . Les règles de similitude à adopter visent une représentation semblable des trajectoires et mouvement de l'aérodyne. Les grandeurs primaires indépendantes en fonction desquelles seront exprimées toutes les variables du problème sont : longueur de référence L , masse volumique du milieu ρ , et accélération de pesanteur g . Une telle représentation conduit dans l'expression des grandeurs réduites caractéristiques à la conservation du nombre de Froude entre maquette et grandeur (exprimant le rapport des forces d'inertie aux forces de gravité). Ainsi si on appelle λ l'échelle géométrique du modèle et m le rapport des masses volumiques de l'air (altitude $Z = 0$ vol maquette/altitude de vol avion) les rapports de similitude des principales grandeurs physiques sont définies par le tableau ci-contre.

Similitude de Froude

Grandeurs fondamentales	Grandeur	Dimension	Rapport
	Longueur	L	λ
	Masse	M	$m \lambda^3$
	Temps	T	$\lambda^{1/2}$
Une telle similitude est appelée restreinte car du point de vue aérodynamique elle ne peut représenter simultanément l'identité des nombres de Reynolds ou de Mach. Notons toutefois que les essais sur maquettes libres ne se rapportent qu'au domaine de vol subsonique incompressible. D'autre part le choix de maquettes de plus grande taille pour de tels essais permet d'atteindre aujourd'hui des nombres de Reynolds voisins de 10^6 (calculés sur la corde moyenne du profil).	Surface	L^2	λ^2
	Volume	L^3	λ^3
	Inertie	$M L^2$	$m \lambda^5$
	Vitesse	$L T^{-1}$	$\lambda^{1/2}$
	Force	$M L T^{-2}$	$m \lambda^3$
	Moment	$M L^2 T^{-2}$	$m \lambda^4$
	Pression	$M L^{-1} T^{-2}$	$m \lambda$
	Fréquence	T^{-1}	$\lambda^{-1/2}$
	Accélération	$L T^{-2}$	1
	linéaire		

2.2 - Similitude directe et indirecte - Application pratique.

La similitude de Froude rappelée ci-dessus détermine des conditions d'essais en vue d'une application directe des résultats de l'expérience sur modèle au cas de l'avion grandeur (fig. 2). Cette démarche n'est appliquée aujourd'hui qu'à l'étude de phénomènes pour lesquels la modélisation apparaît délicate (phénomènes décrochés ou d'impact ...), elle conduit au niveau de l'expérience à des constatations.

La seconde démarche possible est celle de la similitude indirecte dans laquelle les résultats d'essais sur maquette constituent un support expérimental pour la validation d'un modèle mathématique de représentation des phénomènes. La modélisation peut ensuite être "transposée" au niveau de l'avion en tenant compte de ces caractéristiques propres (exemple : introduction des modes souples). Cette seconde procédure est actuellement utilisée pour la plupart des travaux relatifs à l'étude des qualités de vol de l'avion et a été retenue pour la présente étude. Les deux modes, dans certains cas, peuvent être associés.

2.3 - Maquette et équipements.

La figure 3 présente une vue générale de la maquette utilisée pour ces travaux. Il s'agit d'une maquette d'un avion de transport actuel (A.T.A.) représentative d'un type Airbus. La forme a été volontairement simplifiée. Cette maquette est de taille moyenne vis-à-vis des possibilités de la station d'essais. Ses caractéristiques principales sont Envergure : 1,6 m. Longueur : 2 m. Corde de référence : 0,236 m. Masse moyenne : 9 Kg.

(x) l'étude a été réalisée sous contrats STAé (France) "Etudes Générales"

2.3.1 - Construction de la maquette

Nous avons fait choix de réaliser une maquette représentant des rigidités élevées (voir identification structurale) vis-à-vis de l'avion afin de réduire dans une première phase de l'étude les couplages structuraux et permettre dans les chaînes de mesure l'interposition de filtres appropriés. Le fuselage est réalisé en panneaux sandwich, avec ossature en nid d'abeille, constituant une poutre creuse pour permettre l'intégration de l'équipement d'essai. La voilure est construite à partir d'une structure maillée organisée entre des longerons principaux et revêtue de fibre de carbone d'épaisseur 8/10 mm.

Afin d'introduire dans les essais des effets instationnaires importants dus à des surfaces de contrôle agissant en portance la voilure a été munie de surfaces mobiles disposées aux emplacements habituels des volets et agissant en rotation simple à la manière d'ailerons. La profondeur relative de ces surfaces mobiles est de 20 % en moyenne (voir fig. 4). Ces surfaces peuvent être actionnées soit au moyen de vérins électriques en commande continue, soit au moyen de lames en flexion précontraintes pour assurer efficacement une commande par échelons ; elles sont solidaires d'un capteur de position.

Le comportement dynamique de ces "gouvernes" a été relevé pour un échelon de braquage d'amplitude 6°. L'enregistrement au sol a été obtenu par l'intermédiaire d'un capteur de proximité. Le temps de montée pour l'ensemble des surfaces mobiles mécaniquement solidaires est de 15 ms, soit environ un temps réduit de 1,5 cordes de référence pour les conditions de vol.

L'identification des effets instationnaires de portance obtenus par le mouvement en vol de ces volets a été réalisée par le Gerbios (voir référence 23).

Dans le but d'analyser les effets induits par l'aile sur les empennages horizontaux ceux-ci ont été dissociés du fuselage et portés par une balance à jauges à deux composantes (force et moment) (voir fig. 5). Les informations obtenues sont associées à des mesures anémométriques locales réalisées dans la région du bord d'attaque des empennages. Des mesures complémentaires réalisées en soufflerie classique sont actuellement poursuivies afin de permettre la séparation des effets induits par le mouvement propre de l'avion de celui des volets.

2.3.2 - Identification massique et inertielle

La précision sur la connaissance des caractéristiques massiques et inertielles des maquettes libres ou semi-libres est bien sur fondamentale pour l'exploitation des données de vols et détermine notamment le niveau de confiance sur les paramètres aérodynamiques recherchés.

Les méthodes d'identification de ces caractéristiques ont été adaptées à ces nécessités nouvelles,

- la masse des maquettes est obtenue par pesées sur des balances de qualité ;
la précision est de $\pm 0,5 \%$
- position du centre de gravité selon X, Y, Z

celle-ci est obtenue en fixant la maquette à l'extrémité d'un fléau reposant sur un couteau de balance équilibré au moyen de masses marquées disposées à l'autre extrémité. Les axes X, Y, Z maquettes sont successivement disposés parallèlement à l'axe du fléau (voir fig. 6).

La précision obtenue est $\pm 0,5 \text{ mm}$ (soit $2 \cdot 10^{-3}$ cordes pour la maquette A.T.A.).

Les inerties autour des axes de référence sont obtenues au moyen d'un montage dynamique constitué d'une barre de torsion encastrée à une extrémité et munie à l'autre d'un plateau recevant la maquette. Celle-ci peut être montée dans trois positions : les axes de référence successivement parallèles à l'axe de la barre de torsion (voir fig. 6).

L'ensemble forme un pendule excité électro-dynamiquement. La mesure s'effectue à la résonance de phase contrôlée sur scope (fermeture du lissajoux entre la tension synthétiseur déphasée de $\pi/2$ et la réponse du pendule) et à amplitude égale à celle de l'étalonnage.

La précision globale du système pour la détermination des inerties est meilleure que 10^{-2} .

2.3.3 - Identification dynamique des maquettes de vol libre

Cette identification a deux buts principaux :

- vérifier la validité des hypothèses de travail en mode rigide ou déterminer ces modes afin de les prendre en compte dans la modélisation, toute représentation semblable exclue ;
- permettre une implantation préférentielle des capteurs dynamiques et prévoir les procédures de filtrage appropriées dans la chaîne de mesure.

La méthode et les moyens mis en œuvre (voir fig. 7) pour l'identification sont ceux appliqués de façon courante aux maquettes de flottement. Seule la suspension diffère car il s'agit d'une maquette de vol libre. Elle est assurée par des suspentes de grande souplesse (très basse fréquence $< 2 \text{ Hz}$).

L'excitation est créée d'une part par un transducteur électro-acoustique émettant en bruit blanc pour les relevés de spectre et d'autre part au moyen d'un excitateur accordé travaillant par contact pour les relevés d'amplitude. Il est associé à un capteur de déplacement.

L'analyse spectrale est faite en temps réel sur signaux accélérométriques. Trois modes ont été retenus : 1er mode flexion voilure 39,6 Hz, flexion des empannages horizontaux 55,8 Hz, flexion deux noeuds fuselage 88,2 Hz.

De l'ensemble des résultats on peut conclure à une maquette rigide vis-à-vis de l'avion (le premier mode voilure correspondrait pour l'avion à 8 Hz environ).

2.3.4 - Instrumentation embarquée

- l'équipement habituel des maquettes de vol libre destiné à la reconnaissance des mouvements se compose d'ensembles accélérométriques et gyrométriques pour définir l'accélération résultante et le vecteur rotation instantané.

Dans la présente étude relative au mouvement longitudinal et compte tenu de la nécessité de déterminer directement avec précision les charges dynamiques sur les empannages horizontaux dissociés, l'instrumentation comporte un ensemble de 3 accéléromètres pendulaires asservis (classe 10^{-5}) disposés dans le plan de symétrie (2 à axe de mesure parallèle à GZ_1 , 1 parallèle à GX_1). Ils permettent la détermination directe de Z_G , X_G et $\dot{\varphi}$ et de l'accélération appliquée à la masse dissociée des empannages.

- Ces moyens de mesure dynamiques sont complétés par des systèmes opto-électroniques.

Pour la trajectographie la maquette est porteuse de spots lumineux déterminant en vol des traces relevées sur les bases optiques au sol.

Pour les mesures cinématiques une lampe à faisceau dirigé portée par la maquette active les barrières optiques.

Un ensemble de photo-cellules équipe la maquette. Ce système a pour fonctions : le déclenchement par l'intermédiaire du codeur embarqué déterminant la base de temps du système (1,28 ms) de l'acquisition des informations (initialisation de l'acquisition), la détermination de la date du largage (initialisation du vol libre), la datation du passage au droit des bases d'enregistrement optique (synchronisation espace-temps), l'activation des repères optiques embarqués.

- Pour la télémétrie l'équipement maquette est composé d'un ensemble codeur émetteur en mode PCM. 30 voies d'entrée sont disponibles, la fréquence de bits ajustable jusqu'à 250 Kb, le format des mots est de 12 bits, la bande passante par voie peut atteindre 250 Hz.

- Le déclenchement en vol des volets peut être obtenu soit par une commande interne temporisée sur l'initialisation du vol, soit par télécommande sur contrôle des paramètres de vol.

- L'équipement est bien sûr complété par la balance à jauges de contraintes à 2 composantes pour les empannages horizontaux et par les capteurs de pressions différentielles inclus dans les bords d'attaque des profils pour les mesures de pression cinétique et d'incidence locale.

2.4 - Moyens Sol-Station d'essais.

2.4.1 - Organisation générale

Sur la vue générale de l'installation d'essais on peut distinguer la zone de mise en vitesse et de largage réalisée au moyen d'une catapulte pneumatique, le domaine du vol libre où les trajectoires peuvent se développer sur des parcours pouvant atteindre 50 m. (soit plus de 200 cordes de référence) et la zone de récupération des maquettes. Dans le domaine de vol libre une soufflerie horizontale à veine ouverte (sur 6 m.) de section (13,5 x 3,5 m) permet de créer des sollicitations extérieures du type vent ou rafales latérales. Cette possibilité n'est pas exploitée dans la présente étude.

Dans la figure 8 sont précisées les principales caractéristiques géométriques de la station d'essai.

2.4.2 - Catapultage

Les solutions retenues pour le catapultage des maquettes permettent l'obtention de conditions initiales au largage précises notamment vis-à-vis de la géométrie de la cinématique, de la dynamique (aspect vibratoire et instrumental) et de l'aérodynamique (voir fig. 9).

La géométrie pente et assiette initiale est définie à 0,03° près.

La vitesse initiale est définie à 5 % au moyen de barrières optiques.

Les niveaux de bruit sur l'accélérométrie dans la phase de propulsion restent inférieurs à 1 g et permettent l'exploitation des informations sous rampe (voir procédure de contrôle des conditions initiales de vitesses angulaires). Afin de permettre l'installation des forces aérodynamiques avant le largage, la loi de mise en vitesse obtenue est telle que sur les quinze dernières cordes du parcours propulsé l'accroissement relatif de vitesse soit inférieur à 1 %. Cette caractéristique est réalisée en contrôlant les conditions génératrices et la détente de l'air comprimé dans le vérin propulseur. L'énergie maximum libérée au largage est de 40.000 joules.

2.4.3 - Trajectographie sol - Bases optiques

Les informations nécessaires à la connaissance de la trajectoire et des attitudes de la maquette en vol sont obtenues sur trois bases au sol équipées de bancs optiques (voir fig. 10).

Chaque base est située dans un plan vertical normal au plan de symétrie du vol. Elle comporte deux bancs d'enregistrements optiques à axes perpendiculaires situés dans le plan de la base. Sur chaque base sont ainsi enregistrées les traces lumineuses des références portées par la maquette ainsi qu'un référentiel local fixe. Le champ moyen d'observation par base est d'environ 4 m. Les traces sont relevées en continu. Le plan de la base est matérialisé par une nappe lumineuse mince destinée à activer une photo-cellule portée par la maquette. Le top délivré sur la télémetrie permet une synchronisation espace-temps. Un flash fournit en même temps un instantané de la maquette en vol permettant notamment le repérage des traces optiques.

La géométrie de cet ensemble est définie sur les cotes à mieux que 0,01 m et 0,05° sur les angles par visées laser et relevés au cathétomètre.

2.4.4 - Acquisition des données - Structure de la chaîne

L'organisation de la chaîne est présentée dans la figure 11. Il s'agit d'un système à vocation très générale bien adapté à la mesure de phénomènes rapidement variables et offrant la possibilité d'élaborer des boucles de commandes simples par le sol ou d'effectuer de la surveillance de paramètres.

Le codeur relié à un émetteur FM est embarqué dans la maquette. Les caractéristiques principales sont : fréquence de bits jusqu'à 250 Kb, 30 voies, mots de 12 bits, bande passante par voie 250 Hz. La précision globale du système est meilleure que 10^{-3} . Les boucles de commandes simples peuvent être réalisées en numérique pur ou élaborées sur machine analogique après convertisseur. L'acquisition des données comporte la prise des zéros sous catapulte, la phase de mise en vitesse et le vol libre.

Les informations au nombre de 10 sont sous cyclées, elles sont filtrées avant numérisation par un filtre à coupure 80 Hz afin de ne pas atténuer les instationnaires. D'autre part les taps de synchronisation espace-temps figurent quatre fois dans le cycle, ce qui détermine la date des événements à 0,3 ms près, soit 0,01 m environ sur les positions.

2.5 - Logiciels.

Deux programmes principaux sont mis en oeuvre pour traiter les informations relatives au vol (voir fig. 12).

- Le programme de trajectographie traite les traces spatiales des références de la maquette obtenues par dépouillement des enregistrements optiques sur bases. Il utilise 48 points de mesure par base pour élaborer un ensemble de valeurs caractéristiques d'une position de la maquette. Une linéarisation par moindres carrés sur chaque trace spatiale est réalisée et un test de cohérence des données est établi sur le critère de géométrie de positionnement des repères optiques dans les axes maquettes. Pour chaque base on obtient ainsi les angles d'Euler et coordonnées du centre de gravité ψ , θ , φ , X_G , Y_G , Z_G , ainsi que les coordonnées de la pente spatiale.

- Le programme de traitement des enregistrements dynamiques traite pour la durée du vol (1,5 sec. maquette, soit 8 sec. avion) 36.000 valeurs. Il opère sur les valeurs obtenues par différence entre le vol libre et les zéros pris sous catapulte immédiatement avant tir. Le premier ensemble de conditions initiales est déterminé, soit par mesures directes (valeurs instantanées fournies par les capteurs à la date du largage) soit par des mesures indépendantes telles que pente, assiette, vitesse initiale, etc... Afin d'éliminer sur les informations dynamiques les bruits structuraux résiduels du largage, un filtrage numérique inverse - direct est mis en oeuvre avec une fréquence de coupure de 30 Hz. Il permet de préciser les conditions initiales dynamiques, ce filtrage n'est pas effectué pour l'identification des transitoires d'établissement de portance.

Pour chaque sous-cycle PCM (1,28 ms) les grandeurs suivantes sont restituées ou visualisées ψ , θ , φ , X_G , Y_G , $Z_G(t)$ et leurs dérivées V , α , β , positions de gouvernes et résultats relatifs aux empenages.

- Les résultats obtenus à partir de ces deux sources d'informations indépendantes sont utilisés ensuite dans un test de validation des données et d'ajustement final des conditions initiales des vols. En effet les informations trajectographiques demeurent les plus précises, elles permettent d'établir des recoupements avec les informations dynamiques intégrées. Les vols sont validés lorsque pour chacune des variables le recoupement s'établit à l'intérieur des "tubes de précision" définis sur les grandeurs géométriques. Un moindre carré est mis en oeuvre pour traiter sur les différentes bases optiques. Les ajustements sont réalisés sur les conditions initiales du vol (ψ_0 , θ_0 , φ_0 , X_0 , Y_0 , Z_0 , dérivées premières et secondes) en tenant compte de l'intervalle de confiance sur chaque paramètre mesuré.

Cette procédure de validation des vols précise donc les conditions initiales et permet alors une exploitation complète des vols V , α , β , p , q , r , C_x , C_y , C_z , C_L , etc....).

- A ces programmes généraux de traitement des données du vol libre sont parfois associées des procédures particulières de contrôle.

En effet un test supplémentaire sur les conditions initiales au largage ψ_0 , θ_0 , φ_0 et leurs dérivées consiste à intégrer les informations dynamiques sous rampe en mode inverse depuis le largage et réaliser qu'en valeur moyenne $\bar{\psi}$, $\bar{\theta}$, $\bar{\varphi}$ sont constants. Des contrôles sur les dates de franchissement des barrières de mesure de vitesse vérifient l'abscisse du large et la synchronisation espace-temps.

L'ensemble des moyens mis en oeuvre permet de valider des vols en laboratoire sur des parcours de 200 cordes à l'intérieur de "tubes de précision" sur les grandeurs géométriques X , Y , Z de 0,01 m et de 0,1° sur les attitudes ψ , θ , φ . La qualité de l'information sur les accélérations et vitesses angulaires et linéaires est donc particulièrement précieuse pour l'exploitation aérodynamique des vols.

3 - PROCEDURES DE DETERMINATION DE PARAMETRES DE STABILITE DYNAMIQUE EN VOL LONGITUDINAL.-

3.1 - Conditions des essais - Coefficients stationnaires.

La détermination de caractéristiques aérodynamiques à partir de vols libres de maquette se rapporte au domaine de vol basse vitesse (incompressible). Le nombre de Reynolds des essais peut atteindre 10^6 . Les vols ne sont pas motorisés. Le domaine d'incidence traité ici est compris entre 3 et 7°.

Dans le domaine de vol considéré les caractéristiques stationnaires de la maquette sont préalablement déterminées par des vols libres permanents. En effet les données aérodynamiques préliminaires, quelles que soient leurs provenances, ne sont pas suffisamment rigoureuses pour déterminer un vol permanent sur 200 cordes à trim imposé. Une phase de réglage de vols symétriques stabilisés est réalisée selon la procédure indiquée dans la figure 13.

L'orientation des termes de corrections à introduire aux conditions initiales ($\Delta V_0, \Delta \alpha_0, \Delta \delta_{m_0}$...) pour obtenir le vol permanent est définie par le simulateur numérique à partir des informations recueillies lors du vol précédent. Lorsque le vol permanent est établi (chaque variable n'évoluant plus qu'à l'intérieur des "tubes de précision" définis) on obtient directement les caractéristiques aérodynamiques équilibrées de la maquette avec une grande précision.

Indépendamment des objectifs présents la comparaison des valeurs obtenues en vol aux valeurs fournies par des mesures corrigées en soufflerie exécutées sur la même maquette au même Reynolds a un intérêt en elle-même.

3.2 - Simulation - Prévion des vols - Validation.

3.2.1 - Simulateur numérique de vol

L'I.M.F.L. dispose à l'heure actuelle de deux simulateurs numériques de vol : l'un simule le vol longitudinal de l'avion, l'autre le mouvement complet. En ce qui concerne la simulation pour le mouvement longitudinal, le modèle est représenté figure 14 en variables réduites et sous forme d'état habituelle.

Il s'agit du modèle linéaire, petites perturbations autour d'un vol quasi permanent.

Cette simulation est adaptée aux "entrées" particulières pouvant être réalisées dans nos expériences. Ainsi nous pouvons simuler des steps aux conditions initiales : steps d'incidence, d'assiette, de vitesse longitudinale, de masse, de centrage, de gouverne de profondeur et de volets.

Le simulateur permet également la mise au point de lois de pilotage. Exemple : maintenir constante l'assiette ou l'incidence ou leur donner une évolution linéaire au cours du temps.

Il permet également de simuler une évolution quelconque des gouvernes, en particulier une évolution ayant effectivement été réalisée lors du vol d'une maquette.

Les rafales verticales longues peuvent également être simulées.

3.2.2 - Prévion des vols et validation

Les utilisations de ce simulateur sont donc multiples :

- comparaison entre simulations et vols réels ;
- détermination des paramètres sensibilisés lors d'une entrée particulière ;

- inversement, détermination du vol à exécuter pour pouvoir identifier tel ou tel paramètre ;
- mais aussi il permet de prévoir les vols, de déterminer les trajectoires de sécurité à partir de coefficients estimés. Comme exemple de prévision de vol, dans la figure 15 on compare prévisions et vols réels.

Les coefficients du modèle sont ceux obtenus en soufflerie pour une maquette semblable géométriquement, mais de taille différente.

- le simulateur est aussi le dernier maillon de la chaîne de validation des vols par comparaison entre vol réel et vol simulé et certains accidents particuliers remarqués sur les courbes peuvent permettre de déterminer le paramètre éventuellement mal restitué.

3.3 - Nature des entrées - Entrées sensibilisantes - Définition d'un protocole de test pour l'identification.

Habituellement les entrées disponibles pour l'identification de paramètres de stabilité dynamique en vol avion sont des actions pilotes sur les commandes de l'avion.

Les méthodes usuelles en soufflerie sur maquettes mettent en oeuvre des entrées le plus souvent harmoniques non représentatives de trajectoire ou bien des entrées commandes.

Les conditions d'expérience sur maquettes catapultées en vol libre permettent, outre les "entrées" habituelles en vol, d'exploiter aux conditions initiales des sollicitations spécifiques et très variées.

.. Elles comportent notamment les entrées du type "échelon" pratiquées sur des grandeurs telles que \dot{Z} , $\dot{\theta}$ obtenues par variation de masse ou de centrage de la maquette pour toutes autres caractéristiques identiques. Une autre gamme d'entrée correspond à pratiquer des variations au largage des V , α ou gouvernes. Pour toutes ces sollicitations les caractéristiques aérodynamiques sont établies avant le largage mais induisent au lâcher une dynamique importante.

On peut souligner pour toutes ces entrées leur parfaite connaissance et par conséquent une excellente reproductibilité des vols qui en découlent.

Les entrées sur gouvernes en cours de vol peuvent être introduites, soit en continu, soit par valeurs discrètes. C'est cette procédure qui a été utilisée pour mettre en évidence les instationnaires d'établissement de portance par manoeuvre en échelon des volets.

Compte tenu du nombre important d'entrées spécifiques aux essais de catapultage, il est apparu indispensable d'étudier le comportement d'un modèle classique de mécanique du vol de l'avion soumis à de telles excitations et de définir ainsi un choix optimal d'entrées sensibilisantes pour l'identification des différents coefficients dérivés.

Cette étude permet en particulier de définir dans ce but un protocole de tests efficace.

L'étude de sensibilité a été réalisée sur le modèle quasi-stationnaire décrit précédemment.

Pour une variation successive de chaque coefficient $P_i (C_{Z\alpha}, C_{Z\dot{\alpha}}, C_{Zq}, C_{m\alpha}, C_{m\dot{\alpha}}, C_{mq}, C_{\dot{\alpha}\alpha})$ de 20 % on examine l'écart relatif $\frac{\Delta j}{j}$ pour $j = V, \alpha, q, \theta$. Pour chaque type d'entrée on compare les $\frac{\Delta j}{j}$ obtenus pour chaque paramètre. Pour une comparaison plus aisée, on définit

$$\delta_i = \frac{(\sum_{V, \alpha, q, \theta} \frac{\Delta j}{j})}{\sum_{i,j} (\sum_{V, \alpha, q, \theta} \frac{\Delta j}{j}) P_i}$$

Les résultats sont donnés dans la figure 16 pour quelques combinaisons d'entrées possibles.

On peut conclure que certaines entrées permettent de sensibiliser fortement les dérivées en α et q par rapport à d'autres conditions initiales. Les dérivées en α restent dans tous les cas aisément accessibles.

Les dérivées telles que C_{xv} , $C_{x\dot{v}}$, $C_{x\dot{\alpha}}$, $C_{x\delta_m}$ et $C_{x\delta_m}$ qui ne figurent pas dans le tableau sont négligeables, quelle que soit l'entrée considérée. Le coefficient $C_{x\dot{\alpha}}$ de faible sensibilité pourrait lui aussi être négligé.

On a donc défini un protocole de test pour l'identification des dérivées de stabilité dynamique longitudinale établi sur 5 vols ($\Delta \dot{Z}$, $\Delta \dot{Z} + \Delta \dot{\theta}$, $\Delta \dot{Z} + \Delta \alpha$, $\Delta \dot{Z} + \Delta \delta_m$, vol de référence).

3-4 - Restitution des paramètres des vols - Vecteur d'état et dérivée - Présentation d'un résultat type.

3.4.1 - Restitution des paramètres

Comme mentionné dans la présentation de la procédure générale, les données de la trajectoire,

des attitudes, vitesses et accélérations sont élaborées à partir de l'accélérométrie embarquée, des mesures sols de vitesse longitudinale, des topages dus aux nappes lumineuses et de plaques photos.

Au cours du même programme informatique de restitution, ces différentes données élaborées sont projetées dans le repère lié à la trajectoire et elles sont exprimées en variables non dimensionnelles.

Il est à noter que toute cette procédure s'effectue sans filtrage. On soustrait les variables non dimensionnelles du vol quasi-permanent utilisé comme référence des variables non dimensionnelles correspondant à un vol avec entrée. On dispose ainsi pour un vol avec entrée des valeurs non filtrées des écarts sur les variables d'état et de leur dérivée compatibles avec le simulateur.

3.4.2 - Présentation d'un résultat type

Dans la figure 17 on présente un résultat type. On notera la présence du Z qui, bien que n'intervenant pas dans le modèle, permet des vérifications ultérieures.

Toutes les variables sont non dimensionnelles.

Le filtrage est alors effectué suivant les besoins : en ce qui concerne l'identification des coefficients quasi-stationnaires de l'A.T.A., on a filtré à 10 Hz à l'aide d'un filtre numérique inverse, puis d'un filtre direct.

3.5 - Identification des dérivées longitudinales.

3.5.1 - Modèle pour identification

On présente figure 18 le modèle d'identification. C'est un modèle linéaire de type "petites perturbations" autour d'un vol quasi-permanent pris comme référence.

Nous l'écrivons sous forme matricielle

$$C\dot{X} = AX + BU \quad \text{où } X^T = [\bar{V}, \bar{\alpha}, \bar{q}, \bar{\theta}] \quad \text{afin d'isoler chaque coefficient à identifier}$$

où \bar{V} est la vitesse non dimensionnelle $\frac{V_2 - V_{Ref}}{V_0}$
 $V_2(t)$ est la vitesse réelle ramenée au ρ de référence
 $V_{Ref}(t)$ est la vitesse du vol de référence
 V_0 est la vitesse initiale du vol de référence.

(On ramène la vitesse réelle au ρ du vol de référence pour tenir compte du fait que l'on travaille en similitude de Froude où on ne peut comparer que des facteurs de charge qui sont proportionnels à $1/2 \rho V^2$. Ainsi un vol à vitesse V_1 et à ρ_1 constant pendant le vol correspond à un vol à vitesse $V_2 = V_1 (\frac{\rho_1}{\rho_2})^{1/2}$ lors d'un ρ_2 constant).

$\bar{\alpha}$ = incidence $\alpha - \alpha_{Ref}$.

\bar{q} = vitesse angulaire de tangage non dimensionnelle $(q - q_{Ref}) \frac{L}{V_0}$

τ est l'unité de temps réduit, c'est-à-dire le nombre de demi-cordes de référence parcourues à V_0

$\bar{\theta}$ = assiette de tangage $\theta - \theta_{Ref}$.

On trouvera sur la figure 18 les grandeurs réduites relatives à :

$$\gamma_0, B, m_0, \Delta\mu, \Delta x, \Delta\delta_m, \Delta\delta_z$$

Pour l'identification, le système $C\dot{X} = AX + BU$ est écrit sous la forme $O = AX - C\dot{X} + BU$

En remplaçant les valeurs simulées X et \dot{X} par les valeurs expérimentales, le premier membre ne sera plus nul et on écrira alors

$$E = My$$

où M est la matrice composée des matrices $[A; -C; B]$ juxtaposées
 et y^T le vecteur composé des vecteurs $[X^T; \dot{X}^T; U^T]$ juxtaposés

le vecteur E est un vecteur d'erreur à 4 composantes et on peut minimiser $\sum_{R=1}^R (E_R^2)$ ligne par ligne par la méthode des moindres carrés.

3.5.2 - Exploitation des conditions initiales

La figure 19 illustre pour deux vols avec échelons de $\Delta\dot{Z} + \Delta\alpha$ l'intérêt des conditions initiales pour la définition de coefficients type $C_{Z\dot{\alpha}}$ et $C_{Z\alpha}$ ou encore du $C_{X\dot{\alpha}}$. Ces caractéristiques apparaissent sur les courbes α obtenues à partir de coefficients préliminaires ainsi que dans l'évolution de \dot{V} courbe centrale.

Cette première estimation est faite à partir des informations géométriques et dynamiques obtenues à l'instant initial pour diverses combinaisons d'entrées.

3.5.3 - Critère forme - distance

Un critère fondé sur la distance modèle - objet n'est en général pas suffisant. En effet cette distance peut être quasiment identique mais avec des formes différentes. Nous avons donc couplé au critère de distance un critère qualitatif de forme utilisé constamment dans l'identification. En particulier notre procédure de restitution nous engage à admettre des ajustements sur les courbes α , V , q , pour préserver l'évolution globale qui est une caractéristique fiable dans l'exploitation de nos vols obtenue à partir d'informations dynamiques.

3.5.4 - Procédure de traitement globale

Un autre principe utilisé dans notre système d'identification est l'utilisation simultanée du plus grand nombre possible d'essais.

Pour illustrer la nécessité de cette procédure, nous présentons dans la figure 20 deux vols simulés chacun avec deux jeux de paramètres différents. Les coefficients du jeu n° 1 ont été identifiés uniquement sur des vols présentant des steps de volets en vol et associés à un step de masse et d'incidence. Avec ce premier jeu, on peut évidemment rendre compte très correctement du vol CLAC05 qui a servi à cette identification. Par contre le vol DFAT06 est très mal représenté à l'aide de ce jeu de coefficients. (Rappelons que ce vol n'a pas été utilisé pour l'identification de ce premier jeu de coefficients).

Le jeu n° 2 par contre a été obtenu sur un ensemble de vols plus important avec des entrées variées.

On peut constater que l'accord reste bon sur le CLAC05 et que par contre l'accord sur le DFAT06 s'est nettement amélioré.

3.5.5 - Présentation des résultats de l'identification

On peut noter dans la figure 21 les résultats d'ensemble de l'identification réalisée sur la base des procédures mentionnées.

Pour 6 évolutions différentes on peut constater un bon accord d'ensemble avec le jeu de coefficients indiqués.

Il faut relever que pour ces essais nous avons réalisé des mouvements de faible amplitude. Tout en restant cohérent avec les hypothèses du modèle, des échelons plus marqués permettront de parfaire la définition des paramètres recherchés.

3.5.6 - Exemple de sensibilité du modèle pour les essais considérés

Dans la figure 22 on peut comparer les simulations d'un vol $\Delta \dot{z} + \Delta \alpha + \Delta \delta_z(t)$ avec tous les coefficients d'une part et sans $C_{Z\dot{\alpha}}$ et $C_{m\dot{\alpha}}$ d'autre part.

On peut donc constater dans l'évolution de α , θ , Z , l'influence de ces termes (pour ce type d'entrée) détectable au plan expérimental.

Ces coefficients sont donc bien sensibilisés comme prévu par l'étude de sensibilité malgré le faible module des échelons pratiqués.

3.5.7 - Approche sur le transitoire des volets

Lorsqu'on simule les vols avec step de volets en cours d'évolution sans filtrer la gouverne, celle-ci par l'intermédiaire du modèle quasi-stationnaire décrit est directement efficace. On constate que l'influence au loin est négligeable. L'influence des transitoires de volets est donc essentiellement locale.

Il est particulièrement remarquable que la réponse aérodynamique de l'avion dans ce cas peut être représentée en première analyse par un filtrage direct du premier ordre à une fréquence d'environ 20 Hz de la simulation "petites perturbations" gouverne non filtrée. Rappelons que dans le cas de nos essais, la gouverne s'effaçait en 0,015 sec.

On pourrait donc faire choix de représenter les transitoires de volets en identifiant la fréquence de ce filtre.

Remarquons toutefois qu'une analyse beaucoup plus approfondie de ce phénomène transitoire a été effectuée par le Gerbios à partir d'un modèle beaucoup plus élaboré, exposé dans le cadre de ce Meeting.

4 - CONCLUSIONS.-

La méthode expérimentale et les moyens mis en oeuvre permettant une restitution précise des caractéristiques des vols. De très nombreuses combinaisons d'entrées sont réalisables. Elles permettent la définition d'un protocole de test efficace pour l'identification des paramètres longitudinaux.

Le modèle quasi-stationnaire utilisé en première approche représente de façon très satisfaisante ces vols, et certains coefficients y ont un rôle tout à fait négligeable.

Les exemples proposés ici constituent un premier développement de la méthode qui est actuellement étendue à l'étude du mouvement général de l'avion. De plus des sollicitations extérieures du type rafales longitudinales ou transversales pourront être introduites combinées à des manœuvres rapides de gouvernes.

Le domaine de vol est également ouvert sur les grandes incidences et sur la caractérisation de l'effet de sol où la représentation des phénomènes est très directe par cette méthode expérimentale.

- Représentation directe des phénomènes caractéristiques du vol.
- Evolution dans un environnement bien connu.
- Haute précision dans la détermination des caractéristiques massiques et inertielles du modèle.
- Possibilité d'une représentation indirecte des modes structuraux parfaitement définis.
- Maîtrise des entrées du système.
- Extension à des domaines de vol particuliers (effet de sol - grande incidence)
- Large complémentarité avec d'autres méthodes expérimentales.

Fig. 1 - INTERET DE LA METHODE EXPERIMENTALE DE VOL LIBRE EN LABORATOIRE

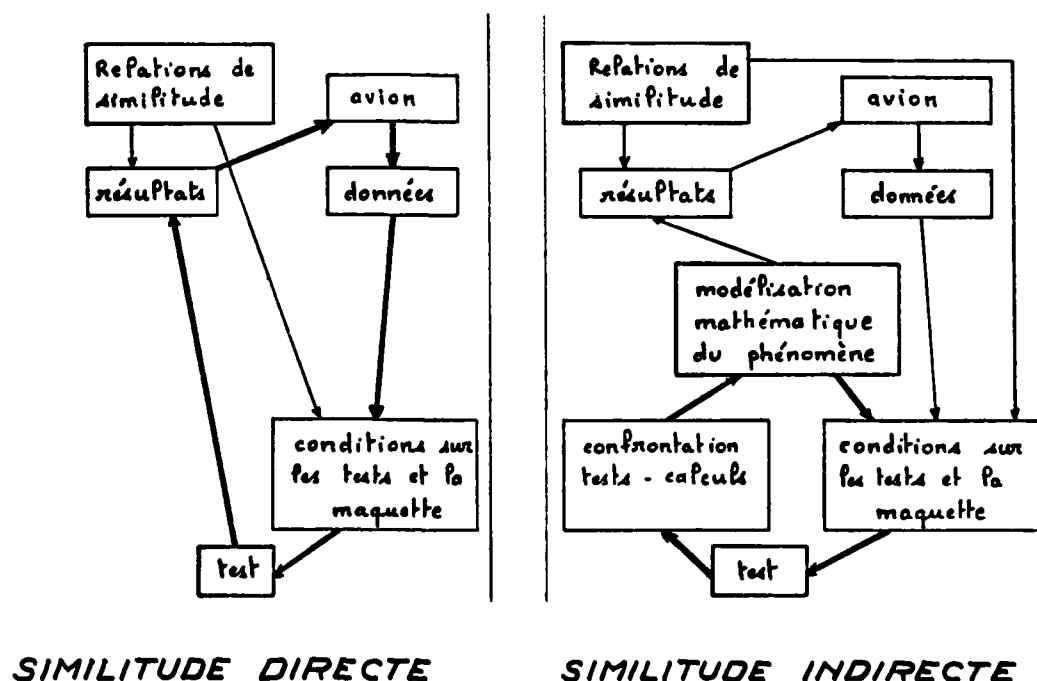
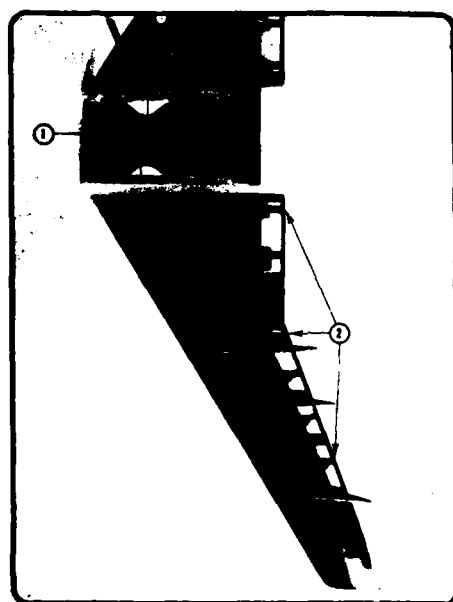


Fig. 2

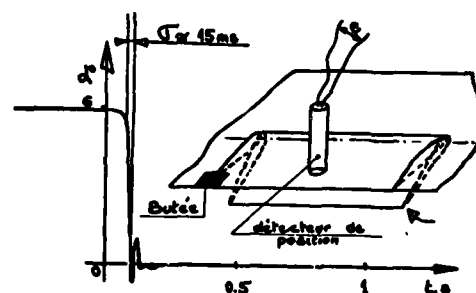


Fig. 3 - VUE D'ENSEMBLE DE LA MAQUETTE A T A



- 1 - Capteur de position
- 2 - La commande par échelon est réalisée par lames en flexion précontraintes.

MAQUETTE A T A
REPONSE D'UN VOLET A UN ECHOLON

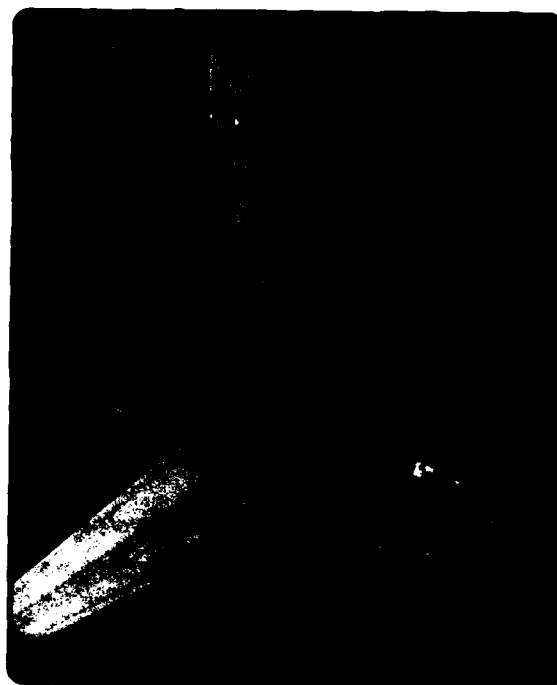


Mesures effectuées sur gouverne interne avec détecteur analogique de proximité.

Fig. 4 - VOILURE MUNIE DE VOLETS MOBILES

1 : Zones d'implantation
des sondes clinométriques
et cinétiques.

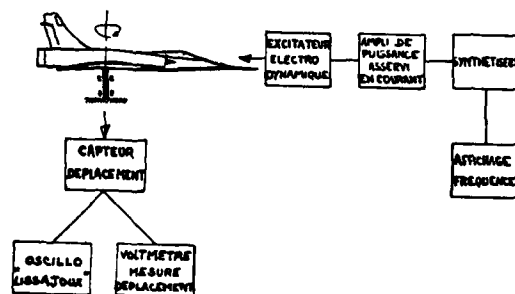
Fig. 5 - BALANCE DE
PESEE D'EMPENNAGES
A 2 COMPOSANTES



Recherche du centre en X.



Détermination de l'inertie de local.



F fréquence d'oscillation.

M masse de la maquette.

d distance du centre de gravité maquette à l'axe
de la barre de torsion.

I inertie de la maquette autour de l'axe considéré
passant par le centre de gravité

I₀ inertie du montage

C raideur angulaire de la barre de torsion

$$I = \frac{C}{4\pi^2 f^2} - (Md^2 + I_0)$$

Précision sur la mesure de I: $\frac{\Delta I}{I} < 1\%$

Fig. 6 - IDENTIFICATION INERTIELLE DES
MAQUETTES DE VOL LIBRE



- Excitation accordée par contact
- Relevé d'amplitude par capteur de déplacement

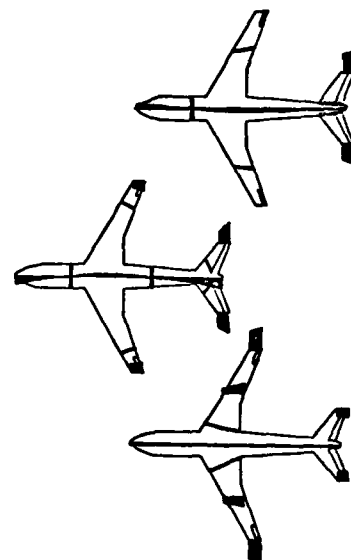
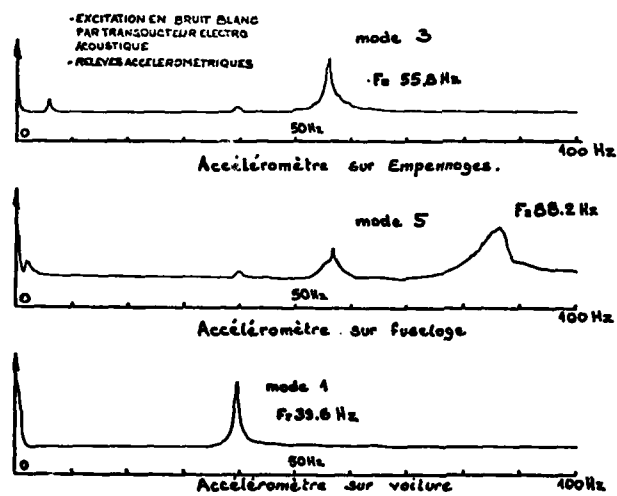


Fig. 7 - EXEMPLE
D'IDENTIFICATION STRUCTURALE

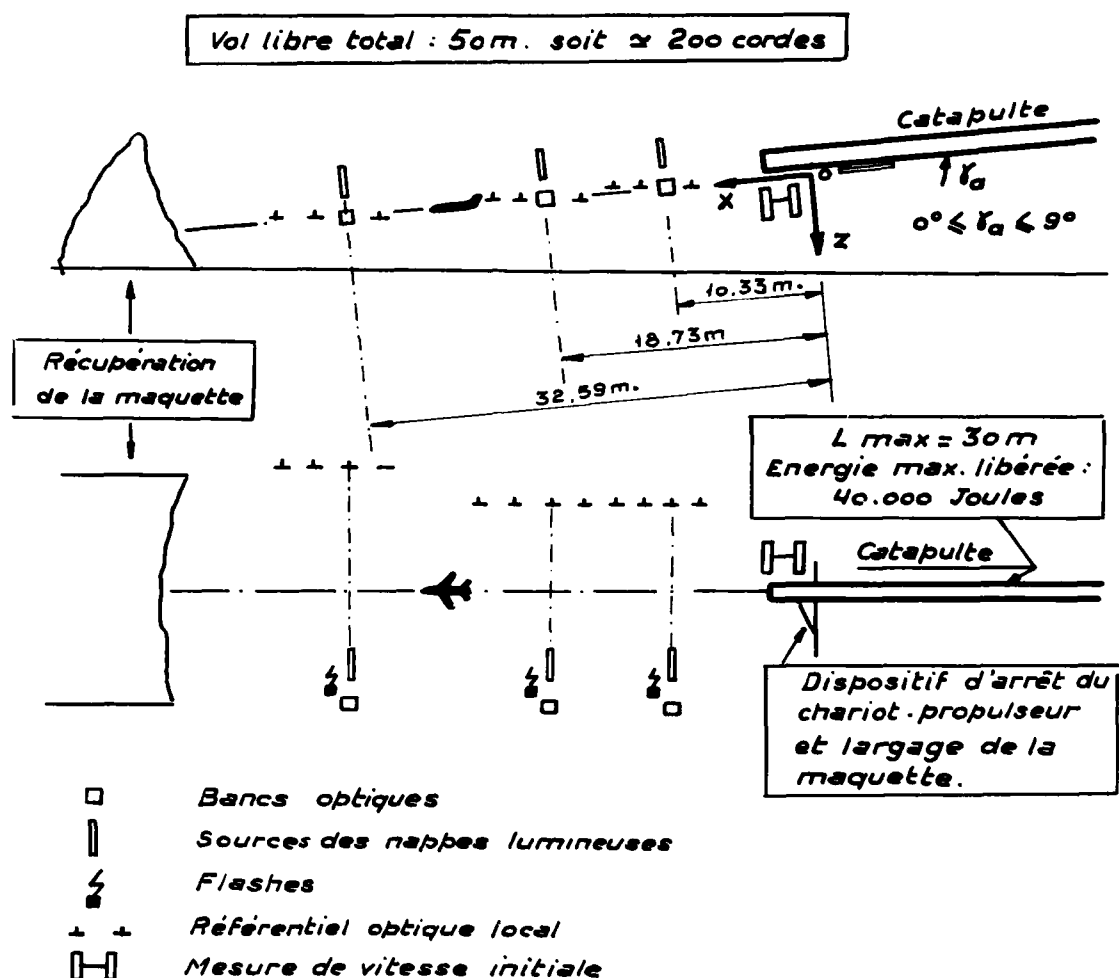


Fig. 8 - GEOMETRIE DE L'ESPACE DE VOL B. 10

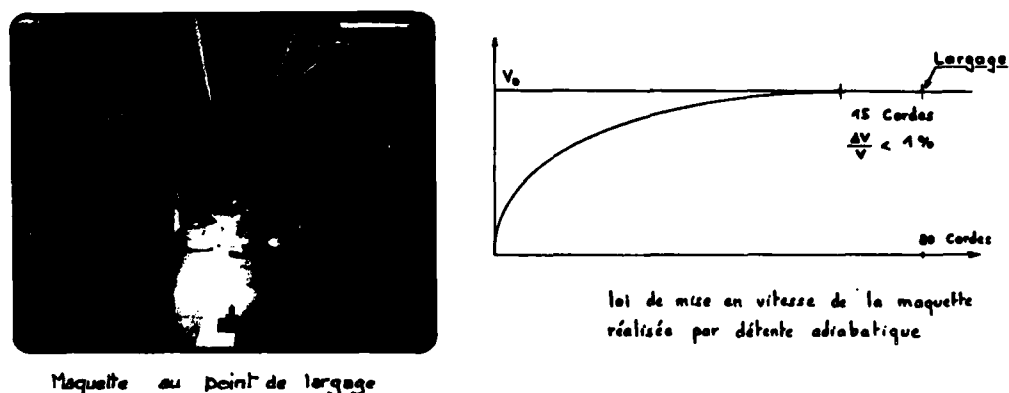


Fig. 9 - DISPOSITIF DE CATAPULTAGE

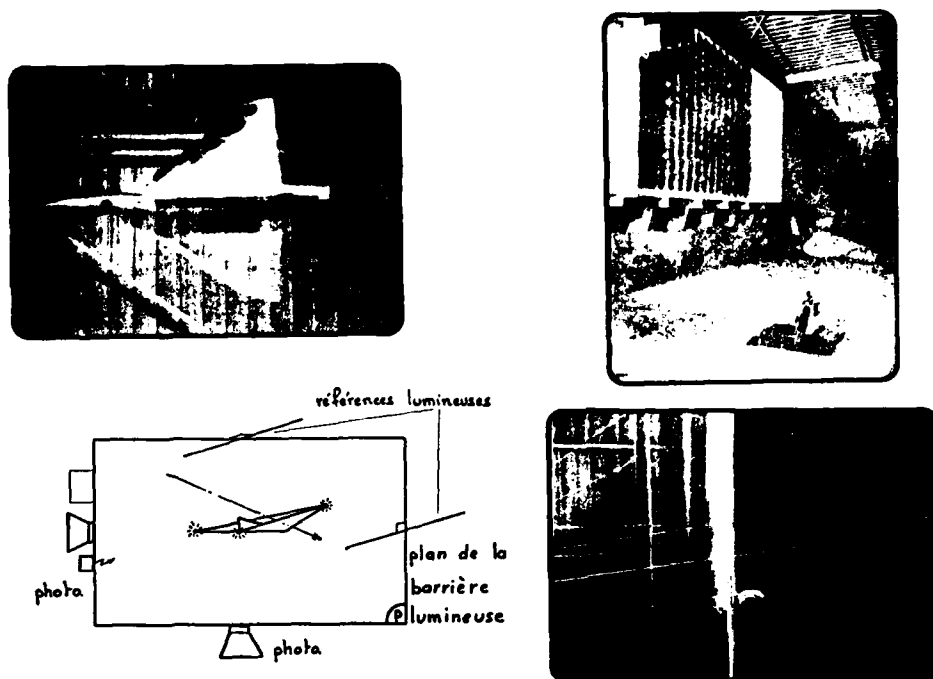


Fig. 10 - BASE OPTIQUE DE TRAJECTOGRAPHIE

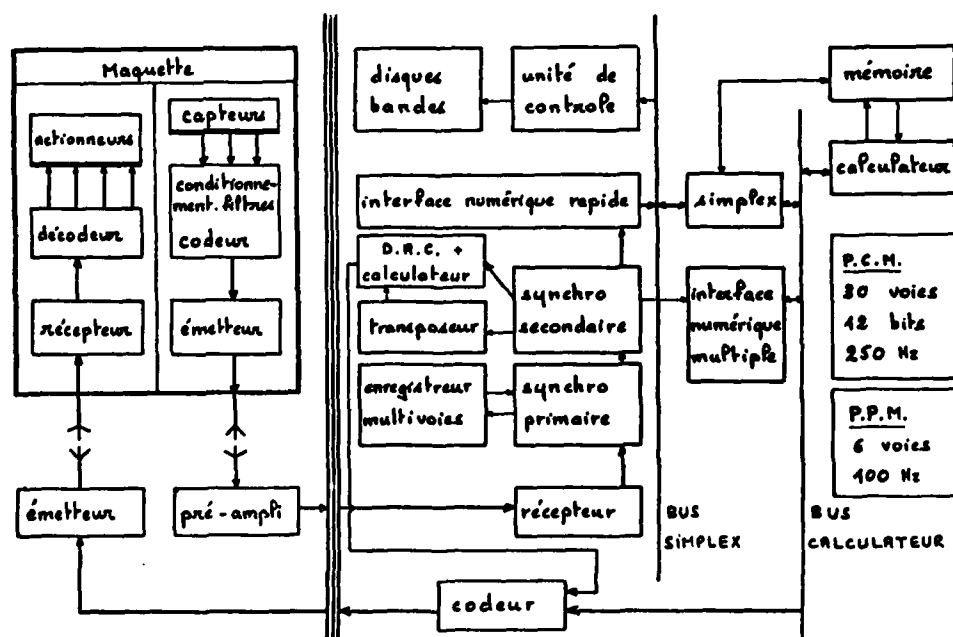


Fig. 11 - ORGANISATION DE LA CHAÎNE DE MESURES ET DE COMMANDES

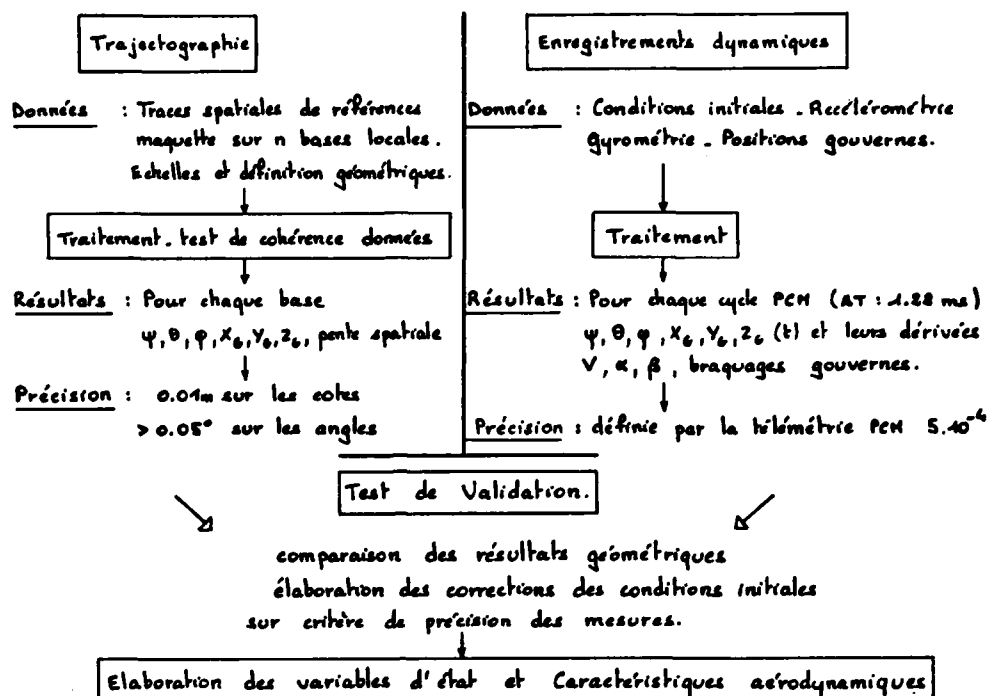


Fig. 12 - RESTITUTION DES VOLS LIBRES

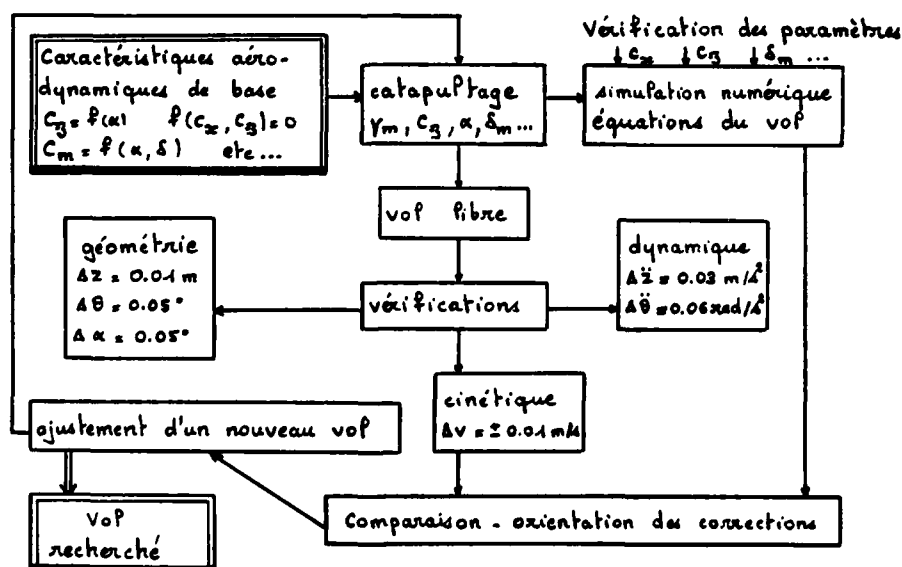


Fig. 13 - PROCEDURE D'AJUSTEMENT DES VOLS

Forme canonique du système :

avec

$$\begin{aligned}\dot{X} &= \bar{A}X + \bar{B}u \\ X^T &= (\bar{V}, \bar{\alpha}, \bar{q}, \bar{\theta}) \\ u^T &= (\Delta \bar{\delta}_m, \Delta \bar{\delta}_z, \Delta \bar{\mu}, \Delta \bar{x})\end{aligned}$$

$$\bar{A} =$$

$-\frac{C_{x\bar{v}} + 2C_{\omega_0} \sin \gamma_0}{2\mu}$	$\frac{C_{\omega_0} \cos \gamma_0 - C_{x\bar{\alpha}}}{2\mu}$	0	$-\frac{C_{\omega_0} \cos \gamma_0}{2\mu}$
$-\frac{C_{z\bar{v}} + 2C_{\omega_0} \cos \gamma_0}{2\mu + C_{z\bar{\alpha}}}$	$-\frac{C_{z\bar{\alpha}} - C_{\omega_0} \sin \gamma_0}{2\mu + C_{z\bar{\alpha}}}$	$\frac{2\mu - C_{z\bar{q}}}{2\mu + C_{z\bar{\alpha}}}$	$-\frac{C_{\omega_0} \sin \gamma_0}{2\mu + C_{z\bar{\alpha}}}$
$\frac{C_{m\bar{v}} - C_{m\bar{\alpha}}}{B} \frac{C_{z\bar{v}} + 2C_{\omega_0} \cos \gamma_0}{(2\mu + C_{z\bar{\alpha}})B}$	$\frac{C_{m\bar{\alpha}}}{B} - C_{m\bar{\alpha}} \frac{C_{z\bar{\alpha}} - C_{\omega_0} \sin \gamma_0}{(2\mu + C_{z\bar{\alpha}})B}$	$\frac{C_{m\bar{q}} + C_{m\bar{\alpha}}}{B} \frac{2\mu - C_{z\bar{q}}}{(2\mu + C_{z\bar{\alpha}})B}$	$-C_{m\bar{\alpha}} \frac{C_{\omega_0} \sin \gamma_0}{B(2\mu + C_{z\bar{\alpha}})}$
0	0	1	0

$$\bar{B} =$$

$-\frac{C_x \delta_m}{2\mu}$	$-\frac{C_x \delta_z}{2\mu}$	$-\frac{g \ell \sin \gamma_0}{2\mu V_0^2}$	0
$-\frac{C_z \delta_m}{2\mu + C_{z\bar{\alpha}}}$	$-\frac{C_z \delta_z}{2\mu + C_{z\bar{\alpha}}}$	$\frac{g \ell \cos \gamma_0}{V_0^2 (2\mu + C_{z\bar{\alpha}})}$	0
$\frac{C_{m\bar{v}} - C_{m\bar{\alpha}}}{B} \frac{C_{z\bar{v}} + 2C_{\omega_0} \cos \gamma_0}{B(2\mu + C_{z\bar{\alpha}})}$	$\frac{C_{m\bar{\alpha}}}{B} - \frac{C_{m\bar{\alpha}}}{B} \frac{C_{z\bar{\alpha}} - C_{\omega_0} \sin \gamma_0}{B(2\mu + C_{z\bar{\alpha}})}$	$\frac{C_{m\bar{q}}}{B} \frac{g \ell \cos \gamma_0}{V_0^2 (2\mu + C_{z\bar{\alpha}})}$	$\frac{C_{\omega_0} \cos \theta_0}{B}$
0	0	0	0

Fig. 14 - MODELE DE SIMULATION

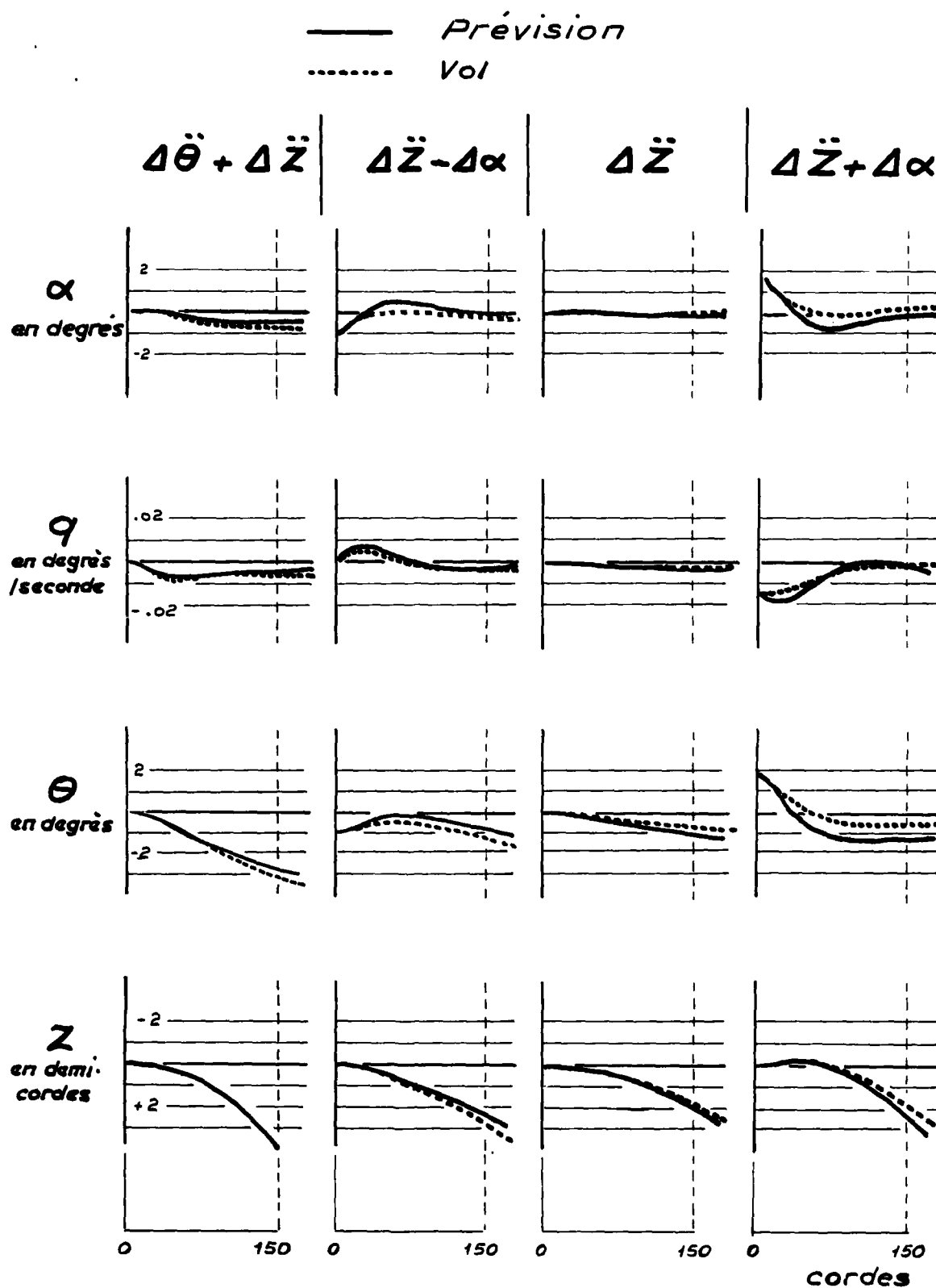


Fig. 15 - COMPARAISON PREVISION • VOL

Détermination des entrées sensibilisantes par variation successive de 20% des paramètres P_i dans l'ordre $C_{z\alpha}$, $C_{z\dot{\alpha}}$, C_{zq} , $C_{m\alpha}$, $C_{m\dot{\alpha}}$, C_{mq} , $C_{x\alpha}$.
Calcul pour un même essai de :

$$\rho_i = \frac{\left(\sum_{v, \alpha, q, \theta} \frac{\Delta j}{\bar{j}} \right) P_i}{\left(\sum_{i=1,7} \left(\sum_{v, \alpha, q, \theta} \frac{\Delta j}{\bar{j}} \right) P_i \right)}$$

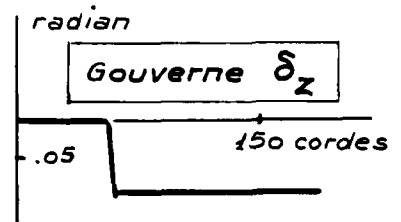
\bar{j} étant la valeur moyenne de v, α, q, θ .

Coefficients Entrées	$C_{z\alpha}$	$C_{z\dot{\alpha}}$	C_{zq}	$C_{m\alpha}$	$C_{m\dot{\alpha}}$	C_{mq}	$C_{x\alpha}$
Centrage (2%)	35	0,1	1,3	44	2	13	5
Gouverne (1°)	35	0,0	1,2	44	2	12	6
Incidence (1°)	28	0,5	1,8	38	11	19	3
Masse (7%)	23	0,1	2,4	36	3	34	3
Centrage + Incidence	37	0,1	0,8	46	3	9	6
Centrage + Gouverne	36	0,1	1,1	44	2	11	5
Centrage + Masse	42	0,1	0,4	44	2	4	9
Gouverne + Incidence	33	0,2	1,4	42	4	14	5
Gouverne + Masse	32	0,1	0,9	50	2	8	8
Incidence + Masse	24	0,6	1,7	39	13	22	1

Fig. 16 - PROTOCOLE D'ESSAI POUR
L'IDENTIFICATION DES TERMES DERIVES
EN STABILITE LONGITUDINALE

CONDITIONS INITIALES :

$$\Delta \ddot{z} + \Delta \alpha + \Delta \delta_z$$



VARIABLES SANS DIMENSION, NON FILTRES

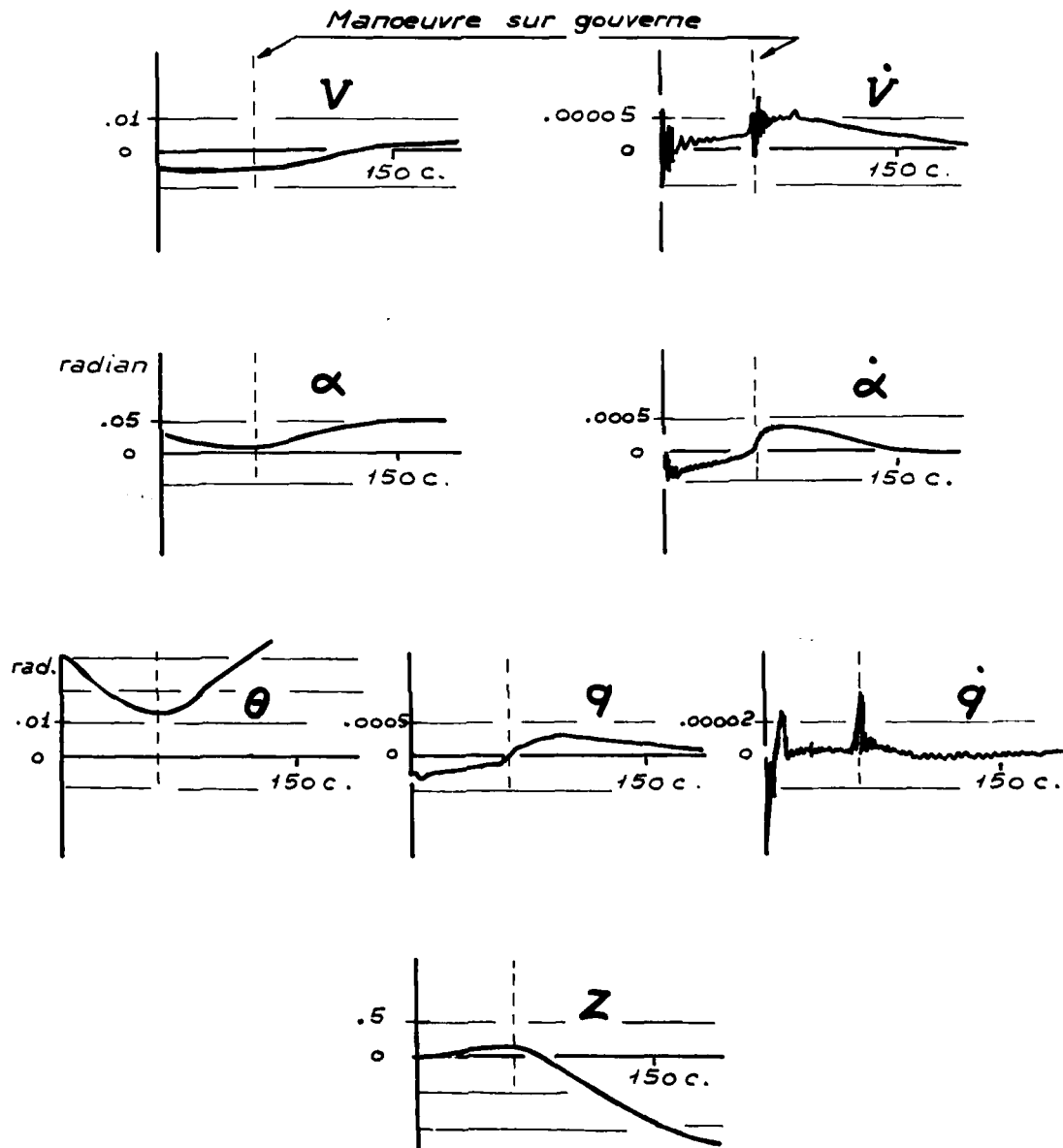


Fig. 17 - RESULTAT TYPE

Ecriture des équations en variables non dimensionnelles

$$0 = AX - CX + BU \text{ soit } \mathcal{E} = MY$$

on minimise $\sum_{j=1}^n (\mathcal{E}_j)^2$ par rapport aux paramètres à identifier ligne par ligne. avec $M = (A; -C; B)$ et $Y^T = (X^T; \dot{X}^T; u^T)$ expérimental

$$X = [\bar{V}, \bar{\alpha}, \bar{q}, \bar{\theta}]$$

$$\bar{V} = \frac{V_2 - V_{\text{réf}}}{V_0} \text{ où } V_2 = V_1 \sqrt{\frac{\rho_1}{\rho_2}}$$

$$\bar{\alpha} = \alpha - \alpha_{\text{réf}}$$

$$\bar{q} = (q - q_{\text{réf}}) \frac{L}{2V_0}$$

$$\bar{\theta} = \theta - \theta_{\text{réf.}}$$

DEFINITION DES VARIABLES NON DIMENSIONNELLES

$$C_{\omega_0} = \frac{m \cdot g}{\frac{1}{2} \rho_0 S V_0^2}$$

$$C_x = \frac{\Delta F_x}{\frac{1}{2} \rho S V_0^2}$$

$$\mu = \frac{m_0}{\frac{1}{2} \rho_0 S L}$$

$$C_{x_0} = C_{\omega_0} \sin \delta_0$$

$$C_z = \frac{\Delta F_z}{\frac{1}{2} \rho S V_0^2}$$

$$B = \frac{I}{\rho_0 S (\frac{L}{2})^3}$$

$$C_{z_0} = C_{\omega_0} \cos \delta_0$$

$$C_m = \frac{\Delta M}{\frac{1}{2} \rho S V_0^2 L}$$

$$d\tau = \frac{2V_0}{L} \cdot dt$$

$$A =$$

$-2C_{x_0}$	$C_{x_0}^{\delta_0}$	0	$-C_{z_0}$
$-2C_{z_0}$	$C_{z_0}^{\delta_0}$	$\frac{1}{2} \rho_0 S L C_{x_0}^{\delta_0}$	C_{x_0}
0	$C_{m\bar{\alpha}}$	$C_{m\bar{q}}$	0
0	0	1	0

$A =$

$$C =$$

2μ	0	0	0
0	$2\mu(C_{x_0}^{\delta_0} + C_{z_0}^{\delta_0})$	0	0
0	$-C_{m\bar{\alpha}}$	B	0
0	0	0	1

$B \cdot u =$

0	$-C_x \bar{\delta}_2$	$\frac{g \sin \delta_0}{V_0^2}$	0
0	$-C_z \bar{\delta}_2$	$\frac{g \cos \delta_0}{V_0^2}$	0
$C_{m\bar{\delta}_m}$	$C_{m\bar{\delta}_z}$	0	$\frac{V_0 \cos \delta_0}{L}$
0	0	0	0

$\Delta \bar{\delta}_m$
$\Delta \bar{\delta}_z$
$\Delta \mu$
ΔX

Fig.18 - MODELE POUR L'IDENTIFICATION

Cas du Step Masse + Incidence

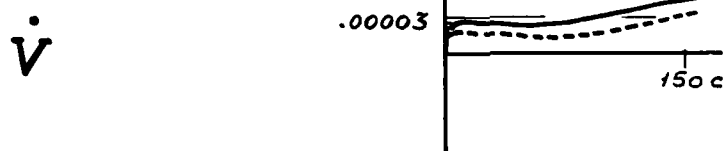
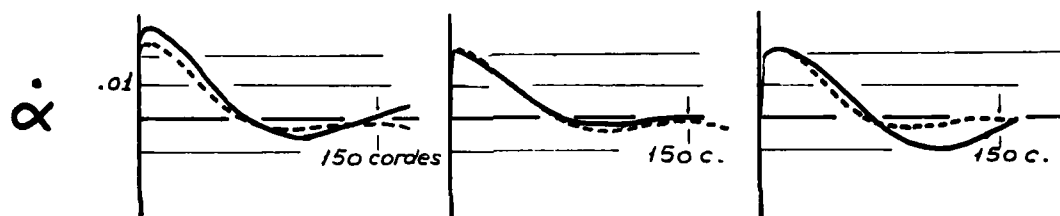
———— *Calcul*
 - - - - - *Expérience*

*Données
préliminaires*

*Identification IMFL
sur l'ensemble
des vols libres*

*1ère identification
sur une base de
données limitées*

$$\Delta \ddot{Z} + \Delta \alpha_1$$



$$\Delta \ddot{Z} + \Delta \alpha_2$$

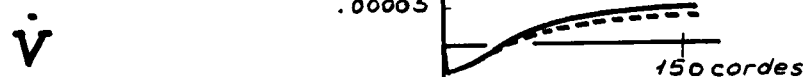
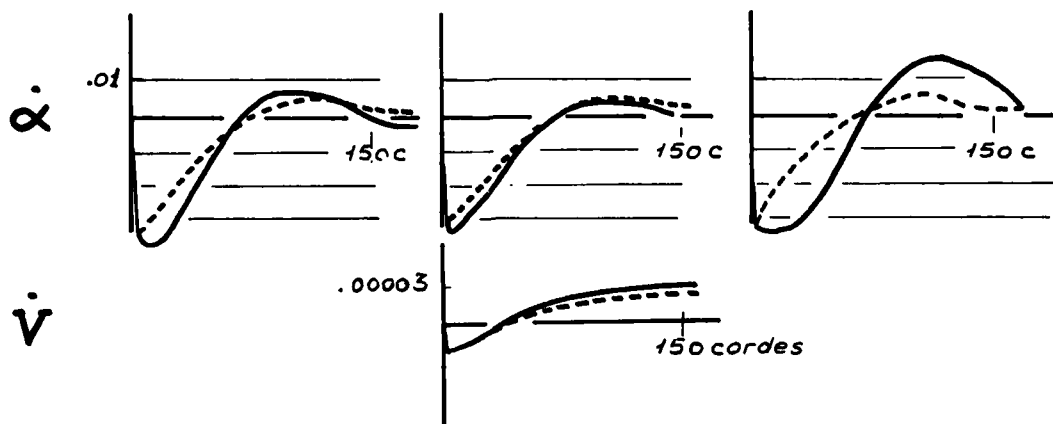


Fig. 19 - EXPLOITATION DES CONDITIONS INITIALES

*Principes : Exploitation séparée des conditions initiales.
Critère couple de forme et de distance.
Utilisation simultanée de tous les vols.*

$C_{x\alpha}$	$C_{x\delta_z}$	$C_{z\alpha}$	$C_{z\delta_z}$	$C_{z\dot{\alpha}}$	$CM\alpha$	$CM\delta_z$	$CM\dot{\alpha}$	CMq
.47	.092	3.9	1.026	7.67	-1.055	-.337	-8.93	-35.3

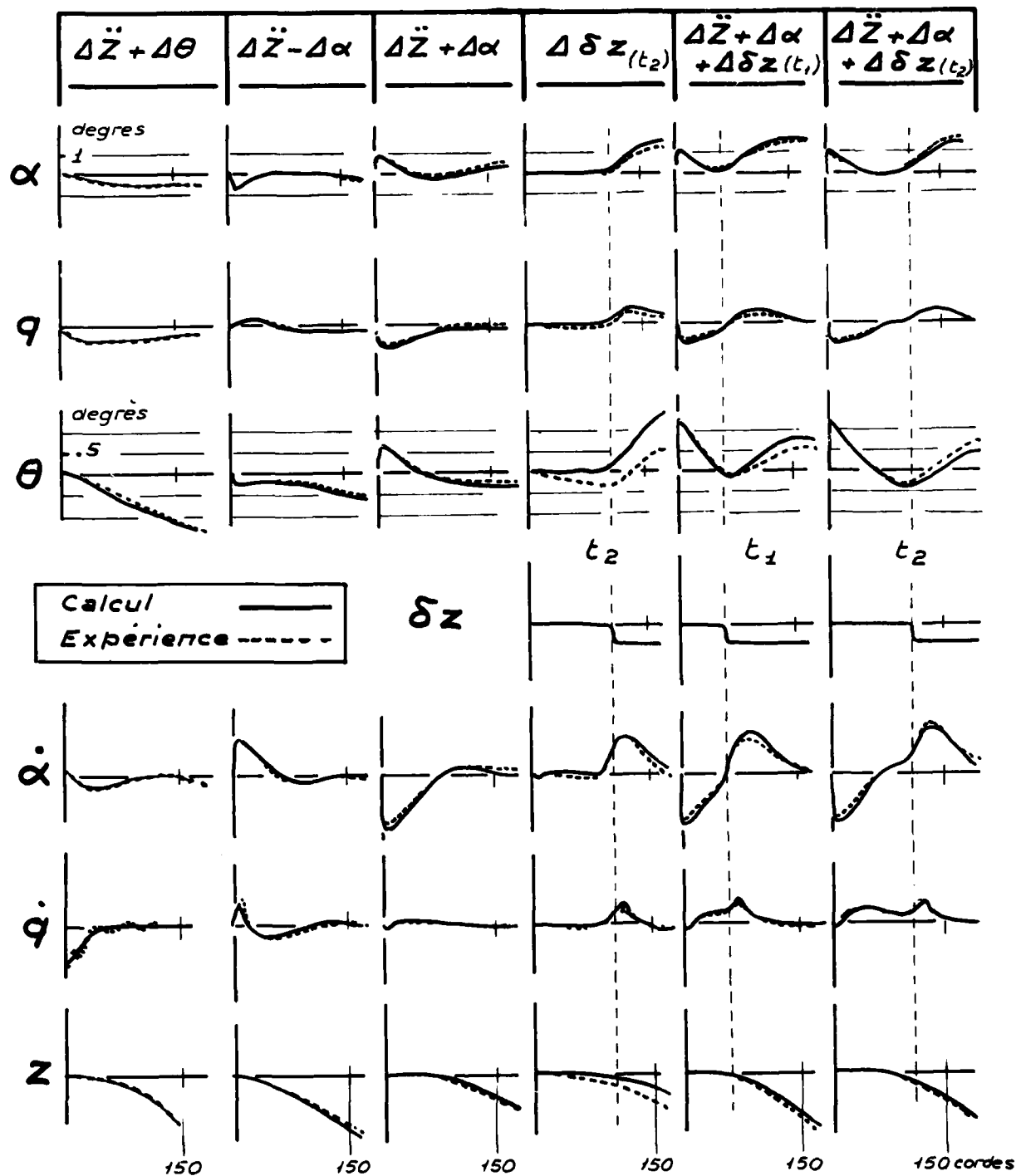
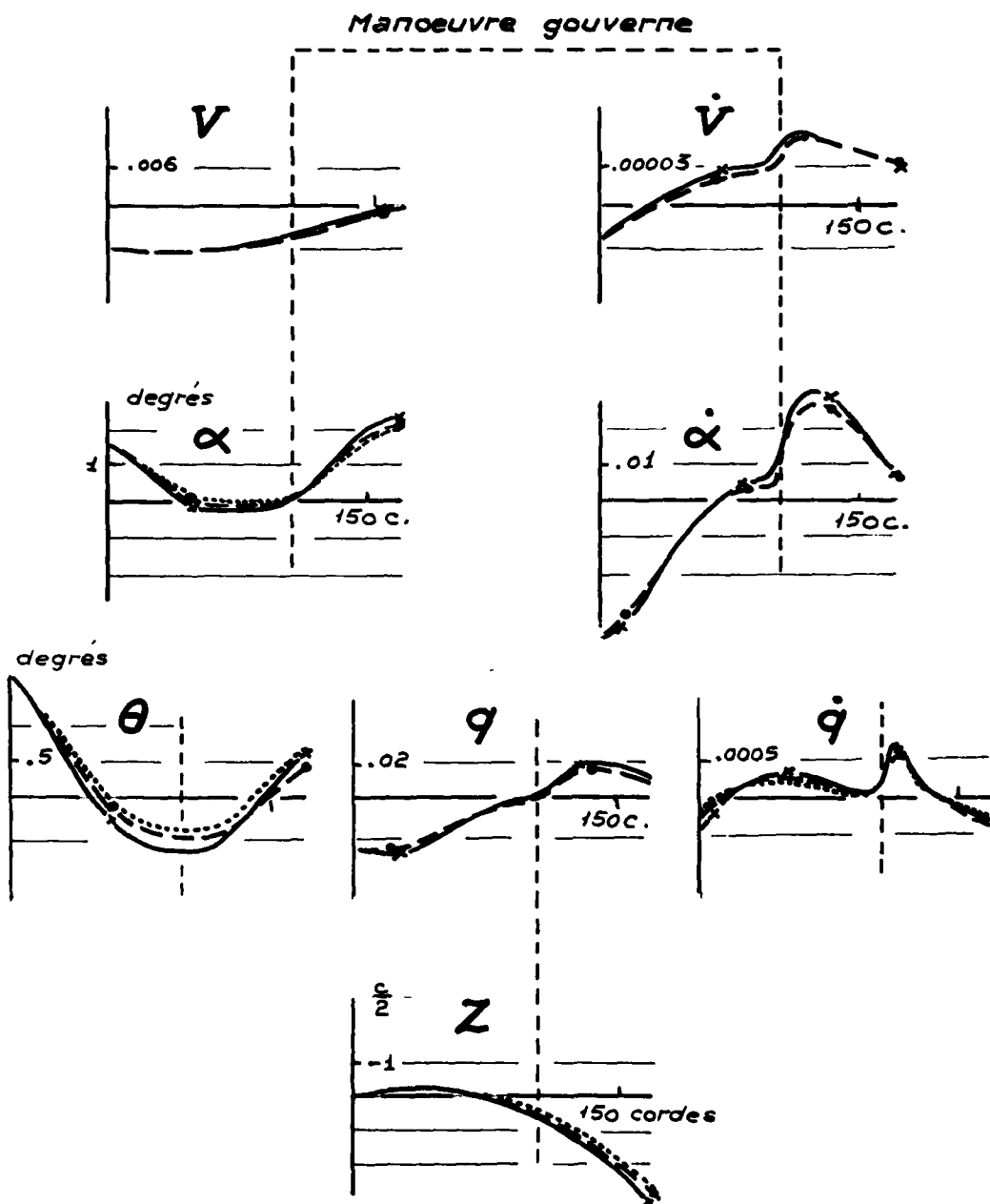
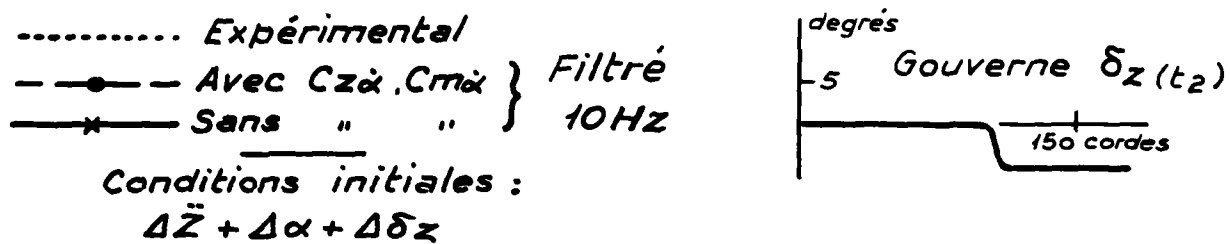


Fig. 21 - RESULTATS DE L'IDENTIFICATION

Fig. 22 - EFFET DE $Cz\dot{\alpha}$ ET $Cm\dot{\alpha}$

NEW NASA-AMES WIND-TUNNEL TECHNIQUES FOR STUDYING AIRPLANE SPIN AND TWO-DIMENSIONAL UNSTEADY AERODYNAMICS

Gerald N. Malcolm and Sanford S. Davis
Ames Research Center, NASA, Moffett Field, California 94035, U.S.A.

SUMMARY

Two new wind-tunnel test apparatuses have been developed at NASA-Ames Research Center. The first is a rotary-balance apparatus to be used in the Ames 12-Foot Pressure Tunnel for investigating the effects of Reynolds number, spin rate, and angle of attack on the aerodynamics of fighter and general aviation aircraft in a steady spin motion. Angles of attack to 100° and angles of sideslip to 30° are possible with spin rates to 42 rad/s (400 rpm) and Reynolds numbers to $30 \times 10^6/\text{m}$ with typical model wing span of 0.7 m.

The second apparatus provides capability for oscillating a large two-dimensional wing (0.5-m chord, 1.35-m span) instrumented with steady and unsteady pressure transducers in the Ames 11- by 11-Foot Transonic Wind Tunnel. The wing and pushrods, which are mounted in a splitter plate arrangement and connected to hydraulic actuators, are constructed of a low-mass high-strength carbon graphite-epoxy material. This allows the system to be oscillated at high reduced frequencies (to 0.30) and Reynolds numbers (to $25 \times 10^6/\text{m}$) at transonic speeds with oscillation amplitudes to $\pm 2^\circ$ around mean angles of attack to 12° . A complete description of both apparatuses, their capabilities, and some typical wind-tunnel results are presented.

1. INTRODUCTION

The National Aeronautics and Space Administration's Ames Research Center has begun basic experimental research programs to assess and understand (1) the aerodynamic behavior of airplane configurations at high angles of attack (Ref. 1) with emphasis on determining Reynolds number effects on a spin motion and (2) the unsteady aerodynamics of two-dimensional wing sections at transonic speeds. Each of these two areas of research has required development of a new and rather complex apparatus for performing tests in large-scale wind tunnels.

The first of these, for the purpose of investigating airplane spin aerodynamics, is an advanced rotary-balance apparatus to be used primarily in the Ames 12-Foot Pressure Tunnel; a five-atmosphere facility capable of attaining Reynolds numbers to $30 \times 10^6/\text{m}$. Exploratory rotary-balance experiments (Refs. 2,3) on a research airplane-type model have shown significant effects of Reynolds number, angle of attack, and spin rate on the aerodynamic characteristics. In some cases hysteresis effects in the nose side force with change in spin rate were observed. For example, Fig. 1 shows a sample of results from Ref. 3 on the "flat spin characteristics" at three Reynolds numbers of a simple model with a forebody shape consisting of a square cross section with radiused corners and hemispherical nose. The forebody side-force coefficient is shown as a function of the reduced spin rate where the reference length, b , is 0.46 m. The important features to note are: (1) the nonlinearity with spin rate, (2) the strong dependence on Reynolds number, and (3) the significant hysteresis effect typical of the intermediate Reynolds numbers. This hysteresis phenomenon occurs as a result of the flow-separation characteristics on the forebody section as the rotational speed is increased and then decreased.

Even before the exploratory experiments were conducted, it had been recognized that in order to efficiently test aircraft models at many different combinations of angle of attack and sideslip in a pressure tunnel, a new improved apparatus would have to be built. It must have larger load capability to accommodate larger models, and, most importantly, it must have the capability to change model attitude remotely. In response to this need a new advanced rotary-balance apparatus has been under development at Ames and is nearing final checkout prior to the first wind-tunnel test. The available combinations of model size and maximum rotation rate of the apparatus will result in a reduced spin-rate parameter consistent with most full-scale spin motions.

Unsteady aerodynamics at transonic speeds is also a critical research area. While computational capabilities have improved considerably, there has been an obvious lack of experimental data with which to compare results. A new experimental apparatus to test two-dimensional wing sections at transonic speeds undergoing both oscillatory pitching and heaving motions has also been under development at NASA-Ames for some time. The apparatus has been designed to operate in the Ames 11- by 11-Foot Transonic Wind Tunnel. This is a continuous-flow tunnel with a Mach number range from 0.4 to 1.4 and total pressure range from 0.5 to 2.0 atmospheres. The purpose of the new oscillatory rig is to provide a means of oscillating large two-dimensional wing sections at high Reynolds numbers at the highest possible reduced frequencies. The apparatus was designed to have two degrees of freedom so that the center of oscillation can be placed anywhere along the chord axis. This provides motions ranging from a pure rotational oscillation to a pure heaving (plunging) motion.

The purpose of this paper is to describe the new rotary-balance apparatus and the two-dimensional oscillating airfoil apparatus. In each case the discussion will include the requirements which influenced the design and a description of the physical characteristics of the apparatus and its capabilities. Both apparatuses were tested extensively in a special test area prior to installation in the wind tunnel. The rotary-balance apparatus is still undergoing pretest checkout for entry into the wind tunnel in late 1978.

The first test in the Ames 11- by 11-Foot Transonic Wind Tunnel using the two-dimensional oscillating airfoil apparatus has recently been completed. Some representative data from the test will be described in this paper.

2. ADVANCED ROTARY-BALANCE APPARATUS

While a small rotary-balance apparatus has been very useful in performing exploratory investigations on simple airplane-like configurations (Refs. 2,3) the need has long been recognized for an improved

apparatus for efficient test operation and for providing the load capability required for large models at high Reynolds numbers. An effort has been under way at Ames for some time to design and construct a large-scale rotary apparatus for use in the Ames 12-Foot Pressure Wind Tunnel and the 11- by 11-Foot Transonic Wind Tunnel. The rotary apparatus was designed to simulate full-scale steady spin motions by use of the proper combination of rotation speed and model size. Figure 2, a plot of reduced spin rate vs free-stream velocity, indicates the region for most full-scale airplane spins of the military fighter class. A rotary apparatus with a rotational speed capability of 42 rad/s (400 rpm) with a model wing span of 0.7 m (2.3 ft) provides a reduced spin rate that encompasses most full-scale spin cases.

2.1 General Description of Apparatus

Avoiding unnecessary startups and shutdowns for model attitude changes is essential for the efficient operation of a pressure tunnel. To accomplish this, the angles of attack and sideslip are capable of being changed remotely from outside the tunnel. The rotary apparatus was also designed to accommodate models of a practical size chosen to maximize the model Reynolds number but to minimize blockage effects or interference with the model. Experiments were run in the 12-Foot Pressure Tunnel with a nonrotating model representing the blockage of the actual apparatus, but no significant effects in the airflow in the vicinity of the model were measured. The effects of rotating the large apparatus structure behind the model are as yet unknown. Figure 3 is a sketch and Fig. 4 is a photograph of the new apparatus. The angle of incidence of the model on a straight base-mounted sting with respect to the flow can be varied up to 30°. With the use of bent stings and top-mounted models, the angle of attack and sideslip can be varied to meet the required envelope of α from -30° to +100° with β ranging between $\pm 30^\circ$. Figure 5 shows the attitude envelope obtainable with the stings selected for the first series of tests, including a base-mounted straight sting ($\alpha_s = 0^\circ$) and two top-mounted bent stings ($\alpha_s = 45^\circ$ and 70°). The angle of attack and sideslip variation is accomplished through rotation about two axes (ϕ_1 and ϕ_2 shown in Fig. 3) which intersect the spin axis at a point on the model coinciding with the center of gravity position of the full-scale free-flight vehicle. Changes in model orientation are made remotely with small electric motors mounted in the apparatus prior to spinning the whole assembly in the tunnel. The counterweight assembly is driven to some predetermined position that statically balances the mass distribution of the system about the spin axis. No attempt is made to balance the system dynamically because of the complexity of moving ballast both longitudinally as well as laterally. The alternative, of course, is to build the apparatus and support system strong enough to accommodate the large rotating dynamic moment associated with the unsymmetrical mass distribution. Once the sting and counterbalance arms are positioned the entire apparatus can then be rotated in the wind-tunnel airstream using a servo-controlled hydraulic drive system that can be varied in speed between zero and 42 rad/s (400 rpm) in either a clockwise or counterclockwise direction.

2.2 Model

Figure 6 shows the first model to be tested, a 0.05 scale F-15 fighter, mounted on each of the stings. Figure 7 is an assembly sketch of the model, balance, and the 70° top-mounted sting. A special solid, six-component strain-gage balance was built for this model to optimize the load capability and to avoid modifying the top of the borrowed model to accommodate a standard balance. The model is presently capable of manually set control deflections in the horizontal tails only. It is planned to also include the capability for setting aileron and rudder control deflections in the near future.

2.3 Instrumentation

Electrical leads to the power positioning drive systems and the power and signal paths from the balance are provided by a slip-ring assembly mounted in the circular housing near the strut mount. This is a low-level signal slip-ring unit containing 84 channels which provides adequate signal paths to run two six-component strain-gage balances simultaneously (nose and tail sections could be mounted on separate balances, for example) in addition to providing for remote changes in model control deflections. If needed, an angle encoder to accurately determine position information about the spin axis is mounted on the rear of the slip-ring unit. A tachometer is mounted on the hydraulic drive motor to determine spin rate. Initially, most experiments will be conducted with the spin axis parallel to the wind stream which will result in a steady force output from the balance at any given rotational speed. The possibility exists, however, that by inclining the rotational axis to the wind stream, say 3° or 4°, one can produce oscillatory force variations that, if measured and interpreted properly, might provide information on damping derivatives. This method of obtaining damping data in lieu of a forced oscillation apparatus is being examined.

2.4 Pretest Setup

Efforts are progressing to check out the operation of the entire system on a special test stand shown in Fig. 8. Because of the large dynamic moment produced by the apparatus, the mount must be very substantial. Also in order to avoid the risk of damaging the model should something fail in the initial rotating tests (since all the components of the system are new, including the stings and balance), a dummy model was built. It is a simple "dumbbell shape" with a center cylinder approximately 0.6 m in length and large enough in diameter to accommodate the balance and with larger diameter cylinders at each end. The total weight and longitudinal and axial moments of inertia are identical to the actual model. Initial tests have been conducted with the dummy model mounted on the rig with the strain-gage balance hooked up to the data acquisition system. Overall, the operational characteristics of the apparatus appear to meet the requirements. Early tests revealed a problem in a bearing retainer ring which was being overstressed at high-rotation rates, and eventually failed. Repairs were made with a redesigned retainer, and the apparatus is now in operation again.

To minimize wind-tunnel occupancy time, most of the measurements of rotating model inertial force and moment tares will be conducted outside the tunnel on this test stand. Only isolated checks will be made on the tares once the model and apparatus are installed in the tunnel. The first wind-tunnel test using the new rotary-balance apparatus will investigate the spin aerodynamics on a model of the advanced high-performance military fighter configuration shown in previous figures. Results from these tests, when completed, will be reported with emphasis on the more interesting aerodynamic phenomena that occur with

Reynolds number variation. In addition, the data will be used in a NASA study as input data for flight history calculations of spin motions which will be compared to actual flight histories of both subscale and full-scale flight tests of the same configuration. If results of these comparisons indicate that the flight motions calculated on the basis of aerodynamic coefficients measured in the wind tunnel are reasonably close to matching those experienced in actual flight, then one can hope to calculate flight histories for other aircraft by using appropriate rotary-balance data.

3. TWO-DIMENSIONAL OSCILLATING WING APPARATUS

Rapid advances in computational techniques have made it possible to compute the unsteady aerodynamics of oscillating airfoils using a variety of governing equations. Until recently, analytical and numerical solutions were only available for incompressible flows (analytical solutions based on the Theodorsen function) and linearized compressible flows (numerical solutions based on the Possio integral equation). Today, solutions are available for a relatively complete spectrum of equations including the Euler equations, the full potential equation, the small-disturbance transonic equation (low-frequency approximation) and the linearized small-disturbance transonic equation. For two-dimensional flows, only the effects of viscosity are lacking. It would be of great value to have experimental data to compare with these computations.

The only detailed experimental data which are available are the results of the recent NLR (National Laboratory for Research, Netherlands) investigations (Ref. 4). These tests proved to be invaluable for their physical insights into the complex flow fields surrounding oscillating airfoils. For subsequent investigations, however, it would be desirable to obtain data at higher Reynolds numbers, more favorable ratios of chord/wind-tunnel height, and more general airfoil motions than were possible with the NLR investigations. Due to the wide operating range of the Ames 11- by 11-foot Transonic Wind Tunnel, this facility was chosen for the installation of a new two-dimensional pitch-plunge apparatus for the study of oscillating airfoils.

Two airfoil sections were examined in the first series of tests. A NACA 64A010 laminar-flow symmetrical airfoil was tested to obtain unsteady aerodynamic data to compare with the numerical computation of Magnus and Yoshihara based on the Euler equations of motion. A NLR 7301 supercritical airfoil section was tested to obtain unsteady aerodynamic data to compare with experiments at NLR.

3.1 General Description of Apparatus Hardware

The selection of model size and ultimately the arrangement of the apparatus and the two-dimensional flow channel in the 11- by 11-foot Transonic Wind Tunnel was based on the choice of an acceptable ratio of wing chord to wind-tunnel height (greater than 6). The lowest hardware cost and tunnel blockage could be obtained with a model spanning the tunnel, but it was obvious that construction of a full-span 0.5-m-chord model was impractical since high priority was placed on obtaining maximum oscillatory frequency and on minimizing aeroelastic effects. A choice was then made of an acceptable span-to-chord ratio of approximately 3 yielding the 1.35-m-model span. This choice dictated the use of the splitter-plate test channel arrangement as shown in Fig. 9. Although previous two-dimensional investigations have utilized splitter plates (e.g., Ref. 5), a preliminary test of this concept was conducted in the Ames 2- by 2-foot Transonic Wind Tunnel which demonstrated that good quality flow could be obtained (Ref. 6).

Figure 9 shows a sketch of the wing splitter-plate actuator system as installed in the wind-tunnel test section. The normal test section, which is 3.4 m \times 3.4 m, is segmented with two splitter plates 3.4 m high by 2.8 m long. In order to minimize blockage effects, the thickness was the minimum that could be used to accommodate adequately sized push-pull rods. In order to prevent excessive deflections of the splitter plates, side struts were added to provide lateral support. The splitters extend into the tunnel's plenum area at the top and bottom where they are bolted to I-beam anchors. Access panels for the instrumentation cables and four slots for the push-pull drive rods are included in the splitter plate.

The wing model, which is instrumented near the midspan and attached to independently-controlled hydraulic actuators through push-pull rods, is free to pitch and plunge in response to the actuators' command signal. The wing is restrained in the fore-aft direction by a pair of carbon-epoxy drag rods, and in the lateral, roll, and yaw directions by sliding cover plates which move with the wing on the inner surface of the splitter plates. The hydraulic actuators, located in the lower plenum area, are supported by flexures and bear directly onto a massive concrete foundation through the four support columns. With this design, the tunnel pressure shell does not have to support the oscillatory reaction loads due to the actuator's motion.

The capabilities of the test apparatus include sinusoidal oscillations over a frequency range of 0 to 60 Hz, with the maximum angle-of-attack oscillation varying from $\pm 2^\circ$ at low frequencies to $\pm 0.8^\circ$ at 60 Hz around any point along the chord axis from $-\infty$ to $+\infty$, and a vertical displacement in heaving motion up to ± 5 cm (2 in.). The mean angle of attack is manually adjustable from -5° to $+15^\circ$.

The various components that make up the system just discussed will now be described in more detail since the basic performance requirements dictated state-of-the-art design in many cases. Many of the components which will be described can be seen in the photograph in Fig. 10 which shows the system installed in the tunnel, and in the photograph in Fig. 11 which shows the basic system set up on a test stand to be discussed later. In the following description it may be helpful to refer to these photographs to visualize the various components and their interrelationship.

3.2 Detailed Description of Apparatus Components

3.2.1 Splitter Plates

Vertical splitter plates with trailing-edge flaps and horizontal side struts form the support structure for the wing and connected apparatus (see Fig. 10). They each have a sharp leading edge and a movable trailing-edge flap which is manually adjustable between $\pm 2^\circ$ from the plane of the splitter plate.

All testing has been done with the flaps at 0° . Horizontal side struts (see Fig. 12) attach to the outside of the splitter plates just below the vertical center and protrude through the test section wall to the exterior tunnel structure. They provide stabilization for the splitter plates and eliminate any excessive deflection in the lateral direction due to aerodynamic loads. The splitter plates are installed with a 0.1° diverging angle from tunnel centerline to account for boundary-layer growth. The thickness of the splitter plates varies along the length (i.e., in the streamwise direction). Following the sharp leading edge the next immediate section is 0.032 m thick and is followed by a 0.05-m thick section in the center to accommodate the push-pull rods. The trailing-edge section is 0.044 m thick and tapers to a sharp trailing edge. The inside surface of the splitter plate is straight with the variations all taking place on the outer surface.

There are openings (Figs. 12 and 13) in the splitter plate to attach the wing to the top of the push-pull rods which are centered in the four channels cut in the splitter plates. In order to seal these openings when the wing is oscillating, sliding covers (Fig. 14) are attached to the wing end plates and slide with the wing on the inside surface of the splitter plate. These are also made from graphite-epoxy to reduce weight and are teflon lined to slide freely.

The splitter plates and trailing-edge flaps contain a total of 130 pressure orifices distributed over the inside and outside surfaces of both plates. The inside orifices are utilized to select the proper channel Mach number and the outer ones, in conjunction with the inner ones, are used to monitor the loading on the splitter plates. While testing, accelerometers are mounted on the trailing-edge flaps to sense any large or potentially destructive flutter motions on the flaps or main splitter plates such as might be produced from the oscillating flow behind the wing or naturally induced from the channel air flow.

3.2.2 Wing and Push-Pull Rods

The wing model is mounted between the splitter plates and is connected to the push-pull rods through flexure bearings. The rods are in turn screwed directly into the actuator pistons. Both the wing and the push-pull rods are fabricated from a lightweight graphite-epoxy material. The 1.35-m span by 0.5-m chord wing is designed to withstand a $2.3 \times 10^3 \text{ m/s}^2$ (230 g) acceleration and a 44,000 (10,000 lb) aerodynamic load. Figure 14 shows a photograph of the NACA 64A010 wing model. The push-pull rods, which are 0.0412 m in diameter, are each capable of a 22,000 N (5000 lb) tension load. The flexures located between the push-pull rods and the wing are also designed for a 22,000 N (5000 lb) load and are strain-gaged to provide a direct measure of the lift load on the wing. A pair of graphite-epoxy rods mounted to the wing with a flexure support and attached to the splitter plates forward of the wing provide a means of counteracting the drag loads (see Fig. 12). These are capable of withstanding 6700 N (1500 lb) each.

The wing is instrumented with as many as 41 static pressure orifices and 41 dynamic pressure transducers. They are all located approximately at midspan. Static pressure tubes are routed from the end of the wing (see Fig. 12), down through a cavity in the splitter plate to the tunnel plenum chamber, and out an access port to scanivalve/transducer units located outside of the tunnel shell. Dynamic transducers are mounted in the wing by inserting the transducer (2.36 mm in diameter) in the end of a long plastic sleeve which is in turn inserted into a cylindrical channel molded into the interior of the wing. The channel terminates at the center of the wing at an orifice communicating to the wing surface. The transducer wires are then routed out the end of the wing (see Fig. 13) through the splitter plates and out through the tunnel walls to the data acquisition equipment in the tunnel control room. A single reference pressure tube from each dynamic transducer is also inserted into the plastic sleeve and routed through the splitter plate to the scanivalve/transducer assembly outside the tunnel. The dynamic reference pressure can be selected to be the static pressure of the adjacent static orifice on the wing or any other selected pressure (such as the tunnel static pressure). Six accelerometers have also been mounted inside the wing, one at each of the attachment points of the four push-pull rods near the corners of the wing and two at the midspan near the leading and trailing edges. The actual motion of the wing can be determined from the accelerometer output and compared to the output of the motion transducers located in the actuator piston rods which will be discussed next.

3.2.3 Motion Generators

The servo-hydraulic actuator system was custom designed and built to the specific requirements for these tests. It is driven by two 11 kW (150 HP) hydraulic pump units rated at $4.1 \times 10^{-3} \text{ m}^3/\text{s}$ (65 gal/min) at $20.7 \times 10^6 \text{ N/m}^2$ (3000 psi). Each of the four actuators consists of two separate pistons on a single rod enclosed in a dual chamber cylinder. The upper piston is used for generating dynamic forces, the lower piston for load biasing. The load bias system is necessary to support the mean aerodynamic lift load, thereby reducing the power required to drive the dynamic piston. As static bias requirements change, the servo-valve system responds to maintain the required force output. Velocity and position transducers are combined into a single physical unit with coils and cores aligned axially for mounting in the center of the actuator.

3.2.4 Pretest Setup

Since every part of this system was new, and there was no test information available to judge the performance and reliability of the apparatus, a special pretest facility was built to permit a detailed check-out program. Many of the components including the wing, push-pull rods, drag restraints, and the hydraulic actuator motion generator system are new designs and would not be a satisfactory risk in the wind tunnel without pretest experiments. A special test stand was built for system verification. Figure 11 is a photograph of the assembly in the test area. A support structure was constructed to which the various components were attached. The hydraulic actuators were mounted at the base with the push-pull rods attached to the top of the pistons. The wing was mounted on the push-pull rods with flexures and angle-of-attack blocks between the rod end and the wing end cap. The drag restraint was fastened on top of the rear flexures and the other end tied to the support frame. Lift loads were simulated by an inflatable bag between the lower surface of the wing and a support cradle fastened to the support stand. Drag loads were simulated by a pneumatically activated piston coupled to cables and straps looped over the wing. A nearly complete envelope of test conditions could be evaluated on the test stand. In the early stages of the

test checkout a wing constructed of fiberglass (shown in Fig. 11) was used before risking the graphite-epoxy test wing. This proved to be an extremely valuable and low-risk method of evaluating the performance of the entire system. The only real limitations were that the fiberglass wing was not stiff enough to prevent large deflections at midspan (particularly in heaving) at frequencies above 30 Hz, and was not strong enough to accept the maximum lift loads. A limited amount of testing was done with the carbon-epoxy wing before installation in the wind tunnel.

3.3 Data Acquisition System

In the past, multichannel unsteady aerodynamic data were acquired with analog tape recorders. Raw data were recorded and stored for future analysis. On-line analysis was restricted to a few selected channels using special purpose "boxes" to extract limited usable data from the great mass of incoming data. These systems suffered from long time lags between acquisition and analysis and the high probability of unknowingly recording spurious data. In the present test a new computational data acquisition and analysis system was developed for on-line display of steady and unsteady aerodynamic data. Figure 15 depicts the main elements of the new system. It has the capability of graphically displaying the first-harmonic pressure distribution (both magnitude and phase) due to arbitrary pitch-plunge motions of the airfoil along with the conventional static pressure distribution. At the user's option, an overlay of selected theoretical or experimental pressure distributions from computer-resident codes or from a dedicated data bank can be accessed.

The system is centered about a Data General Eclipse minicomputer, a high speed (500 kHz) multichannel analog-to-digital converter, a large capacity (92 Mbyte) storage device, and a graphics terminal. The software system consists of approximately 50 independent Fortran-coded programs which are controlled by two executive programs: one for dynamic data, the other for static data.

3.3.1 Dynamic Data Acquisition

The same sinusoidal signal generator that drives the four-channel hydraulic actuator system, which in turn drives the four push-pull rods attached to the wing, is also used to trigger a pulse to initiate the unsteady data acquisition process. Once the actuator control system is adjusted to impart the desired pitching and/or heaving motion to the wing, the motion of the four push-pull rods is continuously monitored and is acquired along with the unsteady pressure data.

The dynamic signals from 41 miniature pressure transducers are amplified and filtered before entering the analog-to-digital converter. Since the signal is periodic, it is possible to obtain good waveform samples with minimum storage per data point by signal-averaging the data. Theoretically, a periodic signal is completely defined by just one cycle of data (e.g., a 40 ms record is all that is necessary to characterize a 25 Hz periodic oscillation). However, the experimental signal is usually so contaminated by random pressure fluctuations due to wind-tunnel and model-induced turbulence that one cycle of data is not very useful.

The signal-averaging technique is implemented as follows: the raw data is synchronized with a pulse train which is triggered at the same phase position for each cycle of the airfoil's motion. These timing relations are shown in Fig. 16. At time t_0 , the sample waveform is recorded for τ seconds. At time $t_0 + n\tau$ the waveform is recorded again for τ seconds. The process is repeated M times. These M samples, each being initiated by the phase-locked pulse, are then ensemble averaged to obtain the averaged signal. In the current experiment τ is chosen to be slightly greater than one period, $n = 2$, and $M = 100$ is sufficient for a good average. At the user's option, the signal averaged waveform and the M th realization for any selected channel can be displayed on the graphics unit.

For on-line analysis, the first harmonic of the response is most useful. A simple Fourier analysis algorithm is implemented to extract the magnitude and phase information at the fundamental frequency. These data are displayed in tabular form on the graphics unit within 30 sec of the termination of data acquisition. This amount of data is usually sufficient to determine if the unsteady data acquisition process was successful. If more on-line analysis is required, the first-harmonic data may be displayed graphically in pressure coefficient form. The magnitude and phase of the chordwise pressure distributions on the upper and lower surfaces of the airfoil are displayed along with certain theoretical curves. The software package currently includes two theoretical options: (1) linear, incompressible small-disturbance theory (Theodorsen function) and (2) linear, compressible small-disturbance theory (Possio integral equation). For time-efficient on-line analysis it does not seem feasible to include unsteady transonic codes on the current generation of minicomputers.

Also available for comparison are the results of other investigations (theoretical and/or experimental) which have been stored in the data bank. For comparing with NACA 64A010 data, the theoretical investigations of Magnus and Yoshihara are available. For the NLR 7301 wing, experimental data obtained at NLR-Amsterdam are available. It is possible to obtain a comparison between the current data and the selected theoretical/experimental overlay in approximately 45 sec after the termination of data acquisition.

3.3.2 Static Data Acquisition

The static pressures are sensed with a conventional system using pneumatic tubing connected to a pressure scanning valve. The electrical output of the pressure cell to which the unknown pressures are multiplexed are read with a digital voltmeter whose BCD output feeds directly into the minicomputer.

The splitter-plate arrangement used for the oscillatory airfoil test requires special attention with regard to the free-stream Mach number (M_∞). As discussed in a previous report (Ref. 6), the Mach number in the channel between the plates is not the same as computed from a static pressure tap in the plenum chamber. In order to obtain the approach Mach number, the splitter plates are equipped with approximately 130 static pressure orifices distributed among 10 rows above and below the plane of the wing on the inner and outer walls of the splitter plates. These pressures are also sensed by the scanning system. The

computed Mach numbers on the splitters are displayed on the graphics unit and the approach Mach number is selected interactively by fairing the graphics unit's horizontal cursor to the data. Using this procedure, the Mach number can be selected to ± 0.002 . Once the Mach number has been chosen, the static pressure distribution is displayed along with selected overlays. A static pressure distribution with overlays can be displayed in approximately 30 sec after the raw data have been acquired.

3.4 Representative Data from the Oscillating Airfoil Test

Steady and unsteady pressure distributions were measured on two airfoils: (1) a NACA 64A010 and (2) a NLR 7301 supercritical. The purpose of the NACA 64A010 tests is to compare the measurements with numerical solutions to the inviscid Euler equations obtained by Magnus and Yoshihara. These calculations were made under AFFDL (U.S. Air Force Flight Dynamics Laboratory, Wright-Patterson AFB, Ohio) sponsorship and were made available to NASA under the terms of a joint NASA-AFFDL cooperative program on the measurement and analysis of unsteady transonic flows. The measurements on the supercritical airfoil will be compared to similar measurements on a 15-cm-chord model that was recently tested at NLR-Amsterdam (Ref. 4). The NLR data were supplied to NASA-Ames under a cooperative program between NASA-Ames and the NLR. Both the NACA 64A010 and NLR 7301 comparison data were stored in the data bank for on-line comparisons with the experimental data.

For the purpose of indicating the capability of the new testing technique, some results will be shown which indicate the versatility and economy of the on-line data acquisition scheme. A comparison between the steady and unsteady (first-harmonic) calculations of Magnus and Yoshihara with the experimental data will be shown for the NACA 64A010 airfoil. The usefulness of the on-line analysis technique will be demonstrated by comparing the NLR experiments with the current experiment for the condition of shockless flow on the supercritical airfoil.

The data to be presented in Figs. 17 through 20 are copies made directly from the graphics terminal. These unedited results contain some spurious data points from plugged tubes, broken transducers, some erroneous printed results, etc., but the value of these displays for on-line analysis will be evident.

Figure 17 depicts the measured and computed static pressure distribution at $M = 0.8$ for the NACA 64A010 airfoil at zero angle of attack. The strength of the shock wave is predicted quite well by the inviscid theory. However, the measured shock position is slightly upstream of the computed position. Further analysis of the viscous effects will be made using measured data at other Reynolds numbers. The calculations do not include the effect of wind-tunnel walls, and the measurements indicate that the ratio of airfoil chord to test-section height for the current experiment was sufficiently small to preclude large interference effects due to blockage.

Figure 18 shows a comparison between the experimental and calculated first-harmonic unsteady pressure distribution. The mean conditions are those shown in Fig. 17. The model was oscillated at 33 Hz about the 0.25-chord location with an amplitude of $\pm 1^\circ$. The first-harmonic response can be expressed as the first term of a Fourier series:

$$p(x/c, t) = a_1 \cos(\omega t) + b_1 \sin(\omega t) \quad (1)$$

where p is the unsteady pressure, ω is the radian frequency, and a_1 and b_1 are Fourier coefficients. The data in Fig. 18 show the magnitude and phase of the pressure normalized by the dynamic pressure q_∞ :

$$\left. \begin{aligned} \text{mag } C_p &= \frac{1}{q_\infty} \left(\sqrt{a_1^2 + b_1^2} \right) \\ \text{phase } C_p &= \tan^{-1} (-b_1/a_1) \quad -\pi < \text{phase} \leq \pi \end{aligned} \right\} \quad (2)$$

The phase reference for the C_p data is arbitrary. The phase reference for the C_p calculations is the α motion. The phase angle for the experimental data (x) has been shifted (\ominus) so that both experimental and calculated results are keyed to the same reference.

Upstream of the shock wave (indicated by a bump in the magnitude and a large phase shift), the magnitudes agree very well. This is probably due to the fact that the mean flows agree with one another and the unsteady response is so closely tied to the mean flow. At the shock wave location the measured peak lies somewhat below the calculated value due to viscous effects. Downstream agreement is again quite good. The phase agrees quite well upstream of the shock. As mentioned above, the Euler equation calculations were made for free-field conditions. The good agreement shown here indicates that wall interference is probably not a problem. These results are typical of other comparison data between the experiment and calculations. Comparisons such as those in Fig. 18 serve as valuable baseline data for confirming the correctness of both the calculations and the experiments. Data have also been obtained at conditions beyond the capabilities of current computer codes (e.g., where strong unsteady shock wave boundary-layer effects exist).

Figures 19 and 20 depict the mean pressure distribution on the NLR 7301 airfoil for two different angles of attack. The NLR data were obtained at an angle of attack of 0.85° . This was the experimentally determined shockless condition in the NLR facility. The Ames and NLR data shown in Fig. 19 are for the same angle of attack. The presence of a shock wave on the upper surface is hard to perceive, but the overall agreement is not very good. After some trial-and-error settings of angle of attack, the best agreement was found when the Ames model was set at $\alpha = 0.37^\circ$ as shown in Fig. 20. It should be noted that the on-line analysis enabled the experiment to be successfully compared with the NLR data in approximately four min. Due to time constraints, the unsteady data from the supercritical airfoil has not yet been closely examined. A complete off-line analysis of all of the data is currently underway.

5. CONCLUSIONS

A new rotary-balance apparatus developed for use in the Ames 12-Foot Pressure Tunnel will provide rotary test capabilities for most airplane configurations at Reynolds numbers previously unobtainable and should provide a reduced spin rate that duplicates that of most full-scale spins. The first configuration to be tested in the near future will be a 0.05-scale model of an advanced U.S. fighter aircraft. Preliminary tests of the apparatus have been performed on a test stand, and results indicate that the desired capability should be achievable.

A new dynamic oscillation apparatus capable of testing two-dimensional wing sections in transonic flow with motions ranging from a pure rotational oscillation to a pure heaving motion has been developed for operation in the Ames 11- by 11-Foot Transonic Wind Tunnel and provides unsteady pressure measurements at Reynolds numbers and reduced frequencies previously unobtainable. Two airfoil sections have recently been tested, a NACA 64A010 and a NLR 7301 supercritical. Steady and unsteady pressure measurements are presently being analyzed and comparisons will be made to other measurements where possible and to various existing theoretical results. Preliminary results indicate excellent agreement between measured results and theory for steady and unsteady pressures on the NACA 64A010 section and between present measurements and NLR measurements on the supercritical section.

REFERENCES

1. Chapman, G. T., Keener, E. R., and Malcolm, G. N.: Stall/Spin Problems of Military Aircraft. AGARD Conference Proceedings No. 199, Stall/Spin Problems of Military Aircraft Flight Mechanics Specialists' Meeting, Rhode Saint Genese, Belgium, November 18-21, 1975.
2. Clarkson, M. H., Malcolm, G. N., and Chapman, G. T.: Experimental Poststall Rotary Aerodynamic Coefficients for Airplane-Like Configurations. AIAA J., Vol. 13, No. 8, Aug. 1976, pp. 565-570.
3. Malcolm, G. N. and Clarkson, M. H.: Wind-Tunnel Testing with a Rotary-Balance Apparatus to Simulate Aircraft Spin Motions. Proceedings of AIAA 9th Aerodynamic Testing Conference, Arlington, Texas, June 7-9, 1976, pp. 143-156.
4. Tijdeman, H.: Investigations of the Transonic Flow Around Oscillating Airfoils. NLR TR 77090 u, 1977.
5. Wyss, J. A. and Herrera, R.: Effects of Angle of Attack and Airfoil Profile on the Two-Dimensional Flutter Derivatives for Airfoils Oscillating in Pitch at High Subsonic Speeds. NACA RMA54H12, October 1954.
6. Davis, S. S. and Satyanarayana, B.: Two-Dimensional Transonic Testing with Splitter Plates. NASA TP 1153, Feb. 1978.

ACKNOWLEDGEMENTS

The authors wish to thank J. Olsen of the Air Force Flight Dynamics Laboratory for making available the calculations on the NACA 64A010 airfoil using the numerical solutions to the inviscid Euler equations obtained by Magnus and Yoshihara.

The authors would also like to thank H. Tijdeman of the NLR-Amsterdam for supplying the experimental data on the NLR 7301 supercritical airfoil obtained at NLR.

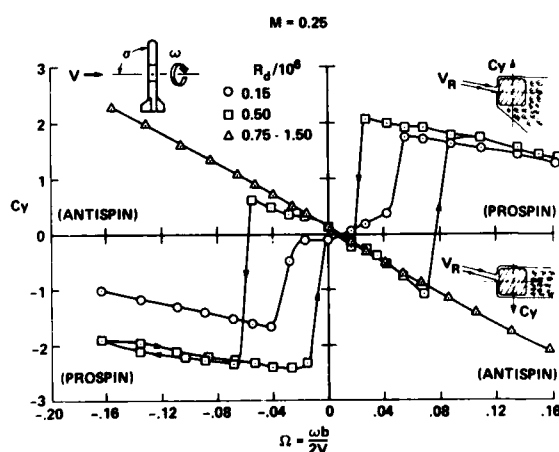


Fig. 1. Nose side force coefficient versus reduced frequency.

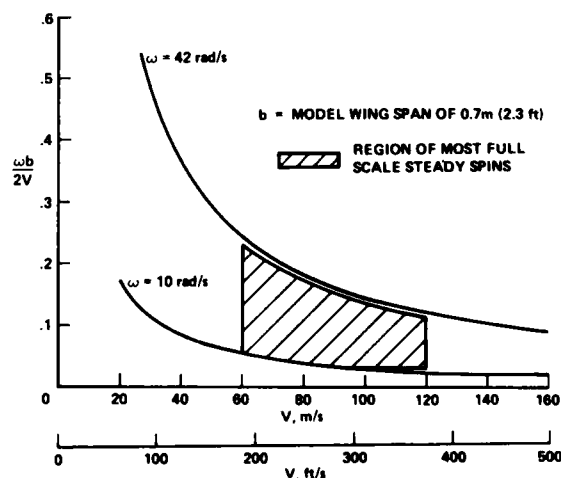


Fig. 2. Reduced spin parameter versus free-stream velocity for simulating steady airplane spins.

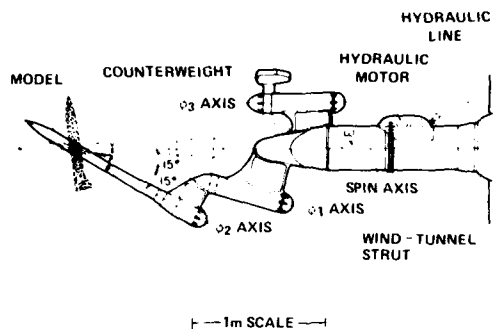


Fig. 3. Planview of new NASA-Ames rotary-balance apparatus.



(a) $\alpha_S = 0^\circ$

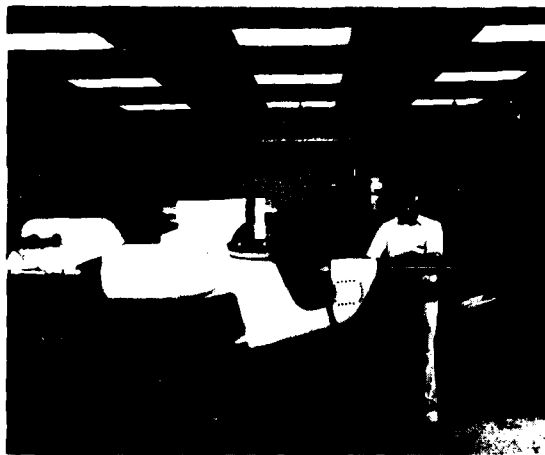


Fig. 4. New NASA-Ames rotary balance apparatus.



(b) $\alpha_S = 45^\circ$

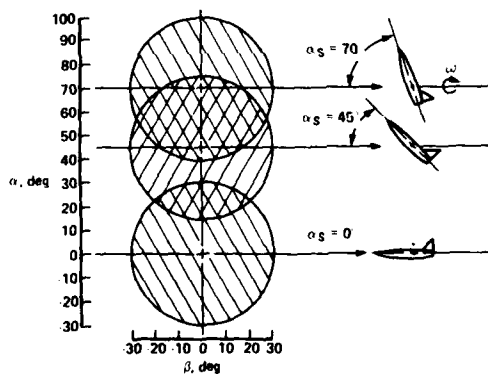


Fig. 5. Angle of attack and sideslip envelope for various sting-model angles.



(c) $\alpha_S = 70^\circ$

Fig. 6. F-15 model mounted on various stings.

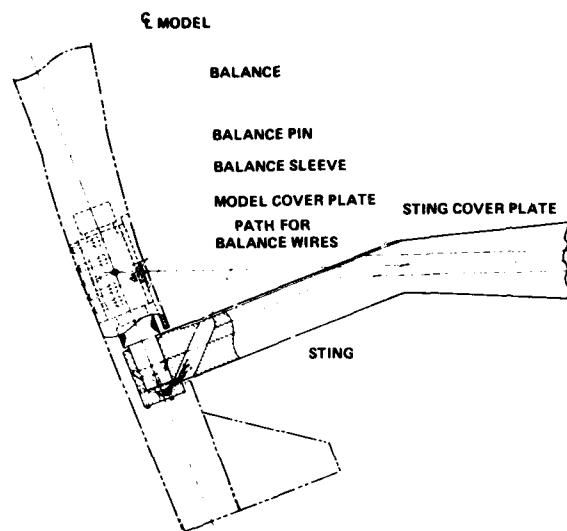


Fig. 7. Assembly of model, balance, and top-mounted sting.

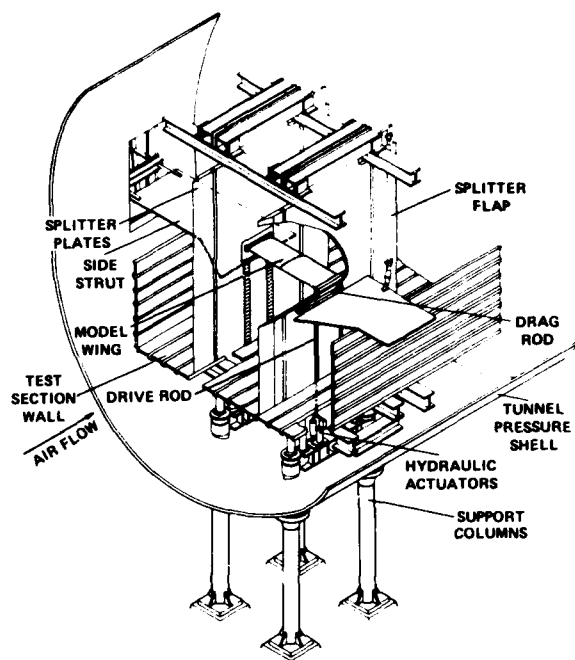


Fig. 9. Two-dimensional oscillating airfoil test apparatus installed in the NASA-Ames 11- by 11-Ft Transonic Wind Tunnel.



Fig. 8. Rotary-balance apparatus mounted on test stand.

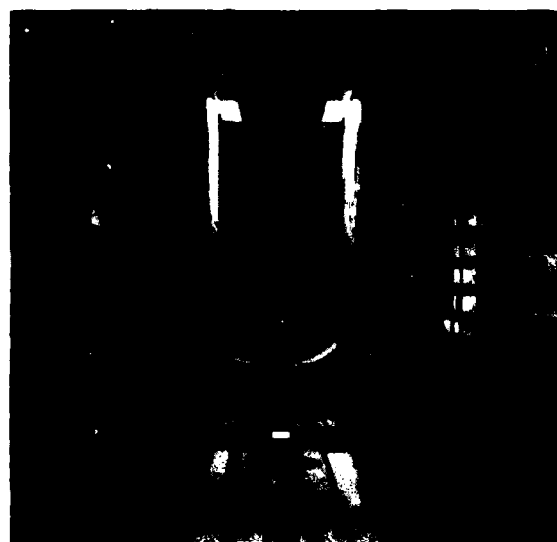


Fig. 10. Two-dimensional oscillating airfoil apparatus installed in the NASA-Ames 11- by 11-Ft Transonic Wind Tunnel.

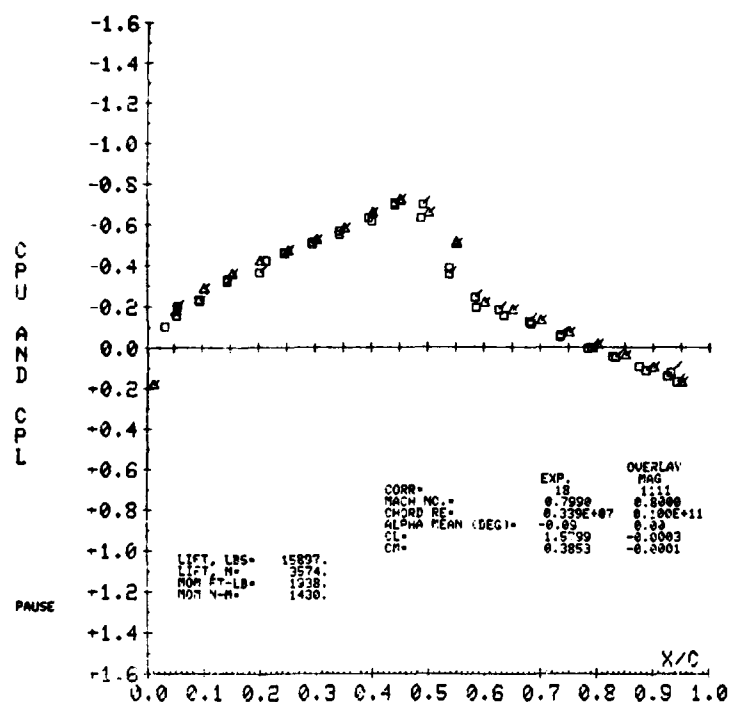


Fig. 17. Static pressure distribution on NACA 64A010 airfoil. $M_\infty = 0.8$, $\alpha = 0^\circ$. Key: Δ calculations of Magnus-Yoshihara; \square experiment, flags denote lower surface.

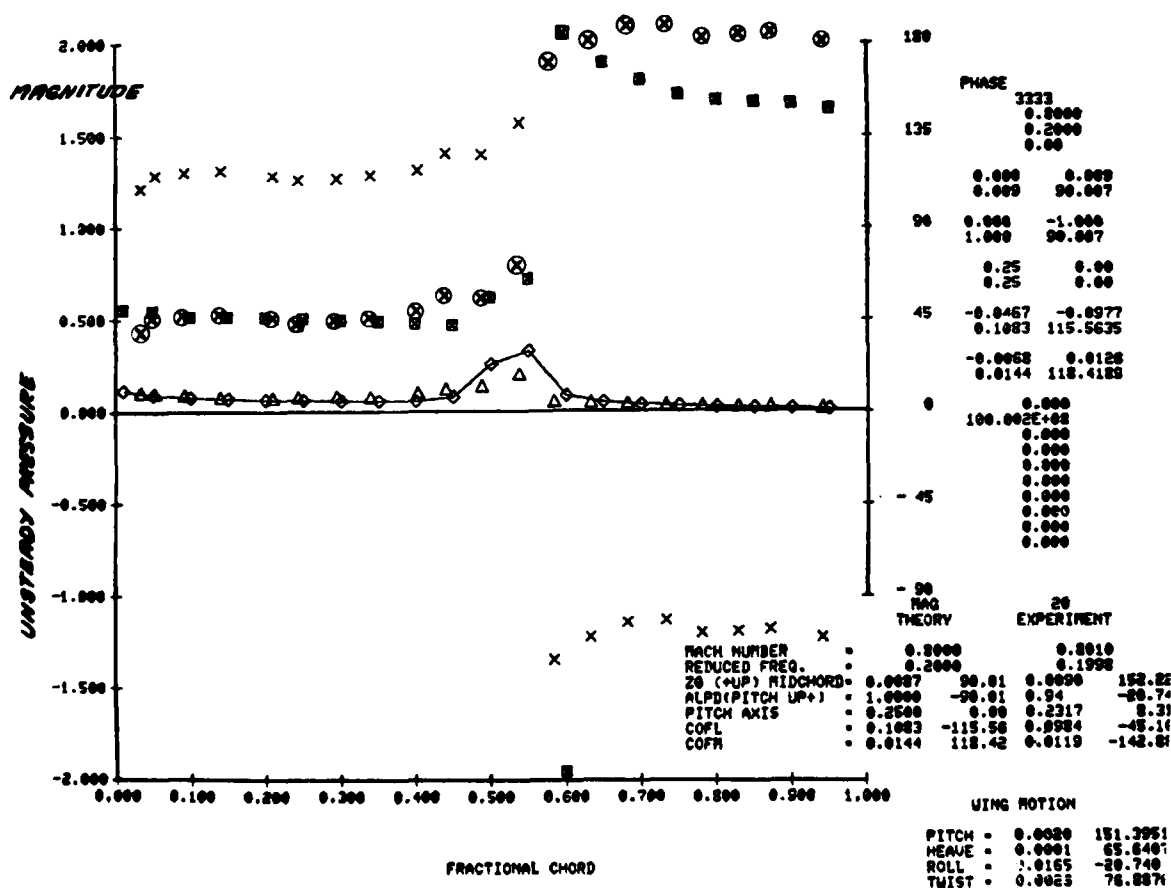


Fig. 18. Distribution of magnitude and phase for first harmonic of the unsteady pressure coefficient on upper surface of NACA 64A010. $M_\infty = 0.8$, $\alpha = 0^\circ$, $k = 0.2$, pitching $\pm 1^\circ$ @ 0.25 chord. Key: \diamond = magnitude, \square = phase of Magnus-Yoshihara calculations; Δ = magnitude, x = phase, \odot = corrected phase of experimental data.

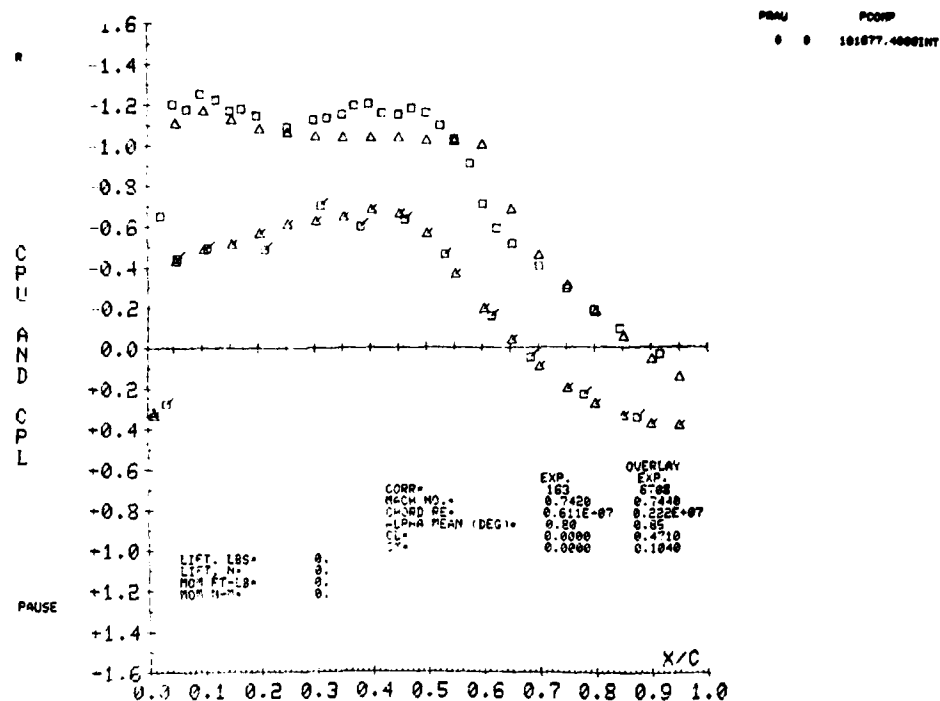


Fig. 19. Static pressure distribution on NLR 7301 supercritical airfoil. $M_\infty = 0.74$, $\alpha = 0.85^\circ$. Key: Δ = NLR experiments; \square = current experiments. Note: Flagged symbols denote lower surface.

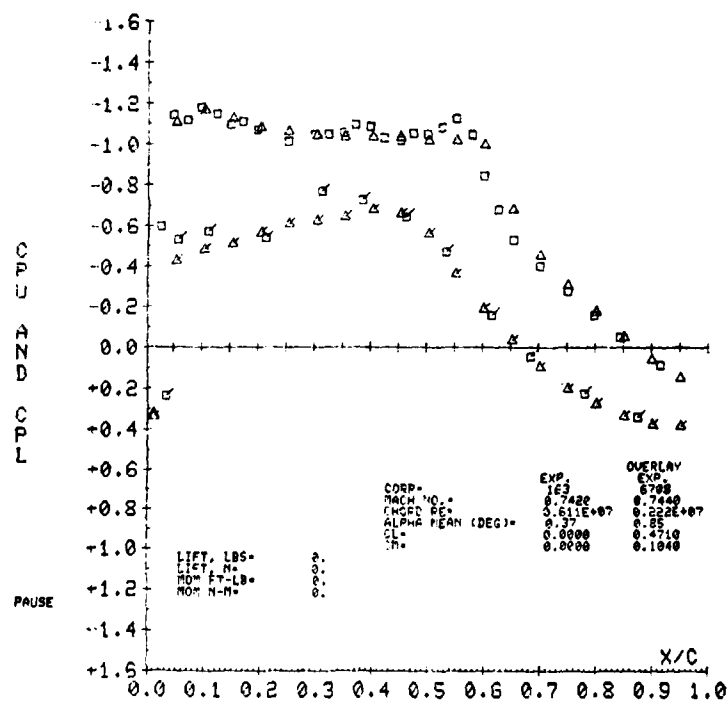


Fig. 20. Static pressure distribution on NLR 7301 supercritical airfoil showing best match between data. $M_\infty = 0.74$. Key: Δ = NLR experiments, $\alpha = 0.85^\circ$; \square = current experiments, $\alpha = 0.37^\circ$. Note: Flagged symbols denote lower surface.

EXPERIMENTAL DETERMINATION OF DYNAMIC DERIVATIVES
DUE TO ROLL AT BRITISH AEROSPACE, WARTON DIVISION

by A.W. Matthews
British Aerospace
Aircraft Group
Warton Division
Warton Aerodrome
Preston
Lancashire
PR4 1AX

SUMMARY

Two rigs for the determination of dynamic derivatives due to roll are under development at B.Ae, Warton Division. Using the principle of continuously rolling a model in a wind-tunnel about an axis parallel to the wind, they are intended to cover a test envelope up to $M = 0.95$, $R_e = 46.10^6/m$, $\alpha = 90^\circ$, $\frac{pb}{2V} = 0.25$.

One has already been used to measure derivatives on complete models at low Mach number and Reynolds number, whilst the second, designed for operation at high subsonic Mach numbers and high Reynolds numbers, is currently undergoing calibration and commissioning prior to tunnel installation. This paper describes the general features of the rigs themselves, together with the instrumentation and control systems. The problems met during design, manufacture, calibration, commissioning and testing are described, together with their solutions. Data from complete models is presented and compared with that compiled for similar configurations from flight testing and other wind-tunnel sources. It is shown that repeatability of data approaching that achievable in steady-state, six-component testing can be obtained.

NOTATION

b wing span

M Mach number

R_e Reynolds number

V Tunnel velocity

X)
Y)
Z) aerodynamic loads in body axes
L)
M)
N)

C_D)
 C_Y)
 C_L) aerodynamic coefficients in wind axes
 C_ℓ)
 C_m)
 C_n)

$$L_p = \frac{\partial C_\ell}{\partial \left(\frac{p_w b}{2V} \right)}$$

$$N_p = \frac{\partial C_n}{\partial \left(\frac{p_w b}{2V} \right)}$$

p)
q) rotational velocities about $\begin{pmatrix} 0_X \\ 0_Y \\ 0_Z \end{pmatrix}$
r)

θ_C) rig setting angles	(sting setting angle
ϕ_B		(body axis roll angle
α) incidence angles	(angle of attack
β		(angle of sideslip
ϕ_w	wind axis roll angle	
$\dot{\phi}_w$	wind axis roll rate ($\equiv p_w$)	
δ_S	slat angle	
δ_F	flap angle	

1. INTRODUCTION

Over the past few years interest in the behaviour of military combat aircraft at extreme attitudes has been growing. Although it is well-known that the relevant dynamic derivatives (e.g. M_q, L_p, N_r, N_p) are highly non-linear at anything above modest values of angle of attack and sideslip, they are also highly configuration-dependent. Since the next generation of combat aircraft will be spending a significant portion of its mission in the relevant regime, it is essential that these derivatives, and thus the behaviour of the aircraft, are known with a reasonable level of confidence prior to any flight testing taking place. Clearly, an empirical technique using models is vital as the theoretical approaches being pursued are unlikely to be sufficiently well-advanced to provide this information with any accuracy. (1,2)*

As this is a dynamic problem, any method used must impart motion to the model. For instance, the technique of oscillating a model through a small amplitude is well-known: when the accuracy of the derivatives obtained in this way is considered however, there exist doubts amongst aerodynamicists with regard to the derivatives due to roll. Other techniques such as free-flight drop models, spinning tunnels and aerodynamically-driven rotary derivative rigs are severely limited by the Mach numbers, Reynolds numbers and attitudes at which they can operate. The continuously-driven rotary derivative rig has benefits for testing large perturbation motions possessed by none of the alternatives mentioned above.

Conceptually, a rotary derivative rig is extremely simple in that all that is required is to continuously rotate a model about an axis aligned with the wind: if the axis passes through the reference centre of the model, then the motion is described at some U.S.A. establishments as 'coning', a graphic and self-explanatory term. It is then possible to measure one of the most important of the aforementioned rotary dynamic derivatives (L_p) by monitoring the input torque required to drive the rig at a steady speed. However, this apparently simple technique has severe problems and results in an extremely limited rig, no measure of any other derivative being possible. Mounting the model on a six-component, internal strain-gauge balance and taking away the signals through a slip-ring unit overcomes this restriction. Used in this way the rotary derivative rig becomes nothing more than a rather complicated sting, and as such it is little more constrained in terms of Mach number, Reynolds number and attitude than a normal sting.

At B.Ae, Warton Division, work has been concentrated on two rigs, one for use at low Mach number and Reynolds number in the 5.5m LSWT, and the other designed primarily for testing in the 1.2m HSWT at Warton, but having the capability of being used at a number of other U.K. facilities. The latter was initiated first, but, due to the problems anticipated, a 12-month feasibility study (3) was made (under the auspices of the Ministry of Defence) before detail design began, and the low-speed rig was designed and manufactured during this period. A table of the test parameters will be found on fig. 1.

2. 5.5m LSWT ROTARY DERIVATIVE RIG

2.1 Test Facility

The rig was designed for exclusive use in the 5.5m LSWT. Although now used as a general-purpose low-speed wind-tunnel (including V/STOL), it was originally built (in 1962/63) purely for V/STOL testing. This resulted in a closed working section, open return circuit tunnel with a maximum speed of 22 m/s ($M = 0.06$, $Re = 1.35 \cdot 10^6/m$). No mechanical balance was installed, all models being sting-mounted from a support system which provided height as well as angle of attack and sideslip variation.

2.2 Specification and Design Features

2.2.1 Specification

The original specification (4) covered the following:

*Figures in parentheses refer to the reference list.

angle of attack range : -45° to $+90^{\circ}$
 sideslip range : -45° to $+45^{\circ}$ (at $\alpha = 0^{\circ}$)
 $\frac{pb}{2V}$: 0 - 0.1 (as a minimum)

The last design point required a wind-axis rotational speed of about 28 rpm for the $1/6$ to $1/7$ scale models of combat aircraft that it was envisaged would be tested on the rig.

Since this was regarded as something of a precursor for the high-speed rig, the time-scale and budget involved demanded certain limitations on the complexity of the approach. Thus, neither remote change of angle of attack and sideslip (all changes being performed manually) or a full closed-loop, servo-controlled, hydraulic motor drive system were considered.

Photographs showing the rig may be found on figs. 2 and 3.

2.2.2 Incidence angles mechanism (fig. 4)

A basic angle of attack range of $0-45^{\circ}$ was achieved by moving the sting around an arc centred at the model reference centre: motion was accomplished by a pinion in the incidence carriage meshing with a rack on the quadrant: the pinion in turn was driven through a worm and wheel. To obtain -45° to 0° the model was simply rotated 180° about its body X-axis. Angles of attack greater than 45° necessitated introducing an upper surface entry sting. The normal rear entry sting was still used but a 90° adapter now connected the sting to the male joint of the balance (fig. 3). Sideslip was obtained by rotating the model about its body X-axis.

Both these motions were infinitely variable, location at the required settings being by clamps. Setting accuracy was of the order of $\theta_c = 0.1^{\circ}$ and $\phi_B = 0.5^{\circ}$, giving a similar overall accuracy for α and β .

2.2.3 Drive

Originally a 1.1 kW air-motor was used, driving the rig through a 103:1 reduction gearbox to provide a maximum rotational speed of about 30 rpm. This was later replaced by a 2.2 kW air-motor and 47:1 reduction gearbox. A maximum rotational speed of about 60 rpm could now be reached, increasing the maximum value of $\frac{pb}{2V}$ to about 0.2. Furthermore, the more powerful motor gave greater speed stability at low values of wind-axis roll rate.

2.2.4 Balancing

It was recognised during the initial consideration of both this and the multi-facility rig that balancing may provide some severe problems (5). There are two aspects of balancing, static and dynamic. Static balancing requires the system to be in equilibrium about the rotational-axis only, dynamic balancing requires equilibrium along this axis also. Because of the low rotational speed and the demand for a simple design, dynamic balancing was not considered for the 5.5m LSWT rig. So that rotational speed fluctuations could be reduced to a minimum however, static balancing was clearly a necessity.

To maintain static balance during an angle of attack traverse both the balancing mass and its radial position could be adjusted: below $\theta_c \approx 8.5^{\circ}$ the balance mass had to be moved from one end of the arc to the other. Setting-up sideslip by rolling about the model X-axis should have no effect on the balance mass or position, as long as the model itself was balanced (i.e. arranging the model c.g. to be coincident with the moment reference centre which was itself the point through which the wind-axis rolling-axis passed at all attitudes). This exercise was carried out for all models tested on the rig. In the case of the strike-fighter model shown in the photographs however, the sting was not aligned with the model X-axis (to reduce model distortion) and so, as sideslip was applied, the balance mass and/or position needed to change to maintain static balance. To alleviate this unsatisfactory situation a secondary balance mass was positioned on the sting itself, which balanced it about the model X-axis at all values of ϕ_B (shown on figs. 2, 3 and 4).

2.2.5 Control and data acquisition

The only control needed was over rotational speed, and this was achieved simply by throttling the air supply to the motor. Motor speed was read via a tachogenerator and inputted directly to the 5.5m LSWT mini-computer based acquisition system, as well as being displayed for the rig operator.

A 25-channel slip-ring unit was fitted over the drive shaft near to the quadrant (fig. 5): the large diameter necessary gave rise to fears that the high-rubbing velocity of the brushes would degrade the signal-to-noise ratio. This proved to be of no consequence whatsoever, the signal-to-noise ratio being lower than that of the complete instrumentation system (5 μ V).

The standard 5.5m LSWT data acquisition system was used, with only one modification: this was an improvement to the integration routine to enable data to be averaged over a cycle instead of a time (cyclic integration). A micro-switch provided the required pulse to start and stop the integration, the number of cycles over which integration was to take place being set-up beforehand. Integrating the data cyclically had two major benefits: the extremely unsteady data, particularly at high angles of attack, was smoothed to give repeatability approaching that of normal steady-state testing, and the need to perform gravitational tares was eliminated.

2.2.6 Data analysis

During a test on a rotary derivative rig the load on the balance has three constituents, gravitational, inertial and aerodynamic. The first (due to the model weight) is purely cyclic, and over a complete revolution its mean value is zero: thus one of the benefits of the cyclic integration described above becomes clear. Inertial loads can be determined by performing a 'wind-off', by calculation or by a combination of the two: either of the first two techniques can be used with the 5.5m LSWT rig (6). The first is straightforward and merely consists of performing, wind-off, the rotation rates to be covered wind-on: the data is interpolated by rpm to correct the wind-on data. The second technique is more complex. It is necessary to know the model attitude, rotational speed, mass, centre of gravity, and moments and products of inertia: the first two are straightforward. To determine the mass and c.g. position the balance loads at a number of attitudes (roll angles) are required under static conditions - a gravitational tare. However, three tares must be performed to determine the model inertias. The model is set-up to provide, in turn, the maximum inertial rolling moment, pitching moment and yawing moment: the rig is obviously run at its maximum speed. Data from the three tares is combined in a computer program which evaluates, using Euler's equations of motion of a rigid body, the moment of inertia differences and products of inertia. (This data was compared with that obtained for one model configuration using a classical laboratory technique (7); data correction using either set of inertias was very similar). These were input as fixed data to the data reduction program. Once the inertial load had been accounted for, the remaining load was assumed to be the aerodynamic load.

Of the two techniques, that of using an inertial tare and interpolating has proved to be rather more accurate for the moments, and significantly so for the forces, and is now used for all 5.5m LSWT rotary derivative rig tests.

2.3 Calibration and Commissioning

2.3.1 Calibration

To statically balance the rig it was mounted on knife edges, one supporting the drive shaft, the other supporting a special calibration fixture replacing the balance. It is now considered that this was not ideal due to the inevitable deflection of the rig being in a different sense to that occurring when the rig was mounted in the tunnel: a somewhat different technique will be used with the multi-facility rotary derivative rig (see section 3.3).

The rig was physically balanced at every $\theta_c = 5^\circ$, except in the range 7° to 10° , where the increments had to be smaller due to the balancing requirements approaching zero. A polynomial fit to the data was made, resulting in a table of balancing masses and positions for every $\theta_c = 0.1^\circ$.

Once in the tunnel angular and translational deflection calibrations were performed, giving two deflection matrices, subsequently used to correct model attitude and inertial loads.

2.3.2 Commissioning

With no regard having been paid to dynamic balancing, the rigidity of the system (particularly the tunnel support which was known to lack stiffness in yaw) under rig rotation was a subject for some speculation. At 30 rpm and $\alpha = 35^\circ$ some oscillation of the support system was visible: the bracing to the tunnel walls (fig. 2) eliminated this completely and allowed operation up to 45° angle of attack. Above 30-35 rpm some twisting about the tunnel yaw axis became noticeable, but an extra brace between the motor and tunnel support reduced this to an acceptable level, and allowed safe operation up to $\phi_w = 50-55$ rpm.

Some variation in rotational speed over a single revolution was noticeable at very low speeds (less than 6 rpm, or $\frac{P_w b}{2V} \approx 0.02$) of about $\pm 8\%$. By 20 rpm this reduced to better than $\pm 1\%$. As has been mentioned earlier, considerable attention was paid to balancing both rig and model, so the effect of rig deflections was clearly important at these low speeds. However, the technique of integrating the data over a cycle had the effect of nullifying this and producing good, repeatable data at all speeds (see section 2.4.2).

2.4 Test Performance

It became necessary to validate this technique of obtaining rotary derivatives in two stages, the second stage being to check the benefits gained by the introduction of a number of improvements recommended as a result of the first test phase.

2.4.1 First test phase

A lightweight fuselage shell was specially built for use on this rig, based on a current strike-fighter: comparison of rig data with flight test data up to moderate angles of attack ($\alpha = 20^\circ$) was therefore possible, and this would determine the satisfactory nature of the technique, or otherwise. Prior to testing, the model was carefully balanced (2.2.4). Due to having to employ existing wings which were much heavier than the ideal, the amount of balancing weight was rather excessive: together, these two factors made the model somewhat heavier than anticipated - this is commented upon later. Immediately following this the moments and one product of inertia were measured by oscillating the model about its various axes, on knife edges. At this stage the instrumentation system had not been modified to provide cyclic integration: since time integration could not usefully be employed, instantaneous data points had to be taken. It was thus necessary to know the roll angle at which the data was taken, in order that the load on the balance could be corrected for the gravitational term. To determine the correction required, a 'gravitational tare' run had to be performed prior to each run: this was extremely time-consuming.

Furthermore, the technique of taking instantaneous data points meant that, under unsteady flow conditions, there would be a large problem of repeatability, and it would be necessary to take more than one data point at each condition (an example of the time-based output of one channel - rolling moment - under steady-state conditions is shown on fig. 6).

A further source of potential error, common to all rotary derivative rig testing and worth mentioning at this stage, is that of the strain-gauge balance load range. The ideal balance for low-speed rotary derivative rig work requires a load range combination totally unlike that for normal six-component testing. For example, the forces are dominated by the need to support the model weight, and so they must all be of the same order. This inevitably results in a degradation of the resolution of aerodynamic forces X and Y, which are generally small anyway. Although they have no gravitational components (as long as the model is balanced) rolling moment, pitching moment and yawing moment will have significant inertial contributions.

The balance used for all testing of the rig to date is an existing balance not designed for rotary derivative rig work: its design load range (in N and Nm) is as follows:

X	Y	Z	L	M	N
700	900	4900	60	160	70

although it was calibrated over a more suitable range for these tests. A new six-component balance has been designed for exclusive use with the rig: its load range is (N, Nm):

700	750	1000	65	90	80
-----	-----	------	----	----	----

and both these ranges may be compared with the maximum aerodynamic loads alone (also N, Nm):

40	60	500	25	50	15
----	----	-----	----	----	----

It is clear that the resolution of the aerodynamic loads is degraded by the need to support the gravitational and inertial loads.

It is not proposed to discuss in detail the results obtained during this phase of testing, since the scatter at angles of attack greater than $\alpha = 15^\circ$ was considerable. Least-square straight line fits to all the C_L v. $\frac{P_{wb}}{2V}$ and C_N v. $\frac{P_{wb}}{2V}$ plots were made, the resulting slopes enabling plots of L_p v. α and N_p v. α to be made: comparison of this data with that obtained from flight testing, wing pressure data and theoretical estimates was sufficiently encouraging to consider the technique validated, but in need of some refinement. Together with a number of other points, it was thus strongly recommended that the cyclic integration technique be incorporated as soon as possible, as the single most cost-effective means of improving the data quality.

2.4.2 Second test phase

A number of improvements were made to the rig and associated systems before a second test programme was begun, the most important of which was cyclic integration. To initiate (and end) the integration period a pulse was required, and this was taken from a micro-switch mounted within the slip-ring unit cover: some additional circuitry was needed to shape the pulse correctly for recognition by the programme. Prior to the test programme proper, an investigation was carried out into the effect of varying the number of cycles (revolutions of the rig) over which the signals were averaged: the data is presented on fig. 7. It can be seen that the number of cycles of integration has very little effect on the data, the sole exception being at high angle of attack and low rotational speed where the data averaged over 2 cycles diverges from that at 3 or 4 cycles (or above - not plotted). On this basis, therefore, 3 cycles was chosen as the optimum level. At the highest rotational speed shown, this represents about $4\frac{1}{2}$ seconds of integration: static, high angle of attack testing in the 5.5m LSWT is carried out using 5 seconds of integration.

The subsequent test programme consisted initially of repeating a number of the runs of the earlier test phase, to assess the benefits gained in terms of scatter and repeatability. Fig. 8 reveals a significant improvement: the scatter is reduced considerably, giving smooth data even at high angles of attack. As far as repeatability is concerned, figs. 9(a) and (b) show that this is of a high order: indeed, as far as the moments are concerned it is approaching that of steady state, six-component testing at high angles of attack. Three separate runs are plotted for two angles of attack and for the two most relevant components, C_L and C_N . Neither angle of attack nor rotational speed have any noticeable effect on the repeatability.

If the plot of L_p - α is examined (fig. 10) it can be seen that up to $\alpha = 30^\circ$ data from the rotary derivative rig generally substantiates the estimated curve. The estimated data is obtained from flight testing (at $\alpha \leq 20^\circ$) and a wind-tunnel tested pressure plotted wing ($\alpha > 20^\circ$). Above $\alpha = 20^\circ$ a divergence between the data occurs, becoming significant above $\alpha = 30^\circ$, when the rig data is indicating a situation approaching auto-rotation. As far as N_p is concerned (fig. 11) the rotary derivative rig is predicting a much smoother change in N_p with α up to $\alpha = 35^\circ$, at which angle of attack the data peaks sharply before declining. These discrepancies have not been successfully explained at the time of writing, but the rig data has been shown to be extremely repeatable.

Some general comments on rotary derivative rig data accuracy are contained in section 4.

3. MULTI-FACILITY ROTARY DERIVATIVE RIG

3.1 Test Facilities

Although designed primarily for the 1.2m HSWT at B.Ae, Warton Division (a blowdown tunnel), it was a pre-requisite that the rig would also function in three other U.K. tunnels: the 2.7 x 2.1m LSWT, B.Ae, Warton Division; the 9' x 8' transonic tunnel at A.R.A., Bedford; and the 8' x 8' HSWT at R.A.E., Bedford. However, because of the impact of the design requirements to allow the rig to operate in a relatively small blowdown tunnel, the effect of considering the other tunnels on the rig design was minimal. The only feature designed specifically for one of the other tunnels (other than the rig supports) was that which allowed testing at angles of attack greater than 40° .

3.2 Specification and Design Features

3.2.1 Specification

The original specification demanded the following test envelope:

maximum Mach number	: 0.95 (1.1 if possible)
maximum Reynolds number	: $46.10^6/m$ (highest at $M = 0.95$ in 1.2m HSWT)
angle of attack range	: 0 to 40° (0- 90° in the 2.7 x 2.1m LSWT)
sideslip range	: 0 to 10° (up to $\alpha = 20^\circ$)
roll rate	: $200^\circ/s$ full-scale

Using models generally associated with the 1.2m HSWT (approximately $\frac{1}{20}$ scale combat aircraft models) the last requirement needed a roll rate of about 600 rpm, giving a maximum value of $\frac{pb}{2V}$ of about 0.14 at the lowest 1.2m HSWT Mach number, $M = 0.4$.

The maximum running time in the 1.2m HSWT is roughly 25 seconds at the minimum Reynolds number at $M = 0.4$, reducing to about 9 seconds at the maximum Reynolds number at $M = 0.95$ (these figures include 2 seconds settling time). This limitation immediately imposed upon the design the impossibility of changing α and β during a run, wind-axis roll rate being the only practical run variable. At the same time positive locking of the motions was adopted (as opposed to the clamping techniques of the 5.5m LSWT rig), owing to the very high loads generated by the rotational speed and attitude.

The components of the rig are shown in photographs on fig. 12, and on a general arrangement on fig. 13.

3.2.2 Incidence angles mechanism

Providing sideslip was straightforward, rolling the model about the body X-axis being adopted as for the 5.5m LSWT rig: the imposition of positive locks gave an increment of $\phi_B = 4^\circ$.

However, the angle of attack variation was approached somewhat differently. Two motions were adopted, one translational and one rotational: this eased some manufacturing problems, but also allowed the possibility of rotating the model with its c.g. off the rolling axis. The translational motion was achieved using a leadscrew to move the incidence carriage along the guide bar: the rotational motion by a worm and wheel rotating the incidence arm (and therefore the sting and model) within the incidence carriage. In both cases tapered pins were used to remove any play between the various components once the required settings had been reached. The increment in θ_C resulting from this was 2° .

This solution for the angle of attack setting can be viewed as a variable-angle cranked sting, demanded by the lack of height in the 1.2m HSWT and the need to reduce blockage.

3.2.3 Drive and control system and operation

A hydraulic motor was chosen at a very early stage in the design study as being the most satisfactory in terms of power for a given physical size. The one finally chosen was of 39 kW driving the rig directly, and having a through-hole in the shaft to allow passage of the instrumentation wires. A full closed-loop servo control system, programmed via a dedicated mini-computer-controlled data acquisition system, was also employed. The system had to automatically run through as wide a range of rotational speeds during a 1.2m HSWT run as possible. By commencing at the highest rotational speed and decelerating great benefits in terms of reduced time between data points would be obtained; the performance demanded of the system is to decelerate by 60 rpm and take data at the new speed, in 2s. In the continuous running tunnels a manual-speed change system could be used as an alternative, the control system functioning only as a constant speed control device. The input to the speed control was from an optical encoder rather than a tachogenerator, as this was considered to provide greater accuracy.

A self-contained hydraulic power unit was used with the rig, avoiding the necessity of having a power unit of the required size at each tunnel and of trying to interface with unfamiliar, and varying, equipment. The system is a low pressure, high volume flow one, the opposite of that found at most wind-tunnel sites so much of the existing equipment could not have been used.

3.2.4 Balancing

Unlike the 5.5m LSWT rig the problem of dynamic balancing was given a great deal of thought (static balancing having been accepted as a necessity). It is possible to show that a single balance mass can be used to dynamically balance a system such as this, the practical problem being to position the mass longitudinally. Two longitudinal positions of the mass were provided so that, during the commissioning phase, the effect of varying this position of the mass on the vibrational characteristics of the rig could be investigated. Other users of high-speed rotary derivative rigs (exclusively in the U.S.A.) benefited from the generally massive tunnel supports available for supporting their rigs, and, as far as can be gathered, have not considered this to be a problem.

For static balancing, both balance mass and radial position could be varied but on only one end of the rig. To reduce the bulk of the mass, the various laminae were made from a special 'heavy metal', approximately twice the density of steel.

As with the 5.5m LSWT rig the model has to be balanced separately, the sting and balance being regarded as part of the rig.

3.2.5 Blockage

The possibility of blockage reducing the performance envelope in the 1.2m HSWT was recognised during the feasibility study, and two static blockage models were subsequently built (fig. 14). A very simple cross-sectional area representation of the scheme that gave rise to these problems was tested in the 1.2m HSWT and significantly reduced the maximum available Mach number. To achieve $M = 0.95$ the frontal area of the drive and incidence angles mechanism had to be reduced; a model of this approach showed that $M = 0.95$ was achievable. However, the reduction in size meant a commensurate reduction in strength such that the maximum loading condition ($M = 0.95$, $\alpha = 40^\circ$, $R_e = 46.10^6/m$, $\dot{\phi}_w = 600$ rpm) could not be achieved. The following are the resulting design points in the 1.2m HSWT:

$$M = 0.95, \quad \alpha = 40^\circ, \quad R_e = 23.10^6/m, \quad \dot{\phi}_w = 600 \text{ rpm};$$

$$M = 0.95, \quad \alpha \approx 15^\circ, \quad R_e = 46.10^6/m, \quad \dot{\phi}_w = 600 \text{ rpm};$$

$$M \approx 0.55, \quad \alpha = 40^\circ, \quad R_e = 40.10^6/m, \quad \dot{\phi}_w = 600 \text{ rpm}.$$

At the same time, a brief investigation into the Mach number distribution in the region of the model was made. This showed a slight longitudinal gradient, but no variation laterally: since any further blockage reduction would have meant a severe contraction of the operating envelope, it was felt that the situation could be accepted, particularly in view of the good lateral distribution.

3.2.6 Strain-gauge balance

It has been suggested that the rapid cyclic variation of loads on a strain-gauge balance demands a dynamic balance calibration (9). As no reference to this being performed on balances used on rotary derivative rigs could be found, a brief experiment to determine the necessity for this was organised. This covered the range 0-15 Hz and used a typical 1.2m HSWT sting/balance/model combination. The result was that, at resonance, phase shifting of the various outputs was found and, as may be expected, the frequency response peaking: ± 2 Hz from resonance, no phase shifting was evident. However, much more importantly from the rotary derivative rig point of view, the mean output was invariant with frequency: thus a static balance calibration was perfectly satisfactory for the determination of cyclically-averaged loads.

3.2.7 Control and data acquisition

Reference has been made to the control of the rig speed through a closed-loop servo system. The overall control of the rig for setting the required speed, speed increment, etc., is through a v.d.u. connected to a mini-computer-controlled data acquisition and control system (fig. 15). Data point settings in the form of initial speed, speed increment, number of speeds, number of rig revolutions over which data is to be integrated and rate of change of speed, are set-up as fixed data prior to a run. Once the tunnel conditions are set the operator starts the control system, which then automatically processes the run through the specified conditions. In a continuous running facility the operator could perform the speed change function manually: on-line data processing would make this a more flexible operation as the programme could be changed, depending upon the results (displayed on the v.d.u.).

In all the test facilities certain tunnel control functions can be interfaced with the rig control system, in particular those concerned with emergency shutdown procedures. If an emergency should occur, making it vital to rapidly stop the rig, power to the motor is cut instantaneously prior to the application of a disc brake mounted on the drive shaft (fig. 13). This may be operated either by the operator having visually observed some failure, or automatically by the exceeding of some pre-set limit in the data acquisition system.

A miniature 95-way slip-ring unit is mounted at the rear of the drive motor, the instrumentation wires passing through the motor shaft.

As the rig was required to have a high degree of versatility with regard to the test facilities, it was decided that the provision of a purpose-built instrumentation package would be preferable to modifying the instrumentation system at each tunnel to conform to the demands of the rig. A number of options for removing the gravitational loads were investigated (filtering, generation of an opposing signal, single and dual data scans), but all were eliminated in favour of multiple data scanning (or cyclic integration). This demands a very high sampling rate (100 μs /sample) in order to minimise the number of revolutions over which data needs to be taken (thus maximising the number of data points taken during a run in the 1.2m HSWT).

A mini-computer is used as the data management tool, the data processing being performed by the B.Ae. Warton Division, IBM 370 via a link by means of modem units (interfaces to code data into a suitable form for transmission over telephone lines). It will, of course, be necessary for each site to have this facility. This technique of data processing has been in use for over two years on the 5.5m LSWT instrumentation, and has been extremely satisfactory (fig. 15).

3.2.8 Data analysis

The problem of analysis of the balance loads is identical to that described earlier (section 2.2.6); gravitational loads are dealt with as above, inertial loads need to be determined, and the remaining load is assumed to be aerodynamic. It was hoped that the inertial loads would be determined by performing a wind-off run prior to each tunnel run: because of the rate at which this could be done, and the length of time between 1.2m HSWT runs, this was no detriment to the overall progress of the programme. However, rig and balance deflections are not so easily accounted for using this technique, and it is therefore planned to use a combination of wind-off testing and calculation (thus making the knowledge of the model moments and products of inertia essential - they will be measured as in section 2.2.6). The accuracy of this approach will be compared to that of wind-off alone, and calculation alone, to determine if any one method is significantly superior.

3.2.9 Tunnel installations

The installations at the four designated facilities are on fig. 16: the relationship between the rig size and the various tunnels is clearly shown.

3.3 Calibration and Commissioning

At the time of writing the rig is undergoing a lengthy period of calibration and commissioning. The rig is being statically-balanced over the complete range of angle of attack for all three sting combinations that are available. Its deflection characteristics will be measured, as will the efficiency of the disc brake. This will be determined by the use of a purpose-designed rig on which the incidence angles mechanism is replaced by a disc of similar inertia. A replacement shaft will be used to support this disc and the disc brake assembly, the whole system being driven by a pneumatic motor: this is being done to avoid possible damage to the rig proper if some catastrophic failure should occur during the disc brake testing. Calculations have shown that application of the disc brake alone should be sufficient to stop the rig from 600 rpm in 10 seconds: of course, in the event of an emergency, the hydraulic motor will be shut-off and will also act as a brake on the system: using figures from the supplier of the motor, it is believed that the combination of brake and motor will stop the rig from 600 rpm in about 5 seconds. Once the disc brake has been shown to be working satisfactorily, the maximum operating speed of the rig will be determined: during this operation accelerometers mounted on the drive casing will be used to monitor vibration. From this data a correlation between rig vibration and speed and attitude will be attempted.

The next task will be to introduce a single-step change of speed automatically: the ability of the drive system to meet the deceleration requirements mentioned earlier will be assessed at this time, and the optimum rate of deceleration and number of cycles of integration to give satisfactory data repeatability in a minimum time will be determined. Assuming that this is satisfactorily accomplished, then a complete wind-off roll rate traverse can be performed, using the automatic control procedure. Finally, it is hoped that forward speed commissioning in the 2.7 x 2.1m LSWT will take place by October, and in one of the high-speed tunnels early in 1979.

4. CONCLUDING REMARKS

It is worthwhile discussing the general problem of obtaining accurate data from rotary derivative rigs. As a starting point the loads which the internal strain-gauge balance has to support will be considered. The total load is made up from: gravitational load (due solely to model weight), inertial load (a function of model mass, rotational speed and attitude) and aerodynamic load (which must be identified).

If the technique of cyclic integration is employed it eliminates the need to account for the model weight, thus removing one source of error. Accounting for the inertial tare can be done in three ways (section 2.2.6), and the best technique will depend on a number of factors, e.g. overall flexibility of the rig, relative flexibility of the sting and balance, model mass c.f. balance load range, etc. Experience with the 5.5m LSWT rig has shown that, of the two techniques available (calculation of inertias, or use of wind-off tares), that of using wind-off tares is the most accurate, but this may not be the case for other model/balance/rig combinations. The possible error in C_L due to incomplete removal of the inertial tare is of the order of .001, roughly 2½% of the highest value of rolling moment: a similar percentage accuracy applies to all the other components. The remaining load is considered to be the aerodynamic load.

However, although the model weight is not needed to be known, it has a bearing on the overall accuracy of the aerodynamic load, inasmuch as it affects the balance load range. For a high-speed tunnel model its effect is trivial, but for a low-speed tunnel model the model weight can obviously affect the ranges required on the forces. Assuming the model to be balanced, the moments will be unaffected. If the inertial load is now considered, then, for a given roll rate and attitude it is in fact dictated by the model weight. In this instance both high-speed and low-speed models are affected, primarily the moments. The weight of a high-speed tunnel model is largely dictated by the strength required to withstand aerodynamic load and little reduction would seem possible. By reducing the weight of low-speed tunnel models however, an improvement in overall accuracy, by ensuring that the aerodynamic load becomes a greater proportion of the balance load range, is clearly possible.

A corollary to this is that the balance must be very carefully designed to ensure also that the available load ranges are not wasted. It is inevitable that some components will have their resolution degraded (see section 2.4.1) by the need to support the model weight and/or inertial load.

	ANGLE OF ATTACK RANGE (AT $\beta=0^\circ$)	SIDSLIP RANGE * (AT $\alpha=20^\circ$)	$\frac{pb}{2V}$ MAX.	ROLL RATE RPM MAX.	MACH. NUMBER MAX.	REYNOLDS NUMBER, MAX. m	BASED ON ξ
5.5M. L.S.W.T. ROTARY DERIVATIVE RIG.	-45(0.1)90	-40(0.5)40	0.22	60	0.06	$1.35 \cdot 10^6$	$0.71 \cdot 10^6$
MULTI-FACILITY ROTARY DERIVATIVE RIG.							
1.2M. H.S.W.T.	-40(2)40	-35(5)35	0.14	600	0.95	$\alpha=40^\circ$ $23 \cdot 10^6$ $\alpha=15^\circ$ $46 \cdot 10^6$	$2.2 \cdot 10^6$ $4.4 \cdot 10^6$
9 x 8 A.R.A.	0.19	$15 \cdot 10^6$	$1.4 \cdot 10^6$
2.7 x 2.1M. L.S.W.T.	-40(2)40 -40(2)90	0.43 0.18	600 250	0.13	$3.05 \cdot 10^6$	$0.29 \cdot 10^6$
8 x 8 R.A.E.	-40(2)40	..	0.43	600	0.87	$30 \cdot 10^6$	$2.8 \cdot 10^6$

* RANGE AND INCREMENT VARY WITH α

FIG. 1. TEST PARAMETERS

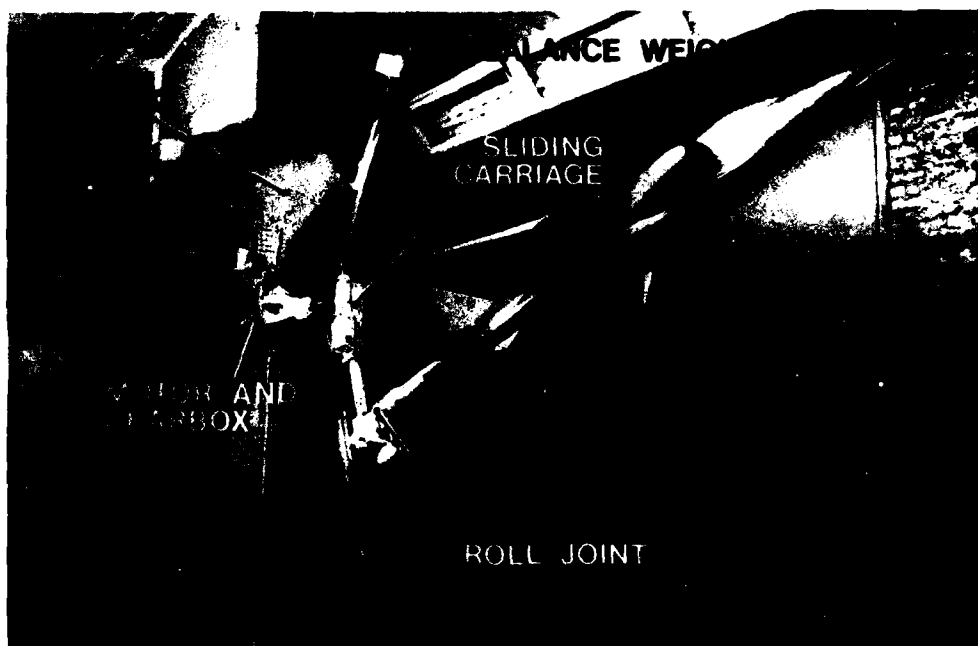
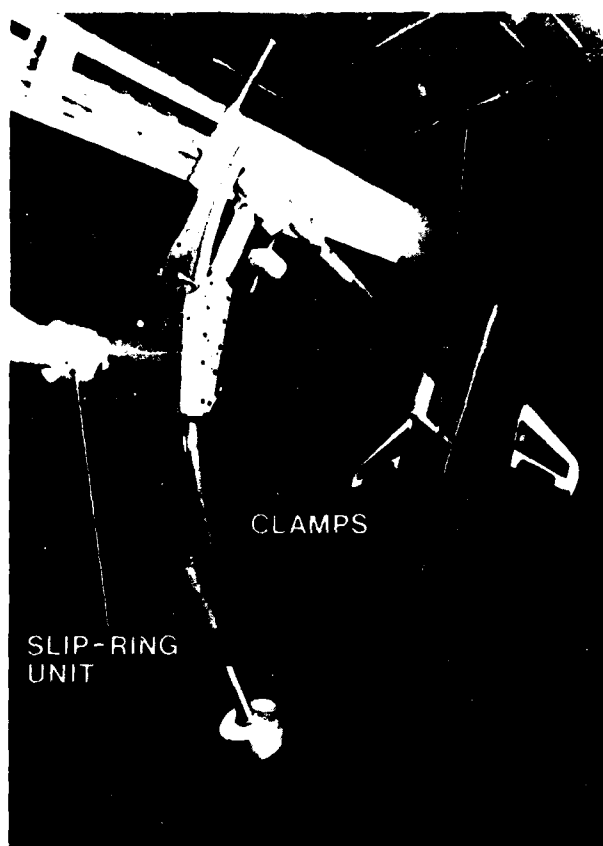


FIG. 2. 5.5M. L.S.W.T. ROTARY DERIVATIVE RIG



**FIG. 3. 5.5M. L.S.W.T. ROTARY DERIVATIVE RIG.
INSTALLATION FOR $45^\circ < \alpha < 90^\circ$**

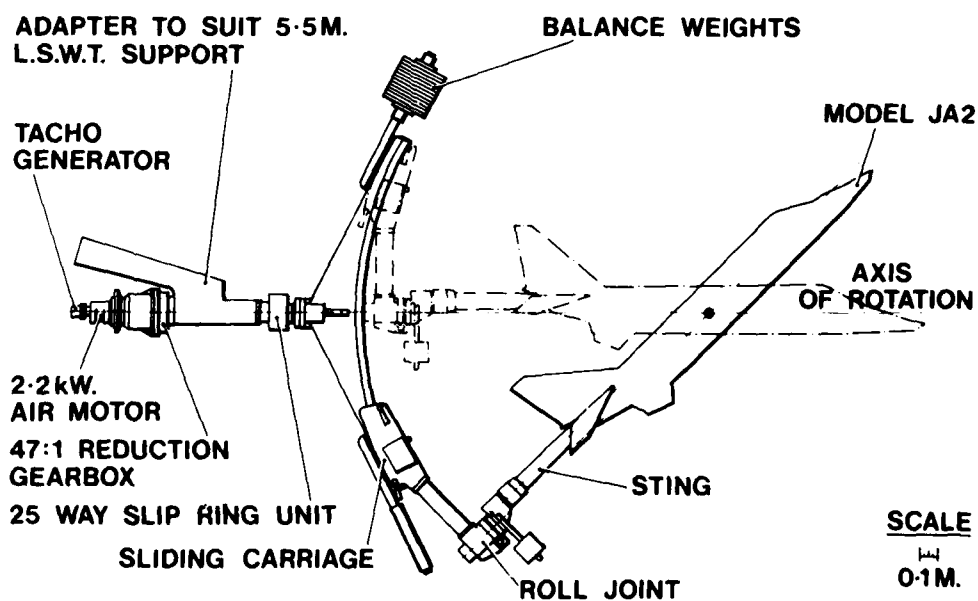


FIG. 4. 5.5M. L.S.W.T. ROTARY DERIVATIVE RIG

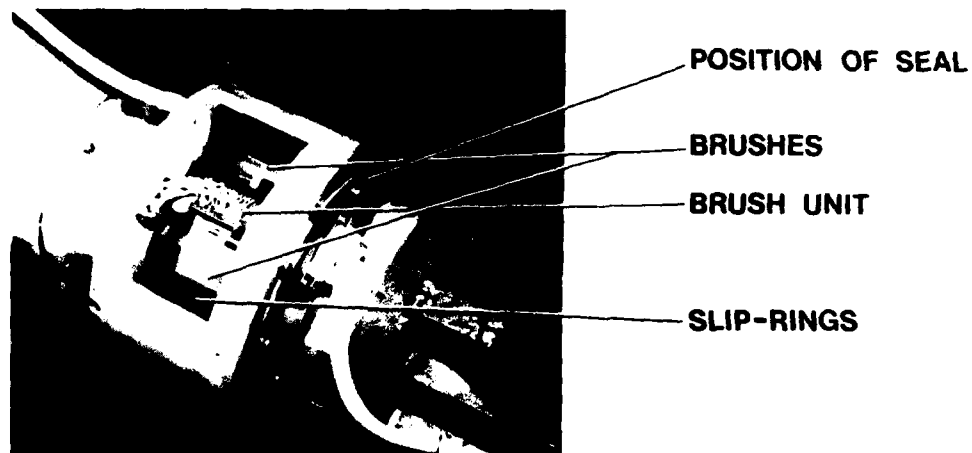
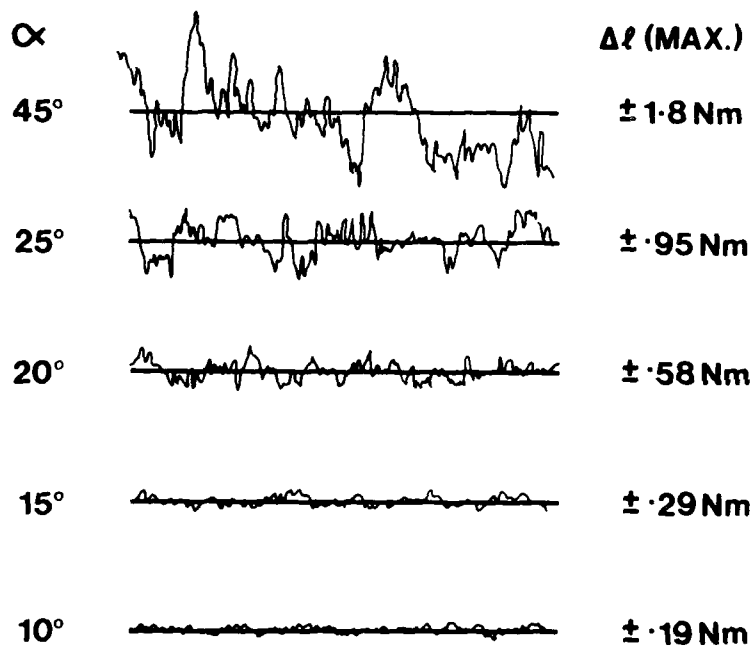


FIG. 5. SLIP-RING UNIT

TYPICAL TRACE (PART ONLY REPRODUCED)



1 SEC.



$$V_{\infty} = 20 \text{ m/s.} \quad \dot{\phi}_w = 0$$

FIG. 6. TIME BASED OUTPUT OF ROLLING MOMENT CHANNEL

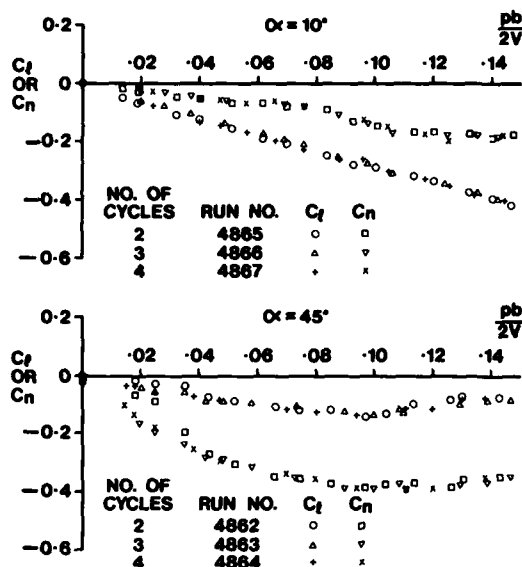


FIG. 7. EFFECT OF NUMBER OF CYCLES OF INTEGRATION ON DATA

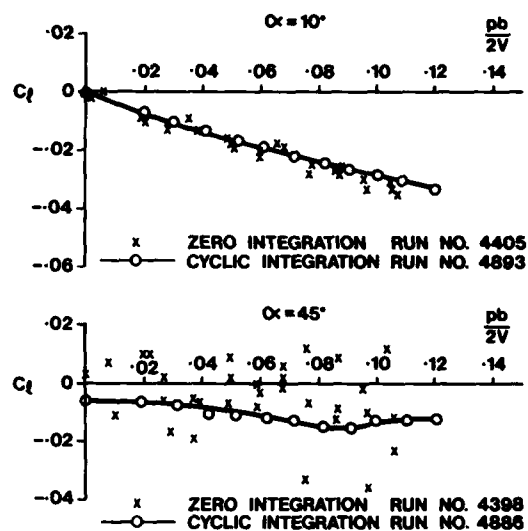
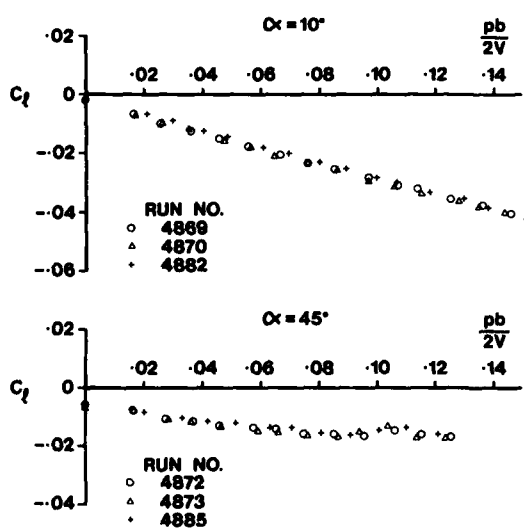
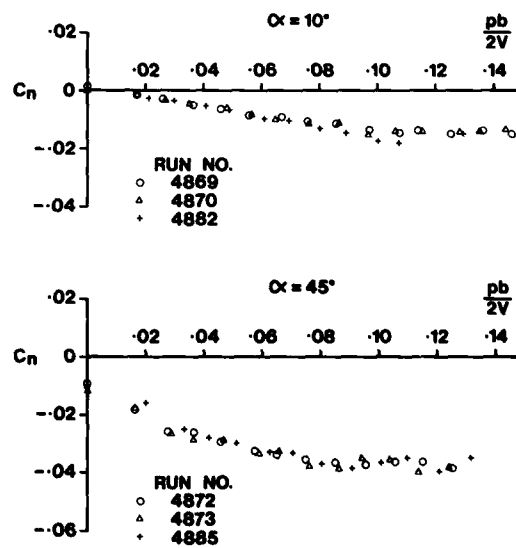


FIG. 8. EFFECT OF CYCLIC INTEGRATION ON DATA SCATTER

FIG. 9(a). DATA REPEATABILITY, C_l FIG. 9(b). DATA REPEATABILITY, C_n

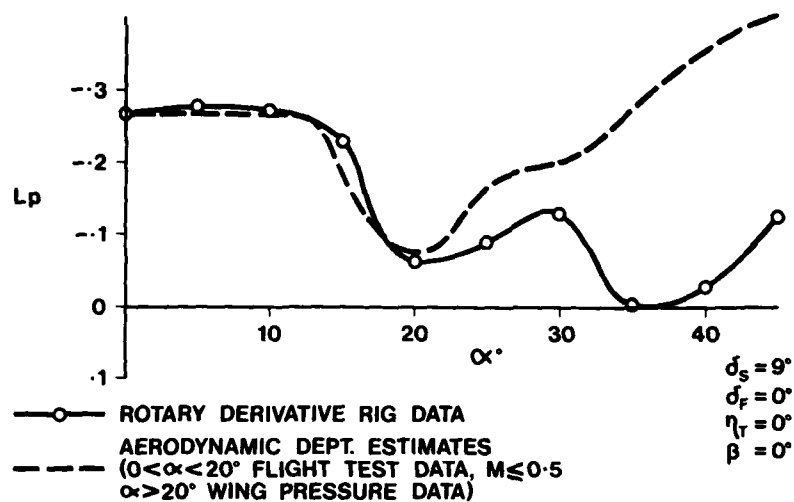


FIG. 10. $L_p - \alpha$ (WIND AXES) FOR A CURRENT COMBAT AIRCRAFT

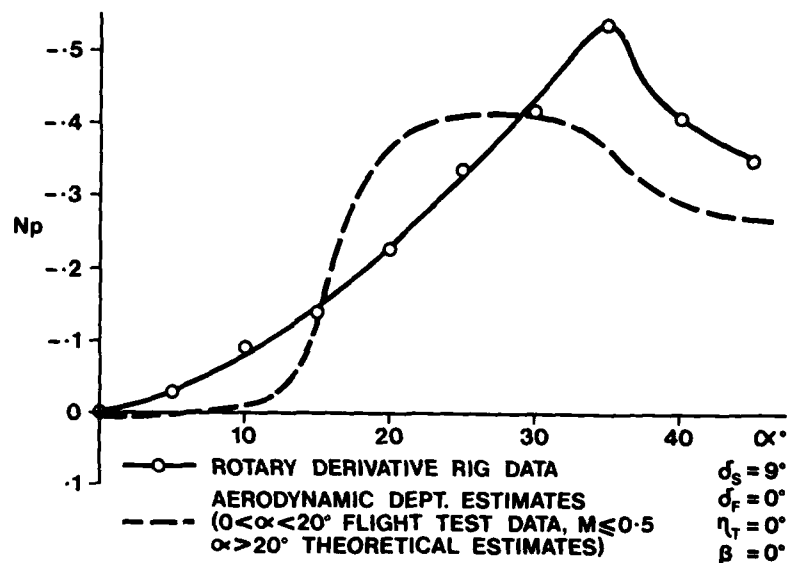


FIG. 11. $N_p - \alpha$ (WIND AXES) FOR A CURRENT COMBAT AIRCRAFT

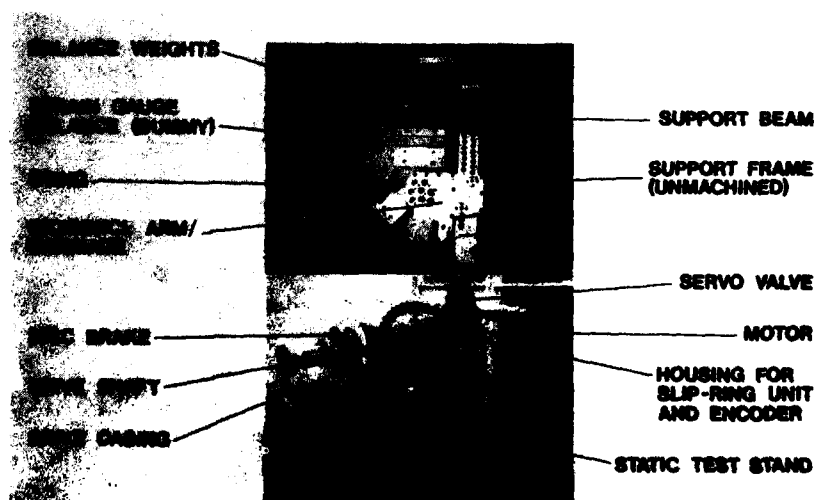


FIG. 12. MULTI-FACILITY ROTARY DERIVATIVE RIG

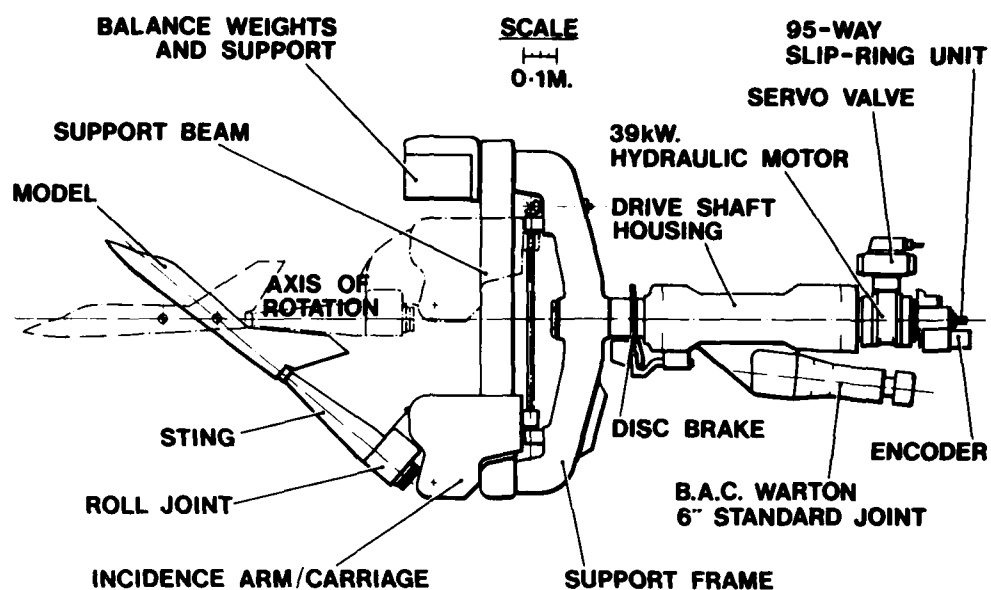
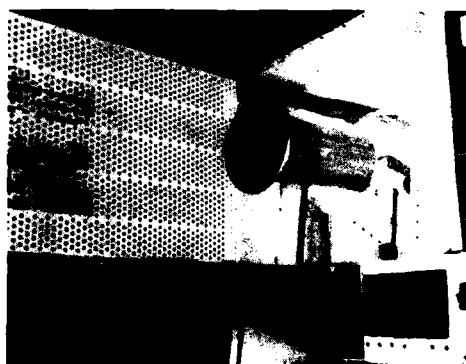


FIG. 13. MULTI-FACILITY ROTARY DERIVATIVE RIG



FIRST BLOCKAGE MODEL



SECOND BLOCKAGE MODEL

FIG. 14. 1-2M. H.S.W.T. BLOCKAGE MODELS

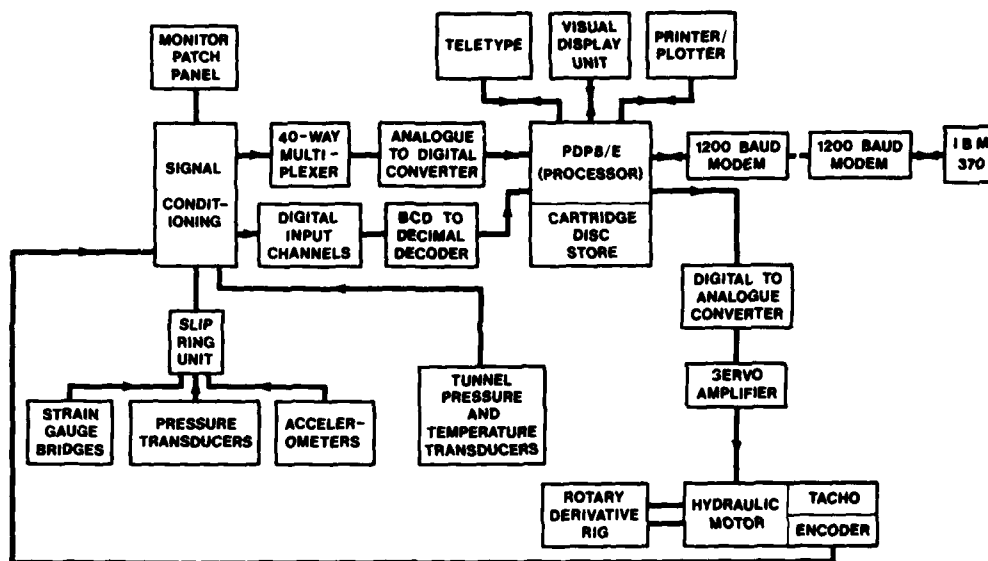


FIG. 15. DATA ACQUISITION AND CONTROL SYSTEM

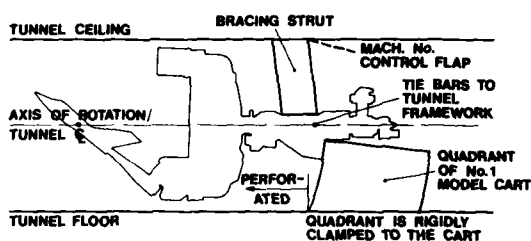


FIG. 16(a). INSTALLATION AT 1.2M. H.S.W.T., B.Ae., WARTON DIVISION

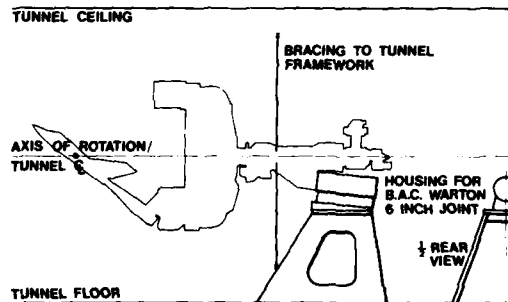


FIG. 16(b). INSTALLATION AT 2.7 x 2.1M. L.S.W.T., B.Ae., WARTON DIVISION

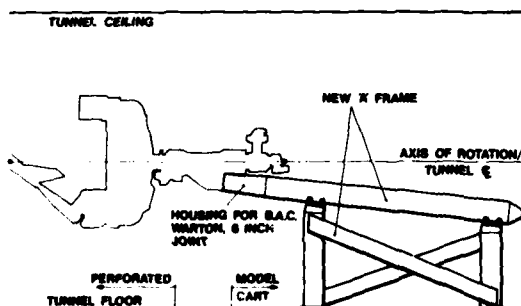


FIG. 16(c). INSTALLATION AT 9'x8' TUNNEL, ARA, BEDFORD

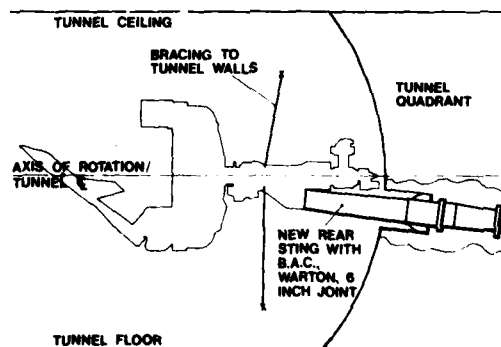


FIG. 16(d). INSTALLATION AT 8'x8' TUNNEL, RAE, BEDFORD

WIND TUNNEL TESTING OF DYNAMIC DERIVATIVES IN W-GERMANY

by

X. Hafer
 Professor of Aeronautics
 Technical University Darmstadt
 Petersenstraße 30, 6100 Darmstadt
 W-Germany

SUMMARY

A survey is given of the activities of the German national working group engaged in the development of dynamic wind tunnel test installations.

Sponsored by the Ministry of Research and Technology, the development of four different test rigs was planned. So far, the development of three test rigs is completed. They are now available for routine investigations, which has been confirmed by many successful tests. Each rig has been designed to meet very specific test requirements which are discussed in detail.

Furthermore, test results are presented giving a comparison of systematic tests with the same model mounted on different test rigs in different wind tunnels. Some flight test results of the corresponding original plane are compared in addition. Finally, some results of linearised flight dynamic investigations are presented to demonstrate the influence of the several dynamic derivatives on the longitudinal and lateral aircraft dynamics.

NOTATIONS

L_p	rolling moment due to roll-rate (damping in roll)
L_r	rolling moment due to yaw-rate
M_q	pitching moment due to pitch-rate (damping in pitch)
N_p	yawing moment due to roll-rate
N_r	yawing moment due to yaw-rate (damping in yaw)
V	velocity
Y_{β}	lateral force due to lateral acceleration
Z_a	vertical force due to vertical acceleration
b	wing span
c	wing chord
f	frequency
n	rate of revolution
p	roll-rate
r	yaw-rate
s	wing half span
Δz	amplitude in heave
θ	pitching displacement
ϕ	rolling displacement
$\Omega = \sqrt{p^2 + r^2}$	resulting rate of revolution
α_0	steady state angle of attack
γ_{Ω}	angle between V and Ω
$\Delta \theta$	amplitude in pitch
$\Delta \phi$	amplitude in roll
$\Delta \psi$	amplitude in yaw

ζ	damping ratio
ω_0	"undamped" circular frequency
ω_a	circular frequency of the aircraft short period motion
ω_β	circular frequency of the aircraft dutch roll motion
ω^*	reduced frequency
$\sigma = -\zeta \omega_0$	exponential damping factor
ν	kinematic viscosity

Subscripts

A/C	aircraft
M	model

1. INTRODUCTION

During several decades much efforts in developing methods for measuring dynamic derivatives can be observed. In 1954, J. Valensi (ref. 1) gives a survey of the methods applied in European wind tunnels until this time. L. Arnold (ref. 2) describes, in 1955, the state of the art in Europe and in the USA, considering besides the test methods also the problems of test instrumentation and the construction of models. The publication of K.J. Orlik-Rückemann (ref. 3) from 1959 gives a systematic and detailed survey of the different techniques also considering free flight test methods. More extensively than W.G. Molyneux (ref. 4), J.B. Bratt (ref. 5) gives in 1960 a survey of test procedures in wind tunnels, analysing especially the ranges of application and sources of errors of the different methods. C.J. Schueler, L.K. Ward and A.F. Hodapp (ref. 6) present in details the state of the art. They describe especially the various kinds of model supporting systems, test instrumentation, construction of balances, and data reduction methods. This publication presents a bibliography containing more than 400 references. K.J. Orlik-Rückemann (ref. 7), (ref. 8) compares the demand for test installations to measure dynamic derivatives with the available facilities and remarks the lack of experimental results especially for large angles of attack and very large Re-numbers. The bibliography of the present paper contains further publications, in which special test installations are described and results are presented as from Langley Research Center (USA) (refs. 9 - 11), RAE-Bedford (UK) (ref. 22), ONERA (F) (refs. 15 and 23) and DFVLR (W-Germany) (refs. 25 - 28) and the German Working Group (refs. 29 - 32).

It was the objective of our efforts, in principle, to obtain testing installations which enable us to measure the most important dynamic derivatives in routine tests. In 1972 a national working group was constituted, the members of which belonged to different aeronautical research institutes (DFVLR, Universities of Bochum and Darmstadt), and the aeronautical industry (Dornier, MBB and VFW-Fokker).

In coordination with the Ministry of Research and Development, a programme was set up in May 1973 to settle upon the technical details, financial aspects, and the course of development of the following four dynamic test facilities:

- Project 1: Industrial testing of the DFVLR multi-degree-of-freedom oscillatory derivative balance
(Programme management Dr. v.d. Decken, Dornier, Subcontractor DFVLR Göttingen)
- Project 2: A mobile oscillatory derivative balance for use in the 3-m low speed wind tunnels of W-Germany
(Programme management Dr. v.d. Decken, Dornier, Subcontractor VFW-Fokker, Techn. University Darmstadt, DFVLR Göttingen)
- Project 3: A rotary derivative balance for use in the 3-m low speed wind tunnel in Cologne mainly
(Programme management H. Schulze, MBB, Subcontractor DFVLR Köln and Braunschweig, Universities of Bochum and Darmstadt)
- Project 4: An oscillatory derivative balance for use in the 1-m transonic wind tunnel DFVLR Göttingen
(Development of the DFVLR Göttingen)

In the following, the projects 1 to 3 which already are successfully developed and tested will be described. The important problems of data-acquisition and -evaluation will be left untouched, for they are the topic of the following paper by Dr. E. Schmidt.

2. DESCRIPTION OF THE TEST FACILITIES

2.1 DFVLR Multi-Degree-of-Freedom Oscillatory Derivative Balance

This balance for oscillatory derivative measurements with rear-sting-mounted wind tunnel models was developed by the DFVLR (ref. 18) based on the experience with the well known Thompson rig of the RAE (ref. 22). The arrangement for longitudinal tests is shown in Fig. 1. The apparatus consists of a very stiff ground fixed support system (1) with angle of attack adjustment from -5 to 25 degrees, the elastic sting (2) at the head of which the model (3) is fitted, and an electro-mechanical exciter (4) with a driving rod fixed to the model at its rear part. The main part of the mechanical set up is the elastic sting, Fig. 2, which consists of two spring elements of different stiffness. The rear flat spring by its bending stiffness defines the natural frequency of the heave oscillation while its torsional stiffness defines the natural frequency of the roll-oscillation. The forward spring, which normally is covered by the model, consists of two parallel bar springs which define the natural frequency of the pitch oscillation. Between these two springs a vertical flat spring provides the stiffness necessary to transfer the normal forces. Two spring units of different stiffness are in use.

For a given spring unit the oscillatory system consisting of the model (mass $m = 46$ kg, moments of inertia in m^2kg : $I_x = 4.1$, $I_y = 12.5$, $I_z = 24.0$), the elastic balance, and the ground fixed support has different natural frequencies. In the following only the values of the weak spring arrangement are mentioned.

In the longitudinal mode two characteristic natural frequencies occur:

- a) Exciting with a frequency of about 2 cps, both springs are deflected in the same direction. This results in a pitch oscillation of the model with a superposition of a small heave portion.
- b) Exciting with a frequency of about 4.5 cps, both springs are deflected in opposite direction. The result is a heave oscillation with a superposition of a small pitch portion.

For the investigation of the lateral motion, the sting, together with the spring system and the exciter, is turned by 90 degrees with the model being left in the usual position. The following three natural frequencies can be observed:

- a) At an excitation frequency of about 2 cps, both springs are deflected in the same direction. From that, a yaw oscillation follows with a superposition of a small transverse portion and a very small roll portion.
- b) At an excitation in the second order frequency (about 4.5 cps), both springs are deflected in opposite direction. From that, a transverse oscillation results with a superposition of a small portion of yaw- and roll oscillation.
- c) At an excitation in the third order frequency (about 6 cps), both springs twist, which results in a roll oscillation of the model with a superposition of a small portion of yaw and transversal oscillation.

The amplitudes of the different modes amount to ± 5 mm for the translational oscillations and ± 0.5 degree for the pitch, yaw, and roll oscillation.

Exciting the model with a frequency different from the resonance frequencies results in mixed harmonic motions of the model.

Normally the tests are performed close to the natural frequencies so that each mode requires a certain frequency. For a given spring arrangement, a change of the reduced frequency ω^* of the model requires a change of the wind tunnel speed, which consequently results in a change of the Reynolds Number.

2.2 Mobile Oscillatory Derivative Balance

Supplementary to the DFVLR derivative balance which uses an electro-mechanical excitation system, a different conception of a dynamic testing facility was realized. It should be a self-sufficient balance including the data acquisition and evaluation system to be used to perform tests in several 3-m low speed wind tunnels of W-Germany. A further important aim of the design was the excitation of single-degree-of-freedom motions for being able to separate the derivatives of the vertical motion. Finally, the exciting frequency should be continuously changeable for being able to select the reduced frequency and the Reynolds Number independently.

In the beginning of the design work, the question of the exciting method was discussed. There are two basic principles: Free oscillations and forced oscillations; in the latter case, elastic or rigid excitation can be used. Fig. 3 gives a survey of the advantages and disadvantages of the different possibilities of solution and demonstrates, that the selected system using a rigid mechanically forced excitation of the model promises convincing advantages.

Due to the dimensions of the 3-m wind tunnels the size of the models is approximately defined. To satisfy an equal magnitude of the reduced frequency ω^* under free flight- and model-test-conditions, the frequency necessary for the model-tests can be estimated by the following equation

$$f_M = \frac{\omega_\alpha}{2\pi} \frac{V_M}{V_{A/C}} \frac{c_{A/C}}{c_M} \quad \text{or} \quad \frac{\omega_\beta}{2\pi} \frac{V_M}{V_{A/C}} \frac{s_{A/C}}{s_M}, \quad (1)$$

where ω_α and ω_β are the angular frequencies of the longitudinal or lateral mode in free flight.

An evaluation of equation (1) for different categories of aircraft, assuming a mean wind tunnel speed of 60 m/s, results in a frequency range of $0.5 < f_M < 2$ cps. Therefore a frequency up to 3 cps was realized for being able to test also models with larger scales.

The electrical drive system was carefully selected considering especially the necessity of keeping the frequency constant and synchronous. These requirements were best satisfied by a 3 kW direct current driving motor with an electronic speed control. The final assembly of the test rig is presented in Fig. 4. The pillar consisting of two parts (1) and (2) is designed as a conical tube of cast-steel screwed on a heavy cast-steel bed-plate having a size of 1.3 x 1.3 m. In this tube, the so called model support (3) is positioned guided in the upper part of the pillar (1). On top of the model support, a square-flange is fastened carrying one of two exchangeable motion heads (4) to which a five component strain gauge balance (5) is flanged. To generate the oscillatory motions of the model, there are three geared driving motors arranged on the bed-plate one of which is engaged while the others are locked in idle position.

The heave-motor (6) drives the model support (3) by means of an eccentric drive over the hinged lever (7). The maximum heave amplitude amounts to ± 30 mm.

The yaw-drive (8) generates by means of an adjustable eccentric disk an oscillating yaw motion of the model support (3) which in this case is bolted with the upper part of the pillar. The maximum yaw amplitude amounts to ± 5 degrees about the vertical wind axis.

The pitch-motor (9) is also used to generate the roll oscillation. In both cases, the rotation of the gear shaft is converted in the lower part of the pillar (2) into an up and down motion. This is transmitted to the motion head (4) by means of a rod (10) arranged at the outer side of the pillar. The maximum amplitudes are ± 5 degrees for each motion. For the roll mode, the oscillation is performed about the wind axis.

To measure the instantaneous position of the model, each mode of motion is supervised by means of a position indicator. For pitch and roll they are to be found in the corresponding motion heads. The position indicator for the heave motion is arranged at the upper part of the pillar and the position indicator for the yaw motion at the lower part. Apart from the heave indicator which is an inductive sensor, all indicators are designed as bending beams fitted with strain gauges. The maximum amplitudes of the different modes, and the range of angle of attack is shown in the following table.

Motion	Amplitudes	Angular-Range
Pitch	$\Delta\theta = \pm 5^\circ$	$\alpha_0 = 0/5/10/15/-5^\circ$
Roll	$\Delta\phi = \pm 5^\circ$	$\alpha_0 = 0/4,5/9/13,5/-4.5^\circ$
Yaw	$\Delta\psi = \pm 5^\circ$	$\alpha_0 = 0/8/10/15/-5^\circ$
Heave	$\Delta z = \pm 30 \text{ mm}$	$\alpha_0 = 0/5/10/15/-5^\circ$
Frequencies	$f = 0 \div 3 \text{ cps}$	

All amplitudes are continuously adjustable up to the indicated maximum values.

The forces in vertical and lateral direction as well as the moments of pitch, roll, and yaw are measured by an internal model-fixed strain gauge balance.

It is of great interest, especially for modern fighter type aircraft, to know the dynamic derivatives at even higher angles of attack than those maximum values being attained by the above described balances when they are placed in the wind tunnel in usual position.

An extension to angles of attack up to 50 degrees is possible by installing the mobile oscillatory balance on a support with a circular guide rail, which is available in the 3-m low speed wind tunnel at Brunswick, Fig. 5. Due to this arrangement, the axes of oscillation of the roll- and yaw mode are inclined with respect to their original directions. The balance excited in roll or yaw respectively, will perform in both cases motions in two degrees of freedom, referred to the wind axis. Supposing that linear superposing of the two modes is allowed, the derivatives can be ascertained by modifying the evaluation method used in conventional tests. For testing the pitch oscillation, no special problems will arise. However, the heave mode needs further considerations in this case.

Here the question arises, whether in tests with high angles of attack an oscillation in the wind system of axes has still its original meaning. So at $\alpha = 90$ degrees the roll oscillation about the wind axis represents a body-fixed yaw oscillation and a yaw oscillation about the wind axis represents a body-fixed roll oscillation.

2.3 Rotary Derivative Balance

With those two test rigs described above, all important dynamic derivatives can be measured up to large angles of attack, supposing oscillations of relatively small amplitudes. Besides the steady state derivatives, the knowledge of accurately tested dynamic derivatives is of fundamental importance to predetermine stability and controllability of aircraft and missiles with high reliability in the vicinity of steady state flight conditions. If manoeuvres of very large amplitudes are in question or continuous rolling or spinning of an aircraft shall be investigated by flight mechanical calculations, the derivatives produced by oscillatory test rigs are no longer valid. Here only a steadily rolling model will supply representative results in wind tunnel tests.

Early rotatory balances constructed in W-Germany (ref. 14 and 33) were limited in size and range of application. In order to meet the requirements of the aircraft industry, a new rotary balance has been constructed. It was designed for use in the 3-m low speed wind tunnel of DFVLR-Cologne mainly. The general arrangement of the complete system is shown in Fig. 6. The rotary balance was constructed as an attachment to an appropriate existing model support (1). The angle between the rotary vector and the speed vector γ_Ω can be varied by changing the attachment with the model support. Flight mechanical investigations of the free flight rolling motion of fighter-type aircraft, which follows constant aileron inputs, showed, however, that the angle γ_Ω fluctuates around a relatively small mean value. So it was decided to select $\gamma_\Omega = 0$ for the rotary tests.

The main mechanical components of the rotary balance are the large bearing box with spindle (2), the hydraulic drive system including a tooth belt transmission with a gear ratio of 1:4.5 (3), a device for remote setting of the angle of pitch (4), interchangeable stings (5), and a six component strain gauge balance joined to the model (6).

The rotary balance is driven by a constant displacement reversible hydraulic motor with a power of four kW. The speed - up to 300 rpm - and the direction of rotation is varied by controlling the fluid flow by means of an electrically controlled servo valve. 10 000 impulses, delivered by an incremental angle encoder mounted at the downstream end of the bearing box, are used to control the speed. Additionally this drive system allows to get the model remotely positioned under every desirable roll angle. This is used e.g. to determine the position of the center of gravity of the model.

On the stream lined arc traverse (1), Fig. 7, a carriage (2) is moved by two screwed spindles (3). These spindles are at one end connected over a gear (4) with high gear ratio to an electrical direct current driving motor (5) fixed downstream at the arc traverse. At the other end of the two spindles, a reversing gear (6) drives a further screwed spindle (7) which rotates inside of the arc traverse and drives a counterweight (8).

The total range of angle of pitch (θ) from 0 to 90 degrees is obtained by using three differently bent stings, Fig. 8. The angle of sideslip is adjusted by rotating the forward part of the sting about its x-body axis (angle ϕ). Only with $\phi = 0$, the angle of pitch is equal to the angle of attack. For values $\phi \neq 0$, the angles of attack and of sideslip can be estimated from the following equations

$$\begin{aligned}\tan\alpha &= \tan\theta \cos\phi, \\ \sin\beta &= \sin\theta \sin\phi.\end{aligned}\tag{2}$$

Future simulation of a finite spin radius can be achieved by rigid adapters, fixed between the bent part and the forward part of the stings.

The span of the model being tested should be about 1 m in order to make use of the whole range of the balance. The maximum Reynolds Number for a given model size is defined by the jet velocity of the wind tunnel (max. 80 m/s). For the Reynolds Number referred to the wing chord (c) of the model, we have with the jet speed V and the kinematic viscosity ν

$$\frac{Re}{c} = \frac{V}{\nu}.\tag{3}$$

The reduced frequency ω^* referred to the wing span b, is defined by $\omega^* = \omega \frac{b}{2V}$ as

$$\frac{\omega^*}{b} = \frac{\pi}{60} \frac{n}{V},\tag{4}$$

where n is the rotary speed in rpm.

Eliminating V from these equations, we get a simple relation between the referred Reynolds Number and the referred reduced frequency

$$\frac{Re}{c} = \frac{\pi}{60v} \frac{n}{\omega^*/b} \quad (5)$$

This relation is presented in Fig. 9 and demonstrates the possibility to investigate the influence of the Reynolds Number at constant reduced frequency and vice versa over a wide range.

3. COMPARISON OF TEST RESULTS

Wind tunnel test were performed with the same Alphajet light-weight-model mounted on the DFVLR oscillatory balance (2.1) and the mobile derivative balance (2.2). The model was to be modified for both sting arrangements by means of changeable fairings. The most important dimensions of the model were

Length 2.32 m , Wing Area 0.70 m² ,
Span 1.82 m .

The tests with the DFVLR-balance were performed in the DFVLR wind tunnel in Göttingen, those with the mobile derivative balance in the wind tunnels of the Technical University of Darmstadt and of the DFVLR in Brunswick. All these tunnels are low speed wind tunnels with approximately equal nozzle size.

In the figures only some of the most important results are presented and compared with flight test results as far as available. All derivatives shown in the figures are referred to the wind system of axes.

In Fig. 10, the derivatives of lift and pitching moment due to pitch oscillation are shown. Both balances produce nearly identical results. Smaller differences might result from the different sting arrangement and different reduced frequencies which were by some factor of three higher in the case of the DFVLR-balance. The wind tunnel results are in good agreement with flight test results.

Fig. 11 presents the damping-in-yaw and damping-in-roll derivatives. Here the results of the two balances correspond very well. Especially the consistency of the values measured by the mobile derivative balance is excellent. Both test results are essentially confirmed by the flight tests.

In Fig. 12 a comparison of the coupling-derivatives rolling moment due to yaw and yawing moment due to roll is given. The slope of the values over the angle of attack of both test results are in reasonably good accordance, while the flight test results show larger differences especially at lower angles of attack. Since the jet of the two turbofan engines was not simulated in the wind tunnel tests, some jet-interference effects may be responsible for this discrepancy. Also the steady state derivatives estimated from the dynamic tests showed excellent results in comparison with steady state wind tunnel tests and flight tests.

With the roll balance some results were received in first tests by a simplified arrangement, for which only three different angles of pitch (0, 15, 30 degrees) could be investigated using three differently bent stings. A comparison with tests performed by Aer Macchi using the same model (apart from a different sting position and different intake fairings) confirms our previous results pretty well, Fig. 13.

4. FLIGHT DYNAMICAL VALUATION OF THE DYNAMIC DERIVATIVES

To estimate the flight dynamic behaviour of new aircraft with sufficient accuracy, the correct knowledge of the total set of derivatives including the dynamic ones is necessary.

Several dynamic derivatives are of quite different influence on the flight dynamics of an aircraft. To know the requirement of accuracy for each derivative, we investigated how the resulting characteristic values are influenced by changing the value of a certain derivative. This was performed for three aircraft configurations having different aspect ratio, wing loading, and ellipsoid of inertia. The results of this investigation are demonstrated in Fig. 13 and 14.

Fig. 14 compares the effect of a relative change of the dynamic derivatives ΔM_q and ΔZ_q on the change of the circular frequency of the undamped system $\Delta \omega_0$ and the damping ratio $\Delta \zeta = -\sigma/\omega_0$ for the short period mode. It is to recognize that the influence of the force derivativ Z_q on the short period mode is some orders of magnitude smaller than the influence of the moment derivative M_q for all aircraft configurations considered. This result is of great importance since an accurate testing of the derivativ Z_q involves fundamental problems since the forces with and without wind are nearly of the same magnitude.

In Fig. 15 the influence of the damping and coupling derivatives of the lateral motion on the damping ratio $\Delta \zeta$ of the dutch-roll-mode is shown for the same aircraft

configurations. Here also the influence of the force due to lateral oscillations, represented by the derivative $C_{y\beta}$, was investigated. Its influence is of such small magnitude that it is not to be represented in the scale used to demonstrate the other derivatives. Therefore one can dispense with its determination in dynamic wind tunnel tests. The influence of the several damping and coupling derivatives depends markedly on the aircraft configuration. It is to be expected e.g. for slender delta configuration, that the derivatives due to the rolling motions are dominant while for the subsonic transport, the derivatives due to the yawing motion are of greater importance. Nevertheless, the four lateral dynamic derivatives considered above are roughly of the same order of magnitude. Their determination in the dynamic tests requires the same degree of accuracy.

5. SUMMARY

In the present paper recent developments of oscillatory and rotary balances for the measurement of dynamic derivatives are described in details. Some typical test results are presented which give a comparison of tests with the same model in different wind tunnels mounted on different balances. It proves the ability of the different test rigs to provide results of high reliability and correspondence. Furthermore it was shown that the results of wind tunnel tests are in reasonable good accordance with flight test results. In a final consideration a contribution is given to recognize the importance of the several dynamic derivatives for the aircraft's dynamic behaviour, from this can be deduced which degree of accuracy for each derivative is required in dynamic wind tunnel tests.

6. REFERENCES

1. J. Válenzi, "A Review of the Techniques of Measuring Oscillatory Aerodynamic Forces and Moments on Models Oscillating in Wind Tunnels in Use on the Continent", AGARD Fourth General Assembly 1965, AG 15/P6.
2. L. Arnold, "Dynamic Measurements in Wind Tunnels", AGARDograph 11 (1955).
3. K.J. Orlik-Rückemann, "Methods of Measurement of Aircraft Dynamic Stability Derivatives", National Research Laboratories, Report LR-254 (1959).
4. W.G. Molyneux, "Measurement of the Aerodynamic Forces of Oscillating Aerofoils", Aircraft Engineering, Vol. XXVIII, No. 323 (1956).
5. J.B. Bratt, "Wind Tunnel Techniques for the Measurement of Oscillatory Derivatives", AGARD Manual on Aero-Elasticity, Vol. IV, Part. 4, Chapter 5 (1960).
6. C.J. Schueler, L.K. Ward, A.E. Hodapp, "Techniques for Measurement of Dynamic Stability Derivatives in Ground Test Facilities", AGARDograph 121 (1967).
7. K.J. Orlik-Rückemann, "Dynamic Stability Testing of Aircraft - Needs Versus Capabilities", NAE, NRC, Ottawa, Ontario, Canada, ICIASF 1973 Record.
8. K.J. Orlik-Rückemann, "Survey of Needs and Capabilities for Wind Tunnel Testing of Dynamic Stability of Aircraft at High Angles of Attack", NASA-CR-114583 (1973).
9. A.L. Braslow, H.G. Wiley, C.Q. Lee, "A Rigidly Forced Oscillation System for Measuring Dynamic-Stability Parameters in Transonic and Supersonic Wind Tunnels", NASA TN D-1231 (1962).
10. L.R. Fisher, J.H. Lichtenstein, K.D. Williams, "A Preliminary Investigation of the Effects of Frequency and Amplitude on the Rolling Derivatives of an Unswept-Wing Model Oscillating in Roll", NACA Tn 3554 (1956).
11. D.C. Freemann, Jr., S.B. Grafton, R.D. Amato, "Static and Dynamic Stability Derivatives of a Model of a Jet Transport Equipped with External-Flow Jet-Augmented Flaps", NASA TN D-5408 (1969).
12. P. Hamel, "Anwendung der Massenkopplung zur Bestimmung der Stabilitätsderivativa", ZFW 15 (1967).
13. D.E. Hewes, "Low-Subsonic Measurements of the Static and Oscillatory Lateral Stability Derivatives of a Sweptback-Wing Airplane Configuration at Angles of Attack from -10° to 90° ", NASA MEMO 5-20-59 L (1959).
14. E. Klinke, A. Müller, "Ein Beitrag zur Messung von Rolldämpfung im Windkanal", Jahrbuch der WGLR (1962), S. 167-170.
15. W. Letko, H.S. Fletcher, "Effects of Frequency and Amplitude on the Yawing Derivatives of Triangular, Swept and Unswept Wings and of a Triangular-Wing-Fuselage Combination with and without a Triangular Tail Performing Sinusoidal Yawing Oscillations", NACA TN 4390 (1958).

16. M. Scherer, P. Mathe, "Mesure des Dérivées Aerodynamiques en Soufflerie et en Vol.", AGARD Rapport 346 (1961).
17. M. Scherer, J. Lopez, "Progrès Réalisés dans les Techniques de Mesure des Dérivées Aerodynamiques en Soufflerie Méthode d'Oscillations Forcées", AGARD CP Nr. 17 (1966).
18. E. Schmidt, "Die AVA-Derivativwaage", DLR-Mitt. 74-32 (1974) and ESA TT-197 (1975).
19. C. Scruton, L. Woodgate, A.J. Alexander, "Measurements of the Aerodynamic Derivatives for Swept Wings of Low Aspect Ratio Describing Pitching and Plunging Oscillations in Incompressible Flow", ARC, R & M No. 2925 (1957).
20. H. Starke, "Design, Construction and Testing of an AGARD Standard Model D for Oscillatory Derivatives Measurements", von Karman Institute, TN 21 (1964).
21. I.C. Statler, O.B. Turfts, W.J. Hirtreiter, "The Development and Evaluation of the VAL/Air Force Dynamic Wind-Tunnel Testing System, Part I + II", AFFDL-TR-66-153 (1967).
22. J.S. Thompson, R.A. Fail, "Oscillatory Derivative Measurements on Sting-Mounted Wind-Tunnel Models at R.A.E. Bedford", Royal Aircraft Establishment TR-66-197 (1966).
23. X. Vaucheret, "Stabilité Dynamique sur Maquettes d'Avion par la Méthode des Oscillations Libres", ONERA T.P. Nr. 390 (1966).
24. K.J. Orlik-Rückemann, "Dynamic Stability Testing of Unconventional Configurations", Journal of Aircraft, Vol. 9, No. 2, pp. 101, 102 (1972).
25. E. Schmidt, "Zweikomponentenwaage zur Messung dynamischer flugmechanischer Derivativa von Flugkörpern", DFVLR-AVA-Bericht Nr. JB-253 73 J 04.
26. E. Schmidt, "Windkanalmessungen mit der AVA-Derivativwaage am Alpha-Jet-Modell (M 1:5), Teil I: Laboreichungen", DFVLR-AVA-Bericht Nr. IB 253-74 J 01 (1974).
27. E. Schmidt, "Windkanalmessungen mit der AVA-Derivativwaage am Alpha-Jet-Modell (M 1:5), Teil II: Dynamische Derivativa der Längsbewegung", DFVLR-AVA-Bericht Nr. IB 253-74 J 09 (1974).
28. E. Schmidt, "Windkanalmessungen mit der AVA-Derivativwaage am Alpha-Jet-Modell (M 1:5), Teil III: Dynamische Derivativa der Seitenbewegung", DFVLR-AVA-Bericht Nr. IB 253-75 J 11 (1975).
29. O. Determann, J. Oser, J.v.d. Decken, R. Joos, B. Ewald, E. Graewe, "Mobile oszillierende Derivativwaage, Entwicklungsphase I, Gesamtauslegung", Dornier Forschungsbericht 74/6/B (1974).
30. O. Determann, J. Oser, J.v.d. Decken, R. Joos, B. Ewald, E. Graewe, "Mobile oszillierende Derivativwaage, Entwicklungsphase II, Voruntersuchung, Detailauslegung, Konstruktion", Dornier Forschungsbericht 75/16/B (1975).
31. O. Determann, J. Oser, J.v.d. Decken, R. Joos, E. Graewe, V. Renken, E. Schmidt, "Mobile oszillierende Derivativwaage, Entwicklungsphase III, Fertigung und Teilerprobung", Dornier Forschungsbericht 76/12/B (1976).
32. E. Graewe, V. Renken, "Mobile oszillierende Derivativwaage, Entwicklungsphase IV, Benutzerhandbuch für die Meßdaten-Erfassungsanlage", Dornier Forschungsbericht 76/13/B (1976).
33. W. Schlottmann, "Stationäre und instationäre Rollmomentenderivative schlanker Flügel in Rollbewegung", ZFW 1974, S. 331-344.

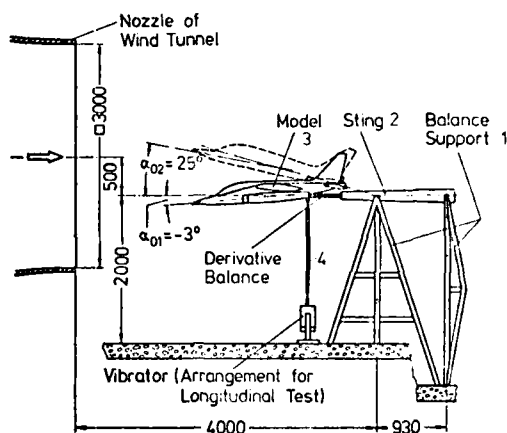


Fig. 1 The DFVLR oscillatory multi-degree-of-freedom derivative balance, final assembly

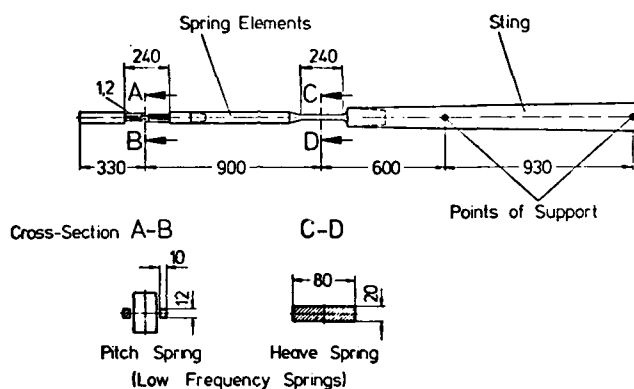


Fig. 2 The elastic sting of the DFVLR-derivative balance

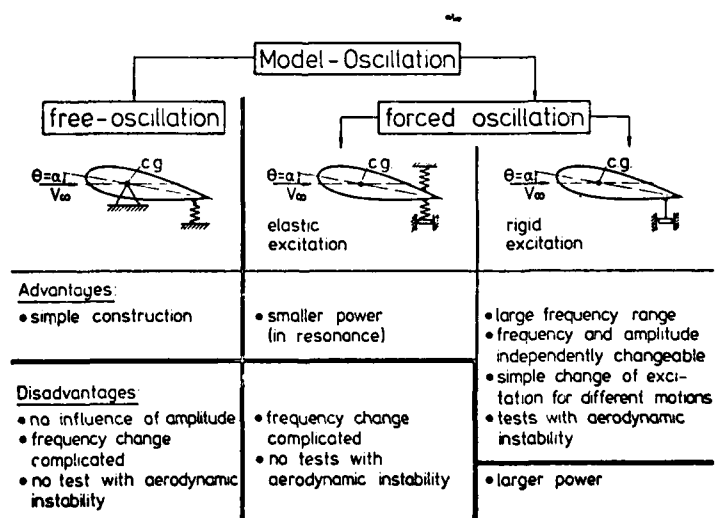


Fig. 3 Basic principles of oscillatory balances

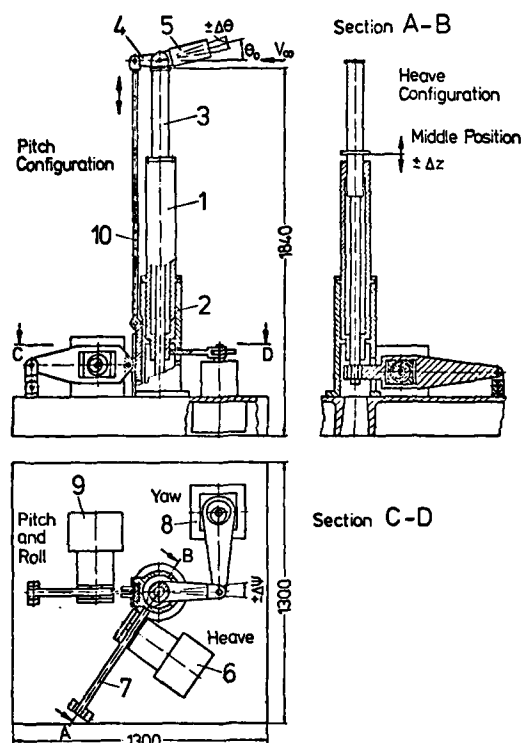


Fig. 4 The mobile oscillatory derivative balance final assembly

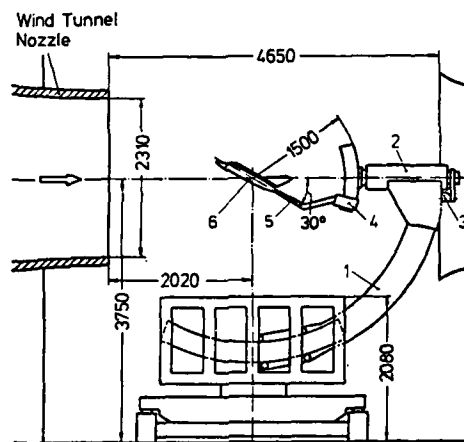


Fig. 6 General arrangement of the rotary derivative balance

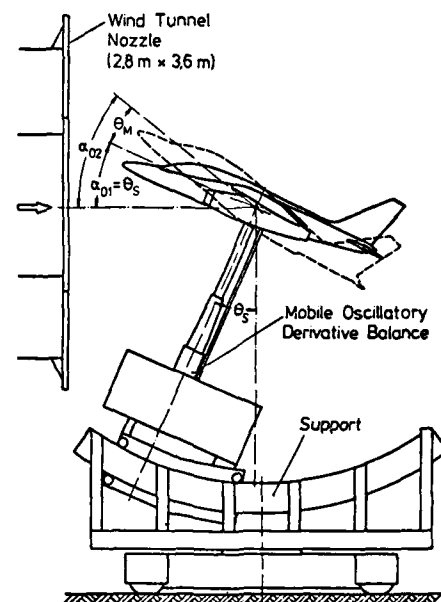


Fig. 5 Installation of the mobile oscillatory derivative balance for high angles of attack

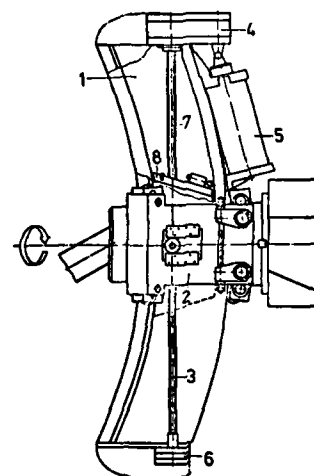


Fig. 7 Arc traverse

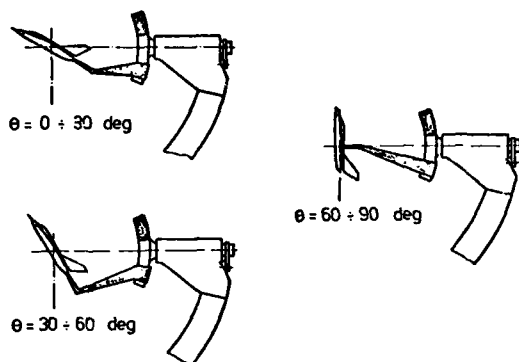


Fig. 8 Sting systems to obtain the total range of pitch

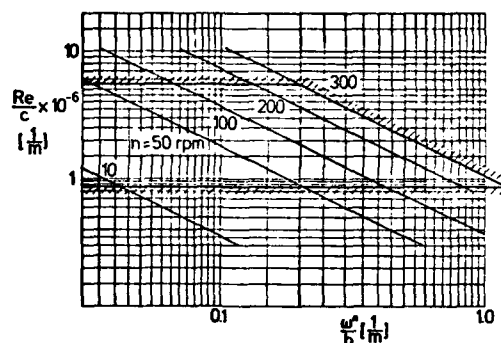


Fig. 9 Reynolds-Number range as function of the reduced frequency and the rotary speed of the balance

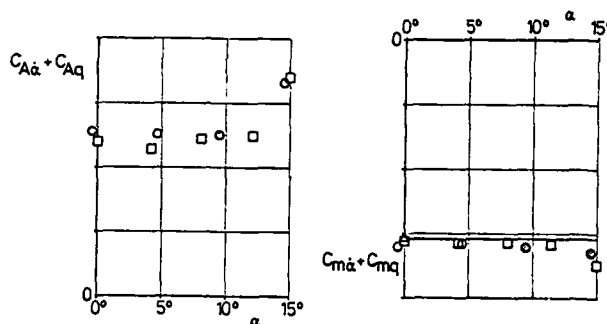


Fig. 10 Lift and pitching moment due to pitch oscillation, comparison of the results of the oscillatory balance and of flight tests

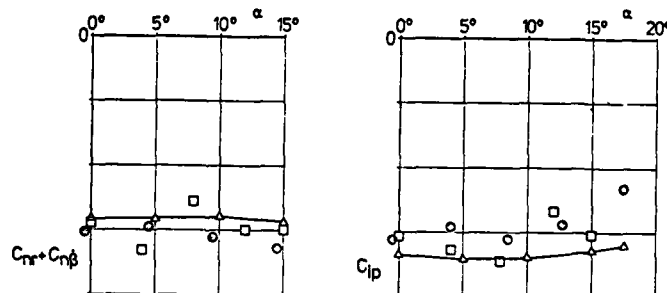


Fig. 11 Damping in yaw and in roll derivatives, comparison of the results of the oscillatory balance and of flight tests

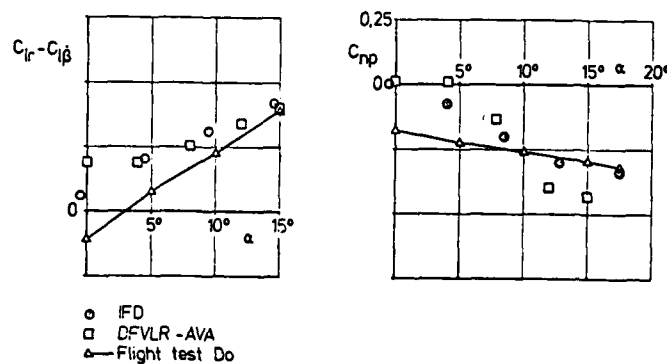


Fig. 12 Lateral coupling derivatives, comparison of the results of the oscillatory balances and of flight tests

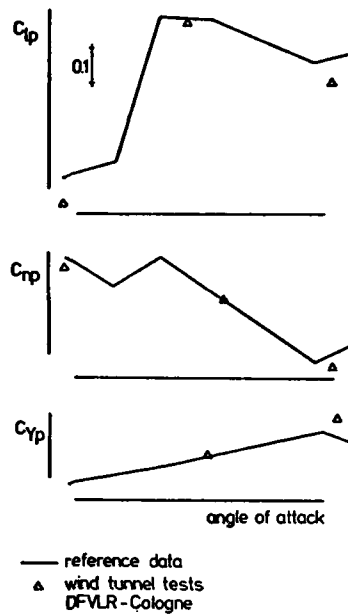


Fig. 13 Rotary derivative balance results (typical fighter configuration)

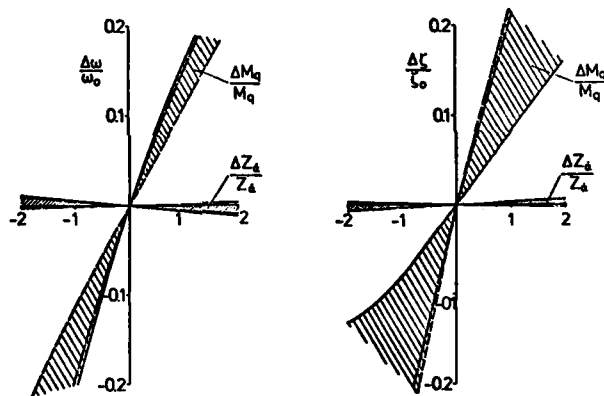


Fig. 14 The relative change of the dynamic derivatives on the results of the short period mode

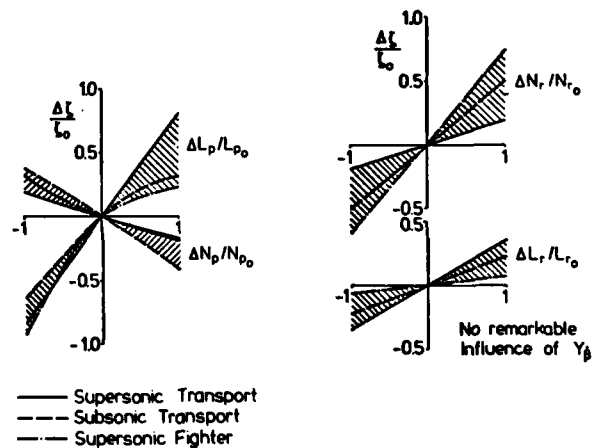


Fig. 15 The relative change of the damping and coupling derivatives on the results of the dutch-roll mode

ON THE TEST PROCEDURES OF THE DERIVATIVE BALANCES USED IN WEST-GERMANY

by

Dr.-Ing. Jan von der Decken, Dornier GmbH, 7990 Friedrichshafen, Pf. 1420,
Dr.-Ing. Eberhard Schmidt, DFVLR, 3300 Braunschweig, Pf. 3267,
Dipl.-Ing. Bernd Schulze, MBB-UF, 8000 München 80, Pf. 801 160.

West-Germany

SUMMARY

The low-speed wind tunnels in West-Germany are equipped with three different test installations to measure dynamic stability derivatives on rigid models of aeroplanes and missiles:

- a mobile oscillatory apparatus with inexorable mechanical drive,
- a multi-degree-of-freedom forced-oscillation apparatus with electrodynamic excitation,
- a steady-state forced-roll apparatus with hydraulic motor drive.

A short description of the measuring technique and the appropriate derivative evaluation method used with each installation will be given in this paper. The good matching of hardware and software used has been demonstrated by the good test results shown by Prof. Hafer in the previous paper.

1. INTRODUCTION

Modern high performance fighter aircraft are often exposed to strong unsteady flow conditions, for instance asymmetric vortex shedding on slender configurations at sideslip, flow separation at high angle of attack and maneuvers in the wake flow of large transport aircraft. A precise prediction of dynamic aircraft motions under such adverse flight conditions has today become essential for a successful advanced aircraft design [1].

Wind tunnel instrumentation for measuring dynamic stability derivatives on aircraft models undergoing longitudinal or lateral motion with one to three degrees of freedom is widely used at the aerodynamic research centers of France, Great Britain and the United States [2], whereas in West-Germany similar equipment has been in operation for only five years. Coordinated work of the German aircraft industry and research facilities on three joint projects sponsored by the Ministry of Research and Technology allows us now to present three different derivative balances operating in our medium-size low-speed wind tunnels. The main features of the installations are summarized in Figure 1.

The mobile oscillatory derivative balance (MOD; main contractor Dornier GmbH, Friedrichshafen) for one-degree-of-freedom operation can be used in three different wind tunnels. Model motions on top of a vertical sting with moderate amplitudes in pitch, heave, roll or yaw are forced by a DC-motor crankshaft drive at frequencies up to 3 Hz.

The three-degree-of-freedom derivative balance (MFD; main contractor DFVLR, Göttingen) is now operated in the 3m wind tunnel at DFVLR, Braunschweig. For a model mounted on an elastic rearward-sting support combined small amplitude oscillations in pitch and heave or roll, yaw and sideslip are rigidly forced by an electrodynamic shaker in the frequency range 2 to 10 Hz.

The steady-state forced-roll derivative balance (RTD; main contractor MBB, Ottobrunn) is constructed for the 3m wind tunnel at DFVLR, Köln. This apparatus consists of a very stiff support with a hydraulic motor on top. The motor drives a circular-arc traverse carrying the model using a rearward sting. The roll axis is kept parallel to the airstream and the arc traverse enables the model angle of attack to be changed continuously.

The design criteria and mechanical arrangements of the three balances together with some typical test results have been discussed by Prof. Hafer in the previous paper [3]. This report gives a short description of the measuring technique and appropriate derivative evaluation method used with each apparatus. Further details can be found in the literature referenced in the following chapters.

2. MOBILE OSCILLATORY DERIVATIVE BALANCE

2.1 Measuring Technique

Prof. Hafer has already referred to the mechanical construction of the crankshaft drive derivative balance which was developed and tested by Dornier as the main contractor. As he indicated, the drive unit is situated outside the wind tunnel test section on the building floor. The models are mounted on a moving head fixed to a vertical sting. Details of the mechanical arrangement are given in Ref. [4].

A block diagram of the measurement technique is shown in Figure 2. The following functions can be distinguished:

- analog measurement of model forces and moments,
- analog measurement of model motion,
- digital measurement of excitation frequency,
- parallel sampling of analog data,
- data storage and processing using a minicomputer,
- real time observation using storage oscilloscope.

A five component (no X-force) strain gauge balance mounted between the moving head and the model with its reference point close to the model center of gravity gives analog voltages representing the total forces or moments caused by inertial and aerodynamic reactions acting on the model. Figure 3 shows the simple construction of the balance specified by Dornier and VFW-Fokker and manufactured by TEM of Crowley, England. The intention was to achieve large signal outputs for small model displacement. The calibration matrix shows very small interference effects.

A simple cantilever beam with a strain gauge bridge gives model position information. The unit is calibrated in the laboratory against absolute model deflection.

A pulse generator on the shaft of the motor drive is used to measure the excitation frequency. A digital counter coupled to the pulse generator gives the time period of excitation with an accuracy of 1 part in 10,000 over the total frequency range used. Routine checks have shown that the oscillation frequency of the total system remains constant within ± 0.001 Hz.

Parallel sampling of analog data is accomplished using a computer controlled data acquisition system built by NEFF. In the configuration chosen, a maximum of 12 parallel low level input channels is available. Each channel is provided with a sample and hold preamplifier with adjustable voltage gain and a Butterworth filter. Four further high level channels to measure voltages of bridge supply and transducers for tunnel pressure and temperature are also included. The sample and hold feature allows all the analog signals to be sampled at the same points in time at a maximum rate of 1000 Hz per channel. The data are serialized using an analog multiplexer. Then they are further amplified with a computer controlled amplifier which provides real time voltage gain adjustment between 1 and 40. The gain is adjusted to provide appropriate input level for the following 20 kHz analog-to-digital converter with 14 bit resolution. The digital output is fed to the minicomputer via direct memory access and immediately stored on magnetic tape using a pair of memory blocks; one of them is filled with input data while the other is read out to the tape unit and then vice versa.

The total measurement error introduced by the sampling and digitizing process is less than $\pm 0.04\%$ of the A/D converter full scale range for temperatures between 20 and 50 degrees C.

The pdp 11/10 minicomputer with 56 kByte core memory, crystal time base, 2.4 megaByte disc cartridge, NEFF analog data acquisition system and 800 bpi magnetic tape unit was purchased by DFVLR. The total data sampling and processing operation is controlled in dialog fashion using a DECwriter keyboard terminal. The keyboard is also used to enter additional test parameter data such as run number, configuration code, test conditions, etc..

The software package necessary for the mentioned features of this stand-alone measuring system was developed by VFW-Fokker in collaboration with the Institute for Flight Techniques of the Technical University Darmstadt. The package also includes strain gauge balance and transducer calibration procedures as well as function tests for all system components. A special FORTRAN driver for the NEFF system developed by DEC with support from VFW-Fokker increased flexibility and greatly lessened the programming workload.

Up to four signals of special interest can be selected from the multiplexer input and displayed on a multiple trace storage oscilloscope. This real-time observation of some input data is necessary because the measurement process appears too fast for step-by-step control by the operator.

Normally a sampling time of 60 sec has been used for wind-on tests, whereas the corresponding wind-off tests lasted 20 sec. The data rate chosen was 1000 samples per sec, giving a typical data string length of 600,000 values. Further details of the complete instrumentation hardware and software for the mobile oscillatory derivative balance (MOD) are given in Ref. [5].

2.2 Derivative Evaluation Method

Modern methods of parameter identification [6] which have been successfully applied to flight test data analysis might be used to evaluate dynamic derivatives from the MOD data which is stored on digital magnetic tape. The disadvantage of those methods is their complexity; this results in inordinate programming workload combined with excessive computer time and memory requirements.

The much simpler classical method of Fourier analysis is applicable to the MOD data because the model is forced to oscillate at essentially constant frequency and amplitude. The good test results shown by Prof. Hafer in the previous paper have been evaluated from MOD measurements using a Fourier technique which used only the fundamental frequency. The main steps of this evaluation method will now be described.

Since the model is excited with a forcing frequency $\omega = 2\pi f$, any deflection signal $D(t)$ as well as any force signal $F(t)$ and moment signal $M(t)$ can be represented by the summations:

$$\left. \begin{aligned} D(t) &= D_0 + D_s \sin \omega t + D_c \cos \omega t, \\ F(t) &= F_0 + F_s \sin \omega t + F_c \cos \omega t, \\ M(t) &= M_0 + M_s \sin \omega t + M_c \cos \omega t. \end{aligned} \right\} \begin{array}{l} \text{plus negligible higher} \\ \text{harmonic terms} \end{array} \quad (1)$$

The Fourier coefficients used for the deflection equation are given by

$$\begin{aligned} D_0 &= \frac{1}{T} \int_{t_0}^{t_0+T} D(t) dt, \\ D_s &= \frac{2}{T} \int_{t_0}^{t_0+T} D(t) \sin \omega t dt, & (\text{in phase component}) \\ D_c &= \frac{2}{T} \int_{t_0}^{t_0+T} D(t) \cos \omega t dt. & (\text{quadrature component}) \end{aligned} \quad (2)$$

It might be remembered from the previous chapter that the MOD data covers a large number of periods in order to eliminate higher harmonics in the signals. Because the measured data are sampled at equidistant time intervals Δt controlled by the crystal clock, and because the exact excitation frequency is measured, a sequence of sampled signals can be chosen in a time interval $n \cdot \Delta t$ equal to a multiple of the period.

In this case the above integrals (2) can be approximated by finite sums:

$$\begin{aligned} D_o &= \frac{1}{n\Delta t} \sum_{i=1}^n D_i \Delta t, \\ D_s &= \frac{2}{n\Delta t} \sum_{i=1}^n D_i \sin \omega t_i \Delta t, \\ D_c &= \frac{2}{n\Delta t} \sum_{i=1}^n D_i \cos \omega t_i \Delta t. \end{aligned} \quad (3)$$

Equivalent equations hold for the force and moment signals. The aerodynamic parts of their Fourier coefficients are easily calculated from the difference of wind-on and wind-off coefficients, for example

$$\begin{aligned} \Delta F(t) &= F(t)_{\text{wind-on}} - F(t)_{\text{wind-off}}, \\ \Delta F(t) &= \Delta F_o + \Delta F_s \sin \omega t + \Delta F_c \cos \omega t. \end{aligned} \quad (4)$$

Normally the aerodynamic reactions contain a constant part κ due to static aerodynamic preloading, a stiffness component λ in phase with the model motion, and a damping component μ which leads the motion by 90 degrees. This means

$$\begin{aligned} \Delta F(t) &= \kappa + \lambda \cdot (D(t) - D_o) + \mu \frac{dD(t)}{dt}, \\ \Delta F(t) &= \kappa + \lambda \cdot (D_s \sin \omega t + D_c \cos \omega t) \\ &\quad + \omega \mu (D_c \cos \omega t - D_s \sin \omega t). \end{aligned} \quad (5)$$

Introducing the relations contained in eq. (1) into eq. (5):

$$\begin{aligned} \kappa &= \Delta F_o \quad (= F_{o, \text{wind-on}} - F_{o, \text{wind-off}}), \\ \lambda &= \frac{\Delta F_s D_s + \Delta F_c D_c}{D_s^2 + D_c^2}, \\ \mu &= \frac{\Delta F_c D_s - \Delta F_s D_c}{\omega (D_s^2 + D_c^2)}. \end{aligned} \quad (6)$$

These relations hold for rotatory oscillations. For translatory motions, the dynamic components are proportional to the motion velocity $\dot{D}(t)$ and the acceleration $\ddot{D}(t)$ instead of the motion $D(t)$ itself.

For each of the different model motions available with the MOD, the three components κ , λ and μ of each force or moment signal can be replaced by the corresponding aerodynamic derivatives. For pitching oscillations ($\Delta \alpha = \Delta \theta$, $\Delta \dot{\alpha} = \Delta \dot{\theta} = \Delta \dot{q}$) flight mechanics nomenclature gives the following relations for the lift force L and pitching moment M

$$\begin{aligned} \Delta L(t) \cos \alpha_o &= q_\infty S [C_{L_o} + C_{L_\alpha} \Delta \theta + (C_{L_q} + C_{L_{\dot{\alpha}}}) \Delta \dot{\theta} 1_\mu / V_\infty], \\ \Delta M(t) &= q_\infty S l_\mu [C_{m_o} + C_{m_\alpha} \Delta \theta + (C_{m_q} + C_{m_{\dot{\alpha}}}) \Delta \dot{\theta} 1_\mu / V_\infty]. \end{aligned} \quad (7)$$

By comparison with eq. (5) and (6) the simple relations between the components κ , λ and μ and the corresponding derivatives can be extracted. Similar relations hold for the roll, yaw and heave derivatives.

The Institute for Flight Techniques has produced a FORTRAN software package for the described derivative evaluation method for use with the 16 bit pdp 11/10 minicomputer. The memory of the minicomputer used with the MOD equipment is large enough to hold the total program in assembler language. Therefore the derivative evaluation process can take place using the MOD equipment itself without the need for additional computer capacity. The processing time needed for a typical data string of 600,000 values is roughly 15 min. Therefore all the data measured during an eight hour work day can easily be evaluated before the next morning.

Finally, based on the test results to date, the accuracy of the resulting derivatives can be discussed. Because of the high noise levels on the measured signals (caused by bearing freeplay in the drive mechanism, free stream wind tunnel turbulence, etc.), each test is repeated several times to obtain sufficient data for statistical analysis. Typical results for a 99% confidence level are given in the following table:

Static Derivatives		Dynamic Derivatives (direct damping)		Dynamic Derivatives (coupled damping)	
C_{L_α}	1,5 %	$C_{L_{\dot{\alpha}}} + C_{L_q}$	7 %		
C_{m_α}	2 %	$C_{m_{\dot{\alpha}}} + C_{m_q}$	2,5 %		
C_{Y_β}	1 %	$C_{Y_r} - C_{Y_{\dot{\beta}}}$	2 %	C_{Y_p}	15 %
C_{l_β}	3 %	C_{l_p}	10 %	$C_{l_r} - C_{l_{\dot{\beta}}}$	10 %
C_{n_β}	2,5 %	$C_{n_r} - C_{n_{\dot{\beta}}}$	2 %	C_{n_p}	12,5 %

The deviations for the static derivatives are not larger than equivalent values from static tests and the deviations of the dynamic derivatives are well within typical values from other dynamic derivative installations (see Ref. [2]).

For further critical examination of the derivative results calculated using the described Fourier analysis, the Institute for Flight Technique has also programmed a regression analysis method. But the regression analysis has not yet been used because, in addition to model motion signals, it also requires velocity and acceleration information. Differentiation of the motion signals would be bad because of the high noise levels. Therefore the MOD is now being instrumented with suitable accelerometers (velocity will be obtained by integration).

It should also be mentioned that cross-coupling derivatives such as $C_{\dot{w}} - C_{\dot{w}p}$, $C_{\dot{w}} + C_{\dot{w}p}$ or $C_{\dot{w}} + C_{\dot{w}p}$ can be evaluated with the MOD as it is now used. This is possible since the required five components (normal force Z, pitching moment M, side force Y, rolling moment L and yawing moment N) are measured for all possible motions (pitch, heave, roll, yaw, and lateral displacement).

3. MULTI-DEGREE-OF-FREEDOM OSCILLATORY DERIVATIVE BALANCE

3.1 Measuring Technique

Prof. Hafer has also described the mechanical arrangement of the Multi-Degree-of-Freedom Derivative Balance (MFD) which takes pattern from an elder RAE balance for slender aircraft models in a large high-speed wind tunnel [7]. In fact our spring-unit has been redesigned for lower stiffness for low-speed wind tunnel application, the excitation force is now directly applied to the model from a more powerful electrodynamic shaker, and variable artificial damping is introduced to smooth model motions due to wind tunnel flow fluctuations [8].

The electronic test equipment is based on a set of special instruments which have been developed by the DFVLR Institute for Aeroelasticity to undertake ground vibration tests on aircraft and spacecraft [9]. Figure 4 shows a schematic block diagram of the MFD instrumentation which can be subdivided into the following functions:

- excitation and damping of model motion,
- measurement of excitation frequency,
- registration of time dependent voltages and transformation into vector component amplitudes,
- integration and display of vector components,
- output of results,
- input data control with oscilloscope.

The control voltage v_c of the electrodynamic shaker (max. force ± 100 N with ± 15 mm displacement at 20 Hz) is produced on a very stable low frequency sine generator and amplified by a feedback power amplifier. An inductive velocity transducer is attached to the shaft of the shaker which is rigidly connected to the model; in a feedback circuit the transducer voltage v_s can be amplified and superimposed on the control voltage v_c thus adding artificial damping to the mechanical system.

The frequency of model excitation is measured by a crystal-based counter with five-digit display. Thereby the short time drift of the sine generator can be checked to within ± 1 per 10^3 digits.

The three output voltages v_1 , v_2 and v_3 from strain gauge bridges measuring bending and torsion of the spring-unit are raised to 1 Volt level via parallel high quality preamplifiers. These voltages together with the voltages v_c and v_s are applied to separate voltmeters which resolve any vector amplitude into a real component (in phase with the 0° reference voltage of the sine generator) and an imaginary component (in phase with the 90° reference voltage). The resolved component voltmeters (RCV) act as selective filters with more than 50 dB/octave minimizing stray voltages at frequencies different from reference (e.g. harmonic distortion and tunnel fluctuation influence). As shown in the diagram the power amplifier for the excitation force is connected to the 90° phase of the sine generator (pure imaginary voltage), so that the model displacement signals v_1 , v_2 and v_3 become real values at phase resonance.

The resolved component voltmeters generate output voltages up to 3 V proportional to the measured components with $\pm 0.3\%$ accuracy related to the full scale value in five ranges from 0.1 to 10 Volts. Each RCV output voltage is applied to an integrating digital voltmeter (IDVM) with variable integration time (typical values used are 6 sec for wind-off tests and 60 sec for wind-on tests). The IDVMs include buffer storage to display and output four-digit results of the previous integration while the actual one is performed.

The digital values of the nine vector components together with the tunnel data (dynamic pressure and temperature), the excitation frequency, and up to four further digital test parameters (run number and model parameters) are applied to a digital multiplexer with party-line control for serial output on paper-tape punch and/or line printer. This data string forms the basis for the further evaluation of dynamic derivatives from the tests.

The most important analog signals are displayed on a four-trace storage oscilloscope for continuous visual checks. The horizontal oscilloscope deflection is triggered by the sine generator to achieve stationary display.

3.2 Derivative evaluation method

The further analysis of the wind tunnel data strings utilizes integral energy equations according to the motions of an aeroelastic vibration system instead of analytical equations of model motion. A similar evaluation method has been successfully employed for flutter calculations of aircraft structures [10], [11]. In the following the main formula algorithm used for the MFD in the case of lateral model motion with three rigid-body degrees of freedom will be given.

The method is based on the assumption that the total oscillating system behaves in a linear manner including the mechanical properties of tunnel ground support, elastic rearward sting, spring-unit and rigid model together with the aerodynamic reactions and the qualities of electronic excitation.

With the principal system outlined in Figure 5 a discrete harmonic excitation force

$$\bar{P}_{E\lambda}(x_E, y_E, z_E, t) = P_{E\lambda}(x_E, y_E, z_E) e^{j\omega_\lambda t} = (P'_{E\lambda} + jP''_{E\lambda}) e^{j\omega_\lambda t} \quad (1)$$

(circular frequency ω_λ , time t , imaginary unit $j = \sqrt{-1}$) is applied to the model, the response of which can be defined by three independent displacement parameters:

$$\begin{aligned} \bar{\varphi}_\lambda(x, y, z, t) &= \varphi_\lambda(x, y, z) e^{j\omega_\lambda t} = (\varphi'_\lambda + j\varphi''_\lambda) e^{j\omega_\lambda t}, \\ \bar{\psi}_\lambda(x, y, z, t) &= \psi_\lambda(x, y, z) e^{j\omega_\lambda t} = (\psi'_\lambda + j\psi''_\lambda) e^{j\omega_\lambda t}, \\ \bar{y}_\lambda(x, y, z, t) &= y_\lambda(x, y, z) e^{j\omega_\lambda t} = (y'_\lambda + jy''_\lambda) e^{j\omega_\lambda t} \end{aligned} \quad (2)$$

(angle of roll φ , angle of yaw ψ , sideslip y).

The introduced complex amplitude notation confines the time dependence to the factor $e^{j\omega_\lambda t}$. Therefore amplitude equations can be employed in the following without restricting the field of validity. It was already mentioned, that the real component of each amplitude is in phase with a common reference vector v_0 (0° reference voltage from sine generator), whereas the imaginary component leads v_0 by 90° .

The stiffness of the mechanical system has been constructed with its three lowest eigenfrequencies giving the three rigid model motions wanted, namely roll, yaw, and sideslip oscillation. Higher eigenfrequencies are far enough above these interesting modes to exclude them from the analysis. If the three eigenmode parameters φ_λ , ψ_λ and y_λ at the eigenfrequencies ω_λ are introduced, any general model motion at the frequency ω_λ can be expressed into the eigenmodes with the Ritz series expansion:

$$\varphi_\lambda = \sum_{r=1}^3 \varphi_r q_{r\lambda}, \quad \psi_\lambda = \sum_{r=1}^3 \psi_r q_{r\lambda}, \quad y_\lambda = \sum_{r=1}^3 y_r q_{r\lambda}. \quad (3)$$

The so-called generalized coordinates $q_{r\lambda} = q'_{r\lambda} + jq''_{r\lambda}$ might be interpreted as weight functions defining the amount of each eigenmode included in the general mode of oscillation.

The general mode parameters φ_λ , ψ_λ , y_λ are related to the voltages v_1 , v_2 , v_3 from the strain gauge bridges in linear form:

$$\begin{aligned} \varphi_\lambda &= c_{\varphi 1} v_{1\lambda} + c_{\varphi 2} v_{2\lambda} + c_{\varphi 3} v_{3\lambda}, \\ \psi_\lambda &= c_{\psi 1} v_{1\lambda} + c_{\psi 2} v_{2\lambda} + c_{\psi 3} v_{3\lambda}, \\ y_\lambda &= c_{y1} v_{1\lambda} + c_{y2} v_{2\lambda} + c_{y3} v_{3\lambda}. \end{aligned} \quad (4)$$

The coefficients are determined with calibrated displacement transducers which are attached to the model during a calibration test.

At any time t equilibrium exists on every volume element of the oscillating model between excitation force, inertial force, mechanical stiffness and damping forces (including artificial electronic damping), and the aerodynamic forces induced by the model motion in the wind stream. Following Galerkin's procedure these elementary forces can be multiplied by each eigenmode in turn and integrated over the body volume to end up with the Rayleigh-Ritz energy equations for the total system. In the case of the MFD lateral motion with wind-on these energy equations read (see Ref. [8]):

$$(\omega_r^2 - \omega_\lambda^2) M_{rr} p_{r\lambda} + j\omega_\lambda \sum_{s=1}^3 D_{rs} p_{s\lambda} = \sum_{s=1}^3 L_{rs} q_{s\lambda} \quad \text{for } r = 1, 2, 3 \quad (5)$$

with the abbreviation

$$p_{r\lambda} = q_{r\lambda} - \frac{P_{E\lambda}}{P_{E\lambda}^0} q_{r\lambda}^0 \quad (6)$$

The quantities ω_λ , $p_{r\lambda}$ and $q_{r\lambda}$ are determined from the data strings given by wind-on and wind-off tests (Index 0); the generalized coordinates can be derived directly from the following linear equation system:

$$\begin{aligned} v_{1\lambda} &= v'_{1\lambda} + jv''_{1\lambda} = \sum_{r=1}^3 v_{1r} (q'_{r\lambda} + jq''_{r\lambda}), \\ v_{2\lambda} &= v'_{2\lambda} + jv''_{2\lambda} = \sum_{r=1}^3 v_{2r} (q'_{r\lambda} + jq''_{r\lambda}), \\ v_{3\lambda} &= v'_{3\lambda} + jv''_{3\lambda} = \sum_{r=1}^3 v_{3r} (q'_{r\lambda} + jq''_{r\lambda}). \end{aligned} \quad (7)$$

It can be seen that the voltage amplitudes v_1 , v_2 and v_3 measured with the strain gauge bridges are used without calibration.

The mechanical system properties are represented by the generalized masses

$$M_{rr} = \iiint_V \rho(x,y,z) u_r^2(x,y,z) dx dy dz \quad \text{for } r = 1, 2, 3 \quad (8)$$

$$= \frac{\omega_r \cdot \Delta m}{2(\omega_r - \omega_{\Delta r})} u_{\Delta r}^2 \quad (\text{calibration formula}) \quad (8a)$$

(local mass density $\rho(x,y,z)$, motion amplitude u_r in direction of the excitation force), the generalized damping matrix

$$D_{rs} = \iiint_V \iiint_V w_{rs}(x,y,z;x',y',z') u_r(x,y,z) u_s(x',y',z') dx dy dz \quad (9)$$

for $r, s = 1, 2, 3$

$$= \frac{P_{Es} \cdot u_{Er}}{\omega_s} \quad (\text{calibration formula}) \quad (9a)$$

(viscous damping coefficients w_{rs} proportional to rate of displacement) and the eigenvalues φ_r , ψ_r and γ_r at eigenfrequencies ω_r .

Calibration tests with an additional mass Δm installed at a model point with the motion amplitude $u_{\Delta r}$ in force direction at eigenfrequency $\omega_{\Delta r}$ give the generalized mass of each eigenmode. The pertinent generalized damping terms D_{rs} are determined from the appropriate data without additional mass, including the force amplitude P_{Es} with the displacement amplitude u_{Er} at the model excitation point.

The unknown quantities of equation system (5) are the aerodynamic force integrals L_{rs} appearing in the expression for the work done by the global aerodynamic reactions:

$$\sum_{s=1}^3 L_{rs} q_{s\lambda} = \varphi_r L_\lambda + \psi_r N_\lambda + \gamma_r Y_\lambda \quad \text{for } r = 1, 2, 3 \quad (10)$$

including rolling moment L_λ , yawing moment N_λ and side force Y_λ . These aerodynamic reactions embody the unknown dynamic stability derivatives of lateral motion defined by the linearized Taylor series expansion:

$$\begin{aligned} L_\lambda &= q_{\infty\lambda} \frac{b}{2} s \left\{ c_{l\phi} \phi_\lambda - \omega_\beta^2 c_{l\dot{\beta}} \bar{y}_\lambda + j\omega_\beta^2 [c_{lp} \varphi_\lambda + (c_{lr} - c_{l\dot{\beta}}) \psi_\lambda + c_{l\dot{\beta}} \bar{y}_\lambda] \right\}, \\ N_\lambda &= q_{\infty\lambda} \frac{b}{2} s \left\{ c_{n\phi} \phi_\lambda - \omega_\beta^2 c_{n\dot{\beta}} \bar{y}_\lambda + j\omega_\beta^2 [c_{np} \varphi_\lambda + (c_{nr} - c_{n\dot{\beta}}) \psi_\lambda + c_{n\dot{\beta}} \bar{y}_\lambda] \right\}, \\ Y_\lambda &= q_{\infty\lambda} s \left\{ c_{y\phi} \phi_\lambda - \omega_\beta^2 c_{y\dot{\beta}} \bar{y}_\lambda + j\omega_\beta^2 [c_{yp} \varphi_\lambda + (c_{yr} - c_{y\dot{\beta}}) \psi_\lambda + c_{y\dot{\beta}} \bar{y}_\lambda] \right\}. \end{aligned} \quad (11)$$

(dynamic pressure $q_{\infty\lambda}$ at free stream velocity v_λ , wing span b , sideslip amplitude parameter $\bar{y}_\lambda = 2y_\lambda/b$).

Three independent model motions at different excitation frequencies ω_λ are necessary to solve the linear equation system (11) on the fifteen unknown derivatives. Therefore the velocity v_λ must be altered to keep the reduced frequency

$$\omega_\beta^* = \omega_\lambda \frac{b}{2} / v_\lambda \quad (12)$$

as the main parameter of unsteady aerodynamics a constant. It is advisable to choose excitation frequencies ω_λ adjacent to the eigenfrequencies ω_r to compensate inertial and mechanical stiffness forces. Then the excitation force becomes a direct measure of the total system damping.

The described derivative evaluation procedure for wind tunnel tests conducted with the multi-degree-of-freedom derivative balance has been established as a package of FORTRAN programs for the IBM 370/158 computer of DFVLR, Göttingen. The case of longitudinal model motion (pitch and heave) is also included in the software.

It might be added that extensive wind tunnel tests on a light-weight Alphajet model were made in the 3m low-speed wind tunnel of DFVLR, Göttingen which show the reliability and serviceableness of the MFD hardware and software [12]. This industrial trial of the equipment qualities was conducted by the DFVLR Institute for Aeroelasticity in close cooperation with Dornier.

4. FORCED-ROLL DERIVATIVE BALANCE

4.1 Measuring Technique

In the previous paper [3] a description of the mechanical arrangement for the new German forced-roll derivative balance (RTD) has been given. Further details can be found in Ref. [13] dealing with the balance design aspects.

It might be remembered that the main mechanical components of the rotary balance are a very stiff and heavy support system carrying a circular-arc traverse which is forced to rotate about the wind axis by means of a hydraulic motor drive, and a cranked sting with the model on top which can be moved on the arc traverse for remote pitch angle setting.

The measuring technique used to obtain aerodynamic data from the rotating model is organized into six

different functions according to Figure 6:

- speed control of the hydraulic drive unit,
- remote setting of the angle of pitch,
- measurement of model forces and moments by use of an internal 6-component strain gauge balance,
- signal transmission from the rotating system to the ground by means of a slip ring assembly,
- signal integration,
- data output.

The four kilowatt hydraulic motor drive can be easily controlled in the whole speed range between 0 and 300 rpm. Its rotational speed is measured by a pulse generator which delivers 2500 pulses per revolution.

The remote setting of the angle of pitch, i.e. the positioning of the sting cart on the arc traverse by means of an electric motor has not yet been tested. The value of the angle of pitch is delivered by a calibrated potentiometer.

The six-component strain gauge balance used has been constructed by VFW-Fokker. While the balance design is conventional, its fabrication procedure is different from others [14]. According to Figure 7 the balance consists of four parts which were machined separately and joined together by electron beam welding under vacuum conditions. Artificial aging was obtained by thermal treatment. The achieved accuracy of the strain gauge balance including temperature effects is given in the following table:

	Mean Accuracy % FS	Zero Shift % FS (20°±50°C)
All components of Forces/Moments	± 0.125	< 0.01

All analog signals from the rotating system are transmitted to the ground-fixed data acquisition system through a commercial quality slip ring unit with gold-plated contacts. Provision was made to transmit 38 connections which means that a future extension of the measuring system is possible including pressure transducers or acceleration pickups. The integral value of the signal-to-noise ratio for multiple revolutions of the slip rings is about 60 dB.

The integration of all balance signals is performed by the standard data acquisition system of the wind tunnel. In each of up to 18 channels in parallel the input voltage is converted into a pulse sequence by using a voltage-to-frequency converter with a cutoff frequency of 100 kHz. Each pulse sequence is integrated by a separate counter with stepwise adjustable gate time from 0.02 to 60 sec.

During forced roll tests the stationary aerodynamic and centrifugal loads acting on the model will be superimposed by periodic loads depending on the number of revolutions of the rotating masses. Therefore accurate mean values of the balance signals can only be obtained, if the gate time of each counter is exactly equal to a multiple period of rotations of the balance [15]. This is achieved by controlling the gate time of the counters externally from a pulse generator connected to the rotating system which produces only one impulse per revolution. As shown in Figure 8 the cycle of measurement is released by external command, but started and concluded by means of impulses delivered from the pulse generator. The actual integration time is terminated by the first impulse following the end of the preselected gate time of the counter.

The counters are provided with digital display and buffer store, so that the last measured value remains indicated while the next integration sequence takes place. The BCD-buffer stores are connected in parallel to a party-line, from which their values will be sequentially transmitted to a minicomputer. The computer collects all measured values from one test run and outputs the raw data on paper tape due to safety considerations. Furthermore the final derivative values are computed and delivered on a line printer using the software package of the rotatory balance developed at DFVLR, Braunschweig.

4.2 Derivative Evaluation Method

The data evaluation method employed is very simple, because it starts from stationary data due to the integration procedure of measurement.

In general a test run is performed so that the rate of rotation is changed stepwise while the model pitch angle θ and the dynamic pressure q_∞ of the wind tunnel is kept constant. For each rate of rotation n a data set consisting of

$$n, \theta, v_x, v_y, v_z, v_L, v_M, v_N, q_\infty, T_\infty$$

is sampled (balance voltages v , tunnel temperature T_∞). The further evaluation is organized according to the following sequence:

- calculation of the balance loads according to the calibration matrix,
- elimination of centrifugal force components,
- correction of the angle of attack due to sting deflection,
- dynamic pressure correction due to displacement of model and support system,
- calculation of nondimensional coefficients and derivatives.

Most of the mentioned evaluation steps are self-explaining. Nevertheless some remarks might be useful:

The unstationary parts of the balance signals due to the model weight need not be considered, because they are eliminated by the integrating measuring technique.

The centrifugal forces are determined by wind-off tests. They are conducted before each wind-on measurement maintaining the same rotation speed.

At the beginning and end of each test the balance zeros are taken by integration over one complete revolution. In doing so the speed of rotation is kept smaller than 3 rpm, so that centrifugal forces can be neglected and the noise level of the slip rings is minimized. The second zero reading is used to correct the measured values due to zero shift during a test.

The angle of attack α of the model is calculated from the angle of pitch θ and the angle of roll ϕ of the model on the cranked sting:

$$\tan \alpha = \tan \theta \cdot \cos \phi,$$

$$\sin \beta = \sin \theta \cdot \sin \phi.$$

The second equation gives the corresponding angle of sideslip.

An empirical correction of the angle of attack due to balance and sting deflections caused by centrifugal and aerodynamic forces is included in the data evaluation program [16]; the force components x and z as well as the pitching moment M influence the sting bending:

$$\Delta\theta = k_1 x + k_2 z + k_3 M.$$

The deflection coefficients k_1 , k_2 and k_3 are determined in a calibration procedure by measuring the deflection due to three different balance loads.

Finally the dynamic pressure correction due to blockage effects of model and support system is calculated according to the semiempirical relation

$$q_{\text{corr.}} = q_{\infty} [1 + \lambda \tau (F_M/F_D)^{3/2}]^2$$

(displacement cross section F_M of model and support system, wind tunnel test section size F_D). The nondimensional factor λ refers to the type of displacement; in the present case the main contribution is caused by the rotating arc traverse and its wake. The nondimensional factor τ represents the influence of the wind tunnel cross section and the model shape; in the present case of an open test section the value of τ is negative.

Further details on the determination of λ and τ can be found in Ref. [17].

First tests with the new RTD equipment, carried out last winter on a light-weight TORNADO model in the 3m wind tunnel of DFVLR, Köln, have shown good results for the roll derivatives c_{l_p} , c_{l_r} and $c_{l_{\dot{r}}}$ as compared to previous measurements on the same model with a roll balance of Aer Macchi^{NP}, Italy. Further wind tunnel tests at DFVLR, Köln, are executed now to figure out values for the confidence levels of the static and dynamic derivatives measured with the RTD.

5. CONCLUDING REMARKS

These short descriptions of instrumentation and test procedures for three derivative balances show how the different tasks of measuring dynamic stability derivatives with low-speed wind tunnel models are solved in West Germany.

Additionally they give an insight into the activities of the national working group on "Dynamic Derivative Measurements in Wind Tunnels" established by the German Ministry of Research and Technology with a fund of nearly two million Dollars.

To conclude, it should be noted that the successful operation of all three installations is due to the joint efforts of ten scientists from the aircraft firms Dornier, MBB and VFW-Fokker and research institutes in the DFVLR and at the Technical Universities of Darmstadt and Bochum. The satisfying test results encourage us to go ahead with the construction of similar derivative balances for use in transonic and supersonic wind tunnels.

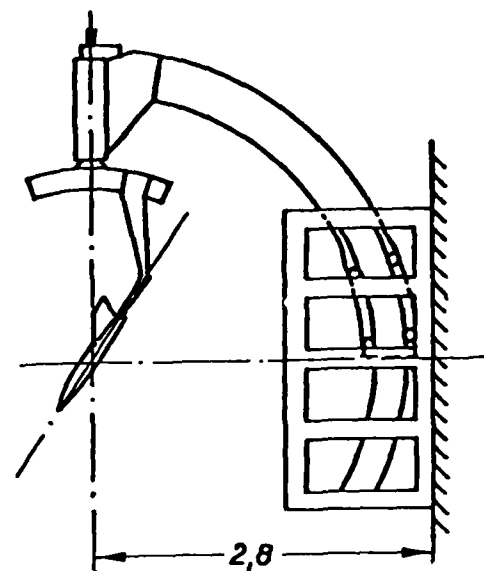
6. REFERENCES

- [1] Orlik-Rückeman, K.J.; Dynamic Stability Testing in Wind Tunnels. VKI Lecture Series 99, (1977)
- [2] Schueler, C.J. et alii; Techniques for Measurement of Dynamic Stability Derivatives in Ground Test Facilities. AGARDograph 121, (1967)
- [3] Hafer, X.; Wind Tunnel Testing of Dynamic Derivatives in W-Germany. AGARD FDP Symp. Athens/Greece, Paper 5 Preprint, (1978)
- [4] EMFT-Arbeitskreis "Derivativwaagen"; Projekt 2: Oszillierende Derivativwaage für die 3m-Unterschall-Windkanäle der BRD; Entwicklungsphase III (1975): Fertigung und Teilerprobung. Dornier-FB 76/12/B, (76)
- [5] EMFT-Arbeitskreis "Derivativwaagen"; Projekt 2: Oszillierende Derivativwaage für die 3m-Unterschall-Windkanäle der BRD; Entwicklungsphase IV (1976): Integration, Laborerprobung, Windkanalmessungen. Dornier-FB 76/13/B, (1977)
- [6] Methods for Aircraft State and Parameter Identification. AGARD FMP CP 172, (1975)
- [7] Thompson, J.S., Fail, R.A.; Oscillatory Derivative Measurements on Sting-Mounted Wind Tunnel Models: Method of Test and Results for Pitch and Yaw on a Cambered Ogee Wing at Mach Numbers up to 2.6. ARC R+M 3355, (1962)
- [8] Schmidt, E.; Die AVA-Derivativwaage. DLR-Mitt. 74-32, (1974) / ESA-TT 197, (1975)
- [9] Breitbach, E.; A Semi-Automatic Modal-Survey Test Technique for Complex Aircraft and Spacecraft Structures. ESRO SP 99, (1974)
- [10] Küssner, H.G.; Theorie und Methode der Flatterrechnung von Flugzeugen unter Benutzung der Eigenschwingungsformen im Stand. Revue Francaise de Mechanique No. 15, (1965), pp. 35 - 41
- [11] Försching, H.; Dynamic Aeroelastic Calculations of Aircraft Based on Ground Vibration Test Data. Progress in Aerospace Sciences, Vol 11, Pergamon Press Oxford & New York, (1970), pp. 1 - 66

- [12] Schmidt, E.; Über die Erprobung der AVA-Derivativwaage mit einem Alphajet-Modell im Göttinger 3m-Windkanal. BMPT FB-W-78-07, (1978)
- [13] Schulze, B.; Entwicklung einer Roll- und Trudeltaage für einen 3m-Niedergeschwindigkeits-Windkanal; Teil I: Systemauslegung. MBB-Bericht UFE 1170, (1974)
- [14] Müller, S., Scheele, E.; DMS-Waage VFW-Fokker W 64; Benutzerhandbuch. VFW-Fokker Bericht 674, (1977)
- [15] Schulz, G.; Roll- und Trudelmessungen im Unterschallwindkanal der DFVLR Köln-Porz: Zwischenbericht 1976. DFVLR IB 157- A 28, (1976)
- [16] Schulz, G.; Die elastische Verformung eines Modellhaltestiels bei Roll- und Trudelmessungen und ihre Berücksichtigung bei der Massenkraft- und Anstellwinkelkorrektur. DFVLR IB 157-77 A 20, (1977)
- [17] Schulz, G.; Die Verdrängungskorrekturen in Unterschallwindkanälen und die Grenzen ihrer Anwendbarkeit. Z. Flugwiss. 20, 7, (1972), S. 261 bis 268

7. LIST OF FIGURES

- Figure 1 Synopsis of low-speed derivative balances
- 2 Block diagram of MOD measuring equipment
 - 3 MOD 5-component strain gauge balance
 - 4 Block diagram of MFD measuring equipment
 - 5 Definitions for lateral model motion
 - 6 Block diagram of RTD measuring equipment
 - 7 RTD strain gauge balance slug
 - 8 Control of integration time for RTD



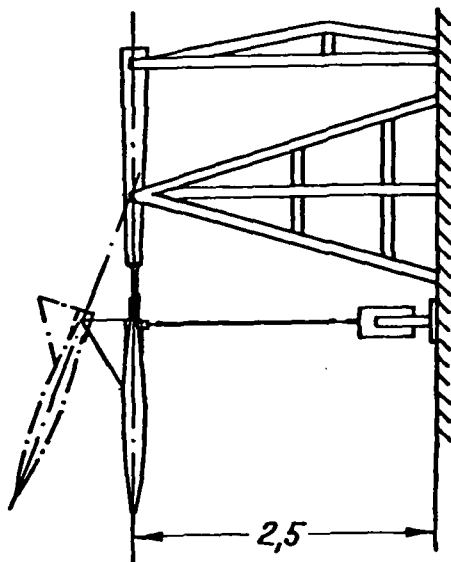
STEADY STATE FORCED-ROLL
DERIVATIVE BALANCE (RTD)

roll
(axis parallel to airstream)

-

10 to 300 rpm

DFVLR Köln-Porz



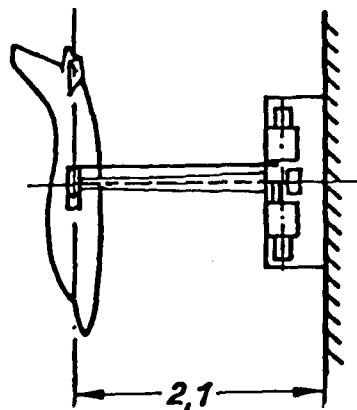
MULTI-DEGREE-OF-FREEDOM
OSCILL. DERIV. BALANCE (MFD)

pitch and heave
or roll, yaw and sideslip

± 0.5 degree; ± 5 mm

2.5 to 10 cps

DFVLR Braunschweig
and Göttingen



MOBILE OSCILLATORY
DERIVATIVE BALANCE (MOD)

model motion:

pitch, heave,
roll, yaw or sideslip

max. amplitude:

± 3 degree; ± 30 mm

frequency range:

0.2 to 3.0 cps

windtunnel operation:

DFVLR Braunschweig
Dornier GmbH
TH Darmstadt

Fig.1 Synopsis of low-speed derivative balances

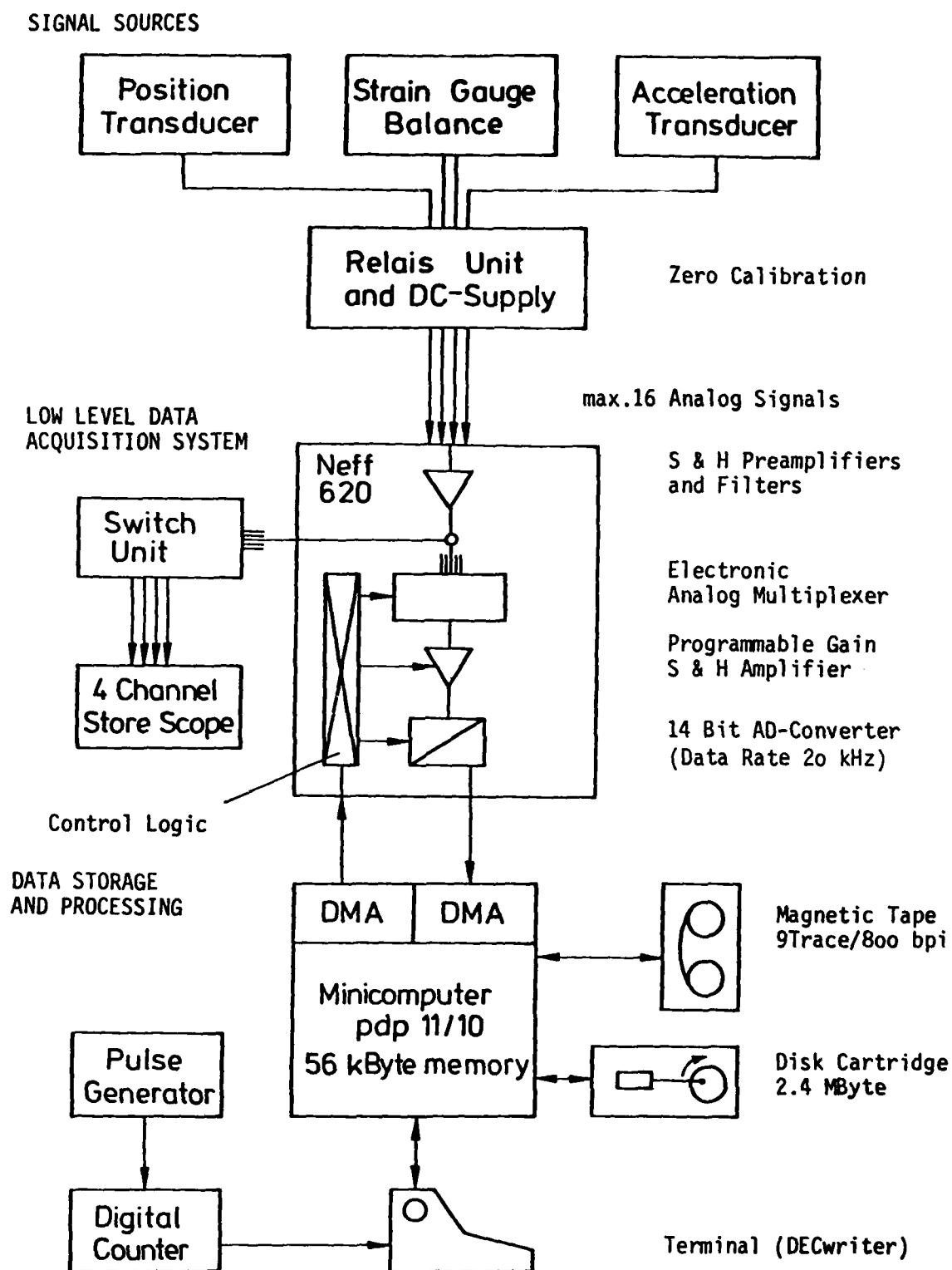
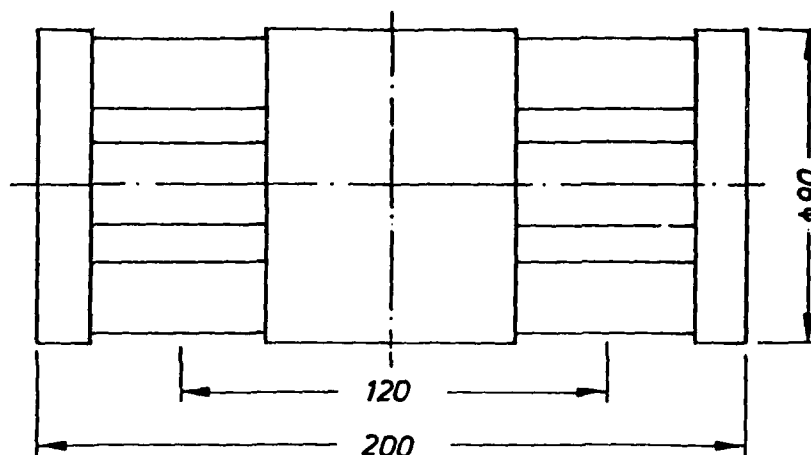


Fig.2 Block diagram of MOD measuring equipment

SIDEVIEW



SENSITIVITY

	FS-Load, 2cps	FS-Output
Normal force Z	500 N	1.66 mV
Pitching moment M	340 Nm	5.22 mV
Side force Y	120 N	.40 mV
Rolling moment L	60 Nm	2.97 mV
Yawing moment N	300 Nm	5.26 mV

CALIBRATION MATRIX

Load	output voltages [mV]				
	v_Z	v_M	v_Y	v_L	v_N
Z [N]	301.218	0	0	1.577	0.527
M [Nm]	0	65.050	0	0	-0.101
Y [N]	-1.628	-0.558	299.968	0.570	0
L [Nm]	0	0	0	20.684	-0.056
N [Nm]	0	0	0	0	57.170

Fig.3 MOD 5-component strain gauge balance

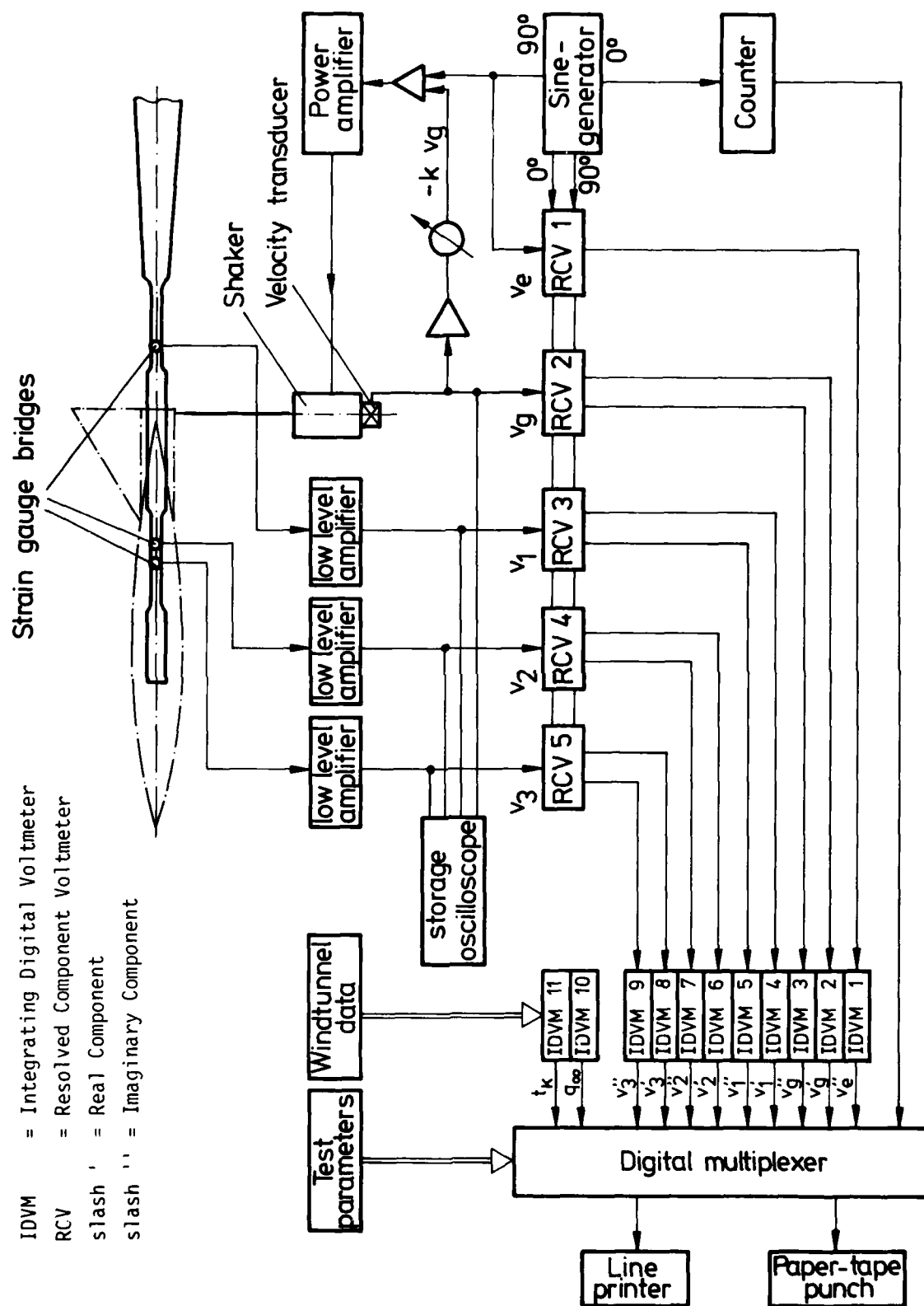


Fig.4 Block diagram of MFD measuring equipment

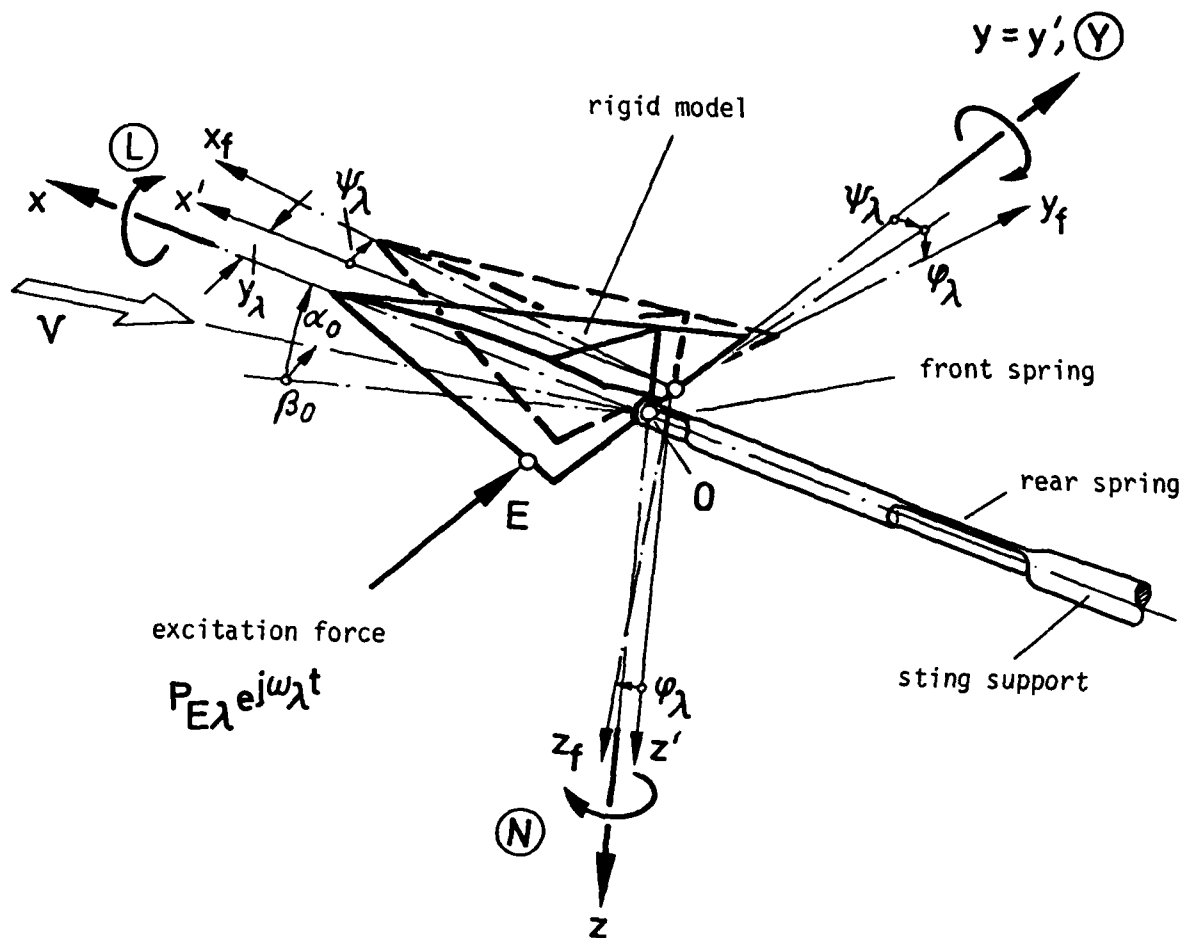


Fig.5 Definitions for lateral model motion

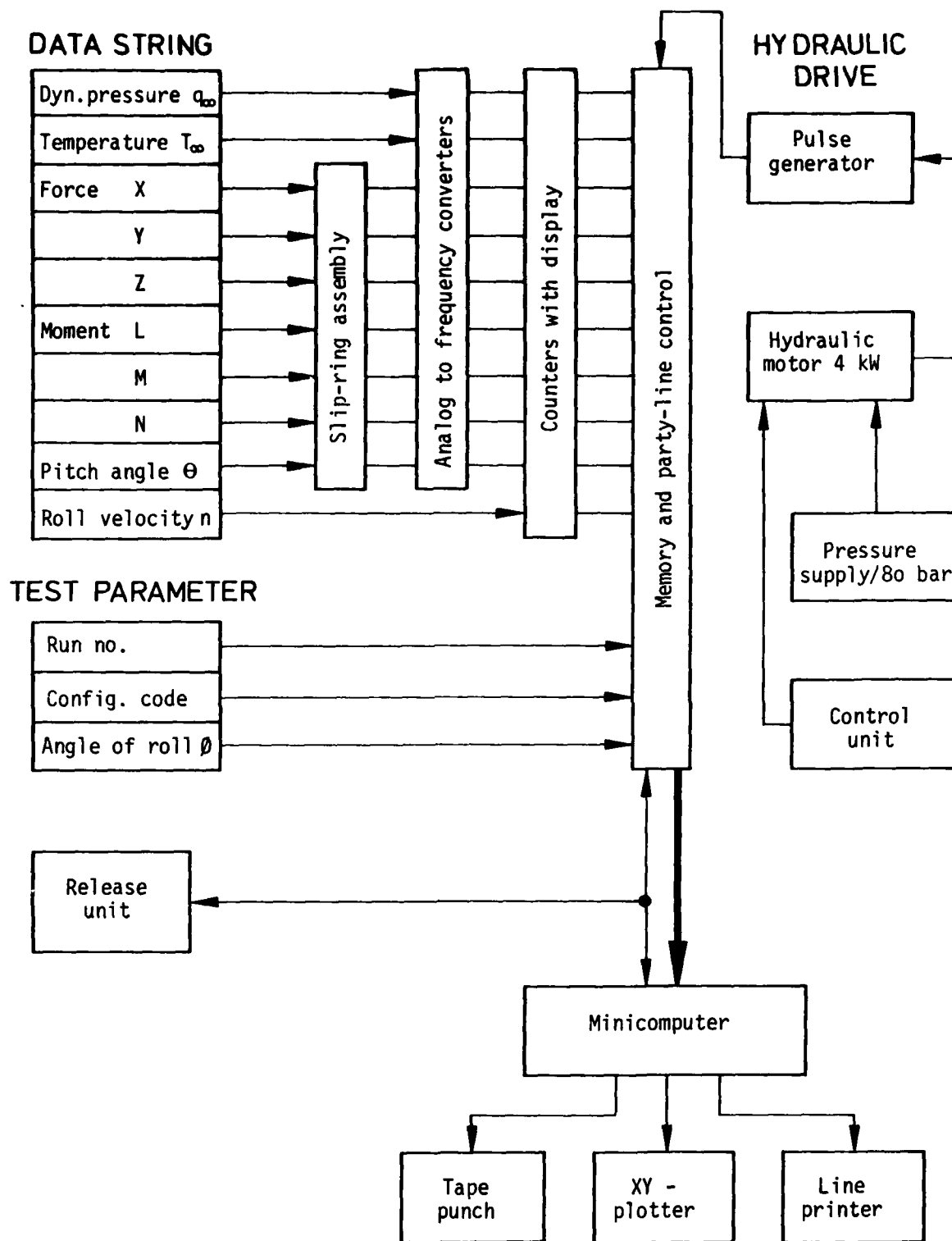
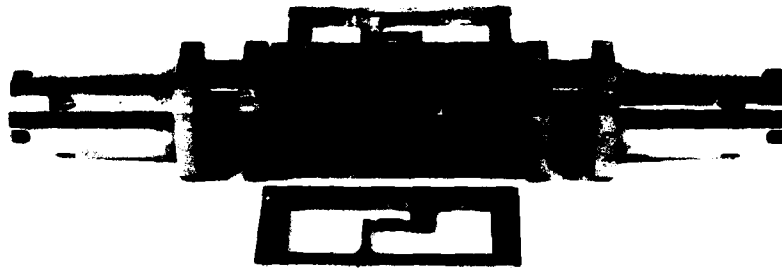
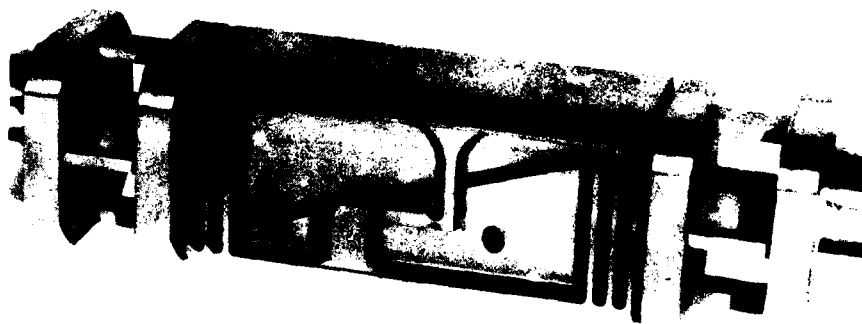


Fig.6 Block diagram of RTD measuring equipment

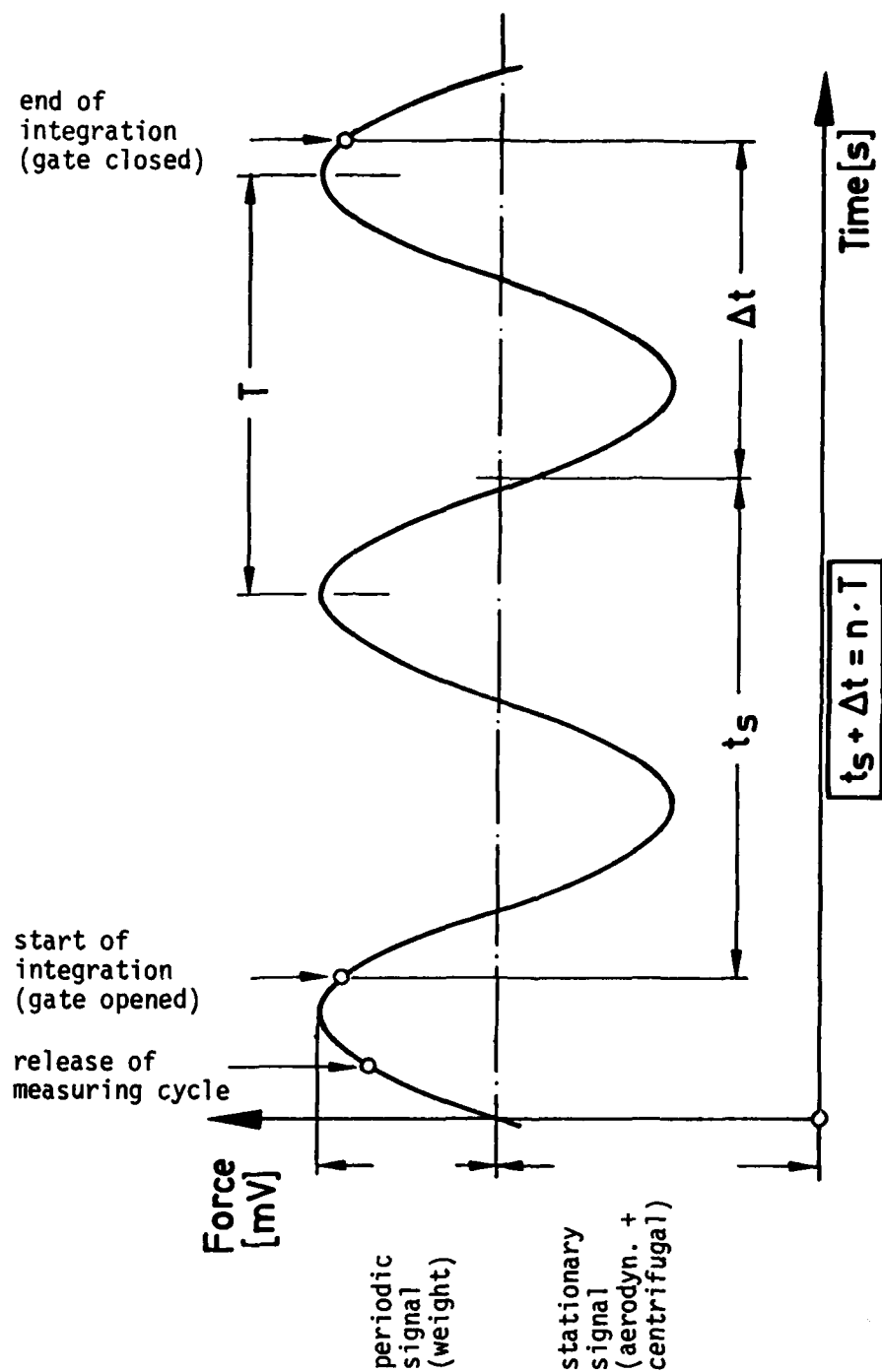


a) Assembly of milled pieces



b) Welded balance unit

Fig.7 RTD strain gauge balance slug



- t_s preselected gate time
- Δt time necessary to complete next cycle
- T period of rotation
- n number of revolutions

Fig.8 Control of integration time for RTD

EXPERIMENTS ON CROSS-COUPLING AND TRANSLATIONAL ACCELERATION DERIVATIVES

by

K. J. Orlik-Rückemann and E. S. Hanff
Unsteady Aerodynamics Laboratory,
National Aeronautical Establishment,
National Research Council of Canada,
Ottawa, Ontario, K1A 0R6,
Canada

SUMMARY

In this paper certain new categories of dynamic stability problems are discussed that are of particular importance for aircraft flying at high angles of attack or at non-zero sideslip angles. These encompass the static and dynamic cross-coupling effects between the lateral and the longitudinal degrees of freedom, the strong non-linear effects at high angles of attack, and the effects of translational acceleration. Experimental techniques developed to determine these effects are briefly described and some illustrative examples of the measured cross-coupling and acceleration derivatives are presented.

1. INTRODUCTION

As mentioned in the introductory paper (Ref. 1) and also in some of the preceding papers of this Symposium, several new problem areas have been identified in recent years in studying the dynamic stability of aircraft. This has been primarily the result of the greatly expanded flight regime of the modern military aircraft and of the advent of the space shuttle. Both these categories of aerospace vehicles are characterized by flight at high angles of attack; in addition, the military aircraft also flies at a non-zero angle of sideslip and performs translational - rather than only rotary - maneuvers. These unusual flight conditions give rise to a whole set of complex aerodynamic phenomena, that have to be properly studied and understood. High on the list are all kinds of separated flow phenomena, shedding and separation of body vortices and their interaction with flow over the leeside of the wing, vortex bursts, and - in general - highly irregular and asymmetric flows. These aerodynamic phenomena affect the stability of aircraft in many different ways. Among the topics that our laboratory has now been studying for some time and that are covered in this paper are

- (1) the significant cross-coupling effects that may be expected to exist between the lateral and the longitudinal degrees of freedom,
- (2) the strong non-linear effects that may affect almost all stability parameters of aircraft at high angles of attack and
- (3) the determination and effects of translational acceleration derivatives.

Some of these studies were performed under a joint research programme with NASA Ames.

2. AERODYNAMIC CROSS-COUPLING

Let us begin with considering the cross-coupling effects. As we know, asymmetric flow results when an aircraft flies at non-zero angle of sideslip and also when it flies at zero sideslip but at high angles of attack. This is so mainly because of the asymmetric shedding of forebody vortices at high angles of attack. In both cases we may expect the occurrence of secondary *lateral* aerodynamic forces and moments in response to a primary *pitching* maneuver and vice-versa, the onset of secondary *longitudinal* reactions in response to a primary *lateral* maneuver. Due to various *time lags*, these secondary reactions will consist of components that are both in-phase and out-of-phase with the primary motion, and will give rise, therefore, to both static and dynamic cross-coupling effects. In the first approximation such effects can be described by introducing the concept of static and dynamic *cross-coupling derivatives*. These quantities, which at the present time may be difficult to determine theoretically or from flight tests, can now be obtained from special dynamic experiments in a wind tunnel. It should be mentioned also, that in the presence of significant cross-coupling it becomes necessary to consider the lateral and the longitudinal equations of motion of an aircraft *all at once*, and not in two separate groups as often done in the past.

In Figure 1 the three equations of angular motion for a captive symmetrical aircraft model are shown. We recognize the three familiar damping derivatives such as damping in roll, damping in pitch and damping in yaw, and the well-known dynamic cross derivatives, rolling moment due to yawing and yawing moment due to rolling. The new dynamic cross-coupling derivatives are represented by terms such as $(L_q + L_{\dot{\alpha}})$, $(M_p + M_{\dot{\beta}} \sin \alpha)$ and $(N_q + N_{\dot{\alpha}})$. By considering the right hand sides of these equations and relating them to a driving motion in another degree of freedom, the basic expressions for the data reduction procedure can be derived.

$$\begin{aligned}
I_x \dot{p} + [\gamma_\phi - (L_p + \sin \alpha L_\beta)] p + (K_\phi - \sin \alpha L_\beta) \phi &= \\
I_{xz} \dot{r} + (L_r - \cos \alpha L_\beta) r - \cos \alpha L_\beta \psi + (L_q + L_d) q + L_\theta \theta + L_T \\
I_y \dot{q} + [\gamma_\theta - (M_q + M_d)] q + (K_\theta - M_d) \theta &= \\
(M_r - \cos \alpha M_\beta) r - \cos \alpha M_\beta \psi + (M_p + \sin \alpha M_\beta) p + \sin \alpha M_\beta \phi + M_T \\
I_z \dot{r} + [\gamma_\psi - (N_r - \cos \alpha N_\beta)] r + (K_\psi + \cos \alpha N_\beta) \psi &= \\
I_{xz} \dot{p} + (N_p + \sin \alpha N_\beta) p + \sin \alpha N_\beta \phi + (N_q + N_d) q + N_\theta \theta + N_T
\end{aligned}$$

Fig. 1 Equations of Angular Motion for a Captive Symmetrical Aircraft Model

Let us consider, as an example, a primary sinusoidal oscillation in yaw

$$\psi = |\psi| e^{i\omega t} \quad (1)$$

and the induced secondary pitching moment

$$\bar{M} = |\bar{M}| e^{i(\omega t + \eta_\theta)} \quad (2)$$

which is synchronous with ψ but, in general, is slightly shifted in phase by a quantity η_θ . Using the equations of Figure 1, this pitching moment can also be expressed as a sum of two contributions depending on r and ψ , respectively

$$\bar{M} = (M_r - M_\beta \cos \alpha) r - M_\beta \psi \cos \alpha \quad (3)$$

Dividing Eq. (2) successively by ψ and by $\dot{\psi}$ we obtain

$$\bar{M} = \psi \frac{|\bar{M}|}{|\psi|} e^{i\eta_\theta} \quad \bar{M} = \dot{\psi} \frac{|\bar{M}|}{i\omega|\psi|} e^{i\eta_\theta} \quad (4)$$

Differentiating Eqs. (4) with respect to ψ and $\dot{\psi}$, respectively, and using the real parts of the complex terms we get

$$\begin{aligned}
\frac{\partial \bar{M}}{\partial \psi} &= \frac{|\bar{M}|}{|\psi|} e^{i\eta_\theta} + \frac{|\bar{M}| \cos \eta_\theta}{|\psi|} \\
\frac{\partial \bar{M}}{\partial \dot{\psi}} &= \frac{|\bar{M}|}{i\omega|\psi|} e^{i\eta_\theta} + \frac{|\bar{M}| \sin \eta_\theta}{\omega|\psi|}
\end{aligned} \quad (5)$$

Setting $\dot{\psi} = r$ and comparing Eqs. (5) with the corresponding derivatives of \bar{M} from Eq. (3) we finally can write the defining expressions for the static and dynamic derivatives of the pitching moment due to oscillation in yaw as

$$\begin{aligned}
-M_\beta \cos \alpha &= \frac{|\bar{M}| \cos \eta_\theta}{|\psi|} \\
M_r - M_\beta \cos \alpha &= \frac{|\bar{M}| \sin \eta_\theta}{\omega|\psi|}
\end{aligned} \quad (6)$$

A full set of such definitions for all the cross-coupling combinations between the primary angular motions and the secondary moments is shown in Figure 2. For each derivative the amplitude of the primary motion, the amplitude of the induced secondary moment and the phase between them is required; in addition, for the dynamic derivatives, also the oscillation frequency is needed. The experimental procedures required to determine these quantities are discussed in Ref. 2.

DOF FORCING/ FORCED	STATIC DERIVATIVE	DYNAMIC DERIVATIVE
YAW/PITCH	$-\cos\alpha M_{\beta} = \frac{ M \cos\eta_{\theta}}{ \psi }$	$M_r - \cos\alpha M_{\dot{\beta}} = \frac{ M \sin\eta_{\theta}}{\omega \psi }$
YAW/ROLL	$-\cos\alpha L_{\beta} = \frac{ L \cos\eta_{\phi}}{ \psi }$	$L_r - \cos\alpha L_{\dot{\beta}} = \frac{ L \sin\eta_{\phi}}{\omega \psi }$
PITCH/YAW	$N_{\alpha} = \frac{ N \cos\eta_{\psi}}{ \theta }$	$N_q + N_{\dot{\alpha}} = \frac{ N \sin\eta_{\psi}}{\omega \theta }$
PITCH/ROLL	$L_{\alpha} = \frac{ L \cos\eta_{\phi}}{ \theta }$	$L_q + L_{\dot{\alpha}} = \frac{ L \sin\eta_{\phi}}{\omega \theta }$
ROLL/PITCH	$\sin\alpha M_{\beta} = \frac{ M \cos\eta_{\theta}}{ \phi }$	$M_p + \sin\alpha M_{\dot{\beta}} = \frac{ M \sin\eta_{\theta}}{\omega \phi }$
ROLL/YAW	$\sin\alpha N_{\beta} = \frac{ N \cos\eta_{\psi}}{ \phi }$	$N_p + \sin\alpha N_{\dot{\beta}} = \frac{ N \sin\eta_{\psi}}{\omega \phi }$

Fig. 2 Defining Expressions for Static and Dynamic Cross and Cross-Coupling Moment Derivatives

3. EXPERIMENTAL TECHNIQUE

In Figure 3 a cut-away drawing is presented of our first cross-coupling apparatus. In the configuration shown this apparatus provides a *primary* oscillatory motion in pitch with resulting *secondary* motions in yaw and roll. By rotating the balance 90° around its longitudinal axis the *primary* motion may be imparted in yaw instead, with the induced *secondary* motions in pitch and roll. The model is driven electromagnetically by means of a single-turn drive coil that can move in a gap between two permanent magnets, and the balance consists of cruciform flexures in yaw and in roll and a crossed-flexure pivot in pitch. All moments are measured around the center of oscillation. Components of the *secondary motions* that are in-phase or out-of-phase with the *primary motion* are

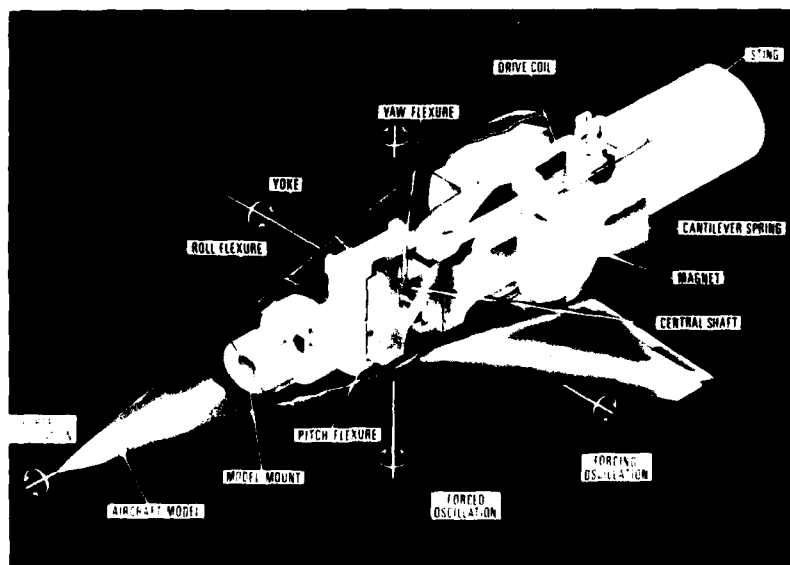


Fig. 3 Cut-away Drawing of the NAE Forced Oscillation Pitch/Yaw Apparatus (Mk 1). Apparatus Set Up for Pitching Oscillation.



Fig. 4 Schematic Model of Delta-Wing Aircraft Installed on the NAE Pitch/Yaw Apparatus in the NASA Ames 6'x6' Wind Tunnel

measured and converted into the corresponding components of the induced secondary moments. In addition, the torque, amplitude, and the frequency of the primary motion are measured. All together a set of two oscillatory experiments, one in pitch and one in yaw, is required to obtain a complete set of four static and four dynamic *cross* and *cross-coupling* moment derivatives as well as two static and two dynamic *direct* moment derivatives. This includes the traditional cross derivative of the rolling moment due to yawing, as well as the well-known damping-in-pitch and damping-in-yaw derivatives. A more advanced version of this pitch/yaw apparatus is now being developed and is described, together with a companion apparatus for oscillatory roll experiments, in Ref. 2.

It should be noted that the technique described provides a *direct* measurement of all the derivatives which is based only on an assumed relation between the secondary moment measured and the causative primary motion, such as given in Eq. (3). In this particular case this relation is linear, but can be replaced by a non-linear or higher order formulation, if the need arises. Since the motion is essentially in one degree of freedom only, the measurement is totally independent of the remaining parts of the equations of motion and therefore the results may be expected to be valid for any

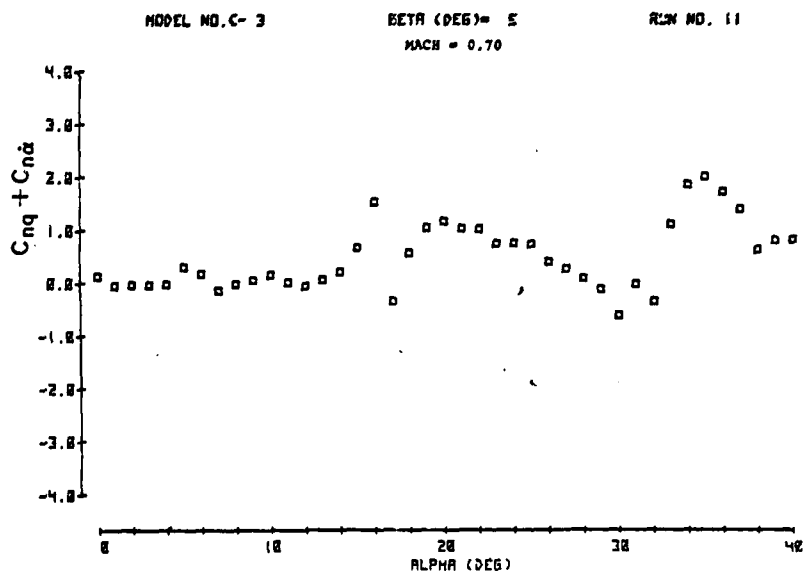


Fig. 5 Dynamic Yawing Moment Derivative due to Pitching
 $M = 0.70; \beta = 5^\circ$

formulation of these equations as long, of course, as the principle of superposition is still applicable, that is as long as the concept of stability derivatives can be used. In this context the stability derivatives need not be constants, but may be functions of some experimental parameters such as the nominal value of angle of attack or sideslip around which the oscillation takes place.

In Figure 4 a schematic model is presented of a delta-wing aircraft mounted on the apparatus just shown, and installed in the NASA-Ames 6' x 6' Wind Tunnel. Several series of oscillatory pitching and yawing experiments were conducted with this model at Mach numbers 0.25 and 0.7, at several angles of sideslip, and in the angle-of-attack range from 0° to 40° . In all cases the axis of oscillation and the point around which the pitching and yawing moments were measured was at a distance of 0.68 of the body length from the nose of the model. In this paper only results obtained at Mach number 0.7 will be discussed.

4. DYNAMIC CROSS-COUPLING DERIVATIVES

An example of one of the dynamic cross-coupling derivatives measured is presented in Figure 5, where derivative $(C_{nq} + C_{n\dot{\alpha}})$, which is the dynamic yawing moment derivative due to oscillatory pitching, is plotted as a function of angle of attack, α . As expected the derivative is practically zero at low angles of attack. There is then a sudden variation around $\alpha = 16^\circ$ or so; according to separate flow visualization studies, that are not included in this paper, this variation may be caused by one of the separated forebody vortices moving over the fin. Another area of rapid variations is in the range of α between 31° and 34° . Note that the derivative may change from -1 to +1 with a change in α of only 1 or 2 degrees. Note also the magnitude of this derivative, which at various angles of attack may reach values from about -1 to +2.

The experiments in the 6' x 6' Wind Tunnel were conducted at a sideslip angle of both $+5^\circ$ and -5° , and this provided a unique opportunity for checking the consistency of the results. As could be expected from basic aerodynamic considerations, all derivatives that were "all longitudinal" or "all lateral" were found to be nearly the same for both positive and negative sideslip, while all the cross-coupling derivatives displayed a reversed sign with a change of sign of the angle of sideslip. An example of this is shown in Figure 6 where the variation with α of the other important cross-coupling derivative, $(C_{lq} + C_{l\dot{\alpha}})$, i.e. the dynamic rolling moment derivative due to oscillatory pitching, is shown. The measured values of the derivative at $\beta = 5^\circ$ are compared to the values of the derivative as obtained at $\beta = -5^\circ$, but with a reversed sign. It can be seen that the various peaks and slopes are quite faithfully reproduced, with only a minor shift, probably due to β not having exactly the same absolute value in the two cases. The overall variation with α of this derivative is in principle similar to that of $(C_{nq} + C_{n\dot{\alpha}})$ shown in Figure 5.

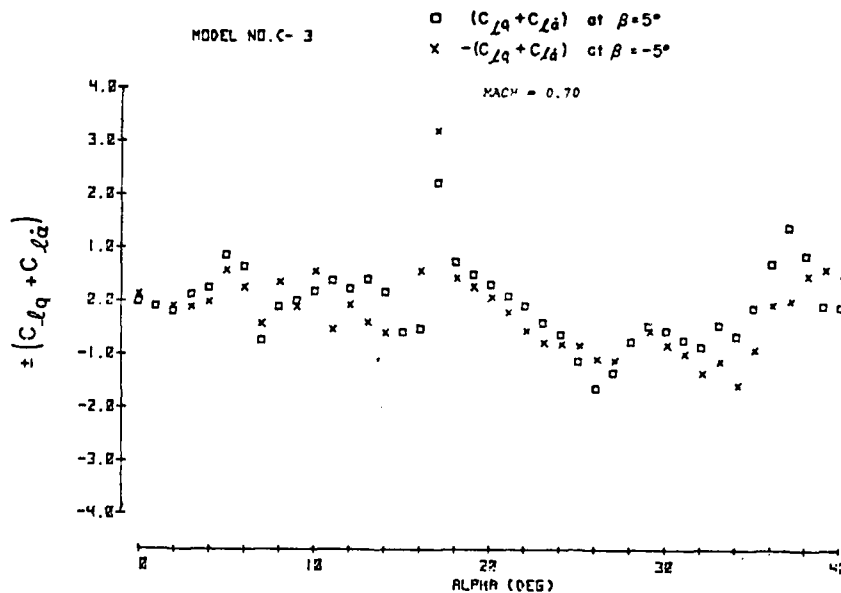


Fig. 6 Dynamic Rolling Moment Derivative due to Pitching. $M=0.70$;
 $|\beta|=5^\circ$. Example of Sign Reversal of Derivative with
 Reversed Direction of Sideslip.

MODEL NO. C-3

BETA (DEG) = 5

RUN NO. 9

MACH = 0.70

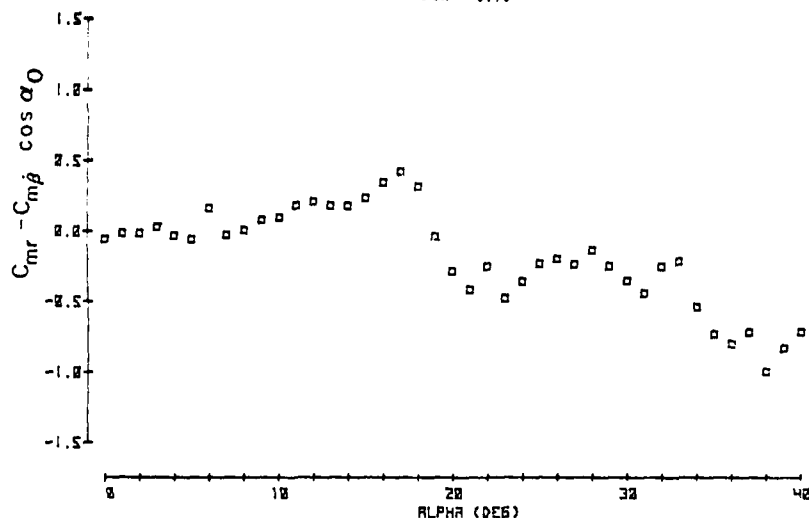


Fig. 7 Dynamic Pitching Moment Derivative due to Yawing.

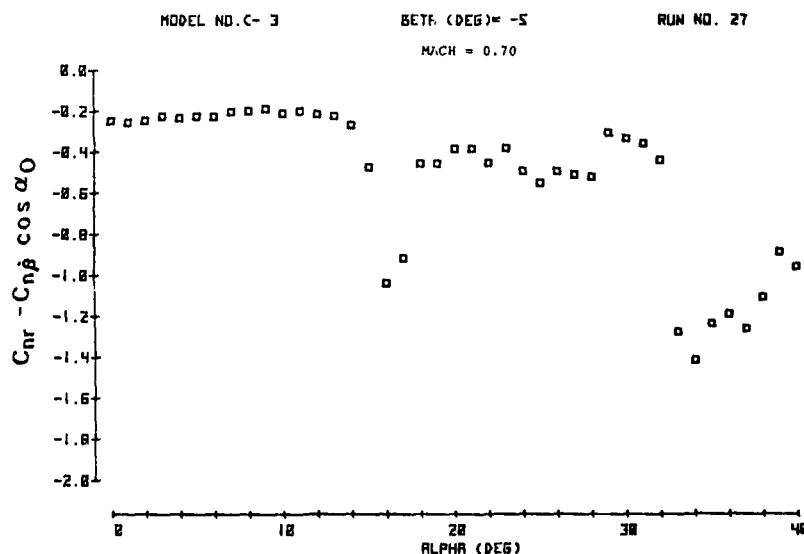
 $M = 0.70$; $\beta = 5^\circ$.

The variation with α of the cross-coupling derivative ($C_{mr} - C_{mb} \cos \alpha_0$), that is the dynamic pitching moment derivative due to oscillatory yawing, is presented in Figure 7. Again the same principal trends may be observed, with small values at low angles of attack and large variations in the vicinity of $\alpha = 18^\circ$ and $\alpha = 34^\circ$; however the magnitudes involved are smaller.

5. NON-LINEAR EFFECTS

All these examples indicate that at higher angles of attack stability derivatives no longer are constants but display significant variations with α . This applies to most static and dynamic derivatives. Furthermore, as we have seen, at certain ranges of angle of attack, the variations with α can be extremely rapid, with the derivative undergoing a major change as the result of a very small variation in α . This means that it may not be sufficient to properly account for the equilibrium values of derivatives, but that in some cases also their local variation about the angle of equilibrium should be suitably modelled. One way of doing that is by local linearization. An example of that is described in Ref. 3. Of course, a more complete but also a more complicated way of modelling is by introducing a complete functional description of a derivative in the equations of motion. However, such a complication may not always be necessary.

In Figure 8 some more non-linearities are presented, this time in the direct deriv-

Fig. 8 Damping-in-Yaw Derivative. $M = 0.70$; $\beta = -5^\circ$.

atives. The apparatus that was developed for the measurement of cross-coupling effects does also provide information on the damping derivatives in the appropriate degrees of freedom. Shown here is the damping-in-yaw derivative, $(C_{nr} - C_{n\beta} \cos \alpha)$. It can be seen that the derivative is almost constant at low angles of attack, has a dramatic peak at $\alpha = 16^\circ$, and is rather irregular at higher angles of attack and particularly so around $\alpha = 32^\circ - 33^\circ$, where an extremely rapid increase of damping takes place. Another interesting aspect is the magnitude of this derivative, which nowhere approaches the value of 2 previously observed for some of the cross-coupling derivatives. Although these are magnitudes of the *dimensionless* derivatives, it can be shown that similar order-of-magnitude considerations also apply to full *dimensional* terms in the appropriate equation of motion.

6. TRANSLATIONAL OSCILLATION EXPERIMENTS

Let us consider now the third topic of the dynamic stability studies conducted in our laboratory, namely the determination of derivatives due to translational acceleration. Translational acceleration may be considered equivalent, from an aerodynamic point of view, to the time rate of change of angular deflection in the same plane of motion. We need this information to be able to separate derivatives appearing in composite expressions such as $(C_{mq} + C_{m\dot{\alpha}})$, which result from traditional oscillatory experiments around a fixed axis. At low angles of attack this separation can sometimes be performed empirically with good chance of success, but at higher angles of attack such a procedure is totally unreliable. The individual derivatives are needed for the proper analysis of all those flight conditions where the aircraft does not follow a straight path. In addition, the translational acceleration derivatives are of special interest for aircraft that use direct-lift or direct-sideforce controls.

The translational oscillation experiments were carried out using the half-model technique. The apparatus consisted of an elastic model suspension in the form of a double-cantilever spring and an electromagnetic oscillator (see Ref. 2), and was mounted on the outside of a circular wind-tunnel plate. Angle of attack could be changed by rotating this plate in the wind-tunnel wall. The half model was firmly attached to the moving end of the spring by means of an adapter which incorporated a small cruciform element for measuring the pitching moment. This adapter passed right through the wind tunnel plate and a reflection plate. The data acquisition and reduction system was similar to that used for measuring cross-coupling derivatives.

Some preliminary results on the pitching moment derivative due to vertical acceleration are shown in Figure 9, for the same configuration as tested before and for a Mach number of 0.7. The width of the band indicates the scatter in the results. The reason why the derivative is not completely symmetric around $\alpha = 0$ axis is not quite clear. The large increase for angles of attack about 20° may be due to the limitations of the half-model technique. More work is needed to clarify this issue. The development of full-model apparatuses for plunging or/and lateral translation experiments is now being contemplated.

7. CONCLUSIONS

In conclusion, a series of oscillatory apparatuses has been developed with which the cross-coupling moment derivatives due to pitching, yawing and rolling, as well as the pitching moment derivative due to vertical acceleration have been measured for a schematic aircraft configuration. It has been found that the dynamic yawing and rolling moment derivatives due to *pitching* were particularly large and of magnitudes comparable to those of traditional damping derivatives. It was also confirmed, that at higher angles of attack *all derivatives*, including several static and damping derivatives not included in this paper, display very large non-linear effects.

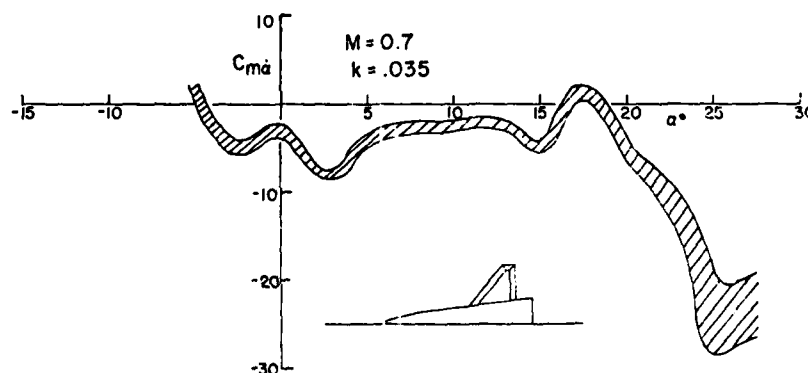


Fig. 9 Pitching Moment Derivative due to Vertical Acceleration. $M = 0.70$.

8. REFERENCES

1. Orlik-Rückemann, K.J. Techniques for Dynamic Stability Testing in Wind Tunnels. AGARD FDP Symposium on Dynamic Stability Parameters, Athens, Greece, 22-24 May 1978. AGARD CP-235, Paper 1.
2. Hanff, E.S.
Orlik-Rückemann, K.J. A Generalized Technique for Measuring Cross-Coupling Derivatives in Wind Tunnels. AGARD FDP Symposium on Dynamic Stability Parameters, Athens, Greece, 22-24 May 1978. AGARD CP-235, Paper 9.
3. Curry, W.H.
Orlik-Rückemann, K.J. Sensitivity of Aircraft Motion to Aerodynamic Cross-Coupling at High Angles of Attack. AGARD FDP Symposium on Dynamic Stability Parameters, Athens, Greece, 22-24 May 1978. AGARD CP-235, Paper 34.

A GENERALIZED TECHNIQUE FOR MEASURING CROSS-COUPLING DERIVATIVES IN WIND TUNNELS

by

E.S. Hanff and K.J. Orlik-Rückemann
Unsteady Aerodynamics Laboratory,
National Aeronautical Establishment,
National Research Council of Canada,
Ottawa, Ontario, K1A 0R6,
Canada

SUMMARY

A novel generalized oscillatory wind-tunnel technique for the determination of dynamic cross and cross-coupling derivatives is described. The technique has been successfully used - by means of specially developed apparatuses - to obtain all moment derivatives due to pitching, yawing and rolling using the full model approach, as well as to determine $C_{m\dot{\alpha}}$ using a half model plunging approach.

A separate three-degrees-of-freedom dynamic calibrator, also described herein, has been developed to *independently* verify the validity of the experimental and analytical procedures used for the determination of the derivatives.

1. INTRODUCTION

Modern high performance military aircraft are subjected to extreme flight conditions - such as flight at high angles of attack and in the presence of small angle of side-slip - where asymmetric flow exists. This phenomenon has been increasingly recognized as a possible cause of significant aerodynamic coupling between the longitudinal and lateral degrees of freedom of the aircraft, resulting in a growing interest in the measurement of the corresponding cross-coupling derivatives; such derivatives were previously neglected in the design of aircraft not subjected to equally demanding flight conditions.

In response to these requirements, a rather general *wind tunnel technique* and associated experimental apparatuses have been developed at the National Aeronautical Establishment over the last few years, and a number of cross and cross-coupling static and dynamic moment derivatives have been determined using this equipment. These include those derivatives due to pitching, yawing and rolling as well as the ones in pitch due to plunging obtained on a half model configuration. It should be noted, however, that these are the cases so far investigated, and that they do not reflect a limitation of the technique, which being quite general appears to be useful for the determination of a number of force and moment derivatives due to the motion in any single degree of freedom. The wind-tunnel results are presented and discussed in Ref. 1, while their significance for the flight mechanics analysis is assessed in Ref. 2.

All the abovementioned experiments have one thing in common, namely, they are dynamic tests in which the model is oscillated sinusoidally in one plane. This "primary oscillation" may be angular or translational, depending on the experiment. Under asymmetric flow conditions, aerodynamic coupling may be present between the primary motion and other degrees of freedom of the model, resulting in induced moments and forces in these degrees of freedom. The objective of the experiments is, then, to determine these "secondary" moments or forces which in turn lead to the pertinent cross and cross-coupling derivatives. The main features of the experiments under consideration are shown in Table I.

TABLE I

Derivatives To Be Measured

Exp.	Primary Motion	Derivatives To Be Measured	
		Direct	Cross and Cross-Coupling
I	Osc. in pitch (full model)	$C_{m\alpha}, C_{mq} + C_{m\dot{\alpha}}$	$C_{n\alpha}, C_{nq} + C_{n\dot{\alpha}}, C_{l\alpha}, C_{lq} + C_{l\dot{\alpha}}$
II	Osc. in yaw (full model)	$C_{n\beta}, C_{nr} - C_{n\dot{\beta}} \cos \alpha_0$	$C_{m\beta}, C_{mr} - C_{m\dot{\beta}} \cos \alpha_0, C_{l\beta}, C_{lr} - C_{l\dot{\beta}} \cos \alpha_0$
III	Osc. in roll (full model)	$C_{l\beta}, C_{lp} + C_{l\dot{\beta}} \sin \alpha_0$	$C_{m\beta}, C_{mp} + C_{m\dot{\beta}} \sin \alpha_0, C_{n\beta}, C_{np} + C_{n\dot{\beta}} \sin \alpha_0$
IV	Vert. plunging (half model)		$C_{m\dot{\alpha}}, C_{m\ddot{\alpha}}$

A common characteristic of these experiments is that they are used to determine derivatives on which little or no information is available, making it very difficult to assess the validity of the results. Consequently, a technique has been developed to *independently* verify the validity of the experimental and analytical procedures used in the wind tunnel experiments.

This paper briefly describes the apparatus and philosophy underlying the various wind tunnel techniques and the verification process.

2. DESCRIPTION OF WIND TUNNEL APPARATUS

In all cases the model is mounted on a balance that is in turn attached to an elastic support system capable of deflecting in the appropriate degree of freedom. The primary motion is imparted by an electromagnetic drive mechanism which oscillates the model with a constant amplitude at the resonant frequency (in the primary degree of freedom) of the mechanical system. Fig. 1 shows a view of the balance and drive mechanism for the pitching and yawing experiments (the latter achieved by rotating the model by 90° relative to the balance). This is a new, more slender apparatus with which more realistic models may be tested than those tested with the previous pitch-yaw apparatus (Ref. 1). The balance has a five component capability (no axial force) and is made in one piece - a very desirable feature for dynamic testing. The balance is attached to a pair of cross flexures that allow it to deflect in pitch (or yaw). The drive mechanism consists of a high-current single turn coil that passes through a magnetic field created by very strong rare earth permanent magnets. A feedback system forces a

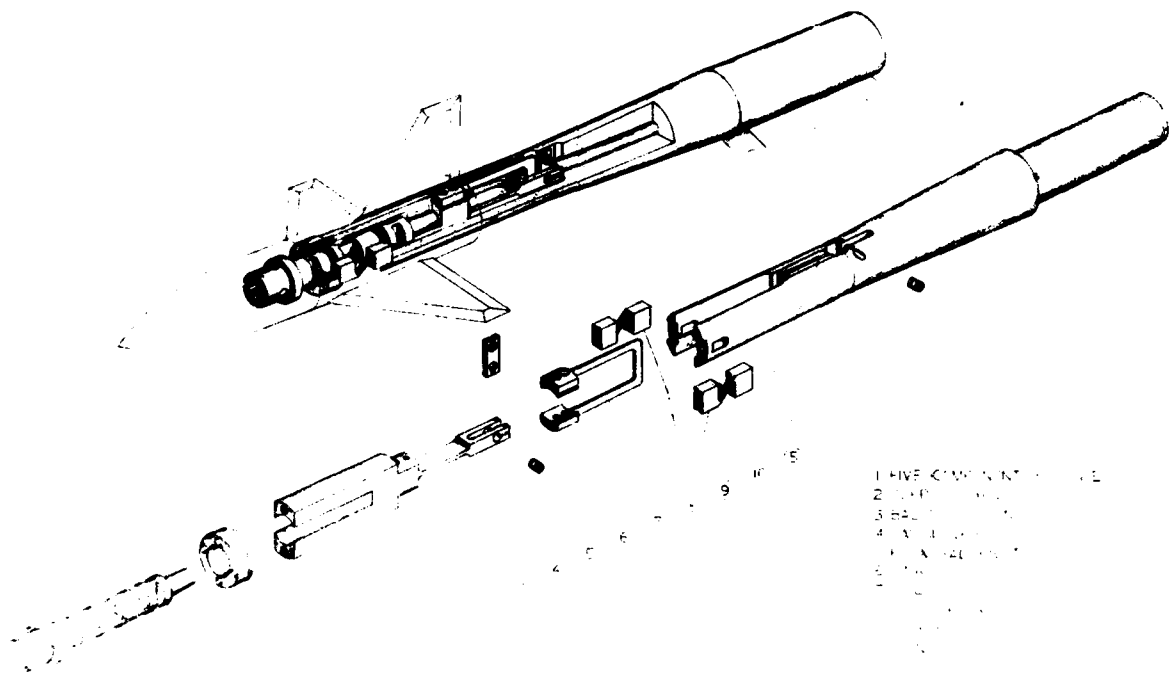


Fig. 1: Pictorial view of pitch-yaw apparatus

suitable current through the coil, that interacts with the magnetic field and results in a moment in the appropriate degree of freedom.

The rolling apparatus is depicted in Fig. 2. In this case the model is mounted on the 5-component dynamic balance mentioned above (although a standard 6-component balance could probably also be used) attached to twelve axially oriented cantilever springs that permit it to oscillate in roll relative to the sting. The drive consists of a rare-earth permanent-magnet "brushless" DC motor-like actuator located at the aft end of the sting and connected to the balance via a drive shaft. As in the previous case, a feedback mechanism ensures that the model oscillates with constant amplitude at the primary mechanical resonant frequency of the system.

For the half-model plunging experiments, the balance is a single pitch-sensitive cruciform flexure attached to a pair of parallel cantilever springs that allow the model to move in the vertical direction (Figs. 3 and 8). The drive mechanism is made up of a pair of electromagnets that produce a magnetic field within which coils are imbedded; these coils, carrying a suitably controlled current, are attached to the balance thus applying the force required to obtain the desired translational oscillation.

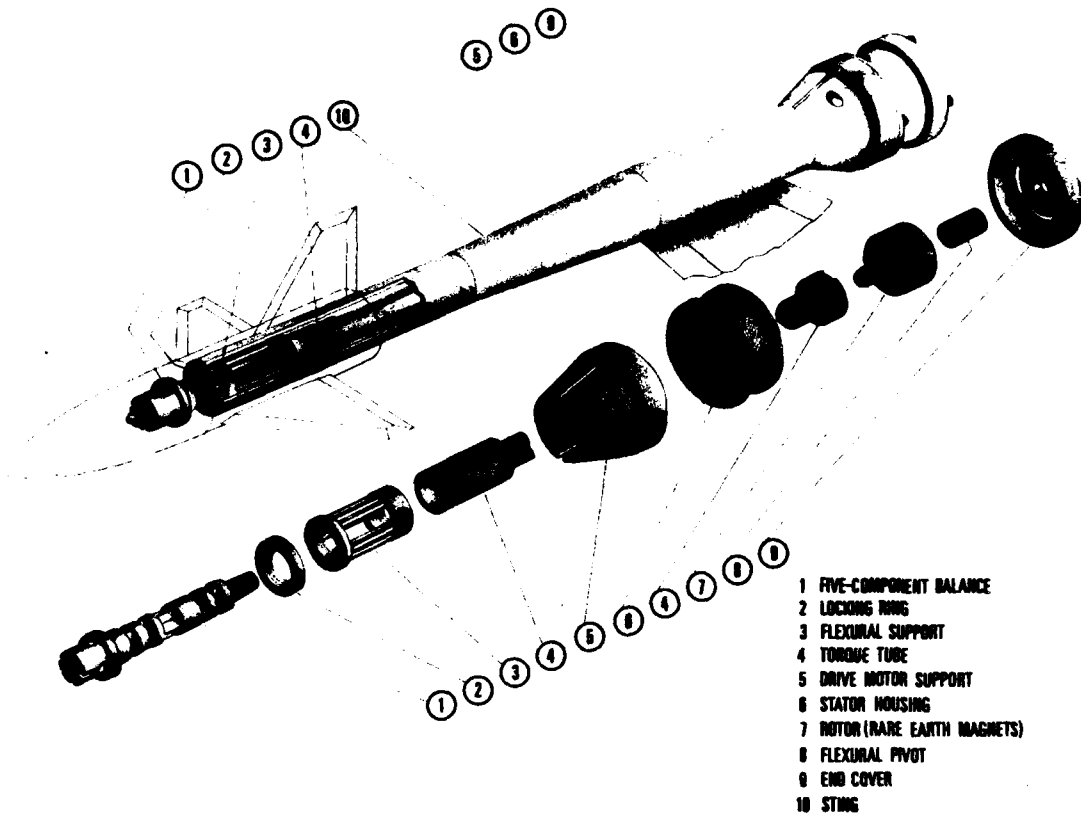


Fig. 2: Pictorial view of roll apparatus

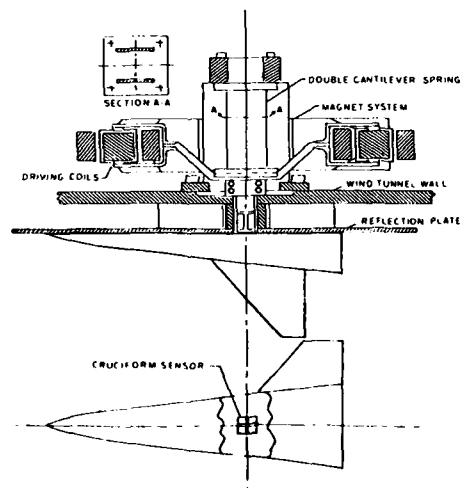


Fig. 3: Schematic of half-model apparatus

3. INSTRUMENTATION

As mentioned above, the purpose of the wind tunnel experiments is to determine the secondary moments (or forces) generated as a result of the primary oscillation and the aerodynamic coupling between the primary and secondary degrees of freedom. In general, signals representing the secondary motions are contaminated with noise to such an extent that conventional filtering methods are inadequate to extract the necessary information. However, the small amplitude of the primary oscillation of the model ($\pm 1.5^\circ$) warrants the assumption that, for a given model attitude, the system is linear about its equilibrium position, in which case the pertinent components of the secondary motions are sinusoidal and of the same frequency as that of the primary motion. The a priori knowledge of the nature of these motions allows the use of correlation methods to extract the information necessary for the eventual determination of aerodynamic derivatives.

Fig. 4 shows a simplified block diagram of the instrumentation system. It is based on five pairs of lock-in amplifiers capable of extracting signals, coherent with a reference signal, that are deeply buried in noise. The signal corresponding to the primary displacement can be used as the reference by virtue of its high signal to noise ratio, and thus the in-phase and quadrature components of the secondary motions with respect to the primary one can be determined.

The primary oscillation amplitude and frequency, as well as the drive current (representing the driving forcing function) also need to be measured in order to obtain the pertinent direct derivatives. The signals of interest are digitized and processed automatically using an off-line calculator-based data acquisition and processing system. Work is currently in progress to implement an on-line fully digital version of the processing system.

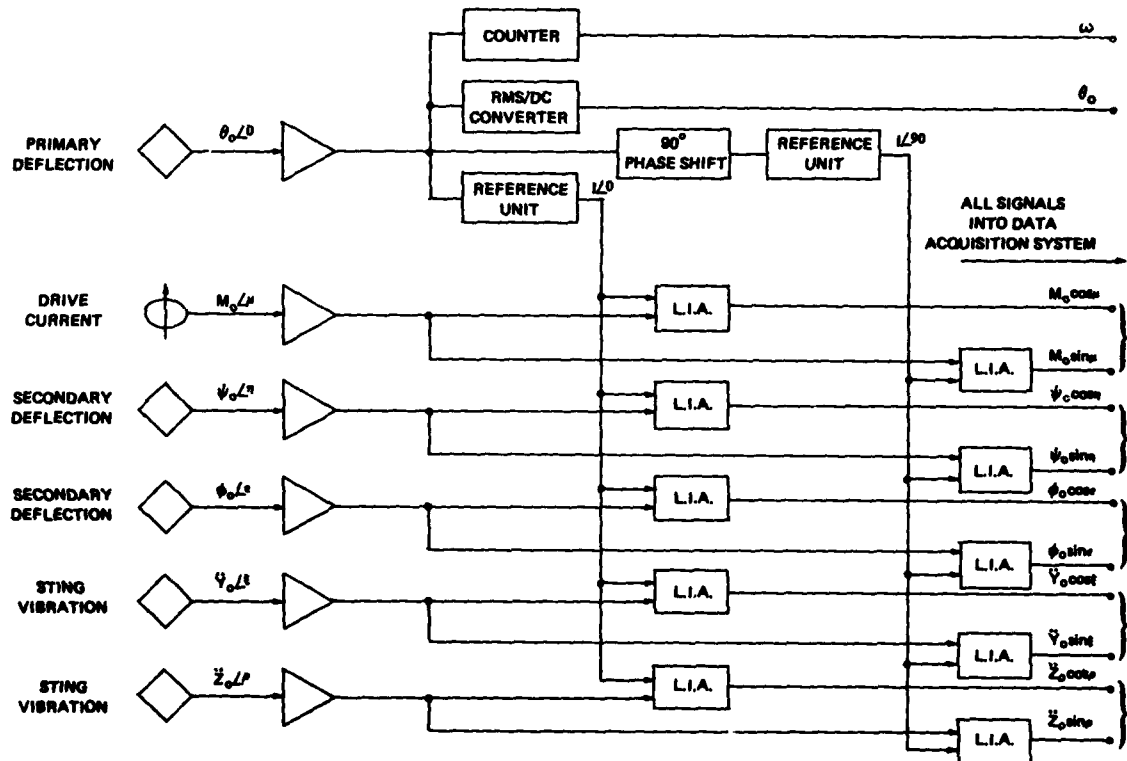


Fig. 4: Instrumentation system block diagram

4. DATA REDUCTION

As is shown in Fig. 5, two distinct reduction procedures are applied to the data obtained from each experiment. Procedure I is applied to the data associated with the primary degree of freedom in order to obtain the corresponding direct derivatives according to the well-known single degree of freedom constant-amplitude oscillation methods, while Procedure II is used to obtain cross and cross-coupling derivatives. The latter is applied to the data associated with the secondary degrees of freedom, namely secondary motions, mechanical stiffnesses and dampings as well as aerodynamic stiffnesses and dampings, which are (in turn) obtained from "complementary" tests where the model is oscillated in the pertinent degree of freedom. It should be noted that the data from the complementary runs must be for the same model attitude as the one under consideration.

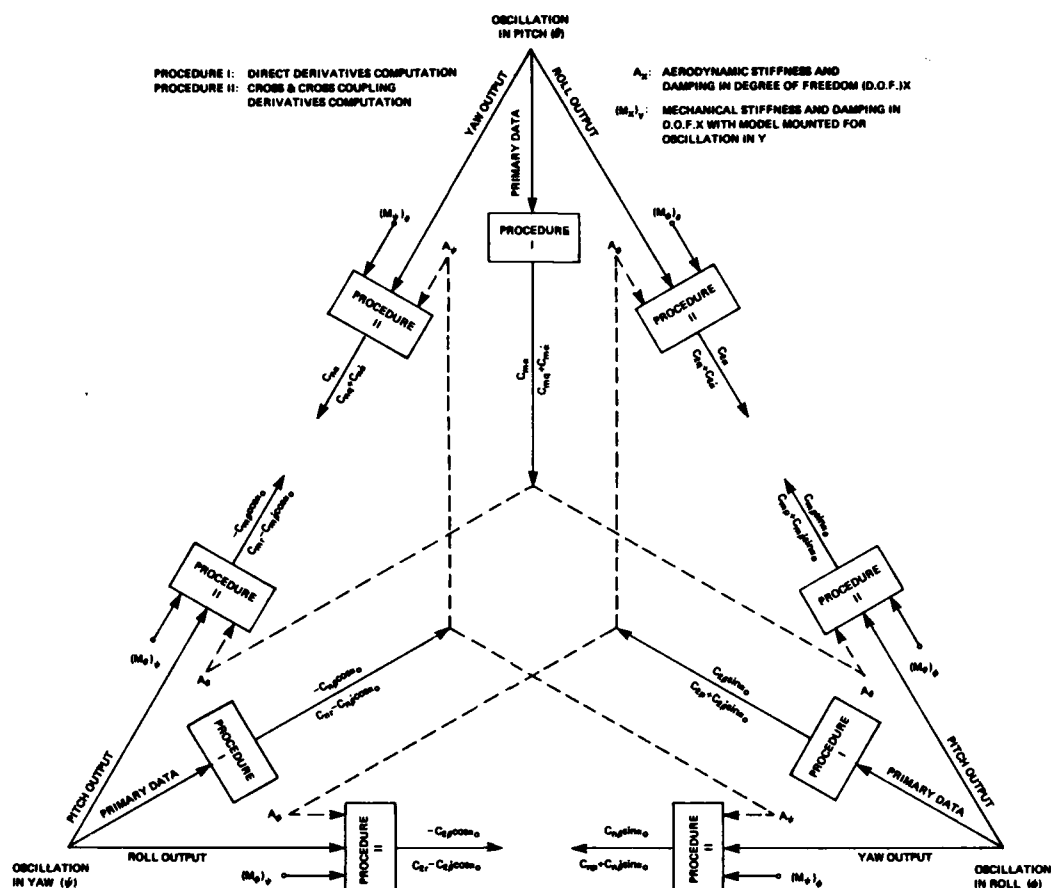


Fig. 5: Interrelation triangle for direct vs. cross and cross-coupling derivatives

It is therefore possible - by means of 3 oscillatory experiments - to obtain a complete set of 9 dynamic and 6 static moment derivatives due to pitching, yawing and rolling. A detailed data reduction flow chart for the specific case of the determination of cross and cross-coupling derivatives due to yawing and direct derivatives due to pitching and rolling is shown in Fig. 6.

In Procedure II, the sinusoidal time variations (coherent with the primary oscillation) of the secondary angular deflections are represented by tare and wind-on vectors. All phases are referred to the primary deflection. The subtraction of the tare vectors from the wind-on vectors gives the "aerodynamic deflection vectors" representing the angular deflections caused solely by aerodynamic moments due to the primary motion.

These aerodynamic deflection vectors are assumed to represent the response of a second-order system to an excitation by sinusoidal aerodynamic moments synchronous with the primary motion. To compute the cross and cross-coupling derivatives involved, the aerodynamic deflection vectors must first be converted into their causative aerodynamic moments which are then resolved into in-phase and quadrature components relative to the primary motion. Considering, for example, the secondary oscillation in pitch caused by a primary oscillation in yaw, $\psi = |\psi| \cos \omega t$, the equation of motion can be written as

$$\ddot{\theta} + (\nu_{\theta})_{\psi} \dot{\theta} + (\omega_{\theta})_{\psi}^2 \theta = |\bar{M}/(I_{\theta})_{\psi}| \cos(\omega t + \eta_{\theta})$$

where the subscript outside the brackets indicate that the model is mounted for oscillation in yaw and the damping coefficient, $(\nu_{\theta})_{\psi}$, and the wind-on natural frequency in pitch $(\omega_{\theta})_{\psi}$ are, respectively

$$(\nu_{\theta})_{\psi} = \frac{(\gamma_{\theta})_{\psi} - M_{\dot{\theta}}}{(I_{\theta})_{\psi}}$$

$$(\omega_{\theta})_{\psi} = \left[(\omega_{n\theta})_{\psi}^2 - \frac{M_{\theta}}{(I_{\theta})_{\psi}} \right]^{1/2}$$

\bar{M} is the aerodynamic moment in pitch - the magnitude and phase of which are to be determined - and t is time.

The direct aerodynamic derivatives $M_{\dot{\theta}}$ and $M_{\dot{\psi}}$ are obtained from the complementary test where the model is oscillated in pitch, and the mechanical characteristics of the system - such as the moment of inertia $(I_{\theta})_{\psi}$, the damping constant $(\gamma_{\theta})_{\psi}$, and the tare natural frequency $(\omega_{n\theta})_{\psi}$ - are determined by separate calibration tests.

The conversion of the aerodynamic pitch deflection vector θ into the aerodynamic moment in pitch \bar{M} is accomplished by considering the equations for amplification and phase shift in a second-order forced-oscillation system (see, e.g. Ref. 3), leading to the following expressions:

$$|\bar{M}| = |\theta| \cdot (I_{\theta})_{\psi} \left[((\omega_{\theta})_{\psi}^2 - \omega^2)^2 + (\nu_{\theta})_{\psi}^2 \omega^2 \right]^{1/2}$$

$$\angle(\bar{M} - \theta) = \epsilon_{\theta} = \arctan \frac{(\nu_{\theta})_{\psi} \omega}{(\omega_{\theta})_{\psi}^2 - \omega^2}$$

In turn, the phase angle between \bar{M} and ψ is determined from

$$\angle(\bar{M} - \psi) = \eta_{\theta} = \angle(\theta - \psi) + \epsilon_{\theta}$$

where $\angle(\theta - \psi)$ is the measured phase angle between θ and ψ .

The static and dynamic cross-coupling derivatives of the pitching moment due to yawing are finally obtained as

$$C_{m\psi} = -C_{m\beta} \cos \alpha_0 = \frac{1}{\bar{q} S \bar{c}} \frac{\partial \bar{M}}{\partial \psi} = \frac{1}{\bar{q} S \bar{c}} \frac{|\bar{M}| \cos \eta_{\theta}}{|\psi|}$$

$$C_{mr} = -C_{m\dot{\beta}} \cos \alpha_0 = \frac{1}{\bar{q} S \bar{c}} \cdot \frac{2V}{b} \frac{\partial \bar{M}}{\partial \dot{\psi}} = \frac{2V}{\bar{q} S \bar{c}} \frac{|\bar{M}| \sin \eta_{\theta}}{\omega |\psi|}$$

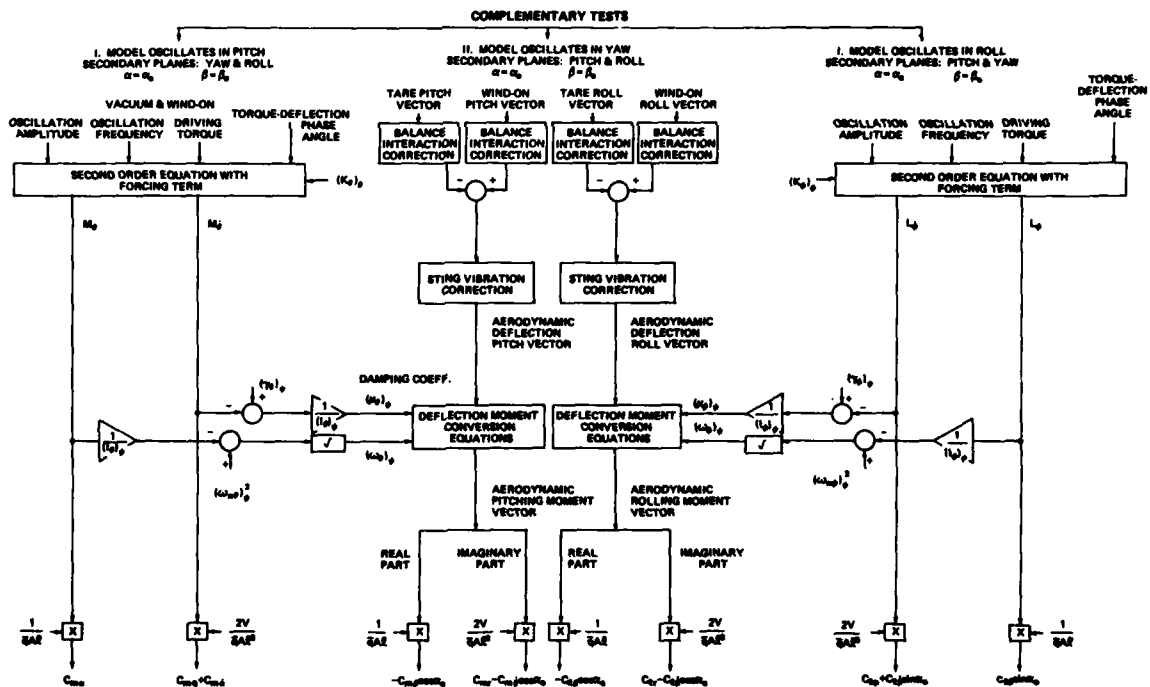


Fig. 6: Wind-tunnel data reduction chart (all vectors referred to primary deflection)

Exactly the same approach is used to obtain the rolling derivatives due to yawing, with the necessary direct derivatives being obtained from the rolling oscillation test. Furthermore, the method is quite general and can, therefore, be used for tests involving oscillations in any single degree of freedom, such as rolling, plunging (etc).

The above data-reduction procedure is based on the assumption that the aerodynamic interactions between the two secondary motions are negligible and that the primary motion is not affected by the two secondary motions. This assumption is considered realistic by virtue of the very high stiffness in the planes of the two secondary motions which results in secondary amplitudes that are small both in an absolute sense and relative to the primary amplitude. This is particularly true with regard to the component of the secondary motion that is coherent with the primary one. Mechanical and electrical interactions, obtained from the static balance calibration, are taken into account by means of a first-order correction. Furthermore, since vertical and lateral accelerations (\ddot{z} and \ddot{y}) may induce moments in the secondary degrees-of-freedom due to the presence of pertinent products of inertia of the moving system, a correction for this effect was incorporated in the data-reduction procedure. The corresponding acceleration effect in the primary degree-of-freedom appeared to be very small for the present experimental set ups and was therefore neglected.

As the method described above is new and based on certain assumptions (Ref. 4), and because little or no data is available on many of the derivatives measured, it was decided to develop a technique that would *independently* verify the validity of the approach. This was accomplished by means of an electromagnetic calibrating system that provides accurately known moments (in vectorial form) in up to three degrees of freedom simultaneously, such that a comparison between these moments and those resulting from the application of the data reduction procedure to the induced deflections provides a measure of the validity of the complete experimental technique and its analytical basis.

5. DESCRIPTION AND OPERATION OF CALIBRATOR

The operation of the calibrator is based on the application of accurately known moments to a calibration frame mounted on the dynamic balance and subjected to the same oscillatory motion in the primary plane as would be encountered in the corresponding wind tunnel test. The applied moments are coherent with the primary motion and their amplitudes and phases can be adjusted to represent a wide range of aerodynamic parameters.

Fig. 7 shows a simplified pictorial drawing of the calibrator. The stationary part is common to all applications and consists of two concentric octagonally-shaped structures that form a magnetic circuit necessary to establish a DC magnetic field across four air gaps located on the horizontal and vertical axes of symmetry of the octagons. Different versions of the moving part are necessary to accommodate the two types of primary motions that are required, namely, angular oscillation for the pitching, yawing and rolling tests, and translational oscillation for the plunging test. The two versions are discussed below.

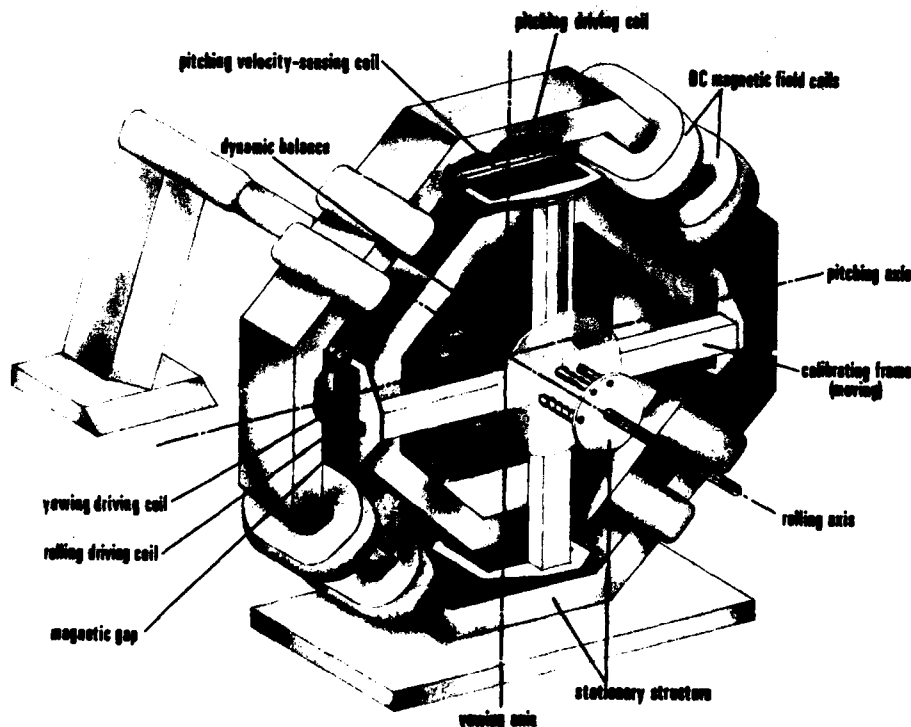


Fig. 7: Pictorial view of calibrator

a) Angular Primary Motion.

In this case the moving part is a very light cruciform-shaped frame. The outer ends of the four arms of the calibration frame support conductors (single-turn driving coils) located within the four air gaps. The necessary moments are obtained by passing suitable alternating currents through the driving coils which thus interact with the surrounding magnetic field. As the calibration frame may be required to move in three rotational degrees of freedom (θ , ψ and ϕ), the calibrator must have spherical symmetry about the point in the balance where the three axes intersect. This requires the magnetic fields across the gap to be radially oriented which is achieved by spherically shaping the pole pieces. Likewise, the driving coils are curved to preserve the necessary angular relationship between the currents and magnetic field.

b) Translational Primary Motion Using Half-Model Technique.

As shown in Table I, in the present context only pitching derivatives due to plunging are obtained, using the half model technique. In the calibration procedure, therefore, it is necessary to apply a pitching moment to a vertically oscillating calibrating frame, which can thus consist of a single horizontal bar to avoid contact between it and the stationary structure at the top and bottom air gaps (which are retained for the sake of simplicity (Fig. 8)). At the ends of the calibrating frame arms there are single turn driving coils oriented in the Y direction (model coordinates) imbedded in the magnetic field present in the side air gaps, which, in this case, are flat in order to accommodate the vertical translation. It should be noted that the pitching motion resulting from the applied moments is very small and thus does not require spherical gaps.

Since the applied moments must have arbitrary phase relationships with respect to the primary motion, the driving currents are synthesized from the signals corresponding to the deflection and angular velocity (90 degrees apart for a sinusoidal motion) in the primary plane. The velocity is sensed directly by means of conductors moving within the magnetic field so as to induce electromotive forces proportional to their velocity.

To ensure a proper calibration operation, the electromagnetically induced loads were carefully calibrated in terms of the corresponding drive currents, and the absence of interactions between the various applied loads - deemed to be essential for obtaining reliable results - was also experimentally confirmed.

The alignment between the stationary and moving parts of the calibrator was found not to be very critical, a situation to be expected as a result of the geometry involved, thus obviating the need for complex alignment procedures.

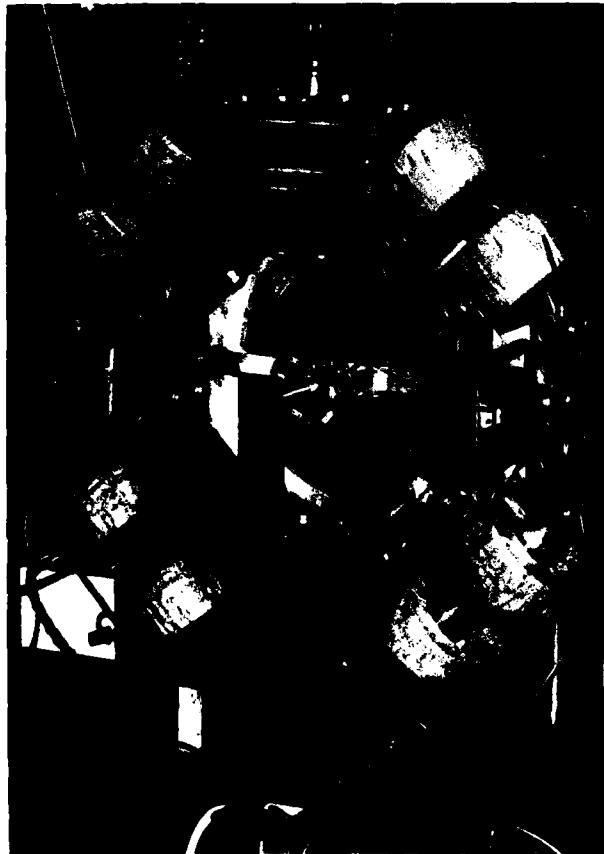


Fig. 8: Half-model calibrator (plunging configuration)

6. CALIBRATION PROCEDURE AND RESULTS

The purpose of the calibration procedure is to verify the validity of the experimental and analytical methods employed in the wind tunnel tests by suitably simulating the conditions encountered by the model in the flow. This is accomplished by substituting the model by the calibration frame and the aerodynamic loads by electromagnetically induced ones. Both "tare" and "wind on" measurements are taken, namely in the absence and presence of applied loads respectively. The same data reduction procedure is applied to the calibration data as used in the aerodynamic tests, that is, the deflection in the secondary degrees of freedom are converted into their causative loads which in this case, however, are known. Consequently, a comparison between the applied and measured loads provides information on the validity of the method. It should be noted that in the calibration experiments the inertia characteristics of the calibration frame rather than those of the model must be used; likewise, the aerodynamic stiffness and damping in the secondary degrees of freedom are zero. It is thus obvious that the calibration tests do not provide a calibration in the sense of obtaining input-output transfer functions, but rather they verify the validity of the experimental approach in a general sense. The calibrator, however, has furthermore proven to be an extremely useful diagnostic tool for the identification of instrumentation faults, computer program errors, etc.

A comparison between applied and measured moments for the pitching apparatus is shown in Fig. 9. Here various combinations of simultaneously applied pitching, yawing and rolling moments (indicated by the flags on the symbols) are plotted in polar form referred to the primary deflection in pitch. A similar plot for the pitching moment in the presence of plunging oscillations is shown in Fig. 10.

It can be seen that these results are very satisfactory; further details on the calibrator, discussion of errors, etc. are given in Ref. 5.

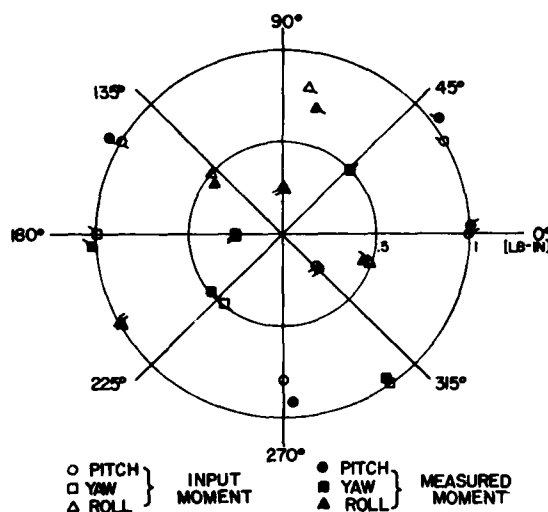


Fig. 9: Comparison between applied and measured L, M, N moment combinations. (Individual runs denoted by flags)

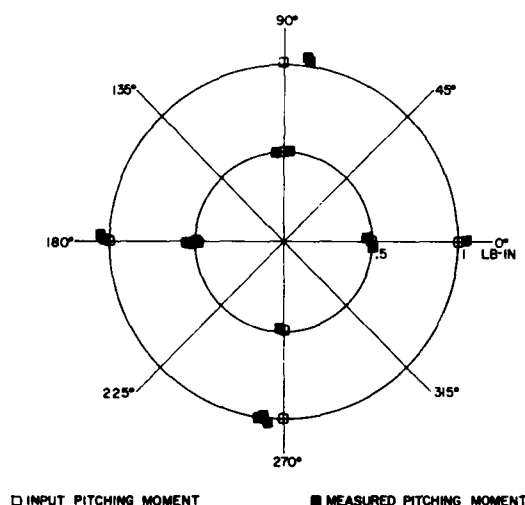


Fig. 10: Comparison between applied and measured pitching moments due to plunging

7. CONCLUSIONS

An oscillatory technique for the determination of static and dynamic cross and cross-coupling derivatives due to pitching, yawing, rolling and plunging has been developed and is available for routine wind tunnel testing of aircraft. A calibrator for the above apparatus has also been developed with which the validity of the experimental approach has been verified.

8. REFERENCES

1. K.J. Orlik-Rückemann
E.S. Hanff Experiments on Cross-Coupling and Translational Acceleration Derivatives. FDP Symposium on Dynamic Stability Parameters, Paper 8, 1978.
2. W. Curry
K.J. Orlik-Rückemann Sensitivity of Aircraft Motion to Aerodynamic Cross Coupling at High Angles of Attack. FDP Symposium on Dynamic Stability Parameters, Paper 34, 1978.
3. S. Timoshenko Vibration Problems in Engineering. D. van Norstrand Co. N.Y., 1937.
4. E.S. Hanff
K.J. Orlik-Rückemann Wind Tunnel Measurements of Dynamic Cross-Coupling Derivatives. J. of Aircraft. Vol. 15, No. 1. 1978.
5. E.S. Hanff Three Degrees of Freedom Dynamic Calibrator for Oscillatory Cross-Derivative Apparatuses. NRC-NAE LTR-UA-39, 1976.

DÉTERMINATION DE NON-LINÉARITÉS DE STABILITÉ DYNAMIQUE

par Xavier VAUCHERET

Office National d'Etudes et de Recherches Aéronautiques (ONERA)
92320 Châtillon (France)

RESUME

Par son balayage complet d'amplitude, au cours d'un transitoire, la méthode des oscillations libres est bien adaptée à l'étude des non-linéarités survenant au cours d'essais de stabilité dynamique de maquettes en soufflerie.

A partir des théories classiques de la mécanique non-linéaire, une classification des non-linéarités, basée sur leurs effets, est proposée. A l'inverse, des évolutions de fréquence et d'amortissement en fonction de l'amplitude, mesurées en cours d'essais, il est possible de remonter à la meilleure représentation non-linéaire du mouvement. Deux cas concrets d'oscillations fortement non linéaires, dont l'un comportant un cycle limite, illustrent les méthodes développées.

INTRODUCTION

La méthode des oscillations libres a été développée à l'ONERA depuis 1957 comme procédé d'étude en soufflerie des caractéristiques de stabilité dynamique des maquettes [1]. La principale raison du choix des oscillations libres était de réduire au maximum le temps d'essai à la durée d'une relaxation en vue de diminuer le coût des essais sur des maquettes de grandes dimensions. Par la suite, cette méthode s'est avérée bien adaptée au cas des souffleries à rafales, de plus en plus brèves, lorsque le nombre de Mach augmente. Des essais ont été alors successivement réalisés à Mach 7 pour une durée de 20 secondes puis Mach 10 pour une durée de 10 secondes en adoptant les montages d'essais et en automatisant toutes les séquences d'essais [2]. Ainsi un programmeur imposait le déroulement successif des déblocages maquettes après amorçage de la veine, armement de la maquette à l'amplitude préaffichée, déverrouillage rapide provoquant l'oscillation libre et reblocage de la maquette avant désamorçage de la veine. Grâce au développement de cette technique, des essais purent être effectués à Mach 17 au cours de tirs d'une durée de 80 à 160 millisecondes.

Dès l'utilisation de la méthode des oscillations libres, le problème des non linéarités a été abordé : en effet, les dispositifs de suspension et de rappel élastique de maquettes pesant environ une tonne soulevaient des difficultés inhérentes à des frottements secs, des jeux ou des discontinuités de rappel [3], qui par la suite furent résolus par l'emploi de montages comportant des articulations à lames croisées monobloc. L'étude des non linéarités d'ordre mécanique a constitué par la suite un acquis profitable pour l'étude des non linéarités d'ordre aérodynamique que tous les engins ou corps de rentrée présentaient par suite de phénomènes de décollements, même lorsque les oscillations étaient réalisées autour d'une incidence nulle.

Les méthodes de résolutions d'équations non linéaires ont été l'objet de nombreux travaux. A partir de cette résolution, une classification des non linéarités relatives aux termes de rigidité et d'amortissement, en non linéarités de courbure et de discontinuité a été établie.

En essais, au cours d'une oscillation libre, les données sont constituées par les évolutions de la fréquence et de l'amortissement en fonction de l'amplitude d'oscillation. Ces évolutions ont pu être obtenues en temps réel à l'aide d'un traitement analogique approprié [4] permettant de se rendre compte, dès la fin de l'oscillation libre, du type de non linéarité en se reportant à la classification des non linéarités basée sur leur effets. Le problème à résoudre consiste alors à déterminer le meilleur modèle mathématique de l'équation non linéaire du mouvement à partir des relevés de fréquence et d'amortissement en fonction de l'amplitude. Ce problème inverse [5] est traité dans chaque cas spécifique en optimisant en pas à pas (fréquence puis amortissement) l'expression mathématique la plus simple de l'équation du mouvement en vue de formuler avec la meilleure précision les non-linéarités.

1 - CLASSIFICATION DES NON LINEARITES1.1 - Méthodes générales de mécanique non linéaire

Les problèmes de mécanique non linéaire ont donné lieu à une abondante littérature de caractère généralement assez mathématique [6],[7],[8] .

Les méthodes utilisées comprennent :

- la méthode topologique de POINCARÉ orientée sur l'étude des points singuliers et des cycles limites
- les méthodes analytiques permettant de traiter des systèmes non linéaires ne s'écartant pas trop d'un modèle linéaire et admettant de ce fait le principe de superposition de faibles non linéarités. Parmi ces méthodes, deux retiennent l'attention :
 - la méthode des perturbations, développée en mécanique céleste par POINCARÉ et LINDSTEDT. L'application de cette méthode conduit souvent à des termes séculaires (produit d'une fonction périodique par une fonction croissant indéfiniment avec le temps) sans réalité physique mais dont l'annulation fournit les évolutions fréquence - amplitude .
 - la méthode de l'équivalent harmonique de KRYLOV et BOGOLJUBOV [9] en relation étroite avec les méthodes de RITZ-GALERKIN et de la variation des constantes.

Ces deux méthodes analytiques donnent des résultats similaires ; la deuxième permet de dégager une classification des non linéarités et a de ce fait été retenue à l'ONERA pour l'étude des non linéarités rencontrées en soufflerie.

1.2 - Non linéarités de courbure

Au cours d'un transitoire, le mouvement est décrit par une équation unique :

$$\ddot{x} + \omega_0^2 x + \varepsilon f(x, \dot{x}) = 0$$

si les non linéarités sont des termes en puissance de x ou de \dot{x} ou une combinaison des deux. La théorie de KRYLOV-BOGOLJUBOV consiste, à partir de la solution de l'équation linéaire pour ε nul, à choisir une solution du type :

$$x = a(t) \sin [\omega_0 t + \phi(t)] = a(t) \sin \psi(t)$$

où les deux fonctions a et ϕ résultent du système de deux équations du premier ordre :

$$\begin{cases} \dot{a} = -\frac{\varepsilon}{\omega_0} f(a \sin \psi, a \omega_0 \cos \psi) \cos \psi \\ \dot{\psi} = \frac{\varepsilon}{a \omega_0} f(a \sin \psi, a \omega_0 \cos \psi) \sin \psi \end{cases}$$

Dans le cas de valeurs faibles de ε , les fonctions a et ϕ peuvent être considérées comme constantes au cours d'une période ; leurs dérivées sont développables en série de FOURIER. La théorie de la première approximation conduit au système :

$$\begin{cases} \dot{a} = -\frac{\varepsilon}{2\pi\omega_0} \int_0^{2\pi} f(a \sin \phi, a \omega_0 \cos \phi) \cos \phi d\phi \equiv F(a) \\ \dot{\psi} = \omega_0 + \frac{\varepsilon}{2\pi a \omega_0} \int_0^{2\pi} f(a \sin \phi, a \omega_0 \cos \phi) \sin \phi d\phi \equiv \Omega(a) \end{cases}$$

A partir de cette théorie, une classification des non linéarités découle selon qu'elles conduisent ou non à des évolutions d'amplitude ou de fréquence.

Une non linéarité du type $\varepsilon |x|^n \frac{x}{|x|}$ n'engendre qu'une variation de fréquence :

$$\Omega(a) = \omega_0 + \frac{\varepsilon}{n} a^{n+p-1} \omega_0^{p-1} \frac{\Gamma(\frac{n+2}{2}) \Gamma(\frac{p+1}{2})}{2 \Gamma(\frac{n+p+3}{2})}$$

Une non linéarité du type $\varepsilon |x^n| |x^0|^p \frac{\dot{x}^0}{|x^0|}$ n'engendre qu'une variation d'amplitude donnée par la loi :

$$F(\alpha) = -\frac{\varepsilon}{\pi} \alpha^{n+p} \omega_0^{p-1} \frac{\Gamma(\frac{n+1}{2}) \Gamma(\frac{p+2}{2})}{2 \Gamma(\frac{n+p+3}{2})}$$

Dans ce cas l'amortissement de l'équation linéarisée de référence

$$\ddot{x} + 2\alpha_E \omega_0 \dot{x} + \omega_0^2 x = 0$$

est donné par la relation

$$\alpha_E = -\frac{F(\alpha)}{\alpha \omega_0}$$

Des non linéarités de type $\varepsilon |x^n| |\dot{x}^0|^p$ ou $\varepsilon |x^n| |\dot{x}^0|^p \frac{x}{|x|} \frac{\dot{x}^0}{|\dot{x}^0|}$ ne conduisent qu'à des fonctions $F(\alpha)$, $\Omega(\alpha)$ contenant des termes en puissances au moins égales à 2 de ε , donc négligeables en première approximation.

1.3 - Non linéarités de discontinuités

Une deuxième catégorie de non linéarités est constituée par des termes discontinus. Au cours d'un cycle d'oscillation, l'équation du mouvement présente autant de formes qu'il existe de discontinuités. La représentation du mouvement dans le plan de phase comporte des tronçons de spirales se raccordant sur autant de lignes de saut qu'il existe de discontinuités.

Un cas général, correspondant aux forces de rappel discontinues, est constitué par le rappel hystérétique rectiligne qui recouvre les cas de frottement sec, jeux ou seuils.

Au cours d'un cycle (figure 1) partant d'une amplitude x_0 positive, le point représentatif parcourt le trajet ACDEFBG composé des 4 droites parallèles deux à deux :

$$F = k_0 (x \pm k_0) , \quad F = \lambda k_0 (x \pm \mu k_0)$$

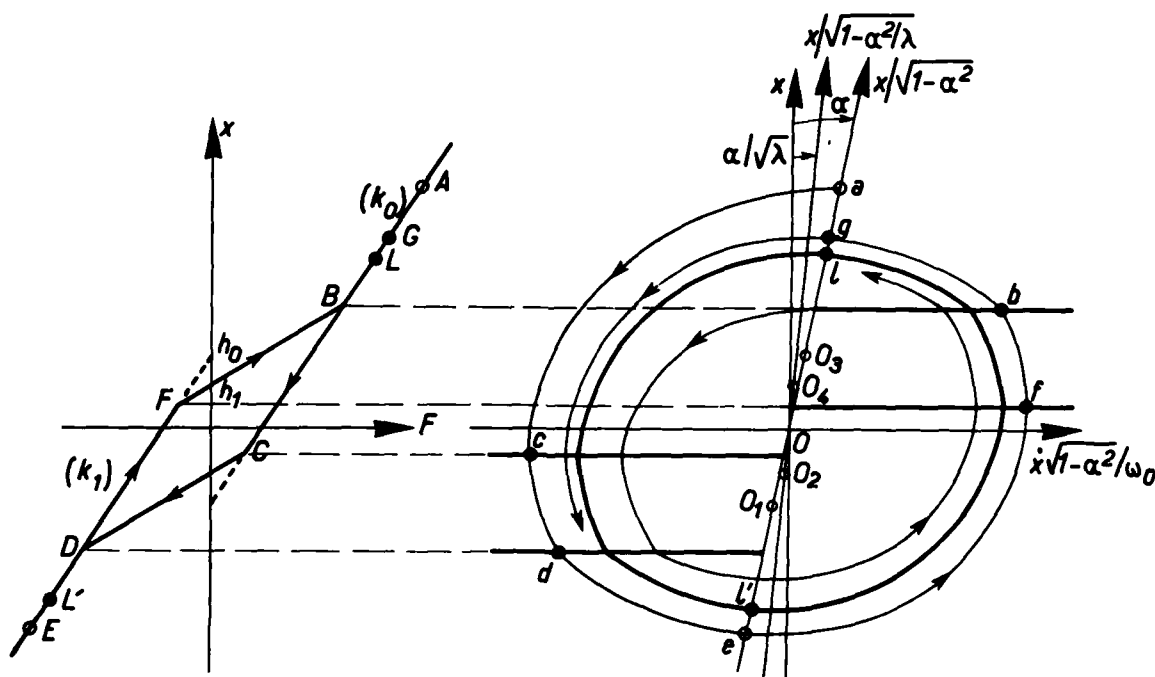


Fig.1 - Force de rappel hystérétique rectiligne - Représentation dans le plan de phase

En prenant pour référence le système linéaire dissipatif de force de rappel $H_0 x$, $\ddot{x} + 2\alpha\omega_0 \dot{x} + \omega_0^2 x$, les quatre équations décrivant le mouvement sont :

$$\begin{cases} \ddot{x} + 2\alpha\omega_0 \dot{x} + \omega_0^2 (x \pm h_0) = 0 \\ \ddot{x} + 2\alpha\omega_0 \dot{x} + \lambda\omega_0^2 (x \pm \mu h_0) = 0 \end{cases}$$

leur résolution peut être effectuée rigoureusement en pas à pas [10]

Partant des conditions initiales A ($t = 0$, $x = x_0$, $\dot{x} = 0$) et posant

$$\omega_p = \omega_0 \sqrt{1-\alpha^2}, \quad \gamma = \alpha / \sqrt{1-\alpha^2}$$

le point C d'élongation $x_c = h_0 \frac{1-\lambda\mu}{\lambda-1}$ sera atteint au temps t_0 , sa vitesse étant \dot{x}_c . t_0, \dot{x}_c sont définis par :

$$\begin{aligned} \text{tg } \xi &= -\frac{1}{\sqrt{1-\alpha^2}} \left(\alpha + \frac{\lambda}{C} \right) & \text{ou} & \quad \xi = \frac{\pi}{2} - \omega_p t_0 \\ e^{-\gamma(\pi-2\xi)} &= \left(\frac{h_0}{x_0+h_0} \right)^2 \left(\frac{1-\mu}{\lambda-1} \right)^2 (C^2 + 2\alpha\lambda C + \lambda^2) & C &= \frac{\lambda-1}{1-\mu} \frac{\dot{x}_c}{\omega_0 h_0} \end{aligned}$$

le point D d'élongation $x_D = h_0 \frac{1+\lambda\mu}{1-\lambda}$ sera atteint au temps t_0+t_1 , sa vitesse étant \dot{x}_D . t_1, \dot{x}_D sont définis par :

$$\begin{aligned} \text{tg } \eta &= -\sqrt{\lambda-\alpha^2} \frac{C+D}{CD+\alpha(D-C)-\lambda} & \text{ou} & \quad \eta = \omega_p t_1 \\ (C^2 + 2\alpha C + \lambda)(1-\mu)^2 e^{-\rho\eta} &= (D^2 - 2\alpha D + \lambda)(1+\mu)^2 e^{\rho\eta} & D &= \frac{\lambda-1}{1-\mu} \frac{\dot{x}_D}{\omega_0 h_0} \end{aligned}$$

avec les notations :

$$\omega_p = \omega_0 \sqrt{\lambda-\alpha^2}, \quad \rho = \alpha / \sqrt{\lambda-\alpha^2}$$

le point E de vitesse nulle sera atteint au temps $t_0+t_1+t_2$, son amplitude étant x_1 . t_2, x_1 sont définis par :

$$\begin{aligned} \text{tg } \xi &= \frac{1}{\sqrt{1-\alpha^2}} \left(\alpha - \frac{\lambda}{D} \right) & \text{ou} & \quad \xi = \frac{\pi}{2} - \omega_p t_2 \\ e^{\gamma(\pi-2\xi)} &= \left(\frac{h_0}{x_1-h_0} \right)^2 \left(\frac{1+\mu}{\lambda-1} \right)^2 (D^2 - 2\alpha D + \lambda^2) \end{aligned}$$

le système des 6 équations rigoureuses ci-dessus permet donc de calculer l'amplitude x_1 et la demi-période ($t_0+t_1+t_2$).

Dans le cas d'amplitudes a suffisamment grandes pour pouvoir négliger les puissances supérieures à 2 du rapport h_0/a devant l'unité, et pour des amortissements faibles, les lois asymptotiques aux grandes amplitudes sont :

$$\begin{aligned} \frac{t_0}{T} &= 1 - \frac{2h_0}{a\pi} \left(1 + \alpha \frac{\pi}{2} - \frac{h_0}{a} \right) & \text{ou} & \quad \omega = \frac{\lambda\mu}{\lambda-1} \\ \Delta a &= a\alpha\pi - \alpha h_0(4-\pi) - 2\omega \frac{h_0^2}{a} \end{aligned}$$

La loi de fréquence, ne contenant ni λ ni μ , est indépendante de la boucle d'hystérésis. La loi de variation d'amplitude, par contre, dépend de ω dont le signe dépend au sens de parcours de la boucle d'hystérésis. La courbe représentative de cette loi (figure 2) est une hyperbole ayant pour asymptotes, d'une part l'axe des ordonnées. d'autre part une droite de pente $\alpha\pi$ et d'abscisse à ordonnée nulle :

$$a^* = h_0 \frac{4-\pi}{\pi}$$

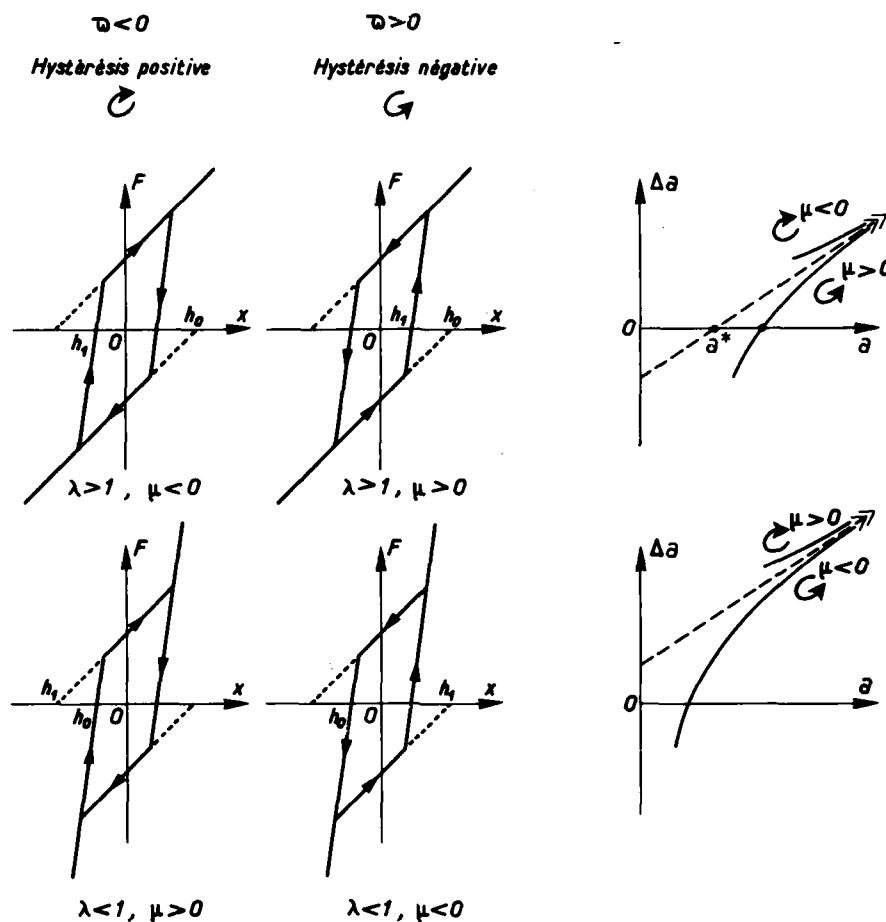


Fig. 2

L'asymptote est atteinte par valeurs supérieures ou inférieures selon que la boucle d'hystérésis est décrite dans le sens positif ($\omega < 0$), ou négatif ($\omega > 0$). Dans ce dernier cas, l'hyperbole coupe l'axe des abscisses en un point correspondant à un cycle limite dont l'étude est donnée au paragraphe suivant.

2 - NON LINEARITES CONDUISANT A DES CYCLES LIMITES

La présence d'oscillations auto entretenues, c'est à dire de cycles limites stables ayant été observée au cours de divers essais en soufflerie, les types de non linéarités pouvant conduire à de telles oscillations sont examinés dans les 2 cas de non linéarités décrites précédemment.

2.1 - Non linéarités de discontinuités

Dans le cas d'une force de rappel hystérétique rectiligne, les équations exactes données au paragraphe 1.3, permettent de calculer les caractéristiques de l'oscillation entretenue en prenant

$$|x_0| = |x_1| = a_L$$

Pour des amortissements faibles, tels que $\alpha^2 \ll 1$, l'amplitude α_L et la fréquence f_L de l'oscillation sont données par les relations :

$$2\omega y_L^2 = \alpha \left\{ \pi - (\xi_0 + \xi_0) + \frac{\eta_0}{\sqrt{\lambda}} \left[1 - y_L^2 (1 + \mu^2) \frac{\lambda}{\lambda - 1} \right] - \frac{\lambda - 1}{\lambda} (\sin \xi_0 + \sin 2\xi_0) \right\}$$

$$\frac{\pi}{\omega_L} = \frac{1}{\omega_0} \left(\pi - \xi_0 - \xi_0 + \frac{\eta_0}{\sqrt{\lambda}} \right)$$

dans lesquelles :

$$\sin \xi_0 = y_L \frac{\lambda}{\lambda - 1} (1 + \mu)$$

$$\sin \xi_0 = y_L \frac{\lambda}{\lambda - 1} (1 - \mu)$$

$$\sin \eta_0 = \frac{\lambda - 1}{\lambda \sqrt{\lambda}} \frac{\sin(\xi_0 + \xi_0)}{1 - y_L^2 (1 + \mu)^2}$$

et avec :

$$y_L = \frac{k_0}{k_0 + \alpha_L}$$

Si les sinus sont assimilables aux angles, les relations se simplifient en :

$$2\omega y_L^2 = \alpha(4 - y_L), \quad f_0 = f_L \left(1 - \frac{2}{\pi} y_L \right)$$

La loi de récurrence d'amplitude, donnée au paragraphe 1.3, pour les grandes amplitudes, peut encore s'écrire :

$$\frac{\Delta \alpha}{\alpha} = -2\omega y^2 + \alpha(\pi - 4y) = f(y, \alpha)$$

le cycle limite, atteint lorsque $f(y, \alpha)$ devient nul, sera stable si :

$$\frac{\partial f(y, \alpha)}{\partial y} < 0$$

ce qui entraîne, pour des valeurs de y comprises entre 0 et 1, la condition ω positif, déjà indiquée au paragraphe 1.3, donc l'un des 2 cas :

$$\mu > 0, \lambda > 1 \quad \text{ou} \quad \mu < 0, \quad 0 < \lambda < 1$$

2.2 - Non linéarités de courbure

Ainsi qu'indiqué au paragraphe 1.2, les seules non linéarités susceptibles de conduire à une variation d'amplitude au cours d'un transitoire sont de la forme $\varepsilon |x|^n |x^b| \text{signe } x$. De telles non linéarités ne donnent aucune variation de fréquences avec l'amplitude ce qui les distingue nettement des non linéarités de discontinuités.

Dans le cas d'une association de plusieurs non linéarités de courbure, génératrices d'évolution d'amplitude, les conditions d'existence de cycles limites stables d'amplitude α_L sont :

$$F(\alpha_L) = 0, \quad F'_\alpha(\alpha_L) < 0$$

Parmi les non linéarités conduisant à un cycle limite, les plus simples seront du type $\sum A_{m,p} x^{2m+2p+1}$ donnant une loi d'amplitude :

$$F(\alpha) = -\sum A_{m,p} \alpha^{2m+2p+1} \omega_0^{2p} \frac{[1 \cdot 3 \cdot 5 \dots (2m-1)][1 \cdot 3 \cdot 5 \dots (2p-1)]}{2^{m+p+1} (m+p+1)!}$$

Deux cas particuliers apparaissent selon que m ou p sont nuls.

Pour un polynôme en m limité à 2 et pour p nul donc un ensemble de 3 non linéarités : $\sum_{m=0}^2 A_{2m} x^{2m}$, la loi d'amplitude est :

$$F(\alpha) = -\frac{\alpha}{16} (8A_0 + 2A_2 \alpha^2 + A_4 \alpha^4)$$

Ce cas, recouvrant l'équation classique de VAN DER POL ($A_4 = 0, A_2 = -A_0$), est rencontré dans le calcul théorique des oscillations d'un corps de rentrée présentant une zone décollée [11]. Le point d'amplitude nulle constitue une singularité stable si A_0 est positif. Pour que des cycles limites existent, il est nécessaire de remplir simultanément 4 conditions :

$$A_0 > 0, \quad A_2 < 0, \quad A_4 > 0, \quad A_2^2 > 8A_0 A_4$$

Seule la racine α_L la plus élevée de $F(\alpha)$ correspond à un cycle limite stable ; selon que l'amplitude initiale d'oscillation sera inférieure ou supérieure à la première racine α_1 de $F(\alpha)$, le mouvement se terminera à amplitude nulle ou égale à α_L .

Pour un polynôme en p limité à 2 et pour m nul, donc pour un ensemble de 3 non linéarités : $\sum_{p=0}^2 A_{0,2p} x^{2p}$, la loi d'amplitude est :

$$F(\alpha) = -\frac{\alpha}{16} (9A_0 + 6A_2 \alpha^2 \omega_0^2 + 5A_4 \alpha^4 \omega_0^4)$$

Les conditions d'existence d'un cycle limite seront :

$$A_0 > 0, \quad A_2 < 0, \quad A_4 > 0, \quad 3A_2^2 > 40A_0A_4$$

une seule racine de $F(\alpha)$, la plus grande, conduira à un cycle limite stable, outre la singularité stable à amplitude nulle pour A_0 positif. Ce cas recouvre l'équation classique de RAYLEIGH ($A_4 = 0, -m A_2 = n A_0$).

3 - OBTENTION DES NON LINEARITES A PARTIR D'ESSAIS EN SOUFFLERIE

De nombreux essais de maquettes de corps de rentrée ont été effectués en soufflerie à l'aide de la méthode des oscillations en utilisant un montage entièrement automatisé (figure 3).

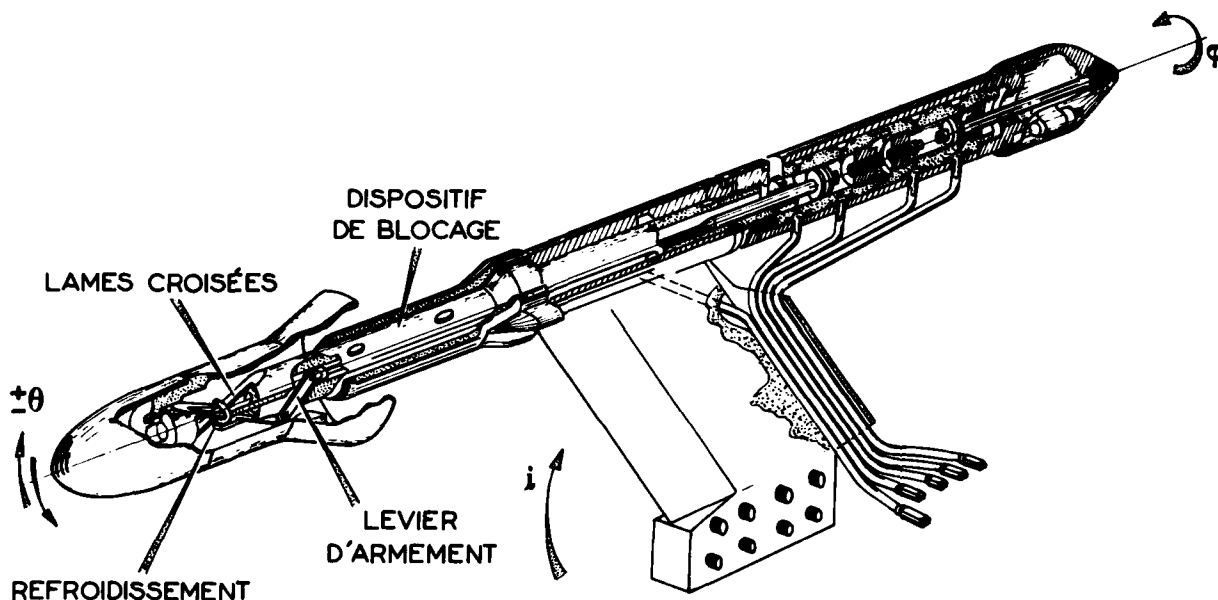


Fig. 3 - Dispositif d'essais de corps de rentrée. $0,75 < M < 10$.

Dans la plupart des cas, de fortes non linéarités ont été rencontrées par suite de la présence de décollements se développant au pied de la partie aval conique des corps de rentrée. Deux types de comportement des maquettes ont été observés : le premier avec des cycles limites d'amplitudes importantes atteintes par valeurs supérieures ou inférieures, donc stables, accompagnés de fortes évolutions de fréquences. De telles oscillations auto entretenues disparaissaient ainsi que l'évolution des fréquences en agissant sur les décollements à l'aide d'aspérités sur la partie avant du corps de rentrée. Une deuxième catégorie concerne des oscillations sans cycles limites, comportant de fortes variations d'amortissement et de fréquence au cours d'un transitoire. Ces deux cas ont été traités en faisant appel à des méthodes de résolution différentes exposés ci-après.

3.1 - Oscillations libres avec cycles limites [10]

Dans le cas d'essais effectués à Mach 4,5 en oscillations libres d'amplitude initiale 7 degrés sur un corps de rentrée, en transition naturelle, comportant une partie cylindrique suivie d'une partie arrière conique, des décollements remontaient jusqu'au milieu de la partie cylindrique à incidence nulle et intéressaient toute la partie cylindrique à l'extrados de la maquette à

l'incidence de 7 degrés, l'écoulement étant bien recollé à l'intrados. Au cours d'oscillations autour d'une valeur moyenne : $\Theta_m = -0,2$ degré, les oscillations se stabilisaient à partir de la 90ème oscillations à une amplitude constante Θ_L de 1,1 à 1,7 degrés pour des nombres de Reynolds de 6 et 4,4 millions (figure 4). A l'inverse, l'amplitude de la maquette débloquée sans armement, augmentait jusqu'à la valeur Θ_L obtenue précédemment.

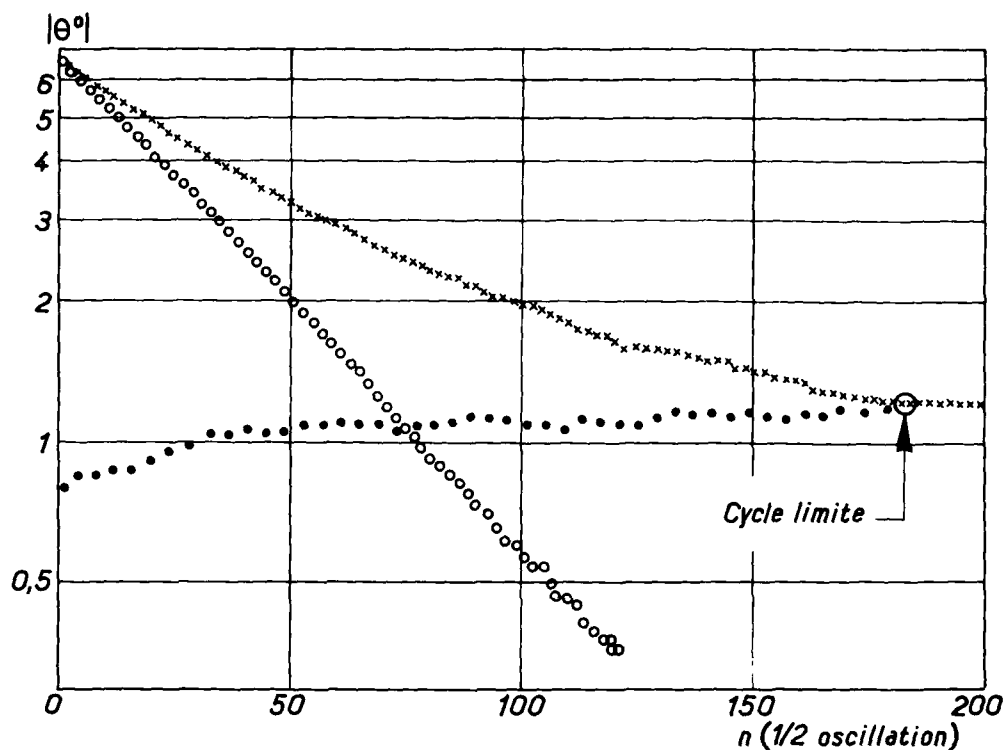


Fig. 4 -

M = 4,5 {
 x Corps de rentrée lisse
 ● Corps de rentrée lisse (régime d'établissement du cycle limite)
 ○ Corps de rentrée avec collerette dentelée

Les courbes classiques d'amplitude tracée en fonction du nombre d'oscillations montrent bien l'évolution obtenue et le cycle limite stable.

En disposant des rugosités sur le nez du corps de rentrée, les ombroscopies montraient un attachement correct de l'onde de pied de jupe et le mouvement est bien linéarisé en amplitude (figure 4) les oscillations auto-entretenuës ont disparu. La comparaison des courbes

$|\Theta| = F(n)$ montre bien la différence de comportement due aux décollements : après 50 oscillations, la maquette rugueuse a une amplitude de 0,6 degré alors que la maquette lisse oscille encore avec une amplitude de 2 degrés.

Une autre différence fondamentale de comportement de la maquette, selon la rugosité du nez, réside dans l'évolution rapide de la fréquence aussi bien avant qu'après cycle limite pour la maquette lisse et une faible variation dans le cas de la maquette rugueuse (figure 5). Sur cette même figure sont portées les lois d'amplitude $\Delta\Theta = F(|\Theta|)$ obtenues.

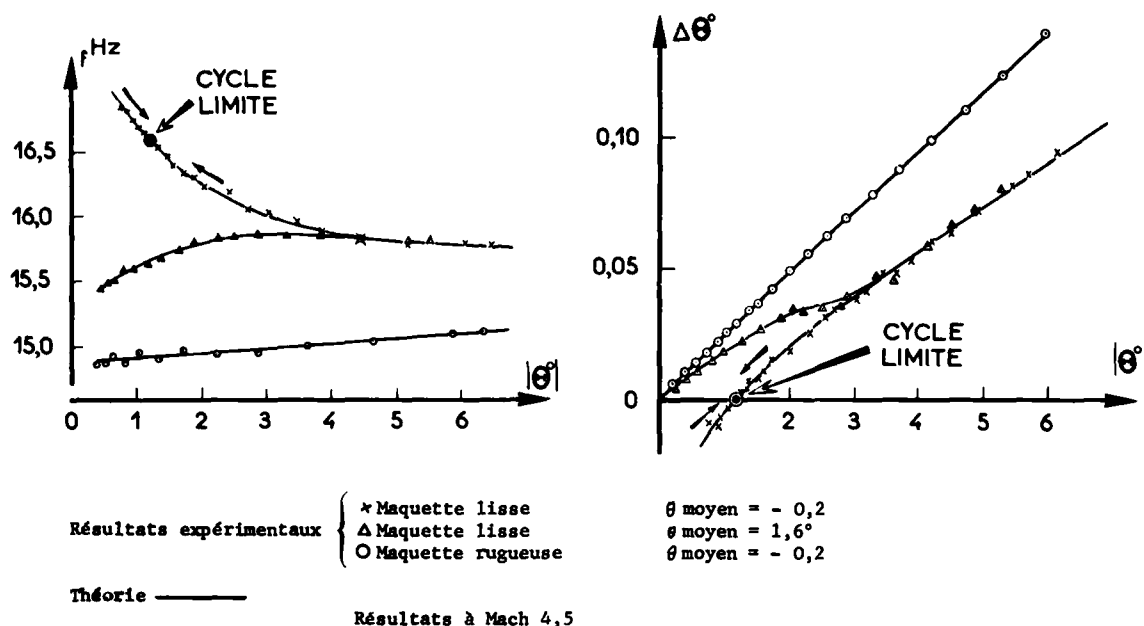


Fig.5 - Lois de fréquence et d'amplitude

3.1.1 - Maquette rugueuse

Les points $\Delta\theta = F|\theta|$ se placent sur 2 droites dont l'une à faibles amplitudes passe par l'origine. La fréquence est pratiquement constante à faible amplitude et croît au delà.

Une modélisation de la force de rappel en trois droites de pentes voisines, sans hystérésis, et un amortissement constant donnent les évolutions de fréquence et d'amplitude tracées en traits continus (figure 5) en bon accord avec les points expérimentaux. En prenant les notations du paragraphe 1.3, les équations du mouvement sont décrites avec des non linéarités de discontinuités caractérisées par :

$$\lambda = 0,95 \quad , \quad \mu = 0 \quad , \quad h_0 = -0,4^\circ \quad , \quad \alpha = 7,3 \text{ ‰}$$

conduisant à une dérivée de stabilité dynamique de tangage constante $C_{mq} = -0,27$.

3.1.2 - Maquette lisse

L'examen des courbes de fréquence et de récurrence d'amplitude (figure 5) et la présence d'un cycle limite stable conduisent à prendre une schématisation de rappel hystérétique rectiligne décrit aux paragraphes 1.3 et 2.1. Ce modèle non linéaire est caractérisé par $\lambda > 1$, $\mu > 0$ et $h_0 > 0$.

La valeur de h_0 découlant de l'amplitude et de la fréquence du cycle limite est $h_0 = +0,13^\circ$. La pente de l'asymptote à la courbe $\Delta\theta = F|\theta|$ donne le coefficient d'amortissement $\alpha = 5,1 \text{ ‰}$. La relation liant ω , y_L et α fournit le paramètre d'hystérésis

$\omega = 0,673$ donc la surface de la boucle d'hystérésis $S_H = 4 h_0 h_0^2 |\omega|$. Il n'est pas possible de séparer λ et μ mais seulement d'indiquer que :

$$\lambda > 1 \quad , \quad 0 < \mu < 0,673 \quad \Rightarrow \quad 0 < h_0 \mu < 0,09^\circ$$

Les courbes théoriques $f(\theta)$, $\Delta\theta = F|\theta|$ obtenues à partir de telles valeurs sont tracées en traits continus figure 5 : elles coïncident parfaitement avec les points expérimentaux. La valeur du coefficient de stabilité dynamique de tangage résultant de la mise en équation non linéaire est constante : $C_{mq} = -0,20$.

Des essais ont été effectués autour d'une valeur moyenne Θ_m de + 1,6 degré. Les lois de fréquence et de récurrence d'amplitude données figure 5 montrent que ce cas est un cas intermédiaire des précédents et ne présente pas de cycle limite. Ce cas peut être traité en prenant une boucle d'hystérésis non centrée autour de la valeur moyenne d'oscillation. Après quelques cycles englobant la boucle d'hystérésis, le mouvement excepte celle-ci et se linéarise aux faibles amplitudes. La courbe théorique obtenue alors est bien conforme aux lois mesurées (figure 5).

3.2 - Oscillations libres non linéaires [12]

Le deuxième exemple d'oscillations libres non linéaires concerne un corps de rentrée en hypersonique (Mach 7). Dans ce cas des évolutions importantes de la fréquence et de l'amortissement équivalent sont enregistrées en fonction de l'amplitude. Aucun cycle limite ne se manifeste. Ce cas peut donc être traité à l'aide d'un ensemble de non linéarités de courbure juxtaposées dont certaines conduisent à la loi de fréquence et d'autres à la loi d'amortissement soit respectivement des types : $\varepsilon |\lambda^n| |\lambda^0|^p$ et $\varepsilon |\lambda^n| |\lambda^0|^p$ ainsi qu'indiqué au paragraphe 12.

Par suite de la présence d'un axe de révolution, les maquettes de corps de rentrée ne peuvent conduire qu'à l'impairité de la force de rappel aérodynamique et à la parité de la force d'amortissement en fonction de l'incidence. L'amortissement de structure de la maquette et de ses liaisons avec son support est une fonction non linéaire de l'élongation instantanée θ de la maquette, nécessairement paire.

L'équation du mouvement de la maquette d'inertie B , rappelée mécaniquement par une suspension à lames croisées de rigidité K , autour d'un axe d'oscillations situé dans un plan vertical et incliné de l'incidence d'équilibre λ_0 est :

$$\ddot{\theta} + \left[\sum_{p=0}^{\infty} \nu_p (\theta^2 + \lambda_0^2)^p + \sum_{q=0}^L \mu_q \theta^{2q} \right] \dot{\theta} + \left[\frac{K}{B} + \sum_{n=0}^N \lambda_n (\theta^2 + \lambda_0^2)^n \right] \theta = 0$$

dans laquelle les coefficients λ_n et ν_p seront liés à des polynômes donnant les coefficients aérodynamiques C_{m_i} et C_{m_q} :

$$B \lambda_n = - p_c S l (2n+1) C_{m_i}, \quad B \nu_p = - \frac{p_c}{V} S l^3 C_{m_q}$$

S, l sont les références géométriques de la maquette, p_c pression cinétique et V la vitesse de l'écoulement.

3.2.1 - Non linéarités de déplacement

Les non linéarités de déplacement, contenues dans l'équation de mouvement sont de la forme $A_{2m+1} \theta^{2m+1}$. Ainsi qu'indiqué au paragraphe 1.2, de telles non linéarités n'entraînent qu'une variation de la fréquence :

$$\Omega(\alpha) = \omega_0 + A_{2m+1} \frac{\alpha^{2m}}{\omega_0} \prod_{k=1}^m \frac{2k-1}{2k+2}$$

Pour l'ensemble des non linéarités, la loi de fréquence est donc

$$\frac{\omega}{\omega_0} = 1 + \frac{1}{\omega_0} \sum_{n=1}^N \lambda_n \left[\alpha^{2n} \prod_{k=1}^{n+1} \frac{2k-1}{2k} + \sum_{m=1}^{n-1} \alpha^{2n-2m} \lambda_0^{2m} \prod_{k=1}^m \frac{n-k+1}{k} \prod_{k=1}^{n-m+1} \frac{2k-1}{2k} \right]$$

dans laquelle ω_0 , pulsation à amplitude nulle, résulte de l'équation linéaire de référence :

$$\ddot{\theta} + \left(\frac{K}{B} + \sum_{n=0}^N \lambda_n \lambda_0^{2n} \right) \theta = 0$$

La loi de fréquence, obtenue au cours d'un transitoire, peut être mise, à l'aide des moindres carrés, sous la forme polynomiale :

$$\omega = \sum_{n=0}^N \alpha_n \alpha^{2n}$$

le premier terme α_0 étant précisément la pulsation ω_0 . En égalant les termes de même puissance de α dans les 2 équations de la fréquence, on obtient un système linéaire de N équations dont les N inconnues sont les coefficients λ_n cherchés :

$$\alpha_0 \alpha_n = \prod_{k=1}^{n+1} \frac{2k-1}{2k} \left(\lambda_n + \sum_{k=1}^{N-n} \lambda_{n+k} \lambda_0^{2k} \prod_{s=1}^k \frac{n+s}{2s} \right)$$

Il suffit qu'un coefficient λ_n quelconque est donné par la relation :

$$\lambda_{n+1} = \alpha_0 \alpha_n \prod_{k=1}^{n+1} \frac{2k}{2k-1} - \sum_{k=1}^{N-n} \lambda_{n+k} \lambda_0^{2k} \prod_{s=1}^k \frac{n+s}{2s}$$

où λ_n dépend donc des termes de degré supérieur, le premier terme λ_0 étant obtenu en dernier par

la relation :

$$\lambda_0 = \alpha_0^2 - \sum_{n=1}^N \lambda_n \lambda_0^{2n} - \omega_0^{*2}$$

où ω_0^* est la pulsation sans vent, obtenue au cours d'essais préliminaires :

$$\omega_0^{*2} = K/B$$

Le choix du degré N du polynôme, représentant au mieux la loi de fréquence mesurée, est effectué par calcul automatique sur ordinateur. L'obtention d'un écart moyen quadratique réduit est un critère nécessaire mais non suffisant ; elle doit être conjuguée avec l'obtention d'un écart individuel maximal le plus faible possible. Dans le cas donné ici à titre d'illustration (figure 6) le degré du polynôme N doit être au moins égal à 3 sinon les écarts sont 2,5 fois trop grands. Pour optimiser le degré N , un critère d'invariance est retenu : effectuant la variation de N , la valeur de N retenue est celle qui assure l'invariance de la fonction $Cm_i(\lambda)$. Les fonctions tracées figure 6 pour des degrés N de 2 à 5 permettent de retenir $N=4$ pour lequel le degré d'invariance est obtenu avec une précision de $\Delta Cm_i / Cm_i = \pm 0,11\%$.

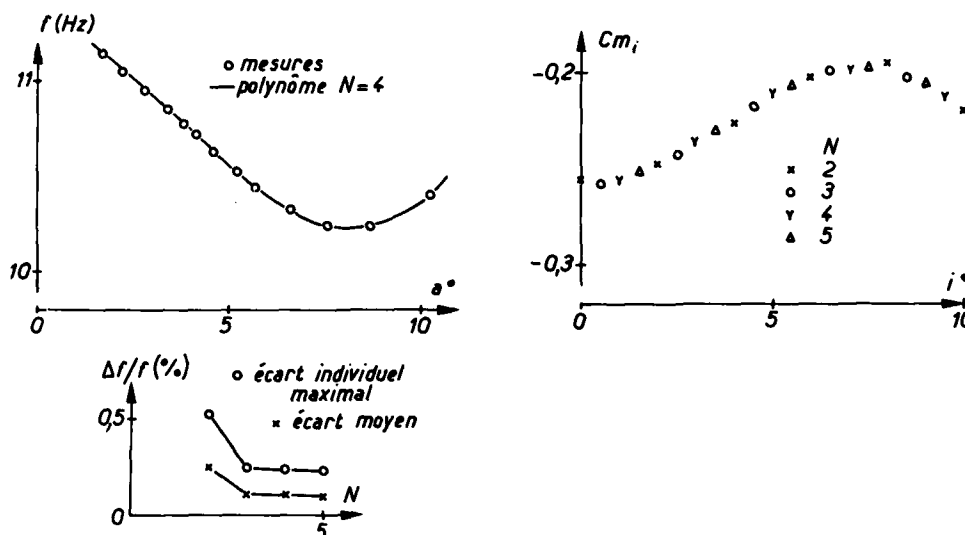


Fig.6 - Evolution de fréquence en amplitude

3.2.2 - Non linéarité de vitesse

Les non linéarités de vitesse, contenues dans l'équation du mouvement sont de la forme $B_{2m} \theta^{2m} \dot{\theta}$. Ainsi qu'indiqué au paragraphe 1.2, de telles non linéarités n'entraînent qu'une variation de l'amortissement équivalent : $2\alpha_E \omega_0 = B_{2m} a^{2m} \pi_{k=1}^m \frac{2k-1}{2k+2}$

Pour l'ensemble des non linéarités, la loi d'évolution de l'amortissement avec l'amplitude

$$\text{sera : } 2\alpha_E \omega = \mu_0 + \sum_{l=1}^L \mu_l a^{2l} \pi_{k=1}^l \frac{2k-1}{2k+2} + \sum_{p=0}^P \nu_p \lambda_0^{2p} + \sum_{p=1}^P \nu_p \left[a^{2p} \pi_{k=1}^p \frac{2k-1}{2k+2} + \sum_{m=1}^{p-1} a^{2p-2m} \lambda_0^{2m} \pi_{k=1}^m \frac{2k-1}{2k+2} \right]$$

Les non linéarités, relatives à l'amortissement de structure, peuvent être considérées séparément à partir d'un essai sans vent au vide. Dans ce cas la loi d'amortissement calculée est :

$$2\alpha_E^* \omega_0^* = \mu_0 + \sum_{l=1}^L \mu_l a^{2l} \pi_{k=1}^l \frac{2k-1}{2k+2}$$

La loi mesurée en cours d'essais est mise sous forme d'un polynôme de degré L :

$$\alpha_E^* = \sum_{l=0}^L \xi_l a^{2l}$$

Les valeurs des coefficients d'amortissements de structure, mesurés au cours de quatre transitoires effectués sans vent au vide (figure 7), peuvent être lissés correctement par un polynôme de degré $L = 2$. L'écart moyen quadratique de 1,9 % pourrait être ramené à 1,4 % en augmentant le degré L à 5 mais le faible gain en résultant est peu intéressant. Comme l'amortissement de structure $\alpha_E^* \omega_0^*$ ne représente qu'environ 10 % de l'amortissement global $\alpha_E \omega$ mesuré avec vent, l'erreur

commise sur α_E^* ne conduit qu'à une erreur relative sur C_{mq} de $\pm 1,2\%$. Il importe de bien souligner ici que les erreurs dues au lissage de la courbe $\alpha_E^*(a)$ sont sans commune mesure avec celles qui résulteraient, soit d'une linéarisation de α_E^* , soit même une absence de ce terme dans les équations du mouvement. Dans de telles hypothèses, les erreurs relatives commises sur C_{mq} seraient alors respectivement de $\pm 4,5\%$ et $\pm 10\%$. Pour la suite du calcul, le degré le plus réduit de L est souhaitable afin de ne pas augmenter le degré de la courbe $C_{mq}(i)$.

Les produits $\alpha_E \omega$, obtenus avec vent, en fonction de l'amplitude, sont mis sous la forme d'un polynôme de degré P

$$\alpha_E \omega = \sum_{p=0}^P (\beta_p \alpha^{2p})$$

En identifiant les termes de même degré de l'amplitude, pour les lois calculées et mesurées, on obtient un système linéaire de $P+1$ équations (pour autant que L soit inférieur à P) dont les inconnues sont les $P+1$ coefficients β_p :

$$2(\beta_p - \omega_0^* \xi_p) = \prod_{k=1}^P \frac{2k-1}{2k+2} \left(\beta_p + \sum_{k=1}^{P-p} \beta_{p+k} i_0^{2k} \prod_{s=1}^k \frac{2s-1}{2s} \right)$$

Les coefficients β_p seront obtenus, à partir de celui de degré P , en abaissant le degré de proche en proche:

$$\beta_{p-1} = 2(\beta_p - \omega_0^* \xi_p) \prod_{k=1}^p \frac{2k+2}{2k-1} - \sum_{k=1}^{P-p} \beta_{p+k} i_0^{2k} \prod_{s=1}^k \frac{2s-1}{2s}$$

le dernier terme β_0 est obtenu par la relation:

$$\beta_0 = 2(\beta_P - \omega_0^* \xi_P) - \sum_{p=1}^P \beta_p i_0^{2p}$$

faisant intervenir tous les coefficients β_p , pour p de 1 à P .

La meilleure représentation de l'évolution du coefficient d'amortissement global avec vent α_E est obtenue à partir d'une mise en équation polynomiale de degré $R = 3$ de la décroissance d'amplitude $\log a(n)$. L'avantage incontestable de la dérivation de cette courbe après lissage permet d'éliminer des fluctuations autour de l'évolution moyenne (figure 8) que la dérivation directe ne ferait qu'exacerber. Ce dernier phénomène, non significatif dans la recherche du coefficient C_{mq} , n'est dû qu'à un mode de pompage de la ligne de dard support. L'invariance autour du degré $R=3$ est observée avec une dispersion relative $\Delta \alpha_E / \alpha_E = \pm 1,75\%$.

En toute rigueur, les degrés retenus $N = 4$ pour le polynôme $\omega(\alpha^2)$ et $R = 3$ pour le polynôme $\log a(n)$ conduisent au degré $P = 6$ pour représenter le produit $\alpha_E \omega(\alpha^2)$. En fait, pour éviter un cumul d'imprécisions dans une résolution matricielle d'ordre trop élevé, il est plus avantageux de réduire le degré P . La figure 9 donne les courbes $C_{mq}(i)$ déduites des polynômes $\alpha_E \omega(\alpha^2)$ pour l'ensemble $N = 4$, $R = 3$ et $L = P$ de 1 à 3. Des calculs effectués avec P jusqu'à 5, il résulte que l'invariance de $C_{mq}(i)$ est observée dès $P = L = 2$ avec une précision $\Delta C_{mq} / C_{mq} = \pm 1,01\%$.

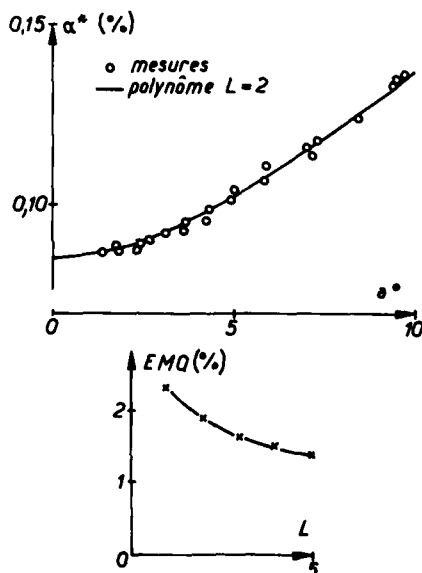


Fig.7 - Coefficient d'amortissement de structure Evolution en amplitude

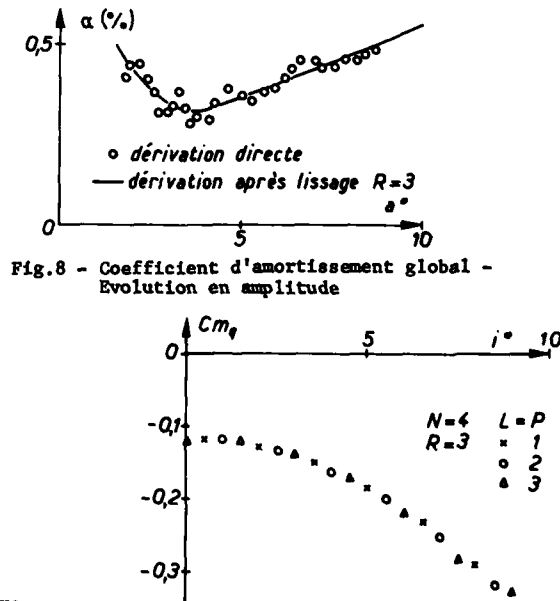


Fig.9 - Stabilité dynamique - Fonction $C_{mq}(i)$

En définitive, les courbes $C_{m_i}(t)$ et $C_{m_q}(t)$, les plus représentatives, sont obtenues avec l'ensemble suivant des degrés : $N = 4$; $R = 3$; $L = 2$; $P = 2$

Dans ces conditions, les dispersions dues à la méthode de calcul sont :

$$\Delta C_{m_i} / C_{m_i} = \pm 0,1\% \quad , \quad \Delta C_{m_q} / C_{m_q} = \pm 1\%$$

4 - EQUATIONS HETERONOMES

Il est bien rare qu'au cours d'un transitoire, effectué dans une soufflerie à rafales, les conditions de l'écoulement soient permanentes et ceci surtout en hypersonique pour les températures génératrices. Il est donc nécessaire de tenir compte de ces évolutions dans le calcul des coefficients aérodynamiques.

4.1 - Evolutions faibles des conditions de l'écoulement

En reprenant le cas des oscillations libres décrites au paragraphe 3.2, un premier calcul des coefficients λ_n et ν_p est effectué pour des valeurs moyennes des conditions génératrices en pression et température : p_{i_m} , T_{i_m} .

Les variations de p_i et T_i au cours du transitoire sont mises sous formes polynomiales à l'aide de la méthode des moindres carrés :

$$p_i = \sum_{q=0}^Q a_q \theta^q, \quad T_i = \sum_{s=0}^S c_s \theta^s$$

d'où la relation

$$\frac{p_i}{T_i} = \sum_{t=0}^T b_t \theta^t$$

Pour chaque valeur de ω_j correspondant à une amplitude α_j , la valeur normée à la pression génératrice moyenne p_{i_m} sera :

$$\omega_{j_m} = \frac{\omega_0^2 + A_N + A_{j_N}}{\omega_0^2 + \frac{p_{ij}}{p_{i_m}} (A_N + A_{j_N})} \left(\frac{\omega_0^2 + \frac{p_{ij}}{p_{i_m}} A_N}{\omega_0^2 + A_N} \right)^{1/2} \omega_j$$

dans laquelle : $\begin{cases} A_N = \sum_{n=0}^N \lambda_n \alpha_0^{2n} \\ A_{j_N} = \sum_{n=1}^N \lambda_n (\alpha_j \prod_{k=1}^{n-1} \frac{2k-1}{2k} + \sum_{m=1}^{n-1} \alpha_j^{2m-2} \alpha_0^{2m} \prod_{k=1}^m \frac{n-k+1}{k} \prod_{k=1}^{n-m-1} \frac{2k-1}{2k} \end{cases}$

De même, les valeurs de $\alpha_E \omega$ normées à la pression génératrice moyenne seront :

$$(\alpha_E \omega)_{j_m} = \frac{\alpha_E^* \omega_0^* + B_P/2 + B_{j_P}}{\alpha_E^* \omega_0^* + \frac{p_{ij}}{p_{i_m} \sqrt{T_{i_m}}} (B_P/2 + B_{j_P})} (\alpha \omega)_j$$

dans laquelle :

$$\begin{cases} B_P = \sum_{p=0}^P \nu_p \alpha_0^{2p} \\ B_{j_P} = \sum_{p=1}^P \nu_p (\alpha_j^{2p} \prod_{k=1}^{p-1} \frac{2k-1}{2k+2} + \sum_{m=1}^{p-1} \alpha_j^{2p-2m} \alpha_0^{2m} \prod_{k=1}^m \frac{p-k+1}{k} \prod_{k=1}^{p-m-1} \frac{2k-1}{2k+2} \end{cases}$$

A partir des valeurs, ainsi normées, de $\alpha_E \omega$ et ω , il est ensuite procédé comme indiqué au paragraphe 3.2 pour obtenir de nouveaux coefficients λ_n et ν_p tenant compte des évolutions des pression et température génératrices.

4.2 - Evolutions importantes des conditions de l'écoulement

En hypersonique, les conditions d'essais peuvent évoluer rapidement en pression et température, au cours d'un transitoire, si bref soit-il. Tel a été le cas des essais à Mach 17, dans la soufflerie ARC 1B de l'ONERA : pour une durée de 100 millisecondes, la pression cinétique variait de 1000 à 500 bars et la température conduisait à une diminution de vitesse de 2900 à 1600 M/s.

La résolution de l'équation à coefficients dépendant du temps :

$$\ddot{x} + P(t) \dot{x} + Q(t) x = 0$$

dépend de la forme des fonctions $P(t)$ et $Q(t)$. Partant de conditions initiales x_0, \dot{x}_0 , la méthode consiste à calculer une solution à partir de la précédente :

$$\begin{aligned} x_{n+1}(t) &= x_0 + \int_0^t \dot{x}_n(t) dt \\ \dot{x}_{n+1}(t) &= \dot{x}_0 - \int_0^t [P(t) \dot{x}_n(t) + Q(t) x_n(t)] dt \end{aligned}$$

Selon le cas, la convergence sera plus ou moins rapide et les formules approchées de la fréquence de l'amortissement dépendent essentiellement des termes inclus dans les fonctions $P(t)$, $Q(t)$.

CONCLUSIONS

Des non linéarités ont été observées, au cours d'oscillations libres à un degré de liberté de corps de rentrée, en présence de décollements. A partir des évolutions de fréquence et d'amortis-

sement en fonction de l'amplitude, mesurées au cours des transitoires, il a été possible de déterminer une équation du mouvement non linéaire rendant bien compte des phénomènes rencontrés. Les méthodes utilisées pour accéder au type et aux valeurs des non linéarités résultent d'une étude générale des phénomènes non linéaires et d'une classification en non linéarités de courbure et de discontinuités.

Le problème peut être étendu à des systèmes à 2 degrés de liberté en vue d'étudier les couplages entre modes longitudinaux et latéraux de maquettes d'avion à grande incidence. Dans ce cas des oscillations libres à grandes amplitudes, sur les 2 degrés de liberté étudiés, constitueront un moyen efficace pour l'étude de comportement singulier des maquettes.

REFERENCES

- [1] VAUCHERET X.
Détermination des coefficients de stabilité dynamique par la méthode des oscillations libres
ONERA TP n° 20 (1963)
- [2] VAUCHERET X - BROUSSAUD P
Dispositif d'oscillations libres pour souffleries à rafales
La Recherche Aérospatiale n° 107 (1965)
- [3] VAUCHERET X.
Méthode pratique de dépouillement d'oscillations libres à un degré de liberté en présence d'une force de rappel discontinue - La Recherche Aérospatiale n° 89 (1962)
- [4] FIQUET J - DUPE J - COMBET P
Un nouvel appareil digital pour la mesure en temps réel de l'amortissement dans l'étude des oscillations libres - TP ONERA n° 1019 (1971)
- [5] TOBAK M
An inverse Problem for a class of non linear differential equations
Jal of mathematical analysis and applications vol 15 n°2 (1966)
- [6] MINORSKY N
Introduction to non linear mechanics - J.W. Edwards - Ann Arbor (1947)
- [7] KAUDERER H.
Nichtlineare mechanik - J. Springer - Berlin (1958)
- [8] GILLE J - DECAULNE P - PELEGRIN M
Méthodes d'études des systèmes asservis non linéaires - Dunod - Paris (1967)
- [9] KRYLOV N - BOGOLJUBOV N
Introduction to non linear mechanics, traduit par S Lefschetz -
Princeton University Press (1947)
- [10] VAUCHERET X
Dépouillement d'oscillations libres d'un corps de rentrée présentant un cycle limite
La Recherche Aérospatiale n°104 (1965)
- [11] VAUCHERET X
Oscillations auto-entretenues d'un corps de rentrée -
La Recherche Aérospatiale 1971-1
- [12] VAUCHERET X
Calcul des fonctions non linéaires de stabilité dynamique d'un corps de rentrée en hypersonique
La Recherche Aérospatiale 1973-3

SOME FACTORS AFFECTING THE DYNAMIC STABILITY
DERIVATIVES OF A FIGHTER-TYPE MODEL

by

W. STAUDACHER

B. LASCHKA

B. Schulze

MBB, W.-Germany

P. POISSON-QUINTON

M. CANU

ONERA, France

S U M M A R Y

In the course of a Franco-German cooperation between ONERA and MBB dynamic stability coefficients of a fighter-type pilot model are derived experimentally. In a first step forced oscillation tests were carried out with a MBB-Pilot model in the ONERA tunnel S2, Modane.

The angle of attack regime investigated was $\alpha = 0 \pm 25^\circ$. This first test phase was concentrated on the investigation of the effects of a strake on the total derivatives of the configuration.

Emphasis of a further second test period will be put on configurational items as strakes, flap systems, tails etc. and experimental characteristics as Reynolds number, frequency and amplitudes.

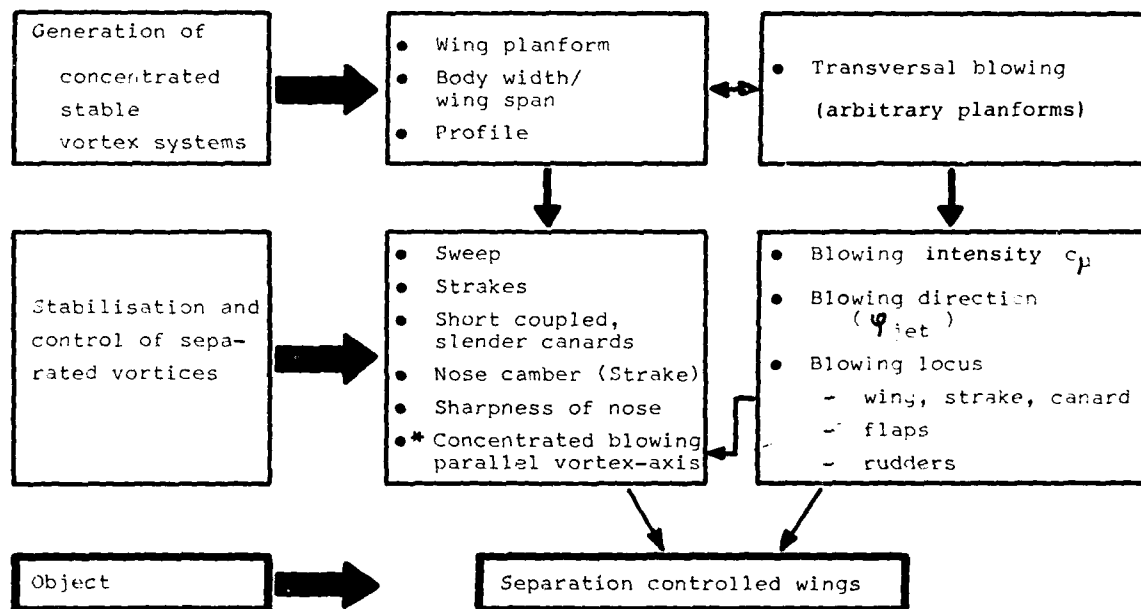
This investigation will be carried out in the new FAUGA F1 tunnel, ONERA Toulouse, a.o.a.-regime is $\alpha = 0 \pm 50^\circ$.

1. INTRODUCTION

The investigation reported herein is part of the activities of a Working Group "WINGS WITH CONTROLLED SEPARATION", which is supported by the German M.O.D. Members of this working group are DFVLR, MBB and VFW-F.

The general approach taken to develop separation controlled wings is depicted in FIGURE 1. All the parameters and modifications, listed in figure 1, were investigated.

A status report concerning these activities was given at AGARD F.D.P. Round Table Discussion on Sept. 30th, 1976 in Moffet Field, California [3].



Working Group "WINGS WITH CONTROLLED SEPARATION": GENERAL APPROACH
(Members: DFVLR, VFW-FOKKER, MBB / *Cooperation with ONERA)

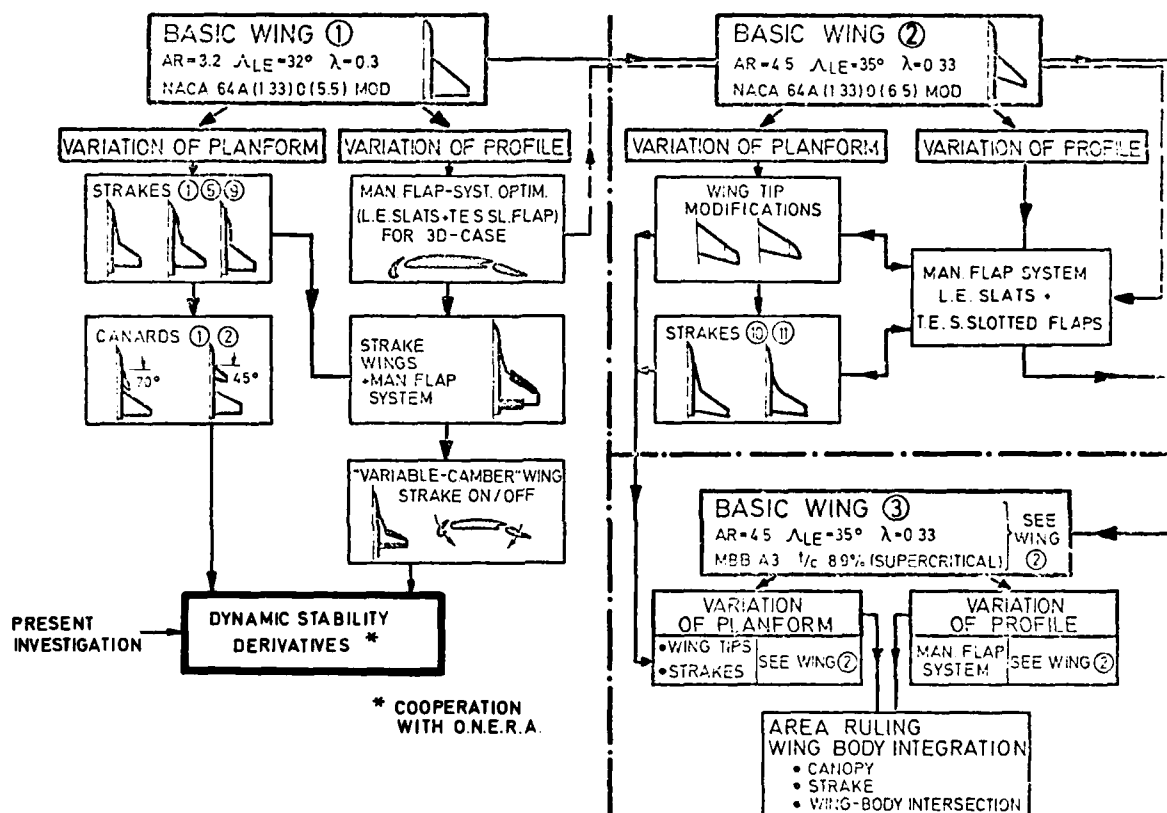
FIG.1

THIS PAGE IS BEST QUALITY PRACTICABLE
FROM COPY FURNISHED TO DDC

The present investigation is embedded in an experimental program for improvement of subsonic/transonic performances of fighter-type aircraft. The scope of this program, conducted by MBB since 1971 and reported in [1], [2], [3], [4], is shown in FIGURE 2.

The derivation of the dynamic stability coefficients is done in close cooperation with ONERA in their test facilities, see Ref. [5], [6], [7].

Preliminary tests were performed in the transonic/supersonic tunnel S2, Modane, which will be completed by further investigations in the new FAUGA F1 tunnel of ONERA, Toulouse.



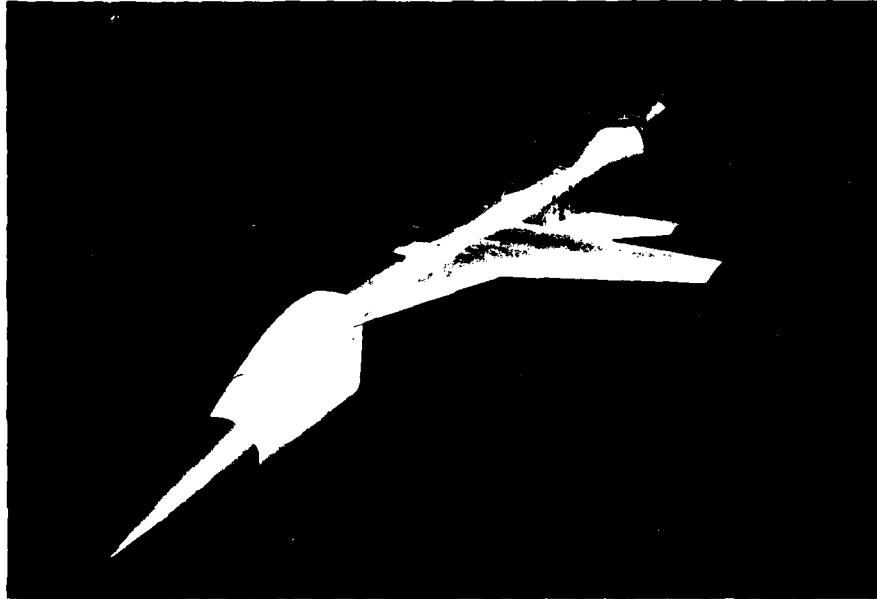
EXPERIMENTAL PROGRAM FOR IMPROVEMENT OF SUBSONIC/TRANSONIC, EMBEDDING OF PRESENT INVESTIGATION

FIG. 2

THIS PAGE IS BEST QUALITY PRACTICABLE
 FROM COPY FURNISHED TO DDC

FIGURE 3 is a photo of the MBB transonic pilot model mounted on the oscillating support of tunnel S2, Modane.

The model is fabricated of steel and plastics, the strakes are detachable from the basic trapezoidal wing; as can be seen the model incorporates a high wing and a low horizontal tail. The wing could further be modified by a L.E. slat-system and T.E. single slotted flap system. The strakes can be replaced by short coupled canards (see figure 2, left).



MBB PILOT-MODEL
IN WIND TUNNEL S2 MODANE (ONERA)

FIG. 3

2. STATIC TEST RESULTS

Some static test results are presented to show the effect of strakes on lift and drag data and maneuver boundaries. In the same time the demonstrated effects of the strake in improving the static performances of the configuration may serve as an aid in explaining some dynamic effects due to the additional strakes.

FIGURE 4 demonstrates the lift-conserving effect of the strake-vortex system. Maximum trimmed lift is increased by more than 60% with an equivalent increase in angle of attack for maximum lift. Simultaneously the induced drag at higher incidences is reduced.

The improvement of maneuver boundaries "BUFFET ONSET" and C_{Lmax} and the reduced buffet intensity of the strake wing relative to the basic wing is shown in FIGURE 5.

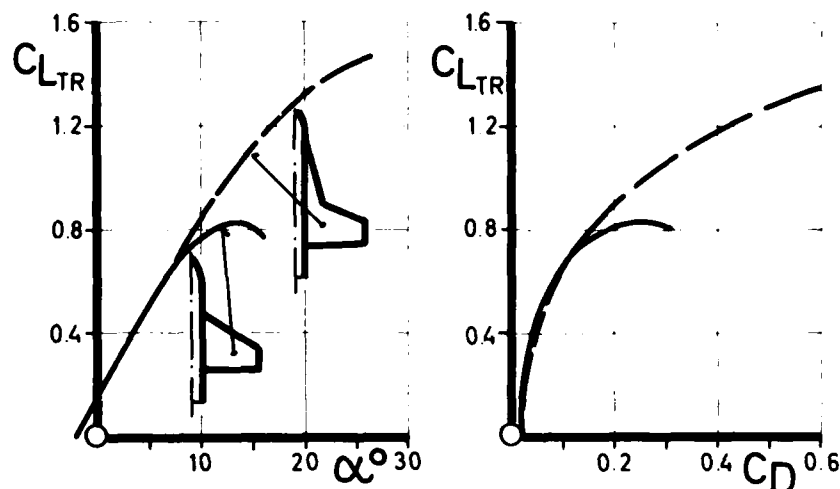


FIG. 4

EFFECT OF STRAKES ON TRIMMED LIFT AND DRAG CHARACTERISTICS

($M = 0.8$, 5% STABILITY MARGIN)

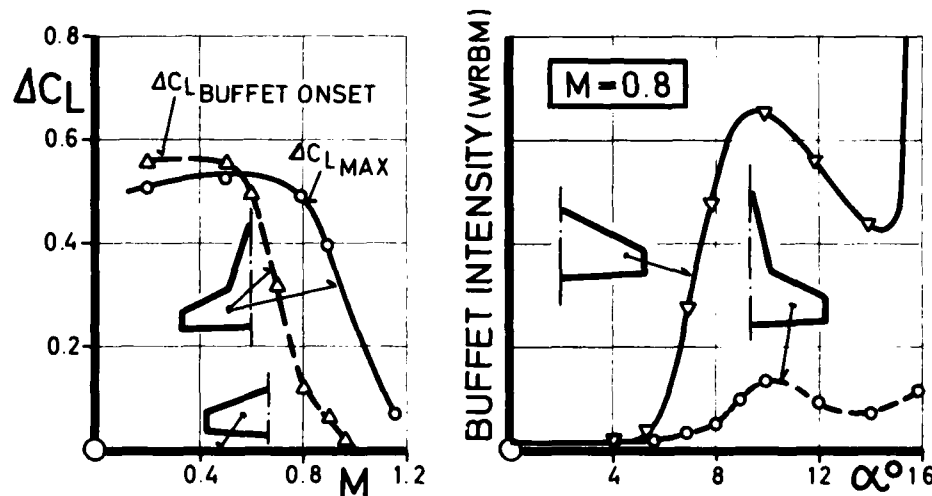


FIG. 5

IMPROVEMENT OF MANOEUVRE BOUNDARIES DUE TO STRAKE

(WING-BODY, CLEAN)

FIGURE 6 summarizes the most important advantages of the strake wing as found from the static tests (see Ref. [1], [2], [3], [4]).

SUBSONIC:

- Increased maximum lift
- Lower level of induced drag for higher a.o.a. regime
- Higher useable lift limits, better buffet penetration

TRANSONIC:

- Higher drag divergence M-Number
- Better buffet characteristics (c_L and intensity)

SUPERSONIC:

- Reduction of wavedrag
- Lower trimmed induced drag

SUMMARY OF STATIC RESULTS:
ADVANTAGES DUE TO STRAKE

FIG. 6

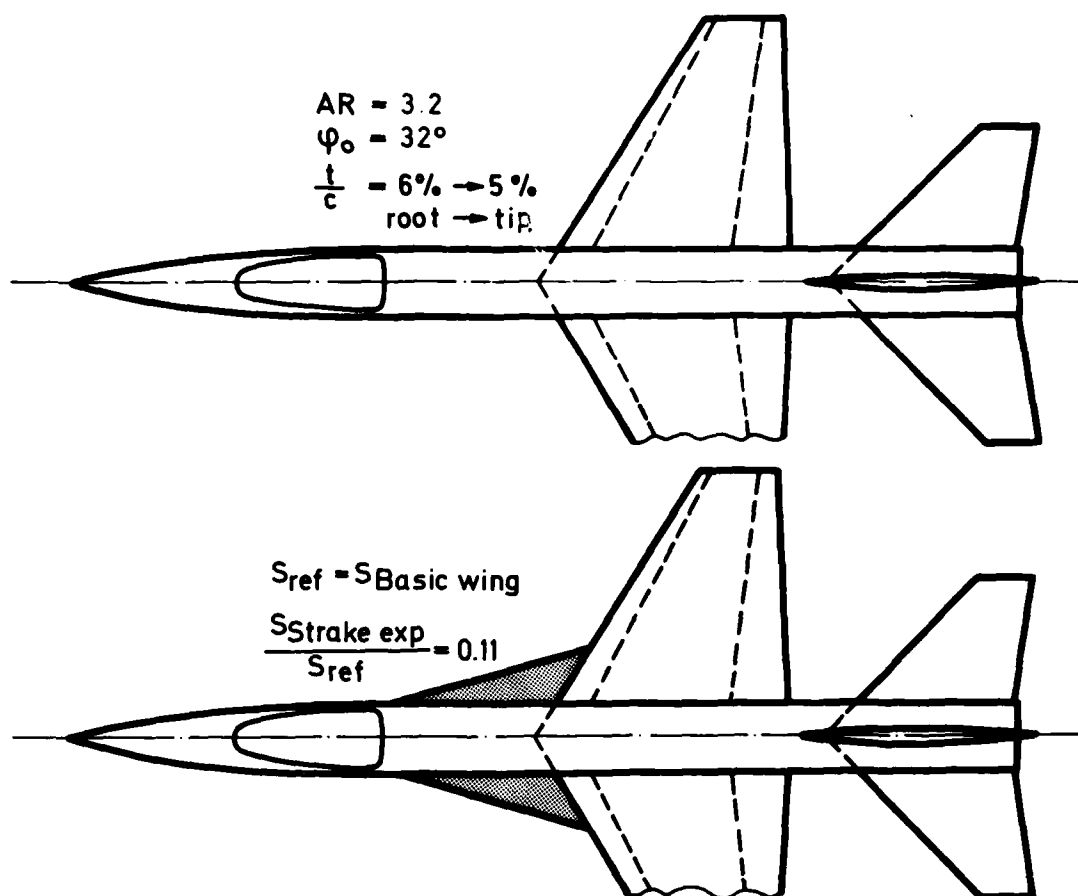
3. FORCED OSCILLATION TESTS

3.1 Model and Apparatus

As mentioned before the model investigated is a MBB high speed pilot model frequently used in the preceding static tests (see figure 2, left column).

The basic wing under consideration is the trapezoidal planform ① (see FIGURE 7), which was modified here by the strake-planform. The body of the model was connected to the rear support-system by means of an internal 3-component strain gauge balance.

Model weight was 120 N, which is relatively heavy for dynamic tests. Therefore the model was made clean later of about 50% of its original weight.



STUDIED MODEL CONFIGURATIONS IN S2, MODANE

FIG. 7

The tests were run with a dynamic balance of ONERA in their tunnel S2, Modane.

The apparatus to generate the harmonic oscillations is located in the corresponding rear strut system. Two struts were available: one for pitch and yaw, the other for rolling motions.

As noted in FIGURE 8 the configurational modifications were restricted to strake on/off in this test phase. Parameters varied in S2, Modane were Mach numbers ($M = 0.3/0.8$), Reynolds number, and frequencies.

CONFIGURATIONS: STRAKE ON/OFF

M [-]	0.3	0.8
α [°]	≤ 25	≤ 15
$Re \cdot 10^{-6}$ [-]	1.8	1.5
$\frac{p \cdot b}{2V}$ [-]	0.047 - 0.07	0.0175 - 0.028
$\frac{q \cdot \bar{c}}{V}$ [-]	0.03 - 0.047	0.012 - 0.0175
$\frac{r \cdot b}{2V}$ [-]	0.05 - 0.068	0.02 - 0.027

RANGE OF STUDIED PARAMETERS IN S2, MODANE

FIG. 8

3.2 Test Results

3.2.1 Rolling motion

The dynamic derivatives due to rolling motion are demonstrated for both the configurations strake off/on in FIGURE 9. The combined derivatives diverge for the basic configuration in the regime of the maximum angle of attack and are then strongly depending on frequency. Force and yawing moment derivatives are of opposite sign, the force derivative giving positive sign for positive roll. Roll damping is gradually lost at the basic configuration and results in an excited motion for higher angles of attack.

The strake wing exhibits increasing roll damping in the a.o.a. regime regarded, the effect of frequency is diminished and the value of the cross coupled derivatives is negligible.

In FIGURE 10 the damping increment of the strake wing relative to the basic wing is shown.

The possible explanation for the excited motion of the basic wing is given in the insert chart on figure 10. The reason may found in earlier wing stall effects (condition on the "back" of the lift polar with negative lift gradients).

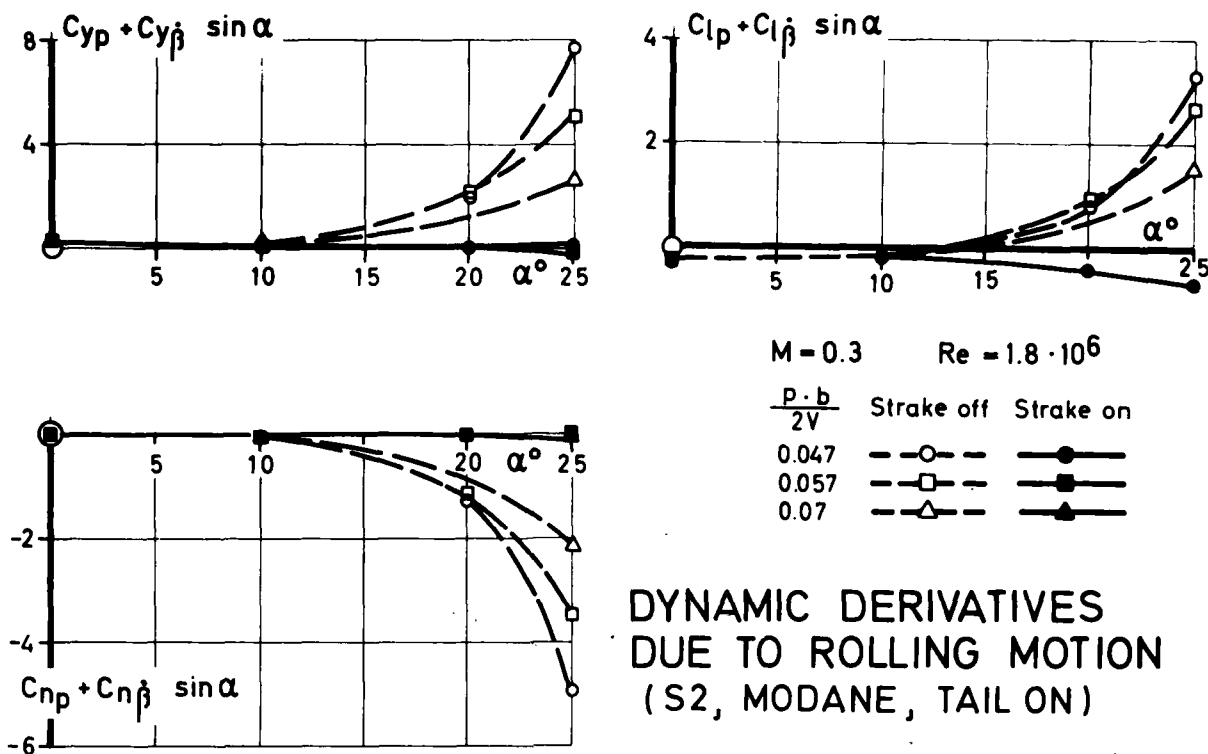
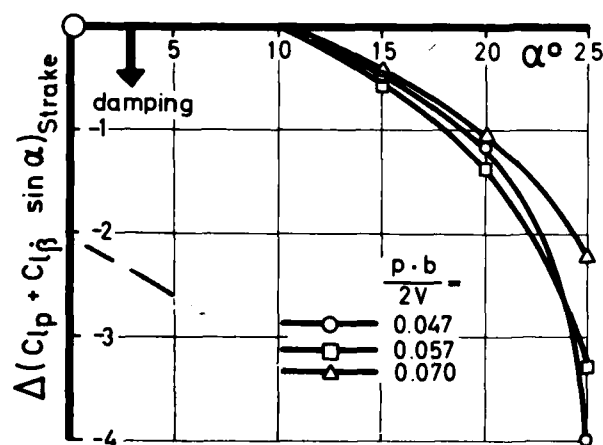
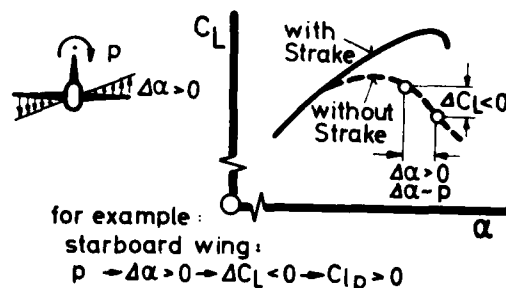


FIG. 9



N o t e:

- frequency effect is found on basic wing (see Fig. 9)
- excited motion of basic configuration is caused by wing-stall effects



**DAMPING INCREMENT DUE TO STRAKE
IN ROLLING MOTION**

FIG. 10

3.2.2 Pitching motion

Similar to the forementioned effects in roll motion deviations from regular behaviour are found for the basic configuration in pitching motion when approaching stall (FIGURE 11).

Normal force and pitching moment derivatives of the configuration "STRAKE OFF" exhibit serious peaks then, whilst the strake configuration gives nearly constant and always damping coefficients in the a.o.a. regime investigated (static α_{max} of this configuration not reached, see figure 4).

FIGURE 12 demonstrates again the damping contribution of the strake, as derived by subtraction of the strake data minus the basic data.

It should be noted here that the excited oscillations for approx. $15^\circ > \alpha > 25^\circ$ of the basic version are caused by hysteresis effects in the stalling regime of the wing ("lag of flow, flow out of phase") and should be due to irregular development of the $C_{z\dot{\alpha}}$ -derivative of the wing (analogous effects are found for the stall flutter phenomenon in aero-elastic motions). This reasoning is further confirmed by the assumption that the tail-contribution is always damping here.

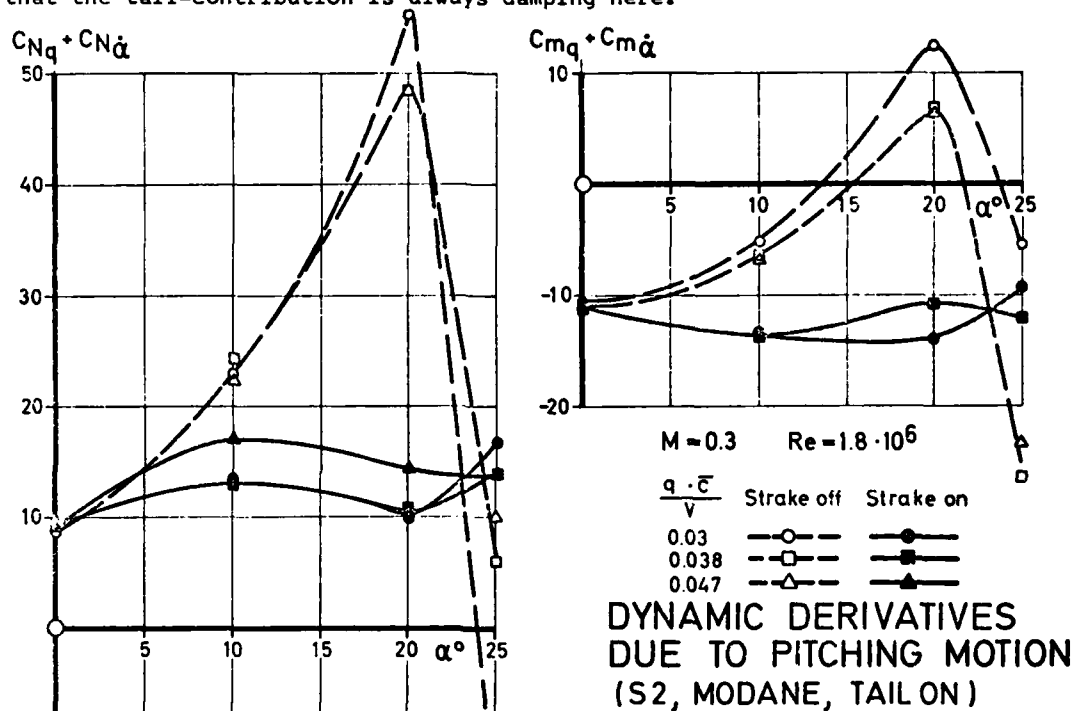
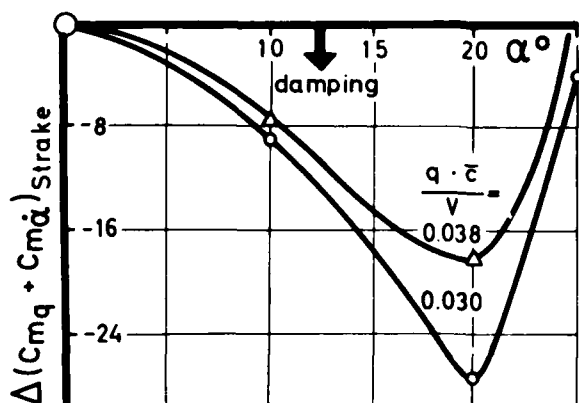


FIG. 11



**DAMPING INCREMENT DUE TO STRAKE
IN PITCHING MOTION**

FIG. 12

Note:

basic configuration (without strake):

- excited oscillation due to
 - hysteresis effects in the stalling regime (flow out of phase)
 - analogous to stall flutter effects at the wing $C_{z\dot{\alpha}}$ wing
- tailplane contribution is probably always damping

3.2.3 Yawing motion

In extensive static tests it was found that the strake vortex system could have very beneficial effects on the development of the flow field at higher angles of attack for the vertical tail, when properly placed.

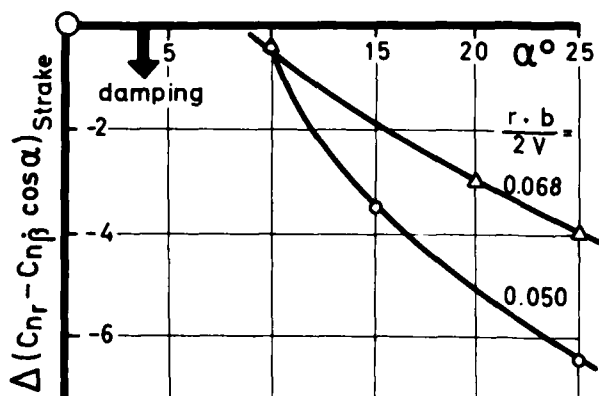
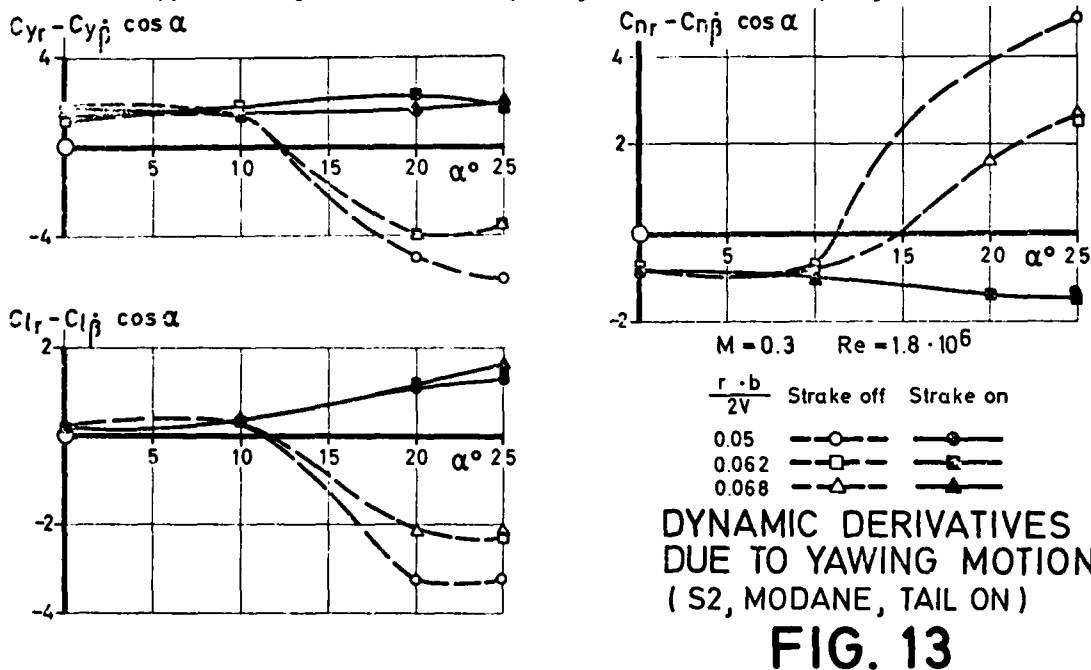
This favourable contributions were caused by prevention from adverse sidewash and by increased dynamic pressure ratios, thus giving improvements of stability and rudder effectiveness as well.

These positive effects are found again in the dynamic derivatives due to yawing motion (FIGURE 13).

The strake configuration exhibits linear development of the derivatives. The influence of frequency is negligible, whilst the basic configuration without strake is very sensitive to frequency and develops diverging characteristics for increasing angles of attack.

The overall contribution of the strakes is shown in FIGURE 14.

Notify, that the apparent sensibility against frequency of the damping increment of the strake configuration is caused by the data of the basic configuration, which are subtracted from the strake-data (see figure 13). Apparently the addition of the strake prevents the configuration from yaw divergence and eliminates the danger of autorotation, effected by adverse sidewash on the vertical tail (opposite sign of force and yawing moment increment, figure 13).



Note:

basic configuration prone to:

- yaw divergence
- danger of autorotation by adverse sidewash at the fin
 $\Delta C_Y < 0$ when $\Delta C_N > 0$

(see Fig. 13)

4. SUMMARY AND OUTLOOK

FIGURE 15 summarizes the advantages due to the strake, as found by the preliminary tests in S2, Modane.

ADVANTAGES DUE TO STRAKE

- excited oscillations are avoided, the addition of strakes always results in additional damping for all axes
- the relation of dynamic stability derivatives and angle of attack is linearized
- hysteresis and frequency effects are almost avoided by the strake vortex-system

SUMMARY OF PRELIMINARY DYNAMIC RESULTS (S2, MODANE, $\alpha = 0 \div 25^\circ$)

FIG. 15

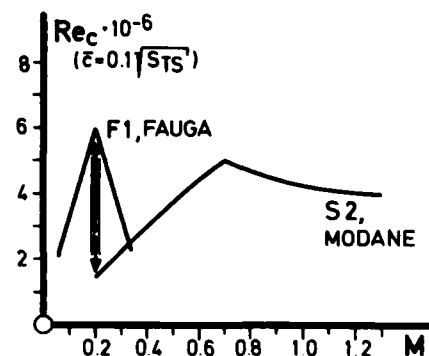
As mentioned before, additional tests are being prepared for the new tunnel FAUGA F1, ONERA Toulouse.

The scope of this program is given in FIGURE 16.

The extension of investigation listed will then give more insight in the behaviour of the configuration.

SCOPE OF ADDITIONAL DYNAMIC INVESTIGATIONS (FAUGA F1-Tunnel, ONERA, Toulouse)

- Extended a.o.a.-range $\alpha = 0 \div 50^\circ$
- Sideslip angles β
- Test parameters varied:
 - frequencies
 - amplitudes
 - Reynolds numbers
- Configurational modifications:
 - Maneuver flap system
 - Tails off/on
 - Strake off/on
- Model weight 50% reduced



FURTHER ACTIVITIES IN 1978 ONERA/MBB

FIG. 16

REFERENCES

- [1] STAUDACHER W.
Verbesserung der Manöverleistungen im hohen Unterschall
MBB-UFE 896-72(Ö) / DGLR 72-126 1972

- [2] STAUDACHER W.
Zum Einfluß von Flügelgrundriß-Modifikationen auf die aerodynamischen
Leistungen von Kampfflugzeugen
MBB-UFE 1033-73(Ö) / DGLR 73-71 1973

- [3] STAUDACHER W.
The Effects of Jets, Wakes, and Vortices on Lifting Surfaces
AGARD F.D.P. RTD
MBB-UFE-AERO-MT-263 1976

- [4] EBERLE A. / STAUDACHER W. / ZECH A.
Advanced Aerodynamics for Transonic Flight
ICAS Paper No. 76-12 1976

- [5] CANU M.
Stabilité dynamique de la maquette au 20e de l'avion de combat MBB,
dans la soufflerie S2MA (V.T.)
ONERA P.V. 3/3302 SNG 1977

- [6] SCHULZE B.
Ermittlung dynamischer Stabilitäts-Derivative der Modellkonfiguration
'FLÜGEL + STRAKES' (M 1:20) im Hochgeschwindigkeitswindkanal S2 der
ONERA, Modane
Mitteilung FE123 1977

- [7] STAUDACHER W.
Dynamische Derivative $\alpha = 0^\circ + 25^\circ$
1. Meßabschnitt / S2, Modane; Pilotmodell
MBB-UFE-AERO-MT-294 1977

AN EXPERIMENTAL STUDY OF THE HYPERSONIC DYNAMIC STABILITY
OF PITCHING BLUNT CONICAL AND HYPERBALLISTIC SHAPES
IN A SHORT RUNNING TIME FACILITY

BY

R. A. East

A. M. S. Qasrawi

M. Khalid *

Department of Aeronautics & Astronautics
University of Southampton
Southampton
Hampshire, SO9 5NH.
U.K.

SUMMARY

New experimental data are presented for the static and dynamic stability of pitching blunt cones and hyperballistic shapes at a Mach number of 6.85. The data have been obtained using a free decaying oscillation technique using a light free piston compression facility having particularly steady flow characteristics during a running time up to 0.5 second. Details of the mode of operation of the facility and the dynamic stability apparatus are described.

The effects of variations of Reynolds number and angles of attack up to 7.5° on the stability derivatives $-C_{m_\alpha}$ and $-(C_{m_q} + C_{m_d})$ are presented. Comparisons of the blunt cone data with previous experimental work and existing theoretical methods are given. Comparison is also made with the predictions of a new theoretical method. The reported experimental values of $-C_{m_\alpha}$ and $-(C_{m_q} + C_{m_d})$ for the hyperballistic shapes highlight the gross errors which can be obtained from Newtonian based prediction methods.

LIST OF SYMBOLS

c	equivalent pointed cone length (see Fig.1)
C_{D_N}	drag coefficient of the hemispherical nose
$C_f(x)$	coefficient of friction at position x
C_m	pitching moment coefficient ($= M/h \rho_\infty V_\infty^2 S_c$ for cones) ($= M/h \rho_\infty V_\infty^2 S_d$ for HB models)
C_{m_α}	pitching moment coefficient due to angle of attack ($= \partial C_m / \partial \alpha$)
C_{m_d}	pitching moment coefficient due to rate of change of angle of attack ($= \partial C_m / \partial (\dot{\alpha} c / 2V_\infty)$ for cones, $= \partial C_m / \partial (\dot{\alpha} d / 2V_\infty)$ for HB models)
C_{m_q}	pitching moment coefficient due to pitch velocity ($= \partial C_m / \partial (q c / 2V_\infty)$ for cones, $= \partial C_m / \partial (q d / 2V_\infty)$ for HB models).
C_p	pressure coefficient
d	centre body diameter HB1, HB2 and HBS shapes
d_b	model base diameter
$h(x,t)$	instantaneous height above 'space fixed' horizontal datum of a point on body axis of symmetry
L	hyperballistic body (HB) length
M	Mach number, also pitching moment (posit nose up)
M_1^*	critical Mach number related to zero angle of attack
M_2^*	critical Mach number related to small angle of attack

* Present address: British Aerospace Dynamics Group,
Hatfield - Luton Division,
Hatfield, Herts.

p	pressure
p_o	compression tube initial pressure
\bar{p}	tunnel 'matching' pressure
Δp	pressure disturbance caused by piston oscillation
q	pitching velocity
R	gas constant
$R(x)$	radius of body at position x
R_n	radius of the blunt nose
R_b	radius of the base
Re	Reynolds number
s	entropy
S	model reference area ($= \pi d_D^2/4$ for cones; $= \pi d^2/4$ for HB models)
t	time
t_*	blast wave parameter ($\approx 2C_{D_N}^{1/2} \times \tan^2 \theta_o/R_n$)
\bar{t}_*	Ericsson's scaling parameter
T_o	test gas initial temperature
\bar{T}	tunnel stagnation temperature
V	velocity
x	axial cylindrical polar co-ordinate
z	co-ordinate measured in vertical direction
α	angle of attack
γ	ratio of specific heats
$\Delta \epsilon_p(x)$	change in angle of inclination of tangent to projected streamline of a particular fluid element between the vertex and a general point on body surface measured in the osculating plane of the streamline
θ	inclination of body axis of symmetry to a horizontal datum
θ_o	cone semi-angle
ρ	density
τ_{run}	tunnel running time
ω	model oscillating angular frequency

Subscripts

b	conditions at base
∞	free stream conditions
x	local conditions
ref	conditions at the reference point
inv	inviscid
vis	viscous

1. INTRODUCTION

A knowledge of hypersonic dynamic stability characteristics is of importance in the context of hyperballistic re-entry vehicles, wing/body combinations of the space shuttle type and integrated vehicles suitable for the hypersonic transport. In comparison with the considerable volume of data regarding the steady flow aerodynamics of such vehicles, relatively less experimental work has been conducted concerning the non-steady flow characteristics. However, there are portions of the flight trajectory of each of these types of vehicle where the dynamic pressures at hypersonic Mach numbers are sufficiently high that an accurate determination of the non-steady forces associated with oscillatory motions is essential.

Traditionally, experimental investigations of hypersonic dynamic stability have been made in continuous flow wind tunnel facilities. In contrast, intermittent facilities of the shock tunnel, arc-heated tunnel and gun tunnel type have proved of value in providing steady aerodynamic characteristics over a wide range of Mach number, Reynolds number and flow stagnation enthalpy whereas only a small number of investigations, see for example refs (1) (2), have been reported concerning non-steady flow measurements. While the short running time facility is attractive as an economic means of achieving flow conditions to simulate Mach number and Reynolds number correctly, the gas heating and compression processes in shock and gun tunnels are usually non-steady in character and result in temporal variations in the test section flow. These variations have in the past prevented the accurate determination of stability derivatives in such facilities (3).

It is one purpose of the present paper to describe a new type of intermittent hypersonic flow facility with a test section Mach number of 6.85 which is based on the light piston compression principle proposed by Jones et al (4) and which is equally suitable for steady flow and dynamic stability investigations. The relatively slow compression process and the novel 'matching' condition achieved when the heated gas is allowed to exhaust through the test section, provide a test section flow with fluctuations in stagnation pressure of about $\pm 1 - 2\%$ over a period up to 0.5 seconds. Some developments of the original concept involving the use of a baffle plate/damping reservoir and compression tube pre-heating to improve the flow quality and flow duration respectively, are described.

As a test of the validity of dynamic stability data obtained from this new type of facility, comparisons are required with data obtained by more conventional means. Measurements have therefore been made of the pitching stability derivatives C_{m_q} and $-(C_{m_q} + C_{m_d})$ for pointed and blunted 10° semi angle

cones shown in Figure 1, for which most theoretical and experimental work exists at hypersonic Mach numbers. For this purpose a relatively conventional free decaying oscillation technique using a sting supported flexure pivot has been used. Data is required over a range of axis positions and angles of attack and the test mechanism has been designed to permit variation of these parameters. The accuracy and speed of data analysis has been improved by using an electronic damping analyser based on an integration method by which the areas under successive blocks of the oscillatory motion containing equal numbers of half-cycles are compared.

Further investigations of the hypersonic dynamic stability characteristics of hyperballistic shapes have been centred around the AGARD standard models HB1 and HB2 and a double flared, spherically blunted shape designated HBS shown in Figure 1. Although HB1 and HB2 are standard shapes, very little non-steady data exist for these models at hypersonic Mach numbers and the present work attempts to provide data in a previously unexplored Mach number and Reynolds number regime.

Previous work on conical bodies (5) has shown significant effects of angle of attack on the measured pitching derivatives. It has been suggested (6) that some of the observed trends associated with angle of attack may be attributed to boundary layer transitional effects and an aspect of the present work has been concerned with an examination of similar effects on the blunt hyperballistic shapes at angles of attack up to 7.5° .

Few theoretical methods exist for comparison with experiments on the HB1, HB2 and HBS and only Newtonian theory has been used in the present context. Gross discrepancies are evident from this comparison and highlight the inadequacy of Newtonian theory for the prediction of the forces on oscillating blunt forebody/afterbody shapes.

For blunted conical bodies, theoretical methods are more fully developed and the experimental results have been compared with Ericsson's generalised embedded Newtonian theory (7), Rie et al's numerical flow field calculation (8) and a new hybrid blast wave analogy/shock expansion method proposed by Khalid (9). The latter theory is outlined briefly in Section 3.

2. APPARATUS AND TEST TECHNIQUE

2.1. Wind Tunnel

The wind tunnel used for the present tests is the Southampton University intermittent hypersonic tunnel which uses a light piston isentropic compression mode of operation. The principle of operation of such a tunnel was described in detail in reference (4) and is outlined briefly here with reference to the schematic diagram in Fig.2(a). The test gas is contained in the compression tube at an initial temperature and pressure and is compressed isentropically by a light piston which is propelled relatively slowly by the driver gas which enters the upstream end of the tube from the high pressure reservoir. When the test gas attains the required stagnation pressure and temperature it is allowed to flow through the expansion nozzle into the test section either by a quick acting valve or a bursting diaphragm. The flow conditions in the test section are maintained constant during the running time by the "matching" process whereby the volumetric flow rate of the driver gas into the compression tube is equal to the flow rate of the test gas into the test section.

If the piston mass is very small and the ratio of the area of the starting valve or diaphragm to the tube area is small, then ideally the stagnation pressure remains constant during the running time. The instantaneous change of velocity of the gas in the compression tube when the matching condition is reached requires that a piston of finite mass will oscillate with an amplitude and period determined by its mass and the effective stiffness of the 'gas spring' acting on both sides of the piston. For a relatively short large diameter tube, theoretical estimates (4) of the pressure fluctuation caused by the piston oscillation based on this model give adequate agreement with observation. For the long, small diameter tube of the present work, the simple model is inadequate and the observed pressure fluctuations are larger than predicted. The problem is minimised by maintaining as low a value of the piston mass as possible, which for the present tube is 290 gm and results in pressure fluctuations, from this source, of $\pm 1-2\%$. A further reduction in this effect can be obtained by the use of a compensator (proposed by Schultz et al) (10) which programmes the volume flow rate of the driver gas to give a piston velocity equal to the matching velocity at the instant just prior to nozzle opening.

Departures from uniform stagnation temperature during the running time are a consequence of heat transfer from the compressed gas to the compression tube wall both during the compression process and during the 'matched' period. The phenomenon results from the relatively cold boundary layer scraped from the wall by the advancing piston and forming a vortex ahead of the piston. Flow visualisation in a transparent water filled model tube has shown that for a long/small diameter tube the vortex is unstable and forms a central turbulent core of colder gas which encroaches into the uniform high temperature compressed gas. The vortex formed during compression causes a steadily falling stagnation temperature with time whereas the relatively more energetic vortex formed when the piston accelerates to the matching condition causes a sharp fall in stagnation temperature during the last 15-20% of the run. These phenomena become less severe as the surface area/volume ratio decreases with increase of scale and the compression vortex effect may be eliminated by preheating the tube with a suitable temperature gradient to compensate for the loss of enthalpy. For the present tests, a linear temperature gradient from 175°C at the nozzle to 195°C at the baffle plate results in a flow stagnation temperature of 600°K uniform to $\pm 2\%$ during a period of 460 ms. The 15-20% loss of 'hot' running time caused by the second vortex is inherent in this type of compression process and is accepted as unavoidable.

The non-steady expansion wave caused by the nozzle opening is a further source of pressure fluctuation and can be minimised by maximising the tube to nozzle valve (or diaphragm) area ratio. For the present tube, a small tube diameter was chosen so that alternative operation as a Ludwig tube is possible and to produce an economic vessel to contain sufficient gas at high pressure to give the running time required at as high as possible Reynolds numbers. This configuration produces higher levels of pressure fluctuation from this source but these have been greatly reduced by the installation of a baffle plate/reservoir system to attenuate the expansion wave reflected from the upstream end of the compression tube. Experiments (11) on a 3.2 cm diameter pilot tube showed that a ratio of open baffle area to tube area of 0.16 was optimum and that although ideally, a very large damping reservoir was required, in practice, a reservoir volume of about 1/3 of the compression tube volume resulted in an acceptable level of pressure fluctuations caused by the non-steady expansion wave of $\pm 4\%$.

Typical records of flow stagnation temperature and pressure, demonstrating the linear pressure rise during compression followed by the steady flow period, are shown in Figure 2 (b). Figure 2 (c) shows the fluctuation in the stagnation pressure caused by piston oscillations, for different values of stagnation pressure and pressure ratios, as predicted by theory (4) and measured experimentally. For $M = 6.85$ operation of the 21 cm diameter test section, steady flow running times in the range of 120 ms to 540 ms are achieved corresponding to an initially unheated (15°C) and preheated (185°C) compression tube. Figure 2(d) shows the theoretical predictions (4) and the experimental values of the flow running time as a function of the initial temperature of the test gas for a flow stagnation temperature of about 600°K . At this temperature the free stream Reynolds number is about $0.45 \times 10^6/\text{m}/\text{bar}$. The tunnel stagnation pressure could be varied from 10 to 60 bars. More information about the wind tunnel is given in reference (12).

2.2. Test Mechanism

The free-oscillation test mechanism used for measurements of dynamic stability in pitch utilises crossed-flexures for model pivot and a long slender sting for model support. Photographs illustrating the sting support system and its geometric relationship to the open jet/diffuser system are shown in Figure 3. The slender sting is stiffened by a pair of crossed steel wires which were fastened to the floor and ceiling of the working section. Displacement and release of the model is made by a spring assisted pneumatic actuator. Measurements of the model motion are made by a bridge of four active resistance type strain gauges bonded to the flexures of the pivot.

Model natural frequencies varied from about 30 Hz to 47 Hz depending on the model and the position of its axis of oscillation.

2.3. Instrumentation and data reduction

The output of the strain-gauge bridge is amplified and recorded on a 6.35 mm ($\frac{1}{4}$ " wide) magnetic tape using frequency modulation and on a transient signal processor. The signal processor uses a digital memory to retain the input signal and the information in the memory can be played back direct for digital processing or in analogue form by digital to analogue conversion. A high resolution is made possible by the use of a 10-bit word system. The processor used has a 0.1% amplitude resolution and a 0.05% time resolution.

Measurements of aerodynamic pitching moment derivatives are made using conventional analysis of wind on and wind off free decaying oscillation records such as those shown in Figure 4. The analyser is used to determine the true mean level of the signal, to rectify the signal and to integrate the rectified signal with respect to time for two successive selected batches of half cycles of model oscillation (n-half-cycles in each batch). The time integrations (performed by voltage to frequency conversion) A and B of each of the two blocks of n half-cycles and the total time of the n-cycles are displayed on a

digital panel. It can be shown that the logarithmic decrement, per half-cycle of the model motion can be expressed as

$$\Delta = \frac{1}{n} \ln \frac{A}{B}$$

Figure 5 shows a block diagram of the data logging system and the model motion analyser. The integration method has the advantage of giving consideration to the complete time history of model motion and averaging out any random noise in the input signal.

2.4. Models

Details of the models tested are shown in Figure 1. The models were machined in two separate aluminium-alloy shells which were screwed to the model attachment ring. The shell thickness was about 1 mm. Tests were conducted with smooth surfaces and with roughness strips glued to the model forebody as shown in Figure 1.

2.5. Test Procedure and Accuracy of Data

2.5.1. Test conditions

The nominal Mach number and flow stagnation temperature in the test section were 6.85 and 600°K respectively. The flow running time was 0.3 sec. for some of the tests (corresponding to an initial temperature of the test gas of 110°C) and 0.53 sec. for the rest of the tests (initial temperature of 185°C). The stagnation pressures and the corresponding Reynolds numbers at which the data were obtained are presented in Table 1. The length of the open-jet for the tests was about 1.25 times the nozzle exit diameter.

TABLE 1 NOMINAL TUNNEL CONDITIONS

Stagnation pressure (bar)	14.2	17.3	23.8	29.8	35.5	46.7	60.0	62.0
(Reynolds number/m) $\times 10^{-6}$	6.43	7.81	10.77	13.48	16.03	21.1	27.12	28.03
Dynamic pressure q_{∞} (bar)	0.129	0.158	0.217	0.271	0.323	0.425	0.546	0.564

2.5.2. Test procedure

The models were initially displaced from the rest incidence by about 1 to 2 degrees and released at about 30 to 50 ms after the flow commencement. Attempts to release the models prior to flow establishment resulted in large perturbations to the oscillation envelope caused by asymmetric loads during starting. For large blunt models, at high incidence, close to the fixed model tunnel blockage boundary, the additional incidence from oscillatory motions produced a very long nozzle starting period which delayed the tunnel start and gave rise to large unsteady forces as indicated on a typical oscillation envelope shown in Figure 4. Restraining the model during the first 50 ms of the run resulted in the elimination of these effects on the model motion.

The corresponding wind-off oscillation was carried out in the evacuated test section just prior to a tunnel run.

These procedures were satisfactory at zero incidence for a wide range of positions of the axis of oscillation both ahead and behind the centre of pressure. At high angles of attack the model restraint and release mechanism permitted axis positions close to and rearward of the centre of pressure only. For axis positions ahead of the centre of pressure the resulting aerodynamic moments caused excessive angular displacements of the flexure supported model. The excess incidence was sufficient to cause flow blockage and hence excessively high sting loads. The stagnation pressure was varied by using Melinex and aluminium diaphragms of different thicknesses at the nozzle inlet.

2.5.3. Accuracy of Data

Uncertainties in the basic tunnel parameters (P , T and M_{∞}) were estimated from calibrations of instrumentation and from repeatability and uniformity of the test section flow during tunnel calibrations. The estimated uncertainties in the free stream properties (Re/m , M_{∞} , q_{∞} and V_{∞}) are summarised in Table 2. The uncertainties in the free stream parameters were combined with the uncertainties in the balance and in the data acquisition and reduction system to estimate the accuracy of the pitching derivatives. The uncertainties in the derivatives are shown on the graphs in Figures 6 to 14 as bars of possible errors. The precision of the measurement of the model pitch is estimated to be ± 0.15 deg.

TABLE 2 TUNNEL PARAMETER UNCERTAINTY

$(Re/m) \times 10^{-6}$	$\Delta(M_\infty)$	$\Delta(Re/m) \times 10^{-6}$	$\Delta(q_\infty)$, bar	$\Delta(V_\infty)$, m/s
6.43	± 0.15	± 0.19	± 0.0032	± 11
7.81	± 0.15	± 0.23	± 0.0040	± 11
10.77	± 0.15	± 0.32	± 0.0054	± 11
13.48	± 0.15	± 0.40	± 0.0068	± 11
16.03	± 0.15	± 0.48	± 0.0081	± 11
21.1	± 0.15	± 0.57	± 0.0106	± 11
27.12	± 0.15	± 0.81	± 0.0137	± 11
28.03	± 0.15	± 0.84	± 0.0141	± 11

3. THEORETICAL METHODS FOR OSCILLATING POINTED AND BLUNTED BODIES

Theoretical methods which have been used to predict the static and dynamic stability of blunted bodies have included simple Newtonian theory, embedded Newtonian theory due to Seiff (13) and applied to oscillating blunted cones by Ericsson (7) and Rie et al's (8) numerical flow field method. Simple Newtonian theory cannot be expected to give reliable predictions for the downstream portions of blunt cones since the assumption of a very thin shock layer is not satisfied especially for long blunted flared or non-flared bodies. This criticism can be alleviated to some extent by using the embedded Newtonian concept which takes account of the fact that the body effectively oscillates within the low dynamic head entropy layer caused by the nose blunting. However, the simple Newtonian method, suitably modified to take account of the lower dynamic pressure, is still used to calculate the local surface pressures due to the relative motion of the surface and the stream. Rie et al's numerical method is the most exact of the available methods but it is less flexible to use and does not result in analytic expressions. Furthermore, this method cannot handle corners or secondary shocks produced by afterbody flares as on the HB2 and HBS shapes. In an attempt to produce a theoretical model which is more soundly based physically than Newtonian theory, yet which still gives analytic results, Khalid (9) has proposed a new method which has been applied to blunted conical bodies and is based on a hybrid blast wave analogy/shock expansion description of the flow. An outline description of the method is as follows.

The steady pressure distribution over a blunt cone is derived from the blast wave analogy. An empirical equation is developed which provides a 'best fit' to the experimental results and numerical solution given by Chernyi (14). This equation has the form

$$\Delta p = 1 + \frac{\sqrt{\gamma-1}}{4(3\gamma-1)} \frac{1}{t_*} - v_1 e^{-\alpha_1 t_*} \cos \beta_1 t_* + (v_1 - 1) e^{-\lambda_1 t_*} \quad (1)$$

$$\Delta p = \frac{C_p}{2 \tan^2 \theta_0} \quad \text{where} \quad C_p = \frac{p - p_\infty}{\frac{1}{2} \rho_\infty v_\infty^2}$$

$$\alpha_1 = 2.8$$

$$\beta_1 = 1.2$$

$$v_1 = 2.1$$

$$\lambda_1 = (\alpha_1 v_1 / \beta_1)^4$$

Modified shock expansion theory due to Eggers and Savin (15) is used to perturb the steady solution downstream of a reference point which is suitably defined as described below, depending on the appropriate entropy layer model used. The use of this theory follows the assumption that $M_{\infty 0} > 1$ and that the flow downstream of the reference point remains conical. It is further required that the plane lamellae of fluid remain plane as they traverse the body surface. The unsteady inviscid pressure distribution is thus given by

$$p(x, t)_{\text{inv}} = p(x)_{\text{inv}} + p'_{\text{inv}} \quad (2)$$

The perturbation term p'_{inv} may be determined from the Prandtl-Meyer flow relationship along a streamline. Thus we have

$$p' = \frac{\rho_x v_x^2}{\sqrt{M_x^2 - 1}} \Delta \epsilon_p(x) \quad (3)$$

where $\Delta \epsilon_p(x)$ (defined in the list of symbols) is given by

$$\Delta \epsilon_p(x) = \left[\tan^{-1} \left\{ \frac{dh}{dx}(x, t) \sin \phi + \frac{dR}{dx}(x) \right\} \right]_0^x \quad (4)$$

and

$$h(x, t) = h(\alpha, \theta, z, z) \quad (5)$$

Two perturbation models were considered:

1. the zero entropy layer model
2. the finite entropy layer model

The finite entropy layer model allows for the presence of a finite entropy layer of lower dynamic pressure in which the blunt cone oscillates. The simplified model assumes the bow shock to be effectively normal to the streamlines which lie close to the apex. These limiting streamlines which run adjacent to the body surface are subsequently perturbed through the shock expansion theory. The reference point in this case is defined to be the position where the pressure on the blunt cone first reaches the sharp cone value. Other flow conditions at this point are calculated using the normal shock and isentropic flow relationships. Thus beyond the reference point

$$\frac{p(x,t)}{p_\infty} \text{inv} = \frac{p(x,t)}{p(x)} \frac{p(x)}{p_{\text{ref}}} \frac{p_{\text{ref}}}{p_{\text{ref}}^*} \frac{p_{\text{ref}}^*}{p_\infty} \quad (6)$$

where * refers to steady pressure conditions and 'ref' gives the reference point condition.

For small bluntnesses it is assumed that the pressure $p(x)$ on a blunt cone at small angle of attack α may be given in terms of the pressure on the unyawed body $p(x)^*$ by

$$p(x) = p(x)^* (1 - \eta \alpha \sin \phi) \quad (7)$$

Thus at the reference point

$$\eta = \frac{1}{p_{\text{ref}}^*} \frac{dp_{\text{ref}}}{d\alpha} \quad \text{at the windward generator where } \sin \phi = -1 \quad (8)$$

For the zero entropy layer model, according to Sims (16),

$$\eta = - \frac{2\gamma M_1^* M_2^*}{(\gamma+1) - (\gamma-1)M_1^*} - \frac{\Delta s}{R} \quad (9)$$

For the finite entropy layer model, from equation 8,

$$\eta = \frac{\gamma M_\infty^2}{2} \frac{p_\infty}{p_{\text{ref}}^*} \frac{\partial C_p}{\partial \alpha}$$

For small α , a tangent cone model gives

$$\frac{C_p}{2 \tan^2(\theta_0 + \alpha)} = f(\bar{t}_*), \text{ is Ericsson's scaling parameter } (17)$$

$$\bar{t}_* = t_* (1 + 8\alpha/3\pi\theta_0)$$

The contribution to the dynamic stability from the front portion of the body, up to the reference point, can be evaluated using the modified Newtonian theory.

The present theory has been adapted to deal with the viscous effects in a manner similar to Orlik-Ruckemann's work (18) on pointed cones and sharp wedges. The viscous contribution to the unsteady pressure distribution may be written as

$$p_{\text{vis}}(\theta, \dot{\theta}, \ddot{\theta}, z, \dot{z}) = (p_{\text{vis}})_0 + \theta_{\text{vis}} \frac{\partial p_{\text{inv}}}{\partial \theta} + \dot{\theta}_{\text{vis}} \frac{\partial p_{\text{inv}}}{\partial \dot{\theta}} + \ddot{\theta}_{\text{vis}} \frac{\partial p_{\text{inv}}}{\partial \ddot{\theta}} + \dots$$

$(p_{\text{vis}})_0$ is the pressure component due to the presence of the steady boundary layer. The remaining

terms are perturbations caused by changes in boundary due to induced incidence or the motion of the body. Considering a plane perpendicular to the direction of motion,

$$\theta_{\text{vis}} = \frac{\partial \delta_*}{\partial x} \sin \phi - \frac{\partial \delta_*}{\partial x} \sin \phi$$

$$\dot{\theta}_{\text{vis}} = \frac{\partial}{\partial t} \theta_{\text{vis}}$$

where δ is the boundary layer displacement thickness. Following Moore and Ostrach (19), Orlik-Ruckemann (18) derives an expression for δ_* in terms of the steady boundary layer displacement thickness at zero angle of incidence δ_{*0} . His expression is

$$\delta_* = \bar{\delta}_* (1 - \theta A_\Delta \sin \phi - \frac{\dot{\theta}}{V_\infty} A'_\Delta \sin \phi)$$

where A_Δ and A'_Δ are related to the geometry and the circumferential mass flow defects of the body. The required steady boundary layer displacement thickness has been obtained approximately using Krasnov's (20) empirical relationship for laminar boundary layers on blunted cones given by

$$\bar{\delta}_* = 2.7 \times C_f(x)$$

Use of the Reynolds analogy, together with an expression for the heat transfer on blunt cones, enables $\bar{\delta}_*$ to be evaluated in terms of the local surface Reynolds number.

Alternatively, the surface pressure gradient has been taken into account by using Curle's (21) solution of the laminar boundary layer equations for constant surface temperature and arbitrary pressure gradient.

For the Reynolds numbers of the reported experiments, the calculated magnitude of the viscous effects on the stability derivatives is less than 5% of the inviscid values (see Figure 10) and either of the boundary layer models give acceptable results.

The overall non-steady pressure distribution is obtained by adding the inviscid and viscous results

$$p(x,t)_{\text{overall}} = p(x,t)_{\text{inv}} + p(x,t)_{\text{vis}}$$

Suitable integration of the resulting pressure coefficients over the body surface, together with appropriate differentiations, result in the evaluation of the pitching stability derivatives $-C_{m_q}$ and

$-(C_{m_q} + C_{m_d})$. Full details of these procedures and of the results of this method are given in reference

9. Typical results showing the predicted effect of bluntness are shown in Figure 7.

4. RESULTS AND DISCUSSION

4.1. Pointed and blunted 10° semi angle cones

4.1.1. Effects of bluntness, axis of oscillation and Reynolds number at zero angle of attack

Data for the static and dynamic stability of pointed conical bodies performing pitching oscillations already exist over a wide range of Mach numbers; see for example (5), (22). The effect of bluntness on the stability derivatives had also been studied experimentally and its dynamically destabilising effect for most axis of oscillation positions has been well demonstrated. The present experiments aim both to confirm the validity of the data obtained from short running experiments in the facility described in Section 2 and to obtain new data to explore the variation of the static and dynamic pitching stability with variation of angle of attack.

Figure 6 shows the variation of $-C_{m_q}$ with nose bluntness for 10° semi angle cones for the axis position $x_o/c = 0.58$. The initial increase in aerodynamic stiffness, followed by a decrease for $R_n/R_b > 0.2$, is similar to the trend reported by previous workers, see for example Ericsson (17), although the observed 30% increase is considerably less than the increases of stiffness of about 100% reported in reference 17 for a different axis of oscillation of $x_o/c = 0.4$.

Comparison of the effect of bluntness on the pitch damping derivative $-(C_{m_q} + C_{m_d})$ with Ericsson's correlation of previous experimental results, is shown in Figure 7. The present results show excellent agreement with previous results for a range of cone semi angles from 5.6° to 20° thereby demonstrating the validity of the present technique in comparison with experiments performed in conventional continuous wind tunnels.

Previous theoretical work concerned with the bluntness effect is also shown in Figure 7. Both Rie et al's numerical method of characteristics calculation (8) and Ericsson's calculation (7) based on Sieff's embedded Newtonian concept (13) over-estimate the destabilising effect of bluntness for $R_n/R_b > 0.15$. Simple Newtonian theory takes no account of the entropy layer which contains relatively low Mach number, low density flow in which the afterbody of the blunted cone effectively oscillates. As a result, the bluntness-induced destabilising effect predicted by Newtonian theory is very small. A new theory proposed by Khalid (9), and described briefly in Section 3, attempts to account for the known physical details of the steady flow past blunted cones by using a hybrid blast wave analogy/shock expansion method. The theory takes account of the thick entropy layer and the good agreement with experiment observed for $R_n/R_b > 0.2$ suggests that this flow model, which attributes the loss of dynamic stability to the local reduction of dynamic head in the entropy layer, is confirmed. For values of $R_n/R_b < 0.2$, this theory over-predicts the destabilising effect, since it is in this region that the entropy layer is relatively thin and the outer higher dynamic head region dominates the dynamic stability.

The results of experiments performed to determine the variation of the damping derivative $-(C_{m_q} + C_{m_d})$ with axis positions in the range $0.58 < x_o/c < 0.78$ are shown in Figure 8. Good agreement is demonstrated with the predictions of the finite entropy layer method for the blunt ($R_n/R_b = 0.3$) cone. The shock expansion method, which ignores the finite thickness entropy layer, shows good agreement with the pointed cone results but, as expected, poor agreement for the blunted cone.

Experiments were also carried out at zero incidence to examine the effect of Reynolds number on the stiffness and damping derivatives. Figure 9 shows the variation of the stiffness derivative $-C_{m_d}$ for Reynolds numbers in the range $0.5 \times 10^6 < Re_b < 2.0 \times 10^6$. The statically stabilising effect evident for $1.0 \times 10^6 < Re_b < 2.0 \times 10^6$ for the pointed cone is similar to that reported for tests in a helium tunnel by Orlik Ruckemann (18) and attributed to effects associated with the movement of the natural transition point on the conical surface. Fixing the position of transition with apex roughness gave results which were more invariant with Reynolds number, which suggests that the unroughened pointed cone flow was naturally transitional.

The considerable decrease in local surface Reynolds number within the entropy layer on the blunt cone should result in naturally laminar flow at the Reynolds numbers of the reported experiments. Attempts to promote transition by surface roughness were unsuccessful; the derivative $-C_{m\alpha}$ being

identical with the smooth model results over the complete range of Reynolds numbers. It seems likely, therefore, that the boundary layer was sufficiently far from natural transition for it to remain laminar.

Evidence of transitional effects on the pointed cone damping derivative results is also shown in Figure 10 which shows the variation of $-(C_{m\alpha} + C_{m\alpha}^q)$ with Reynolds number. The movement of the natural transition point as the model oscillates, results in an increase of the damping derivative in the region of Reynolds number between 1.0×10^6 and 2.0×10^6 . This effect is similar to that reported by Orlick-Ruckemann (17) and Ericsson (6). Artificial fixing of the transition point by apex roughening resulted in the damping derivative being invariant with Reynolds number. No variations in $-(C_{m\alpha} + C_{m\alpha}^q)$ with

Reynolds number were observed for the cone of 0.3 bluntness either with or without surface roughness. It was concluded that the boundary layer remained laminar throughout.

Calculations by Khalid (9), plotted in Figure 10, show that the magnitudes of the viscous effects due to the oscillatory boundary layer displacement thickness are expected to be less than 5% of the inviscid value over the range of Reynolds number (from 0.5×10^6 to 2.0×10^6) of the experiments. This theoretical model assumes quasi-steady behaviour of a laminar boundary layer. No significant viscous effects from this cause can be detected within the limits of experimental errors.

4.1.2. Effects of angle of attack on $-C_{m\alpha}$ and $-(C_{m\alpha} + C_{m\alpha}^q)$

The effects of angle of attack on the static and dynamic pitching stability, as obtained from experiments performed on blunted cones ($R_n/R_b = 0, 0.1, 0.2, 0.3$) at the highest Reynolds number condition ($Re_b = 2.0 \times 10^6$), are summarised in figures 11 and 12. No immediate consistency is observed between the trends with increase of incidence up to 7.5° for cones of different bluntness. Walchner and Clay's (5) experiments also show highly non-linear trends both in $-C_{m\alpha}$ and $-(C_{m\alpha} + C_{m\alpha}^q)$ with angle of attack for blunt cones and Ericsson (7) has shown how these effects may be predicted by application of his generalised unsteady Newtonian theory, providing due consideration is given to viscous effects.

It seems probable that the pointed cones results of ref 5 were transitional, whereas, for the Reynolds numbers of the present angle of attack experiments, turbulent boundary layer behaviour is most likely for the pointed cone. The observed trend of a small increase in $-C_{m\alpha}$ and almost constant

$-(C_{m\alpha} + C_{m\alpha}^q)$ with increase of α up to 7.5° supports this conjecture. It is noted that the small +ve value of $-C_{m\alpha}^q$ shows that the centre of pressure is slightly ahead of the position of the oscillation axis at $0.68c$ and moves to almost coincide with the axis at $\alpha = 7.5^\circ$.

The decrease in $-C_{m\alpha}$ with angle of attack for the 0.1 and 0.2 bluntness cones appears consistent with previously observed effects (6) (22) of non steady transition point movement. The increase in local Reynolds number with angle of attack causes these effects to occur at higher angles of attack, whereas, they are absent from zero angle of attack experiments. The increase in damping derivative with increase of α for the 0.2 bluntness cone is consistent with transitional boundary layer behaviour but, it is surprising that the 0.1 bluntness cone does not show this trend.

It is possible, however, that the observed trends for these blunted cones are due to both transitional boundary layer behaviour and also centre of pressure movements due to changes in the surface pressure distribution with angle of attack.

The results for the 0.3 bluntness cone show an increase of both $-C_{m\alpha}$ and $-(C_{m\alpha} + C_{m\alpha}^q)$ with increase of angle of attack. For this bluntness, the flow over the majority of the conical surface is dominated by the nose bluntness-induced entropy layer. For $\alpha = 0$ the body effectively oscillates within the inner low dynamic pressure region, but, as α increases the windward surface extends progressively into the higher dynamic pressure outer region with consequent increases in the local non-steady aerodynamic forces. Since the stiffness and damping derivatives will be progressively more dominated by the windward surface forces as α increases, it is suggested that the bluntest cone results are caused by this effect. Any effects due to transitional boundary layer behaviour are likely to be small since the local surface Reynolds numbers are lowest for the bluntest cone and the boundary layer probably remains laminar over the incidence range tested.

4.2. Blunt Hyperballistic Shapes

4.2.1. Stability derivatives at zero angle of attack

Figure 13 shows the variation of the pitching derivatives with the position of the axis of model oscillation for the models HBl and HBS at zero angle of attack as measured experimentally and as predicted by the simple Newtonian theory. The linearity of the stiffness derivative (as measured from experiments) with the position of the axis of model oscillation is good. The concluded position of the centre of pressure (where $-C_{m\alpha} = 0$) for the model HBl agrees very well with that previously obtained from static force measurements (see reference 23 figure 7b) at Mach number 7.0. The damping derivative shows a minimum, for the model HBl, at a position of the axis of model oscillation corresponding to the centre of pressure, while the damping derivative for the model HBS is decreasing with positions of the axis of model oscillation closer to the centre of pressure.

It is apparent that the simple Newtonian theory does not predict satisfactorily the pitching derivatives for either of the models. For the model HB1 it predicts a less stiff body and a position of the centre of pressure well ahead of the true one (at $\frac{x}{L} \approx 0.1$ compared to 0.27). This is because the

Newtonian theory completely ignores the pressures on the long after-body of this model. This is also reflected in the estimates of the damping derivative which are much smaller than the experimental values. For the model HBS, the Newtonian theory predicts a stiffer body with a position of the centre of pressure behind the experimentally concluded position (at $\frac{x}{L} \approx 0.72$ compared to 0.64). The reason for this

discrepancy is that the Newtonian theory over predicts the dynamic pressure on the flares of this model since the bow shock wave is assumed to coincide with the flare's surfaces. The reduced dynamic pressure on the surface, caused by the entropy gradient through the flow shear-layer produced by the nose-bluntness, is not predicted correctly. This is also reflected in the estimates of the damping derivative, which are larger than the experimental values. It is concluded that the simple Newtonian theory is totally inadequate to describe the complex flow field around such blunt-nose-cylinder-flare type of bodies. A method which more closely describes the flow field around such bodies is required in order to arrive at better estimates of the pitching derivatives in hypersonic flows.

4.2.2. Effects of angle of attack on $-C_{m_{\alpha}}$ and $-(C_{m_q} + C_{m_{\dot{\alpha}}})$

Figure 14 shows the variation of the pitching derivatives of the three tested models with angle of attack in the range 0 to 7.5 deg. and at a Reynolds number of 0.82×10^6 to 0.85×10^6 . The position of the axis of model oscillation was chosen to be close to the centre of pressure of each model at zero angle of attack. If the position of the axis of model oscillation is far behind the centre of pressure then the resulting large pitching moment produces large model deflections when it is released. On the other hand, if the position of the axis of model oscillation was far ahead of the centre of pressure then the resulting nose-down pitching moment would release the displaced model if the pitching moment exceeded the pivot restoring moment, since the models were not locked in the displaced position.

It is seen that the stiffness derivative generally increases with the increase in the angle of attack; this is equivalent to a rearward shift of the centre of pressure with angle of attack. A similar trend was observed (see section 4.1.2) for the bluntest of the conical bodies tested.

The damping derivative for the model HB1 is almost independent of the angle of attack in the range 0 to 7.5 deg. The same derivative shows a substantial non-linear increase with angle of attack for the model HB2 and to a lesser extent for the model HBS. Similar non-linear increases in the damping derivative with angle of attack were observed for some of the conical bodies tested (see 4.1), for a space shuttle orbiter configuration (24) and a pointed slender missile configuration with lifting and control surfaces (25).

It is likely that these non-linear increases in the damping derivative are partly caused by boundary layer transition on the windward side of the flare surface at angle of incidence, where the flow density and the local value of Reynolds number are relatively large. It is important to attempt the separation of the effects of boundary layer transition (promoted by angle of incidence) from those of inviscid angle of attack effects (if any). The experimental evidence suggests that the flow is naturally laminar for the model HB1 through the range of angle of attack considered and that the low values of Reynolds number over the after body of this model are much below the value of Reynolds number for natural transition at this Mach number.

It is worth noting that for conical bodies, cross-flows at an angle of incidence are more likely to promote transition on the leeward side of the body. However, for blunt hyperballistic shapes these cross flow effects are less significant.

Finally, it is important to stress that entirely new flow phenomena are likely to occur at higher angles of incidence in the range 10 to 30°, such as flow separation on the cylindrical afterbody surface or on the flare's surfaces and the all important inter-action between the nose bow shock wave and the flare surface on the windward side. These phenomena are likely to have dramatic effects on the pitching stability of this type of body.

5. CONCLUSIONS

A brief description has been given of a newly developed $M = 6.85$ intermittent wind tunnel, based on the light piston isentropic compression concept, which has very suitable characteristics for the economic acquisition of dynamic stability data. Equipment suitable for the measurement of pitching stability derivatives during tunnel running times of less than 0.5 seconds is described.

New data for the pitching dynamic stability derivatives of a range of pointed and blunted axisymmetric shapes have been obtained at $M = 6.85$ using this equipment. The present data for pointed and blunted cones at zero incidence show good agreement with previous work. New data showing the effects of Reynolds number, axis of oscillation and the non-linear effects of angles of attack up to 7.5° are presented for a range of conical and hyperballistic shapes.

The results have been compared with existing theories and with a new theory developed by Khalid for blunted conical shapes. The bluntness induced effects at zero incidence are well correlated by theory but further work is required on the non-linear effects of angle of attack, especially in flow regimes for which the boundary layer is transitional. Simple Newtonian theory was found to be quite inadequate in predicting the experimentally observed pitching static and dynamic stability of the hyperballistic shapes HB1, HB2 and HBS. Further work is required concerning suitable theoretical methods for these shapes.

REFERENCES

1. East, R.A. "Oscillatory experiments in short duration hypersonic testing facilities". Proceedings of the 1st International Congress on Instrumentation in Aerospace Simulation Facilities, Paris 1964.
2. Enkenhus, K.R., Richards, B.E. and Culotta, S. "Free flight stability measurements in the Longshot tunnel". Shock Tube Research, Chapman and Hall, London, 1971.
3. Ghesh, K. "Dynamic tests using a gas bearing model-pivot in hypersonic flow". Ph.D.Thesis, University of Southampton, 1973.
4. Jones, T.V., Schultz, D.L. and Hendley, A.D. "On the flow in an isentropic light piston tunnel". ARC R & M 3731, 1973.
5. Walchner, O. and Clay, J.T. "Nose bluntness effects on the stability derivatives of cones in hypersonic flow". Transactions of the Second Technical Workshop on Dynamic Stability Testing, I, Paper 8, April 1965, Arnold Engineering Development Centre, Arnold Air Force Station, Tennessee, U.S.A.
6. Ericsson, L.E. "Effect of boundary layer transition on vehicle dynamics". Journal of Spacecraft and Rockets, 6, 12, pp 1404-1409, December 1969.
7. Ericsson, L.E. "Generalised unsteady embedded Newtonian flow". Journal of Spacecraft and Rockets, 12, 12, pp 718-726, December 1975.
8. Rie, H., Linkiewicz, E.A. and Bosworth, F.D. "Hypersonic dynamic stability, Part III: Unsteady flow Program". General Electric Company FDL-TDR-64-149, 1967.
9. Khalid, M. "A theoretical and experimental study of the hypersonic dynamic stability of blunt axisymmetric conical and power law shapes". Ph.D.Thesis, University of Southampton, 1977.
10. Schultz, D.L., Jones, T.V., Oldfield, M.L.G. and Daniels, L.C. "A new transient cascade facility for the measurement of heat transfer rates". Oxford University Engineering Laboratory Report 1207/77, 1977.
11. East, R.A. Unpublished work. University of Southampton, 1974.
12. Qasrawi, A.M.S. "Measurements of hypersonic dynamic stability of pitching blunt-nosed bodies in a short duration facility". University of Southampton, Ph.D.Thesis, 1977.
13. Seiff, A. "Secondary flow fields embedded in hypersonic shock layers." NASA TN D - 1304, May 1962
14. Chernyi, G.G. "Introduction to hypersonic flow". Translation Editor R. F. Probstein, Academic Press, New York 1961.
15. Eggers, A.J. and Savin, R.C. "Approximate methods for calculating the flow about non-lifting bodies of revolution at high supersonic airspeed." NASA TN 2579, 1951.
16. Sims, J.L. "Tables for supersonic flow around circular cones at zero angles of attack". NASA SP-3004, 1964.
17. Ericsson, L.E. "Unsteady embedded Newtonian flow". Astronautica Acta, 18, 309-330, 1973.
18. Orlik-Ruckemann, K.J. "Dynamic viscous pressure interactions in hypersonic flow". National Research Council of Canada, Aeronautical Report LR-535, July 1970.
19. Moore, R.K. and Ostrach "Displacement thickness of the unsteady boundary layer". Journal of Aeronautical Sciences, 24, 1, pp 72-78, 1957.
20. Krasnov, N.F. "Aerodynamics of bodies of revolution" edited and annotated by Deane N. Morris, American Elsevier Publishing Company, Inc., New York 1970.
21. Curle, N. "The steady compressible laminar boundary layer with arbitrary pressure gradient and uniform wall temperature". Proc. Roy. Soc. (A) 249, pp 206, 1958.
22. Schueler, C.J. "Dynamic stability results for a 10° cone at Mach numbers 0.8 to 20". AEDC TDR 64-226. December 1964.
23. Gray, J.D. "Summary report on aerodynamic characteristics of standard models HB-1 and HB-2". AEDC-TDR-64-137, July 1964.
24. Uselton, B.L., Freeman, D.C.Jnr, and Boyden, R.P. "Experimental dynamic stability characteristics of a shuttle orbiter at $M_\infty = 8$ ". Journal of Spacecraft and Rockets, 13, 10, pp 635-640, October 1976.
25. Morrison, A.M. and Ingram, C.W. "Stability coefficients of a missile at angles of attack." Journal of Spacecraft and Rockets, 13, 5, pp 318-9, May 1976.

ACKNOWLEDGEMENTS

This work has been supported by the Procurement Executive, Ministry of Defence. One of the authors (M. Khalid) wishes to acknowledge the financial support of a Science Research Council Research Studentship during the period of this work.

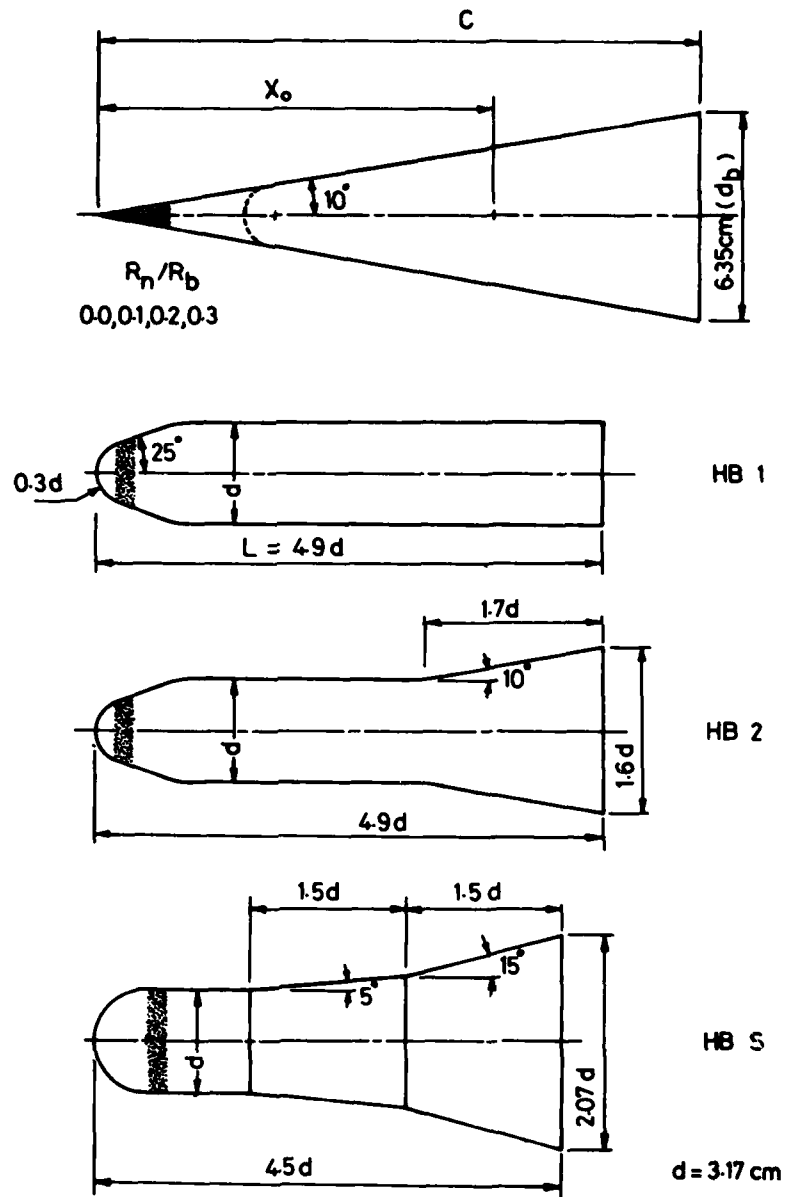
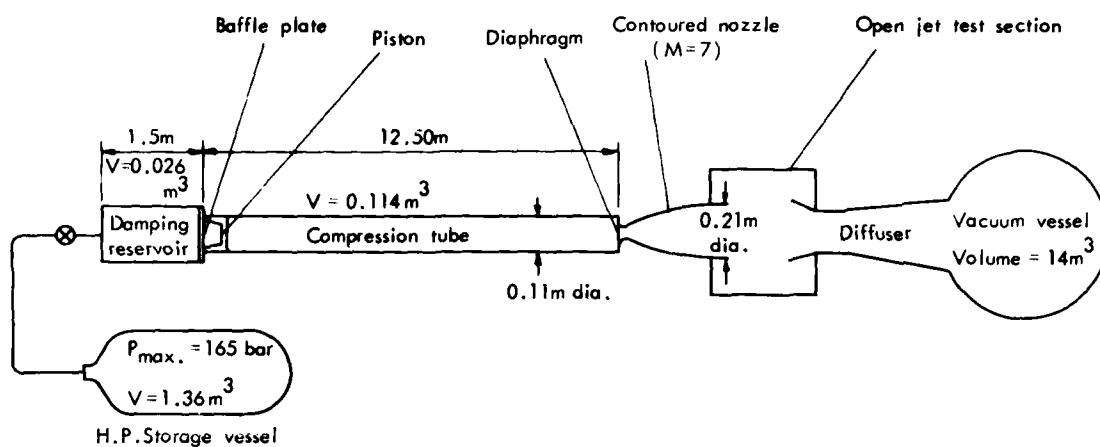


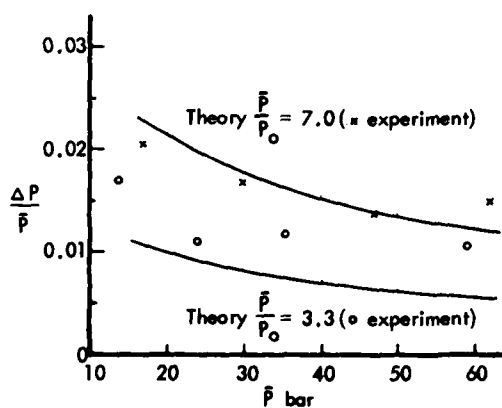
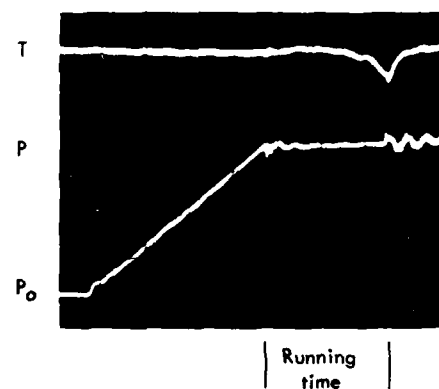
Fig.1 Shapes tested for dynamic stability



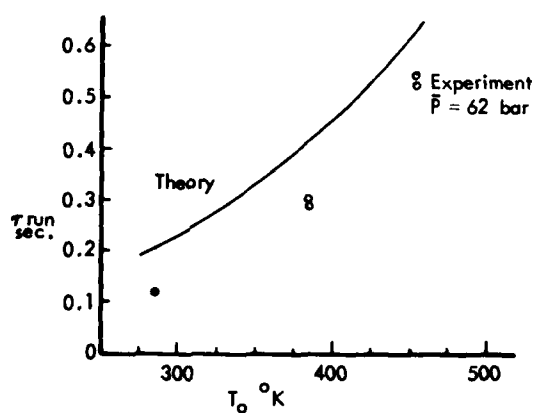
(a) Schematic diagram of test facility

(b) Records of flow temperature and pressure

$T_{ref.} = 597^\circ \text{K}$ ($50^\circ \text{C}/\text{div.}$)
 $\bar{P} = 60.7 \text{ bar}$ ($12.1 \text{ bar}/\text{div.}$)
 Time scale $0.2 \text{ sec.}/\text{div.}$

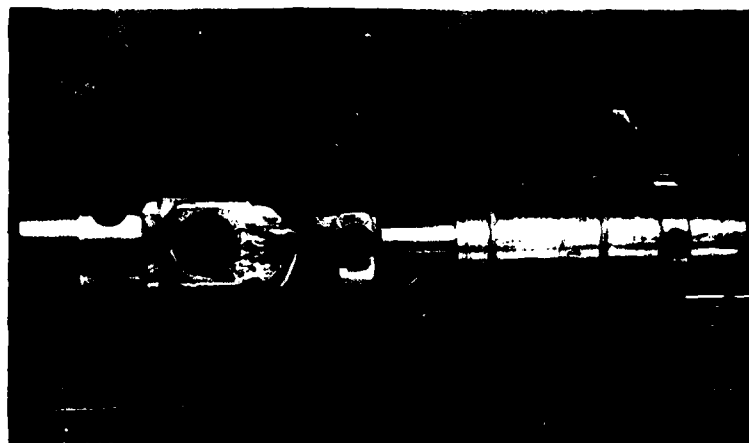


(c) Pressure fluctuations



(d) Running time vs. initial temperature

Fig.2 Description of test facility and its performance



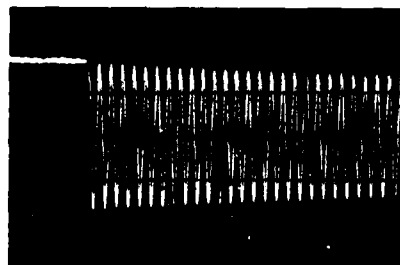
(a) Model pivot and attachment assembly



(b) Sting - supported model in test - section

Fig.3 Free-oscillation test mechanism

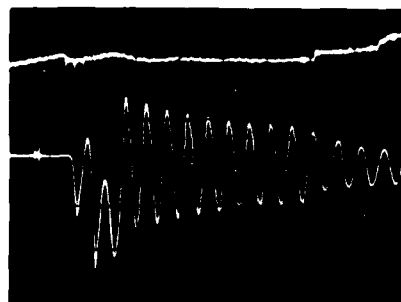
HB1 Model oscillation
Wind off
1.0 deg/div, 0.1 sec/div.



HB1 Model oscillation
Wind on
1.0 deg/div, 0.1 sec/div.



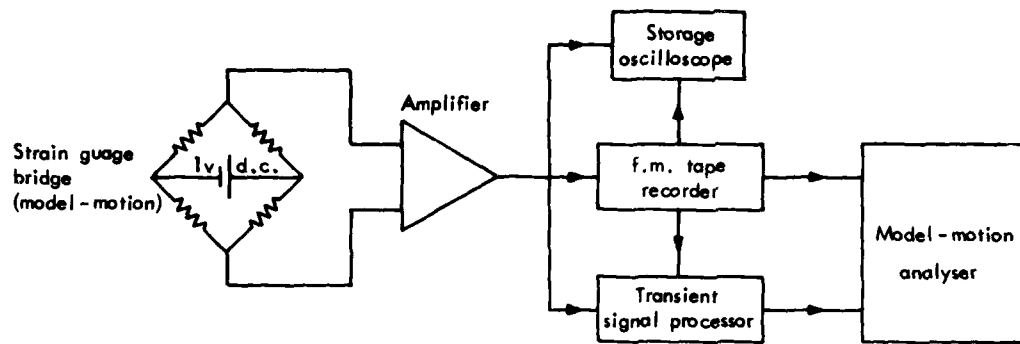
Effect of flow start on model
oscillation ($\alpha = 7.5^\circ$)
1.0 deg/div, 0.05 sec/div.



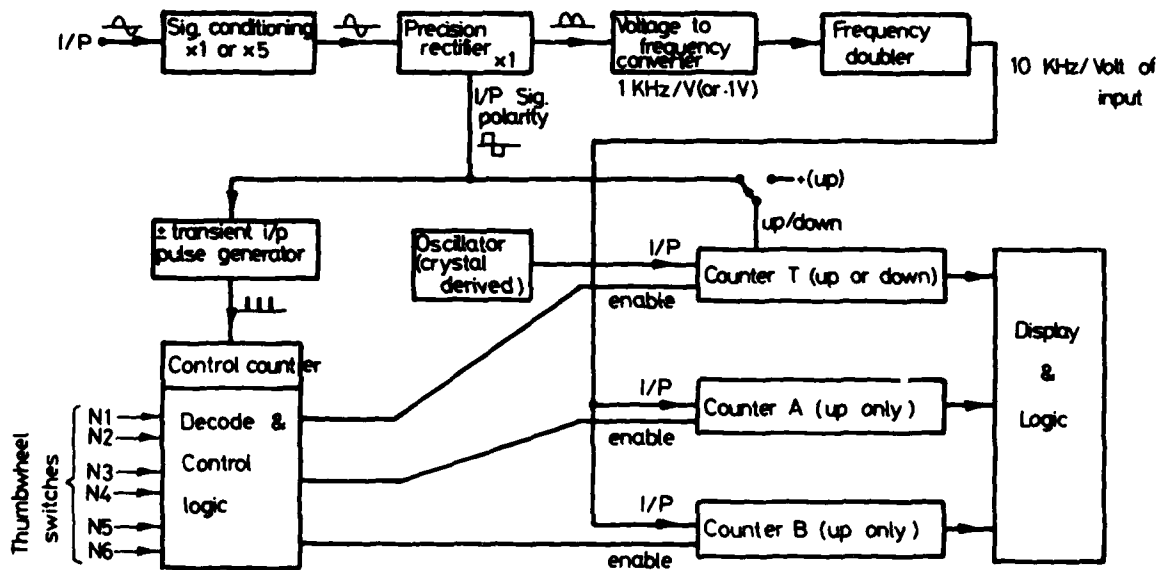
Schlieren photograph of flow
around the model HBS
 $\alpha = 0$ deg. , at 0.3 sec.



Fig.4 Records of model free oscillations and a Schlieren photograph of flow



Block diagram of data-logger



Block diagram of model-motion analyser

Fig.5 Block diagrams of data acquisition and reduction system

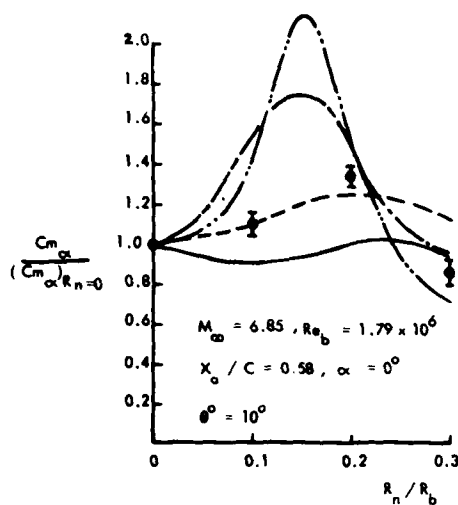


Fig.6 Variation of 10° cone stiffness derivative $C_{m\alpha}$ with bluntness \sim comparison of theory with experiment

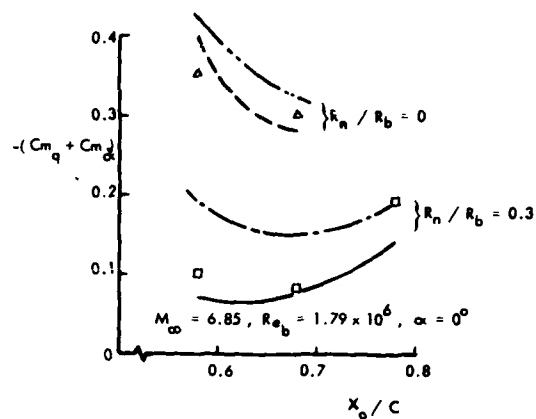


Fig.8 Variation of dynamic stability of 10° cones with axis of oscillation

KEY TO THEORIES FOR FIGURES 6, 7, 8.

LINE	AUTHOR	REFERENCE No.
— — — —	KHALID (ZERO ENTROPY LAYER MODEL) $M_{\infty} = 5.85$	9
————	KHALID (FINITE ENTROPY LAYER MODEL) $M_{\infty} = 5.85$	9
— . . . —	ERICSSON (EMBEDDED NEWTONIAN) $M_{\infty} = 14$	7
— . . . —	RIE ET AL (NUMERICAL) $M_{\infty} = 20$ (Fig 7) $M_{\infty} = 7$ (Fig 8)	8

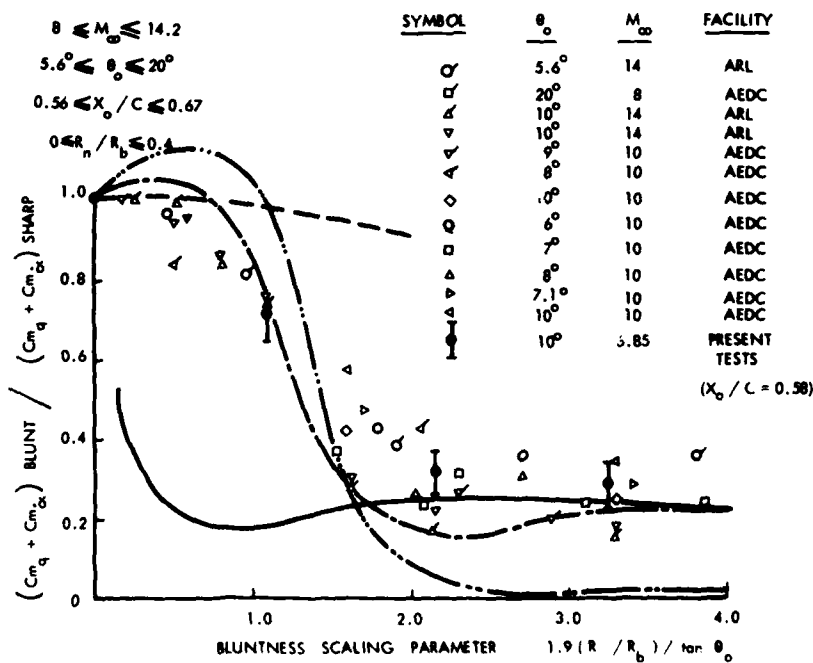


Fig.7 Scaling of damping derivatives for slender blunted cones. Comparison of theory and experiment

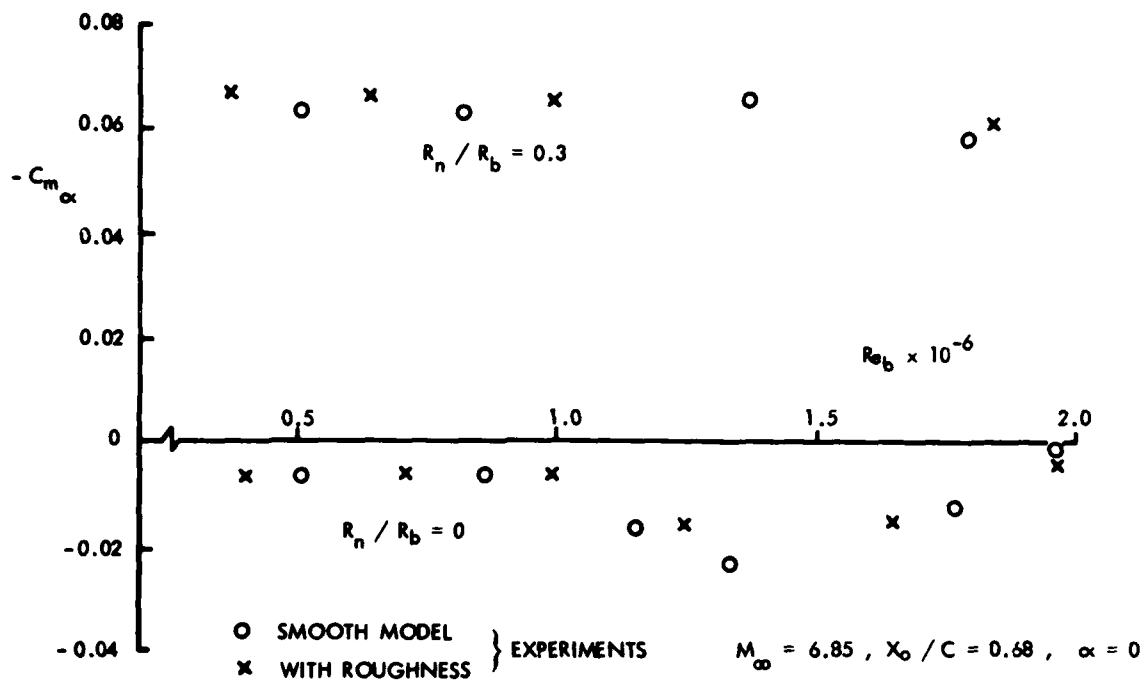


Fig.9 Variation of static stability $-C_{m_\alpha}$ with Reynolds number for 10° cones

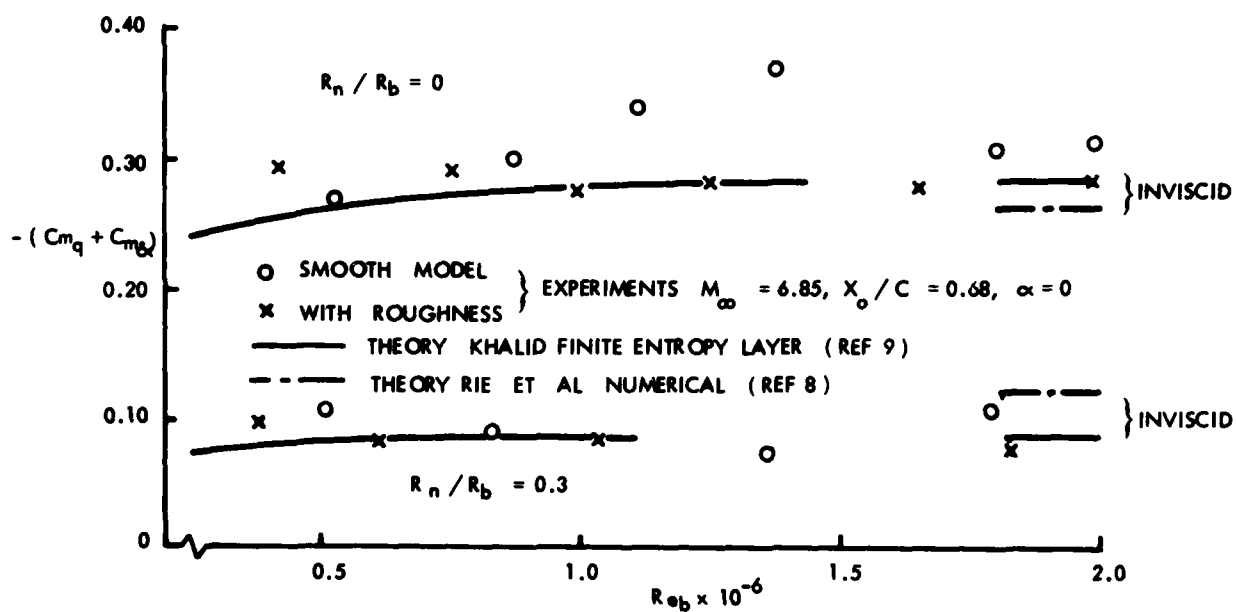


Fig.10 Variation of dynamic stability $-(C_{m_q} + C_{m_{\dot{\alpha}}})$ with Reynolds number for 10° cones

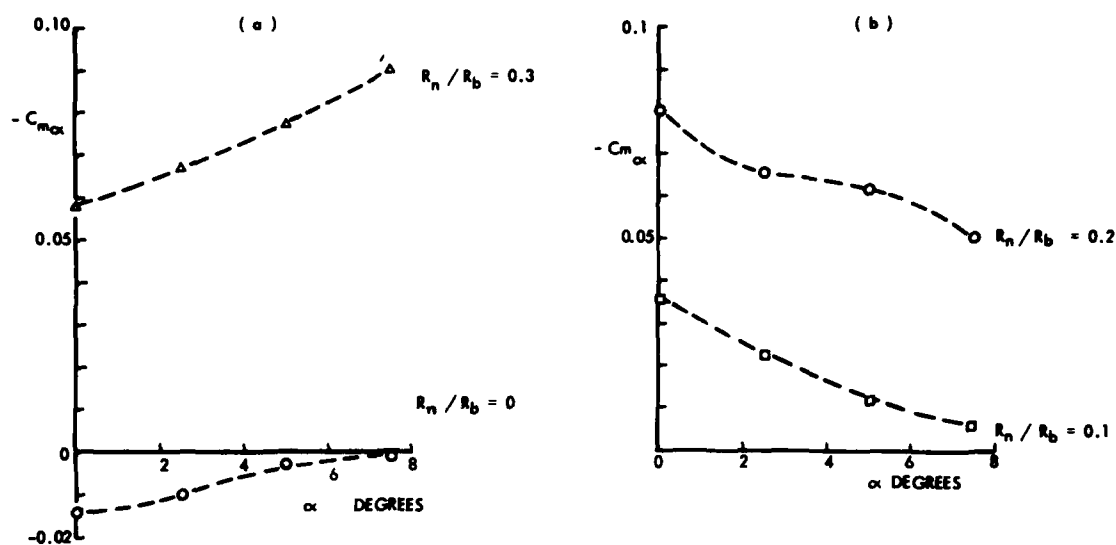


Fig.11 Variation of static stability $C_{m\alpha}$ of 10° cones with angle of attack. $M_\alpha = 6.85$, $Re_b = 1.79 \times 10^6$, $X_0/C = 0.68$

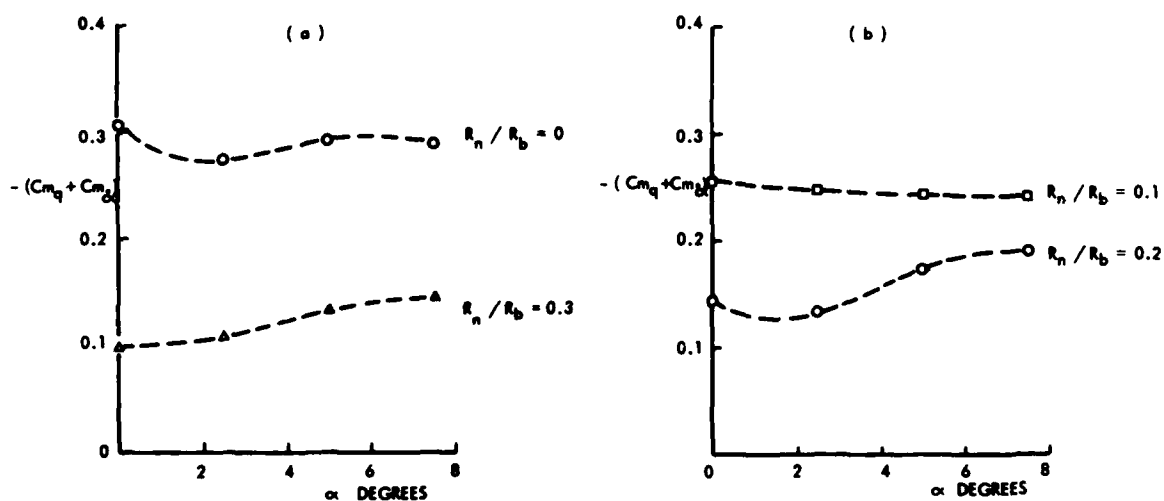


Fig.12 Variation of dynamic stability $-(C_{mq} + C_{m\alpha})$ of 10° cones with angle of attack. $M_\infty = 6.85$, $Re_b = 1.79 \times 10^6$, $X_0/C = 0.68$

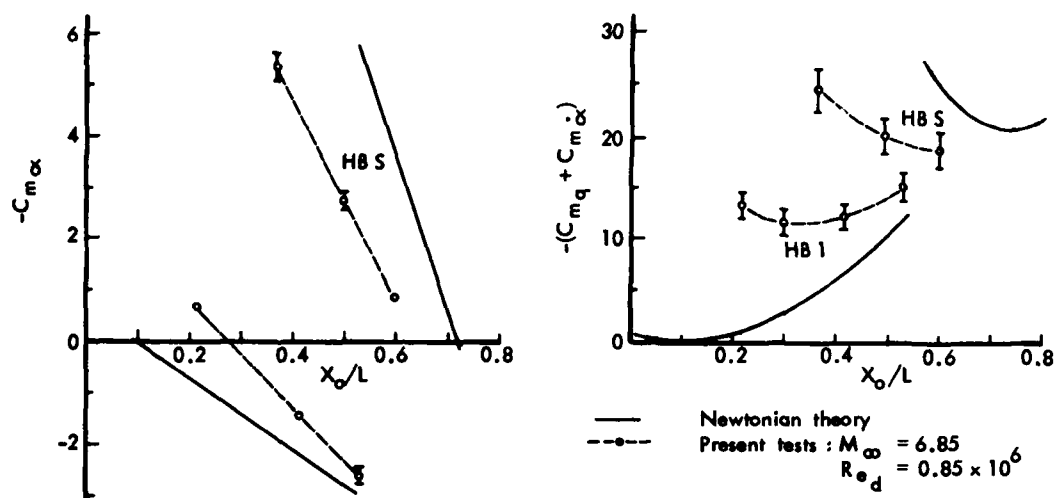


Fig. 13 Stability derivatives of blunt hyperballistic shapes at zero angle of attack

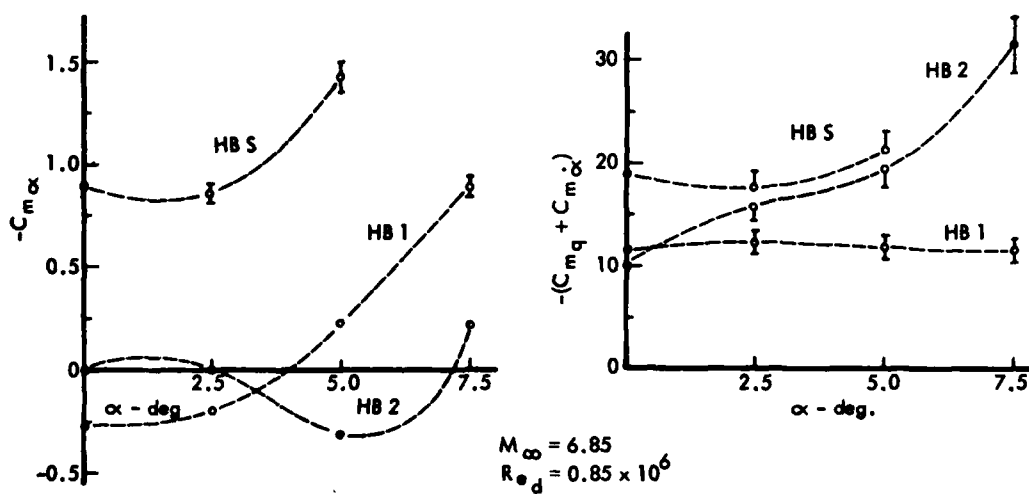


Fig. 14 Effects of angle of attack on stability derivatives

UNSTEADY AERODYNAMICS OF OSCILLATING CONTAINERS AND APPLICATION TO THE
PROBLEM OF DYNAMIC STABILITY OF HELICOPTER UNDERSLUNG LOADS

by A. Simpson and J. W. Flower

Department of Aeronautical Engineering,
University of Bristol, Bristol, BS8 1TH, England.

SUMMARY

Loads slung beneath helicopters can develop alarming oscillations at quite low air-speeds due to aerodynamic forces, and hence severely curtail the performance of the helicopter. The present investigation highlights the (sometimes overriding) importance of load movement on the aerodynamic forces for the particular case of the standard 20' x 8' x 8' container.

Forces and moments have been derived from pressure measurements on two models, inexorably oscillated in a variety of modes and at various amplitudes, with some comparison with other results from decaying oscillation investigations. Extreme non-linearities are evident; for example, the case where static stability changes to instability as yaw angle is changed, while dynamic instability for small yaw oscillations changes to dynamic 'stability' for large yaw oscillations.

Flow visualisation techniques show complex flow situations and extreme phase lags in the separated flow patterns. A mathematical model based on the observed patterns compares well with the force and moment results.

LIST OF SYMBOLS

b	Spacing between upper strops. (Also viscous damping coefficient)
B	Total damping coefficient (Equation 3)
C	Total stiffness coefficient (Equation 3)
C_x, C_y, C_z	($= X/\frac{1}{2}\rho V^2 h d, Y/\frac{1}{2}\rho V^2 h^2, Z/\frac{1}{2}\rho V^2 h d$) Aerodynamic force coefficients
C_{mx}, C_{my}, C_{mz}	($= M_x, M_y, M_z/\frac{1}{2}\rho V^2 d h^2$) Aerodynamic moment coefficients
C_p	($= \text{pressure}/\frac{1}{2}\rho V^2$) Pressure coefficient
d	Length of container
f	Natural frequency (Hz)
h	Depth (and breadth) of container
I_z	Moment of inertia of container about axis O_z
l	Upper strop length
M_x, M_y, M_z	Aerodynamic moments about O_x, O_y, O_z
O_x, O_y, O_z	Body fixed right handed Cartesian axis system with O at container geometric centre
p (or p_n)	Static pressure at some point on the container
p_s	Reference static pressure
p	Aerodynamic phase lag
q	Dynamic pressure ($= \frac{1}{2}\rho V^2$)
t	Time variable
V	Free stream velocity
w_d, w_h	Frequency parameter based on d and h ($= w d/V, w h/V$)
X, Y, Z	Aerodynamic forces along O_x, O_y, O_z directions
θ, ϕ, ψ	Rotations about O_x, O_y, O_z axes
$\delta x, \delta y, \delta z$	Deviations of container from equilibrium position in O_x, O_y, O_z directions
$\delta \theta, \delta \phi, \delta \psi$	Angular deviations of container from equilibrium position about O_x, O_y, O_z axes
v	Frequency parameter based on d and f ($= f d/v$)
Suffix o	Denotes datum when affixed to θ, ϕ, ψ , etc.
Suffixes x, y, ψ , etc.	Denote derivative of suffixed quantity with respect to suffix when affixed to $C_x, C_y, C_z, C_{mx}, C_{my}$ and C_{mz}

1. INTRODUCTION

Over the past thirty years, a considerable number of philosophies on the air transport of freight has evolved. One of the more important of these in the military context concerns the use of helicopters to convey freight externally by suspending it directly, or within containers, beneath the helicopter fuselage by using strop and lifting-hook configurations. In this way loads whose bulk and accessibility would preclude air transport by any other means may be carried successfully. Furthermore, turn-round times are minimised by such procedures - an important factor in many civil as well as military applications. Ordnance, strategic supplies and even troops may be transported efficiently by this means and recovery operations may be performed with optimum speed. On the civil side, crane helicopters have been used in the erection of bridges, towers and other buildings and structures, and even for the transport of mobile operating theatres.

However, inevitably, there are limitations of this simple external mode of freight transportation, these being associated with the aerodynamic forces which arise when there is motion of air relative to the suspended body. These forces can lead to static or dynamic states of instability of the suspended body or of the combined helicopter-freight system. Severe instabilities have led to the loss of freight in the worst cases and generally to handling problems of varying degrees of severity and/or speed limitations. Many of these problems are associated with the poor Dutch Roll characteristics of most helicopters - particularly at high forward speeds.

While it is not possible a priori to rule out the possibility of instability modes requiring motions of both freight and helicopter, it is recognised generally that most of the troublesome motions arise from the freight aerodynamics per se. In this paper, therefore, attention is confined to the freight aerodynamics and to the related natural stability problems which arise therefrom. Indeed, before a successful study of the helicopter-freight combination can be undertaken, it is essential to develop an understanding of the aerodynamic characteristics of the freight per se. Herein, attention is focussed on one particular type of freight container; the familiar 5:2:2 rectangular box.

2. OSCILLATION OF RECTANGULAR CONTAINERS SUSPENDED BENEATH HELICOPTERS: THE NEED FOR UNSTEADY AERODYNAMIC RESEARCH

The simplest type of strop system is the single-strop sling (Figure 1a). This carries the advantage of simplicity since only one lifting hook is required on the aircraft: also, rigging time is minimised. A major disadvantage of the single-strop sling is its lack of yaw restraint, and this carries with it two consequences - both of them serious:- (i) As soon as the helicopter moves forward, the container will align itself with its major axis crosswind thus maximising drag. (ii) While this equilibrium position is statically stable, it transpires to be dynamically unstable in the sense that yaw oscillations are initially negatively damped and build up to limit cycles whose frequencies and amplitudes are completely determined by aircraft forward speed. Depending upon the length of the upper strop, amongst other things, sideslip oscillation might accompany the yaw.

An obvious development of the single-strop sling is the twin-strop arrangement (Figure 1b). This provides yaw restraint in the manner of bifilar suspension and, provided the upper strops are sufficiently well separated, this will be adequate to maintain the container near its minimum drag position (major axis along wind direction). However, this position is shown herein (see also Reference 1) to be dynamically unstable in yaw and the resulting yaw oscillations couple strongly with sideslip under certain conditions. The ensuing combined motions may achieve large amplitudes in only a few oscillation cycles: indeed, containers have had to be jettisoned on occasions so severe have been the motions. The price one pays for minimum drag is thus high!

In order to avoid the negative yaw damping which characterises the minimum drag position, the container can be rigged with a nose-down attitude of about 10° . In this attitude, positive yaw damping obtains, drag is only marginally increased, but the aircraft now has to support a negative lift load. If the upper strops are parallel, the 10° nose-down orientation does not change with aircraft forward speed. Ostensibly, this would appear to solve the lateral oscillation problem completely: Naturally it doesn't! Reference 1 shows such arrangements to be highly flutter prone in combined sideslip and yaw motions. Amplitudes can once again be very large, and flutter onset is usually of the 'hard' type. Criteria for flutter onset involve many parameters, e.g. strop length, separation and disposition relative to the container c.g., container weight and yaw moment of inertia, etc. The type of flutter mode obtained therefore depends, amongst other things, on how the container is loaded¹.

An extension of the twin-strop arrangement, known as the 'double V strop' configuration (Figure 1c) has been proposed by Sheldon². Independent yaw motion of a rigid container is excluded with this strop configuration, provided all cables are inextensible and the aircraft itself is sensibly rigid. Indeed, the only kinematically permissible motions are the longitudinal and lateral pendulum modes. The type of flutter mentioned above is thus avoided, as is pure yaw (negatively damped) motion.

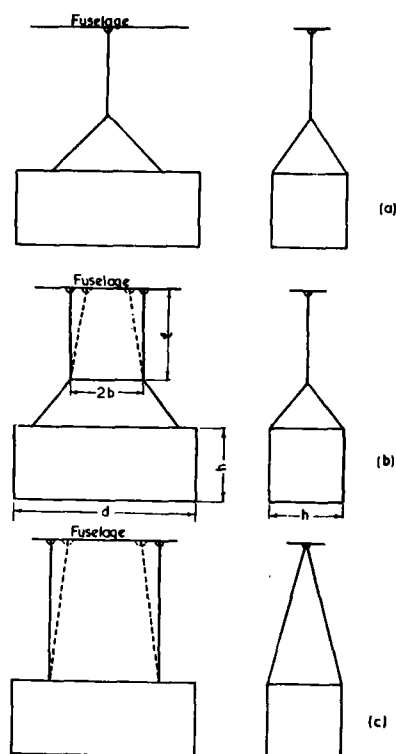


FIGURE 1 Strop Configurations
(a) Single Strop Configuration
(b) Twin Strop Arrangements
(c) Sheldon 'Double V Strop' Arrangement

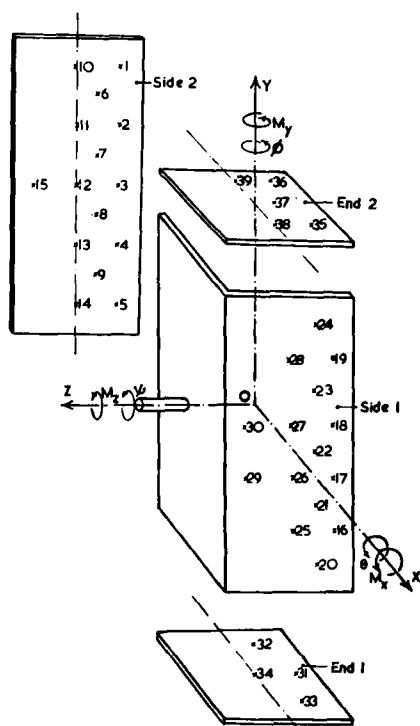


FIGURE 2 Single Degree of Freedom
(1' x 0.4' x 0.4') Model -
Pressure Tappings and Axes

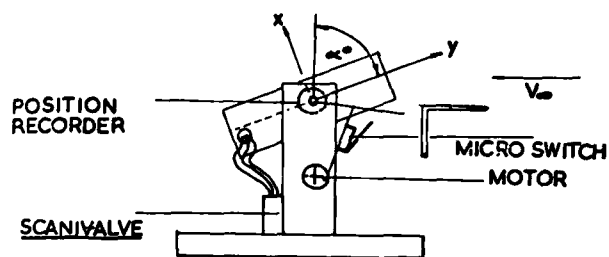


FIGURE 3 Single Degree of Freedom Rig -
General Layout

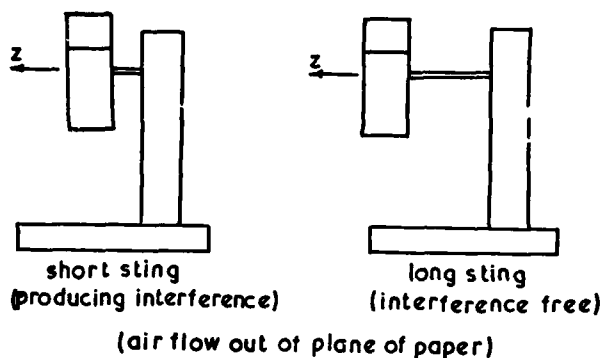


FIGURE 4 Single Degree of Freedom Model -
Support Arrangements

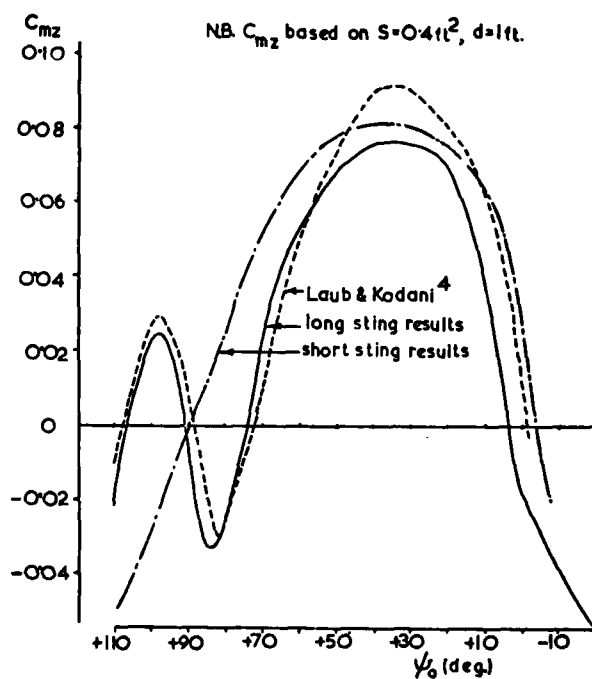


FIGURE 5 1' x 0.4' x 0.4' Model - Yawing
Moment Results

Wind tunnel model tests¹ of this arrangement have given reason for encouragement, but at full scale two problems are likely to arise:- (a) In view of the additional kinematic constraints, there is more likelihood of interaction between the aerodynamic forces on the container and motions of the aircraft. (b) Lateral gusts could give rise to a structurally nonlinear yaw mode in which pairs of opposite strops become alternately slack. The latter problem is exacerbated at high forward speeds if the two pairs of V strops are parallel: in the 'blown back' equilibrium position, tensions in the leeward V strops can become very small. (This effect can be overcome by the trapezoidal arrangement shown dotted in Figure 1c, but then the negative lift induced by nose-down container incidence would grow with speed, as indeed would drag coefficient).

Many other methods of stropping have, of course, been employed, but none has been entirely successful. Lateral oscillations of the underslung container are clearly the major cause for concern, even though these sometimes couple with longitudinal motions to produce quite dramatic combined instability modes.

Most of the previously published studies of the underslung load stability problem rely upon wind tunnel-measured static aerodynamic derivatives⁴. One exception is the work of Liu⁵ who used viscous cross-flow theory to compute a set of quasi-static force derivatives for the 5:2:2 container at attitudes close to the minimum drag position. Liu also calculated pitch and yaw derivatives, but these proved to be grossly in error owing to the presence of separation bubbles which exert a profound influence on the moments (but less so on the forces). In the opinion of the present authors, the use of quasi-steady derivatives is not justified over a considerable portion of the usually accepted flight envelope. Referring to Figure 1b one readily obtains the following expression for the frequency of yaw oscillations, assuming a uniformly dense container:-

$$f = \frac{1}{2\pi} \sqrt{\frac{12g b^2}{\ell(d^2+h^2)}} \text{ Hz} \dots\dots\dots (1)$$

Assuming zero aerodynamic stiffness in yaw, the frequency parameter, v , is given by

$$v = \frac{fd}{V} = \frac{\text{time for a fluid particle to travel distance } d}{\text{yaw oscillation period}} = \frac{d}{2\pi V} \sqrt{\frac{12g b^2}{\ell(d^2+h^2)}} \dots\dots (2)$$

Typically $d = 20 \text{ ft}$, $h = 8 \text{ ft}$, $b = 10 \text{ ft}$ so that $v = 29/V\sqrt{\ell}$, approximately.

Now in conventional aeroelastic applications, a sensible upper limit to the applicability of quasi-static aerodynamic theories is $\omega d/V \approx 0.5$ where $\omega = 2\pi f$. This implies an upper limit of v of about 0.1 (ten chords traversed per oscillation period). Hence for quasi-static theories to apply $V\sqrt{\ell} > 290 \text{ ft}^{3/2}/\text{sec}$. For $\ell = 25 \text{ ft}$, which is a relatively long upper strop dimension, one must have $V > 58 \text{ ft/sec}$. Thus, at all speeds below 58 ft/sec , the use of quasi-steady theories is questionable, and this represents a very large segment of the operational flight envelope of freight-carrying helicopters. Furthermore, the configuration of Figure 1b is a statically stable one implying positive aerodynamic stiffness in yaw; hence the above frequency, f , underestimates the actual yaw frequency by a progressively greater amount as V increases. Hence, the range of inapplicability of quasi-static theories is even greater than that implied by the above simple formulae. Shortening of the upper strop length, ℓ , widens the range of inapplicability even further. It is therefore hardly surprising that previous treatments of underslung load instability based on quasi-static aerodynamic data have proved to be patently unsuccessful in predicting full-scale behaviour. With such reservations firmly in mind, the 'unsteady aerodynamics' approach reported herein was instituted under contract support from the United States Army.

Throughout the remainder of the paper, the aerodynamic aspects only will be considered. Actual applications to stropped containers will not be considered: the necessary aerodynamic tools required in such applications, however, will be provided along with an understanding of the flow processes involved.

3. SCOPE OF THE WIND TUNNEL MODEL TESTS

In order to gain an insight into the aerodynamic actions on an oscillating rectangular container, it was decided at the outset to perform the following tests on typical container shapes:-

- (i) Pressure distribution tests for stationary and inexorably oscillating container models. In the first place, these tests were to involve motions in a single degree of freedom, namely pitch about the various principal axes (or, what amounts to the same thing, yaw); subsequently simple binary combinations of the individual degrees of freedom were to be considered. The pressures were to be ultimately integrated to provide force and moment time history diagrams, loop diagrams (which immediately illustrate stability of motion) and finally 'overall aerodynamic derivatives'. The term 'overall' prefixing 'aerodynamic derivatives' implies that the imposed motions need not necessarily be small; the aerodynamics will therefore be generally nonlinear and the 'overall aerodynamic derivatives' thus have the nature of describing functions for the forces and motions being considered.

- (ii) Flow visualisation tests for stationary and inexorably oscillating container models. In both stationary and dynamic cases, various techniques were to be considered; e.g. 'surface', 'smoke' and 'helium bubble'.
- (iii) Single degree of freedom decaying oscillation tests. These were to be performed for pitch oscillations only, to provide a rapid means of assessing aerodynamic derivatives.

All tests outlined above were to be performed for a wide variety of equilibrium configurations and oscillation amplitudes over a wide range of frequency parameter

$$w_d = \omega d/V.$$

The majority of tests were to be performed at equilibrium positions close to that of minimum drag since this is the preferred orientation for practical transport applications. However, the maximum drag orientation is obviously important when single strop carriage is employed; hence several tests were to be performed for this configuration in order, amongst other things, to explain the limit cycle oscillation in yaw.

In the contract report¹, two container shapes were investigated, namely the 5:2:2 and the 5:1:1; the former (being the most common) in much greater detail than the latter. In this paper, results are presented for the 5:2:2 container only.

4. THE PRESSURE DISTRIBUTION TESTS

Chronologically, the single degree of freedom pitching tests preceded the design of a multi degree of freedom test facility and will therefore be described first. Static tests were performed only on the single degree of freedom apparatus.

4.1 THE SINGLE DEGREE OF FREEDOM APPARATUS AND TEST RESULTS

4.1.1 Models

Two 1' x 0.4' x 0.4' models were constructed from perspex. The first was designed to be pitched about a minor axis, the second about the major axis. However, since pitch about a major axis is of limited interest only, the first model only will be described herein. It was provided with 39 pressure tappings as shown in Figure 2, these being connected to a scanivalve. In order to improve coverage of the container surface area, the matrix of points was different on each face of the model.

Each pressure point was assumed to give an average pressure over some area, and this area to have some moment arm about the axis of the model. These areas and moment arms represent weightings to be applied to each pressure value when integrating to give total force and moment contributions. Details of weightings are omitted here in the interests of conciseness, but can be found in Reference 1.

4.1.2 Model Support and Actuation

The model support and associated apparatus is shown schematically in Figure 3. The axis of the model contains a position recorder to record angular position at any instant of time.

The forcing mechanism consists of a simple slider crank chain with a sufficiently long connecting rod to provide a close approximation to simple harmonic motion. This was driven by an induction motor through a reduction gear. Oscillation amplitudes could be varied from 10° in steps of about 5° to 29.5° by varying crank length.

4.1.3 Instrumentation

This subject is best introduced by describing the process by which the final results were obtained:-

The pressure points on the model are connected by tubes to the tabulations of the scanivalve. The latter contains a reluctance type transducer which converts an unsteady pressure into an electrical signal directly proportional to and in phase with it. This is done by means of an amplitude modulated 3 KHz carrier signal which is demodulated before being passed through a DC amplifier. The signal is then fed into one of the channels of an analogue to digital converter (ADC), being triggered by a pulse generated by a micro-switch on the slider crank chain. When the trigger pulse attains a preset voltage, the ADC begins to scan the unsteady pressure signal at a pre-determined rate and the digitised output is passed to a Hewlett-Packard 2100A computer and thence on to magnetic tape. Signals from a position recorder on the model are passed into another ADC channel simultaneously and thence via the computer on to the magnetic tape. This tape then forms the input of a second suite of computer programs for evaluation of aerodynamic forces and moments as functions of time, the plotting of moment/attitude loop diagrams and the evaluation of 'overall aerodynamic derivatives' according to the procedure described in Appendix I.

4.1.4 Wind Tunnels

Most of the tests were performed in the 3' 6" open-jet wind tunnel at Bristol University although some comparative tests were performed in the 18' x 8' 6" return section of the University's 7' x 5' wind tunnel. The speed range in the former is 25-135 ft/s and in the latter 0-50 ft/s: the free-stream turbulence intensities in both facilities are between 1 and 1.5%.

4.1.5 Test Technique

To obtain the static aerodynamic characteristics, the container model was set at various incidence angles and the pressures recorded. Each pressure point was selected in turn on the scani-valve and two seconds of signal recorded on magnetic tape. These signals were then averaged and integrated to produce all components of overall forces and moments.

In the dynamic tests, an equilibrium incidence angle was first defined and an oscillation amplitude preset on the slider crank chain mechanism. Then with fixed frequency (just below 1 Hz) and for a selection of windspeeds, the individual pressure points were selected in turn and the pressure signals recorded and duly processed. The parameters selected for the averaging process were such that 31 sample values were taken for each signal trace at a time interval of 0.05 sec; i.e. a total length of signal of 1.5 sec. The voltage traces of the unsteady signals were averaged over four such signal traces. The process was repeated for a selection of equilibrium (datum) attitudes and pitch amplitudes.

The single degree of freedom model tests were really proving tests for the ultimate multi-freedom study and it was decided that aerodynamic nonlinearity with amplitude should be studied in the low frequency parameter regime, $w_d < 0.125$, for which the aerodynamic actions would usually be viewed as quasi-steady.

4.1.6 Results from the Single Degree of Freedom Model Tests

Owing to the exploratory nature of the single degree of freedom tests, only a brief selection of the results will be presented herein.

Static Tests

The initial static tests involved the use of a shorter support sting (length 4") than the 12" sting ultimately employed (see Figure 4). The consequences of aerodynamic interference resulting from the use of the short sting were dramatic, as will be seen in Figure 5. In this Figure $\psi_0 = 0$ denotes the broadside-on configuration. Results from pressure integrations for C_{mz} , the yawing moment coefficient, are shown juxtaposed against results obtained by direct moment measurement⁴. The most significant error ascribable to the use of the short sting is probably that the small region of static stability, $80^\circ < \psi_0 < 100^\circ$, is missed completely. Provision of the longer sting removed this error (see Figure 5) and gave good agreement with the direct moment results.

It is apparent that the 5:2:2 container has the following static stability characteristics in low turbulence flow:-

$0 < \psi_0 < 32^\circ$	stable	(maximum drag region)
$32^\circ < \psi_0 < 82^\circ$	unstable	
$82^\circ < \psi_0 < 90^\circ$	stable	(minimum drag region)

It will be shown later that free stream turbulence of higher intensity can alter this state of affairs near to $\psi_0 = 90^\circ$. It is also apparent that the yaw aerodynamics is highly nonlinear for modest excursions from the minimum drag position - at least in low turbulence flow.

Dynamic Tests

The results presented here were obtained for an impressed yaw oscillation of amplitude $|\delta\psi| = 29.5^\circ$ about equilibrium positions defined by $\psi_0 = 90^\circ, 45^\circ$ and zero at $w_d = 0.12$. Detailed pressure results are presented for the $\psi_0 = 90^\circ$ case only. Force and moment time histories for this case are also presented along with $M_z/q-v-\delta\psi$ loop diagrams for all three equilibrium attitudes.

The pressure traces (Figure 6) for the $\psi_0 = 90^\circ$ case show that as the container yaws to port (i.e. $\delta\psi$ moving from zero to negative values), the pressures at points 10-14 on the starboard face increase to maxima at $\delta\psi = -29.5^\circ$. As this yaw develops, the separated region on the starboard face shrinks, the curved reattachment line moving forward until at $\delta\psi = 29.5^\circ$ the separated region (bubble) has virtually disappeared and the flow is attached across the entire face. Meanwhile, on the port face the pressure traces from points 25-28 indicate decreasing pressures as the separation bubble grows. The position of the reattachment line can be related to the points of near discontinuity on the pressure traces. For example, in the case of pressure point 10, reattachment occurs at about $t = 0.27$ sec where $\delta\psi$ is about -10° . At pressure points 11, 12 and 13,

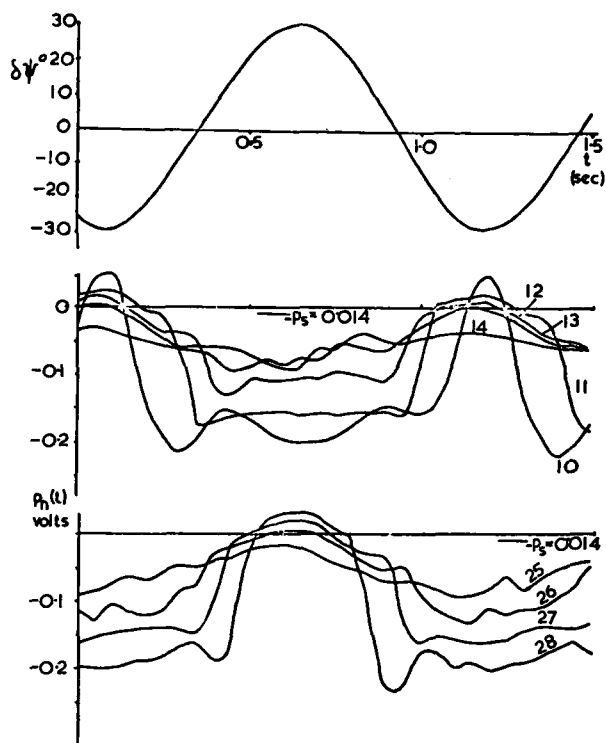


FIGURE 6 1' x 0.4' x 0.4' Model -
Pressure ~ Time
 $\psi_0 = 90^\circ$, $w_d = 0.12$

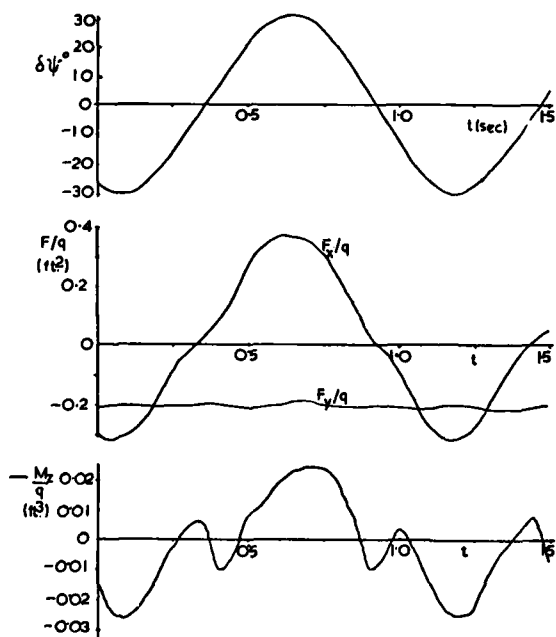


FIGURE 7 1' x 0.4' x 0.4' Model -
Integrated Forces and Moments
 $\psi_0 = 90^\circ$, $w_d = 0.12$

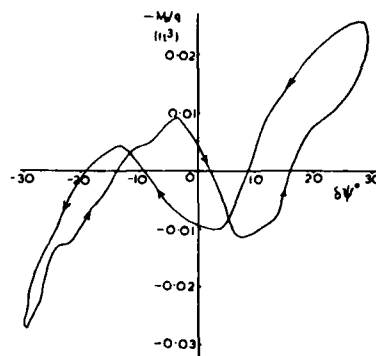


FIGURE 8 1' x 0.4' x 0.4' Model -
Moment ~ Angle Loop Diagram
 $\psi_0 = 90^\circ$, $w_d = 0.12$

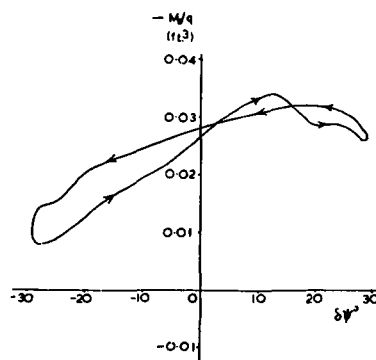


FIGURE 9 1' x 0.4' x 0.4' Model -
Moment ~ Angle Loop Diagram
 $\psi_0 = 45^\circ$, $w_d = 0.12$

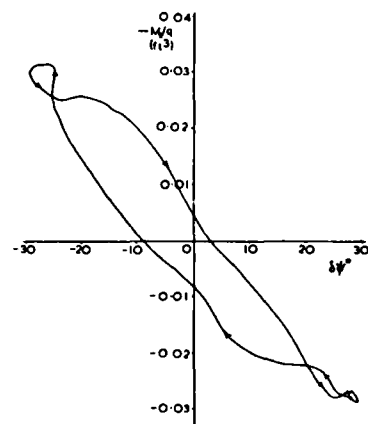


FIGURE 10 1' x 0.4' x 0.4' Model -
Moment ~ Angle Loop Diagram
 $\psi_0 = 0^\circ$, $w_d = 0.12$

it occurs at $t = 0.34, 0.42$ and 0.45 sec. respectively where $\delta\psi$ is zero, $+10^\circ$ and $+12^\circ$ respectively. At the rearmost point, 14, there is no obvious discontinuity and one might conclude that a separation bubble which embraces this point does not exist. While too close a comparison with the static case should not be attempted (for even at $w_d = 0.12$ there will be some noticeable lag), it should be noted that these results accord with the static flow visualisation results to be presented later.

It should be noted that the level of suction beneath a separation bubble increases as the bubble size shrinks and that for a bubble of a given length, the suction beneath it decreases generally with distance from the separation line at the leading edge. The asymmetries in the pressure traces of Figure 6 would not exist had the frequency of the motion been very low: Their existence is indicative, even at $w_d = 0.12$, of dynamic effects other than simple phase lag.

Figure 7 shows the integrated force and moment traces for the $\psi_0 = 90^\circ$ case. The X force is seen to follow the impressed motion reasonably faithfully while the Y force is substantially constant. The yawing moment curve is seen to follow closely the static moment characteristic (Figure 5) as the container passes through the $\psi_0 = 90^\circ$ equilibrium position. However, there are phase lags between the motion of the container and the quasi-steady yawing moment and it is therefore instructive to present the information in terms of a loop diagram (Figure 8).

The rules for interpreting loop diagrams are as follows:-

- (a) If there is no separation (loop) between the moment loci for increasing and decreasing values of $\delta\psi$, then there is no dynamic effect and the system can be said to be dynamically neutrally stable.
- (b) If the points associated with increasing $\delta\psi$ lie above those for decreasing $\delta\psi$ (clockwise loops), then there is positive work done by the incident wind tending to overdrive the motion. In this situation the container is dynamically unstable.
- (c) Anticlockwise loops indicate dynamically stable (damped) situations.
- (d) When coupled loops appear, then over the cycle, the system is damped (driven) if the area enclosed by anticlockwise loops is greater (less) than that enclosed by clockwise loops. When these areas balance, there is no net energy input over the cycle.
- (e) Stable limit cycles occur when there is no net energy exchange over the cycle and there is a destabilising (clockwise) loop in the vicinity of the mean position of the container.

Figure 8 shows that there is an unstable loop in the region of $\delta\psi = 0$ for the $\psi_0 = 90^\circ$ case. The two outer loops tend to stabilise the motion by virtue of being anticlockwise in direction. Thus one has the ingredients for a limit cycle oscillation about the $\psi_0 = 90^\circ$ position provided that at full scale there is sufficient yaw restraint (say from twin, bifilar type, strops) to overcome the state of static instability (positive $\partial M_z / \partial \psi$) which exists as soon as motion builds up beyond the regime of the dynamically unstable central loop. If there is no such yaw restraint (i.e. if single strop suspension is used) then a limit cycle about $\psi_0 = 90^\circ$ will not exist, for as soon as the motion builds up beyond the regime of the central loop a statically unstable situation exists which will diverge the container rapidly to its next statically stable state, i.e. at $\psi_0 = 0$ - the broadside-on position. Indeed, in practice, only a very short time is spent in the unstable oscillatory state near to $\psi_0 = 90^\circ$ and the casual observer would conclude that the divergence to $\psi_0 = 0$ implies static instability at $\psi_0 = 90^\circ$. Such erroneous reasoning, based on free model dynamic tests, has led to much confusion in the past.

Figure 9 shows the loop diagram for the inclined case where $\psi_0 = 45^\circ$. Here there is a small unstable loop centred on $\delta\psi = 10^\circ$ flanked by two stable loops. However, as the unstable loop is not centred on $\psi_0 = 45^\circ$, the ingredients for a limit cycle there are not satisfied. Indeed, the $\psi_0 = 45^\circ$ position is stable in the oscillatory sense, being within an anticlockwise loop, but unstable in the divergence sense since $\partial M_z / \partial \psi$ is positive. Figure 10 shows the loop diagram for the broadside-on position, $\psi_0 = 0$. Here, the unstable central loop is a dominant feature so that any limit cycle in practice could well have amplitudes in excess of 30° . Since static stability obtains throughout the region encompassed by the diagram, an oscillatory situation will exist in practice whatever the nature of the strop suspension (assumed passive).

4.2 THE MULTI-DEGREE OF FREEDOM APPARATUS AND TEST RESULTS

Consideration of the results of some preliminary freely suspended model tests indicated that

- (a) comprehensive dynamic model tests with prescribed motion would need to cater for more than one degree of freedom; probably two, possibly three or even four
- (b) the particular degrees of freedom needed with their associated amplitudes and phase relationships would be difficult to anticipate.

It was therefore decided to attempt to design a rig with six degrees of freedom where any combination of freedoms could be used, with selected amplitudes and phase lags. One type of rig might have involved three degrees of freedom angular movement of a model about a universal joint mounted on sets of rails giving the three translational freedoms. Such a rig would, however, seem extremely difficult to engineer and would be unduly costly. Furthermore, problems of aerodynamic interference (the importance of which has already been demonstrated, Figure 5) would abound. The design chosen moves the complexity from inside the model and tunnel by using wire supports, and concentrates it in the actuating mechanism outside the tunnel. The tunnel used for the six degree of freedom rig was the 18' x 8' 6" return section of the 7' x 5' tunnel at Bristol University.

The wire supports (Figure 11) are in the form of eight wire circuits with one additional wire with spring to take the dead weight of the model. (NB. The spring could not act dynamically.) The eight circuits are two more than necessary to define six degrees of freedom, but were deemed desirable as being more versatile and able to cope with a variety of model shapes. The over-constraint is taken out by suitable springs. Each circuit passes from the model over four pulleys back to the model and incorporates a spring tensioning device which ensures that any extension required in a circuit - say in a vertical circuit when the model is moved horizontally - is split equally between the two halves of the circuit (see Figure 12). The tensioning device thus acts kinematically, but not dynamically. Four circuits are vertical defining vertical, pitch and roll motions; four are horizontal defining fore-and-aft, side and yaw motions. The tensioning device for each circuit (Figure 12) is on a vertical lever pivotted at its upper end, with the circuit wires passing over pulleys at the lower end and with attachment for actuation also near the lower end.

Actuation for each circuit is from outside the tunnel and operates below the glass walls of the tunnel. The actuator design is illustrated for one circuit in Figure 13. The motor is a 3.5 HP, 1440 rpm Crompton-Parkinson 230 V D.C. machine controlled to $\pm 1\%$ on speed by an air-cooled thyristor unit. It drives two pulleys with 90° phase difference; these pulleys incorporate tensioning devices similar to that of Figure 12 and are attached by wire circuitry to a pyramid of pulleys with 2:1 diameter ratios between consecutive pulleys. Six pulleys defining movement in six degrees of freedom are driven by the pyramid pulleys at chosen amplitudes and with phase relationships of 0, 90° , 180° or 270° degrees. Individual circuits are connected to three of these pulleys in a way that compounds the individual movements into the single appropriate movement for the circuit. At constant motor speed, the device is capable of producing virtually pure SHM of the model at translational amplitudes up to 1 ft.

4.2.1 Container Model

A 2' x 0.8' x 0.8' plywood model was provided with 78 standard pressure tappings; 15 on each major face and 9 on each minor face. Additionally 10 tappings were provided on each major face and 4 on each minor face for the purpose of obtaining more-detailed pressure distributions when desired. For the most part, the 78 standard tappings were used to assess the overall forces. In contradistinction to the single degree of freedom model, it was decided that the basic arrangement of pressure points should be entirely regular and symmetrical: this facilitates computation and also allows for the use of a technique for minimisation of temperature drift errors to which scani-valves are susceptible. (Pressure point locations are shown in Figure 14.) Two scani-valves were incorporated inside the container model; all pressure tube lengths were thus less than 1 ft.

4.2.2. Instrumentation and Test Technique

In view of the necessity for lower speeds (higher values of w_d), the instrumentation was slightly different from that used in the single degree of freedom tests since smaller pressures had to be sensed. It was therefore necessary to use more sensitive scani-valve transducers requiring separate auxiliary equipment. These transducers work on the principle of the condenser microphone. When sensing unsteady pressures a diaphragm, two microns thick, moves and in so doing varies the frequency of the 5.5 MHz carrier wave. Thus, frequency demodulation now has to be applied to give a voltage signal proportional to and in phase with the unsteady pressure. This type of transducer requires an oscillator to be mounted in its vicinity; therefore it was necessary to mount two oscillators within the model alongside the scani-valves. Output signals were processed in much the same way as in the single degree of freedom case.

It was decided to improve the accuracy of the triggering device (see Section 4.1.3) by reducing the pulse rise time and by improving the manner by which the computer program triggers at the instant the pulse rises. In this way, the average error in phase angle prediction was reduced from 5% to below 3%. Model position, as before, was monitored by using an angular position recorder on the motor drive shaft.

The integration procedure used in the single degree of freedom tests involved a point by point march around the container and an ultimate weighted summation. Such a procedure applied in the multidegree of freedom tests would lead to unintelligible force and moment results since the tunnel used is recirculatory and temperature rises, through the (sometimes lengthy) duration of a test, produce drifts in the scani-valve transducer outputs. It was possible to overcome this problem without having to expend heavily on temperature control within the tunnel. The solution of the drift problem

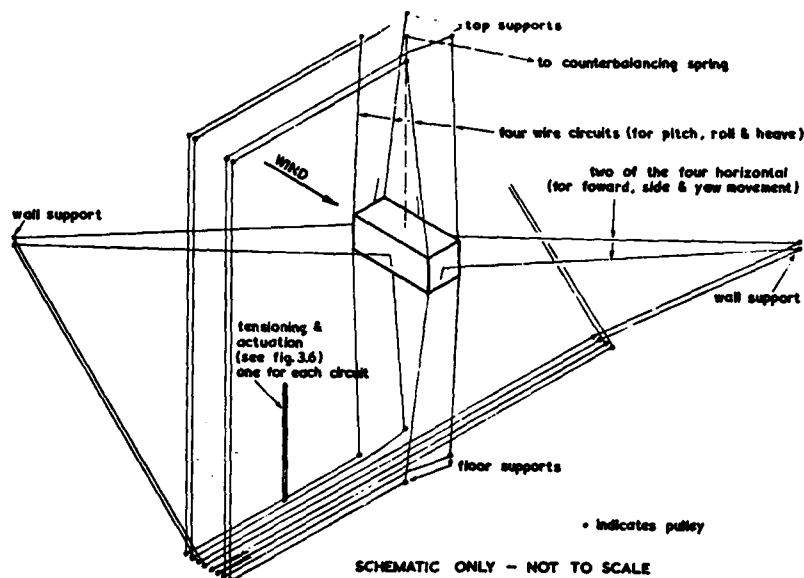


FIGURE 11 Multi-Degree of Freedom Wire Support Rig

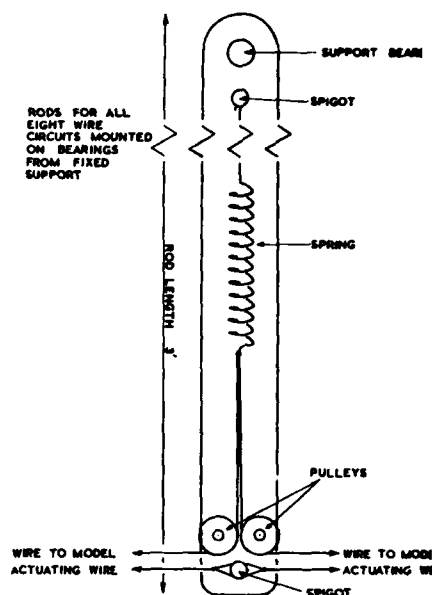


FIGURE 12 Multi-Degree of Freedom Rig - Arrangement of Tensioning Devices

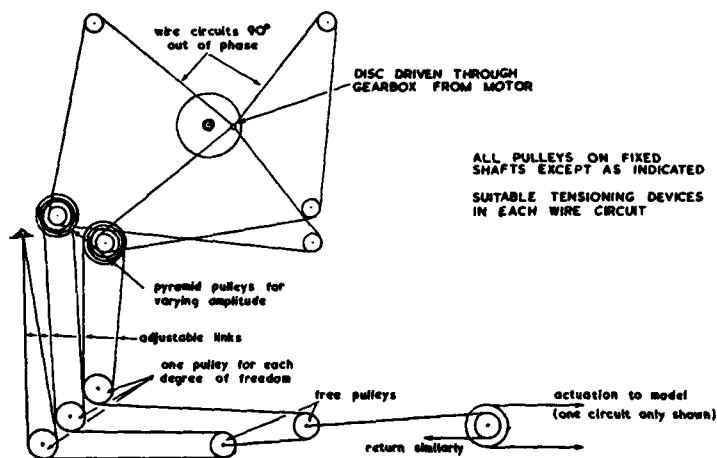


FIGURE 13 Multi-Degree of Freedom Rig - Actuation Design (Schematic)

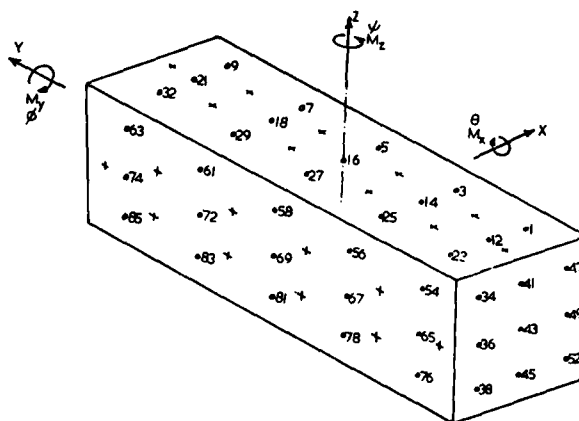
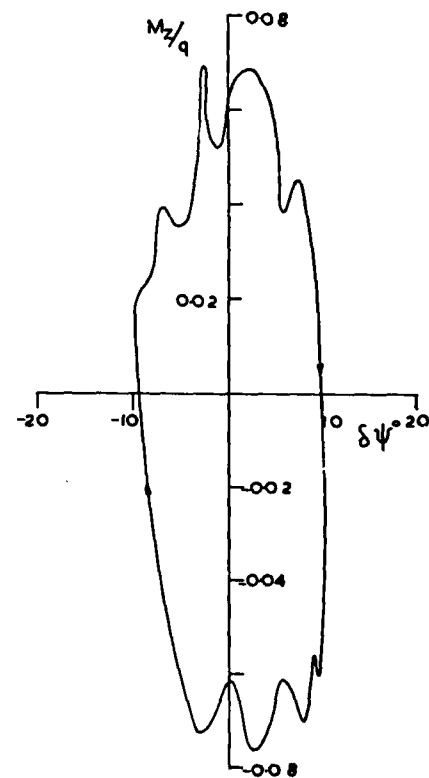


FIGURE 14 Multi-Degree of Freedom (2'x0.8'x0.8') Model - Pressure Tappings and Axes. (opposite points on unseen faces are one number more than those shown)

FIGURE 15 2' x 0.8' x 0.8' Model Moment - Angle Loop Diagram. $\psi_0 = 90^\circ$, $\theta_0 = 0^\circ$, $w_d = 0.45$

consisted of adopting an order of marching through the mesh of points which involved, alternately, reading points on opposite faces of the container. The time between readings for these opposite points is optimally short and the temperature effect on the difference (which is always implied in overall force and moment calculation) is minimised. Also, at every tenth tabulation of the scani-valve, reference static pressure is measured so that the temperature drift can be subtracted from the raw pressure readings, again minimising temperature effects.

The actual test procedure was virtually the same as that already described for the single degree of freedom case.

4.2.3 Results from the Multi-Degree of Freedom Tests

A massive amount of information was obtained in these tests and it would be clearly inappropriate to attempt to present all of it here. Only those features having particular interest will be discussed herein and the reader is referred to Reference 1 for greater detail.

Unfortunately, time did not permit the rig to be used to the full extent of its versatility and the largest number of degrees of freedom employed in combination was two. However, the facility for rigging any desired datum position and imposing any one of the six possible motions was fully exploited.

(a) Minimum Drag Configuration: $\psi_0 = 90^\circ$, $\theta_0 = 0$. Yaw Motion Imposed

This case has already been discussed for low frequency parameters in Section 4.1.6. Detailed pressure distributions will therefore not be shown and it suffices to say that the previous results were confirmed in the present tests. Loop diagrams at the smaller yaw amplitude of $|\delta\psi| = 10^\circ$ are found, as might have been expected, to comprise just one clockwise loop corresponding to the central loop of Figure 8; see for example Figure 15 which relates to $w_d = 0.45$. (The spikes on the loop are due to support wire vibration: the wires were inadequately tensioned). The loop for $w_d = 0.32$ (not shown) was of smaller area and was rotated bodily in the anticlockwise sense by some 15° relative to the $w_d = 0.45$ loop. The increase in loop area between these two w_d values was small, but suggested a destabilising effect of w_d in this range for a yaw oscillation of 10° amplitude. The body rotation of the loop as w_d increases in this small w_d range would indicate a statically stabilizing effect of w_d , if such can be conceived! This is clearly an acceleration effect. Comparison with the loop diagram for $w_d = 0.12$ of Figure 8 would seem to confirm this effect, but the validity of comparison of loops obtained at different amplitudes is questionable.

In order to provide data for stability analyses (asymptotic type), it is instructive to evaluate 'overall aerodynamic derivatives' for small amplitude excursions from the datum position. These may then be viewed as conventional stability derivatives, and the manner in which these vary with w_d is of paramount interest. This has been done in Table I for the present case for a yaw amplitude of 5.5° . The important

TABLE I AERODYNAMIC 'OVERALL DERIVATIVES'

$$\psi_0 = +90^\circ, \theta_0 = 0^\circ, \delta\psi = \pm 5.5^\circ$$

w_d	.3740	.4208	.5611	.8416
$C_{x\psi}$	-.9406	-.9172	-.9994	-.6074
$C_{y\psi}$	-.1126	-.1059	-.2317	-.3408
$C_{z\psi}$.1446	-.0152	.0477	.0269
$C_{mx\psi}$.0491	-.0574	-.0543	-.0986
$C_{my\psi}$	-.0117	.0164	.0363	.0194
$C_{mz\psi}$	-.1780	-.0126	.1751	.3039
$C_{\dot{x}\psi}$	1.0182	1.4277	.5705	.3179
$C_{\dot{y}\psi}$	-.4202	-.2039	-.0606	-.1226
$C_{\dot{z}\psi}$.1326	.0439	.1111	-.0207
$C_{m\dot{x}\psi}$	-.1338	.0522	-.0223	-.0317
$C_{m\dot{y}\psi}$	-.0876	.0512	.0235	-.0162
$C_{m\dot{z}\psi}$	1.2346	.8605	.7822	.3462

derivatives in respect of single freedom yaw stability are $C_{mz\psi}$ and $C_{\dot{m}z\psi}$. The former represents the mean slope of the loop and the latter the loop area. A positive value of the former implies a static destabilizing effect and of the latter a dynamic destabilising effect (negative direct damping). It is seen that $C_{mz\psi}$ is negative at low values of w_d becoming positive beyond $w_d = 0.45$. On the other hand $C_{m\dot{z}\psi}$ is initially

positive and diminishes as w_d increases. Thus, over the range $0.374 < w_d < 0.8416$, the role of w_d determining yaw stability is statically destabilising and dynamically stabilising. (Note that the converse appeared to be true for $w_d < 0.45$ above, but that the above conclusions related to larger amplitude motions, namely $|\delta\psi| = 10^\circ$, over which the static variation of C_{mz} (Figure 5) is highly nonlinear).

All of the important cross derivatives, namely $C_{x\psi}$, $C_{y\psi}$, $C_{z\psi}$ and $C_{mz\psi}$ all show substantial variations with w_d . The appearance of unexpected derivative values (e.g. $C_{z\psi}$, $C_{my\psi}$, etc.) is possibly due to small rigging errors or to flow swirl in the tunnel. Loop diagrams relating to the extremities of the w_d range are presented in Figure 16. Their dispositions and areas bear out the $C_{mz\psi}$ and $C_{mz\dot{\psi}}$ derivative values given in the first and last columns of Table I.

In order to throw more light on variations of stability parameters with w_d at large amplitude, some tests were performed over the range $0.15 < w_d < 1.08$ for an impressed yaw amplitude of 11.5° . The results are presented here in the form of 'overall aerodynamic derivatives' in Table II. (The term 'overall' is again prefixed

TABLE II AERODYNAMIC 'OVERALL DERIVATIVES'

$$\psi_0 = +90^\circ, \theta_0 = 0^\circ, \delta\psi = \pm 11.5^\circ$$

w_d	.1509	.1783	.2268	.3441	.3562	.4424	.6452	1.07547
$C_{x\psi}$	-1.2419	-1.1723	-1.1589	-1.1779	-1.0738	-1.1085	-.9651	-.7853
$C_{y\psi}$	-.0427	.1595	-.0373	-.0622	.0478	-.0180	-.0065	.0068
$C_{z\psi}$	-.0144	-.0222	-.0063	.0484	-.0206	-.0018	-.0429	.0241
$C_{mx\psi}$	-.0223	-.0244	-.0349	.0240	-.0566	-.0092	-.0547	-.0388
$C_{my\psi}$.0001	.0124	.0200	-.0052	.0164	-.0146	.0089	.0119
$C_{mz\psi}$	-.2040	-.1820	-.2201	-.0268	-.0944	-.0363	.1235	.3792
$C_{x\dot{\psi}}$	1.3986	1.1802	-.5212	1.0679	.4967	.2130	.4036	-.0827
$C_{y\dot{\psi}}$	-.2799	-.2294	.1190	-.0607	.0098	-.1730	-.1602	-.0283
$C_{z\dot{\psi}}$.2884	-.1229	.2333	-.0123	-.0451	.0920	.0309	.0760
$C_{mx\dot{\psi}}$.0632	-.0385	.0905	-.1060	-.0751	-.0454	.0551	.0289
$C_{my\dot{\psi}}$.0228	.0674	-.1137	-.0029	.0074	.0376	.0090	.0244
$C_{mz\dot{\psi}}$.8226	.7066	.7281	.7240	.6973	.7042	.3765	.1958

since the yawing motions now embrace a highly nonlinear region of the static yawing moment curve; Figure 5). The variations of the stability derivatives $C_{mz\psi}$ and $C_{mz\dot{\psi}}$ are anything but monotonic over this w_d range. There is an overall tendency, however, for $C_{mz\psi}$ to increase from negative values, becoming positive as before at $w_d \sim 0.45$; as w_d is increased and for $C_{mz\dot{\psi}}$ to become less positive, again as before. The $C_{x\dot{\psi}}$ values are clearly less than those in Table I for corresponding w_d values. This behaviour is expected because there is a small incursion into stabilising loops (Figure 8) when $|\delta\psi| = 11.5^\circ$.

Note that the derivatives presented in Table II should not be used in an asymptotic stability analysis in view of the large amplitude used in their determination.

(b) $\psi_0 = 90^\circ, \theta_0 = 5^\circ$: Yaw Motion Imposed

This is the situation where the major axis is 5° from the stream direction in the nose-up incidence sense and where a yaw oscillation (of amplitude 5.5°) is imposed about the z body axis.

The aerodynamic derivatives for this case are presented in Table III. The important derivatives $C_{x\psi}$, $C_{y\psi}$, $C_{mz\psi}$, $C_{x\dot{\psi}}$, $C_{y\dot{\psi}}$ and $C_{mz\dot{\psi}}$ show similar variations with w_d as those of the minimum drag case (Table I). Note, however, that $C_{x\dot{\psi}}$ actually changes sign at the highest w_d value in the present case. Note also the appearance of $C_{my\psi}$ and $C_{my\dot{\psi}}$ as important derivatives, perhaps unexpectedly, for this case. This can be ascribed to the separation bubble asymmetry with regard to the median major axes of the port and starboard faces: the bubbles are biased above these axes at equilibrium and as their sizes fluctuate in a yaw oscillation, a rolling moment is produced. The $C_{mz\psi}$ values show that the sign is reversed from negative to positive at a much lower w_d value than in the $\theta_0 = 0$ case. Indeed, it is known from the static results of Reference 4 that small angles of incidence from the minimum drag configuration render yaw statically unstable (i.e. they effectively remove the nonlinearity from the C_{mz}/ψ_0 characteristic near $\psi_0 = 90^\circ$ in Figure 5). The $C_{mz\dot{\psi}}$ values are smaller than those of the $\theta_0 = 0$ case, indicating that the effect on yaw of a small incidence is dynamically stabilizing. It will be shown later that when $\theta_0 \approx 10^\circ$, the dynamic instability in yaw is completely eliminated.

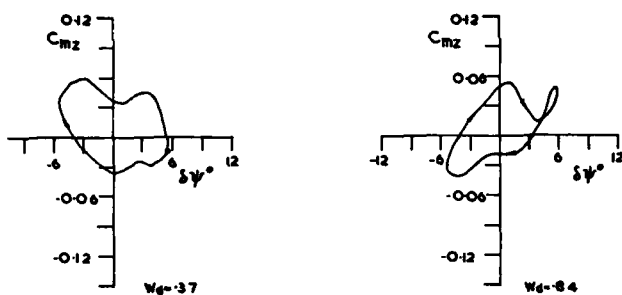


FIGURE 16 2' x 0.8' x 0.8' Model - Moment Coefficient - Angle Loop Diagrams. $\psi_0 = 90^\circ$, $\theta = 0^\circ$

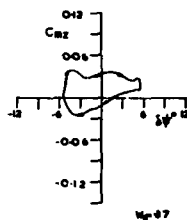


FIGURE 17 2' x 0.8' x 0.8' Model - Moment Coefficient - Angle Loop Diagram. $\psi_0 = 90^\circ$, $\theta = 5^\circ$

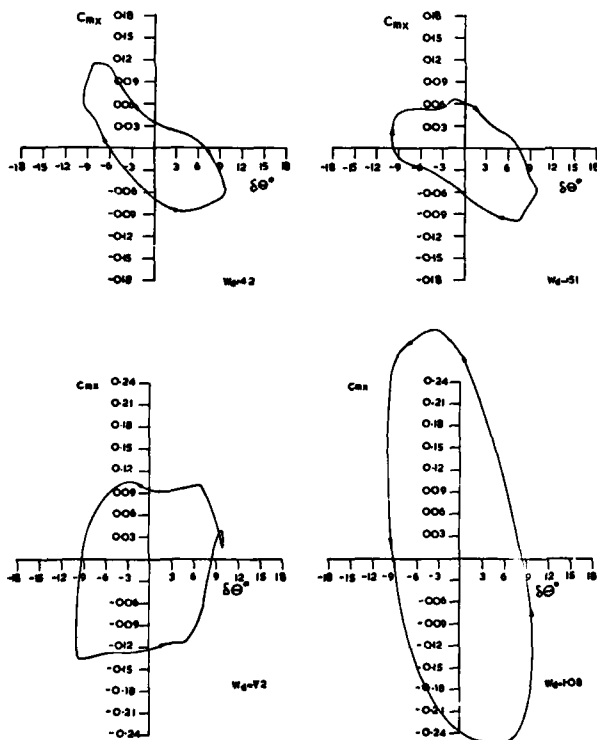


FIGURE 19 2' x 0.8' x 0.8' Model - Moment Coefficient - Angle Loop Diagrams. $\psi_0 = 90^\circ$, $\theta_0 = -90^\circ$

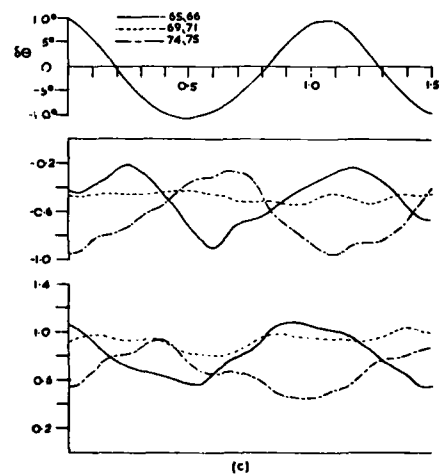
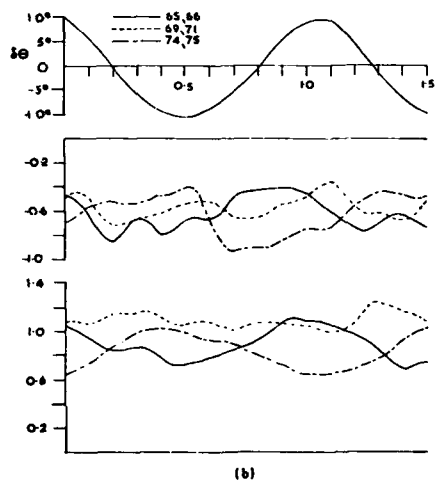
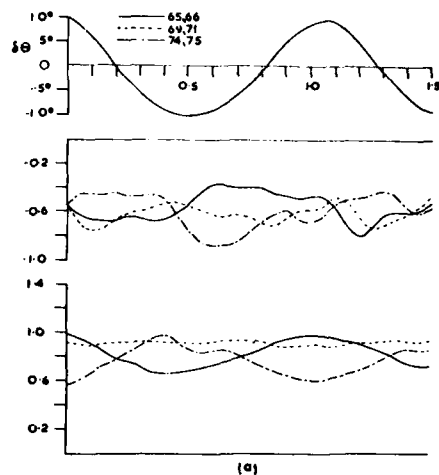


FIGURE 18 2' x 0.8' x 0.8' Model - Pressure Traces for Broadside-On Oscillation. Front and Rear Faces. $\psi_0 = 90^\circ$, $\theta_0 = -90^\circ$.
(a) $w_d = 0.44$
(b) $w_d = 0.57$
(c) $w_d = 0.88$

TABLE III AERODYNAMIC 'OVERALL DERIVATIVES'

$$\psi_0 = +90^\circ, \theta_0 = +5^\circ, \delta\psi = \pm 5.5^\circ$$

w_d	.3441	.3871	.5377	.8416
$C_{x\psi}$	-1.2937	-1.3096	-1.2558	-.9905
$C_{y\psi}$	-.1839	-.1234	.1052	-.2551
$C_{z\psi}$	-.0386	-.0556	-.2263	.1552
$C_{mx\psi}$	-.0169	-.0439	-.0868	.0348
$C_{my\psi}$	-.2182	-.1695	-.1854	-.1820
$C_{mz\psi}$	-.0133	.0452	.2302	.4008
$C_{x\dot{\psi}}$	1.2686	.7818	.6500	-.1182
$C_{y\dot{\psi}}$	-.3639	-.3016	-.2296	-.1765
$C_{z\dot{\psi}}$.1804	-.0051	-.0016	.1144
$C_{mx\dot{\psi}}$.0965	.1125	.1744	.0517
$C_{my\dot{\psi}}$.2656	.2484	.2175	.0228
$C_{mz\dot{\psi}}$.8076	.6459	.5439	.2843

The same is also true, of course, at $\theta_0 = -10^\circ$ which gives the basis for carrying containers in a nose-down attitude.

A typical loop diagram is presented in Figure 17 for $w_d = 0.84$. This should be compared with the corresponding diagram of Figure 16, and it will be seen that the behaviour of the corresponding $C_{mz\psi}$ and $C_{mz\dot{\psi}}$ values accord with the behaviour of the loop diagrams.

The appearance of C_{my} derivatives of appreciable magnitude points to the possibility of significant yaw/roll coupling in the full scale problem. Note that these derivatives are of the opposite sign when $\theta_0 = -5^\circ$. Full details of the latter case will be found in Reference 1.

(c) Broadside-on Position: $\psi_0 = 90^\circ, \theta_0 = -90^\circ$

As this configuration is fundamentally important to full scale single-stop carriage of a container load, it warrants detailed consideration. The reasons for considering the configuration $\psi_0 = 90^\circ, \theta_0 = -90^\circ$ with θ oscillations imposed rather than simply $\psi_0 = 0, \theta_0 = 0$ with ψ oscillations imposed need not be of concern here. The broadside-on configuration has already been shown to be dynamically unstable at low values of w_d and to exhibit a large amplitude limit cycle (Figure 10). However, at first sight one might suspect that the angular motion should be damped by drag. Clearly, stagnation type pressures on the windward face cannot contribute to the instability. Again, pressures on the small end faces, while being interesting, are hardly likely to contribute strongly since their moment arms about the rotation axis are small. (Tests on a container with hollow ends of considerable depth, thus relieving the suctions in the region under the shear layer, had also exhibited negative damping when allowed to oscillate about a central minor axis. This supports the contention that pressures on the small end faces are not responsible for the instability.) Pressures on the major faces parallel to the free stream clearly cannot contribute. The inescapable conclusion is that it is the outboard base pressures which must support the instability. It is therefore appropriate to study these pressures in some detail.

Figure 18 gives the base pressure time histories at points 65, 74 (outboard) and 69 (central) along with the opposite front face pressures 66, 75 (outboard) and 71 (central) for an impressed amplitude $|\delta\theta| = 10^\circ$, for $w_d = 0.44, 0.57$ and 0.88 . The front face pressures are broadly in phase with the impressed motion for each of the w_d values. At $w_d = 0.44$, Figure 18a shows that the pressures at the outboard points 65 and 74 are in antiphase (as expected) and broadly in quadrature with the motion and in directions which support the motion. At $w_d = 0.57$, Figure 18b shows similar characteristics, but with greater net pressures supporting the motion. At $w_d = 0.88$, Figure 18c shows that the antiphase pressures at points 65 and 74 have now reversed their directions and, still being broadly in quadrature with the impressed motion, conspire to damp it. This is clearly a most radical effect of frequency parameter on the stability characteristics of the container.

To confirm these pressure-based deductions, Figure 19 presents loop diagrams for $w_d = 0.42, 0.51, 0.72$ and 1.08 . The loops for $w_d = 0.42$ and 0.51 are clockwise and hence indicate negative damping while those for $w_d = 0.72$ and 1.08 are anticlockwise and hence indicate positive damping. The larger area of the loop for $w_d = 1.08$ indicates that the damping effect is stronger there than in the $w_d = 0.72$ case.

To add further weight to what has already been said, Table IV presents the overall

TABLE IV AERODYNAMIC 'OVERALL DERIVATIVES'

$$\psi_0 = 90^\circ, -\theta_0 = 90^\circ, \delta\theta = \pm 10^\circ$$

w_d	.2809	.3795	.4176	.5121	.5259	.6938	.7169	1.0754
$C_{x\theta}$.0674	.0186	-.1294	-.0666	-.1652	-.0318	.2352	.1009
$C_{y\theta}$.7435	.3634	-.1843	-.0861	-.7925	-2.9043	-3.4900	-3.0443
$C_{z\theta}$.0037	.1245	-.0166	-.2061	-.0923	-.1708	-.3557	-.6973
$C_{mx\theta}$	-.6279	-.5651	-.3906	-.2083	-.2090	.2501	.2972	-.7786
$C_{my\theta}$	-.0469	-.0521	.0905	-.0159	.0867	-.0278	.0043	.0294
$C_{mz\theta}$.0485	.0850	.1509	.1459	.1347	.0485	.0753	-.0840
$C_{x\dot{\theta}}$	-.1831	.1320	-.1860	-.2886	.3391	.3512	-.0881	-.0904
$C_{y\dot{\theta}}$	-3.1131	-3.6412	-3.2447	-3.3970	-3.3400	-1.8473	-.8090	2.5476
$C_{z\dot{\theta}}$.0155	-.1710	.0360	-.2608	.1136	-.0196	-.0635	.4850
$C_{mx\dot{\theta}}$.7467	.7864	.7716	.6504	.8277	.1132	-.9130	-1.3648
$C_{my\dot{\theta}}$.0043	.0289	.0813	.0401	.0678	.020	-.1072	.0442
$C_{mz\dot{\theta}}$.2148	-.0575	-.0314	-.1128	-.0513	-.1178	.0362	-.0637

derivatives for this case for a wide range of frequency parameters. The derivatives $C_{mx\theta}$, $C_{my\theta}$ are those which indicate stability about the rotation axis. It is interesting to note that static stability ($C_{mx\theta}$) is continuously eroded as w_d increases, is lost between $w_d = 0.6$ and 0.8 and regained thereafter up to $w_d = 1.08$. Dynamic damping ($-C_{mx\dot{\theta}}$), while fluctuating somewhat, is negative up to $w_d = 0.7$ and increasingly positive thereafter, in accordance with the loop diagrams and indeed with the base pressure traces.

The C_x , C_{my} and C_{mz} derivatives should be zero in truly symmetric flow. Table IV shows that some of these derivatives have sizeable values, though exhibit little consistency over the range of frequency parameter.

Finally, it might be observed with more than a little concern, that the appropriate frequency parameter for the broadside-on case should not be w_d , which is based on major axis length, d , but rather $w_h = 0.4 w_d$, based on minor axis length. The above dynamic stability changeover thus occurs at $w_h = 0.28$ or thereabouts, which in conventional aerodynamics terms is a very modest value indeed. However, for bluff bodies with major axis normal to the flow (or two dimensional bluff bodies) the most pertinent criterion defining the applicability limit of quasi-static ideas is some fraction of the Strouhal number which describes the frequency parameter of the vortex shedding process. Regrettably, the vortex shedding frequency was not measured in the tests described herein, but for a 3:1:1 half model⁶ a Strouhal number of 0.55 has been measured. This has to be doubled to give the frequency parameter at which yaw motions would 'lock-on' to the shedding frequency, and the above critical value of w_h is almost exactly one quarter of this value. While this fraction might be significant, it seems unlikely that the natural vortex formation process could be 'entrained' through such a frequency ratio. Further work is clearly called for in this area.

(d) Minimum Drag Position: $\psi_0 = 90^\circ$, $\theta_0 = 0$: Sideslip Motions Imposed

This case was studied for $w_d = 0.32$ and 0.84 for an impressed x motion of amplitude 2 inches. Loop diagrams for both C_x and C_{mz-y-x} are presented in Figure 20. The former are stable in the dynamic damping sense, the damping being greater at the higher w_d value, but the latter merely show x/C_{mz} coupling.

(e) $\psi_0 = 90^\circ$, $\theta = 5^\circ$: Sideslip Motions Imposed

This case is covered in more detail than the previous one in view of its relevance to the nose-down container carriage position. Loop diagrams for $w_d = 0.34$ and 0.88 are given in Figure 21. These are stable, as in the previous case, with stability increasing with w_d , but an unexpected mean sideforce has appeared. This suggests erroneous rigging at a mean yaw angle different from $\psi_0 = 90^\circ$ by a small amount. Overall derivatives are presented in Table V from which it is seen that the C_{xx} derivative is substantially constant as w_d varies: the net increase in damping between $w_d = 0.34$ and 0.88 is only about 5%.

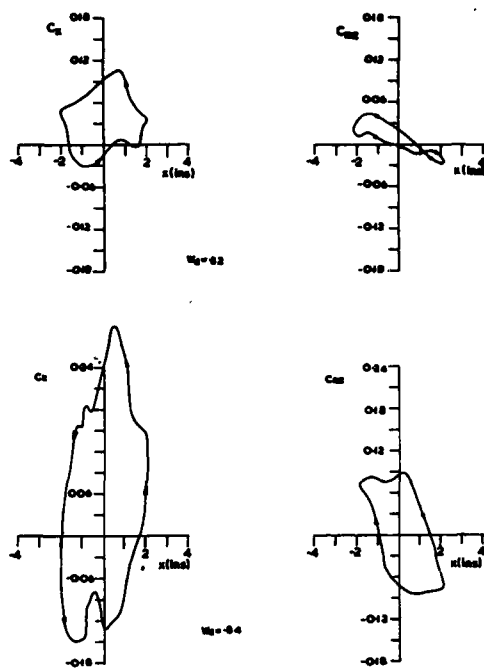


FIGURE 20 2' x 0.8' x 0.8' Model - Force & Moment Coefficient - Linear Displacement Loop Diagrams. $\psi_0 = 90^\circ$, $\theta_0 = 0^\circ$

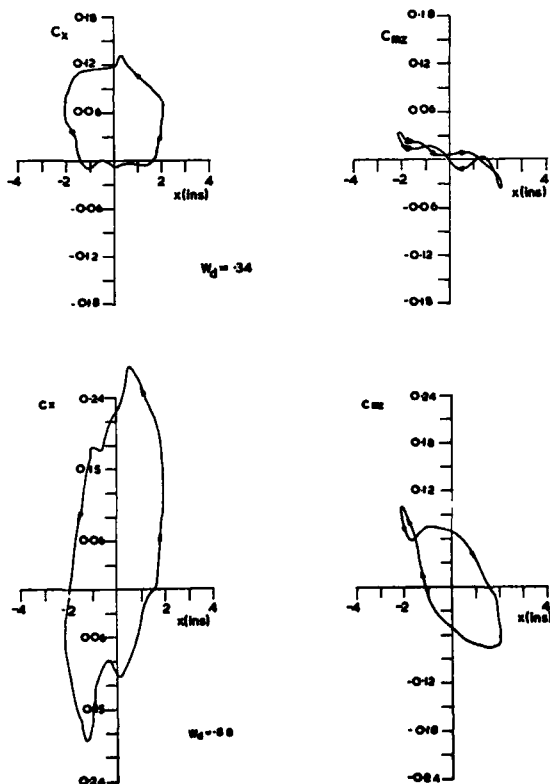


FIGURE 21 2' x 0.8' x 0.8' Model - Force & Moment Coefficient - Linear Displacement Loop Diagrams. $\psi_0 = 90^\circ$, $\theta_0 = 5^\circ$

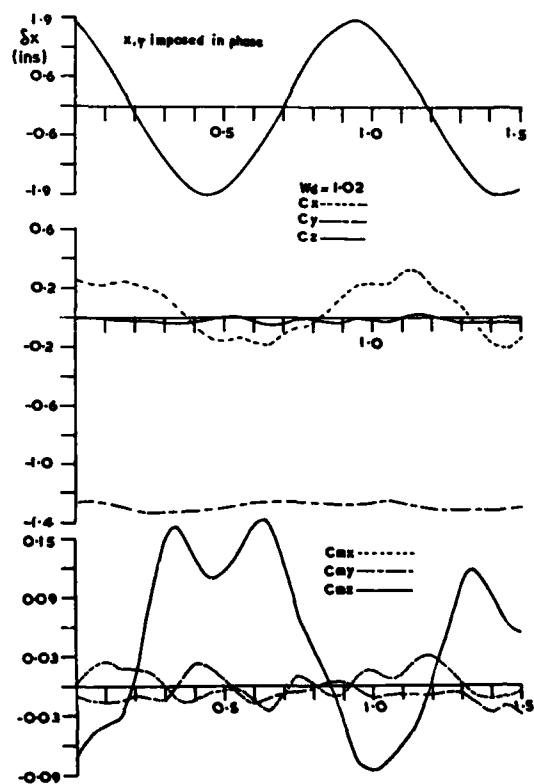
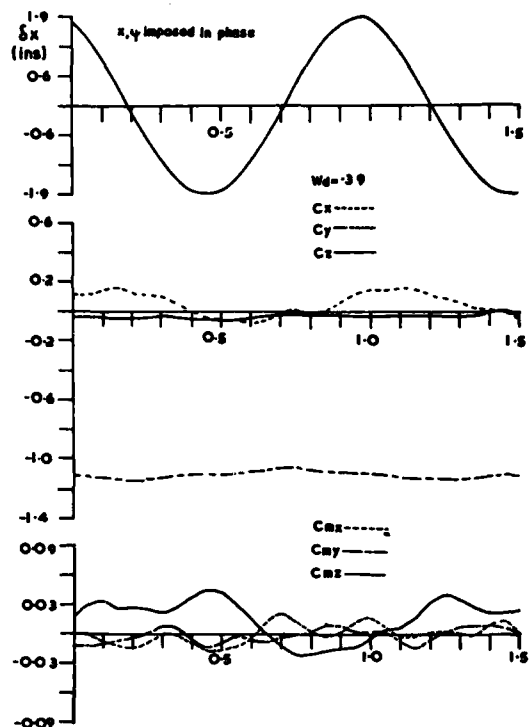


FIGURE 22 2' x 0.8' x 0.8' Model - Force and Moment Traces for Combined Angular and Linear Displacement. $\psi_0 = 90^\circ$, $\theta_0 = 0^\circ$, $\delta x = 1.9''$, $\delta \psi = 3.5^\circ$.

TABLE V AERODYNAMIC 'OVERALL DERIVATIVES'

$$\psi_0 = +90^\circ, \theta_0 = 5^\circ, \delta x = 2.5''$$

w_d	.3366	.4208	.5611	.8799
C_{xx}	-.0655	-.1826	.1436	1.0162
C_{yx}	.4183	.3462	.3467	.0195
C_{zx}	-.1373	-.1249	-.1717	-.0417
C_{mxx}	-.1079	-.0239	-.0079	-.1576
C_{myx}	-.0925	-.0730	-.1596	-.1350
C_{mzx}	-.201	-.1854	-.5155	-.6912
$C_{\dot{x}x}$	-1.9002	-2.0094	-2.0354	-2.0159
$C_{\dot{y}x}$.2674	.3487	.2798	.3526
$C_{\dot{z}x}$	-.1807	-.3212	.1658	-.0150
$C_{m\dot{x}x}$	-.2073	-.1136	-.0576	-.2260
$C_{m\dot{y}x}$	-.3224	-.0766	-.2171	-.1793
$C_{m\dot{z}x}$.1365	.2554	.3363	.4940

The derivative $C_{\dot{x}x}$, which on quasi-static theory should be zero, shows some interesting dependence on w_d . It should be noted (see Appendix I) that the translational overall derivatives include all in-phase actions so that the variation of $C_{\dot{x}x}$ with w_d represents a virtual inertia or acceleration effect. This is true for all translational derivatives presented, but the very large values of C_{yx} at low frequency parameter defy explanation and could be attributed to experimental error, although it should be remembered that the derivative is based on area $h^2 = 0.64 \text{ ft}^2$ while C_{xx} and C_{zx} are based on $hd = 1.6 \text{ ft}^2$. The C_{myx} derivative is significant here for the same reasons as in case (b) above.

The contention that the highest value of $C_{\dot{x}x}$, namely 1.0162 at $w_d = 0.88$, is a virtual inertia effect warrants closer investigation: The mass of air displaced by the container is $m_c = 2' \times 0.8' \times 0.8' \times 23.8 \times 10^{-4} \text{ slug} = 30.4 \times 10^{-4} \text{ slug}$. Let m_a be actual mass of air moved to give $C_{\dot{x}x} = 1.016$; then $1.016 q h d = X_{\dot{x}} = \omega^2 m_a$. In this case $V = 12.5 \text{ ft/sec}$, $\omega = 5.65 \text{ rad/sec}$, hence $m_a = 95 \times 10^{-4} \text{ slug}$. This suggests that the mass of air moved in this case is about three times greater than that actually displaced by the container. The positive value of $C_{\dot{x}x}$ indicates that the acceleration experienced by this mass is in phase with the x displacement of the container; i.e. in antiphase with the acceleration of the container. At the lower values of w_d , a smaller virtual mass is accelerating in phase with container acceleration, thus producing numerically small $C_{\dot{x}x}$ derivatives of negative sign.

(f) Minimum Drag Configuration: $\psi_0 = 90^\circ, \theta_0 = 0$: Combined Yaw and Sideslip Motions Applied in Phase

As an example of the effects of combined motion, the simultaneous imposition of a $3\frac{1}{2}^\circ$ amplitude yaw motion and a 2° amplitude sideslip motion, in phase, was studied. The results are presented in Figure 22 in terms of time histories of force coefficients. In this Figure, which relates to two values of w_d , 0.39 and 1.02, the x (sideslip) signal is displayed as a displacement reference. A symmetric C_x force is recorded broadly in quadrature with the motion and in the sense to oppose it. The C_x amplitude is greater at the higher w_d value indicating a stabilizing effect of w_d . C_y , the steady drag, is virtually constant, as expected, for both w_d values although it is marginally larger at the higher w_d value. C_z is sensibly zero, again as expected.

The dominant moment coefficient is C_{mz} in both cases, but it has much larger amplitude at the higher w_d value. At $w_d = 0.39$, quadrature components of C_{mz} are seen to oppose the yaw motion. (It should be remembered that yaw per se was negatively damped: with in-phase sideslip at this particular amplitude ratio it is now positively damped). At $w_d = 1.02$, however, a large destabilizing quadrature component exists on a motion upstroke while on a downstroke this component is close to zero. Thus, in a net sense, one should expect negative damping. (Cf. case (a) above where, for yaw per se, w_d increases were stabilizing.) These deductions are confirmed by the loop diagrams presented in Figure 23: the x loops are stable while the ψ loops are stable/unstable at the lower/higher w_d . Overall stability of the combined motion might be assessed by algebraic addition of the x and ψ loop areas. In view of the x and ψ units used, a factor must be applied to, say, the ψ loop area before addition. This factor transpires to be 0.168 and so obviously the combined motion is damped at both w_d values.

(g) Minimum Drag Configuration: Effect of Free Stream Turbulence

Helicopters flying at low speed near the ground will experience wind turbulence intensities of 15% or more. At altitude, while flying at high speed, the effective turbulence intensity is greatly reduced, say 5% or less. The results from the cases described above, being performed at intensities of 1.5%, relate to the latter case. The former needs to be studied, and this is the objective of this section, albeit the investigation was only brief.

The case $\psi_0 = 90^\circ, \theta_0 = 0, |\delta\psi| = 9^\circ$ was considered at $w_d = 0.41$ and 1.02 in grid-generated turbulence of 10% intensity. The results are presented in terms of overall derivatives in Table VI. Of

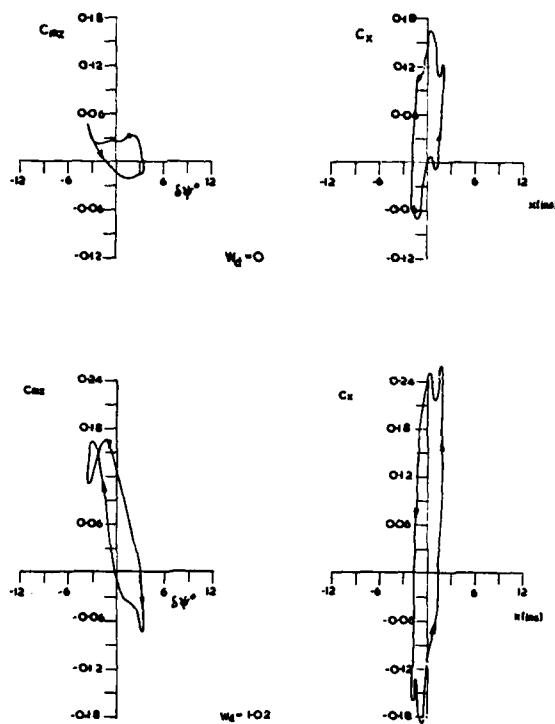


FIGURE 23 2' x 0.8' x 0.8' Model - Direct Force and Moment Coefficient Loop Diagrams for Combined Angular & Linear Displacements. $\psi_0 = 90^\circ$, $\theta_0 = 0^\circ$, $\delta x = 1.9''$, $\delta \psi = 3.5^\circ$.

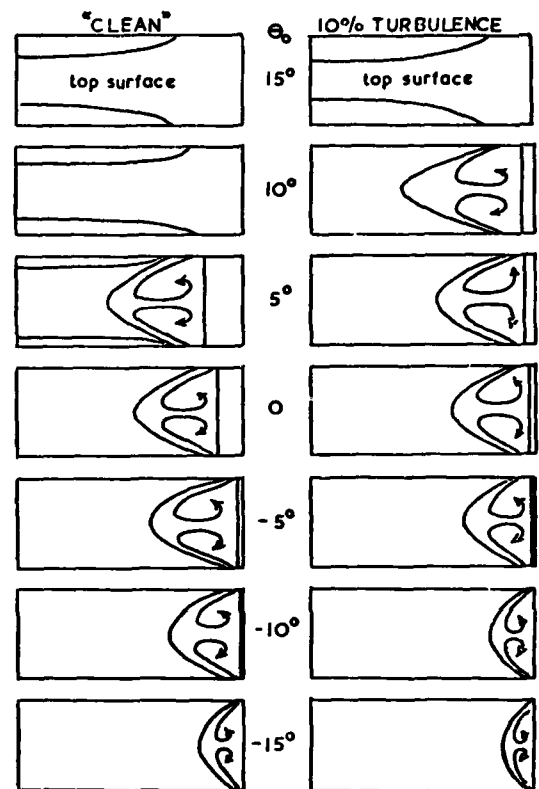


FIGURE 25 Separation Bubbles and Vortex Lines on Upper Surface of 1:0.4:0.4 Model

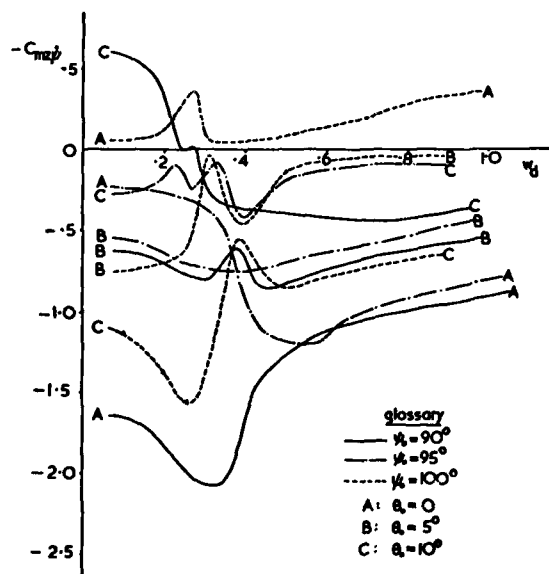


FIGURE 24 Yaw Damping Derivative ~ Frequency Parameter for 1:0.4:0.4 Container From Decaying Oscillation Technique

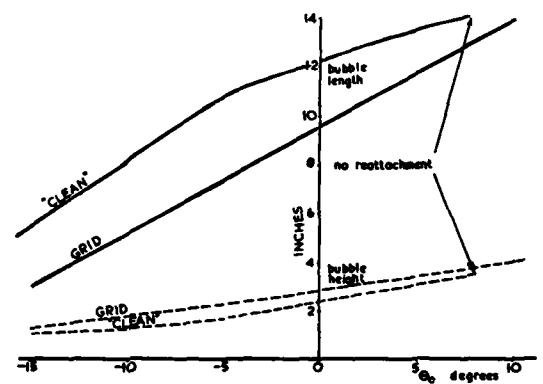


FIGURE 26 Variation of Bubble Length and Height on Upper Surface of 1:0.4:0.4 Model

TABLE VI AERODYNAMIC OVERALL DERIVATIVES

$$\psi_0 = +90^\circ, \theta_0 = 0^\circ, \delta\psi = \pm 9^\circ$$

10% Free Stream Turbulence

w_d	.4075	1.0188
$C_{x\psi}$	-1.1053	-.3065
$C_{y\psi}$	-.1481	-.0090
$C_{z\psi}$	-.0328	.0267
$C_{mx\psi}$	-.0626	.0044
$C_{my\psi}$.0475	.0029
$C_{mz\psi}$.0661	.1479
$C_{x\dot{\psi}}$	1.4234	.0634
$C_{y\dot{\psi}}$	-.2407	-.1019
$C_{z\dot{\psi}}$	-.0010	-.0076
$C_{mx\dot{\psi}}$.0217	-.0134
$C_{my\dot{\psi}}$	-.0309	.0117
$C_{mz\dot{\psi}}$	1.0973	-.1894

particular importance are the $C_{mz\psi}$ and $C_{mz\dot{\psi}}$ derivatives. $C_{mz\psi}$ is positive at both w_d values, moreso at the higher value, implying static instability increasing with w_d . Comparing with the corresponding low turbulence case (Table II), it is seen that the higher level of turbulence has changed a statically stable state into a statically unstable one at the lower w_d value while reducing the degree of static instability at the higher w_d value. Again, in Table VI, $C_{mz\dot{\psi}}$ is strongly positive at low values of w_d , moreso than in the low turbulence case (Table II) indicating a dynamically destabilising effect of turbulence intensity. At high w_d , $C_{mz\dot{\psi}}$ (Table VI) is negative implying instability. These results show the profound effect of moderate levels of free stream turbulence on container yaw stability. It is an area which requires further extensive study.

4.3 CONCLUDING COMMENTS: PRESSURE TESTS

The tests described in this section have provided a great deal of information on container stability and in particular how this is influenced by aerodynamic nonlinearity, history effects and free stream turbulence. It is, however, appreciated that pressure integration is not the most expedient means of obtaining derivative information: direct force measurement or the decaying oscillation technique (where it is applicable) provide much more rapid results, albeit with less understanding of the underlying aerodynamic mechanisms.

5. DECAYING OSCILLATION TESTS

In order to confirm the variability with frequency parameter, w_d , of the damping derivative $C_{mz\dot{\psi}}$, a series of small amplitude decaying oscillation tests was conducted on a 1' x 0.4' x 0.4' plywood model in the 3' 6" open jet wind tunnel. The tests were of a straightforward nature and procedural details are omitted here in the interests of brevity. A full description of the test procedure and instrumentation is to be found in Reference 1. For the present purposes, suffice it to say that the governing equation of yawing motion was assumed to be of the form

$$\delta\ddot{\psi} + B\delta\dot{\psi} + C\delta\psi = 0 \quad \dots \quad (3)$$

wherein $\delta\psi$ = yaw excursion from equilibrium (near to $\psi_0 = 90^\circ$, $\theta_0 = 0$),

$$B = \{b - \frac{1}{2}\rho V h^2 d^2 C_{mz\dot{\psi}}\} / I_z,$$

$$C = \{\omega_0^2 - \frac{1}{2}\rho V^2 h^2 d C_{mz\psi} / I_z\},$$

$$b = \text{equivalent viscous damping coefficient of model suspension at } V = 0,$$

$$\omega_0 = \text{circular natural frequency in yaw of model at } V = 0 \text{ for } b = 0,$$

$$\text{and } I_z = \text{total moment of inertia of model and suspension about the yaw axis (central minor axis).}$$

The parameters b and ω_0 were determined from wind-off decaying oscillation tests and I_z from a wind-off 'displaced frequency' procedure. The parameters B and C were determined,

for a variety of w_d values, from wind-on decaying oscillation tests; hence the derivatives $C_{mz\dot{\psi}}$ and $C_{mz\ddot{\psi}}$ were finally obtained by difference. This procedure was carried out (for $|\delta\psi| < 2^\circ$) over a number of equilibrium configurations near to the minimum drag position.

Such were the dynamic proportions of the model that the procedure outlined above was conditioned towards accurate assessments of $C_{mz\dot{\psi}}$; $C_{mz\ddot{\psi}}$ being obtained with much less resolution. That is, I_z and ω_0 were chosen such that smooth S.H.M. behaviour obtained over the entire velocity range of the tests. This led to comparatively large values of I_z and hence to very small variations of C with windspeed. With such a system, where the structural frequency ω_0 predominates, controlled studies of the damping, B , could be carried out under conditions of virtually pure damped S.H.M. Values of $C_{mz\dot{\psi}}$ could therefore be obtained with extreme rapidity - a small computer program being used to calculate this derivative when digitised segments of wind-on and wind-off decaying oscillation traces were provided as data.

Figure 24 presents the results from some of the decaying oscillation tests. It should be noted first that the values of $C_{mz\dot{\psi}}$ for $\psi_0 = 90^\circ$, $\theta_0 = 0$ (minimum drag position) are numerically larger than those (for corresponding w_d values) obtained from the pressure integrations (Tables I and II). The reason for this is that the present tests were performed at very small amplitudes while the pressure tests were performed at amplitudes in excess of 5° (Table I) and 10° (Table II); the nonlinearities of damping as well as stiffness being very pronounced near to the minimum drag position (see Figures 5 and 8). The same is true of the $\psi_0 = 90^\circ$, $\theta_0 = 5^\circ$ case (Table III for comparison).

The most significant features of the curves of Figure 24, however, are the dramatic changes of $C_{mz\dot{\psi}}$ with w_d in the range $0.25 < w_d < 0.4$. These effects remain unexplained except that one might expect small changes of phase angle to exert a significant moment effect when the latter is very sensitive to the size of and pressures within the separation bubbles on the side faces. (The phase angle referred to here is that between the real flow characteristics at time t and those hypothetical characteristics which would have obtained under static conditions for the container attitude evaluated at t).

Referring to the solid lines of Figure 24, which refer to $\psi_0 = 90^\circ$, it is seen that the minimum drag configuration (line A) is the most unstable over the whole w_d range. The instability is reduced by provision of $\theta_0 = 5^\circ$ (or -5°) incidence (line B). For $\theta_0 = 10^\circ$ (or -10°), the container is stabilised provided $w_d < 0.25$, (line C). This provides the basis for 10° nose-down container carriage which clearly removes negative damping in yaw at low values of w_d . For higher values of w_d , however, negative damping again appears, so the nose-down solution is by no means a universal one.

Referring to the broken lines of Figure 24, which refer to the asymmetric container position $\psi_0 = 95^\circ$, line A shows that this is much less unstable than the minimum drag configuration at low values of w_d . Provision of $\theta_0 = 5^\circ$ renders this configuration more unstable in yaw at low w_d and less unstable at higher w_d values, (line B), while $\theta_0 = 10^\circ$ yields less instability at all w_d values. From the dashed lines, which refer to $\psi_0 = 100^\circ$, the container is positively damped in yaw when $\theta_0 = 0^\circ$ (line A), but is destabilised progressively (lines B and C) as θ_0 is increased to 10° .

Laying aside the $\psi_0 = 90^\circ$, $\theta_0 = 10^\circ$ case, increasing w_d beyond about 0.45 is seen to be stabilising in all cases. In general, the values of $C_{mz\dot{\psi}}$ obtained at or near to $w_d = 0$ (i.e. the quasi-static results) have little relevance when w_d is of the order of magnitude usually encountered in practice (see Section 2).

6. FLOW VISUALISATION TECHNIQUES APPLIED TO THE 1:0.4:0.4 CONTAINER

Flow visualisation, in providing an understanding of the complex flow situations obtaining around the container - while stationary and in motion, was a central feature of the research effort. In this section, a very small batch of the results obtained is presented; fuller details being available on reference to the contract report¹.

6.1 STATIC CASES

6.1.1 Surface Patterns

A 2' x 0.8' x 0.8' blackened plywood model was mounted in the 18' x 8' return section of the large wind tunnel. 'Dayglo' pigment/paraffin mixture was applied to the upper surface (usually a major face) and allowed to dry in the highest-speed flow available. The surface etchings were then photographed in ultra-violet light and the photographs subsequently analysed. The vast majority of the tests centred on the minimum drag configuration; $\psi_0 = 90^\circ$, $\theta_0 = 0$ and involved two free-stream flow conditions: (i) Clean flow, and (ii) grid-generated turbulent flow at about 10% intensity.

The surface flow patterns obtained in these tests are summarised in Figure 25. In clean flow at $\theta_0 = 0$, the separation bubble is seen to extend to about half the container length. As θ_0 is decreased to -15° , the extent of the bubble becomes less, occupying about one quarter of the container length at $\theta_0 = -15^\circ$. For positive θ_0 , the bubble grows and ceases to exist at about $\theta_0 = 8^\circ$. The effect of free stream turbulence is seen to be to shorten the separation bubble and to increase to some 10° the incidence at which a

bubble is still present. In order to supplement the above information, smoke and helium bubble visualisation techniques were used to determine bubble height, the complete results being summarised in Figure 26. Free stream turbulence is seen to increase bubble height in roughly the same proportion that it decreased bubble length.

6.1.2 Smoke and Helium Bubble Studies

The investigations to determine separation bubble height were extended to provide an appreciation of the entire flow field around the container model in the symmetrical orientation where $\psi_0 = 90^\circ$. Initial tests were with smoke. In the $\theta_0 = 0$ configuration, smoke introduced at the leading edge was entrained into the bubble at a remarkably slow rate. However, smoke introduced at the sides of the container near the leading edge filled the bubble rapidly. The secondary vortex parallel to the leading edge (see Figure 25) is clearly a stable arrangement relative to the major vortex 'pair' and the direction of flow in this secondary vortex is therefore such as to carry fluid windward along the surface and thence upwards and forwards towards the shear layer and the leading edge. When incidence was introduced ($\theta_0 > 0$), the rate of entrainment of smoke into the bubble from the sides of the container was found to increase. For $\theta_0 > 8^\circ$ the upflow from the container sides meeting the streamwise air above the upper surface rolled up into a streamwise vortex pair (c.f. Figure 25), one effect of which was to prevent the shear layers generated at the leading edge from reattaching to the container upper surface; i.e. the bubble as such ceased to exist.

In order properly to study the flow behaviour above the upper surface, the helium bubble technique was employed in conjunction with selective halogen lighting. This consisted of illumination of a vertical plane of small width and positioning this plane so as to illuminate a given streamwise segment of the upper surface flow. Helium bubbles were then introduced upstream and photographs taken of the segment of flow. A typical set of flow sections for the case $\psi_0 = 90^\circ$, $\theta_0 = 0$ is presented in Plate I. As a result of the analysis of these and other segmental flow studies, an overall picture of the flow processes around a stationary container was formulated (Figure 27).

6.2 DYNAMIC CASES

In order to distinguish the significant differences between the steady and unsteady flows over a container model, it is necessary to capture the history of the flow whilst the model is oscillating. Some cinefilm records were taken, using helium bubble visualisation, but in order to obtain good quality still photographs at representative positions during an oscillation, a switching technique was evolved. A pentax camera was arranged to be operated by a solenoid. The solenoid was first energised by closing a switch in a circuit after the model had reached a steady oscillating condition, with final closing of the circuit coming from a microswitch attached to the driving motor mechanism (on the six degree of freedom rig, Section 4). The position of the microswitch was varied to provide eight photographs at equi-spaced time intervals during an oscillation cycle. Illumination was from a floor-mounted 250 W Halogen projector downstream of the model.

6.2.1 Pitch Oscillation

(a) Minimum Drag Configuration

Results are presented in Plates II and III for two frequency parameters, $w_d = 0.97$ and 1.94 respectively, in pitch oscillation at 11.5° amplitude. At $w_d = 0.97$, the pictures resemble those for a steady model, but with some phase lag evident. The separated region is smallest in positions (e) and (f), largest in (a) and (b), i.e. the bubble size lags the motion by perhaps $\pi/4$ radians. For $w_d = 1.94$, the leading edge bubble is smallest in (f) and (g) and the shedding of the separated flow can be clearly seen. Starting from (g) and following through (h) and (a), the bubble can be seen to be somewhat over half the model length in (b). In (c) and (d), the separated flow can be seen to be extending to the leeward edge of the model and in (e) no longer separating from the leading edge. In (f) and (g), the mass of fluid once in the bubble approaches the leeward edge, passing that edge in (h) while another bubble is growing at the front. The lag of bubble growth relative to the motion in this case approaches $\pi/2$ radians.

Much more detailed, segmental visualisation was performed for the above cases, but the results are not included here for reasons of brevity. (See Reference 1 for details)

(b) Broadside-On Configuration

A limited investigation of this case was performed using smoke. This followed the obtaining of the results of Section 4.2.3 (c) where the damping derivative was found to change sign with modest variations of w_d . For a static model, the flow separates from all leading edges and contains the separated, or rather dead air, region behind the model. The division between the two regions is essentially in line with the small side faces - as sketched in Figure 28 (a). With changes of attitude, the side flow can re-attach, with the division between the side flow and the base region still being in line with the side face. With oscillation at moderate to high w_d , there was evidence that (i) the vorticity shed in the base region could 'lock on' to the model oscillation and (ii) the line dividing the side and base flows changed for certain parts of the cycle to being in line with the base rather than the side as indicated in Figure 28 (c). It seems probable that the change from negative to positive damping with increase of w_d is associated with the latter of these factors.

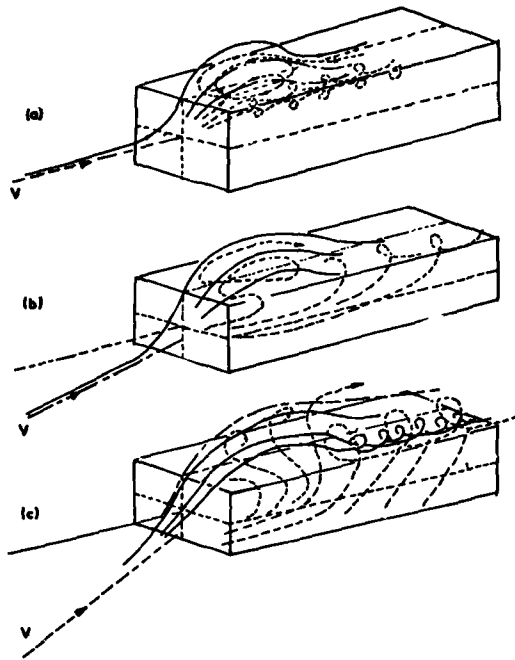


FIGURE 27 Idealised Flow Patterns Over Container Model at Various Pitch Incidences
 (a) Approx. $\psi_0 = 90^\circ$, $\theta_0 = 0^\circ$
 (b) Approx. $\psi_0 = 90^\circ$, $\theta_0 = 5^\circ$
 (c) $\psi_0 = 90^\circ$, $\theta_0 > 10^\circ$

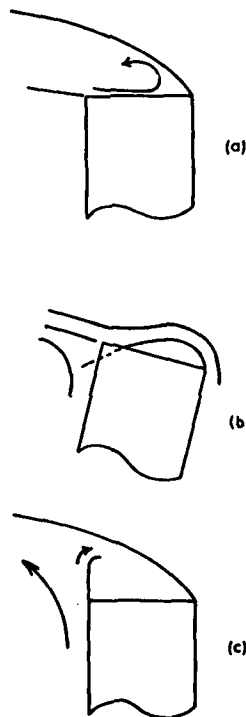


FIGURE 28 End Flow for Broadside-On Position

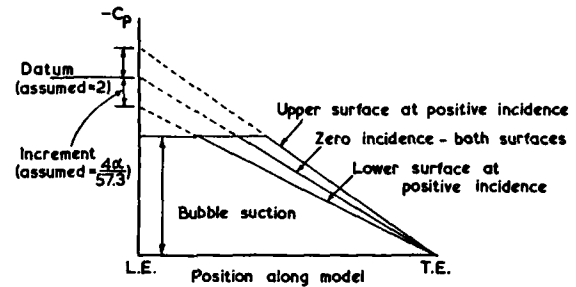
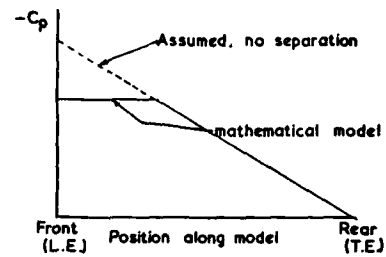


FIGURE 29 Mathematical Model - Static Pressure Distributions

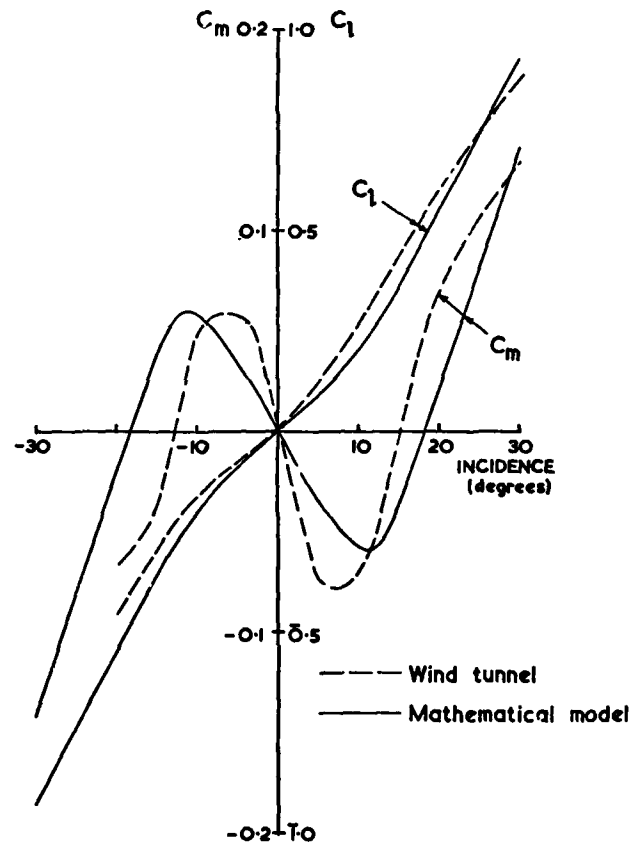


FIGURE 30 Mathematical Model - Comparison with Experiment

6.2.2 Fore and Aft Oscillation (Minimum Drag Configuration)

While this case does not fit into the overall pattern of the investigation as described in this paper, the results obtained are of great interest and two illustrative figures are included here. Plate IV refers to $w_d = 1.94$ while Plate V refers to $w_d = 5.54$ in an impressed fore and aft oscillation of amplitude 3.54 inches.

As the model moves rearwards at $w_d = 1.94$, the separated flow collects and thickens near the front until the rearward position is reached, plate (d). In (e), the separated flow is shed with a new bubble growing from the leading edge. In (f), this flow clears the rear of the model with evidence of a smaller secondary vortex of opposite sense being shed later. For $w_d = 5.54$ the same major features are evident, although in this case the rapid rearward model movement can, for a short time, leave the separation bubble ahead of the model.

7. MATHEMATICAL MODELLING BASED ON SIMPLIFIED FLOW ASSUMPTIONS

As mentioned previously Liu⁵ used viscous crossflow theory successfully to compute a set of quasi-static force derivatives for a 5:2:2 container, but this technique failed to provide meaningful estimates of the moments owing to the profound influence of separation bubbles on the latter. Rather than attempt to modify Liu's theory, which at most would have provided linear quasi-steady moment derivatives, it was decided to use the knowledge of experimental results (pressures and loop diagrams in particular) gained herein to formulate a simple working model which would (a) provide quasi-steady linear moment derivatives; (b) simulate the shape of experimental loop diagrams and (c) show all the expected variations with frequency parameter. These studies were restricted to the important case of pitch motions about an equilibrium position near to the minimum drag configuration, $\psi_0 = 90^\circ$, $\theta_0 = 0$.

Following some preliminary calculations on conceptual mathematical models of pressure variations along the upper and lower surfaces of pitching container, it was (on the basis of wind tunnel pressure results) decided to model the pressure within the separation bubble by a constant pressure value, which tails-off linearly aft of the bubble to zero at the trailing edge. (See Figure 29(a)) No attempt was made to model the pressure variation across the container. Static results were first computed for the values of the parameters illustrated in Figure 29(b) chosen to give moments of the correct order of magnitude. The results for pitching moment and lift are shown in Figure 30, these comparing favourably with measured values. The level of pressure within the bubble was taken as $C_p = -1$, according roughly with measured values. The variation of bubble length with incidence also compares favourably with the experimental results (See Figure 31).

Detailed wind tunnel results with turbulence are not available, but indications are that bubble length would be shorter, depth larger and levels of suction greater. Computed moment curves for varying levels of suction within the bubble are shown in Figure 32. This shows the same trend as inferred from experiment, i.e. a decrease in static stability near to the minimum drag position for increases in bubble suction.

The modelling of unsteady flow required further assumptions to be made. It had been observed that bubble size lags the motion giving, for incidence increasing, bubble lengths shorter than those for the same attitude when static. Now the smaller bubble implies a higher suction, partly to turn the flow round a smaller radius and partly to entrain more air. It was assumed that the effect of lag could be computed by applying a phase lag to incidence, computing bubble length for that incidence, and assuming that length to apply at the correct incidence with a corresponding change of bubble suction (Figure 33).

Results for oscillations of amplitude 15° and 30° and with phase lags of 0, 30, 60 and 90 degrees are shown in Figure 34. Points of interest, all in agreement with measurement, are

- (i) a phase lag results in unstable loops,
- (ii) the energy input is stronger for smaller angles, and
- (iii) a mean line through the loop shows increasing slope (decreasing static stability) with increasing phase lag.

Note that phase lag, P , is simply related to frequency parameter, w_d , by

$$w_d \propto \tan P$$

Now the loops formed are all destabilising, in no case having the stabilising sub-loops observed in the experimental results (e.g. Figure 8). It should be noted, however, that the only dynamic effect assumed can in no way represent conventional damping that occurs, for example, with attached flow past streamlined shapes in pitching motion, or with completely detached flows past bluff bodies in fore-and-aft motion. If this type of damping is added, loops such as those shown in Figure 35 are produced. With increase of conventional or viscous-type damping, the destabilising loop becomes progressively more stable with, for the amplitude of 30° illustrated, stabilising subloops appearing at the extremities of the motion.

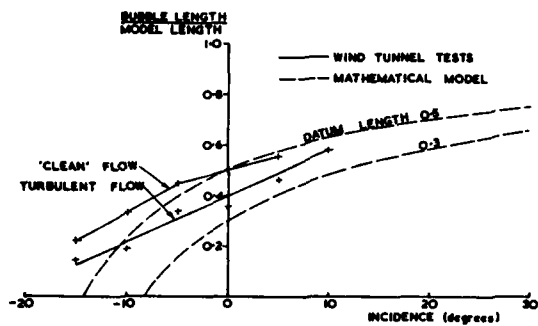


FIGURE 31 Variation of Bubble Length with Incidence

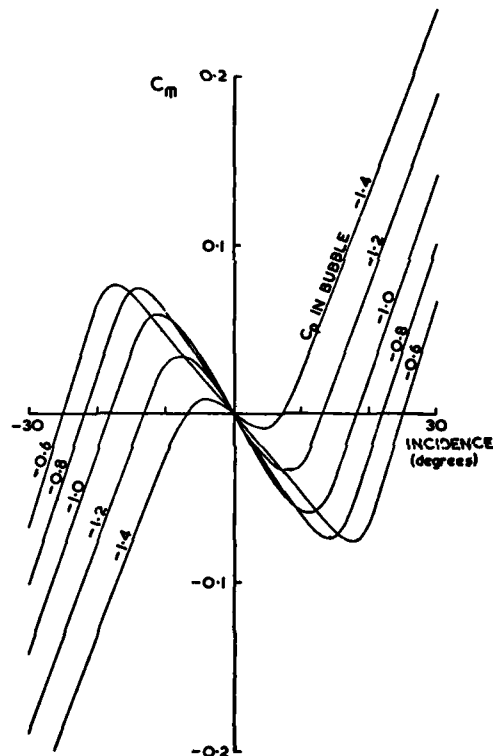


FIGURE 32 Mathematical Model - Effect of Bubble Suction on Moment Coefficient

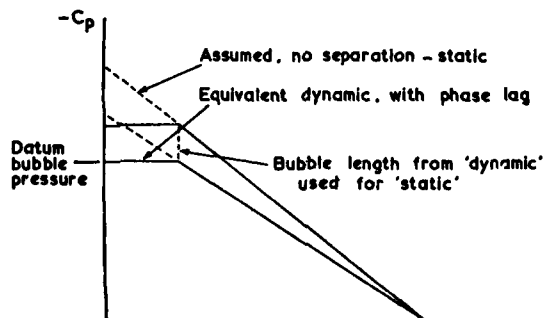


FIGURE 33 Mathematical Model - Effect of Motion on Bubble Pressure

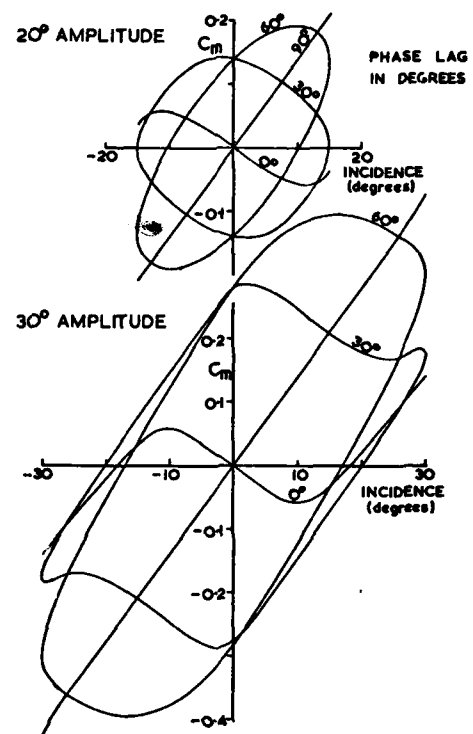


FIGURE 34 Mathematical Model - Effect of Phase Lag on Moment-Angle Loop Diagrams

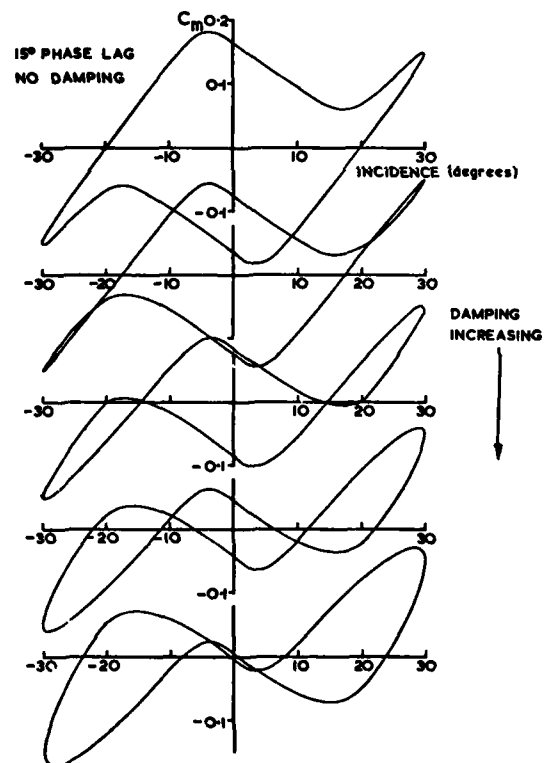


FIGURE 35 Mathematical Model - Effect of Conventional Damping on Moment-Angle Loop Diagrams

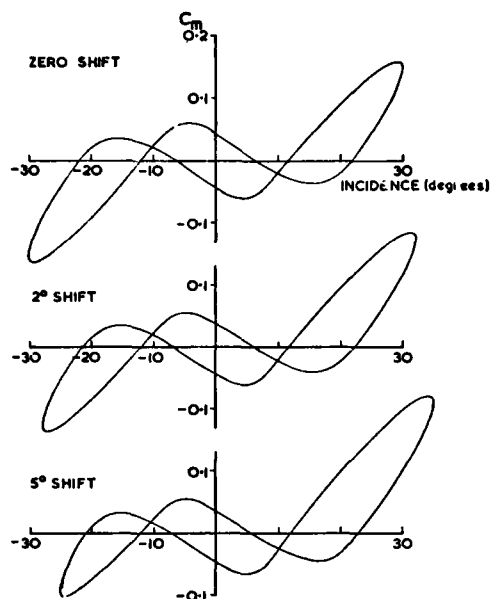


Figure 36 Mathematical Model - Effect of Datum Shift on Moment ~ Angle Loop Diagrams

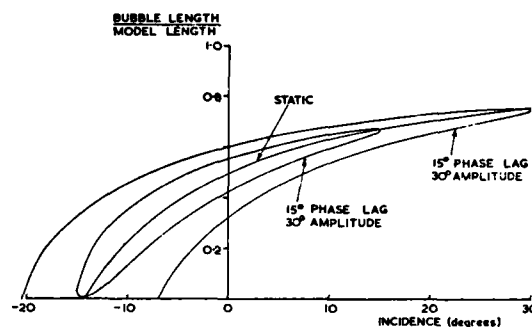


Figure 37 Mathematical Model - Bubble Length During Motion with Phase Lag

Figure 36 shows the effect of datum error. This is of interest in comparison with the wind tunnel results of Section 4 indicating that certain asymmetries in the results may be due simply to comparatively small changes in relative flow direction.

Finally, the bubble lengths implied in these models may be readily computed: these are shown in Figure 37.

In summary, the highly simplified flow model seems to lead to lift, moment and bubble characteristics that follow closely those obtained from experiment, in particular representing many of the static and dynamic instability regions. The curious results obtained for low frequency parameters in the decaying oscillation tests (Section 5) however are not explained by the simple model.

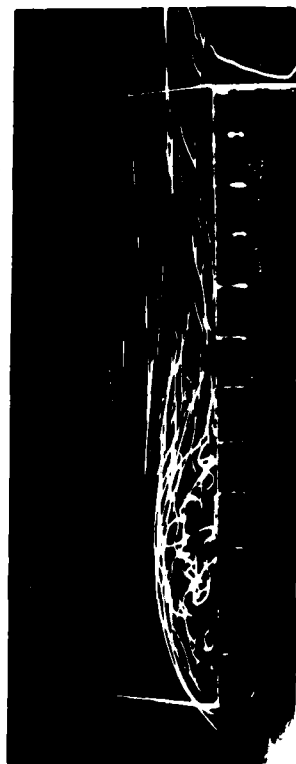
8. CONCLUSIONS

The extensive pressure and flow visualisation studies described herein have revealed extreme complexity in the flow situation around a particular cargo container shape. The separated flows may or may not reattach and will usually involve strong interaction between component flows on normal streamwise faces. The dynamic tests clearly showed pronounced history effects at very modest frequency parameters indicating that it will hardly ever suffice to use quasi-static aerodynamic derivatives when attempting to predict the stability of underslung bluff loads. Attempts to model the flow by using simple, quasi empirical, mathematical expressions show considerable promise, and it is felt that this will provide the most suitable means of representing the complex, hysteresis bound, nonlinear aerodynamic characteristics for use in future stability investigations. Alternatively, these characteristics might be represented adequately by 'overall derivatives' measured on oscillating wind tunnel models, as described herein. However, this would involve more dynamical testing to define 'overall derivatives' as curve-fitted functions of amplitude as well as of frequency parameter.

Stability characteristics of the container have been shown to depend strongly on free stream turbulence intensity, rendering it futile to attempt to predict full scale container stability at low forward speeds and low altitude in a natural wind using 'clean tunnel' results.

9. REFERENCES

1. CHAN, D.
FLOWER, J.W.
SIMPSON, A. 'Aerodynamically Induced Motions of Bluff Bodies Suspended Beneath Helicopters' 1975; United States Army Contract No. DAJA 37-73-C-0477: Final Technical Report.
2. SHELDON, D.F.
PRYOR, J. 'A Wind Tunnel Investigation of Yaw Instabilities of Box-shaped Loads Underslung from a Helicopter on a Tandem Suspension' RMCS Tech Note AM/62 Dec. 1974, R.M.C.S. Shrivenham, U.K.
3. PRABHAKAR, A. 'A Study of the Effects of an Underslung Load on the Dynamic Stability of a Helicopter' Ph.D. Thesis, R.M.C.S. Shrivenham, U.K. June 1976.
4. LAUB, G.H.
KODANI, H.M. 'Wind Tunnel Investigation of Aerodynamic Characteristics of Scale Models of Three Rectangular-shaped Cargo Containers' 1972; NASA TMX-62, 169.
5. LIU, D.T. 'In Flight Stabilisation of Externally Slung Helicopter Loads' 1973; USAAMRDL Tech. Report 73-5 Contract DAJA 02-70-C-0067.
6. COOK, N.J. 'The Effect of Turbulence Scale on Flow Around High Rise Building Models' 1971; Ph.D. Thesis, Department of Aeronautical Engineering, University of Bristol, England.



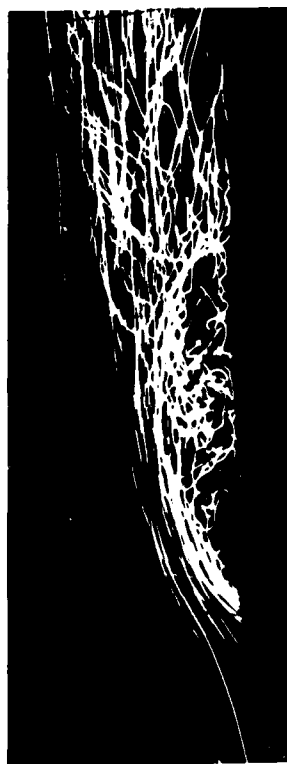
(a)

0 - 1.6" SECTION



(d)

4.8" - 6.4" SECTION



(b)

1.6" - 3.2" SECTION



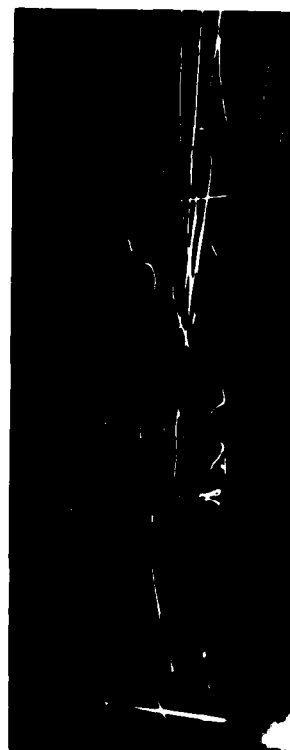
(e)

6.4" - 8.0" SECTION



(c)

3.2" - 4.8" SECTION



(f)

8.0" - 9.6" SECTION

PLATE I SECTIONS OF HELIUM BUBBLE FLOW OVER A STATIONARY BOX $\psi_0 = 90^\circ$ $\Theta_0 = 0$

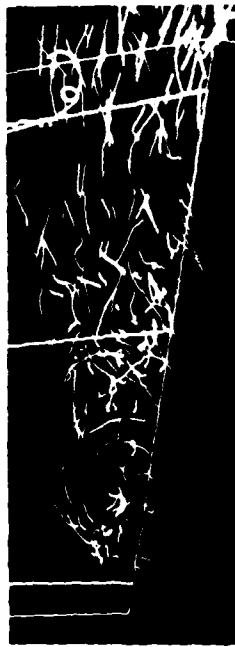
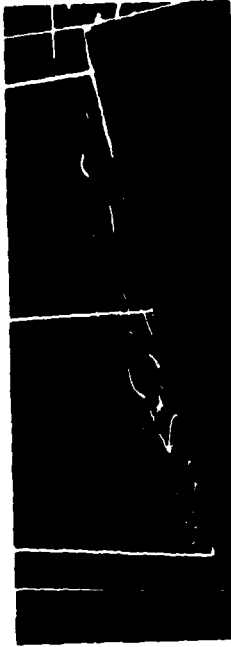
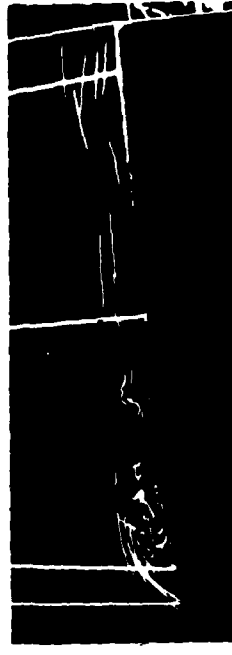
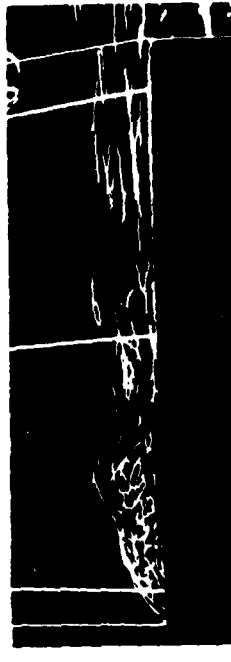
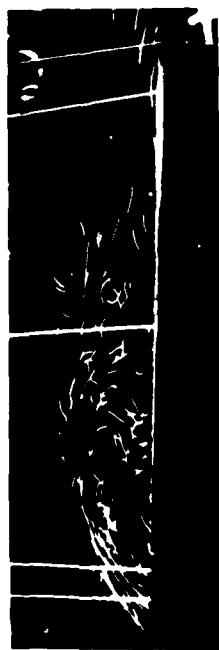
(a) $\theta = 11\frac{1}{2}^\circ$ (b) $\theta = 5^\circ$ (c) $\theta = 2^\circ$ (d) $\theta = 7^\circ$ (e) $\theta = -11\frac{1}{2}^\circ$ (f) $\theta = -3^\circ$ (g) $\theta = 3^\circ$ (h) $\theta = 9^\circ$

PLATE II HELIUM BUBBLE UNSTEADY FLOW FOR A PITCH OSCILLATION $\psi_s = 90^\circ$ $\psi_s = \pm 15^\circ$ $W_0 = 0.968$



(a) $\theta = 11\frac{1}{2}^\circ$



(b) $\theta = 5^\circ$



(c) $\theta = -2^\circ$



(d) $\theta = -7^\circ$



(e) $\theta = -11\frac{1}{2}^\circ$



(f) $\theta = -3^\circ$



(g) $\theta = 3^\circ$



(h) $\theta = 9^\circ$

PLATE III HELIUM BUBBLE UNSTEADY FLOW FOR A PITCH OSCILLATION $\psi_0 = 90^\circ$ $|\theta| = 11\frac{1}{2}^\circ$ $W_0 = 1.94$

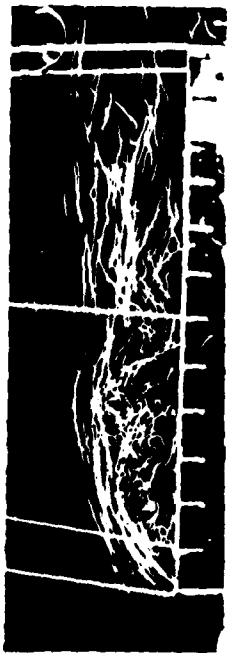
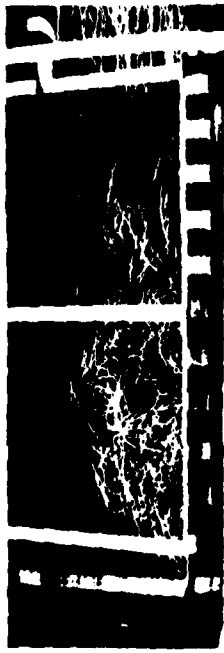
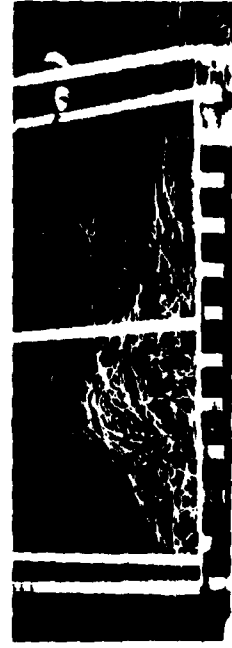
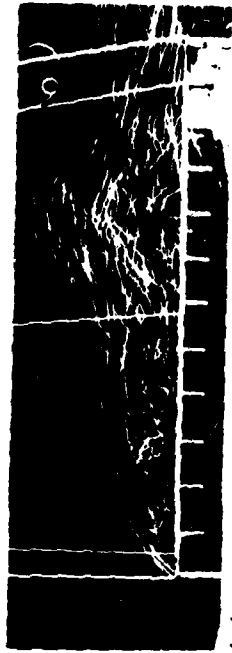
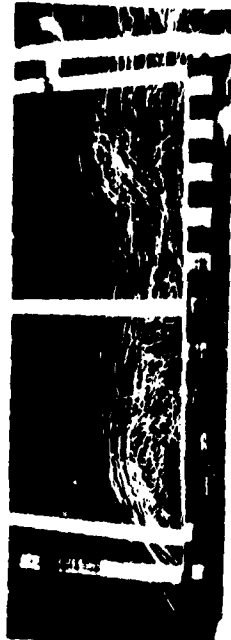
(a) $y = +dy$ (b) $y = +dy/2$ (c) $y = 0$ (d) $y = -dy/2$ (e) $y = -dy$ (f) $y = -dy/2$ (g) $y = 0$ (h) $y = +dy/2$

PLATE IV HELIUM BUBBLE UNSTEADY FLOW FORE AND AFT MOTION $\theta_c = 90^\circ$ $dy = \pm 3.54''$ $W_B = 1.94$

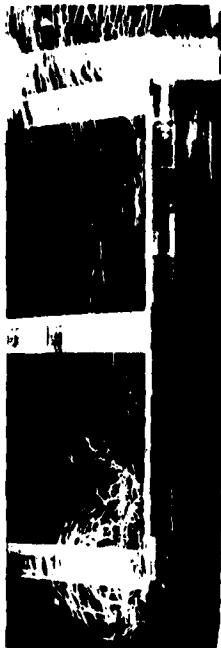
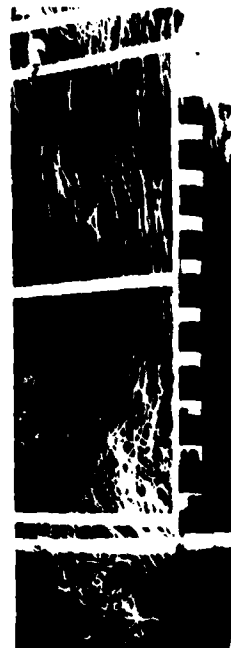
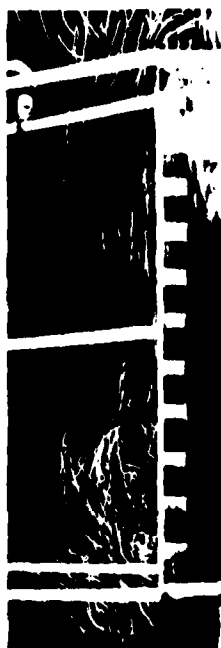
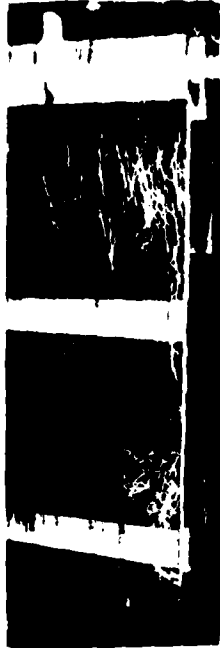
(a) $y = +dy$ (b) $y = +dy/2$ (c) $y = 0$ (d) $y = -dy/2$ (e) $y = -dy$ (f) $y = -dy/2$ (g) $y = 0$ (h) $y = +dy/2$

PLATE V HELIUM BUBBLE UNSTEADY FLOW FOR AND AFT MOTION $\psi_0 = 0^\circ$ $dy = \pm 3.54''$ $w_0 = 5.54$

APPENDIX I CALCULATION OF 'OVERALL DERIVATIVES'

Consider the case of pitch oscillation impressed at circular frequency ω , i.e.

$$\theta = a \cos \omega t + b \sin \omega t \quad \dots \dots \dots (4)$$

where it is desired to obtain 'overall' pitching moment derivatives. In general, the pitching moment can be expanded in the Fourier series

$$M = A_0 + \sum_{j=1}^{\infty} A_j \cos j\omega t + B_j \sin j\omega t \quad \dots \dots \dots (5)$$

$$\text{where } A_0 = \frac{\omega}{2\pi} \int_0^T M(t) dt, A_j = \frac{\omega}{\pi} \int_0^T M(t) \cos j\omega t dt, B_j = \frac{\omega}{\pi} \int_0^T M(t) \sin j\omega t dt \quad \dots (6)$$

where $T = 2\pi/\omega$ = periodic time of impressed oscillation.

Now consider for simplicity data acquired over just one complete period of length $T = t_p - t_0$:-

t_0	t_1	t_2	t_p
θ_0	θ_1	θ_2	θ_p
M_0	M_1	M_2	M_p

and define the column vectors $\theta = \{\theta_0, \theta_1, \dots, \theta_p\}$, $M = \{M_0, M_1, \dots, M_p\}$

$$C_j = \{\cos j\omega t_0, \cos j\omega t_1, \dots, \cos j\omega t_p\} \text{ and } S_j = \{\sin j\omega t_0, \sin j\omega t_1, \dots, \sin j\omega t_p\} \quad (7)$$

For evaluating the integrals (6) above, Simpson's rule has been found to be entirely adequate; the weighting matrix for this is simply $W = \text{Diag}[1, 4, 2, 4, 2, 4, \dots, 1]$ (8) whereupon the integrals (6) become

$$\begin{aligned} A_0 &= \frac{1}{3p} M^T W \underline{1} \\ A_j &= \frac{2}{3p} M^T W C_j \quad j \neq 0 \quad \dots \dots \dots (9) \\ B_j &= \frac{2}{3p} M^T W S_j \quad j \neq 0 \end{aligned}$$

where $\underline{1} = \{1, 1, \dots, 1\}$; $(p+1 \times 1)$.

In the majority of the tests, the θ motion was virtually pure S.H.M., but in any event a and b in equation (4) were determined from

$$a = \frac{2}{3p} \theta^T W C_1, \quad b = \frac{2}{3p} \theta^T W S_1 \quad \dots \dots \dots (10)$$

the higher harmonic coefficients $a_j = \frac{2}{3p} \theta^T W C_j$, $b_j = \frac{2}{3p} \theta^T W S_j$ being found in all cases to be vanishingly small.

Now when assessing derivatives, one has only to take account of the harmonic components of response, viz A_1 and B_1 , although for completeness the higher order harmonic components A_j and B_j for $j > 1$ were also considered as important indicators of departure from linearity. From the linear expression

$$\begin{aligned} \Delta C_m &= (M_\alpha \theta + M_\alpha \dot{\theta}) / \frac{1}{2} \rho V^2 h^2 d = [M_\alpha (a \cos \omega t + b \sin \omega t) + M_\alpha \omega (-a \sin \omega t + b \cos \omega t)] / \frac{1}{2} \rho V^2 h^2 d \\ &\equiv (A_1 \cos \omega t + B_1 \sin \omega t) / \frac{1}{2} \rho V^2 h^2 d \end{aligned}$$

one obtains on comparing coefficients

$$C_{m\alpha} = M_\alpha / \frac{1}{2} \rho V^2 h^2 d = \frac{aA_1 + bB_1}{\frac{1}{2} \rho V^2 h^2 d (a^2 + b^2)} \quad \dots \dots \dots (11)$$

$$C_{m\dot{\alpha}} = M_\alpha / \frac{1}{2} \rho V h^2 d^2 = \frac{bA_1 - aB_1}{\frac{1}{2} \rho V h^2 d^2 \omega (a^2 + b^2)} \quad \dots \dots \dots (12)$$

Note that in the above connotation, $C_{m\alpha}$ embraces all in-phase components of ΔC_m , including acceleration effects, and $C_{m\dot{\alpha}}$ embraces all quadrature components of ΔC_m . As they represent averages over, perhaps, large amplitude oscillations and are obtained on the basis of fundamental harmonic balance, $C_{m\alpha}$ and $C_{m\dot{\alpha}}$ are termed 'overall derivatives'. $C_{m\dot{\alpha}}$ represents the area of a 'smoothed' loop diagram of C_m -v- θ .

The higher harmonic contributions to the derivatives are

$$C_{maj} = \frac{aA_j + bB_j}{\frac{1}{2}\rho V^2 h^2 d(a^2 + b^2)} \quad \text{and} \quad C_{mdj} = \frac{bA_j - aB_j}{\frac{1}{2}\rho V h^2 d^2 \omega(a^2 + b^2)} ; \quad j > 1$$

Summing all significant C_{maj} terms yields the area of the actual loop diagram $C_m-v-\theta$. In each of the many cases considered, values of j up to 4 were considered and several of the derivatives were found to possess significant higher harmonic components even when impressed amplitudes were small.

The above procedure is obviously applicable to any combination of forces (or moments) and displacements/rotations. The results presented in Tables I - VI were obtained using the above procedure.

AIR FORCE FLIGHT TEST CENTER EXPERIENCE
in the
IDENTIFICATION OF STABILITY AND CONTROL PARAMETERS
from
DYNAMIC FLIGHT TEST MANEUVERS

PAUL M. JEGLIUM, LtCol, USAF
DIRECTOR OF SAFETY (FORMERLY: CHIEF, PERFORMANCE
and FLYING QUALITIES BRANCH)
AIR FORCE FLIGHT TEST CENTER
EDWARDS AFB, CALIFORNIA U.S.A. 93523

SUMMARY

Air Force Flight Test Center experience in the flight test determination of stability derivatives is generalized in terms of the attainment of known benefits, and the practical and philosophical necessity for the use of the technique are discussed. Data from recent flight test programs is used to illustrate that Stability Derivative Extraction (STABDEX) techniques result in savings of flight time, a significantly better and safer flight test program and high quality data which would otherwise be unobtainable. Concluding remarks discuss the importance of the technique for the flight testing of advanced designs.

INTRODUCTION

The Air Force Flight Test Center has been engaged in the determination of the coefficients of "model" equations (stability derivatives) which describe the flight characteristics of air vehicles since 1948. From 1948 to 1961, no less than twenty two publications on the subject were authored by the National Aeronautics and Space Administration (then NACA), the United States Air Force and other agencies (reference 1).

Researchers and "flight testers" alike recognized the advantages and benefits that could accrue from a complete description of an air vehicle's stability and control characteristics. These included (reference 2):

1. Improved verification of specification requirements,
2. An analytical model to facilitate flight test envelope expansion (primarily because of the improved dependability of extrapolated flight characteristics),
3. A tool to implement the correction of deficiencies and the developmental optimization of the vehicle,
4. A tool to more precisely implement the "standardization" of stability and control characteristic
5. The means by which engineering and operational simulators could be updated to more accurately represent the air vehicle, and
6. The reduction of the amount of flight test time required to adequately assess the flight characteristics of an air vehicle, resulting in a reduction of the cost of flight test development.

Despite the recognition of the desirability of accomplishing such a task, early parameter identification efforts were limited to the synthesizing of major stability derivatives from data produced by small, linear control inputs. The manual matching of analog computer outputs with flight test traces (Analog Matching), using linear equations of motion was the most commonly used method of determining these major derivatives (reference 3.) Although good results were (and are) achieved, this technique was time consuming and was strongly dependent on the sophistication of the operator. The development of faster, more accurate methods was recognized as being dependent on more accurate instrumentation of the flight variables and improved mathematical techniques which would accommodate the basically statistical and discrete nature of flight test data.

Hindsight shows that the imperative nature of these developments was not universally recognized in the flight test community. Pilots and Flight Test Engineers were reluctant to depart from classical, proven, methods and managers were hesitant to commit resources to a method of "unproven" value which appeared to go beyond the requirements for a "demonstration" of characteristics. It was (and is) mandatory for us, the advocates of quantitative descriptions of the stability and control and flying qualities characteristics to demonstrate that these techniques provide tangible cost and technical benefits over more qualitative methods. Such evidence now exists and provides a compelling motivation for the use of the technique. More of this later.

THE REQUIREMENT

As a point of philosophy, it is worthwhile mentioning that an "evaluation" of an air vehicle's characteristics may differ significantly from a "demonstration" of those same characteristics. Current U.S. Air Force guidance requires acquisition and test agencies within the Air Force to evaluate, as well as demonstrate, all new systems.¹ To this end, all agencies are involved, jointly, from the genesis of a particular design.

1. See references 4, 5, 6 and 7.

This involvement ideally continues until all production items, (and support equipment) are delivered to the user. The determination of the "stability derivatives" of the air vehicle lends itself well to this philosophy.

METHODOLOGIES

The Air Force Flight Test Center has used several recent methodologies for the determination of the "stability derivatives" of at least eight flight test vehicles. All of our early efforts utilized the Modified Maximum Likelihood Extraction (MMLE) (Newton-Raphson) program developed by Richard Maine and Ken Iliff of the NASA Dryden Flight Research Center (reference 8.) Although we now utilize four individual methodologies to accomplish the task, an updated MMLE is still used as the standard method of evaluation and as a "baseline" when results are not as anticipated. Further local developments include a formally structured but highly versatile library of operator selectable computer routines for the relatively rapid determination of characteristic derivatives and for the confirmation of their validity; along with an evaluation of the associated open loop parameters. This semi-formalized procedure and library has been christened "STABDEX" (which stands for STABILITY Derivative EXtraction and verification.) In a general sense, our experience in the determination and use of flight test determined stability derivatives has resulted in at least the partial achievement of all those benefits previously mentioned. Several specific lessons are worthy of mention.

RESULTS

From an implementation point of view, we feel that we have demonstrated significant reductions in the amount of flight test time necessary to define the stability and control characteristics of an air vehicle. During the evaluation of several prototype and production aircraft, records were maintained with respect to the amount of dedicated flight time devoted to classical stability and control maneuvers and those flight hours devoted to stability derivative extraction (STABDEX) maneuvers.

TABLE 1
A COMPARISON OF CLASSICAL AND STABDEX
FLIGHT REQUIREMENTS FOR A TYPICAL CONFIGURATION

	<u>Classical</u>	<u>STABDEX</u>
Total Maneuver	159(89)	117(53)
Total Flight Hours	20.8(11.7)	4.2(1.9)
Maneuvers per Flight Hour	7.6(7.6)	27.9(27.9)
Parameters per Maneuver	2.9(2.9)	10.5(10.5)
Parameters per Flight Hour	22(22)	293(293)

Note 1: Numbers in parentheses are for an idealized flight test program.

Note 2: Courtesy of Lt David Maunder, AFFTC/DOEEP.

Table 1 is a listing of the actual experience during one of these programs in which both classical and STABDEX methods were used. The numbers in parentheses are an estimate of an idealized test program, based on hindsight, which could have been flown to obtain the same data. Two points are obvious. The first is that efficient test planning can effect a significant reduction in flight test time regardless of the analysis method used. The second is that the total flight time can be reduced nearly 75% by the application of STABDEX techniques. It must be noted that the flight time indicated in the tables is not exactly representative of the total flight time required since the evaluation of characteristics such as the variation of pitch control force and deflection with velocity and certain roll performance parameters must be obtained by classical techniques. Similarly, in a properly implemented active control system, the longitudinal short period frequency and damping ratios can only be quantified by STABDEX techniques.

We have found that a second, somewhat complimentary, benefit of the use of STABDEX techniques is the ease with which the stability and control envelopes can be mapped, leading to a valid and efficient matrix of flight test conditions (reference 9.) Since stability derivatives depend on Mach Number (M), Angle of Attack (AOA), Angle of Sideslip (β), normal acceleration (g) and equivalent airspeed (V_e) (for a specific configuration), the specification of flight test points becomes a matter of insuring that the Mach, AOA, β , g and V_e envelopes are adequately covered. Special emphasis is placed on the predicted "boundaries" and "limits". This is especially important in those areas where aerodynamic non-linearities or active control system irregularities are anticipated. Figure 1 is a generalized representation of the "Flying Qualities" envelopes used by the AFFTC. Representative test points are indicated. Note that the entire range of each independent variable is explored. It is important to emphasize that some very important independent variables, such as aggregated control inputs, are not represented on this figure, and that the figure is for one configuration only. Both of these considerations become extremely important if aerodynamic cross-coupling or significant changes in stability derivatives occur (reference 7.)

During the past decade the Dryden Flight Research Center and the AFFTC have determined stability derivatives for a significant number of conventional and unusual configurations. Figure 2 presents a summary of the maximum variation of predicted stability and control derivatives from those determined by flight test for the X-24B, the F-111E, the X-15, the M2-F2, M2-F3, HL-10, X-24A, F-15A, YF-16, and YF-17. This compilation is not meant to be a criticism or condemnation of either flight test or wind tunnel results.

but is intended to show that significant differences do occur between predicted and flight test values of stability and control derivatives. The results, with respect to rotary derivatives, are not particularly surprising. Flight test, wind tunnel and analytically estimated values of these derivatives all contain significant uncertainty. The area of concern, in this author's opinion, is in the variation experienced in the major derivatives. For instance, Figure 3 illustrates the estimated and flight test derived values of the directional stability derivative $C_{n\dot{\beta}}$ for a fighter aircraft tested at the AFFTC. As the flight test program progressed, the differences in predicted and measured directional stability were noted and the aircraft was placarded to an angle-of-attack limit which provided adequate static and dynamic directional stability. In the course of the operational evaluation of the aircraft, however, it was inadvertently flown beyond the placard angle-of-attack limit on two occasions; and on both occasions departed from controlled flight. The data obtained during these departures indicates that the chosen limit was correct, and, incidentally, filled in the curve nicely.

These two data points coincidentally provided us with a welcome confirmation of the versatility of the Newton-Raphson (MMLE) methodology. In both cases, the first determination of the stability derivatives was accomplished by an experienced flight test engineer using an analog matching technique. The data was subsequently evaluated using the MMLE program, which duplicated the manually obtained results with significant precision.

A final comment on the data of Figure 2 is in order. The "side force" data of columns 13, 14 and 15 indicates that estimates of aileron and rudder induced side forces can be significantly in error. Experience on recent programs at the AFFTC indicates that the magnitude of these side forces is extremely important when designing toward or optimizing a precision, pilot-in-the-loop, nose pointing task.

It is an obvious, but sometimes neglected, fact that engineering and operational simulators must be representative of flight hardware with respect to the implementation of the equations of motion and the coefficients of these equations. The foregoing discussion illustrates that flight test verification of estimated characteristics is absolutely essential.

The determination of stability and control "limits" remains as a difficult, and sometimes hazardous, task. Angle-of-Attack limits have been shown to depend on a fairly complex array of independent variables including roll and roll-yaw coupling, control system interactions and rate effects, as well as the effects of aerodynamic non-linearities and apparent time dependency. Although we conventionally consider limits to exist only at the extremes of attainable parameters, we have demonstrated departures well within normally obtainable values of both angle of attack and sideslip. As an example, in the case of one sideslip generated departure, a non-linearity (reversal) in roll-with-yaw ($C_{x\dot{\beta}}$) was experienced at large sideslip angles with near zero angle-of-attack at a mach number of 0.9. The rapid roll rate which resulted subjected the aircraft to over seven negative 'g's. Fortunately, no damage was incurred by the airframe. Subsequent evaluation showed that a departure area existed at the mid-point of the envelope, as shown in Figure 1.

In the effort to more safely and effectively determine stability and control limits, the AFFTC plans to implement a flight test mission complex in which engineering simulations can be operated simultaneously with flight tests. We plan to utilize telemetered data from specified test points to evaluate, update and extrapolate estimated characteristics. It is anticipated that this technique can further reduce required flight test time and contribute toward safer and more effective flight testing for the determination of aerodynamic limits.

THE FUTURE

The coming decade promises to be a productive and exciting time for air vehicle designers and developers. The necessity to provide increased mission capabilities in more fuel efficient vehicles will require significant aerodynamic sophistication, especially if Design-to-Cost formulae are enforced. Increased dependence on active control systems and non-conventional configurations will tax our ingenuity and creativity.

The products of the next decade may also result in a basic change in the philosophical concept of flight testing for adequate flying qualities. This will depend on the degree of sophistication (or conversely, simplicity) which is necessary to accomplish a mission. Unusual aerodynamic configurations and active control system(s) may require the establishment of tight limits to protect the airframe and the crew, but these limits will have to permit operations at the limits of capability. The flying(or handling) qualities and the departure resistance of these vehicles may be totally dependent on the quality of our evaluation of the aerodynamic parameters: We must be ready to accept this responsibility; along with the accolades which will certainly come our way.

REFERENCES

1. Cox, J.F., "Literature Survey of Methods for Determination of Stability Derivatives from Flight Test Data," Flight Research Branch Information Bulletin 61-3, Air Force Flight Test Center, Edwards AFB, CA, Aug 1961.
2. Kirsten, Paul W. and Ash, Lawrence G., "A Comparison and Evaluation of Two Methods of Extracting Stability Derivatives from Flight Test Data," AFFTC-TD-73-5, Air Force Flight Test Center, Edwards AFB, CA, May 1974.
3. Zaleski, Charles D. and Rampy, Johnny M., "Detailed Procedure for Obtaining Stability Derivatives from Flight Test Data by Analog Matching," FTC-TIM-65-1020, Air Force Flight Test Center, Edwards AFB, CA, Jan 1965.

6. MIL-D-8708, Military Specification, "Demonstration Requirements for Airplanes."

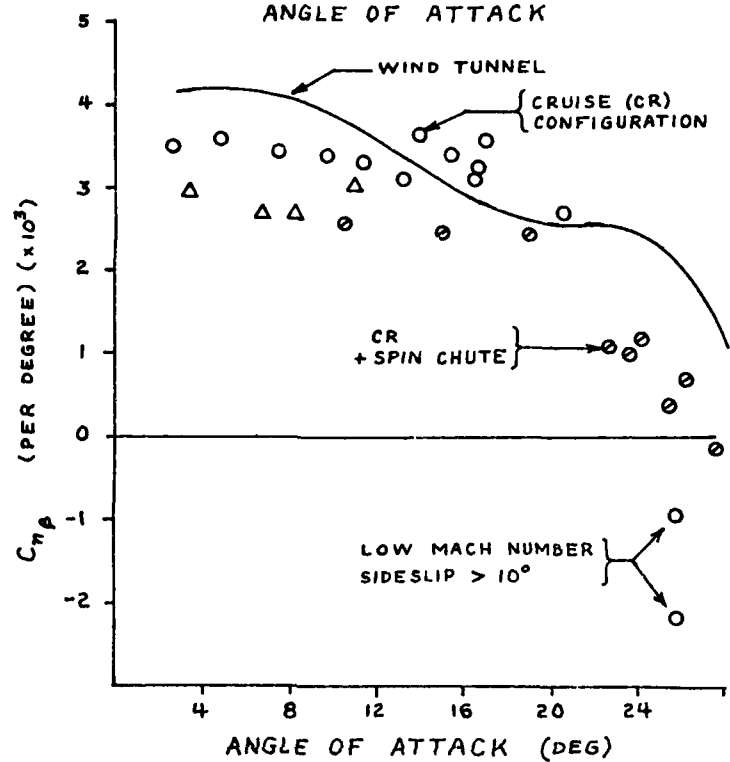
7. MIL-S-83691A (USAF), Military Specification, "Stall/Post-Stall/Spin Flight Test Demonstration Requirements for Airplanes," 15 Apr 1972.

8. Maine, Richard E. and Iliff, Kenneth W., "A Fortran Program for Determining Aircraft Stability and Control Derivatives from Flight Data," NASA TN D-7831, National Aeronautics and Space Administration, Washington, DC, Apr 1975.

9. Hoey, Robert G., "Choosing Test Conditions for Stability Derivative Maneuvers," AFFTC-TDM-75-4, Air Force Flight Test Center, Edwards AFB, CA 93523, Apr 1975.



FIGURE 3. STATIC LATERAL-DIRECTIONAL STABILITY
VERSUS
ANGLE OF ATTACK



ESTIMATION OF AERODYNAMIC CHARACTERISTICS FROM DYNAMIC FLIGHT TEST DATA

by

Kenneth W. Iliff
Aerospace Engineer
NASA Dryden Flight Research Center
Edwards, California 93523
USA

SUMMARY

There is a need to obtain estimates of aerodynamic characteristics from flight data. Advanced mathematical techniques can provide the unknown coefficients that describe the mathematical phenomenon if the phenomenon can be accurately modeled. These techniques have proved successful in obtaining information from flight data where proven models are available. This paper is intended to acquaint analysts working in ground testing and theoretical aerodynamics with the state of the art of obtaining aerodynamic characteristics from dynamic flight data. The flight data analyst needs guidance from ground testing and theoretical aerodynamic experts to properly define the necessary phenomenology for the high angle of attack flight regions. When this phenomenology has been defined, it will be possible to obtain more useful information from the analysis of dynamic flight data obtained in the high angle of attack regime.

SYMBOLS

All data are referenced to fuselage body axes according to right-handed sign conventions.

a_n	normal acceleration, g	M	aircraft mass, kg
a_x	longitudinal acceleration, g	M_r	drag-rise Mach number ratio
a_y	lateral acceleration, g	n	state noise vector
b	reference span, m	p	roll rate, deg/sec or rad/sec
C_D	coefficient of drag	\hat{p}_g	estimated gust roll rate, deg/sec
C_L	nondimensional lift	q	pitch rate, deg/sec or rad/sec
C_R	nondimensional rolling moment	\bar{q}	dynamic pressure, N/m ²
C_m	nondimensional pitching moment	R	covariance of weighted residual measurement error
C_n	nondimensional yawing moment	r	yaw rate, deg/sec or rad/sec
C_Y	nondimensional side force	s	reference area, m ²
c	reference chord, m	T	maneuver duration, sec
$f(\)$	general function	t	time, sec
G	spectral density of measurement noise	u	input vector
g	acceleration due to gravity, m/sec ²	V	velocity, m/sec
$g(\)$	general function	x	state vector
I_X	moment of inertia about roll axis, kg-m ²	y	observation vector
I_{Xp}	propeller moment of inertia about roll axis, kg-m ²	y_ξ	computed observation vector based on ξ
I_{XY}	cross product of inertia between roll and pitch axes, kg-m ²	z	measured observation vector
I_{XZ}	cross product of inertia between roll and yaw axes, kg-m ²	\hat{z}_ξ	Kalman-filtered estimate of the observation vector
I_Y	moment of inertia about pitch axis, kg-m ²	α	angle of attack, deg
I_Z	moment of inertia about yaw axis, kg-m ²	$\hat{\alpha}_g$	angle of attack induced by vertical velocity component of turbulence, deg or rad
J	cost functional	α_m	measured angle of attack, deg
		α_0	angle of attack of principal axis, deg or rad

β	angle of sideslip, deg	ψ	heading angle, deg
$\hat{\beta}_g$	estimated gust angle of sideslip, deg	ω_p	propeller speed, rad/sec
δ_a	aileron deflection, deg	Superscripts:	
δ_D	differential tail deflection, deg	*	matrix adjoint
δ_e	elevator deflection, deg	.	derivative with respect to time
δ_r	rudder deflection, deg	Subscripts:	
η	noise vector	$p, q, r,$	derivative with respect to indicated
θ	pitch attitude, deg	$\alpha, \dot{\alpha}, \beta, \delta_a,$	quantity
ξ	vector of unknowns	δ_e, δ_r	
ρ	atmospheric density, kg/m ³	trim	trimmed value
φ	bank angle, deg	wt	wind tunnel
		0	bias

INTRODUCTION

Significant effort has been spent in estimating unknown aircraft coefficients, such as stability and control derivatives, from dynamic flight maneuvers. The techniques used to estimate these coefficients are becoming increasingly complex; however, these techniques make it possible to obtain estimates of coefficients that in the past were nearly impossible to obtain.

This paper presents a survey of the investigations that have been undertaken to obtain estimates of coefficients from dynamic flight maneuvers. One of the methods, the maximum likelihood estimation technique, is described briefly and some of the successful applications of this technique at the Dryden Flight Research Center are presented. Possible techniques for analyzing responses obtained in the stall/spin regime are discussed. Finally, recent data obtained in the stall/spin flight regime are presented along with a discussion of how some basic results can be obtained with simple analysis techniques.

OVERVIEW OF AIRCRAFT COEFFICIENT ESTIMATION

The extraction of stability and control derivatives and other unknown coefficients or derivatives from flight data has been of interest for many years (refs. 1 and 2). The derivatives are used to provide final verification of the predicted full-scale aircraft aerodynamic characteristics and to verify the prediction techniques. The derivatives are needed to improve vehicle design and to assist in the flight testing and verification of overall aircraft system performance (ref. 3). After the analysis of the flight test data, the aircraft stability and control characteristics can be compared with calculated derivatives and wind tunnel predictions, and this comparison can be used to update prediction methods for the improvement of future aircraft designs (ref. 4). Once an aircraft is built, the derivatives play an important role in the expansion of the flight test envelope (ref. 5). As estimates of the derivatives become available, they are used to upgrade fixed-base simulators to assist in flight planning and the modification of the aircraft control system (ref. 6). In addition, the flight-determined derivatives can be used to establish compliance with the desired design specifications. Stability and control derivatives are also used to establish the accuracy of airborne simulations (ref. 7) and to identify aircraft parameters for adaptive control.

Initially, fairly straightforward methods of manual calculations were used to obtain estimates of these unknown coefficients. These methods have evolved into a very complex application of advanced mathematical techniques requiring digital computers. The advanced mathematical techniques can improve the efficiency of flight testing and can infer information not obtainable from flight data by less sophisticated techniques. The maximum likelihood estimator (ref. 8) is one of these techniques that has been successfully applied to the analysis of flight data (refs. 9 and 10).

The maximum likelihood estimator technique requires a mathematical model that adequately describes the phenomenon being studied. The technique can be used to estimate unknown coefficients for either linear or nonlinear systems, although its primary use to date has been for linear systems. Most of the proven formulations based on phenomenological considerations that are available to the analyst have been linear. The definition of the drag polar from flight data is an example of a nonlinear formulation based on phenomenological considerations. If a phenomenon is not well understood, it may be possible to gain insight into the proper mathematical model describing the phenomenon through the analysis of dynamic flight response data. Great care must be exercised or the resulting mathematical model may be representative of only the response data used to define the model.

Another type of model that occurs in the less well understood flight regimes, such as high angle of attack, is one that is stochastic in nature. If the forcing functions are stochastic, and the model is otherwise known, then the basic framework for defining the maximum likelihood estimator is available. If the unknown coefficients are stochastic, the procedure for extracting information from the data is not well defined. Although stochastic coefficients have been noted, it is difficult to discern the difference between deterministic coefficients that are not general enough to describe the phenomenon and stochastic coefficients. Some attempts are now being made to extract information from these less well understood flight regimes.

The following discussion is a chronological survey of the investigations that have led to the development and subsequent widespread acceptance of the maximum likelihood estimation technique for aircraft coefficient estimation. The more straightforward deterministic analyses are discussed first, followed by a brief discussion of nondeterministic analysis. Most of the investigations in estimation of unknown coefficients of general systems since 1960 have been surveyed in references 11 to 13. Some of the investigations in estimations of unknown coefficients from aircraft dynamic response data are contained in references 14 and 15.

Deterministic Analyses

The sophistication and complexity of methods being used to estimate the unknown coefficients from aircraft dynamic flight responses has continued to increase over the past 30 years. In the late 1940's and early 1950's the frequency response methods gained popularity in aircraft analysis as well as in other types of analysis. Steady-state oscillator analysis (ref. 16) and Fourier analysis (ref. 17) are representative of the frequency methods. Use of these methods yields the frequency response of the vehicle and not the coefficients of the differential equations. Attempts were then made to extract these coefficients by selecting values of the aircraft coefficients that resulted in the best fit of the frequency response (refs. 18 and 19). Regression techniques, such as the linear least square (ref. 20) and weighted least square (ref. 19), were also applied to flight data at about this time. Unfortunately, the regression techniques give poor results in the presence of measurement noise and yield biased estimates. The time vector technique (ref. 21) has also been applied to flight data. It suffers because an incomplete set of coefficients is obtained and the types of responses that can be analyzed are restricted to fairly simple motions.

Analog matching techniques (refs. 21 and 22) have also been applied to flight data. Analog matching is limited because resulting estimates vary with the skill and technique of the operator. A summary of some of the early work and comparisons of the various techniques are given in references 23 and 24. These comparisons show that a more complete method of identification is needed.

In 1968, two independent studies (refs. 25 and 26) of obtaining aerodynamic coefficients by methods of nonlinear minimization without state noise (output error methods) were published. Reference 25 describes the use of the maximum likelihood estimator with a modified Newton-Raphson technique (ref. 27) to obtain a complete set of aerodynamic coefficients from flight data. Reference 26 discusses the results of using a quasilinearization technique (ref. 28) to estimate some coefficients of an aircraft. One reason for the early success of these two attempts is that the previous research had furnished a well defined model that adequately described the resulting motion of the vehicle. These two early results of aircraft identification by nonlinear minimization generated a renewed interest in analysis of flight data. A modification of the cost functional to include *a priori* information was reported in reference 29. The minimization of this modified cost functional does not result in a maximum likelihood estimator, as it is based on the joint probability distribution rather than the conditional probability. The maximum likelihood estimation method has been successfully applied to a wide variety of vehicles, as described in references 9, 10, and 30. Efforts similar to these have provided maximum likelihood estimation computer programs tailored to suit specific aircraft applications. These programs are reported in references 31 to 34. Extensive experience has been obtained using the maximum likelihood estimator technique on dynamic flight responses. These results have been obtained from investigations carried out at many installations. A sampling of these results are contained in references 3, 4, 14, 15, and 35 to 42. The NASA Dryden Flight Research Center has estimated stability and control derivatives from over 3000 maneuvers performed by 30 different aircraft.

Another approach, similar to the output error methods discussed above, is the application of the Kalman filter (ref. 43) to obtain an estimate of the aerodynamic coefficients. Some of the early results obtained by the Kalman filter technique were unsatisfactory; that is, the estimates of both the states and the parameters were biased and did not always converge to reasonable results. Reference 44 showed that an improvement resulted from adding the derivative of the state. The Kalman filter estimation technique can be shown for certain uses to be equivalent to some of the maximum likelihood estimator (output error) methods. Reference 44 points out a weakness of the Kalman filter method in that it is dependent on the covariance matrix obtained from the filter. Reference 43 offers a technique for obtaining estimates of the covariance matrix with a sub-optimal Kalman filter. References 45 and 46 describe an application of the Kalman filter to provide the state estimates used for the estimation of stability and control derivatives as well as of performance parameters.

Nondeterministic Analysis

To date there appear to be broadly two techniques for the estimation of systems with unknown stochastic inputs - the Kalman filter or, more generally, the extended Kalman filter technique (refs. 43, 44, 47, 48, 49, and 50) and the maximum likelihood technique (refs. 9, 10, 51, 52, and 53). Many of the precise applications of these techniques do not truly fall into these classes, but tend to mimic one of these two techniques.

The general application of the extended Kalman filter is discussed in references 47 and 48. The extended Kalman filter for the discrete case was applied to simulated aircraft data with a stochastic input, and the results are shown in reference 44. Reference 49 presents a similar application to aircraft flight response data that shows inconclusive results because the stochastic input is small and the system is nonlinear. Somewhat better results are given in reference 50 with an application of a greatly simplified extended Kalman filter technique.

Reference 53 shows an application of the maximum likelihood estimator to response data of an aircraft flying in atmospheric turbulence. The results are in agreement with results obtained for the same aircraft flying in smooth air - that is, without the stochastic input. More discussion of these results is presented in the Nondeterministic Estimation section.

Most of the successful extractions of unknown coefficients from aircraft dynamic flight response data have been based on a simple linear mathematical model. This model has been found to be extremely good for obtaining stability and control derivatives in stabilized flight at low to moderate angles of attack. The mathematical model has been defined by a standard linear deterministic set of uncoupled equations with two or three degrees of freedom for the longitudinal modes and three degrees of freedom for the lateral-directional modes. The next section discusses some of the recent investigations conducted at the Dryden Flight Research Center that have successfully gone beyond the restrictions of this linear mathematical model. As more of these restrictions are eliminated, it is hoped that information previously not obtainable from dynamic flight responses will become available for comparisons with calculated aerodynamic and wind tunnel predictions.

ESTIMATION OF AIRCRAFT CHARACTERISTICS

The estimation problem considered in this paper can be defined in general terms as follows: The system investigated is assumed to be defined by the mathematical model which is described by a set of dynamic equations containing unknown parameters. The actual system response to some input is measured. The values of the unknown parameters are then inferred from the requirement that the model response match the actual system response. Formulated in this manner, the identification

of the unknown parameters could easily be accomplished by many methods; however, complicating factors arise when application to real systems is considered.

The first complication results from the impossibility of obtaining perfect measurements of the response of any real system. The sensor errors are usually included as additive measurement noise in the dynamic model. Once this noise is introduced, the theoretical nature of the problem changes drastically. It is no longer possible to exactly identify the values of the unknown parameters; rather, the values must be estimated by some statistical criterion.

For discrete time systems, the theory of estimation in the presence of measurement noise is relatively straightforward, requiring only basic probability. In continuous time, however, rigorously defining a useful probability measure requires considerable background in functional analysis.

The second complication of real systems is the presence of state noise or unknown stochastic inputs. State noise is random excitation of the system from unmeasured sources. Standard examples for the aircraft are buffeting and atmospheric turbulence. When both state and measurement noise are considered, the continuous time theory involves extensive mathematical background for a rigorous treatment. The algorithm that results, however, is actually simpler than the discrete time algorithm and more versatile from several viewpoints. The results presented in this paper are based on the continuous time formulation and discretized only at the stage of implementation on a digital computer. The theory will not be presented, but it is discussed in detail in references 51 and 53.

The final problem to be faced for a real system is modeling. It is assumed throughout the above discussion that for some value of each of the unknown coefficients, the system is correctly and exactly described by a simple dynamic model; therefore, the question of modeling error arises. In this paper, modeling error is treated as state noise or measurement noise, or both, in spite of the fact that the modeling errors may be deterministic rather than random. The assumed noise statistics can then be adjusted to include the contribution of the modeling error. This procedure is not rigorously justifiable, but combined with careful choice of the model, it is probably the best approach available.

The following section describes the method that results in the best compromise for estimating the unknown aircraft coefficients under the restrictions on the data discussed above.

Maximum Likelihood Estimation

The problem considered is: Given a set of flight time histories of an aircraft's response and input variables, find the values of some unknown parameters in the system equations that result in the best representation of the actual aircraft response. An intuitive mathematical approach to this problem is to minimize the difference between the flight response and the response computed from the system equations. This difference could be defined for each response variable as the integral of the error squared. These responses could then be multiplied by weighting factors proportional to the relative confidence in each signal and summed to obtain the total weighted response error. This defines an integral squared error criterion.

A mathematically more precise probabilistic formulation can be made. For each possible estimate of the unknown parameters, a probability that the aircraft response time histories attain values near the observed values can be defined. The estimates should be chosen so that this probability is maximized. This process results in the maximum likelihood formulation of the problem.

The maximum likelihood estimation method (ref. 8) is one technique that can be used to estimate unknown coefficients of a dynamic system. The mathematical model of this dynamic system may, in most instances, be described as

$$\dot{x}(t) = f(x, u, n, t) \quad (1)$$

$$y(t) = g(x, u, t) \quad (2)$$

$$z(t) = y(t) + \eta(t) \quad (3)$$

where

- x state vector
- u control vector
- n state noise vector
- y observation vector
- z measured observation vector
- η measurement noise vector

The maximum likelihood estimates are obtained by maximizing the log likelihood functional, the form of which depends on the type of the dynamic equations. This is actually done by minimizing the negative of the log likelihood functional. If there is no state noise, the cost functional to be minimized is

$$J = \frac{1}{T} \int_0^T [z(t) - y_{\xi}(t)]^* (GG^*)^{-1} [z(t) - y_{\xi}(t)] dt \quad (4)$$

where G is the spectral density of the measurement noise. A more complete discussion of this cost functional is given in references 8, 9, 33, 54, and 55.

If the system to be analyzed is described by a linear set of dynamic equations that include state noise, the cost functional

to be minimized is

$$J = \frac{1}{T} \int_0^T (z - \hat{z}_\xi)^* (GG^*)^{-1} (z - \hat{z}_\xi) dt + \text{Trace } (R) \quad (5)$$

where \hat{z}_ξ is the Kalman-filtered (ref. 51) estimate of y and R is the covariance matrix of the weighted observation estimation error. This algorithm (refs. 51, 53, 56, and 57), in contrast to the extended Kalman filter method, uses the Kalman filter to estimate only the states and measurements, not to estimate the unknown coefficients. Equation (5) is equivalent to equation (4) if there is no state noise because \hat{z}_ξ is then equivalent to y_ξ , and R is the null matrix.

Figure 1 illustrates the maximum likelihood estimation concept. The measured response of the aircraft is compared with the estimated response. The difference between these responses is called the response error. The Newton-Balakrishnan computational algorithm (formerly referred to as the modified Newton-Raphson algorithm) is used to find the derivative values that maximize the likelihood functional. Each iteration of this algorithm provides a new estimate of the unknown coefficients on the basis of the response error. The new estimates of the coefficients are then used to update the mathematical model of the aircraft. The updated mathematical model is used to provide a new estimated response and, therefore, a new response error. The updating of the mathematical model continues iteratively until a convergence criterion is satisfied. The estimates resulting from this procedure are the maximum likelihood estimates.

The maximum likelihood estimator also provides an estimate of the reliability of each estimate based on the information content of each dynamic maneuver. The estimate of the reliability analogous to the standard deviation is called the Cramér-Rao bound (ref. 8). This bound is sometimes multiplied by a scalar and is then referred to as the uncertainty level. The uncertainty level has been found useful in assessing the validity of estimates (ref. 9). Recently, greater insight has been gained into determining the scalar factor that relates the Cramér-Rao bound to the uncertainty level (ref. 10). The maximum likelihood estimator and the Cramér-Rao bound (uncertainty level) are used to assess the estimation throughout the remainder of this section.

Deterministic Estimation

Linear Aerodynamic Mathematical Model

The linear aerodynamic mathematical model considered in the following discussion is defined by the requirement that the first-order partial derivatives be used to describe the aerodynamic behavior of the aircraft. The differential equations of motion used to describe this linear model are nonlinear in the kinematic coupling terms. These nonlinear five-degree-of-freedom equations of motion, which allow for nonzero I_{XZ} and I_{XY} , are written as follows:

$$\dot{\alpha} = -\frac{\bar{q}s}{MV} C_L + q + \frac{g}{V} [\cos(\theta) \cos(\varphi) \cos(\alpha) + \sin(\theta) \sin(\alpha)] - \tan(\beta) [p \cos(\alpha) + r \sin(\alpha)] \quad (6)$$

$$\dot{\beta} = \frac{\bar{q}s}{MV} C_Y + \frac{g}{V} \cos(\theta) \sin(\varphi) + p \sin(\alpha) - r \cos(\alpha) \quad (7)$$

$$\dot{p} I_X - \dot{r} I_{XZ} - \dot{q} I_{XY} = \bar{q} s b C_l + q r (I_Y - I_Z) + p q I_{XZ} - r p I_{XY} \quad (8)$$

$$\dot{q} I_Y - \dot{p} I_{XY} = \bar{q} s b C_m + r p (I_Z - I_X) + (r^2 - p^2) I_{XZ} + q r I_{XY} + r \omega_p I_{Xp} \quad (9)$$

$$\dot{r} I_Z - \dot{p} I_{XZ} = \bar{q} s b C_n + p q (I_X - I_Y) - q r I_{XZ} + (p^2 - q^2) I_{XY} - q \omega_p I_{Xp} \quad (10)$$

$$\dot{\theta} = q \cos(\varphi) - r \sin(\varphi) \quad (11)$$

$$\dot{\phi} = p + r \cos(\varphi) \tan(\theta) + q \sin(\varphi) \tan(\theta) \quad (12)$$

The standard equations of motion are defined by ignoring the kinematic coupling. The underlined terms are omitted; the remaining terms are linearized about average values of θ , ϕ , and α . If the aircraft is inertially symmetric in the horizontal plane, the I_{XY} term is zero and the terms including I_{XZ} disappear.

For the purposes of this paper, the linear expansions of the nondimensional moments and forces are written as follows:

$$C_L = C_{L_\alpha} \alpha + C_{L_{\delta_e}} \delta_e + C_{L_0} + C_{L_\beta} \beta \quad (13)$$

$$C_Y = C_{Y_\beta} \beta + C_{Y_{\delta_a}} \delta_a + C_{Y_{\delta_r}} \delta_r + C_{Y_0} + C_{Y_\alpha} \alpha \quad (14)$$

$$C_l = C_{l_\beta} \beta + C_{l_p} \frac{pb}{2V} + C_{l_r} \frac{rb}{2V} + C_{l_{\delta_a}} \delta_a + C_{l_{\delta_r}} \delta_r + C_{l_0} + C_{l_q} \frac{qc}{2V} + C_{l_\alpha} \alpha \quad (15)$$

$$C_m = C_{m_\alpha} \alpha + C_{m_q} \frac{qc}{2V} + C_{m_{\delta_e}} \delta_e + C_{m_0} + C_{m_{\delta_a}} \delta_a + C_{m_p} \frac{pb}{2V} + C_{m_r} \frac{rb}{2V} + C_{m_\beta} \beta \quad (16)$$

$$C_n = C_{n_\beta} \beta + C_{n_p} \frac{pb}{2V} + C_{n_r} \frac{rb}{2V} + C_{n_{\delta_a}} \delta_a + C_{n_{\delta_r}} \delta_r + C_{n_0} + C_{n_q} \frac{qc}{2V} + C_{n_\alpha} \alpha \quad (17)$$

The underlined terms are normally not included in the linear analysis when the data are gathered during stabilized flight at low angles of attack. The underlined terms (referred to as the aerodynamic cross-coupling terms) are only needed when the aircraft is expected to have aerodynamic cross-coupling between the longitudinal and lateral-directional aerodynamic modes. For instance, these terms would be significant for an aircraft that is flying at high angles of attack or that is aerodynamically asymmetric.

In the absence of either kinematic or aerodynamic cross-coupling terms, the equations can be divided into two sets—that is, the two-degree-of-freedom longitudinal equations and the three-degree-of-freedom lateral-directional equations. The longitudinal equations are defined by equations (6), (9), and (11) with δ_a , δ_r , ϕ , β , p , and r assumed constant. The lateral-directional equations are defined by equations (7), (8), (10), and (12) with δ_e , θ , α , and q assumed constant.

The next two sections discuss the estimation of aerodynamic coefficients from dynamic flight maneuvers without and with cross-coupling effects, respectively. The figures showing estimated stability and control derivatives presented in the remainder of this section show each estimate of the unknown coefficient as a symbol with an associated vertical line indicating the uncertainty level for that estimate. The longer the vertical line, the less certain the estimate (refs. 8, 9, and 10).

Examples without coupling effects

Many examples of obtaining maximum likelihood estimation of unknown coefficients from dynamic flight maneuvers exhibiting no coupling are available in the literature. When coupling is present, the analysis becomes more difficult.

Evaluating aircraft scale effects: One way to assess the quality of flight estimates is to compare these estimates with predictions from other sources. When making this comparison, great care must be taken to assess any possible sources of error that may contaminate the estimates or predictions. Errors may enter into the flight-determined maximum likelihood estimates from many sources, some of which are discussed elsewhere in this paper. Other sources of error are discussed in reference 54. Sometimes, after all apparent sources of error have been investigated, differences between the estimates from different sources still exist. Such differences have been observed when comparing wind tunnel estimates with flight-determined estimates. These differences are frequently attributed to either scale effects or the differences in aerodynamic flow between the static wind tunnel tests and the dynamic flight maneuvers. It is therefore of interest to compare flight-determined estimates from the same configuration for two scales.

Stability and control maneuvers were performed in flight on both a full-scale highly maneuverable jet aircraft and a large-scale unpowered remotely piloted vehicle (RPV) with the same configuration. The maneuvers on the jet aircraft were performed at three engine mass flow rates to assess the effect of the propulsion system on the stability and control derivatives. A complete set of stability and control derivatives were obtained for both vehicles using the maximum likelihood estimation method. These derivatives were obtained on both vehicles over an angle of attack range of approximately -15° to 20° . The propulsion system appeared to have little effect on the derivatives. In general, very good agreement was found between the estimates from the two vehicles.

Figure 2 shows the maximum likelihood estimates of $C_{n\beta}$, C_{nr} , and $C_{n\delta_r}$ from the RPV. The vertical bars represent the uncertainty levels. The fairing of the data was determined by considering the estimates with the smaller uncertainty levels to be more reliable. Figure 3 presents estimates from the full-scale airplane of the same derivatives in the same format. The various symbols represent various mass flow rates. The fairing from figure 2 is repeated in figure 3. The agreement between the two vehicles is good for $C_{n\beta}$ and C_{nr} . The trend for $C_{n\delta_r}$ is the same for both vehicles, but the full-scale airplane indicates more rudder control effectiveness. There is no trend in $C_{n\delta_r}$ for the full-scale airplane to indicate that an extrapolation of the mass flow rates would account for the difference. Since $C_{n\beta}$ and C_{nr} for both vehicles are in good agreement, it is unlikely that an error in the moment of inertia in one of the vehicles would account for the difference. These results imply the difference in $C_{n\delta_r}$ between these vehicles may be attributable to scale effects.

Assessing angle of attack: Sometimes discrepancies between derivatives estimated from a given flight and the previously available estimates can be explained by uncertainties in the measured angle of attack, α_m . This uncertainty can be resolved by making an independent estimate of angle of attack. The angle of attack of the principal axis, α_0 , can be estimated by using the unknown coefficient $\sin \alpha_0$, which occurs in the lateral-directional equations of motion (eq. (7)). This coefficient is extremely important when no measurement of angle of attack is made. In this case, an estimate of angle of attack can be obtained from $\sin \alpha_0$ so that the derivatives obtained from flight can be compared more meaningfully with derivatives obtained by other methods. This technique for obtaining angle of attack is particularly effective when many maneuvers are available. Figure 4 compares $\sin \alpha_0$ with α_m for a measured angle of attack range from -20° to 53° . The solid line corresponds to perfect agreement between α_0 and α_m . For the data plotted, the cross moment of inertia is approximately zero, so the principal axis is nearly coincident with the body axis; therefore, α_0 should equal α_m . As the figure shows, most of the data fall near the line for α_0 equals α_m , verifying that the measured angle of attack is a fairly good indication of the actual angle of attack. As figure 4 shows, if no measurement of angle of attack had been made for this vehicle, the actual value of angle of attack could have been determined fairly accurately from $\sin \alpha_0$.

Determining translational acceleration derivatives: It is difficult to obtain the translational acceleration derivatives independent of the angular rate derivatives from dynamic flight maneuvers. These derivatives are difficult to obtain in flight for the same reason they are difficult to obtain in standard wind tunnels—that is, translational acceleration and angular rate are normally dependent variables. In flight, these variables are nearly dependent, but due to the normally small terms containing g/V in equations (6) and (7), they are technically independent. This is a small effect, and therefore, determining the effects of these two variables falls into the category of nearly dependent variables (ref. 54), making any meaningful estimate of their separate effects difficult.

In the past, the sum of the two effects (translational acceleration and angular rate) has been determined and the separate effects then estimated by analytical means, just as was done with wind tunnel estimates. At relatively low angles of attack, the analytical techniques usually indicated the translational acceleration effect was negligible; all of the effect was attributed to the angular rate. Recently, renewed interest in the translational acceleration and rate derivatives has emerged due to the predicted predominant effect of these derivatives at high angles of attack (refs. 58 and 59). If these derivatives are significantly different from zero, then it is of great interest to know their value when conducting flight tests, as the resulting flight responses are affected by them.

The appendix discusses several maneuvers that can be performed to allow the independent estimation of the translational acceleration and angular rate derivatives. The appendix shows that two different maneuvers should allow separate estimation of these derivatives. The first maneuver discussed in the appendix is an aileron roll that includes elevator pulses. The second maneuver is accomplished by obtaining erect and inverted elevator pulse maneuvers at the same angle of attack and analyzing them simultaneously with multiple maneuver analysis (refs. 8, 9, 33, and 54).

To assess these two types of maneuvers, the T-37 twin jet aircraft was chosen because it is able to fly inverted and because a complete set of flight-determined stability and control derivative estimates were already available for comparison (ref. 60). To test the erect and inverted maneuver approach, four inverted and four erect longitudinal maneuvers were obtained at the same angle of attack. The maximum likelihood estimates were obtained for four pairs of double maneuvers (an erect maneuver paired with an inverted maneuver).

The estimates of $C_{m\dot{\alpha}}$ from all the maneuvers were in good agreement, which resulted in a small deviation. The Cramér-Rao bounds obtained for each estimate were even smaller than the resulting standard deviations. Similar results were obtained for C_{m_q} . The consistency of the estimates, standard deviations, and Cramér-Rao bounds adds confidence to the meaningfulness of obtaining $C_{m\dot{\alpha}}$ from this type of maneuver. The sum of C_{m_q} and $C_{m\dot{\alpha}}$ obtained from the double maneuvers is approximately equal to the value of $C_{m_q} + C_{m\dot{\alpha}}$ given by reference 60, as would be expected. Figure 5 shows a typical fit of the double maneuvers obtained with the maximum likelihood estimator. The fit is very good. Another way to assess the validity of the estimate of $C_{m\dot{\alpha}}$ is to attempt the estimation based on the same maneuvers, forcing $C_{m\dot{\alpha}}$ to be zero. Since conflicting information is given for the damping erect and inverted (due to the $C_{m\dot{\alpha}}$ contribution), the fit would be expected to be poorer, resulting in a more poorly damped calculated response from the maximum likelihood estimator. The results of this estimation are shown in figure 6 for the same two maneuvers. The estimated damping is obviously significantly lower in figure 6 than in figure 5. In addition, note that the value for $C_{m_q} + C_{m\dot{\alpha}}$ is about the same as it was for C_{m_q} alone in the analysis that allowed $C_{m\dot{\alpha}}$ to vary. It is important to note here that quality of fit, in itself, is not a good criterion for assessing the desirability of adding a new term to the unknown coefficients being determined. In the example given here, the need for $C_{m\dot{\alpha}}$ was strongly motivated from physical laws. $C_{m\dot{\alpha}}$ was also assessed on its agreement with the results given in reference 60 and on the size of the standard deviation and Cramér-Rao bounds of the estimates.

It is of interest to see the resulting fit of the aileron roll maneuver. This very good fit is shown in figure 7. The analysis of this maneuver would logically fall in the next section, as it is a highly kinematically coupled maneuver; however, since it is intended to enhance the information on $C_{m\dot{\alpha}}$, it is included here for completeness.

Examples with coupling effects

As pointed out before there are basically two types of coupling, kinematic and aerodynamic. In this section, an example of kinematic coupling is studied first, and then an example of kinematic coupling along with aerodynamic coupling is examined. Investigations of aerodynamic coupling are of great interest currently because aircraft flying at high angles of attack exhibit aerodynamic coupling due to the effects of separated flow.

Response with kinematic coupling terms: Estimation of the aerodynamic coefficients is sometimes desirable in the presence of kinematic coupling between the longitudinal and the lateral-directional aerodynamic modes. Coupling usually occurs during stability and control maneuvers when the vehicle cannot be completely stabilized. This lack of stability occurs frequently during steady turns or high angle of attack maneuvers. If the measurements of the motions in the modes not being analyzed are assumed to be sufficiently accurate, these motions can be treated as known. Therefore, the coupling terms appear as known external inputs (eqs. (6), (9), and (11)) to the mode under investigation. The model is once again linear, and the maximum likelihood estimator can be applied and the additional terms treated as extra controls.

Figure 8(a) is a time history of a longitudinal maneuver during which lateral-directional motion was significant. The fit of the flight and estimated data is not particularly good because the aircraft was at an extreme angle of attack and was difficult to stabilize in the lateral-directional mode. Figure 8(b) shows the fit that results when the kinematic coupling terms are included. This fit is considered exceptionally good for a high angle of attack maneuver, and the resulting derivatives are in good agreement with derivatives obtained from maneuvers performed at the same flight condition but with little lateral-directional motion at the same angle of attack.

Response with kinematic and aerodynamic coupling terms: The previous section showed the results that could be obtained when the kinematic coupling terms were accounted for. This section discusses some of the results obtained from the oblique wing aircraft (ref. 61). The oblique wing aircraft was a powered remotely piloted aircraft. A sketch of the vehicle is shown in figure 9.

The oblique wing aircraft configuration is of current interest because of its potential for transonic drag reduction and corresponding fuel savings. Before the oblique wing concept can be developed to its full potential, it is necessary to develop techniques to verify the asymmetrical aircraft's aerodynamic characteristics in flight. The maneuvers obtained from the oblique wing aircraft were analyzed by using a technique similar to that used to account for the kinematic coupling in the previous

section. In addition to this, the underlined terms (aerodynamic coupling terms) in equations (13) to (17) were allowed to vary. The estimation was done with the two-degree-of-freedom longitudinal and the three-degree-of-freedom lateral-directional equations of motion. Therefore, as described in detail in reference 61, the state variables used to determine the aerodynamic coupling terms were the measured values. A complete set of stability and control derivatives including the aerodynamic coupling terms were successfully determined. Figure 10 shows the comparison of the estimated values from flight with the wind tunnel estimates obtained for wing skew angles of 0° and 45° for the aerodynamic coupling terms $C_{m\delta_a}$ and $C_{m\delta_p}$. There is reasonable agreement between the two sets of estimates. These derivatives are important when leaving or entering a turn.

The analysis above is for estimating stability and control derivatives for an asymmetric aircraft. At high angles of attack, the cross-coupling terms result from separated flow, but the resulting flight responses are similarly affected. By using the same technique used in reference 61, it is hoped that in some instances the cross-coupling terms can be estimated from dynamic maneuvers at high angles of attack.

Nonlinear Aerodynamic Mathematical Model

The previous section discussed the techniques that can be applied to flight data to make the correlation of flight estimates with other predictive estimates more valid. This section discusses two analysis techniques that can be used to aid in correlating flight estimates with other predictive techniques when it is known that the mathematical model is nonlinear—that is, the form of the model is based on sound physical principles or on independent measurement.

Example of unknown nonlinear model

An instance for which no proven model exists is when maneuvers are performed at high angles of attack. One way to treat this problem, when perturbations about the nominal are small, is to assume that the system is still described by the linear equations of motion. For example, the pitching coefficient, C_m , as a function of angle of attack is quite nonlinear over a large angle of attack range. If the change in angle of attack can be kept small enough for a given flight condition, the derivative $C_{m\alpha}$ can be estimated and plotted as a function of angle of attack. Figure 11 shows $C_{m\alpha}$ as a function of angle of attack for an angle of attack range from -20° to 50° . The estimates show a consistent trend which is in fairly good agreement with the wind tunnel estimates. Therefore, by linearizing for small excursions from the nominal condition, a linearly approximated model can sometimes be used where there is no known nonlinear model.

Example of known nonlinear model

Sometimes the linear model of the aircraft becomes inadequate, and the nonlinear model is known but cannot be put into linear form. For example, to obtain drag information from a dynamic flight maneuver it is necessary to include the nonlinear drag polar in the model. The nonlinear model for the estimation of the lift and drag coefficients is derived in reference 55, and the complete set of results is given. The equations of motion are now nonlinear in the state variables, so they are more complex than those described in equations (6) to (17). Although the equations are nonlinear, they still fit the general form of equations (1), (2), and (3); therefore, the cost functional given by equation (4) can still be used to obtain the maximum likelihood estimates.

To obtain estimates of the drag polars, pushover-pullup maneuvers were performed in flight. Figure 12 is a comparison of longitudinal maneuver data and data computed on the basis of estimates from a nonlinear model for the algorithm just discussed. The fit is excellent. The drag polar obtained from this maneuver is compared in figure 13 with wind tunnel estimates of the drag polar. Agreement is reasonably good.

To assess the usefulness of the maximum likelihood estimation technique for obtaining drag information from dynamic maneuvers, the maximum likelihood estimates were compared with the wind tunnel estimates as a function of the drag-rise Mach number ratio at four constant lift coefficients. Drag-rise Mach number ratio, M_r , is calculated by dividing Mach number by the wind tunnel estimate of the drag-rise Mach number at a lift coefficient of 0.25. The drag-rise Mach number is defined as the Mach number where $\frac{\partial C_D}{\partial \text{Mach number}} = 0.1$. The maximum estimates of the trimmed drag are compared with wind tunnel results in figure 14. The dashed line is a fairing of the maximum likelihood estimates (similar to those shown in fig. 13) obtained at various Mach numbers. In general, the comparison is good and indicates that the drag-rise Mach number determined by the maximum likelihood estimation technique is somewhat lower than that determined by the wind tunnel estimates.

Nondeterministic Estimation

All the analysis discussed previously was based on estimating coefficients from deterministic mathematical models. If the vehicle is known to be in the presence of unknown stochastic inputs, then the problem can no longer be put into a completely deterministic form. In this section, the analysis of two examples with unknown stochastic inputs are discussed—an aircraft flying in turbulence and an aircraft experiencing wing rock at a high angle of attack.

Analysis Including Atmospheric Turbulence

Aircraft cannot always avoid flying in atmospheric turbulence, so it is desirable to be able to obtain stability and control derivatives in the presence of turbulence. In addition, it can also be important to obtain an estimate of the turbulence time history. The technique described in references 51, 53, 56, and 57 can account for the effect of turbulence. With this technique, maximum likelihood estimates of the stability and control derivatives as well as estimates of the turbulence time histories are obtained by minimizing the cost functional given by equation (5).

Figure 15(a) is a comparison of the longitudinal flight response obtained in atmospheric turbulence with the estimated response obtained with the maximum likelihood estimator of equation (4). The fit is obviously unacceptable as were the estimated coefficients (refs. 53 and 57). The data shown in figure 15(b) were analyzed using the maximum likelihood estimator

that accounts for the unknown stochastic input by minimizing the cost functional of equation (5). The fit that results is virtually perfect. The resulting estimated coefficients were also shown to be very close to the estimates obtained while flying at the same flight condition in smooth air (refs. 53 and 56). The estimated spectrum of the unknown stochastic input was also in excellent agreement with the theoretical Dryden spectrum for atmospheric turbulence (refs. 53, 56, and 57).

To show the general applicability of the algorithm, a similar test was made on lateral-directional flight data obtained in atmospheric turbulence. Figure 16(a) shows the results when the estimator does not account for the unknown input, and figure 16(b) shows the results when the estimator does account for the unknown input. The fit shown in figure 16(b) is virtually perfect, and the maneuver provided acceptable estimated coefficients and good agreement with the theoretical power spectrum (ref. 10).

It has been shown that the maximum likelihood estimator that accounts for turbulence (eq. (5)) provides a good fit for both longitudinal and lateral-directional maneuvers obtained in turbulence. In addition, the resulting estimated stability and control derivatives and the estimated spectrum of the turbulence were found to be in good agreement with other techniques.

Analysis Including Separated Flow

Another situation in which the aircraft is driven by an unknown stochastic input is when the aircraft is flying with separated flow. Although there are many causes of flow separation, the time at which the separation occurs and the frequency with which it occurs are apparently random. Thus, little can be done to extract meaningful stability and control derivatives unless the separation is mild enough to permit a known model to approximate the overall resulting motion adequately. Figure 17 shows data obtained during a period when flow separation was known to exist. These data are compared with data computed from the maximum likelihood estimates obtained by using equation (4). The fit, although sometimes poor, indicates that the computed data approximate the flight data. Therefore, a fairly good linear approximation of the data was obtained with flow separation. The separation shows as a poor fit in roll rate, but the resulting estimated coefficients agreed well with those obtained when aerodynamic separation was not evident. The effect of separated flow shown in figure 17 is mild. Where separated flow becomes predominant at very high angles of attack, the cross-coupling terms from the lateral-directional modes need to be included. These types of problems are currently being studied. The estimator that accounts for an unknown stochastic input (eq. (5)) also may serve as a useful tool in analyzing data obtained where the flow is predominantly separated. Analyses of this type are now being conducted on maneuvers obtained in the stall/spin flight regime.

ESTIMATION AT HIGH ANGLES OF ATTACK

The problems that have been discussed in this paper have had quantitative solutions that were in some sense satisfactory. There are, of course, far more problems in the physical world that have no satisfactory quantitative solutions. Frequently, no apparent quantitative solutions exist because no model that is satisfactorily precise has been proposed. High angle of attack problems are understood in a qualitative sense, but no exact model that will serve the flight data analysts in all eventualities has been defined.

It is well known that when flying at high angles of attack small changes in the flight condition can result in large changes in the resulting forces and moments on the aircraft. This phenomenon has many qualitative explanations, such as flow separation, vortex shedding, asymmetric vortex shedding, and vortex bursting. However, none of these explanations are of much immediate use to the analyst of flight data. These phenomena are very difficult to study from any point of view, but simulation and wind tunnel studies at high angles of attack can be better controlled than studies performed in flight. Reference 62 points out some of the recent successes and remaining difficulties encountered in these types of studies at high angles of attack. Before much progress can be made in analyzing flight data at high angles of attack, the flight data analyst must await further guidance from the theoretical aerodynamicists and wind tunnel testing experts on how to best model the phenomenon. The problem faced in the analysis of high angles of attack flight data is that the aircraft behaves in a highly dynamic, highly variable manner. No good general models exist. The vehicle appears to behave differently at different times at essentially the same conditions. Without a suitable model, the flight data analyst is forced to resort to *ad hoc* techniques, such as infinite power series expansion and spline fitting procedures (refs. 63, 64, 65, and 66). The explanation in the following section concerning the difficulties facing the flight data analyst may help clarify the problem.

Definition of Stall/Spin Modeling Problems

When studying responses obtained at high angles of attack from a purely analytical point of view, the problem can be treated as deterministic. With existing theory, a model that predicts the overall reaction for each consecutive time interval can be stated or simulated. The analytical solution from this deterministic approach is plausible and results in responses that realistically represent the actual problem.

The problem becomes completely different when its inverse is viewed. The resulting flight response is given, and the task becomes one of determining what values of the unknown coefficients of some unspecified model would account for the given response. The analyst is then faced with a problem for which there is little precise physical insight. In addition, the flight data are transient, so little information is contained in any one maneuver. The analyst then tries to model the problem with a high-order power series, since it is well known that any finite set of data can be fit to any degree of accuracy if one is willing to use enough terms in a power series.

References 63 to 66 are examples of studies done to try to perfect the technique of selecting the most meaningful terms in a power series. Some frustration results from trying to use these power series, since frequently the problem is not really deterministic. The problem is perhaps deterministic, in a very large sense, but it becomes a problem involving stochastic coefficients (or at least an unknown stochastic input) when realistically sized. That is, repeating an experiment with exactly the same initial conditions and exactly the same known inputs to the system results in a completely different response. Solving the inverse problem under these circumstances will result in two completely different power series with very little similarity in the values of like coefficients and probably a different set of significant terms in the power series. Therefore, the analyst ends up with little information that can be used to provide a meaningful mathematical model to describe a phenomenon in general. Since it appears that there are many problems that are of current interest that fall into this class, a philosophy needs to be developed on how to approach problems without appropriate phenomenology. In the future, theoretical or experimental

results that remove a given problem from the above confusion may develop. However, until this happens, a procedure is needed to obtain the most meaningful results when analyzing problems of this sort.

To avoid meaningless results, the following guidelines are proposed for application to the analysis of problems requiring a power series expansion solution. If the resulting model does not satisfy all these guidelines, the results may be meaningless. When evaluating the estimates obtained from flight test data for comparison with other estimates, the analysis should be scrutinized to see if these guidelines were applied.

- The higher order statistics of the estimated coefficients of the power series (such as f tests) must indicate that the estimates are valid.
- The quality of the fit must be good, and even small discrepancies must be explained since these discrepancies can result in serious misinterpretations of nonlinear systems.
- The simplest model that adequately fits the data should be chosen; a more complex model cannot be justified.
- A consistent trend must result for each estimated coefficient as each independent variable is changed.
- A plausible physical explanation for each resulting model should be found.
- The resulting model must be evaluated on a completely independent set of data.

References 63 to 66 report results of applying one or more of these rules to data obtained in the high angle of attack regime. This regime is also being investigated at the Dryden Flight Research Center, and all these guidelines are being applied. In the high angle of attack regime, it is sometimes possible to describe the flight responses with relatively simple models. The application of the other guidelines becomes fairly straightforward once the model has been simplified. The following section discusses some of the results obtained with the simplified model approach.

Investigation of Stall/Spin Characteristics at the Dryden Flight Research Center

A program is underway at the Dryden Flight Research Center to investigate the flight characteristics in the stall/spin flight regime. Some information has already been obtained in the stall region at angles of attack up to 55° . The analysis was conducted with a linearized model of the equations of motion. Some results of the analysis of data obtained in the stall/spin regime are given in reference 3. In addition, analysis is being attempted on data obtained in the wing rock region, which allows unknown cross-coupling terms and stochastic inputs.

Investigations are also in progress to analyze data obtained while an aircraft is in a spin. The approach being taken for these investigations is to start with the simplest model possible. Then, as the need arises and the system being studied becomes more general, the model is made more complex. The steady-state spinning condition appears to be the simplest dynamic system to model in the stall/spin regime because the kinematic terms equal the aerodynamic terms of equations (6) to (12) in a steady-state fashion. The steady-state spinning condition is established when the controls have remained at a fixed position allowing the vehicle to stabilize in a smooth mode with little variation in the response variables. Then the steady-state aerodynamic effects can be approximated by equating them to the kinematic effects (which are known). This steady-state condition can also be analyzed in rotary balance tunnels where the effects of changing variables on the forces and moments can be investigated. With these predicted parameters from the wind tunnel as starting values, the necessary adjustments can be made to the flight estimates to match the flight responses. Once this problem has been solved, small perturbations about the steady-state spinning condition can be made and their effects can be estimated. This approach can be expanded to the point that much of the spinning phenomenon observed on the aircraft may be explained and accounted for. The flight vehicle being used is the spin research vehicle (SRV) described below.

Spin Research Vehicle Description

The spin research vehicle (SRV) is a large-scale unpowered remotely piloted vehicle that is representative of current high performance fighter aircraft. The SRV is 7 meters long with a span of about 4 meters. The vehicle instrumentation consisted of the standard package used for the measurement of altitude and airspeed, three axis angular rate gyros, attitude gyros, linear accelerometers along with control position transducers, and boom-mounted angle of attack and angle of sideslip vanes. Pressure sensors mounted on the nose, wings, and stabilizers, and tufts on the aft portion of the vehicle are included for flow visualization. The data are acquired by means of a pulse code modulation system at 200 samples per second. The control system is implemented on a ground-based computer to allow the investigation of various spin avoidance and automatic spin recovery techniques. Aerodynamic modifications can be made to the vehicle to observe the effects on the stall/spin characteristics of the vehicle.

Stall/spin Results

The smooth spin modes referred to previously were obtained from the SRV. The most repeatable quantitative spin characteristic is the zero control smooth spin mode. This is the stabilized condition of the aircraft when it remains in a spin with the lateral-directional controls set to zero. The important responses depicting a zero control smooth spin mode are shown for the SRV in figure 18. An example of perturbations about these smooth modes can be seen in figure 19, where a control pulse was put in after the vehicle had been stabilized in a zero control smooth spin mode. It is hoped that with pulses of this sort, a fairly linear perturbation model can be defined and the aerodynamic characteristics can be estimated with the maximum likelihood estimator. The results from this analysis can be compared to the results being obtained with computational aerodynamics and with the rotary balance wind tunnel tests on the SRV configuration.

One of the reasons the steady-state spin is being investigated first is that this appears to be repeatable from flight to flight. The spin entries are not as repeatable even when the initial inputs and conditions are fairly closely matched. It is hoped that the entries can be investigated more completely by allowing unknown stochastic inputs to be determined during the entry while trying to determine some of the more important aerodynamic characteristics.

The SRV has different spin characteristics for spins to the left and to the right. This is probably caused by the asymmetric shedding of the vortices caused by a slight misalignment of the nose. Figure 20 shows the effect of this spin asymmetry for left and right spins with nearly identical control motions (the lateral-directional controls have the same magnitude but are opposite in sense). The figure shows that the vehicle spins much more readily to the right than to the left: To reach a yaw rate of 100 degrees per second when spinning to the left, the SRV takes twice as long as it takes to reach the same yaw rate when spinning to the right.

The effect of the asymmetry can also be seen in terms of the two primary variables that define the spinning condition: yaw rate and angle of attack. The zero control smooth spin modes (such as those shown in figs. 18 and 19) can be repeated during a given flight and from flight to flight. There may be one or more such modes for a given aircraft configuration; however, the same combination of yaw rate and angle of attack is repeatable again and again. An example of this repeatability is shown in figure 21, where the vehicle attains the same zero control smooth spin mode twice during the same flight. The yaw rate and angle of attack are the same for both steady-state spin conditions. The same mode was indicated on several other flights as well.

Research is just beginning to extract information from spins that may help in the understanding of the phenomenon. The preliminary results shown here give examples of some of the characteristics that can easily be investigated. This is an example of one area where investigations are being carried out. However, these results are just a start and much more must be done to define satisfactory models in the stall/spin regime.

CONCLUDING REMARKS

Much of the estimation of aerodynamic characteristics from dynamic flight maneuvers has been confined to analysis of the linear aircraft mathematical model. Some success has been achieved in obtaining estimates of characteristics where the model is nonlinear or nondeterministic and the phenomenon being analyzed is fairly well understood. Attempts are being made to obtain information from flight data in the high angle of attack regime. These attempts suffer from the lack of physical insight into the phenomenon being analyzed, so very minimal results have been obtained from flight data to date.

Some flight results obtained at the Dryden Flight Research Center indicate that analysis techniques currently available can be used to extract basic stall/spin characteristics from responses obtained in the stall/spin regime. The more complex problems in the stall/spin regime still remain. Therefore, the flight data analyst needs guidance from wind tunnel and theoretical aerodynamic experts to properly define the necessary phenomenology. When this phenomenology is defined, more useful information will be obtained from the analysis of flight data obtained in the high angle of attack regime.

APPENDIX

Methods of Estimating Translational Acceleration Derivatives

The translational acceleration derivatives are of general interest, especially if they are sufficiently large because they impact the comparison of many of the stability and control derivatives obtained from flight with those obtained from wind tunnels. This impact is most easily seen in the translational acceleration derivative $C_{m_{\dot{\alpha}}}$ and its effect on $C_{m_{\alpha}}$. The $C_{m_{\alpha}}$ in equation (16) can be estimated from flight data and is actually $C_{m_{\alpha_{wt}}} - \frac{\rho s c}{4M} C_{L_{\alpha}} C_{m_{\dot{\alpha}}}$, where $C_{m_{\alpha_{wt}}}$ is the value that would be obtained from a wind tunnel. In the past, with $C_{m_{\dot{\alpha}}}$ assumed to be appropriately zero, the $C_{m_{\alpha}}$ measured in flight was roughly equivalent to that measured in the wind tunnel. If $C_{m_{\dot{\alpha}}}$ is other than zero, the flight $C_{m_{\alpha}}$ must be corrected to be comparable to the wind tunnel value. To make this correction, it becomes necessary to have an estimate of $C_{m_{\dot{\alpha}}}$.

Three methods of estimating $C_{m_{\dot{\alpha}}}$ from dynamic flight maneuvers can be envisioned:

1. Estimate $C_{m_{\dot{\alpha}}}$ independent of C_{m_q} for an aircraft flying in turbulence (ref. 53) where the $\dot{\alpha}$ is quite independent of q .
2. Estimate $C_{m_{\dot{\alpha}}}$ at high and low altitudes at the same angle of attack so that the flight estimate of $C_{m_{\dot{\alpha}}}$ will change as a function of atmospheric density.
3. Design an aircraft maneuver in smooth air that forces $\dot{\alpha}$ and q to be independent.

The first method seems to be a sound way of estimating $C_{m_{\dot{\alpha}}}$ but this may not be the same $C_{m_{\dot{\alpha}}}$ that is desired for standard aircraft maneuvering. That is, the $C_{m_{\dot{\alpha}}}$ obtained in turbulence may be the result of a different aerodynamic interaction than the one obtained for normal flight maneuvers. At the very least, since $C_{m_{\dot{\alpha}}}$ is predicted to be frequency dependent, the frequency range of $\dot{\alpha}$ in turbulence is much different than the frequency range in normal aircraft maneuvering.

The second method, that of performing similar maneuvers at different altitudes and calculating the $C_{m_{\dot{\alpha}}}$ that would be required to make the difference in $C_{m_{\alpha}}$, is not very direct, but may be a way of checking the values obtained by other flight test and analytical means. It should be pointed out that aerolastic effects are often evaluated by comparing estimates obtained from similar maneuvers at different altitudes. Some of the differences in the estimates may be attributable to $C_{m_{\dot{\alpha}}}$.

The third method, that of designing new aircraft maneuvers to force $\dot{\alpha}$ to be independent of q , appears to be the most promising. There are three types of maneuvers that should force $\dot{\alpha}$ to be independent of q , all of which force the g/V term in equation (6) to actually act as an independent input. The three methods are: (1) to perform a more or less parabolic trajectory at constant angle of attack to get the maximum change in θ ; (2) to perform aileron rolls while pulsing the elevators; and (3) to perform erect and inverted conventional elevator pulse maneuvers at the same angle of attack, and to use multiple maneuver analysis as discussed in references 8, 9, 33, and 54. The first method does not create as much difference between $\dot{\alpha}$ and q as do the second two.

The second maneuver type may be easier to perform than the third type, but the second type will require the use of the cross-coupling terms and will result in a gradient in angle of attack across the span. With either of these methods the sum of $C_{m_{\dot{\alpha}}}$ and C_{m_q} should be the same as the value obtained for C_{m_q} when $\dot{\alpha}$ and q are nearly dependent. The same considerations given to $C_{m_{\dot{\alpha}}}$ apply to other translational acceleration derivatives.

REFERENCES

1. Norton, F. H.: The Measurement of the Damping in Roll on a JN4h in Flight. NACA Rep. 167, 1923.
2. Norton, F. H.: A Study of Longitudinal Dynamic Stability in Flight. NACA Rep. 170, 1923.
3. Iliff, Kenneth W.; Maine, Richard E.; and Shafer, Mary F.: Subsonic Stability and Control Derivatives for an Unpowered, Remotely Piloted 3/8-Scale F-15 Airplane Model Obtained From Flight Test. NASA TN D-8136, 1976.
4. Sim, Alex G.: A Correlation Between Flight-Determined Derivatives and Wind-Tunnel Data for the X-24B Research Aircraft. NASA SX-3371, 1976.
5. Jeglum, Paul M.: AFFTC Experience in the Use of Flight-Test Derived Stability Derivatives. Paper 14, AGARD Fluid Dynamics Panel Symposium on Dynamic Stability Parameters, Athens, Greece, May 22-24, 1978.
6. Holleman, Euclid C.: Summary of Flight Tests to Determine the Spin and Controllability Characteristics of a Remotely Piloted, Large-Scale (3/8) Fighter Airplane Model. NASA TN D-8052, 1976.
7. Smith, Harriet J.: Flight-Determined Stability and Control Derivatives for an Executive Jet Transport. NASA TM X-56034, 1975.
8. Iliff, Kenneth W.; and Taylor, Lawrence W., Jr.: Determination of Stability Derivatives From Flight Data Using a Newton-Raphson Minimization Technique. NASA TN D-6579, 1972.
9. Iliff, Kenneth W.; and Maine, Richard E.: Practical Aspects of Using a Maximum Likelihood Estimator. Methods for Aircraft State and Parameter Identification, AGARD-CP-172, May 1975, pp. 16-1-16-15.
10. Iliff, Kenneth W.; and Maine, Richard E.: Further Observations on Maximum Likelihood Estimates of Stability and Control Characteristics Obtained From Flight Data. AIAA Paper 77-1133, Aug. 1977.
11. Cuenod, M.; and Sage, A. P.: Comparison of Some Methods Used for Process Identification, Automatica, vol. 4, 1968, pp. 235-269.
12. Balakrishnan, A. V.; and Peterka, V.: Identification in Automatic Control Systems. Automatica, vol. 5, Nov. 1969, pp. 817-829.
13. Åström, K. J.; and Eykhoff, P.: System Identification - A Survey. Identification and Process Parameter Estimation, Academia (Prague), 1970, pp. 0.1.1-0.1.38.
14. Parameter Estimation Techniques and Applications in Aircraft Flight Testing. NASA TN D-7647, 1974.
15. Methods for Aircraft State and Parameter Identification. AGARD-CP-172, May 1975.
16. Breuhaus, W. O.: Summary of Dynamic Stability and Control Flight Research Conducted Utilizing a B-25J Airplane. Rep. no. TB-405-F-10, Cornell Aeronautical Lab., Buffalo, N. Y., May 1948.
17. Seamans, R. C., Jr.; Blasingame, B. P.; and Clementson, G. C.: The Pulse Method for the Determination of Aircraft Dynamic Performance. J. Aeronaut. Sci., vol. 17, no. 1, Jan. 1950, pp. 22-38.
18. Greenberg, Harry: A Survey of Methods for Determining Stability Parameters of an Airplane From Dynamic Flight Measurements. NACA TN 2340, 1951.
19. Shinbrot, Marvin: On the Analysis of Linear and Nonlinear Dynamical Systems From Transient-Response Data. NACA TN 3288, 1954.
20. Howard J.: The Determination of Lateral Stability and Control Derivatives From Flight Data. Canadian Aeronaut. & Space J., vol. 13, Mar. 1967, pp. 127-134.
21. Wolowicz, Chester H.: Considerations in the Determination of Stability and Control Derivatives and Dynamic Characteristics From Flight Data. AGARD Rep. 549. Part I, 1966.
22. Rampy, John M.; and Berry, Donald, T.: Determination of Stability Derivatives From Flight Test Data by Means of High Speed Repetitive Operation Analog Matching. FTC-TDR-64-8, Air Force Flight Test Center, Edwards, Calif., May 1964.
23. Denery, Dallas G.: Identification of System Parameters From Input-Output Data With Application to Air Vehicles. NASA TN D-6468, 1971.
24. Rynaski, Edmund G.: Application of Advanced Identification Techniques to Nonlinear Equations of Motion. Proceedings of the Stall/Post-Stall/Spin Symposium, Wright Patterson Air Force Base, Ohio, Dec. 1971, pp. Q-1-Q-18.
25. Taylor, Lawrence W., Jr.; and Iliff, Kenneth W.: A Modified Newton-Raphson Method for Determining Stability Derivatives From Flight Data. Computing Methods in Optimization Problems, Lofti A. Zadeh, Lucien W. Neustadt, and A. V. Balakrishnan, eds., Academic Press, 1969, pp. 353-364.
26. Larson, Duane B.; and Fleck, John T.: Identification of Parameters by the Method of Quasilinearization. Cal Rep. 164, Cornell Aeronautical Lab., Buffalo, New York, May 1968.

27. Balakrishnan, A. V.: *Communication Theory*, McGraw-Hill, Inc., c. 1968.
28. Bellman, Richard E.; and Kalaba, Robert E.: *Quasilinearization and Nonlinear Boundary-Value Problems*. American Elsevier Publishing Co., Inc., 1965.
29. Taylor, Lawrence W., Jr.; Iliff, Kenneth W.; and Powers, Bruce, G.: *A Comparison of Newton-Raphson and Other Methods for Determining Stability Derivatives From Flight Data*. AIAA Paper 69-315, Mar. 1969.
30. Wolowicz, Chester H.; Iliff, Kenneth W.; and Gilyard, Glenn B.: *Flight Test Experience in Aircraft Parameter Identification*. Paper 23, CP-119, 1972.
31. Grove, Randall D.; Bowles, Roland L.; and Mayhew, Stanley C.: *A Procedure for Estimating Stability and Control Parameters From Flight Test Data by Using Maximum Likelihood Methods Employing a Real-Time Digital System*. NASA TN D-6735, 1972.
32. Ross, A. Jean; and Foster, G. W.: *FORTTRAN Programs for the Determination of Aerodynamic Derivatives From Transient Longitudinal or Lateral Responses of Aircraft*. TR-75090, Royal Aircraft Establishment, Sept. 1975.
33. Maine, Richard E.; and Iliff, Kenneth W.: *A FORTRAN Program for Determining Aircraft Stability and Control Derivatives From Flight Data*. NASA TN D-7831, 1975.
34. Nagy, Christopher J.: *A New Method For Test and Analysis of Dynamic Stability and Control*. AFFTC-TD-75-4, Air Force Flight Test Center, Edwards, Calif., May 1976.
35. Suit, William T.: *Aerodynamic Parameters of the Navion Airplane Extracted From Flight Data*. NASA TN D-6643, 1972.
36. McBrinn, D. E.; and Brassell, B. B.: *Aerodynamic Parameter Identification for the A-7 Airplane at High Angles of Attack*. Proceedings of the AIAA 3rd Atmospheric Flight Mechanics Conference, c. 1976, pp. 108-117.
37. Frei, D. R.: *Practical Applications of Parameter Identification*. AIAA Paper 77-1136, Aug. 1977.
38. Ross, A. Jean: *Determination of Aerodynamic Derivatives From Transient Responses in Manoeuvring Flight*. Methods for Aircraft State and Parameter Identification, AGARD-CP-172, May 1975, pp. 14-1-14-10.
39. Gould, D. G.; Hindson, W. S.: *Estimates of the Stability Derivatives of a Helicopter and a V/STOL Aircraft From Flight Data*. Methods for Aircraft State and Parameter Identification, AGARD-CP-172, May 1975, pp. 23-1-23-9.
40. Klein, V.: *Longitudinal Aerodynamic Derivatives of a Slender Delta-Wing Research Aircraft Extracted From Flight Data*. CIT-FI-74-023, Cranfield Inst. of Technology, July 1974.
41. Schuetz, A. J.: *Low Angle-of-Attack Longitudinal Aerodynamic Parameters of Navy T-2 Trainer Aircraft Extracted From Flight Data: A Comparison of Identification Technique*. Volume I—Data Acquisition and Modified Newton-Raphson Analysis. NADC-74181-30, Dept. of the Navy, Washington, D.C., June 1975.
42. Marchand, M.; and Koehler, R.: *Determination of Aircraft Derivatives by Automatic Parameter Adjustment and Frequency Response Methods*. Methods for Aircraft State and Parameter Identification, AGARD-CP-172, May 1975, pp. 17-1-17-18.
43. Mehra, Raman, K.: *Maximum Likelihood Identification of Aircraft Parameters*. Eleventh Joint Automatic Control Conference of the American Automatic Control Council, Paper 18-C, June 1970, pp. 442-444.
44. Tyler, James S.; Powell, J. David; and Mehra, Raman K.: *The Use of Smoothing and Other Advanced Techniques for VTOL Aircraft Parameter Identification*. Final Report. Naval Air Systems Command Contract No. N00019-69-C-0534, Systems Control, Inc., Palo Alto, Calif., June 1970.
45. Gerlach, O. H.: *The Determination of Stability Derivatives and Performance Characteristics From Dynamic Manoeuvres*. Rep. VTH-163, Delft Univ. of Technology, Dept. of Aerospace Eng., Delft, The Netherlands, Mar. 1971.
46. Jonkers, H. L.: *Application of the Kalman Filter to Flight Path Reconstruction From Flight Test Data Including Estimation of Instrumental Bias Error Corrections*. Rep. VTH-162, Delft Univ. of Technology, Dept. of Aerospace Eng., Delft, The Netherlands, Feb. 1976.
47. Åström, K. J.: *Control Problems in Papermaking*. Proceedings of the IBM Scientific Computing Symposium on Control Theory and Applications, IBM Data Processing Div., White Plains, N.Y., c. 1966, pp. 135-167.
48. Kashyap, R. L.: *A New Method of Recursive Estimation in Discrete Linear Systems*. IEEE Transactions on Automatic Control, vol. AC-15, no. 1, Feb. 1970, pp. 18-24.
49. Chen, Robert T. N.; and Eulrich, Bernard, J.: *Parameter and Model Identification of Nonlinear Dynamical Systems Using a Suboptimal Fixed-Point Smoothing Algorithm*. Twelfth Joint Automatic Control Conference of the American Automatic Control Council, Paper 7-E2, Aug. 1971, pp. 731-740.
50. Yazawa, Kenji: *Identification of Aircraft Stability and Control Derivatives in the Presence of Turbulence*. AIAA Paper 77-1134, Aug. 1977.
51. Balakrishnan, A. V.: *Stochastic Differential System I. Filtering and Control—A Function Space Approach*. Lecture Notes in Economics and Mathematical Systems, 84, M. Beckmann, G. Goos, and H. P. Künzi, eds., Springer-Verlag (Berlin), 1973.

52. Balakrishnan, A. V.: *Modelling and Identification Theory: A Flight Control Application. Theory and Applications of Variable Structure Systems*. Academic Press, Inc., New York, c. 1972.
53. Iliff, K. W.: *Identification and Stochastic Control With Application to Flight Control in Turbulence*. UCLA-ENG-7340, School of Engineering and Applied Science, Univ. Calif., Los Angeles, Calif., May 1973.
54. Iliff, Kenneth W.; and Maine, Richard E.: *Practical Aspects of Using a Maximum Likelihood Estimation Method to Extract Stability and Control Derivatives From Flight Data*. NASA TN D-8209, 1976.
55. Iliff, Kenneth W.: *Maximum Likelihood Estimates of Lift and Drag Characteristics Obtained From Dynamic Aircraft Maneuvers*. Proceedings of AIAA 3rd Atmospheric Flight Mechanics Conference, c. 1976, pp. 137-150.
56. Iliff, Kenneth W.: *An Aircraft Application of System Identification in the Presence of State Noise*. New Directions in Signal Processing in Communication and Control, J. K. Skwirzynski, ed., Noordhoff International Publishing (Leyden, The Netherlands), c. 1975, pp. 529-541.
57. Iliff, Kenneth W.: *Estimation of Characteristics and Stochastic Control of an Aircraft Flying in Atmospheric Turbulence*. Proceedings of AIAA 3rd Atmospheric Flight Mechanics Conference, c. 1976, pp. 26-38.
58. Coe, Paul L., Jr.; Graham, A. Bruce; and Chambers, Joseph R.: *Summary of Information of Low-Speed Lateral-Directional Derivatives Due to Rate of Change of Sideslip β* . NASA TN D-7972, 1975.
59. Orlik-Rückemann, K. J.: *Recent Advances in Techniques for Dynamic Stability Testing at NAE*, Reprinted from DME/NAE Quarterly Bulletin No. 1976 (1), National Research Council Canada, National Aeronautical Establishment, Ottawa, Canada, Apr. 1976.
60. Shafer, Mary F.: *Stability and Control Derivatives of the T-37B Airplane*. NASA TM X-56036, 1975.
61. Maine, Richard E.: *Maximum Likelihood Estimation of Aerodynamic Derivatives for an Oblique Wing Aircraft From Flight Data*. AIAA Paper 77-1135, Aug. 1977.
62. Anglin, Ernie L.: *Recent Research on Aerodynamic Characteristics of Fighter Configurations During Spins*. AIAA Paper 77-1163, Aug. 1977.
63. Hall, W. Earl, Jr.; Gupta, Narendra K.; and Tyler, James S., Jr.: *Model Structure Determination and Parameter Identification for Nonlinear Aerodynamic Flight Regimes*. Methods for Aircraft State and Parameter Identification, AGARD-CP-172, May 1975, pp. 21-1-21-21.
64. Ramachandran, S.; Schneider, H.; Mason, J. D.; and Stalford, H. L.: *Identification of Aircraft Aerodynamic Characteristics at High Angles of Attack and Sideslip Using the Estimation Before Modeling (EBM) Technique*. AIAA Paper 77-1169, Aug. 1977.
65. Fiske, Philip H.; and Price, Charles F.: *A New Approach to Model Structure Identification*. AIAA Paper 77-1171, Aug. 1977.
66. Gupta, Narendra K.; Hall, W. Earl, Jr.; and Trankle, Thomas L.: *Advanced Methods of Model Structure Determination From Test Data*. AIAA Paper 77-1170, Aug. 1977.

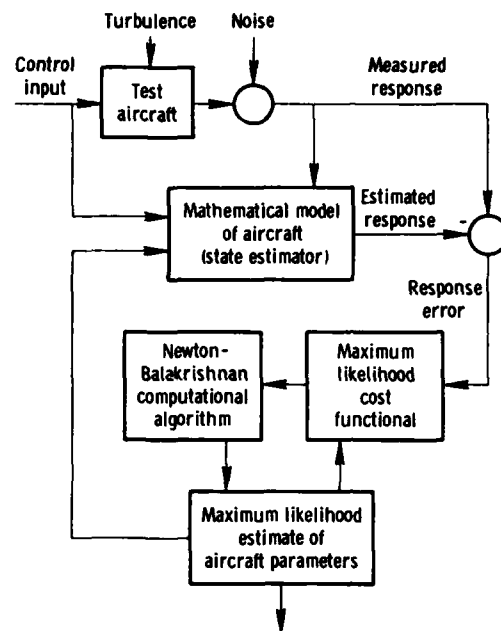


Figure 1. Maximum likelihood estimation concept.

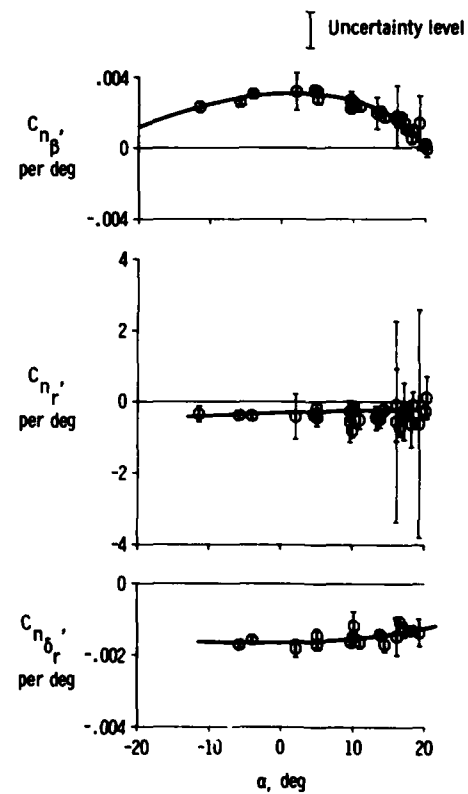


Figure 2. Selected low-speed stability and control derivatives as functions of angle of attack obtained from RPV.

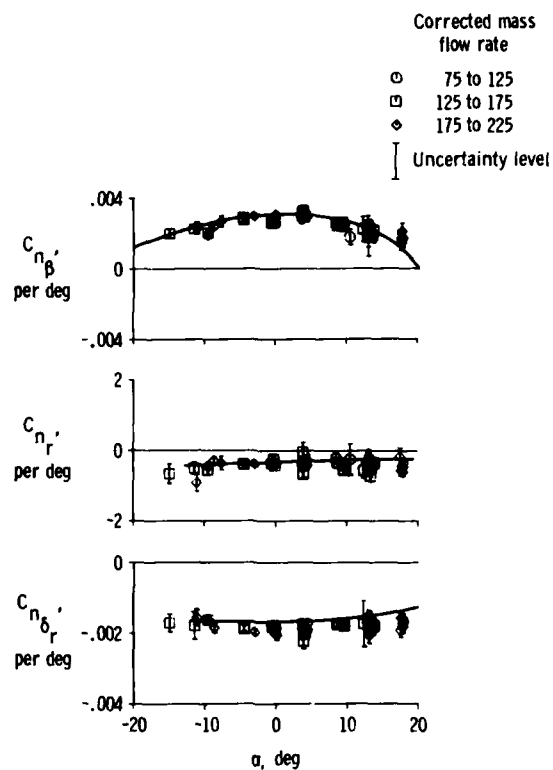


Figure 3. Selected low-speed stability and control derivatives as functions of angle of attack obtained from full-scale airplane at three engine mass flow rates.

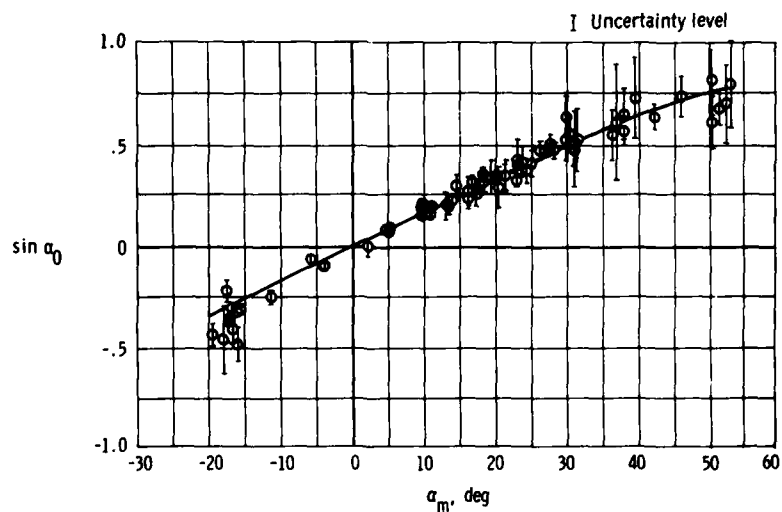
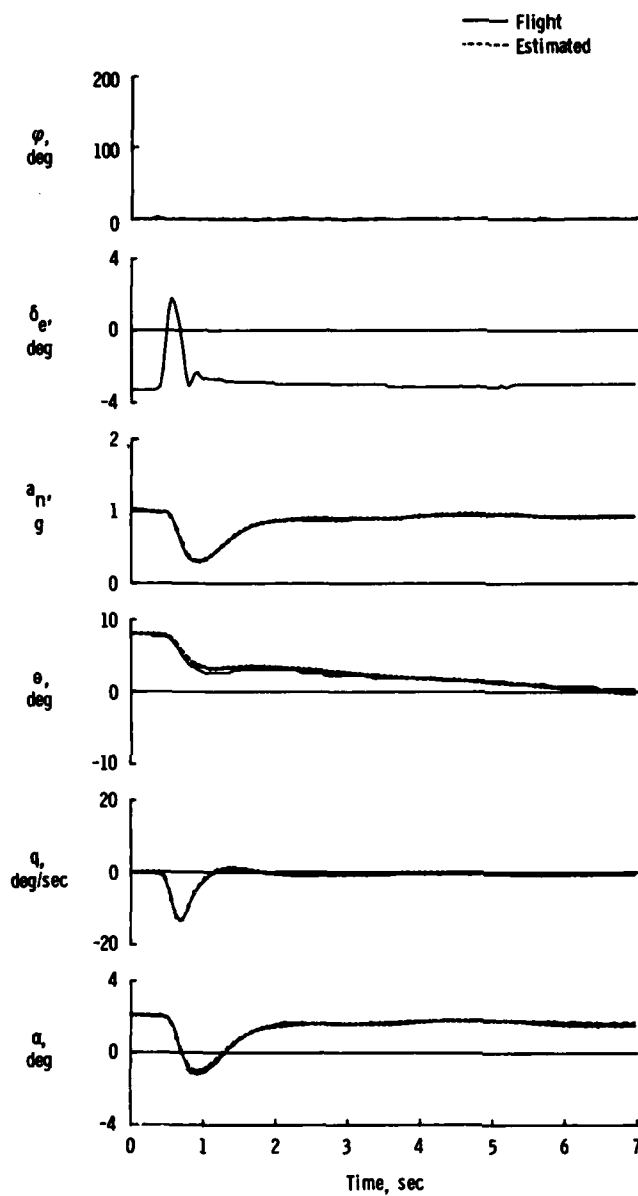
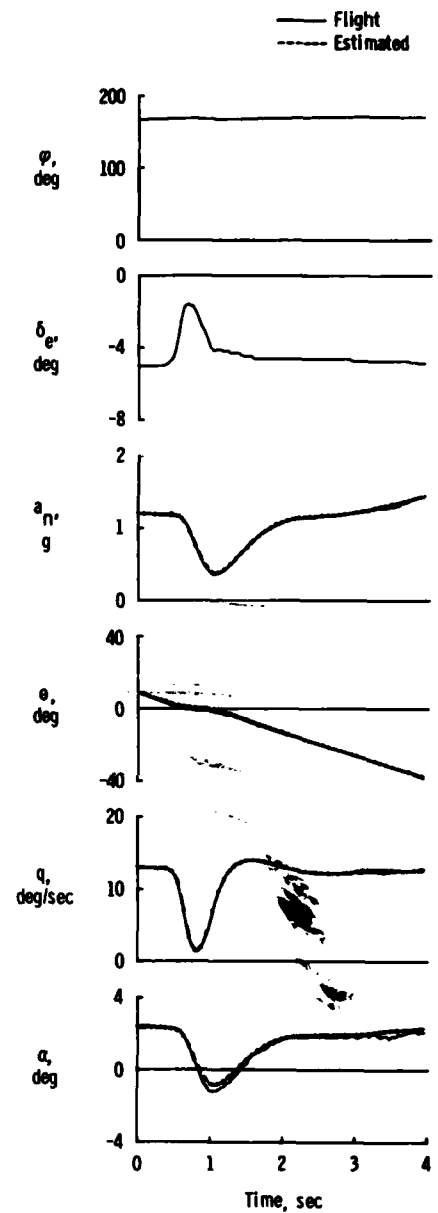


Figure 4. Comparison of angle of attack estimated from flight data and measured angle of attack.

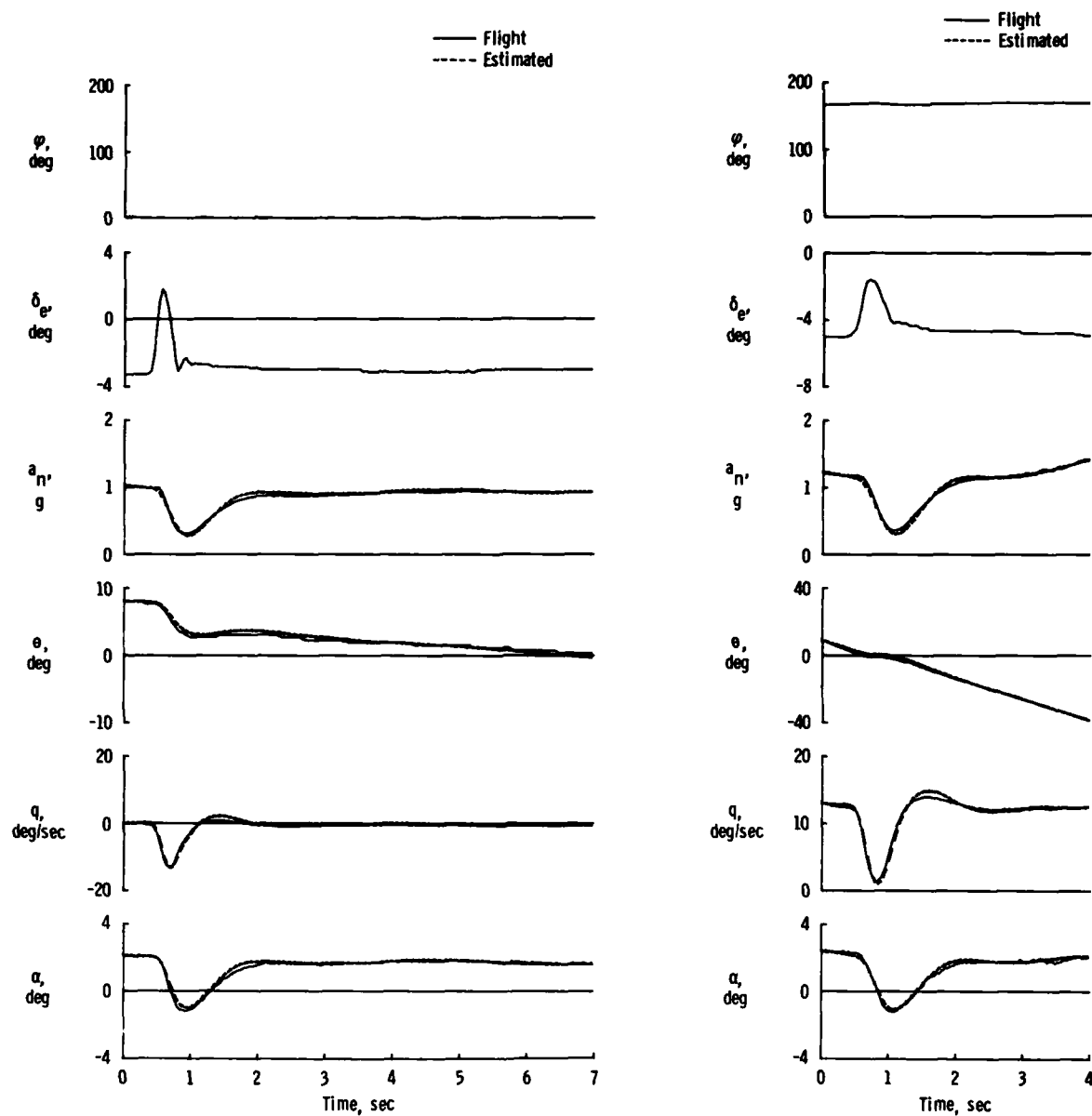


(a) Erect maneuver.



(b) Inverted maneuver.

Figure 5. Double maneuver for elevator pulse with aircraft inverted and erect with $C_{m_{\dot{\alpha}}}$ independent of C_{m_q} .



(a) Erect maneuver.

(b) Inverted maneuver.

Figure 6. Double maneuver for elevator pulse with aircraft inverted and erect with $C_{m_{\dot{\alpha}}}$ forced to zero.

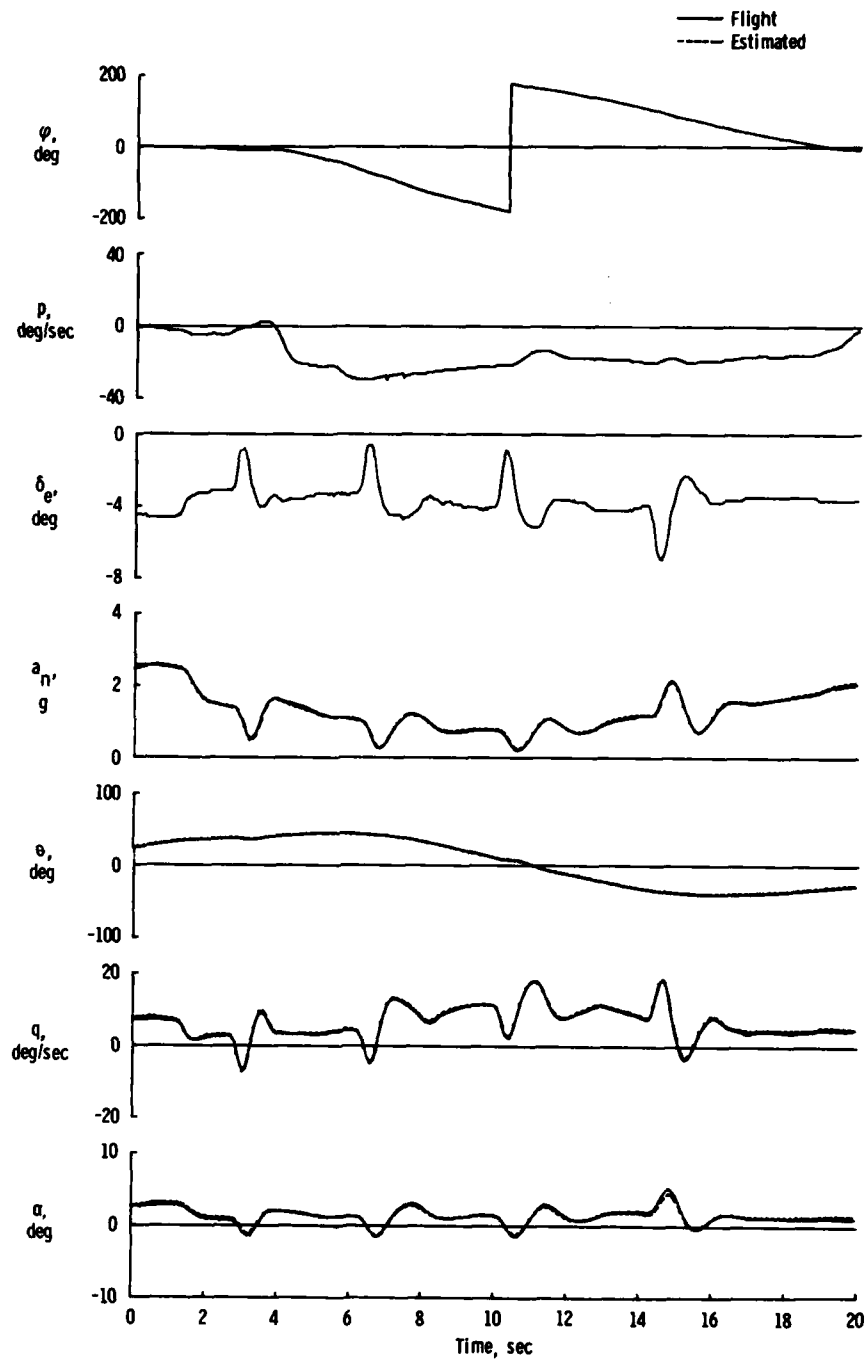
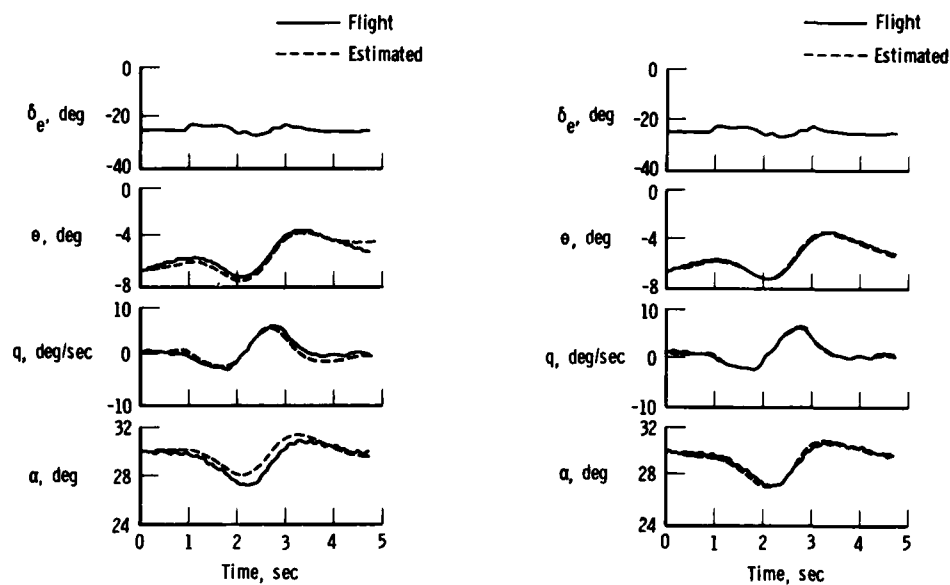


Figure 7. Comparison of measured and computed responses for aileron roll maneuver designed to make $C_{m_{\dot{\alpha}}}$ independent of C_{m_q} .



(a) Lateral-directional kinematic coupling terms ignored.

(b) Lateral-directional kinematic coupling terms included.

Figure 8. Effect of lateral-directional kinematic coupling terms on fit of computed and flight data for a longitudinal maneuver.

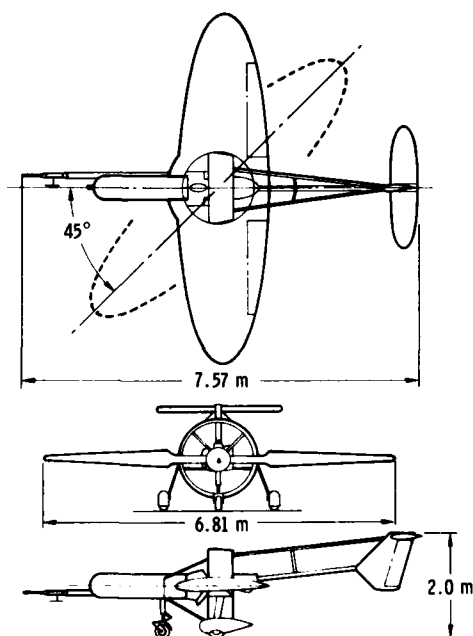


Figure 9. Three-view drawing of remotely piloted oblique wing aircraft.

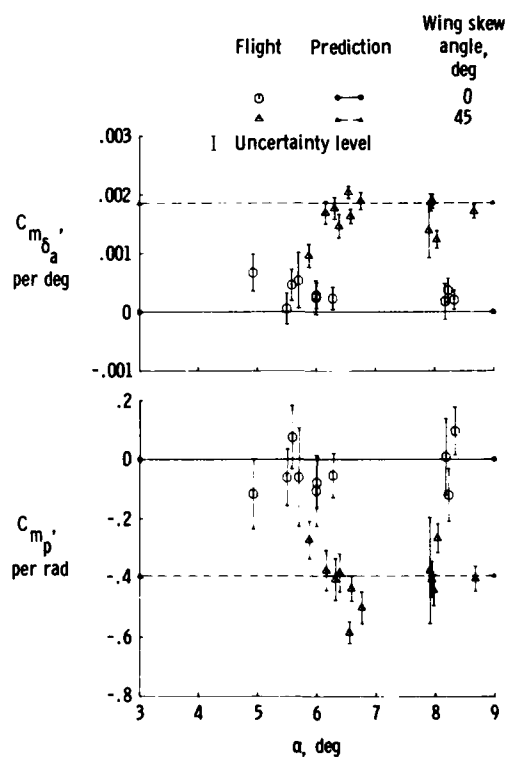


Figure 10. Maximum likelihood estimates of aerodynamic cross-coupling derivatives obtained for the oblique wing aircraft at two wing skew angles.

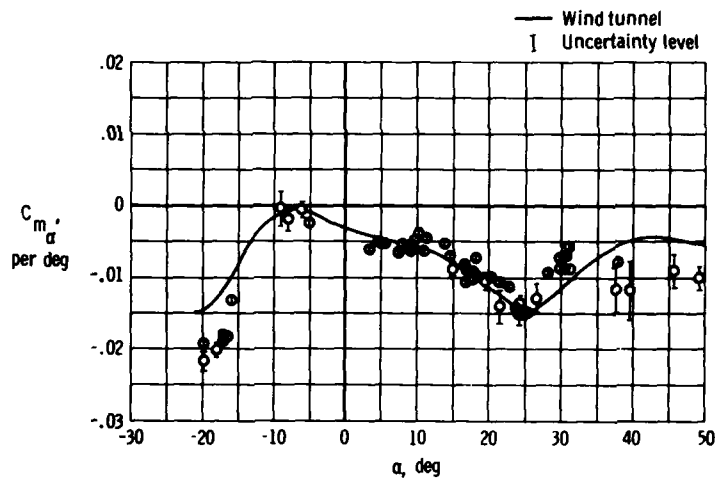


Figure 11. Comparison of flight and wind tunnel estimates of C_{m_α} over a large angle of attack range.

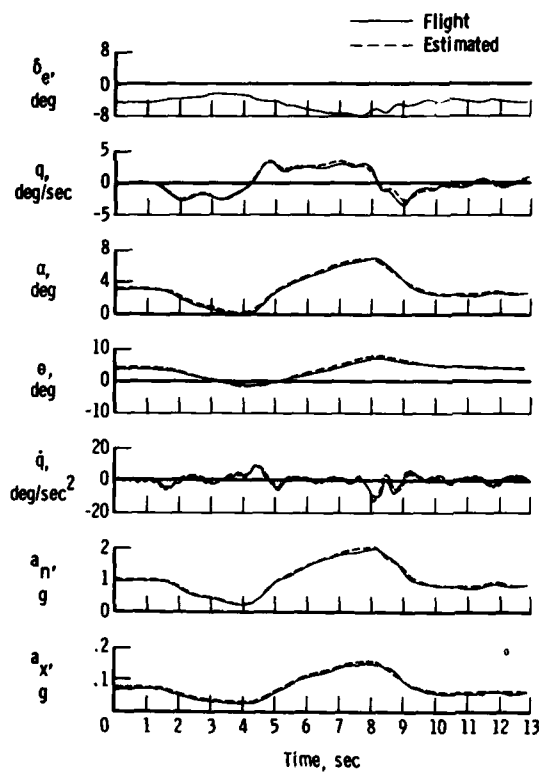


Figure 12. Comparison of flight data and data estimated by using a nonlinear model.

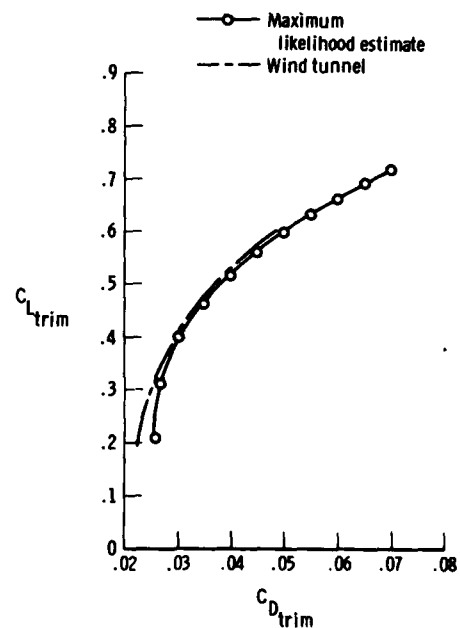


Figure 13. Comparison of drag polars obtained from estimates based on wind tunnel and flight data.

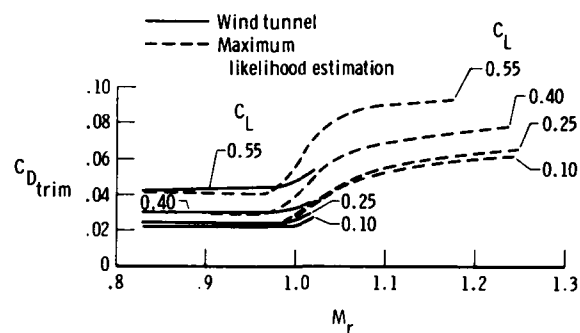
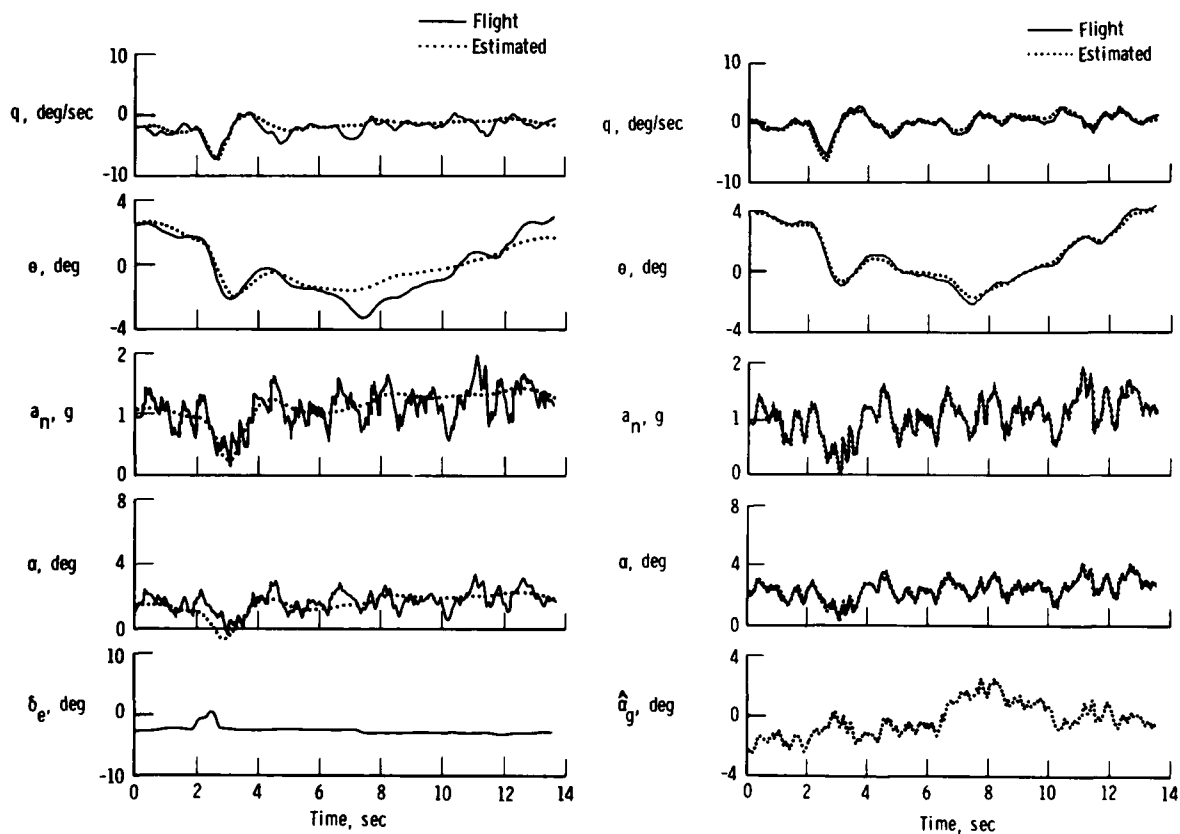


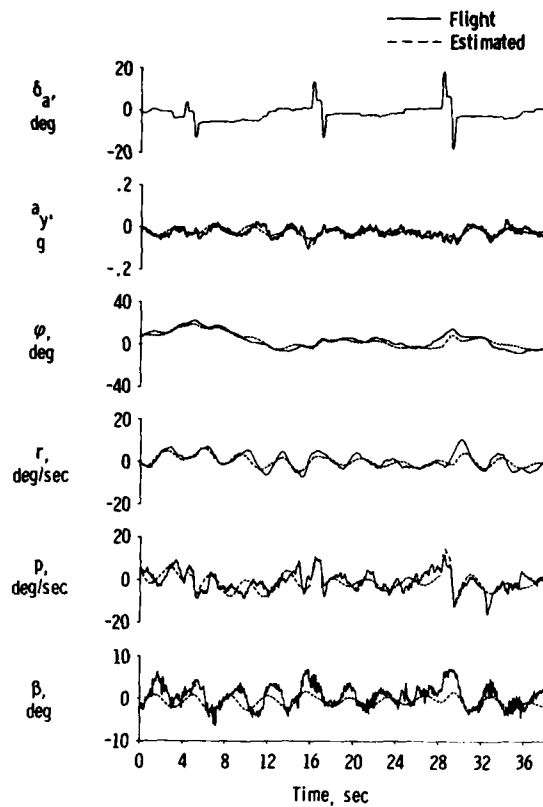
Figure 14. Summary of coefficient of drag as a function of M_r for estimates from the wind tunnel and the maximum likelihood estimation technique.



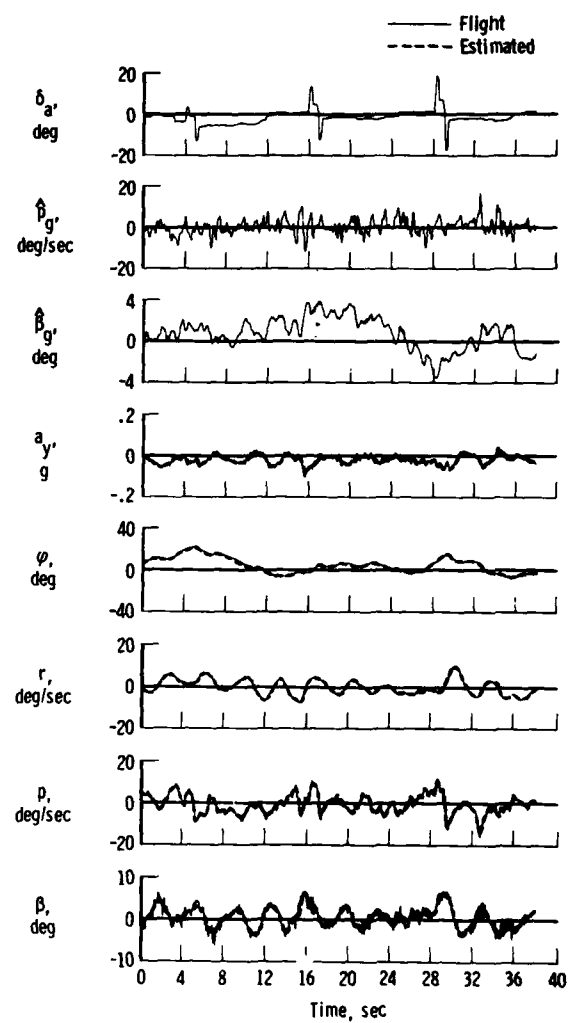
(a) Estimator that does not account for turbulence.

(b) Estimator that accounts for effects of turbulence.

Figure 15. Fit of computed and flight data when turbulence effects are present.



(a) Estimator that does not account for turbulence.



(b) Estimator that accounts for effects of turbulence.

Figure 16. Fit of flight data obtained in turbulence and computed data obtained from maximum likelihood estimator.

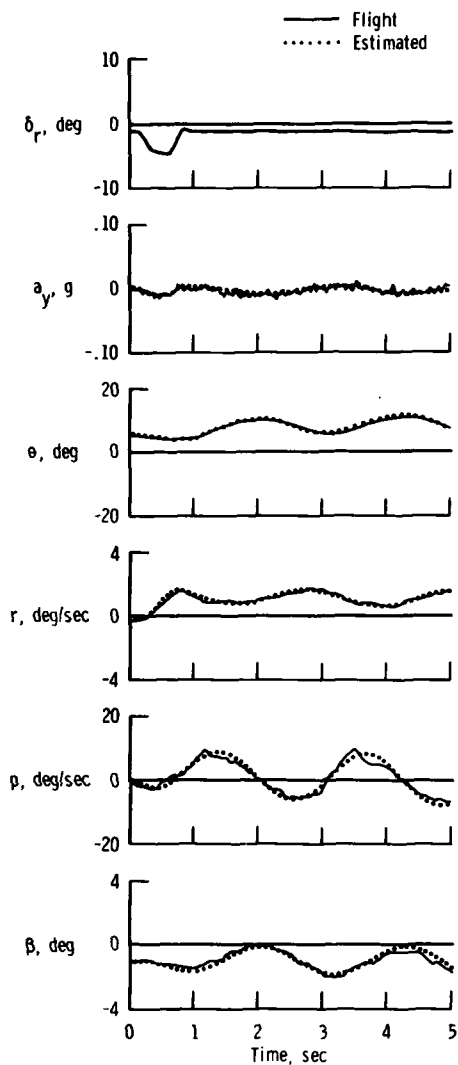


Figure 17. Comparison of flight data obtained in separated flow with data estimated without accounting for effects of separated flow.

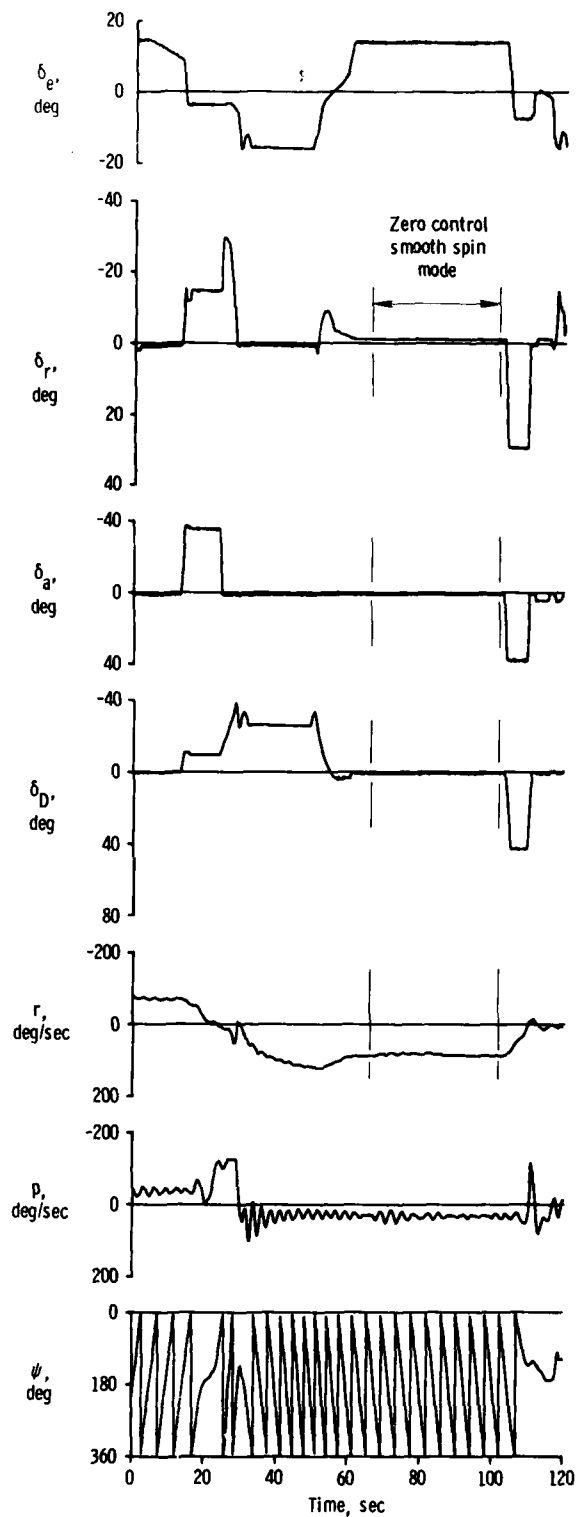


Figure 18. Time history obtained from SRV that demonstrates the steady-state nature of a zero control smooth spin mode.

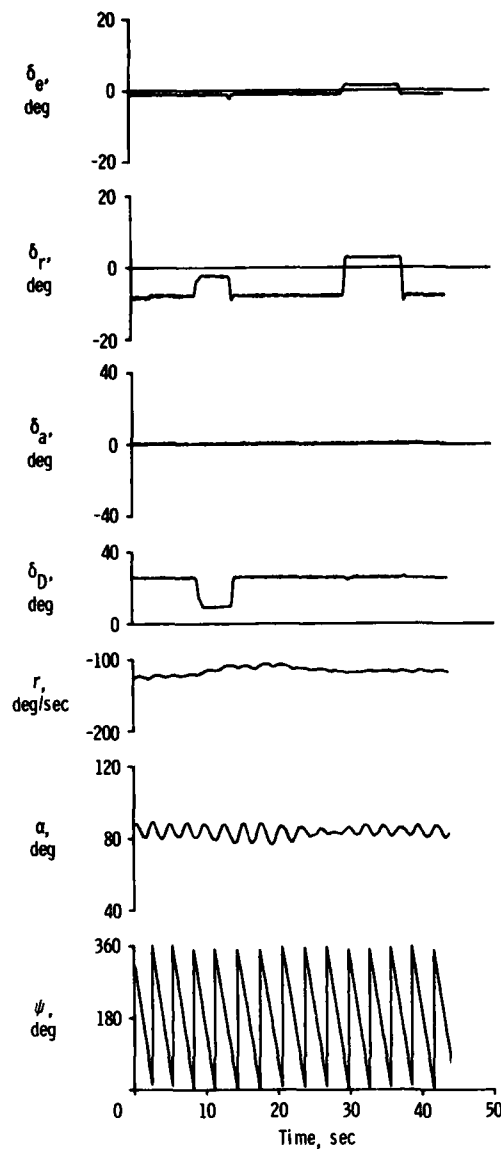


Figure 19. Time history obtained from SRV showing effect of control pulse on zero control smooth spin mode.

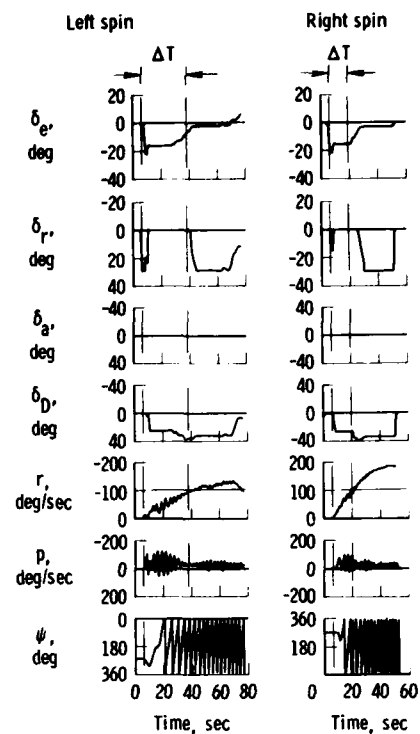


Figure 20. Comparison for left and right spin entries on the SRV with misaligned nose.

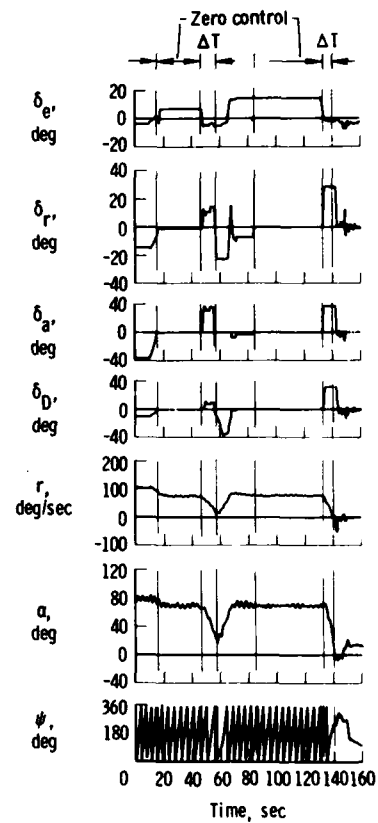


Figure 21. Time histories obtained from SRV where repeatability of zero control smooth spin modes are demonstrated.

AERODYNAMIC INTERACTIONS ON THE FIGHTER CCV TEST AIRCRAFT

By

Robert A. Whitmoyer
Air Force Flight Dynamics Laboratory
Wright-Patterson AFB, Ohio, 45433, USA

SUMMARY

The Fighter CCV YF-16 testbed aircraft completed an 87-flight 125-hour test program in June 1977. The aircraft achieved higher levels of direct force control than had previously been flight tested. Direct sideforce levels up to 0.9g were reached on the CCV YF-16 through the twin vertical canard/rudder combination. Direct lift levels of $\pm 1.2g$'s were obtained from the flap/horizontal tail combination. These direct force capabilities were used to implement six unconventional control modes on the aircraft, consisting of flat-turns, decoupled normal acceleration control, independent longitudinal and lateral translations, and uncoupled elevation and azimuth aiming. The aircraft was also flown at a range of center-of-gravity positions corresponding to subsonic static margin levels from 2% stable to 12% unstable to investigate performance and flying qualities sensitivities to degree of relaxed static stability. The flight test program, and supporting wind tunnel testing, produced a wealth of data concerning the complex aerodynamic interactions between the force and moment producers on a Control Configured Vehicle design. This paper documents the specific aerodynamic coupling effects observed during flight testing of the CCV YF-16. These interactions were prime factors in determining the viability of the unconventional control concepts investigated.

LIST OF SYMBOLS

α	angle of attack
β	angle of sideslip
CCV	Control Configured Vehicle
c.g.	center of gravity
$C_{l\beta}$	rolling moment coefficient due to sideslip angle (dihedral effect)
C_m	pitching moment coefficient
$C_{n\beta}$	yawing moment coefficient due to sideslip angle (directional stability)
$C_{n\beta}$ DYNAMIC	dynamic directional stability coefficient
$C_{n\delta_{vc}}$	yawing moment coefficient due to vertical canard deflection
δ_H	horizontal tail (stabilator) deflection
δ_{TEF}	trailing edge flap deflection
δ_{vc}	vertical canard deflection
Δ	increment or change
defl	deflection
deg	degrees
DLC	direct lift control
DN	down
DSFC	direct sideforce control
FWD	forward
F.S.	fuselage station
fps	feet per second
ft., FT.	feet
g	acceleration due to gravity
H.T.	horizontal tail (stabilator)

in., IN.	inches
I_x	aircraft moment of inertia about the longitudinal axis
I_z	aircraft moment of inertia about the vertical axis
L/D	ratio of lift to drag
m	meters
MAC	mean aerodynamic chord
P_s	specific excess energy
REF	reference
RMS	root mean square
RSS	Relaxed Static Stability
sec	seconds
S.S.	span station
T.E.	trailing edge
V	forward velocity
V.C.	vertical canard
W.L.	water line

1. INTRODUCTION

The Fighter Control Configured Vehicle (CCV) YF-16 testbed aircraft (Figure 1) completed an 87-flight 125-hour test program in June 1977. The purpose of the Fighter CCV Program was to demonstrate specific new control degrees of freedom incorporated in an existing high-performance fighter and to quantify the advantages of Relaxed Static Stability (RSS). This program offered the first true test of decoupled, six degree-of-freedom flight path control. The ability to decouple the translational and rotational degrees of freedom and to exercise independent control of each can create unique maneuvering capabilities. Application to air-to-air and air-to-ground mission tasks has the potential to significantly improve maneuverability, weapon delivery, and survivability.

The process of designing and flight testing the unconventional control concepts produced a wealth of data concerning the complex aerodynamic interactions between the force and moment producers on a CCV design. The YF-16 Number 1 prototype aircraft was modified to provide direct lift and direct sideforce capabilities which were used to implement six independent decoupled control modes. A two-view layout of the CCV YF-16 is presented in Figure 2. The only external change from the prototype configuration is the addition of twin moveable 8-square-foot-per-surface (0.74m^2) canards mounted on the engine inlet. The flaperon mechanism was also modified so that these surfaces could be deflected symmetrically in up-and-away flight to provide direct lift control. These changes produced significant aerodynamic interactions on the aircraft which influenced the flight evaluations of the CCV concepts.



FIG 1: CCV YF-16 Testbed Vehicle

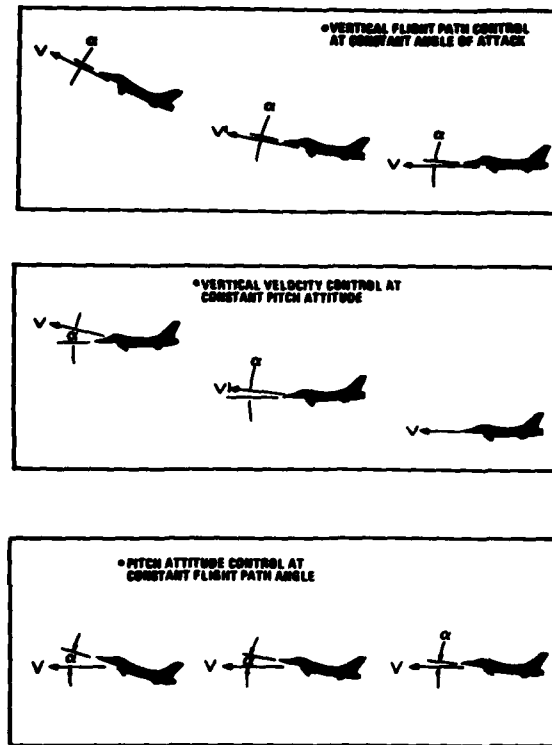


FIG 3: Direct Lift Control Modes

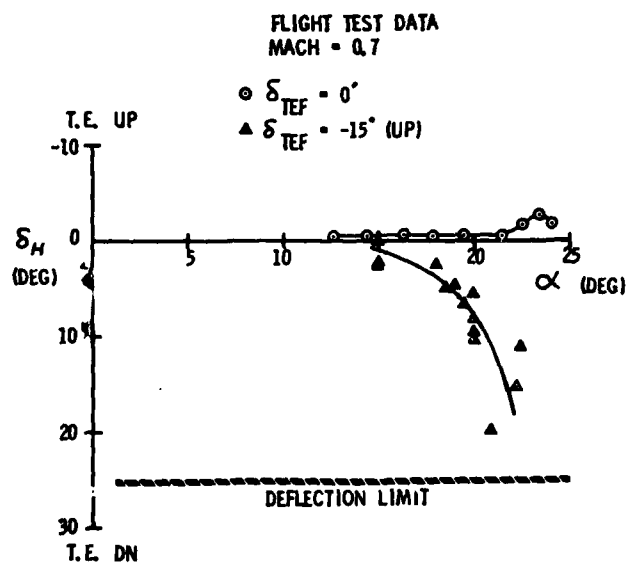


FIG 4: Horizontal Tail Defl. Vs. Angle Of Attack

combined with the flap pitching moments, the tail power loss produced the effect shown in Figure 4. On a statically unstable aircraft such as the CCV YF-16, it is vital that recovery pitching moment be available at all times to prevent departure. The trend shown in Figure 4 resulted in a circuit modification in the auxiliary flight control computer preventing DLC application above 18 degrees angle of attack.

DLC flap deflections also modified the YF-16's buffet characteristics. The baseline YF-16 has very low maneuvering buffet levels because of the forebody strakes and automatically-scheduled leading edge flaps. While using the DLC modes at elevated angles of attack, the pilots reported an increase in buffet intensity over the normally mild YF-16 levels. Although the CCV flap-induced buffet levels were judged objectionable, none of the pilots thought that the buffet was severe enough to impair tracking ability. Flight test results from earlier prototype testing was used to verify the CCV pilot's opinions of the buffet intensities. Figure 6, taken from Reference 3, shows the effect of trailing-edge flap deflection on the buffet level at the pilot station. This plot shows that flap deflections progressively reduce the angle of attack for buffet onset and increase the peak intensity. Of particular interest is the fact that flap deflections of up to 13 degrees can be used at low angles of attack with no increase in buffet level. Figure 6 also shows a large buffet penalty over the entire α range for 20 degree flap deflection. By limiting maximum DLC commands to 15 degrees of flap, the CCV YF-16 maintained mild buffet levels at low angles of attack, and kept the peak buffet intensities within the moderate region.

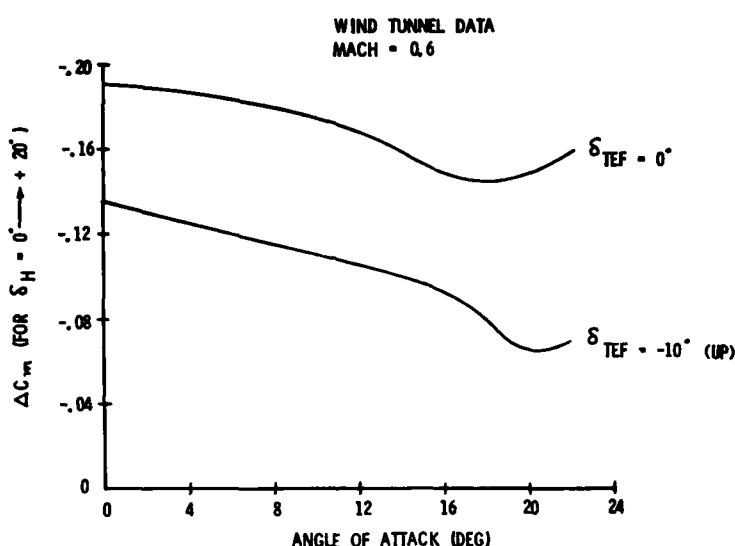


FIG 5: Effect Of Trailing Edge Flap Deflection On Longitudinal Control Power

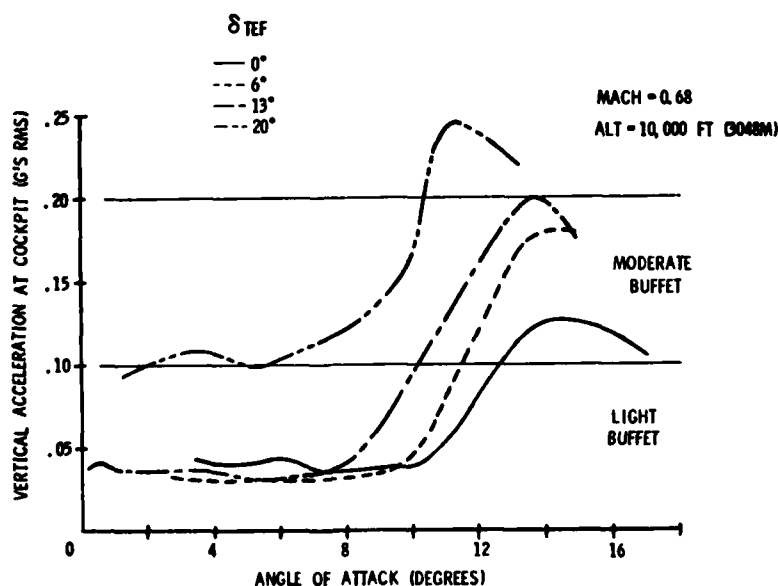


FIG 6: Effect Of Trailing Edge Flap Deflections On YF-16 Buffet Level

The optimum implementation of DLC would produce only the desired decoupled motion with no change in forward speed. This goal is unlikely to be achieved in practice. On the CCV YF-16, maximum DLC inputs were nearly always accompanied by a decrease in airspeed, averaging about 30 knots depending on the particular flight condition, mode, and duration of input (Reference 2). Force coupling between DLC and the x-axis was considered to be an important factor in the operational utility of the CCV modes. Quantitative guidelines need to be established defining the acceptable levels of energy change associated with direct force control inputs.

The effects of DLC inputs on subsonic aircraft performance are shown in Figure 7 in terms of Specific Excess Energy (P_S) versus normal load factor. At low load factors, any DLC command decreased the aircraft P_S level because of profile drag increases. This effect caused the speed losses reported above. At high load factors, positive flap deflections decreased induced drag by increasing wing camber, resulting in a P_S improvement. Negative flap deflections at high g subsonic flight conditions had a very detrimental effect on aircraft specific energy. Supersonically, the high load factor flap effects were reversed; decambering the wing with negative flap deflections had a beneficial effect on aircraft energy, while positive flap deflections caused a substantial supersonic performance loss.

Figure 8 shows CCV YF-16 flight test data on the incremental energy change as a function of flap deflection for the pitch pointing mode. These data were taken at 1 g flight and demonstrate an energy maneuverability loss of about 70 fps (21 m/sec) for full pointing in either direction. It should be noted, however, that the maneuverability losses typical of DLC are transitory in nature and must be weighed against predicted increases in overall combat effectiveness resulting from the unconventional control modes. Also, the trailing edge flap effects reported here are for the CCV YF-16 configuration only, and may vary strongly for different wing planform geometries.

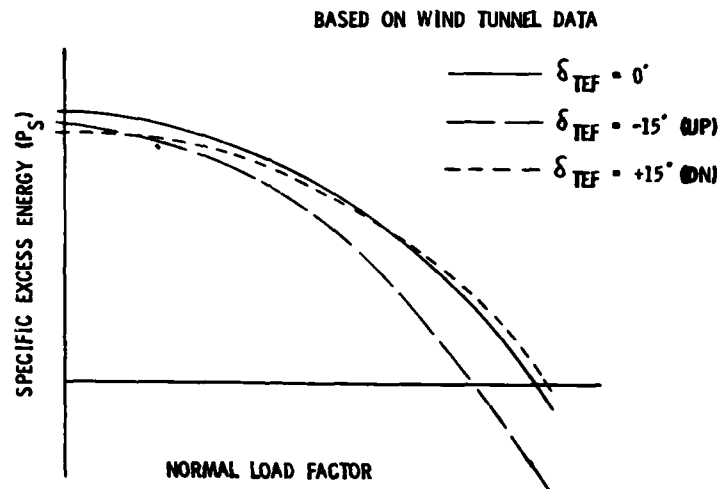


FIG 7: Effect Of DLC On Subsonic Maneuver Potential

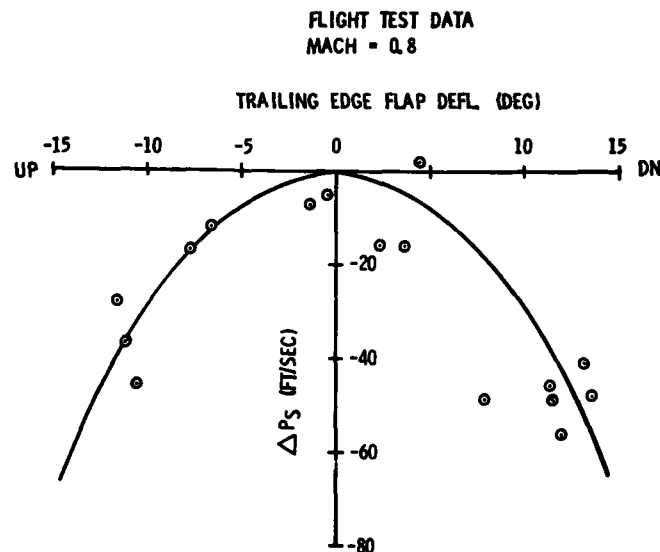


FIG 8: Effect Of Pitch Pointing On Aircraft Energy

3. DIRECT SIDEFORCE CONTROL INTERACTIONS

Direct Sideforce Control (DSFC) was obtained on the Fighter CCV aircraft by means of coordinated deflections of "vertical" canard surfaces and the rudder. As shown in Figure 2, the canards were not truly vertical, but were canted outward 30 degrees. Three distinct uncoupled lateral-directional control modes were implemented on the aircraft through different interconnect gains between canards and rudder. The first DSFC mode provided direct control over lateral acceleration permitting coordinated flat turns. The second mode allowed lateral translational velocities at a constant aircraft heading. The third DSFC mode produced the capability for independent fuselage azimuth pointing at a constant flight path angle. These DSFC modes are graphically illustrated in Figure 9.

The canards deflected a maximum of ± 25 degrees at a system rate of 94 deg/sec. Maximum DSFC deflections produced decoupled lateral accelerations of up to 0.9 g, decoupled translational velocities of up to 40 knots, and decoupled azimuth aiming angles of up to ± 5 degrees. During flight testing, the pilots identified several actual and potential applications for these Direct Sideforce capabilities. As was the case for the longitudinal modes, the control surface deflections required to produce the DSFC modes produced significant aerodynamic interference effects. In addition, the canards modified the YF-16 aerodynamic characteristics even when no CCV modes were being commanded.

Stability derivatives extracted from flight test maneuvers were used to document the effect of the vertical canards on CCV YF-16 aerodynamics. These derivatives were calculated using a National Aeronautics and Space Administration (NASA) computer program incorporating a Newton-Raphson technique called the Modified Maximum Likelihood Estimator. Engineers from the Air Force Flight Test Center at Edwards AFB, California extracted all the stability derivatives presented herein. Canard off derivatives were taken from Reference 4, while the derivatives for the CCV configuration were taken from the Reference 5 unpublished letter report.

An obvious effect of the vertical canard installation was to destabilize the aircraft directionally. Figure 10 compares subsonic directional stability levels between canard on and off configurations as a function of angle of attack. At low angles of attack, the total airplane directional stability level was reduced nearly 50% by the vertical canards. Figure 10 also shows that for angles of attack above about 12 degrees, the vertical canard effectiveness begins to fall off rapidly, as evidenced by the bending of the canard-on stability curve toward the stability level for canards-off. The YF-16 stability augmentation system was not modified for CCV testing to compensate for the reduced directional stability of the canard configuration. In spite of this, the pilots noticed the reduced directional stiffness only during intentional rudder doublets. Although the large directional stability loss due to the canards was not critical subsonically, it was a primary reason for imposing a supersonic limit of Mach 1.7 on the CCV airplane.

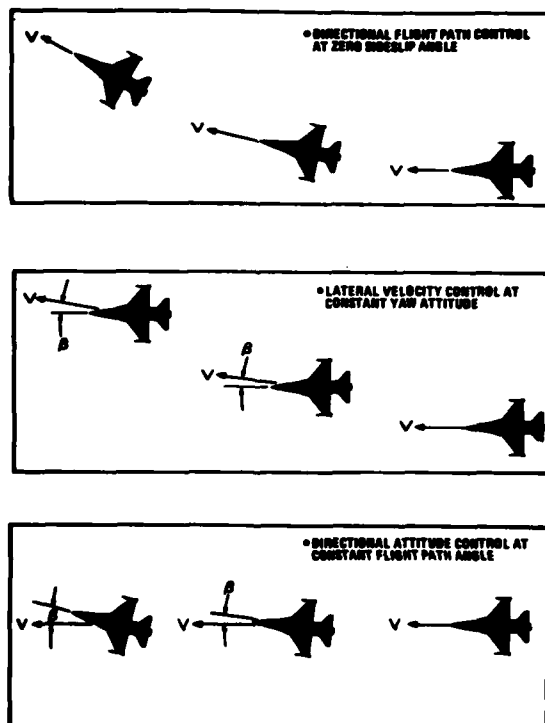


FIG 9: Direct Sideforce Control Modes

While the lowered directional stability of the CCV configuration was expected, the effect of canards on the dihedral effect ($C_{l\beta}$) was not anticipated. Figure 11 compares the dihedral effect as a function of angle of attack for vertical canards on and off. Flight test data was used in Figure 11, except for the regions of initial flow separation, where flight test data did not adequately define the curves. In these areas, wind tunnel data was used. Figure 11 shows that the vertical canards increase $C_{l\beta}$ over the entire angle of attack range investigated. This effect was attributed to flow interference from the canards on the downstream wing.

The tendency of an aircraft to depart from controlled flight is of prime importance for all configurations. It is an especially valid concern for aircraft with reduced levels of longitudinal and/or directional stability, such as encountered on CCV designs. A parameter which is commonly used to predict yaw departure tendencies is the dynamic directional stability coefficient defined by:

$$C_{n\delta} \text{ DYNAMIC} = C_{n\delta} \text{ BODY} \cos \alpha - C_{l\beta} \text{ BODY} \left(\frac{I_z}{I_x} \right) \sin \alpha .$$

Flight test data was used to calculate and compare the dynamic directional stability parameters for the baseline YF-16 and the CCV configuration. Figure 12 shows that for angles of attack above 15 degrees, the dynamic stability parameter is greater with canards installed than with them off. This occurred because the canards increase the dihedral effect sufficiently to offset the reduced directional stability. Other flight conditions

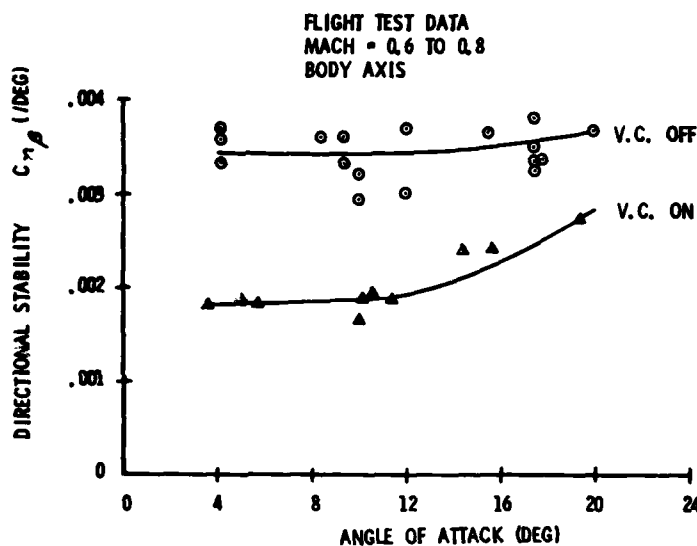


FIG 10: Effect Of Vertical Canards On Directional Stability

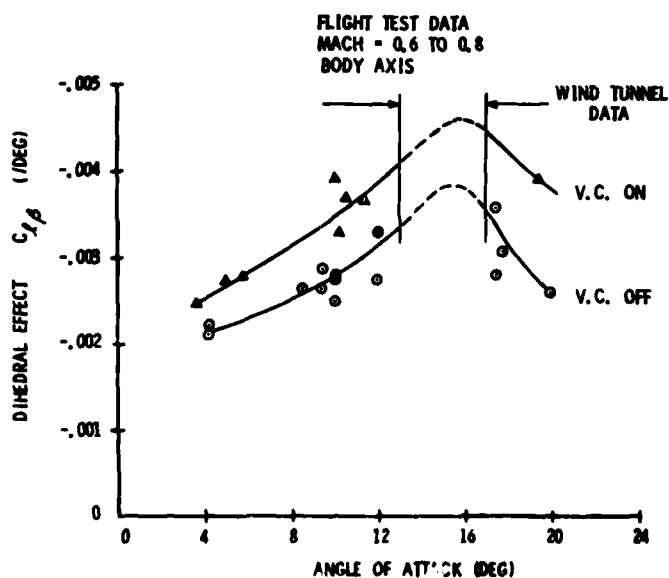
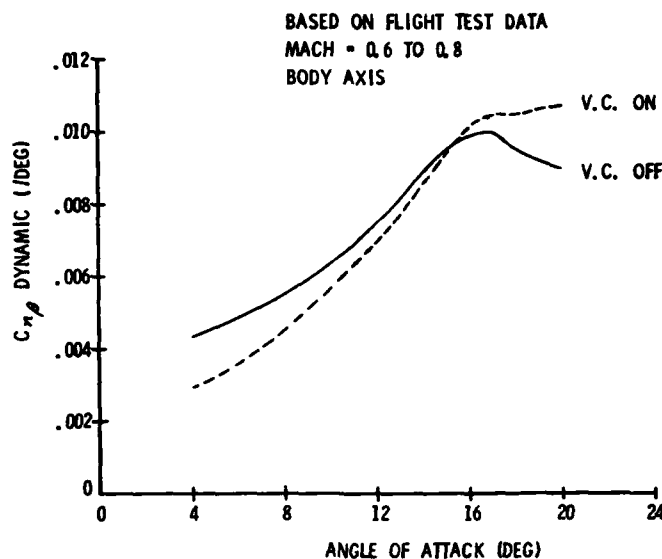


FIG 11: Effect Of Vertical Canards On Dihedral Effect

FIG 12: Effect Of Vertical Canards On $C_{n\delta}$ DYNAMIC

showed similar trends in $C_{n\delta}$ DYNAMIC such that the CCV configuration was comparable in dynamic directional stability with the baseline YF-16. Although flight test data was not available above 20 degrees angle of attack, wind tunnel results further indicated that the vertical canards would not degrade high- α dynamic directional stability. Spin tunnel tests conducted at the NASA Langley Research Center on the CCV configuration prior to flight testing showed that the spin and recovery characteristics of the YF-16 were not significantly altered by the addition of vertical canards.

Although the canards had only a small effect on yaw departure tendencies as measured by $C_{n\delta}$ DYNAMIC, they were found through analysis to degrade pitch departure tendencies. This came about for several reasons. First, because the canards were canted outward, the additional forward lifting surface reduced the aircraft static margin by 2 to 3% MAC. Second, adverse aerodynamic interference between the canards and the horizontal tail reduced the recovery moments available from the tail. Finally, the lower directional stability made the aircraft more susceptible to pitch/roll coupling during sustained rolling maneuvers.

Figure 13 presents simulator results defining the angle of attack boundaries for performing 360-degree rolling maneuvers. The boundaries were set on the basis of full trailing edge down tail deflections being encountered during the maneuvers. Rolls initiated above the Figure 13 boundaries would be expected to saturate the tail and result in possible aircraft departure in pitch. The curves show that the presence of the vertical canards reduces the permissible rolling maneuver envelope. Moving the center-of-gravity

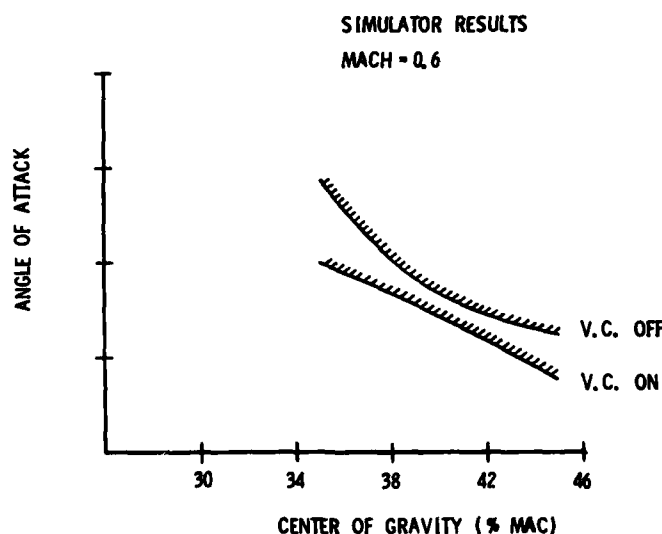


FIG 13: Maneuver Boundaries For 360° Rolls

aft of its nominal 35% MAC location also had a strong adverse effect on rolling maneuver capabilities. The reduction in the rolling maneuver envelope caused by the canards was the main reason for the decision to conduct Relaxed Static Stability (RSS) flight testing with the vertical canards removed.

The same canard interference effect which reduced tail pitching moments also caused a reduction in roll control effectiveness from the differential horizontal tails. This degradation was not too important since the differential tails provide only a small percentage of total aircraft roll power. Unfortunately, the flaperons, which provide most of the YF-16 roll control, also experienced effectiveness losses due to vertical canard interactions. The flaperon losses were fairly small and were effectively masked by the YF-16 roll rate command system, especially since maximum rate rolls were not part of the CCV flight test program.

The overall canard interference effects on CCV YF-16 pitch and roll control power were not completely documented during wind tunnel or flight tests. The available data were for undeflected canards. Interferences would be expected to be stronger for deflected surfaces. As mentioned earlier, upward deflected flaps had a strong influence on longitudinal tail power which was not fully recognized prior to flight test. A complete wind tunnel parameter matrix for the CCV YF-16 would have included control power measurements as functions of flap and canard deflections as well as functions of the more traditional variables. The important point to be made is that added CCV control surfaces can be expected to interact strongly with other force and moment producers, and the definitions of these interactions may significantly increase the cost and scope of the design process.

Aerodynamic non-linearities associated with the vertical canards were discovered during early wind tunnel tests. Figure 14 presents wind tunnel data of $C_{n\delta_{vc}}$ versus angle of attack and shows a reduction in vertical canard yaw effectiveness at high angles of attack. The two flight test points available, while inadequate to completely define canard effectiveness, lend credence to the wind tunnel values. Flight test directional stability data shown previously in Figure 10 also indicated these canard effectiveness losses. Figure 14 confirms the sharp fall-off in canard effectiveness that begins at about 12 degrees angle of attack, and also shows a more gradual decline in the low angle of attack region. This nonlinearity required that the gains of the CCV directional modes be scheduled with angle of attack. A less severe aerodynamic nonlinearity occurred with canard deflection angle. However, it was impractical to also gain schedule with δ_{vc} , although this might have resulted in improved mode response.

In addition to complicating the mode implementation task, the vertical canard aerodynamic nonlinearities could compromise operational usefulness of the DSFC modes. During CCV flight evaluations, the flat turn mode was rated highly on its potential for improving air combat maneuvering. However, the pilots believed that higher authority levels than implemented on the CCV YF-16 were required. The rapid decline in canard effectiveness with increasing angle of attack suggests that high DSFC levels may not be obtainable at maneuvering conditions with practical size vertical canards. This canard characteristic is not unique to the CCV configuration. Wind tunnel data covering a wide range of vertical canard locations and planforms on several different aircraft show the same rapid reduction in canard effectiveness with increasing angle of attack.

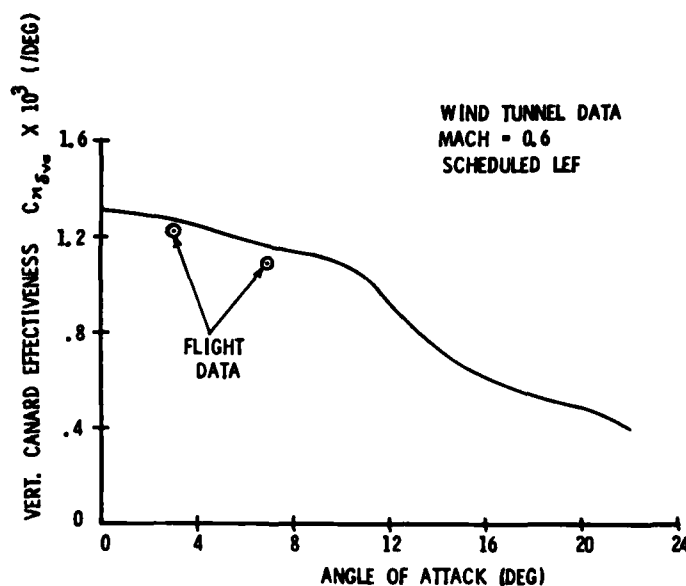


FIG 14: Vertical Canard Effectiveness

As with DLC commands, direct sideforce control inputs changed the energy state of the aircraft. However, unlike flap deflections which sometimes resulted in slight drag reductions, vertical canard deflections always increased the aircraft drag. The minimum drag penalty for the undeflected canards was relatively small, ranging from 10 drag counts subsonically to 20 counts supersonically. In fact, because the canards were canted outward, the increased lifting area resulted in minor L/D improvements with streamlined canards at some flight conditions. Significant drag increases occurred when the canards were deflected through large angles to command the DSFC modes. Figure 15 shows CCV YF-16 flight test data on the incremental energy change as a function of canard deflection for the flat turn mode. An energy maneuverability loss of about 90 fps (27 m/sec) occurred for maximum flat turn performance. The speed loss which accompanied DSFC inputs was quite apparent to the pilots and was judged to be a feature which could influence operational suitability. Again, the transitory nature of DSFC commands in operational usage may reduce the importance of these drag increases.

4. RELAXED STATIC STABILITY

The final facet of the CCV YF-16 flight test program was research into the benefits and limitations of relaxed longitudinal stability. The aircraft's fuel system was modified to enable pilot control of aircraft center-of-gravity position to permit evaluation over a wide range of aerodynamic stability levels. Figure 16 shows the relationships between the neutral point and the c.g. range tested. Note that the unmodified YF-16 aircraft was designed to take advantage of the Relaxed Static Stability (RSS) concept by operating at a nominal 2% MAC negative static margin at 0.8 Mach. The purpose of the CCV testing was to quantify performance sensitivity to the degree of static margin and verify experimentally that RSS provides maneuverability improvements over conventionally balanced designs. RSS testing was conducted with the vertical canards removed, all unconventional control modes disabled, and with the baseline YF-16 flight control system.

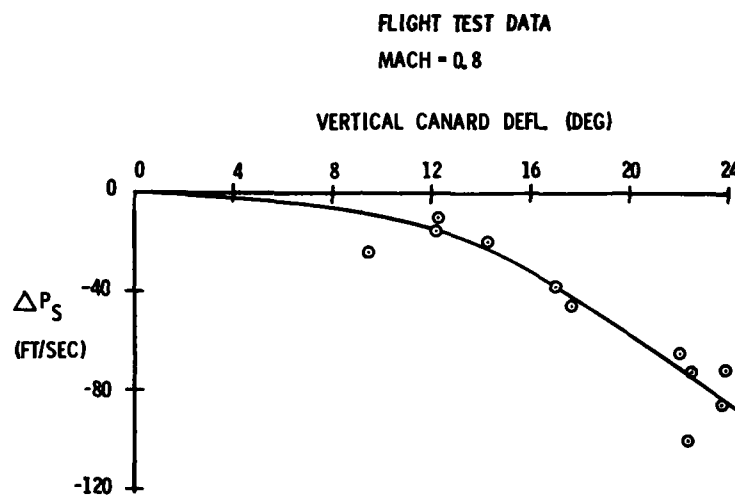


FIG 15: Effect Of Flat Turn Mode On Aircraft Energy

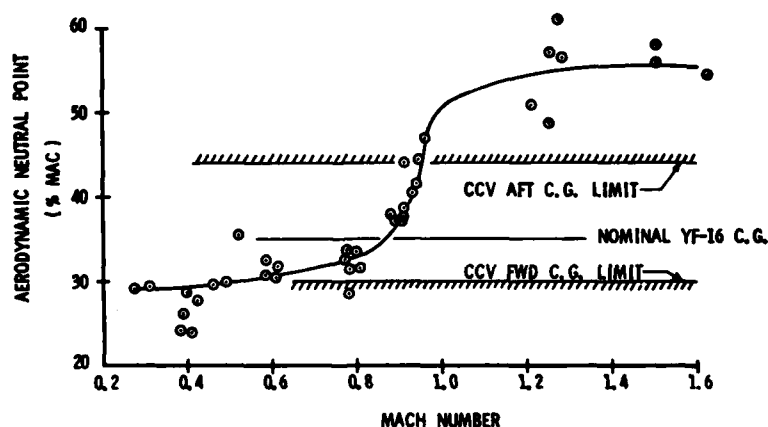


FIG 16: Neutral Point/C.G. Relationships For RSS Testing

The RSS testing verified that significant performance improvements can be obtained at aft c.g. locations. Figure 17 shows the change in sustained normal load factor as a function of c.g. location at 1.2 Mach. The load factors are shown as incremental variations from the YF-16 nominal c.g. of 35% MAC. The improvements with aft c.g. movement comes from increased lift-to-drag ratios resulting from favorable changes in horizontal tail trim loads. Reference 1 completely documents the RSS flight test performance results.

The RSS performance improvements were measured from the standpoint of gathering engineering data without regard to whether these improvements could be realized in a practical operational scenario. No attempt was made to modify the YF-16 aerodynamic or control system configuration to prevent handling qualities degradation at the aft c.g. locations. Prior to the performance tests, a series of four handling qualities flights were conducted with a spin recovery parachute assembly installed to make sure that the aft c.g. performance tests could be safely flown. These tests, and previous simulations, showed that control system and aerodynamic changes would have been necessary to produce an aircraft that could have taken maximum advantage of RSS and still have acceptable operational characteristics. Results indicated that the YF-16 design achieved a good compromise in applying the RSS concept without sacrificing operational suitability.

As described in Reference 6, the baseline YF-16 aft c.g. limit was established on the basis of having adequate pitch control power available for recovery from high angle of attack. The CCV program went beyond this guideline, so that at the CCV aft limit of 44% MAC, it would have been possible for the aircraft to encounter a locked-in stall situation. This was acceptable risk during the closely-controlled RSS experiments, but would be unsatisfactory for normal operations. The need for additional pitch control power at the aft c.g.'s was also demonstrated in Figure 13. Tail saturation caused by roll coupling resulted in unacceptable maneuvering limitations at aft c.g.'s. It is unfortunate that the RSS concept has sometimes been associated with smaller tail surfaces. While this may be true for low maneuverability aircraft, fighter aircraft can be expected to experience increased control power requirements as a result of RSS. Inadequate pitch control power requires an aerodynamic solution and cannot be alleviated by advanced control system technology.

Several handling qualities deficiencies which may have been correctable through control system modifications were also discovered during the RSS safety clearance flights. Although performance testing to a c.g. of 44% had been planned, aft limits forward of this were set based on pilot observations of handling quality changes as the c.g. moved aft. In up-and-away flight, the pilot reported:

"A considerable loss of precision in pitch control was evident while operating with the c.g. at 44% MAC. Based on the specific changes seen in rolling behavior and the loss of precision in pitch control, I believe that the end point has been reached as regards aft c.g. testing for this program. The airplane should not be used for subsequent performance testing with the c.g. aft of 43% MAC."

In simulated landing approaches, the pilot reported:

"The airplane exhibited some rather unpleasant flying qualities in landing configuration flight with the c.g. at 41.5% MAC. A horizontal tail deflection of approximately 8 degrees trailing edge down was required for trim at 1 g. Very mild pitch disturbances produced large positive horizontal tail deflections

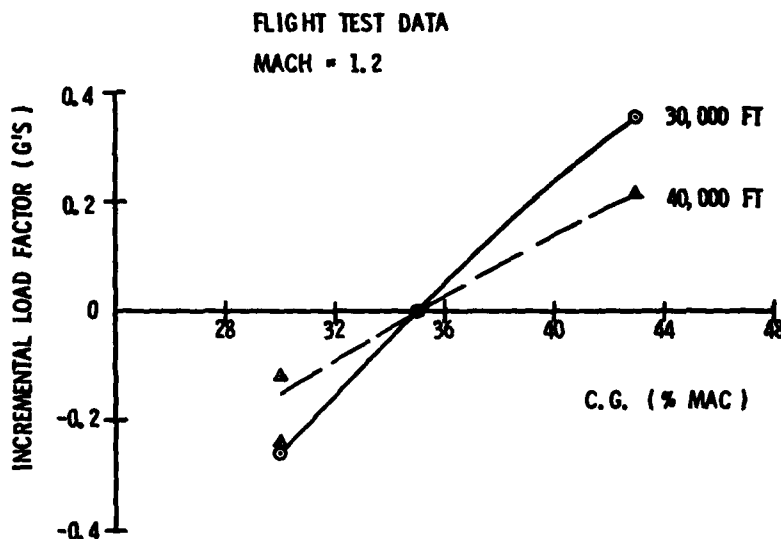


FIG 17: Effect Of C.G. Location On Maximum Sustained Load Factor

during damping. In this flight condition, the airplane appears to respond very unfavorably to turbulence. Pitch control is very imprecise and the lateral-directional damping is somewhat weak. The piloting task is such that almost constant reference must be made to the angle-of-attack indicator. Based on the test runs flown, performing an actual landing with the c.g. at 41.5% MAC would be challenging in calm air and quite hazardous in turbulence. Landing configuration flight with the c.g. at 41.5% MAC is to be avoided if at all possible, and if no alternative is available, should be approached with caution, especially in turbulence."

Although the above pilot comments were difficult to substantiate using the available recorded data, it was clear that handling qualities had severely deteriorated requiring revised aft c.g. limits of 41.5 and 43% MAC for landing and up-and-away flight, respectively. By proper ballasting and fuel management, the 43% MAC performance testing was accomplished and then fuel was pumped forward to land at a c.g. giving acceptable approach handling qualities. While RSS testing verified that significant performance improvements are available from reduced static margins, it also pointed out the difficulties in realizing the maximum benefits in a practical fighter aircraft.

4. CONCLUSIONS

The CCV YF-16 flight test program demonstrated that the Control Configured Vehicle concept, rather than reducing the importance of bare airframe aerodynamics, has resulted in an increased requirement for a thorough and accurate definition of aerodynamic characteristics. The control surfaces used to decouple aircraft motions and implement CCV concepts can be expected to exhibit nonlinearities and interference effects which should be accounted for in the design process. On the CCV YF-16, the closed-loop flight control system was generally effective in compensating for aerodynamic deficiencies. However, there are limits beyond which control system fixes of aerodynamic characteristics are not practical or possible. Future CCV designs may require an increased scope of wind tunnel testing in the form of larger parameter matrices to identify and solve adverse aerodynamic interaction and nonlinearity effects. Guidelines are needed to define acceptable levels of buffet and energy changes associated with decoupled control modes. On the CCV YF-16, these aerodynamic effects were primary factors in determining the viability of the unconventional control concepts investigated.

REFERENCES

1. McAllister, J.D., et al, (General Dynamics Corp.), Fighter CCV Phase IV Report, AFFDL-TR-78-9, Air Force Flight Dynamics Laboratory, Wright-Patterson AFB, OH February 1978.
2. Wood, R.A., Garland, M.P. and Meschko, E.T., Major, USAF, YF-16 Control Configured Vehicle (CCV) Operational Potential, Flying Qualities, and Performance Evaluation, AFFTC-TR-77-23, Air Force Flight Test Center, Edwards AFB, CA, January 1978.
3. Benepe, D.B., Sr., High-Angle-of-Attack Aerodynamics, Part I: Investigations of YF-16 Lightweight Fighter Prototype Buffet Characteristics, ERR-FW-1654, General Dynamics Corp., Fort Worth, TX, 15 December 1975.
4. Eggers, J.A., Major, USAF and Bryant, W.F., Jr., Major, USAF, Flying Qualities Evaluation of the YF-16 Prototype Lightweight Fighter, AFFTC-TR-75-15, Air Force Flight Test Center, Edwards AFB, CA, July 1975.
5. Ettinger, R.A., Lt/Col, USAF, and Jones, G.L., Interim Results of the YF-16 CCV Evaluation Through 24 June 1976, Letter Report, Air Force Flight Test Center, Edwards AFB, CA, 30 March 1977 (unpublished).
6. Lamers, J.P., "YF-16 High Angle of Attack Flight Test Experience", AGARD Flight Mechanics Panel CP-199, June 1976.

IDENTIFICATION OF THE STABILITY PARAMETERS OF AN AEROELASTIC AIRPLANE*

Edmund G. Rynaski
Staff Engineer

Dominick Andrisani II
Senior Systems Engineer

Norman Weingarten
Research Aeronautical Engineer

Flight Sciences Department
Calspan Corporation
Buffalo, New York 14225

1.0 SUMMARY

This paper addresses the problem of the parameter identification of large scale dynamic systems involving a system matrix characterized by approximately 200 elements. By using phase variable transformations, a mathematical model of an aeroelastic airplane is described in a form that is amenable to partial or piecemeal acceptance of parameters estimated from flight data. A mathematical model of the U.S. Air Force (USAF) Total In-Flight Simulator (Ref. 1) was computed using the FLEXSTAB (Ref. 2) digital computer program. As data became available during the progress of the flight test program, this data was processed and substituted in the mathematical model for parameters analytically obtained from the FLEXSTAB program. The results tend to show a progressive and orderly transition from an analytically defined mathematical model to one obtained from the flight tests of the actual aircraft.

2.0 INTRODUCTION

An accurate and adequate mathematical model of an aircraft is needed before a flight control system can be designed for an aircraft that exhibits a high degree of aeroelastic flexibility. Many investigations have recently been concerned with the problem of aircraft identification, i.e., the determination of the stability and control derivatives of these equations of motion. Concurrent with the development of identification techniques has been the development of digital computer programs to analytically predict the required dynamical equations. Perhaps the best known program is FLEXSTAB (Ref. 2), a comprehensive digital program that predicts not only rigid body dynamics, but also aeroelastic natural frequencies and damping ratios and a complete set of aeroelastic equations of vehicle motion. It is likely, however, that programs such as FLEXSTAB will be used only for preliminary prediction and analysis until verification of the accuracy of the computer predictions can be established by analysis of compatible flight test data.

The mathematical model of an aeroelastic airplane involves the definition of an order of magnitude more parameters or stability derivatives than has ever been accomplished in the past. No known method of parameter identification, including weighted least squares, maximum likelihood or minimum variance methods can now accurately estimate the hundred or more parameters required to establish a mathematical model of an aeroelastic airplane. Perhaps the most significant difficulty in trying to simultaneously identify a large number of parameters is the specification of an optimal input that would enable each of the parameters to be independently identifiable.

The method of parameter identification presented in this paper was conceived to circumvent the problems discussed above. The main idea is to transform the original equations of motion into a canonical form that would allow for partial or piecemeal analysis of the data. By doing this one can avoid the dimensionality problem, guarantee a minimum dimensionality representation, allow for the direct use of existing and conventional "frequency sweep" inputs ordinarily used in structural mode and flutter analysis, and allow for the assimilation of both flight data and an analytically computed FLEXSTAB representation. In addition, it has been found that the method can yield an estimate of the accuracy of the final estimates of the parameters of the aeroelastic vehicle.

3.0 MATHEMATICAL METHODS

3.1 The Phase Variable Transformation

The linearized equations of motion of an aeroelastic airplane are normally available in the usual matrix-vector form

$$\begin{aligned} \dot{A}x &= Bx + Cu \\ \text{or} \quad \dot{x} &= Fx + Gu \end{aligned} \quad (1)$$

where x is a vector whose components represent the rigid body motion variables such as angle of attack, pitch rate and pitch angle and the conventional normal elastic variables and their time derivatives. The vector u represents the input variables such as the commands to the elevator and direct lift flap electrohydraulic actuation system. The elements of the matrices F and G represent respectively the dimensional stability and control derivatives of the mathematical model of the aircraft.

*The research reported upon in this paper was performed under U.S. Air Force Contract F33615-73-C-3051 and funded by the Langley Research Center of the National Aeronautics and Space Administration.

A transformation, called a phase variable transformation of the form

$$x = T_i y, \quad (2)$$

is defined, one for each control input, u_i , that transform the equations of motion Eq. (1) into the set

$$\begin{aligned} \dot{y} &= T_i^{-1} F T_i y + T_i^{-1} G_i u_i \\ &= F_0 y + G_0 u_i \end{aligned} \quad (3)$$

where F_0 and G_0 are of the form

$$F_0 = \begin{bmatrix} 0 & 1 & 0 & 0 & \dots & 0 \\ 0 & 0 & 1 & 0 & \dots & 0 \\ \vdots & \vdots & \vdots & \vdots & \ddots & \vdots \\ 0 & 0 & \dots & 0 & 1 & 0 \\ -d_0 & -d_1 & \dots & 0 & -d_{n-1} & 1 \end{bmatrix} \quad G_0 = \begin{bmatrix} 0 \\ \vdots \\ 0 \\ 1 \end{bmatrix} \quad (4)$$

The coefficients d_i of the last row of the matrix F_0 are obtained from the coefficients of the characteristic polynomial of the system matrix of Eq. (1), i.e.

$$|Is - F| = s^n + d_{n-1}s^{n-1} + d_{n-2}s^{n-2} + \dots + d_1s + d_0 \quad (5)$$

The rows of the square, non-singular transformation matrix T_i of Eq. (2) are obtained from the coefficients of the numerator polynomials of the transfer functions obtained from the equation of motion Eq. (1). This transformation can be defined from the equation

$$T_i S = |Is - F| [Is - F]^{-1} G_i \quad (6)$$

$$\text{or} \quad T_i S = [Is - F]^{\text{adj}} G_i \quad (7)$$

where $S^T = [1, s, s^2, \dots, s^{n-1}]$ is a vector composed of powers of the Laplace transform variable s and $[Is - F]^{\text{adj}}$ defines the adjugate of the $[Is - F]$ matrix. Eqs. (2) and (3) are therefore sufficient to define all of the transfer functions of the state variables that can be represented by Eq. (1) with respect to the input u_i . The rows of the transformation T_i consist of the coefficients of the numerator polynomials of these transfer functions. Eqs. (2) and (3) can be looked upon as a matrix representation of the transfer functions of the system.

If the aircraft is represented in the phase variable model form, individual transfer functions may be identified separately, thereby significantly reducing the dimensionality of the identification process. When a sufficient number of transfer functions have been identified, the transformation given by Eq. (2) can be constructed. The original equations of motion Eq. (1) are then obtained by the relatively simple computation given by

$$\begin{aligned} \dot{x} &= T_i F_0 T_i^{-1} x + T_i G_0 u_i \\ &= F x + G u \end{aligned} \quad (8)$$

Because a separate transformation for each control input can be obtained, the process of estimating transfer functions for a second control can be repeated and a second estimate of the matrix of the stability derivatives F can be obtained. In fact, the two transformations associated with two control inputs, T_1 and T_2 , can be combined in any linear way to obtain a better estimate of the matrix F of stability derivatives as, for example, given by Eq. (9),

$$\begin{aligned} \dot{x} &= (T_1 + T_2) F_0 (T_1 + T_2)^{-1} x + T_1 G_0 u_1 + T_2 G_0 u_2 \\ &= F x + G u \end{aligned} \quad (9)$$

Because both transformations must yield the same matrix F , i.e.

$$T_1 F_0 T_1^{-1} = T_2 F_0 T_2^{-1} = F \quad (10)$$

a mathematically rigid expression can be obtained from Eq. (10) that will, if satisfied, yield a precise measure of accuracy of the identification process. This expression is

$$F_0 T_1 T_2^{-1} = T_1 T_2^{-1} F_0 \quad (11)$$

In other words, F_0 and $T_1 T_2^{-1}$ must mathematically commute. Eq. (11) states that the eigenvectors of the matrices F_0 and $T_1 T_2^{-1}$ must coincide, resulting in an extremely precise and highly constrained mathematical relationship.

3.2 Treatment of Partially Identified Aircraft Data

The complete identification of a system using the procedure developed in this paper requires as many independent measurements of the aircraft dynamic motions as there are degrees of freedom of motion of

the dynamic model of the aircraft. In practice, a separate sensor is desirable for each state variable of the vehicle mathematical model. If a sufficient number of sensors are not available for a complete identification of the system dynamics, the data obtained from flight test can be combined or used to partially or selectively replace portions of the analytically computed FLEXSTAB model in the following fashion:

1. The FLEXSTAB equations of motion are transformed to the phase variable form.
2. Transfer functions from flight data are estimated using a conventional least squares matching process (Refs. 3 and 4).
3. Rows of the transformation obtained from the analytical model, step 1, are replaced by the coefficients of the numerator polynomials of the corresponding transfer functions estimated from the flight data, step 2.
4. The resulting transformation, obtained partially from an analytical model and partially from flight data, is used as in Eq. (8) to transform back to obtain estimates of the stability and control parameters for the mathematical model of the aircraft.

The four-step procedure described above yields a method of gradually or systematically replacing analytical predictions with flight test data as it becomes available, thereby assuring an increasingly more accurate description of the aircraft dynamics.

4.0 APPLICATION TO THE USAF/CALSPAN TOTAL IN-FLIGHT SIMULATOR (TIFS)

To verify the principles described in the previous section, it was decided to obtain a FLEXSTAB computer model of the Total In-Flight Simulator (TIFS) (Ref. 5), compare the response of this model to that of the actual aircraft and finally to try to determine the practical feasibility of combining analytical and experimental data sources to obtain increasingly more accurate estimates of the dynamics of the airframe.

The TIFS airplane is well suited for an experimental program of this type. In addition to a complete complement of instrumentation designed for rigid body measurements of the vehicle dynamic motions, six linear accelerometers used initially for flutter tests were available for aeroelastic measurements. The elevator and direct lift (inboard) flaps of the airplane are driven directly by wide band, high performance electrohydraulic servos. Sine wave inputs up to 15 Hz could be electronically injected into the servos to oscillate the elevator and the direct lift flaps, thereby exciting the first five symmetrical elastic modes of motion of the aircraft.

4.1 FLEXSTAB Model Development

The structural and aerodynamic properties of the symmetric degrees of freedom of the TIFS aircraft were analytically computed through use of the Level 2.01 FLEXSTAB computer program using the residual flexibility formulation. This finite element computer program used lumped masses and equivalent uniform beams for the structural model and thin bodies, slender bodies and interference bodies for the aerodynamic model. A low frequency unsteady aerodynamic modeling feature is also an integral part of this computer program.

The structural and aerodynamic description of TIFS developed for input into the FLEXSTAB program is subject to several limitations. The mass distribution and stiffness data were based on Convair 580 data originally prepared over 25 years ago and subsequently updated to include the special TIFS modifications. Only limited ground vibration data was available. The dynamics of the turboprop engine on its engine mounts were not represented nor were the aerodynamic effects of propeller slipstream. Most significantly, the data to be presented herein showing TIFS responses to sinusoidal inputs are outside the range of applicability of the low frequency aerodynamic theory incorporated into the FLEXSTAB program. As may be expected, the analytical model of the TIFS airplane behaved somewhat differently from the actual airplane, yet the natural frequencies of the structural modes of the TIFS aircraft were accurately predicted. The FLEXSTAB program, then, is a valuable tool not only to provide a preliminary mathematical model for the aircraft, but also to define the range of frequencies and amplitudes that should be used to sinusoidally excite the aircraft.

4.2 Procedure for Combining Data Sources

The aeroelastic equations of motion for the symmetric degrees of freedom were obtained from the FLEXSTAB program in the general matrix-vector form

$$\dot{A}\dot{x} = Bx + Cu \quad (12)$$

and are readily transformed to the more familiar state space form by premultiplication by A^{-1}

$$\begin{aligned} A^{-1} \dot{A}\dot{x} &= A^{-1} Bx + A^{-1} Cu \\ \dot{x} &= Fx + Gu \end{aligned} \quad (13)$$

where the state and control vector have been defined as

$$\begin{aligned} x^T &= [\Delta V, \Delta \alpha, q, \Delta \theta, \eta_1, \eta_2, \eta_3, \eta_4, \eta_5, \dot{\eta}_1, \dot{\eta}_2, \dot{\eta}_3, \dot{\eta}_4, \dot{\eta}_5] \\ u^T &= [\delta_z, \delta_e] \end{aligned}$$

The state variables η_i ($i = 1, \dots, 5$) and $\dot{\eta}_i$ ($i = 1, \dots, 5$) represent the first five symmetrical normal elastic mode variables and their time derivatives, while ΔV , $\Delta \alpha$, q and $\Delta \theta$ represent the rigid body change in velocity, angle of attack, pitch rate and pitch angle. The control variables δ_f and δ_e represent respectively the incremental deflection of the direct lift flap and the elevator.

Several additions, deletions or transformations were made to the FLEXSTAB dynamical system Eq. (13) in order to reflect the actual physical differences of representation between the FLEXSTAB computation and the TIFS airplane. Specifically, actuator dynamics were added to the equations of motion (Eq. (13)), and the equations were transformed into a set that reflected as accurately as possible the signal outputs of actual flight measurements or sensors used on the TIFS airplane.

4.3 Additions of Servo Dynamics

The flight data was obtained by driving the input to the control surface actuators with a sine wave oscillator at specific incremental frequencies to span the range of natural frequencies of the normal mode variables, thus obtaining amplitude/frequency or Bode plots of the aircraft response to sine wave actuator input commands. The flight records included measurements of the oscillator output and the actual aerodynamic control surface position. Therefore, Bode plots were obtained of the actuator response. Examination of these flight recordings indicated that the elevator and the direct lift flap servos' dynamic behavior could be approximated by first order mathematical models and expressed in the usual form

$$\dot{u} = F_1 u + G_1 u_c \quad (14)$$

where $u^T = [\delta_f, \delta_e]$ represents the deflection of the direct lift flap and elevator and $u_c^T = [\delta_{fc}, \delta_{ec}]$ represents the input (sine wave oscillator output) to the surface servos. Eq. (14) was then appended to Eq. (13) to yield the combined set

$$\begin{bmatrix} \dot{x} \\ \dot{u} \end{bmatrix} = \begin{bmatrix} F & G \\ 0 & F_1 \end{bmatrix} \begin{bmatrix} x \\ u \end{bmatrix} + \begin{bmatrix} 0 \\ G_1 \end{bmatrix} u_c \quad (15)$$

$$\text{or} \quad \dot{x}_A = F_A x_A + G_A u_c \quad (16)$$

4.4 Transformation to a Partially Measurable Set

The instrumentation complement used during the flights of the airplane included normal accelerometers, rate and attitude gyros, and sensors to measure velocity and angle of attack change. Although each of the instruments measured a function of the state variables of Eq. (15), no instrument did or was able to sense a state variable independently. The ten sensors used during flight represent outputs of the equations of motion Eq. (16), and were calculated from the FLEXSTAB program in the vector matrix form

$$z_m = H_1 x \quad (17)$$

where z_m is a vector that represents the sensor outputs and H_1 is a 12x16 output matrix representing the linearized functional relationship between the state variables of Eq. (16) and the sensors used in the airplane. Relationship Eq. (17) was used to form a transformation matrix

$$z = Hx \quad (18)$$

where

$$H = \begin{bmatrix} H_1 \text{ (12x16)} \\ 0 \mid I_{4x4} \end{bmatrix}$$

$$\text{and } z^T = [\Delta V, \Delta \theta, q, \Delta \alpha, \delta_e, \delta_f, \eta_{zp}, \eta_{zc}, \eta_{ztr}, \eta_{ztc}, \eta_{znr}, \eta_{znc}, \eta_4, \eta_5, \dot{\eta}_4, \dot{\eta}_5]$$

The matrix H is square and non-singular. Therefore, the equations of motion, Eq. (16), can be transformed directly using Eq. (18) to obtain

$$\begin{aligned} \dot{z} &= H F_A H^{-1} z + H G_A u_c \\ \text{or} \quad \dot{z} &= F_B z + G_{B_1} \delta_{fc} + G_{B_2} \delta_{ec} \end{aligned} \quad (19)$$

4.5 Transformation to Phase Variable Form

The FLEXSTAB equations of motion, Eq. (19), were written as two single input systems

$$\dot{z} = F_{B_1} z + G_{B_1} \delta_{fc} \quad (20a)$$

$$\dot{z} = F_{B_2} z + G_{B_2} \delta_{ec} \quad (20b)$$

where the state vector for Eq. (20a) contained the direct lift flap position as a state variable but not the elevator position while the reverse was true for Eq. (20b). These equations were then transformed into the phase variable form of Eq. (3) by means of two transformations T_{δ_f} associated with the direct lift flap servo input and T_{δ_e} associated with the elevator servo input.

The fifteen state variables of Eq. (20a) $\mathbf{z}^T = [\Delta V, \Delta \theta, \delta, \Delta \alpha, \delta_z, \eta_1, \eta_2, \eta_3, \eta_4, \eta_5, \dot{\eta}_1, \dot{\eta}_2, \dot{\eta}_3, \dot{\eta}_4, \dot{\eta}_5]$. Eight of these states, designated with the subscript, namely $\eta_m, \delta_m, \eta_{pm}, \eta_{cgm}, \eta_{NTm}, \eta_{TCm}, \eta_{HTm}, \eta_{MMm}$ were measured directly in flight and transfer functions for these eight variables were estimated from the flight data. These eight variables represent respectively the output of a rate gyro, the direct lift flap incremental deflection and linear accelerometer outputs at the pilot station (η_{pm}), the aircraft center of gravity (η_{cgm}), the starboard wing tip (η_{NTm}), the tail cone (η_{TCm}), stabilizer tip (η_{HTm}), and the acceleration at a mid-wing station (η_{MMm}).

The transfer functions were estimated using direct and straightforward least squares regression methods adequately described by Levi (Ref. 1) and Sanahanan and Koerner (Ref. 2). The techniques were slightly modified to improve accuracy by estimating transfer functions from two Bode plots simultaneously and including the constraint that both transfer functions have the same denominator or characteristic polynomial. This constraint essentially eliminated the known fault of this technique of occasionally estimating transfer functions having unstable or right-half plane poles. By working with only two transfer functions at one time, only a maximum of 43 coefficients had to be simultaneously estimated, rather than the 240 or so parameters of Eq. (20a), thereby greatly reducing the dimensionality problem for each computer computation run.

4.6 Partial Replacement of Analytical Results with Flight Data

The first step was to replace the characteristic polynomial or phase variable system matrix F_0 of the analytical model with the measured system matrix F_{0m} obtained from the transfer function estimates.

Then eight of the rows of the analytically calculated phase variable transformations were replaced, row by row with the coefficients of the eight numerator polynomials obtained from the flight data, and expressed in the form

$$\mathbf{z}_m = T_m y \quad (21)$$

where \mathbf{z}_m represents the eight measured state variables and T_m is an 8×15 matrix made of the numerator polynomial coefficients of the transfer functions of the eight variables estimated from flight data. The remaining portion of the phase variable transformation calculated analytically T_c was then appended to Eq. (21) to yield the mixed measured-calculated transformation

$$\begin{bmatrix} \mathbf{z}_m \\ \mathbf{z}_c \end{bmatrix} = \begin{bmatrix} T_m \\ T_c \end{bmatrix} y$$

or

$$\mathbf{z}_{mc} = T_{mc} y \quad (22)$$

where \mathbf{z}_c represents the state variables not measured in flight, namely $\mathbf{z}_c^T = [\Delta V, \Delta \alpha, \Delta \theta, \eta_1, \dot{\eta}_1, \eta_2, \dot{\eta}_2, \eta_3, \dot{\eta}_3, \eta_4, \dot{\eta}_4, \eta_5, \dot{\eta}_5]$.

The transformation T_{mc} is now full rank and invertible, so the equations of motion in the form of Eq. (20a) now containing a mixture of measured and calculated data, can be obtained from

$$\dot{\mathbf{z}}_{mc} = T_{mc} F_{0m} T_{mc}^{-1} \mathbf{z}_{mc} + T_{mc} G_0 \delta_z \quad (23)$$

There is no way known at this time to transform Eq. (23) back to the original form of Eq. (13), nor does there seem to be a practical reason for wishing to do this. The in-vacuum normal mode variables η_i and derivatives $\dot{\eta}_i$ are not directly measurable, so they cannot be used, as the sensor outputs can, for control system design purposes. The transformation H that transforms the Eq. (23) into the set Eq. (13) requires accurate knowledge of the mode shapes and slopes which comes from accurate knowledge of the mass and stiffness distribution. This data can be more easily obtained by ground measurements or calculations rather than from flight measurements.

4.7 Multi-Input Data Analysis

The procedure of generating Bode plots, estimating transfer functions from these Bode plots and replacing the calculated characteristic polynomial and selected rows of the phase variable transformation was repeated for an elevator actuator command input, resulting in a second set of combined measured-calculated equations of motion of the form

$$\dot{\mathbf{z}}_{mc} = T_{mc} F_{0m} T_{mc}^{-1} \mathbf{z}_{mc} + T_{mc} G_0 \delta_e \quad (24)$$

Combining Eqs. (23) and (24) in the manner defined by Eq. (9) required a minor but straightforward modification because Eq. (23) contains direct lift flap actuator dynamics with no elevator actuator dynamics while with Eq. (24) the reverse is true. The modification requires a redefinition of a system matrix F_{0m} to include the dynamics of both elevator and direct lift flap actuators. When this is done, the resulting dimensionally expanded phase variable transformation T_{e} and T_{δ} will each contain a row and column of zero or null elements. Because a row of null elements produces a singular, non-invertible matrix, neither of the two matrices can be used as a similarity transformation but their sum will be non-singular. The multicontrol, mixed-measured and calculated equations of motion can be obtained by combining as follows:

$$\hat{z}_{mc} = \begin{pmatrix} T_{mc\delta_z} & T_{mc\delta_e} \end{pmatrix} F_{om} \begin{pmatrix} T_{mc\delta_z} & T_{mc\delta_e} \end{pmatrix}^{-1} \hat{z}_{mc} + T_{mc\delta_z} G_o \delta_z + T_{mc\delta_e} G_o \delta_e \quad (25)$$

By combining data from several different excitation sources in the manner defined by Eq. (25), it is felt that the identifiability of the system and therefore the accuracy of the results can be significantly improved. Often one aeroelastic mode is only nominally excited by a particular input, yet that mode can be strongly excited by a second input. Every phase variable transformation can contain within it information related to the elastic modes in different degrees. By combining the transformations as indicated by Eq. (25), more complete information about the modes is available. In a mathematical sense, this means that the matrix $T_{\delta_e} + T_{\delta_z}$ will likely be better conditioned than will T_{δ_z} or T_{δ_e} alone.

5.0 RESULTS

Typical results showing a comparison of FLEXSTAB-computed amplitude and phase responses of the TIFS airplane with the data collected in flight are shown in Figs. 1-4. The measured and computed responses shown were for the normal acceleration at the wing tip of the aircraft. The flight conditions approximated the landing approach speed of the aircraft at low altitudes. Figs. 1 and 2 show the amplitude and phase response comparisons when the aircraft was excited by a sine wave input to the direct lift flap actuator while Figs. 3 and 4 show the responses to an elevator actuator sine wave input. In some instances, like those shown in Figs. 1 and 2, the general character of the responses was similar but amplitudes differed considerably. Although not shown, the natural frequencies of the modes calculated from FLEXSTAB and estimated from flight data were nevertheless in close agreement, as could be judged from the phase vs. frequency plot of Fig. 2.

Figs. 5 and 6 show typical comparisons between the flight data and the Bode plot generated from a transfer function estimated from the flight data, and are therefore a measure of the accuracy of the transfer function identification method used.

Once the transfer functions were obtained from flight, the data was used to replace the characteristic polynomial of the FLEXSTAB-computed results and selected rows of the phase variable transformations in sequential fashion. First the characteristic polynomial was replaced, and the equations transformed back from phase variable form to the form of Eq. (20a). Then both the characteristic polynomial and one of the rows of the phase variable transformation were replaced with data estimated from flight, and then again transformed to the form of Eq. (20a). This process was sequentially repeated replacing progressively more of the rows of the calculated transformation with flight estimates.

In Table 1 are listed some of the results of the gradual substitution of experimentally estimated data for analytically computed parameters. The table shows the progression of change in twelve of the 256 parameters contained in the matrix F_B . This table shows data substitutions for one control input only, the direct lift flap. These selected results indicate substantial differences between the FLEXSTAB and mixed FLEXSTAB/experimental calculations. Many of the elements have changed mathematical signs, and the numerical values have changed by several orders in magnitude. In general, the numerical values of the elements of the system matrix tend to show a progressive and relatively smooth change as increasingly more analytically computed data was replaced by experimental results. The numbers in the F_B matrix change substantially because of the strict mathematical requirement that some numerator polynomials corresponding to F_B match the FLEXSTAB polynomials while other numerator polynomials match the flight identified results. This latter property appears to be the most significant result of this procedure, the actual numbers appearing in the F_B matrix being of lesser importance. A tentative conclusion from the relatively smooth transition indicated by the results shown in Table 1 is that the gradual replacement of analytical predictions with experimentally determined estimates as described in this paper is a reasonable approach to the problem of identification of large scale systems as characterized by the aeroelastic airplane. More research, however, is required in order to answer questions concerning the sensitivity of the elements of Eq. (25) to errors in the determination of the numerator and denominator polynomials from the flight data and to investigate the possibility of optimally combining rather than directly substituting analytically computed data for flight data.

Table 2 shows some preliminary results obtained after the mixed calculated-measured results for the transformation matrices of the direct lift flap and the elevator were combined according to Eq. (25). The first column of the two columns of data in Table 2 shows the roots of the numerator polynomial of two transfer functions. The $n_{z\delta_z}/\delta_e$ roots were identified from flight data and were substituted into the corresponding row of the $T_{\delta_z mc}$ matrix of Eq. (23). The $\Delta v/\delta_z$ roots are those calculated by FLEXSTAB and were retained in $T_{\delta_z mc}$. In both cases, the roots shown in column one are the numerators corresponding to the system matrix $T_{\delta_z mc} F_{om} T_{\delta_z mc}^{-1}$, of Eq. (23). In a similar manner the numerator of $n_{z\delta_z}/\delta_e$ was computed from flight data, $\Delta v/\delta_e$ was computed by FLEXSTAB, and these two results were combined into the matrix $T_{\delta_e mc}$. The second column of Table 2 shows the numerator roots for δ_e input corresponding to the system matrix $[T_{\delta_e mc} + T_{\delta_z mc}] F_{om} [T_{\delta_e mc} + T_{\delta_z mc}]^{-1}$ of Eq. (25). When this second transformation $T_{\delta_e mc}$ is added to $T_{\delta_z mc}$ a gradual but significant change in the transfer function representation of the mathematical model occurs, particularly among the variables measured directly in flight such as the $n_{z\delta_z}/\delta_z$ transfer function. Through further research, it is expected that the mathematical relationships, constraints, and limitations of this procedure will be more accurately defined.

6.0 CONCLUSIONS

The method of data handling for large scale systems identification presented in this paper appears to be a reasonable approach to the problem. The technique is independent of the particular method of system identification used. Both time domain and frequency domain methods have been shown to be

successful for low dimensional systems, and the preliminary results presented in this paper indicate a useful application to the in-flight identification of the aeroelastic airplane.

The potential advantages of using the method described in this paper are significant. Fewer parameters need be identified at one time than with direct time domain methods, so the dimensionality and the input design problems are significantly simplified. Because either transients or the sinusoidal inputs described in this paper can be used to dynamically excite the aircraft, the experimental requirements are compatible with present flutter testing methods. The phase variable transformation is canonical, which means that the minimum number of parameters required to completely define the dynamic characteristics of the airplane are obtained. Finally, both stability and control derivatives and flying qualities parameters may be obtainable, thereby presenting the data in the correct form for aerodynamicists, flying qualities engineers and flight control system designers.

REFERENCES

1. Andrisani II, D., et. al.: "The Total In-Flight Simulator (TIFS). Aerodynamics and Systems - Description and Analysis," January 1976, Calspan Report No. AK-5280-F-10.
2. Boeing Commercial Airplane Company and Boeing Computer Services, Inc.: "A Method for Predicting The Stability Characteristics of Control Configured Vehicles," Vol. 1, "FLEXSTAB 2.01.00 Theoretical Description," November 1974, Air Force Flight Dynamics Laboratory Report No. TR-74-91, Vol. 1.
3. Levy, E. C.: "Complex Curve Fitting," May 1959, IEEE Transactions on Automatic Control, Vol. AC-4.
4. Sanahanan, C. K. and Koerner, J.: "Transfer Function Synthesis as a Ratio of Two Complex Polynomials," January 1963, IEEE Transactions on Automatic Control, Vol. AC-8.
5. Rynaski, E., Andrisani II, D. and Weingarten, N.: "Active Control for the Total In-Flight Simulator (ACTIFS)." April 1977, Calspan Report No. AK-5280-F-11.

ACKNOWLEDGMENTS

The authors would like to express their gratitude to Mr. L. Taylor, Mr. R. Hood and Mr. D. Middleton of NASA for their helpful suggestions and stimulating conversation. The FLEXSTAB results obtained during the program were obtained only with the very generous and expert assistance of Mr. R. Schwarz and Mr. C. Stockdale of the Air Force Flight Dynamics Laboratory, Wright Field, Ohio.

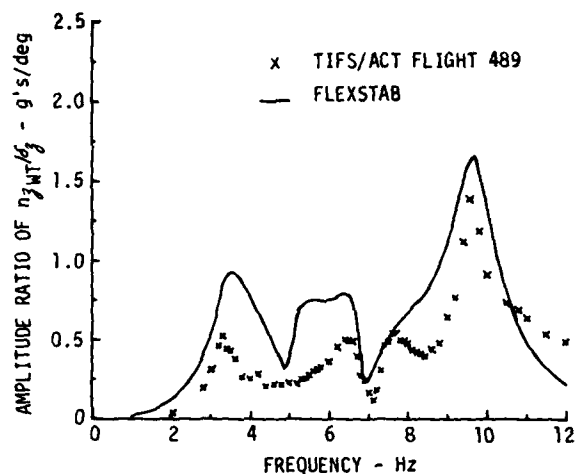


Figure 1. Frequency Response, Wing Tip Acceleration (n_{jWT})/DLF Deflection (δ_j) Landing Condition

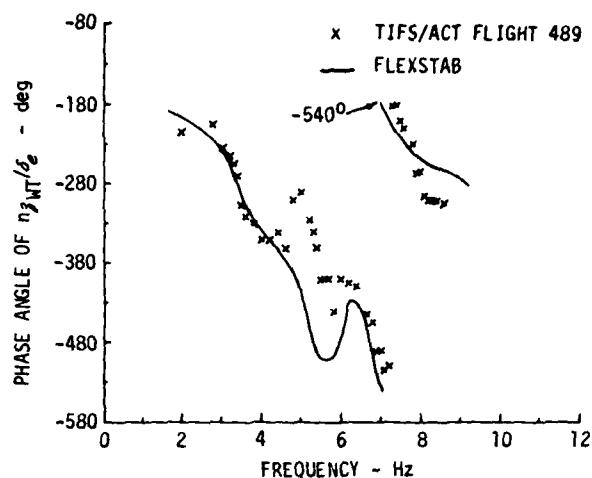


Figure 4. Frequency Response, Wing Tip Acceleration (n_{jWT})/Elevator Deflection (δ_e) Landing Condition

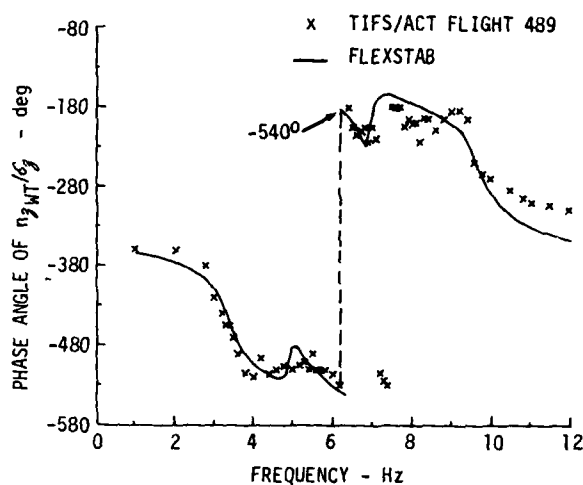


Figure 2. Frequency Response, Wing Tip Acceleration (n_{jWT})/DLF Deflection (δ_j) Landing Condition

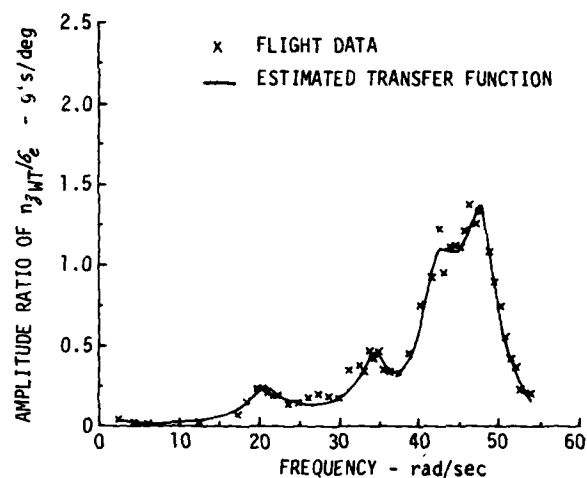


Figure 5. Frequency Response, Wing Tip Acceleration (n_{jWT})/Elevator Deflection (δ_e) Landing Condition

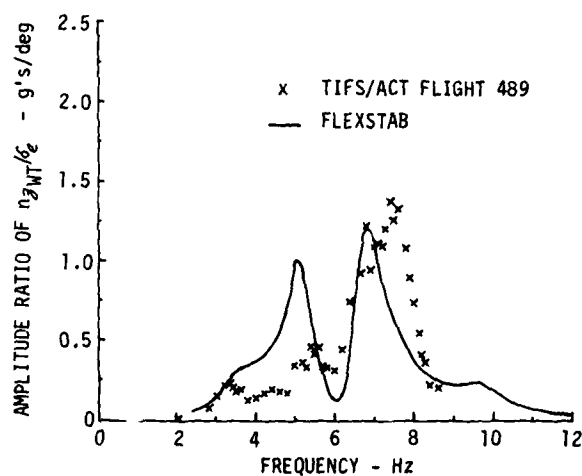


Figure 3. Frequency Response, Wing Tip Acceleration (n_{jWT})/Elevator Deflection (δ_e) Landing Condition

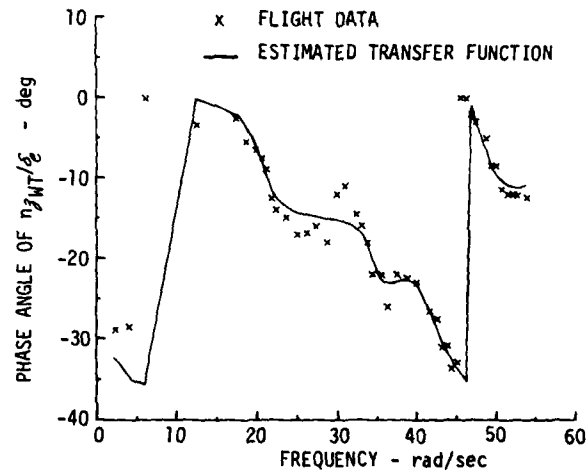


Figure 6. Frequency Response, Wing Tip Acceleration (n_{jWT})/Elevator Deflection (δ_e) Landing Condition

Table 1
Trend of Changes of System Matrix as Flight Data
Is Substituted For Analytically Computed Data

FLIGHT DATA SUBSTITUTED	ELEMENTS OF SYSTEM MATRIX											
	$\frac{\partial \dot{q}_{cg}}{\partial q_{cg}}$	$\frac{\partial \dot{q}_{cg}}{\partial n_{zp}}$	$\frac{\partial \dot{q}_{cg}}{\partial \dot{\eta}_1}$	$\frac{\partial \dot{q}_{cg}}{\partial \alpha_v}$	$\frac{\partial n_{zp}}{\partial q_{cg}}$	$\frac{\partial n_{zp}}{\partial n_{zp}}$	$\frac{\partial n_{zp}}{\partial \dot{\eta}_1}$	$\frac{\partial n_{zp}}{\partial \alpha_v}$	$\frac{\partial \ddot{\eta}_1}{\partial q_{cg}}$	$\frac{\partial \ddot{\eta}_1}{\partial n_{zp}}$	$\frac{\partial \ddot{\eta}_1}{\partial \dot{\eta}_1}$	$\frac{\partial \ddot{\eta}_1}{\partial \alpha_v}$
No substitutions (FLEXSTAB re- sults)	1.06	-18.1	-.154	8.10	-527.0	5795.0	87.0	-4659.0	.000716	219.8	-.000126	.00637
Characteristic Eqn. plus num- erators of $\delta_g/\delta_c, \dot{\delta}_g/\delta_c$ transfer func- tions	.134	-27.9	-.00167	.0517	20.0	-979.8	3.04	-165.3	-6.8×10^{-6}	98.1	-1.5×10^{-5}	.00042
Above substitu- tions plus num- erator of n_{zp}/δ_c Transfer func- tion	-1.02	5.9	-.0722	2.03	-6.19	68.4	.171	-28.0	4.05	-20.7	.248	-6.96
Above substitu- tions plus num- erators of $n_{zp}/\delta_c, n_{zp}/\delta_c$ and \dot{q}_{cg}/δ_c transfer func- tions	-4.71	59.1	-.197	1.67	3.74	79.1	-.0095	1.75	-.0138	288.4	-2.16	-102.3

Landing Flight Condition
Direct Lift Flap Inputs Only

Table 2
Comparison of Numerator Polynomial Roots Using
One or Two Phase Variable Transformation

Transfer Function	Numerators Estimated From Flight Data for n_{zp}/δ_c and By FLEXSTAB for $\Delta V/\delta_c$			Numerator Transfer Function Zeros Calculated From $\dot{\delta}_{mc} - (T_{\delta_{mc}} + T_{\dot{\delta}_{mc}}) \dot{\delta}_{mc} + T_{\delta_{mc}} \ddot{\delta}_{mc} + T_{\dot{\delta}_{mc}} \ddot{\delta}_{mc}$		
	ζ	$\frac{\omega}{\text{rad/sec}}$	τ sec	ζ	$\frac{\omega}{\text{rad/sec}}$	τ sec
n_{zp}/δ_c (Numerator of response at pilot location to direct lift flap input)	.0468 .0158 .0975 -.0527	76.2 47.1 36.5 30.7	-.050 -22.2 -.0517 31.1 .361 -.937	-.0599 .539 .0374 .924	54.3 42.9 36.4 14.3	-.0577 10.8 -.0395 -.005 -.647 -6.04
$\Delta V/\delta_c$ (Numerator of change in airspeed response to direct lift flap input)	.0418 .145 .056 .076 .455 .0225	61.2 45.3 43.9 31.7 23.1 1.57	-.741	.0513 .0131 -.143 .071 .918 .365	63.3 43.6 39.4 35.2 25.4 .972	.010 -.081

Nonlinear Parameter Identification and Its Application to Transport Aircraft

T.J. Galbraith

T.J. Petersen

Boeing Commercial Airplane Company
Renton, Washington

ABSTRACT

The need for accurate identification of aircraft force and moment coefficients has long been realized but only recently has it been feasible with the aid of high speed computers. This need is continually increasing due to the growing complexity of flight control systems and the expanding role of flight simulators. Parameter identification was first successful in the study of linear systems where the linear approximation was made to keep the order of the system tractable. Since airplanes must be described in both the linear and nonlinear flight regimes the more complex nonlinear parameter identification problem must also be addressed. The problems associated with the identification of nonlinear parameters are being overcome and the results look promising. This paper is a description of one such nonlinear parameter identification program with analysis results.

The purpose of this paper is to describe a nonlinear parameter identification computer program and results obtained from analyzing jet transport flight data characterized by nonlinear motion and parameters. The program is called NLAK for nonlinear aerodynamics and kinematics and is part of a system of computer programs developed at Boeing for analyzing airplane dynamic response data. NLAK's formulation is based on the full six-degrees-of-freedom equations of motion and up to third order polynomials for aerodynamic coefficients and thrust parameters. NLAK employs a maximum likelihood estimation algorithm which is capable of both recursive and batch processing.

The flight data analyzed was low speed, below 150 knots. The low speed data was characterized by kinematic cross-coupling, large motion variations and nonlinear forces and moments.

The analysis system will be outlined and all interfaces with the NLAK program will be described. The basic concepts and some of NLAK's formulation details will also be described in relation to obtaining consistent estimation results, especially for the nonlinear problem.

From the analysis by the NLAK program the results were generally consistent between different maneuvers at the same flight conditions, which helps substantiate the particular values identified. The NLAK analysis also showed the need for the high order polynomials in the nonlinear low speed flight records, and at present there also appears to be a need for velocity dependent coefficients in the low speed cases.

INTRODUCTION

Major advances have been made in flight control technology during the past decade; particularly in the areas of fly-by-wire, active controls, and more recently, digital control systems. To remain competitive, the next generation of aircraft--whether commercial or military--must take advantage of the benefits achievable from these concepts. The degree to which a new airplane design can be based on such advanced concepts depends to a large extent upon the confidence with which the aerodynamic and structural characteristics can be predicted and related to actual flight qualities.

Boeing Flight Controls Technology initiated the development of a system of programs for parameter identification in order to provide a tool which would enable both a qualitative and quantitative evaluation of the design processes used to arrive at the static and dynamic characteristics of an airplane. This means that it is desired to verify the ability of the design equations and/or the wind tunnel data to accurately represent the aerodynamic characteristics over the aircraft's flight regime. Additionally, it is desired to verify the accuracy of the models and data with respect to the actual values attained by the production airplane. A further requirement was that the analysis be accomplished by the engineers involved in the design process and not by a separate group isolated from the preliminary design.

The results obtained from parameter identification (PI) analyses would be used to :

1. Verify the analytical design procedures.
2. Isolate and identify nonanticipated aerodynamic effects.

3. Provide values for the stability and control derivatives that can be used by the flight simulators to more faithfully reproduce the airplanes static and dynamic characteristics for training and engineering studies.

These objectives for the parameter identification system indicated that the program must be flexible with respect to the force and moment models that could be incorporated into the equations of motion and relatively insensitive to initial values and tolerances applied to the system parameters. Additionally, since many of the anomalous aerodynamic effects will be discerned post-flight test, the program should be able to obtain the maximum information from available flight testing. To enhance its use by the Flight Controls staff, valid analysis cues and procedures must be developed which lead to consistent results.

To satisfy the overall objectives, a system of computer programs has been developed (Figure 2) and is briefly described in subsequent paragraphs. The system of programs is operational and has been used to identify all of the Boeing family of commercial aircraft as well as the YC-14 and the NASA C-8A augmented wing Buffalo. The results of the parameter identification analyses have been used to verify results from previous (manual) analyses, update simulator values and to provide parameters for characteristic motion analysis when normal methods are not applicable (i.e., phugoid frequency and damping in STOL flight).

FLIGHT DATA ANALYSIS SYSTEM

Figure 2 shows the Boeing Flight data analysis system. The first step in the system operation is the preparation and evaluation of the flight test data with the REF360 program. The output data from REF360 may be interactively plotted by the PILOT program or sent directly to KASD. The KASD program evaluates the flight data for kinematic consistency and will determine biases and scale factors that should be applied to the data. The actual parameter identification takes place in either the MMLE (linearized equations) or the NLAK (nonlinear equations) programs. The results of the MMLE/NLAK analysis can then be saved and statistically combined in the CIDS program with results from other records at the same flight conditions. Additionally, the results of the MMLE/NLAK analyses can be received by the PILOT program.

SUPPORT PROGRAMS

Program REF360

Boeing flight test data is reduced on an IBM360 computer having various formats and data organization. The primary purpose of REF360 is to decode and reformat the data for the parameter identification programs. However, the program also serves as an interface between flight test and the various flight simulators in the Boeing Company. The program also statistically defines the data with respect to averages, variations, noise and signal to noise characteristics. Additional processing by differentiating five other sensors can be accomplished for inspection of time derivatives that may have importance in an airplane's dynamics but are not usually available measurements (e.g., $\dot{\alpha}$, $\dot{\beta}$).

Program PILOT

The PILOT program was developed to provide a semi-interactive method of evaluating the incoming flight test data and the results of the identification analyses. The program will provide either quick look plots or document quality plots via Calcomp and several other plotting programs. The program provides a very flexible capability for overlaying the measured sensor values over the calculated values or over the time history of the corrections developed by the recursive estimators in the KASD and NLAK (see examples, Figure 3) programs. This capability allows the analyst to see the response of the parameter corrections to variations in the state, a very significant cue in determining the parameters dependence on the state. Additionally, the time history of the recursive corrections to the parameters, along with the respective $\pm 1\sigma$ conditional standard deviations can be plotted.

Program CIDS

The CIDS program combines the results from various flight records at the same flight condition to provide a single "best estimate" for the flight condition. Due to improper excitation, process noise and other unaccountables, the parameters will be better identified in some flight records than in others. The CIDS program compensates for this by using the implied error distribution of the individual covariance matrices with a Bayesian estimation algorithm (Ref. 5) to provide a single "best estimate" for a given flight condition. The CIDS estimates of the parameters are then used in the equations of motion for simulations of the flight maneuvers and compared to the measurement data. No dynamic fit of the data is attempted. The response match must be acceptable for all the flight records before the parameter estimates are accepted. Generally very little degradation in the response match occurs. In thirty to forty percent of the cases, there is a slight improvement of the match. The CIDS program is particularly useful for those flight records which have not been designed for the Parameter Identification process in that proper state excitation had not been achieved.

The CIDS results are obtained simply by

$$S_{cids} = [S_1^{-1} + S_2^{-1} + \dots + S_n^{-1}]^{-1} \quad (1)$$

$$P_{cids} = S_{cids} [S_1^{-1} p_1 + S_2^{-1} p_2 + \dots + S_n^{-1} p_n]$$

where

$S_{cids}, S_i \ (i=1,n)$ the respective covariance matrices of the estimates

$P_{cids}, p_i \ (i=1,n)$ the respective parameter estimates from fits of different flight records.

IDENTIFICATION PROGRAMS

Program KASD

The KASD computer program is a parameter identification (PI) scheme designed to identify sensor biases and scale factors in dynamic flight test data. This program is currently used as a preprocessor of flight data before the stability and control derivatives are identified by other PI programs. The KASD results can improve both the PI and conventional techniques of analyzing dynamic flight motion data.

The KASD program can identify sensor biases and scale factors for: true airspeed, angles of attack and sideslip, the three Euler angles, and body axis angular rates and accelerations. Biases only are identified for the altimeter and linear accelerometers. All or any combination of the above parameters can be identified depending on the sensor information available in the flight record.

The KASD concept employs the classical six degree-of-freedom kinematic relations, modeled sensor errors and an estimator to produce a kinematically consistent set of sensor time histories. Sensor errors can only be determined if redundant measurements are obtained. The kinematic equations are used to transform some measured variables into a form which are directly compared with other measured variables to check for sensor consistency. In the program the measured angular rates and linear angles of attack and sideslip, airspeed, altitude and the three Euler angles are called "measurements" which are compared to the integrated "input" results. Since the angular acceleration measurements are not always available, a separate identification routine is used for these measurements. The angular rates are differentiated and compared to the measured angular accelerations for sensor error determination and if the accelerations are not available the generated accelerations can be written on the output tape.

An example of the programs procedure is as follows. The three angular rates are integrated to yield the three Euler angles which can be compared to the measured Euler angles to check for consistency. Any inconsistency between the calculated and measured sensor time histories would be due to sensor errors, assuming a perfect numerical integration. An example of a sensor bias would be for the sensor to have been zeroed incorrectly and as a scale factor error, to use the wrong conversion between the recorded units and the units output (e.g., inches of water to degrees).

Expressions for the sensor errors are incorporated into the kinematic equations as unknown parameters and then adjusted until the sensor inconsistencies are minimized. The estimator performs the adjustment of all unknown parameters simultaneously to minimize the sensor inconsistencies while being under some user constraints based on a priori information or engineering judgment. Typical of this judgment would be to set a larger than usual value for the initial tolerance of a sensor error to be identified based on the knowledge that during flight testing the instrument was not always functioning properly.

To model sensor errors for a measured variable the true value and the measured value are related by the expression:

$$\text{TRUE VALUE} = \text{SCALE FACTOR} * \text{MEASURED VALUE} + \text{BIAS}$$

In this expression a bias and scale factor error are modeled for one measurement. This expression is substituted into the kinematic equations for each measured variable of interest and the biases and scale factors are identified. Once the errors are identified they can be used to correct the flight record at each time point.

The estimator used in this program is an iterated Kalman filter with fixed interval and fixed point smoothing routines, similar to those used in Reference 7. This form of

estimator will estimate a new set of parameters at each time point, (recursive), which converges to a constant set with time.

Program MMLE

The MMLE program was received from NASA-Flight Research Center, Edwards AFB, and is capable of identifying linear stability and control derivatives for either longitudinal or lateral-directional flight maneuvers. The program has linearized equations of motion and the estimation algorithm is a modified maximum-likelihood method. A full description of the program is given in Reference 8.

The program is being used by stability and control staff personnel for simulator updating and the results have been satisfactory. A minimum of guidance has been required from the research staff.

Program NLAK

The NLAK program is specifically designed to derive values of the linear and nonlinear stability and control derivatives from flight measurements of the aircraft state and related accelerations. NLAK is formulated with 6 DOF equations of motion incorporating nonlinear aerodynamics and kinematics. The estimation process is based on a maximum likelihood algorithm and is formulated for batch (accumulative) and recursive processing.

The original base for the NLAK program was a set of 6 DOF equations of motion received from NASA-Langley Research Center (Ref. 6). The program was extensively modified with respect to the estimation algorithm and additional nonlinear parameters. NLAK can solve for 40 parameters out of a possible 156 defined elements.

The general problem addressed by the NLAK program is given; a flight time history of an aircraft's motion as seen in measurements of:

- α (angle of attack),
- β (angle of sideslip),
- V_T (true airspeed),
- P (roll rate),
- Q (pitch rate),
- R (yaw rate),
- ϕ (roll angle),
- θ (pitch angle),
- n_x (longitudinal acceleration),
- n_y (side acceleration),
- n_z (normal acceleration),
- \dot{p} (roll acceleration),
- \dot{q} (pitch acceleration),
- \dot{r} (yaw acceleration);

find the parameters (i.e., the stability and control derivatives) which will reproduce that motion when incorporated in the differential equations of motion and integrated on a computer.

The basic solution technique used by NLAK is to define a mathematical model which will represent the aircraft motion with the stability and control derivatives as parameters in the model. Then, using the aircraft's measured control input to excite the equations of motion and a set of assumed parameters, the computed model accelerations are integrated and the resultant states and accelerations are compared to their respective flight test measurements. The differences between the calculated and measured values are then related to corrections of the stability and control derivatives by a set of parameter sensitivity equations and the estimation algorithm.

Force and Moment Equations

The equations of motion utilized by the NLAK program are taken directly from Ref. 4. A summary of the equations (in body axis) is given below.

$$\begin{pmatrix} \dot{U} \\ \dot{V} \\ \dot{W} \end{pmatrix} = \frac{1}{m} \begin{pmatrix} F_x \\ F_y \\ F_z \end{pmatrix} - \begin{pmatrix} P \\ Q \\ R \end{pmatrix} \times \begin{pmatrix} U \\ V \\ W \end{pmatrix} \quad (2)$$

$$\begin{pmatrix} \dot{P} \\ \dot{Q} \\ \dot{R} \end{pmatrix} = I^{-1} \begin{pmatrix} M_x \\ M_y \\ M_z \end{pmatrix} - \begin{pmatrix} P \\ Q \\ R \end{pmatrix} \times I \begin{pmatrix} P \\ Q \\ R \end{pmatrix}$$

where: I is the inertia matrix and m the mass of the aircraft;

and F_x, F_y, F_z are the forces in the body directions x, y and z .

with M_x, M_y , and M_z , the moments about the body axes x, y and z .

F_i ($i=x+z$) is of the form

$$F_i = \bar{Q} S C_{F_i}(\alpha, \dot{\alpha}^2, \beta, \beta^2, V_T, P, Q, \dots) + f_i + g_i$$

and M_i ($i=x+z$) is of the form

$$M_i = \bar{Q} S C_{M_i}(\alpha, \dot{\alpha}^2, \beta, \beta^2, V_T, P, Q, \dots) + m_i$$

where f_i and m_i are applied external forces and torques respectively and g_i the gravity force on the airplane

The nonlinear parameters in NLAK are stability and control derivatives which are postulated as polynomials in the state. For example,

$$\text{from } C_m = C_m|_{\alpha=\alpha_R} + C_{m_\alpha}|_{\alpha=\alpha_R} \cdot [\alpha - \alpha_R] + C_{m_{\alpha^2}}|_{\alpha=\alpha_R} \cdot [\alpha - \alpha_R]^2$$

we get by differentiating with respect to α

$$C_{m_\alpha}|_{\alpha} = C_{m_\alpha}|_{\alpha=\alpha_R} + 2C_{m_{\alpha^2}}|_{\alpha=\alpha_R} \cdot [\alpha - \alpha_R]$$

where

$C_{m_\alpha}|_{\alpha}$ is the change in pitching moment with α at α .

$C_{m_\alpha}|_{\alpha_R}$ is the change in pitching moment with α evaluated at α_R . This parameter is the classic linear derivative for C_{m_α}

$C_{m_{\alpha^2}}|_{\alpha_R}$ is the change in the stability derivative C_{m_α} with α evaluated at α_R

α_R is the reference angle of attack used in the analysis.

The total list of parameters used by the NLAK program is given in Table I.

A particular feature utilized in the equations is the separation of the lateral-directional and longitudinal modes for the analysis.

The 6-DOF equations of motion can be reduced to force and moment components representing either the longitudinal or lateral-directional modes. This feature allows the analyst to concentrate on those parameters related to the predominant motion in the flight record. The motion separation feature does not preclude solutions using parameters for the full 6-DOF system equations. It is up to the user to decide the scope of the analysis.

The separation of the motion into lateral-directional or longitudinal modes is accomplished in the dynamic equations only (i.e., the modeled states). The nonlinear kinematic cross coupling is fully accounted for in the reduced equations by defining the states complementary to the mode being analyzed directly from the measurement data. For example, if a lateral-directional analysis was being performed, the "dynamic states" would be V, P, R, ϕ ; while the "kinematic states" would be U, W, Q, θ . The situation would be reversed for a longitudinal analysis. The KASD program will remove any bias or scale factor errors that may impact the solution and in fact, make all the measurement data kinematically consistent.

NLAK Estimation Algorithm

The estimation algorithm used by the NLAK program has evolved through several phases in the program's development. The first estimator incorporated was identical to that used in the MMLE program. The results were satisfactory, but the solution required six to ten iterations. To reduce the computer time and allow more analysis cues for the analyst, recursive estimation techniques were formulated and incorporated into the program. The two recursive algorithms used were the Iterated Kalman Filter defined in Ref. 7 and an estimation process based on perturbations as postulated by Kalman, et al (Ref 2) and Canon, et al (Ref. 3). The general performance of both recursive estimators was good and gave consistent answers. However, because the perturbation technique was faster, less sensitive to the input tolerances and by its method of operation gave quicker insight into modeling errors (i.e., missing parameters), the perturbation method is being used as the primary estimator in NLAK. The batch estimation process (MMLE) is still available.

The two estimation processes (i.e., the MMLE batch and recursive) used in the NLAK program have advantages and disadvantages relative to one another. Overall, the recursive formulation has given the best performance in terms of computer time used and consistency of results. Depending on the options used, the recursive estimator can calculate solutions in 1/4 to 1/2 the computer time required by the batch process. In addition, when results are compared over several flight records at the same flight conditions, the answers are more consistent for the recursive estimator. However, the recursive estimator requires an initial estimate of how well the parameter values are known before the solution is attempted (e.g., $C_{y\delta} = -.042 \pm .005$) similar to accuracies ascribed to the measurement data. If the motion is properly excited, such that the parameter effects can be separated and identified, an arbitrary assignment of tolerances at 25%-30% of the initial parameter values will give good answers and have no significant effect on the solution. For a general motion which has not been chosen for its capability to identify the stability and control derivatives (i.e., not designed for parameter identification), the initial parameter tolerances can affect the final solution--particularly for short records. To circumvent this situation, the batch MMLE algorithm is used to generate a set of parameter tolerances proportional to the flight records information content for each parameter. The batch process does not require initial parameter tolerances and in fact generates an estimate of the parameters statistics without a priori information. The parameter statistics from the batch process can then be input to subsequent runs using the recursive estimator.

The basic problem in handling the nonlinear estimation process is to develop a system linearization that is both accurate and efficient. The linearization approach taken for the perturbation estimator is to use a variant parameter technique and include second order effects in the perturbation equations. The main assumption for the estimator is that the developed perturbation equations can accurately represent a mapping of the error distribution from the parameter error space to the measurement system.

The linearization scheme in NLAK is based on the variation of a functional rather than the differential of a function. This approach is used because the identification process is parametrically based and the solution can be considered as the difference between parametric curves. Consider that the differential of a function is an approximation to the change in that function along a particular curve, while the variation of a functional is an approximation to the change curve to curve.

To orient the reader, suppose that the basic system model is given by

$$x(t_k) = \phi(t_k, t_j)x(t_j) + \int_{t_j}^{t_k} \phi(t_k, \tau)B(\tau)u(\tau)d\tau \quad (3)$$

where

$$t_k > t_j$$

$\phi(t_k, t_j)$ = the time varying transition matrix

$x(t_k), x(t_j)$ = the state at times t_k, t_j

$B(\cdot)$ = the time varying control matrix

$u(\cdot)$ = the control input

then the variation of $x(t_k)$; i.e., $\delta x(t_k)$ is given by

$$\delta x(t_k) = \delta \phi x(t_j) + \phi \delta x(t_j) + \int_{t_j}^{t_k} [\delta \phi(t_k, \tau)B + \phi(t_k, \tau)\delta B]u d\tau$$

Considering the above, the model for the variation, then by differentiating with respect to time, the differential equations of the variation are obtained. Using

$$\frac{d}{dt}[\delta x(t)] = \delta \frac{dx}{dt}$$

the differential equations for this system reduces to

$$\delta \dot{x}(t_k) = F \delta x(t_k) + \delta F x(t_k) + \delta B u \quad (4)$$

Considering second order variation (i.e., the variation of the variation) and adding subscripts to the δ quantities to identify the variation order.

$$\delta_2(\delta_1 \dot{x}) = F \delta_2(\delta_1 x) + \delta_2 F \delta_1 x + \delta_2(\delta_1 F) x + \delta_1 F \delta_2 x + \delta_2(\delta_1 B) u$$

$$\begin{aligned} \text{then } \delta_1 \dot{x} &= F[\delta_1 x + \delta_2(\delta_1 x)] + [\delta_1 F + \delta_2(\delta_1 F)] x \\ &\quad + \delta_1 F \delta_2 x + \delta_2 F \delta_1 x + [\delta_1 B + \delta_2(\delta_1 B)] u \end{aligned} \quad (5)$$

The main interest in the variational equations is their dependence on changes in the parameters (i.e., $\delta p_i, i=1, n$). Therefore,

ignoring the parametric dependence of $\delta_2(\delta_1)$ (i.e., $\frac{\partial \delta_2(\delta_1)}{\partial p_i} = 0$)

and assuming $\frac{\partial \delta_1 x}{\partial p_i} = \frac{\partial \delta_2 x}{\partial p_i}$ also that $\frac{\partial \delta_1 F}{\partial p_i} = \frac{\partial \delta_2 F}{\partial p_i}$

$$\frac{\partial \delta_1 \dot{x}}{\partial p_i} = [F + \delta_1 F + \delta_2 F] \frac{\partial \delta_1 x}{\partial p_i} + \frac{\partial \delta_1 F}{\partial p_i} [x + \delta_1 x + \delta_2 x] + \frac{\partial \delta B}{\partial p_i} u \quad (6)$$

setting

$$\frac{\partial \delta x}{\partial p_i} = P, \quad \text{and} \quad [\delta_1 F + \delta_2 F] \frac{\partial \delta x}{\partial p_i} + \frac{\partial \delta F}{\partial p_i} [x + \delta_1 x + \delta_2 x] + \frac{\partial \delta B}{\partial p_i} u = U_p$$

$$P = FP + U_p \quad (7)$$

which has the form of a dynamic system with control input.

Equation 7 can now be evaluated with respect to two concepts; the first presented by Gura and Hendrikson (Ref. 1), the second by Kalman et al (Ref. 2), and Canon et al (Ref. 3).

The first concept involves incorporating the corrections due to nonlinearities prior to minimization of the cost function. For example, suppose the scalar J was to be minimized for a single stage estimation, that is

$$J = \frac{1}{2} [z - h(y)]^T R^{-1} [z - h(y)]$$

z = measured variable
 $h(y)$ = calculated variable
 r = weighting matrix

Using standard linearization; i.e., differential corrections, $h(y)$ is assumed to be

$$h(y) = h(\bar{x}) + \frac{\partial h(\bar{x})}{\partial x} [y - \bar{x}]$$

then minimizing with respect to y gives

$$\left(\frac{\partial J}{\partial y} \right) = - \frac{\partial h(\bar{x})}{\partial x} R^{-1} [z - \bar{x} - \frac{\partial h(\bar{x})}{\partial x} [y - \bar{x}]]$$

so that

$$y = \bar{x} + \left[\left(\frac{\partial h(\bar{x})}{\partial x} \right)^T R^{-1} \cdot \left(\frac{\partial h(\bar{x})}{\partial x} \right) \right]^{-1} \cdot \left(\frac{\partial h(\bar{x})}{\partial x} \right)^T R^{-1} \cdot [z - h(\bar{x})]$$

the alternative forwarded by Reference 1 is to first perform the minimization with respect to y , so that

$$\left(\frac{\partial J}{\partial y} \right) = - \left(\frac{\partial h(y)}{\partial y} \right)^T R^{-1} [z - h(y)] = 0$$

Then assume that $(\partial(J)/\partial y)$ is a linear function of $(y-x)$ and obtain

$$y = \bar{x} + [-\frac{\partial}{\partial x} [\frac{\partial h(\bar{x})}{\partial x}]^T R^{-1} [z-h(\bar{x})]]^{-1} [\frac{\partial h(\bar{x})}{\partial x}]^T R^{-1} [z-h(\bar{x})]$$

or

$$y = \bar{x} + [[\frac{\partial h(\bar{x})}{\partial x}]^T R^{-1} [\frac{\partial h(\bar{x})}{\partial x}] - [\frac{\partial^2 h(\bar{x})}{\partial x^2}]^T R^{-1} [z-h(\bar{x})]]^{-1} \cdot [\frac{\partial h(\bar{x})}{\partial x}]^T R^{-1} [z-h(\bar{x})] \quad (8)$$

The same essential result can be obtained by assuming that $h(y)$ is a quadratic function of $(y-x)$ and minimizing that approximation.

In either case, the main idea is to correct or condition the perturbation equations as indicated by the difference between z and $h(x)$; i.e., a control on the perturbation equations. Under proper conditions, the corrected perturbation equations will represent a linear mapping or transformation between the parameter error space and the residual error space.

The second concept is that of defining an attainable set of states relative to a given class of control input. From Reference 2, the conditions for an optimal control are stated; if there is a specific (target) state to be reached which is not exclusive of the attainable states (the class of control inputs being the same), then there is an optimal control relative to the input for the attainable states.

This is interpreted in the NLAK program to mean: if there are given states attained by perturbations to the parameters, and if there is a desired state that can be reached by proper scaling of the parameter perturbations (value of the scaling factor between zero and one), then there is an optimum set of scale factors on the perturbations which will enable the desired state to be attained.

To illustrate the use of these concepts in the NLAK program, the variation of the system perturbation is written as

$$\frac{\partial \delta \dot{x}}{\partial p_i} = \bar{F} \frac{\partial \delta x}{\partial p_i} + [\delta_1 F + \delta_2 F] \frac{\partial \delta x}{\partial p_i} + \frac{\partial \delta F}{\partial p_i} [\bar{x} + \delta_1 x + \delta_2 x] \quad (9)$$

where the bar signifies present values of the system matrix and state.

If a perturbation π is incorporated into the parameters and results in a simultaneous ΔF and Δx such that

$$\Delta F = [\delta_1 F + \delta_2 F]$$

and

$$\Delta x = [\delta_1 x + \delta_2 x]$$

one can then calculate the variation of the perturbation equations as

$$\left. \frac{\partial \delta \dot{x}}{\partial p_i} \right|_{\substack{p=\bar{p} \\ \delta p=\pi}} = \bar{F} \frac{\partial \delta x}{\partial p_i} + \Delta F \frac{\partial \delta x}{\partial p_i} + \frac{\partial \delta F}{\partial p_i} [\bar{x} + \Delta x] \quad (10)$$

If an optimum set of parameters is calculated (i.e., $\hat{p} = \bar{p} + \delta \hat{p}$) and incorporated into the state vector and system matrix, one can also write

$$\left. \frac{\partial \delta \dot{x}}{\partial p_i} \right|_{\substack{p=\hat{p} \\ \pi = \pi - \delta p}} = \hat{F} \frac{\partial \delta x}{\partial p_i} + \delta_2 F \frac{\partial \delta x}{\partial p_i} + \frac{\partial \delta F}{\partial p_i} [\hat{x} + \delta_2 x] \quad (11)$$

so that

$$\left. \frac{\partial \delta \dot{x}}{\partial p_i} \right|_{\substack{p=\hat{p} \\ \pi = \pi - \delta p}} = \left. \frac{\partial \delta \dot{x}}{\partial p_i} \right|_{\substack{p=\hat{p} \\ \pi = \pi - \delta p}} \quad (12)$$

under the condition

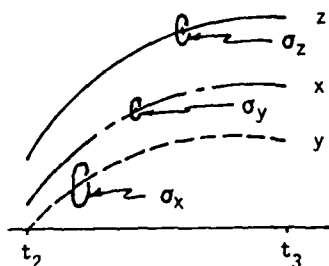
$$|\pi| > |\delta\hat{p}|$$

This equivalence allows the definition of a perturbation cone relative to the best estimate trajectory (BET); i.e., the use of \hat{p} and \hat{x} in the state equations. The BET perturbation cone in turn admits continuing optimal correction of the system in response to the observed residual error.

The basic premise in generating the perturbation equations is determining the proper conditioning for the equations. By this, it is meant to determine the proper direction; i.e., sign, and magnitude of the perturbation; i.e., an optimum perturbation, so that the optimal control is a proper subset of the perturbation input.

The problem is differentiating between the optimum perturbations and the final optimum corrections. The differentiation between perturbations and parameter corrections is accomplished in NLAK by solving the single stage optimum control problem under two different constraint conditions; i.e., the perturbation problem is solved with no constraints, while the parameter correction problem is constrained to a specified target state.

To illustrate this operation, consider the figure below



z is defined as the observation data with dispersion σ_z
(covariance R)

x is defined as the modeled state with error dispersion σ_x
(covariance S)

y is the best estimate of the state with dispersion σ_y
(covariance \hat{S})

that a best estimate state y can be determined is seen by:

$$\min \int_{t_1}^{t_2} \{ [y-x]^T S^{-1} [y-x] + [z-y]^T R^{-1} [z-y] \} dt$$

$$\frac{\partial J}{\partial y} = 2S^{-1}[y-x] - 2R^{-1}[z-y] = 0$$

so that

$$y = \hat{S}R^{-1}[z-x] \quad (13)$$

where

$$\hat{S} = [S^{-1} + R^{-1}]^{-1}$$

The next step is to add a control or correction vector π to the basic integral such that

$$\min \int_{t_1}^{t_2} \{ [y-x]^T S^{-1} [y-x] + [z-y]^T R^{-1} [z-y] + \pi^T Q^{-1} \pi \} dt$$

with respect to π . Setting ($y = x$) or ignoring the constraining statistics of x

$$\frac{\partial J}{\partial \pi} = \left(\frac{\partial [y-x]}{\partial \pi} \right)^T S^{-1} [y-x] - \left(\frac{\partial [y-x]}{\partial \pi} \right)^T R^{-1} [z-y] + Q^{-1} \pi = 0$$

for ($y-x$) = 0

$$\pi = QP^T R^{-1} [z-x] \quad ; \quad P = \frac{\partial(y-x)}{\partial \pi} = \frac{\partial \delta x}{\partial \delta p_i} = \int_0^t \dot{P} dt + P(0) \quad (14)$$

The next step is to minimize the integral

$$\min \int_{t_1}^{t_2} ([y-x]^T S^{-1} [y-x] + [y-z]^T R^{-1} [y-z] + \delta p^T Q^{-1} \delta p) dt$$

with respect to δp

subject to the constraints

$$y(t) = \phi x(t_1) + [SH^T + rL][HSH^T + R]^{-1} [z(t_1) - Hx(t_1)]$$

and

$$y(t_1) = x(t_1) + \frac{\partial \delta x(t_1)}{\partial \pi_i} \delta p_i$$

The particular form of the constraint equation is that of the 'best estimate state' given by Kalman in reference 9. This form was chosen because it incorporates the correlation between process noise and the residuals and propagates the effect from t_1 to t_2 . In general the correlation matrix L is given by

$$L(t_1) = E\{\delta w(t_1) \delta z(t_1)^T\}$$

where

δw is the system process noise

δz is the best estimate of the change in the residuals.

In the NLAK formulation, corrections to the parameters are considered process noise relative to the state estimates such that

$$\delta w(t_1) = \frac{\partial \delta \dot{x}}{\partial \delta \pi}(t_1) \delta p(t_1)$$

$$\delta z(t_1) = \frac{\partial \delta x}{\partial \delta \pi}(t_1) \delta p(t_1)$$

so that

$$L(t_1) = \frac{\partial \delta x(t_1)}{\partial \pi} E\{\delta p_i(t_1) \delta p_j(t_1)^T\} \left[\frac{\partial \delta x(t_1)}{\partial \pi}\right]^T$$

$$L(t_1) = \frac{\partial \delta \dot{x}(t_1)}{\partial \pi} Q(t_1) \left[\frac{\partial \delta x(t_1)}{\partial \pi}\right]^T$$

where

$Q(t_1)$ is the error covariance of the parameters.

Thus the correlation between the system process noise (δp) and the expected residuals (δz) implies the continuous update of the parameters during the estimation process.

This formulation is equivalent to defining y as the target set for the interval $[t_2, t_1]$ with the final result being

$$\delta p(t_1) = QP^T [PQP^T]^{-1} \hat{S} R^{-1} [z(t_1) - Hx(t_1)]$$

assuming that $\bar{S} = PQP^T$ (i.e., the uncertainty of the state space is a mapping of the parameter uncertainty).

$$\delta p(t_1) = QP^T [PQP^T + R]^{-1} [z(t_1) - Hx(t_1)] \quad (15)$$

The parameter and the state are then updated to $\hat{x} = y$ so that the perturbation required at t_2 is given by

$$\pi(t_2) = \hat{Q}P^T R^{-1}[z(t_2) - H\hat{x}(t_2)]$$

where

$$\hat{Q} = [I - QP^T[PQP^T + R]^{-1}P]Q$$

Comparing the perturbation $\pi(t_1)$ to the correction $\delta p(t_1)$, it is apparent

$$|\pi(t_1)| \geq |\delta p(t_1)|$$

Satisfying the conditions for the existence of an optimal correction.

Procedure and Results of YC-14 and C8A Analysis

To fully test and verify the nonlinear capability of the NLAK program, flight records of the YC-14 and C-8A aircraft in the STOL flight regime were obtained and analyzed. The YC-14 aircraft STOL concept is based on the Upper Surface Blowing (USB) concept while the C-8A uses the augmented wing to amplify the wing circulation for low speed flight.

In the case of the YC-14, test cases were obtained from the flight simulator and the basic YC-14 model verified—all parameters used by the NLAK program matched within 3 percent with 90% of the parameters within 1 percent of their true values.

An interesting anomaly occurred during the initial identification runs in YC-14 simulator data. When the initial identification was attempted, the results showed inconsistency between different maneuvers at the same flight conditions. The problem was traced to a time skew in the simulator data between the aerodynamic force calculation and the determination of the state variables; i.e., between the acceleration calculations and the state calculations. The difference in response to a pilot flying the simulator is imperceptible, but the identification program was notably affected. This problem is similar to commutation lags in a flight data system. When the acceleration and the states were made consistent by shifting the states relative to the acceleration by the amount of delay in the simulation data, identification consistency was achieved and satisfactory results were obtained.

When the actual flight test data was obtained, the same type of inconsistency was noted. Since the commutation lags had been corrected by the Flight Test group, an evaluation of the data conditioning was considered. The problem was traced to the YC-14 Electronic Flight Control System (EFCS). Before the acceleration and rate data is processed by the EFCS and then recorded, it is smoothed by a second order filter resulting in variable time skews and inconsistent amplitude variations between the accelerations and the states. This problem was overcome by modeling the filter in the identification programs and applying it to the programs calculated states. The residual comparison was then between two filtered states. This was a satisfactory fix in that the identification results became consistent between flight records.

The high speed YC-14 data was evaluated first with both the linear MMLE program and the NLAK program to isolate and identify any source of inconsistencies. After incorporating the second order filter into both programs, the programs gave equivalent results for the high speed motion which was characterized by low excitation and resultant linear motion.

Due to the significant nonlinearities in the STOL flight regime, only the NLAK program was able to produce consistent parameter estimates. The linear MMLE program was outside its applicable flight regime.

The YC-14 STOL flight data was characterized by large variations in the angle of attack ($20^\circ < \alpha < 120^\circ$) and large velocity excursions (90-120 knots) in conjunction with high lift coefficients ($C_L > 3$).

Significant nonlinear terms were identified for the longitudinal maneuvers. In the longitudinal maneuvers, the force and moment equations required the use of third order terms in α ; e.g., $C_x \alpha^3$, $C_z \alpha^3$, $C_m \alpha^3$. Additionally, a strong velocity dependence in the force and moment equations was identified. This dependence is postulated as caused by C_j effects on the aircraft's aerodynamics. See Table II for the parameters used and identified in matching the YC-14 flight measurements. Figure 4 is an example of the nonlinear parameters identified by NLAK for STOL flight. The parameter shown in figure 4 is a third order polynomial in α for C_m , the pitching moment coefficient. From two flight records using the same reference angle of attack but having different angle of attack excitation, two separate third order solutions for pitching moment were obtained. A "best estimate" of the polynomial was obtained by a CIDS combination of the two solutions. The CIDS best estimate is compared to the predicted C_m curve obtained from the YC-14 simulation for further evaluation.

Figures 6 and 7 show the response matches that resulted from the YC-14 analysis. Several points must be explained relative to the response match. First is that the response match is considered a necessary, but not sufficient criteria for judgment as to the quality of the identification process. For the identified parameters to be accepted as representative of the aircraft flying qualities, they must be able to reproduce the flight motion indicated by other test records. A case in point is the response match for the measurement A_x . The calculated values for A_x have only a relative resemblance to the values indicated by the measurement itself. A simple force balance along the longitudinal axis will indicate that the values calculated by the program are more representative of the actual values than the measurement. The fact there is a conflict between the program values and the measurement is reflected in the tolerances assigned to C_{x0} by the program.

In order to isolate sensor errors of this type, one has two choices. The weighting (tolerances) assigned to the measurements can be made larger or smaller or the force and moment model can be expanded or developed to force the program to ignore the erroneous measurement by the sheer preponderance of contrary information. The second alternative has produced the most favorable results (i.e., consistent answers, although less than ideal response matches for all measurements). After a satisfactory model had been developed and the results obtained, a final combination of the parameters was made by the CIDS programs. The combined parameter set was then input into the NLAK program and the verification passes were made. A CIDS verification pass solves only for the trim values of the force and moment equations (i.e., C_{x0} , C_{z0} , etc.) and the initial states values. The resulting response matches are shown in Figures 8 and 9.

C-8A Buffalo

In all, three longitudinal, and two lateral-directional records were analyzed. The lateral-directional records were characterized by relatively high excitation in all states, while the longitudinal record had large excursions for α and V_T but minimal for Q . All of the flight data was checked and made kinematically consistent by the KASD program.

The analysis was started by initializing with the models and parameters determined by the YC-14 analysis. While the initial runs showed relatively good response matches, several indicators used in the NLAK program indicated that the system model was not properly defined.

The first indicator was the time history of the recursive corrections to the parameters. After fitting the data, it was easily seen that although the conditional covariance of the parameter was converging, the actual parameter correction was not stabilizing. This indicated that unmodeled effects are impacting the estimates for that parameter. $C_{\dot{\delta}p}$ and $C_{\dot{\delta}a}$ are shown in figure 5. The first column of figure 5 (5a) shows the time history of the parameter corrections with the initial model of the rolling moment equation.

From the simulator documents, it was known that the augmentor flap position had an effect on $C_{\dot{\delta}p}$. This effect was modeled as $C_{\dot{\delta}p, \delta F_A}$, the second column (5b) shows the corrections time history with this parameter incorporated. $C_{\dot{\delta}p}$ has smoothed out considerably, but $C_{\dot{\delta}a}$ remains unstabilized. Carrying the modeling process one step further, a dependence of $C_{\dot{\delta}a}$ on C_j was postulated and incorporated into the model. The final column (5c) indicated a stabilization of both parameter estimates.

The second indicator used by NLAK is a fit quality calculation which is merely the difference of the average CHI square of the residuals during the recursive fitting process and that attained by a fit verification pass using the solved for parameters as the elements in a strict response simulation.

$$\Delta FIT = \left\{ \frac{1}{n} \sum \delta r^T R^{-1} \delta r \right\}_{verify} - \left\{ \frac{1}{n} \sum \delta r^T R^{-1} \delta r \right\}_{fit} \quad (16)$$

It is a characteristic of the NLAK program that if the initial weightings of the parameters are in error and are affecting the solution, the CHI square factor will be slightly larger for the fit verification pass than for the actual fitting process. If the tolerances are correct or do not affect the solution, then the CHI square factor for the fit verification pass will be equal or less than the factor for the estimation pass. However, if the model is incorrect or inadequate, the CHI-square factor will always be significantly greater for the verification pass than for the estimation pass.

A third cue used in the analysis is the convergence of the conditional covariance (dispersion) of the parameters. If the dispersion envelope as seen in figure 5 remain constant or almost constant it indicates one of two things--(1) there is no information available for the parameters estimate, or (2) the parameter is at its best estimate. In the case of the second alternative, this satisfies the criteria for an optimum solution.

The longitudinal analysis of the C8-A data has rather tentative results. The sensor correction program (KASD) and the nonlinear identification program (NLAK) had problems maintaining consistency between the velocity and the translational accelerometers and the alpha pitch measurements. The identified parameters shown in Table III are the result of segmenting a 105 second flight record into three overlapping 50 second segments. The parameters identified by each segment were then combined in the CIDS program and the

combined parameter set used to generate a response match over the entire flight record. Except for an obvious gust at 65-70 seconds, the source of the inconsistencies is unknown. The operation of the θ measurement is somewhat suspect with the possibility of the measurement having a threshold on Q before responding. (There is a longitudinal Stability Augmentation System on the aircraft.) Some confidence is maintained in the parameters, however, by the ability to maintain coincident response over the entire flight record. However, the possibility exists that the model is not properly defined with respect to certain transient effects. Figure 10 shows the results of the longitudinal verification pass. It should be remembered that no dynamic fit of the data was attempted for the verification run.

After developing the basic lateral-directional model to be used in the analysis (see Table IV), two lateral-directional records were analyzed. One record had a C_j of .45, the other a C_j of 1.05. Since the two records were not at the same nominal flight condition, a CIDS combination of the identified parameters was not attempted. The resulting response matches are the result of the parameter identification analysis. The parameter comparisons shown in Table 14 can only be analyzed with respect to the predicted trends. The general predicted trends are confirmed, but the actual values are not. Further analysis is required to confirm both the PI analysis values and the indicated trends. The response matches attained by the analysis are presented in figures 11 and 12.

Conclusions and Recommendations

The basic objectives of the Flight Data Analysis system were to enable the qualitative and quantitative evaluation of the models used to predict the airplane's dynamic performance through parameter identification. These objectives have been met over a large flight regime (STOL to high speed flight, including simulator identification). A first attempt to allow nonspecialists to use the programs has had success with the linear MMLE program in the determination of parameter values for the flight simulators. Still to be determined is the quality of the results using the nonlinear program NLAK in the hands-on mode of operation. Training for orientation in the use of the Flight Data Analysis system has been scheduled for personnel in the Flight Controls group.

Further investigation into the sensor documentation should be undertaken to resolve problems with the sensor data conditioning, sensor dynamic response and sensor alignments.

Particularly valuable in the development of the Boeing Flight Data Analysis system was the feedback from the Stability and Control design groups. Their demand for consistent and understandable analysis was a "real world" constraint on the operational characteristics of the program. Without the confidence of these groups, Parameter Identification will not be accepted as an alternative method of flight data analysis.

To develop this confidence, the programs must be released to and used by the design groups and their comments regarding the program's utility must be considered in the further development of Parameter Identification.

References

1. Gura, I.A. and Henrikson, I.J., "A Unified Approach to Nonlinear Estimation," The Journal of Astronautical Science, Vol.XVI, No.2, Mar-Apr, 1968
2. Kalman, R.E., Falb, P.L. and Arbib, M.A., Topics in Mathematical System Theory, McGraw-Hill, Inc., 1969
3. Canon, M.D., Cullum, C.D., Polak, E. Theory of Optimal Control and Mathematical Programming, McGraw-Hill, Inc., 1970
4. Etkin, Bernard, Dynamics of Flight, John Wiley and Sons, Inc., 1970
5. Morrison, Norman, Introduction to Sequential Smoothing and Prediction, McGraw-Hill, Inc., 1969
6. Ramachandran, S. and Well, W.R., "Estimation of Nonlinear Aerodynamic Derivatives of Variable Geometry Fighter Aircraft from Flight Data," AADA paper No. 74-790, AIAA Mechanics and Control of Flight Conference, August 1974
7. Chen, R.T.N., Eulrich, B.J., Lebacqz, J.V., "Development of Advanced Techniques for the Identification of V/STOL Aircraft Stability and Control Derivatives," Cal Report No. BM-2820-F-1, August 1971
8. Iliff, K.W. and Taylor, L.W., Jr., "Determination of Stability Derivatives from Flight Data Using a Newton-Rapson Minimization Technique," NASA TN D-6579, NASA Flight Research Center, Edwards, California, 1972.
9. Kalman, R.E., "New Methods in Wiener Filtering Theory," Predictions of the First Symposium on Engineering Applications of Random Function Theory and Probability." J.L. Bogdanoff, F. Kozin, Editors, John Wiley & Sons, Inc., 1963.

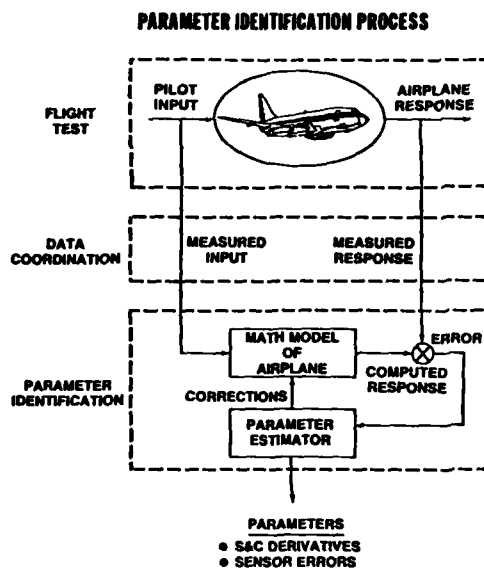


Figure 1

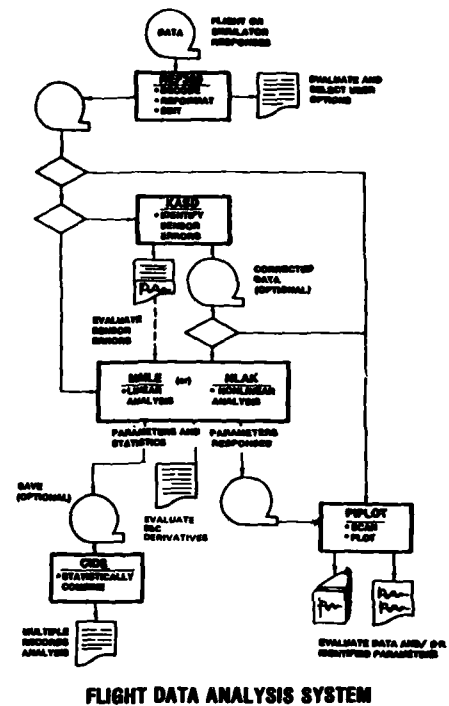


Figure 2

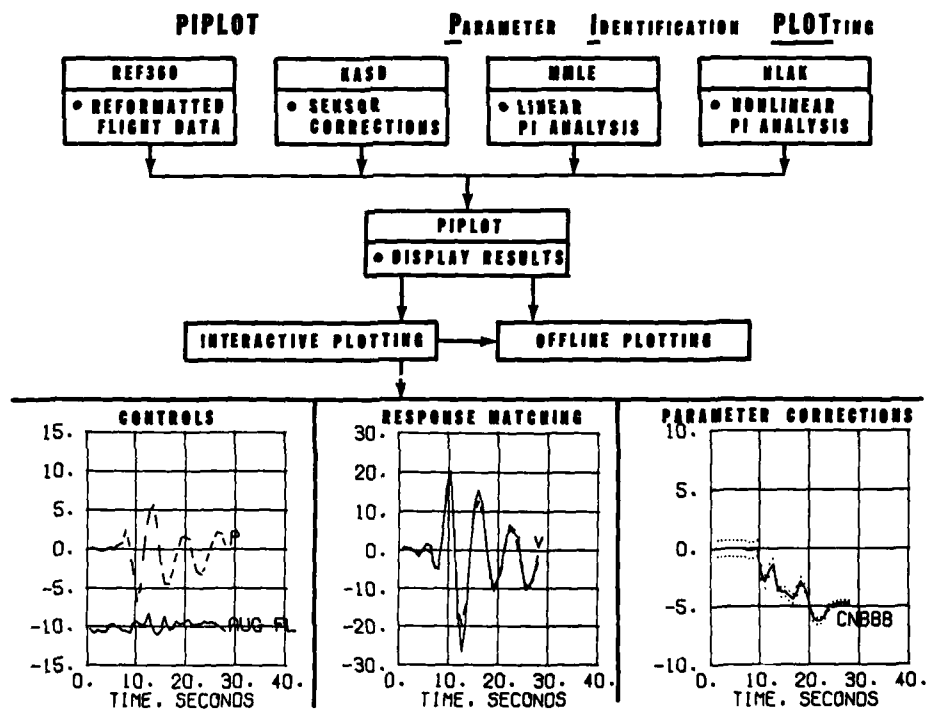
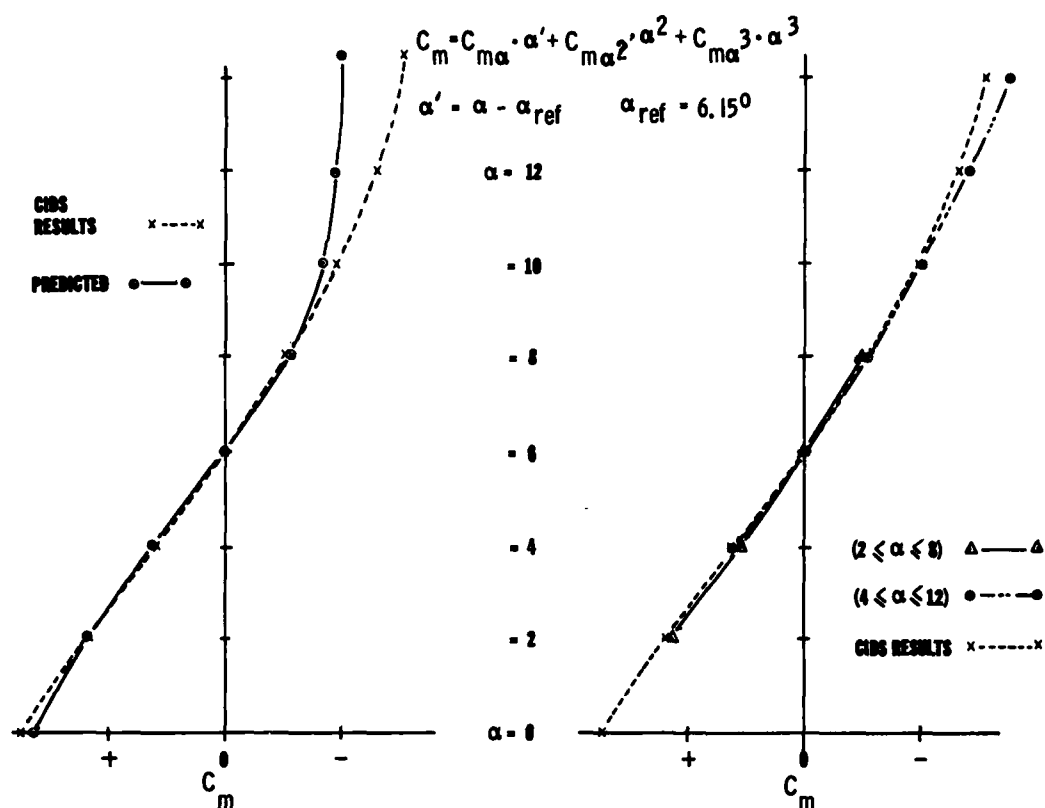


Figure 3



IDENTIFICATION OF THE YC-14 NONLINEAR PITCHING MOMENT (LOW SPEED, FLAPS 60° , $C_{Df} = 1$, $C_{Df} = .25$)

Figure 4

C-8A MODEL DEVELOPMENT

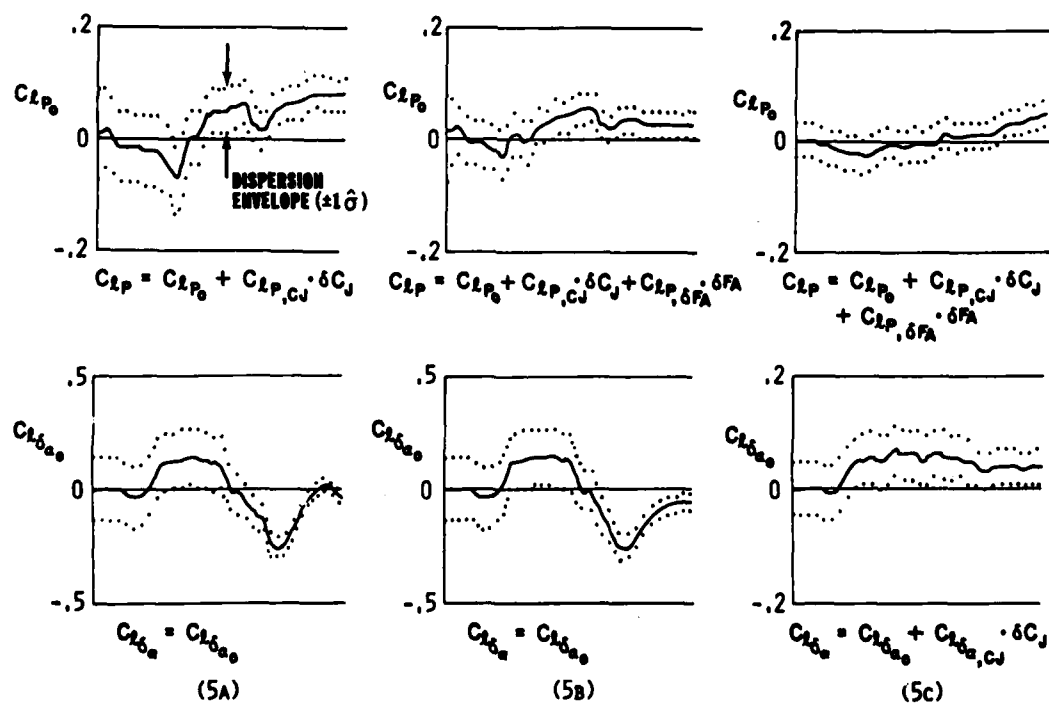


Figure 5

FIT OF RECORD 1 VC-14

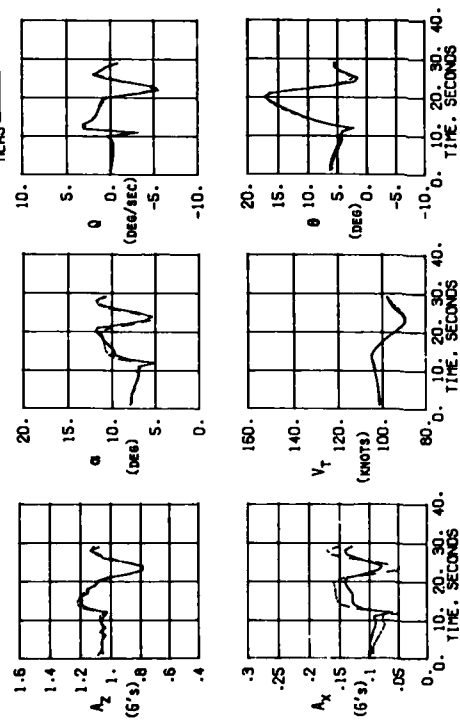


Figure 6

CIDS VERIFICATION RECORD 1 VC-14

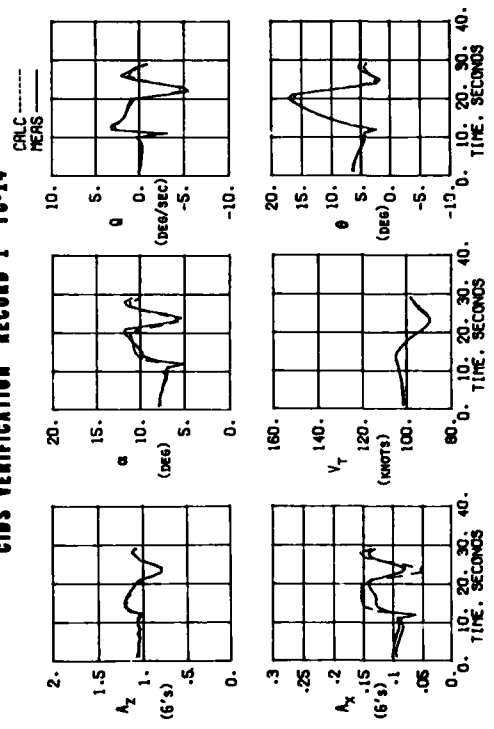


Figure 8

FIT OF RECORD 2 VC-14

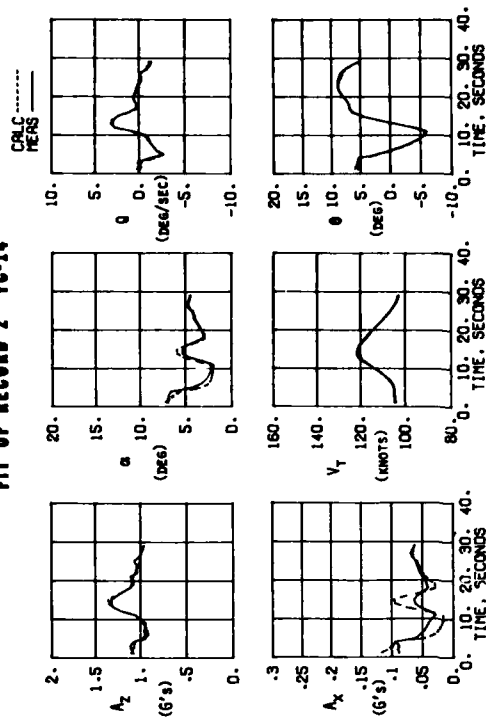


Figure 7

CIDS VERIFICATION RECORD 2 VC-14

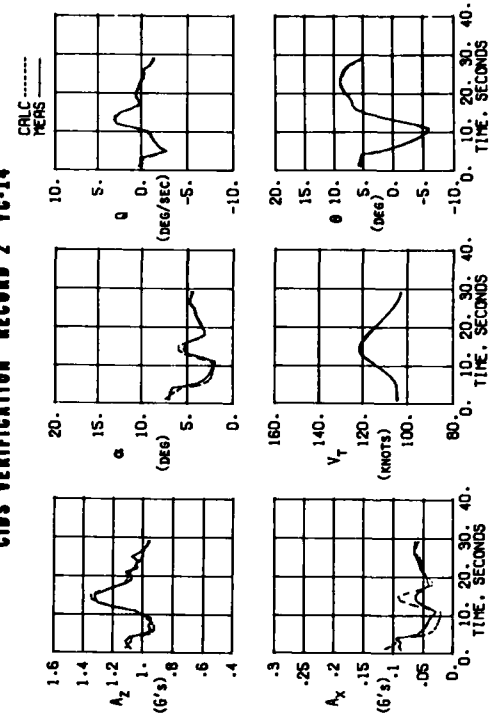


Figure 9

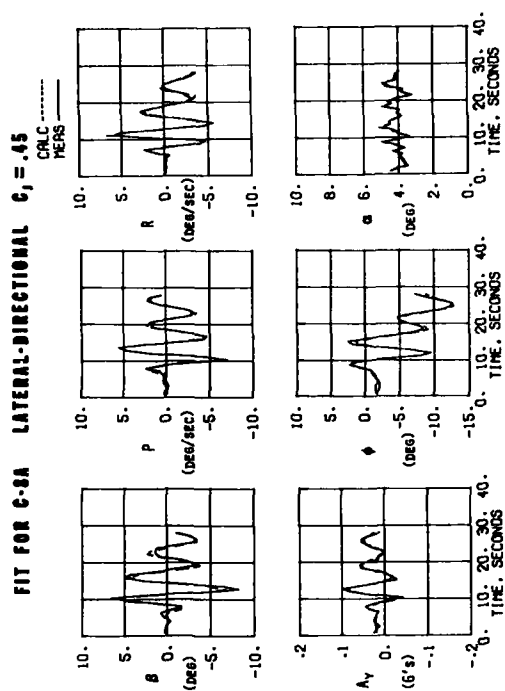


Figure 11

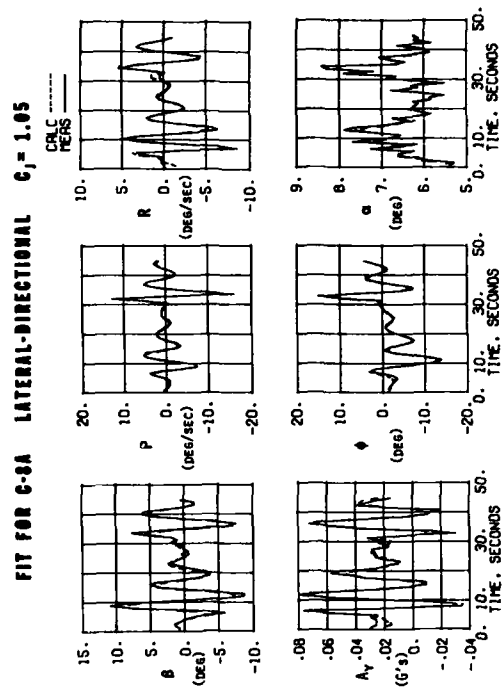


Figure 12

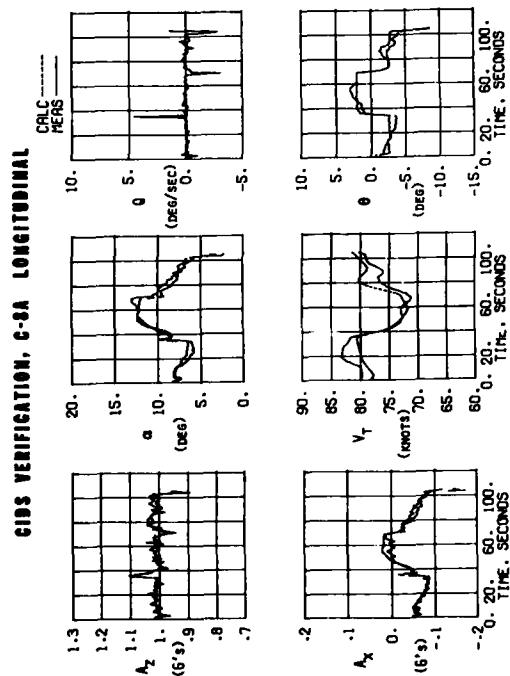


Figure 10

TABLE II

VC-14 LONGITUDINAL IDENTIFICATION

BODY AXIS CG @ .25C $\alpha_R = 6.0^\circ$ $C_j = 1$ $\delta_{F,USB} = 60^\circ$

PARAMETER	PREDICTED	RECORD 1	RECORD 2	COMBINED ESTIMATE	95% TOLERANCE
C _x	0.544	0.481	0.482	0.496	1 %
C _{xa}	2.369	1.276	0.038	0.280	23 %
C _{xa} ²	-	-11.430	-2.727	-4.086	21 %
C _{xa} ³	-	3.399	3.425	3.424	12 %
C _{xq} ⁺	0.335	0.497	0.347	0.359	16 %
C _{xcj}	-	0.571	0.600	-	-
C _{xcja}	-	-0.020	-0.020	-0.020	16 %
C _{xge}	-0.025	-	-	-	-
C _z	-3.261	-3.198	-3.189	-3.187	1 %
C _{za}	-7.961	-8.246	-8.630	-8.524	2 %
C _{za} ²	-	-1.149	-1.156	-1.144	13 %
C _{za} ³	-	-19.067	-20.283	19.909	12 %
C _{zq} ⁺	-3.191	-7.940	-7.559	-7.653	16 %
C _{zcj}	-	-0.297	-0.437	-0.381	-
C _{zcja}	-	-5.442	-2.599	-	-
C _{zge}	-1.544	-0.809	-0.925	-0.893	11 %
C _m	-0.103	-0.018	0.001	-0.005	1 %
C _{ma}	-1.829	-1.771	-1.543	-1.543	7 %
C _{ma} ²	-	2.227	1.672	1.867	6 %
C _{ma} ³	-	1.979	-0.904	3.937	48 %
C _{mq} ⁺	-92.591	-81.906	-73.520	-75.522	2 %
C _{mcj}	-	-0.168	-0.313	-0.272	5 %
C _{mcja}	-	-1.933	1.297	-	-
C _{mge}	-7.143	-5.255	-5.057	-5.140	1 %

TABLE III

C-3A LONGITUDINAL IDENTIFICATION

BODY AXIS CG @ .34C $\alpha_{REF} = 6^\circ$ $C_j = 0.6$ $\delta_{F,AUG} = 65^\circ$

PARAMETER	PREDICTED	SEGMENT 1	SEGMENT 2	SEGMENT 3	COMBINED ESTIMATE	95 % TOLERANCE
C _x	-0.016	-0.105	-0.183	-0.137	-0.130	2 %
C _{xa}	1.522	1.115	1.152	0.739	1.012	7 %
C _{xa} ²	-	-5.114	-3.752	-7.756	-4.801	23 %
C _{xa} ³	-	-14.087	-9.892	-9.533	-10.904	70 %
C _{xq} ⁺	-	3.161	2.761	41.000	9.067	50 %
C _{xcj}	-	-0.290	-0.421	-0.264	-0.326	23 %
C _{xge}	0.060	0.319	0.137	0.393	-	39 %
C _{xgl}	-	0.002	-0.071	0.003	-0.050	150 %
C _z	-3.772	-2.617	-2.663	-2.792	-2.681	1 %
C _{za}	-6.013	-4.852	-5.325	-5.461	-5.186	3 %
C _{za} ²	-	-13.951	-11.750	-3.320	-11.172	18 %
C _{za} ³	-	-6.150	0.248	-5.649	-5.279	200 %
C _{zq} ⁺	-	-106.145	-103.665	-123.258	-108.657	10 %
C _{zcj}	-	-0.163	-0.505	-0.324	-0.320	47 %
C _{zge}	-0.570	-0.592	-0.648	-0.426	-0.550	21 %
C _{zgl}	-	-1.155	-0.597	-0.436	-0.880	15 %
C _m	0.000	0.003	0.011	0.008	0.007	1 %
C _{ma}	-1.143	-1.157	-1.113	-0.941	-1.099	3 %
C _{ma} ²	-	7.981	8.499	4.023	7.207	6 %
C _{ma} ³	-	-34.187	-34.089	-12.265	-25.391	13 %
C _{mq} ⁺	-26.180	-19.334	-18.725	-21.459	-20.182	15 %
C _{mcj}	-	-0.051	-0.062	0.021	-0.034	43 %
C _{mge}	-	-1.848	-1.842	-1.801	-	2 %
C _{mgl}	-	0.105	0.011	0.063	0.047	18 %

TABLE IV

C-8A LATERAL-DIRECTIONAL IDENTIFICATION

BODY AXIS CG @ .32c $\alpha_{REF} = 4^\circ$ $\delta_{F AUG} = 65^\circ$

PARAMETER	$C_j = .45$		$C_j = 1.05$	
	PREDICTED	RECORD 1	PREDICTED	RECORD 2
$C_{y\beta}$	-1.261	-0.994	-1.301	-1.003
$C_{y\beta^3}$	-	-3.154	-	2.442
$C_{y\dot{\beta}}$	-	-0.699	-	-0.448
$C_{y\delta r}$	0.768	0.390	0.768	0.308
$C_{L\beta}$	0.000	-0.203	-0.022	-0.234
$C_{L\beta^3}$	-	-1.597	-	-4.113
$C_{L\beta a}$	-	-2.834	-	0.455
$C_{L\dot{\beta}}$	-0.501	-0.592	-0.644	-1.218
$C_{L\dot{R}}$	0.232	0.412	0.306	0.495
$C_{L\dot{\beta} a}$	-	-16.187	-	8.630
$C_{L\dot{R} a}$	-	-14.719	-	-1.600
$C_{L\delta r}$	0.049	0.041	0.049	0.053
$C_{L\delta a}$	-	0.366	-	0.196
$C_{L\delta a a}$	-	3.920	-	4.378
$C_{L\delta a C_j}$	-	-	-	-
$C_{L\beta \delta l}$	-	0.005	-	0.007
$C_{L\dot{\beta} \delta l}$	-	-0.022	-	0.024
$C_{L\dot{R} \delta l}$	-	-0.006	-	0.005
$C_{n\beta}$	0.241	0.167	0.211	0.147
$C_{n\beta^3}$	-	4.998	-	-2.116
$C_{n\beta a}$	-	-0.571	-	0.376
$C_{n\dot{\beta}}$	-0.131	-0.336	-0.194	-0.584
$C_{n\dot{R}}$	-0.083	-0.455	0.032	-0.287
$C_{n\dot{\beta} a}$	-	-1.475	-	-0.662
$C_{n\dot{R} a}$	-	-46.021	-	-6.408
$C_{n\delta r}$	-0.461	-0.231	-0.461	-0.298
$C_{n\beta \delta l}$	-	-0.006	-	0.027
$C_{n\dot{\beta} \delta l}$	-	0.102	-	0.095
$C_{n\dot{R} \delta l}$	-	0.034	-	-0.021
$C_{n\delta a}$	-	-	-	0.047

A SURVEY OF ANALYTICAL AND EXPERIMENTAL TECHNIQUES TO PREDICT AIRCRAFT DYNAMIC CHARACTERISTICS AT HIGH ANGLES OF ATTACK

by

A. M. Skow, Manager, Aerosciences Research Department
Northrop Corporation, Aircraft Division
3901 West Broadway, Hawthorne, California 90250

A. Titiriga, Jr., Manager, F-5 Aerosciences and Propulsion Analysis Department
Northrop Corporation, Aircraft Division
3901 West Broadway, Hawthorne, California 90250

CONTENTS

1.0	Introduction	1	4.0	Analytical/Experimental/Flight Test	
2.0	Experimental Techniques	3		Correlation	26
2.1	Wind Tunnel Tests	3	4.1	Experimental Studies	26
2.2	Water Tunnel Tests	9	4.2	Analytical Prediction	27
2.3	Tethered Model Tests	10	4.3	Flight Tests	32
2.4	Vertical Tunnel Tests	12	4.4	Analytical Flight Test Comparison	34
2.5	Remotely Piloted Drop Model Technique	12	5.0	Synopsis	34
2.6	Manned Simulation	13	5.1	Stall/Post-Stall Prediction	34
2.7	Full Scale Flight Tests	13	5.2	Departure/Spin-Entry	35
3.0	Analytical Techniques	13	5.3	Oscillatory and Steady Spin	35
3.1	Approach to Stall/Post-Stall	13	5.4	Spin Recovery	36
3.2	Departure/Spin Entry	17	5.5	Conclusion	36
3.3	Oscillatory and Steady Spin	21		References	36
3.4	Spin Recovery	24			

SUMMARY

Fighter aircraft are required to have excellent maneuverability to succeed in most air combat scenarios. Angle of attack, airspeed, roll rate and/or pitch rate limiters incorporated to prevent the pilot from placing the aircraft in a region of poor lateral-directional stability may also limit the aircraft's capability to accomplish its basic mission. It is possible, however, to combine an airframe which has good post-stall aerodynamics and a sophisticated control system in such a way as to enhance the total system performance capability. In order to ensure that an airframe design will have these good aerodynamics, experimental test techniques and analytical prediction methodologies must provide reliable information early in the preliminary design phase. This paper presents a survey of some of the techniques that will aid the fighter aircraft designer in building good high angle-of-attack aerodynamic characteristics into the airframe.

1.0 INTRODUCTION

Many papers have been written on the subject of predicting high angle-of-attack characteristics of aircraft. They have dealt with analytical as well as experimental techniques. This paper will summarize some of the more well known analytical and experimental methods and endeavor to highlight the contributions each method provides.

Much has been said about the poor correlation which has been obtained over the years between flight test and analytical stall departure and spin-entry predictions for a variety of aircraft. The cause of some of the poor correlation has been attributed to inherent limitations of conventional static aerodynamics and a lack of fundamental understanding of the aerodynamic phenomena which are present. While the latter is certainly true, a large percentage of the poor results obtained in high angle-of-attack analysis can in many cases be attributed to poorly measured static aerodynamic data rather than any limitation imposed on a simulation because of a lack of dynamic derivatives. It is also true that extrapolation from one configuration to another in the angle-of-attack region where vortex interaction and separated flows predominate has led to poor prediction of stall characteristics. Also, many digital stimulation programs in the past have had a limited capacity to store data as a nonlinear function of angle of attack and sideslip. Linearization of these data sometimes obscured the problem and again poor correlation was obtained.

Aerodynamic hysteresis, Reynolds number, rotary derivatives, unsteady aerodynamics and other effects are certainly important and in some cases are not totally understood. However, fundamental procedures such as expanding the storage capabilities of 6 degree of freedom analysis programs, improving static wind tunnel test techniques, taking more data and providing adequate stability criteria which take coupling between the longitudinal and lateral degrees of freedom into account can greatly increase our ability to confidently predict the high angle-of-attack behavior of an aircraft early in a development program.

What are the limiting factors on maneuverability that make predictions of stall/departure characteristics of fighter aircraft important? Figure 1-1 shows a typical lift curve. Buffet onset is not usually a limiting factor but may be a warning in some cases of impending difficulties. Buffet intensity is a potential limiting parameter. Wing rock onset is certainly a limit on tracking accuracy but not necessarily a limit on usable lift. Some aircraft have wing rock which diverges initially and then becomes bounded at a moderate oscillation amplitude. This provides information to the pilot that he is approaching or exceeding maximum wing lift which he may want to do in a defensive role to force an attacker to overshoot. If the oscillation amplitude is not extremely large and if no departure from controlled flight is imminent, he will not hesitate to pull into fairly heavy wing rock. However, if wing rock is merely the first step in a sequence of events leading to a departure, then the first onset of wing rock is a limit. Roll reversal implies the aircraft has to unload to roll so that the usable lift in the airframe is limited. Directional divergence is another limit because if the angle of attack for divergence is exceeded, nose slice or departure and possible spin entry will result.

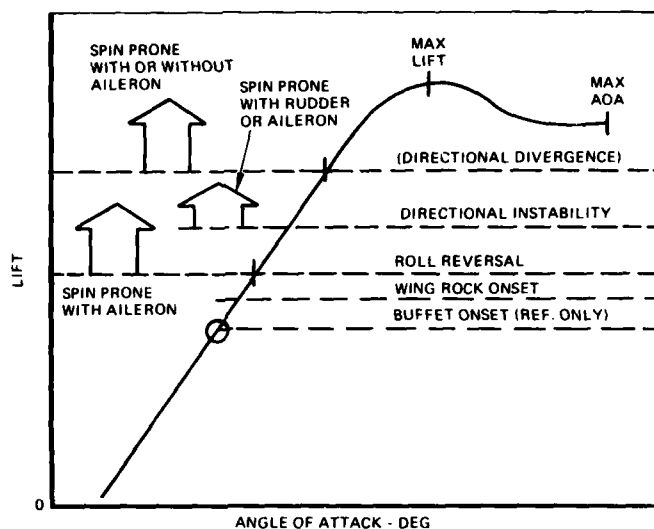


FIGURE 1-1. USABLE LIFT

Automatic control systems can be designed to improve departure resistance and such systems may also allow higher usable lift to be obtained. Roll/yaw interconnects can prevent the build-up of adverse sideslip during a rolling maneuver, thereby allowing higher roll rates to be obtained. Aircraft with poor aerodynamic stability characteristics require the control system to provide the needed levels of stability, both longitudinal and lateral-directional, to prevent loss of control. If these control system requirements become too restrictive, they may lead to angle-of-attack, airspeed, load factor and/or roll rate limits all of which reduce the potential maneuver performance which an airframe with good aerodynamics might otherwise achieve. Figure 1-2 shows how the maximum maneuver boundary can be affected due to a control system which limits the aircraft to prevent departure. The significant reduction in the maneuver boundary indicates that it is clearly more desirable to have an airframe which contributes a high level of resistance to loss of control which might be enhanced by a sophisticated control system, than to have a control system attempt to compensate for poor lateral-directional aerodynamic characteristics thus limiting the maximum maneuver capability of the aircraft.

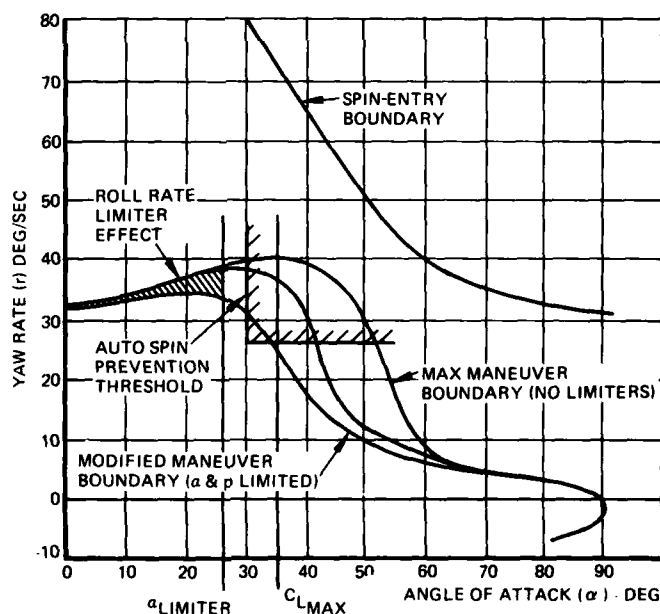


FIGURE 1-2. EFFECTS OF ANGLE OF ATTACK AND LIMITERS ON MANEUVER CAPABILITY

The departure prediction techniques which are appropriate and the level of accuracy required from them generally vary with time and depend on what stage the aircraft is in the design phase. Major configuration decisions must often be made early in preliminary design stages when only a limited amount of data is available. Complicated prediction techniques involving vast data arrays are useless at this time because the required data are not yet available. Consistent simple prediction techniques are important in the early design phase to establish the configuration and make trade studies between performance and departure resistance. Later in the development cycle, increased accuracy is required to avoid costly configuration changes and reduce risk during flight test. If the program is large, further refinements in the aero/math model are required to be able to accurately estimate the effects of future design changes.

This paper will present a synopsis of the current prediction techniques and discuss their relation to various stages of the design phase. It will also attempt to show which methodologies are most accurate or appropriate when parameters such as time and cost effectiveness are considered.

2.0 EXPERIMENTAL TECHNIQUES

Significant advances have been made in recent years in the state-of-the-art of theoretical, computational aerodynamics. In spite of these advances, rational, purely theoretical tools based on first principles which can be used with confidence to analyze the high angle-of-attack characteristics of aircraft have not yet been developed and are not likely to be developed in the foreseeable future. The best analytical techniques and methodologies currently in use which deal with the high angle-of-attack area of the flight envelope rely almost completely on experimentally measured response characteristics and aerodynamic forces and moments. Hence, the discussion of the experimental test techniques which should be used to acquire these data becomes extremely important.

Much has been said over the years about the aerodynamicists' capability to adequately represent the post-stall behavior of an aircraft. In all fairness to our fellow aerodynamicists, however, the problem which we face is extremely formidable. The aerodynamic phenomena present are highly complex, nonlinear, not too well understood and, in some cases, impossible to functionally quantify. A great volume of data which demonstrates poor correlation with flight test results has been generated. In general, the correlations have been acceptable only when the simulation is performed after the fact. When we know the answer, the solution to the problem becomes a great deal easier to find.

In the pursuit of accurate prediction of the high angle-of-attack characteristics of an aircraft, the aerodynamicist has many tools potentially available to him. These tools include: static, forced oscillation, rotary balance, curved or rotating flow wind tunnel tests, water tunnel tests for flow visualization, tethered model tests, vertical spin tunnel tests, drop model tests and manned simulation. Each of these tools can provide an increment to the level of accuracy which can be achieved. It would, of course, be unreasonable to expect that all of these tools could be utilized during the development of a new aircraft. The realities of the aircraft design process force us to "take our best shot" early in the design phase when there has not been sufficient time (or funds) to thoroughly wring out a configuration. It is with these realities in mind that this paper has been written.

2.1 Wind Tunnel Tests

The wind tunnel is, of course, the primary experimental tool used to predict the high angle-of-attack characteristics of aircraft. Several different test techniques are used to isolate the various components of the equations of motion which may be functions of position angles, rotational rates or oscillation frequency or amplitude. There is, however, no way at present that an aerodynamicist can isolate, experimentally, all the required parameters. The effects of aerodynamic hysteresis have been measured and can be important near the stall angle of attack; the effect of Reynolds number can be extremely important; the inability to separate the β and rate derivatives obtained from forced oscillation tests has restricted our ability to mathematically model the aircraft dynamics correctly, and the effect of unsteady aerodynamics at high angles of attack is automatically filtered by the wind tunnel data acquisition system before the data is used to formulate an aerodynamic model. In spite of the many gaps in experimental capability, small-scale wind tunnel data, measured accurately over adequate angle-of-attack and sideslip ranges in sufficiently small incremental steps, can be used to estimate with reasonable confidence the stall/departure/spin characteristics of fighter aircraft.

2.1.1 Static Wind Tunnel Tests

Initial prediction of the high angle-of-attack characteristics of an aircraft configuration are made from static wind tunnel data. Prediction parameters such as $C_{n\beta}$ DYN and Lateral Control Departure Parameter (LCDP) can be used with a high level of confidence if care is taken when measuring the data from which these parameters are calculated. As shown in Figure 2-1, data taken at angle-of-attack increments of 5 degrees can produce deceptive answers. Also, the sideslip angles which are used to determine lateral-directional stability must be carefully chosen.

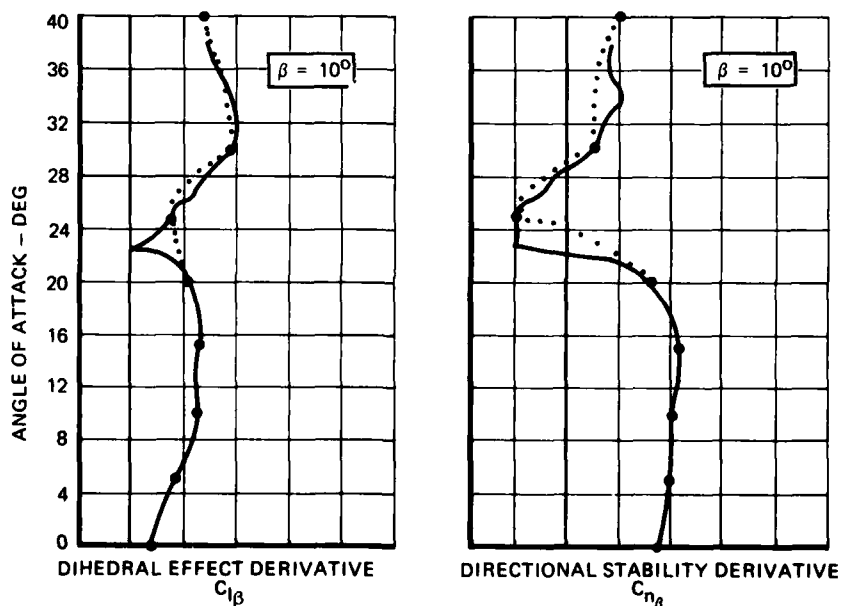


FIGURE 2-1. EFFECT OF ANGLE OF ATTACK INCREMENTS

Figure 2-2 presents a typical variation of lateral-directional coefficients as a function of sideslip for a fixed post-stall angle of attack. As evidenced, there is a large degree of nonlinearity at large sideslip angles and a high degree of hysteresis at smaller sideslip angles. In order to accurately measure these aerodynamic nonlinearities, especially in angle-of-attack and sideslip regimes where vortex decay or breakdown is occurring, it is advisable to measure data in increments as shown in Figure 2-3.

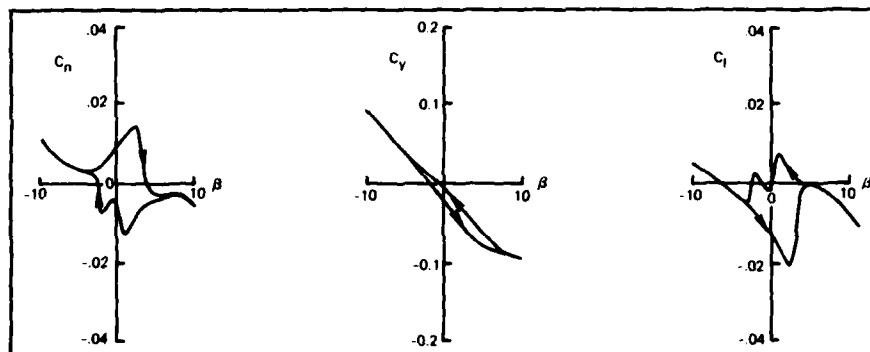


FIGURE 2-2. AERODYNAMIC HYSTERESIS IN A REGION OF VORTEX BREAKDOWN

α RANGE	$\Delta\alpha$	CONSTANT β
$ \alpha < 20^\circ$	1.0°	$0, \pm 2, \pm 5, \pm 10, \pm 15, 30$
$20^\circ < \alpha < 35^\circ$	0.5°	$0, \pm 2, \pm 5, \pm 10, \pm 15, 30$
$35^\circ < \alpha < 60^\circ$	2.0	$0, \pm 2, \pm 5, \pm 10, \pm 15, 30$
$60^\circ < \alpha < 90^\circ$	5.0°	$0, \pm 2, \pm 5, \pm 10, \pm 15, 30$

FIGURE 2-3. TEST ANGLE RANGES

2.1.2 Rotary Balance Tests

An experimental tool which has been used to uncover much valuable information about the characteristics of aircraft in a steady, smooth spin is the rotary-balance test technique. This technique is used to gather six-component force data on aircraft scale models at a constant value of angle of attack of from 45° to 90° for a range of non-dimensional spin rate ($Qb/2V$) of ± 0.30 .

The spin has for many years been recognized as a maneuver with no tactical utility. As the requirement to spin aircraft in training was declared nonexistent, the emphasis in fighter design in the past 20 years or so has moved away from a thorough analysis of the developed spin characteristics and more toward the near post-stall region where departure prevention is the key objective. In this period, the use of the rotary balance rig to test fighter configurations has slackened.

In the near future, it is not likely that this emphasis will change, because of the ever increasing tendency in the industry to rely on sophisticated control systems to "automatically" prevent the pilot from placing his aircraft in a region of the flight envelope where departure is possible. In spite of this current emphasis, more research is required to determine the influence of such variables as forebody cross-sectional shape and fineness ratio, after body shape and empennage and wing geometry on the aerodynamic forces and moments present in a steady spin. Based on these studies recovery capability from unintentional spins could probably be improved. This research should be carried out on rotary test rigs, and in spite of the specific results being, perhaps, configuration dependent, overall, the research could be used to develop design guidelines which would aid designers in choosing departure and spin resistant configurations. Rotary-balance testing is almost certainly out of the question during the preliminary design phase of aircraft development. Rotary data on a final configuration can, however, when combined with forced oscillation data, provide a more accurate simulation of the expected developed spin rates, modes and recovery characteristics of an aircraft.

2.1.3 Forced Oscillation Tests

As stated in paragraph 2.1.1, static wind tunnel data can be used with some degree of confidence to predict the behavior of an aircraft at high angles of attack. Prediction of certain types of maneuvers which contain highly oscillatory aircraft motions (such as large amplitude wing rock), has, however, been poor in the past when the aerodynamic model lacked accurately measured damping derivatives. Here again, the best match between simulated response data and experiment has come after the fact when the aerodynamic model has been altered (in a reasonable way) to force a match. Such studies as shown in Figure 2-4 have shown the acute sensitivity predicted high angle-of-attack response characteristics can have to small changes to damping derivatives. In the case shown, only roll damping was changed in the stall region.

Figure 2-5 illustrates an example of an attempt to develop a configuration modification in the wind tunnel which would have a large beneficial effect on wing rock characteristics. Static, lateral-directional stability data are shown

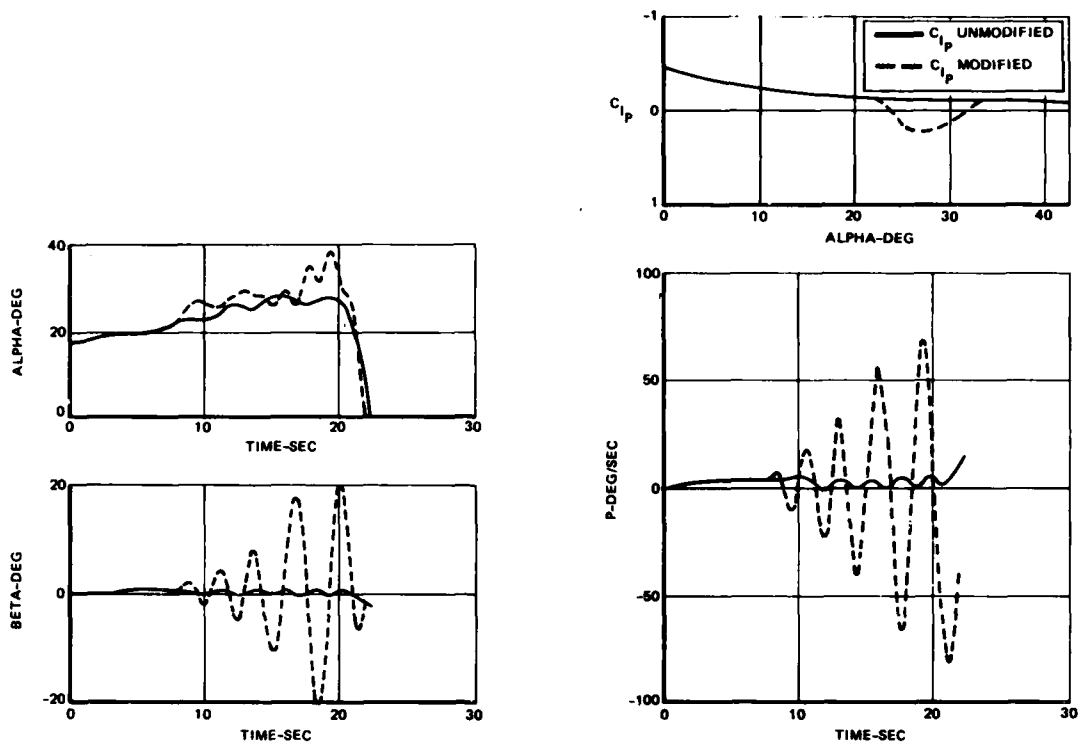


FIGURE 2-4. EFFECT OF ROLL DAMPING ON PREDICTED STALL CHARACTERISTICS

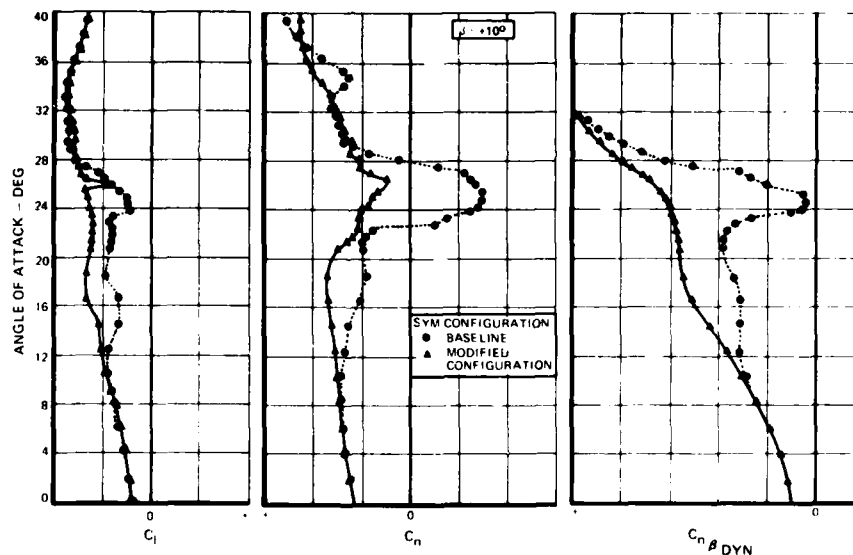


FIGURE 2-5. STABILITY CHARACTERISTICS

for the initial configuration exhibiting a local loss of dihedral effect and a local directional instability in the stall angle-of-attack region. The minimum value of $C_n \beta_{DYN}$ in the stall approaches zero, indicating that wing rock oscillations would be expected in flight. This was indeed the case as the aircraft exhibited a bounded wing rock behavior. The wind tunnel data for the modified configuration showed a significant improvement in lateral-directional stability values in the stall region, indicating the configuration should have a stall behavior with little or no roll oscillations. Such was not the case in flight, however, and the apparent cause of this lack of correlation is thought to be due to the fact that neither configuration exhibited damping-in-roll in the stall region. The example is presented merely to illustrate how futile predicting changes in oscillatory high angle-of-attack characteristics due to a configuration modification can sometimes be when the experimental tools are limited to static wind tunnel data.

The primary airframe contributor to both static lateral stability ($C_{l\beta}$) as well as dynamic roll damping (C_{lp}) is the wing. Certain wing selection and planform geometries can result in significantly different airframe roll damping characteristics. Figure 2.6 illustrates three possible variations of C_{lp} with angle of attack and the expected stall and wing rock behavior associated with each.

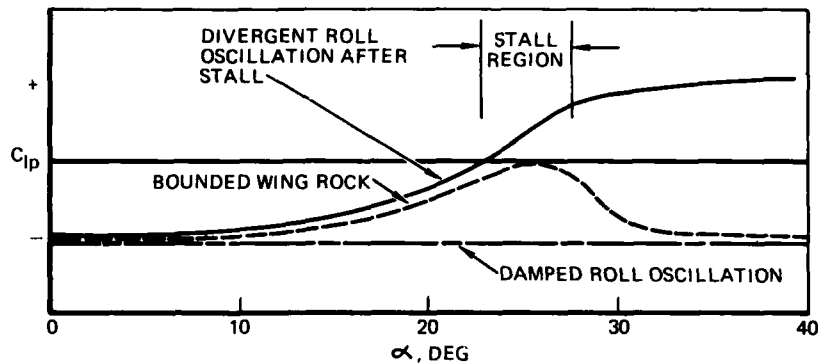


FIGURE 2-6. EFFECT OF ROLL DAMPING FOR THREE CONFIGURATIONS

A significant variation of roll damping with oscillation amplitude has been measured for some configurations. This effect is illustrated in Figure 2-7 and could result in an initial divergence in roll oscillation until a threshold amplitude is attained followed by neutrally damped, bounded oscillations. It is obvious from these data that accurate prediction of the oscillatory stall characteristics of an aircraft requires equally accurate damping derivative data. Such data may be determined from forced oscillation tests or curved or rotating flow wind tunnel tests.

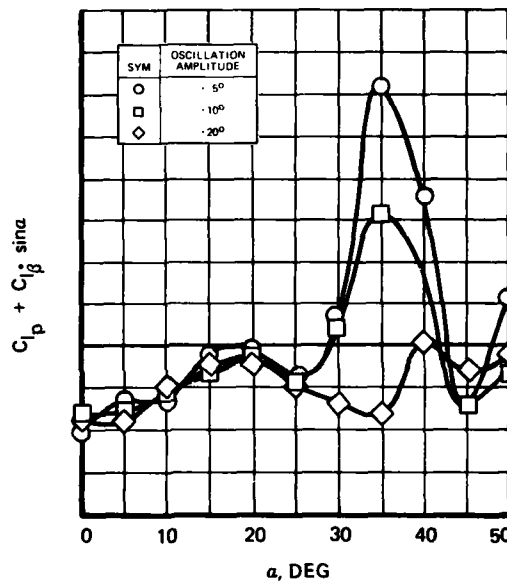


FIGURE 2-7. EFFECT OF OSCILLATION AMPLITUDE

Empirical guidelines should be developed to relate wing section and planform geometry parameters to expected stall characteristics as a guide to the designer.

2.1.4 Curved or Rotating Flow Wind Tunnel Tests

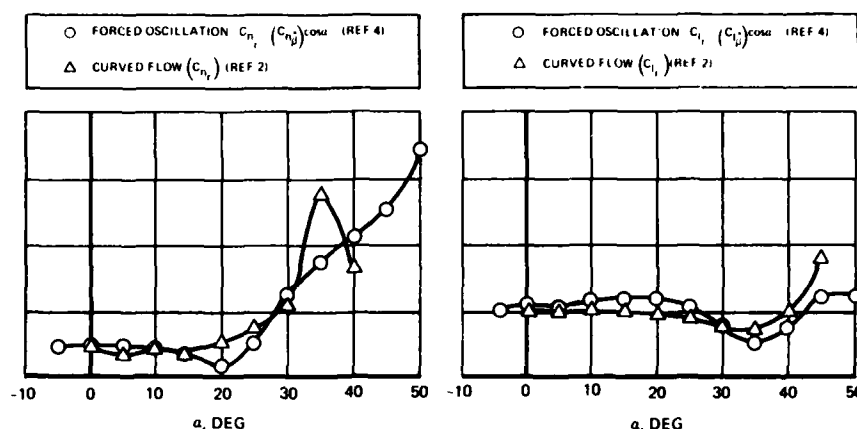
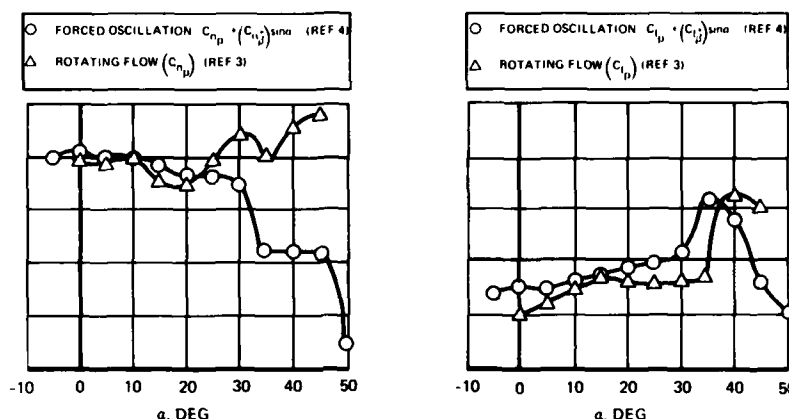
One technique which has been used to separate rate derivatives (C_{n_r} , C_{l_p} , C_{m_q}) from the unsteady derivatives ($C_{n_{\dot{\beta}}}$, $C_{l_{\dot{\beta}}}$, $C_{m_{\dot{\alpha}}}$) is by using a wind tunnel with a curved or rotating flow through the test section. Such a wind tunnel is described in Reference 1. This wind tunnel has been specially designed to obtain pure rotary derivatives in the yaw, roll and pitch axes.

Curved flow past the model is produced by deforming the walls of the test section in a prescribed way and by tuning the velocity profile in the radial direction by means of a graduated wire mesh screen. In the rolling flow tests, a motor driven rotor located upstream of the test section is used to impart a rotary motion to the flow. The rotor vanes are specially designed to provide a velocity distribution which simulates a solid vortex. This allows the fixed model to experience a flow field similar to that which an aircraft rolling about its velocity vector would see in flight.

Figures 2-8 and 2-9 present a comparison of rotary derivative data from forced oscillation tests and from curved and rotating flow wind tunnel tests. As can be seen, the agreement at low angles of attack is good; the $\dot{\beta}$ contribution is quite small. At higher angles of attack, significant unsteady effects are present.

2.1.5 Reynolds Number Effects

The question of the effect of Reynolds number on the analysis of an aircraft's characteristics at high angles of attack is a popular one. Prediction of high angle-of-attack flying qualities of all classes of aircraft geometries with confidence by extending analytical results obtained using small scale, low Reynolds number aerodynamic data to full

FIGURE 2-8. EFFECT OF β DERIVATIVESFIGURE 2-9. EFFECT OF β DERIVATIVES

scale flight test may not be possible. There is strong evidence which indicates that Reynolds number effects are small for fighter aircraft with thin wings having sharp leading edges which fix the separation point and incorporating large wing-body strakes or leading edge extensions which generate strong vortices at high angles of attack. There also exists, however, equally strong experimental evidence of large Reynolds number effects, particularly for aircraft with relatively thick wing sections and large leading edge radii and on forebodies which generate strong secondary vortices fed from a sheet originating at the separation line on the side of the nose. The effect of Reynolds number on the more dominant apex vortex pair is thought to be small. Small model imperfections can cause these Reynolds number effects to be amplified, particularly at angles of attack above 35 degrees. This will be discussed in greater detail in a later section. Examples can be found where the best correlation with flight test is obtained only with small scale data measured at the highest Reynolds numbers. Other examples exist where such a wide variation in the data exists that, in some cases, the lowest Reynolds number data shows the best agreement. Clearly, accurate prediction of high angle-of-attack characteristics is impossible under such circumstances.

In the absence of an adequate experimental data base, the question of the general effect of Reynolds number cannot be answered here. Even with such a data base, the answer will likely be extremely configuration dependent. For current generation fighter aircraft, the available data indicate a critical Reynolds number exists somewhere below 1 million above which variations in aerodynamic parameters tend to damp out. Testing should, of course, always be conducted at the highest Reynolds number available, but, it is felt that data measured carefully at Reynolds numbers greater than 2 million should yield sufficiently reliable results. Figure 2-10 shows an example of yawing moment data at zero sideslip for two different aircraft taken at several Reynolds numbers. Aircraft A and B exhibit a good correlation between small scale data taken at Reynolds numbers of 1.0 to 2.0×10^6 and flight test data taken at in the range of 5.5 to 6.5×10^6 .

2.1.6 Data Repeatability

A lack of repeatability in aerodynamic data at high angles of attack can be caused by many factors. Low Reynolds number aerodynamic hysteresis; wind tunnel model imperfections; wind tunnel turbulence level and unsteady aerodynamic phenomenon can all contribute. Figure 2-11 shows an example of typical but poor repeatability at high angles of attack at zero sideslip. Unsteady aerodynamic effects cannot be studied by using conventional wind tunnel support apparatus and instrumentation due to the limitations of data acquisition systems. Aerodynamic hysteresis can be measured but its effect cannot easily be factored into an analytical methodology so that it can be useful. Reynolds number effects were discussed in the previous section and wind tunnel turbulence level is beyond our control, generally.

Data have recently been gathered on several configurations which indicate that the effect of small model forebody imperfections (perhaps amplified by the low test Reynolds number) can be quite large. Figure 2-12, taken from Reference 5, illustrates the effect of the roll angle of an axisymmetric nose on the side force generated at zero sideslip.

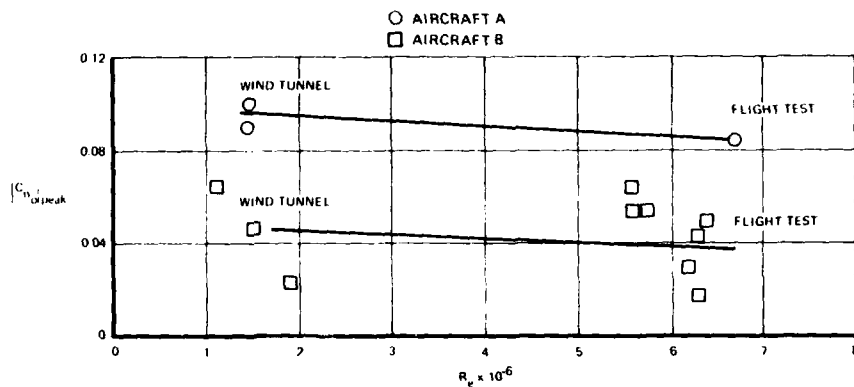


FIGURE 2-10. REYNOLDS NUMBER EFFECT

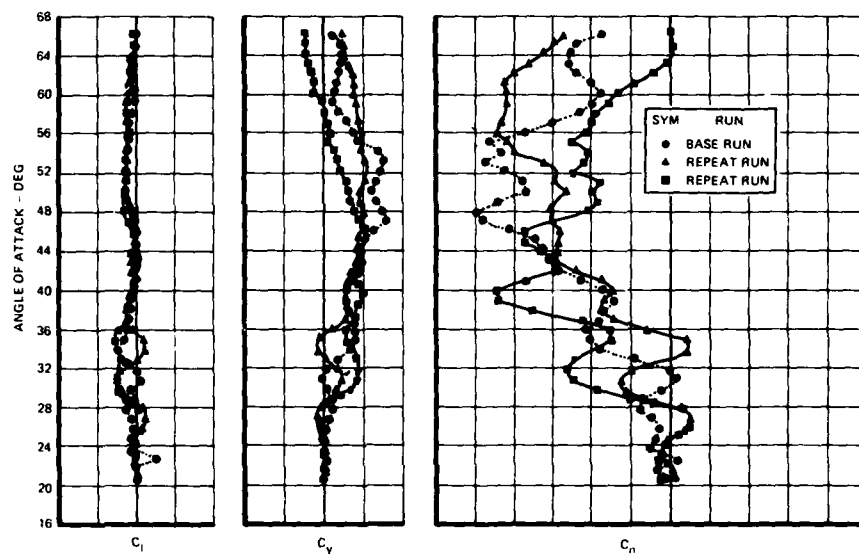


FIGURE 2-11. EFFECT OF REPEATABILITY AT HIGH ANGLES OF ATTACK

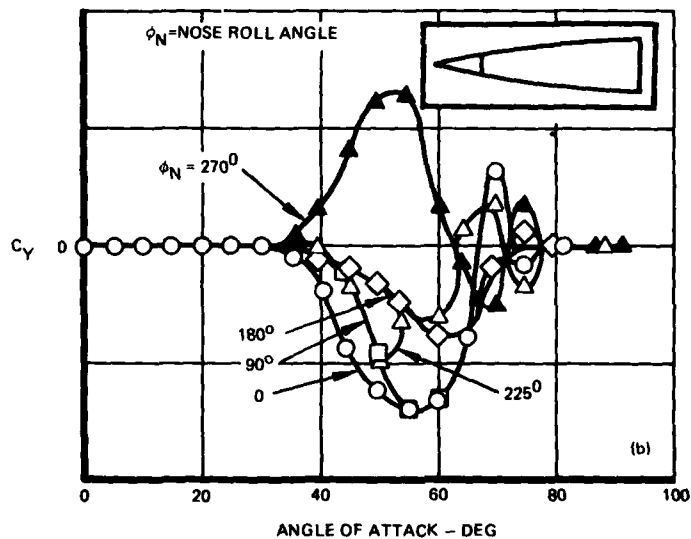


FIGURE 2-12. EFFECT OF THE TIP ROLL ANGLE OF AN AXISYMMETRIC NOSE

Figure 2-13 illustrates a similar effect on a nonaxisymmetric forebody where the roll angle was varied by only ± 0.5 degree. Data variation at angles of attack of greater than 40 degrees is unacceptable. However, repeatability within the same test for a fixed forebody roll orientation is quite good as shown in Figure 2-14.

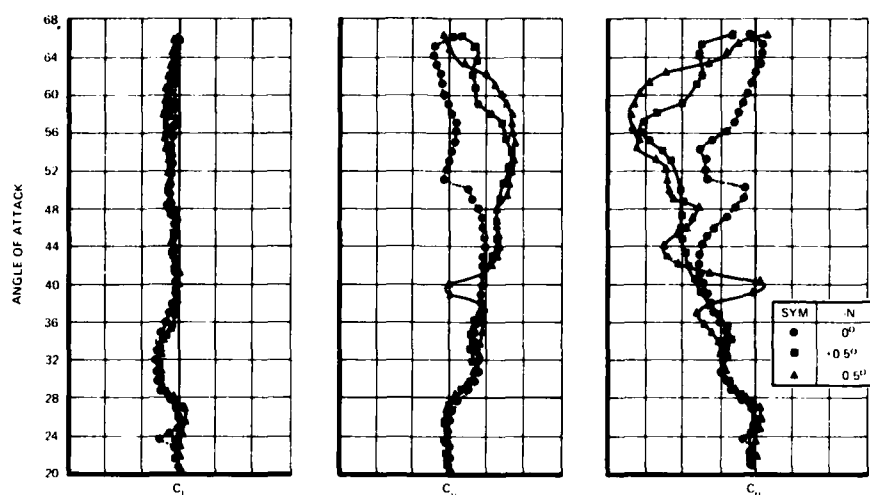


FIGURE 2-13. EFFECT OF THE ROLL ANGLE OF A NON-AXISYMMETRIC NOSE

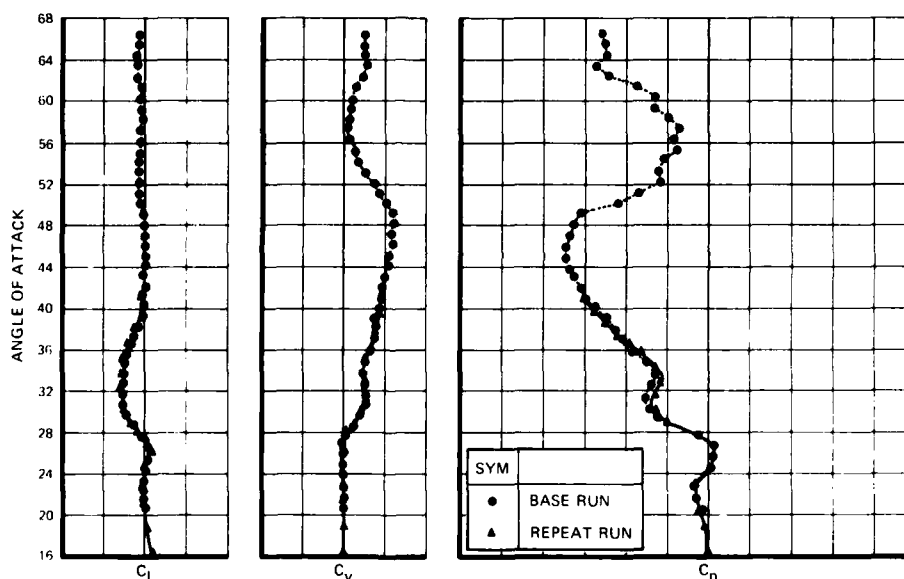


FIGURE 2-14. REPEATABILITY FOR A FIXED ROLL ANGLE

This effect, as with others which have been discussed, is possibly very configuration dependent. During the development of an aircraft configuration, the sensitivity of a particular forebody geometry to these small imperfections should be investigated. If the effect is found to be significant, care should be exercised to use test techniques which would minimize its influence on the data gathered. Numerous repeat runs are always very valuable to monitor any shift in the data.

2.2 Water Tunnel Tests

Accurate visualization of the flow field around an aircraft has long been recognized as a valuable aid to an aerodynamicist, regardless of the Mach number or the angle of attack being considered. Well known techniques such as Schlieren, shadow graph or laser interferometer photographs, surface oil flow or tuft patterns and smoke or hydrogen bubble generators have been applied to a wide class of aerodynamic problems with good success.

However, satisfactory visualization of the fluid mechanic phenomena associated with an aircraft operating at a high, post-stall angle of attack is not really possible with any of the aforementioned techniques. Northrop has selected a water tunnel as the best available experimental tool to provide convenient, vivid and easily controlled flow visualization studies of vortex interactions at high angles of attack. The reason for this is two-fold. First, the density of water is 800 times that of air. Any dyes or other tracers put into the fluid for flow visualization can be roughly 800 times more dense in water than in air with resulting light reflecting characteristics orders of magnitude better. Second, at the same unit Reynolds number and model scale, the velocity in water is $1/15$ that in air, and

thus, a "slow motion" view of the flow can be observed. Most aerodynamic phenomena are easier to follow and better understood at the slow speed.

Prior to development of the Northrop water tunnel, the question of whether flow-field characteristics in air could be properly simulated in water with sufficient accuracy was considered. It is well known that if cavitation is avoided and compressibility does not enter the problem, then the flow of water and air at the same Reynolds number are similar. At the same model scale and velocity, the Reynolds number in water is higher by a factor of 15. Because of practical limitations in speed and model scale, water tunnel tests are generally run at Reynolds numbers well below those of wind tunnels. However, for present day fighter aircraft operating at high angles of attack, flow separation occurs at wing leading edges at all Reynolds numbers, provided the Reynolds number is above a critical value. The water tunnel is operated above the critical value corresponding to leading edge separation. As a result, aircraft leading edge separation phenomena, including the downstream influence on the flowfield, is properly simulated in the water tunnel.

Following construction of the Northrop water tunnel and development of adequate flow visualization techniques, tests were performed to check out the water to air analogy. Figure 2-15 shows for sharp-edged delta wings of different sweep angles the variation in vortex burst location as a function of angle of attack as determined from water tunnel tests. These data were correlated with wind tunnel data for identical wing planforms as shown in Figure 2-16. A comparison of trailing edge vortex burst angles of attack determined from the Northrop water tunnel and from wind tunnel tests of Wentz (Reference 22) and Poisson-Quinton (Reference 6) was made. Excellent agreement is exhibited.

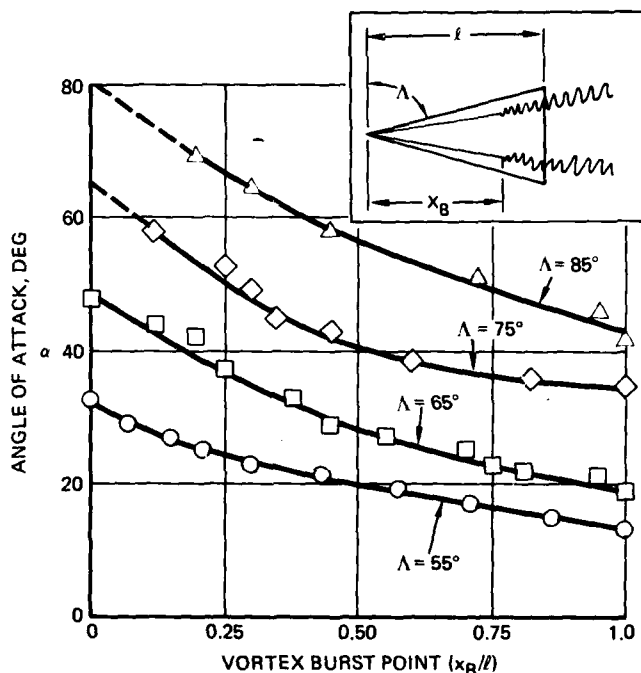


FIGURE 2-15. VORTEX BURST POINT FROM WATER TUNNEL TESTS

Comparisons of motion pictures and photographs of various flowfield phenomenon generated by several other aerodynamic configurations have shown equally good agreement between the observed flowfield structure obtained in the water tunnel and in various wind tunnels.

Water tunnels have been used with great success in the past, especially during the era of the SST. Work at ONERA (References 7, 8, 9, 10) analyzing the vortex flow around ogee and delta wings and slender fuselages has proven the utility of hydrodynamic facilities. Work at Northrop in the water tunnel has consisted of extensive research into forebody shaping to augment stability at high angles of attack, leading edge extension (LEX) contouring to delay vortex breakdown, spanwise blowing to enhance vortex strength and configuration studies to aid in location of wings, inlets, tails and control surfaces to take maximum advantage of vortex induced lift and to minimize adverse interactions. Figures 2-17 through 2-20 present some examples of studies conducted in the Northrop hydrodynamic facility.

2.3 Tethered Model Tests

This test technique consists of free flight testing of a scale model in the wind tunnel. The dynamically scaled model is flown by remote control in the open throat test section of the Langley 30 x 60 foot full-scale wind tunnel. Control commands, electrical power for servo actuators and compressed air for ejector drive thrust simulation are fed through an umbilical cable, attached to the model. Control augmentation laws are stored in a peripheral computer.

This technique has a valuable, but restricted application. It can provide information on the flying qualities of an aircraft at angles of attack at or below stall. Flight above the stall angle of attack is possible if the aircraft has no unstable characteristics, therefore this testing technique can also be used for VTOL transition tests. Experiments using this technique can greatly aid the safety of a flight test program by uncovering potential dynamic stability problems near the stall angle of attack or at large values of sideslip at lower angles of attack. It can also be used to evaluate a control augmentation system and its effect on flight characteristics prior to first flight.

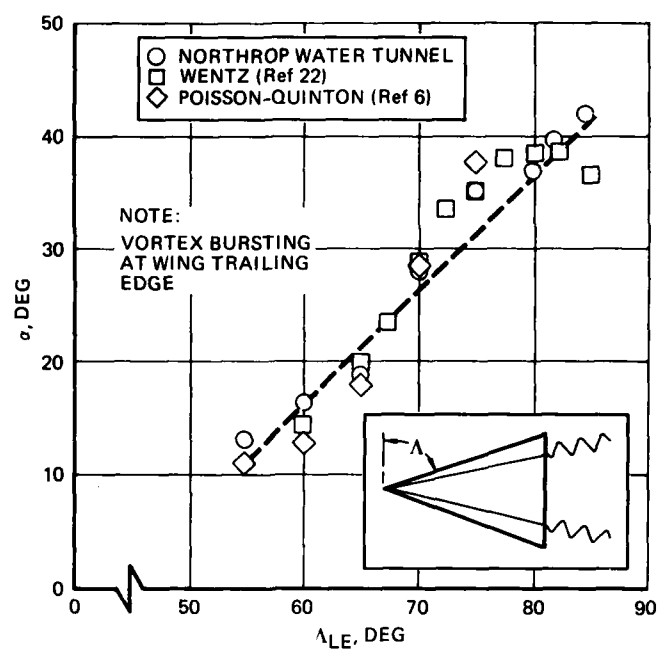


FIGURE 2-16

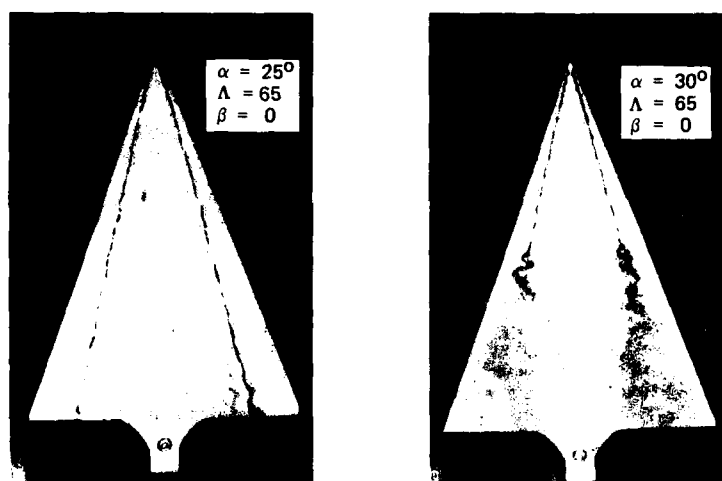
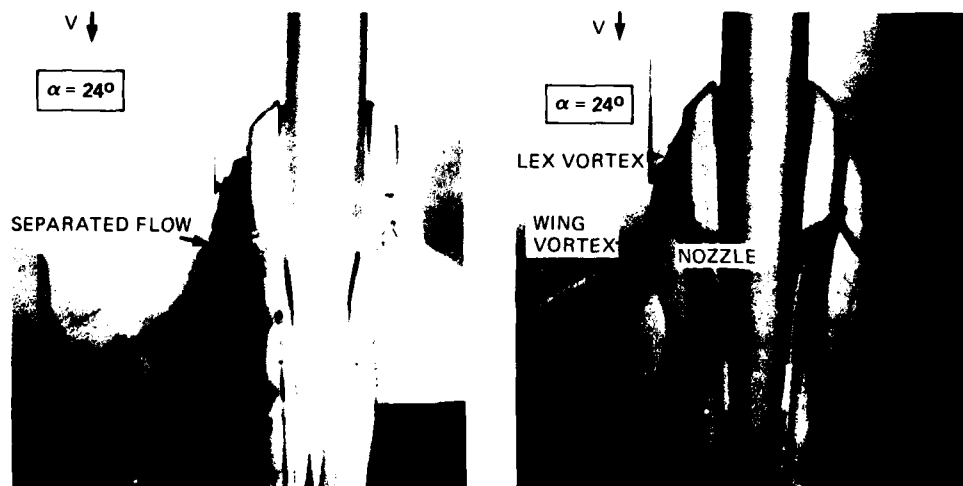
FIGURE 2-17. DELTA WING VORTEX BURST PROGRESSION
WITH ANGLE OF ATTACK

FIGURE 2-18. EFFECT OF SPANWISE BLOWING ON VORTEX BURST

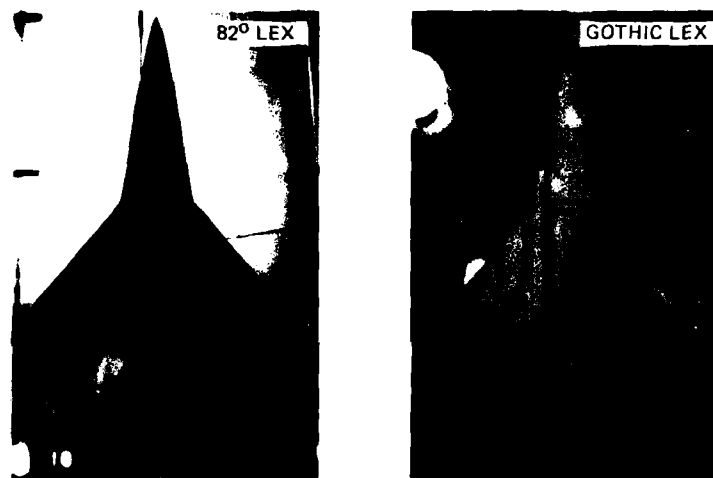


FIGURE 2-19. EFFECT OF LEX CONTOUR ON VORTEX BURST

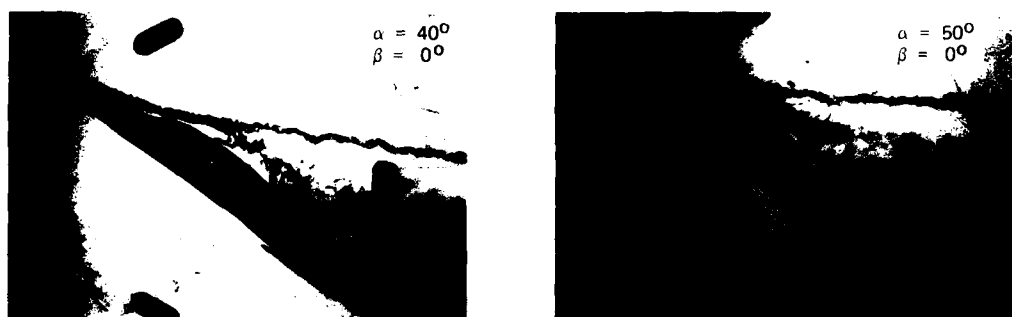


FIGURE 2-20. FOREBODY VORTEX PATTERNS AT HIGH ANGLES OF ATTACK

This technique will, however, only provide an indication of a tendency of an aircraft to depart from controlled flight at near-stall angles of attack or at large sideslip angles. Neither the severity or duration of a departure nor the expected recovery characteristics can be evaluated with this method. The susceptibility of an aircraft to progress from a post-stall gyration (PSG) or departure to a spin cannot be investigated either. Maneuvers are limited, in general, to 1-g, however, mild maneuvering such as bank-to-bank rolls or steady-state sideslips can be accomplished.

One additional comment is appropriate with regard to the tethered test technique. As with many of the experimental tools available within the current state-of-the-art, this technique is, unfortunately, not a tool which is likely to be used during the preliminary design phase of most aircraft. The costs associated with a wind tunnel free-flight test can be high, but because the models can be used for low speed force, moment and forced oscillation tests, the costs associated with tethered testing can possibly be offset.

2.4 Vertical Tunnel Tests

Vertical wind tunnels are used primarily to investigate the spin modes and recovery characteristics of an aircraft. Because of the launch methods used, no stall or departure motions can be obtained. In addition to spin mode identification, vertical tunnels are very useful in evaluating spin recovery devices to be used during the flight test phase of a spin test program. Sizing of the spin chute canopy diameter and determination of the proper riser and suspension line lengths to ensure positive recovery are best suited for evaluation in the vertical wind tunnel.

The vertical wind tunnel is a minimum cost facility and many repeat runs can be obtained inexpensively to establish trends. It is an indoor facility and not subject to adverse weather conditions.

2.5 Remotely Piloted Drop Model Technique

The free flight drop model technique consists of launching a radio controlled, dynamically scaled model from either a helicopter at low altitudes (approximately 5000 feet) or from a parent aircraft such as a B-52 at very high altitudes (up to 40,000 feet). Helicopter-launched free flight drop models of several aircraft have been tested at NASA Langley and B-52-launched models of the F-15 has been tested at NASA Dryden. The YF-16 was tested by AFFDL at the USAF Flight Test Center at Edwards AFB.

This technique is useful in determining the post-stall and spin entry motions of aircraft. This information can not be obtained from any other test technique short of full scale flight testing. The drop model technique can be used to evaluate the effect of adverse control inputs during the post-stall gyration (PSG) phase. Accelerated as well as 1 g stalls can be performed.

The techniques used in this type of testing are very similar to those which are used during full scale testing and the spin susceptibility of an aircraft determined from drop testing is usually very representative. Complex control laws can be programmed into computers in the ground station and up-linked to the model to properly simulate highly augmented flight control systems.

The major limitation associated with this method is cost of the models as well as support costs for the test program. The time required to complete such a program is also a serious drawback. The major justification of such a test technique is in the increased level of safety that the results lend to a full scale, manned, flight test program. Certain areas of the flight envelope can be explored with a bit more vigor when an unmanned drop model is used. Drop model tests are used to predict departure and spin entry susceptibility and can identify recommended controls to be used for recovery from the PSG or spin phase prior to flight testing.

2.6 Manned Simulation

Meaningful manned simulation of aircraft departure and spin characteristics is a difficult task. Not only are there limitations inherent due to the aerodynamic modeling, but also limitations exist which are imposed by the simulator itself. In most cases, aircraft motions during departures are usually random, and require both visual and "seat of the pants" pilot cues. For this reason, moving base simulation or fixed base simulation with motion cues should be used in an investigation of stall and departure characteristics. Even when moving base simulation is available, care must be taken to use the best set of nonlinear aerodynamic data and any available flight data to produce a good model of the aircraft or results could be misleading. Preceding the flight test phase of the F-5E Spin Susceptibility Program, a simulation of the aircraft was implemented on the NASA Langley Differential Maneuvering Simulator. Fortunately, stall flight test data, both 1-g and accelerated, were available to improve the aircraft model. The Northrop and the USAF pilots both flew the simulator prior to flight tests. Both agreed that there were some high angle-of-attack characteristics identified during the simulator tests that were later encountered during the spin tests. Due to their exposure to these characteristics on the simulator, they were better prepared to react to them in flight. Certain areas of the test matrix were explored first on the simulator prior to performing them in flight to gain confidence. Manned simulation can also be used to determine the effect of certain configuration modifications prior to testing.

Good simulation is particularly useful in development of control systems, saving flight test time and reducing risk. Although at this time, simulation will not replace stall departure or spin flight testing, it can be used as a "confidence builder" (albeit an expensive one) to augment flight test programs or as a familiarization tool or training device.

2.7 Full Scale Flight Tests

A discussion of full scale flight test techniques may seem misplaced in a survey paper which deals with the prediction of an aircraft's characteristics at high angles of attack in as much as this phase of an aircraft development should represent the "final answer." However, some discussion of the aerodynamic effects of certain required configuration features peculiar to a test aircraft is appropriate.

Instrumentation requirements for an aircraft which will be used in stall-spin testing are among the most demanding that an engineer must deal with. Comprehensive analysis of stall-spin flight test data requires accurate knowledge of the aircraft's angular position relative to both the velocity vector and the earth, its angular rates and acceleration, its airspeed, Mach number, altitude, engine operating conditions, inertial distribution, control surface positions and configuration (flaps, gear, speed brake, etc). Care must be exercised to insure that the effect of the emergency recovery system installation, external camera protuberances or special instrumentation package installations on the test aircraft has a minimal effect on the aerodynamics and the inertia characteristics of the aircraft. If their effect is not negligible, this must be adequately taken into account in any preflight analysis or prediction which is done. It goes without saying that the test aircraft must be representative, aerodynamically and inertially, of the production aircraft.

One area which deserves special attention is the installation of a large flight-test nose boom to mount an angle-of-attack and sideslip vane and pitot-static system. This modification to a test aircraft can significantly affect the lateral-directional stability of the configuration at high angles of attack and could, potentially, alter the departure susceptibility and recovery characteristics which would be determined.

Figure 2-21 illustrates the variation in lateral-directional stability which can be caused by the installation of a large (4-inch diameter) flight test nose boom on a fighter aircraft. A significant change to the forebody vortex system is produced by the nose boom.

3.0 ANALYTICAL TECHNIQUES

This section presents some of the current analytical techniques to predict aircraft stall/departure/spin characteristics. The categories of buffet onset, wing rock, roll reversal, roll departure, yaw departure, post stall/spin entry, steady spins and spin recovery will be addressed.

3.1 Approach to Stall/Post Stall

3.1.1 Buffet Onset

Buffet onset is not usually a limiting factor. However, severe buffet may prevent adequate tracking capability and therefore could effectively limit turn rate capability. Breaks in the lift curve slope prior to reaching maximum lift have been used to predict buffet onset. Wing root strain gages have also been used to predict buffet onset and buffet intensity in the wind tunnel. Flight test results of Reference 11 showed that breaks in the slope of aileron hinge/moment, trailing edge flap hinge/moment and trailing edge static pressure coefficients with angle of attack correlated well with initial flow separation and buffet onset.

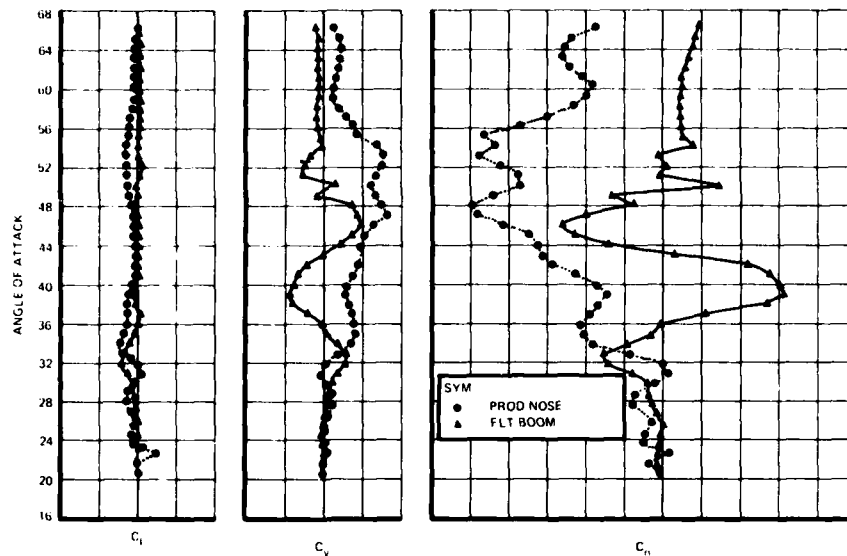


FIGURE 2-21. EFFECT OF FLIGHT TEST NOSE BOOM

3.1.2 Wing Rock

The occurrence of wing rock is common to most fighter aircraft when operating in a tactical environment. Wing rock usually becomes the limiting condition, in conjunction with buffet, for adequate gun tracking capability. It can occur in the transonic Mach number region at moderate angles of attack as a result of shock/boundary layer interaction. It can also degrade air combat maneuvering capability at airspeeds/Mach numbers at or below the corner speed of the aircraft in the vicinity of the stall angle of attack.

Many aspects of wing rock, such as the triggering mechanisms and the sustaining forces, are not well understood. Wind tunnel data on several individual aircraft have been analyzed and a fairly good correlation with full scale flight results demonstrated. Unfortunately, prediction methodologies derived from these analyses have not proven to be sufficiently reliable on present day aircraft which have moderately swept, highly cambered wings and employ complex vortex systems for lift augmentation at high angles of attack.

Tests performed on the F-5A at NASA Ames Research Center (Reference 12) using a specially designed flexible support system which allowed the model to oscillate in roll have provided some insight into the flow mechanism responsible for the medium angle of attack (11-12 degree), transonic, small amplitude wing rock phenomenon. Based on pressure and response data acquired when the model was constrained by a fixed support and when it was free to oscillate in roll, it was concluded that the wing rock was generated by a limit cycle mechanism due to the pressure changes on the wing upper surface, especially near the wing tip. The primary reason for the pressure changes was the induced changes to local wing panel angles of attack which alternately caused leading edge stall and recovery.

3.1.3 Roll Reversal/Roll Departure

Roll reversal can be accurately predicted using LCDP or the aileron alone divergence parameter (AADP) as shown in Reference 13 and 14. The parameter LCDP has been used in various forms for different purposes and is derived from the simplified rolling and yawing moment equation. As a lateral control departure parameter, it predicts roll reversal or the point where rolling moment due to adverse yaw overcomes the aileron power.

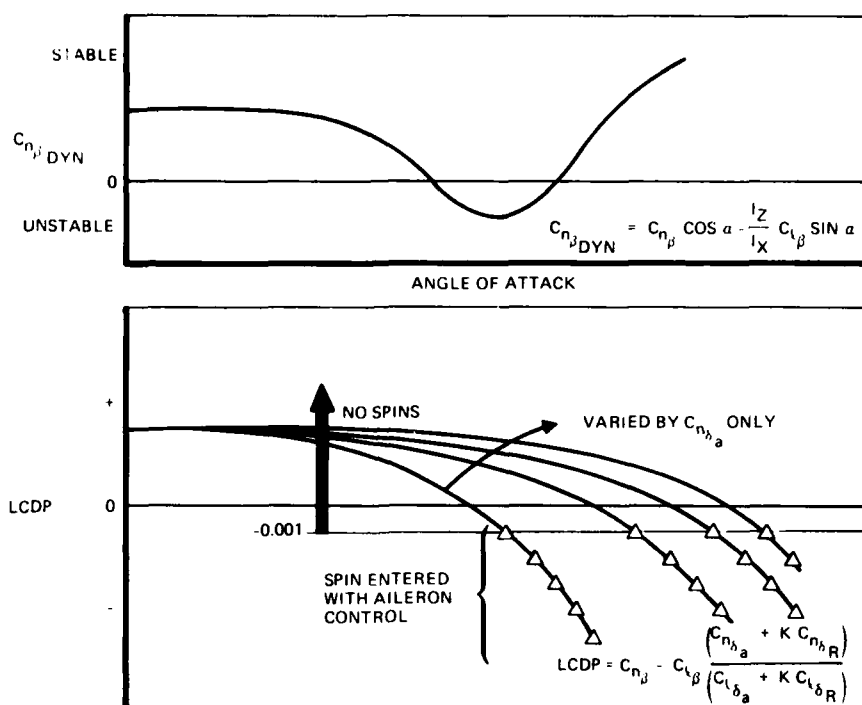
$$\text{LCDP (AADP)} = C_{n\beta} - \left(\frac{C_{n\delta a}}{C_{l\delta a}} \right) C_{l\beta} \quad (\text{no rudder})$$

$$\text{LCDP} = C_{n\beta} - C_{l\beta} \left(\frac{C_{n\delta a} + KC_{n\delta r}}{C_{l\delta a} + KC_{l\delta r}} \right) \quad (\text{with rudder})$$

$$\text{where} \quad K = \frac{\delta r}{\delta a}$$

When LCDP approaches zero, the aircraft will not roll with aileron input. When LCDP becomes negative the aircraft will experience a rolling departure, i.e., the aircraft rolls opposite to roll control input. At large negative values of LCDP the aircraft will depart in yaw opposite to the aileron input and spin entry is probable. A computer study varying $C_{n\delta a}$ making LCDP more positive or negative for a modern fighter configuration is shown in Figure

3-1. As shown, as LCDP became more negative than -0.001 spin entry was possible with aileron inputs even though $C_{n\beta \text{ DYN}}$ was positive.

FIGURE 3-1. LCDP AND $C_{n\beta DYN}$ CORRELATION

3.1.4 Yaw Departure

Many attempts have been made to derive a simple expression for predicting yaw departure. One expression which has received a lot of attention in past years is $C_{n\beta DYN}$. The expression is derived from the open loop lateral-directional quartic equation and represents an approximation of the "C" term. It is a measure of the aircraft's stability about the flight path and predicts departure from longitudinal control inputs.

$$C_{n\beta DYN} = C_{n\beta} \cos \alpha - \frac{I_z}{I_x} C_{l\beta} \sin \alpha$$

Reference 15 presents data which compares $C_{n\beta DYN}$ with flight results of seventeen different aircraft, ten of which included more than one aerodynamic configuration. A good to fair correlation was obtained for 90 percent of the cases studied. Using these and other flight test data, Figure 3-2 presents various ranges of $C_{n\beta DYN}$ which predict aircraft behavior in a stall with longitudinal control inputs only. During the early design stages of an aircraft, trade-offs for performance advantages between the solid stall and acceptable stall region may be made. However, $C_{n\beta DYN}$ should never be allowed to penetrate the random yaw departure values otherwise nose slices and departures can be expected.

Other correlations have also been made to predict departures where lateral-directional control inputs are considered. These methods incorporate both the $C_{n\beta DYN}$ and LCDP departure criteria. The first is the $\beta + \delta$ axis stability indicators.

$$\alpha_{-\beta} = \alpha - \tan^{-1} \left(\frac{C_{n\beta}}{C_{l\beta}} \cdot \frac{I_x}{I_z} \right)$$

$$\alpha_{\delta} = \alpha - \tan^{-1} \left(\frac{C_{n\delta a}}{C_{l\delta a}} \cdot \frac{I_x}{I_z} \right)$$

For stability

$$\alpha_{-\beta} > \alpha_{\delta} \quad \text{and} \quad \alpha_{-\beta} > 0$$

This criterion essentially shows that $C_{n\beta DYN}$ has to be greater than zero and where $\alpha - \beta = \alpha_{\delta}$, LCDP will be zero. Another correlation of $C_{n\beta DYN}$ and LCDP described in Reference 14 identifies regions of predictable stall characteristics (see Figure 3-3). A comparison of the Reference 14 criterion which considers $C_{n\beta DYN}$ and AADP

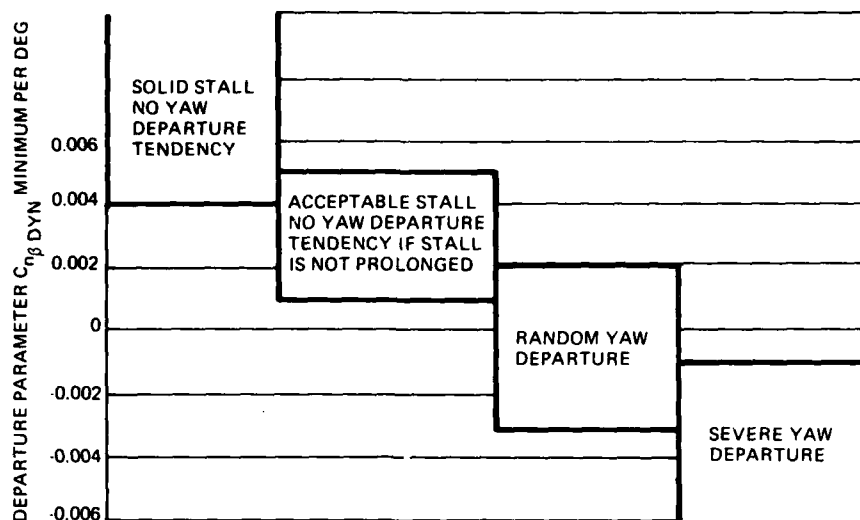


FIGURE 3-2. EXPECTED STALL BEHAVIOR AS A FUNCTION OF $C_{n\beta DYN}$

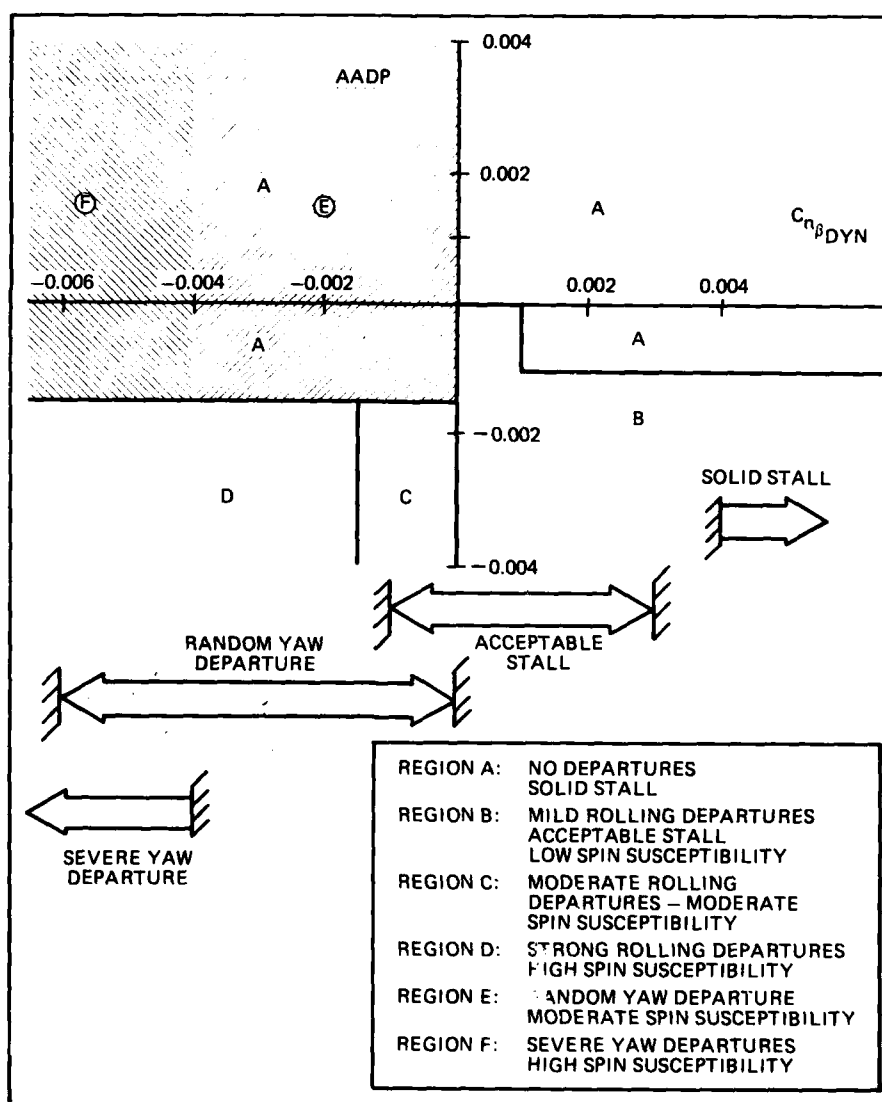


FIGURE 3-3. COMPARISON OF WEISSMAN AND NORTHROP DEPARTURE CRITERIA

with the Figure 3-3 criterion which considers $C_{n\beta DYN}$ only has been made. The comparison of these data indicates that two more regions, E and F, can be identified which would improve correlation with flight test results. These regions would define aft stick yaw departures because of the relatively high negative values of $C_{n\beta DYN}$.

3.1.5 Pitch Departure

Coupling between the lateral-directional and longitudinal axes can be large in the stall and post-stall angle-of-attack region. Nose up pitching moment due to sideslip ($C_m|\beta|$) can produce significant increases in angle of attack especially during heavy wing rock. Figure 3-4 presents a typical variation of this parameter and identifies maximum trim angle of attack for two levels of horizontal tail authority. Figure 3-5 presents the corresponding effect of the nose up pitching moment due to sideslip on maximum trim angle of attack. The data indicate that a near zero or a slightly nose down value of $C_m|\beta|$, similar to that shown for -17 degrees tail authority, is desirable to avoid coupling effects which may place the aircraft in a region of poor lateral directional stability or poor pitch response to recovery control surface inputs.

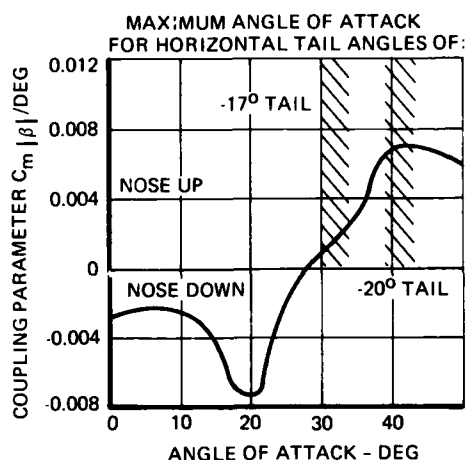


FIGURE 3-4. EFFECT OF LIMITING TAIL AUTHORITY ON SIDESLIP/ANGLE-OF-ATTACK COUPLING PARAMETER

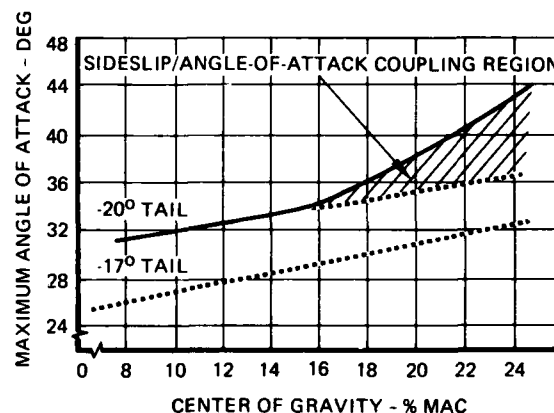


FIGURE 3-5. EFFECT OF LIMITING TAIL AUTHORITY ON MAXIMUM ANGLE OF ATTACK

3.1.6 Coupled Pitch and Yaw Departure

A technique has been developed by Kalviste for predicting departure tendencies in aircraft (Reference 16). The new Kalviste Criteria is derived in a manner similar to the current $C_{n\beta DYN}$ criteria. As shown in Figure 3-6, a characteristic polynomial is formed and an analysis of the roots of this equation and Routh's discriminate reveal the important stability parameters. The strength of the Kalviste method is based upon two facts: (1) it employs coupled equations in angle of attack and sideslip, and (2) it is based upon a fully non-linear static aero data model.

The Kalviste criteria results in instability, or a departure tendency, being determined by the sign of three parameters: $C_{n\beta COP}$, $C_{m\alpha COP}$, and K . The subscript COP indicates that these parameters are from coupled equations. Figure 3-7a shows a typical $C_{n\beta DYN}$ stability curve. A negative value of $C_{n\beta DYN}$ indicates an unstable configuration. $C_{n\beta DYN}$ is normally shown only as a function of α because the data has been linearized over some range of β . The Kalviste method does not linearize variations with β but rather uses the partial derivative at each value of β . The stability parameters therefore become a function of both α and β . One can then employ contour mapping techniques to define regions in which the aircraft will be unstable; i.e., where $C_{n\beta COP}$, $C_{m\alpha COP}$ or K are of the unstable sign (see Figure 3-7b). These three types of unstable regions correspond to slicing departures, pitch-up departures, and oscillatory departures, respectively.

3.2 Departure/Spin Entry

The post-stall and spin-entry regions are areas where simple prediction techniques do not correlate well with flight test. Part of the problem may be due to inadequately measured wind tunnel data. In the past, even with adequately measured wind tunnel data, computer storage limitations often forced the analyst to linearize the data and in some cases eliminate any chance for correlation with flight test.

3.2.1 Aerodynamic Asymmetries

A significant interest has developed in recent years in the study of aerodynamic asymmetries at high angles of attack. Historically, the phenomenon had been primarily concentrated in missile aerodynamics, due to the characteristically long and slender bodies of most missiles. Reference 17 presents a good survey and bibliography of the missile problem. Recent trends in fighter aircraft design have led to aircraft fuselages which have forebody fineness ratios in the same range as some missiles, thus forcing aircraft designers to deal with the problem of asymmetries. Figure 3-8 shows the variation in absolute magnitude of yawing moment coefficient at zero sideslip developed from the analysis of data on several aircraft whose fineness ratios varied from approximately 3.5 to 6.0. Also shown in the variation of onset angle of attack with fineness ratio taken from Reference 13.

CHARACTERISTIC POLYNOMIAL

$$(S^4 + AS^2 + E)(S) = 0$$

CURRENT APPROACH

● UNCOUPLED EQUATIONS

$$(\beta = 0, M_\beta = N_\alpha = \mathcal{L}'_\alpha = 0)$$

$$A = N_\beta \text{ DYN} - M_\alpha$$

$$B = -(N_\beta \text{ DYN}) (M_\alpha)$$

$$N_\beta \text{ DYN} = N_\beta \cos \alpha - \mathcal{L}'_\beta \sin \alpha$$

PRESENT CRITERIA

$$N_\beta \text{ DYN} > 0 \text{ OR } C_{n\beta} \text{ DYN} > 0$$

$$M_\alpha < 0 \text{ OR } C_{M_\alpha} < 0$$

KALVISTE METHOD● COUPLED EQUATIONS
(LOCAL SLOPES AT α & β)

$$A = N_\beta \text{ DYN} - M_\alpha$$

$$+ (N_\alpha \sin \alpha + \mathcal{L}'_\alpha \cos \alpha) \tan \beta$$

$$B = -(N_\beta \text{ DYN}) (M_\alpha)$$

$$+ (N_\alpha \cos \alpha - \mathcal{L}'_\alpha \sin \alpha) M_\beta$$

$$+ (\mathcal{L}'_\alpha N_\beta - \mathcal{L}'_\beta N_\alpha) \tan \beta$$

KALVISTE CRITERIA

$$\text{DISCRIMINANT, } K = (A^2 - 4B) > 0$$

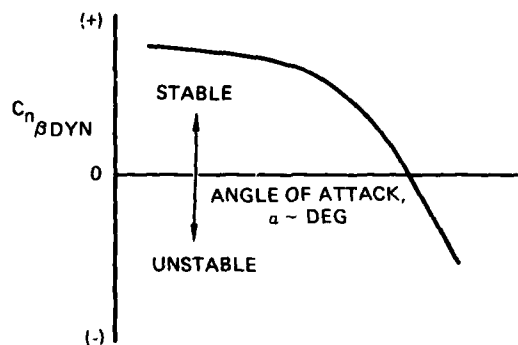
$$N_\beta \text{ COP} > 0 \text{ OR } C_{n\beta} \text{ COP} > 0$$

$$M_\alpha \text{ COP} < 0 \text{ OR } C_{m_\alpha} \text{ COP} < 0$$

FIGURE 3-6. AIRCRAFT STATIC STABILITY PERTURBATION EQUATIONS

CURRENT CRITERIA

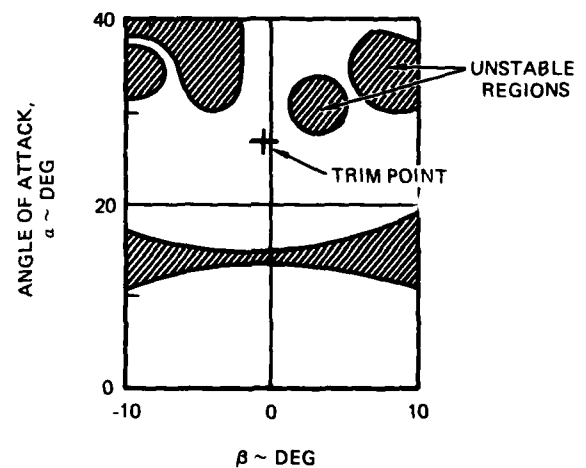
- FIXED δ_H
- UNCOUPLED EQUATIONS
- LINEARIZED WITH β



(a)

KALVISTE CRITERIA

- FIXED δ_H
- COUPLED α, β EQUATIONS
- FULL NONLINEAR STATIC AERO DATA SET



(b)

FIGURE 3-7. COMPARISON OF KALVISTE CRITERIA WITH $C_{n\beta \text{ DYN}}$ CRITERIA

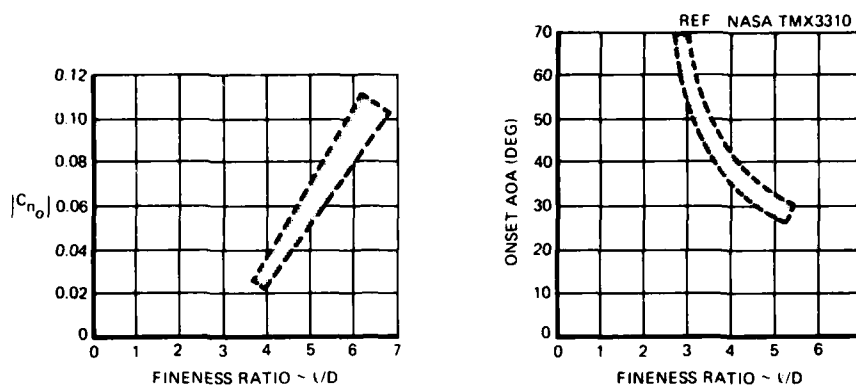


FIGURE 3-8. EFFECT OF FINENESS RATIO

The definition of forebody length used in the calculation of fineness ratio depends on the aircraft geometry. For aircraft with fairly long forebodies, a reference line is drawn four body diameters forward of the wing trailing edge. The forebody length is defined as the length forward of that reference line. This convention is taken from Reference 18 and is illustrated in Figure 3-9. a. For aircraft with large wing-body strakes (LEX's) or large inlets which extend fairly far forward, a different definition for forebody length is used as shown in Figure 3-9. b.

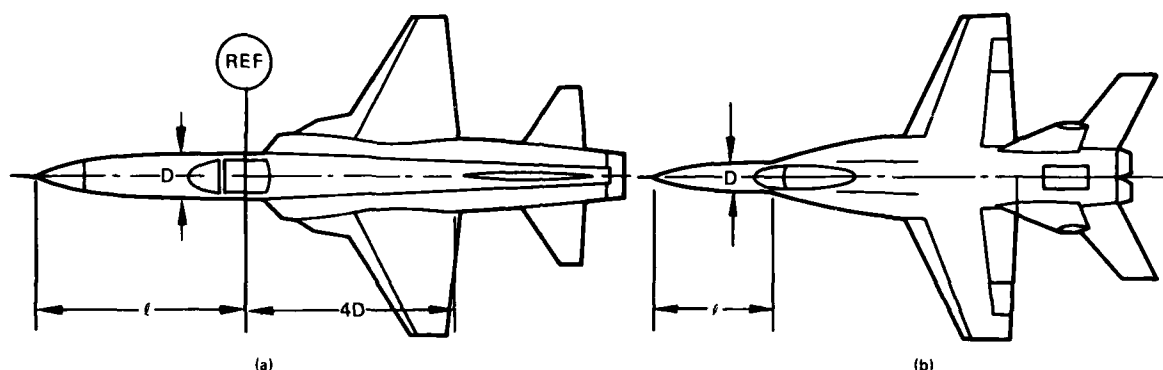


FIGURE 3-9. DEFINITION OF FINENESS RATIO

It has been convincingly shown in small scale wind tunnel and water tunnel experiments that the aerodynamic phenomenon which is responsible for these asymmetric forces and moments is the growth of a strong vortex system from the aircraft forebody. For sufficiently slender forebodies, this vortex system becomes asymmetric at high angles of attack and exerts a significant effect on the other components of the airframe. Figure 3-10 illustrates these vortices. Figure 3-11 shows dye patterns emanating from an isolated aircraft forebody at a high angle of attack taken during a water tunnel test. An asymmetric vortex pattern is clearly shown.

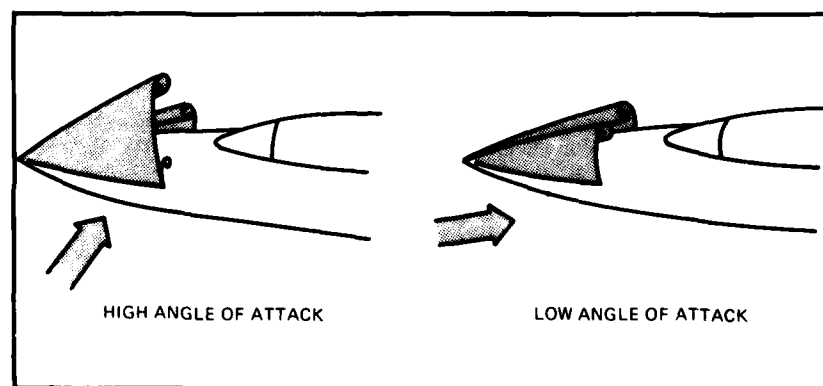


FIGURE 3-10. FOREBODY VORTEX PATTERNS

Until recently, however, it had not been convincingly shown that this asymmetric vortex system and the resulting asymmetric forces which have been measured on wind tunnel models actually exist on the full scale aircraft at flight Reynolds number. Figure 3-12 shows a comparison of yawing moment coefficient at zero sideslip for a small scale wind tunnel model and the full scale aircraft. The wind tunnel data was gathered at Reynolds number of 2.0×10^6 and the flight test data was extracted at Reynolds numbers of between 5.5 and 6.5×10^6 .



FIGURE 3-11. VORTEX PATTERNS

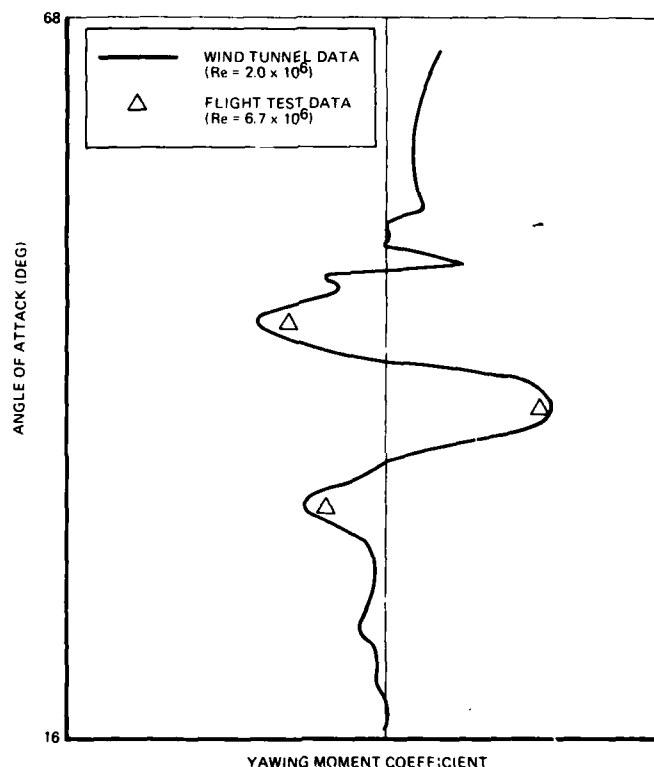


FIGURE 3-12. WIND TUNNEL/FLIGHT TEST CORRELATION

Figure 3-13 shows a comparison of a digital computer simulation and actual flight test results of a longitudinal stick snap maneuver. Control inputs used in the simulation were identical to those of the flight test and consisted of a rapid application of full trailing-edge up horizontal stabilizer to its maximum travel and no rudder or aileron inputs. The aerodynamic model used in the simulation included all nonlinearities and asymmetries which were measured in the wind tunnel. The excellent match of flight test and simulation for this maneuver, as well as many others not shown, strongly suggests that the asymmetries measured in the wind tunnel at low Reynolds number are accurate both in terms of onset angle of attack and peak magnitudes and do, indeed, represent the same phenomenon present on the full scale aircraft at higher Reynolds numbers.

A further discussion of aerodynamic asymmetries, including methods to attenuate their magnitude, is included in Section 4 of this paper.

3.2.2 Six Degree of Freedom Analysis

Open loop six degree of freedom analysis can be helpful in defining spin characteristics of an aircraft. In order to be confident in the predicted results a good set of nonlinear aero data is necessary.

Initially, boundaries of no spin, oscillatory spin and steady-state spin in terms of yaw rate and angle of attack are established, as shown in Figure 3-14. An oscillatory spin is a combination of yaw rate and angle of attack that returns to the trim angle of attack after transitioning through at least two (2) turns. A steady spin is that combination of yaw rate and angle of attack where the initial values of yaw rate and angle of attack reach a steady value.

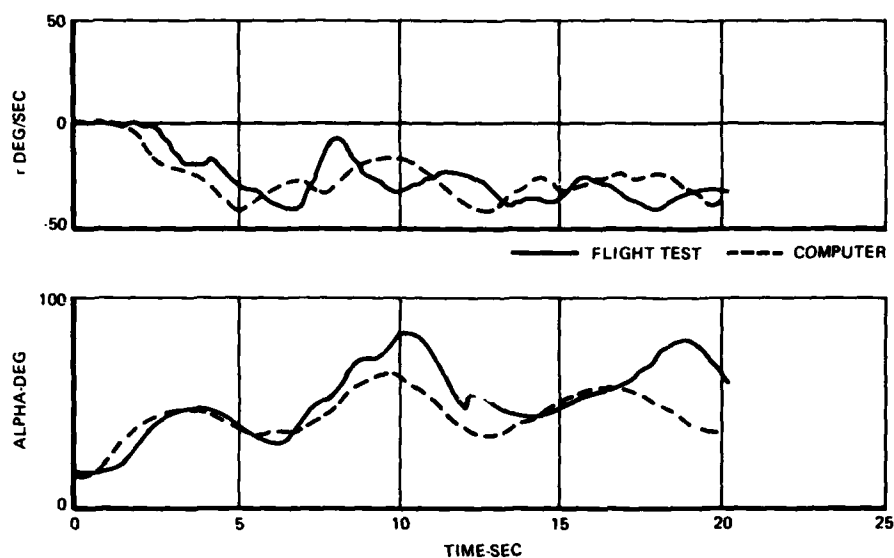


FIGURE 3-13. COMPARISON OF DIGITAL COMPUTER SIMULATION AND FLIGHT TEST RESULTS

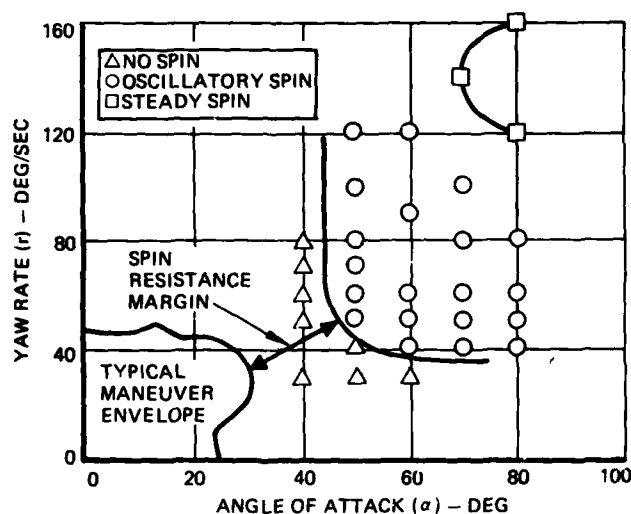


FIGURE 3-14. LOCATING SPIN BOUNDARIES

Classification of spins, i.e., no spin, oscillatory spin or steady spin defines two boundaries; the spin-entry boundary and the steady-state spin boundary. Once these boundaries are established, a maneuver envelope can be generated. Combination of control inputs and recoveries from unusual attitudes that may arise during combat maneuvering are used to map the maneuver boundary. The margin between the maneuver envelope and the spin entry boundary is a measure of the aircraft's spin resistance. Figure 3-15 shows various spin entry envelopes and defines aircraft maneuver limitations associated with each boundary.

Figure 3-16 presents the effect of the aerodynamic asymmetries on the analytical spin-entry boundary. When the asymmetries are ignored, the calculated boundary is symmetric and indicates a false level of spin resistance. When the asymmetries are included, a strong bias is evidenced. Flight test results of two spins are shown, indicating an agreement with the asymmetric spin boundary, thus further substantiating the existence of the aerodynamic asymmetries.

3.3 Oscillatory and Steady Spin

3.3.1 Angular Acceleration Method

This method assumes that $\dot{p} = \dot{q} = \dot{r} = 0$ in the three moment equations and that the cross products of inertia terms are small and can be neglected. It predicts the steady state spin condition.

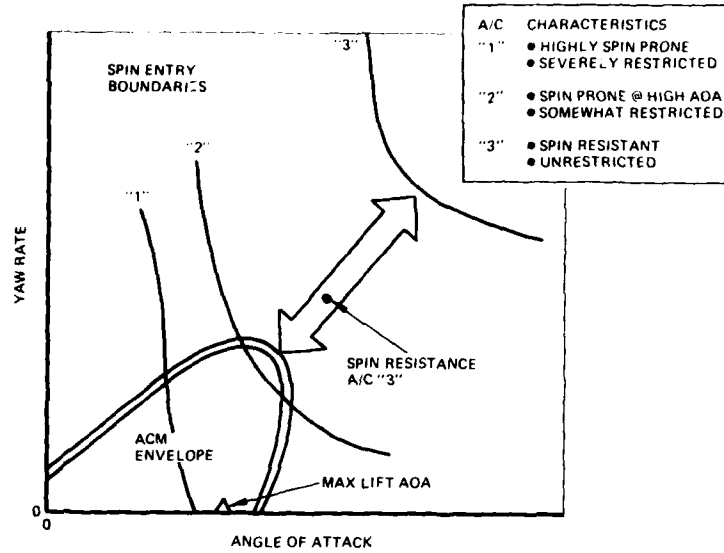


FIGURE 3-15. RELATIVE SPIN ENTRY CHARACTERISTICS

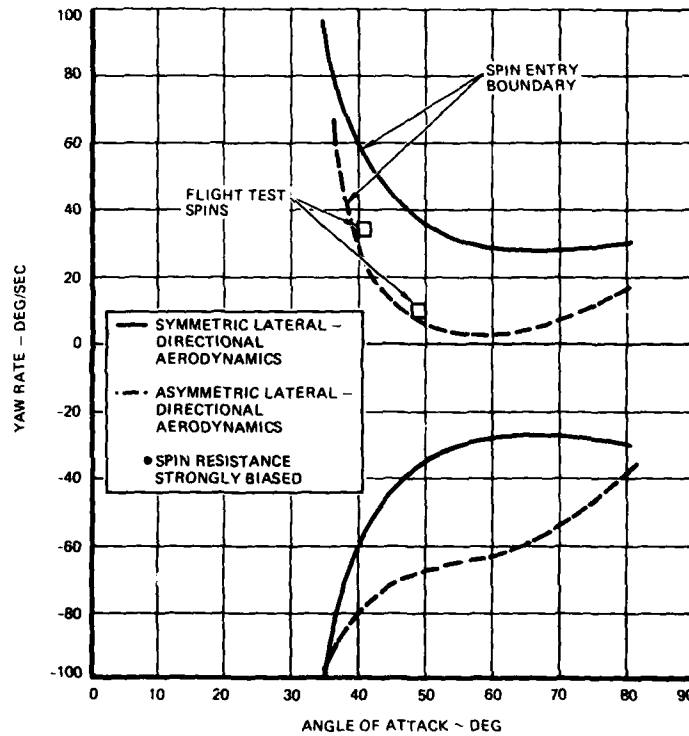


FIGURE 3-16. EFFECT OF AERODYNAMIC ASYMMETRIES

From the equation for pitch acceleration \dot{q} we have:

$$(I_z - I_x) pr = - \frac{\bar{c} S_w q_0 C_m}{I_y}$$

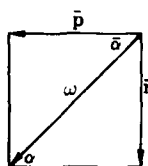
$$pr = - \frac{\bar{c} S_w q_0 C_m}{I_y (I_z - I_x)}$$

From the \dot{p} and \dot{r} moment equations:

$$C_{l_p} \beta + C_{l_r} \frac{rb}{2V} + C_{l_p} \frac{pb}{2V} + C_{l_{\delta_a}} \cdot \delta_a + C_{l_{\delta_r}} \cdot \delta_r = 0$$

$$C_{n_{\beta}} \beta + C_{n_r} \frac{rb}{2V} + C_{n_p} \frac{pb}{2V} + C_{n_{\delta_a}} \cdot \delta_a + C_{n_{\delta_r}} \cdot \delta_r = 0 \quad (3)$$

Assuming that the resultant angular velocity is aligned with the flight path and that the angle of roll and pitch are small:



$$\frac{r}{p} = \tan \alpha \quad (4)$$

$$p = \omega \cos \alpha \quad \text{and} \quad r = \omega \sin \alpha \quad (5)$$

From equations 1 and 5 we see that $pr = \omega^2 \cos \alpha \sin \alpha$ and that

$$\omega^2 = \frac{\bar{c} S_w q_0 C_m}{(I_z - I_x) \sin \alpha \cos \alpha} \quad (6)$$

Solution of equations 2 through 6 as functions of α and β for a typical aircraft is presented in Figure 3-17. The crossover point indicates simultaneous solutions of equations 2, 3 and 6. These crossover points also represent balances between the aerodynamics and inertial torques.

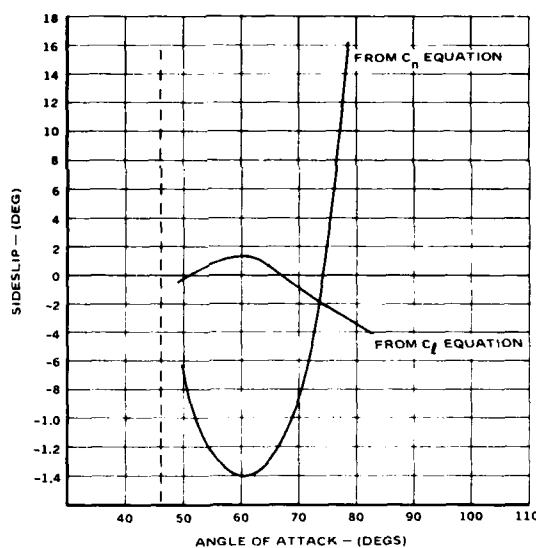


FIGURE 3-17. STEADY-STATE SPIN PREDICTION

The values of p and r corresponding to these points are presented in Figure 3-18. Six degree of freedom computer results are shown for comparison. The values of r and α are in fair agreement. The predicted values of roll rate are not in good agreement and no explanation is offered at this time.

c.g.	δ_H	δ_a	δ_n	PREDICTED SIMPLIFIED METHOD			PREDICTED 6 DOF COMPUTER		
				$r(^{\circ}/\text{SEC})$	$\alpha(^{\circ})$	$p(^{\circ}/\text{SEC})$	$r(^{\circ}/\text{SEC})$	$\alpha(^{\circ})$	$p(^{\circ}/\text{SEC})$
16%	-20	0	0	178	72.5	56	173	83	20
22%	-20	0	0	168	73.5	49	154	84	17

FIGURE 3-18. PREDICTED STEADY-STATE SPIN

3.3.2 Side Area Method

Reference 19 presents a method where the ratio of aircraft side area and aircraft mass properties are combined to predict whether the steady spin will be oscillatory or smooth (see Figure 3-19). It is well known that if an aircraft has an oscillatory spin, recovery is much more probable.

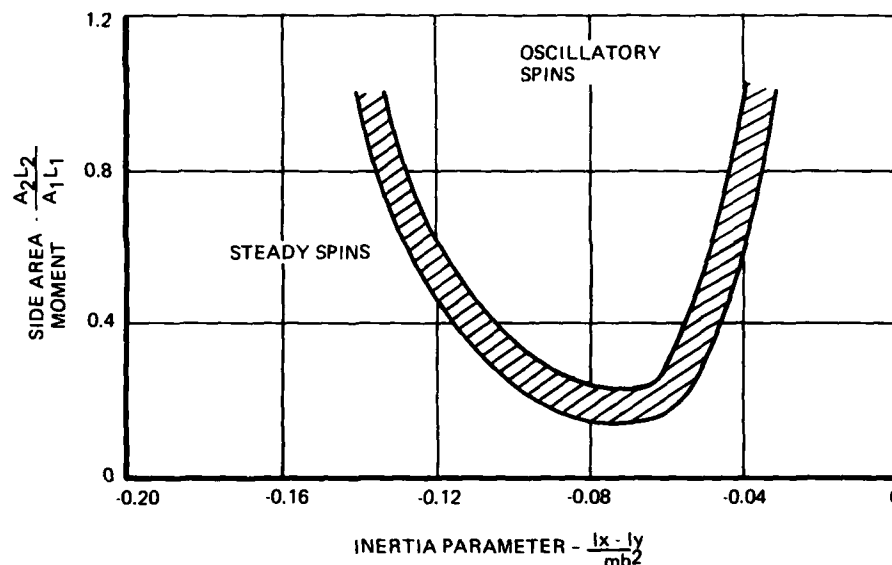


FIGURE 3-19. SIDE AREA EFFECT ON SPIN CHARACTERISTICS

3.3.3 Six Degree of Freedom Analysis

Six degree of freedom studies similar to vertical tunnel tests can be accomplished to determine the steady spin characteristics of an aircraft as described in Section 3.2.2. The resultant aircraft motion from initial values of yaw rate and angle of attack with various control inputs can be analyzed to determine whether the aircraft will have a steady oscillatory or smooth spin. Because the aircraft is in a spinning condition, non-linearity of the aerodynamic data due to rotational rates must be considered. This information can be obtained from rotary balance tests described in paragraph 2.1.2. A correlation between vertical tunnel, computer and flight test results is shown in Figure 3-20.

ITEM	PREDICTION		
	SPIN TUNNEL	COMPUTER	FLIGHT TEST
ANGLE OF ATTACK	+75° TO +85°	75°	84°
WING TILT	±7° (SMOOTH)	LARGE & OSCILLATORY (CAN PROGRESS TO SMOOTH ±3°)	LARGE & OSCILLATORY (CAN PROGRESS TO SMOOTH ±3°)
SPIN RATE	169°/SEC	175°/SEC	160°/SEC
AXIS	CG	CG	CG
SINK RATE	236 FT/SEC	260 FT/SEC	280 FT/SEC

FIGURE 3-20. STEADY-STATE SPIN CORRELATION

3.4 Spin Recovery

3.4.1 Inertial/Tail Damping Power Factor (TDPF)

The TDPF criterion was developed for application to light aircraft and trainers. The criterion considers spin recovery characteristics for the aileron neutral case only. The definition of TDPF is illustrated in Figure 3-21 taken from Reference 19. The criterion boundaries are shown in Figure 3-22 and indicate satisfactory recoveries above the boundary and both satisfactory and unsatisfactory recoveries below the boundary. The boundary definition considers a 2-1/4 turn or less recovery by rudder reversal as satisfactory.

The evolution of the TDPF relates to work done in the 1930's and 1940's, both at RAE and at NACA. Much experience has been gained since the criterion was first published. It has been found that some other factors other than tail geometry can have a dominating effect on recovery characteristics from spins. Fuselage shape, including

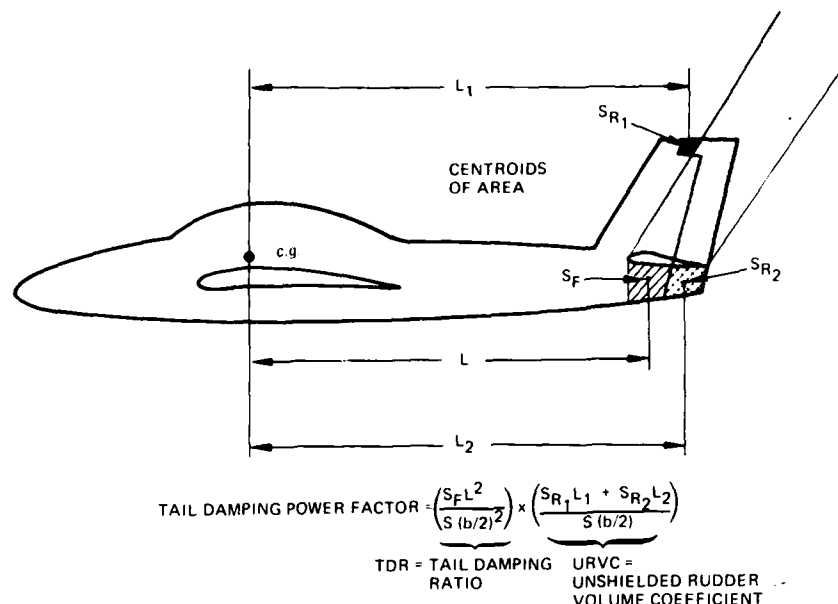


FIGURE 3-21. TAIL DAMPING POWER FACTOR (TDPF) DEFINITION

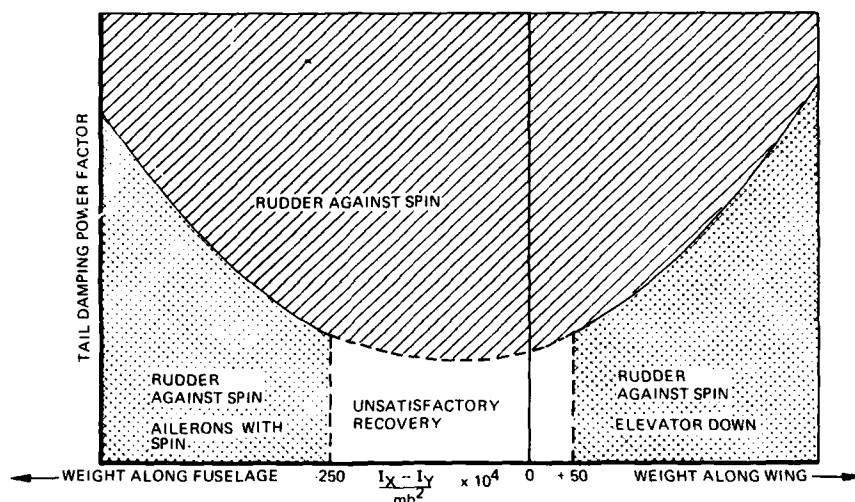


FIGURE 3-22. CONTROL MOVEMENT FOR SPIN RECOVERY

both the forebody and afterbody, can have a significant effect on recovery as can the center of gravity position, aileron deflection and tail length. It is not recommended to use TDPF solely as a prediction of spin recovery but it can be used as a guideline for tail design. As shown in Figure 3-22, inertia distributions of wing heavy configurations favor recovery from spins with rudder and inertia distributions of fuselage heavy configurations favor aileron recoveries.

3.4.2 Negative LCDP

As presented in Section 3.1.3 large negative values of LCDP promote spin entry from aileron inputs. This same mechanism promotes spin recovery for aircraft that rely on aileron for recovery. Spin recovery control techniques that require aileron inputs with the spin or in the direction of yaw rate, produce yaw accelerations in the anti-spin direction, thus promoting spin recovery.

3.4.3 Six Degree of Freedom Analysis

Once the steady spin correlation has been identified on the computer, spin recovery from these conditions can be investigated. From the steady spin condition various control inputs (aileron rudder and pitch) can be used and the resultant recovery characteristics determined. See Figure 3-23. Non-linearity of the aerodynamic control power due to rotational rates must be identified using rotary balance techniques to improve the computer to flight test correlation. Spin recovery comparisons between the six degree of freedom analysis, vertical spin tunnel tests, drop model tests, RPRV and flight test are shown in Figure 3-24.

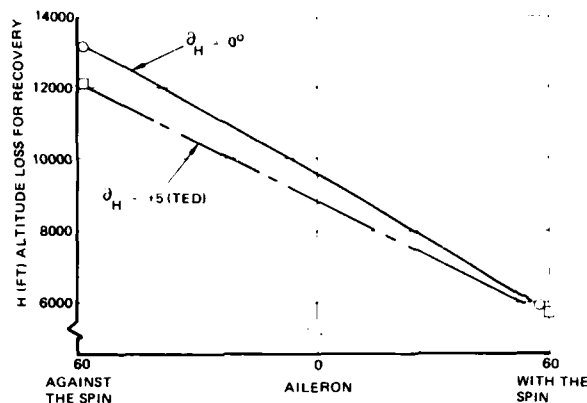


FIGURE 3-23. EFFECT OF RECOVERY CONTROL POSITIONS

SPIN MODES	COMPUTER	SPIN TUNNEL	DROP MODEL	RPRV	FULL SCALE
OSCILLATORY	--	REC BY δa , $\delta r = 1.2$	$\frac{1}{2}$, $2\frac{1}{4}$	NA	$2\frac{1}{2}$
SMOOTH HIGH α	$4\frac{1}{2}$	REC BY δa , $\delta r = 4.5$	$3\frac{1}{2}$	4.5	$3\frac{1}{2}$, 5

FIGURE 3-24. CORRELATION OF MODELS AND FULL SCALE

4.0 ANALYTICAL/EXPERIMENTAL/FLIGHT TEST CORRELATION

The following section presents an example of a development program for an aircraft modification which was conducted in a very compressed time frame. Approximately 4 months time elapsed between the development of the configuration and the completion of a verification spin test program. In light of the limited time available, the experimental test techniques used consisted of low speed static wind tunnel tests and selected water tunnel studies. No forced oscillation or rotary balance testing was performed; damping derivatives were estimated from static wind tunnel build up data. No vertical spin tunnel tests or drop model or tethered model tests were performed. In addition, no pilot in-the-loop simulation was conducted.

Analytical prediction techniques employed included a study of $C_{n\dot{\delta}}$ DYN and LCDP values, an analysis of aerodynamic asymmetries, r - α boundary determination, the Kalviste stability criterion and digital 6 degree of freedom open loop maneuver simulation.

The flight tests which were conducted thoroughly evaluated the departure and spin characteristics and provided a basis for a critical evaluation of the prediction techniques used.

4.1 Experimental Studies

The favorable contribution of properly shaped aircraft forebodies to flying qualities at high angles of attack has been the subject of considerable analysis in the past. In Reference 4, NASA investigated the F-5A nose shape and found it to be the major contributor to the directional stability of the aircraft above the stall angle of attack as shown in Figure 4-1. The primary cause of this stabilizing effect was found to be the unique orientation which the forebody vortex system assumes when the aircraft is sideslipped.

As discussed in Section 3.2.1, sufficiently long forebodies can produce vortices of such strength that they assume an asymmetric orientation at zero sideslip. The most common means of ensuring that the forebody vortices will shed symmetrically at zero sideslip has been the use of thin strakes placed on the maximum half-breadth of the forebody. Unfortunately, in many cases these nose strakes prevent the formation of the unique vortex orientation at nonzero sideslip, eliminating the positive directional stability contribution of the forebody. This is illustrated in Figures 4-2 and 4-3.

As a part of Northrop's ongoing research into forebody/wing vortex interactions, a special forebody shape and wing leading edge extension (LEX) planform were developed which together produce a vortex system which is symmetric at zero sideslip and which retains (or actually enhances) the favorable stability effects at nonzero sideslip. The forebody geometry is called the "Shark Nose" due to its flat, broad nose, resembling the nose of a shark and the LEX planform is denoted by its wind tunnel model part number, "W6." The combination will henceforth be referred to as "Shark Nose/W6 LEX." The Shark Nose geometry is depicted in Figure 4-4 and the W6 LEX planform in Figure 4-5.

The effect of the Shark Nose/W6 LEX on post-stall aerodynamic asymmetries is shown in Figure 4-6. Body-axis yawing moment at zero sideslip is reduced from a maximum value of 0.10 to a maximum of approximately 0.01 at angles of attack below 60 degrees angle of attack. This reduction is even more positive than that provided by radome strakes as illustrated in Figure 4-2.

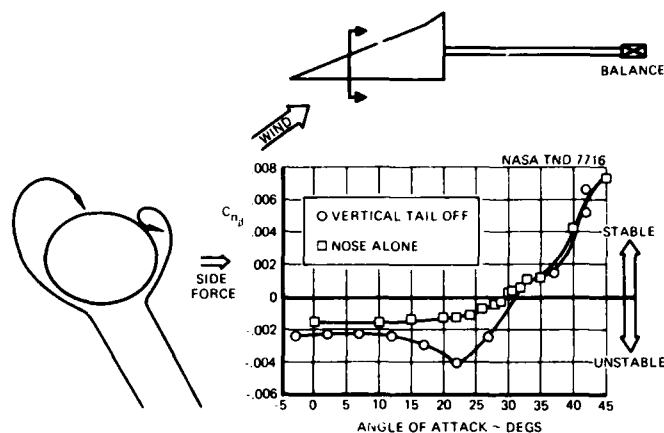


FIGURE 4-1. NOSE EFFECT ON STABILITY

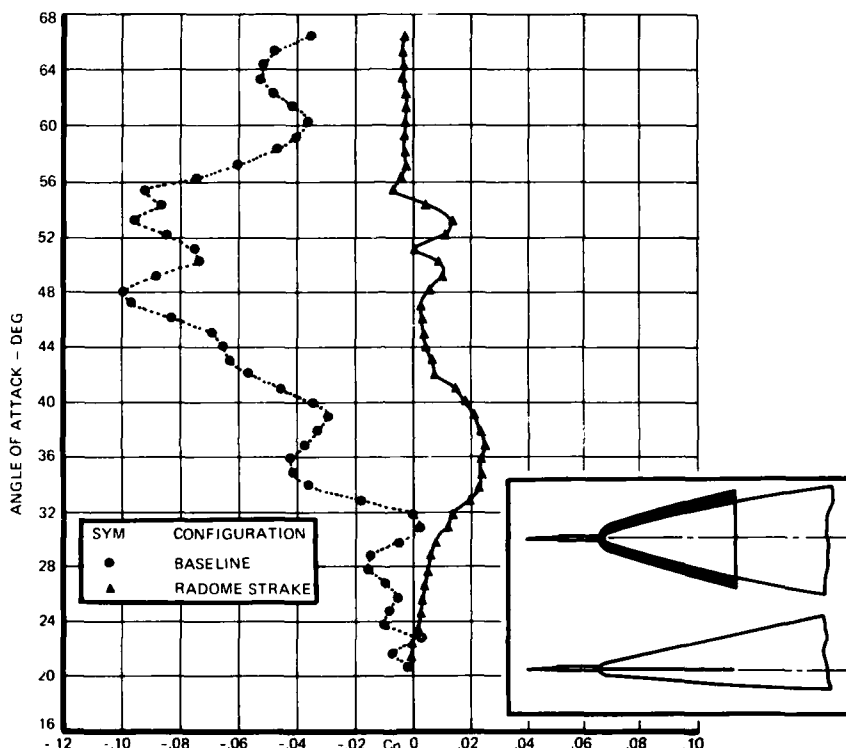


FIGURE 4-2. STRAKE EFFECT ON AERODYNAMIC ASYMMETRIES

The effect of the Shark Nose on directional stability at an angle of attack of 46 degrees is shown in Figure 4-7. Not only is the stability dramatically increased, but the $\beta = 0$ offset is eliminated.

4.2 Analytical Prediction

Figure 4-8 illustrates the effect of the Shark Nose alone and in combination with the W_6 LEX on the minimum value of $C_{n\beta_{DYN}}$ in the stall. The Shark Nose geometry causes the favorable stability influence due to the nose to become effective at a lower angle of attack when compared to the basic nose. The W_6 LEX is responsible for delaying the unfavorable breakdown in the LEX vortex to a higher angle of attack when compared to the basic LEX. When the Shark Nose/ W_6 LEX are combined, a very desirable benefit is produced with no local dip in $C_{n\beta_{DYN}}$. The effect of the Shark Nose/ W_6 LEX on LCDP is shown in Figure 4-9.

An analysis of the three-axis coupled stability characteristics of the Shark Nose was performed using the method of Kalviste (Reference 16). This method is briefly discussed in Section 3.1.4. Figure 4-10 presents a summary of the results of this analysis. The basic aircraft exhibits a tendency to trim at a nonzero value of sideslip and displays large regions of angle of attack and sideslip where local instabilities are present. The Shark Nose, however, exhibits a tendency to trim at much smaller values of sideslip (due to its symmetric vortex formation) and also has few regions of local instabilities. Figure 4-10 does not illustrate the relative levels of local instability of the Shark Nose and Basic Nose but does clearly indicate that the Shark Nose departure tendencies would be improved over the Basic Nose configuration.

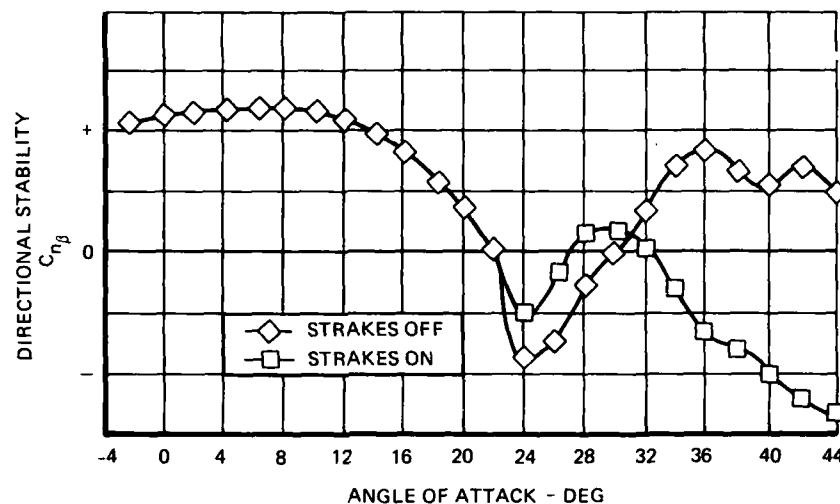


FIGURE 4-3. STRAKE EFFECT ON STABILITY

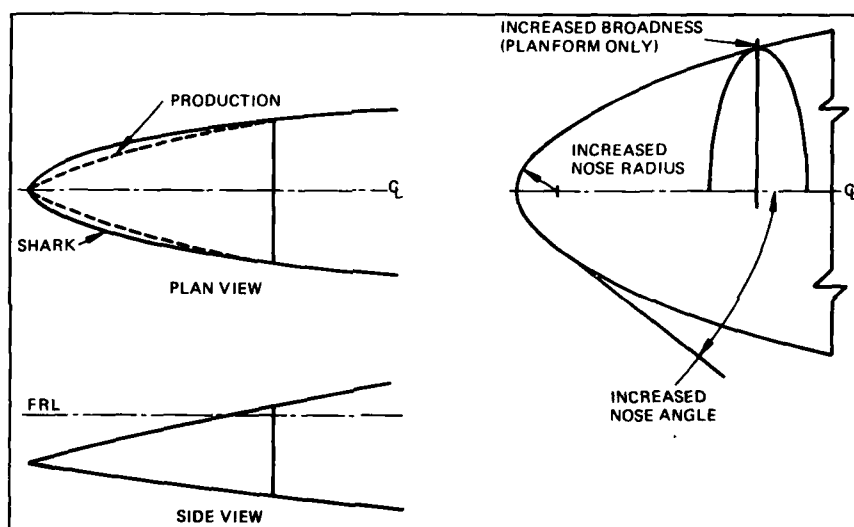
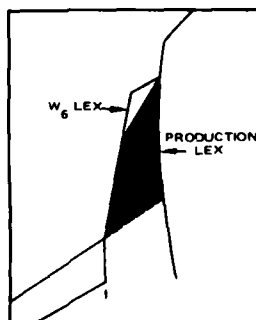


FIGURE 4-4. SHARK NOSE GEOMETRY

FIGURE 4-5. W_6 LEX GEOMETRY

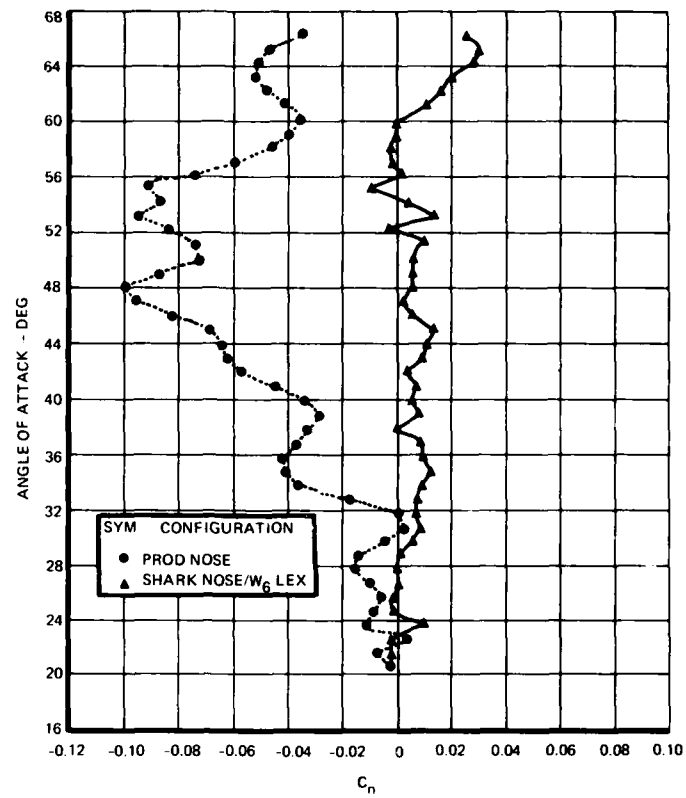


FIGURE 4-6. SHARK NOSE EFFECT ON AERODYNAMIC ASYMMETRIES

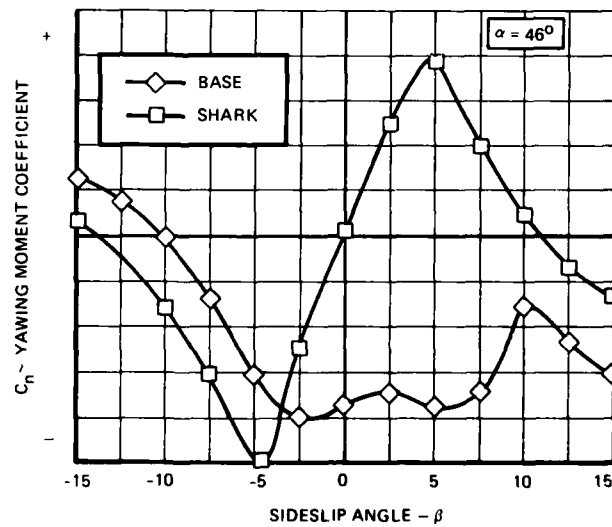


FIGURE 4-7. SHARK NOSE EFFECT ON STABILITY

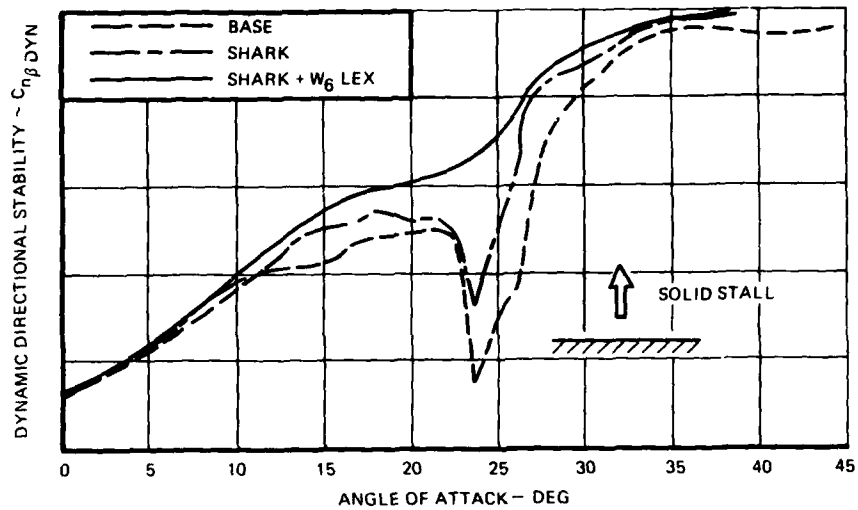


FIGURE 4-8. DYNAMIC STABILITY COMPARISON

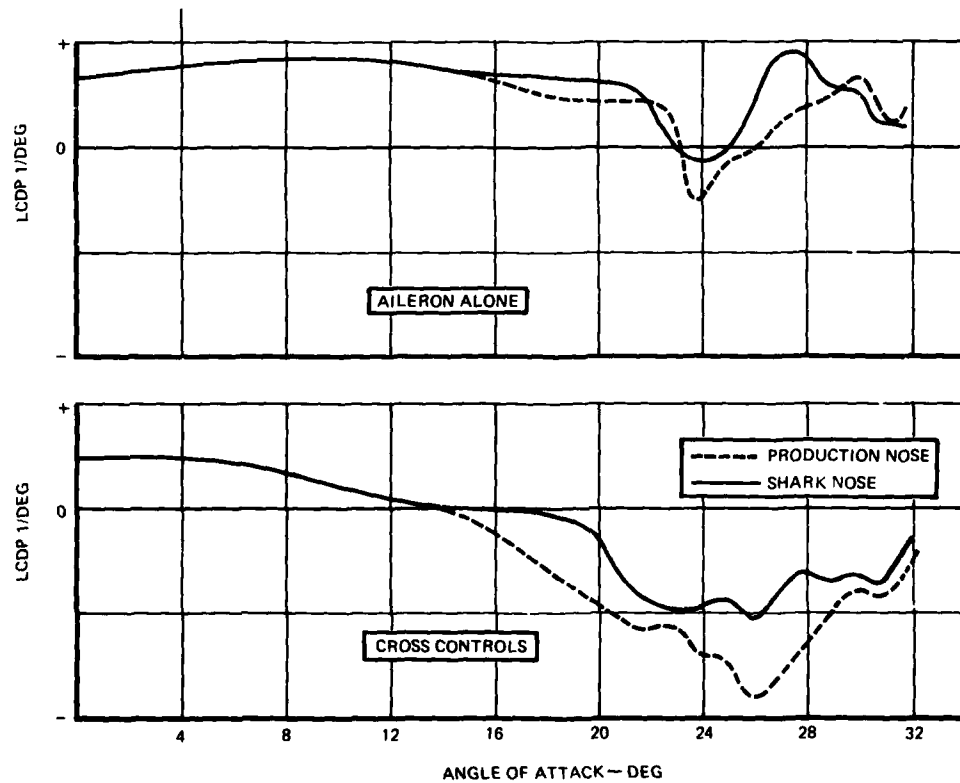


FIGURE 4-9. SHARK NOSE EFFECT ON LCDP

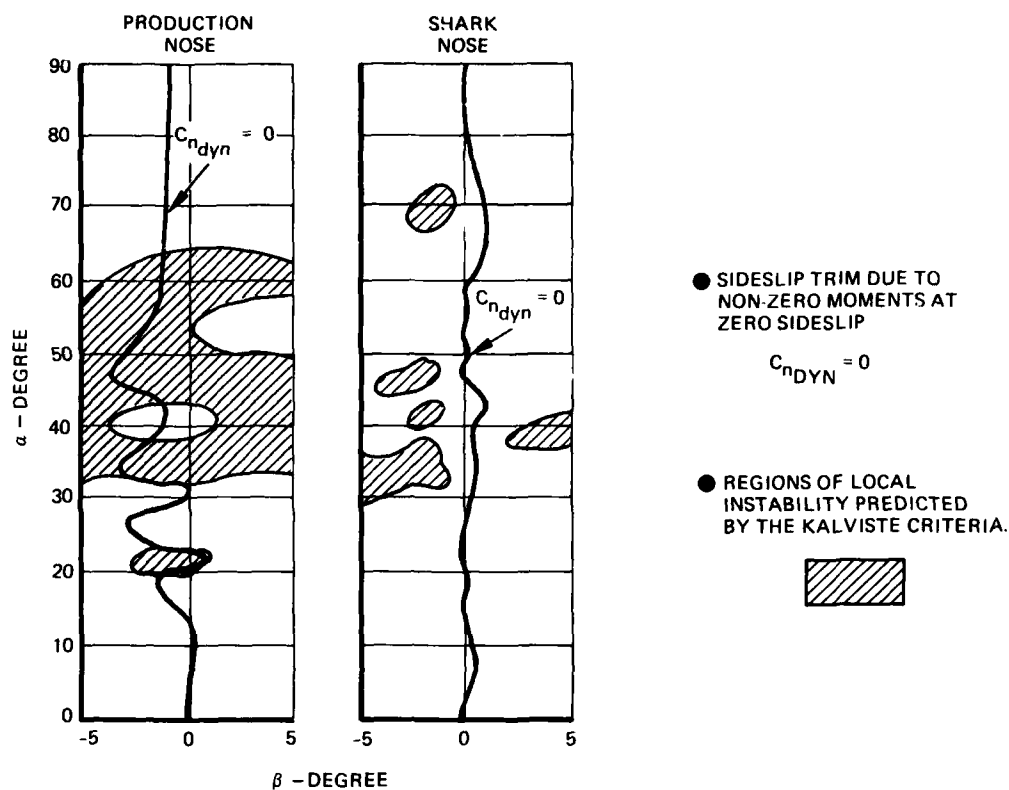


FIGURE 4-10. EFFECT OF SHARK NOSE ON COUPLED STABILITY PARAMETERS

Figure 4-11 shows the effect of the Shark Nose on analytical spin-entry boundaries, indicating an increased level of spin resistance.

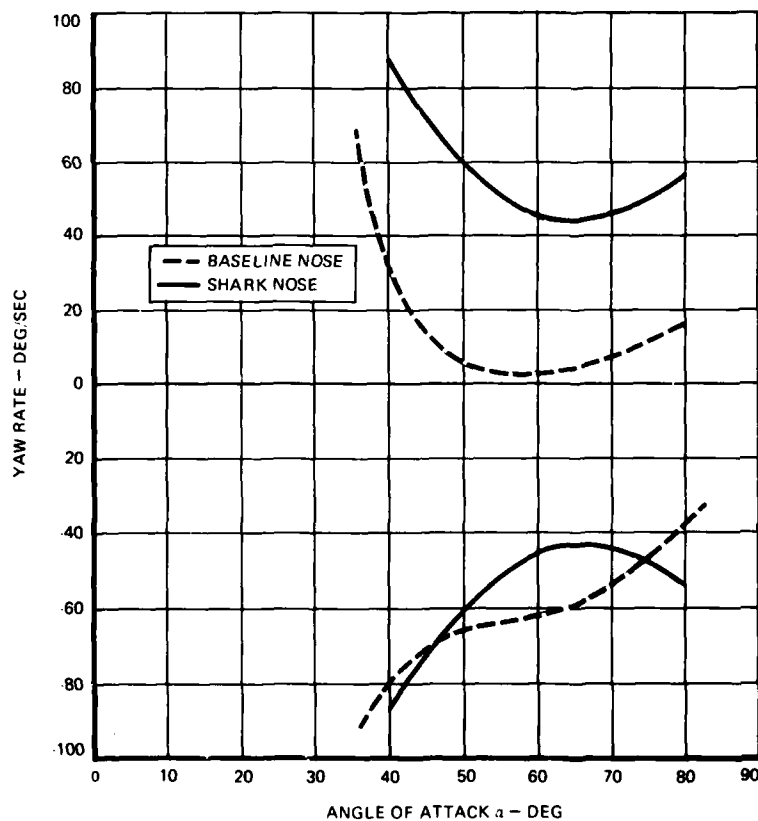


FIGURE 4-11. SHARK NOSE EFFECT ON ANALYTICAL SPIN ENTRY BOUNDARY

Figure 4-12 presents one selected time history from an extensive open-loop 6 DCF analysis of the Shark Nose/ W_6 LEX. The maneuver simulated was the abrupt application of full nose-up horizontal stabilizer at time $t = 0$ from a trim condition at 150 knots at 35,000 feet altitude. No lateral-directional control inputs were applied. Full-up stabilizer was maintained throughout the maneuver. Only yaw rate and angle of attack are presented here. The aerodynamic data package for this simulation consisted of unaltered small scale low speed, static wind tunnel data with estimated rotary derivatives (strip theory method). As can be clearly seen in the figure, the base configuration experiences a large, uncommanded increase in yaw rate at $t = 2.3$ seconds as an angle of attack of approximately 45 degrees is attained. This yaw rate couples inertially with roll rate (not shown) to produce a further increase in angle of attack, producing a spin condition. The same control inputs to the Shark Nose/ W_6 LEX configuration produces a higher initial angle of attack, but no uncommanded yaw departure, and the angle of attack begins to converge to a full aft stick trim value of approximately 30 degrees.

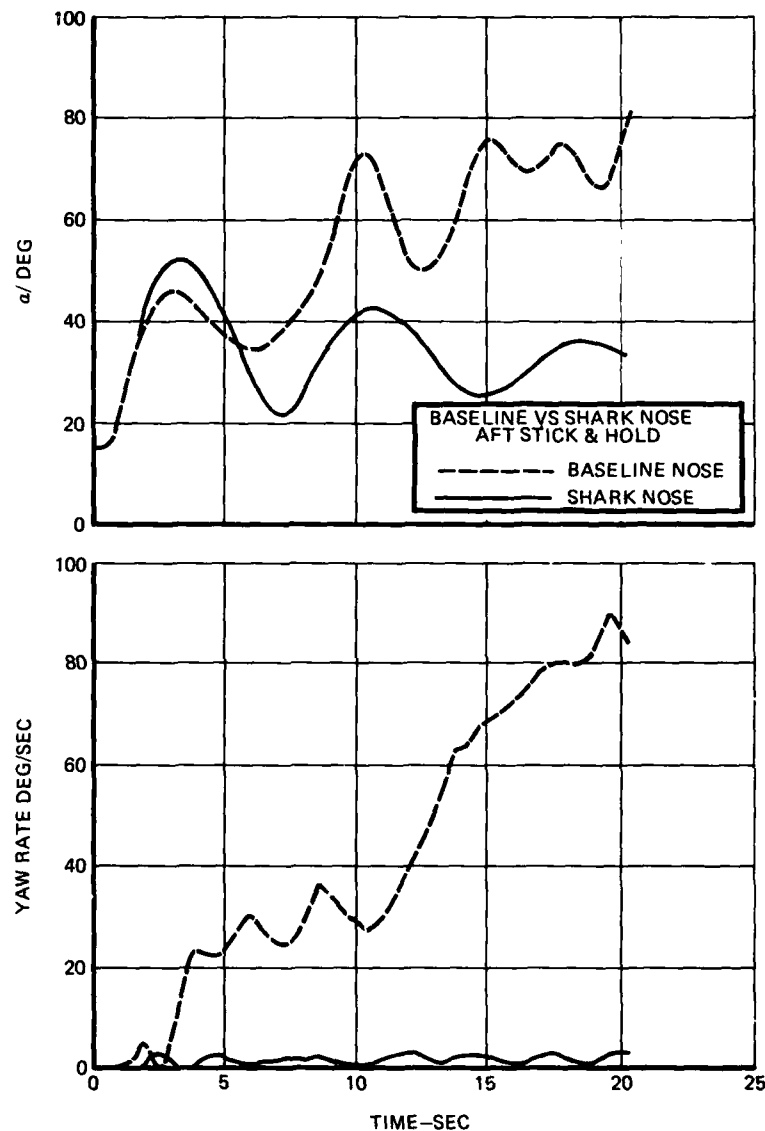


FIGURE 4-12. DIGITAL 6 DOF SIMULATED MANEUVER — EFFECT OF SHARK NOSE

The results of this maneuver and many others indicated a dramatic increase in departure resistance could be expected from the Shark Nose/ W_6 LEX configuration when compared to the baseline.

4.3 Flight Tests

Based on the small scale experimental tests and analytical predictions, a full scale Shark Nose was constructed and a flight test investigation of its effects was made using a specially modified spin test aircraft. Figure 4-13 presents a photograph of the Shark Nose alongside the basic nose. Figure 4-14 presents a photograph of the W_6 LEX. Figure 4-15 presents a photograph of the test aircraft. The results of this flight program verified the analytical predictions and confirmed that the nose vortex system had been stabilized and the asymmetric yawing moments previously experienced were eliminated.

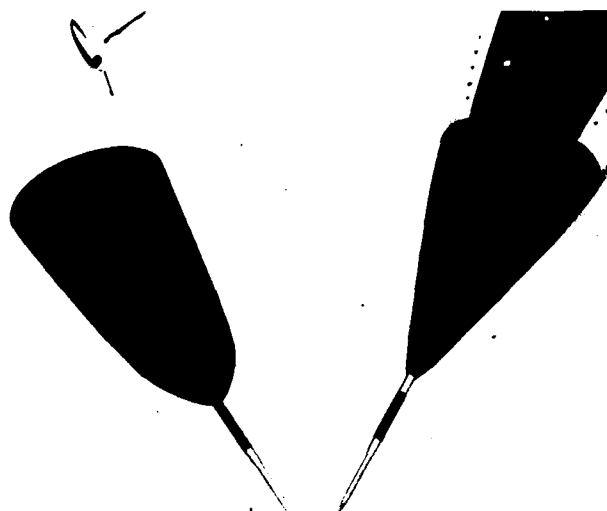
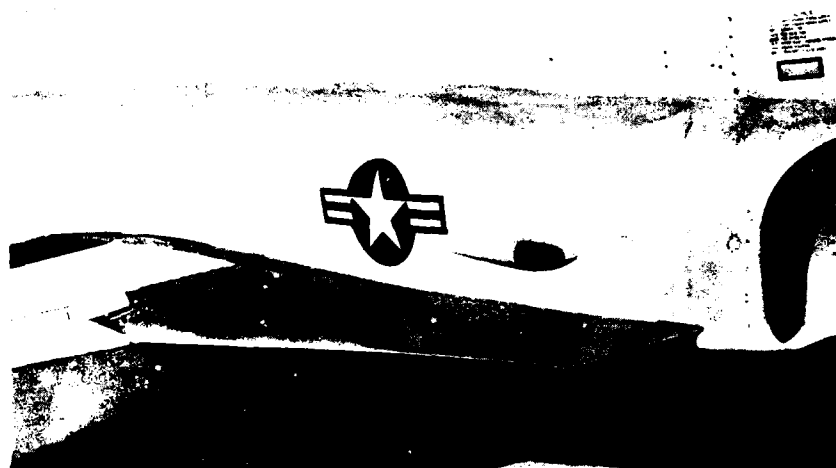
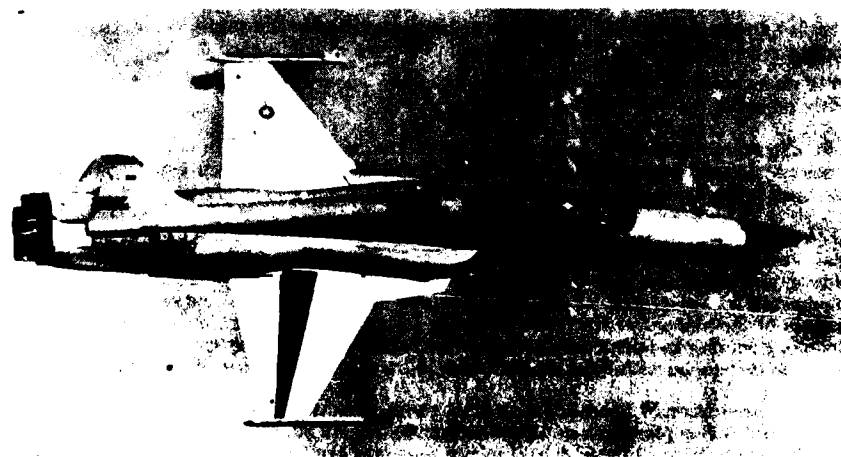


FIGURE 4-13. COMPARISON OF SHARK NOSE AND PRODUCTION NOSE



77-00927-5

FIGURE 4-14. W₆ LEX



C-658-77

FIGURE 4-15. FLIGHT TEST VEHICLE WITH SHARK NOSE AND W₆ LEX INSTALLED

4.4 Analytical Flight Test Comparison

Figures 4-16 and 4-17 present a comparison of full scale flight test results with 6 DOF simulation for two maneuvers. Figure 4-16 is a longitudinal stick snap similar to that described in Figure 4-12 but with slightly different initial conditions. The exact flight test control inputs and initial condition were used in the digital simulation. The agreement shown is excellent. Figure 4-17 is a 1 g stall, and again, except for a slight phase discrepancy in roll angle, the agreement is excellent.

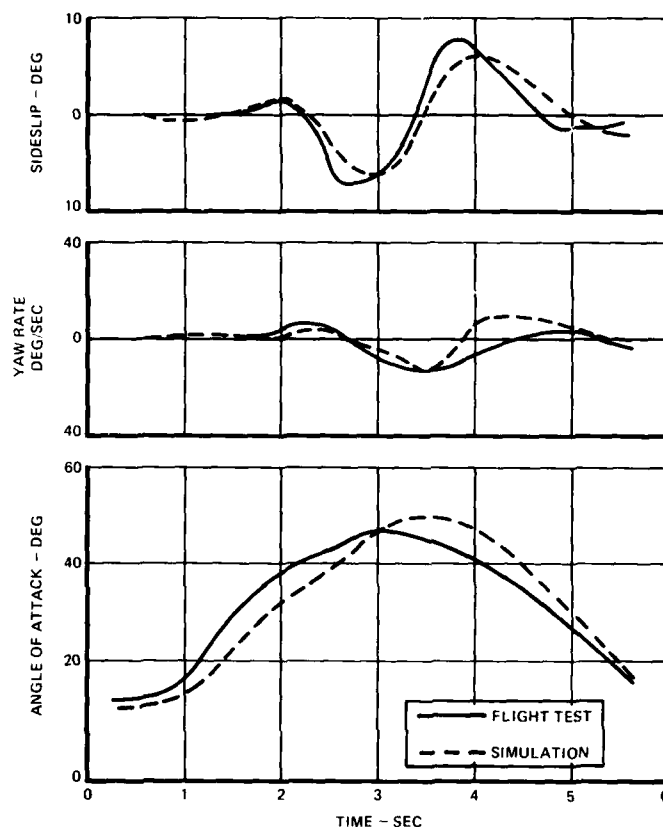


FIGURE 4-16. DIGITAL/FLIGHT TEST CORRELATION
STICK SNAP MANEUVER

5.0 SYNOPSIS

This section highlights the points made in the paper concerning prediction techniques and recommended further studies.

5.1 Stall/Post-Stall Prediction

Early in the design phase when the available experimental data base usually consists of static wind tunnel data only, the best analysis tools which can be used with some degree of confidence are $C_{N\beta}$, C_{DYN} , LCDP and $C_m|\beta|$. When the effects of these parameters are considered together, accurate prediction of stall/post-stall departure tendencies can usually be made.

The Kalviste criterion can further improve the prediction accuracy at this stage of the design development by analyzing non-linear static wind tunnel data in a manner which takes into account coupling between the longitudinal and lateral-directional degrees of freedom.

Later in the development of an aircraft, more data become available to the engineer and the level of confidence can be improved. For instance, when the aircraft's dynamic stability derivatives are known, the characteristics of wing rock oscillatory motion can be more accurately estimated. The effects on dynamic stability derivatives of such parameters as frequency and amplitude of oscillation can be factored into the analysis if these data are available. However, regardless of the amount of static and dynamic wind tunnel data available, there exists today no consistent prediction methodology which can accurately estimate the highly coupled wing rock oscillations of an aircraft. Such a methodology should be developed with due consideration to the fluid mechanics of the phenomenon.

A very accurate prediction of the stall/post-stall characteristics of an aircraft can be derived from very sophisticated experimental test techniques such as the wind tunnel-free flight model technique or the remotely piloted drop model technique. However, both of these experimental methods are time consuming and costly, usually being performed very late in the development phase; sometimes after the first flight of the prototype.

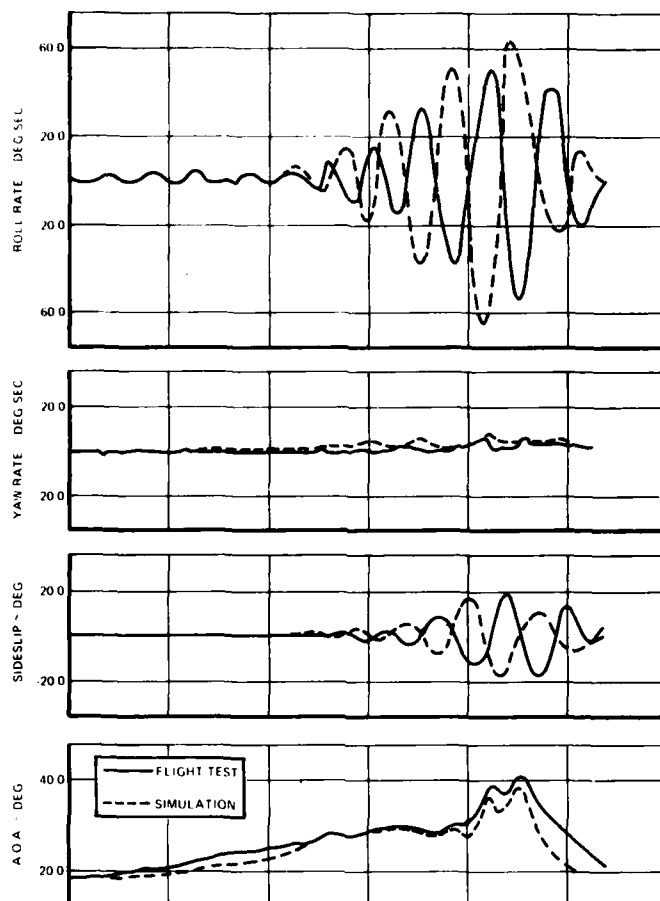


FIGURE 4-17. DIGITAL/FLIGHT TEST CORRELATION 1.0g STALL MANEUVER

Pilot in-the-loop effects and the effects of complex, highly augmented automatic control systems must be analyzed by manned simulation. Again, this can be a costly experimental procedure, but the results in most cases correlate well with flight test and can actually save flight test development time and money and reduce risks later in the program.

5.2 Departure/Spin-Entry

This area of high angle-of-attack analysis is one where prediction methodologies have not correlated well with flight test in the past. However, it has been recently shown that aerodynamic asymmetries associated with the forebody vortex system can have a strong influence on the departure and spin-entry characteristics of an aircraft. These asymmetries can be measured in small-scale wind tunnel tests and a good correlation of onset angle of attack has been demonstrated. The effect of Reynolds number on the measured magnitude of the asymmetries is not adequately known at this time. Also, there exists no criterion for the maximum allowable asymmetry which can guide a designer.

Remotely piloted drop model tests can serve to bridge the gap in Reynolds number between wind tunnel and flight test and can help to answer the question of allowable magnitude also.

The Reynolds number sensitivity of the vortex asymmetries may not be related to a viscous phenomenon and may instead be related to an inviscid, hydrodynamic instability. If this is the case, representative flow characteristics associated with these vortex asymmetries can be studied at very low Reynolds number in a water tunnel. If an understanding of the fluid phenomenon can be developed, analysis of wind tunnel data can be done with more confidence.

Six degree-of-freedom analysis of departure and spin characteristics, either open-loop or manned, must adequately represent the aerodynamic non-linearities associated with these vortex asymmetries in order to be valid.

5.3 Oscillatory and Steady Spin

Currently the vertical wind tunnel is the most reliable method of predicting the spin modes of an aircraft. Vertical spin tunnel experiments are relatively inexpensive and many repeat runs can be obtained to establish the trends.

Best analytical predictions are derived from methods which consider the full six degree-of-freedom equations. However, the impact of rotary derivatives on the prediction of steady spin characteristics area can be critical. Rotary balance wind tunnel data should be included in any analysis. Similarly, aerodynamic asymmetries can have

a significant effect on the predicted spin characteristics and should be included in the aerodynamic model. Analytically determined spin entry boundaries in terms of yaw rate and angle of attack have shown good correlation with flight test.

5.4 Spin Recovery

Prediction methods for spin recovery have demonstrated good correlation for some aircraft and poor correlation for others. A six degree-of-freedom analysis method can be used to determine trends in recovery characteristics but should not be relied upon to predict absolute magnitudes. The experiment data base required for a good six degree-of-freedom analysis is a formidable one. Such effects as aileron effectiveness as a function of spin rate can be very important and are not generally measured.

Recovery characteristics predicted from vertical spin tunnel tests are generally quite accurate for fighter aircraft configurations. Although Reynolds number effects are determined prior to and accounted for during vertical spin tunnel tests, the remotely piloted drop model can serve to bridge the gap between the Reynolds number of the vertical spin tunnel and the full scale aircraft. Vertical spin tunnel models are generally 1/30 to 1/20 scale whereas drop models range from 1/10 to 1/3 scale.

Accurate sizing of emergency recovery systems such as spin chutes or other more advanced recovery concepts must be performed in a vertical spin tunnel.

5.5 Conclusion

Future stall/departure prediction requirements should be directed toward uncovering the tools necessary to allow the engineer to successfully design highly maneuverable fighter aircraft within the time and money constraints of the program.

Vast amounts of data, from both small scale wind tunnel experiments and small and full scale flight tests, are available on a number of aircraft. Because of many constraints, individual contractors seldom have the opportunity to fully correlate the data. Even if it is correlated it is only one segment of the total problem. All these data must be brought together, analyzed, and conclusions obtained. Individual successes with correlation between certain parameters and flight test results indicate available data may produce other pertinent relationships if the data were analyzed across the board instead of aircraft by aircraft.

REFERENCES

1. Lutze, F.H., Jr.; Marchman, J.F., III; Cliff, E.M. and Mutchler, M.S.; "The Determination of Yawing Rotary Derivatives Using a Curved Flow Testing Technique," VPI-AERO-009, Dept. of Aerospace and Ocean Engr., November 1973.
2. Lutze, Frederick H.; Curved Flow Wind Tunnel Test of a Spin-Resistant Aircraft Configuration, VPI-AERO-067, August 1977.
3. Lutze, Frederick, H.; Rolling Flow Wind Tunnel Test of a Spin Resistant Aircraft Configuration, VPI-AERO-075, December 1977.
4. Grafton, Sue B.; Chambers, Joseph R.; Coe, Paul L., Jr.; Wind-Tunnel Free-Flight Investigation of a Model of a Spin-Resistant Fighter Configuration, NASA TN-D-7716.
5. Chapman, G. T.; Keener, E. R.; Malcolm, G. N.; Asymmetric Aerodynamic Forces on Aircraft Forebodies at High Angles of Attack - Some Design Guides, AGARD CP-199, June 1976.
6. Poisson-Quinton, P.; Erlich, E.; Hyperlift and Balancing of Slender Wings, NASA TT-F-9523, August 1965.
7. Werle, H., "Possibilités Experimentales due Tunnel Hydrodynamique a Visualisation," ONERA, N.T. 48 (1958); "The Hydrodynamic Analogy Laboratory at ONERA," ONERA Publication No. 103 (1961).
8. Werle, H. and Fiant, C., "Visualisation Hydrodynamique de l'Ecoulement a Basse Vitesse Autour d'une Manquette d'Avion du Type 'Concorde'," ONERA, La Recherche Aerospatiale No. 102 (1964).
9. Werle, H. and Fiant, C., "Sur l'Eclatement des Tourbillons d'Apex D'une Aile Delta Aux Faibles Vitesses," ONERA, La Recherche - Aeronautique No. 74 (1960).
10. Poisson-Quinton, P., "From Wind Tunnel to Flight, the Role of the Laboratory in Aerospace Design," AIAA 30th Wright Brothers Lecture (January 1967).
11. Titiriga, Andrew, Jr.; F-5A Transonic Buffet Flight Test, AFFDL TR-69-110, December 1969.
12. Hwang, Chintsun; Pi, W.S.; F-5A Wind Tunnel Investigation, NAS 2-8734, December 1977.
13. Titiriga, A., Jr.; Ackerman, J.S.; Skow, A.M.; Design Technology for Departure Resistance of Fighter Aircraft, AGARD CP-199, June 1976.
14. Wiessman, R.; Preliminary Criteria for Predicting Departure Characteristics/Spin Susceptibility of Fighter-Type Aircraft, AIAA Journal of Aircraft, April 1973.
15. Greer, H. Douglass; Summary of Directional Divergence Characteristics of Several High-Performance Aircraft Configurations, NASA TN D-6993, 1972.
16. Kalviste, Juri; Aircraft Stability at High Angles of Attack, AGARD Symposium, Athens, Greece, May 1978.

17. Nielsen, J.N.; Nonlinearities in Missile Aerodynamics, AIAA Paper 78-20, January 1978.
18. Jorgensen, Leland H.; Nelson, Edgar R.; Experimental Aerodynamic Characteristics for Slender Bodies with Thin Wings and Tail at Angles of Attack from 0° to 58° and Mach numbers from 0.6 to 2.0, NASA TM X-3310, March 1976.
19. Lamers, John P.; Design for Departure Prevention, AIAA Paper No. 74-794, August 1974.
20. Burk, S.M.; Bowman, J.S.; White, W.C.; Spin Tunnel Investigation of the Spinning Characteristics of Typical Single Engine General Aviation Airplane Designs, NASA Tech Paper 1009, September 1977.
21. Neihouse, A.I., et al; Status of Spin Research for Recent Airplane Designs, NASA TR R-57, 1960.
22. Wentz, W.H., Jr.; "Wind Tunnel Investigation of Vortex Breakdown on Slender Sharp-Edged Wing," CR-98737, 1968, NASA.

PRESENTATION OF STABILITY DERIVATIVES IN
MISSILE AERODYNAMICS AND THEORETICAL METHODS
FOR THEIR PREDICTION

by
C.P. Schneider
Messerschmitt-Bölkow-Blohm GmbH
Munich

SUMMARY

This literature survey serves as a directive for present and future theoretical studies of stability derivatives of missiles. The aim is to indicate analytical procedures for the determination of pitching derivatives and coefficients essentially - of wings of arbitrary planform, of bodies of revolution and of combinations thereof in the linear and non-linear angle-of-attack range in subsonic and supersonic flow. With regard to the abundance of literature treating unsteady flow problems in general, a frame for a classification of theory for missile design in particular is prepared. Within this frame, procedures as tools for prediction rate second behind their product, i.e. the derivatives of the flight configurations of interest as functions of given flight conditions. In this investigation steady derivatives have been referred to only if needed in connection with the unsteady stability problem. The study results in a presentation of the literature on the subject in literature tables. The tables, besides rating the significance of derivatives with respect to missile stability, intend to show which derivatives of importance are available in the open literature and which not.

The prediction methods are grouped in those which lead to simple expressions for the derivatives - such as the slender body theory does - and numerical procedures - such as the panel method for example. Essentially, the methods for the prediction of pitching derivatives and for solving stability problems arising with the longitudinal acceleration of missile are described.

LIST OF SYMBOLS

a	speed of sound (table 3.1)
c, c_o, \bar{c}	total body length, wing root chord, aerodynamic mean chord of wing
f	natural frequency (table 3.1)
f_o, f_1	functions according to ref. 14 (fig. 3.10 and eqs. 5 - 8)
k, k'	reduced frequency: $k = \frac{qc_o}{V}$ or $\frac{qc}{V}$, $k' = kD_o/c$ (chapter 3.1, table 3.1, figs. 3.37 - 3.39)
l	length (table 1.1)
m	parameter specified in ref. 14, $m = \beta \cdot \tan \delta$ (fig. 3.10)
p, q, r	angular velocities (fig. 1.1)
u, v, w	translational velocities (fig. 1.1)
\bar{v}	term specified in ref. 5 (chapter 3.2.2, eqs. 9, 10, 12)
A	altitude (table 3.1)
AR	aspect ratio
C	aerodynamic coefficient of forces and moments and their derivatives (tables 1.1, 2.2, figs. 1.1, 1.2)
C_N	normal force coefficient (table 1.1)
$C_{N\alpha}, C_{N\delta}$	linear normal force slope, non-linear normal force coefficient, wing reference area S , body reference area $S_o = \pi D_o^2/4$ (table 1.1, figs. 3.29, 3.30, 3.37-3.39)
$C_{Nq}, C_{N\dot{\delta}}$	normal force damping coefficients, wing reference length and area \bar{c} , S , body reference length and area D_o , $S_o = \pi D_o^2/4$ (table 1.1)
C_m	pitching moment coefficient (table 1.1)
$C_{m\alpha}, C_{m\delta}$	linear pitch stiffness, non-linear pitching moment coefficient; reference lengths and areas are the same as for $C_{Nq}, C_{N\dot{\delta}}$ (table 1.1, figs. 3.29, 3.30)
$C_{mq}, C_{m\dot{\delta}}$	pitch damping coefficients, reference lengths and areas see $C_{Nq}, C_{N\dot{\delta}}$

C_{Nc}	normal force correction term specified in ref. 64 (fig. 3.6, eq. 3)
$(C_{m_c})_0$	moment correction term specified in ref. 64 (fig. 3.6, eq. 4)
C_L, C_D	lift and drag force coefficients (fig. 1.2)
D_0, D_{max}	body base diameter, maximum body diameter (figs. 3.1, 3.39)
F, G	functionals according to ref. 99
F_1	indicial function area (fig. 3.31, chapter 3.4)
F_2	indicial function area (fig. 3.31, chapter 3.4)
$K_{B(W)}$	interference factor specified in ref. 126, $K_{B(W)} = N_{B(W)}/N_W$ = body normal force due to wing interference/wing normal force (chapter 3.6)
M	Mach number
Re	Reynolds number
S	surface area
$T, \Delta T$	time, constant time lag specified in ref. 85 (chapter 3.4)
V	resultant velocity (fig. 1.2)
\ddot{V}	acceleration (fig. 4.1, chapter 4)
X, Y, Z	coordinates (fig. 1.3)
X_p, X_1, X_2	locations of pitching axis (fig. 3.28, eq. 13)
X_N, X_{Pr}	location of neutral point (fig. 3.5, chapter 3.2.1), location of pressure point (fig. 4.1, chapter 4)
$\alpha, \dot{\alpha}$	angle of attack $\sin \alpha = w/V$, time derivative of α , (fig. 1.2)
β	angle of sideslip (fig. 1.2)
β	Prandtl-Glauert factor, ref. 14
γ	Euler constant, $\gamma = 0.5772$, used in ref. 5 (chapter 3.2.2, eqs. 9, 10, 12)
δ	leading edge sweep angle according to ref. 14, angle between leading edge and root chord of the wing (chapter 3.2.2)
ϵ	thickness parameter, maximum wing thickness divided by root chord length c_0 (figs. 3.26, 3.27, chapter 3.4)
λ	wing taper ratio
ξ, η, ζ	dimensionless coordinates, refs. 85, 90 (chapter 3.4)
ξ	running variable in time, ref. 99 (chapter 3.4)
τ	time variable, ref. 99 (chapter 3.4)
Δ	deviation from mean value (fig. 3.25)
Γ	parabolic constant, ref. 56 (fig. 3.26, chapter 3.4), vortex strength, refs. 85, 90 (chapter 3.4)
ϕ	potential
ϕ, θ, ψ	roll, pitch and yaw angle (fig. 1.1)

1. INTRODUCTION

"Unsteady" is the comprehensive designation of the property of a flow with superimposed time dependent and time independent components. The results of the superposition may be a flow whose properties changes slowly with time. In this case, the forces on an immersed body may be considered as first order functions of the steady flow conditions. Their dependence on flow rates is significant only to second order. These forces are quasi-steady. In case of rapidly changing flow conditions, the forces are strongly dependent on the rates of the flow properties. A time varying angle of attack ($\dot{\alpha}$) for instance causes the forces to accept terms depending on the vertical acceleration. These terms are "unsteady" in the true sense of the designation. The terminology of the independent dynamic variables u, v, w, p, q, r is chosen in accordance with notations which are common in the literature. The translatory velocity components u, v, w point in the positive direction of the space coordinates X, Y, Z . The rotatory velocity components p, q, r are related to the space angles ϕ, θ and ψ . The flight mechanical notations and coordinate system in figs. 1.1 and 1.2 where the body axes coincide with the geodetical axes are common in experimental aerodynamics. The body fixed system with reversed X and Z shown in fig. 1.3 is often used in theoretical aerodynamics, so it is in the present paper.

Steady and unsteady aerodynamic forces and moments being single valued and monotonous functions of independent variables (of the flight condition) over a specified time interval, can be developed in a series. In the case of linear dependence on the state variables, the coefficient derivative series of the normal force and the pitching moment are listed in table 1.1. Numerous derivatives result in such a development, but only few are significant for the flight stability (refs. 1 and 2). Still a large number of derivatives remain, any single of which is dependent on various flow properties and body

parameters. The first task arising with this study is therefore the design of a frame work which allows a survey of the derivatives and influence parameters important to missile stability.

2. FRAME WORK FOR A CLASSIFICATION OF LITERATURE ON AERODYNAMIC "MISSILE" DERIVATIVES

The diagram of fig. 2.1 serves this purpose. Here, the aerodynamic derivatives are grouped in two major sections, experimental and theoretical. For detailed partitioning according to physical and mathematical view points, the theoretical terminology is more appropriate than the experimental, as the latter cannot specify the various conditions imposed on the theoretical treatment of derivatives. As example, the differences between real and ideal gas conditions defined in theory are non-existing in the experiment. In fig. 2.1 these conditions as specified in gas- and aerodynamic text books (refs. 3 - 5) are chosen as the two major partitions in the section on theoretical work. In experimental work, the differences need not be considered. Linearity and non-linearity are chosen for further classification of aerodynamic coefficients. This draws a "historical" line through literature. As the expense of treating non-linear problems theoretically as well experimentally (ref. 6) increases substantially over that needed for the solution of the linear case, non-linearity and numerical solutions by use of the computer became inseparable. A change in the present terminology is involved if a non-linearity of the normal force or the pitching moment with the angle of attack is given. In the coefficient series of table 1.1, the derivative αC_{m_0} for instance is to be replaced by the non-linear coefficient αC_{m_0} , where C_{m_0} is some function of the angle of attack. The difficulty and expense especially of the theoretical determination of aerodynamic derivatives is also dependent on the body geometry. This defines whether a flow around it can be treated as planar or as spatial problem. Therefore, in the diagram of fig. 2.1, the difference between two- and three-dimensional flow is taken into account. This defines twelve sections for the grouping of derivatives. Each section has three subdivisions according to the flight velocity. The flight velocity generally dictates the type of differential equation (refs. 7, 8, 9), which describes the flow conditions around a flight vehicle. The flight velocity is the most important parameter for flow simulation in an experiment. Therefore, in fig. 2.1 the final partitioning of derivatives is provided in terms of subsonic, transonic and supersonic flight velocity. The numbers in the partitions obtained this way denote the reports referenced in the literature list of this study.

From the diagram of fig. 2.1 is seen, that most experimental and theoretical work in the past was concerned with linear forces on flight vehicles in three-dimensional sub- and supersonic flow. In the recent literature, non-linear forces on three-dimensional flight vehicles in subsonic and supersonic flow are examined experimentally and theoretically to great extent.

Fig. 2.1 is complimented by table 2.1, which coordinates the classification of derivatives according to mathematical and physical considerations with a more practical listing for designers needs indicating the type of flight vehicle and the type of motion. The numbers in the top row of table 2.1 refer to the sections (1-12) in fig. 2.1. The topics in the first column of table 2.1 were selected with the purpose of condensing the contents in the viewed literature under the least number of headings possible. The result shows that simple components of flight vehicles such as wings and rotationally symmetric bodies are preferred in literature, to enable comparison to other data. Table 2.1 and fig. 2.1 were used to outline the scope of this survey, which is based on the literature study of ref. 10. Theoretical and experimental work on unsteady viscous flow over wings and bodies as for instance reported in ref. 11 is now receiving new attention - according to a comprehensive review on this field (ref. 12). Wings and bodies in unsteady two-dimensional flow of an ideal fluid are treated at length in text books (refs. 5, 13, 14). Results are listed in data collections such as DATCOM and the "Engineering Sciences Data Unit" (refs. 15, 16). Although of importance to missile aerodynamics, these fields are referred to only if necessary. Most current literature deals with three-dimensional inviscid flow about wings and bodies with small-amplitude motion perpendicular to the main flow. Therefore, the main part of this review (chapter 3) deals predominantly with "Theoretically determined stability derivatives of missiles, projectiles, and their components in three-dimensional flow". Linear and non-linear dependence of forces and moments on influence parameters, and the type of unsteady motion are the topics of the subdivisions. The longitudinal acceleration as additional characteristic in missile motion and its influence on the distribution of pressure or normal force over bodies and on the location of the aerodynamic center is investigated in very few reports. Some of them (refs. 17 - 20) are briefly discussed in chapter 4.

In ref. 10, the literature on derivatives of delta wings and other common wing shapes and of bodies of revolution is classified in tables. One of them on theoretical work concerning linear derivatives of delta wings in subsonic flow is reproduced here as table 2.2. It serves as sample and does not cover all reports on derivatives presented in this paper. The tables in ref. 10 give a survey of references and a rating of the significance of the derivatives on the stability of delta wings and flight vehicles with delta planforms. The derivatives of pitching and plunging motions, of yaw and roll and of coupled motions are arranged in the top row. Wing control flaps are seldom used in missile design. So, the corresponding derivatives are excluded from the tables. As the main influence parameters, the Mach number, angle of attack, reduced frequency, location of the pitching axis, aspect ratio, taper ratio and wing thickness are chosen. They are arranged in the first column. Each field obtained this way defines a derivative dependent on a specific parameter. Not all fields are meaningful. The normal force slope for instance is independent of the location of the pitching axis, so are the roll derivatives. These fields are marked with dark hatching. The fields with light hatching indicate

derivatives or parameters of minor significance to the delta wing stability. The pitching and roll inertia for instance are much less influential than the pitch and roll damping. The influence of wing parameters such as aspect ratio, taper ratio, wing thickness is small on the yaw derivatives, if the wing incidence is small. Within small angle of attack also the rolling moment derivative $C_{l_r} = C_{l_p} \sin \alpha$ - some authors use C_{l_q} instead of C_{l_r} - is negligible. According to ref. 21, the roll damping caused by yawing motion (C_{l_r}) and yaw damping caused by roll (C_{n_p}) are second order derivatives. The normal force due to rolling (C_{n_p}) becomes important only at larger wing incidence. The blank fields define derivatives and influence parameters which are of interest to missile design. Whenever literature is available, a reference number (without brackets) is filled in the appropriate field. The symbols in brackets give additional information on wing shapes deviating slightly from the triangular form, or on the notation of derivatives in the various reports - should they be different from the terminology of this review. The explanation to the abbreviations are found as footnotes with each table. In ref. 10 - the tables served as directive for the planning of theoretical work on missile longitudinal stability, i.e. for the selection of appropriate and most accurate theoretical procedures for the determination of derivatives. The tables are found useful as filing unit of available literature on unsteady missile aerodynamics. With little effort a large amount of literature can be registered on little filing space. With regard to the readiness of availability of literature in documentation centers, this appears to be a very useful means of classification.

3. THEORETICALLY DETERMINED STABILITY DERIVATIVES OF MISSILES AND PROJECTILES AND THEIR COMPONENTS IN THREE-DIMENSIONAL FLOW

The amount and variety of reported theoretical studies on unsteady flow-body-interaction requires restriction to a certain category of aerodynamic derivatives and type of flight vehicle as well and - as compensation for the lack of completeness - a brief survey on other reviews (refs. 1, 2, 7, 8, 12, 29, 31, 33, 38, 39) of unsteady fluid mechanics. This survey is given in chapter 3.3. The results of theoretical procedures are discussed here with the derivatives of longitudinal stability of wings of simple shape - such as delta wings - and of simple body forms - such as cones and ogive - cylinder configurations.

The significance of longitudinal stability derivatives chosen as guideline through this review, may be demonstrated on the example of the "evolution" of a ballistic projectile. In the initial concept, shown in fig. 3.1, a non-rolling projectile with a very simple shape was designed in order to minimize production cost. Windtunnel experiments with a static model at incidences up to 10° confirmed the effectiveness of the design. Free flight experiments and dynamic measurements showed a susceptibility to initial perturbation and revealed the alternating appearance of flow separation bubbles on top and bottom of the shoulder of the inclined body, leading to instability and - in the case of free flight - to deviations from the anticipated flight path. In the flight path prediction, the initial disturbance was simulated with the assumption of an initial low pitching frequency q_1 . A positive value of the pitch damping derivative C_{m_q} was chosen for the representation of the combined action of a time varying pitch stiffness non-linear with the angle of attack and the sum of unsteady coefficients C_{m_α} and C_{m_q} . In the final design, lifting surfaces distributed over the length of the weapon including fixed fins and a flare at the end, turned the intended simple form in a more complicated one, but provided longitudinal stability over the angle of attack range of the mission (see fig. 3.2)

3.1 Mathematical modelling of unsteady vertical motion

In general, the velocity and its change with time of the unsteady vertical motion of a rigid missile is slow compared to the cruising speed. Expressed in terms of the reduced frequency $k = q \cdot c/V$ for the pitching velocity q , a value most times smaller than 0.05 (see table 3.1) allows to treat the motion mathematically as a quasisteady one. In this case the pitching motion can be represented with a constant rotational velocity which adds a non-constant angle of attack distribution over the length of the body to the constant angle of attack at cruise velocity.

The slow or quasisteady vertical motion may be considered a special case ($k \rightarrow 0$) of harmonic pitching and plunging with small amplitude. The latter is the most frequently used model with numerical procedures as solution to the unsteady linear potential equation.

Another model which is suited to describe linear and non-linear motions as well is proposed by Tobak (ref. 32) and Belotserkovskii (ref. 33). A discontinuous - vertical steplike - change of q or α initiates the unsteady motion. Before this event the body had a steady flight phase, after it the steady phase is approached or restored in a "transient phase", where α or q may change slowly. A superposition of a sequence of steps can simulate a non-linear motion. In another version of this model, the body receives its steady cruise velocity at the same instant the vertical step occurs.

3.2 Stability derivatives of wings with harmonic pitching and plunging at low frequency

3.2.1 Delta wings in subsonic flow

The difficulty of solving an unsteady flow problem is greatly reduced if the unsteady motion occurs at low frequency $k \rightarrow 0$. All quadratic frequency terms in the unsteady potential equation and in the boundary condition become negligibly small. In the solu-

tion, only linear frequency terms are retained - for instance in the integral equation, with other words: the pressure distribution in the solution to the steady potential equation oscillates with low frequency.

This characterization is inherent in Garner's formulation of the integral equation (ref. 22), based on Multhopp's subsonic lifting surface theory, which differs from the classical one by Küssner (ref. 30) only by the frequency condition. In ref. 59, Garner and Fox present a program for the determination of aerodynamic forces and moments caused by thin wings pitching, plunging and rolling at low frequency in subsonic flow. The program is based on the theory of ref. 22 and suited for thin wings of arbitrary planform. The load is determined over four sections parallel to the wing root chord, distributed over half the wing span. Results for a low aspect ratio delta wing ($AR = 0.924$) are compared to other analytical and experimental data (refs. 14, 66, 67, 68) in figs. 3.3 and 3.4. Here, the normal force slope, pitch stiffness, normal force damping and pitch damping are displayed against the Mach number of the flight velocity. Further theoretical results for low aspect ratio delta wings in subsonic, transonic and supersonic flow are presented by Acum and Garner (ref. 60) and discussed with respect to their accuracy. Some of their data are also shown in fig. 3.4. A further example of the analytical treatment of vertical low frequency motion is given by Milne and Garner (ref. 61). An asymptotic expansion in terms of the oscillation frequency is applied to the Kernel function in the integral equation of the quasisteady subsonic lifting surface theory (ref. 22). The derivatives with respect to the frequency obtained this way are examined for continuity or discontinuity at zero frequency. The discontinuous derivatives are retained with the intention to determine the leading transient term of the asymptotic expansion for large time due to an oscillatory vertical (or upwash) velocity. The expansion has direct relevance to the use of aerodynamic derivatives. In the report by Goethert and Otto (ref. 62), various solutions to the quasisteady potential equation leading to the determination of pitching derivatives are compared on the example of delta wings. The comparison covers the theories of Schlichting and Truckenbrodt (ref. 63), Garner (ref. 22), Tobak and Lessing (ref. 64) and Ribner (ref. 65). The quasisteady method of ref. 63 for thin wings in subsonic flow makes use of a Prandtl-Glauert transformation reducing thereby the potential of a compressible flow to a potential equation of an incompressible flow. The upwash condition to the integral equation provides for an angle of attack distribution due to a constant rotational velocity about the pitching axis in addition to the steady unit angle of attack distribution. Each distribution yields a pressure distribution of its own. Results of this procedure (ref. 66) are shown in figs. 3.3 and 3.4. Ref. 64 deals with damping coefficients of thin wings of arbitrary planform. The analysis of C_{m_q} and C_{N_q} corresponds to that of ref. 63. The coefficients $C_{m_{\dot{\alpha}}}$ and $C_{N_{\dot{\alpha}}}$ are proportional to a constant vertical acceleration. The estimation of the latter derivatives is possible with a solution of the unsteady potential equation suitable for supersonic speed which is a combination of two steady-flow potentials one due to a steady pitching velocity, the other due to a steady angle of attack. A third steady flow potential is introduced for adaptation to subsonic speed, where the Kutta-Joukowski condition is to be satisfied at the trailing edge. The solution for delta wings is obtained by use of the loadings of slender wing theory which are multiplied by a chordwise correction factor accounting for the non-slenderness. Very simple expressions are derived this way. The pitch damping is given by

$$(C_{m_q})_0 = \frac{9}{8} \left(\frac{c_0}{c} \right)^2 (C_{m_{\dot{\alpha}}})_0 \cdot (C_{N_q})_0 / (C_{N_{\dot{\alpha}}})_0 \quad (1)$$

where the subscript "0" on the derivatives indicates that the terms are evaluated for an axis located at the wing apex. In eq. 1, the normal force damping is

$$(C_{N_q})_0 = -\frac{3}{2} \left(\frac{c_0}{c} \right) (C_{m_{\dot{\alpha}}})_0 \quad (2)$$

while the functions $X_N/c_0 = -(C_{m_{\dot{\alpha}}})_0 (c_0/c) / C_{N_{\dot{\alpha}}}$ and $C_{N_{\dot{\alpha}}}$ needed in eqs. 1 and 2 are displayed in fig. 3.5 as functions of the reduced aspect ratio $\beta \cdot AR$, where $\beta = (1-M^2)^{1/2}$. The unsteady damping coefficients are determined with the relations

$$(C_{N_{\dot{\alpha}}})_0 = \frac{1}{2} \left(\frac{c_0}{c} \right) \left(\frac{X_N}{c_0} C_{N_{\dot{\alpha}}} + C_{N_C} \right), \quad (3) \quad \text{and} \quad (C_{m_{\dot{\alpha}}})_0 = -\frac{9}{16} \left(\frac{c_0}{c} \right)^2 \left(\left(\frac{X_N}{c_0} \right)^2 C_{N_{\dot{\alpha}}} + (C_{m_C})_0 \right) \quad (4)$$

The correction terms C_{N_C} and $(C_{m_C})_0$ in eqs. 3 and 4 are given as functions of $\beta \cdot AR$ in fig. 3.6. Results for C_{m_q} and $C_{m_{\dot{\alpha}}}$ for delta wings with $AR = 1.45, 2$ and 4 are plotted versus the Mach number in figs. 3.7 - 3.9 respectively. They are compared to experimental and other theoretical results (refs. 55, 69). Although different approaches to solving the potential equation are chosen by Garner (ref. 22) and by Tobak and Lessing (ref. 64), the load distributions obtained with refs. 22 and 64 are the same, as demonstrated in ref. 62. The two-dimensional method of Ribner (ref. 65) determines the initial slope of the derivatives at $AR = 0$ in plots versus the aspect ratio. Without the correction terms introduced in ref. 62, the Kutta-Joukowski condition remains unsatisfied in the slender wing theory of ref. 65.

3.2.2 Delta wings in supersonic and transonic flow

Several procedures reduce the boundary value problem associated with a given plan-

form in unsteady supersonic flow to an equivalent problem in steady flow. One of them is developed by Miles (ref. 14) applying a frequency expansion to the solution of the Fourier transformed potential equation. At very low frequency, of the expanded terms only the ones of first order in frequency are retained. For a slender delta wing, Miles constructs a simple exact solution to the problem. The resulting relations for the steady and unsteady derivatives of longitudinal stability of delta wings with supersonic leading edges involve the functions f_0 and f_1 representing the zero'th and first order potentials, corresponding to a constant unit angle of attack and to the angle of attack distribution along the wing chord due to a constant rotational velocity about the pitch axis X_p . The functions f_0 and f_1 are dependent on $m = \beta \tan \delta$ (see fig. 3.10). The leading edge sweep angle δ lies between leading edge and root chord of the wing. The parameter $m > 1$ or $m < 1$ designates a delta wing as one with subsonic or supersonic leading edge respectively. The derivatives of a delta wing with subsonic leading edge ($m \geq 1$) are determined with a set of closed relations, which are used to calculate complimentary data in figs. 3.3, 3.4, 3.11 and 3.12. The damping derivatives, presented as sums $C_{Nq} + C_{N\dot{\alpha}}$ and $C_{mq} + C_{m\dot{\alpha}}$ in ref. 14 are separated into their components for $m \leq 1$ in eqs. 5-8, in order to show the influence of either $C_{N\dot{\alpha}}$ and C_{Nq} or $C_{m\dot{\alpha}}$ and C_{mq} on the wing stability, which may differ depending on the parameter m .

$$C_{Nq} = (4/\beta) (c_o/\bar{c}) \left(\frac{2}{3} f_1 - \frac{X_p}{c_o} f_0 \right), \quad (5)$$

$$C_{N\dot{\alpha}} = (4/\beta) (c_o/\bar{c}) \left[\frac{1}{3} f_0 - \frac{M^2}{\beta^2} \left(f_0 - \frac{2}{3} f_1 \right) \right], \quad (6)$$

$$C_{mq} = -(4/\beta) (c_o/\bar{c})^2 \left\{ \left[\left(\frac{X_p}{c_o} - \frac{2}{3} \right)^2 + \frac{1}{18} \right] f_0 + \left(\frac{1}{2} - \frac{2}{3} \frac{X_p}{c_o} \right) (f_1 - f_0) \right\} \quad (7)$$

and

$$C_{m\dot{\alpha}} = (4/\beta) (c_o/\bar{c})^2 \left[f_0 - \frac{3M^2}{\beta^2} \left(f_0 - \frac{2}{3} f_1 \right) \right] \left(\frac{1}{3} \frac{X_p}{c_o} - \frac{1}{4} \right). \quad (8)$$

Setting $f_0 = f_1 = 1$ in eqs. 5-8, yields the derivatives for delta wings with subsonic leading edge. The results obtained with eqs. (5-8) for a delta wing of $AR=4$ are compared to experimental data for a cropped delta wing $AR=3$, $\lambda = 0.072$ by Orlik-Rückemann and Laberge (ref. 70) in fig. 3.12. Also, in fig. 3.4, theoretical results by eqs. (5-8) are displayed.

Estimating pitching and plunging derivatives of wings in transonic flow, Landahl (ref. 5) uses a Fourier transformed differential equation, a slender wing potential as first order solution and higher order terms according to Adams and Sears (ref. 71), accounting for deviation from slenderness. The solution is simple if the requirements of a continuous leading edge slope and curvature of the wing is satisfied and if the angle of attack distribution and its first two derivatives with X have no discontinuities. The delta wing fulfils the requirements. For low frequency pitching and plunging oscillations, Landahl derives the stability derivatives from generalized force coefficients for low aspect ratio delta wings at transonic speed. The damping derivatives are

$$C_{Nq} = \frac{\pi AR}{2} (c_o/\bar{c}) \left[1 - \frac{X_p}{c_o} - \frac{\pi k AR^2}{64} \left(\frac{3}{2} - \frac{X_p}{c_o} \right) \right] + \frac{\pi AR}{2} \frac{c_o}{\bar{c}} \frac{\pi k AR^4}{4096} \left(6\bar{v} - \frac{15}{8} \right), \quad (9)$$

$$C_{N\dot{\alpha}} = \frac{\pi AR}{2} (c_o/\bar{c}) \left[\frac{1}{3} - \frac{AR^2}{64} \left(2\bar{v} + \frac{k\pi}{2} \right) \right], \quad (10)$$

$$C_{mq} = - \frac{\pi AR}{2} (c_o/\bar{c})^2 \left\{ \frac{3}{4} - \frac{5}{3} \frac{X_p}{c_o} + \left(\frac{X_p}{c_o} \right)^2 - \frac{AR^2}{64} \left[\frac{3}{8} + \pi k \left(\frac{6}{5} - \frac{9}{4} \frac{X_p}{c_o} + \left(\frac{X_p}{c_o} \right)^2 \right) \right] \right\}, \quad (11)$$

$$C_{m\dot{\alpha}} = - \frac{\pi AR}{2} (c_o/\bar{c})^2 \left\{ \frac{1}{3} \left(\frac{3}{4} - \frac{X_p}{c_o} \right) - \frac{AR^2}{64} \left[2\bar{v} \left(\frac{3}{4} - \frac{X_p}{c_o} \right) - \frac{1}{2} + \pi k \left(\frac{2}{5} - \frac{1}{2} \frac{X_p}{c_o} \right) \right] \right\}, \quad (12)$$

where $\bar{v} = \ln \frac{128}{kAR^2} - \gamma$, and $\gamma = 0.5772$ denotes the Euler constant. Similar to eq. 9 for C_{Nq} , eq. 11 may contain higher order terms in the aspect ratio (AR^4). They are not given here (following ref. 74), as an apparent misprint of the generalized force coefficients in ref. 5 cannot be eliminated without greater effort or consulting Landals original work (ref. 72). The results obtained for a delta wing with $AR = 4$ at $M = 1$ are meant as complimentary data for figs. 3.11 and 3.12. There, they are not plotted because of their relatively large amounts exceeding the scale of the ordinates. The normal force slope is $C_{Nq} = 6$, and for $X_p/c_o = 0$ the pitch stiffness ($C_{m\dot{\alpha}}$) = -6 according to ref. 5. The second order terms containing AR^2 reduce the absolute values of both derivatives by approximately 4 % of the first order term, when a low frequency $k = 0.05$ is assumed. The absolute value

of $C_{m\dot{q}} = -8.6$ by eq. 11 is 20 % lower than the value of the first order term by itself. The unsteady derivative $C_{m\dot{\alpha}} = 18.7$ provides a "positive" damping coefficient $C_{m\dot{q}} + C_{m\dot{\alpha}} = 11.1$ for a pitch axis at the apex. The normal force damping coefficient equals $C_{N\dot{q}} = 8.9$ without and 11.2 with the third order term containing AR^3 . This amounts to a 25 % increase over the value obtained from the first and second term of eq. 9. Both, the unsteady damping coefficient $C_{N\dot{\alpha}} = -18$ and the sum $C_{N\dot{q}} + C_{N\dot{\alpha}} = -9.1$ are negative.

3.2.3 Accuracy of the delta-wing derivatives, transformation of the pitch axis

For various pitch axis locations and aspect ratios, the derivatives of delta wings are displayed in figs. 3.3, 3.4, 3.7-3.9, 3.11 and 3.12. The results are either obtained from eqs. 1 - 12 (refs. 5, 14 and 64), or determined with relations from ref. 69, or taken from numerical calculations (refs. 22, 55, 66). They cover the velocity range $0 < M < 3.5$. All theoretical data collected in a single diagram for each derivative and the addition of corresponding experimental results will provide a survey on the accuracy of derivatives of delta wings. This survey may be generalized to other wing shapes, as for the numerical results the delta wing is usually chosen as "testing" shape offering the possibility of comparison to exact solutions. The collection of data in a single diagram for each derivative, requires a transformation of $C_{m\dot{\alpha}}$, $C_{N\dot{q}} + C_{N\dot{\alpha}}$ and $C_{m\dot{q}} + C_{m\dot{\alpha}}$ to a common pitch axis. This is done with relations taken from refs. 66 and 70 which are adapted to the present notation of derivatives and to the coordinate system of fig. 1.3. A common pitch axis location $X_p/c_o = 0.5$ is chosen. The shift of $\Delta X/\bar{c} = (X_1 - X_2)/\bar{c}$ from X_1 to the new axis X_2 with $|X_2| < |X_1|$ yields in case of the new damping moment

$$(C_{m\dot{q}} + C_{m\dot{\alpha}})_2 = (C_{m\dot{q}} + C_{m\dot{\alpha}})_1 + (\Delta X/\bar{c})(C_{m\dot{\alpha}})_1 - (\Delta X/\bar{c})(C_{N\dot{q}} + C_{N\dot{\alpha}})_1 - (\Delta X/\bar{c})^2 \cdot C_{N\dot{\alpha}}. \quad (13)$$

The efficiency of the transformation relations (refs. 66, 70) is demonstrated with figs. 3.13-3.16, where the derivatives of delta wings in subsonic flow are shown as functions of the pitch axis location: The theoretical results match well with measured data. The theoretical data of figs. 3.3, 3.4, 3.7-3.9, 3.11 and 3.12, complimented by the analytical results of Martin, Smith et al. (refs. 24 and 73), are collected in figs. 3.17-3.20. The common pitch axis is $X_p/c_o = 0.5$; the aspect ratios $AR = 0.9, 1.5, 2$ and 4 are chosen as parameters. The scattering of results provided by the various theories for a specific aspect ratio leads to data bandwidths, which - in the case of $AR = 0.9, 1.5$ and 2 - are transferred to the diagrams (figs. 3.21-3.24) with experimental results by refs. 9, 70, 75-80. This display enables to determine the deviation from the mean values for each derivative. For delta wings with $AR \leq 2$, the average deviations of $C_{N\dot{\alpha}}$, $C_{m\dot{\alpha}}$, $C_{N\dot{q}} + C_{N\dot{\alpha}}$ and $C_{m\dot{q}} + C_{m\dot{\alpha}}$ from the mean values are displayed in percentage as function of the Mach number $0 \leq M \leq 3$ (see fig. 3.25). The theories alone would give narrower bands of data scattering. The derivatives of fig. 3.25 include experimental results. The relatively large deviation of $C_{N\dot{q}} + C_{N\dot{\alpha}}$ is caused by the use of eq. 13 for the provision of additional values, which often are missing in theory or experiment. This procedure involves a double transformation of the coefficients $C_{m\dot{q}} + C_{m\dot{\alpha}}$ introducing two times the inaccuracy of this derivative to $C_{N\dot{q}} + C_{N\dot{\alpha}}$. The overestimation of the deviation of $C_{N\dot{q}} + C_{N\dot{\alpha}}$ is apparent in fig. 3.25. Values in the order of the deviations of $C_{m\dot{q}} + C_{m\dot{\alpha}}$ appear more appropriate.

3.3 Stability derivatives of wings with harmonic pitching and plunging at arbitrary frequency

If the frequency of the pitching and plunging motion does not permit the low frequency approximation, numerical procedures become necessary for the solution of the unsteady boundary value problem involved. Several recent reviews cover the wide scale of numerical techniques applied in the subsonic, transonic and supersonic speed range. Therefore, the stability derivatives of wings with harmonic pitching and plunging at arbitrary frequency will be discussed in connection of presenting some of the reviews on the subject.

3.3.1 Survey on numerical procedures

Surveys on numerical procedures give the refs. 1, 2, 7, 8, 12, 29, 31 and 33. Thomas' (ref. 1) and Ellisons and Hoaks (ref. 2) literature surveys rate the significance of stability derivatives. The authors of refs. 1 and 2 discuss the state of art in 1961 and '68 on the example of experimental and theoretical data which are published in DATCOM (ref. 15) and ANON (ref. 16). At this time, most analytical procedures did not consider non-linearities. As subjects

wings of large aspect ratio were treated with Multhopp's lifting line theory. Wings of small aspect ratio with taper and sweep of the leading and/or trailing edge were analyzed with the lifting surface theory of Multhopp and Garner (ref. 22) and slender pointed wings treated with the slender body theory by Cole, Margolis, Malvestuto et al. (refs. 23-25). Bodies were handled with slender body theory. Ellison and Hoak (ref. 2) and Thomas (ref. 1) as well suggested the development of half-empirical methods in order to predict non-linear and viscous flow effects and the influence of flow separation in unsteady body-flow-interaction, particularly as at this time progress was made in non-linear steady wing theory (ref. 26). Especially with missile components - slender wings, cones, ogive-cylinder configurations - their suggestions were realized in recent work (refs. 27, 28).

The review of Landahl and Stark on unsteady potential theory (ref. 29) discusses the possible forms of the integral equation mainly for subsonic and transonic wing application. Directions are given on the appropriate load function in the velocity potential:

For wings of large aspect ratio for instance the load functions of surface elements can be composed of two load functions derived from the two dimensional lifting line theory. This procedure fails in the case of wings of small or medium aspect ratio, where the load variation near the wing root cannot be simulated accurately this way. Here, load functions of a closed form as for instance given with dipoles (ref. 30) are practicable. An example for the application of this concept to the unsteady boundary value problem is the work of Laschka (ref. 51).

Reviews of Bland (refs. 7, 8) discuss linearization methods of the unsteady potential equation and numerical procedures for its solution. Ref. 7 is mainly concerned with transonic flow, ref. 8 with the entire velocity range. An abstract of linearization techniques and numerical procedures is given in table 3.2. Some of the results of numerical procedures presented (ref. 55) are displayed in figs. 3.8, 3.9, 3.12, 3.17-3.20. For the transonic flow case Bland describes the separation of the general potential equation in steady and unsteady parts, which is possible with the introduction of velocity potentials containing a main steady term and a time dependent "small perturbation" term simulating a harmonic motion. The boundary condition is given a similar treatment. The separation yields a non-linear potential equation for the steady flow and a linear one for the unsteady flow. In the transonic case, the latter contains variable coefficients, which depend on the solution of the steady flow problem. In sub- and supersonic flow, only terms with constant coefficient remain in the unsteady wave equation. Here the linearization is complete providing the degree of unsteadiness satisfies the conditions of a "small disturbance".

The review of Conlan (ref. 31) on methods predicting the longitudinal damping derivatives discusses the application of the indicial response technique (ref. 32) to slender wings. Piston theory and Allens cross flow theory (ref. 28) may be used to complete a synthesis of unsteady aerodynamic forces and moments of slender wing-body combinations.

A review on recent Russian studies concerning the solution of unsteady lifting surface problems by use of the computer is given by Belotserkovskii (ref. 33). The schematization of an aircraft in steady and unsteady flow for the purpose of modeling it and its wake for description by linearized or non-linear boundary conditions, is one of the major concerns of this report. For example: The slender wing and the circular cylinder as simplest and oldest schemes are frequently employed also in modern approaches (refs. 34, 35, 36). According to Belotserkovskii, the main deficiency of the simple schemes is that they provide only partial description of the actual configuration, which most times is much more complicated. For the complicated configurations a modelling with plane base elements is appropriate. They are the loci on the body surface where a distribution of gas dynamic singularities such as vortices, dipoles and sources satisfies the continuity equation. Methods of solution such as the integral representation of the velocity potential and the panel method in subsonic and supersonic flow problems, the discrete vortex method in subsonic flow and the "direct" method in supersonic flow (where the conditions of a boundary value problem are satisfied directly) are interpreted and discussed with regard to steady and unsteady flow problems. Some of the solutions are characterized briefly in table 3.2. For the time history of unsteady forces and moments, transient functions between an initial step deviation and the approximation of steadiness are proposed. The same approach of modelling unsteady events is suggested by Tobak (ref. 32). For the treatment of non-linear body-flow interaction, Belotserkovskii esteems the discrete-vortex method as most effective among numerical approaches. For example, results on the formation of separated flow, i.e. the development of vortex structures on rectangular and triangular wings at high angle of attack are shown.

In the review of McCroskey (ref. 12), the main areas of fluid dynamics where unsteady flow phenomena occur are covered. Some methods of analysis are discussed as in Bland's and Belotserkovskii's review. Particularly a hypothetical interpretation of the real trailing edge condition in unsteady flow is extracted from various sources, for instance from a report by Sears (ref. 37). This "real" condition is presented in contrast to the classical one of Kutta-Joukowski, which implies that the pressure jump across an airfoil approaches zero at the trailing edge, and that here the velocity be finite. So far, the latter condition is used in all unsteady potential theories. In reality, when blunt trailing edges and boundary layer separation are involved, upper and lower surface pressures at the trailing edge are not equal. The new "real" condition implies that the change of the circulation at the trailing edge is given by an integral relation over the boundary layer thickness, summing the flux of vorticity out of the boundary layer into the wake. In ref. 12, consequences in the solutions of the potential theory on the results of forces, moments and circulation of wings are pointed out. The "real" trailing edge condition may be of major significance to the circulation about missile fins which often lie in the influence field of the propellant flow. McCroskey lists several recent symposia and meetings on theoretical and experimental progress in unsteady aerodynamics. His list should be complimented with the 99th lecture series of the VKI, April 1977 in Bruxelles and the 15th and 16th Aerospace Sciences Meetings of the AIAA in Los Angeles (1977) and Huntsville (January 1978). In the VKI lectures, Försching (ref. 38) and Labrujere, Roos and Erkelenz (ref. 39) summarized numerical solutions to the unsteady potential theory. A paper by C. Rehbach (ref. 40) presented at the 16th AIAA meeting gives new results on the discrete vortex method, preferred by Belotserkovskii.

3.4 Non-linear forces and moments of wings with thickness or at high angle of attack in unsteady flow

In unsteady aerodynamics, most theoretical studies of non-linear effects on forces and moments of wings and bodies rely on empirical assumptions. This is true for all methods treated in this chapter.

The effect of wing thickness is examined in the work of Ruo, Liu et al. (refs. 56, 42). The method of reference 56 is related to the procedure of refs. 41 and 81, where non-lifting and lifting bodies of revolution with oscillation of low frequency in subsonic and transonic flow are examined by application of a steady flow linearization technique (see table 3.2).

In ref. 41, firstly a solution to the potential equation for transonic flow past plunging bodies is developed which yields the same basic flow structure as in steady non-lifting transonic flow. This means, the solution has two parts, a cross flow in planes normal to the free stream and a spatial influence. For transonic flow past pitching bodies a general solution is derived which contains steady and oscillatory subsonic and transonic flow terms. A low frequency expansion is used for the sonic flow, which leads in connection with the Adam-Sears interaction (ref. 71) to the stability derivatives. Transferred to delta wings in transonic flow (ref. 56), the method differs from the theory of Landahl (ref. 5) by the non-linear potential term $\phi_x \phi_{xx}$ and the frequency range. In the non-linear potential term, the derivative ϕ_{xx} is replaced by a parabolic constant Γ . The solution to the potential equation is useable at low frequency motion; the solution of Landahl is valid only at high frequency, allowing to eliminate the non-linear term in the potential equation. The parabolic constant Γ of ref. 56 is a thickness parameter relating the cross section of a thick delta wing to an equivalent body of revolution (cone). The dependence of Γ on the body thickness is shown in fig. 3.26. Here, also the damping derivative $C_{m\dot{q}} + C_{m\ddot{q}}$ is displayed as function of Γ and as function of the reduced frequency $0 \leq k \leq 0.08$. A solution to the transonic unsteady potential equation based on local linearization and application of the sonic-box method is presented in ref. 42 also with the purpose of predicting the influence of delta wing thickness on the damping derivative $C_{m\dot{q}} + C_{m\ddot{q}}$. The values of $C_{m\dot{q}} + C_{m\ddot{q}}$ plotted versus the reduced frequency with the wing thickness ϵ as parameter differ at low frequency $k \leq 0.2$ from the result of ref. 56. According to ref. 42, the thickness effect reduces the damping at low frequency (fig. 3.27c). The opposite effect is apparent from fig. 3.26, showing the result of ref. 81. The damping reduction predicted in ref. 42 is confirmed by experiments of Statler (ref. 77). For a delta wing, the thickness effect on the normal force slope $C_{N\dot{q}}$ is weak (fig. 3.27b). It is strong in case of a rectangular wing (fig. 3.27a). The local linearization technique involves a coordinate transformation, converting a locally linear small perturbation velocity-potential equation into a linearized transonic equation with constant coefficients. The transformation limits the application of the sonic-box solution to simple wing shapes. The limitation can be avoided replacing the transformation by a modified source strength distribution dependent on the local Mach number.

The non-linear angle-of-attack dependence of forces and moments of wings, oscillating about a mean incidence may be predicted by using the free vortex model of Bollay (ref. 82). The model was successfully applied in subsonic steady wing aerodynamics in refs. 26 and 83: The free vortices of a horse shoe vortex distribution over the wing surface at the incidence α separate at an angle $\alpha/2$, as shown in fig. 3.28. In connection with a low frequency expansion, Garner and Lehrian (ref. 84) used the model assuming a small amplitude oscillation of the vortices about $\alpha/2$. In ref. 84 their analytical procedure is based on Multhopp's subsonic lifting surface theory (ref. 22) and is applied to a slender gothic wing. The damping coefficient $C_{m\dot{q}} + C_{m\ddot{q}}$ and the non-linear static stability coefficient $C_{m\eta}$ obtained in ref. 84 are shown in fig. 3.29. Using the approach of ref. 63, which leads to two steady angle-of-attack distributions (as described in chapter 3.2.1 and shown in fig. 3.28), the free vortex model of Bollay may be applied to derive the non-linear static stability coefficients $C_{N\eta}$, $C_{m\eta}$ and the damping derivatives $C_{N\dot{q}}$ and $C_{m\dot{q}}$ for arbitrary wing shapes. The delta wing results obtained this way (ref. 66) are compared in figs. 3.29 and 3.30 to the theories of Garner and Lehrian, Ericsson and Reding (ref. 85), and to experimental data by Schmidt (ref. 76). In ref. 85, Ericsson and Reding develop a half-empirical procedure for the determination of non-linear coefficients for static longitudinal stability and of non-linear damping derivatives of sharp-edged delta wings with low pitching and plunging frequency. The method is applicable over the entire speed range. Considering - as usual - small perturbations from a mean static angle of attack, the non-linear coefficients and derivatives are obtained by superposition of attached and separated flow components. The steady coefficients $C_{N\eta}$ and $C_{m\eta}$ are derived with Polhamus' modification of potential theory for attached flow, and leading-edge suction analogy for separated flow (refs. 86, 87). Polhamus' concept is applicable only to the steady lift and moment coefficients preferably of simple pointed wings. The coefficients for attached flow are determined with potential theory assuming that a Kutta-Joukowski flow condition exists at the sharp leading edges. This way no leading edge suction is developing. At higher angles of attack however, leading edge suction does cause a loss of lift which must be accounted for. Rather than treating the loss as a phenomenon associated with leading edge vortex separation, i.e. with the vortex lift, as it truly is; it is assumed for convenience, that the potential lift is lowered by the loss. A correction factor is defined which compares well with a correction term in R.T. Jones slender wing theory (ref. 88), accounting there for the effect of a finite aspect ratio. In order to determine the vortex lift, Polhamus finds an analogy between the flows around a sharp and a round leading edge: The flow ahead of the stagnation point of a sharp leading edge reverses near the lower wing surface and separates from the wing leaving the leading edge tangentially. Then it rolls

up to a spiral vortex sheet. Air drawn over this vortex sheet is accelerated downward to the upper surface reattachment line. Since the flow over the vortex sheet reattaches, the basic idea of the analogy is that the total force on the sharp-edged wing associated with the pressure required to maintain the equilibrium of the flow over the separated spiral vortex is essentially the same as the leading edge suction force associated with the pressure required to maintain attached flow around a round leading edge. The latter pressure distribution is used for the determination of the vortex lift coefficients. The unsteady derivatives are defined with the piston theory (ref. 89) in case of attached supersonic flow. The subsonic derivatives follow from the supersonic ones by referring them to an equivalent "subsonic" wing area, which is the true geometric area diminished by sections near the trailing edges. The sections carry no load which accounts for the delta wing trailing edge condition at $M = 0$ (ref. 85). The "vortex lift" derivatives of unsteady separated flow are calculated with an unsteady pressure variation over the wings which has a constant phase lag with respect to the steady pressure variation. The latter follows from Polhamus' analogy. The pressure amplitude remains unaffected by the unsteadiness. The constant phase or constant time lag concept was concluded by Lambourne et.al. (ref. 90) from experimental observations of the behavior of the leading-edge vortices over a delta wing following a sudden change of incidence. According to ref. 90, the strength of the separated vortex at any position ξ of the wing surface can be regarded as the integral result of the vorticity shed from all positions upstream of ξ . For small perturbations from a mean angle of attack, the change of vortex strength in ξ -direction can be assumed a linear function of the local angle of attack. The local effective perturbation angle is $\alpha(\xi) = \partial\zeta/\partial\xi + (c_0/V) \cdot \partial\zeta/\partial T$ with $\zeta = \zeta_0 \cos qT$ for a pitching motion or - as defined in ref. 85 - for pitching deformation of the surface. Hence, $\alpha(\xi)$ determines the change of vortex strength with ξ . The chordwise integration over the deforming part of the surface renders the vortex strength perturbation at any station downstream of the deformation proportional to the apex deflection independent of the shape of deformation $\alpha(\xi)$. At station ξ_1 at time T_1 , the vortex strength Γ would be the sum of the vorticity shed from each position upstream of ξ_1 at the earlier time $T_1 - Kc_0(\xi_1 - \xi)/V$, where $Kc_0(\xi_1 - \xi)/V = \Delta T$ is the constant time lag mentioned above. The constant K is obtained by comparison of steady and unsteady pressure distributions over η of the wing at a station ξ_1 . The local vortex strength will determine the local pressures as long as the reduced frequency is low. Then the vortex strength deviations in the neighborhood upstream or downstream of the local value can be assumed negligibly small. The coefficients and derivatives C_{N_1} , C_{m_1} and $C_{m_q} + C_{m_{\dot{\alpha}}}$ are presented in closed form relations (refs. 69, 85, 91). The normal force damping deviations $C_{N_{\dot{\alpha}}} + C_{N_{\ddot{\alpha}}}$ may be determined for an arbitrary pitch axis location X_1 with eq. 13, using the values of C_{N_1} , $(C_{m_q} + C_{m_{\dot{\alpha}}})_1$ at X_1 and in addition $(C_{m_q} + C_{m_{\dot{\alpha}}})_2$ for another arbitrary location X_2 with $\Delta X = X_1 - X_2$. Linear derivatives by Ericsson and Reding are shown in figs. 3.7, 3.8, 3.11, 3.12, 3.17-3.20. Non-linear results are displayed in figs. 3.29 and 3.30 in comparison to other theoretical and experimental data. The method of Ericsson and Reding involves in a simplified version the "indicial function" concept specified by Tobak (ref. 32): Counting the time from a sudden change of incidence of the wing, the steady aerodynamic forces and moments are approached with a step occurring after a constant time lag. The unsteady forces and moments are approximated with the product of the corresponding steady state values times the time lag.

The use of the indicial function (ref. 32) is demonstrated in fig. 3.31 on the example of determining C_N from the transient $C_N(T)$ of two delta wings of different aspect ratio in a subsonic flow field. The function in fig. 3.31 involves a single step, i.e. a sudden change $\Delta\alpha$ at $T_0=0$. The value of C_N at T_0 can be calculated with the piston theory (ref. 89). The value of the linear steady C_{N_α} which is approached at T_1 is given for instance with the theories of R.T. Jones (ref. 88) or Schlichting-Truckenbrodt (ref. 63). The aerodynamic reactions to the initial step are termed the indicial response or indicial function. The transient values of the indicial response may be determined for simple wing shapes using the theories of refs. 92-96. For a two-dimensional wing, the formation of the transient values of pressure or the indicial loading is shown in fig. 3.32. From the indicial load distributions of delta wings at subsonic speed (ref. 94), the transient values $C_{N_\alpha}(T)$ in fig. 3.31 are to be integrated. The areas F_1 and F_2 in fig. 3.31 determined by the difference between $C_{N_\alpha}(T)$ and the constant steady value C_{N_α} are proportional to the unsteady derivative $C_{N_{\dot{\alpha}}} \sim F_1 - F_2$. The method is applicable to non-linear unsteady aerodynamics, as shown by Schiff (ref. 97) in case of coning motions of bodies of revolution. In non-linear wing aerodynamics, the initial value of the non-linear coefficient C_{N_1} for instance had to be obtained from a non-linear piston theory, where the step $\Delta\alpha$ occurs from a mean steady value α . The static final value at T_1 would be given by non-linear steady flow theories (refs. 66, 83, 86, 87). For the transient values one would get first order approximations from linear theory. The approximations are consistent with observations of Murphy (ref. 98), provided the forces and moments are "weak" non-linear functions. As weak non-linearity Murphy understands a quadratic dependence of forces and moments on the angle of attack. A superposition of indicial function as response to subsequent small deviations $\Delta\alpha$ or Δq would lead to truly non-linear transient values. A superposition is demonstrated with the pitching moment in fig. 3.33, taken from reference 99. Here it is assumed that the response $\Delta C_m/\Delta\alpha$ or $\Delta C_m/\Delta(qc/V)$ is quasisteady, i.e. independent of the variable $C_m(T)$ earlier than or at τ when the step occurs and independent of $C_m(T)$ after this event. The increment of the transient function is then given by

$$\Delta C_m(T) = \frac{\Delta C_m(T-\tau)}{\Delta\alpha} \Delta\alpha + \frac{\Delta C_m(T-\tau)}{\Delta(qc/V)} \Delta(qc/V),$$

indicating that the differential quotients are functions of the interval $(T-\tau)$ only, but neither of T or τ alone. This implies that $\Delta C_m/\Delta\alpha$ and $\Delta C_m/\Delta(qc/V)$ are always the same

functions of $(T-\tau)$, regardless of the absolute magnitude of α or q . The transient pitching moment obtained by integrating from T_0 to T is

$$C_m(T) = C_m(0) + \int_{T_0=0}^T C_{m\alpha}(T-\tau) \frac{d}{d\tau} (\alpha(\tau)) d\tau + \frac{C}{V} \int_{T_0=0}^T C_{mq}(T-\tau) \frac{d}{d\tau} (q(\tau)) d\tau. \quad (14)$$

The integration of $C_{m\alpha}$ in eq. 14 for instance would yield a non-linear pitch stiffness coefficient $C_{m\alpha}/\alpha$. An improvement removing the limitation of quasisteady increments is proposed in ref. 99. The simple functions $f(T-\tau)$ in eq. 14 are to be replaced by functionals $G(\alpha(\xi), q(\xi))$ where $\alpha(\xi)$ and $q(\xi)$ denote functions of time, and ξ a running variable in time from T_0 to T . In our example, C_m and C_{mq} become functionals of the type $F(\alpha(\xi), q(\xi), T, \tau)$. A detailed explanation is given in refs. 97 and 99. According to ref. 99, the indicial response method is applicable to rigid bodies only. However, recently also flutter problems were treated with the indicial method (ref. 129). A further condition of constant Mach number and cruise altitude limits the method to small unsteady perturbation of a steady state variable, in particular to small increments in lateral or longitudinal acceleration, or small changes in atmospheric density. This excludes for instance the application to problems involving longitudinal acceleration in the launch phase of a missile. The restrictions do not impair the treatment of longitudinal stability derivatives.

3.5 Steady and unsteady derivatives of longitudinal stability of bodies of revolution

The slender body theory of steady flow was corrected for thickness, compressibility and viscous effects and for angle of attack dependence by concepts of Lighthill (ref. 100), Van Dyke (ref. 101), Oswatitsch and Keune (ref. 102), Maeder and Thommen (ref. 103), Allen (ref. 104), Bryson (ref. 105) and others. These concepts were utilized in non-linear unsteady aerodynamics of bodies of revolution, for example in the theories in refs. 28, 41, 106, 107, 108. In non-linear missile aerodynamics, the work of Murphy (refs. 98, 109-112), Nicolaides (ref. 113), Stone et al. (ref. 114), Morrison et al. (ref. 115) - to name a few experimental studies - and reformulations of stability derivatives (ref. 116) gave inputs to unsteady theory either confirming or improving it or verifying empirical assumptions.

3.5.1 Non-slender bodies, thickness effect

The procedure of Liu et al. (ref. 41) predicting static and dynamic stability derivatives for bodies of revolution with thickness at subsonic and transonic speeds was briefly described in connection with the delta wing thickness effect. A linearization technique of refs. 102, 103 is applied replacing the second order derivative ϕ_{xx} of the velocity potential in the non-linear term $\phi_x \phi_{xx}$ of the potential equation by a parabolic constant. Then a low frequency expansion for sonic flow and the Adam-Sears iteration procedure (ref. 71) lead to the stability derivatives of the oscillating body. The latter two means of approximation are also used by Revell (ref. 107) in his second-order slender body theory for steady or unsteady subsonic flow past slender lifting bodies of finite thickness. Because of the body thickness, a coupling between axial flow and cross flow is present as a consequence of non-linearity of the velocity potential equation. Revell calculates the corrections for thickness and compressibility from a second-order approximation to the non-linear time-dependent velocity potential. The crossflow theory by Miles and Munk (refs. 14, 117) predicting the stability derivatives as functions of body shape only, and Adams-Sears axial flow theory are the starting points to Revell's successive approximation scheme. The second order slender body theory of Lighthill (ref. 100) applicable to steady flow past bodies of revolution is utilized to account for the thickness effects. Essentially, the solution is obtained by approximating the non-linear terms in the second-order potential equation by their first order values and by solving the resulting inhomogeneous partial differential equation which is subject to more refined boundary conditions. The isentropic pressure equation is likewise refined and integrated to give the second-order corrections to lift and pitching moment coefficients. Prior to ref. 107, the method was applied to unsteady supersonic flow past pointed bodies by the same author (ref. 106). The concept of maintaining the correct boundary conditions and pressure equation, i.e. avoiding the approximations inherent with slender body theory, is the essence of Van Dyke's theory (ref. 101) for steady flow past thick bodies. His method is extended to unsteady supersonic flow over cones by Tobak and Wehrend (ref. 108). As in refs. 106 and 107, a low frequency approximation is required. A second method, also proposed by Van Dyke, is utilized in ref. 108. This combines the first order crossflow potential with an axial flow potential correct to second order. Applied to slender cones, both methods have closed-form solutions. Some results, the derivatives $C_{mq} + C_{m\dot{q}}$ and $C_{nr} - C_{n\dot{r}}$ for a ten degree cone at $M = 2$ and low "total" angle of attack (specified in refs. 114, 116), are shown in fig. 3.34 together with experimental results by Schiff and Tobak (ref. 118) and experimental and theoretical data by Stone et al. (ref. 114).

3.5.2 Non-linearity with the incidence

The data of Stone et al. (ref. 114) are obtained with the Newtonian theory following assumptions by Maple and Synge in reference 119: The forces and moments are considered functions of the instantaneous values of translational and rotational velocity components, and may be represented in a multi-dimensional Taylor series. The results of reference 114 (fig. 3.34) reveal non-symmetrical damping moments at high angle of attack. The asymmetry in dynamic damping is assumed being caused by asymmetrical vortices and by the presence of separated flow on the lee side of the body. The asymmetric vortex formation is confirmed by recent experimental "steady flow" studies (ref. 120, 121). The flow mechanism of

ref. 114 may well explain the behavior of the ballistic weapon shown in fig. 3.1. The Newtonian theory accounts for the phenomena with a non-linear variation of the surface pressure due to the variation of the local air velocity. Also in ref. 122, the Newtonian theory is used. It is applied to pointed slender bodies of revolution. A modification, the "embedded" Newtonian is employed with blunted slender bodies in order to determine the non-linear damping behavior at angle of attack.

The concept of functionals (ref. 99) is used by Schiff (ref. 97), who gives in an advanced version of ref. 116 a non-linear formulation of the aerodynamic force and moment system acting on bodies with arbitrary motions of large amplitude. Applied to a slow varying non-planar motion of a body of revolution, this formulation suggests that the forces and moments on the body are superpositions of components due to basic motions: steady angle of attack, pitch oscillations, roll or yaw oscillations and coning motion. This refined model of body motions yields functionals, i.e. forces and moments which are linear at low angle of attack and which become non-linear at larger incidence. A numerical finite-difference technique is used to compute the inviscid flow field surrounding a body in coning motion in a supersonic stream.

Viscous steady flow effects on bodies of revolution are examined by Wardlaw (ref. 120) and Deffenbaugh and Koerner (ref. 121). Both concepts can be extended to study non-linear unsteady aerodynamics of slender bodies with incidence. An evaluation of the vortex models in refs. 120 and 121 and of their impact to steady missile aerodynamics is given in a recent review by Nielsen (ref. 123).

3.6 Steady and unsteady derivatives of configurations including interference effects

The slender body crossflow theory (ref. 104) and the discrete vortex model of Jorgensen and Perkins (ref. 105) are applied to calculate steady and quasisteady aerodynamic coefficients of configurations in the non-linear angle-of-attack range (ref. 125). In figs. 3.35 and 3.36, the pitch damping coefficients for two configurations at $M = 0.8$ with the same pitching axis location $X_p = 5.67 D_0$ but different fin positions are broken up into their components of the body $(C_{mq})_{2+3}$, the wing $(C_{mq})_4$ and their mutual interference $(C_{mq})_{5+6}$. The coefficient of the body $(C_{mq})_{2+3}$ consists of a slender body term and a crossflow term. The latter implies a laminar boundary layer. The wing coefficient $(C_{mq})_4$ is calculated with the non-linear lifting surface theory (refs. 26, 66). The interference coefficient $(C_{mq})_{5+6}$ consists of the influence of the wing on the body and of the body on the wing. The latter is estimated with discrete vortices (ref. 105) superimposed on the slender body potential for crossflow around a cylinder. Two methods based on the non-linear lifting surface theory are investigated in order to assess the angle-of-attack dependent interference of the wing on the body $(K_{B(W)}(\alpha))$, following the terminology of Nielsen et al. (refs. 13, 126, 128). One procedure is based on the horse shoe vortex model replacing the wing-body combination. In the second procedure, which has been employed prior in linear aerodynamics (ref. 63), the section of an infinitely long cylinder between the wing root chords is replaced by a rectangular flat wing, the area of which equals the root chord length times the body diameter. In figs. 3.37 and 3.38, the normal force and pitching moment coefficients C_N and C_m of the two missile configurations at $M=0.8$ with different fin positions are compared. The low reduced frequency $k=qc/V=0.05$ is suggested by the natural frequencies usually encountered with missiles (see table 3.1). Unfortunately no experimental data for a comparison were available. A comparison to experimental data from ref. 127 was possible for the missile configuration of fig. 3.39. Here, the coefficients $C_N = \alpha C_{Nn} + k' C_{Nq}$ and $C_m = \alpha C_{mn} + k' C_{mq}$ with $k' = k D_0 / c$ are plotted as functions of the angle of attack. In the body crossflow terms a laminar boundary layer was used. In case of a turbulent boundary layer, the coefficient αC_{Nn} would approximately match experimental data and the values predicted with the steady non-linear theory (ref. 124) based on Wardlaw's vortex model. The moment αC_{mn} for a turbulent layer would deviate stronger from experimental and the vortex model results than it does in the laminar case, whereas the sum $\alpha C_{mq} + k' C_{mq}$ would coincide with the data of refs. 124 and 127. In unsteady aerodynamics linear with incidence, a slender body procedure of Chao (ref. 130) gives the pressure distribution over cylindrical pointed bodies with wings or fins arranged in "plus" position. The configurations roll, pitch or plunge with harmonic oscillations at $k=qc/V=1$ with small amplitudes compared to the body radius. Recent results of Chao (ref. 131) from an exact solution of the linearized potential equation for spheroidal bodies oscillating harmonically in subsonic flow, are utilized in a comparison to numerical data by Geissler (ref. 132) in the review by Försching (ref. 38). Geissler's panel method is suited for application to harmonically oscillating thick bodies of complicated shape. Other recent numerical approaches which can be applied to linear unsteady aerodynamics of wing-body combinations with harmonic oscillations are reported by Roos, Bennekens and Zwaan (refs. 49, 133), by Dusto, Epton and Johnson (ref. 134) and Morino (refs. 43, 135). Roos et al. (ref. 133) apply the doublet lattice method combined with unsteady source panels. The body thickness effect to the steady flow field is accounted for with a combined vortex-lattice/steady source panel method. The method of Dusto et al. employs a panel distribution of quadratically varying doublets and linearly varying sources over arbitrarily positioned boundary surfaces. This way, a method applicable to arbitrary arrangements of wings and bodies is obtained. The solution makes use of the aerodynamic coefficient concept in the integral equation - as in ref. 55. Morino's general unsteady theory involves an integral representation for the potential of subsonic and supersonic flow by applying the Green function method. The solution suited for lifting bodies having arbitrary shape and motion is obtained with a panel distribution for body schematization. A condensed description of Morino's non-planar method is given in the review of Labrujere et al. (ref. 39). An extensive survey on numerical procedures applicable to unsteady interference problems is given in the review by Försching (ref. 38).

Work of Laschka (ref. 136), Becker (ref. 57), Rodden et al. (refs. 34, 35, 36), Cunningham (ref. 137), Tijdemann and Zwaan (ref. 138) is covered with some detail. This work however is geared towards airplane aerodynamics, involving complicated configurations and high frequency flutter. In missile aerodynamics, the rigid body concept appears still appropriate with the size of most present configurations. Of current interest is the extension of steady methods such as ref. 128 to quasisteady or unsteady procedures apt to solve interference problems governed by a non-linear dependence of forces and moments on the angle of attack.

4. INFLUENCE OF THE LONGITUDINAL ACCELERATION

The load distribution over the length of a missile or missile component changes with the longitudinal acceleration during the starting or boost phase and with deceleration. The consequence is a change of the center of pressure location. Compared to the dynamic-pressure-dependent quantities of the steady normal force and pitching moment, the perturbation due to acceleration is of the order $\nabla c/V^2$, where ∇ is the acceleration and c the body length. This effect is often very small, but not in the starting phase of high accelerated missiles. Although the acceleration effect can be of great impact to missile aerodynamics, little information on this phenomenon exists in the open literature. Work of Schmidt (ref. 18) employing the slender body theory to bodies alone was recently revised and extended by Erber to wing-body combinations (ref. 20). A result of ref. 20 is given in fig. 4.1, showing the shift of the center of pressure X_{pr}/c of an ogive-cylinder body as function of the acceleration parameter $\nabla c/V^2$. Earlier studies of Ballmann (ref. 19) concentrated on supersonic flow and based on the concept of moving singularities were applied to the aerodynamics of accelerated missile bodies in subsonic and supersonic flow in ref. 139. The pressure distribution of accelerated bodies with a parabolic profile or with slight deviations from this shape were investigated by Foote (ref. 17). His analytical procedure is based on results of Coles theory on accelerated slender bodies (ref. 140). Gardner and Ludloff (ref. 141) investigated the acceleration effects on the aerodynamic characteristics of thin airfoils at supersonic and transonic speed. The experimental simulation of accelerated flight is difficult in conventional wind tunnels. Also drop tests in the open air are inaccurate as they are impaired by changing atmospheric conditions. In supersonic flow, recent acceleration tests of the lift of an airfoil in a pressure driven shock tube by Minkinen et al. (ref. 142) utilized the expansion waves propagating in the driver tube immediately after the diaphragm rupture. For subsonic accelerated flow experiments, the expansion waves in a Ludwig tube may be suitable.

5. CONCLUSION

A field of quasisteady or unsteady aerodynamics inherent in missile aerodynamics and less significant to airplane aerodynamics is concerned with high longitudinal acceleration effects. A shifting pressure point due to acceleration and a shifting center of gravity due to mass reduction of a propelled missile account for the significance of the aerodynamic forces and moments of longitudinal stability. Dynamic longitudinal stability problems in missile aerodynamics have the appearance of being easier to solve than problems in the same field encountered in airplane aerodynamics. This is true with respect to the frequency of vertical motions, superimposing to the steady flight motion. The frequencies are low with the size and mass of missiles and projectiles where the assumption of body rigidity is close to reality. Not so in airplane aerodynamics where body and wing sizes most times involve high flutter frequency. The reduced frequency of pitching, plunging or yawing motion of missiles is of the order of $k=0.1$. This permits to treat vertical motion as nearly steady. The analysis of such a problem with the potential theory is essentially a steady one, which involves a more complicated yet steady upwash field over the configuration. If a low frequency approximation is necessary, the analytical procedure becomes quasisteady providing solutions which depend linearly on the frequency. In some literature this type of motion is termed "unsteady". The low frequency approach should be satisfactory for most dynamic stability problems in missile aerodynamics. It is needed for instance, when analytical results are to be compared to experimental data which are usually achieved with small scale models oscillating at higher frequency than $k=0.1$. Both, steady and quasisteady solutions simplify the analysis. On the other hand, the amplitudes of oscillation of vertical motions can become large which is not consistent with the usual assumption of small perturbations in potential theory. This renders missile aerodynamics non-linear and difficult. Some methods of this literature study which are considered suitable to the requirements of missile aerodynamics are called to attention in this conclusion.

Provided missile derivatives are linearly dependent on the state variables, various procedures mentioned in the previous sections can be applied. One of them, Morino's unsteady "general" theory (refs. 43, 135) suitable for rather complicated configurations at subsonic and supersonic speeds fulfills the requirements of unsteady missile aerodynamics. For bodies of revolution alone, the theory of Revell (refs. 106, 107) and for wings, the theory of Brune and Dusto (ref. 55) appear appropriate for sub- and supersonic speeds. In case of non-linear problems, at present an analysis geared toward the treatment of single missile components and a subsequent data synthesis is more promising than a complete configuration analysis. With respect to the attainable accuracy of linear aerodynamic coefficients and derivatives of missile wings (chapter 3.23, fig. 3.25), at least an approximate description of non-linear stability behavior of the main components should be possible. Interference effects may be approximated by linear theory. On this basis, the following theories are of interest, either for immediate application or for adaptation to the problems in question: The method of indicial functions proposed by Tobak and Belotserkovskii (refs. 32, 33) is suitable to handle quasisteady motions of small

or of larger amplitude of wings and bodies in subsonic and supersonic flow. The piston theory (ref. 89) had to be extended to high-incidence application. Subsonic and supersonic indicial functions should be available for more complicated wing forms than the delta and rectangle (refs. 92-96). At low frequency, the quasisteady functions with differential quotients would be appropriate. An additional quasisteady method applicable to wings of arbitrary shape in the high angle of attack range could be derived by the combination of Brune's and Dusto's (ref. 55) procedure with Bollay's (ref. 82) vortex model. This way, a comparison of analytical results for wings in quasisteady motion were possible. In the case of bodies, the utilization of Wardlaws (ref. 120) or Deffenbaughs and Koerners (ref. 121) vortex models for quasisteady aerodynamics at high angle of attack should not be difficult. Again assuming quasisteadiness, the interference of the body on the wing could be determined with the symmetric body nose vortex model of Mendenhall and Nielsen (ref. 128). The wing influence on the body and on the tail could be obtained with one or several horse shoe vortices representing the non-linear quasisteady wing circulation. The interference loads on body and tail will be obtained with these vortices adapting to the body flow and vortex field. A more refined way for solution of the wing-body interference problem would be obtained by extending the method of Gregoriou (ref. 143) to quasisteady application.

REFERENCES

1. H.H.B.M. Thomas, "State of the art of estimation of derivatives", 1961, AGARD Rep. 339.
2. D.E. Ellison, D.E. Hoak, "Stability derivative estimation at subsonic speeds", 1968, Annals New York Academy of Sciences, International Congress on Subsonic Aeronautics New York, N.Y. Academy of Sciences, pp. 367-396.
3. H.S. Tsien, "Fundamentals of gas dynamics", Princeton N.J., Princeton University Press, 1958, Article on "The equations of gas dynamics".
4. I. Serrin, "Handbuch der Physik" Bd. VIII/1 Strömungsmechanik I, Berlin-Göttingen-Heidelberg, 1959, Article on "Mathematical principles of classical fluid dynamics".
5. M.T. Landahl, "Unsteady transonic flow", International Series of Monographs in Aeronautics and Astronautics Division II: Aerodynamics Vol. 2, Oxford, Pergamon Press, 1961.
6. R.L. Pope, "A FORTRAN program to extract static and dynamic moments from free oscillation in a wind tunnel", 1976, Australian Defence Scientific Service, WRE-Technical Note-1729 (WR&D).
7. S.R. Bland, "Comments on NASA Langley research on transonic unsteady aerodynamics", 1973, AGARD Rep. 619.
8. S.R. Bland, "Recent advances and concepts in unsteady aerodynamic theory", 1975, NASA SP-347, NASA conference on aerodynamic analysis requiring advanced computers.
9. E. Khaski, "Transonic/supersonic longitudinal aerodynamic derivatives", 1977, v.K.I.F.D. Lecture Series 99: Aerodynamic input for problems in aircraft dynamics.
10. C.P. Schneider, "Instationäre Flugkörper-Aerodynamik", 1975, MBB-Bericht UA-306-75, Messerschmitt-Bölkow-Blohm GmbH, München.
11. W.J. McCroskey, J.J. Philippe, "Unsteady viscous flow on oscillating airfoils", AIAA Journal, Vol. 13, No. 1, January 1975, 71-79.
12. W.J. McCroskey, "Some current research in unsteady fluid dynamics", J. Fluids Engineering, Vol. 99, No. 1, March 1977.
13. J.N. Nielsen, "Missile Aerodynamics", New York, Toronto, London, McGraw-Hill Book Company, Inc., 1961.
14. J.W. Miles, "The potential theory of unsteady supersonic flow", Cambridge monographs on mechanics and applied mathematics, Cambridge at the university press, 1959.
15. D.E. Hoak et al., "U.S.A.F. Stability and Control Datcom", Revised edition, 1970.
16. ANON, Royal Aeronautical Society data sheets-Aerodynamics, 1955.
17. J.R. Foote, "The C for accelerated slender bodies", J. Applied Mechanics, Transactions of ASME, March 1966, pp. 1-6.
18. W. Schmidt, "Aerodynamische Kräfte und Momente bei beschleunigter oder verzögerter Längsbewegung", 1960/1961, Bölkow-Berichte FM-A-95, FM-A-108, FM-A-114.
19. J. Ballmann, "Berechnung von Überschallströmungen um schlanke Körper mit Hilfe bewegter Singularitäten", Juli 1967, Dissertation TH Aachen.

20. F. Erber, "Aerodynamische Kräfte und Momente bei instationären Längsbewegungen an Flügel-Rumpfkombinationen", 1977, MBB TN-AE12-44/77, Messerschmitt-Bölkow-Blohm, München.
21. K.J. Turner, A.J. Ross, Geraldine Earley, "The dynamic stability derivatives of a slender wing, a comparison of theory with free-flight model test at near-zero lift, $M = 0.8$ to 2.4 ", 1966, R.A.E. TR 66170.
22. H.C. Garner, "Multhopp's subsonic lifting-surface theory of wings in slow pitching oscillations", 1952, A.R.C., R.&M. 2885.
23. I.J. Cole, K. Margolis, "Lift and pitching moment at supersonic speed due to constant vertical acceleration for thin sweptback tapered wings with streamwise tips. Supersonic leading and trailing edges", 1954, NACA TN 3196.
24. J.C. Martin, K. Margolis, I. Jeffreys, "Calculation of lift and pitching moments due to angle of attack and steady pitching velocity at supersonic speeds for thin sweptback tapered wings with streamwise tips and supersonic leading and trailing edges", 1952, NACA TN 2699.
25. F.S. Malvestuto, D.M. Hoover, "Lift and pitching derivatives of thin sweptback tapered wings with streamwise tips and subsonic leading edges at supersonic speeds", 1951, NACA TN 2994.
26. K. Gersten, "Nichtlineare Tragflächentheorie insbesondere für Tragflächen mit kleinem Seitenverhältnis", Ing.-Archiv, Bd. 30, 1961, pp. 431-452.
27. L.E. Ericsson and J.P. Reding, "High attitude delta wing unsteady aerodynamics", J. Aircraft, Vol. 12, No. 11, Nov. 1975.
28. M.L. Robinson, "The estimation of pitch damping derivatives of missile configurations at subsonic speeds", 1970, AIAA Paper 70-537, AIAA Atmospheric Flight Mechanics Conference, Tullahoma, Tennessee.
29. M.T. Landahl, V.J.E. Stark, "Numerical Lifting-Surface Theory-Problems and Progress", AIAA Journal, Vol. 6, No. 11, Nov. 1968, pp. 2049-2060.
30. H.G. Küssner, "Allgemeine Tragflächentheorie", Luftfahrtforschung, Bd. 17, Lfg. 11/12, pp. 370-378.
31. R.W. Conlan, "Methods for predicting the longitudinal damping coefficients $C_{m\dot{\alpha}}$ and $C_{m\ddot{\alpha}}$ ", 1974, AFATL-TR-74-47.
32. M. Tobak, "On the use of the indicial function concept in the analysis of unsteady motions of wings and wing tail combinations", 1954, NACA TR 1188.
33. S.M. Belotserkovskii, "Study of the unsteady aerodynamics of lifting surfaces using the computer", Ann. Rev. Fluid Mech. 1977.9, pp. 469-494.
34. T.P. Kalman, W.P. Rodden, J.P. Giesing, "Application of the doublet-lattice method to nonplanar configurations in subsonic flow", 1970, AIAA Paper No. 70-539, AIAA Atmospheric Flight Mechanics Conference, Tullahoma, Tennessee.
35. W.P. Rodden, J.P. Giesing, T.P. Kalman, "New developments and applications of the subsonic doublet-lattice method for nonplanar configurations", 1971, AGARD-CP-80-71, Part II.
36. J.P. Giesing, T.P. Kalman, W.P. Rodden, "Subsonic unsteady aerodynamics for general configurations", 1972, AIAA Paper No 72-26.
37. W.R. Sears, "Unsteady motion of airfoils with boundary layer separation", AIAA Journal, Vol. 14, No. 2, Feb. 1976, pp. 216-220.
38. H. Förssching, "Prediction of unsteady aerodynamic forces in high frequency oscillatory flow", 1977, VKI LS 99 on "Aerodynamic Inputs for problems in aircraft dynamics".
39. T.E. Labrujere, R. Roos, L.J.J. Erkelens, "The use of panel methods with a view to problems in aircraft dynamics", 1977, VKI LS 99 on "Aerodynamic Inputs for problems in aircraft dynamics"; and NLR MP 77009 U.
40. C. Rehbach, "Numerical calculation of three-dimensional unsteady flows with vortex sheets", 1978, AIAA Paper No. 78-111, AIAA 16th Aerospace Sciences Meeting, Huntsville, Alabama.
41. D.D. Liu, M.F. Platzler, S.Y. Ruo, "On the calculation of static and dynamic stability derivatives for bodies of revolution at subsonic and transonic speeds", 1970, AIAA Paper No. 70-190, AIAA 8th Aerospace Sciences Meeting, New York, N.Y..
42. S.Y. Ruo, E.C. Yates Jr., J.G. Theisen, "Calculation of unsteady transonic aerodynamics for oscillating wings with thickness", J.Aircraft, Vol. 11, No. 10, 1974, pp. 601-606.

43. L. Morino, "A general theory of unsteady compressible potential aerodynamics", 1974, NASA CR-2464.
44. D.E. Davies, "Calculation of unsteady generalized airforces on a thin wing oscillating harmonically in subsonic flow", 1963, A.R.C. R.&M. No. 3409.
45. D.E. Lehrian, H.C. Garner, "Theoretical calculation of generalized forces and load distribution on wings oscillating at general frequency in a subsonic stream", 1971, A.R.C. R.&M. No. 3710.
46. E. Albano, W.P. Rodden, "A doublet-lattice method for calculating lift distributions on oscillating surfaces in subsonic flows", AIAA Journal, Vol. 7, No. 2, Feb. 1969, pp. 279-285.
47. W.P. Rodden, J.P. Giesing, "Application of oscillatory aerodynamic theory to estimation of dynamic stability derivatives", J. Aircraft, Vol. 7, No. 3, June 1970, pp. 272-275.
48. B. Bennekers, T.E. Labrujere, "Calculation of unsteady subsonic aerodynamic characteristics by means of the doublet lattice method", 1972, NLR TR 73031 V.
49. R. Roos, B. Bennekers, R.I. Zwaan, "A calculation method for unsteady subsonic flow about harmonically oscillating wing-body configurations", 1975, AIAA Paper No. 864.
50. W. Geissler, "Ein numerisches Verfahren zur Berechnung der instationären aerodynamischen Druckverteilung der harmonisch schwingenden Tragfläche mit Ruder in Unterschallströmung, Teil I: Theorie und Ergebnisse für inkompressible Strömung", 1975, DLR-FB 75-37, "Teil II: Theorie und Ergebnisse für kompressible Strömung", 1977, DFVLR-AVA-Rep. IB 253-77J04.
51. B. Laschka, "Zur Theorie der harmonisch schwingenden tragenden Fläche bei Unterschallströmung", Z. Flugwissenschaften, 11. Jahrgang, Heft 7, Juli 1963, pp. 265-292.
52. H. Ashley, S. Windall, M.T. Landahl, "New Directions in lifting surface theory", AIAA Journal, Vol. 3, No. 1, January 1965, pp. 3-16.
53. P. Salaün, "Calcul précis des pression aérodynamiques instationnaires en subsonic", 1970, ONERA NT No. 163.
54. J. Fromme, D. Halstead, "The use of local basis functions in unsteady aerodynamics", 1975, AIAA Paper No. 75-100, AIAA 13th Aerospace Sciences Meeting, Pasadena, Cal..
55. G.W. Brune, A.R. Dusto, "Slowly oscillating lifting surfaces at subsonic and supersonic speeds", J. Aircraft, Vol. 9, No. 11, Nov. 1972, pp. 777-783.
56. K.R. Kimble, D.D. Liu, S.Y. Ruo, J.M. Wu, "Unsteady transonic flow analysis for low aspect ratio pointed wings", AIAA Journal, Vol. 12, No. 4, April 1974, pp. 516-222.
57. J. Becker, "Vergleich gemessener und berechneter instationärer Druckverteilungen für den hohen Unterschall an einem elastischen gepfeilten Flügel", 1969, Messerschmitt-Bölkow-Blohm, EWR-Report Nr. 403-69.
58. Appa Kari, G.C.C. Smith, "Further developments in consistent supersonic aerodynamic coefficients", 1971, AIAA Paper No. 71-177, 9th Aerospace Sciences Meeting, New York, N.Y..
59. H.C. Garner, D.A. Fox, "ALGOL 60 programme for Multhopp's low-frequency subsonic-surface theory", 1966, A.R.C. R.&M. 3517.
60. W.E.A. Acum, H.C. Garner, "The estimation of oscillatory wing and control derivatives", 1964, A.R.C. C.P. No 623.
61. H.C. Garner, R.D. Milne, "Asymptotic expansion for transient wing theory", Aeronautical Quarterly 17, 1966, pp. 343-350.
62. R. Göthert, H. Otto, "Berechnung der Stabilitätsderivativa für die Nickbewegung von Deltaflügeln im Unterschallbereich", Z. Flugwissenschaft, Vol. 15, Heft 10, 1967, pp. 363-368.
63. H. Schlichting, E. Truckenbrodt, "Aerodynamik des Flugzeuges", Vol. 2, Chapter 8.2, Springer-Verlag, Berlin, Heidelberg, New York, 1969.
64. M. Tobak, H.C. Lessing, "Estimation of rotary stability derivatives at subsonic and transonic speeds", 1961, AGARD Rep. 343.
65. H.S. Ribner, "The stability derivatives of low-aspect-ratio triangular wings at subsonic and supersonic speeds", 1947, NACA TN 1423.
66. C.P. Schneider, D. Nikolitsch, "Längsmomentenderivative von Flügeln bei hohen Anstellwinkeln in Unterschallströmung", 1976, BMVg-FBWT 76-26.

67. G.Z. Harris, "The calculation of generalized forces on oscillating wings in supersonic flow by lifting surface theory", 1966, A.R.C. R.&M. 3453.
68. J.S. Thompson, R.A. Fail, "Oscillatory-derivative measurements on sting-mounted wind-tunnel models: Method of test and results for pitch and yaw on a cambered ogee wing at Mach numbers up to 2.6", 1962, A.R.C. C.P. 3355.
69. L.E. Ericsson, J.P. Reding, "Effect of angle of attack and Mach number on slender wing aerodynamics", 1977, AIAA Paper No. 667.
70. K.J. Orlik-Rückemann, J.G. Laberge, "Static and dynamic longitudinal stability characteristics of a series of delta wings and sweptback wings at supersonic speeds", 1966, National Research Council of Canada, Aeron. Rep. LR-396.
71. M.C. Adams and W.R. Sears, "Slender-Body Theory-Review and Extension", J. Aero. Sci., Vol. 20, No. 2, 1953, pp. 85-98.
72. M.T. Landahl, "The flow around oscillating low aspect ratio wings at transonic speeds", 1954, KTH AERO TN 40, Stockholm.
73. J.H.B. Smith, J.A. Beasley, A. Stevens, "Calculations of the lift slope and aerodynamic centre of cropped delta wings at supersonic speeds", 1960, R.A.E. Techn. Note Aero 2697, A.R.C. 22200, C.P. 562.
74. K. Orlik-Rückemann, C.O. Olsson, "A method for the determination of the damping-in-pitch of semi-span models in high-speed wind-tunnels, and some results for a triangular wing", 1956, FFA Rep. 62, Stockholm.
75. K.J. Turner, A.J. Ross, G. Earley, "The dynamic stability derivatives of a slender wing, a comparison of theory with free-flight model test at near-zero lift, $M = 0.8$ to 2.4 ", June 1966, R.A.E. T.R. No. 66170.
76. E. Schmidt, "Experimentelle und theoretische Untersuchungen über die instationären flugmechanischen Derivativa der Längsbewegung an schlanken Flugkörpern bei mäßiger Geschwindigkeit", 1971, Jahrbuch der DGLR, pp. 71-97.
77. I.C. Statler, "Dynamic wind-tunnel tests of a delta-wing model at transonic speeds", 1970, AFFDL-TR-69-97, Air Force Flight Dynamics Lab., Wright-Patterson Air Force Base, Ohio.
78. L. Woodgate, P.G. Pugh, "Measurements of the pitching-moment derivatives on a sharp-edged delta wing in incompressible flow", 1963, A.R.C. R.&M. No. 3379.
79. N. Treinies, "Die Ermittlung aerodynamischer Derivativa mit Hilfe der diskreten Fourier-Transformation freier Schwingungen", 1974, DLR-FB 74-17.
80. H.F. Emerson, C.R. Robinson, "Experimental wind-tunnel investigation of the transonic damping-in-pitch characteristics of two wing-body combinations", 1958, NASA Memo 11-30-58A, Washington.
81. S.Y. Ruo, D.D. Liu, "Calculation of stability derivatives for slowly oscillating bodies of revolution at Mach 1.0", 1971, LMSC HREC D1 62375, Lockheed Missiles & Space Co., Huntsville, Ala..
82. W. Bollay, Z. angew. Math. Mech. 19, 1939, p. 21, and J. Aero. Sci. 4, 1937, p. 294.
83. D. Nikolitsch, "Über die nichtlineare Tragflügeltheorie von Gersten", 1967, Bölkow Bericht FM 370, 67.
84. H.C. Garner, Doris E. Lebrin, "Pitching derivatives for a gothic wing oscillating about a mean incidence", 1963, A.R.C. C.P. No 695.
85. L.E. Ericsson, J.P. Reding, "Unsteady aerodynamic analysis of space shuttle vehicles, Part II: Steady and unsteady aerodynamics of sharp-edged delta wings", 1973, Lockheed Missiles and Space Company, LMSC-D 352320.
86. E.C. Polhamus, "A concept of the vortex lift of sharp-edge delta wings based on a leading-edge-suction analogy", 1966, NASA TN D-3767.
87. E.C. Polhamus, "Predictions of vortex-lift characteristics by leading-edge-suction analogy", J. Aircraft, Vol. 8, No. 4, April 1971, pp. 193-199.
88. R.T. Jones, "Properties of low-aspect-ratio pointed wings at speeds below and above the speed of sound", 1945, NACA Rep. 1105.
89. R.L. Bisplinghoff, H. Ashley, R.L. Halfman, "Aeroelasticity", 1955 Addison-Wesley, Cambridge, Mass., pp. 418-419.
90. N.C. Lambourne, D.W. Bryer, J.F.M. Maybre, "The behavior of the leading-edge vortices over a delta wing following a sudden change of incidence", 1969, A.R.C. R.&M. 3645.

91. L.E. Ericsson, J.P. Reding, "Approximate non-linear slender wing aerodynamics", J. Aircraft, Vol. 14, No. 12, December 1977, pp. 1197-1204.
92. M.A. Heaslet, H. Lomax, "Two-dimensional unsteady lift problems in supersonic flight", 1949, NACA Rep. 945.
93. H. Wagner, "Über die Entstehung des dynamischen Auftriebes von Tragflügeln", Z.f.a.MM. Bd. 5, Heft 1, Feb 1925, pp. 17-25.
94. H. Lomax, M.A. Heaslet, F.B. Fuller, L. Sluder, "Two-and three-dimensional unsteady lift problems in high-speed flight", 1952, NACA Rep. 1077.
95. J.W. Miles, "Transient loading of wide delta airfoils at supersonic speeds", 1950, NAVORD Rep. 1235.
96. J.W. Miles, "Transient loading of supersonic rectangular airfoils", J. Aero. Sci., Vol. 17, No. 10, Oct. 1950, pp. 647-652.
97. L.B. Schiff, "A study of the non-linear aerodynamics of bodies in non-planar motion", 1974, NASA TR R-421.
98. C.H. Murphy, "The measurements of non-linear forces and moments by means of free flight tests", 1958, BRL Rep. No. 974.
99. M. Tobak, L.B. Schiff, "On the formulation of the aerodynamic characteristics in aircraft dynamics", May 1975, v.K.I.F.D. Lecture Series on Aircraft Stability and Control.
100. M.J. Lighthill, "Supersonic flow past slender pointed bodies of revolution at yaw", Quart. J. Mech. & Appl. Math., Vol. 1, 1948, pp. 76-89.
101. M.D. Van Dyke, "First and second order theory of supersonic flow past bodies of revolution", J. Aero. Sci., Vol. 18, No. 3, 1951, pp. 161-178.
102. K. Oswatitsch, F. Keune, "Flow around bodies of revolution at Mach number one", 1955, Paper presented at the Brooklyn Polytechnic's Conference on High-Speed Aeronautics.
103. P.F. Maeder, H.U. Thommen, "Some results of linearized transonic flow about slender airfoils of bodies of revolution", J. Aero. Sci., Vol. 23, 1956, pp. 187-188.
104. H.J. Allen, "Estimation of the forces and moments acting on inclined bodies of revolution of high fineness ratio", 1949, NACA RM 9126.
105. L.H. Jorgensen, E.W. Perkins, "Investigation of some wake vortex characteristics of an inclined ogive-cylinder body at Mach number 2", 1959, NACA Rep. 1371.
106. J.D. Revell, "Second-order theory for unsteady supersonic flow past slender, pointed bodies of revolution", J. Aerospace Sci., Vol. 27, Oct. 1960, pp. 730-740.
107. J.D. Revell, "Second-order theory for steady or unsteady subsonic flow past slender lifting bodies of finite thickness", AIAA Journal, Vol. 7, No. 6, June 1969, pp. 1070-1078.
108. M. Tobak, W.R. Wehrend, "Stability derivatives of cones at supersonic speeds", 1956, NACA TN 3788.
109. C.H. Murphy, "The prediction of non-linear pitching and yawing motion of symmetric missiles", J. Aero. Sci., Vol. 24, No. 7, July 1957, pp. 473-479.
110. C.H. Murphy, "Non-linear motion of a symmetric missile acted on by a double valued static moment", AIAA Journal, Vol. 6, No. 4, April 1968, pp. 713-717.
111. C.H. Murphy, "Non-linear motion of a missile with slight configurational asymmetries", 1970, AIAA Paper No. 70-534, AIAA Atmospheric Flight Mechanics Conference, Tullahoma, Tenn..
112. C.H. Murphy, "Gravity-induced angular motion of a spinning missile", 1971, BRL Rep. No. 1546.
113. J.D. Nicolaides, "On the free flight motion of missiles having slight configurational asymmetries", 1953, Institute of the Aeronautical Sciences 21st Annual Meeting, Reprint No. 395.
114. G.W. Stone, E.L. Clark Jr., G.E. Burt, "An investigation of nonsymmetrical aerodynamic damping moments", 1972, AIAA Paper No. 72-29, AIAA 10th Aerospace Sciences Meeting, San Diego, Cal..
115. A.M. Morrison, J.E. Holmes, W.R. Lawrence, "An investigation of the damping in pitch characteristics of a ten degree cone", 1975, NSWC/WOL/TR 75-84, Naval Surface Weapon Center, White Oak, Silver Spring, Md..

116. M. Tobak, H.C. Lessing, "Study of the aerodynamic forces and moments on bodies of revolution in combined pitching and yawing motions", 1960, NASA TN D-316.
117. M. Munk, "The aerodynamic forces on airship hulls", 1923, NACA Rep. 184.
118. L.B. Schiff, M. Tobak, "Results from a new wind-tunnel apparatus for studying coning and spinning motions of bodies of revolution", AIAA Journal, Vol. 8, No. 11, 1970, pp. 1953-1957.
119. C.G. Maple, J.L. Synge, "Aerodynamic symmetry of projectiles", Quarterly of Applied Mathematics, Vol. 6, No. 4, 1949, pp. 345-366.
120. A.B. Wardlaw, "Prediction of normal force, pitching moment, and yawing force on bodies of revolution at angles of attack up to 50 degrees using a concentrated vortex flow-field model", 1973, NOLTR 73-209.
121. F.D. Deffenbaugh, W.G. Koeber, "Asymmetric vortex wake development on missiles at high angles of attack", J. Spacecraft, Vol. 14, No. 3, March 1977, pp. 155-162.
122. L.E. Ericsson, "Generalized unsteady embedded Newtonian flow", 1975, AIAA Paper No. 75-210, AIAA 13th Aerospace Sciences Meeting, Pasadena, Cal..
123. J.N. Nielsen, "Nonlinearities in missile aerodynamics", 1978, AIAA Paper No. 78-20, AIAA 16th Aerospace Sciences Meeting, Huntsville, Ala..
124. D. Nikolitsch, "Theoretisches Verfahren zur Beiwertberechnung von Rumpfen und Flügel-Rumpfanordnungen bis zu extrem hohen Anstellwinkeln", 1976, BMVg-FBWT 76-10.
125. C.P. Schneider, "Derivative der Längsstabilität von Flügel-Rumpf-Anordnungen mit hohen Anstellwinkeln in Unterschallströmung", 1978, MBB Bericht No. UA-420-78.
126. W.C. Pitts, J.N. Nielsen, G.E. Kaattari, "Lift and center of pressure of wing-body-tail combinations at subsonic, transonic and supersonic speeds", 1953, NACA Rep. 1307.
127. H. Esch, "Windkanalmessungen zum Einfluß der Rollage auf die Normalkraft eines Flugkörperleitwerks", 1975, DFVLR-Bericht No. IB 351-75/7.
128. M.R. Mendenhall, J.N. Nielsen, "Effect of symmetrical vortex shedding on the longitudinal aerodynamic characteristics of wing-body-tail combinations", 1975, NASA CR-2473.
129. W.F. Ballhaus, P.M. Goorjian, "Computation of unsteady transonic flows by the indicial method", AIAA Journal, Vol. 16, No. 2, Feb. 1978, pp. 117-124.
130. K.L. Chao, "Berechnung der instationären Druckverteilung an harmonisch schwingenden kreiszylindrischen Flugkörpern mit kreuzförmig angeordneten Flügeln oder Leitflächen", 1971, DLR, FB 71-87.
131. K.L. Chao, "Analytische Lösung der verallgemeinerten Helmholtz-Wellengleichung für kompressible Unterschallströmung und Berechnung der instationären Druckverteilung an harmonisch schwingenden rotationselliptischen Körpern", 1976, DFVLR-AVA-Rep. IB 253-76J11.
132. W. Geissler, "Berechnung der Druckverteilung an harmonisch oszillierenden dünnen Rumpfen in kompressibler Strömung", 1976, DLR-FB 76-48.
133. R. Roos, B. Bennekers, R.J. Zwaan, "Calculation of unsteady subsonic flow at harmonically oscillating wing/body configurations", J. Aircraft, Vol. 14, No. 5, May 1977, pp. 447-454.
134. A.R. Dusto, M.A. Epton and F.T. Johnson, "Advanced Panel type influence coefficient methods applied to unsteady three dimensional potential flows", 1978, AIAA Paper No. 78-229, AIAA 16th Aerospace Sciences Meeting, Huntsville, Ala..
135. L. Morino, L.T. Chen, E.O. Suciu, "Steady and oscillating subsonic and supersonic aerodynamics around complex configurations", AIAA J., Vol. 13, 1975, pp. 368-374.
136. B. Laschka, "Interfering lifting surfaces in subsonic flow", Z. Flugw. 18, Heft 9/10, 1970, pp. 359-368.
137. A.M. Cunningham Jr., "Oscillatory supersonic kernel function method for interfering surfaces", J. Aircraft, Vol. 11, No. 11, Nov. 1974, pp. 664-670.
138. H. Tijdeman, R.J. Zwaan, "On the prediction of aerodynamic loads on oscillating wings transonic flow", 1974, AGARD Rep. No. 612.
139. W. Arrenbrecht, J. Ballmann, "Untersuchung des Einflusses der Beschleunigung auf die Druck- und Normalkraftverteilung eines Flugkörpers", 1976, Bericht der RWTH Aachen, Lehrgebiet Mechanik.
140. J.D. Cole, "Acceleration of slender bodies of revolution through sonic velocity", J. Applied Physics, Vol. 26, 1955, pp. 322-327.

141. C.S. Gardner and H.F. Ludloff, "Influence of acceleration on aerodynamic characteristics of thin airfoils in supersonic and transonic flight", JAS, Vol. 17, 1950, pp. 47-59.

142. G.T. Minkinen, T.A. Wilson, G.S. Beavers, "An experiment on the lift of an accelerated airfoil", AIAA Journal, Vol. 14, No. 5, May 1976, pp. 687-689.

143. G. Gregoriou, "On the calculation of the pressure distribution of wing-body combinations in the non-linear angle-of-attack range", 1977, AGARD-CP-204.

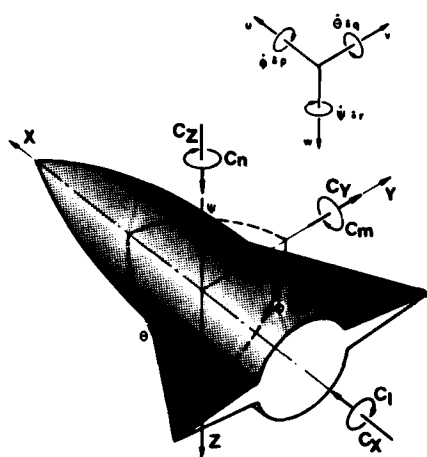
Table 1.1: Coefficients of the normal force, the pitching moment and their derivatives. Reference lengths and surfaces of wing, body and their combination		
Normal force and pitching moment coefficient		
$C_N = N / (\frac{1}{2} \rho V^2 S) \quad ; \quad C_m = M / (\frac{1}{2} \rho V^2 S l)$		
Reference lengths, reference surfaces for C_N and C_m		
Wing	Body	Wing-Body-Combinations
$l = c_o$ or \bar{c}	$l = D_o$ or c	$l = D_o$ or c
$S = S_{(W)}$	$S = S_o$	$S = S_o$
Coefficient derivative series, linear dependence on the variables of the flight condition		
$C_N = \alpha C_{N\alpha} + q \left(\frac{1}{V}\right) C_{Nq} + \dot{\alpha} \left(\frac{1}{V}\right) C_{N\dot{\alpha}} + \ddot{\alpha} \left(\frac{1}{V}\right)^2 C_{N\ddot{\alpha}} + \ddot{\alpha} \left(\frac{1}{V}\right)^2 C_{N\ddot{\alpha}} + \dots$ $= \alpha \frac{\partial N}{\partial \alpha} \left(\frac{2}{\rho V^2 S}\right) + \frac{q}{V} \frac{\partial N}{\partial q} \left(\frac{2}{\rho V S l}\right) + \frac{\dot{\alpha}}{V} \frac{\partial N}{\partial \dot{\alpha}} \left(\frac{2}{\rho V S l}\right) + \frac{\ddot{\alpha}}{V^2} \frac{\partial N}{\partial \ddot{\alpha}} \left(\frac{2}{\rho S l^2}\right) + \frac{\ddot{\alpha}}{V^2} \frac{\partial N}{\partial \ddot{\alpha}} \left(\frac{2}{\rho S l^2}\right) + \dots$		
$C_m = \alpha C_{m\alpha} + q \left(\frac{1}{V}\right) C_{mq} + \dot{\alpha} \left(\frac{1}{V}\right) C_{m\dot{\alpha}} + \ddot{\alpha} \left(\frac{1}{V}\right)^2 C_{m\ddot{\alpha}} + \ddot{\alpha} \left(\frac{1}{V}\right)^2 C_{m\ddot{\alpha}} + \dots$ $= \alpha \frac{\partial M}{\partial \alpha} \left(\frac{2}{\rho V^2 S l}\right) + \frac{q}{V} \frac{\partial M}{\partial q} \left(\frac{2}{\rho V S l^2}\right) + \frac{\dot{\alpha}}{V} \frac{\partial M}{\partial \dot{\alpha}} \left(\frac{2}{\rho V S l^2}\right) + \frac{\ddot{\alpha}}{V^2} \frac{\partial M}{\partial \ddot{\alpha}} \left(\frac{2}{\rho S l^3}\right) + \frac{\ddot{\alpha}}{V^2} \frac{\partial M}{\partial \ddot{\alpha}} \left(\frac{2}{\rho S l^3}\right) + \dots$		

Table 2.1: Coordination between an application - oriented classification of aerodynamic derivatives and the theoretical classification of fig. 2.1

	1	2	3	4	5	6	7	8	9	10	11	12
wings with harmonic oscillations of small amplitude		1, 21, 34, 56, 57, 68, 69, 70, 74 - 80, 142			1, 2, 5, 14-17, 21, 24, 25, 32, 62, 65, 72, 75, 83, 94, 96, 141	5, 7, 8, 9, 14-16, 22, 29, 30, 33-35, 42, 44, 45-46, 51-64, 67, 72, 73, 64, 94, 94-96, 114, 136-138						
bodies of rotational symmetry with harmonic oscillations of small amplitude		34, 41, 113, 114, 122				28, 34, 41, 50, 106, 107, 108, 113, 131, 139						
wings with arbitrary motion, non-linear effects			6, 11, 12, 138	6, 27, 64, 69, 77, 85, 90, 91, 127, 129, 142			27, 37, 64, 69, 85, 91, 134	28, 27, 33, 40, 42, 54, 64, 69, 82-87, 80, 91			11	
bodies of rotational symmetry with arbitrary motion, non-linear effects				65, 98, 99, 113, 114, 115, 116, 122			28, 31, 100, 101, 123	51, 97, 99, 102, 108, 106-114, 116, 122			120, 121	
bodies or wings with unsteady boundary layer			11, 12	11, 12							11, 12	
wing-body configuration, wing-body-tail configuration, interference in unsteady flow		1, 34, 87,	4, 138	28	1, 32, 150	7, 8, 9, 28, 31, 34-36, 48, 52, 131, 134-136	28, 31, 36, 56, 125, 126	28, 31, 49, 99, 125, 133				

Table 3.1: Reduced frequency of various MBB missiles at cruise-speed and -altitude

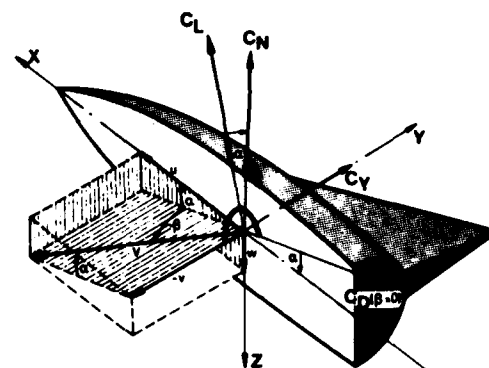
missile (No.)	cruise Mach number M	flight altitude A [\bar{km}]	body length c [\bar{m}]	natural pitch frequency f [s^{-1}]	reduced frequency $k = \frac{2\pi fc}{aM} = \frac{qc}{V}$
1	0.7	<1	0.5	3.6	~0.05
2	3.3	20	3.3	0.45	0.02
3	1.8	10	3.3	1.15	0.06
4	0.97	<1	4.4	0.04	0.04
5	2.5	<1	3.6	1.6	0.043



translatory degrees of freedom	longitudinal	lateral	normal
coordinates	X	Y	Z
velocities	u	v	w
axial forces	C_X	C_Y	C_Z

rotatory degrees of freedom	roll	pitch	yaw
angles	ϕ	θ	ψ
angular velocities	p	q	r
moments	C_l	C_m	C_n

Fig. 1.1: Body-fixed coordinates, velocity components, axial forces and moments according to the standard of flight mechanics, assuming coincidence of body coordinates and geodetical coordinates



resultant velocity	V	lift	C_L
velocity components	u, v, w	normal force	C_N
angle of attack	α	side force	C_Y
angle of sideslip (yaw)	β	drag force	C_D

Fig. 1.2: Body-fixed coordinates, angle of attack, aerodynamic forces

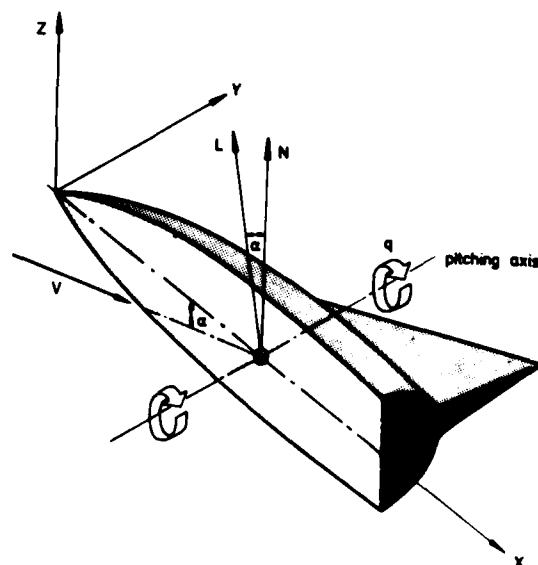


Fig. 1.3: Body-fixed coordinate system for the determination of pitching derivatives (theoretical aerodynamics)

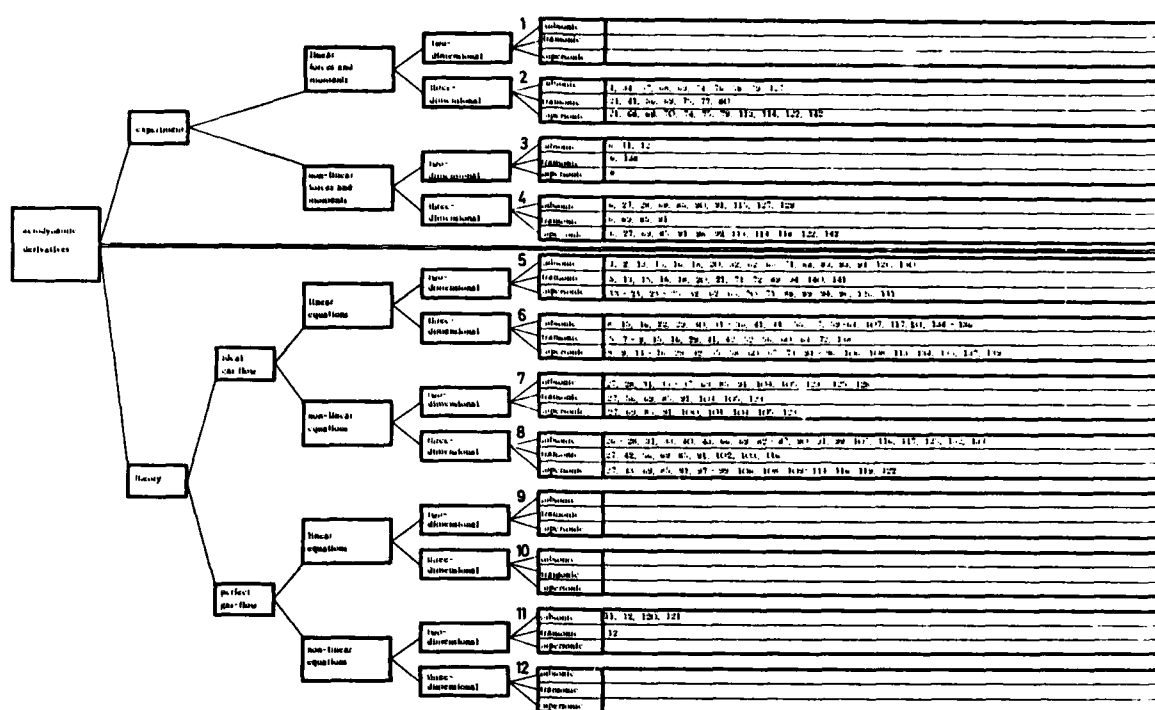


Fig. 2.1: Frame for the classification of aerodynamic derivatives and literature on the subject under a theoretical viewpoint

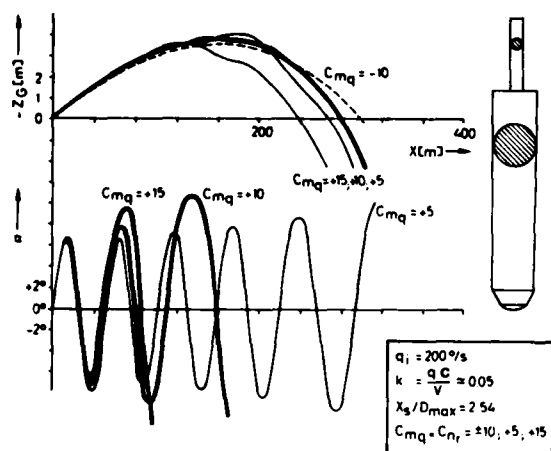


Fig. 3.1: Computer simulation of the flight path and the vertical motion of a ballistic projectile

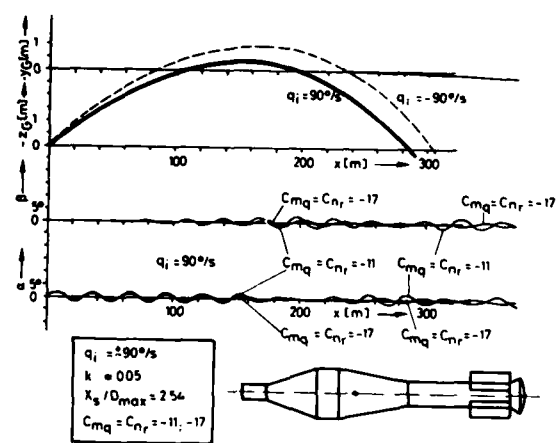


Fig. 3.2: Computer simulation of the flight path and the lateral motion of a projectile with fin and flare stabilization

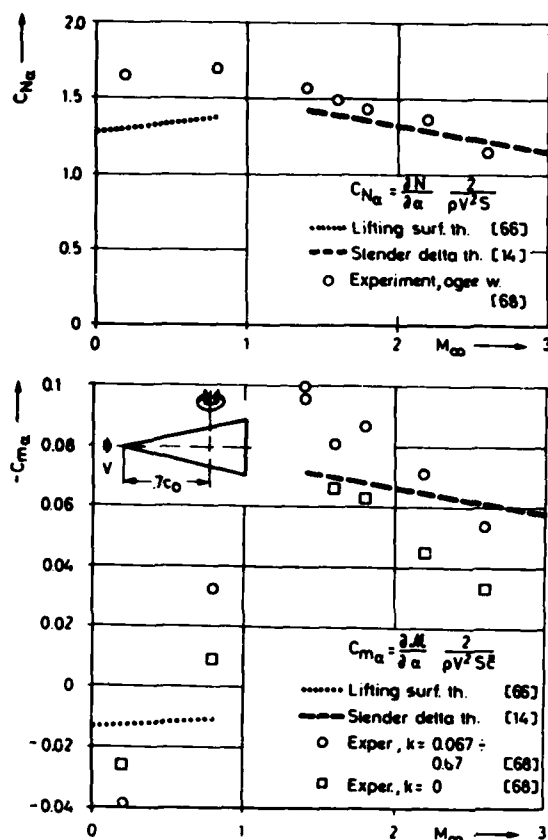


Fig. 3.3: Normal force slope and pitch stiffness of low aspect-ratio delta and ogee wings, $AR=0.924$

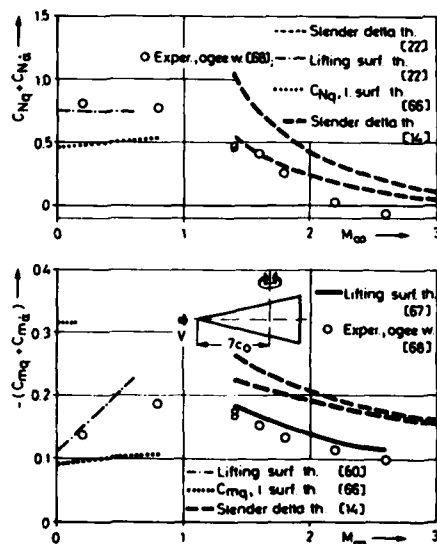


Fig. 3.4: Normal-force and pitching moment damping of low-aspect-ratio delta and ogee-wings $AR=0.924$, comparison of theoretical and experimental results, pitch frequency of experiment $k=q \cdot \bar{c}/V=0.067 \pm 0.67$

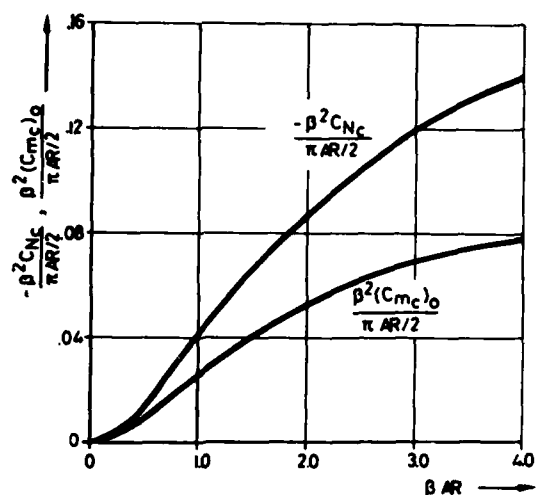


Fig. 3.5: Variation of $C_{N\alpha}/(1/2\pi AR)$ and X_N/c_0 with reduced aspect ratio, βAR

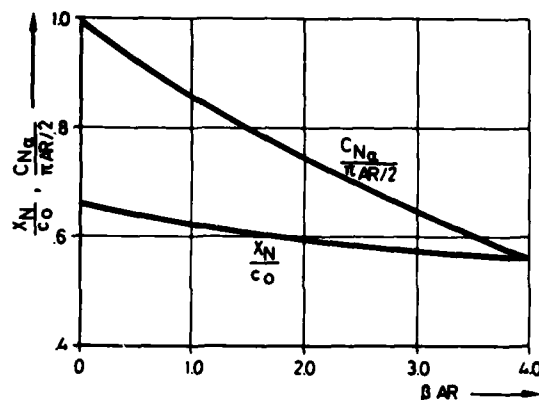


Fig. 3.6: Variation of lift- and moment-coefficient correction terms with reduced aspect ratio, βAR

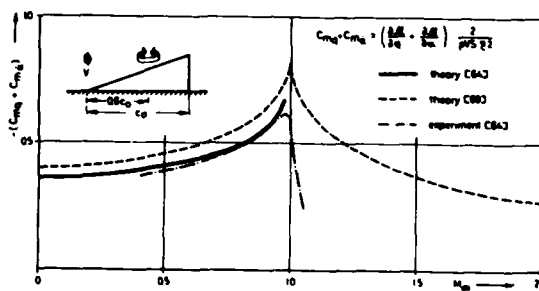


Fig. 3.7: Pitch damping of a delta wing $AR=1.45$ in subsonic and supersonic flow, comparison of theoretical and experimental results

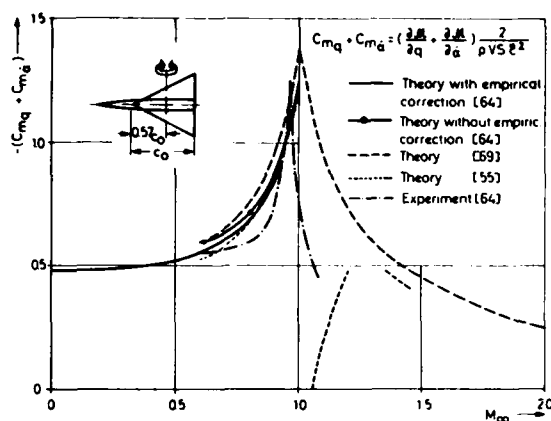


Fig. 3.8: Pitch damping of a delta wing AR=2 in subsonic and supersonic flow, comparison of theoretical and experimental results

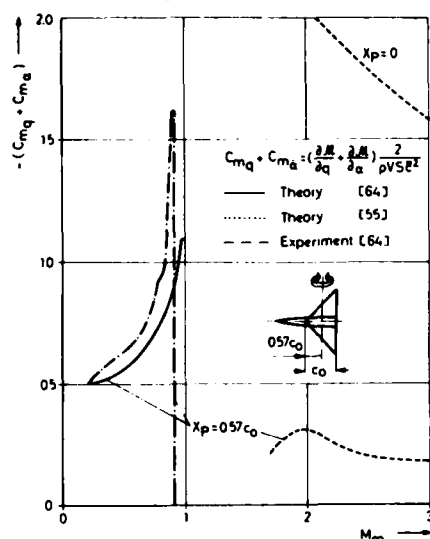


Fig. 3.9: Pitch damping of a delta wing AR=4 in subsonic and supersonic flow, comparison of theoretical and experimental results

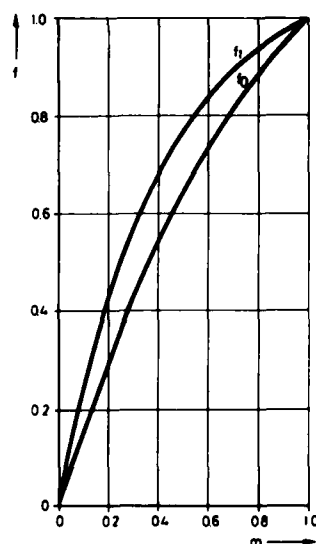


Fig. 3.10: The functions $f_0(m)$ and $f_1(m)$ of Miles' supersonic theory of slender delta wings (ref. 14)

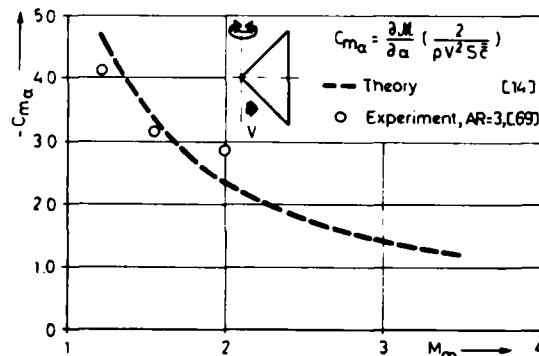
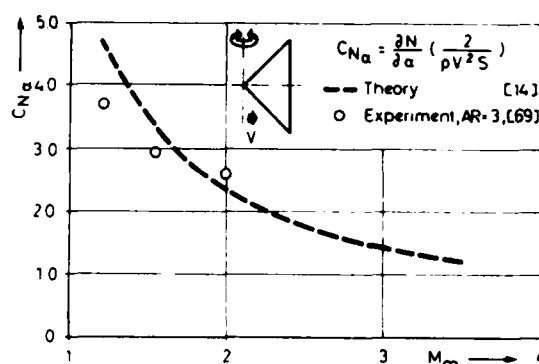


Fig. 3.11: Normal-force slope and pitch stiffness of a delta wing AR=4 in supersonic flow, comparison of theoretical and experimental results

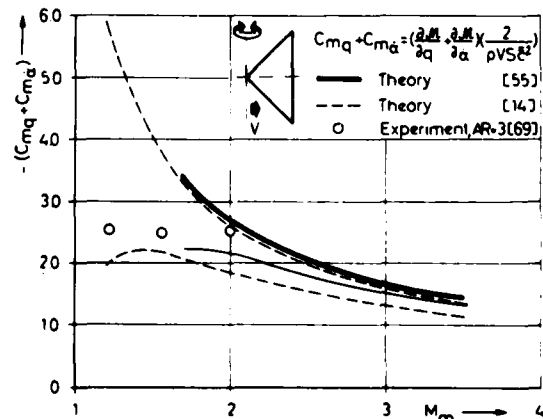
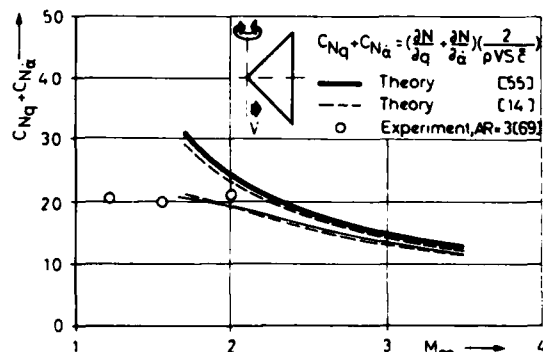


Fig. 3.12: Normal-force- and pitch damping of a delta wing AR=4 in supersonic flow, comparison of theoretical and experimental results

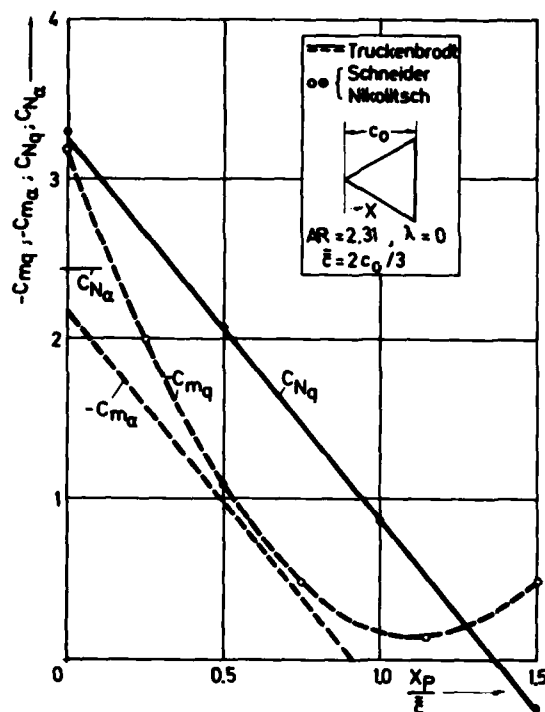


Fig. 3.13: Normal-force slope, pitch stiffness, normal-force and pitch-damping of a delta wing in subsonic flow ($M=0.2$), influence of the location of the pitching axis, comparison of theoretical data

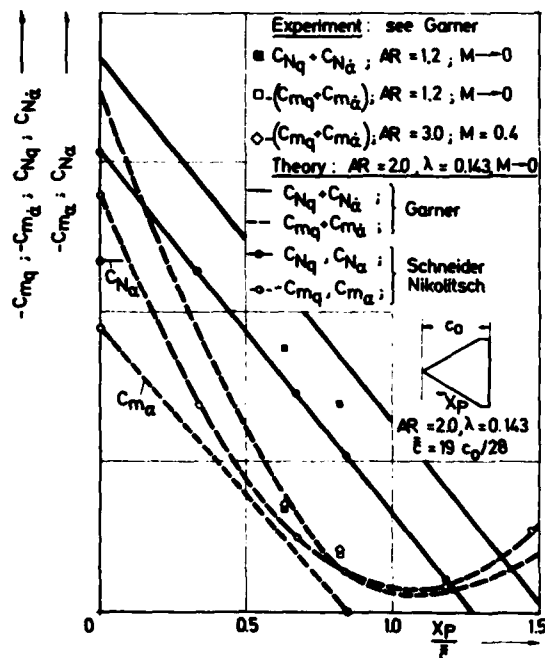


Fig. 3.14: Normal-force- and pitch-damping of delta wings in subsonic flow as function of the location of the pitching axis, comparison of theory and experiment

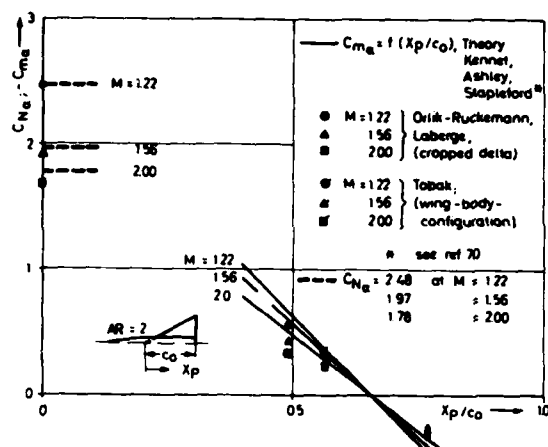


Fig. 3.15: Normal-force slope and pitch stiffness of a cropped delta wing ($AR=2$, $\lambda=0.072$) and a delta wing-body-configuration ($AR=2$) in supersonic flow, influence of the locations of the pitching axis on the pitch stiffness, comparison of theory and experiment

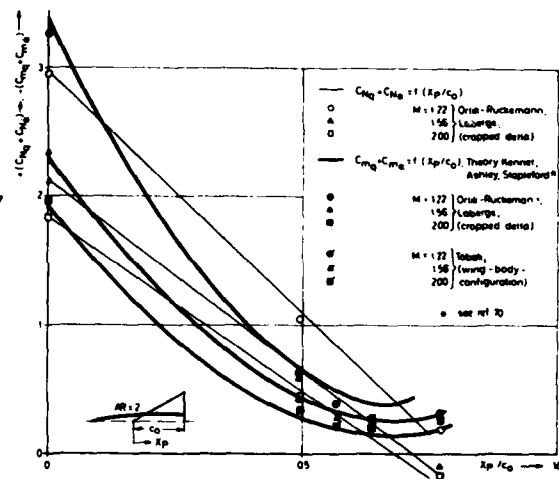


Fig. 3.16: Normal-force- and pitch-damping of a cropped delta wing ($AR=2$, $\lambda=0.072$) and a delta wing-body-configuration ($AR=2$) in supersonic flow, influence of the location of the pitching axis, comparison of theory and experiment

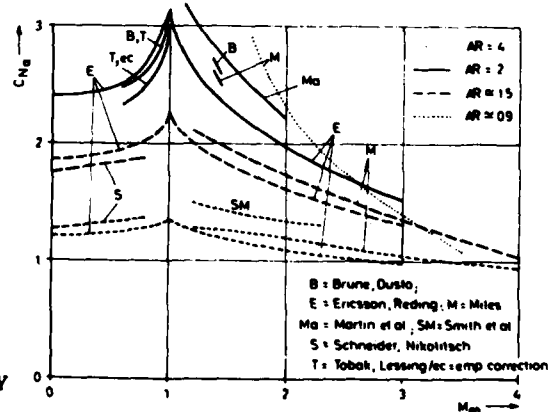


Fig. 3.17: Theoretical data of the normal force slope of delta wings at zero angle of attack

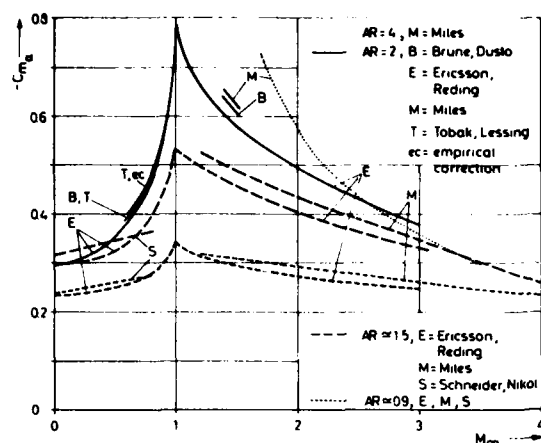


Fig. 3.18: Theoretical data of the pitching moment slope of delta wings at zero angle of attack, location of pitching axis at $X_p/c_0=0.5$

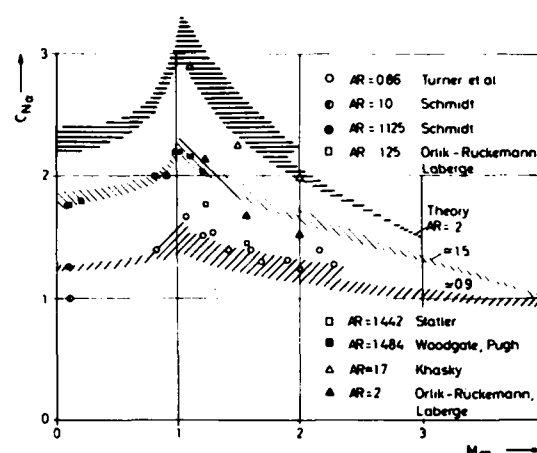


Fig. 3.21: Experimental results of the normal force slope of delta wings compared to the bandwidth of theoretical data of fig. 3.17

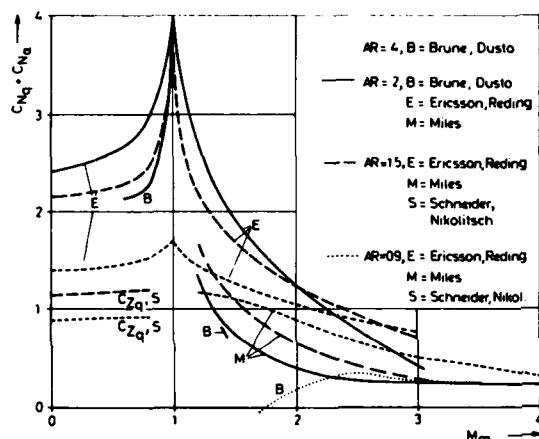


Fig. 3.19: Theoretical data of normal-force damping of delta wings at zero angle of attack, location of pitching axis at $X_p/c_0=0.5$

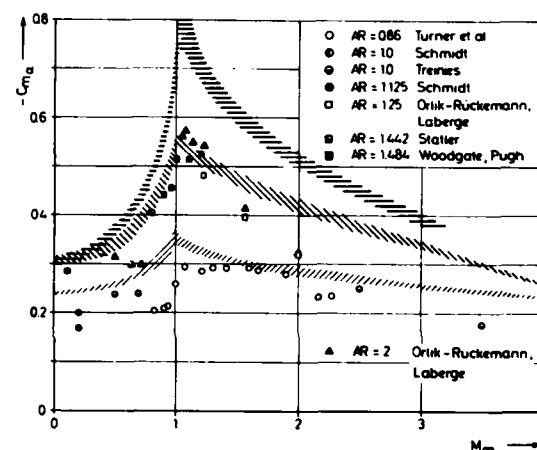


Fig. 3.22: Experimental data for the pitch stiffness of delta wings compared to the bandwidth of theoretical data of fig. 3.18, location of pitching axis $X_p/c_0=0.5$

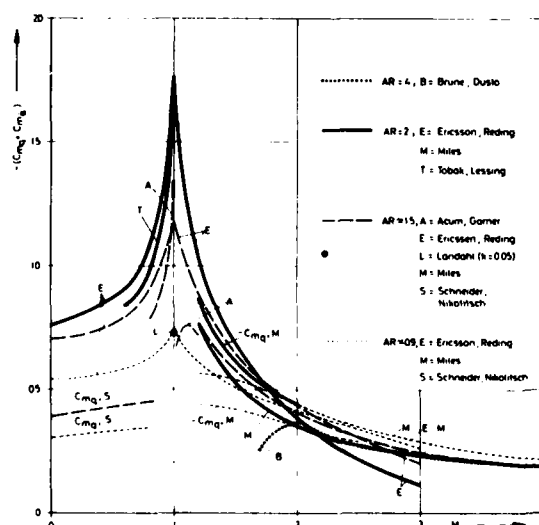


Fig. 3.20: Theoretical data of pitch damping of delta wings at zero angle of attack, location of pitching axis at $X_p/c_0=0.5$

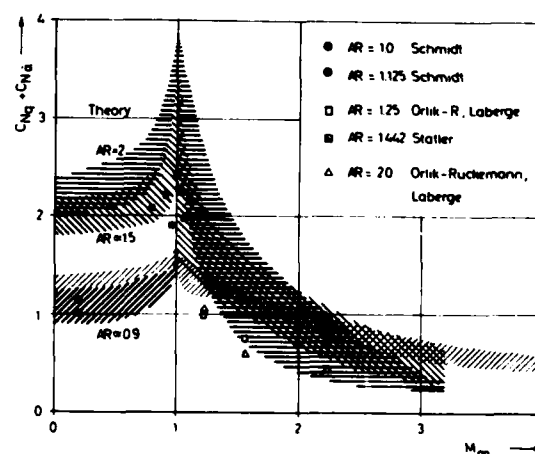


Fig. 3.23: Experimental data of the normal force damping of delta wings compared to the bandwidth of theoretical data of fig. 3.19, location of pitching axis $X_p/c_0=0.5$

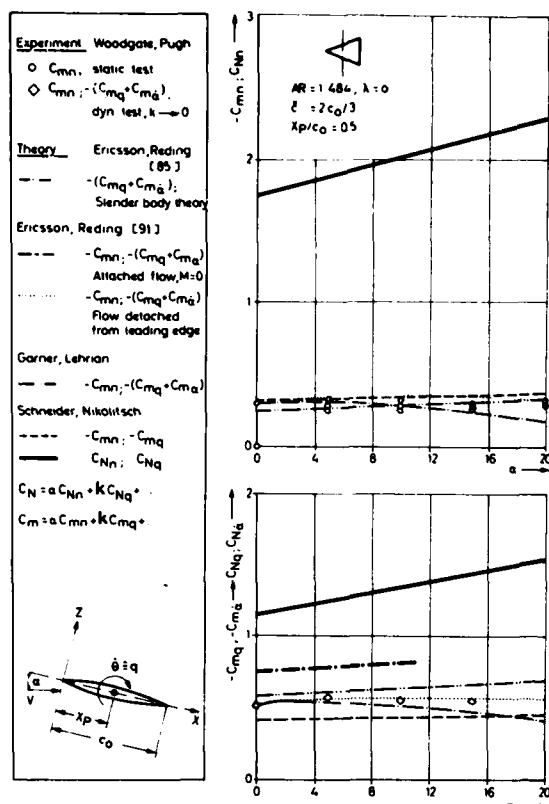


Fig. 3.29: Nonlinear normal-force and pitching moment coefficients C_{Nn} , C_{mn} , normal-force- and pitch-damping of a delta wing in subsonic flow ($M=0.2$) as functions of the angle of attack, comparison of theory and experiment

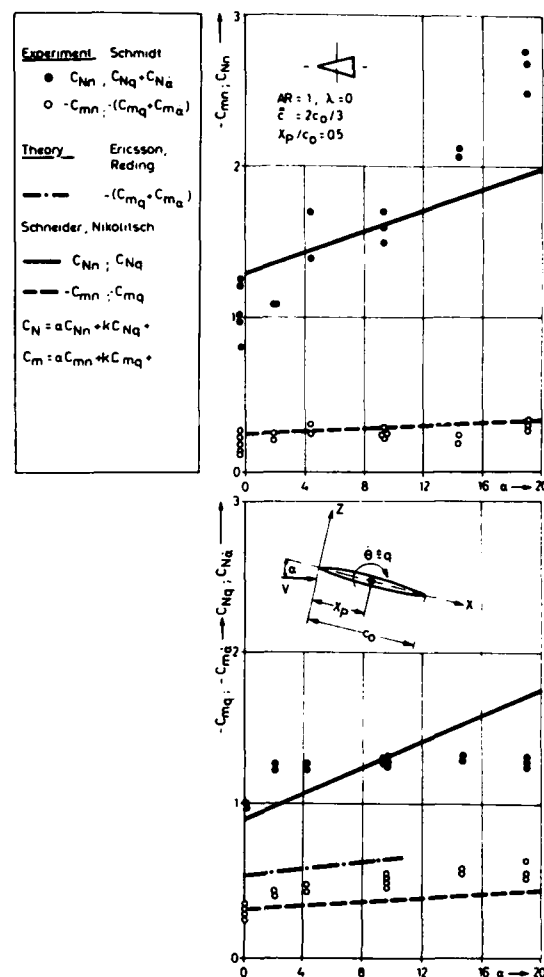


Fig. 3.30: Nonlinear normal-force and pitching moment coefficients C_{Nn} , C_{mn} , normal-force- and pitch damping of a delta wing in subsonic flow ($M=0.2$) as functions of the angle of attack, comparison of theory and experiment

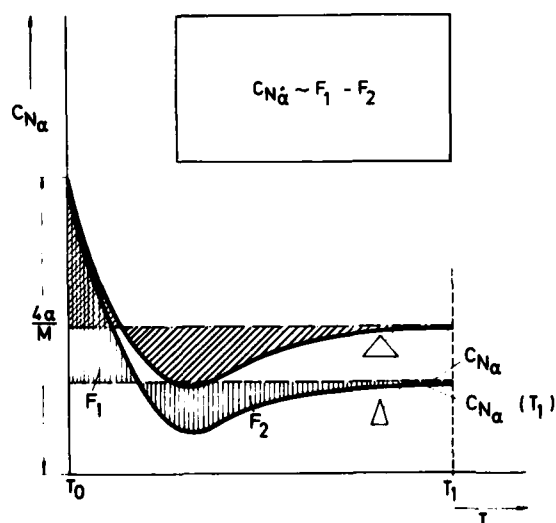


Fig. 3.31: Schematic presentation of the time dependent normal force slope following a sudden change $\Delta\alpha$, influence of the aspect ratio of delta wings in subsonic flow

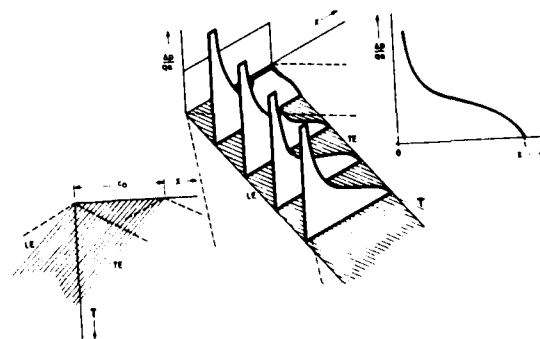


Fig. 3.32: Transient values of the pressure distribution on a two-dimensional wing at subsonic speed

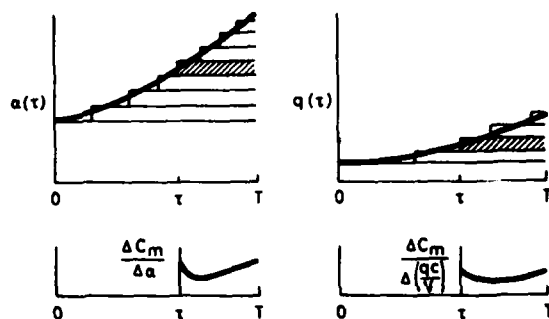


Fig. 3.33 Reaction of the pitching moment upon a sudden change $\Delta\alpha$, and upon a change of the pitching velocity $\Delta(qc/V)$, time independent differential quotients

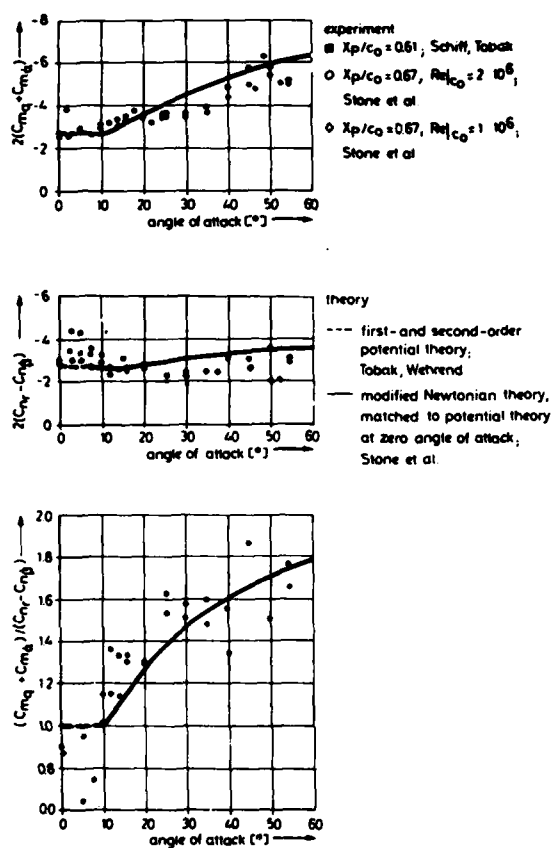


Fig. 3.34: High angle-of-attack effect on the damping moments of a cone of 10° half angle at $M=2$, comparison of experimental data with Newtonian and potential theory

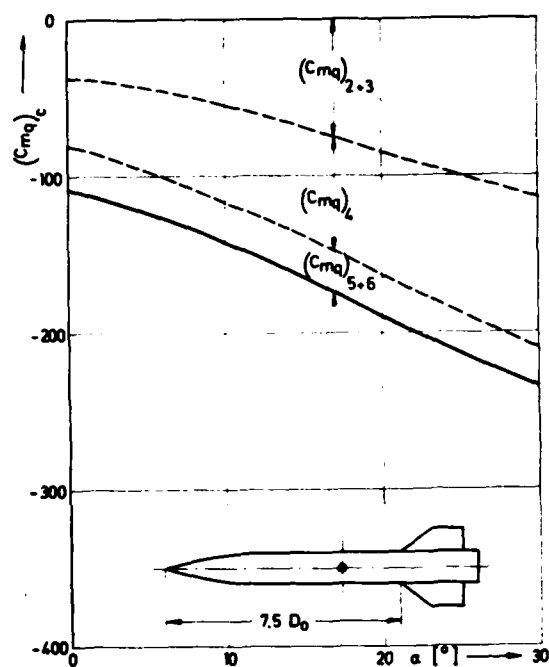


Fig. 3.35: Pitch damping of a missile configuration with the fin tip and pitch axis at $X_p=5.67 D_0$, $M=0.8$; indices: 2+3 ≡ body, 4 ≡ wing, 5+6 ≡ wing/body interference

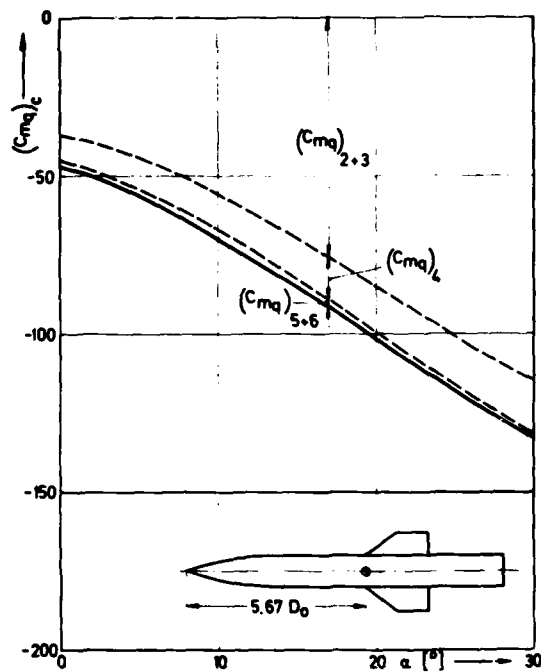


Fig. 3.36: Pitch damping of a missile configuration with the fin tip at $7.5 D_0$ and the pitch axis at $X_p=5.67 D_0$, $M=0.8$; Indices see fig. 3.35

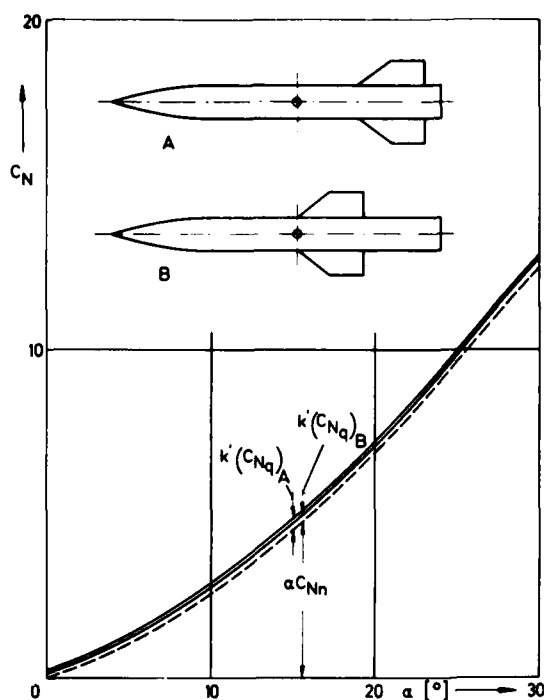


Fig. 3.37: Normal force coefficient $C_N = \alpha(C_{Nn})_C + k'(C_{Nq})_C$ of the configurations A and B at $M=0.8$ with $k'=kD_0/c$ and $k=qc/V=0.05$

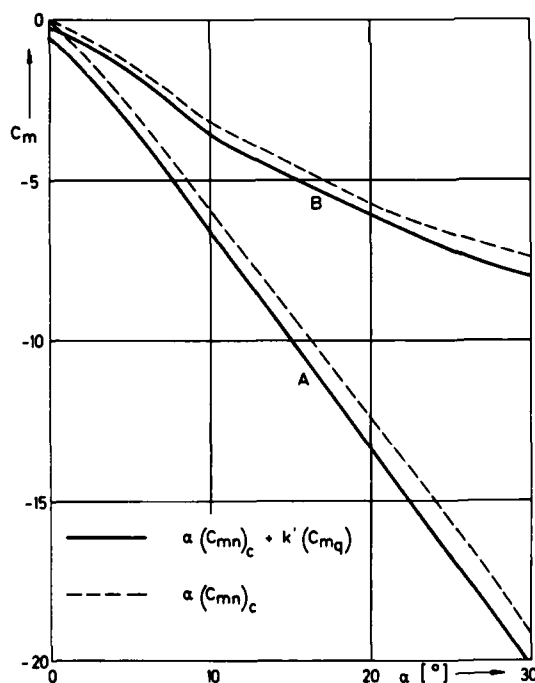


Fig. 3.38: Pitching moment $C_m = \alpha(C_{mn})_C + k'(C_{mq})_C$ of the configurations A and B at $M=0.8$ with $k'=kD_0/c$ and $k=qc/V=0.05$

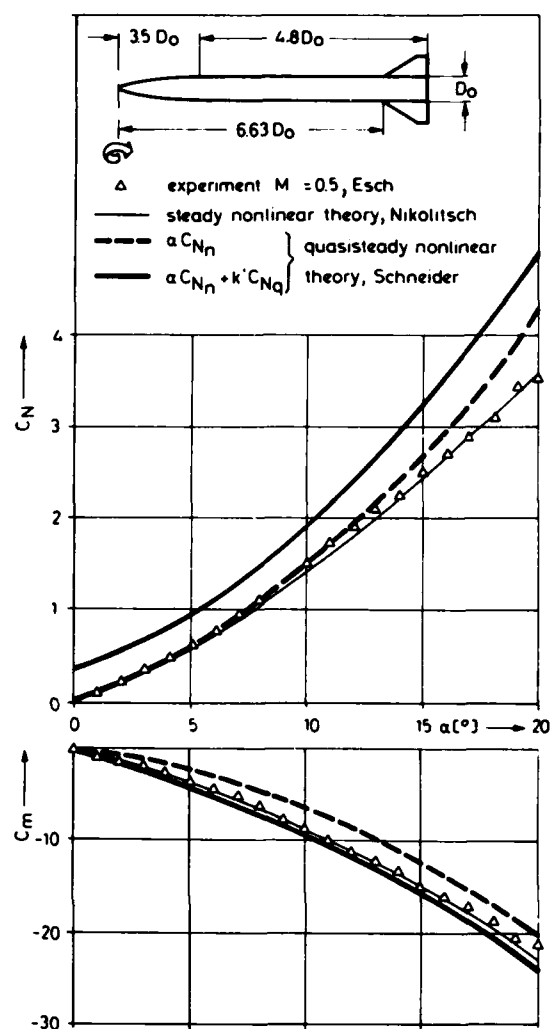


Fig. 3.39: Normal force and moment coefficients of a missile configuration with laminar body boundary layer, comparison of theoretical and experimental results, reduced frequency $k'=kD_0/c$ with $k=qc/V=0.05$

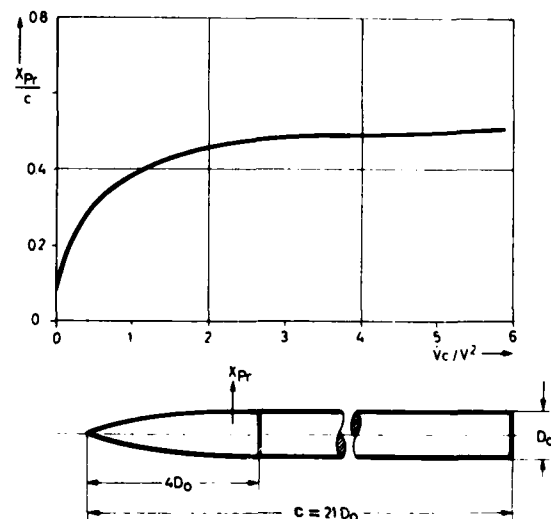


Fig. 4.1: Shift of the center of pressure X_{Pr}/c of an ogive-cylinder body as function of the acceleration parameter Vc/V^2

THE USE OF PANEL METHOD* FOR
STABILITY DERIVATIVES

by

R. Roos

National Aerospace Laboratory, NLR
Amsterdam
The Netherlands

SUMMARY

The possibilities of panel methods for computing aerodynamic stability derivatives are reviewed. Emphasis is put on unsteady panel methods, results of which are compared with experimental data.

LIST OF SYMBOLS

A_{ij}	aerodynamic force (eq. A1)	S	shape function
a	speed of sound	Ω_w	wing surface area
C_l	rolling-moment coefficient	s_w	semi span
C_m	pitching-moment coefficient	t	time
C_n	yawing-moment coefficient	U_∞	free stream velocity
C_y	side-force coefficient	u	perturbation in forward velocity
C_z	normal-force coefficient	V_n	prescribed normal wash
\bar{c}	mean chord	w_n	normal wash
F	functional dependence of a singularity distribution	x, y, z	Cartesian co-ordinate system
g	density of a singularity distribution	α	angle of attack
h	displacement	β	angle of side slip
K	wave number (eq. 6)	β	subsonic: $(1-M_\infty^2)^{1/2}$; supersonic: $(M_\infty^2-1)^{1/2}$
k	reduced frequency	γ_0	flight path angle
	symmetric motions: $k = \omega l / U_\infty$	δ_0	control surface deflection
	antisymmetric motions: $k = \omega l / 2U_\infty$	ξ, η, ζ	Cartesian co-ordinate system
l	reference length	n	state variable of structural vibration mode
M	Mach number	θ	angle of pitch
\vec{n}	unit normal	ρ	density
p	roll rate	ϕ	velocity potential; mode shape
Q_{ij}	generalized aerodynamic force	ϕ	perturbation velocity potential;
q_{ij}	pitch rate		angle of roll
r	yaw rate	ψ	angle of yaw
		ω	oscillation frequency

Superscripts

- ' transformed variable (eq. 4.6)
- ' time derivative

Subscripts

- e referring to a aerodynamic co-ordinate axis system
- g referring to a gust
- s referring to a stability co-ordinate axis system
- ∞ referring to the free stream condition

1. INTRODUCTION

The panel methods referred to in this paper have been developed to determine the potential flow about complex airplane configurations. Their name follows from the fact that the surface of the configuration is divided into a set of small segments, called "panels". Each of these panels is assumed to carry a distribution of so-called singularities, which form elementary solutions of the potential flow equation. By requiring the flow to follow the contour of the particular configuration the density of the singularity distribution on each panel can be found. The combined effect of all singularities results in a description of the sought flow field.

In this paper it is explained in what way panel methods can be instrumental in evaluating the aerodynamic input for investigations on aircraft dynamics. This aerodynamic input is required in the form of aerodynamic derivatives such as stability derivatives, control surface derivatives and gust derivatives. The use of panel methods to compute these derivatives is not new. For example, already in 1969 one finds applications of panel methods for computing stability derivatives (Refs 1,2).

The potentialities of panel methods are clear. In the design phase of an airplane it is necessary to know how changes in the configuration will affect the stability characteristics. While for such studies wind tunnel experiments are prohibitively expensive, the flexibility of panel methods allows for parameter studies at relatively low costs. Further, for configurations like the wide-body transports, the SST or for aircraft equipped with multiple stores, the traditional methods to estimate the derivatives (aerodynamic strip theory or data sheets) have become marginal in their applicability. Here also, panel methods can be extremely useful.

Next to this, it becomes more and more necessary to account for the effects of structural deformations. The introduction of large transport planes and higher flight speeds has set off a trend towards increased structural flexibility, which cannot always be ignored in flight dynamic investigations. Similarly the increased application of flight control systems in modern military aircraft may lead to adverse effects due to coupling with structural deformations. This increased importance of the structural deformations results in an aerodynamic coupling of the rigid body motions and the structural motions, making a time dependent or frequency dependent analysis of the stability derivatives necessary. In this respect it is important to recognize the existence of unsteady (harmonic) panel methods, used in aeroelastic investigations.

* This investigation was carried out under contract for the Scientific Research Branch, Air Materiel Directorate, Royal Netherlands Air Force, (RNLAF).

In the following it is tried to give some insight how panel methods may be used for computing aerodynamic derivatives. First the basics of both steady and unsteady panel methods are touched upon. Next some observations are made as to the possibilities of the different methods. Finally some comparisons are made between calculated and measured stability derivatives. Here emphasis is put upon the use of unsteady panel methods, which introduce the possibility to compute "dynamic" stability derivatives. The material presented in this paper is based partly on reference 3.

2. PANEL METHODS

2.1. Fundamentals

The starting point for the description of the compressible flow field about an aircraft configuration, as applied in panel methods, is the assumption of irrotational, (inviscid), flow. This makes it possible to introduce a velocity potential $\phi = U_\infty x + \phi$, in which U_∞ is the freestream velocity and ϕ a perturbation potential. After linearization this perturbation potential satisfies the equation

$$(1-M_\infty^2) \phi_{xx} + \phi_{yy} + \phi_{zz} - \frac{1}{a_\infty^2} \phi_{tt} - 2 \frac{M_\infty}{a_\infty} \phi_{xt} = 0 \quad (1)$$

and is subject to the boundary condition

$$\frac{\partial \phi}{\partial t} + (\vec{U}_\infty + \vec{V}\phi) \cdot \vec{VS} = 0, \quad (2)$$

which states that at all times the flow should be tangential to the surface of the configuration, described by the shape function $S(x,y,z,t) = 0$.

For incompressible flow equation (1) reduces to the well known Laplace equation

$$\phi_{xx} + \phi_{yy} + \phi_{zz} = 0 \quad (3)$$

which then in addition holds for the full potential ϕ . In the case of steady compressible flow the Göthert co-ordinate transformation

$$x' = x, \quad y' = \beta y, \quad z' = \beta z \quad (4)$$

transforms for subsonic conditions equation (1) into a Laplace equation, while for supersonic conditions the wave equation

$$\phi_{x'x'} - \phi_{y'y'} - \phi_{z'z'} = 0 \quad (5)$$

is obtained. In many unsteady flow applications the perturbation potential ϕ can be assumed to have a harmonic behaviour: $\phi = \phi_1 e^{i\omega t}$. Here the Göthert transformation combined with the substitution

$$\phi' = \phi_1 e^{-iKM_\infty x}, \quad K = \frac{\omega}{a_\infty \beta^2} \quad (6)$$

results in a Helmholtz equation

$$\phi_{x'x'} + \phi_{y'y'} + \phi_{z'z'} + K^2 \phi' = 0 \quad (7)$$

In all types of panel methods the solutions of the Laplace, Helmholtz or Wave equation are found by a linear superposition of fundamental solutions of these equations. For this purpose in general the "source", "doublet" and "vorticity" distributions are used. For the source and doublet distributions the general solutions for the equations then are found as an integral over the weighted distributions placed on the surface of the configuration and the wake:

$$\phi(x',y',z',K) = \iint_{S(\xi',\eta',\zeta')} g(\xi',\eta',\zeta') F(x'-\xi',y'-\eta',z'-\zeta',K) dS \quad (8)$$

in which the fundamental solution F depends on the type of distribution used. A general solution for the velocity field is easily found by differentiation. When using a vorticity distribution a similar surface integration gives immediately the general solution for the velocity field. In all cases the weighting function g indicates the still unknown density of a particular distribution.

After having applied the reverse of the transformations defined by (4) and (6), the general solution for the velocity field can be substituted in equation (2), thus effecting the tangential flow condition. This results in an integral equation for the normal wash:

$$\frac{\partial}{\partial n} \iint_{S(\xi,\eta,\zeta)} g(\xi,\eta,\zeta,\omega) F(x,y,z,\omega) dS = V_n(x,y,z,\omega) \quad (9)$$

from which the unknown density g can be solved.

In panel methods the surface, of the configuration, is divided in individual elements, called panels. On the panels the source, doublet or vorticity density are taken to vary in a certain way: the earlier methods, such as the source panel method of Hess and Smith (Ref. 4), use a constant density over each panel; the newer methods use higher order functions to approximate the variation of the density per panel, with at the same time enforcing some continuity condition on the panel edges.

This division in panels reduces the integral equation to a system of linear algebraic equations. The unknowns are the coefficients in the approximations for the distributions per panel. The right-hand side of each equation contains the specified normal velocity in one or more points per panel (depending on the number of unknowns). Substitution of the coefficients in the pertinent formulae, results in values for the velocity and pressure distribution along the surface of the configuration.

For a more detailed description of the fundamentals the reader is referred to references 5 and 6.

2.2. Types of panel methods

Over the years several kinds of panel methods have been devised. The major difference lies in the type of fundamental singularity or combination of singularities used. In the following only a few of them are mentioned.

As far as steady methods are concerned, the Vortex-lattice (VL) method is perhaps the first and most simple panel method ever developed. The original idea of Falkner (Ref. 7) was implemented on the computer a.o. by Hedman (Ref. 8). The wing, which is regarded as infinitely thin, is covered with a network of horseshoe-vortices, with their trailing legs extending downstream to infinity and composing the wake. This method is capable of treating lifting surfaces, but due to its neglect of thickness it can not handle complete configurations.

The first method to describe the potential flow about thick bodies was the method of Hess and Smith (Ref. 3), who employed constant source panels. A source distribution is not capable of describing a wake in which the vorticity, shed from a lifting configuration, is carried off to infinity. Therefore this method is limited to non-lifting configurations.

The earlier methods for thick lifting configurations used a combination of two types of distributions: a source distribution on the surface of the configuration and a vorticity or doublet distribution on the wake surface and on the internal camber surface. This scheme forms the basis for methods developed a.o. at Boeing (Ref. 9), Douglas (Ref. 10), NLR (Ref. 11), BAC (Ref. 12) and MBB (Ref. 13). Clearly other set-ups are possible to describe this type of flows, such as a doublet or vorticity distribution on both the surface of the configuration and the wake surface. Lately a trend is developing towards methods with higher order distributions.

The most popular panel method for unsteady flow is the Doublet-lattice (DL) method. This method originally developed by Albano and Rodden (Ref. 14) can be regarded as the unsteady version of the Vortex-lattice method. It describes the unsteady flow field about an infinitely thin, harmonically oscillating lifting surface configuration. The singularity used is the pressure doublet, which through chordwise integration over a panel reduces to an unsteady lifting line formulation equivalent to the horseshoe-vortex approach.

Based on the Doublet-lattice formulation several attempts were made to incorporate also the effects of the fuselage and stores into the description of the unsteady flow field. First Kalman, Rodden and Giesing (Ref. 15) computed oscillatory wing/body interference by panelling the body as a ring wing. Later a slender body formulation was added to be able to calculate the unsteady forces on the bodies also (Ref. 16).

At the NLR, the Doublet-lattice method was combined with an unsteady source panel method (Ref. 17). In this (NLRI) method the surfaces of the bodies are covered with panels containing a harmonically oscillating constant source distribution, for which the basic formulation was developed earlier by Hess (Ref. 18). The thickness of the lifting surfaces is still neglected.

Finally Morino (Ref. 19) has developed an unsteady panel method in which source and dipole distributions are placed on the surfaces of both the bodies and the lifting elements of the configuration.

3. POSSIBILITIES FOR CALCULATING STABILITY DERIVATIVES

When considering the use of panel methods to compute aerodynamic derivatives necessary for flight dynamic investigations it is useful first to examine the possibilities of such methods more closely. In doing so, certain derivatives can be excluded beforehand, since the assumptions inherent to panel methods make it impossible to compute them with sufficient accuracy. Further a preliminary choice as to the type of panel method most suitable for computing a particular derivative may be made.

3.1. Limitations due to the neglect of viscosity

Common to all panel methods is the assumption of potential flow, implying the neglect of viscosity. This means that the viscous boundary layer along the surface of the configuration is taken to be non-existing. For the high Reynolds number condition encountered with aircraft, this approximation is acceptable when computing coefficients depending on lift. But for estimates on the drag a modelling of viscous effects is indispensable. Some attempts have been made to combine a panel method approach with a 3D-boundary layer calculation, however, such methods are not yet available for routine computations.

This neglect of the boundary layer has several consequences. Some of the derivatives used in stability investigations depend very much on the drag experienced by the aircraft. This drag is built up of viscous drag and induced drag, while for flows with shock waves the wave drag may give an appreciable contribution also. It is clear that this type of derivatives cannot be computed with panel methods in which the boundary layer is not modelled. One possible exception should be mentioned. When the drag derivatives depend mainly on the induced drag, being a function of the lift coefficient, a reasonable estimate might be obtained.

Further the forces experienced by control surfaces depend strongly on the boundary layer also. Therefore panel methods do not seem very promising for predicting control surface derivatives. On the other hand it is possible that although no accurate values may be obtained, trends may be predicted reasonably well, provided that no flow separation occurs.

This introduces an additional serious limitation of the neglect of viscosity namely that flow separation cannot be modelled. A possible exception is the case of leading edge separation, as occurring for delta wings at high angles of attack, where recently some progress was made. Here the assumption of potential flow could be retained by assuming a vortex sheet to be shed from the leading edge and to roll up into a core of concentrated vorticity. Typical examples of panel methods following this approach are presented in references 20 and 21.

3.2. Modelling of compressibility

The assumption of a perturbation potential and the linearization, makes it impossible to treat transonic flow conditions with panel methods based on equation (1). In addition the results of such methods will have a Mach number dependence following the $(1-M^2)$ behaviour of the Götthert rule, which is acceptable up to moderately subsonic flow. For high subsonic flow conditions compressibility corrections such as the one devised at NLR (Ref. 3) may be used. In unsteady methods a "local Mach number correction" Ref. (22) may be useful.

Derivatives with respect to the forward velocity are usually expressed in terms of a sum of derivatives with respect to Mach number, dynamic pressure and thrust coefficient. Of these, only derivatives with respect to Mach number can be evaluated with panel methods. This may be done by performing computations for two different Mach numbers and determining the coefficient according to

$$\frac{\partial C}{\partial M} \sim \frac{C(M + \Delta M) - C(M)}{\Delta M}$$

3.3. Representation of thickness of wings and bodies

For panel methods a clear distinction can be made between planar and non-planar methods. In the planar methods the thickness of the lifting surfaces and the fuselage type parts of the configuration are neglected, while in the fully non-planar methods the thickness of all parts of the configuration is taken into account. A mixture of both is obtained when the lifting surfaces are taken to be thin, while the fuselage is represented correctly. An example of this approach is the NLRI method mentioned in section 2.2

Experience with panel methods has shown that including the wing thickness while neglecting the boundary layer leads to an overestimation of the normal force derivatives on the wing. Due to that the results of planar methods often compare better with experimental data. Clearly, for derivatives to which the fuselage or other thick bodies (such as stores) contribute significantly, non-planar methods or the mixture type methods seem suited most.

In general, applying non-planar methods is more expensive than using planar methods. Therefore, including the effects of fuselage or stores is relatively costly. However, it is possible to introduce the effects of such bodies in an approximate way in planar methods. This is done by representing these bodies in the form of a ring wing, an endplate or a cross. Of course, one has to be careful in applying this type of idealizations, as a certain representation might give good results for one derivative but not for another.

3.4. Application of methods for harmonic motions

The aerodynamic derivatives may be divided in two groups. One group can be computed in principle by a steady method, while the second one can only be evaluated with an unsteady method. In table 1 it is indicated which coefficient belongs to which group. Of course, when making this distinction it should be mentioned that in principle all derivatives can be computed with an unsteady method. The type of unsteady panel methods most commonly in use are those in which small harmonic motions are assumed. In the appendix it is indicated how such methods can be used to obtain the necessary aerodynamic coefficients. In this context it is of interest to mention that all coefficients given in tables A.2 and A.3 can be computed individually. This may be in aid of interpreting results of unsteady windtunnel experiments where many coefficients can be measured only in combination.

TABLE 1

The method of computation of the aerodynamic derivatives depending on their state variable

	Symmetric motions	Antisymmetric motions
Steady method	u, α, q, n δ	β, p, r, η δ
Unsteady method	$\dot{\alpha}, \dot{q}, \dot{n}$ $\dot{\delta}, \dot{\alpha}_g, \alpha_g$	$\dot{\beta}, \dot{p}, \dot{r}, \dot{\eta}$ $\dot{\delta}, \dot{\alpha}_g, \dot{\beta}_g, \alpha_g, \beta_g$

3.5. Relation between aircraft motions and input for steady methods

In the stability axis system an α -variation is equivalent to a variation in the constant upwash experienced by the airplane (Fig. 1). Therefore it is equivalent also to the angle of attack variation to be prescribed in the panel methods, where an aerodynamic axis system is used. A variation with respect to q as defined in the stability axis system is felt by the airplane as a linearly varying upwash (see Fig. 2). Computation of the corresponding derivatives is possible with steady panel methods when the normal wash is specified individually for each panel.

These observations made for the derivatives with respect to the symmetric variables α and q , are valid also for the derivatives with respect to the anti-symmetric variables β , p and r . However, for the derivatives with respect to β and r the accuracy may become questionable at large yawing angles, when there is a large shadow-effect of the fuselage on the lee side wing and a strong interference of the wake of the weather-side wing with the fuselage (see Fig. 3). The shadow effect depends very much on the development of the boundary layer along the fuselage and therefore is not represented in inviscid panel methods. The direct interference of the wake with the fuselage cannot be represented either, although alignment of the trailing vortices with the free stream direction will account for part of the wake effect.

Derivatives resulting from structural deformation, may be calculated also with steady panel methods by specifying the local normal wash per panel. This normal wash is then derived from a given upwash distribution over the configuration, an example of which is given in figure 4.

4. RESULTS OBTAINED WITH UNSTEADY PANEL METHODS

The applicability of steady panel methods for computing stability derivatives is well documented in the literature. Therefore in this paper the emphasis is put on results obtained with unsteady panel methods, which are hard to find in the literature. As far as planar methods are concerned, Hotten and Giesing (Ref. 24) showed the possibilities of the Doublet-lattice method by computing the longitudinal dynamic stability derivatives for a jet transport wing. Unfortunately no comparison with experimental data was given.

To the authors knowledge the first application of an unsteady non-planar method was reported in reference 22. Using the NLRI-method, discussed in section 2.2, the longitudinal dynamic stability derivatives were computed for a delta wing-fuselage configuration at zero angle of attack. The panelling scheme (for symmetry reasons only one half of the configuration) and the results are given in figure 5. For the few derivatives, obtained in an oscillatory windtunnel experiment (Ref. 25), the theory shows a reasonable agreement.

Recently the NLRI panel method was applied also to calculate the lateral stability derivatives for a T-tail transport configuration. For this configuration experimental data were obtained with the small amplitude forced oscillatory roll mechanism at Nasa Langley (Ref. 26). The panelling scheme used in the calculations is shown in figure 6 (again for symmetry reasons only one half is shown). The fuselage of the configuration was approximated by a blunt nosed cylinder with in contrast to the experimental model, no tapering at the rear. The fuselage mounted engine nacelles were not modelled in the calculations, since in the tests their effect was found to be negligible.

In table 2 a comparison is presented of the calculated and measured derivatives for the configurations with and without wings. For the configuration without the wing the agreement between theory and experiment is reasonably good. The effect of adding the wing is predicted fairly well also, except for the cross derivative C_{np} . However, this latter difference can be expected since the main contributions of the wing to this derivative come from profile drag and leading edge suction, which are not modelled in the NLRI-method.

TABLE 2

Comparison of calculated and measured lateral stability derivatives for a T-tail transport

	Fuselage + T-tail		Fuselage + wings + T-tail	
	Theory	Experiment	Theory	Experiment
C_{lp}	-0.029	-0.025	-0.531	-0.465
$k^2 C_{lp}$	0	0	0	0.004
C_{np}	0.052	0.060	0.012	-0.04
$k^2 C_{np}$	0	0	0.001	0

Calculations were performed also for isolated parts of the configuration such as the fuselage, the wing and the T-tail. The results (table 3) clearly show the effect on the derivatives when the configuration is made more complex by adding T-tail and wings to it. They indicate also that summing up the contributions due to the isolated parts of the configuration in general is not allowed, because of aerodynamic interference. A typical example for this is the C_{yp} derivative.

To illustrate in more detail the importance of the aerodynamic interference, the individual contributions of the different parts of the configuration to the derivatives have been listed in table 4. Comparison of tables 3 and 4 show that in general the wing itself is less affected by interference. However, the presence of the wing has a marked influence on the body and even more strongly on the T-tail. Clearly the wake of the wing should be taken into account when computing the contribution due to the T-tail.

5. CONCLUDING REMARKS

In the foregoing the use of panel methods for computing stability derivatives has been discussed. Reasons were given why not all derivatives, especially those which are dominated by viscous drag, can be computed with the same level of accuracy.

The unsteady panel methods, developed for aeroelastic applications, were shown to be very useful for computing "dynamic" stability derivatives. With the aid of some computed examples compared with experimental data, the value of such methods was demonstrated. In addition the calculations showed that parameter studies, in which the contribution of different parts of the configuration are evaluated, can be carried out very successfully with panel methods.

It was further indicated that planar panel methods, which are cheaper to use, in many cases will give satisfactory results.

TABLE 3

Calculated lateral stability derivatives for different parts of a T-tail transport configuration

	Fuselage	Wings	T-tail	Fuselage T-tail	Fuselage wings T-tail
$C_{y\beta}$	-0.052	-0.001	-0.082	-0.200	-0.237
$C_{y\dot{\beta}}$	-0.133	0	-0.006	-0.105	-0.072
C_{yp}	0	0.029	0.039	0.060	-0.035
$C_{y\dot{p}}$	0	0	0.003	-0.011	0.116
C_{yr}	-0.618	0	-0.191	-0.804	-0.675
$C_{y\dot{r}}$	20.8	0.020	32.9	80.0	95.0
$C_{l\beta}$	0	0.015	0.030	0.043	0.025
$C_{l\dot{\beta}}$	0	0	-0.001	-0.002	-0.005
C_{lp}	0	-0.506	-0.027	-0.029	-0.531
$C_{l\dot{p}}$	0	0.010	0	0.007	-0.008
C_{lr}	0	-0.001	0.058	0.081	0.066
$C_{l\dot{r}}$	0	-3.04	-11.8	-17.1	-9.95
$C_{n\beta}$	0.052	0	-0.071	-0.073	-0.080
$C_{n\dot{\beta}}$	-0.007	0	-0.006	0.014	0.037
C_{np}	0	0	0.035	0.052	0.012
$C_{n\dot{p}}$	0	0	0.003	-0.008	0.077
C_{nr}	-0.124	0	-0.169	-0.296	-0.206
$C_{n\dot{r}}$	-21.0	0	28.4	28.9	31.9

TABLE 4

Contributions of the different parts of the configuration to the calculated lateral stability derivatives

	Fuselage	Wings	Stabi- lizer	Fin	Fuselage wings stabilizer fin
$C_{y\beta}$	-0.115	0.003	0	-0.126	-0.237
$C_{y\dot{\beta}}$	-0.077	0	0	0.005	-0.072
C_{yp}	-0.065	0.031	0	-0.001	-0.035
$C_{y\dot{p}}$	0.068	-0.001	0	0.049	0.116
C_{yr}	-0.463	0.001	0	-0.232	-0.675
$C_{y\dot{r}}$	46.0	-1.162	0	50.2	95.0
$C_{l\beta}$	0	-0.023	0.017	0.030	0.025
$C_{l\dot{\beta}}$	0	0.002	-0.006	-0.001	-0.005
C_{lp}	0	-0.523	-0.008	0	-0.531
$C_{l\dot{p}}$	0	0.016	-0.012	-0.012	-0.008
C_{lr}	0	0.007	0.008	0.051	0.066
$C_{l\dot{r}}$	0	9.2	-6.9	-12.2	-9.95
$C_{n\beta}$	0.029	0	0	-0.109	-0.080
$C_{n\dot{\beta}}$	0.034	0	0	0.003	0.037
C_{np}	0.010	0.001	0	0	0.012
$C_{n\dot{p}}$	0.034	0	0	0.043	0.077
C_{nr}	-0.016	0	0	-0.190	-0.206
$C_{n\dot{r}}$	-11.8	0.129	0	43.5	31.9

6. REFERENCES

- 1 Dusto, A.R., Chevalier, H.C., Dornfeld, G.M. and Schwanz, R.C.: An analytical method for predicting the stability and control characteristics of large elastic airplanes at subsonic and supersonic speeds. Part I and II. AGARD Conf. Proc. 46, 1969.
- 2 Roskam, J.: Comments, interpretation and application of a method for predicting aerodynamic characteristics of large flexible airplanes. AGARD Conf. Proc. 46, 1969.
- 3 Labrujère, Th.E., Roos, R. and Erkelens, L.J.J.: The use of panel methods with a view to problems in aircraft dynamics. VKI lecture series 99, 1977. Also NLR MP 77009 U.
- 4 Hess, J.L. and Smith, A.M.O.: Calculation of potential flow about arbitrary bodies. Progress in Aeronautical Sciences, Vol 8, Pergamon, London 1967, pp 1-138.
- 5 Labrujère, Th.E.: A survey of current collocation methods in inviscid subsonic lifting surface theory. Part I: Numerical Aspects. VKI Lecture series 44, Febr. 1972.
- 6 Hunt, B.: The panel method for subsonic aerodynamic flows. VKI Lecture series 1978-4.
- 7 Falkner, V.M.: The calculation of aerodynamic loading on surfaces of any shape. ARC, R and M 1910, 1943.
- 8 Hedman, S.G.: Vortex lattice method for calculation of quasi-steady state loadings on thin elastic wings in subsonic flow. FFA report 105, 1966.
- 9 Rubbert, P.E. et al: A general method for determining the aerodynamic characteristics of fan-in-wing configurations. The Boeing Co Report D6-15047-1, 1967.
- 10 Hess, J.L.: Calculation of potential flow about arbitrary three-dimensional lifting bodies. Phase I Final report. McDonnell Douglas Rept.No.MDC-J 0545, 1969.
- 11 Labrujère, Th.E., Loeve, W. and Slooff, J.W.: An approximate method for the calculation of the pressure distribution on wing-body combinations at sub-critical speeds. AGARD C.P. No. 71, paper 11, 1970. Also NLR MP 70014 U.
- 12 Hunt, B. and Semple, W.G.: The BAC(MAD) program to solve the 3D lifting subsonic Neumann problem using the plane panel method. BAC doc. ARG 97, 1976.
- 13 Kraus, W.: Das MBB-UFE Unterschall-Panelverfahren. UFE 633-70, 1970.
- 14 Albano, E. and Rodden, W.P.: A doublet-lattice method for calculating lift distributions on oscillating surfaces in subsonic flow. AIAA. J. Vol.7, No.2, 1969, pp 279-285.
- 15 Kalman, T.P., Rodden, W.P. and Giesing, J.P.: Application of the Doublet-Lattice method to Non planar configurations in subsonic flow. J. of Aircraft, Vol.8, June 1971, pp 406-413.
- 16 Rodden, W.P., Giesing, J.P. and Kalman, T.P.: New developments and applications of the subsonic doublet-lattice method for non-planar configurations. Douglas Aircraft Co paper 5826. AGARD Conf. Proc. no.80-71, part II, No.4, 1971.

- 17 Roos, R., Bennekens, B. and Zwaan, R.J.: Calculation of unsteady subsonic flow about harmonically oscillating wing/body configurations. J. Aircraft, Vol. 14, No. 5, May 1977, pp 447-454.
- 18 Hess, J.L.: Calculation of acoustic fields about arbitrary three-dimensional bodies by a method of surface source distributions based on certain wave number expansions. Douglas Aircr. Comp. Long Beach, Calif., DAC 66901, March 1968.
- 19 Morino, L.: A general theory of unsteady compressible potential aerodynamics. NASA CR-2464, 1974.
- 20 Johnson, F.T., Lu, P., Brune, G.W., Weber, W. and Rubbert, P.E.: An improved method for the predictions of completely three-dimensional aerodynamic load distributions of configurations with leading edge vortex separation. AIAA paper 76-417.
- 21 Kandil, O.A., Mook, D.T. and Nayfeh, A.H.: Nonlinear prediction of the aerodynamic loads on lifting surfaces. J. of Aircraft, Vol. 13, No. 1, Jan. 1976, pp 27-28.
- 22 Roos, R.: Application of panel methods for unsteady subsonic flow. NLR MP 76010 U, 1976.
- 23 Meyer, J.J. and Zwaan, R.J.: Calculations of frequency response functions for flexible aircraft. NLR TR 75147 U, 1975.
- 24 Rodden, W.P. and Giesing, J.P.: Application of oscillatory aerodynamic theory to estimation of dynamic stability derivatives. J. of Aircraft, Vol. 7, No. 3, 1970, pp 272-275.
- 25 Scherer, M.: Mesure des coefficients de stabilité dans les souffleries transsoniques et supersoniques de l'ONERA. Communication à la session de l'AGARD à Marseille, Sept. 1959.
- 26 Boyden, R.P.: Aerodynamic roll damping of a T-tail transport configuration. NASA TM X-3115, 1974.

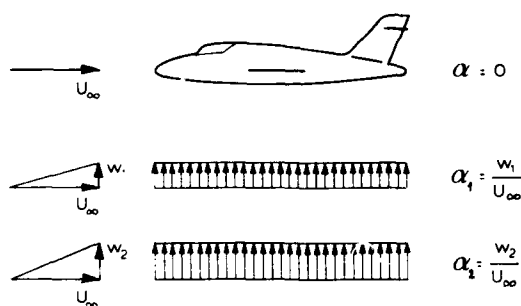


Fig. 1 An α variation in terms of an upwash variation

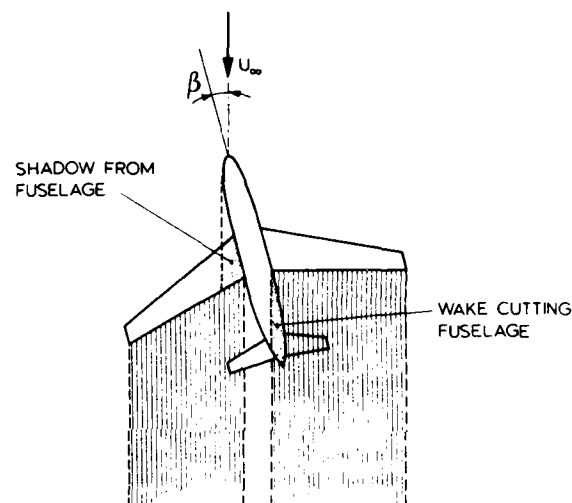


Fig. 3 Poor modelling capabilities for an aircraft subject to a yaw angle

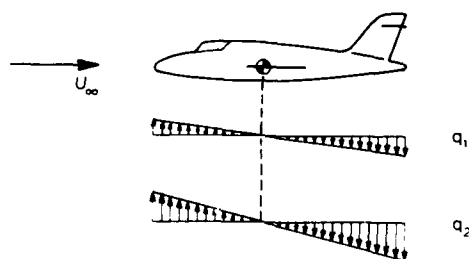


Fig. 2 A q variation in terms of an upwash variation

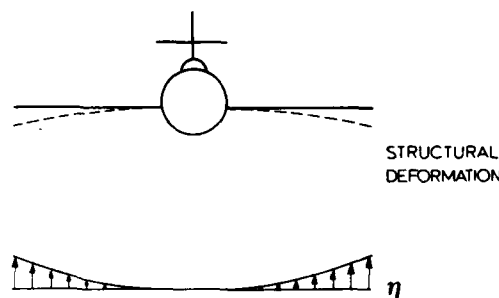
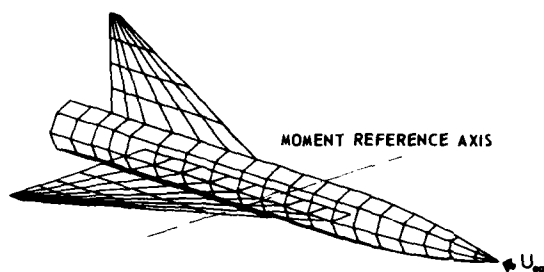


Fig. 4 Example of an upwash distribution for the computation of derivatives with respect to η



$M_{\infty} = 0.6 \quad k = 0.014$		
	CALCULATED	MEASURED
$C_{z, \dot{\alpha}}$	-2.574	-2.510
$C_{z, \dot{\beta}}$	0.487	
$C_{z, q}$	-1.211	
$C_{m, \dot{\alpha}}$	-0.443	-0.420
$C_{m, \dot{\beta}}$	0.226	
$C_{m, q}$	-0.382	-0.315

Fig. 5 Comparison of dynamic stability derivatives as measured in a windtunnel and computed with an unsteady non-planar panel method

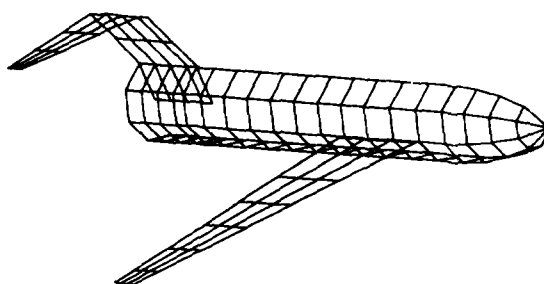
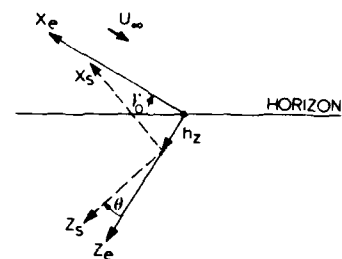
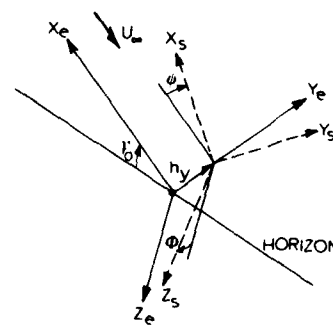


Fig. 6 Panelling scheme for a T-tail transport configuration



a. SYMMETRIC MOTIONS



b. ANTISYMMETRIC MOTIONS

Fig. 7 Orientation of the space-fixed axis system x_e, y_e, z_e and the stability axis system x_s, y_s, z_s

APPENDIX : ANALYTICAL DESCRIPTION OF THE AERODYNAMIC DERIVATIVES

In the stability axis system a typical aerodynamic force is defined as:

$$A_{ij}(t) = \frac{1}{2} \rho U_\infty^2 S_w C_{i_{\xi_j}}(t) \xi_j(t) \quad (A.1)$$

in which ξ_j represents a state variable (rigid or flexible), a control surface deflection or gust variable. The index i refers to one of the rigid body motions or one of the structural vibrations. The non-dimensional aerodynamic derivative is defined as:

$$C_{i_{\xi_j}}(t) = \frac{1}{S_w} \iint C_{p_{\xi_j}}(t) \vec{n} \cdot \vec{\phi}_i dS \quad (A.2)$$

with $C_{p_{\xi_j}}$ being the change in the local pressure distribution due to a change in the state variable ξ_j .

$\vec{\phi}_i$ represents the i^{th} mode shape. For the rigid body motions $\vec{\phi}_i$ takes very simple forms; for symmetric motions e.g.: longitudinal $\vec{\phi}_x = (1, 0, 0)$, normal $\vec{\phi}_z = (0, 0, 1)$ and in pitch $\vec{\phi}_m = (\frac{z-z_m}{c}, 0, -(\frac{x-x_m}{c}))$.

The aerodynamic force as defined in (A.1), can be expanded as follows:

$$A_{ij}(t) = \frac{1}{2} \rho U_\infty^2 S_w \left[C_{i_{\xi_j}} \xi_j + C_{i_{\dot{\xi}_j}} \dot{\xi}_j + O(\xi) \right] \quad (A.3)$$

Neglecting the terms involving ξ and higher order derivatives, the aerodynamic force can be regarded as being built up of a steady term and an unsteady term. The derivative $C_{i_{\dot{\xi}_j}}$ is a quasi-steady quantity and thus can be computed with a steady aerodynamic method (see table 1).

The derivative $C_{i_{\dot{\xi}_j}}$ can be obtained with the existing aerodynamic methods for harmonic aircraft motions, developed for aeroelastic applications. As a rule, the output of these methods comes in the form of generalized aerodynamic forces which refer to an axis system $x_e y_e z_e$ with the x_e -axis pointing in the direction of the undisturbed flight path, while the origin is translating in that direction with a speed U_∞ . These generalized aerodynamic forces are defined as a function of the oscillation frequency ω :

$$A_{mn}(\omega) = \frac{1}{2} \rho U_\infty^2 s^2 \left[Q'_{mn} + i Q''_{mn} \right] \xi_j \quad (A.4)$$

in which

$$Q_{mn} = \frac{1}{s^2} \iint C_{p_n} \vec{n} \cdot \vec{\phi}_m dS \quad (A.5)$$

As small disturbances have been assumed, simple conversion rules exist between harmonic motions in both the $x_s y_s z_s$ stability axis system and the $x_e y_e z_e$ axis system. For the rigid body motions with a frequency ω these rules are given in table A.1.

TABLE A.1

Conversion rules between the stability and the aerodynamic axis system

	$x_s y_s z_s$ stability system		$x_e y_e z_e$ aerodynamic space- oriented axis system
Symmetric motions	α	=	$ik \frac{h_z}{c} + \theta$
	q	=	$ik\theta$
Antisymmetric motions*	β	=	$ik \frac{h_y}{c} - \psi$
	p	=	$\frac{1}{2} ik\phi$
	r	=	$\frac{1}{2} ik\psi$

* The factor $\frac{1}{2}$ in the expressions for p and r enters due to non-dimensionalizing with $2 U_\infty$ instead of U_∞ as in the case of q .

In this table k is the non-dimensional (reduced) frequency and h_z and h_y are translatory motions in the z_e and y_e directions respectively. The orientation of both axis systems is illustrated in figure 7. The expressions describing the structural vibrations, control surface deflections and atmospheric gusts are the same in both axis systems.

Applying a Fourier transformation the aerodynamic force defined in (A.3) can be written as:

$$A_{ij}(\omega) = \frac{1}{2} \rho U_\infty^2 S_w \left[C_{i_{\xi_j}} + ik C_{i_{\dot{\xi}_j}} \right] \xi_j \quad (A.6)$$

Comparing the expressions (A.4) and (A.6) and using the conversion rules as given in table A.1 relations between the two types of aerodynamic derivatives are derived easily. They are given in tables A.2 and A.3 for the symmetric and antisymmetric derivatives respectively, (taken from ref. 23).

TABLE A.2
Relation between symmetric aerodynamic derivatives
and generalized aerodynamic forces

	C_z	C_m	C_{ξ_i}
α	$\frac{s^2}{S_w} \frac{Q_{22}''}{k}$	$\frac{s^2}{S_w} \frac{Q_{32}''}{k}$	$\frac{s^2}{S_w} \frac{Q_{12}''}{k}$
$\dot{\alpha}$	$-\frac{s^2}{S_w} \frac{Q_{22}'}{k^2}$	$-\frac{s^2}{S_w} \frac{Q_{32}'}{k^2}$	$-\frac{s^2}{S_w} \frac{Q_{12}'}{k^2}$
q	$\frac{s^2}{S_w} \left(\frac{Q_{23}''}{k} + \frac{Q_{22}'}{k^2} \right)$	$\frac{s^2}{S_w} \left(\frac{Q_{33}''}{k} + \frac{Q_{32}'}{k^2} \right)$	$\frac{s^2}{S_w} \left(\frac{Q_{13}''}{k} + \frac{Q_{12}'}{k^2} \right)$
\dot{q}	$-\frac{s^2}{S_w} \left(\frac{Q_{23}'}{k^2} - \frac{Q_{22}''}{k^3} \right)$	$-\frac{s^2}{S_w} \left(\frac{Q_{33}'}{k^2} - \frac{Q_{32}''}{k^3} \right)$	$-\frac{s^2}{S_w} \left(\frac{Q_{13}'}{k^2} - \frac{Q_{12}''}{k^3} \right)$
ξ_j	$\frac{s^2}{S_w} Q_{2j}'$	$\frac{s^2}{S_w} Q_{3j}'$	$\frac{s^2}{S_w} Q_{1j}'$
$\dot{\xi}_j$	$\frac{s^2}{S_w} \frac{Q_{2j}''}{k}$	$\frac{s^2}{S_w} \frac{Q_{3j}''}{k}$	$\frac{s^2}{S_w} \frac{Q_{1j}''}{k}$
δ	$\frac{s^2}{S_w} Q_{2\delta}'$	$\frac{s^2}{S_w} Q_{3\delta}'$	$\frac{s^2}{S_w} Q_{1\delta}'$
$\dot{\delta}$	$\frac{s^2}{S_w} \frac{Q_{2\delta}''}{k}$	$\frac{s^2}{S_w} \frac{Q_{3\delta}''}{k}$	$\frac{s^2}{S_w} \frac{Q_{1\delta}''}{k}$
α_g	$\frac{s^2}{S_w} Q_{2\alpha_g}'$	$\frac{s^2}{S_w} Q_{3\alpha_g}'$	$\frac{s^2}{S_w} Q_{1\alpha_g}'$
$\dot{\alpha}_g$	$\frac{s^2}{S_w} \frac{Q_{2\alpha_g}''}{k}$	$\frac{s^2}{S_w} \frac{Q_{3\alpha_g}''}{k}$	$\frac{s^2}{S_w} \frac{Q_{1\alpha_g}''}{k}$

Subscripts of Q_{mn} indicate the mode shape:

2 = vertical translation, 3 = pitching motion, i, j = structural vibration,
 δ = control surface deflection, α_g = gust

TABLE A.3

Relation between antisymmetric aerodynamic derivatives and generalized aerodynamic forces

	C_y	C_ℓ	C_n	C_{ℓ_1}
β	$\frac{s^2}{S_w} \frac{Q_{11}''}{k}$	$\frac{s^2}{S_w} \frac{Q_{21}''}{k}$	$\frac{s^2}{S_w} \frac{Q_{31}''}{k}$	$\frac{s^2}{S_w} \frac{Q_{i1}''}{k}$
$\dot{\beta}$	$-\frac{s^2}{S_w} \frac{Q_{11}'}{k^2}$	$-\frac{s^2}{S_w} \frac{Q_{21}'}{k^2}$	$-\frac{s^2}{S_w} \frac{Q_{31}'}{k^2}$	$-\frac{s^2}{S_w} \frac{Q_{i1}'}{k^2}$
p	$\frac{s^2}{S_w} \frac{2Q_{12}''}{k}$	$\frac{s^2}{S_w} \frac{2Q_{22}''}{k}$	$\frac{s^2}{S_w} \frac{2Q_{32}''}{k}$	$\frac{s^2}{S_w} \frac{2Q_{i2}''}{k}$
\dot{p}	$-\frac{s^2}{S_w} \frac{2Q_{12}'}{k^2}$	$-\frac{s^2}{S_w} \frac{2Q_{22}'}{k^2}$	$-\frac{s^2}{S_w} \frac{2Q_{32}'}{k^2}$	$-\frac{s^2}{S_w} \frac{2Q_{i2}'}{k^2}$
r	$\frac{s^2}{S_w} \left(\frac{2Q_{13}''}{k} - \frac{2Q_{11}'}{k^2} \right)$	$\frac{s^2}{S_w} \left(\frac{2Q_{23}''}{k} - \frac{2Q_{21}'}{k^2} \right)$	$\frac{s^2}{S_w} \left(\frac{2Q_{33}''}{k} - \frac{2Q_{31}'}{k^2} \right)$	$\frac{s^2}{S_w} \left(\frac{2Q_{i3}''}{k} - \frac{2Q_{i1}'}{k^2} \right)$
\dot{r}	$-\frac{s^2}{S_w} \left(\frac{2Q_{13}'}{k^2} + \frac{2Q_{11}''}{k^3} \right)$	$-\frac{s^2}{S_w} \left(\frac{2Q_{23}'}{k^2} + \frac{2Q_{21}''}{k^3} \right)$	$-\frac{s^2}{S_w} \left(\frac{2Q_{33}'}{k^2} + \frac{2Q_{31}''}{k^3} \right)$	$-\frac{s^2}{S_w} \left(\frac{2Q_{i3}'}{k^2} + \frac{2Q_{i1}''}{k^3} \right)$
ξ_j	$\frac{s^2}{S_w} Q_{1j}'$	$\frac{s^2}{S_w} Q_{2j}'$	$\frac{s^2}{S_w} Q_{3j}'$	$\frac{s^2}{S_w} Q_{ij}'$
$\dot{\xi}_j$	$\frac{s^2}{S_w} \frac{Q_{1j}''}{k}$	$\frac{s^2}{S_w} \frac{Q_{2j}''}{k}$	$\frac{s^2}{S_w} \frac{Q_{3j}''}{k}$	$\frac{s^2}{S_w} \frac{Q_{ij}''}{k}$
δ	$\frac{s^2}{S_w} Q_{1\delta}'$	$\frac{s^2}{S_w} Q_{2\delta}'$	$\frac{s^2}{S_w} Q_{3\delta}'$	$\frac{s^2}{S_w} Q_{i\delta}'$
$\dot{\delta}$	$\frac{s^2}{S_w} \frac{Q_{1\delta}''}{k}$	$\frac{s^2}{S_w} \frac{Q_{2\delta}''}{k}$	$\frac{s^2}{S_w} \frac{Q_{3\delta}''}{k}$	$\frac{s^2}{S_w} \frac{Q_{i\delta}''}{k}$
α_g	$\frac{s^2}{S_w} Q_{1\alpha_g}'$	$\frac{s^2}{S_w} Q_{2\alpha_g}'$	$\frac{s^2}{S_w} Q_{3\alpha_g}'$	$\frac{s^2}{S_w} Q_{i\alpha_g}'$
$\dot{\alpha}_g$	$\frac{s^2}{S_w} \frac{Q_{1\alpha_g}''}{k}$	$\frac{s^2}{S_w} \frac{Q_{2\alpha_g}''}{k}$	$\frac{s^2}{S_w} \frac{Q_{3\alpha_g}''}{k}$	$\frac{s^2}{S_w} \frac{Q_{i\alpha_g}''}{k}$
β_g	$\frac{s^2}{S_w} Q_{1\beta_g}'$	$\frac{s^2}{S_w} Q_{2\beta_g}'$	$\frac{s^2}{S_w} Q_{3\beta_g}'$	$\frac{s^2}{S_w} Q_{i\beta_g}'$
$\dot{\beta}_g$	$\frac{s^2}{S_w} \frac{Q_{1\beta_g}''}{k}$	$\frac{s^2}{S_w} \frac{Q_{2\beta_g}''}{k}$	$\frac{s^2}{S_w} \frac{Q_{3\beta_g}''}{k}$	$\frac{s^2}{S_w} \frac{Q_{i\beta_g}''}{k}$

Subscripts of Q_{mn} indicate the mode shape:

1 = horizontal translation, 2 = rolling motion, 3 = yawing motion,

i, j = structural vibration, δ = control surface deflection, α_g, β_g = gust

AN ANALYTIC THEORY OF SUPERSONIC/HYPERSONIC

STABILITY AT HIGH ANGLES OF ATTACK

W. H. HUI

Associate Professor

Department of Applied Mathematics

University of Waterloo

Waterloo, Ontario, Canada N2L 3G1.

Summary

The problem of dynamic stability of supersonic/hypersonic vehicles of simple shapes at high angles of attack is studied based on inviscid flow theory. The amplitude and frequency of the pitching oscillation are assumed small and a perturbation method employed. Systematic investigations of the closed form analytic formulae for the stability derivatives of oscillating wedges, flat plates, delta wings (with attached shock waves or detached shock waves) lead to the following general conclusions: (a) Increasing flight Mach number M_∞ tends to increase the dynamic stability and the stability derivatives tend to constant for large M_∞ ; (b) the sweep-back angle of a delta wing has only small effects on its dynamic stability; (c) for small angles of attack α the damping-in-pitch derivative increases with α but after α reaches certain critical angle the trend is reversed and further increase in α may rapidly cause dynamical instability; and (d) the effects of the specific heat ratio γ of the gas on dynamical stability are small for small angles of attack α , but are large for large α , and in the latter case increasing γ can also cause dynamic instability.

List of Symbols

A	reference area, Eq. (4)
b	semi-span of delta wing
C_m	pitching moment coefficient, Eq. (4)
$-C_{m_\theta}$	stiffness derivative, Eq. (5)
$-C_{m_\dot{\theta}}$	damping-in-pitch derivative, Eq. (5)
h	pivot position measured in body length ℓ from the apex
i	$= \sqrt{-1}$
k	$= \omega \ell / U_\infty$, reduced frequency parameter.
ℓ	body length
M	Mach number
p	pressure
t	time variable
U_∞	free stream velocity
\vec{V}	velocity vector
ρ	density of gas
α	mean angle of attack, also semi-vertex angle of wedge and cone
γ	ratio of specific heats of gas
χ	sweep-back angle of delta wing
ϵ	amplitude of pitching oscillation
ω	circular frequency of oscillation
Ω	similarity parameter defined in Eq. (12)
λ	shock layer parameter defined in Eq. (13)

Subscripts

() _{∞}	free stream
() ₀	steady wedge flow behind the shock

- ()₁ steady flow on upper surface of flat plate
 ()_u upper surface
 ()_l lower surface

1. INTRODUCTION

This paper is concerned with the aerodynamic stability of supersonic/hypersonic vehicles of simple shapes at high angles of attack. The need for investigating stability characteristics at high angles of attack was clearly shown by Orlik-Rüchemann in his survey paper¹, which largely deals with experimental facilities. On the theoretical side, the problem was investigated by the author and his associates in a series of recent studies based on the inviscid flow assumption. These include pitching wedges, flat plates, delta wings with detached shock waves, delta wings with attached shock waves (compression side only), oscillating cones at zero angle of attack, and the caret wing at certain design conditions. Some of these work are already published²⁻⁷ and some are reported here for the first time. In all cases, analytic formulae for the stability derivatives are obtained in closed form.

Whilst the unsteady flow fields over any practical vehicles are very complicated and would require experimental or numerical investigations, it is expected that the inviscid analytical results given here for the simpler shapes will give some insight to the unsteady flow and indicate trends for the stability characteristics of more complex shapes. Especially when there is no flow separation, the effects of viscosity on dynamic stability are known to be generally small^{8,9} and the inviscid flow theory should be reasonably accurate.

Specifically, the problem to be considered is that of a uniform supersonic/hypersonic stream of gas symmetrically past a "vehicle" which performs a small-amplitude, slow pitching oscillation. The gas is assumed to be non-viscous, perfect and with constant specific heats, and the aim is to calculate the resulting unsteady flow and hence the stability derivatives. The governing equations are

$$\begin{aligned}\frac{\partial \rho}{\partial t} + \nabla \cdot (\rho \vec{v}) &= 0 \\ \frac{\partial \vec{v}}{\partial t} + \vec{v} \cdot \nabla \vec{v} + \frac{\nabla p}{\rho} &= 0 \\ \frac{\partial (\rho / \rho^\gamma)}{\partial t} + \vec{v} \cdot \nabla \left(\frac{\rho}{\rho^\gamma} \right) &= 0\end{aligned}\quad (1)$$

where \vec{v} , p , ρ are, respectively, the velocity, pressure and density, and γ the ratio of specific heats of the gas. The boundary condition to be satisfied at the body surface is

$$\text{at } B = 0, \quad \frac{\partial B}{\partial t} + \vec{v} \cdot \nabla B = 0 \quad (2)$$

where $B = 0$ is the equation of the body surface. The boundary conditions at the shock wave are the well-known Rankine-Hugoniot conditions

$$\begin{aligned}\text{at } s = 0, \quad [\rho (\frac{\partial s}{\partial t} + \vec{v} \cdot \nabla s)] &= 0 \\ [\rho (\frac{\partial s}{\partial t} + \vec{v} \cdot \nabla s)^2 + p (\nabla s)^2] &= 0 \\ [\vec{v} \times \nabla s] &= 0 \\ [\frac{1}{2} (\frac{\partial s}{\partial t} + \vec{v} \cdot \nabla s)^2 + \frac{\gamma}{\gamma-1} \frac{p}{\rho} (\nabla s)^2] &= 0\end{aligned}\quad (3)$$

where the unknown shock shape is described by $s = 0$ and the square brackets denote the change in the enclosed quantity across the shock.

There are two major difficulties in solving the problem as formulated: (a) the non-linearity in the equations as well as in the shock boundary conditions; (b) the existence of the shock wave whose position is not known a priori but has to be determined as part of the solution. Since the boundary conditions are to be satisfied at the shock wave, this renders the mathematical problem a free boundary one. At present, there exists no general method for solving non-linear partial differential equations with a free boundary.

At low supersonic Mach number and at very low angles of attack, the shock wave is weak and can be replaced by Mach waves. In that case the equation can be linearized, resulting in the supersonic potential flow theory and both difficulties mentioned above disappear. The problem can then be solved in a fairly general way by the method of integral transform, and most results were summarized in Miles' monograph¹⁰.

With increasing flight Mach number and angle of attack, or both, the shock wave becomes strong and no longer can be replaced by Mach waves. In this case the supersonic potential flow theory does not apply and the integral transform method is generally useless. However, in all the problems mentioned above the difficulties associated with non-linearity and with existence of a shock wave are overcome by using a perturbation method in which the unsteady flow field is regarded as a small perturbation to some reference steady flow. Thus the problem of calculating an unsteady flow with shock waves is to be solved in two steps: the first step is to find a corresponding steady flow solution which is then used in the second step as a reference flow in calculating the unsteady perturbation flow. Whilst the problem encountered in the first step is still non-linear and with free boundary -- but is a steady one, that in

the second step is a linear problem with fixed boundaries.

As a number of exact or accurate steady flow solutions already exist, they are utilized in finding the corresponding unsteady flow solutions. These results will be summarized in Section 2, whereas in Section 3 a systematic study is given of the dependence of the dynamic stability derivatives on the flight parameters, namely the flight Mach number M_∞ , the mean angle of attack α , the sweep-back angle χ of the delta wing, and the ratio γ of the specific heats of the gas.

2. RESULTS

Consider a supersonic stream of gas with uniform velocity U_∞ past a given body performing a small amplitude, slow pitching oscillation. Let ϵ denote the amplitude and ω the circular frequency of the oscillation, so that the departure of the instantaneous position of the body from its mean steady position is described by an angle equal to $\epsilon e^{i\omega t}$. Let the pivot axis be perpendicular to the plane of symmetry of the body. The pitching moment of the resulting unsteady aerodynamic forces about the pivot axis will be denoted by $M_{pitching}$ (positive values of $M_{pitching}$ corresponds to nose-down). The pitching moment coefficient C_m is defined as usual by

$$C_m = \frac{M_{pitching}}{\frac{1}{2} \rho_\infty U_\infty^2 \ell A} \quad (4)$$

where ρ_∞ is the gas density in the free stream, ℓ is the body length and A a reference area which is taken to be $\ell \cdot 1$ for the cases of a wedge and of a flat plate, but in the case of a delta wing, A is taken to be equal to the wing area. The stiffness derivative $-C_{m_\theta}$ and the damping-in-pitch

derivative $-C_{m_\dot{\theta}}$ are also defined as usual by

$$C_m = \epsilon e^{i\omega t} [(-C_{m_\theta}) + ik(-C_{m_\dot{\theta}}) + O(k^2)] \quad (5)$$

where

$$k = \frac{\omega \ell}{U_\infty} \quad (6)$$

is the reduced frequency parameter and is, for slow oscillations, much smaller than unity.

2.1. Oscillating Wedges with Attached Shock Waves

In this case the reference steady flow is the well-known exact supersonic wedge flow which is uniform. The governing equations for the perturbation unsteady flow are linear with constant coefficients and are solved exactly. In particular, we have

$$\begin{aligned} -C_{m_\theta} &= \frac{FE}{\cos^2 \alpha} (\frac{1}{2} - h \cos^2 \alpha) \\ -C_{m_\dot{\theta}} &= \frac{F}{\cos^3 \alpha} (\frac{U_\infty}{u_0}) [I(h \cos^2 \alpha)^2 - Gh \cos^2 \alpha + \frac{1}{3}(2G-I)] \end{aligned} \quad (7)$$

where α is the semi-vertex angle of the wedge (see figure 1) and is equal to θ in Ref. 2, and h is the pivot position measured in the body length ℓ from the apex and along the body's symmetry line. The constants E, F, G and I are given in Ref. 2, and u_0 is the velocity behind the shock in the steady reference flow. The apparent differences between Eq. (7) above and Eq. (29) of Ref. 2 are due to the difference in defining the frequency parameter k . It should also be noted that due to a misprint the constant \tilde{C} in Ref. 2 (Eq. (15)) should be corrected by multiplying it by a factor of 2. (The numerical results in Ref. 2, however, requires no correction).

2.2. Oscillating Flat Plates

In the case the shock wave is attached to the leading edge of the flat plate the flows on the lower surface (compression sides) and on the upper surface (expansion side) are independent of each other and can be treated separately. The flow on the lower surface are the same as that on an oscillating wedge surface. Thus using the solution for unsteady pressure given in Ref. 2 (Eq. (26)) we have the lower surface contributions to the stability derivatives (see fig. 2) as follows

$$\begin{cases} (-C_{m_\theta})_\ell = \frac{1}{2} FE (\frac{1}{2} - h) \\ (-C_{m_\dot{\theta}})_\ell = \frac{1}{2} F (\frac{U_\infty}{u_0}) [Ih^2 - Gh + \frac{1}{3}(2G - I)] \end{cases} \quad (8)$$

The reference steady flow for the upper surface is the famous Prandtl-Meyer supersonic flow over a convex corner. The governing equations for the unsteady flow are derived by perturbing the steady Prandtl-Meyer flow. They are solved exactly to $O(\epsilon^2)$, and $O(\epsilon k^2)$, and we obtain the following formulae for the upper surface contribution to the stability derivatives (see fig. 2).

$$\begin{cases} (-C_{m_\theta})_u = 2\left(\frac{\rho_1}{\rho_\infty}\right)\left(\frac{u_1}{U_\infty}\right)^2 \frac{1}{(M_1^2-1)^{1/2}} \left(\frac{1}{2} - h\right) \\ (-C_{m_\theta})_u = 2\left(\frac{\rho_1}{\rho_\infty}\right)\left(\frac{u_1}{U_\infty}\right) \frac{1}{(M_1^2-1)^{1/2}} \left[h^2 - \frac{1}{2}\left(1 + \frac{M_1^2-2}{M_1^2-1}\right)h + \frac{1}{3} \frac{M_1^2-2}{M_1^2-1}\right] \end{cases} \quad (9)$$

where ρ_1 , u_1 , and M_1 are, respectively the density, velocity and Mach number on the upper surface of the flat plate in the steady reference flow.

The stability derivatives of the flat plate are then given by

$$\begin{cases} -C_{m_\theta} = (-C_{m_\theta})_u + (-C_{m_\theta})_l \\ -C_{m_\dot{\theta}} = (-C_{m_\dot{\theta}})_u + (-C_{m_\dot{\theta}})_l \end{cases} \quad (10)$$

2.3 Oscillating Delta Wings With Detached Shock Waves

We consider now a flat delta wing placed symmetrically in a supersonic stream of gas (fig. 3). The shock wave developed may be attached to the leading edges of the wing or detached from them, depending on the combination of the free stream Mach number M_∞ , the angle of attack α , the sweep-back angle χ , and the ratio of specific heats γ of the gas. (A criterion for shock attachment may be found in Ref. 11, say). Generally speaking, for large enough α and χ the shock will be detached from the leading edges. In this subsection we consider the detached shock case, whereas the attached shock case will be considered in subsection 2.4.

In the detached shock case we use Messiter's thin shock layer solution¹² (with some corrections given in Ref. 5) as the reference steady flow solution. It is an approximate theory and gives the first order correction to the Newtonian flow. The linearized (in the amplitude of oscillation ϵ) equations governing the unsteady flow are derived by perturbing Messiter's steady flow solution. They are of variable coefficients but are solved exactly⁵ for general values of the reduced frequency k . In particular we have the following formula (fig. 3) for the stiffness derivative $-C_{m_\theta}$ and the damping-in-pitch derivative $-C_{m_\dot{\theta}}$.

$$\begin{cases} -C_{m_\theta} = 2 \sin 2\alpha \left(\frac{2}{3} - h\right) \\ -C_{m_\dot{\theta}} = 4 \sin \alpha \left[h^2 - \frac{2}{3} (2 + G(\Omega))h + \frac{1}{2} (1 + G(\Omega))\right] \end{cases} \quad (11)$$

where the similarity parameter Ω is defined as

$$\Omega = \frac{b}{\lambda^{1/2} \tan \alpha} \quad (12)$$

where

$$\lambda \equiv \frac{\gamma-1}{\gamma+1} + \frac{2}{(\gamma+1)M_\infty^2 \sin^2 \alpha} \quad (13)$$

This parameter Ω is the scaled aspect ratio of the wing and, detached shock flow corresponds approximately to $0 \leq \Omega \leq 2$. The function $G(\Omega)$ is given in fig. 4. The apparent differences between Eq. (11) and Ref. 5 (Eqs. (29) and (30)) are again due to the different definitions used for the reduced frequency parameter.

2.4 Oscillating Delta Wings with Attached Shock Waves

In this case the flows on the upper surface and on the lower surface are independent and can be calculated separately. Only the lower surface (compression side) flow is considered here. It is expected, however, that with increasing Mach number or increasing angle of attack the lower surface flow will become dominant.

For the attached shock case we use Hui's analytic solution¹³ for unified supersonic/hypersonic flow over delta wings as the reference steady flow. This solution is exact in the outboard region where the cross flow is supersonic but is only approximate in the central region where the cross flow is subsonic. However, it gives almost identical results as large scale numerical solutions. The linearized (in the amplitude of oscillation ϵ) equations governing the unsteady flow are derived by perturbing Hui's steady flow solution. They are of variable coefficients. In the outboard region they are exactly solved⁶ in a manner similar to the oscillating wedge case. The result is rather too tedious to be reproduced here.

In the central region where the cross flow is subsonic, a group-theoretic method is first used to reduce the three space coordinates to two. The resulting problem of partial differential equations in two independent variables is integrated spanwisely, yielding a problem of ordinary differential equations whose solution is obtained analytically in closed form. Thus both the stiffness derivative and the damping-in-pitch derivative of a delta wing with attached shock wave are obtained in

closed form which explicitly show their dependence on $M_\infty, \alpha, \chi, \gamma$ and h . (For details, see Ref. 6)

3. DISCUSSIONS AND CONCLUSIONS

A comparison of the theoretical damping value with the measurements of Pugh and Woodgate¹⁴ for an oscillating wedge is shown in figure 5. It is seen that the inviscid theory, including the prediction of negative damping, is well verified by experiments, except when the pivot axis is along the wedge leading edge.

With the closed form formulae given in Section 2 for various cases, we are in a position to investigate the effects of the flight Mach number M_∞ , the mean angle of attack α , the sweep-back angle χ of the delta wings and the specific heat ratio γ on the stability derivatives, in particular, the damping-in-pitch derivative $-C_{m\dot{\theta}}$. It should be noted that because of the different ways in measuring the body length, the $m_{\dot{\theta}}$ stability derivatives for the flat plate at large M_∞ or large α do not approach one-half of that for a wedge. Also because of the different reference areas A used in Eq. (4), the stability derivatives for a delta wing with attached shock wave at large M_∞ and $\chi \rightarrow 0$ do not approach that for a flat plate.

Systematic investigations of the stability derivatives have led to the following general conclusions.

- (a) Increasing flight Mach number M_∞ generally tends to increase the dynamic stability, and $-C_{m\dot{\theta}}$ tends to a constant for large M_∞ (Fig. 6), in consistence with the principle of Mach number independence for steady hypersonic flow.
- (b) The angle of attack α has a very important effect on the damping-in-pitch derivative. Typically, $-C_{m\dot{\theta}}$ increases with increasing α , but after α reaches certain critical value it begins to decrease rapidly with further increase in α (Fig. 7). Furthermore, in the cases of a wedge, a flat plate aerofoil and a delta wing with attached shock waves $-C_{m\dot{\theta}}$ can take very large negative values, an indication that in those cases the unsteady aerodynamic forces tend to strongly destabilize the pitching motion. However, there is an exception for hypersonic slender wings with detached shock waves. In that case Eq. (11) together with the fact that $G(\alpha) < 1$ (see Fig. 4) shows that the damping derivative is always positive.
- (c) The effects of the sweepback angle χ on the $-C_{m\dot{\theta}}$ for a delta wing with either attached or detached shock waves are generally small, except near the shock detachment or when α nearly 90° (Fig. 8). In these cases the present theory does not apply.
- (d) The effects of the specific heat ratio γ on $-C_{m\dot{\theta}}$ are small for small α (Fig. 9) but can be unexpectedly large for large α . In the latter cases, increasing γ tends to decrease the damping-in-pitch derivative and, for the cases of a wedge or a flat plate aerofoil, can cause instability of the pitching motion. This is in sharp contrast to the linearized supersonic potential flow theory, according to which the flow is independent of γ . This rather drastical theoretical prediction of the γ -effects remains to be verified experimentally.

Results for the stiffness derivatives are also presented in Figs. 10-13, showing similar effects, except that of α .

Finally, in this series of analytical study the relation between unsteady Newtonian flow theory and the limiting gasdynamic theory is clarified. Thus for the cases of the oscillating wedge, the flat plate, the cone and the delta wing with attached shock wave it is shown¹⁵ that, contrary to existing theories,¹⁶ the centrifugal effect is important and cannot be neglected. For example, it contributes one half of $-C_{m\dot{\theta}}$ for a wedge and one third for a cone. Furthermore, it is shown that for these cases unsteady Newtonian flow theory with centrifugal corrections agrees identically with gasdynamic theory in the double limit as $\gamma \rightarrow 1$ and $M_\infty \rightarrow \infty$, independently. It is thus conjectured that general three-dimensional unsteady Newtonian flow theory plus centrifugal corrections will agree with gasdynamic theory in the double limits as $\gamma \rightarrow 1$ and $M_\infty \rightarrow \infty$, independently. This conjecture would enable dynamic stability derivatives to be calculated somewhat easier using unsteady Newtonian theory as a first approximation for hypersonic flow.

REFERENCES

1. Orlik-Rückemann, K. J., "Dynamic stability testing of aircraft -- needs versus capabilities", Prog. Aerospace Sci., 16, 431-447, 1975.
2. Hui, W. H., "Stability of oscillating wedges and caret wings in hypersonic and supersonic flows", AIAA Journal, 7, 1524-1530, 1969.
3. Hui, W. H., "Interaction of a strong shock with Mach waves in unsteady flow", AIAA Journal, 7, 1605-1607, 1969.
4. Hui, W. H., and Hamilton, J., "Higher order solutions for unsteady hypersonic flow", Aeronautical Quarterly, 25, 59-68, 1974.

5. Hui, W. H. and Hemdan, H. T., "Unsteady hypersonic flow over delta wings with detached shock waves", AIAA Journal, 14, 505-511, 1976.
6. Liu, D. D. and Hui, W. H., "Oscillating delta wings with attached shock waves", AIAA Journal, 15, 804-812, 1977.
7. Hui, W. H. and Mahood, G. E., "Modified thin shock layer method for supersonic flow past an oscillating cone", J. Spacecraft and Rockets, 13, 481-487, 1976.
8. Orlik-Fückemann, K. J., "Stability derivatives of sharp wedges in viscous hypersonic flow", AIAA Journal, 4, 1001-1007, 1966.
9. Hui, W. H. and East, R. A., "Stability derivatives of sharp wedges in viscous hypersonic flow", Aeronautical Quarterly, 22, 127-145, 1972.
10. Miles, J. W., "Potential Theory of Unsteady Supersonic Flow", Cambridge University Press, 1959.
11. Babaev, D. A., "Numerical solution of the problem of supersonic flow past the lower surface of a delta wing", AIAA Journal, 1, 2224-2231, 1963.
12. Messiter, A. F., "Lift of slender delta wings according to Newtonian Theory", AIAA Journal, 1, 794-802, 1963.
13. Hui, W. H., "Supersonic and hypersonic flow with attached shock waves over delta wings", Proc. Roy. Soc. London, A325, 251-267, 1971.
14. Pugh, P. G. and Woodgate, L. "Measurements of pitching -- moment derivatives for blunt-nosed aerofoils oscillating in two-dimensional supersonic flow", A.R.C. Repts. and Memoranda 3315, Aeronautical Research Council of Britain, 1963.
15. Mahood, G. E. and Hui, W. H., "Remarks on unsteady Newtonian flow theory", Aeronautical Quarterly, 27, 66-74, 1976.
16. Tobak, T. and Wehrend, W. R., "Stability derivatives of cones at supersonic speeds", Technical Notes 3788, NACA, 1956.

Acknowledgement: This work was supported by the National Research Council of Canada.

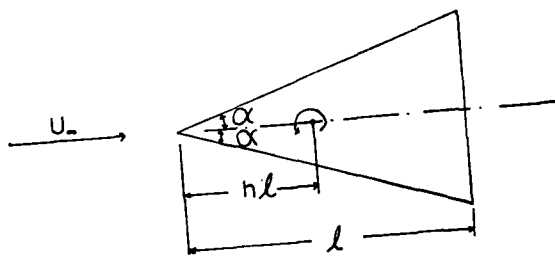


Fig. 1. Oscillating Wedge

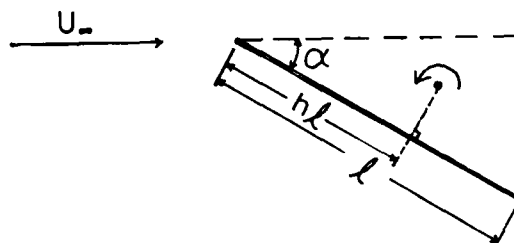


Fig. 2. Oscillating Flat Plate

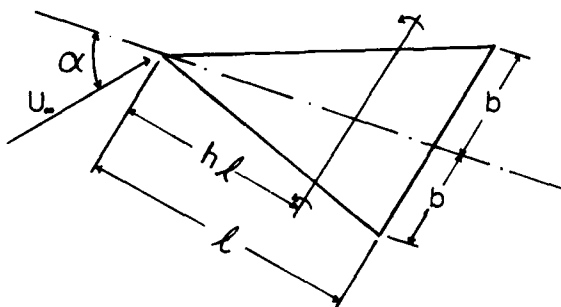


Fig. 3. Oscillating Delta Wing

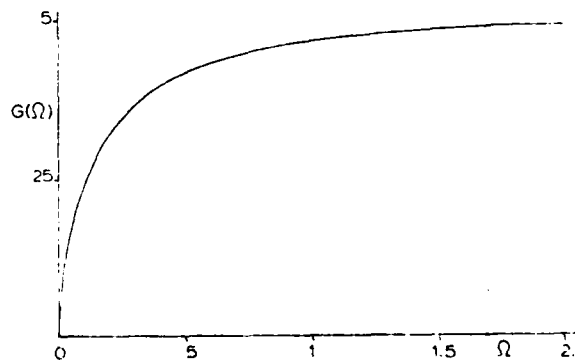


Fig. 4. Universal Function $G(\Omega)$

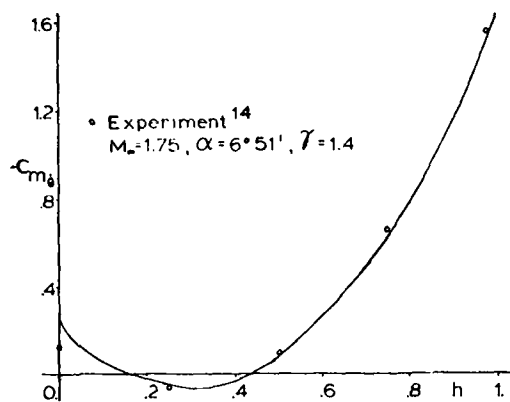


Fig. 5. Damping Derivatives $-C_{m_{\dot{\theta}}}$ of Wedge. Comparison with Experiments

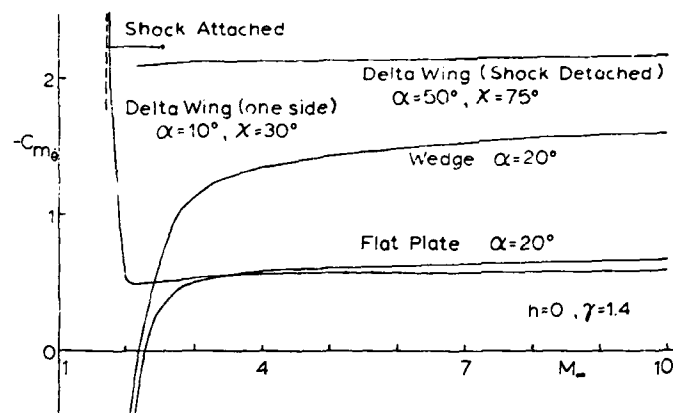


Fig. 6. Damping Derivative $-C_{m_{\dot{\theta}}}$ versus Flight Mach Number M_{∞}

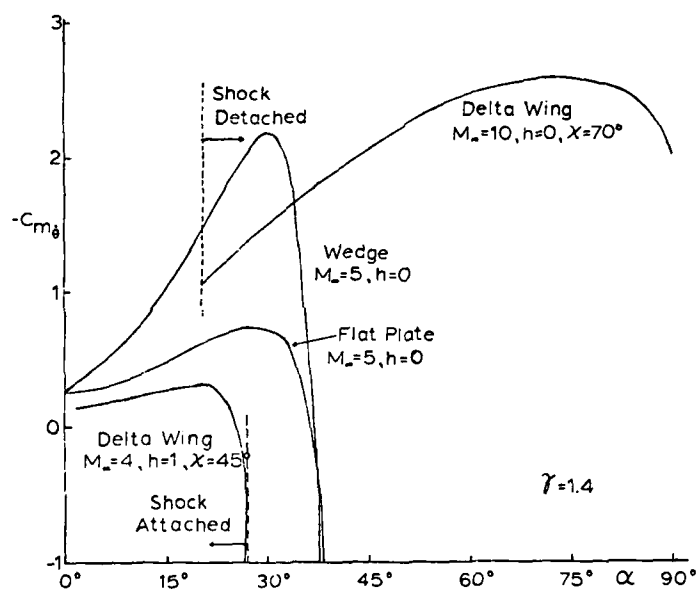


Fig. 7. Damping Derivative $-C_{m_{\dot{\theta}}}$ versus Angle of Attack α

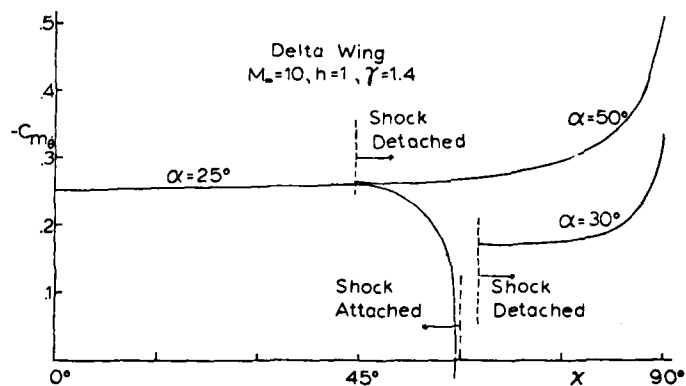


Fig. 8. Damping Derivative $-C_{m_{\dot{\theta}}}$ of Delta Wing versus Sweepback Angle X

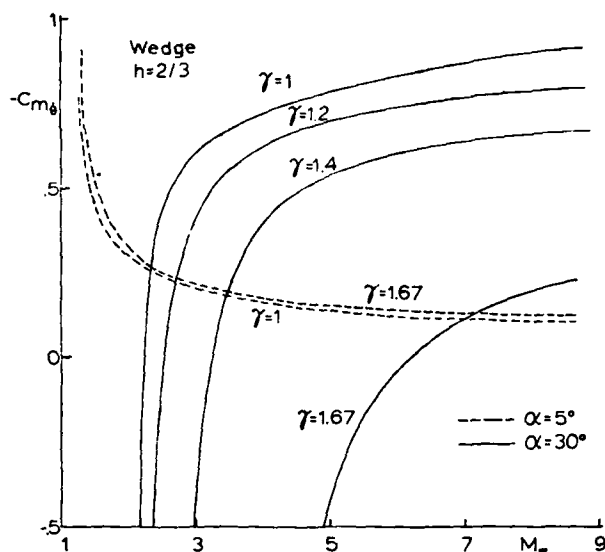


Fig. 9_a. Damping Derivative $-C_{m\dot{\theta}}$ of Wedge
Showing γ effects

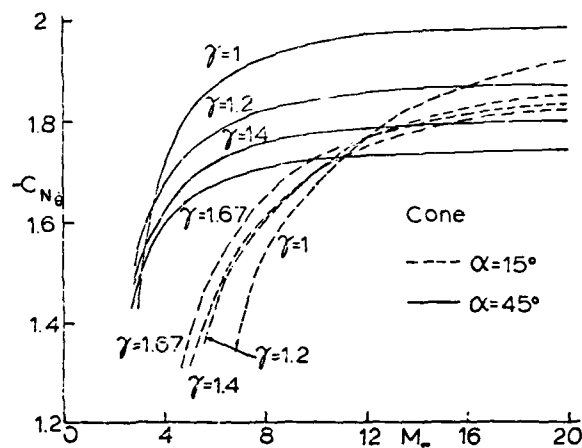


Fig. 9_b. Damping Derivative $-C_{N\dot{\theta}}$ of Circular
Cone Showing γ effects

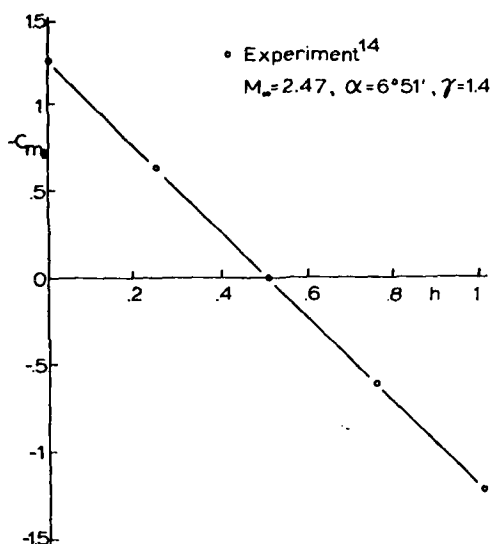


Fig. 10. Stiffness Derivative $-C_{m\theta}$ of
Wedge Comparison With Experiments

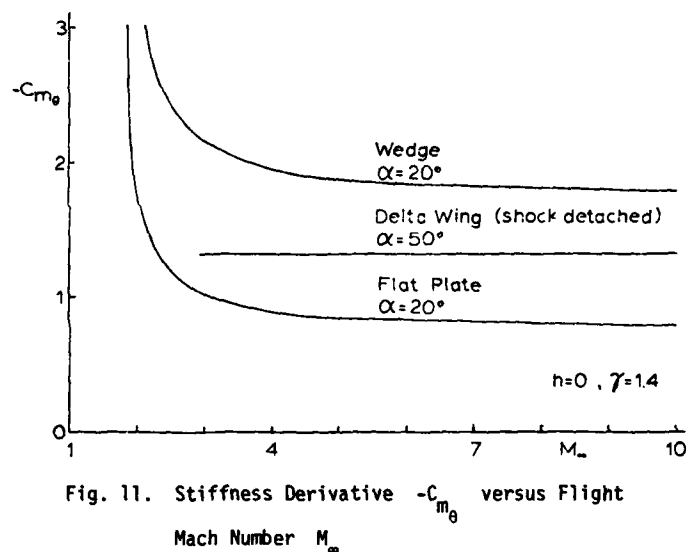


Fig. 11. Stiffness Derivative $-C_{m\theta}$ versus Flight
Mach Number M_∞

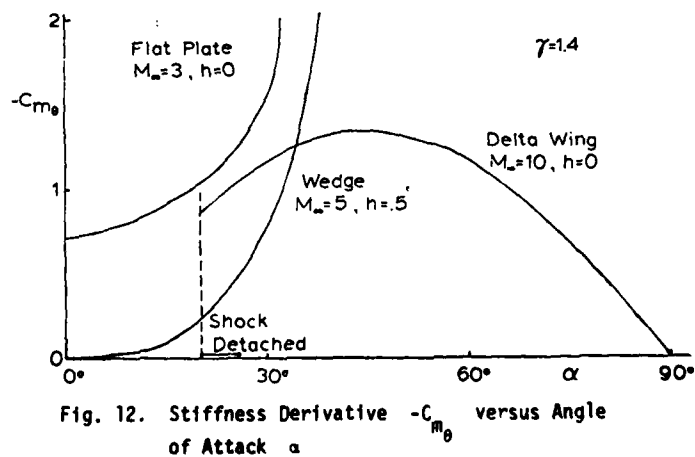


Fig. 12. Stiffness Derivative $-C_{m\theta}$ versus Angle
of Attack α

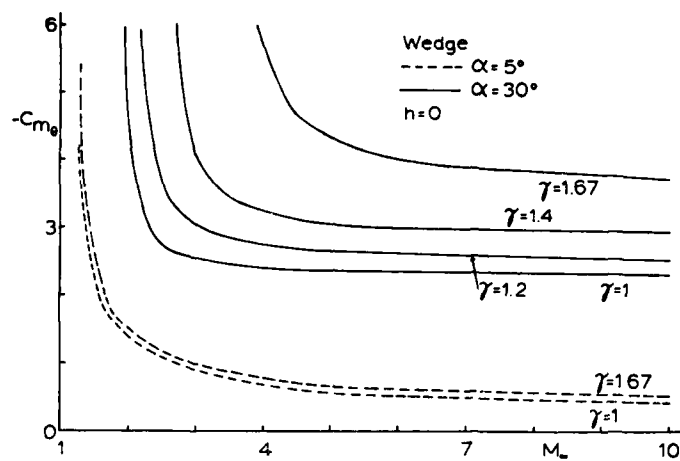


Fig. 13. Stiffness Derivative $-C_{m_{\theta}}$ of Wedge
 Showing γ effects

IDENTIFICATION OF UNSTEADY EFFECTS

IN LIFT BUILT UP*

P. Mereau, R. Hirsch, G. Coulon, A. Rault

ADERSA/GERBIOS

53 Avenue de l'Europe

F78140 Vélizy (France)

SUMMARY

A methodology to identify unsteady aerodynamic forces from flight test data is proposed and developed in the case of uncoupled longitudinal motion. Based upon linearity and frequency separation of the involved phenomena, this method includes several steps : data filtering, classical stability and control parameters identification, transient forces estimation, unsteady terms identification. The mathematical model includes state equations and convolution integrals, thus requiring particular identification algorithms, well adapted to each form of representation. The results obtained in the case of non-powered flights of a reduced scale plane are very satisfactory in the sense that their comparison with existing theoretical developments are very close and thus validate the theoretical characterizations.

SYMBOLS

C_{z_i}	aircraft aerodynamic parameter with respect to variable i
$C_{z_i}^t$	tail aerodynamic parameter with respect to variable i
D	average distance between flap trailing edge and tail aerodynamic center
\underline{E}	input vector
f_i	lift difference between steady-state and transient step responses due to variable i
I	longitudinal moment of inertia
l	reference chord
L	distance between the aircraft and the tail centers of gravity
m	aircraft mass
m_t	tail mass
q	pitch angular velocity
\underline{R}_t	tail unsteady residual vector
\underline{R}_w	wing unsteady residual vector
R_{z_i}	aircraft lift term due to variable i
S	aircraft reference surface
S_t	tail reference surface
V_0	reference speed
\underline{X}	state vector
$f \otimes g$	convolution integral between functions f and g
α	angle of attack
$\delta(i)$	variation of variable i
ρ	air density
μ_i	theoretical transient coefficient in the lift term due to variable i
χ_i	theoretical jump coefficient in the lift term due to variable i
θ	pitch angle
τ	flap deflection
\ddot{z}	normal acceleration

* This research has been conducted under D.R.E.T. research contract N° 76.235 and S.T.Aé research contract N° 76.98213 in close cooperation with the Institute of Fluid Mechanics of Lille.

1 INTRODUCTION

In the framework of recent trends like the CCV concept, direct lift control or high angle of attack flights, short duration phenomena such as unsteady aerodynamics and aircraft flexible modes can no longer be neglected. A good knowledge of these phenomena is therefore important and the question on how to determine them with precision arises.

Several theoretical characterizations, based on the initial works of Wagner, Theodorsen and Jones (ref. 1,2,3), have been made to model unsteady aerodynamics, and computational methods have been developed in the case of subsonic flow (ref. 4,5,6). However, to the best knowledge of the authors there have been few satisfactory experimental verifications in the three dimensional cases. In this paper, we describe a method to identify unsteady aerodynamic forces from flight test data.

Identification from flight test data has been used in several instances, and is now well developed, for the determination of the classical aircraft stability and control derivatives (ref. 7,8,9). The identification procedure includes three steps :

- characterization of a model in which several unknown parameters appear.
- estimation of the unknown parameter values by using test data.
- validation of the model.

This procedure has been used for the identification of unsteady aerodynamic forces. However, due to the particular problem investigated, an appropriate methodology had to be developed.

The characterization of unsteady aerodynamic forces and the derivation of a model are described in section 2. The identification methodology is presented in section 3 and the various steps of this methodology are developed in section 4. The results obtained in the case of non-powered flights of a reduced scale plane are given and compared with the theoretical results derived from existing mathematical characterizations.

2 CHARACTERIZATION OF UNSTEADY TERMS

In order to obtain a model for unsteady effects, one must express transient aerodynamic forces through a mathematical formulation. The lift force is written :

$$R_z = R_{z_0} + \delta R_{z_\alpha} + \delta R_{z_q} + \delta R_{z_\tau} \quad (1)$$

where R_{z_0} is the lift value at some reference conditions and the other terms of (1) are respectively due to variations in the angle of attack α , the pitch angle derivative q and the flap deflection τ .

From an automatic control viewpoint, the variational terms can be represented as the output of a bloc diagram (Figure 1).

If only steady-state forces are considered, the transfer operator between the input $\delta\alpha$ and the output δR_{z_α} is a constant gain

$$H_\alpha = H_\alpha^0 = \frac{1}{2} \rho S V_0^2 C_{z_\alpha} \quad (2)$$

where ρ , S , V_0 are reference values for the air density, the lifting surface and the flying speed. C_{z_α} is the aircraft stability derivative with respect to the angle of attack.

If transient forces are considered, the transfer operator between $\delta\alpha$ and δR_{z_α} is no longer constant. Assuming linear phenomena, let $h_\alpha(t)$ be the impulse response of this transfer operator, the response $\delta R_{z_\alpha}(t)$ due to an arbitrary input $\delta\alpha(t)$, with $\delta\alpha(t) = 0$ for all $t < 0$, can then be expressed as,

$$\delta R_{z_\alpha}(t) = \int_0^t h_\alpha(t-u) \delta\alpha(u) du \quad (3)$$

Integrating (3) by parts leads to

$$\delta R_{z_\alpha}(t) = \int_0^t g_\alpha(t-u) \frac{d}{du} [\delta\alpha(u)] du \quad (4)$$

where,

$$g_\alpha(v) = \int_0^v h_\alpha(u) du$$

Similar expressions can be written for the variational terms due to δq and $\delta \tau$.

Assuming a discontinuity at starting time and first order transients, $h_\alpha(t)$ and $g_\alpha(t)$ have the following form. (These are the classical hypotheses made by Hirsch (ref.10,11))

$$\begin{aligned} h_\alpha(t) &= a e^{-bt} \\ g_\alpha(t) &= \frac{b}{a} (1 - e^{-bt}) + c \end{aligned}$$

where the constant terms a , b and c are bound through the steady-state relationship

$$\lim_{t \rightarrow \infty} g_{\alpha}(t) = \frac{b}{a} + c = H_{\alpha}^0 = \frac{1}{2} \rho S V_0^2 C_{z_{\alpha}}$$

then,

$$\delta R_{z_{\alpha}}(t) = \frac{1}{2} \rho S V_0^2 C_{z_{\alpha}} \int_0^t \left[1 - \frac{b/a}{b/a+c} e^{-b(t-u)} \right] \frac{d}{du} [\delta \alpha(u)] du$$

which is of the form,

$$\delta R_{z_{\alpha}}(t) = \frac{1}{2} \rho S V_0^2 C_{z_{\alpha}} \int_0^t [1 - \chi_{\alpha} e^{-\mu_{\alpha}(t-u)}] \frac{d}{du} [\delta \alpha(u)] du \quad (5)$$

Expression (5) was derived from whirl flow considerations and used to simulate unsteady terms in longitudinal motion (ref. 12,13).

It is not necessary to assume transients to be of the first order. The only hypothesis we shall make is linearity and thus equation (4) can also be written as

$$\delta R_{z_{\alpha}}(t) = - \int_0^t g_{\alpha}(u) \frac{d}{du} [\delta \alpha(t-u)] du$$

defining

$$f_{\alpha}(u) = 1 - \frac{g_{\alpha}(u)}{\frac{1}{2} \rho S V_0^2 C_{z_{\alpha}}}$$

and using $\delta \alpha(0) = 0$, we have

$$\delta R_{z_{\alpha}}(t) = \frac{1}{2} \rho S V_0^2 C_{z_{\alpha}} \left\{ \delta \alpha(t) + \int_0^t f_{\alpha}(u) \frac{d}{du} [\delta \alpha(t-u)] du \right\} \quad (6)$$

Comparing (6) and (2) shows that an expression for the lift force, including transients, can be obtained from the steady-state lift expression by changing

$\delta \alpha(t)$ into $\delta \alpha(t) + f_{\alpha} \otimes \delta \alpha$, where $f_{\alpha} \otimes \delta \alpha$ summarizes the convolution integral in (6). Similarly for the variational terms due to δq and $\delta \tau$, expressions including transients can be derived from steady-state expressions by the following operations:

$$\begin{aligned} \delta q(t) &\rightarrow \delta q(t) + f_q \otimes \delta q \\ \delta \tau(t) &\rightarrow \delta \tau(t) + f_{\tau} \otimes \delta \tau \end{aligned} \quad (7)$$

This approach allows one to obtain a model for both, steady-state and transient forces, directly from the usual state equations derived from classical flight mechanics. For uncoupled longitudinal motion, these classical equations can be represented by (ref. 14,15):

$$\dot{\underline{X}} = \underline{A} \underline{X} + \underline{B} \underline{E} \quad (8)$$

where \underline{X} is the state vector ($\underline{X}^T = [V \alpha \theta q]$), \underline{E} is the input vector (in our case $\underline{E}^T = [\tau \Delta m]$, Δm being the mass variation). The matrices \underline{A} and \underline{B} depend on the aircraft stability and control derivative coefficients.

Using operations (7), a complete model including unsteady aerodynamic terms, can then be written as (ref. 15):

$$\dot{\underline{X}} = \underline{A} \underline{X} + \underline{B} \underline{E} + \underline{R}_w + \underline{R}_t \quad (9)$$

where \underline{R}_w and \underline{R}_t are residual vectors due respectively to wing and tail lift unsteady effects.

Assuming that variations due to $\delta \alpha$, δq and $\delta \tau$ have the same transient dynamics, the functions in the convolution integrals (6) and like are such that

$$f_{\alpha} = f_q = \frac{1}{k} f_{\tau} = f$$

and we can write

$$\underline{R}_w = \underline{A}_1 (f \otimes \dot{\underline{X}}) + \underline{B}_1 (k f \otimes \dot{\underline{E}}) \quad (10)$$

where \underline{A}_1 and \underline{B}_1 are appropriate constant matrices (cf appendix).

A similar expression can be derived for tail unsteady residuals

$$\underline{R}_t = \underline{A}_1 (\underline{f}_t \otimes \dot{\underline{X}}) + \underline{B}_1 (k_t \underline{f}_t \otimes \dot{\underline{E}}) \quad (11)$$

3 IDENTIFICATION METHODOLOGY

The characterization developed in section 2 reduces the unsteady terms identification to the determination of the functions \underline{f} , \underline{f}_t and the constants k , k_t in (10) and (11), using data on \underline{X} and \underline{E} . This type of identification problem involving a model with both state equations and convolution integrals is new and difficult to solve in general because :

- the residual terms in (9) have a much smaller magnitude than the other terms.
- the data obtained from measurements contain information on several phenomena such as classical flight mechanics, unsteady effects, aircraft vibrations and noises from several origins (wind disturbances, measurements).

The first difficulty can be reduced by choosing adequate test signals sensitizing transient terms. The second difficulty can be solved by adequate data filtering in order to reduce, or eliminate, information on non-desired phenomena. However, this is possible only in the case of a clear frequency separation of the phenomena.

Based on these considerations, the procedure developed to identify unsteady terms includes the following steps :

1. Identification of the aircraft classical flight mechanics parameters (i.e., coefficients of matrices A and B), using low-pass filtered data.
2. Identification of the tail classical flight mechanics parameters from measured tail forces, also using low-pass filtered data.
3. Evaluation of the tail unsteady residual terms \underline{R}_t by subtracting tail steady-state forces, calculated after identification in 2, from measured non-filtered tail forces.
4. Evaluation of the wing unsteady residual terms \underline{R}_w from (9) using non-filtered data.
5. Identification of the wing unsteady terms using model (10) where \underline{R}_w , $\dot{\underline{X}}$, $\dot{\underline{E}}$, \underline{A}_1 and \underline{B}_1 are known. Data are not filtered.
6. Identification of the tail unsteady terms using model (11).

These steps will be explained in details, and results will be given, in the next section concerning the case of a reduced scale plane.

4 IDENTIFICATION

4.1 Data collection

Data were obtained from reduced scale plane launches. The tests were conducted at the Fluid Mechanics Institute of Lille (IMFL), France, which has developed facilities and a new methodology for experimental studies from reduced scale planes (ref. 16).

Test runs consisted of non-powered flights with perturbed flight conditions. The inputs used were :

- changes of the reduced scale plane mass and center of gravity position with respect to a reference flight.
- quick flap deflection during flights.

The measured quantities were :

- the normal acceleration of the center of gravity.
- the longitudinal accelerations of two distinct points of the reduced scale plane.
- the tail normal force.
- the flap deflection.

The values of the state variables (V , α , θ , q) and their rate of change were obtained from the acceleration measurements (ref. 15).

4.2 Identification of classical flight mechanics parameters

This identification consists in finding values for the unknown coefficients of the matrices A and B of model (8), using state and input data. Three steps were used (ref. 14) :

1. Estimation of the parameter values using a last square method.
2. Improvement of the estimates by minimizing a sum of squares, differences between the computed state variables (\underline{X}_c) and the available data properly low-pass filtered,

$$F(\underline{P}) = \sum_{k=1}^K [\underline{X}_c(t_k, \underline{P}) - \underline{X}(t_k)]^T W [\underline{X}_c(t_k, \underline{P}) - \underline{X}(t_k)] \quad (12)$$

where \underline{P} is the vector of unknown parameters, t_k are sampled times, W is a weighting matrix and K is the number of data points used.

A Newton-Raphson method (ref. 17) was used to minimize (12).

3. Estimation of bounds on the values found.

Calculated state variables, after identification, and the data used are shown in figure 2. Knowing matrices A and B of (8), one can compute the reduced scale plane stability and control derivatives. The values obtained are given in table 1, together with upper and lower bounds.

4.3 Identification of tail classical flight mechanics parameters

The tail normal force can be written as

$$F = F_I + F_{Ae}$$

where F_I is the normal acceleration force due to pitch motion and F_{Ae} is the tail aerodynamic force. In steady-state, these forces can be expressed as (ref. 15)

$$F_I = m_t (\ddot{z} + L \ddot{\theta}) \quad (13)$$

$$F_{Ae} = \frac{1}{2} \rho S_t V_o^2 (C_{z_o}^t + C_{z_\alpha}^t \delta\alpha + C_{z_\tau}^t \delta\tau)$$

where m_t is the tail mass, L is the distance between the plane center of gravity and the tail center of gravity, \ddot{z} is the plane normal acceleration and $\ddot{\theta}$ is the pitch angle acceleration. ρ , S_t and V_o are reference quantities and $C_{z_o}^t$, $C_{z_\alpha}^t$, $C_{z_\tau}^t$ are coefficients to be identified.

Coefficient values were found by using a least square method and low-pass filtered data on F , z , θ , $\delta\alpha$ and $\delta\tau$. Figure 3 shows the calculated tail aerodynamic force after identification and the data used. The coefficient values found are given in table 2 together with upper lower bounds.

Using the parameters obtained through identification the tail steady-state lift can be computed with arbitrary non-filtered $\delta\alpha$ and $\delta\tau$. Then, subtracting this steady-state lift from the total measured tail lift, we obtain a good estimate of the tail transient forces and thus of the tail residual vector \underline{R}_t in (9).

4.4 Identification of wing unsteady terms

Following previous identifications (4.2., 4.3), matrices A, B and vector \underline{R}_t in (9) can be computed. Then, using data on \underline{X} , $\underline{\dot{X}}$ and \underline{E} , the wing residual vector \underline{R}_w in (9) can be calculated as well as the matrices A_1 and B_1 in (10) (cf. Appendix).

In the investigated case, only transient states of $\delta\alpha$ and $\delta\tau$ had a significant value. Consequently, only the second and the fourth equations of model (10) were considered. These equations can be developed as

$$\underline{R}_{w_\alpha} = f \otimes (a_{22}^1 \delta\dot{\alpha} + a_{24}^1 \delta\dot{q} + k b_{21}^1 \delta\dot{\tau}) \quad (14)$$

$$\underline{R}_{w_q} = f \otimes (a_{42}^1 \delta\dot{\alpha} + a_{44}^1 \delta\dot{q} + k b_{41}^1 \delta\dot{\tau})$$

where the operator \otimes stands for a convolution integral and a_{ij}^1 , b_{ij}^1 are coefficients of the matrices A_1 and B_1 .

Putting relations (14) into a more compact form leads to

$$\begin{aligned} S_1 &= f \otimes (e_1^1 + k e_1^2) \\ S_2 &= f \otimes (e_2^1 + k e_2^2) \end{aligned} \quad (15)$$

Since data are available at sampled times t_n , a discrete version of (15) is used :

$$\begin{aligned} S_1(t_n) &= \sum_{i=1}^N h_i [e_1^1(t_{n-i}) + k e_1^2(t_{n-i})] \\ S_2(t_n) &= \sum_{i=1}^N k_i [e_2^1(t_{n-i}) + k e_2^2(t_{n-i})] \end{aligned} \quad (16)$$

were the parameters h_i are related to the sampled values of function f through the sampling period T :

$$h_i = T f(iT)$$

Now, the identification problem consists in finding values for h_i , $i = 1, N$, and k , knowing data points on S_j , e_j^1 , $1 = 1, 2$, $j = 1, 2$

4.4.1 Identification algorithm

First a value for k is fixed, then knowing

$$S_j(n) = S_j(t_n)$$

and

$$U_j(n-i) = e_j^1(t_{n-i}) + k e_j^2(t_{n-i}) \quad j = 1, 2 ; n = 1, \dots, N$$

the estimates of h_i are updated at each step according to,

$$h_i(n+1) = h_i(n) - \lambda \frac{SM_j(n) - S_j(n)}{v + \sum_{i=1}^N [U_j(n-i)]^2} U_j(n-i) \quad (17)$$

$i = 1, \dots, N ; j = 1, 2$

where, $h_i(n)$ is the estimate of h_i after the use of n data points

$SM_j(n)$ is the calculated value of $S_j(t_n)$, using (16) with $h_i = h_i(n)$

λ and v are coefficients chosen according to data quality to keep a smooth identification. If λ and v are well chosen, algorithm (17) converges and is not sensitive to reasonable data noise (ref. 18, 19).

The value of k is periodically updated by minimizing a functional of square differences between data on $S_j(n)$ and the corresponding values calculated using (16) with h_i fixed.

4.4.2 Results

The sampling time and the number of parameters were respectively $T = 0.00256$ sec. and $N = 40$.

Due to the particular test inputs used, the quantities e_j^1 and e_j^2 , $j = 1, 2$, in (15) did not have the same order of magnitude; e_2^2 , which is related to the flap deflection rate of change, was larger ($e_2^2 = 20 e_1^1$ and $e_2^2 = 60 e_1^1$). Consequently the terms $f \otimes e_j^1$ were not sensitized in the identification and only the product $k f$ was identified. That is, we were able to obtain unsteady terms related to the flap motion, but not those related to the plane motion.

The results obtained are summarized in figures 4 and 5 showing respectively :

- plots of unsteady wing lift and pitch moment residuals evaluated from the data and calculated from (16), after identification.
- transient step responses (i.e. function f in (6)) obtained from identification and from theory, together with upper and lower bounds.

The so-called theoretical value for function f has been computed from whirl flow considerations using characterization (5). The value found for coefficients χ_r and μ_r related to the flap motion were $\chi_r = 0.75$ and $\mu_r = 0.55 \frac{V_0}{T}$ (V_0 and l being a reference speed and a reference chord).

The following comments can be made :

1. The results, shown here for a particular run, have been confirmed with two other runs.
2. The data noise in figure 4 is due to fuselage vibrations (frequency ≈ 80 Hz). Compared to the signal of interest, this noise is important and identification was possible by improving algorithm performances with non-stationary matched filtering based upon projection procedures (ref. 20).

3. The important confidence interval found for function f is due to the high data noise level and the rough hypothesis made to estimate these intervals. The closeness of the identification results for several runs seems to indicate that these intervals are exaggerated upper limits on uncertainty.
4. The jump amplitude at $t = 0$ in figure 5 can be calculated from the value of parameter h_1 in (16). The amplitude found was 53% of the steady-state value, with bounds at 33% and 70%. The large bounds are due to the important uncertainty on h_1 (cf 3 above). These results seem to imply that the theoretical value of 25% (i.e., $1 - \chi_1$) for the jump amplitude is too small.
5. Figure 5 shows a good match between identification and theoretical results. This shows the feasibility of unsteady effects identification from flight data and validates the theoretical characterization. It also confirms the value of $0.55 \frac{V_0}{l}$ for μ_1 which was found different ($0.35 \frac{V_0}{l}$) in computations based on wind tunnel measurements on bi-dimensional periodic tests (ref. 21).

4.5 Identification of tail unsteady terms

The characterization of section 2 leads to a model similar to (16) (with only one equation) for the tail unsteady residuals. The identification algorithm was the same as that used in 4.4.1 and the results obtained are summarized in figures 6 and 7 showing respectively :

- plots of unsteady tail lifts evaluated from the data and calculated from the model, after identification.
- tail lift transient step responses obtained from identification and from theory, together with upper and lower bounds.

The following comments can be made :

1. Only unsteady terms due to flap motion have been obtained.
2. The theoretical transient response was obtained with a characterization similar to (5) with a pure delay in the convolution integral to account for the air flow travelling time between wing and tail. Theoretical values were : delay = $1.7 \frac{V_0}{l}$ where D is an average distance between the flap trailing edge and the tail aerodynamic center, and V_0 is the air flow speed.
 $\chi_1^t = 1$ (i.e., no jump)
 $\mu_1^t = \frac{V_0}{D}$
3. Identification results seem to indicate (figure 7) an initial jump of about 17% of the steady-state value and a shorter transient duration than theoretical results.

5 CONCLUSION

A methodology to determine transient aerodynamic forces through modeling and identification has been developed and used in the case of uncoupled longitudinal motions of a reduced scale plane.

The problem investigated is difficult because unsteady aerodynamic effects have a short duration and the test data contain information about other phenomena. The proposed method is based upon linearity and frequency separation of the phenomena and includes a number of specific steps.

The model characterization, including state equations and convolution integrals, makes straight forward the passage from the classical steady-state representation to a complete representation including transient states. This characterization does not rely on assumptions about transients order and it is very well adapted to the numerical identification algorithm used.

The results obtained concerning unsteady effects related to flap motions are very satisfactory and establish the feasibility of the identification from flight data and the validity of existing theoretical characterizations of unsteady effects. Identification confirms the theoretical values for wing lift transient duration and tail lift delay, but it indicates a higher wing lift jump and a smaller tail transient duration than theory.

Unsteady lift terms related to the aircraft motion could have been obtained by using the same method with adequately sensitized data (for instance data obtained from non-powered flights crossing a known wind gust).

REFERENCES

1. Wagner, H. *Über die Entstehung des dynamischen Auftriebes von Trag flugeln*, Z.fa.MM., Bd.5, Heft 1 (1925), S 17-35
2. Theodorsen T. *General Theory of Aerodynamic Instability and the Mechanism of Flutter*, NACA Rept., N° 496, 1935
3. Jones, R.T. *The Unsteady Lift of a Finite Wing*, NACA T.N., N° 682, 1939
4. Giesin, J.P. *Nonlinear two-dimensional unsteady potential flow with lift*, Journal of Aircraft, Vol. 5, N° 2, 1968, p. 135-143
5. Djojodihardjo, R.H. *A Numerical Method for the Calculation of Nonlinear, Unsteady Lifting Potential Flow Problems*, AIAA Journal, Vol.7, N° 10, 1969, p. 2001-2009
6. Giesin, J.P. *Air Force Flight Dynamics Lab., Wright-Patterson Air Force Base (Ohio), Subsonic Unsteady Aerodynamics for General Configurations*, 1972, USAF AFFDL-TR-71-5, Part I, Nov. 1971, AFFDL-TR-71-5, Part II
7. Mehra, R.K. *A generalized method for the identification of aircraft stability and control derivatives from flight test data*, JACC, 1972, p. 525-534
8. Rault, A. *Identification applications to Aeronautics*, IFAC Symposium on Identification and System Parameter Estimation, The Hague, The Netherlands, 1973
9. - *Parameter Estimation Techniques and Applications in Aircraft Flight Testing*, NASA Symposium, April 24-25, 1973, NASA TN-D-7647
10. Hirsch, R. *Determination et Calcul des hélices d'avion*, Publication scientifique et technique du Ministère de l'Air (France), PST N°220, 1948
11. Hirsch, R. *Réponse à la rafale OACT d'un avion conventionnel et d'un avion absorbeur de rafales*, Congrès de Mécanique d'Istanbul, 1954
12. Hirsch, R. *ADERSA/GERBIOS, Simulation d'un avion, Chaîne longitudinale, Modèle de connaissance, Modèle de représentation*, Avril 1976, Contrat S.T.Aé N° 75.98522, Fasc. 2
13. Coulon, G. *Simulation of an airplane with structural and nonstationary effects*, 8th AICA Congress, Delft, The Netherlands, 1976
14. Coulon, G. *ADERSA/GERBIOS, Modélisation en aérodynamique asservie*, April 1977, Contrat S.T.Aé N° 76.98213, Lot 1
15. Coulon, G. *ADERSA/GERBIOS, Modélisation en aérodynamique asservie*, Octobre 1977, Contrat S.T.Aé N° 76.98213, Lot 2
16. Charon, W. *Nouvelle technique d'essais sur maquettes libres en laboratoire pour la détermination des caractéristiques aérodynamiques instationnaires*, AGARD Symposium on Dynamic Stability Parameters, Athens, May 1978
17. Himmelblau, D.M. *Applied Nonlinear Programming*, Mc Graw Hill, New York, 1972
18. Lecamus, F. *Identification des systèmes discrets linéaires multivariables par minimisation d'une distance de structure*, Electronic Letters, Vol. 4, N° 24, Nov. 1968
19. Richalet, J. *Identification des processus par la méthode du modèle*, Gordon & Breach, London, 1971
20. Mereau, P. *ADERSA/GERBIOS, Pilotage automatique numérique transparent*, Déc. 1977, Contrat D.R.E.T. N° 75/195, Lot 4

21. Coulon, G.
Hirsch, R.
Mereau, P.
Rault, A.

ADERSA/GERBIOS, *Modélisation et commande en aérodynamique asservie*,
Juin 1977, Contrat D.R.E.T. N° 76/235, Lot 2

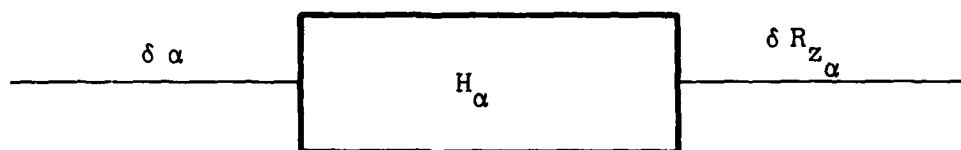


Figure 1 - Bloc-diagram representation between lift and angle of attack variations

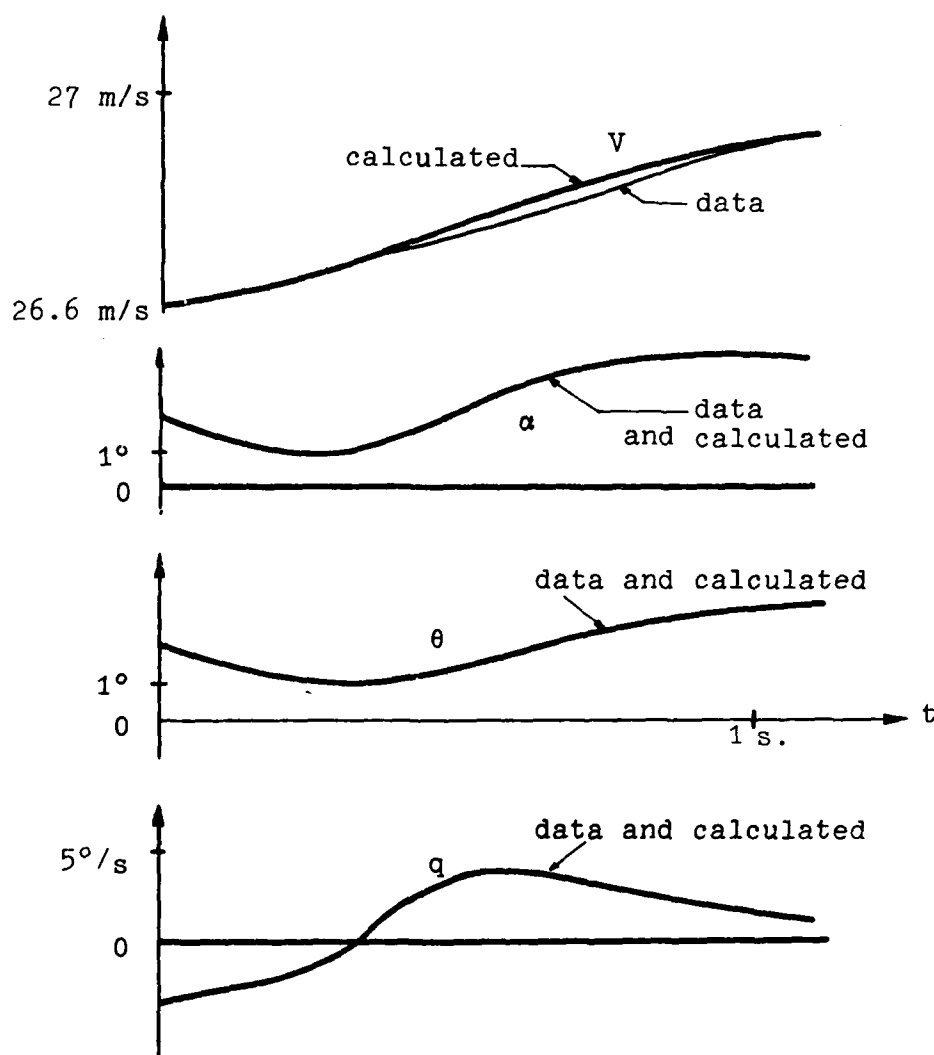


Figure 2 - Comparison of data and calculated state variables

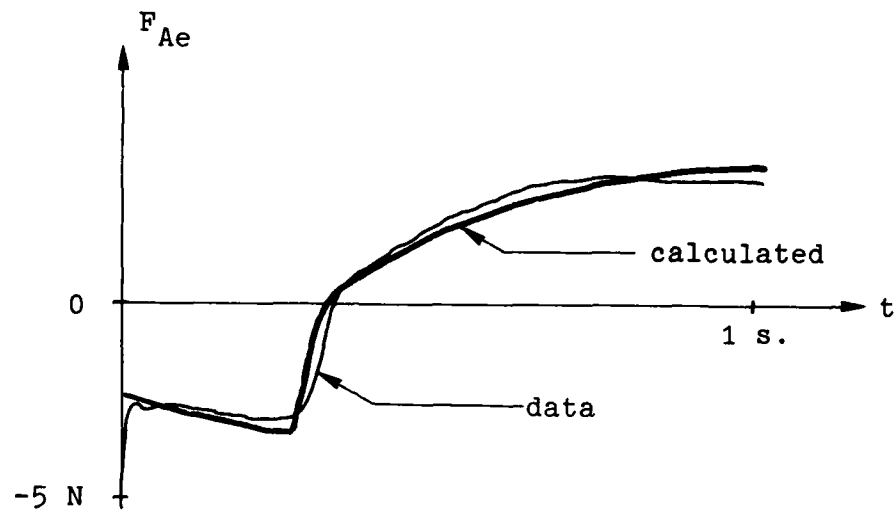


Figure 3 - Comparison of data and calculated tail aerodynamic force

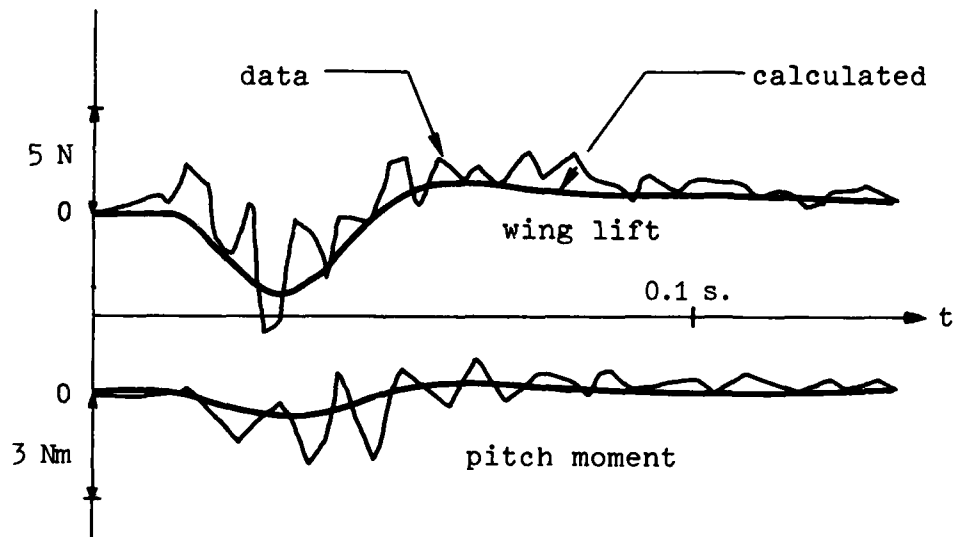


Figure 4 - Comparison of data and calculated unsteady wing lift and unsteady pitch moment

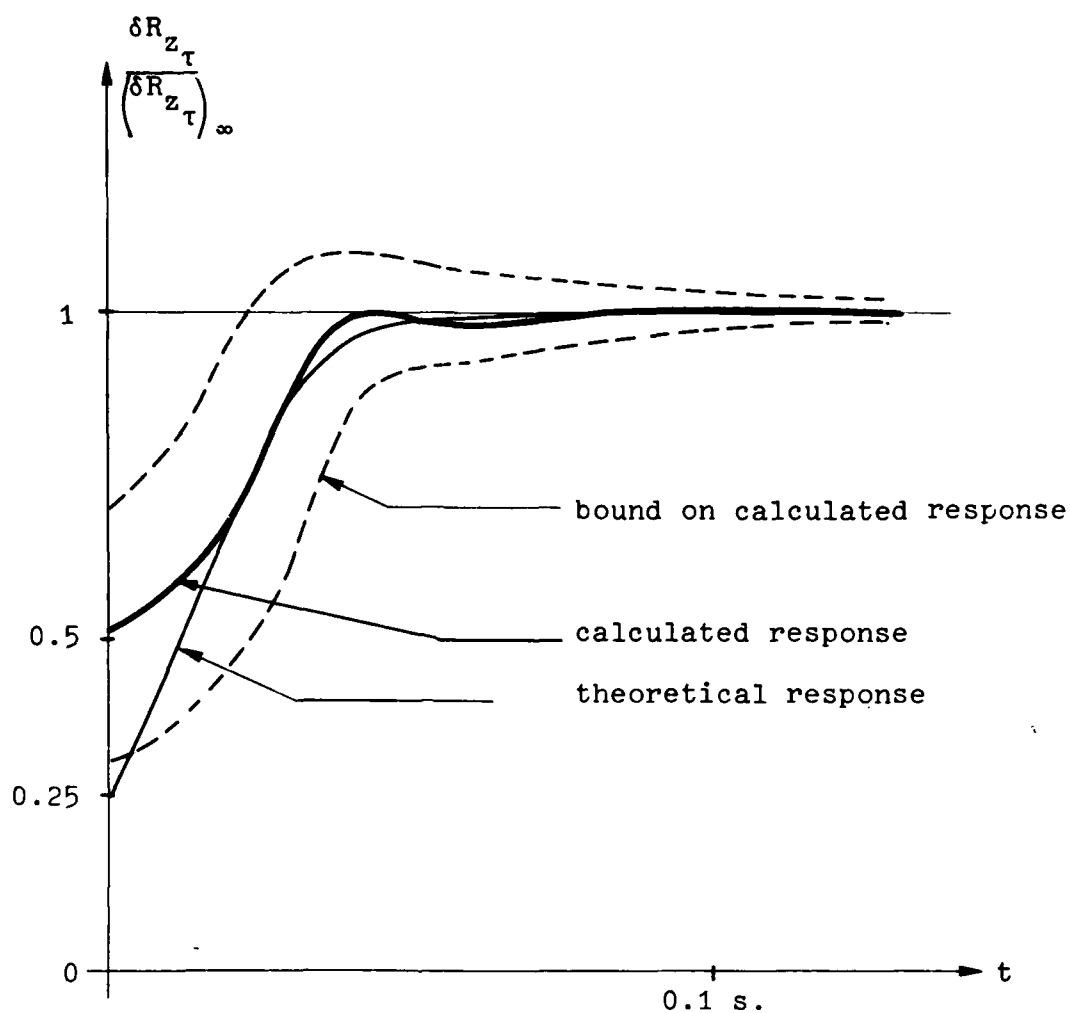


Figure 5 - Comparison of theoretical and calculated transient step responses for wing lift variation due to flap motion

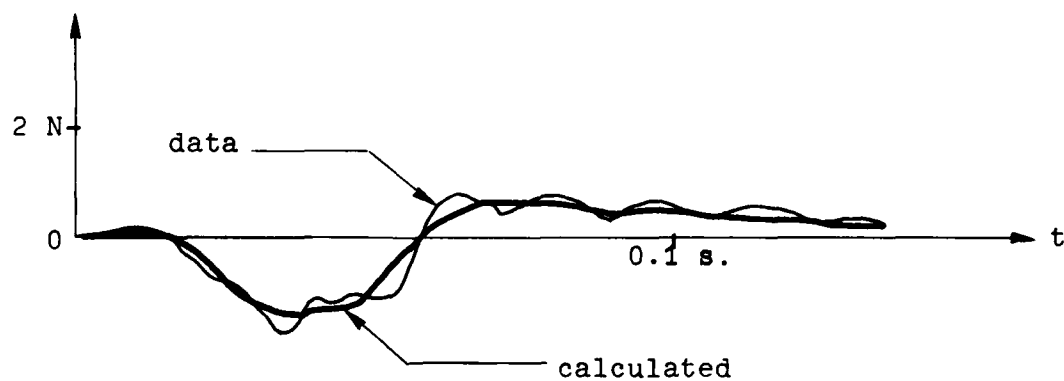


Figure 6 - Comparison of data and calculated unsteady tail lift

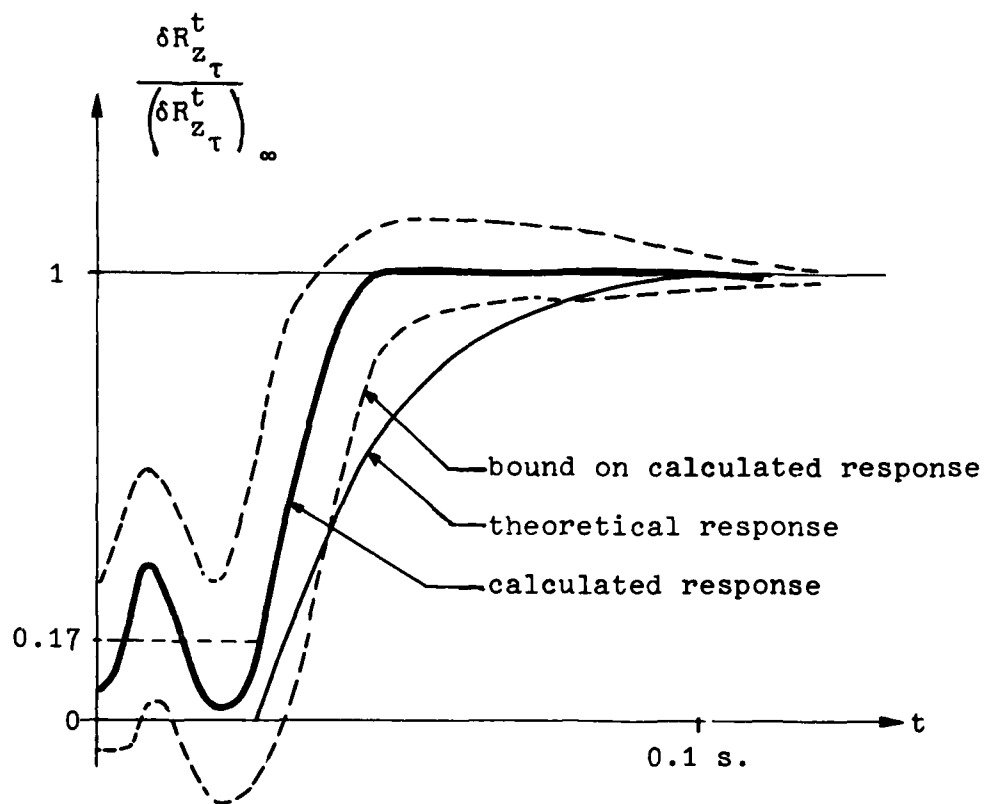


Figure 7 - Comparison of theoretical and calculated transient step responses for tail lift variation due to flap motion

APPENDIX

EXPRESSIONS OF THE RESIDUAL VECTORS IN MODEL (9)

The residual vector due to wing lift unsteady terms is given by (10) where $f \otimes \dot{\underline{x}}$ stands for a convolution integral between the function, f and each component of the vector $\dot{\underline{x}}$. Thus the i -th component of vector $f \otimes \dot{\underline{x}}$ according to (6) has the following forms :

$$\int_0^t f(u) \frac{d}{du} [x_i(t-n)] du$$

If the transient terms in V and θ are not considered (e.g. not sensitized in the identification), matrices A_1 and B_1 have the following form (ref. 14)

$$A_1 = \begin{bmatrix} 0 & 0 & 0 & 0 \\ 0 & a_{22}^1 & 0 & a_{24}^1 \\ 0 & 0 & 0 & 0 \\ 0 & a_{42}^1 & 0 & a_{44}^1 \end{bmatrix} \quad B_1 = \begin{bmatrix} 0 & 0 \\ b_{21}^1 & 0 \\ 0 & 0 \\ b_{41}^1 & 0 \end{bmatrix}$$

with,

$$\begin{aligned} a_{22}^1 &= -\frac{\rho S V_0}{2m} C_{z_\alpha}^w ; & a_{24}^1 &= -\frac{\rho S V_0}{2m} C_{z_q}^w \\ a_{42}^1 &= \frac{\rho S l V_0^2}{2I} C_{m_\alpha}^w ; & a_{44}^1 &= \frac{\rho S l V_0^2}{2I} C_{m_q}^w \\ b_{21}^1 &= -\frac{\rho S V_0}{2m} C_{z_\tau}^w ; & b_{41}^1 &= \frac{\rho S l V_0^2}{2I} C_{m_\tau}^w \end{aligned}$$

where m is the aircraft mass, l a reference chord, I the longitudinal moment of inertia. $C_{z_i}^w$ and $C_{m_i}^w$ are wing stability and control derivatives. ρ, S, V_0 are reference values defined in section 1.

Concerning the residual vector due to tail lift unsteady terms given by (11), the matrices \bar{A}_1 and \bar{B}_1 are :

$$\bar{A}_1 = \begin{bmatrix} 0 & 0 & 0 & 0 \\ 0 & \bar{a}_{24}^1 & 0 & 0 \\ 0 & 0 & 0 & 0 \\ 0 & 0 & 0 & 0 \end{bmatrix} \quad \bar{B}_1 = \begin{bmatrix} 0 & 0 \\ \bar{b}_{21}^1 & 0 \\ 0 & 0 \\ 0 & 0 \end{bmatrix}$$

with,

$$\bar{a}_{24}^1 = \frac{\rho S_t V_0}{2m} C_{z_\alpha}^t ; \quad \bar{b}_{21}^1 = \frac{\rho S_t V_0}{2m} C_{z_\tau}^t$$

where superscript t and subscript t refer to tail quantities.

Coefficient	Value	Bounds
C_{z_α}	3.44	2.95 ; 3.7
C_{z_τ}	0.87	0.78 ; 0.98
C_{m_α}	-0.85	-1.0 ; -0.8
C_{m_β}	-0.12	-0.29 ; -0.1
C_{m_τ}	-0.26	-0.27 ; -0.25

Table 1 - Reduced scale plane aerodynamic coefficients obtained by identification

Coefficient	Value	Bounds
$C_{z_0}^t$	-0.03	-0.05 ; -0.02
$C_{z_\alpha}^t$	1.9	1.67 ; 2.5
$C_{z_\tau}^t$	-0.54	-0.63 ; -0.47

Table 2 - Tail aerodynamic coefficients obtained by identification

EFFECT OF FLOW SEPARATION VORTICES ON AIRCRAFT UNSTEADY AERODYNAMICS*

by

L. E. Ericsson, Consulting Engineer and J. P. Reding, Research Specialist
Lockheed Missiles & Space Company, Inc.
Sunnyvale, California, 94088, U.S.A.

SUMMARY

A study of the unsteady aerodynamic flow field over the space shuttle orbiter has recently been completed (Ref. 1). The results are summarized in the present paper. The study showed that at moderate to high angles of attack separation-induced vortices exert a dominating influence on the unsteady aerodynamics of the space shuttle orbiter and of high performance aircraft. The distinguishing characteristics are as follows:

- 1) The vortex-induced aerodynamic loads are large and highly nonlinear, sometimes discontinuous in character.
- 2) The vortex-induced loads have opposite effects on static and dynamic stability characteristics.

Analytic approximations are presented which can predict these vortex-induced aerodynamic effects with the accuracy needed for most engineering design.

NOMENCLATURE

A	aspect ratio, $A = b^2/S$
b	wing span
\bar{c}	reference length (mean aerodynamic chord; for a delta wing $\bar{c} = 2 c_o/3$)
c_o	slender wing root chord
K_{Ma}, K_{MV}	Mach number parameters, Eqs. (1) and (4)
K_p, K_v	potential flow and vortex lift factors
L	lift: coefficient $C_L = L/(\rho_\infty U_\infty^2/2)S$
M	Mach number
M_p	pitching moment: coefficient $C_m = M_p/(\rho_\infty U_\infty^2/2)S\bar{c}$
N	normal force: coefficient $C_N = N/(\rho_\infty U_\infty^2/2)S$
q	pitch rate
Re	Reynolds number (based on root chord and free stream conditions)
S	reference area (= projected wing area)
s	local semi-span
t	time
T	period of oscillation
U	horizontal velocity
\bar{U}	convection velocity
x	axial body-fixed coordinate
α	angle of attack
α_o	trim angle of attack
$\tilde{\alpha}$	generalized angle of attack, Eq. (8)
$\bar{\beta}$	M-parameter, $\bar{\beta} = \sqrt{1 - M_\infty^2}$
Δ	increment
η	dimensionless y-coordinate, $\eta = y/s$
θ	angular perturbation in pitch
θ_{LE}	apex half angle
θ_{TE}	trailing edge sweep angle
ξ	dimensionless x-coordinate, $\xi = x/c_o$
ρ	air density
ψ	phase angle, $\psi = \omega t$
$\omega, \bar{\omega}$	pitching frequency, $\bar{\omega} = \omega \bar{c}/U_\infty$

Subscripts

A	apex
a	attached flow

*The paper is based on results obtained in studies made for Mr. J. C. Young, NASA JSC, and Mr. W. W. Clever, NASA MSFC, under Contracts NAS 9-11445, NAS 8-28130, and NAS 8-30652.

CG	center of gravity
crit	critical
D	discontinuity
EW	equivalent wing
eff.	effective
LE	leading edge
SW	slender wing
s	separated flow
TE	trailing edge
V	vortex
2D	two-dimensional flow
∞	freestream conditions

Superscripts

(-) barred quantities denote integrated mean values

Derivative Symbols

$$\dot{\theta} = \partial \theta / \partial t$$

$$C_{N\alpha} = \partial C_N / \partial \alpha; C_{m\dot{\theta}} = \partial C_m / \partial \dot{\theta}$$

$$C_{m\dot{\theta}} = C_{mq} + C_{m\dot{\alpha}} = \partial C_m / \partial (c\dot{\theta}/U_\infty)$$

$C_{m\dot{\theta}}$ and $C_{m\dot{\alpha}}$ are mean coefficients for nonlinear characteristics, Eqs. (15)-(17).

1. INTRODUCTION

The increased operational range of high performance aircraft and tactical missiles as well as the unique operational requirements of the space shuttle have created new demands on our understanding of the high angle of attack characteristics of lifting surfaces. This is especially true in regard to the unsteady aerodynamics. In the case of low aspect ratio wings with highly swept leading edges separated flow exhibits itself in form of leading edge vortices which affect the aerodynamics throughout the angle of attack range and can have a decisive influence on dynamic stability characteristics already at low angles of attack.

The space shuttle orbiter is a configuration of special current interest which exhibits a multitude of separation-induced vortices (see Figs. 1a and 1b). Orbiter dynamic data (Ref. 1) shows the opposite α -trends in dynamic and static stability derivatives indicative of the flow field time lag effects typical of separation-induced loads (Ref. 2) (Fig. 2). The steps leading to the development of analytic means whereby the highly nonlinear characteristics in Fig. 2 can be predicted are described in what follows.

2. ANALYSIS

The static aerodynamic loads induced by the leading edge vortices on sharp-edged slender delta wings are determined by a simple analytic method based upon Polhamus' leading edge suction analogy (Ref. 3), modified to agree with the experimentally observed longitudinal distribution of the vortex-induced lift (Refs. 4 and 5). The vortex-induced unsteady aerodynamic characteristics are obtained equally simply using an analytic method suggested by the systematic investigations performed by Lambourn et al (Refs. 6 thru 8). For the more complicated configuration of the space shuttle orbiter experimental static characteristics are used to define an equivalent slender wing and its separation-induced loads.

2.1 Static Aerodynamics

K_P and K_V are constants determining the magnitudes of attached flow and vortex lift components, respectively (Refs. 3, 9, 10 and 11). In Jones' slender wing theory (Ref. 12) $(K_P)_{SW} = \pi A/2$. According to Ref. 13 Jones did himself derive a correction for the effect of finite aspect ratio, which in the case of compressible flow can be written

$$K_P = K_{Ma} : (K_P)_{SW}$$

$$K_{Ma} = 2/[1 + A\bar{\beta}/4 + \sqrt{1 + (A\bar{\beta}/4)^2}] \quad (1)$$

$$\bar{\beta} = \sqrt{|1 - M^2|}$$

Applying Eq. (1) also for supersonic Mach numbers gives slightly lower lift than the inviscid value derived in Ref. 14. At the limit $A\bar{\beta}/4 = 1$, when the leading edge ceases to be subsonic, the difference is 8%. As it does not seem unreasonable that such a decrease from the two-dimensional inviscid value could be caused by viscous edge conditions, Eq. (1) will be used for both subsonic and supersonic Mach numbers. Thus, in the Mach number range for subsonic leading edge conditions, $0 \leq M_\infty \leq \sqrt{1 + (A/4)^{-2}}$, the formulation for the attached flow aerodynamics is as follows (Ref. 9).

$$\begin{aligned}
C_{Na} &= (C_{Na})_{SW} K_{Ma} \\
(C_{Na})_{SW} &= (\pi A/2) \sin \alpha \cos \alpha \\
C_{ma} &= - (c_o/\bar{c}) C_{Na} (\bar{\xi}_a - \xi_{CG}) \\
K_{Ma} &= 2 / \left[1 + A \bar{\beta}/4 + \sqrt{1 + (A \bar{\beta}/4)^2} \right] \\
\bar{\xi}_a &= \begin{cases} 0.667 \sqrt{K_{Ma}} : 0 \leq M_\infty < 1 \\ 0.667 : 1 \leq M_\infty \leq \sqrt{1 + (A/4)^{-2}} \end{cases}
\end{aligned} \quad (2)$$

Polhamus' expression for the vortex lift at supersonic speeds (Ref. 3) can be written

$$K_V = \pi [1 + (A/4)^2]^{1/2} K_{Ma}^2 [1 - (A \bar{\beta}/4)^2]^{1/2} \quad (3)$$

Thus, the vortex-induced aerodynamics can be approximated as follows (Refs. 9 thru 11)

$$\begin{aligned}
C_{NV} &= (C_{NV})_{SW} K_{MV} \\
(C_{NV})_{SW} &= \pi [1 + (A/4)^2]^{1/2} \sin^2 (\alpha - \alpha_s) \\
C_{mV} &= - (c_o/\bar{c}) C_{NV} [0.3 (\bar{\xi}_a - \xi_{CG}) + 0.7 (\bar{\xi}_V - \xi_{CG})] \\
K_{MV} &= [1 - (A \bar{\beta}/4)^2]^{1/2} \begin{cases} 1 : 0 \leq M_\infty < 1 \\ K_{Ma}^2 : 1 \leq M_\infty \leq \sqrt{1 + (A/4)^{-2}} \end{cases} \\
\bar{\xi}_V &= 0.587 \begin{cases} (1 - 0.046 \bar{\beta}) [1 - \bar{\eta}_V (A \bar{\beta}/4)^2] : 0 \leq M_\infty < 1 \\ 1 : 1 \leq M_\infty \leq \sqrt{1 + (A/4)^{-2}} \end{cases} \\
\bar{\eta}_V &= 0.56 + 0.36 / [1.75 + (\alpha/\theta_{LE})]
\end{aligned} \quad (4)$$

The vortex-induced loads generated at non-zero angle of attack are determined by Eq. (4) and are superimposed on the attached flow loads defined by the modified slender wing theory, Eq. (2). The total aerodynamic loads of an $A = 1.15$ delta wing determined in this manner agree well with experimental results (Refs. 5, 15) (Fig. 3). The figure shows how the vortex-induced loads decrease continually with increasing Mach number. The present modification of Polhamus' theory (Ref. 3) affects mainly the moment prediction, which is improved substantially judging by available experimental results (Refs. 5, 16, 17) (Fig. 4). In Ref. 10 a simple method was derived to account for moderately swept (forward or back) trailing edges. Two equivalent delta wings were defined, one for attached flow loads and another for the vortex-induced loading. These equivalent delta wing characteristics were referenced ("back") to the true wing geometry by multiplication through the following ratios.*

$$\begin{aligned}
\frac{C_N}{(C_N)_{EW}} &= \frac{1 - \tan \theta_{LE} \tan \theta_{TE}}{(1 - \bar{\eta} \tan \theta_{LE} \tan \theta_{TE})^2} \\
\frac{c_o}{(c_o)_{EW}} &= (1 - \bar{\eta} \tan \theta_{LE} \tan \theta_{TE}) \\
\bar{\eta}_a &= 4/3\pi ; \bar{\eta}_V = 0.56 + 0.36 / [1.75 + (\alpha/\theta_{LE})]
\end{aligned} \quad (5)$$

Combining Eqs. (2), (4), and (5) gives the results shown in Fig. 5, indicating that the simple Eq. (5) suffices even when the trailing edge sweep angles are of significant magnitudes.

2.2 Unsteady Aerodynamics

The unsteady aerodynamic characteristics for a delta wing in incompressible flow were derived in Ref. 9. In the present notation the attached flow derivatives are

$$\begin{aligned}
C_{m\theta a} &= (c_o/\bar{c}) C_{N\theta a} \cos^2 \alpha_o [\bar{\xi}_a - \xi_{CG}] \\
C_{m\dot{\theta} a} &= (c_o/\bar{c})^2 C_{N\theta a} \cos \alpha_o [(c_{eff}/c_o) - \xi_{CG}]^2 \\
C_{N\theta a} &= (\pi A/2) K_{Ma} \\
c_{eff}/c_o &= [K_{Ma} (2 - \cos^2 \alpha_o)]^{1/2}
\end{aligned} \quad (6)$$

and the vortex-induced contributions are

$$\begin{aligned}
C_{m\theta v} &= - (c_o/\bar{c}) C_{N\theta v} [0.3 (\bar{\xi}_a - \xi_{CG}) + 0.7 (\bar{\xi}_V - \xi_{CG})] \\
C_{m\dot{\theta} v} &= - (c_o/\bar{c})^2 C_{N\theta v} \left\{ 0.3 \sec \alpha_o [(c_{eff}/c_o) - \xi_{CG}]^2 \right. \\
&\quad \left. + 0.7 (U_\infty/\bar{U}) \bar{\xi}_{CG} (\bar{\xi}_V - \xi_{CG}) \right\} \\
C_{N\theta v} &= \pi K_{MV} \sin^2 (\alpha_o - \alpha_s) [1 + (A/4)^2]^{1/2}
\end{aligned} \quad (7)$$

* For the present the incompressible spanwise load center is used for all Mach numbers.

The incompressible stability derivatives at $\alpha = 0$ determined by use of Eqs. (2) and (6) are compared with experimental results (Refs. 18 thru 20) in Fig. 6.[#] The simplified present formulation does give a fairly good account of the effect of aspect ratio. Noticing that both $C_{m\dot{\alpha}}$ and $C_{m\ddot{\alpha}}$ as measured in the dynamic test of the $A = 1.458$ wing are 25% below the prediction, whereas the static test gave a stability derivative C_{m0} that agrees with the prediction, it is hard to judge how good the present prediction of the aspect ratio effect is. That the prediction is good for low aspect ratios is confirmed by the results shown in Fig. 7 for an $A = 0.75$ Gothic wing. The present prediction of the effect of oscillation center on $C_{m\dot{\alpha}}$ agrees with experimental results (Refs. 23, 24) as well as with the computations from lifting surface theory (Ref. 25). Fig. 8 shows that the prediction of Mach number effects for an $A = 1.45$ delta wing agree well with experimental data (Ref. 26) for the subsonic speed range, and also agrees well with other theories (Refs. 27 thru 29) in the supersonic speed range. The poor agreement between experiment and theory at supersonic speeds could be due to shockwave-boundary layer interaction at the trailing edge of the half model, as is suggested in Ref. 26. A similar and probably stronger shock-boundary layer interaction might explain the sharp drop-off of the damping when the sonic speed is exceeded. According to the results in Ref. 30, the aspect ratio is too low for the wing to realize any of the degraded damping at low supersonic speeds caused by inviscid α -effects. In Fig. 9 comparison is made with wind tunnel test data on a sting-mounted $A = 2$ delta wing. Although the aspect ratio is rather high, the present predictions agree well with experimental data (Refs. 30, 31) and available theory (Ref. 30). It can be seen that the transonic behavior of the experimental data is not as violent as for the half-model data in Fig. 8. However, even wing-mounted models can experience data distortion due to support interference (Ref. 32), especially if boundary layer transition is occurring on or near the sting-model juncture (Ref. 33). The subsonic test data (Ref. 31) in Fig. 9 were obtained using a very large diameter sting and support interference is a distinct possibility. At supersonic speeds support interference is less of a problem. All in all the experimental data in Fig. 9 probably provides a good representation of the correct Mach number trend. In Fig. 10 free-flight data (Ref. 34) for an $A = 0.865$ Gothic wing are shown to compare well with present predictions. There is also good agreement between present theory and other available supersonic (Refs. 35,36) and subsonic (Ref. 37) theories.

The main purpose of the present analysis is to provide simple analytic means for computation of the contribution to the dynamic stability derivatives from the leading edge vortices that are generated at non-zero angles of attack. Combining Eqs. (2), (4), (6), and (7) the results shown in Fig. 11 were obtained. It can be seen that the experimentally observed large vortex-induced loads, with opposite effects on static and dynamic stability (Ref. 18), are well predicted (Fig. 11a). Considering the delay in leading edge separation caused by leading edge roundness, determined by using two-dimensional airfoil stall data in the cross-flow plane normal to the leading edge (Ref. 10), gives the results shown in Fig. 11b, which are also in good agreement with experiments (Ref. 38). At high angles of attack the leading edge vortex breaks down causing a reversal of the vortex-induced effects on the stability derivatives for increasing angle of attack (Ref. 19) (Fig. 12). Over the wing area where vortex breakdown occurs not only is the vortex-induced suction loading lost but also the attached flow suction is in large part eliminated. That is, at vortex breakdown the vortex-induced loads, to be super-imposed on the attached flow loads, are reversed. In addition vortex burst introduces significant buffeting loads (Ref. 39).

2.3 Orbiter Dynamics

When trying to extend the analytic methods developed for the delta wing to apply to the space shuttle orbiter, one encounters several complications. First, the space shuttle has a double-delta wing planform (Fig. 13a). The inner delta wing or strake induces a substantial loading on the main wing (Ref. 40) (Fig. 13b). In addition to the complication introduced by the strake there is a considerable influence by the orbiter fuselage. The absence of any wing-body fairing causes flow separation to occur in the wing-fuselage juncture, starting just forward of the OMS pods at $\alpha = 0$. This "axial corner flow" separation grows with increasing angle of attack as crossflow-induced collection of forebody boundary layer "spills" over the strake into the wing-body juncture (Refs. 41, 42). The addition of low energy boundary layer to the corner flow region causes the flow separation to grow, occurring closer to, and finally at the strake apex. The separation is vented by a vortex which generates lift on the aft main wing. This vortex is similar to the free body vortices generated on slender bodies of revolution (Ref. 43). Thus, the crossflow over the forebody and strake determines the vortex-induced lift on the aft main wing. At high angles of attack the corner vortex interacts with the main wing vortex to form one large size vortex, which is swept outboard to the outer wing panel where, when some critical angle of attack is exceeded, it starts to burst over the wing initiating the loss of lift associated with three-dimensional slender wing stall.

The unsteady aerodynamic characteristics of the orbiter are computed in the following manner. An equivalent slender wing is defined for computation of the attached flow unsteady aerodynamics, similarly to what was done in the delta wing analysis (Ref. 10). The trailing edge of the equivalent wing is located such that the computed slender wing force derivative $C_{Y\dot{\alpha}}$ at $\alpha = 0$ agrees with $C_{Y\dot{\alpha}}$ measured in static tests. That determines c_{eff}/c in Eq. (6) and is used to obtain the attached flow damping derivative $C_{m\dot{\alpha}}$. The corresponding static stability derivative C_{m0} is computed from Eqs. (2) and (6) as $C_{m0}(\alpha) = C_{m0}^{\text{measured}}(0) \cos^2 \alpha$, where $C_{m0}^{\text{measured}}(0)$ is C_{m0} at $\alpha = 0$ measured in the static test. The vortex-induced loads are defined as the difference at angle of attack between the actually measured static characteristics (Ref. 44) and the computed attached flow characteristics.

In this manner the flow complications caused by the fuselage are accounted for in regard to the magnitude of the vortex-induced loads. In order to obtain the unsteady aerodynamics one has to determine the phasing of these vortex-induced loads. The situation is different from that for the pure delta wing analysis. For the strake vortex and its induced loads on the strake of a pure double-delta wing (Fig. 13b), the delta wing analysis would apply. However, for the vortex-induced loads on the main orbiter wing

[#]The ordinate scale reflects the fact that $\bar{c} = c/2$ was used in Refs. 18-20. In order to avoid confusion the definition in the Nomenclature will be followed strictly, and when the data taken from another data source defines the derivatives in a different manner, this fact will be reflected as shown in Fig. 6, following the example set by Schneider in his current review of the state of the art in this field (Refs. 21,22).

(Fig. 13a), the delta-wing analysis does not apply. The vortex is a free vortex, like a forebody vortex (Refs. 41-43) or a part-span vortex (Ref. 45). Its strength is determined by the feeding from the strake, and the change of vortex strength is convected downstream with free stream speed, $\bar{U} = U_\infty$. Furthermore, the fuselage cannot be treated as a reflection plane. The corner flow vortex is fed by forebody crossflow. It appears reasonable that the combined crossflow effects can be represented in lumped form by the crossflow at strake apex (Refs. 41,42). That is, the vortex-induced force C_{NV} at a station $x - x_A$ downstream of strake apex is a function of the angle of attack at strake apex a time increment Δt earlier, where $\Delta t = (x - x_A)/U_\infty$. For rigid body oscillations around x_{CG} the generalized angle of attack at strake apex (x_A) is

$$\tilde{\alpha}_A = \alpha_0 + \theta + (x_A - x_{CG}) \dot{\theta}/U_\infty \quad (8)$$

With θ being the infinitesimal amplitude perturbation in pitch around α_0 at a low reduced frequency, one can represent $\tilde{\alpha}_A(t - \Delta t)$ by the first order terms in a Taylor expansion.

$$\tilde{\alpha}_A(t - \Delta t) = \alpha_0 + \theta - \dot{\theta} \Delta t + (x_A - x_{CG}) \dot{\theta}/U_\infty \quad (9)$$

The vortex-induced load at x at time t is

$$C_{NV}(t) = C_{NV}(\alpha_0) + C_{N\dot{\alpha}V}(\alpha_0) \tilde{\alpha}_A(t - [x - x_A]/U_\infty) \quad (10)$$

Combining Eqs. (9) and (10) gives

$$C_{NV}(t) = C_{NV}(\alpha_0) + C_{N\dot{\alpha}V}(\alpha_0) [\theta + (2x_A - x - x_{CG}) \dot{\theta}/U_\infty] \quad (11)$$

For the vortex-induced total load centered at \bar{x}_V Eq. (11) gives

$$C_{NV}(t) = C_{NV}(\alpha_0) + C_{N\dot{\alpha}V} \theta + C_{N\dot{\theta}V} \frac{\dot{\theta}}{U_\infty} \quad (12)$$

$$C_{N\dot{\theta}V} = C_{N\dot{\alpha}V}(\alpha_0)$$

$$C_{N\dot{\theta}V} = C_{N\dot{\alpha}V}(2x_A - \bar{x}_V - x_{CG})/\bar{c}$$

Thus, with $C_{mV} = -C_{NV}(\bar{x}_V - x_{CG})/\bar{c}$, the moment derivatives become

$$\begin{aligned} C_{m\dot{\theta}V} &= -C_{N\dot{\theta}V}(\bar{x}_V - x_{CG})/\bar{c} \\ C_{m\dot{\theta}V} &= -C_{m\dot{\alpha}V}(\bar{x}_V + x_{CG} - 2x_A)/\bar{c} \end{aligned} \quad (13)$$

As in the case of the pure delta wing (Fig. 11) the vortex-induced loads affect static and dynamic stability in opposite ways. This vortex contribution is added to the attached flow derivatives for angles of attack $\alpha > \alpha_V$ where the strake-fuselage vortex occurs. Thus, the total derivatives are

$$\begin{aligned} C_{m\theta} &= \begin{cases} C_{m\theta a} & : \alpha < \alpha_V \\ C_{m\theta a} + C_{m\dot{\theta}V} & : \alpha \geq \alpha_V \end{cases} \\ C_{m\dot{\theta}} &= \begin{cases} C_{m\dot{\theta} a} & : \alpha < \alpha_V \\ C_{m\dot{\theta} a} + C_{m\dot{\theta}V} & : \alpha \geq \alpha_V \end{cases} \\ C_{m\theta a} &= -C_{N\dot{\alpha} a} \cos^2 \alpha_0 (\bar{x}_A - x_{CG})/\bar{c} \\ C_{m\dot{\theta} a} &= -C_{N\dot{\alpha} a} \cos \alpha_0 [(x_{TE})_{eff} - x_{CG}]^2/\bar{c}^2 \\ C_{m\theta V} &= -C_{N\dot{\alpha} V}(\bar{x}_V - x_{CG})/\bar{c} \\ C_{m\dot{\theta} V} &= -C_{m\dot{\alpha} V}(\bar{x}_V + x_{CG} - 2x_A)/\bar{c} \end{aligned} \quad (14)$$

In Fig. 14 the predicted stability derivatives obtained through Eq. (14) are compared with subsonic dynamic experimental results (Ref. 46). The agreement is gratifying. At high angles of attack, $\alpha > 12^\circ$, the combined strake-body vortex starts to burst at the trailing edge. As the burst location moves forward with increasing angles of attack the lift loss increases resulting in a loss of static stability. Because of the time lag the effect on the dynamic stability is the opposite, Eq. (13), and the damping is increased. The static data (Ref. 44) used for the dynamic prediction were obtained with a different OMS-pod configuration. Inspection of Fig. 14, keeping the above time lag effect in mind, reveals that if the correct static data had been available (they would have coincided with the dynamic $C_{m\dot{\theta}}$ -data) improved agreement would result between predicted and measured damping characteristics at high angles of attack.

At transonic speed a shock emanates from the corner separation and extends outboard over the wing (Refs. 41,42). At some critical angle of attack the wing-body corner separation jumps discontinuously to the strake apex in response to the increase of the crossflow at strake apex above the critical value. This in turn causes the shock to jump forward close to the leading edge of the main wing resulting in a sudden, discontinuous change in the wing loading. Thus, the crossflow at the strake apex determines the separation-induced discontinuous load change and its effects on the vehicle dynamics. However, because of the discontinuous variation of the aerodynamic forces the derivative concept, Eq. (14), has to be abandoned. An equivalent effective derivative that varies with the amplitude can be defined which agrees with the derivative-representation in dynamic experiments (Refs. 47,48). With ΔC_m being the discontinuous moment jump

* The pod containing the Orbital Maneuver System is very bulbous, (it can be seen in Fig. 13a, located at the root of the orbiter fin) and has a significant effect on the orbiter aerodynamics.

** Note that $\bar{\omega}^2 \ll 1$.

which occurs when α exceeds α_D one obtains the following effective aerodynamic spring coefficient for pitch oscillations around α_0 of amplitude $\Delta\theta$.

$$C_{m\theta} = \frac{1}{\Delta\theta^2} \int_{-\Delta\theta}^{\Delta\theta} C_m d\theta = C_{m\alpha} + \frac{\Delta C_m}{\Delta\theta} \left[1 - \frac{\alpha_D - \alpha_0}{\Delta\theta} \right] \quad (15)$$

provided that $\alpha_0 \leq \alpha_D \leq \alpha_0 + \Delta\theta$. Likewise, the equivalent damping derivative is obtained by integrating the work over one cycle.

$$C_{m\dot{\theta}} = \frac{1}{\pi \Delta\theta \omega} \int_{\psi_0}^{\psi_0 + 2\pi} C_m(\psi) \cos \psi d\psi \quad (16)$$

where $\psi = \omega t$ and $\omega T = 2\pi$ with ω and T being the frequency and period of the pitch oscillation. Integration gives

$$C_{m\dot{\theta}} = C_{m\dot{\theta}a} - \frac{2\Delta C_m}{\pi \Delta\theta} \frac{\bar{x}_V + x_{CG} - 2x_A}{\bar{c}} \quad (17)$$

As the static data (Ref. 44) did not have the resolution needed to determine ΔC_m , it was determined from the dynamic measurements of C_m using Eq. (15). The ΔC_m -value obtained in this manner* was used in Eq. (17) to determine the corresponding damping spike. For the rest of the angle of attack range, $\alpha < \alpha_0 - \Delta\theta$ and $\alpha > \alpha_0 + \Delta\theta$, Eq. (14) applies. In Fig. 15 the computed results for $M_\infty = 0.9$ are compared with the Langley damping measurements (Ref. 11). The agreement is as good as for the lower Mach number in Fig. 14, and would have been even better if the correct static data had been available. This conclusion is based upon the same observation that was applied earlier to the results in Fig. 14.

In the sonic and low supersonic portion of the transonic speed range the flow separation becomes very sensitive to the OMS-pod configuration (Refs. 41, 42, 49, 50) (Fig. 16), and the error incurred by using the incorrect static data becomes more severe than at the lower Mach numbers. However, even with access to the correct static data it may not be possible to predict the dynamic characteristics using the present approach. The results in Fig. 16 indicate that separation induced unsteady loads at $M_\infty = 0.98$ and $M_\infty = 1.2$ have a more complicated character than what is represented by the present formulation, which is based upon the assumption that the crossflow at strake apex controls the separation-induced loads. Further work is needed to pinpoint the reason for the loss of dynamic stability at transonic speeds, for $8^\circ < \alpha < 14^\circ$ at $M_\infty = 0.98$ and for $8^\circ < \alpha < 12^\circ$ at $M_\infty = 1.2$ (Fig. 16). When one considers how difficult it is to extrapolate from transonic subscale dynamic test data to full scale (Refs. 51, 52) the dynamic characteristics shown in Fig. 16 give cause for concern.

3. CONCLUSIONS

The presented analysis shows how the classical slender wing theory can be extended to provide the analytic means needed for computation of the unsteady aerodynamics of present high performance vehicles operating at high angles of attack. The results are as follows:

- o The effect of Mach number for a subsonic leading edge is accounted for by a simple modification of Jones' slender wing theory for the attached flow loads and by an extension of Polhamus' theory for the vortex-induced loads.
- o The effect of moderate trailing edge sweep (forward or back) is accounted for by the use of two equivalent delta wings, one for the attached flow loads and another for the vortex-induced loads.
- o Static and dynamic longitudinal aerodynamic characteristics determined by the presented closed form solutions are in good agreement with experimental data in the complete Mach number range $0 \leq M_\infty \leq 2.8$.
- o In the α - M_∞ regions where other theoretical methods exist they give results that are in good agreement with present predictions.
- o The slender wing analysis is extended as follows to the orbiter wing with its double-delta planform.

The attached flow loads are given by an equivalent slender wing that gives the $C_{N\alpha}$ and $C_{m\alpha}$ at $\alpha = 0$ which was measured in static tests.

The vortex-induced loads are defined as the difference at $\alpha > 0$ between the measured total static loads and the computed attached flow loads. The crossflow effects on the unsteady vortex-induced loads are represented in lumped form by the crossflow at the strake apex.

- o The unsteady aerodynamic characteristics of the orbiter computed in this manner are in good agreement with dynamic experimental results in the Mach number range $0.3 \leq M_\infty \leq 0.9$. At transonic speeds, however, the experimentally observed dynamic instability could not be predicted. Thus, further work is needed in the critical Mach number range $0.9 < M_\infty < 1.4$.

4. REFERENCES

1. Boyden, R. P. and Freeman, D. C., "Subsonic and Transonic Dynamic Stability Derivatives of a Modified 089B Shuttle Orbiter," NASA TM X-72631, DMS-OR-2107, Dec. 1974.
2. Ericsson, L. E. and Reding, J. P., "Analysis of Flow Separation Effects on the Dynamics of a Large Space Booster," J. Spacecraft and Rockets, Vol. 2, No. 4, July-August 1965, pp. 481-490.

* See Ref. 41 for a detailed discussion.

3. Polhamus, E. C., "Predictions of Vortex-Lift Characteristics by a Leading-Edge Suction Analogy," *Journal of Aircraft*, Vol. 8, No. 4, April 1945.
4. Hummel, D., "Zur Umströmung scharfkantiger schlanker Deltaflügel bei grossen Anstellwinkeln," *Z. Flugwiss*, Vol. 15, No. 10, 1967, pp. 376-385.
5. Davenport, E. E. and Huffman, J. K., "Experimental and Analytical Investigation of Subsonic Longitudinal and Lateral Aerodynamic Characteristics of Slender Sharp-Edge 74° Swept Wings," NASA TN D-6344.
6. Lambourne, N. C., Bryer, D. W., and Maybrey, J.F.M., "A Preliminary Note on the Behavior of the Leading-Edge Vortices on a Delta Wing Following a Sudden Change of Incidence," NPL Aero Note 1006, Aer. Res. Council, Great Britain, Nov. 1962.
7. Lambourne, N. C., Bryer, D. W., and Maybrey, J.F.M., "The Behavior of the Leading-Edge Vortices over a Delta Wing Following a Sudden Change of Incidence," ARC R&M No. 3645, Aer. Res. Council, Great Britain, March 1969.
8. Lambourne, N. C., Bryer, D. W., and Maybrey, J.F.M., "Pressure Measurements on a Model Delta Wing Undergoing Oscillatory Deformation," NPL Aero Report 1314, Aer. Res. Council, Great Britain, March 1970.
9. Ericsson, L. E. and Reding, J. P., "Unsteady Aerodynamics of Slender Delta Wings at Large Angles of Attack," *J. Aircraft*, Vol. 12, No. 9, Sept. 1975, pp. 721-729. Errata, *J. Aircraft*, Vol. 14, No. 8, Aug. 1977, p. 832.
10. Ericsson, L. E. and Reding, J. P., "Approximate Nonlinear Slender Wing Aerodynamics," *J. Aircraft*, Vol. 14, No. 12, Dec. 1977, pp. 1197-1204.
11. Ericsson, L. E. and Reding, J. P., "Effect of Angle of Attack and Mach Number on Slender Wing Aerodynamics," AIAA Paper No. 77-667, June 1977.
12. Jones, R. T., "Properties of Low-Aspect-Ratio Pointed Wings at Speeds Below and Above the Speed of Sound," NASA Report No. 835, May 1975.
13. Lomax, H. and Sluder, L., "Chordwise and Compressibility Corrections to Slender Wing Theory," NACA Report 1105 (1952).
14. Brown, C. E., "Theoretical Lift and Drag of Thin Triangular Wings at Supersonic Speeds," NACA Report 839 (1946).
15. Davenport, E. E., "Aerodynamic Characteristics of Three Slender Sharp-Edge 74° Swept Wings at Subsonic, Transonic, and Supersonic Mach Numbers," NASA TN D-7631, Aug. 1974.
16. Wendtz, W. H., Jr., "Effects of Leading-Edge Camber on Low-Speed Characteristics of Slender Delta Wings," NASA CR-2002, 1972.
17. Peckham, O. H., "Low-Speed Wind-Tunnel Tests on a Series of Uncambered Slender Pointed Wings with Sharp Edges," R&M No. 3186, Aer. Res. Council, Great Britain, 1958.
18. Woodgate, L., "Measurements of the Oscillatory Pitching Moment Derivatives on a Slender Sharp-Edged Delta Wing in Incompressible Flow," R&M No. 3628, Part 2, Aer. Res. Council, Great Britain, 1968.
19. Woodgate, L. and Pugh, P. G., "Measurements of Pitching-Moment Derivatives on a Sharp-Edged Delta Wing in Incompressible Flow," R&M No. 3379, Aer. Res. Council, Great Britain, 1963.
20. Woodgate, L. and Halliday, A. S., "Measurements of Lift, Drag, and Pitching Moments on a Series of Three Delta Wings, R&M No. 3628, Part 4, Aer. Res. Council, Great Britain, 1968.
21. Schneider, C. P., "Instationäre Flugkörper-Aerodynamik," MBB Bericht Nr. UA-306-75, Messerschmitt-Bölkow-Blohm, West Germany, 1975.
22. Schneider, C. P., "Presentation of Stability Derivatives in Missile Aerodynamics and Theoretical Methods for Their Prediction," Paper 20, AGARD Symposium on Dynamic Stability Parameters, Athens, Greece, 21-24 May 1978.
23. Wright, J. G. and Wilkinson, A., "Low Speed Wind-Tunnel Measurements of Oscillatory Derivatives for a Family of Slender Wings, Part II, Damping in Pitch," Report W.T. 348, Bristol Aircraft Ltd., 1960.
24. Wright, J. G., "Low Speed Wind-Tunnel Measurements of the Oscillatory Longitudinal Derivatives of a Gothic Wing of Aspect Ratio 0.75," A.R.C. 24, 357, Aer. Res. Council, Great Britain, 1962.
25. Garner, H. C. and Lehrian, D. E., "Pitching Derivatives for a Gothic Wing Oscillating About a Mean Incidence," C.P. No. 695, Aer. Res. Council, Great Britain, 1963.
26. Orlik-Rückemann, K. and Olsson, C. O., "A Method for the Determination of the Damping-in-Pitch of Semi-Span Models in High-Speed Wind-Tunnels, and Some Results for a Triangular Wing," Report 62, The Aer. Res. Inst. of Sweden, 1956.
27. Ribner, H. S. and Malvestuto, F. S., Jr., "Stability Derivatives of Triangular Wings at Supersonic Speeds," NACA Report 908, 1948.

28. Watkins, C. E. and Berman, J. H., "Airforces and Moments on Triangular and Related Wings with Subsonic Leading Edges Oscillating in Supersonic Potential Flow," NACA Report 1099, 1952.
29. Berndt, S. B., "On the Theory of Slowly Oscillating Delta Wings at Supersonic Speeds," Report 43, The Aer. Res. Inst. of Sweden, 1951.
30. Tobak, M., "Damping in Pitch of Low-Aspect-Ratio Wings at Subsonic and Supersonic Speeds," NACA RM A52104a, 1953.
31. Emerson, H. F. and Robinson, R. C., "Experimental Wind Tunnel Investigation of the Transonic Damping-in-Pitch Characteristics of Two Wing-Body Combinations," NASA Memo 11-30-58A, 1958.
32. Reding, J. P. and Ericsson, L. E., "Dynamic Support Interference," J. Spacecraft and Rockets, Vol. 9, No. 7, July 1972, pp. 547-553.
33. Ericsson, L. E. and Reding, J. P., "Boundary Layer Transition and Dynamic Sting Interference," AIAA Journal, Vol. 8, No. 10, Oct. 1970, pp. 1886-1888.
34. Ross, A. J., Edwards, G. F., and Waterfall, A. F., "The Dynamic Stability Derivatives of a Slender Wing at Zero and Moderate Lift. A Comparison of Theory with Free-Flight Model Tests, $M = 0.8$ to 2.0 ," C.P. No. 1310, Aer. Res. Council, Great Britain, 1973.
35. Malvestuto, F. S. and Hoover, D. M., "Lift and Pitching Derivatives of Thin Sweptback Tapered Wings with Streamwise Tips and Subsonic Leading Edges at Supersonic Speeds," NACA TN 2294, 1951.
36. Malvestuto, F. S. and Hoover, D. M., "Supersonic Lift and Pitching Moment of Thin Sweptback Tapered Wings Produced by Constant Vertical Acceleration, Subsonic Leading Edges and Supersonic Trailing Edges," NACA TN 2315, 1951.
37. Garner, H. C., "Multhopp's Subsonic Lifting-Surface Theory of Wings in Slow Pitching Oscillations," R&M No. 2885, Aer. Res. Council, Great Britain, 1952.
38. Woodgate, L., "Measurements of the Oscillatory Pitching Moment Derivatives on a Delta Wing with Rounded Leading Edges in Incompressible Flow," R&M No. 3628, Part 1, Aer. Res. Council, Great Britain, 1968.
39. Earnshaw, P. B. and Lawford, J. A., "Low-Speed Wind Tunnel Experiments on a Series of Sharp-Edged Delta Wings," RAE Tech. Note Aero 2780, Aer. Res. Council, Great Britain, Aug. 1961.
40. Wendtz, W. H., Jr. and McMahon, M. C., "An Experimental Investigation of the Flow Fields About Delta and Double-Delta Wings at Low Speeds," NASA Cr-521, 1967.
41. Reding, J. P. and Ericsson, L. E., "Unsteady Aerodynamic Flow Field Analysis of the Space Shuttle Configuration Part II: Launch Vehicle Aeroelastic Analysis," NASA CR 144,333, April 1976.
42. Reding, J. P. and Ericsson, L. E., "Effects of Flow Separation on Shuttle Longitudinal Dynamics and Aeroelastic Stability," J. Spacecraft and Rockets, Vol. 14, No. 12, Dec. 1977, pp. 711-718.
43. Reding, J. P. and Ericsson, L. E., "Review of Delta Wing Shuttle Vehicle Dynamics," Vol. III, Proceedings Space Shuttle Aerothermodynamics Conference, NASA/Ames Research Center, Moffett Field, Calif., Dec. 15-16. NASA TM-X-2508, pp. 861-931.
44. Allen, E. C., "An Investigation to Verify the Static Scability and Control Characteristics of the 0.004 Scale Model (74-0) of the Shuttle 5 Orbiter (OA108)," NASA CR 141,537, June 1975.
45. Garner, H. C. and Bryer, D. W., "Experimental Study of Surface Flow and Part-Span Vortex Layers on a Cropped Arrowhead Wing," R&M No. 3107, Aer. Res. Council, Great Britain, 1957.
46. Boyden, R. P. and Freeman, D. C., "Subsonic and Transonic Dynamic Stability Derivatives of a Modified 089B Shuttle Orbiter," NASA TM X-72631, DMS-OR-2107, Dec. 1974.
47. Ericsson, L. E., "Separated Flow Effects on the Static and Dynamic Stability of Blunt-Nosed Cylinder-Flare Bodies," NASA CR 76,919, Dec. 1965.
48. Ericsson, L. E., "Unsteady Aerodynamics of Separating and Reattaching Flow on Bodies of Revolution," Recent Research on Unsteady Boundary Layers, Vol. 1, IUTAM Symposium, Laval University, Quebec, May 1971, pp. 481-512.
49. Ericsson, L. E. and Reding, J. P., "Unsteady Aerodynamic Flow Field Analysis of the Space Shuttle Configuration, Part I, Orbiter Aerodynamics," NASA CR 144,332, April 1976.
50. Sparks, V. H. and Moser, M. M., Jr., "Wind Tunnel Tests of an 0.015 Scale Configuration 140 A/B Space Shuttle Orbiter Model (67-0) in the NASA LRC 8-Foot TPT to Obtain Transonic Aerodynamic Force Data (OA-106)" NASA CR 134,426, June 1975.
51. Ericsson, L. E. and Reding, J. P., "Scaling Problems in Dynamic Tests of Aircraft Like Configurations," AGARD Symposium on Unsteady Aerodynamics, Ottawa, Canada, Sept. 26-28, 1977.
52. Ericsson, L. E. and Reding, J. P., "Reynolds Number Criticality in Dynamic Tests," AIAA Paper No. 78-166, Jan. 1978.

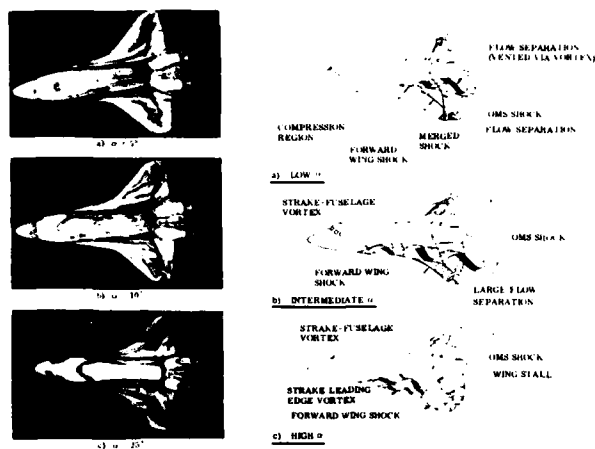
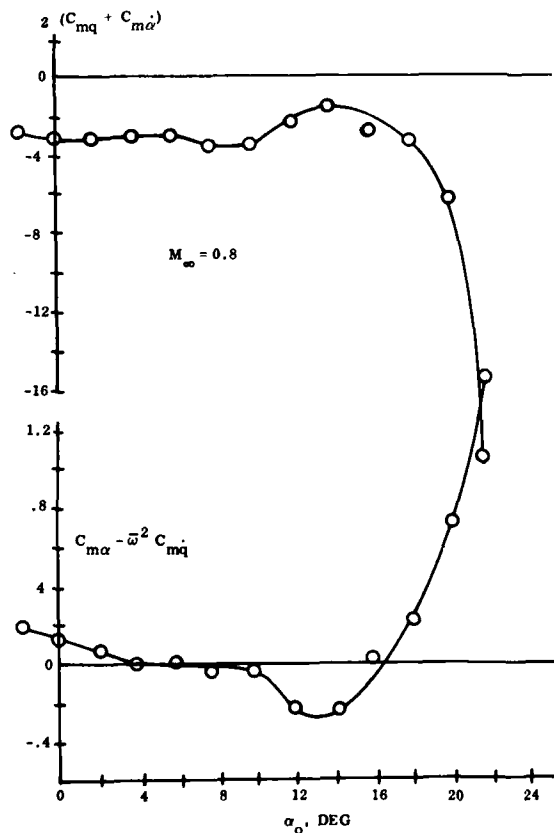
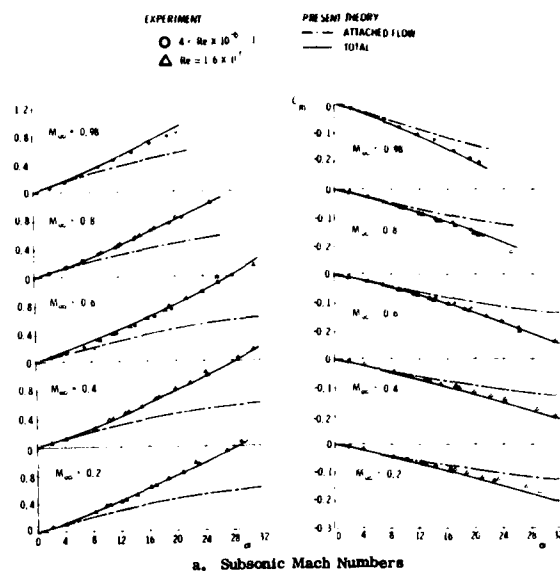
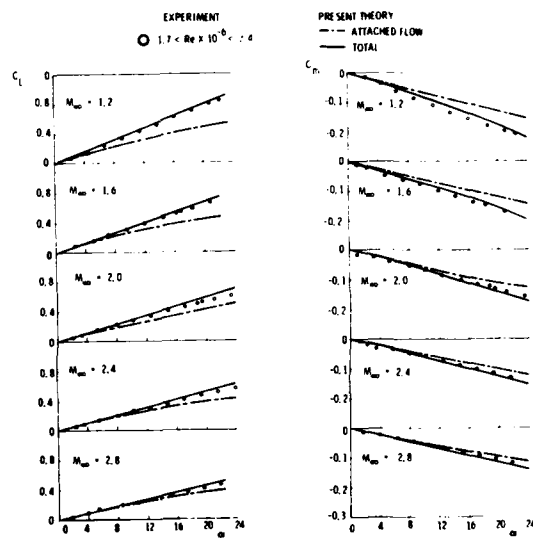


Fig. 1 Flow Pictures of the Space Shuttle Orbiter

Fig. 2 Dynamic Orbiter Characteristics at $M_\infty = 0.8$ 

a. Subsonic Mach Numbers



b. Supersonic Mach Numbers

Fig. 3 Static Aerodynamic Characteristics of an A = 1.15 Sharp-Edged Delta Wing

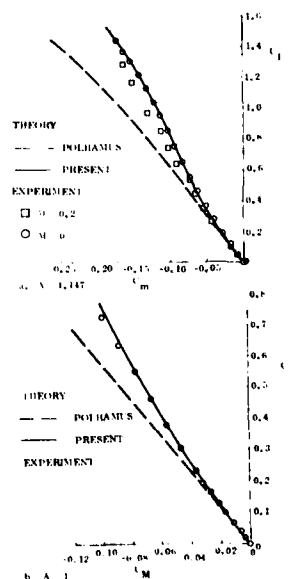


Fig. 4 Static Stability Characteristics of Sharp-Edged Delta Wings

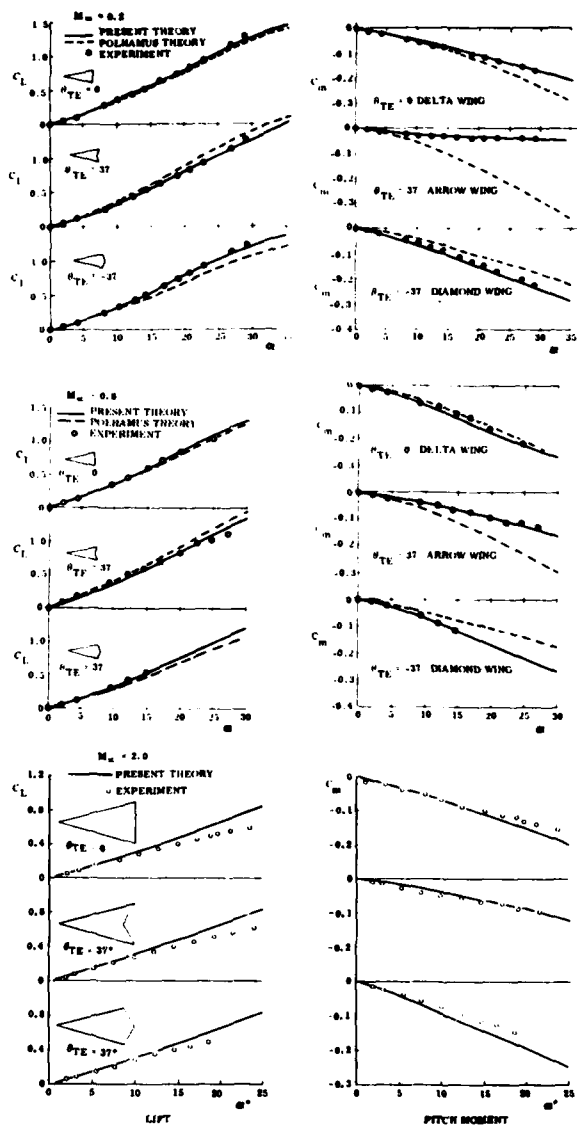


Fig. 5 Effect of Trailing Edge Sweep on Static Slender Wing Characteristics

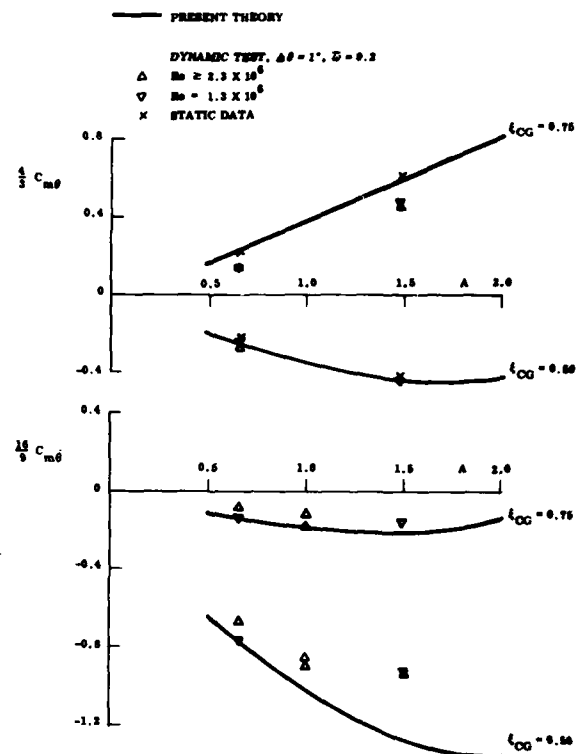


Fig. 6 Dynamic Delta Wing Characteristics at $M_\infty = 0$ and $\alpha = 0$.

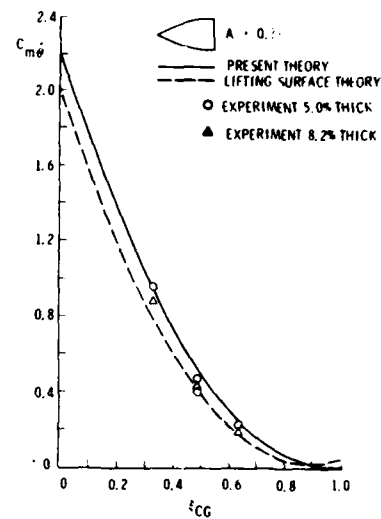


Fig. 7 Pitch Damping of an $A = 0.75$ Gothic Wing at $M_\infty = 0$ and $\alpha = 0$

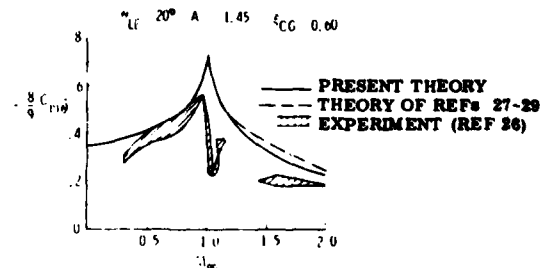


Fig. 8 Pitch Damping of an $A = 1.45$ Delta Wing at $\alpha = 0$ as a Function of Mach Number

$\theta_{LE} = 26.6^\circ$; $A = 2$
 — PRESENT THEORY
 - - - THEORY OF (REF 30)
 EXPERIMENT $Re > 1.7 \times 10^6$ (REF 30)
 Δ EXPERIMENT $Re > 6 \times 10^6$ (REF 31)

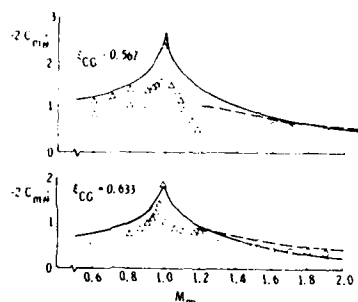
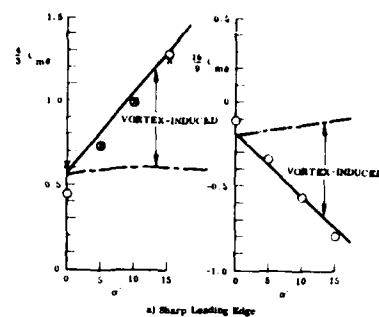


Fig. 9 Pitch Damping of an $A = 2$ Delta Wing at $\alpha = 0$ as a Function of Mach Number



— ATTACHED FLOW
 — TOTAL
 — EXPERIMENT $l_{CG} = 0.75$
 O DYNAMIC TEST, $\Delta\theta = 1^\circ$, $\omega = 0$
 X STATIC TEST

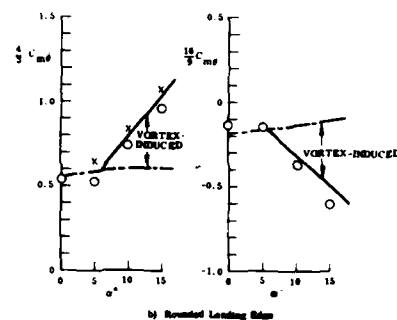


Fig. 11 Dynamic Characteristics of an $A = 1.484$ Delta Wing at $M = 0$ as a Function of Angle of Attack

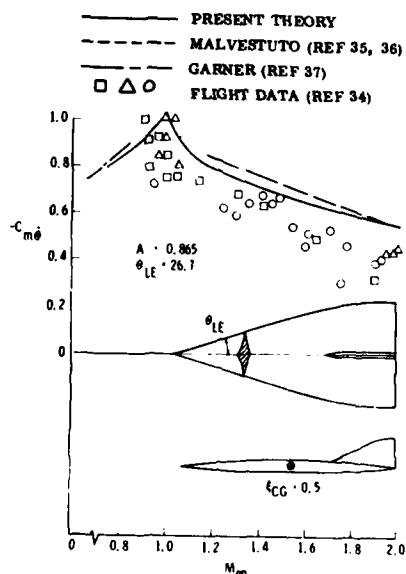


Fig. 10 Pitch Damping of an $A = 0.865$ Gothic Wing at $\alpha = 0$ as a Function of Mach Number

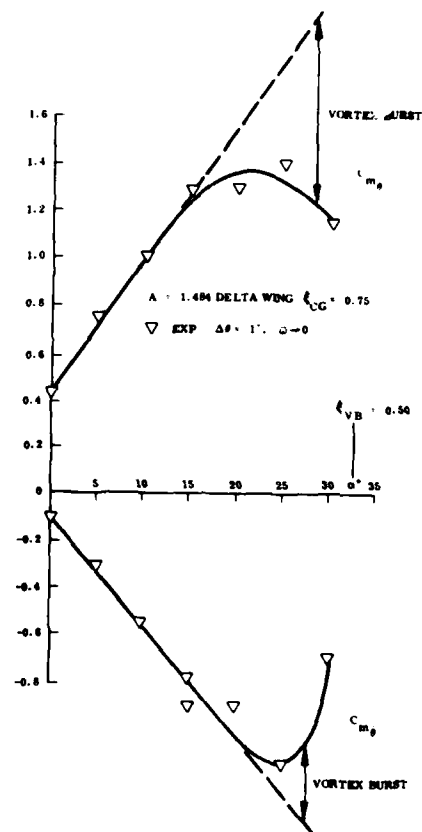


Fig. 12 Effect of Vortex Burst on Delta Wing Static Aerodynamic Characteristics (Ref. 19)

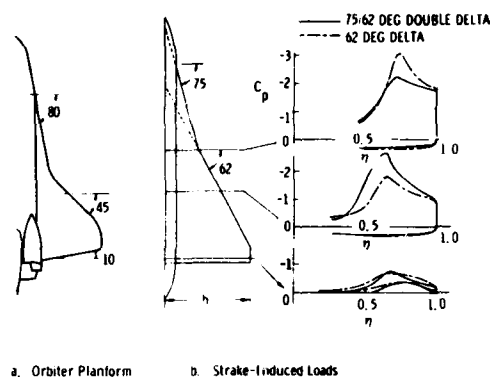


Fig. 13 Double-Delta Planforms

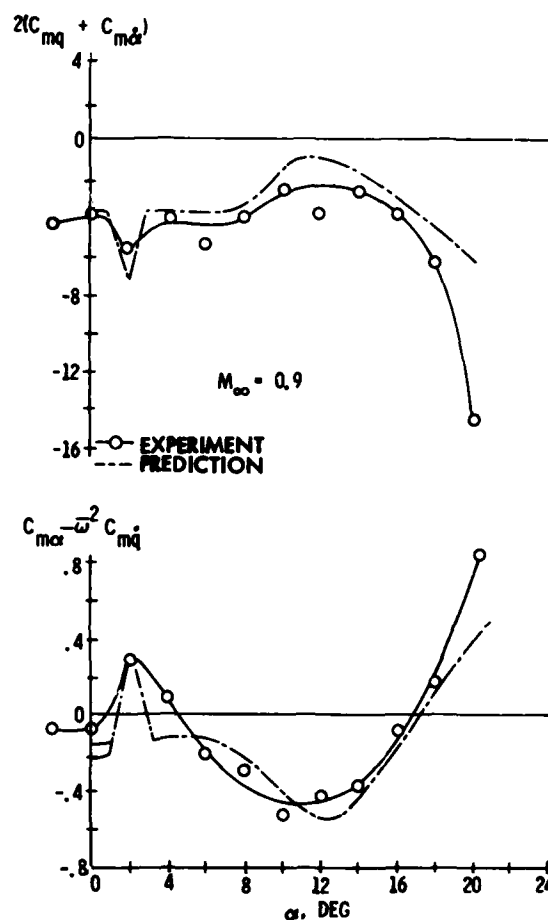
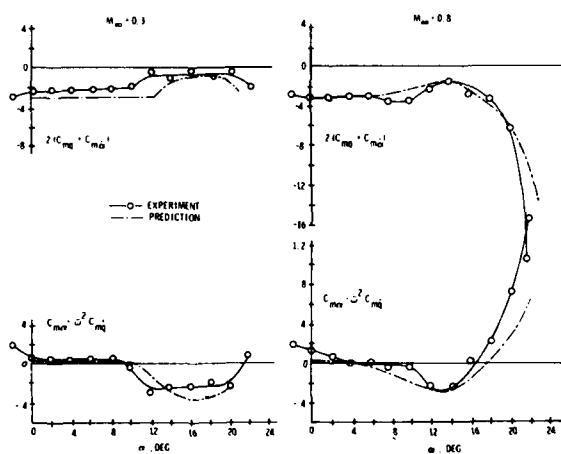
Fig. 15 Predicted and Measured Orbiter Dynamics at $M_\infty = 0.9$ 

Fig. 14 Predicted and Measured Orbiter Dynamics at Subsonic Mach Numbers

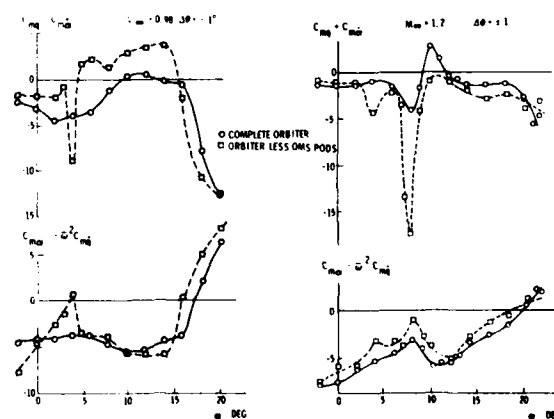


Fig. 16 Effect of OMS Pods on Orbiter Dynamics at Transonic Mach Numbers (Ref. 30)

OSCILLATORY AERODYNAMICS AND STABILITY DERIVATIVES FOR AIRFOIL SPOILER MOTIONS

by

R. Bernier
Graduate Student
California Institute
of Technology

and

G.V. Parkinson
Professor
Department of Mechanical
Engineering
University of British Columbia

SUMMARY

Using an extension of a previously developed linearized incompressible potential-flow theory, the lift, pitching moment, and spoiler hinge moment for a thin airfoil section with an upper-surface spoiler oscillating about a mean erection angle are calculated. Using integral transforms, the transient lift and moment following spoiler erection are calculated from the oscillatory results. Either the oscillatory or the transient loadings can be related to the conventional stability derivatives for spoiler displacement and rate. The oscillatory loadings produce frequency-dependent functions for the stability derivatives, while the transient loadings lead to a conventional constant displacement derivative, but a time-dependent function for the rate derivative.

NOTATION

z	linearized physical plane (steady flow)	$\mu = \frac{\omega h}{U}$	reduced frequency
z'	linearized physical plane (unsteady flow)	$\hat{t} = \frac{Ut}{c}$	dimensionless time
\mathcal{J}	transform plane	$\hat{T} = \frac{UT}{c}$	dimensionless erection time
c	airfoil chord	p_c	cavity pressure
s	spoiler distance from airfoil leading edge	p	free stream pressure
h	spoiler height	C_L	lift coefficient
U	free stream velocity	C_M	pitching moment coefficient
ω	circular frequency	C_H	spoiler hinge moment coefficient
δ	spoiler angle	$()_s$	quasi-steady, or steady-state
t	time	$()_\delta$	displacement derivative
T	spoiler erection time	$()_{\dot{\delta}}$	rate derivative

1. INTRODUCTION

Although wing upper-surface spoilers are being increasingly used for aircraft roll and flight path control, their partially separated flow fields create difficult problems for theoretical analysis, particularly in the unsteady flow situations of flutter and dynamic stability calculations. Theoretical and experimental research on the aerodynamics of spoilers has been conducted in the Department of Mechanical Engineering at the University of British Columbia in recent years, and earlier results of the program were reported at previous AGARD Conferences (1,2).

In the work reported here, the linearized theory described in Ref. 1 is extended and applied to the problem of calculating aerodynamic loadings caused by spoiler motions. Further details are given in Ref. 3.

2. THEORY

The theory is applied to a thin airfoil of arbitrary profile with an upper surface spoiler of arbitrary position and height. The flow is two dimensional, incompressible, and irrotational, and the complex acceleration potential is used as the flow variable. The separated wake bounded by streamlines from the spoiler tip and airfoil trailing edge is treated as a semi-infinite cavity at free-stream pressure. (In the linearized theory for the steady-state aerodynamics, described in Ref. 1 and given in detail in Ref. 4, the constant cavity pressure is empirically given and the cavity is of finite length, but the simpler assumption is believed to be adequate for the time-dependent theory).

Because the linearized theory permits the superposition of effects of airfoil incidence, camber, and thickness on those caused by the spoiler, only the configuration of Fig. 1 needs to be considered here, since the paper deals only with the effects of

spoiler motion. The other effects are given by the methods of Ref. 4. Fig. 2 shows the sequence of conformal transformations used in the steady-state aerodynamics, with an arbitrary cavity pressure. In the present problem, since cavity length l is infinite, the linearized physical z - plane is identical with the z' - plane, and one transformation is eliminated. The linearized airfoil and cavity boundary is a slit along the positive real axis in the physical z' - plane. This slit is transformed so that the airfoil and spoiler wetted surface become the upper half unit circle in a ζ - plane, while the upper and lower cavity boundaries become the positive and negative real axes in the ζ - plane, outside the unit circle. The flow field is the upper half ζ - plane, and the boundary conditions of uniform flow at infinity, tangent flow on the airfoil and spoiler wetted surfaces, constant pressure on the cavity boundary, and Kutta conditions at spoiler tip and airfoil trailing edge are expressed conventionally in terms of the complex acceleration potential.

3. APPLICATIONS

3.1 Oscillating Spoiler

The first problem considered is the oscillation of the spoiler about a mean erection angle. The complex acceleration potential is found in the ζ - plane in terms of elementary functions plus a Laurent series, and the unknown coefficients are evaluated from the boundary conditions. The airfoil lift and pitching moment are integrated analytically, and the spoiler hinge moment numerically from the calculated pressure distribution. Fig. 3 shows examples of the usual phase plane plots of the lift and pitching moment vectors, normalized by their quasi-steady values, as functions of reduced frequency based on spoiler height h . Fig. 4 shows corresponding results for spoiler hinge moment.

3.2 Spoiler Erection

The second problem considered is the transient aerodynamic loading following spoiler actuation. Both unit-step and constant-rate actuations are treated. The method is to use Fourier integral transforms of the above oscillatory solutions to give the unit-step solutions, and to use Duhamel integrals of the unit-step solutions to give the constant-rate solutions. Results for the unit-step case are shown in Fig. 5, and for the constant-rate case in Fig. 6, in the form of transient lift and pitching-moment coefficients normalized by their asymptotic steady-state values.

3.3 Stability Derivatives

Finally, the calculation of stability derivatives is of interest. For the spoiler erection problem, pertinent derivatives are of lift and moment with respect to spoiler angle and actuation rate, and they can be extracted from the transient solution for constant-rate actuation just considered, which had been obtained using Duhamel's integral. This is easily reworked into a differential form whose partial derivatives are formally identical to the above stability derivatives. The results, normalized by the values of the displacement derivatives, are shown in Fig. 7 for a typical case. It can be seen that the rate derivatives are not constant, in contrast to the usual assumption of stability derivative theory. This anomaly has been discussed by Etkin (5), and the asymptotic value (zero in the present case) should be used if a constant value is required. Any use of the asymptotic value would, however, be inaccurate for small time.

For the oscillating spoiler problem, pertinent stability derivatives include those of spoiler hinge moment with respect to angular displacement and rate. As Etkin (5), and Rodden and Giesing (6), have noted, such derivatives can be extracted from the solution of the appropriate oscillatory aerodynamic problem. However, derivatives obtained in this way are frequency-dependent. Here, the appropriate solutions are those of Fig. 4, and for one of the cases the displacement and rate derivatives are calculated and plotted as functions of reduced frequency on Fig. 8. The curves are normalized by the zero-frequency (quasi-steady) value of the displacement derivative.

4. DISCUSSION

It would be desirable to conduct wind tunnel tests to investigate the validity of the theoretical results presented here. The actual flow would have a separation bubble at the upstream base of the spoiler, and would not have constant free-stream base pressure as assumed in the model. However, some experiments conducted in the second author's laboratory on the transient lift following constant-rate spoiler actuation, and reported in Ref. 1, give encouragement that the theory does lead to quite accurate predictions of unsteady aerodynamic loadings.

The next step in the theoretical studies is to extend them to configurations of finite aspect ratio. This has already been done for the steady-state aerodynamics of spoilers, using a lifting-line theory for configurations of relatively high aspect ratio, and the results, reported in Ref. 2, were in good agreement with experimental values for wing lift and rolling moment.

The oscillatory results were presented in terms of reduced frequency M based on spoiler height h instead of airfoil chord c . This is a more reasonable parameter, since only the spoiler was oscillating. In Fig. 8 it is interesting to note that the rate

derivative C_H is nearly constant for $\mu > 0.1$, and that the displacement derivative $C_{H\delta}$ is nearly constant for $\mu < 1$. Also, the small-disturbance theory could scarcely be considered applicable for $\mu > 1$. Thus, in the range $0.1 < \mu < 1$, which would be of practical interest for application of the theory, both derivatives are approximately constant, as the conventional formulation of stability derivatives assumes.

REFERENCES

1. Parkinson, G.V., Brown, G.P., and Jandali, T.; 'The Aerodynamics of Two-Dimensional Airfoils with Spoilers', Proc. AGARD Conf. on V/STOL Aerodynamics, Delft, April, 1974, pp. 14-1 to 14-10.
2. Parkinson, G.V., and Tam Doo, P.; 'Prediction of Aerodynamic Effects of Spoilers on Wings', Proc. AGARD Conf. on Prediction of Aerodynamic Loading, NASA Ames, Sept., 1976, pp. 4-1 to 4-9.
3. Bernier, R., 'Steady and Transient Aerodynamics of Spoilers on Airfoils', M.A.Sc. Thesis, U.B.C., August, 1977.
4. Brown, G.P., and Parkinson, G.V.; 'A Linearized Potential Flow Theory for Airfoils with Spoilers', Jour. Fluid Mech., 57, 1973, pp. 695-719.
5. Etkin, B.; 'Dynamics of Atmospheric Flight', Wiley, 1972, pp. 276-283.
6. Rodden, W.P., and Giesing, J.P.; 'Application of Oscillatory Aerodynamic Theory to Estimation of Dynamic Stability Derivatives', Jour. Aircraft, 7, 3, May-June, 1970, pp. 272-275.

ACKNOWLEDGEMENTS

The research reported here was supported by Grant A586 of the National Research Council of Canada. Some of the calculations, and an improvement in the calculation methods were contributed by Dr. Peter Tam Doo.

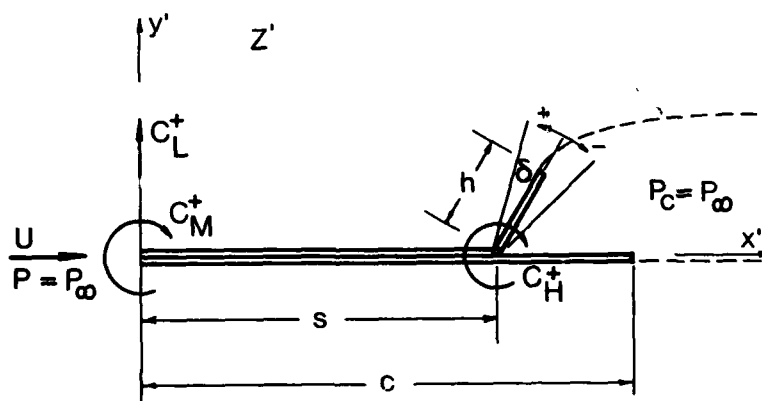


Fig. 1. Configuration for Moving Spoiler Problems.

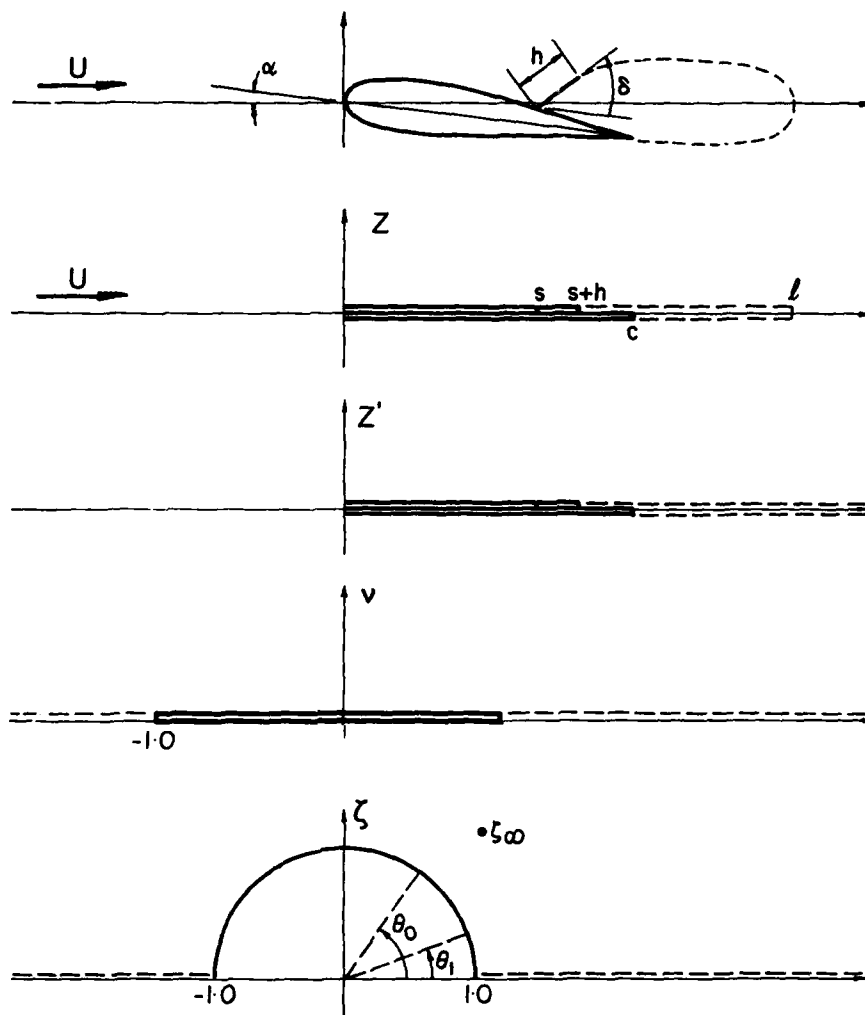


Fig. 2. Conformal Transformations for Spoiler Problems.

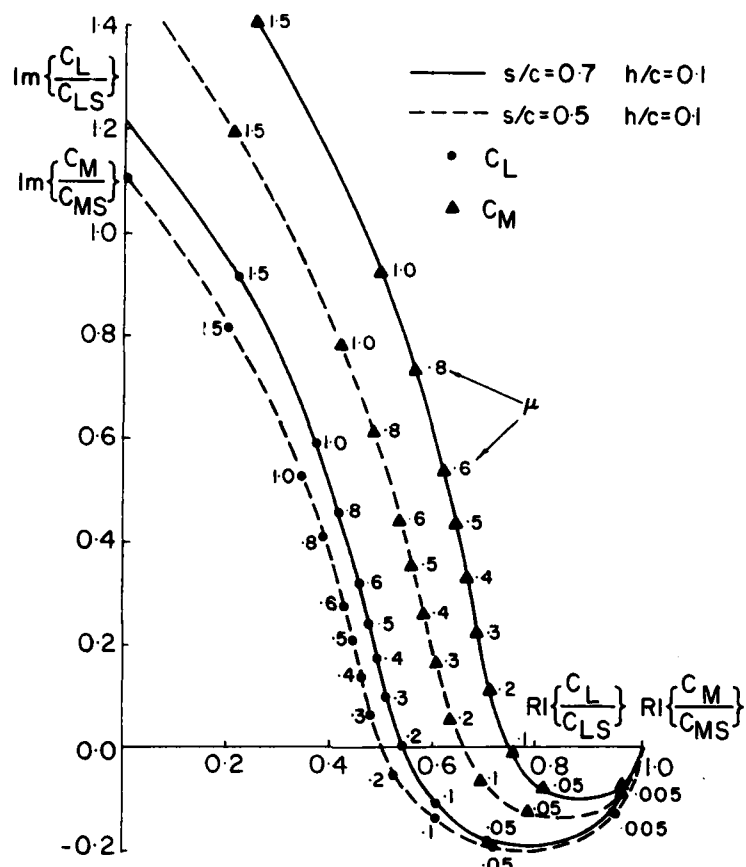


Fig.3. Lift and Pitching Moment on Airfoil with Oscillating Spoiler.

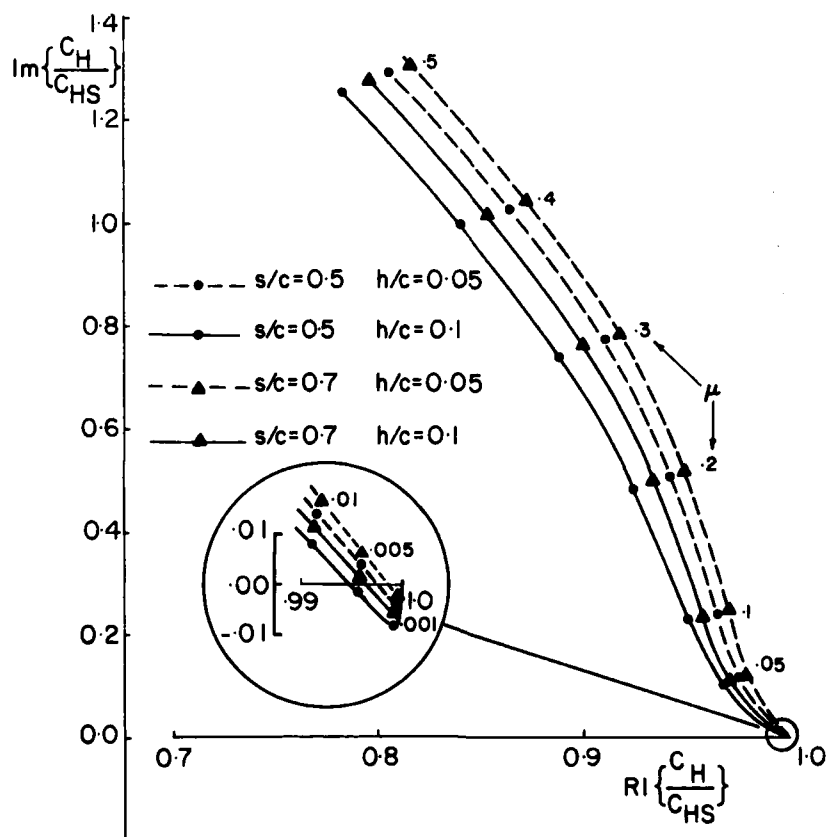


Fig.4. Hinge Moment on Oscillating Spoiler.

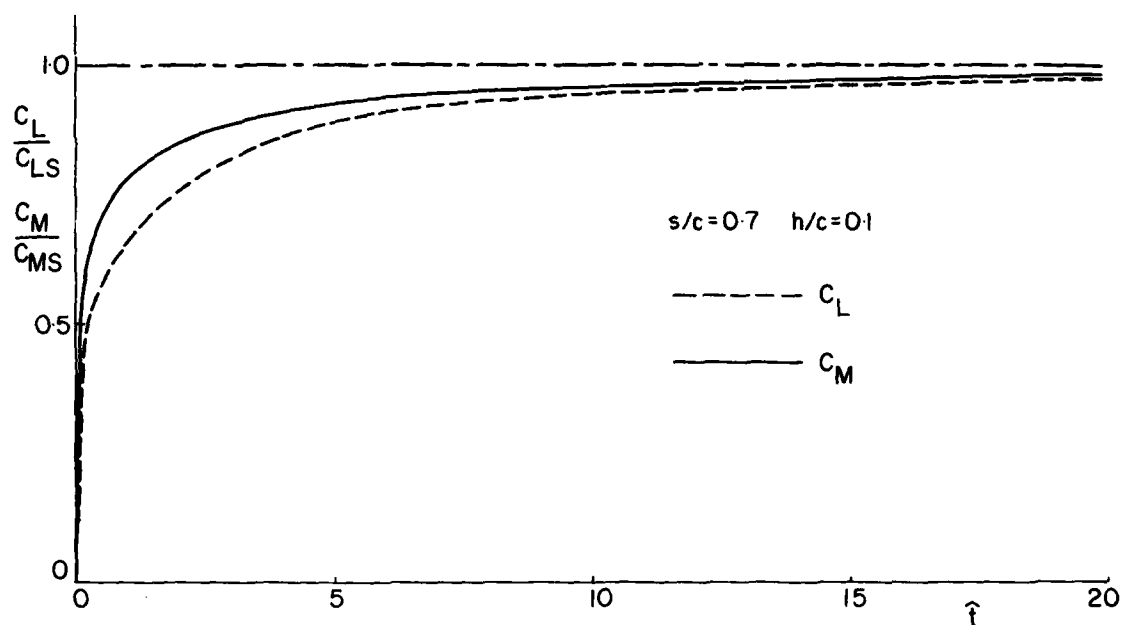


Fig.5. Lift and Pitching Moment on Airfoil after Unit-Step Erection.

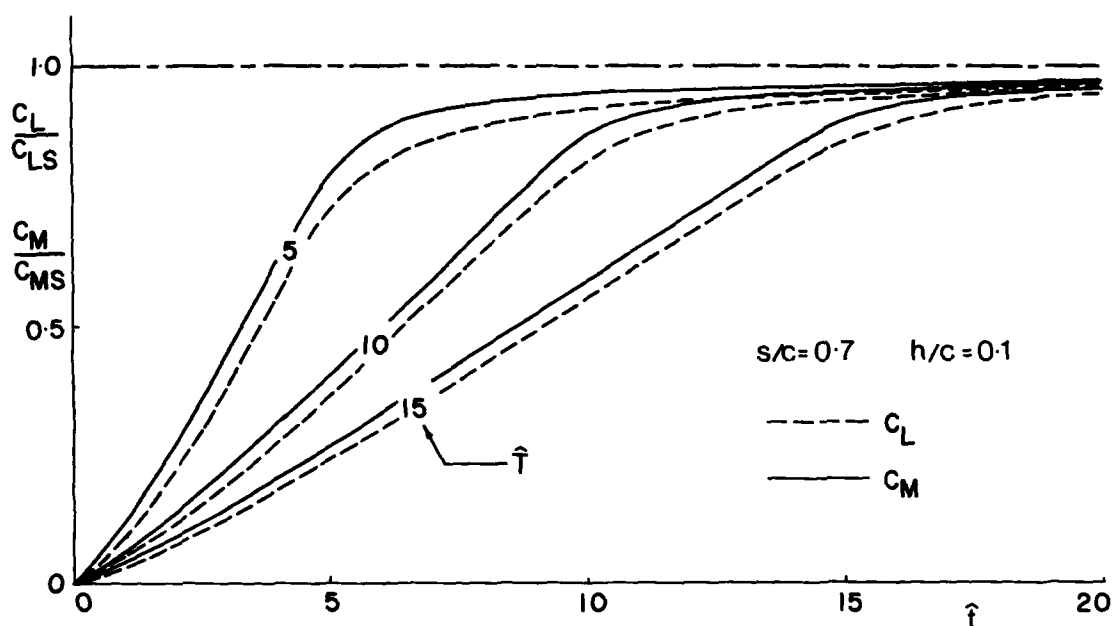


Fig.6. Lift and Pitching Moment on Airfoil with Constant-Rate Erection.

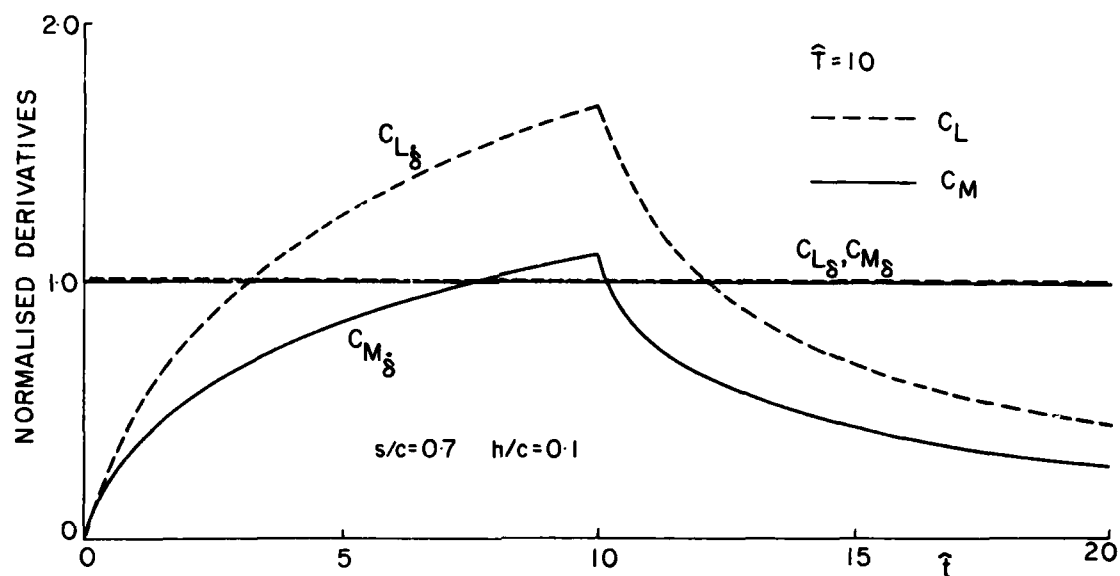


Fig.7. Stability Derivatives for Airfoil with Constant-Rate Erection.

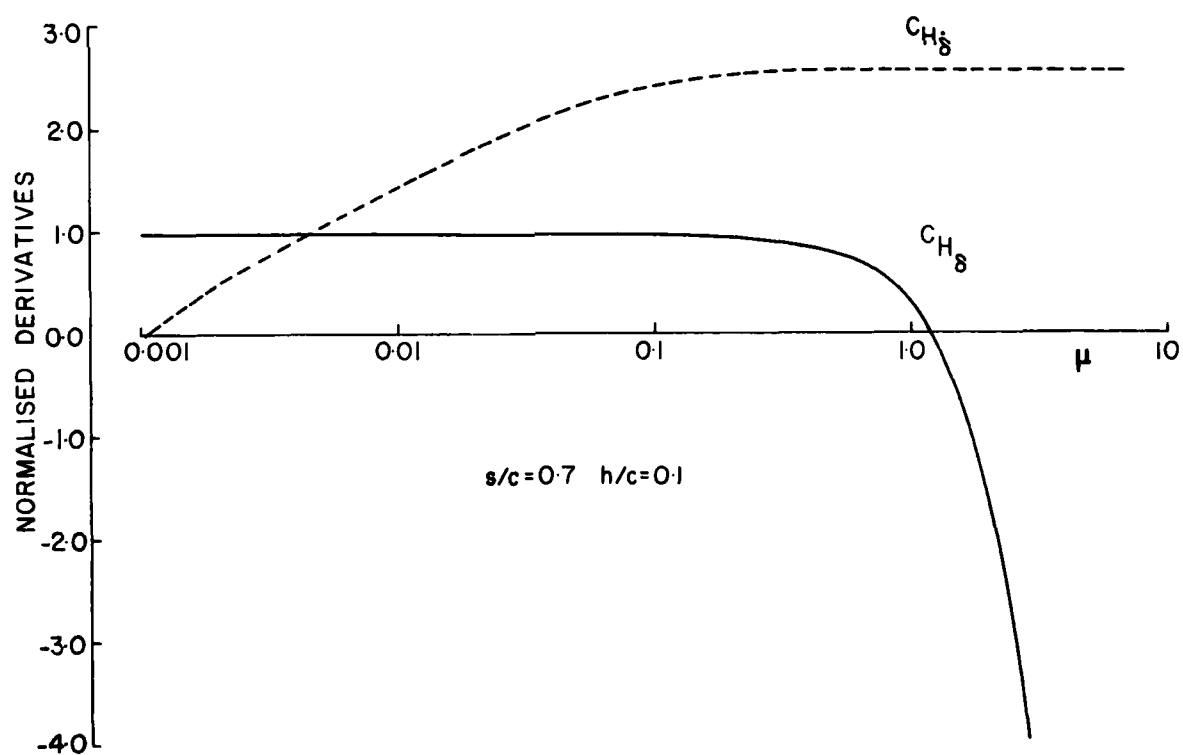


Fig.8. Stability Derivatives for Oscillating Spoiler.

THE ROLE OF TIME-HISTORY EFFECTS IN THE FORMULATION OF THE AERODYNAMICS OF AIRCRAFT DYNAMICS

Murray Tobak* and Lewis B. Schiff**
Ames Research Center, NASA, Moffett Field, California 94035, U.S.A.

SUMMARY

The scope of any aerodynamic formulation proposing to embrace a range of possible maneuvers is shown to be determined principally by the extent to which the aerodynamic indicial response is allowed to depend on the past motion. Starting from the linearized formulation, in which the indicial response is independent of the past motion, two successively more comprehensive statements about the dependence on the past motion are assigned to the indicial response (1) dependence only on the recent past and (2) dependence additionally on a characteristic feature of the distant past. The first enables the rational introduction of nonlinear effects and accommodates a description of the rate-dependent aerodynamic phenomena characteristic of airfoils in low-speed dynamic stall; the second permits a description of the double-valued aerodynamic behavior characteristic of certain kinds of aircraft stall. An aerodynamic formulation based on the second statement, automatically embracing the first, may be sufficiently comprehensive to include a large part of the aircraft's possible maneuvers. The results suggest a favorable conclusion regarding the role of dynamic stability experiments in flight dynamics studies.

LIST OF SYMBOLS

C_m	pitching-moment coefficient, $\frac{\text{pitching moment}}{qSz}$
$G[\sigma(\xi)]$	functional notation: value at $\xi = t$ of a time-dependent function which depends on all values taken by the argument function $\sigma(\xi)$ over the time interval $0 < \xi < t$
I	moment of inertia about the pitching axis
l	reference length
q	dynamic pressure, $\frac{1}{2} \rho V^2$
S	reference area
t	time
V	magnitude of flight velocity vector
σ	angle of attack, Fig. 1
ρ	atmospheric density
ω	frequency of harmonic oscillatory motion

1. INTRODUCTION

One of the difficult problems in aircraft flight dynamics is that of formulating an aerodynamic force and moment system with sufficient scope to cover the wide range of maneuvers typical of modern aircraft (Refs. 1,2). What is the nature of the problem?

Consider the questions that arise in the prediction of a maneuver from a known initial state. Let an essentially rigid aircraft with known inertial properties undergo an arbitrary motion. At a certain time t_0 , allow a measurement of the aircraft's state (i.e., its linear and angular velocity components) and its aerodynamic response (i.e., the aerodynamic force and moment). Given this information at t_0 , what is needed to predict the aircraft's motion over the succeeding increment of time? The ability to carry the motion forward over the first increment of time implies, of course, the ability to predict the entire subsequent motion. What is needed principally is a form for the incremental changes in the aerodynamic force and moment, that is, the indicial response, over the increment of time. Assigning an adequate form constitutes the problem of formulation. The difficulty of the problem arises in assigning a form that applies not only to the motion under study, but to all of the other motions of which the aircraft is capable, and which might have occurred prior to t_0 . This way of describing the difficulty allows one to appreciate the great virtue of a linearized version of the aerodynamic indicial response. Invoking linearity supposes that the aerodynamic indicial response is independent of anything that happened prior to the origin of the response. Thus, the calculation can be carried forward without any acknowledgment whatever of the motion prior to t_0 . Although there are flow regimes where use of the linearized formulation can be justified (e.g., attached flows with small perturbations), these regimes do not embrace the whole range of flows that a modern aircraft may experience. A formulation applicable to the remaining regimes must be freed of the limitation imposed by linearization. This means, of course, that the aerodynamic indicial response must be allowed to depend on the past motion.

In a series of papers (cf. Ref. 3 for a connected account), the authors have tried to show how concepts from functional analysis could be used to construct a mathematical framework allowing a general

*Research Scientist, Entry Technology Branch

**Research Scientist, Computational Fluid Dynamics Branch

dependence of the aerodynamic indicial response on the past motion. Having a rigorous framework has enabled the introduction of rational approximations which, in effect, limit the dependence on the past motion to some definite property, applicable to an appropriate class of flows. One can argue in favor of limited statements about the dependence on the past motion as follows: Since the linearized formulation has found application to a certain class of flows, a formulation based on a limited statement, which includes the linearized formulation as a special case, must find application to a wider class of flows. A sequence of successively more comprehensive statements, each embracing all of the preceding ones, must eventually reach a stage where the resulting formulation is applicable to a sufficiently wide class of flows to accommodate a description of all of the motions of interest. It remains to discover whether this stage can be reached well short of having to account for the whole past motion in detail for any of the motions of interest.

Thus, the role assigned to time-history effects, that is, the statement about the dependence on the past motion, constitutes a determining criterion by which the merits and shortcomings of any aerodynamic formulation may be judged. The purpose of this report is to investigate how far the first few statements go toward fulfilling the goal of a sufficiently comprehensive statement. Starting from the linearized formulation, in which the indicial response is independent of the past motion, two successively more comprehensive statements about the dependence on the past motion are assigned to the indicial response (1) dependence only on the recent past and (2) dependence additionally on a characteristic feature of the distant past. The successive statements allow the effects of successively larger bodies of aerodynamic phenomena to be acknowledged within the scopes of the resulting formulations. The first enables the rational introduction of nonlinear effects and accommodates a description of the rate-dependent aerodynamic phenomena characteristic of airfoils in low-speed dynamic stall; the second permits a description of the double-valued aerodynamic behavior characteristic of certain kinds of aircraft stall. It is suggested that an aerodynamic formulation based on the second statement, automatically including the first, may be of sufficient scope to embrace a large part of the aircraft's possible maneuvers. Implications of the results with regard to dynamic stability experiments are discussed.

2. DEFINITION OF MANEUVER

To focus directly on the question of time-history effects, it is advisable to avoid the complications introduced by coordinate systems and motions with multiple degrees of freedom. In all of the study to follow, the aircraft's maneuver is restricted to be planar with only a single degree of freedom. Extension to more general motions will be straightforward, paralleling that described in Ref. 3.

Let the aircraft be in level steady flight prior to time zero. At time zero let it begin an arbitrary pitching maneuver during which the center of gravity continues to follow a rectilinear path at constant velocity V . Hence flight-path properties such as dynamic pressure, Mach number, and Reynolds number remain constant throughout the maneuver. The pitching maneuver is defined by the angle of attack α (Fig. 1), the angle between the aircraft's longitudinal axis and the velocity vector. The motion, of course, may be specified to reproduce that of a wind-tunnel model in an oscillations-in-pitch experiment.

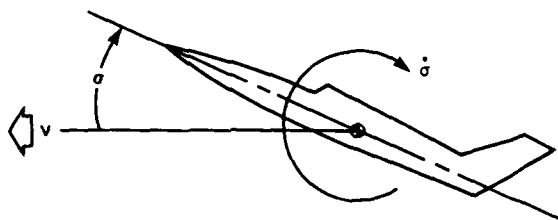
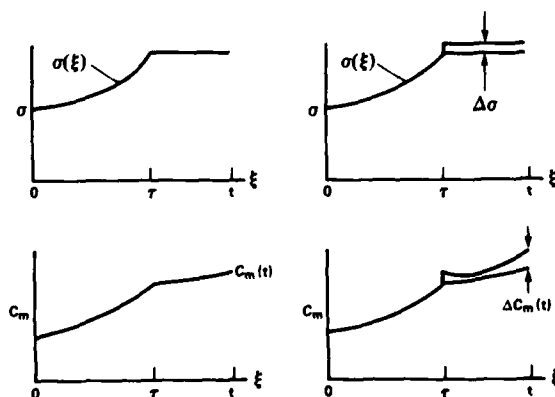


Fig. 1. Single-degree-of-freedom pitching maneuver.

Thus, focusing on this motion will facilitate a later discussion of the implications of the results with regard to wind-tunnel experiments.

3. FORMATION OF INDICIAL PITCHING-MOMENT RESPONSE AND INTEGRAL FORMS



Since it will be necessary in later sections to consider the influence of random fluctuations, the formation of the indicial pitching-moment response will be described in a way that acknowledges their presence. Two motions have to be considered (cf. Fig. 2). First, beginning at $\xi = 0$, the aircraft is made to undergo the motion under study $\alpha(\xi)$. At a certain time τ the motion is constrained so that the value of α at time τ , that is, $\alpha(\tau)$, remains constant thereafter. The pitching moment corresponding to this motion is measured at a time t . Now if $\alpha(\tau)$

Fig. 2. Formation of indicial response.

is sufficiently large so that, for example, flow separation occurs in the course of a maneuver, then as a result of the ensuing fluctuations in the flow, any single measurement of the pitching moment at time t will include a random component. This circumstance calls for repeating the maneuver and the corresponding measurement at time t many times and taking the arithmetic mean of the measurements. If the fluctuating part of the response is truly random, its contribution to the measurement at time t should cancel in the mean, and the resulting mean value should be representative of the deterministic part of the response. It will be assumed that this is true for any time t , and that as a result, a deterministic part of the response will exist that is continuous for all ξ in the interval $0 \leq \xi \leq t$. Second, the aircraft is made to execute precisely the same motion, beginning at $\xi = 0$ and constrained in the same way at $\xi = \tau$, except that at the latter time, σ is given an incremental step $\Delta\sigma$ over its value at $\xi = \tau$. Hence, for all time subsequent to τ , σ is equal to $\sigma(\tau) + \Delta\sigma$. The pitching moment corresponding to this motion is again measured at time t . Just as before, the second maneuver and the corresponding measurement at time t must be repeated many times, and the arithmetic mean of the measurements taken to be the deterministic part of the response. The difference between mean values for the two measurements, $\Delta C_m(t)$, is divided by the incremental step $\Delta\sigma$. The limit of this ratio (if it exists) as the magnitude of the step approaches zero is called the indicial pitching-moment response at time t per unit step change in σ at time τ . Since the two maneuvers prior to $\xi = \tau$ are identical (in the mean), the ratio must be identically zero for $0 \leq \xi < \tau$. At $\xi = \tau$ a discontinuity in the ratio is permissible, reflecting the discontinuous change in σ . For all $\xi > \tau$ the ratio is assumed to be continuous. With the understanding that the pitching-moment response to each maneuver and at each time t is the result of an ensemble average of measurements, the indicial pitching-moment response is defined as:

$$\lim_{\Delta\sigma \rightarrow 0} \frac{\Delta C_m(t)}{\Delta\sigma} = C_{m_\sigma}[\sigma(\xi); t, \tau] \quad (1)$$

As the functional notation indicates, the indicial response is allowed to depend in an unspecified way on the entire history of the motion $\sigma(\xi)$.

When the assumptions leading to the definition of a deterministic indicial response can be said to hold within each increment of the stepwise representation of an arbitrary motion $\sigma(t)$, the pitching-moment response $C_m(t)$ to the motion $\sigma(t)$ follows from a summation of incremental responses over the time interval 0 to t :

$$C_m(t) = C_m(0) + \int_0^t C_{m_\sigma}[\sigma(\xi); t, \tau] \frac{d\sigma}{d\tau} d\tau \quad (2)$$

This is the general integral form for $C_m(t)$ corresponding to an arbitrary motion $\sigma(t)$. The form is essentially exact, but its further use without approximation is exceedingly difficult. The nature of the difficulty becomes clear if one writes the equation of motion for the single-degree-of-freedom pitching motion $\sigma(t)$, and asks for a solution of $\sigma(t)$ for specified initial conditions. The equation of motion is:

$$\ddot{\sigma}(t) = \left(\frac{gSz}{I} \right) \left\{ C_m(0) + \int_0^t C_{m_\sigma}[\sigma(\xi); t, \tau] \frac{d\sigma}{d\tau} d\tau \right\} \quad (3)$$

Since the indicial response within the integral is a functional, dependent in general on the whole past motion $\sigma(\xi)$, it is unknown when σ is unknown. Thus, both the indicial response and the motion must be found simultaneously, an awesome prospect. Cases can be envisioned (e.g., massively ablating reentry vehicles) where the mutual dependence between the motion and the indicial response cannot be uncoupled. However, for rigid aircraft of fixed shape, the past success of the linearized formulation lends credence to the belief that the interdependence may be at least partially uncoupled. Now if the indicial response were somehow known, Eq. (3) would become an integro-differential equation of the Volterra type for which solutions can be found by known, albeit numerical, techniques. The indicial response could be considered known, at least in principle, if its dependence on the past motion were specified in a way that allowed it to be an identifiable member of a collection of indicial responses, all of which had been obtained beforehand from, for example, a suitable series of experiments. Thus, Eq. (3) can be made tractable by assigning to the indicial response appropriate statements about how it depends on the past motion which allow it to be determined in advance. Let it be noted, however, that since every statement assigned to the indicial response will multiply the number of responses in the collection required to be known in advance, it becomes imperative to make the least number of statements possible. In succeeding sections, two such statements will be introduced, which it is hoped, may suffice to cover the cases of interest.

Finally, it is recognized that counting on the availability of a collection of indicial responses may be somewhat unrealistic in view of the difficulty of experimentally determining an indicial response. In a later section, however, it will be shown how the results from suitably designed oscillations-in-pitch experiments, which, it may be presumed with greater reason, are technically feasible, may be used in place of the integral in Eq. (3). Thus, for the availability in principle of a collection of indicial responses may be read the availability of an equivalent collection of results from oscillations-in-pitch experiments.

4. DEPENDENCE OF THE INDICIAL RESPONSE ON THE RECENT PAST

First, Eq. (1) for the indicial pitching-moment response will be put in an equivalent form that will suggest a first statement about its dependence on the past motion. If $\sigma(\xi)$ can be considered to be analytic in a neighborhood of $\xi = \tau$ (corresponding to the most recent past for an indicial response with origin at $\xi = \tau$), in principle, its history can be reconstructed from a knowledge of all of the coefficients of its Taylor series expansion about $\xi = \tau$. Then, since $\sigma(\xi)$ is equally represented by the coefficients of its expansion, the functional, with its dependence on $\sigma(\xi)$, can be replaced without approximation by a function with a dependence on all of the coefficients of the expansion of $\sigma(\xi)$ about $\xi = \tau$; that is,

$$C_{m_0}[\sigma(\xi); t, \tau] = C_{m_0}(t - \tau; \sigma(\tau), \dot{\sigma}(\tau), \ddot{\sigma}(\tau), \dots) \quad (4)$$

The additional replacement of a dependence on elapsed time $t - \tau$ rather than on t and τ separately is justified within the specification already invoked of constant flight-path properties.

Now it is argued that a class of flows exists for which disturbances originating at times far removed from the vicinity of $\xi = \tau$ will have died out before they are able to influence events in the vicinity of $\xi = \tau$. In such cases, it can be assumed that the indicial response will have "forgotten" long-past events, and so will depend only on events occurring in the most recent past. Therefore, to the extent that the indicial response can be influenced by the past motion, the form of the past motion just prior to the origin of the step might just as well have existed for all earlier times. Accordingly, only the first few coefficients of the expansion of $\sigma(\xi)$ need be retained to characterize correctly the most recent past, which is all the indicial response is assumed to remember. Retaining the first two coefficients of $\sigma(\xi)$, for example, implies matching the true past history of σ in magnitude and slope at the origin of the step, thereby approximating $\sigma(\xi)$ by a linear function of time $\sigma(\xi) = \sigma(\tau) + \dot{\sigma}(\tau)(\tau - \xi)$. With an approximation of this order in force in Eq. (1), the integral form replacing Eq. (2) and the right-hand side of Eq. (3) becomes

$$C_m(t) = C_m(0) + \int_0^t C_{m_0}(t - \tau; \sigma(\tau), \dot{\sigma}(\tau)) \frac{d\sigma}{d\tau} d\tau \quad (5)$$

The steady-state value of the indicial response can be put in evidence with the additional (consistent) assumption that events in the recent past, that is for $\xi < \tau$, will again be far removed and so, forgotten, so far as the indicial response is concerned when $t - \tau \rightarrow \infty$. This means that the steady-state value of the indicial response will depend only on local conditions, that is, on the constant value of $\sigma(\tau)$. The latter behavior is put in evidence by the substitution

$$C_{m_0}(t - \tau; \sigma(\tau), \dot{\sigma}(\tau)) = C_{m_0}(\infty; \sigma(\tau)) - F(t - \tau; \sigma(\tau), \dot{\sigma}(\tau)) \quad (6)$$

where $C_{m_0}(\infty; \sigma(\tau))$ is the steady-state value of the indicial response. Notice that it must be a single-valued function of $\sigma(\tau)$. The function $F(t - \tau; \sigma(\tau), \dot{\sigma}(\tau))$ is called the deficiency function; it approaches zero as $t - \tau \rightarrow \infty$ and, in practice, will be essentially zero for all elapsed time $t - \tau$ larger than a relatively small value t_a . When Eq. (6) is substituted in Eq. (5), the steady-state term multiplied by $(d\sigma/d\tau)d\tau$ forms a perfect differential which can be integrated. The resulting formulation for $C_m(t)$ becomes

$$C_m(t) = C_m(\infty; \sigma(t)) - \int_0^t F(t - \tau; \sigma(\tau), \dot{\sigma}(\tau)) \frac{d\sigma}{d\tau} d\tau \quad (7)$$

Here, $C_m(\infty; \sigma(t))$ is the pitching-moment coefficient that would be measured in a steady flow with σ fixed at the instantaneous value $\sigma(t)$. Again, note that $C_m(\infty; \sigma(t))$ must be a single-valued function of σ according to this formulation.

Equation (7) actually includes three increasingly comprehensive formulations, each of which may be applicable in appropriate circumstances. The simplest, of course, is the linear formulation, for which the indicial response is said to be independent of both $\sigma(\tau)$ and $\dot{\sigma}(\tau)$. The resulting simplification is reflected in the equation of motion, Eq. (3), which becomes

$$\ddot{\sigma}(t) = \left(\frac{qS\bar{z}}{I} \right) \left\{ \sigma(t) C_{m_0}(\infty) - \int_0^t F(t - \tau) \frac{d\sigma}{d\tau} d\tau \right\} \quad (8)$$

The equation is linear and the integral term is of the convolution type, which enables an immediate solution for σ by the aid of Laplace transforms. A considerable additional virtue is that the collection of indicial responses required to be known in advance consists of one member.

The second formulation, applicable in particular to slowly varying motions, is obtained by omitting the dependence on $\dot{\sigma}(\tau)$ from the indicial response. Omitting this dependence in Eq. (6) means that, so far as the indicial response is concerned, the motion prior to the origin of a step is being approximated by the time-invariant motion $\sigma(\xi) = \sigma(\tau)$. The equation of motion, Eq. (3), becomes

$$\ddot{\sigma}(t) = \left(\frac{qS\bar{z}}{I} \right) \left\{ C_m(\infty; \sigma(t)) - \int_0^t F(t - \tau; \sigma(\tau)) \frac{d\sigma}{d\tau} d\tau \right\} \quad (9)$$

a nonlinear Volterra integro-differential equation, solvable by numerical techniques. Here, the collection of indicial responses required to be known in advance must consist of members corresponding to a range of values of $\sigma(\tau)$. This formulation also lends itself to reduction to a form correct to the first order in frequency, resulting in a nonlinear generalization of the classical stability derivative formulation. The form has been studied at length in the authors' previous work (Ref. 3). Approximation at the level of the second formulation thus enables the rational introduction of nonlinear effects.

Finally, the third, most comprehensive formulation is that represented in full by Eq. (7). This form is of sufficient scope to allow the treatment of motions involving hysteresis effects caused by rate-dependent aerodynamic phenomena. It is believed to be applicable, for example, to the complex set of aerodynamic phenomena characteristic of airfoils in low-speed dynamic stall (Refs. 4-6). Retaining a dependence on $\dot{\sigma}(\tau)$ allows assigning different indicial responses to a step at a single value of $\sigma(\tau)$, depending on the magnitude and sign of $\dot{\sigma}(\tau)$. It is possible, for example, to distinguish between indicial responses where σ was increasing or decreasing prior to the step. The motion that would be required to obtain the indicial response experimentally with positive $\dot{\sigma}(\tau)$ is essentially the same as the maneuver that has been used to study the overshoot in lift that occurs following a rapid pitch-up (Ref. 7). It would also be necessary to carry out experiments involving pitch-down maneuvers to allow for the possibility

that the indicial response for a given $\sigma(\tau)$ and a negative value of $\dot{\sigma}(\tau)$ will be different from that for a positive $\dot{\sigma}(\tau)$ of the same magnitude. Here, the collection of indicial responses required to be known in advance must embrace a range of values of $\sigma(\tau)$ and a range of both positive and negative values of $\dot{\sigma}(\tau)$.

While Eq. (7) goes some distance toward fulfilling the goal of a sufficiently comprehensive formulation, it is still incapable of accounting for the existence of multivalued aerodynamic phenomena that need not depend on the pitching rate. This is evident, in particular, in the representation of the steady-state aerodynamic pitching moment $C_m(\omega; \sigma(t))$, and its derivative $C_{m\dot{\sigma}}(\omega; \sigma(t))$, which must be single-valued functions of σ . Admitting the possibility of multivalued aerodynamic responses, not necessarily dependent on the pitching rate, will require an acknowledgment of the influence of the distant past on the indicial response.

5. DEPENDENCE OF THE INDICIAL RESPONSE ON THE DISTANT PAST

In the preceding treatment, on the assumption that events in the distant past should be incapable of influencing the indicial response, the indicial response functional $C_{m\sigma}[\sigma(\xi); t, \tau]$ was replaced by a function $C_{m\sigma}(t - \tau; \sigma(\tau), \dot{\sigma}(\tau))$ which depends only on the magnitude and slope of the past motion $\sigma(\xi)$ at the origin of the step. This replacement can be viewed either as an approximation of the actual motion $\sigma(\xi)$ by a linearly varying motion $\sigma(\xi) = \sigma(\tau) - \dot{\sigma}(\tau)(\tau - \xi)$ for all past time, or, as a substitution applicable only in the vicinity of $\xi = \tau$ with the implicit understanding that the distant-past motion, being immaterial to the indicial response, can be assigned at will. In what follows, the latter interpretation will be the desired one to the extent possible. However, the presence of fluctuations appears to represent a condition where events occurring in the distant past (e.g., the initiation of fluctuations due to flow separation) can affect the present evolution of the indicial response. For suppose that certain distant-past motions, but not others, can initiate fluctuations that persist up to the measuring time, and that the indicial response measured in the presence of fluctuations can differ from the measurement in the absence of fluctuations. Then this must be taken into account somehow, and in a way that does not require assigning the actual distant-past motion to every indicial response.

5.1 Reformulation of Pitching-Moment Response

It is convenient to consider first a typical motion qualifying as the first of the two motions required to form the indicial response (cf. Fig. 3). The motion for values of $\xi < \tau$ is given by $\sigma(\xi)$; it is held constant at $\sigma(\tau)$ for all $\xi > \tau$. The time $\xi = t$ is the time at which the pitching moment is measured. The whole time period prior to $\xi = \tau$ will be called the past relative to any value of $\xi = t > \tau$. Let the past be divided into two parts so that there is an interval T just prior to $\xi = \tau$. The interval of duration T will be called the recent past and the remaining interval the distant past. Let T be chosen sufficiently large so that under normal circumstances, the particular form of the motion $\sigma(\xi)$ in the distant past is immaterial to the pitching-moment response for values of $\xi = t > \tau$. This is the condition that has been used in the preceding section.

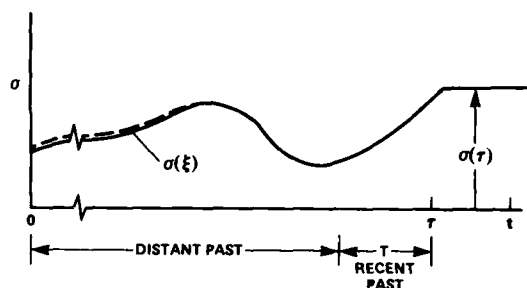


Fig. 3. Recent past and distant past.

How can motion in the distant past influence the measurement for the pitching moment at time t ? It is clear that it will do so if it is capable of changing the nature of the flow in the recent past, to which the measurement is certainly sensitive. This is possible if motion in the distant past has initiated fluctuations that persist into the recent past. The following is an explicit argument. Suppose that the pitching moment is measured at time t for the motion shown in Fig. 3. (Recall that the measurement is actually the ensemble average of repeated measurements at t corresponding to repetitions of the same motion.) With everything else remaining the same, make an infinitesimal change in the distant-past motion as shown by the dotted curve in Fig. 3. After many repetitions of this motion and the corresponding measurement for the pitching moment at time t , compare the ensemble-averaged result with that of the original motion. Suppose first that there is no difference between the two measurements. This, of course, is the expected result according to the preceding formulation. However, there are two conditions under which it should hold: (1) neither distant-past motion has initiated fluctuations that persist into the recent past or (2) both distant-past motions have initiated fluctuations that attain similar statistical properties over the identical recent past, thereby altering the ensemble-averaged flow over the recent-past motion in the same way. Both conditions can be incorporated within a single assertion that in neither case did only one motion initiate fluctuations persisting into the recent past. Now suppose that the two measurements differ at time t . Then the infinitesimal change in the distant-past motion must have exceeded a critical condition for the initiation of fluctuations, and the persistence of these fluctuations into the recent past must have changed the form of the flow in the recent past in ensemble average. The argument of exceeding a critical condition is equally valid for cases in which an infinitesimal change in the distant-past motion stops previously existing fluctuations from persisting into the recent past. Thus, if the distant-past motion is able to influence the measurement at t , the cause is attributable to the existence of a critical condition for the initiation or cessation of persistent fluctuations.

Finally, consider a second infinitesimal change in the distant-past motion that also exceeds the critical condition. Consistent with condition (2) already noted, it is argued that the pitching-moment response to this motion at time t will be the same as the response to the previous motion which had also exceeded the critical condition. The argument is that relative to values of $\xi = t > \tau$, there is sufficient time over the duration T of the recent past for fluctuations originating in the distant past to attain statistical properties that no longer depend on their origin, but rather depend only on their experience over the recent past. Since the recent-past motion is the same for both distant-past motions, the statistical properties of their respective fluctuations should have become the same by the time they have reached the vicinity of $\xi = \tau$. With identical statistical properties, ensemble averaging of repetitions of the pitching-moment responses to the two motions should then yield the same result at $\xi = t$. Now the same argument should hold for any distant-past motion that has initiated fluctuations persisting into the recent past. According to this argument then, the pitching-moment response at time t for a given past motion can be duplicated by the pitching-moment response for a motion whose form in the distant past is assigned at will, so long as it is known that both have initiated fluctuations persisting into a same recent past. Likewise, a distant-past motion whose fluctuations do not persist into the recent past can be replaced, according to the argument, by one assigned at will, so long as fluctuations originating in the latter motion also do not persist into the recent past. The argument translates into a mathematical statement that the pitching-moment response at $\xi = t > \tau$ must be a unique functional of the recent-past motion and additionally, must depend on a parameter that designates by say, one of two numbers, whether fluctuations originating in an otherwise arbitrary distant-past motion do or do not persist into the recent past. Accordingly, the pitching-moment response is written in the functional form

$$C_m(t) = C_m[\sigma(\xi); t, \tau, \lambda(\tau)] \quad (10)$$

where it will be understood that the range of ξ over which there is a functional dependence on $\sigma(\xi)$ is now restricted to cover the recent past only, that is, $\tau - T < \xi < \tau$, and where λ designates the type of distant-past motion, otherwise arbitrary, by one of two numbers; that is,

$$\left. \begin{aligned} \lambda(\tau) = 0: & \text{fluctuations originating in distant past do not persist into recent past;} \\ \lambda(\tau) = 1: & \text{fluctuations originating in distant past persist into recent past.} \end{aligned} \right\} \quad (11)$$

Notice in Eqs. (10) and (11) that although λ can take only one of two values, nevertheless it is a function of τ . This is because the event characterized by λ must originate in the distant past, and by definition, what is called the distant past depends on τ . That is, an event is said to occur in the distant past if the time ξ at which it occurs satisfies $\tau - \xi > T$.

5.2 Reformulation of Indicial Response and Integral Form

Now it is necessary to consider the role of fluctuations in the formation of the indicial response. Consider again the motion illustrated in Fig. 3, for which the pitching-moment response is of the form Eq. (10). Just as before, with everything else remaining the same, make a small change $\Delta\sigma$ in the constant value $\sigma(\tau)$. Repetitions of this motion and the corresponding measurement at time t yield an ensemble-average value for the pitching moment at time t . The procedure is repeated for successively smaller values of $\Delta\sigma$, as many times as necessary, to carry out the limiting process indicated formally in Eq. (12):

$$\lim_{\Delta\sigma \rightarrow 0} \frac{\Delta C_m(t)}{\Delta\sigma} = \lim_{\Delta\sigma \rightarrow 0} \left\{ \frac{C_m[\sigma_2(\xi); t, \tau, \lambda(\tau)] - C_m[\sigma_1(\xi); t, \tau, \lambda(\tau)]}{\Delta\sigma} \right\} \\ \equiv C_m[\sigma(\xi); t, \tau, \lambda(\tau)] \quad (12)$$

where

$$\begin{aligned} \sigma_1(\xi) &= \sigma(\xi); & 0 < \xi < \tau \\ &= \sigma(\tau); & \xi > \tau \\ \sigma_2(\xi) &= \sigma(\xi); & 0 < \xi < \tau \\ &= \sigma(\tau) + \Delta\sigma; & \xi > \tau \end{aligned}$$

The result (if it exists) is the definition of the indicial response. Suppose first that the limit exists, and moreover, that the pitching-moment response to the second motion is very similar in character to that of the first. Again, there are two conditions: (1) neither motion $\sigma_1(\xi)$ nor $\sigma_2(\xi)$ contains flow fluctuations or (2) both motions $\sigma_1(\xi)$ and $\sigma_2(\xi)$ contain flow fluctuations of similar statistical character. Both conditions are incorporated within a single assertion that in neither case did the infinitesimal change $\Delta\sigma$ either initiate fluctuations or stop prior fluctuations. Now suppose that the ensemble-averaged pitching-moment response to the second motion differs from that of the first in such a marked way that the limiting process $\lim_{\Delta\sigma \rightarrow 0} (\Delta C_m(t)/\Delta\sigma)$ almost fails to converge. In this event, it will be said that the infinitesimal change $\Delta\sigma$ has either initiated fluctuations or stopped prior fluctuations. In other words, if the infinitesimal change $\Delta\sigma$ required to form the indicial response itself either initiates fluctuations or stops prior fluctuations, the evidence of this will be a marked, almost discontinuous, change in the indicial response. This abrupt change will be evidenced, in particular, in the steady-state value of the indicial response. While the cause of an abrupt change in the indicial response most often can be attributed to the initiation or termination of fluctuations, let it be noted that nothing in the analysis prevents associating the abrupt change with other, perhaps nonfluctuating,

phenomena as well; for example, an abrupt shift in the pattern of flow separation or an abrupt shift in the location of a shock wave (Ref. 8). All that the analysis requires in principle is the existence of two distinct regimes of flow separated by critical conditions. Thus, the phrase "initiation (or termination) of fluctuations" may stand for any flow phenomenon leading to an abrupt change in the indicial response.

To complete the reformulation, it is necessary to consider the summation process leading to an integral form for the pitching-moment response to an arbitrary motion. Although, as noted, the possibility is allowed of a near-discontinuity with respect to σ in the indicial response, this possibility will exist only at certain isolated values of σ where the exceeding of a critical condition by the infinitesimal change $\Delta\sigma$ either initiates or stops fluctuations. Since the nearly singular behavior of the indicial response thus will be confined to discrete events in the history of σ , these events will not invalidate the general applicability of the summation procedure. Then, as before, the result of summation yields for $C_m(t)$:

$$C_m(t) = C_m(0) + \int_0^t C_{m_0}[\sigma(\xi); t, \tau, \lambda(\tau)] \frac{d\sigma}{d\tau} d\tau \quad (13)$$

The form differs from the one presented earlier (Eq. (2)) in two respects: (1) the functional dependence of the indicial response on $\sigma(\xi)$ extends only over the recent past; (2) the indicial response depends additionally on the parameter λ , designating the type of distant-past motion that is to be attached to the recent-past motion.

Finally, the same argument that was used before can be invoked to replace the indicial response functional in Eq. (13) by a function dependent on a limited number of parameters, rather than on all values of $\sigma(\xi)$ over the interval T of the recent past. If it is assumed again that the recent-past motion is adequately represented by the first two terms of its Taylor series expansion about $\xi = \tau$, then Eq. (13) becomes

$$C_m(t) = C_m(0) + \int_0^t C_{m_0}(t - \tau; \sigma(\tau), \dot{\sigma}(\tau), \lambda(\tau)) \frac{d\sigma}{d\tau} d\tau \quad (14)$$

Again, it can be argued that as the indicial response approaches its steady-state value with increasing values of $t - \tau$, it must become independent of any particular recent-past motion (characterized by $\dot{\sigma}(\tau)$ in Eq. (14)), since the statistical properties of disturbances originating in the recent past will have become independent of their origin as $t - \tau \rightarrow \infty$. The dependence on λ remains, however, and this means that the steady-state value of the indicial response may now be a double-valued function of $\sigma(\tau)$, corresponding to the two possible values of λ . The substitution

$$C_{m_0}(t - \tau; \sigma(\tau), \dot{\sigma}(\tau), \lambda(\tau)) = C_{m_0}(\infty; \sigma(\tau), \lambda(\tau)) - F(t - \tau; \sigma(\tau), \dot{\sigma}(\tau), \lambda(\tau)) \quad (15)$$

puts the steady-state value of the indicial response in evidence. If Eq. (15) is substituted in Eq. (14) and the interval $0 < \tau < t$ is divided into segments, each of which contains only a single value of λ , then the steady-state term can be integrated over each of the segments. The intermediate terms always cancel, however, so that the formulation for $C_m(t)$ takes the form:

$$C_m(t) = C_m(\infty; \sigma(t), \lambda(t)) - \int_0^t F(t - \tau; \sigma(\tau), \dot{\sigma}(\tau), \lambda(\tau)) \frac{d\sigma}{d\tau} d\tau \quad (16)$$

As before, $C_m(\infty; \sigma(t), \lambda(t))$ is the pitching-moment coefficient that would be measured in a steady flow with σ fixed at the instantaneous value $\sigma(t)$. Like its derivative, it may now be a double-valued function of σ corresponding to the two possible values of λ .

5.3 Decision Logic for Choice of λ

It remains to determine a logic for assigning the appropriate value of λ to an indicial response. Recall that the influence of the distant-past motion on an indicial response at current time, characterized by λ , was associated with the exceeding of a critical condition in the distant past which either initiated or terminated persistent fluctuations. It was noted also that at the time of exceeding a critical condition the initiation or cessation of fluctuations would be evidenced by a marked change in the behavior of the indicial response, and in particular the steady-state value of the indicial response, accompanying an infinitesimal change in σ . This suggests that a suitable experiment for determining where the onset and cessation of fluctuations occur is simply the experiment that would be required in any case to determine the steady-state pitching moment as a function of angle of attack. A suitable program for changing the angle of attack is illustrated in Fig. 4, where, at each level, sufficient time is allowed before measuring the pitching moment for the pitching-moment response to reach a steady state (in the mean). Advancing through a series of increasing angles of attack, and then similarly, through a series of decreasing angles of attack, should allow determining whether double-valued behavior of the steady-state pitching moment is possible. Suppose that the result of measurements for the steady-state pitching-moment coefficient resembles that shown on Fig. 5(a). The curve has two distinct branches, reflecting the nonfluctuating and fluctuating regimes of flow. A region of overlap, $\sigma_R < \sigma < \sigma_S$, exists in which the pitching-moment coefficient is double-valued. As illustrated schematically in Fig. 5(b), passage from one regime to the



Fig. 4. Angle-of-attack program for measuring steady-state pitching moment.

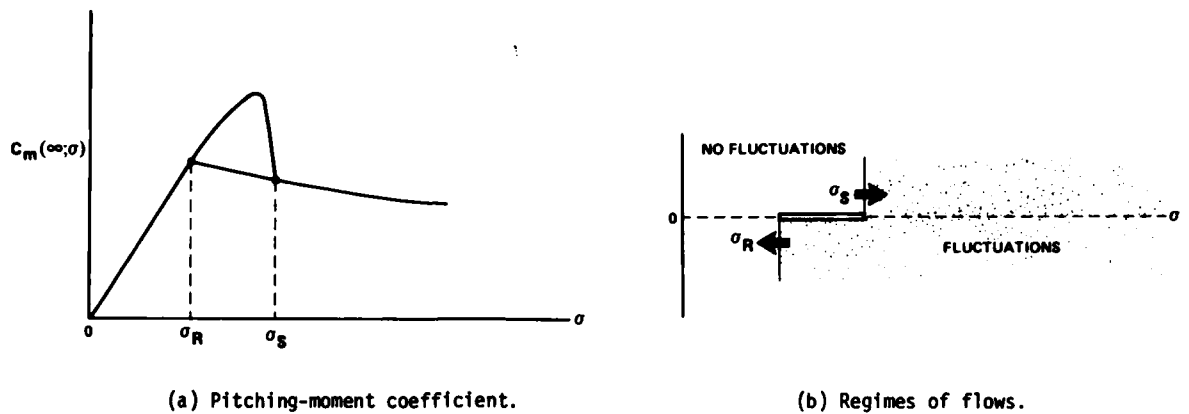


Fig. 5. Steady-state pitching-moment coefficient with region of double-valued dependence on angle of attack.

other is barred (indicated by the double line) except by traversing the critical points $\sigma = \sigma_S$, $\sigma = \sigma_R$ in the directions indicated by the arrows. Then, having the values of σ_S and σ_R should suffice to determine a logic for the choice of λ .

Assume that a step-by-step calculation is being made of a maneuver, and that the calculation has advanced to the point $\xi = \tau$ (cf. Fig. 6). To continue the calculation one more step, it is necessary to assign the appropriate indicial response to the point $\xi = \tau$. Can it now be done? The form of the indicial response, Eq. (15), indicates the parameters that have to be known: $\sigma(\tau)$, $\dot{\sigma}(\tau)$, and $\lambda(\tau)$. Since $\sigma(\xi)$ is known for $\xi \leq \tau$, the values of $\sigma(\tau)$, $\dot{\sigma}(\tau)$ can be specified. It remains to determine whether $\lambda = 0$ or 1 to complete the specification. The following three questions are asked: (1) Is there at least one ξ_0 with $\tau - \xi_0 > T$ such that $\sigma(\xi_0) = \sigma_S$? (2) Is there at least one ξ_1 with $\tau - \xi_1 > T$ such that $\sigma(\xi_1) = \sigma_R$? (3) If the answers to (1) and (2) are yes, is $\min(\tau - \xi_1) > \min(\tau - \xi_0)$? Yes or no answers to the three questions determine the value of λ . Results are given in Table 1:

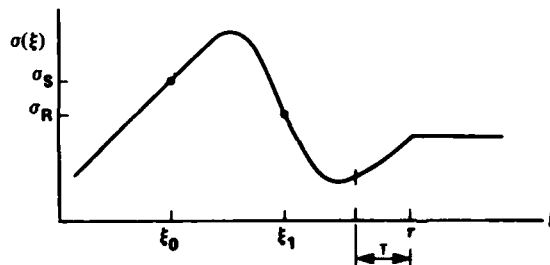


Fig. 6. Step-by-step calculation of a maneuver.

TABLE 1. DECISION LOGIC FOR λ

	1	2	3	λ
No	---	---	---	0
Yes	No	---	---	1
Yes	Yes	No	---	0
Yes	Yes	Yes	---	1

6. IMPLICATIONS FOR DYNAMIC STABILITY EXPERIMENTS

The formulation Eq. (16) is considered to be the principal result of this study. Given the information required to determine λ , its scope may be sufficiently wide to embrace motions involving both nonlinear aerodynamic responses and the double-valued aerodynamic behavior evident in certain kinds of aircraft stall (Refs. 8-10). However, its usefulness in practice appears to hinge on the availability of a collection of indicial responses, forming the kernel of the integral term in Eq. (16). As noted earlier, the eventual availability of such a collection is very unlikely in view of the great difficulty of experimentally determining an indicial response. The purpose of this section will be to show that the usefulness of the formulation in fact is not contingent on the availability of indicial responses. It will be shown that the integral term in Eq. (16) is replaceable by results from a technically more feasible experiment: the oscillations-in-pitch experiment.

For an arbitrary motion $\sigma(t)$, the contribution to $C_m(t)$ of the integral term in Eq. (16) may be approximated as a finite sum of responses to discrete steps $\Delta\sigma(\tau)$. The form of the summation, that is, the integrand, is illustrated in Fig. 7. At each step, the deficiency function $F(t - \tau; \sigma(\tau), \dot{\sigma}(\tau), \lambda(\tau))$ dies out to zero as $t - \tau \rightarrow \infty$, and will be essentially zero for all $t - \tau$ larger than a relatively small value t_a . This is shown schematically in Fig. 7. It is clear that in the summation of responses at time t , only the responses in the interval $t - t_a < \tau < t$ yield measurable contributions at t . Thus, the form of the motion $\sigma(\tau)$ outside the interval $t - t_a < \tau < t$ is immaterial to the summation, except insofar as it determines the value of λ . On the assumption that the motion outside the interval is such that it ensures the correct value of λ , the motion within the interval $t - t_a < \tau < t$ can be approximated without serious error by any convenient substitute motion. If, for example, the substitute motion is harmonic, the resulting summation of responses at time t will be that corresponding to an equivalent harmonic oscillatory motion.

phenomena as well; for example, an abrupt shift in the pattern of flow separation or an abrupt shift in the location of a shock wave (Ref. 8). All that the analysis requires in principle is the existence of two distinct regimes of flow separated by critical conditions. Thus, the phrase "initiation (or termination) of fluctuations" may stand for any flow phenomenon leading to an abrupt change in the indicial response.

To complete the reformulation, it is necessary to consider the summation process leading to an integral form for the pitching-moment response to an arbitrary motion. Although, as noted, the possibility is allowed of a near-discontinuity with respect to σ in the indicial response, this possibility will exist only at certain isolated values of σ where the exceeding of a critical condition by the infinitesimal change $\Delta\sigma$ either initiates or stops fluctuations. Since the nearly singular behavior of the indicial response thus will be confined to discrete events in the history of σ , these events will not invalidate the general applicability of the summation procedure. Then, as before, the result of summation yields for $C_m(t)$:

$$C_m(t) = C_m(0) + \int_0^t C_{m\sigma}[\sigma(\xi); t, \tau, \lambda(\tau)] \frac{d\sigma}{d\tau} d\tau \quad (13)$$

The form differs from the one presented earlier (Eq. (2)) in two respects: (1) the functional dependence of the indicial response on $\sigma(\xi)$ extends only over the recent past; (2) the indicial response depends additionally on the parameter λ , designating the type of distant-past motion that is to be attached to the recent-past motion.

Finally, the same argument that was used before can be invoked to replace the indicial response functional in Eq. (13) by a function dependent on a limited number of parameters, rather than on all values of $\sigma(\xi)$ over the interval T of the recent past. If it is assumed again that the recent-past motion is adequately represented by the first two terms of its Taylor series expansion about $\xi = \tau$, then Eq. (13) becomes

$$C_m(t) = C_m(0) + \int_0^t C_{m\sigma}(t - \tau; \sigma(\tau), \dot{\sigma}(\tau), \lambda(\tau)) \frac{d\sigma}{d\tau} d\tau \quad (14)$$

Again, it can be argued that as the indicial response approaches its steady-state value with increasing values of $t - \tau$, it must become independent of any particular recent-past motion (characterized by $\dot{\sigma}(\tau)$ in Eq. (14)), since the statistical properties of disturbances originating in the recent past will have become independent of their origin as $t - \tau \rightarrow \infty$. The dependence on λ remains, however, and this means that the steady-state value of the indicial response may now be a double-valued function of $\sigma(\tau)$, corresponding to the two possible values of λ . The substitution

$$C_{m\sigma}(t - \tau; \sigma(\tau), \dot{\sigma}(\tau), \lambda(\tau)) = C_{m\sigma}(\infty; \sigma(\tau), \lambda(\tau)) - F(t - \tau; \sigma(\tau), \dot{\sigma}(\tau), \lambda(\tau)) \quad (15)$$

puts the steady-state value of the indicial response in evidence. If Eq. (15) is substituted in Eq. (14) and the interval $0 < \tau < t$ is divided into segments, each of which contains only a single value of λ , then the steady-state term can be integrated over each of the segments. The intermediate terms always cancel, however, so that the formulation for $C_m(t)$ takes the form:

$$C_m(t) = C_m(\infty; \sigma(t), \lambda(t)) - \int_0^t F(t - \tau; \sigma(\tau), \dot{\sigma}(\tau), \lambda(\tau)) \frac{d\sigma}{d\tau} d\tau \quad (16)$$

As before, $C_m(\infty; \sigma(t), \lambda(t))$ is the pitching-moment coefficient that would be measured in a steady flow with σ fixed at the instantaneous value $\sigma(t)$. Like its derivative, it may now be a double-valued function of σ corresponding to the two possible values of λ .

5.3 Decision Logic for Choice of λ

It remains to determine a logic for assigning the appropriate value of λ to an indicial response. Recall that the influence of the distant-past motion on an indicial response at current time, characterized by λ , was associated with the exceeding of a critical condition in the distant past which either initiated or terminated persistent fluctuations. It was noted also that at the time of exceeding a critical condition the initiation or cessation of fluctuations would be evidenced by a marked change in the behavior of the indicial response, and in particular the steady-state value of the indicial response, accompanying an infinitesimal change in σ . This suggests that a suitable experiment for determining where the onset and cessation of fluctuations occur is simply the experiment that would be required in any case to determine the steady-state pitching moment as a function of angle of attack. A suitable program for changing the angle of attack is illustrated in Fig. 4, where, at each level, sufficient time is allowed before measuring the pitching moment for the pitching-moment response to reach a steady state (in the mean). Advancing through a series of increasing angles of attack, and then similarly, through a series of decreasing angles of attack, should allow determining whether double-valued behavior of the steady-state pitching moment is possible. Suppose that the result of measurements for the steady-state pitching-moment coefficient resembles that shown on Fig. 5(a). The curve has two distinct branches, reflecting the nonfluctuating and fluctuating regimes of flow. A region of overlap, $\sigma_R < \sigma < \sigma_S$, exists in which the pitching-moment coefficient is double-valued. As illustrated schematically in Fig. 5(b), passage from one regime to the

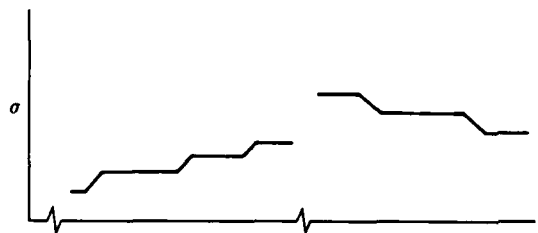


Fig. 4. Angle-of-attack program for measuring steady-state pitching moment.

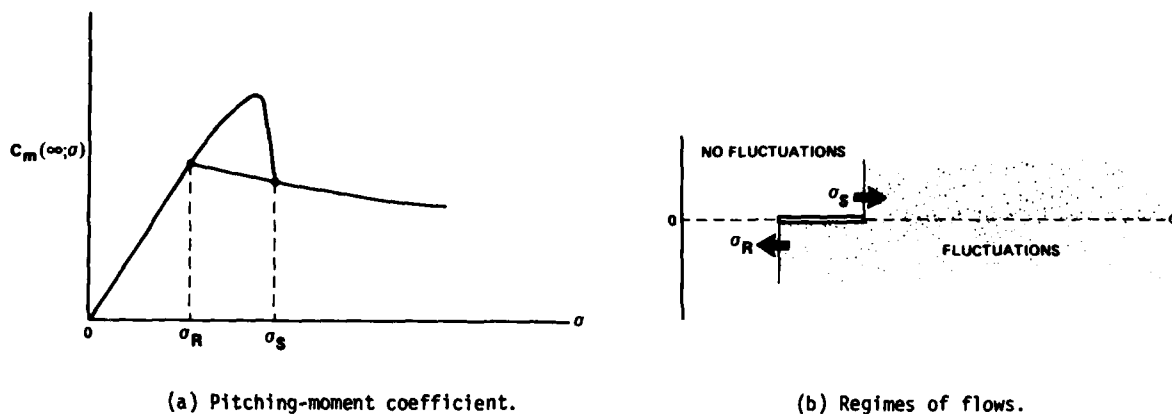


Fig. 5. Steady-state pitching-moment coefficient with region of double-valued dependence on angle of attack.

other is barred (indicated by the double line) except by traversing the critical points $\sigma = \sigma_S$, $\sigma = \sigma_R$ in the directions indicated by the arrows. Then, having the values of σ_S and σ_R should suffice to determine a logic for the choice of λ .

Assume that a step-by-step calculation is being made of a maneuver, and that the calculation has advanced to the point $\xi = \tau$ (cf. Fig. 6). To continue the calculation one more step, it is necessary to assign the appropriate indicial response to the point $\xi = \tau$. Can it now be done? The form of the indicial response, Eq. (15), indicates the parameters that have to be known: $\sigma(\tau)$, $\delta(\tau)$, and $\lambda(\tau)$. Since $\sigma(\xi)$ is known for $\xi < \tau$, the values of $\sigma(\tau)$, $\delta(\tau)$ can be specified. It remains to determine whether $\lambda = 0$ or 1 to complete the specification. The following three questions are asked: (1) Is there at least one ξ_0 with $\tau - \xi_0 > T$ such that $\sigma(\xi_0) = \sigma_S$? (2) Is there at least one ξ_1 with $\tau - \xi_1 > T$ such that $\sigma(\xi_1) = \sigma_R$? (3) If the answers to (1) and (2) are yes, is $\min(\tau - \xi_1) > \min(\tau - \xi_0)$? Yes or no answers to the three questions determine the value of λ . Results are given in Table 1:

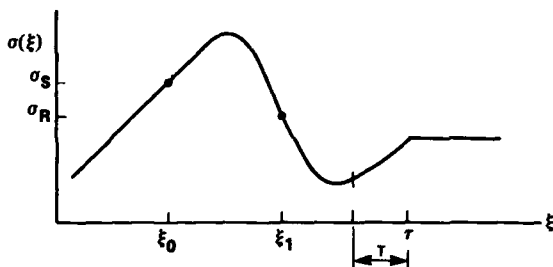


Fig. 6. Step-by-step calculation of a maneuver.

TABLE 1. DECISION LOGIC FOR λ

1	2	3	λ
No	---	---	0
Yes	No	---	1
Yes	Yes	No	0
Yes	Yes	Yes	1

6. IMPLICATIONS FOR DYNAMIC STABILITY EXPERIMENTS

The formulation Eq. (16) is considered to be the principal result of this study. Given the information required to determine λ , its scope may be sufficiently wide to embrace motions involving both nonlinear aerodynamic responses and the double-valued aerodynamic behavior evident in certain kinds of aircraft stall (Refs. 8-10). However, its usefulness in practice appears to hinge on the availability of a collection of indicial responses, forming the kernel of the integral term in Eq. (16). As noted earlier, the eventual availability of such a collection is very unlikely in view of the great difficulty of experimentally determining an indicial response. The purpose of this section will be to show that the usefulness of the formulation in fact is not contingent on the availability of indicial responses. It will be shown that the integral term in Eq. (16) is replaceable by results from a technically more feasible experiment: the oscillations-in-pitch experiment.

For an arbitrary motion $\sigma(t)$, the contribution to $C_m(t)$ of the integral term in Eq. (16) may be approximated as a finite sum of responses to discrete steps $\Delta\sigma(\tau)$. The form of the summation, that is, the integrand, is illustrated in Fig. 7. At each step, the deficiency function $F(t - \tau; \sigma(\tau), \delta(\tau), \lambda(\tau))$ dies out to zero as $t - \tau \rightarrow \infty$, and will be essentially zero for all $t - \tau$ larger than a relatively small value t_a . This is shown schematically in Fig. 7. It is clear that in the summation of responses at time t , only the responses in the interval $t - t_a < \tau < t$ yield measurable contributions at t . Thus, the form of the motion $\sigma(\tau)$ outside the interval $t - t_a < \tau < t$ is immaterial to the summation, except insofar as it determines the value of λ . On the assumption that the motion outside the interval is such that it ensures the correct value of λ , the motion within the interval $t - t_a < \tau < t$ can be approximated without serious error by any convenient substitute motion. If, for example, the substitute motion is harmonic, the resulting summation of responses at time t will be that corresponding to an equivalent harmonic oscillatory motion.

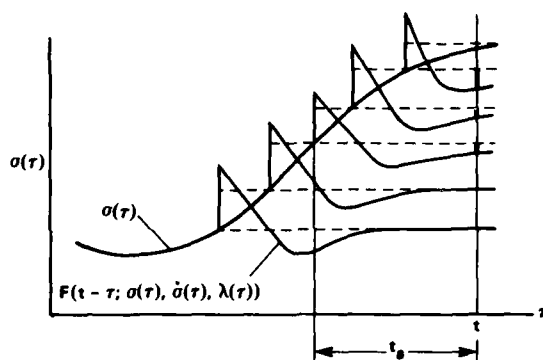


Fig. 7. Summation of indicial responses.

An arbitrary harmonic motion $\sigma_h(\tau)$ about a constant mean provides three arbitrary constants (assuming that the frequency ω is chosen to match a characteristic frequency of the actual motion) which may be chosen to match three properties of the actual motion. It is especially important to match the actual motion in the immediate vicinity of $\tau = t$ where the contributions to the summation are largest. If it is chosen to match the actual values of $\sigma(t)$, $\dot{\sigma}(t)$, and $\ddot{\sigma}(t)$ by a harmonic motion $\sigma_h(\tau)$, then the form of the harmonic motion is given by

$$\sigma_h(\tau) = \left[\sigma(t) + \frac{\ddot{\sigma}(t)}{\omega^2} \right] - \frac{\dot{\sigma}(t)}{\omega} \sin \omega(t - \tau) - \frac{\ddot{\sigma}(t)}{\omega^2} \cos \omega(t - \tau) \quad (17)$$

so that

$$\dot{\sigma}_h(\tau) = \dot{\sigma}(t) \cos \omega(t - \tau) - \frac{\ddot{\sigma}(t)}{\omega} \sin \omega(t - \tau) \quad (18)$$

Substituting Eqs. (17) and (18) for $\sigma(\tau)$, $\dot{\sigma}(\tau)$ in the integral term in Eq. (16) yields for the integral term (letting the lower limit be $t - t_a$ for consistency):

$$\begin{aligned} J(t) = & -\dot{\sigma}(t) \int_{t-t_a}^t F(t - \tau; \sigma_h(\tau), \dot{\sigma}_h(\tau), \lambda(\tau)) \cos \omega(t - \tau) d\tau \\ & + \frac{\ddot{\sigma}(t)}{\omega} \int_{t-t_a}^t F(t - \tau; \sigma_h(\tau), \dot{\sigma}_h(\tau), \lambda(\tau)) \sin \omega(t - \tau) d\tau \end{aligned} \quad (19)$$

or, with a change of variable,

$$\begin{aligned} J(t) = & -\dot{\sigma}(t) \int_0^{t_a} F(u; \sigma_h(t - u), \dot{\sigma}_h(t - u), \lambda(t - u)) \cos \omega u du \\ & + \frac{\ddot{\sigma}(t)}{\omega} \int_0^{t_a} F(u; \sigma_h(t - u), \dot{\sigma}_h(t - u), \lambda(t - u)) \sin \omega u du \end{aligned} \quad (20)$$

This is the contribution to $C_m(t)$ from the integral term, and it is the same contribution that would be obtained from an oscillations-in-pitch experiment for an oscillation constructed according to Eq. (17). This means matching $\sigma(t)$, $\dot{\sigma}(t)$, and $\ddot{\sigma}(t)$ requires that an equivalent harmonic motion have a mean value equal to $[\sigma(t) + \ddot{\sigma}(t)/\omega^2]$ and an amplitude equal to $[(\dot{\sigma}(t)/\omega)^2 + [\ddot{\sigma}(t)/\omega^2]^2]^{1/2}$. The contribution from the term multiplied by $\ddot{\sigma}(t)$ in Eq. (20) is actually of second order in ω and probably negligible for the very low reduced frequencies typical of most aircraft motions. For rapid maneuvers, however, (e.g., a rapid pitch-up maneuver) it may be necessary to retain the term, since it accounts for the very large deviation from the steady-state aerodynamic contribution (i.e., $C_m(\omega; \sigma(t), \lambda(t))$ in Eq. (16) at $\sigma = \sigma_{\max}$ (where $\dot{\sigma} \equiv 0$) which has been observed in wind-tunnel experiments with oscillating airfoils in the low-speed dynamic stall regime (Refs. 4,5).

The result represented by Eq. (20) mathematically expresses the major theme of this study. However, couched in more general terms, it leads to an almost self-evident conclusion that should hold in the general case: the instantaneous aerodynamic force and moment corresponding to an arbitrary motion can be duplicated with the instantaneous force and moment corresponding to an assigned motion, so long as both motions are essentially the same in the recent past relative to the instant, and are in the same flow regime determined by the otherwise immaterial distant-past motion.

7. CONCLUDING REMARKS

The scope of any aerodynamic formulation proposing to embrace a range of possible aircraft maneuvers has been shown to be determined principally by the extent to which the aerodynamic indicial response is allowed to depend on the past motion. Allowing the indicial response to depend only on motion in the recent past resulted in an aerodynamic formulation enabling the rational introduction of nonlinear effects and a description of the rate-dependent aerodynamic phenomena characteristic of airfoils in low-speed dynamic stall. Allowing the indicial response to depend additionally on a characteristic feature of

motion in the distant past, that is, the initiation or termination of persistent fluctuations, resulted in a more comprehensive formulation permitting a description of the double-valued aerodynamic behavior characteristic of certain kinds of aircraft stall. The scope of the latter formulation should be sufficiently wide to include any pitching maneuver having no more than two distinct regimes of flow, separated by critical conditions. Straightforward extensions of the formalism already developed should yield formulations permitting a description of any number of flow regimes and embracing motions with multiple degrees of freedom. A general conclusion that can be drawn from this study, favorable regarding the role of dynamic stability experiments, is the following: the instantaneous aerodynamic force and moment corresponding to an arbitrary motion can be duplicated with the instantaneous force and moment corresponding to an assigned motion, so long as both motions are essentially the same in the recent past relative to the instant, and are in the same flow regime determined by the otherwise immaterial distant-past motion.

REFERENCES

1. Thomas, H. H. B. M.: On Problems of Flight Over an Extended Angle-of-Attack Range. J. Roy. Aeronaut. Soc., Aug. 1973, pp. 413-423.
2. Hancock, G. J.: Problems of Aircraft Behavior at High Angles of Attack. AGARDograph No. 136, 1969.
3. Tobak, M. and Schiff, L. B.: On the Formulation of the Aerodynamic Characteristics in Aircraft Dynamics. NASA TR R-456, Jan. 1976.
4. McCroskey, W. J.: Recent Developments in Dynamic Stall. Unsteady Aerodynamics, Vol. 1, edited by R. B. Kinney, University of Arizona, 1975, pp. 1-33.
5. Carr, L. W., McAlister, K. W., and McCroskey, W. J.: Analysis of the Development of Dynamic Stall Based on Oscillating Airfoil Experiments. NASA TN D-8382, Jan. 1977.
6. Ericsson, L. E. and Reding, J. P.: Quasi-Steady and Transient Dynamic Stall Characteristics. Prediction of Aerodynamic Loading, AGARD CP-204, 1976, paper 24.
7. Harper, P. W. and Flanigan, R. E.: The Effect of Rate of Change of Angle of Attack on the Maximum Lift of a Small Model. NACA TN 2061, 1950.
8. Ericsson, L. E.: Unsteady Aerodynamics of Separating and Reattaching Flow on Bodies of Revolution. Recent Research on Unsteady Boundary Layers, Vol. 1, IUTAM Symposium, 1971, edited by E. A. Eichelbrenner, Les Presses de l'Université Laval, Quebec, Canada, 1972, pp. 481-512.
9. Lowson, M. V.: Some Experiments with Vortex Breakdown. J. Roy. Aeronaut. Soc., Vol. 68, No. 641, May 1964, pp. 343-346.
10. Lambourne, N. C. and Bryer, D. W.: The Bursting of Leading-Edge Vortices; Some Observations and Discussion of the Phenomenon. Aeronautical Research Council, London, England, R&M 3282, 1961.

MATHEMATICAL MODELS OF AIRCRAFT DYNAMICS FOR EXTREME FLIGHT CONDITIONS
(THEORY AND EXPERIMENT)

by

H. H. B. M. Thomas and Geraldine Edwards
Aerodynamics Department
Royal Aircraft Establishment
Farnborough, Hampshire, England

SUMMARY

An examination of the basic features of various formulations of the aerodynamic forces and moments acting on an aircraft, or in other words the mathematical modelling of an aircraft, indicates that motions such as spin entry pose new problems. These relate to the question of which contributions to the aerodynamic forces and moments may be linearized and which have to be included within a term, which is a function of some of the state variables.

The essential overall validation that tests using free-flight models can provide is discussed together with a sample of the results of trials already undertaken, as well as other tasks to which the technique can be successfully applied. A related wind-tunnel test programme, which can provide validation, or otherwise, of the proposed formulations for specific motions, is also outlined.

Finally the sensitivity of the motion to changes in the detail of a particular model used in conjunction with the free-flight tests already mentioned is examined by comparing the motion calculated including a particular term with that calculated ignoring that term.

1 INTRODUCTION

The existence of an adequate mathematical model of an aircraft is essential to the understanding of its dynamics and to the design of control systems intended to render it safe and to endow it with good handling qualities.

It was in the context of the study of the stability of the aircraft's steady state that the earliest form of mathematical model evolved. Here was developed a linearized model, in which the forces and moments called into play by the deviations in the motion variables were assumed to be proportional to the said deviations. The linearized model so evolved centred around the concept of a force or moment derivative and is clearly well suited to an analysis of the stability of an aircraft. Not unnaturally the same model was pressed into service to calculate the response of an aircraft to control inputs by the pilot or to external disturbances, such as a gust. Its success in the treatment of seemingly quite violent motions of this kind may be not easy to understand at first sight. To appreciate why such a simple model should be so successful it is necessary to examine the problem as expressed in terms of normalized variables, which are the appropriate non-dimensionalized counterparts of the state variables. We are then concerned with parameters of the form u/V_e , v/V_e (or its equivalent, the sideslip angle, β), w/V_e (or its equivalent, the angle of attack, α), $p\ell/V_e$, $q\ell/V_e$ and $r\ell/V_e$. It is evident that provided V_e is not small, quite large changes in the motion variables u , v , w , p , q and r fall within modest changes in their normalized (or non-dimensional counterparts). Furthermore, away from proximity to the Earth, it may be assumed that position has nil effect on the aerodynamic forces experienced.

By the same token it is possible to adapt this model to the treatment of the rapid rolling motion of an aircraft, provided the speed in the equilibrium flight is sufficiently large, by the simple expediency of incorporating second-order inertial terms, which are usually ignored in the strictly linear model. However, the angles of attack and sideslip can attain appreciable values in such a motion which, in combination with high Mach number, would indicate the advantage of generalizing the mathematical model by using a formulation of the aerodynamics based on coefficients and their derivatives. Thus typically we have,

$$Y = \frac{1}{2}\rho V^2 S C_Y ; \quad C_Y = C_Y(\alpha, \beta) + C_{Yp}(\alpha, \beta) \frac{p\ell}{V} + C_{Yr}(\alpha, \beta) \frac{r\ell}{V}$$

and

$$L = \frac{1}{2}\rho V^2 S c_{\ell} ; \quad C_{\ell} = C_{\ell}(\alpha, \beta) + C_{\ell p}(\alpha, \beta) \frac{p\ell}{V} + C_{\ell r}(\alpha, \beta) \frac{r\ell}{V} + C_{\ell \dot{\beta}}(\alpha, \beta) \frac{\dot{\beta}\ell}{V} .$$

This represents an expansion of the force and moment coefficient around a notional steady state defined by the instantaneous values, α , β and V . Such modified mathematical models have been arrived at on a pragmatic basis, but Tobak and Schiff² have shown that such formulations can be rigorously justified for non-linear conditions, if the characteristic feature of hysteresis, multivalued aerodynamic responses, are excluded. In the absence of these effects the transition from the strict treatment of a force or a moment as a functional of the variables to its representation by a function of the above type is possible as the formulation contains an adequate cognizance of the past motion. In addition to the presence of high rates of rotation in the motion let us suppose that the speed is low. We are now entering upon conditions in which even the normalized variables can become large. This would be the natural consequence of manoeuvring to high angles of attack resulting in post-stall gyrations and possibly entry into a spin. In these conditions the representation of angular velocity effects by coefficient derivatives, as in the

formulation given above, has to be questioned. It becomes necessary to incorporate these effects to a certain degree, at least, within the general functions which form the initial terms of the expressions for the force and moment coefficients. How is this to be done and how can the necessary validation of the mathematical model be best achieved? These are the questions which the present paper considers.

2 THE GENERAL MATHEMATICAL MODEL

In a general motion the components of the acceleration of the centre of gravity of the aircraft along a system of body axis are given by,

$$\begin{bmatrix} a_x \\ a_y \\ a_z \end{bmatrix} = \begin{bmatrix} \dot{u} \\ \dot{v} \\ \dot{w} \end{bmatrix} + A_p \begin{bmatrix} u \\ v \\ w \end{bmatrix} \quad (1)$$

$$\text{where } A_p = \begin{bmatrix} 0 & -r & q \\ r & 0 & -p \\ -q & p & 0 \end{bmatrix}.$$

Let us assume that the direction of the resultant axis about which the aircraft rotates is aligned with the direction of the resultant velocity of the centre of gravity, so that,

$$\frac{1}{V} \begin{bmatrix} u \\ v \\ w \end{bmatrix} = \frac{1}{\omega} \begin{bmatrix} p \\ q \\ r \end{bmatrix} = \begin{bmatrix} \cos \sigma \\ \sin \beta_s \\ \sin \alpha_s \end{bmatrix} = \begin{bmatrix} \cos \alpha_t \cos \beta_s \\ \sin \beta_s \\ \sin \alpha_t \cos \beta_s \end{bmatrix}. \quad (2)$$

It then follows that

$$\begin{bmatrix} a_x \\ a_y \\ a_z \end{bmatrix} = \begin{bmatrix} \dot{u} \\ \dot{v} \\ \dot{w} \end{bmatrix} = \dot{V} \begin{bmatrix} \cos \sigma \\ \sin \beta_s \\ \sin \alpha_s \end{bmatrix}, \quad (3)$$

provided α_s , β_s and σ are constant, since

$$A_p \begin{bmatrix} p \\ q \\ r \end{bmatrix} = 0.$$

The resultant angular velocity is written as ω to avoid confusion with Ω , which is the resultant of p , q , r in a general motion.

For the particular motion being considered here the accelerations of the centre of gravity along the air-path axis are given by,

$$\begin{bmatrix} a_{x_a} \\ a_{y_a} \\ a_{z_a} \end{bmatrix} = S_a^{-1} \begin{bmatrix} a_x \\ a_y \\ a_z \end{bmatrix} \quad (4)$$

$$\text{where } S_a^{-1} = \begin{bmatrix} \cos \sigma & \sin \beta_s & \sin \alpha_s \\ -\cos \sigma \tan \beta_s & \cos \beta_s & -\sin \alpha_s \tan \beta_s \\ -\sin \alpha_s \sec \beta_s & 0 & \cos \sigma \sec \beta_s \end{bmatrix}.$$

On evaluating the right-hand side of this equation we have,

$$a_{x_a} = \dot{V}; \quad a_{y_a} = 0; \quad a_{z_a} = 0.$$

This demonstrates that if the velocity of the centre of gravity is fixed at its instantaneous value of V , similarly the incidence angles (α_t , β_s or α_s , β_s or σ , λ) a steady rotational motion of the aircraft

would ensue, in which the aircraft performs a coning motion about the instantaneous tangent to the flight path (or the direction of the resultant velocity, V) with some prescribed angular rate ω .

Expansions of the force and moment coefficients may proceed on the basis of such a steady motion. Whilst the choice of the angles of incidence and the velocity for this motion seem natural, there is no straight-forward basis for choosing a value of the coning rate. The formulation of the aerodynamics arrived at by Tobak and Schiff in their analysis of Ref 2 corresponds to taking ω to be such that its component along the body x-axis is equal to the instantaneous rate of roll, that is, $\omega = p \sec \sigma$.

In a steady spin, or a rapid roll essentially about the flight path, the direction of the axis of rotation at a given instant is nearly aligned with the velocity vector, so that,

$$\begin{bmatrix} p \\ q \\ r \end{bmatrix} \approx \Omega \begin{bmatrix} \cos \sigma \\ \sin \beta_s \\ \sin \alpha_s \end{bmatrix}$$

where Ω is the resultant angular velocity or

$$\Omega^2 = p^2 + q^2 + r^2.$$

For this type of motion $\omega \approx \Omega$ and whilst $\Omega \approx p \sec \sigma \approx q \csc \beta_s \approx r \csc \alpha_s$, all these forms are not equally appropriate for all flight conditions. Thus for small values of α_s and β_s the two latter forms are counter indicated. In most motions β_s is small but α_s or σ can be moderately large, as in a steep spin, or very large, as in a flat spin.

In general, the resultant angular velocity is not aligned to the axis of the rotation and the question, that faces us then, is what constitutes a reasonable choice of a steady coning motion with respect to which the development of the forces and moments may be made. There are three motions, which are worthy of further examination. These are,

- (1) A steady coning motion for which $\omega = p \sec \sigma$, that is, one for which the component of the angular velocity about the body x-axis equals the current value of the rate of roll.
- (2) A steady coning motion for which $\omega = p \cos \sigma + q \sin \beta_s + r \sin \alpha_s$, in other words, one for which the coning rate equals the current component of angular velocity about the flight path (or the direction of V).
- (3) A steady coning motion for which $\omega = \Omega = (p^2 + q^2 + r^2)^{1/2}$, that is, one which has a coning rate equal to the resultant angular velocity.

The particular choice may present advantages, or difficulties, according to the degree to which the formulation of the force and moment coefficients can be simplified or according to the closeness of approximation to the actual motion to be represented.

Each of the above steady coning motions gives rise to three steady components of angular velocity, which we may designate, p_s , q_s and r_s . These are given by the equations,

$$\begin{bmatrix} p_s \\ q_s \\ r_s \end{bmatrix} = \omega \begin{bmatrix} \cos \sigma \\ \sin \beta_s \\ \sin \alpha_s \end{bmatrix} = \omega \begin{bmatrix} \cos \sigma \\ \sin \lambda \sin \sigma \\ \cos \lambda \sin \sigma \end{bmatrix} = \omega \begin{bmatrix} \cos \alpha_t \cos \beta_s \\ \sin \beta_s \\ \sin \alpha_t \cos \beta_s \end{bmatrix}. \quad (5)$$

These give for the three motions in question,

$$(1) \quad p_s = p,$$

$$\begin{aligned} (2) \quad p_s &= p \cos^2 \sigma + (q \sin \beta_s + r \sin \alpha_s) \cos \sigma \\ &= p \cos^2 \sigma + (q \sin \lambda + r \cos \lambda) \sin \sigma \cos \sigma \\ &= \left\{ (p \cos \alpha_t + r \sin \alpha_t) \cos \beta_s + q \sin \beta_s \right\} \cos \alpha_t \cos \beta_s, \end{aligned}$$

and

$$(3) \quad p_s = \Omega \cos \sigma = \Omega \cos \alpha_t \cos \beta_s.$$

For all three motions we may write,

$$q_s = p_s \sec \sigma \sin \beta_s = p_s \sec \alpha_t \tan \beta_s \quad \text{and} \quad r_s = p_s \sec \sigma \sin \alpha_s = p_s \tan \alpha_t \sec \beta_s,$$

as being convenient forms for computational purposes.

For the formulation of the aerodynamic forces and moments a given motion characterised by the set of variables $(V, \alpha, \beta, p, q, r, \dot{\alpha}, \dot{\beta})$ is then regarded as a perturbation of the chosen steady coning motion.

Accordingly a force or moment coefficient is written in the form (k stands for X, Y, Z or l, m, n),

$$C_k = C_k(\alpha, \beta, \omega^*, \delta = 0) + C_k(\alpha, \beta, \omega^*, \delta) + C_{kp}(\alpha, \beta, \omega^*) \left(\frac{p' \ell}{V} \right) + C_{kq}(\alpha, \beta, \omega^*) \left(\frac{q' \ell}{V} \right) \\ + C_{kr}(\alpha, \beta, \omega^*) \left(\frac{r' \ell}{V} \right) + C_{k\dot{\alpha}}(\alpha, \beta, \omega^*) \left(\frac{\dot{\alpha} \ell}{V} \right) + C_{k\dot{\beta}}(\alpha, \beta, \omega^*) \left(\frac{\dot{\beta} \ell}{V} \right) \quad (6)$$

where $\omega^* = \frac{\omega \ell}{V}$; $p' = p - p_s$, $q' = q - q_s$, $r' = r - r_s$ and the first term represents the force or moment during a coning motion with ω constant and the motivators (control surfaces etc) centralized (as indicated by the generic symbol $\delta = 0$). The second term represents the effect deflection of the said motivators has on the coefficient being considered (δ would be replaced by ξ , η , ζ , singly or in combination, as appropriate). It is implicit in this formulation that it is convenient to treat this as an additive effect. The remaining terms involve coefficient derivatives which strictly speaking should be evaluated for the chosen coning steady state.

Some simplifications may be permissible, for example, the influence of sideslip may not be significant except within the first two terms. It may further be the case that all terms excepting that which relates specifically to the steady coning motion are only weakly dependent on the coning rate. In this case the expression for C_k breaks down into simpler terms, thus,

$$C_k = C_k(\alpha, \beta, \delta = 0) + C_k(\alpha, \frac{\omega \ell}{V}, \delta = 0) + C_k(\alpha, \beta, \delta) + C_{kp}(\alpha) \left(\frac{p' \ell}{V} \right) + C_{kq}(\alpha) \left(\frac{q' \ell}{V} \right) \\ + C_{kr}(\alpha) \left(\frac{r' \ell}{V} \right) + C_{k\dot{\alpha}}(\alpha) \left(\frac{\dot{\alpha} \ell}{V} \right) + C_{k\dot{\beta}}(\alpha) \left(\frac{\dot{\beta} \ell}{V} \right) \quad (7)$$

On the contrary there could be an effect of motivator deflection on the derivative terms. For example, a change in the value of η alters the value of, say, C_{kr} , in which case the term in this derivative would appear in the form $C_{kr}(\alpha, \delta) \left(\frac{r' \ell}{V} \right)$. There is no 'a priori' argument upon which we can either include or exclude such modified terms. In an expansion of the force and moment coefficient around the steady coning motion it would be logical to have the values of parameters represented collectively by δ adjusted to those corresponding to the steady motion, but this represents no simplification. Accordingly current values of the motivator parameters would be used instead.

The third term of the expression just given refers to the main influence of the motivator deflections, that is, the direct effect on the derivative. It is assumed in the formulation that the contributions due to motivator deflection are approximately the same in the steady rectilinear flight defined by V , α and β and in the steady coning flight defined by V , α , β and ω .

When the individual aerodynamic coefficients are considered further simplifications may be justified. Examples of such simplifications would be accepting a linearized form for each of the contributions due to individual motivators, thus the rolling moment coefficient contributions corresponding to deflections ξ , η and ζ would be written $C_{\ell\xi}(\alpha, \eta)\xi$, $C_{\ell\eta}(\alpha, \xi)\eta$ and $C_{\ell\zeta}(\alpha)\zeta$, say. It may be noted that in the particular examples cited a cross-coupling influence is admitted in the modification of the aileron effectiveness ($C_{\ell\xi}$) with the amount of elevator (tailplane) applied, as is likely to be the case when differential tailplane is used for lateral control. Similarly we have coupling via the rolling moment produced by a tailplane deflection in an asymmetric flow condition ($C_{\ell\beta\eta}$).

There is also no 'a priori' case for dropping any of the cross-coupling terms in the expressions given above, but this should not be taken to mean that all, or any of these terms, which are usually neglected, are important. We shall return to this question later.

In the foregoing discussion it has been tacitly assumed that dynamic analysis is made in terms of aerodynamic quantities related to a body system of axes. For this axis system the steady state coning motion used to develop the expressions for the forces and moments has an angular velocity corresponding to components, which we have designated p_s , q_s , r_s . If the air-path axis had been adopted for formulating the aerodynamic forces the steady coning motion has components of angular velocity of ω , 0, 0 and the expansion would take place about this datum.

A completely different approach to the construction of a mathematical model for high angle-of-attack and rapid rotary conditions has been adopted by the aerodynamic design staff at BAe (Warton). In this it is assumed that the influence of the high rotational rates can be embodied in a term $C_k(\alpha, \frac{p \ell}{V})$ and that this can be isolated from rotary test data (force and moment data obtained during a steady coning motion) by transformation between axis systems assuming that the contribution due to the rate of yaw can be represented by a derivative term $C_{kr}(\alpha, \eta)$.

How this scheme turns out in detail may be illustrated by writing down the expanded forms obtained for the force and moment coefficients in a particular case,

$$\left. \begin{aligned}
 C_x &= C_x(\alpha, \eta), \\
 C_Y &= C_Y(\alpha, \beta) + C_{Y\eta}(\alpha, \beta)\eta + C_{Y\xi}(\alpha, \eta)\xi + C_{Y\zeta}(\alpha)\zeta + C_{Yp}(\alpha)\frac{p\ell}{V} + C_{Yr}(\alpha)\frac{r\ell}{V}, \\
 C_z &= C_z(\alpha, \eta) + C_{zq}(\alpha)\frac{q\ell}{V} + C_{z\dot{\alpha}}(\alpha)\frac{\dot{\alpha}\ell}{V}, \\
 C_\ell &= C_\ell(\alpha, \beta) + C_{\ell\left(\alpha, \frac{p\ell}{V}\right)} + C_{\ell\eta}(\alpha, \beta)\eta + C_{\ell\xi}(\alpha, \eta)\xi + C_{\ell\zeta}(\alpha)\zeta + C_{\ell r}(\alpha)\frac{r\ell}{V} + C_{\ell\dot{\beta}}(\alpha)\frac{\dot{\beta}\ell}{V}, \\
 C_n &= C_n(\alpha, \beta) + C_{n\left(\alpha, \frac{p\ell}{V}\right)} + C_{n\eta}(\alpha, \beta)\eta + C_{n\xi}(\alpha, \eta)\xi + C_{n\zeta}(\alpha)\zeta + C_{nr}(\alpha)\frac{r\ell}{V} + C_{n\dot{\beta}}(\alpha)\frac{\dot{\beta}\ell}{V},
 \end{aligned} \right\} \quad (8)$$

and

$$C_m = C_m(\alpha) + C_{m\eta}(\alpha, \eta) + C_{mq}(\alpha)\frac{q\ell}{V} + C_{m\dot{\alpha}}(\alpha)\frac{\dot{\alpha}\ell}{V}.$$

The representative length ℓ was taken as b in C_ℓ and C_n but as \bar{c} in C_m , to conform with the notation scheme adopted here.

To some extent the ready availability of the data in the above form brought about the adoption of this particular mathematical model as the basic one to be used in the planning of the free-flight model tests to be described later.

We now turn from consideration of the nature of the mathematical model to the means by which experimental validation of the adequacy of a particular model might be sought.

3 VALIDATION OF THE MATHEMATICAL MODEL

In order to justify the use of a particular mathematical model in design studies it is necessary to demonstrate that it represents sufficiently faithfully the behaviour of the aircraft (or a scaled model) over a range of possible motions. The ultimate test here is, of course, its capability to predict reasonably accurately all features of the motion in free unrestricted flight. Data of this nature could have been obtained from tests of a fully-instrumented aircraft, but such tests are potentially hazardous as is borne out by the losses suffered during spinning tests. This caused us to opt for a quarter-scale model of a typical combat aircraft as the test vehicle.

3.1 Free-flight model tests

The model used in the present series of tests are unpowered. For ease of handling on the ground they are carried on a trolley, which is so designed as to enable the model to be lifted clear of the ground and trolley by means of jacks. From this elevated position the model is lifted off by a helicopter, to which it is attached by a cable about 50 m long. As soon as the weight of the model is removed from the jacks they retract automatically and rapidly to reduce the possibility of damage to the model during lift-off. To provide greater safety and stability on tow the cable is ballasted by additional mass and a drogue parachute attached to the rear of the model. Once the helicopter has towed the model to the required height a trial run down the range is made. Provided everything is satisfactory during this dummy run the actual run is made at the desired speed and height towards the release point. When over the release point the flight observer simultaneously releases the drogue from the model and the latter from the cable.

As at present arranged the control-surface inputs are initiated by a timer mechanism and are thus preprogrammed. At the completion of a test a recovery sequence is initiated by either the above-mentioned timer mechanism at some preset time or by a barometric switch operating at some preset height. The recovery sequence consists of the application of fully-up tailplane followed by forcible ejection of an auxiliary parachute, which pulls out a cluster of recovery parachutes. The up-tailplane deflection acts as a safety recovery measure in the event of failure of the parachute system.

Data from on-board instrumentation provides measured values of the linear accelerations along each axis, angle of attack, angle of sideslip (strictly β_c , see notation), the angular acceleration (\dot{p} , \dot{q} , \dot{r}), the angular velocity components (p , q , r), the attitude of inclination and bank (Θ , Φ) as well as the speed over a wide range in the angle of attack. The data are recorded using the telemetry and data recording systems already available at the range. Other data are available from trajectory observations and these are the speed (V), the angle of glide and the angle of track of the aircraft model. Some redundancy of information is implied in this comprehensive set of measurements and in due course full use is to be made of this fact. Certain compatibility tests can be made using the two sets of data. There is the usual difficulty in obtaining a uniformly high standard of measurement for all quantities.

In the longer term it is hoped that some generalized form of 'parameter identification' technique may be applied to the data to yield some of the terms in the mathematical model. For the present purposes the ideal free-flight test programme would consist of a steady progression from the simplest to the most complicated form of motion. Thus, as a start the model would be flown in a series of trimmed glides. This to be followed by small amplitude motion of either essentially longitudinal or lateral type. Next would come post-stall gyrations of differing form and severity till spin-entry conditions would be finally reached. Pressure to extend the work in other directions with a more immediate application to current projects caused us to partly abandon this basic research approach. However, as an immediate overall check on the usefulness of the mathematical model it is possible to compare the history of the measured motion with that predicted. A number of such comparisons have been made and we now examine a sample of these.

The first set of curves (Figs 1 and 2) refer to trials 5 and 6, which were intended to produce identical motions on the assumption that gusts and launch distributions were sufficiently small to have

had a negligible effect on the motion during its later stages. In these trials the model left the cable with a speed of 37 m/s and at its trim angle of attack when on tow, 3° (this angle is always low due to the large drag force of the drogue parachute). The tailplane angle was -6° whilst both the differential tail deflection and the rudder angle were zero. On release the aircraft model experienced a transient motion in response to the out-of-balance forces and moments and an interval of about 7.5 seconds was allowed for this motion to damp out. The application, at approximately this time, of 30° port rudder launched the model into fairly violent post-stall gyrations with a large content of rolling. This strongly coupled motion drove the model to angles of attack well beyond the 25° of the near-trim condition, see Fig 2.

There are slight differences in the timing of the control inputs during the two drops and response of the model reflects these. Furthermore, larger disturbances appear to have been present during the release in drop 6 as compared with drop 5. Figs 1 and 2 refer specifically to drop 6.

As regards the comparison of predicted and measured behaviour it seems that there are additional disturbances present, which are not accounted for in the prediction. The calculated excursions in sideslip following rudder application are larger than those measured.

The degree of mismatch (in Fig 2) is greatest for the rate-of-roll history and it is considered that this reflects the inability of the particular mathematical model used to represent the angular velocity effects accurately enough.

Incidentally the ease of recovery from such a post-stall gyration was examined and it was shown that reduction of the up-tailplane angle combined with centralizing the rudder brought about a prompt return to normal flying conditions.

An earlier trial (drop 4) had explored entry into one of the spin motions that the configuration is capable of executing. Calculations had indicated that entry into the particular spin investigated during drop 4 could be effected by increasing the amount of up-tailplane from -6° to -12° after about 5 seconds of flight, followed, about 2 seconds later, by combined application of full port rudder ($+30^\circ$) and against-spin differential tailplane (-5°), see Fig 3. As can be seen from Fig 4 appreciable and highly oscillatory roll rates ensued combined with large rates of yaw of a less oscillatory nature. Associated with these angular rates are a marked growth in the angle of attack and a departure trend in sideslip.

After about 10 seconds of flight the model began to settle into the intended spin motion, which was characterised by an angle of attack of about 72° and a nose-down attitude of about -25° on average. The spin rate was one turn per 2.2 seconds (this is model rate, which is twice the full-scale rate).

Here again the predicted motion is generally more oscillatory than that measured and, as before, this is an indication that the mathematical model is not sufficiently representative when high rates of roll and yaw are present. Calculations had indicated that full up-tailplane, reversed differential tailplane and neutral rudder would bring about a rapid recovery from the spin. The trial confirmed this finding as can be seen from Fig 4.

The computer-based studies had shown that the aircraft model was capable of executing a fast, flat spin. It was further found that, if during the previous spin mode the tailplane was returned to its neutral position the rate of rotation increased and so did the angle of attack with the result that the aircraft model entered a fast, flat spin. Thus for drop 7 the results of which we now examine, the opening stages of the motion were nearly the same as for drop 4. Such differences as exist were not intended. Once the model was established in the spin previously described the tailplane was centralized, but the rudder and differential tail deflections were maintained at their previous values of $+30^\circ$ and -5° respectively (see Fig 5). As can be seen from Fig 6 the model soon entered the expected flat, fast spin, characterized by angles of attack of about 85° , a very small nose-down attitude and a high rate of turn (one turn per 1.17 seconds). Once again the type of discrepancy between the predicted and measured motion previously noted is still present.

Among the drops already made were two which featured small amplitude 'Dutch-roll' type motions covering the angle-of-attack range, 20° to 35° , approximately. In the first of these, drop 9, the aim was to apply in two stages tailplane angles of -6° and -10° , which were expected to give near trimmed conditions in which the angles of attack would oscillate around 20° and 25° respectively. Calculations based on previous experience had suggested that random launch and other disturbances would suffice to excite the Dutch-roll motion. Apart from the fact that the upper level achieved in the angle of attack was somewhat lower than 25° these objectives were realized. On the contrary in drop 10 the mean angles of attack reached, as a result of using tailplane deflections of -10° and -15° were somewhat larger than expected.

An examination of the recorded data for drop 9, see Fig 7, points to the presence of sustained lateral inputs since the aircraft model enters a nearly steady turn. Shown on the same figure is a calculated history of the motion assuming the presence of rolling and yawing moments during most of the motion as indicated in the figure. No ready explanation of such inputs is forthcoming as attempts were made to immobilize the rudder during these two trials and there was no direct evidence to suggest that either rudder or differential tailplane was at other than zero setting. The fact that the Dutch-roll oscillation is superimposed on a more or less steady turning motion does not inhibit in any way the analysis of the motion on a linearized basis using one of the established parameter-identification methods. In the present analysis the derivatives $C_{Y\beta}$, $C_{l\beta}$, $C_{n\beta}$, C_{lp} and C_{np} were allowed to vary in order to obtain the best match between measured and calculated values of the following motion variables - angle of sideslip ($\beta \equiv \beta_g$), rate of roll (p), rate of yaw (r) and the sideways acceleration (A_y) - for certain portions of the history. Figs 8 and 9 show the degree of match obtained whilst the results obtained for the individual derivatives are displayed in Fig 10 where they are compared with some wind-tunnel measurements and estimates. Of the differences that are shown by these comparisons the most striking are those present in the $C_{n\beta}$ results. It should be emphasized that these are preliminary results and it is too

early to ascribe the discrepancy to any particular effect. However, it has been noted in tests on another configuration that a long probe of the sort fitted to the nose of the model can have a significant effect in the angle-of-attack range where the differences are most marked in Fig 10. If later tests confirm the trends indicated by the above two trials it will be necessary to modify the mathematical model, which was constructed on the basis of data drawn from various sources. How far we shall fall short of the ideal of having a comprehensive set of wind-tunnel tests on an aircraft model identical with one of those flown remains to be seen.

3.2 Supporting wind-tunnel testing

It is evident from what has been said already that there is a need to establish a wind-tunnel test procedure to give data for the synthesis of the mathematical model and to this end the wind tunnel must also play its part in the validation of the assumptions made in the course of formulating the mathematical model. The constraints imposed by wind-tunnel tests represent on the one hand undesired restrictions on the motion (hence the need for free-flight tests), but on the other hand they can by reduction of the number of variables involved enable particular features of a mathematical model to be examined in isolation.

The coning motion about the relative velocity direction is a key feature of the generalized mathematical model as envisaged. Furthermore there seems to be general acceptance of this conclusion and this has accounted for a resurgence of interest in rotary rigs. New rigs of this type are being developed and brought into use in a number of countries. What emerges from our deliberations thus far is that there is not such a universally accepted view on how to utilize the data output of rotary-rig tests.

If the generally acceptable mathematical model conforms to the formulations outlined in this paper, the rotary rig is a means of providing the data for the opening terms of the expansions for the force and moment coefficients. Whether it is, in general, necessary to retain a general single function or whether this can be split into two simplified terms remains to be demonstrated. Strictly speaking the derivative type terms should be evaluated at the datum condition of the steady coning motion and the development of rigs to comply with this requirement could pose difficult problems. This being so it seems all the more necessary to ensure that there is a real need to return to the most general and basic formulation outlined in order to achieve an adequate mathematical model. In this context the measurement of forces and moments during some specialized forms of motion in a wind-tunnel merit careful consideration. Four such motions are suggested and these are:

- (1) Rotation, about a line through the model's centre of gravity parallel to the airstream, during which the speed of rotation is varied.

Here the three steady coning rates ω_1 , ω_2 and ω_3 are all equal to the instantaneous rate of rotation. Hence in accord with any of the proposed mathematical models it is expected that the forces and moments at any instant of the motion equal those generated during a steady coning motion about the relative velocity vector with a rate equal to that of variable motion at the given time. Thus $C_k(\alpha, \beta, \omega(t)) \approx C_k(\alpha, \beta, \omega)$, $\omega = \text{const} = \omega(t)$. However in the same type of experiment it is possible to arrange for the rate of rotation to be a perturbation of a steady rate. For example, suppose $\omega = \omega_0 + \omega_1 \sin \tau t$, $\omega_1 \ll \omega_0$, then we may treat the motion and the aerodynamic coefficients as perturbations around the steady coning motion defined by V , α_t , β_s and ω_0 . The perturbations in the angular velocity components are,

$$p' = \omega_1 \sin \tau t \cos \alpha_t \cos \beta_s,$$

$$q' = \omega_1 \sin \tau t \sin \beta_s,$$

$$r' = \omega_1 \sin \tau t \sin \alpha_t \cos \beta_s.$$

In the motion in question the values of the angle of attack (α_t) and the angle of sideslip (β_s) remain invariant. When considered as a perturbation of a steady coning motion the test would enable a check to be made on the validity of a derivative formulation for the incremental force and moment coefficients due to p' , q' and r' . In the particular case mentioned these would vary in a cyclic manner and vanish for $\tau t = n\pi$, where n is an integer.

- (2) Rotation about a direction through the centre of gravity of the model, but not aligned with the airstream direction. This motion may be interpreted physically as corresponding to a general rotational but still rectilinear motion. The kinematics of this motion and the setting of the model attitudes for a test of this kind are discussed fully in Appendix 1.

During this motion the angle of attack (α_t) and the angle of sideslip (β_s) vary and the amount of variation can be adjusted by either altering the direction of the axis of rotation or the rate of rotation about a fixed axis direction. The forces and moments acting during the motion depend on all parameters, that is, α , β , $\dot{\alpha}$ and $\dot{\beta}$ are added to the parameters involved in motion (1). During these tests the motivator settings may be held at zero or constant deflection.

Non-alignment of the angular velocity and the linear velocity will provide an opportunity of assessing the most appropriate datum steady coning motion (about the linear velocity direction) with respect to which expansions of the functions for the forces and moments may be developed.

- (3) A rotary motion about a line offset from the centre of gravity of the model, but parallel to the direction of the airstream, so that the resulting motion is analogous to a spin motion. The centre of gravity of the model describes the equivalent of the aircraft's helical path.

The angles of incidence (α_t, β_s) differ somewhat from those for the corresponding steady rotation about the airstream direction passing through the centre of gravity of the model by an amount, which depends on the magnitude of the parameter, $\lambda_\omega = \omega r/V_R$, see Appendix 2.

This particular motion is the basis of a test that can be used to check that the effects associated with the angular velocity can be superimposed upon the angle-of-incidence effects, as given by static wind-tunnel tests.

(4) If a varying rate of rotation is introduced into the motion just described, we shall have all the features present in motion (2). Such a variant of the spin motion would provide a basis for checking all aspects of the mathematical modelling.

The properties of a number of motions having been examined, we pass on to outline in some more detail a wind-tunnel test programme for validation of the mathematical model and acquisition of data.

3.3 A possible series of wind-tunnel tests

In what follows various expressions are given for a typical coefficient symbolized by C_k . The first is the general form in each case and implies no assumption other than the functional may be replaced by a function. Other expressions follow this and C_k is written as approximately equal to some expansion or other. These forms are at present speculative and it remains to be seen how far the approximation by simplified forms can be pressed in individual cases.

(1) Static tests

$$\begin{aligned} C_k &= C_k(\alpha, \beta, \delta) \\ &\approx C_k(\alpha, \beta, \delta = 0) + C_{k\xi}(\alpha, \beta, \eta)\xi + C_{k\eta}(\alpha, \beta)\eta + C_{k\zeta}(\alpha, \beta, \eta)\zeta \\ &\approx C_k(\alpha, \beta, \delta = 0) + C_{k\xi}(\alpha, \eta)\xi + C_{k\eta}(\alpha)\eta + C_k(\alpha, \eta)\zeta \end{aligned} \quad (9)$$

Here we shall drop the suffices on α and β so that these should be interpreted as α_t and β_s . The symbol δ is used as a generic symbol for motivator deflection, so that in the particular case developed δ stands for ξ, η, ζ either individually or collectively.

(2) Steady coning about the airstream

In this case

$$C_k = C_k\left(\alpha, \beta, \frac{\omega l}{V}, \delta\right) \quad (10)$$

It may be possible to replace this relationship by one of the following forms,

$$\begin{aligned} C_k &\approx C_k\left(\alpha, \beta, \frac{\omega l}{V}, \delta = 0\right) + C_{k\xi}\left(\alpha, \beta, \frac{\omega l}{V}, \eta\right)\xi + C_{k\eta}\left(\alpha, \beta, \frac{\omega l}{V}\right)\eta + C_{k\zeta}\left(\alpha, \beta, \frac{\omega l}{V}, \eta\right)\zeta \\ &\approx C_k\left(\alpha, \beta, \frac{\omega l}{V}, \delta = 0\right) + C_{k\xi}(\alpha, \beta, \eta)\xi + C_{k\eta}(\alpha, \beta)\eta + C_{k\zeta}(\alpha, \beta, \eta)\zeta \\ &\approx C_k\left(\alpha, \beta, \frac{\omega l}{V}, \delta = 0\right) + C_{k\xi}(\alpha, \eta)\xi + C_{k\eta}(\alpha)\eta + C_{k\zeta}(\alpha, \eta)\zeta \end{aligned} \quad (11)$$

The first term in these last three expressions may itself be capable of being broken down into two simpler terms, thus,

$$C_k\left(\alpha, \beta, \frac{\omega l}{V}, \delta = 0\right) \approx C_k(\alpha, \beta, \delta = 0) + C_k\left(\alpha, \frac{\omega l}{V}, \delta = 0\right)$$

It is evident that if some of these simpler forms are acceptable certain of the terms are already available from static tests.

(3) Coning at varying rate about a line in the airstream direction through the centre of gravity

With $\omega = \omega_0 + \omega_1 \sin \omega t$, say, we have constant angles of incidence and the value of a coefficient at time t is the same as that for steady coning at the rate $\omega = \omega(t)$. This latter is available for a range of angular rates from the tests under (2).

Alternatively if $\omega_1 \ll \omega_0$ we may write

$$C_k \approx C_k\left(\alpha, \beta, \frac{\omega_0 l}{V}, \delta\right) + C_{kp}\left(\alpha, \beta, \frac{\omega_0 l}{V}\right) \frac{p'l}{V} + C_{kq}\left(\alpha, \beta, \frac{\omega_0 l}{V}\right) \frac{q'l}{V} + C_{kr}\left(\alpha, \beta, \frac{\omega_0 l}{V}\right) \frac{r'l}{V} \quad (12)$$

where p', q', r' are expressible in terms of $\omega_1 \sin \omega t$, α and β .

It will be particularly interesting to see whether the two formulations implied here are equally successful, or if one is more so than the other which that is.

(4) Coning about a line through the centre of gravity not parallel to the airstream

In this case the aircraft model is rotated with an angular velocity ω , say, about an axis the direction of which is defined by $\alpha_\omega, \beta_\omega$ (analogous to but not equal to the incidence angles α_t, β_s). We have,

$$C_k = C_k\left(\alpha, \beta, \frac{\omega l}{V}, \alpha_\omega, \beta_\omega, \delta\right) . \quad (13)$$

Here the wind-tunnel set-up simulates a general rotational motion in which the centre of gravity of the aircraft describes a rectilinear path. A test of this type permits us to assess the relative merits of the different choices for the coning rate of the steady datum condition with respect to which the expansion of C_k is developed. We have already mentioned three such coning rates (see section 2) and let us designate these $\omega_1, \omega_2, \omega_3$ respectively. The components, with respect to the body axes, of the angular velocity of the aircraft model are given by,

$$\begin{bmatrix} p \\ q \\ r \end{bmatrix} = \omega \begin{bmatrix} \cos \sigma_\omega \\ \sin \lambda_\omega \sin \sigma_\omega \\ \cos \lambda_\omega \sin \sigma_\omega \end{bmatrix} = \omega \begin{bmatrix} \cos \alpha_\omega \cos \beta_\omega \\ \sin \beta_\omega \\ \sin \alpha_\omega \cos \beta_\omega \end{bmatrix} . \quad (14)$$

For the three steady coning motions to be examined the rates of roll are,

$$\begin{aligned} p_{s1} &= \omega_1 \cos \sigma = p , \\ p_{s2} &= \omega_2 \cos \sigma = \omega_2 \cos \alpha_t \cos \beta_s , \\ p_{s3} &= \omega_3 \cos \sigma = \omega_3 \cos \alpha_t \cos \beta_s , \end{aligned}$$

while in each case the other two components q_{sn}, r_{sn} are related to the rate of roll p_{sn} by the relationships,

$$\left. \begin{aligned} q_{sn} &= p_{sn} \sin \lambda \tan \sigma = p_{sn} \sec \alpha_t \tan \beta_s \\ r_{sn} &= p_{sn} \cos \lambda \tan \sigma = p_{sn} \tan \alpha_t \end{aligned} \right\} n = 1, 2, 3 .$$

In accord with the proposed scheme for formulating the aerodynamic coefficients we write,

$$C_k \approx C_k\left(\alpha, \beta, \frac{\omega_s l}{V}, \delta\right) + C_{kp} \frac{p' l}{V} + C_{kq} \frac{q' l}{V} + C_{kr} \frac{r' l}{V} + C_{k\dot{\alpha}} \frac{\dot{\alpha} l}{V} + C_{k\dot{\beta}} \frac{\dot{\beta} l}{V} . \quad (15)$$

In this motion the angles of incidence (λ, σ or α_t, β_s) change during the test and the first term in the above expression represents the value the particular coefficient C_k has in a steady coning motion about the velocity vector, \vec{V} , for which the angular velocity is constant and equal to ω_s , whilst α and β are constant and equal to the instantaneous values of these angles. Furthermore $\omega_s = \omega_1, \omega_2$ or ω_3 and

$$\begin{aligned} p' &= p - p_{sn} , \\ q' &= q - q_{sn} , \\ r' &= r - r_{sn} . \end{aligned}$$

The individual terms of the above expression are open to the same treatment as those which occur in the motions already discussed.

There are two ways in which a given motion may differ from a steady coning motion namely through varying coning rate (as in 3) or by misalignment (as in 4). Another form of misalignment is that in which the motion of the model simulates spin conditions, that is, rotation takes place about a line parallel to the airstream, but offset from the centre of gravity of the model. A varying coning rate may be introduced into this form of motion and the effects of doing so are now considered.

(4a) Rotary motion about the tunnel axis, with variable rate of rotation and the model's centre of gravity offset from the tunnel axis

The angular velocity of the model may take on any form, in principle, but let us examine the case where

$$\omega = \omega_0 + \omega_1 \sin \nu t \quad (16)$$

where ω_0 and ω_1 are constant.

As shown in Appendix 2 the angles of incidence are given by,

$$\tan \alpha_t = \cos \phi_e \tan \theta_e + \frac{\omega r}{V_R} \sin \phi_e$$

and

$$\left\{ 1 + \left(\frac{\omega r}{V_R} \right)^2 \right\}^{\frac{1}{2}} \sin \beta_s = \sin \phi_e \sin \theta_e - \frac{\omega r}{V_R} \cos \phi_e,$$

where $V_R^2 = V^2 + \omega^2 r^2$ and V is the tunnel airspeed.

Since by virtue of equation (16) the angular velocity varies with time, so do the angles of incidence, α_t and β_s . Accordingly terms in $\dot{\alpha}$ and $\dot{\beta}$ must be added to the expression for a typical aerodynamic coefficient C_k . Furthermore, as explained earlier, we may write

$$C_k = C_k \left(\alpha, \beta, \frac{\omega l}{V_R}, \delta \right) + C_{k\dot{\alpha}} \left(\alpha, \beta, \frac{\omega l}{V_R} \right) \left(\frac{\dot{\alpha} l}{V_R} \right) + C_{k\dot{\beta}} \left(\alpha, \beta, \frac{\omega l}{V_R} \right) \left(\frac{\dot{\beta} l}{V_R} \right) \quad (17)$$

in accord with the suggested formulations for the general case. Here α, β and ω are the instantaneous values of these parameters at time t . The leading term of this expression may be simplified as indicated earlier, if this proves to be justified.

If ω_1 is small compared with ω_0 an alternative interpretation is permissible, namely to regard the motion as a perturbation of the motion for the constant angular velocity, ω_0 . With this approach we write

$$C_k \approx C_k \left(\alpha, \beta, \frac{\omega_0 l}{V_R}, \delta \right) + C_{kp} \left(\alpha, \beta, \frac{\omega_0 l}{V_R} \right) \frac{p' l}{V_R} + C_{kq} \left(\alpha, \beta, \frac{\omega_0 l}{V_R} \right) \frac{q' l}{V_R} + C_{kr} \left(\alpha, \beta, \frac{\omega_0 l}{V_R} \right) \frac{r' l}{V_R} \\ + C_{k\dot{\alpha}} \left(\alpha, \beta, \frac{\omega_0 l}{V_R} \right) \frac{\dot{\alpha} l}{V_R} + C_{k\dot{\beta}} \left(\alpha, \beta, \frac{\omega_0 l}{V_R} \right) \frac{\dot{\beta} l}{V_R} \quad (18)$$

The terms of this expression are open to the same simplifying treatment as accorded to terms in other motions should such simplifications prove valid.

Although some of the motions just outlined may present no difficulty and could thus form part of a data acquisition scheme, others may be more troublesome. It is possible, of course, to envisage a more direct means of providing aerodynamic data. Just as it is appropriate for say departure studies to perform oscillatory tests around a datum flight condition defined by α_t and β_s (usually reduced to α_t , $\beta_s = 0$), so more generally oscillatory tests may be made with respect to a datum flight condition defined by α_t, β_s and ω (a steady coning motion). Rigs of this kind are clearly more complicated than existing oscillatory test rigs. If some of the speculations made here are found to result in adequate representations of the aerodynamic coefficients, we may not need such rigs for they may be capable of being replaced by existing rigs (or developments of these) for the determination of some terms in the expansion of the coefficient. The question which must now be resolved is whether the problems associated with the conduct of tests involving different rotary motions are significantly less than those involved in the design of the generalized oscillatory rig.

4 SOME STUDIES IN SENSITIVITY OF PREDICTED MOTIONS TO CERTAIN PARAMETERS

In a formal manner many novel features have been included in the mathematical model. For instance, we have not excluded interference effects due to the deflection of particular motivators, which give rise to derivatives such as $C_{k\zeta}(\alpha, \eta)$ or $C_{k\xi}(\alpha, \eta)$. All primary effects, however small, have been included although it has been customary to ignore some of these in the linearized model. The derivatives C_{yp} and C_{yr} come in this category. Cross-coupling terms, representing forces and moments which couple the longitudinal and lateral motions, are also not excluded. In this way there is a danger of over complicating the mathematical model and thereby rendering interpretation and analysis (parameter identification) more difficult. It was considered worthwhile even on the basis of the mathematical model adopted for the planning of the free-flight tests to make an analysis of the sensitivity of the predictions to the inclusions or otherwise of certain terms. We now consider the results of the studies so far made.

4.1 Effect of C_{Yp} and C_{Yr}

It has long been customary to ignore these terms in calculations using the linearized model. However large values of the rates of roll and yaw in departure or spin entry flight conditions urges caution in doing so when these conditions are the subject of investigation.

The calculated histories of drops 6 and 7 have been chosen for the present analysis. As shown in Fig 11 the quality of the agreement is hardly affected for any of the variables α , β , p , q and r by ignoring the C_{Yp} term in predicting the motion for drop 6. The influence of the same term was examined in the case of drop 7 and the effect of ignoring the C_{Yp} term is very small.

Since it is found that as expected the omission of the term in C_{Yr} affects the motion to the same slight degree, the results are displayed only for the case of drop 7 where large rates of yaw occur. Even so the predicted motion with the C_{Yr} term ignored is in close agreement with that predicted including the contribution of the C_{Yr} term except near the end of the test programme (see Fig 12). This phase of the motion corresponds to a reduction in the amount of up-tailplane applied (-24° to -6°), the intention being to return to normal flying conditions. It turns out that this action is a little premature in that the rate of yaw is still high (about $100^\circ/\text{s}$). This combined with a reduction in the angle of attack below 40° accounts for the local significant effect of the C_{Yr} term.

However, in the light of the overall discrepancies between predicted and measured motion histories it is considered that there is no strong case to be made for including the contributions of the rate of roll and of rate of yaw to the sideforce.

4.2 Effect of tailplane deflection on $C_Y(\alpha, \beta)$, $C_l(\alpha, \beta)$ and $C_n(\alpha, \beta)$

The large close-coupled tailplanes of present-day combat aircraft, when deflected to provide control in pitch, can affect the force and moments due to sideslip. These contributions to the sideforce, rolling moment and yawing moment vary with the angle of attack. Within some range in the angle of attack their magnitudes for the configuration featured in the free-flight tests are such that it is advisable to include them within the mathematical model adopted for prediction purposes. Nevertheless it is interesting to examine the result of omitting each of the effects in turn individually. These contributions to the force and moment coefficients have been linearized with respect to both sideslip angle and tailplane angle and so give rise to derivatives $C_{Y\beta\eta}(\alpha)$, $C_{l\beta\eta}(\alpha)$ and $C_{n\beta\eta}(\alpha)$.

Ignoring the sideforce derivative $C_{Y\beta\eta}$ has only a small and localized effect on the predicted motion, see Fig 13, in the case of drop 6. For the same drop the omission of $C_{l\beta\eta}$ has a somewhat more persistent effect, but this is still small when compared to the differences that exist between the predicted and measured histories, see Figs 14 and 2.

When the contribution of the tailplane deflection to the yawing moment coefficient due to sideslip, represented by the derivative $C_{n\beta\eta}$, is omitted in the calculation of the motion for drop 6 the effect is little short of startling. Instead of a normal recovery from the post-stall gyration the calculations indicate a departure into a fast, flat spin in opposite sense to the yaw rate experienced earlier in the motion. Examination of the histories of α , β , p , q and r displayed in Fig 15 shows that up to 15 seconds from the release of the aircraft model there is a slight but progressive shift in the oscillations in the variables α , β , p and q particularly in the sideslip angle (β). Superficially the differences do not seem significant but the very oscillatory nature of the motion means that a small shift in phase can result in, for example, the values of the sideslip angle in the two predicted motions being of opposite signs. Thus a careful and detailed analysis of the variation of the different contributions to the total rolling and yawing moment coefficients is necessary in order to explain the precise manner in which the (aircraft) model's behaviour differs according to which mathematical model is used.

The difficulties associated with providing such an explanation are more readily appreciated by reference to the equations of motion, see Appendix 3.

However, there is in these results a clear indication that conditions must be near to critical as regards departure into a spin. As a check on this another computation was made in which $C_{n\beta\eta}$ assumed its non-zero values only over the angle-of-attack range 20° to 50° . The calculated motion is now in fair agreement with the original prediction, that is, with $C_{n\beta\eta}$ as a function of the angle of attack throughout the full range, as shown in Fig 16.

We now examine the motion of drop 7 in the same way. Again it is found that the nature of the motion is hardly affected by the neglect of the sideforce contribution due to the combined effects of sideslip and tailplane angle. The results of this calculation are not displayed. If, however, the rolling moment contribution from the same source is ignored, that is, $C_{l\beta\eta}$ is set to zero, significant, but still undramatic, changes are noted in the history of all the motion variables (see Fig 17). In particular, the angle of attack increases more rapidly and the rate of yaw is numerically larger. It is interesting that the amplitudes of the oscillations are reduced, but the agreement with the test results remains on the same level as for the basic prediction (cf Fig 6). Moreover, there are indications that the prescribed recovery action would be ineffective in the absence of the $C_{l\beta\eta}$ term.

Smaller changes yet occur if the yawing moment due to combined sideslip and tailplane angles is ignored. This involves setting the $C_{n\beta\eta}$ derivative to zero and as can be seen (Fig 18) the effect on the motion is negligible except during the closing stages of the test. Here again the recovery action seems likely to prove ineffective in the absence of the $C_{n\beta\eta}$ term.

4.3 Effect of tailplane deflection on the force and moments generated by differential tailplane deflection (effect of $C_{Y\eta\eta}$, $C_{L\eta\eta}$ and $C_{n\eta\eta}$)

In the free-flight model tests roll control is effected by differential deflection of the port and starboard tailplane panels. The forces and moments generated in this way are subject to appreciable modification according to the amount of tailplane applied and these effects are represented by derivatives, $C_{Y\eta\eta}$, $C_{L\eta\eta}$ and $C_{n\eta\eta}$, which are complicated functions of the angle of attack.

There being no differential tailplane applied in the course of drop 6 the effect of ignoring each of these derivatives in turn can only be examined in relation to drop 7. Once again it is seen that the influence of the sideforce contribution (due to $C_{Y\eta\eta}$) is extremely small except in the recovery stage where it assumes some significance in the reduction of the magnitude of the rate of yaw (see Fig 19). Neglect of the rolling moment contribution, however, has a dramatic effect on the predicted motion (see Fig 20). Instead of an entry into spin conditions, as in the original prediction, the calculations now yield numerically much reduced rates of yaw and a containment of the angle of attack. This results in a return to low angle-of-attack conditions and the calculation is terminated by want of data for negative angles of attack. The values of all the motion variables begin to differ from the instant at which differential tailplane is applied (about 7.5 seconds). These differences are most pronounced in the case of the yaw rate during the next 2 seconds, see Fig 20.

Neglect of the yawing moment due to combined differential and symmetrical tailplane deflection has a significant, if less dramatic, effect on the motion associated with the control inputs for drop 7 as can be seen from Fig 21. Here again there are indications of the inadequacy of the prescribed recovery action when $C_{n\eta\eta}$ is taken as zero.

4.4 The effect of tailplane deflection on the damping-in-yaw (influence of the $C_{nr\eta}$ term)

Wind-tunnel tests also indicate that the damping-in-yaw moment would be dependent on the tailplane deflection and this is represented by a derivative $C_{nr\eta}$ in the basic mathematical model. Such a moment derivative arises in much the same manner as the corresponding sideslip derivative, $C_{n\beta}$. If in the calculation of the motion for drops 6 and 7 this additional damping term is ignored the motion changes to that displayed in Figs 22 and 23. Here again both calculations would predict entry in much the same manner into the fast, flat spin, but with no $C_{nr\eta}$ term the indications are that the spin motion persists in spite of the attempt to recover.

4.5 Influence of cross-coupling terms (C_{nq} and C_{mr})

In Ref 2 Orlik-Rückemann has demonstrated that at large angles of attack significant forces and moments of a cross-coupling nature can arise. Unfortunately no wind-tunnel data of this kind are available for the configuration which forms the subject of this investigation. To provide some assessment of the relative importance of these terms in the calculation of the motion for the inputs of drops 6 and 7 it is assumed that C_{nq} has the constant value of 0.25 in the angle-of-attack range indicated in Figs 24 and 25 and is otherwise zero.

The assumed non-zero values of C_{mr} are given in Fig 26.

In both the cases examined the inclusion of a term in C_{nq} of the above magnitude produces some significant localized difference, but the overall effect on the two motions is small, see Figs 24 and 25.

The influence of including non-zero values of C_{mr} on the predicted motions for drops 6 and 7 is small and so only the results for drop 7 are displayed, see Fig 26.

It is important to stress that the values assumed for the two derivatives C_{nq} and C_{mr} are arbitrary. In particular, these derivatives are certain to exhibit greater variation with angle of attack than is implied in these assumed values. The derivative C_{Lq} , which has not featured in the present sensitivity study, is probably smaller and more subject to variation with angle of attack.

5 CONCLUDING REMARKS

The present preliminary examination of the nature of what is likely to constitute an adequate mathematical model of an aircraft for the calculation of large excursion motion such as encountered in spin entry conditions has led to the following specific conclusions.

- (1) Only a specially designed series of wind-tunnel tests in combination with free-flight model tests can provide a comprehensive validation of the basic framework for the mathematical model of an aircraft for the above mentioned flight conditions.
- (2) In addition to this fundamental role, the free-flight model is a useful vehicle for the testing of recovery techniques, influence of control systems and spin prevention systems. It, therefore, has an important part to play in the testing of specific projects and their systems.
- (3) Comparison of predicted and measured motion histories indicate some shortcomings in the particular mathematical model used for the predictions. A mathematical model adhering more closely to the proposed form discussed in the text could be more successful. However, it has not been possible, at this stage, to construct from the available aerodynamic data a mathematical model based on any of the three basic steady coning motions, but it is hoped that this will be attempted in the near future.

(4) It seems that free-flight test technique yields data of a sufficiently high quality to permit analysis using parameter identification techniques.

(5) The sensitivity of the predicted motions to detailed changes in the mathematical model as determined by the addition or omission of certain terms leads to the following observations.

(a) The motion, in each case, is relatively insensitive to changes in the sideforce coefficient contributions from sources other than sideslip (and possibly rudder) alone.

(b) It is difficult to generalize about how changes in the effect of tailplane deflection on the rolling and yawing moments due to sideslip affect the calculations, as their influence can vary from one type of motion to another. It is considered advisable to include such terms unless there is good reason to suppose that the derivatives themselves are numerically very small.

(c) In the case of an aircraft equipped with differential tailplane for roll control it seems essential to include the effect of the symmetric deflection of the tailplane (elevator effect) on both the rolling and the yawing moments due to the differential deflection.

(d) Other cross-coupling terms seem relatively unimportant.

(e) There is no clear indication that adjustment of even the more important aerodynamic effects listed above could significantly improve the overall match of the predicted and the measured motion.

(6) The partial success in calculating the response of the aircraft model to the various control inputs suggests that some of the simplifications discussed in section (3.3) are justified in the present application.

NOTATION

The notation used here is basically that of R & M 3562 (Ref 1).

Aerodynamic coefficients

$$C_x = \frac{X}{\frac{1}{2}\rho V^2 S}, \quad C_y = \frac{Y}{\frac{1}{2}\rho V^2 S}, \quad C_z = \frac{Z}{\frac{1}{2}\rho V^2 S}$$

$$C_l = \frac{L}{\frac{1}{2}\rho V^2 S b}, \quad C_m = \frac{M}{\frac{1}{2}\rho V^2 S \bar{c}}, \quad C_n = \frac{N}{\frac{1}{2}\rho V^2 S b}.$$

Thus the representative lengths used are

$l = l_1 = \bar{c}$ for longitudinal motion quantities,

$l = l_2 = b$ for lateral motion quantities.

Coefficient derivatives are based on these and differ from the usual US derivatives, in particular,

$$C_{mr} = \frac{1}{2} C_{m_r} = \frac{1}{2} \frac{\partial C_m}{\partial \left(\frac{rb}{V} \right)}$$

$$C_{nq} = \frac{1}{2} C_{n_q} = \frac{1}{2} \frac{\partial C_n}{\partial \left(\frac{qb}{V} \right)}.$$

In Fig 10 the derivatives plotted are the usual US derivatives, eg

$$C_{lp} = \left\{ \frac{\partial C_l}{\partial \left(\frac{pb}{2V} \right)} \right\}_e.$$

REFERENCES

- 1 H. R. Hopkin, 'A scheme of notation and nomenclature for aircraft dynamics and associated aerodynamics', ARC R & M 3562 (Parts 1 to 5) (1966)
- 2 M. Tobak, L. B. Schiff, 'On the formulation of the aerodynamic characteristics in aircraft dynamics', NASA TR R-456 (1976)

Copyright

©
Controller, HMSO, London
1978

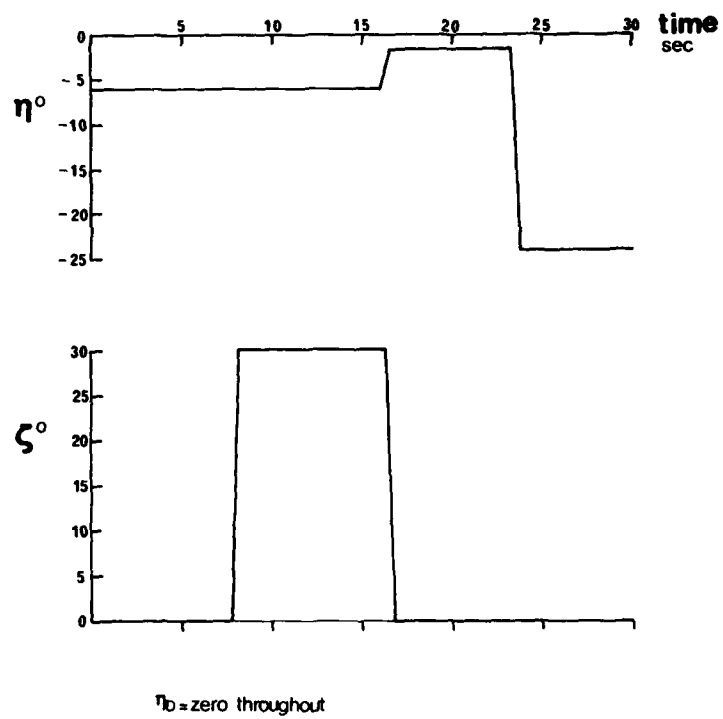


Fig 1 Control-surface inputs for drop 6 (post-stall gyration)

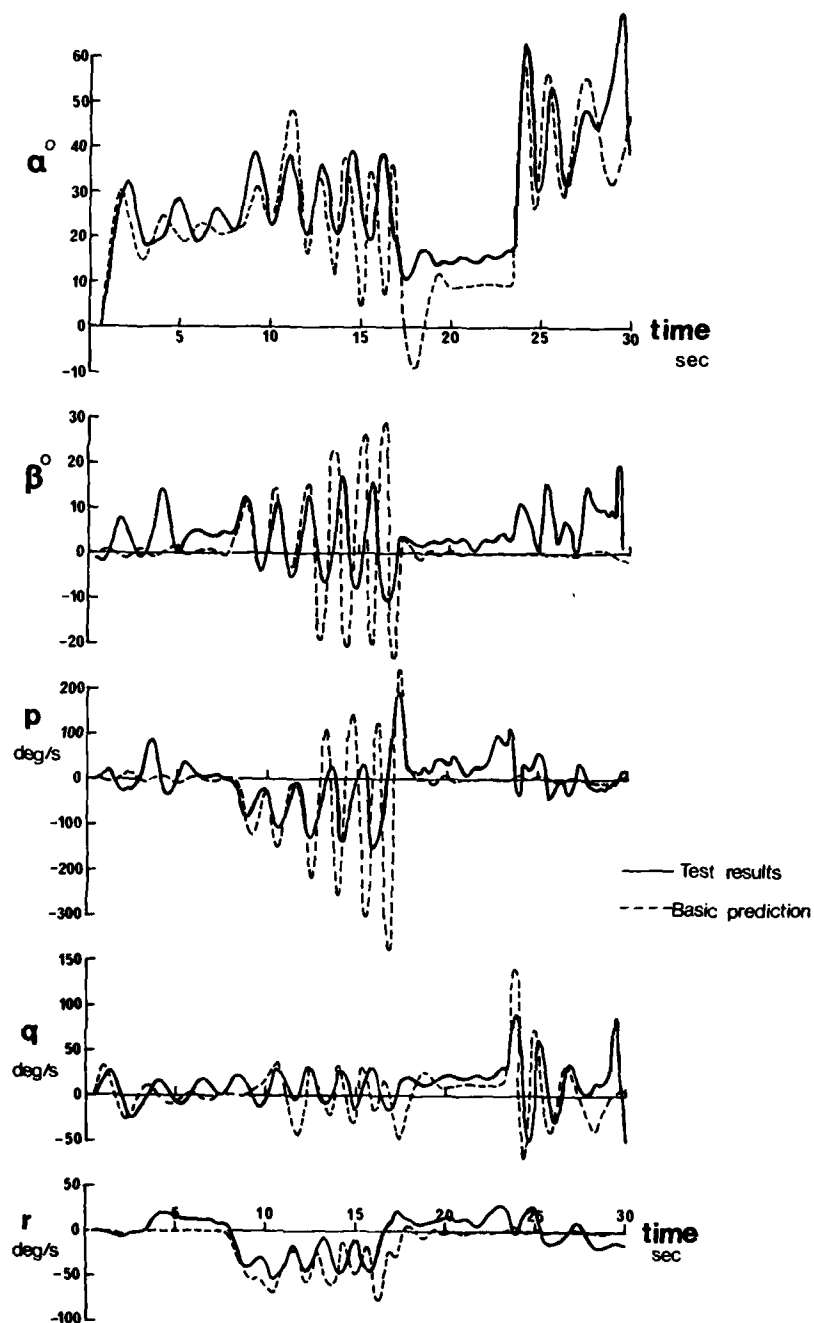


Fig 2 Histories of certain motion variables during drop 6
(comparison of measured and predicted values)

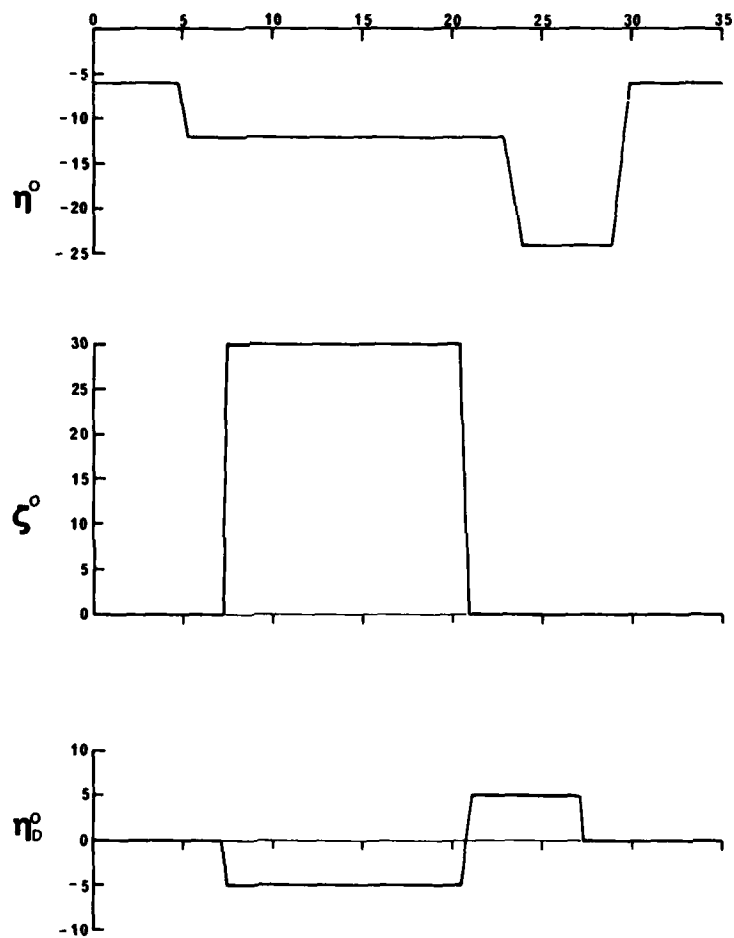


Fig 3 Control-surface inputs for drop 4 (entry into and recovery from moderately steep spin)

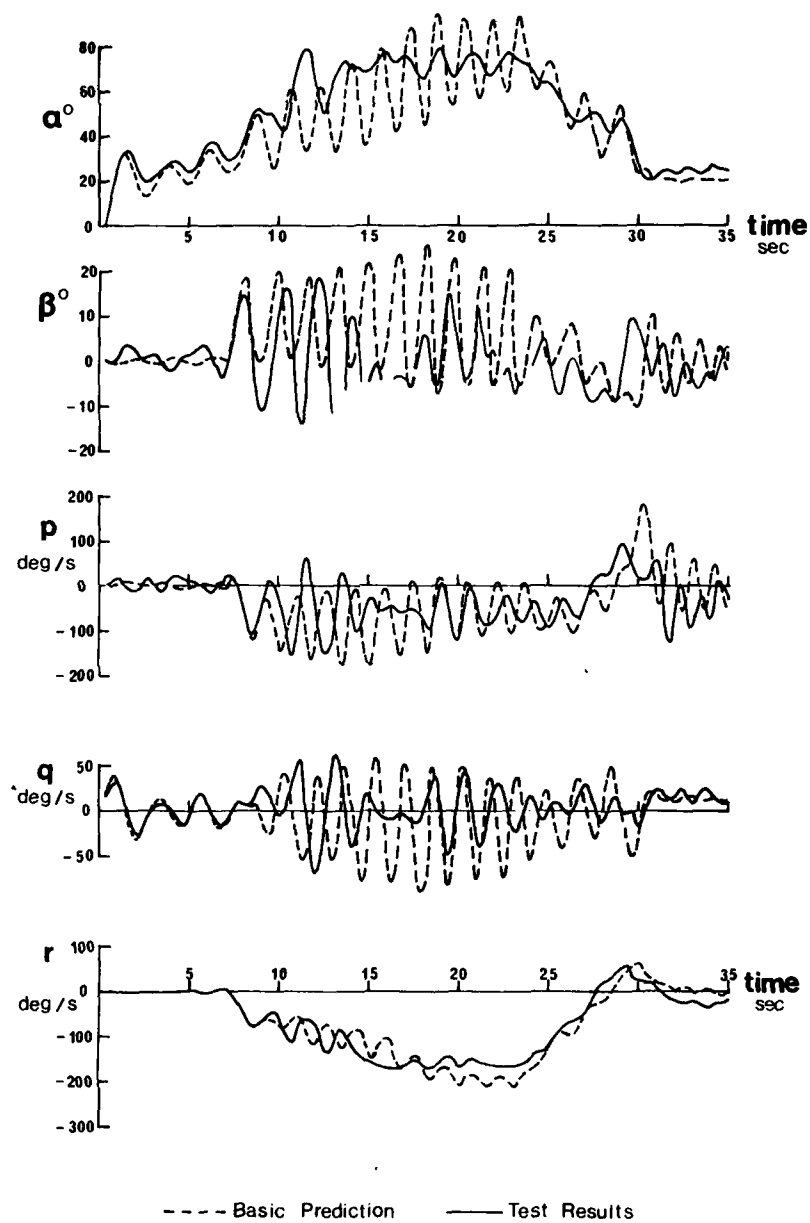


Fig 4 Histories of certain motion variables during drop 4
(comparison of measured and predicted values)

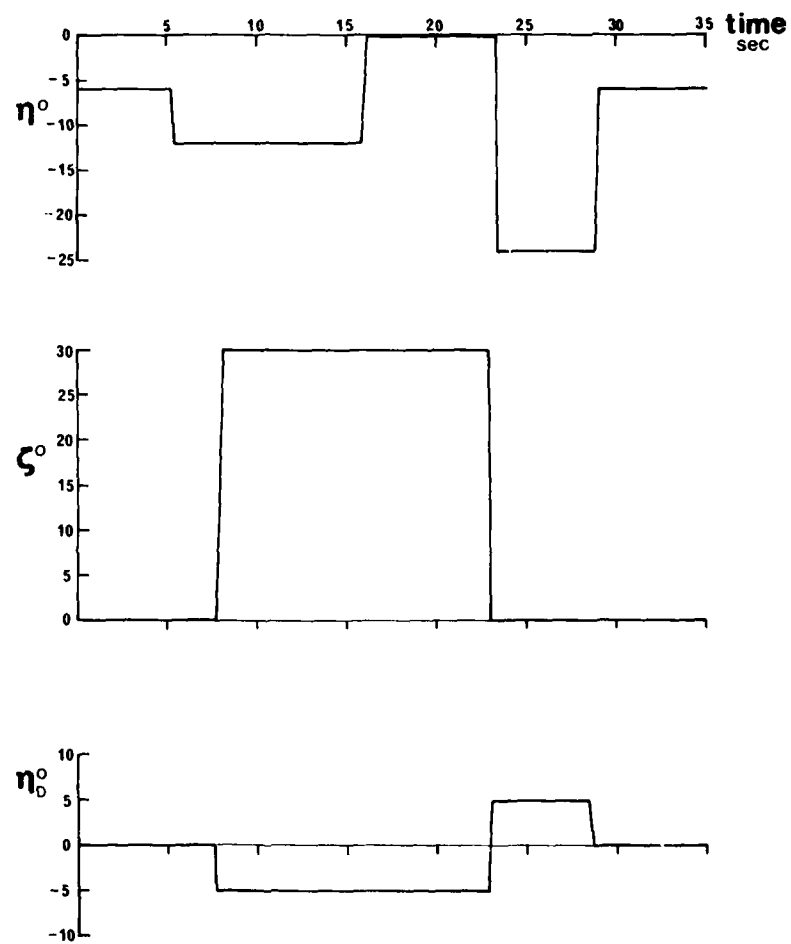


Fig 5 Control-surface inputs for drop 7 (entry into and recovery from a fast, flat spin)

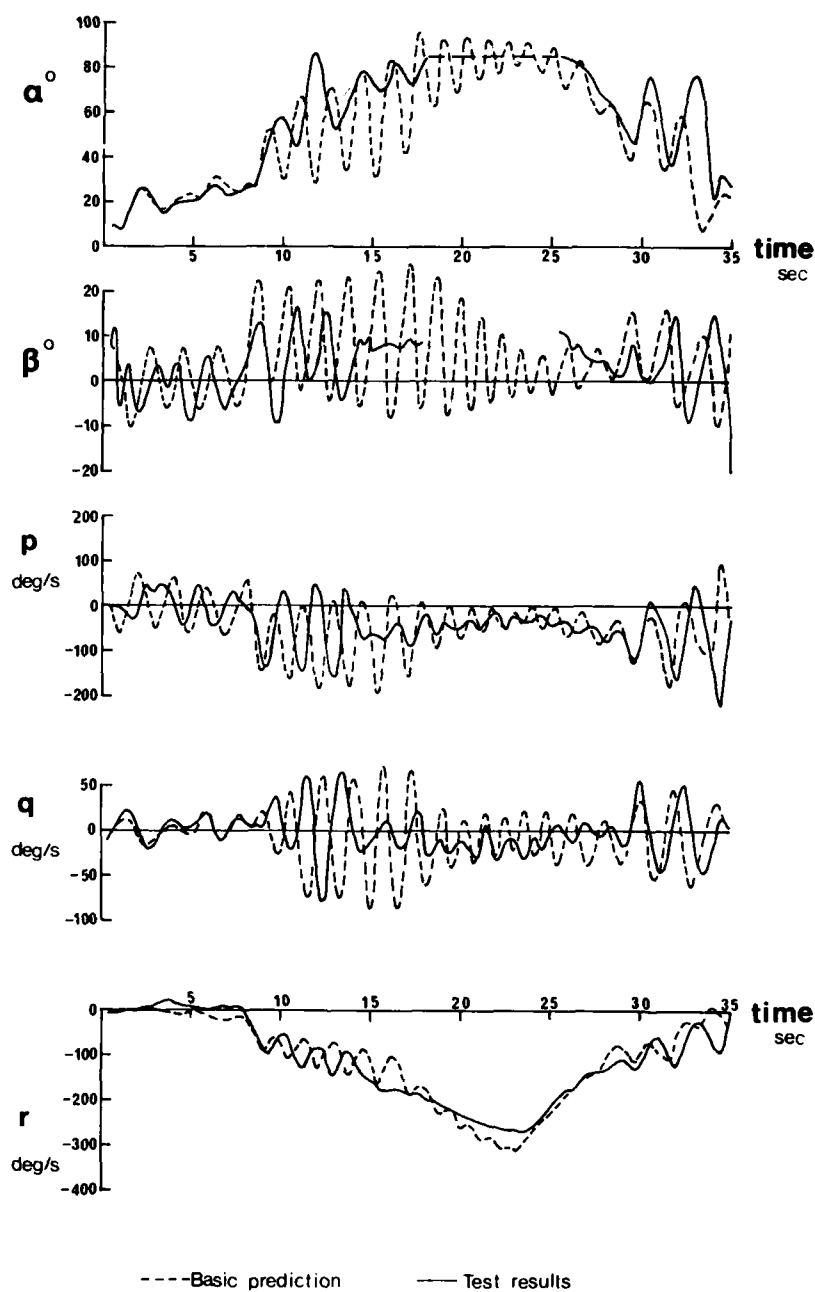


Fig 6 Histories of certain motion variables during drop 7
 (comparison of measured and predicted values)

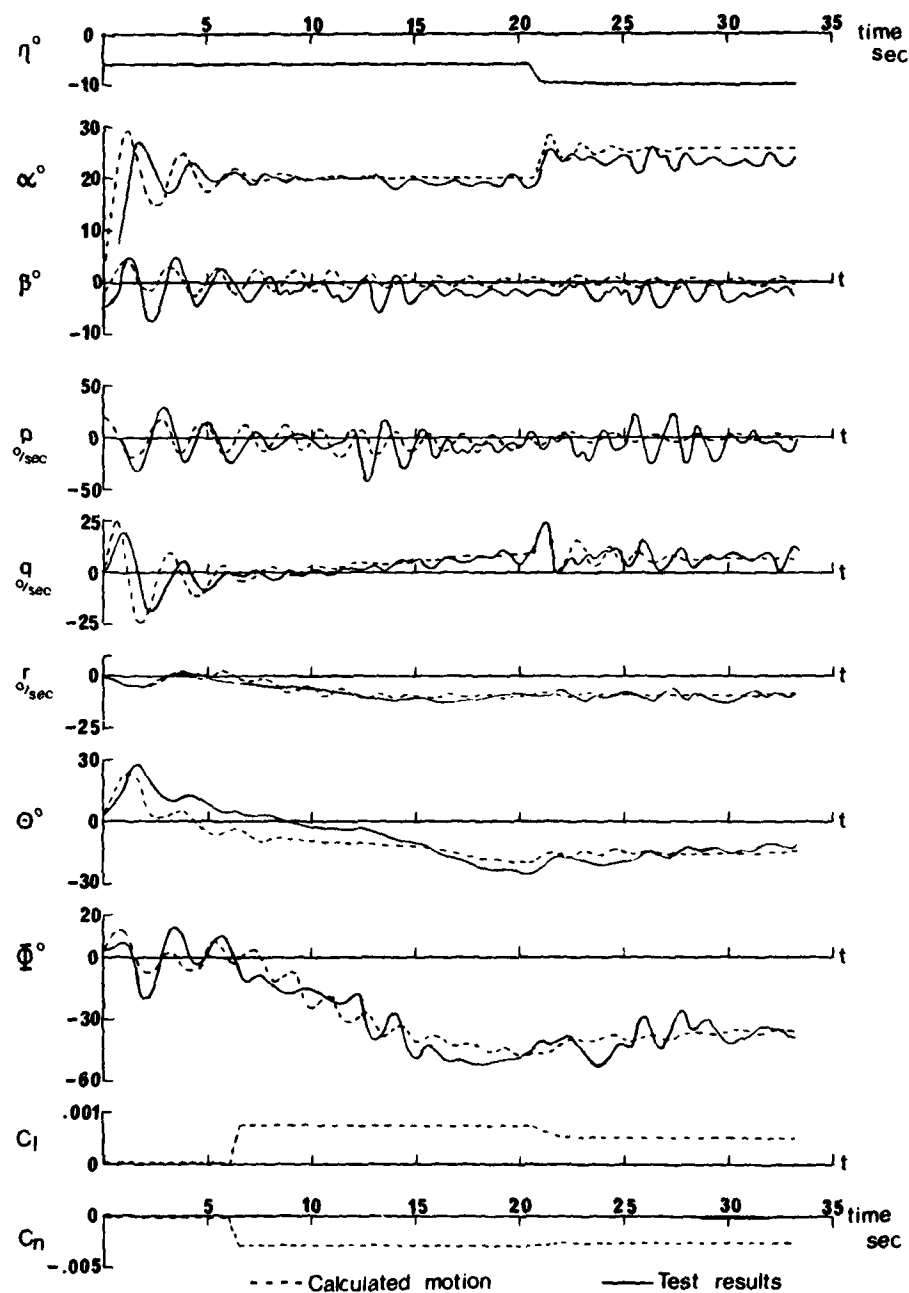


Fig 7 Match obtained using derivatives identified in Fig 8 for a Dutch roll oscillation about $\alpha = 19^\circ$

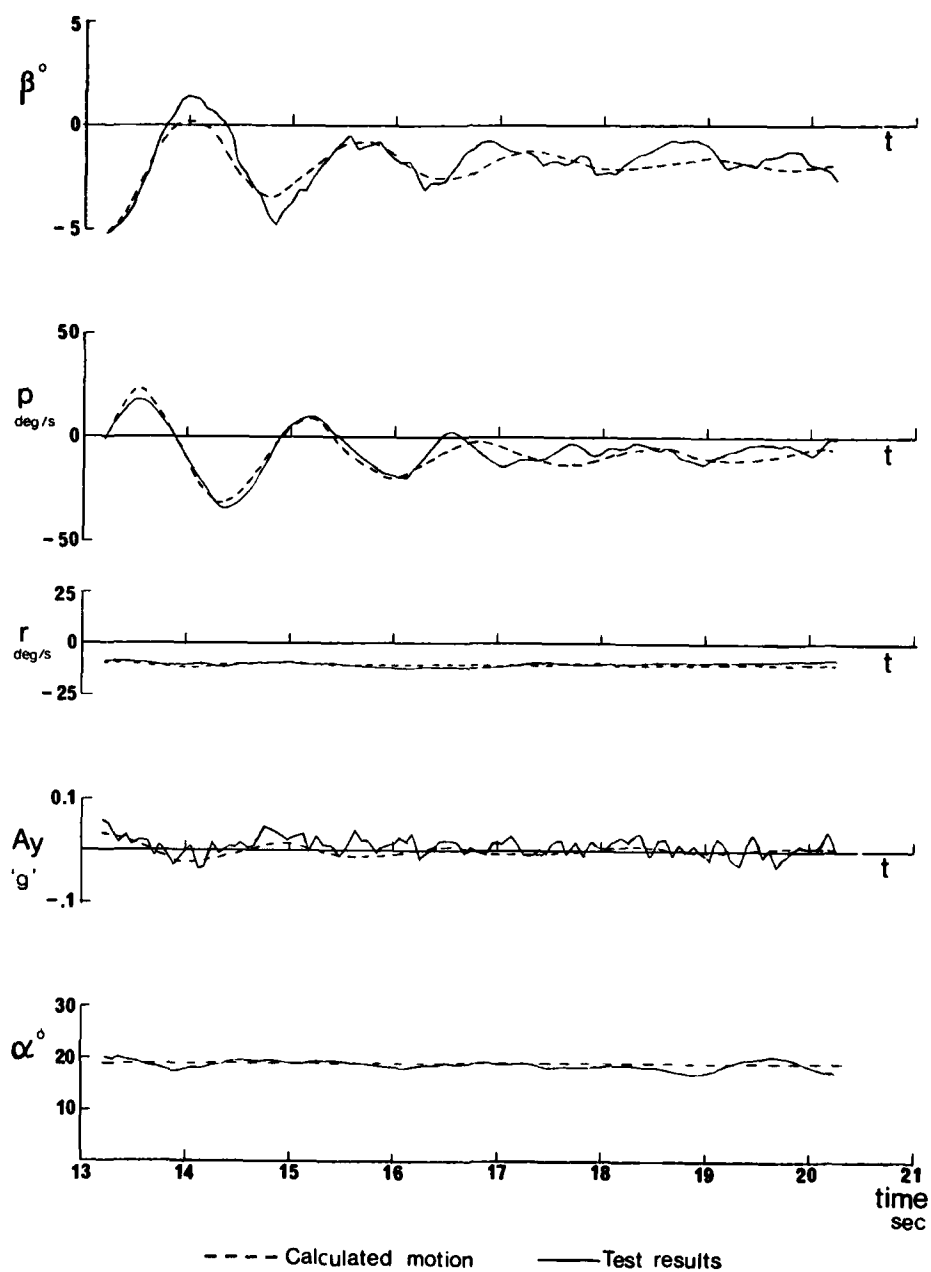


Fig 8 Matched histories of a calculated and measured motion (drop 9)

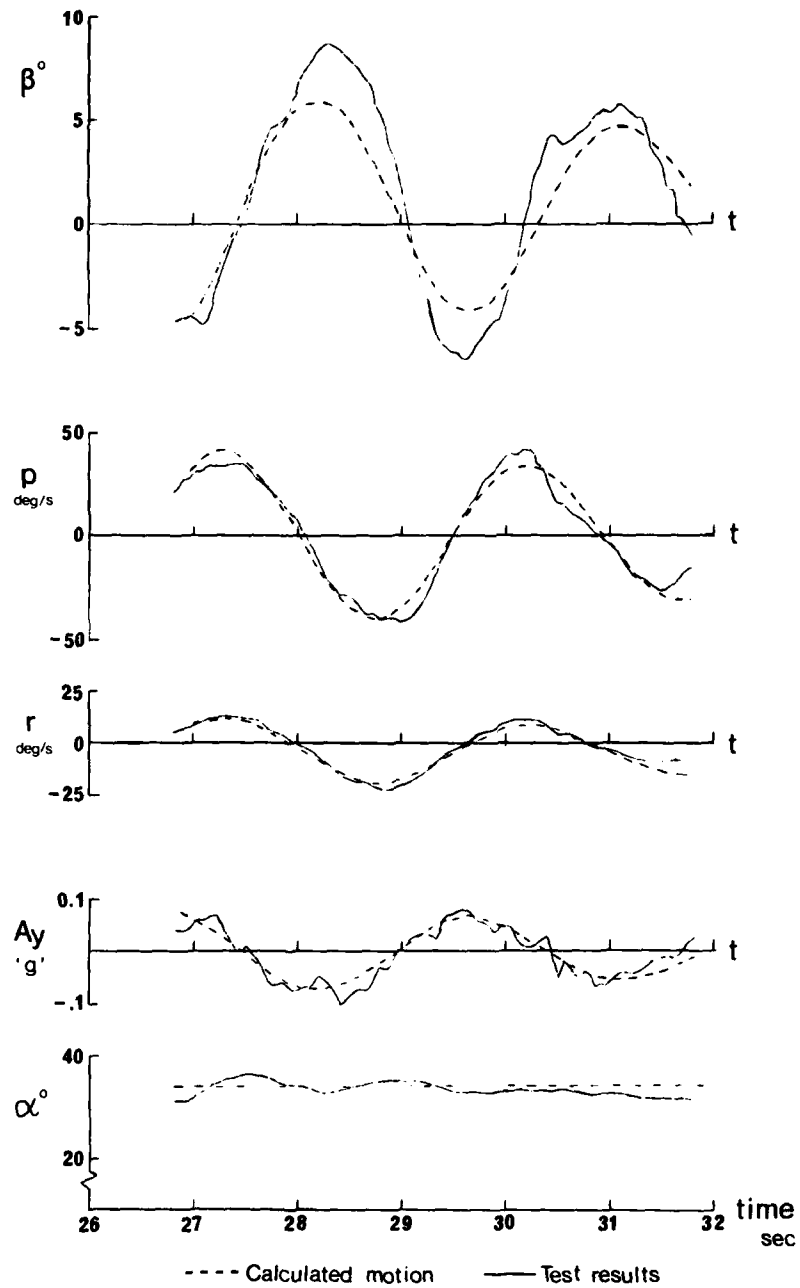


Fig 9 Matched histories of a calculated and measured motion (drop 10)

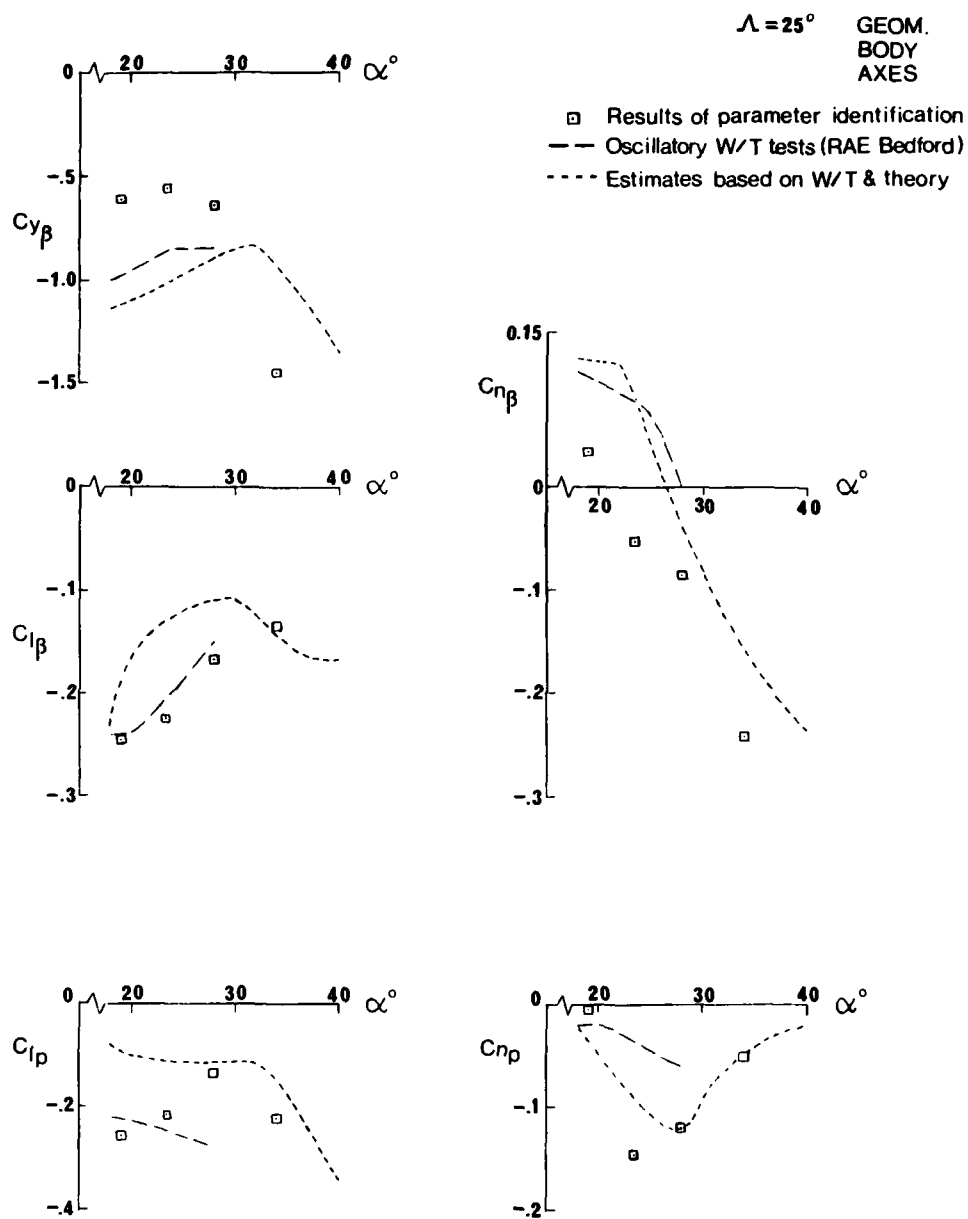


Fig 10 Analysis of Dutch roll oscillations

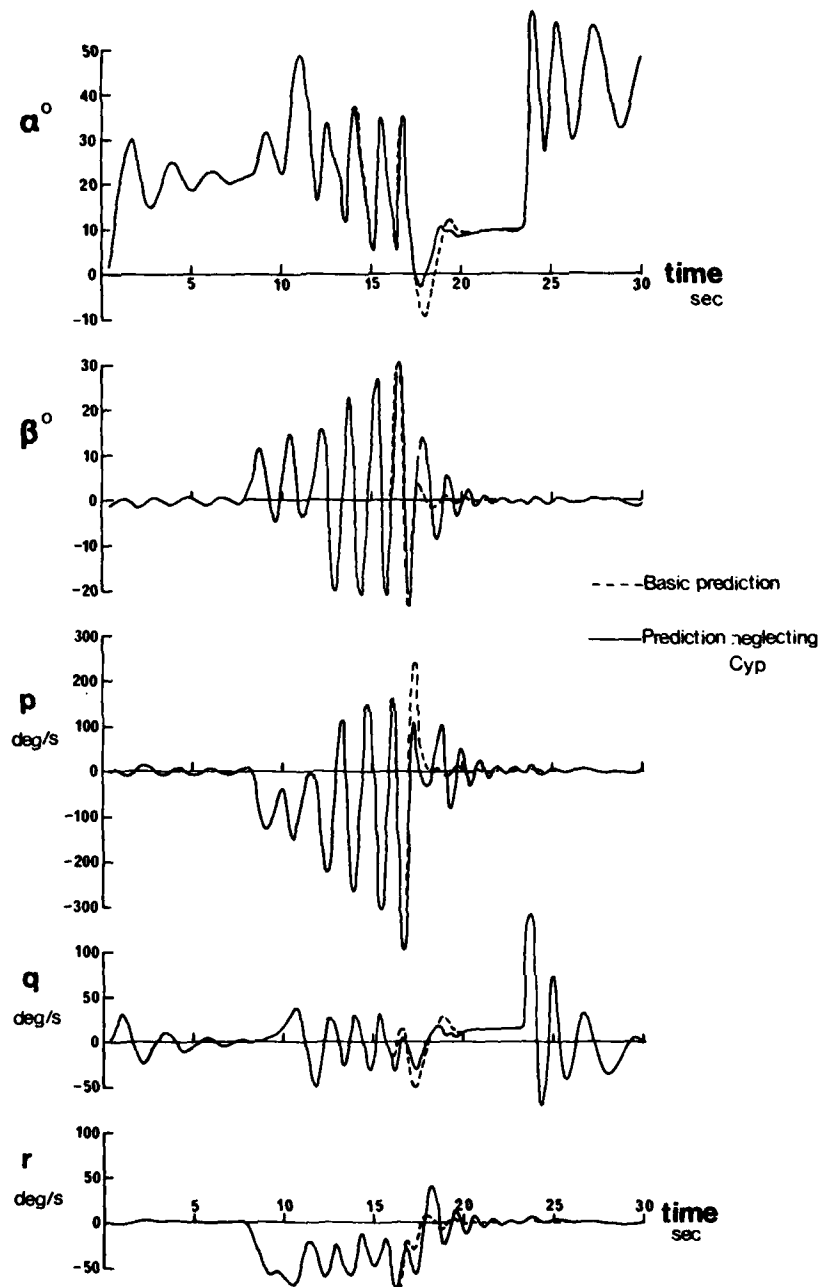


Fig 11 Effect of ignoring the sideforce due to rate of roll on the predicted motion for drop 6

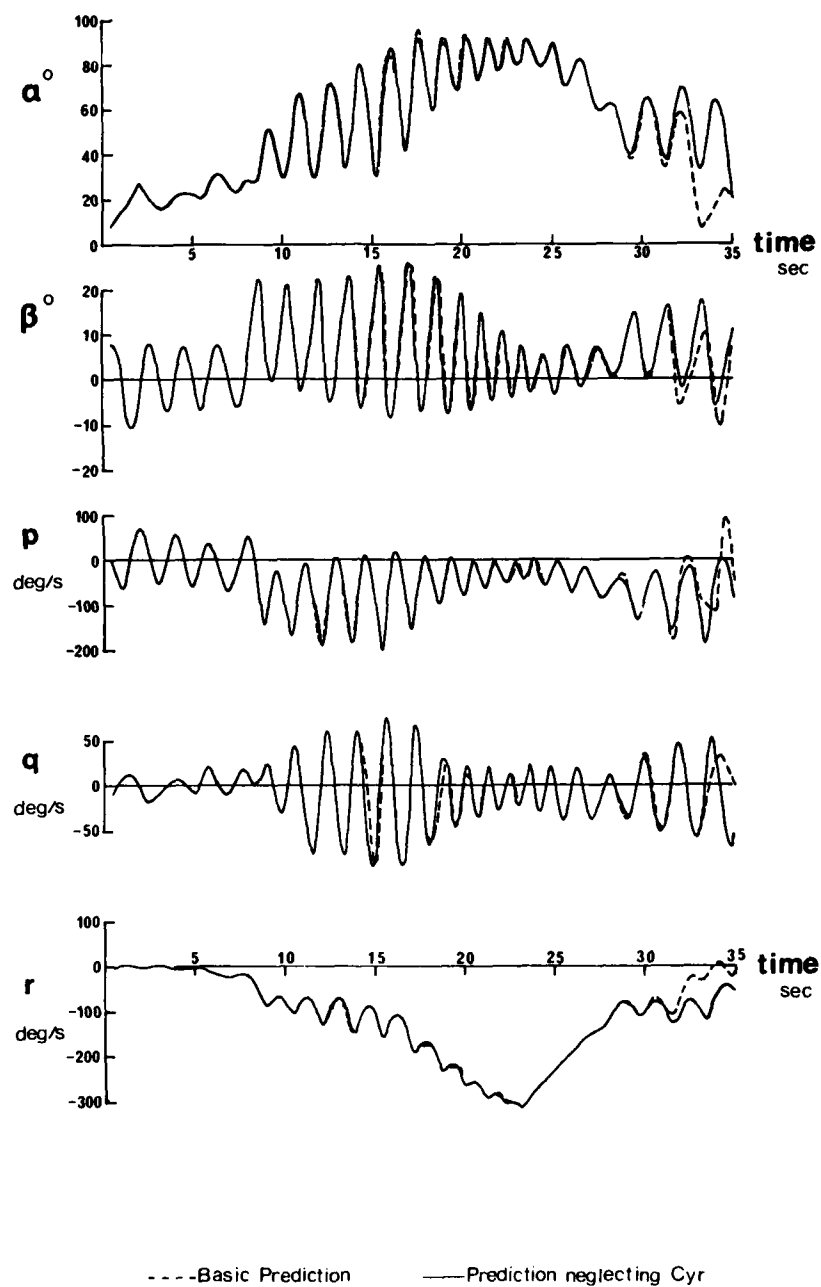


Fig 12 Effect of ignoring the sideforce due to rate of yaw on the predicted motion for drop 7

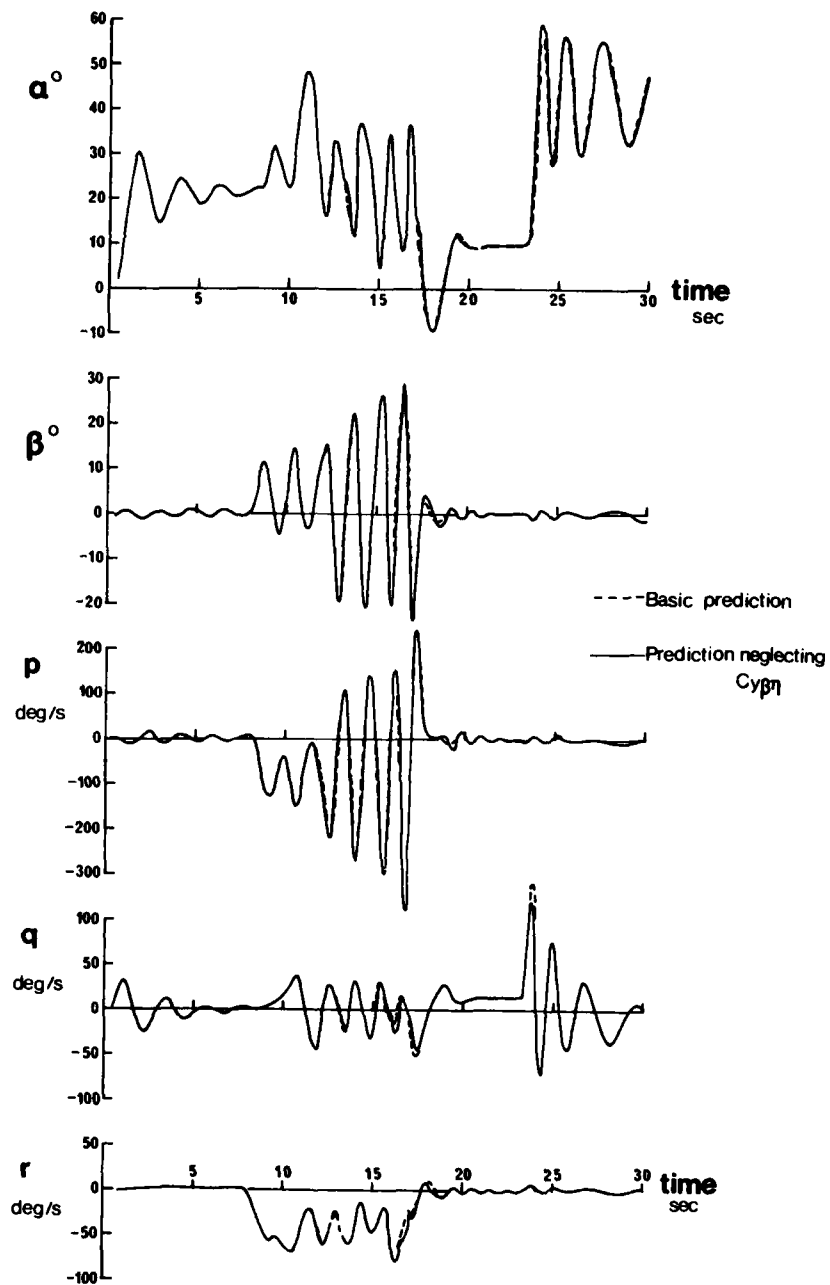


Fig 13 Effect of ignoring the sideforce due to combined side-slip and tailplane angle on the predicted motion for drop 6

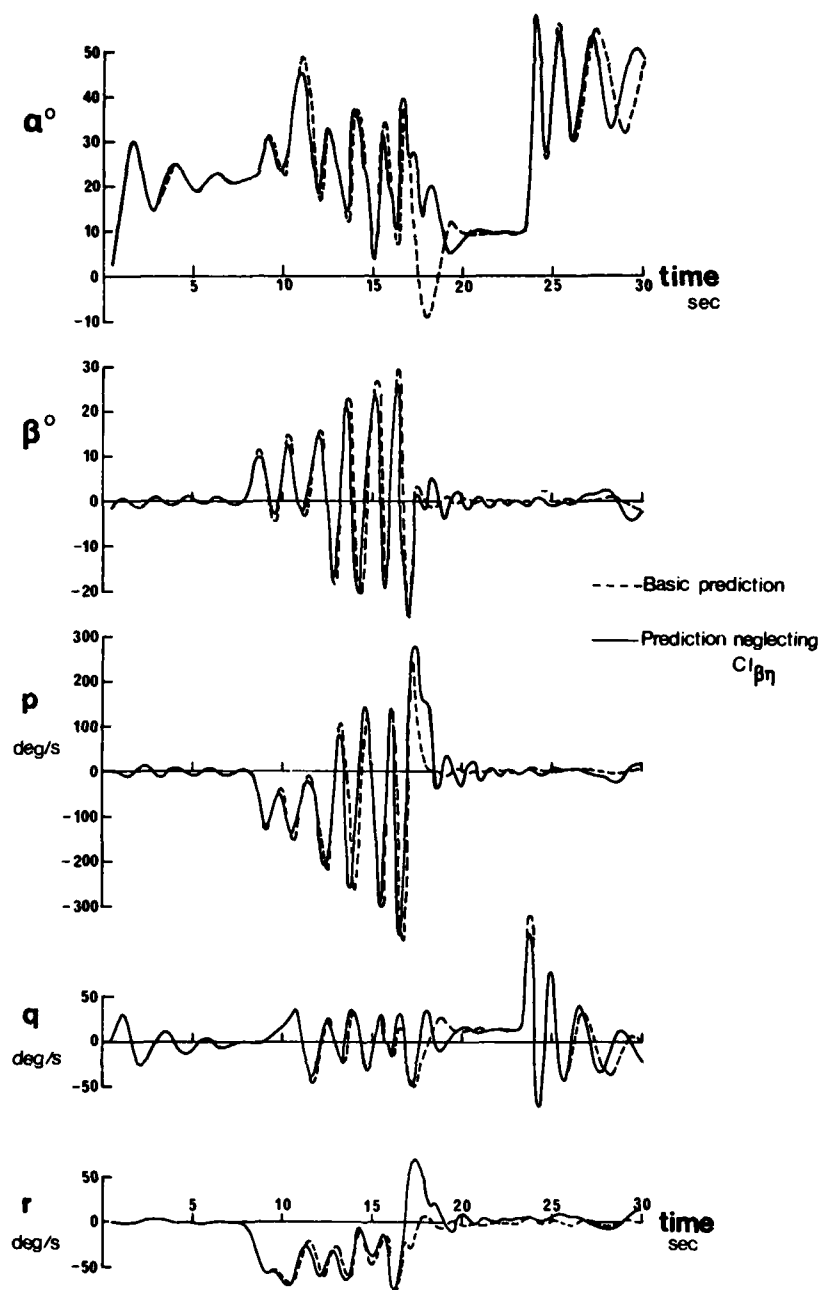


Fig 14 Effect of ignoring the rolling moment due to combined sideslip and tailplane deflection on the predicted motion for drop 6

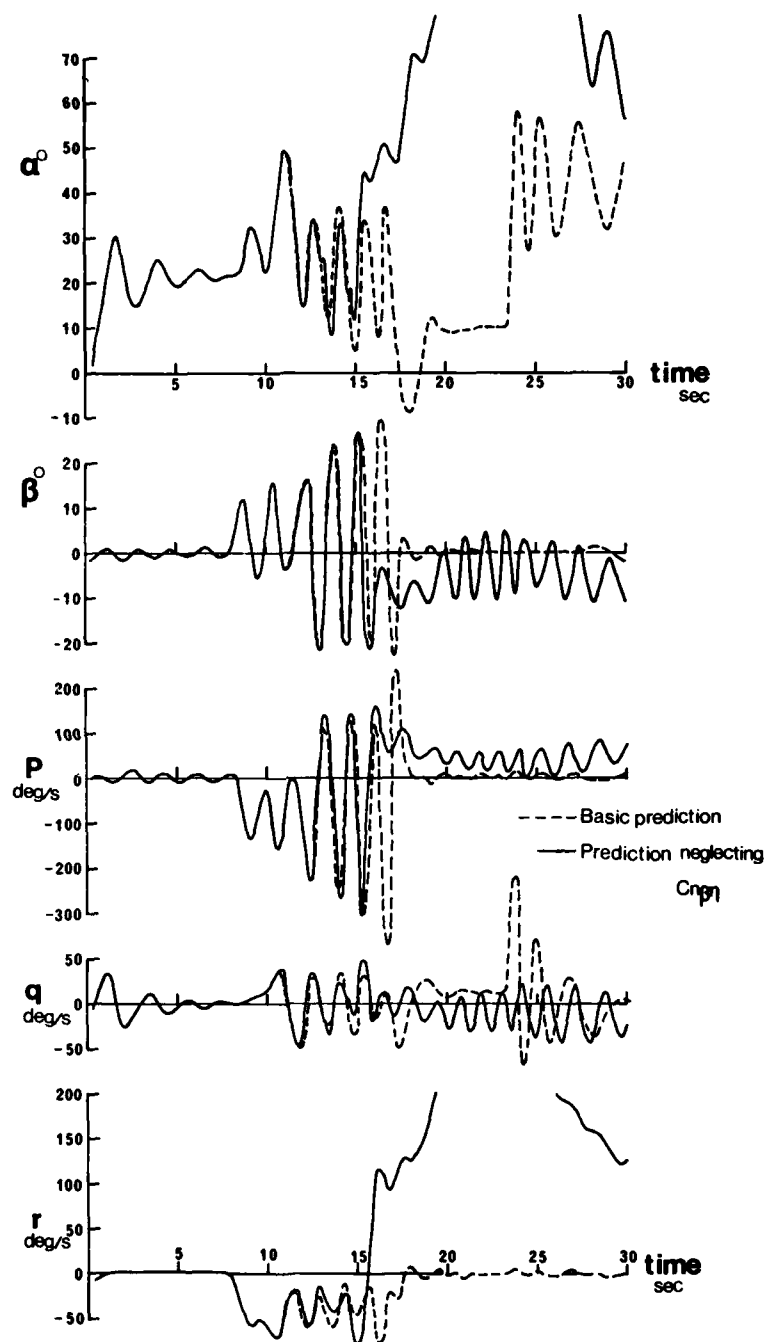


Fig 15 Effect of ignoring the yawing moment due to combined sideslip and tailplane deflection on the predicted motion for drop 6

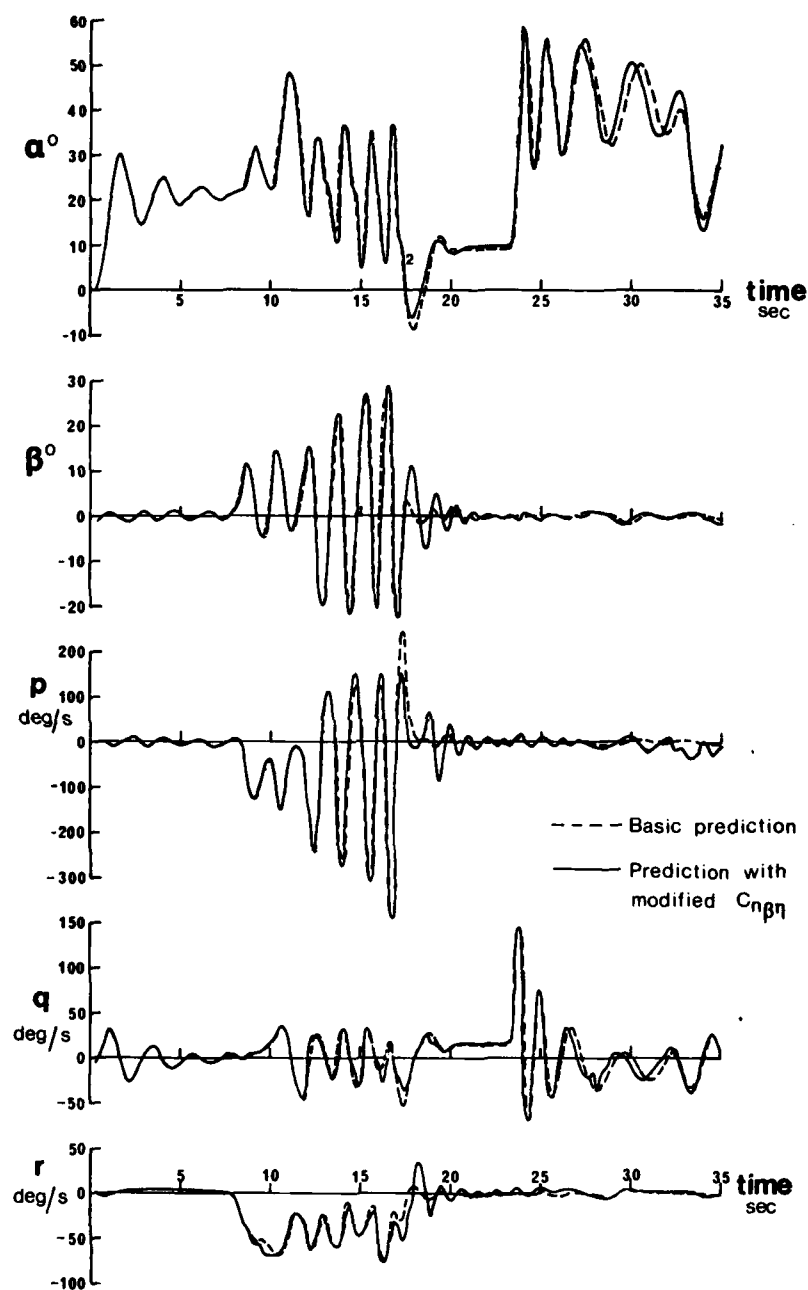


Fig 16 Effect of a modified yawing moment due to combined sideslip and tailplane deflection on predicted motion for drop 6 (see section (4.2))

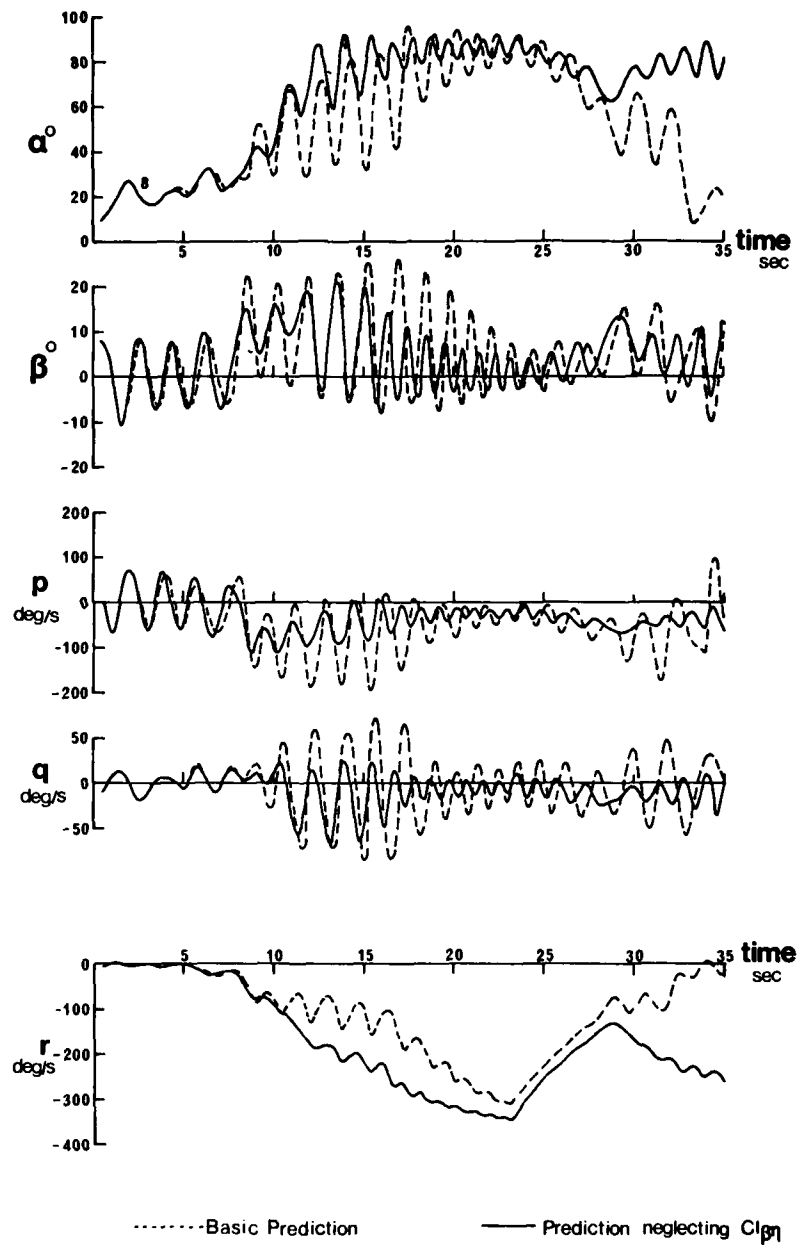


Fig 17 Effect of ignoring the rolling moment due to combined sideslip and tailplane deflection on predicted motion for drop 7

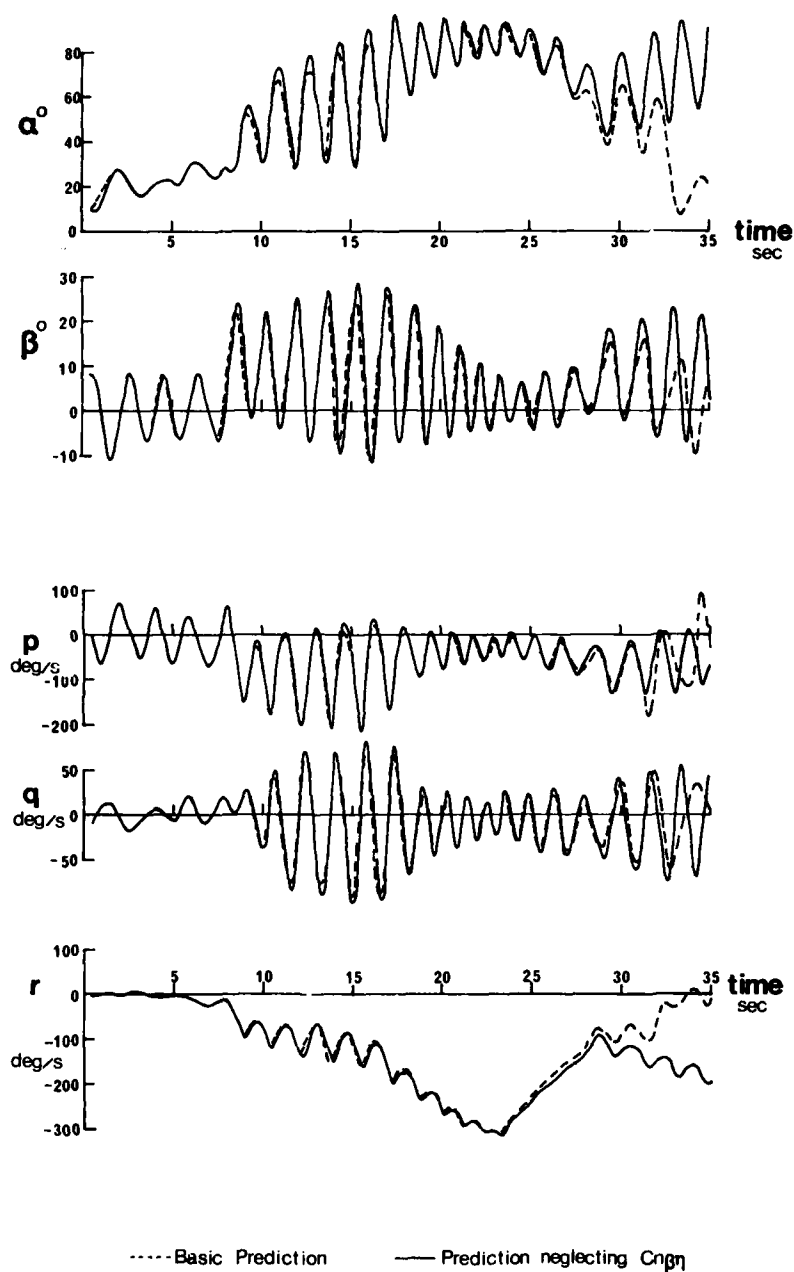


Fig 18 Effect of ignoring the yawing moment due to combined sideslip and tailplane deflection on the predicted motion for drop 7

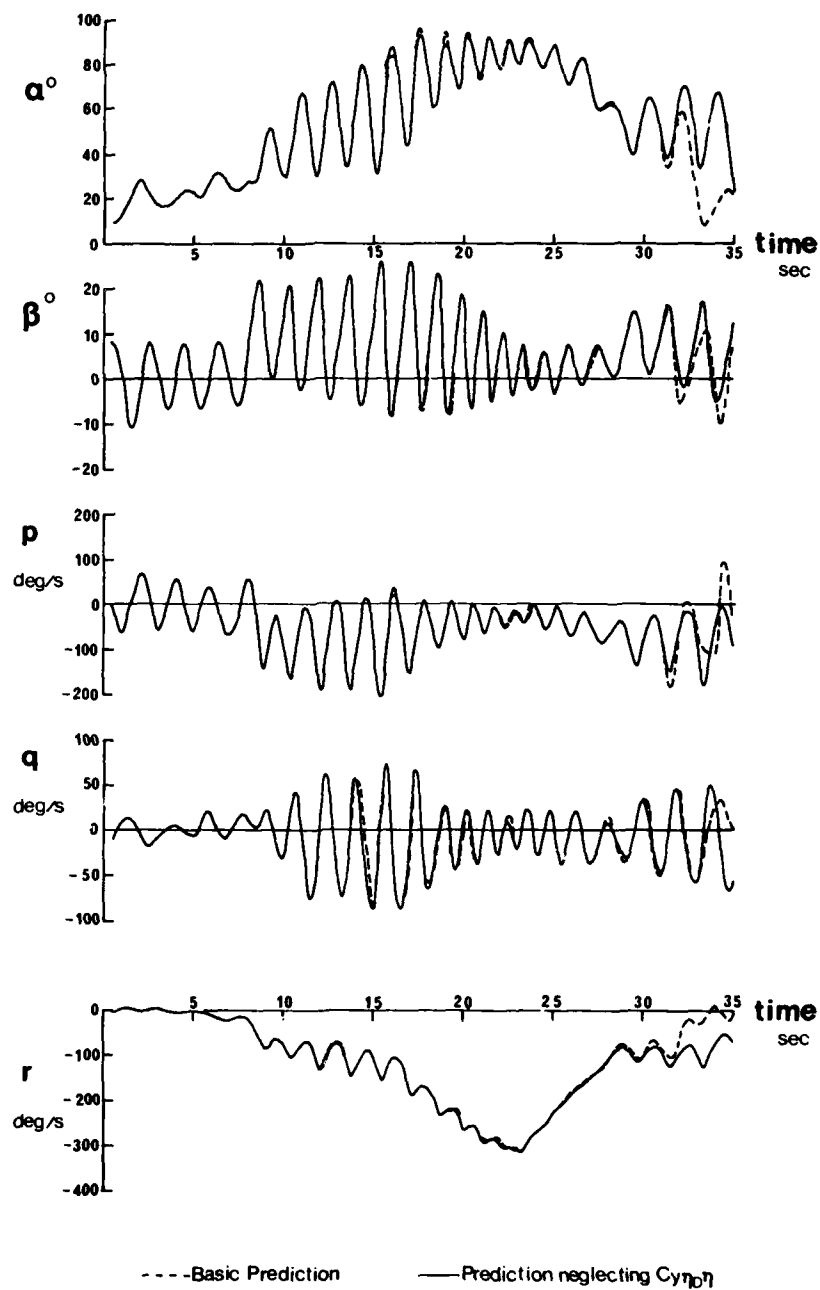


Fig 19 Effect of ignoring the sideforce due to combined differential and symmetrical tailplane deflection on predicted motion for drop 7

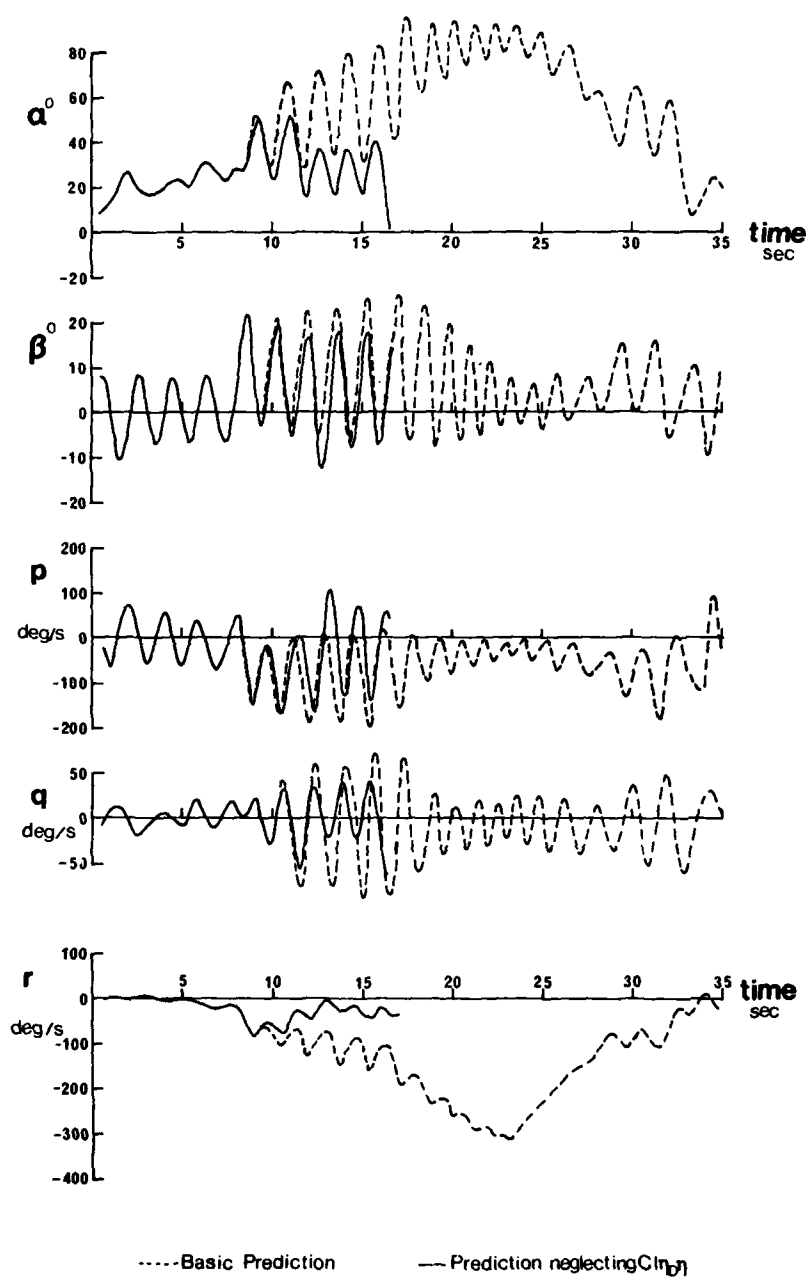


Fig 20 Effect of ignoring the rolling moment due to combined differential and symmetrical tailplane deflection on the predicted motion for drop 7

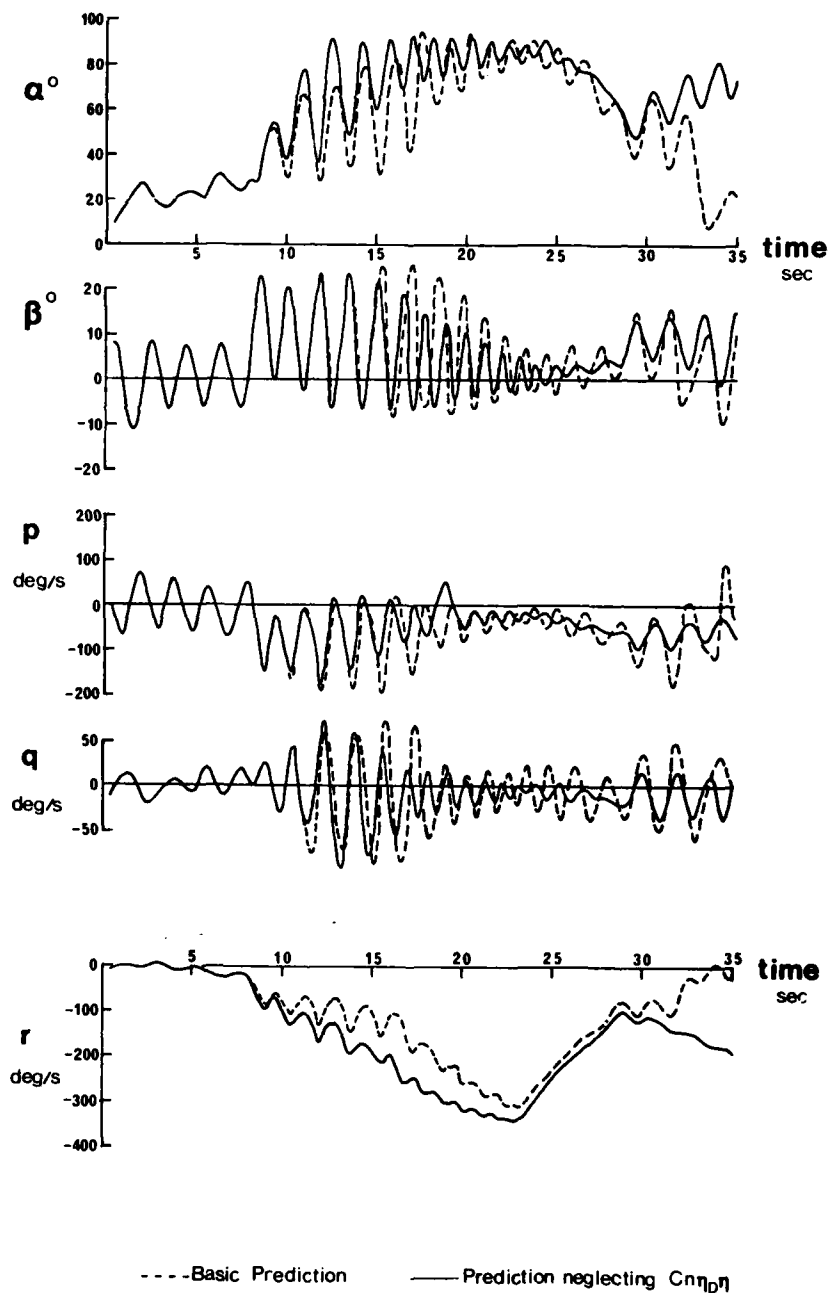


Fig 21 Effect of ignoring the yawing moment due to combined differential and symmetrical tailplane deflection on the predicted motion for drop 7

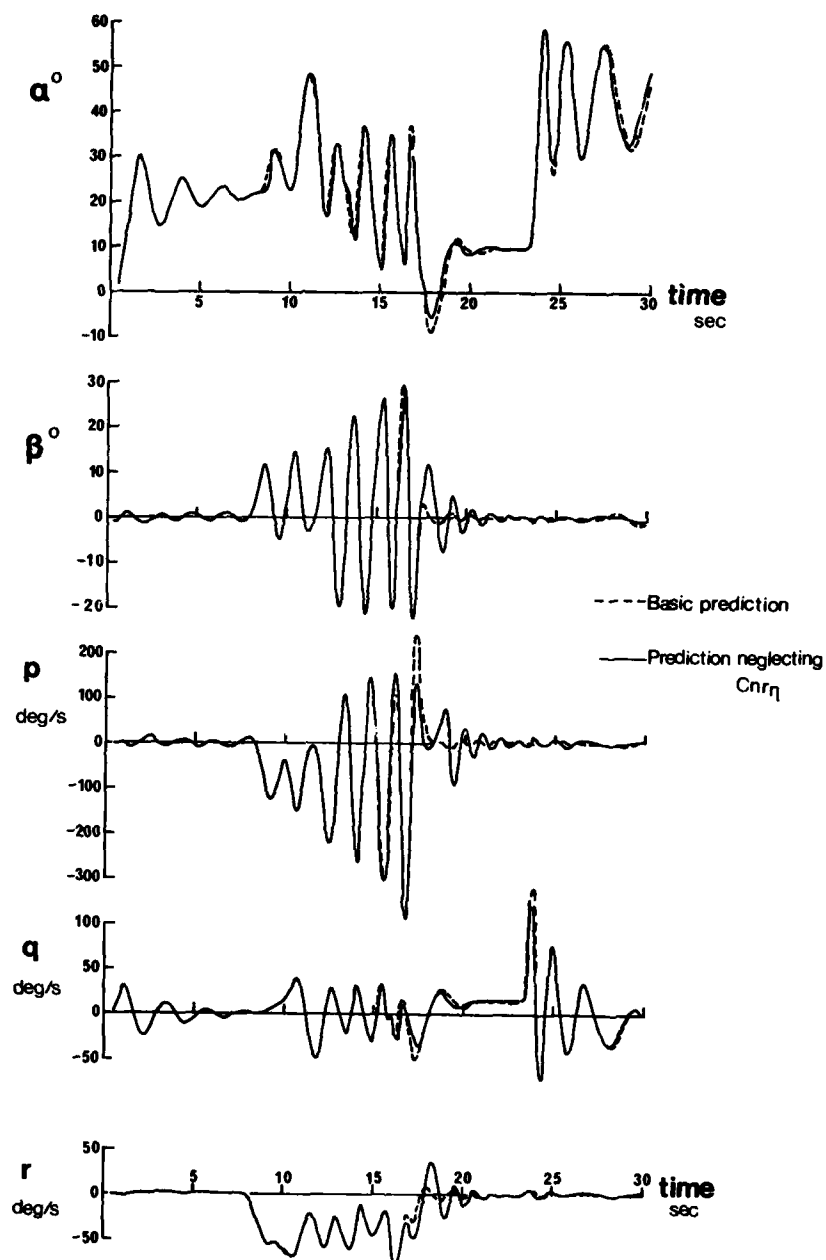


Fig 22 Effect of ignoring the yawing moment due to combined rate of yaw and tailplane deflection on the predicted motion for drop 6

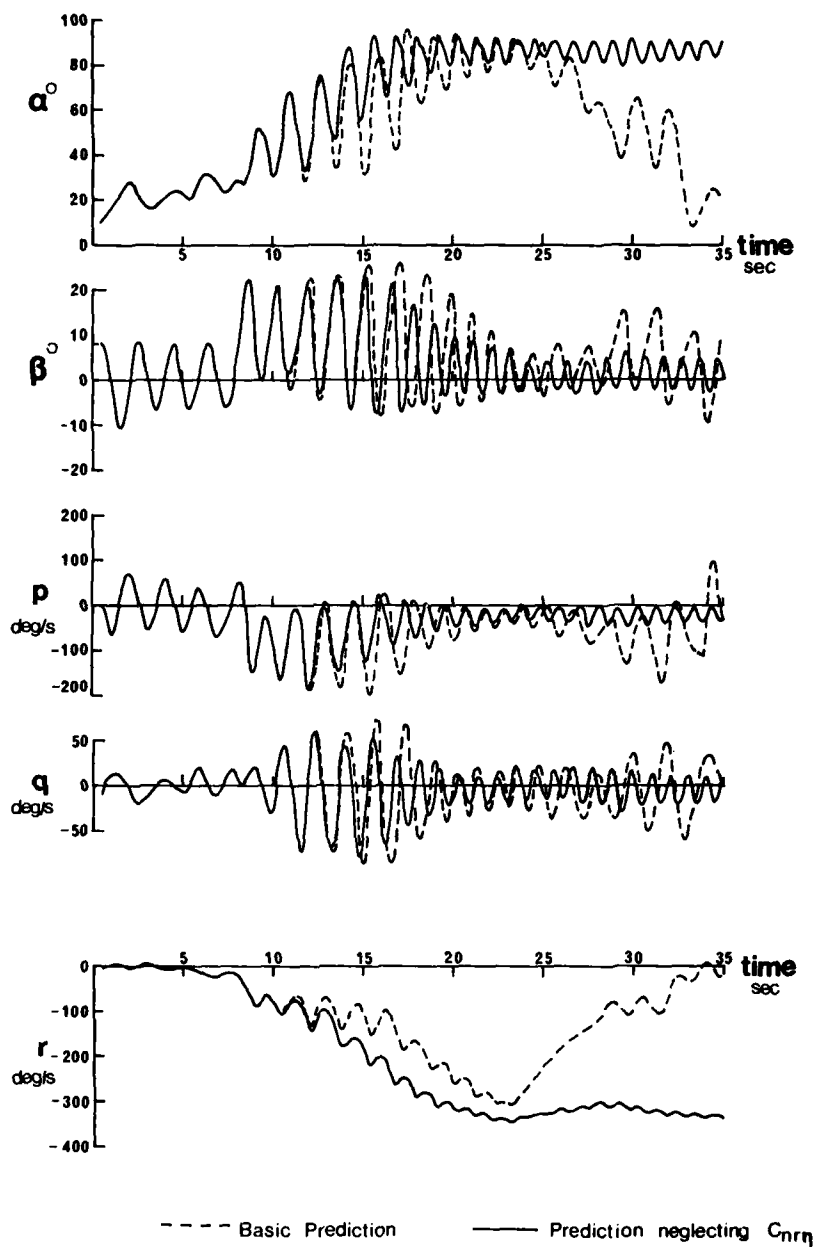


Fig 23 Effect of ignoring the yawing moment due to combined rate of yaw and tailplane deflection on the predicted motion for drop 7

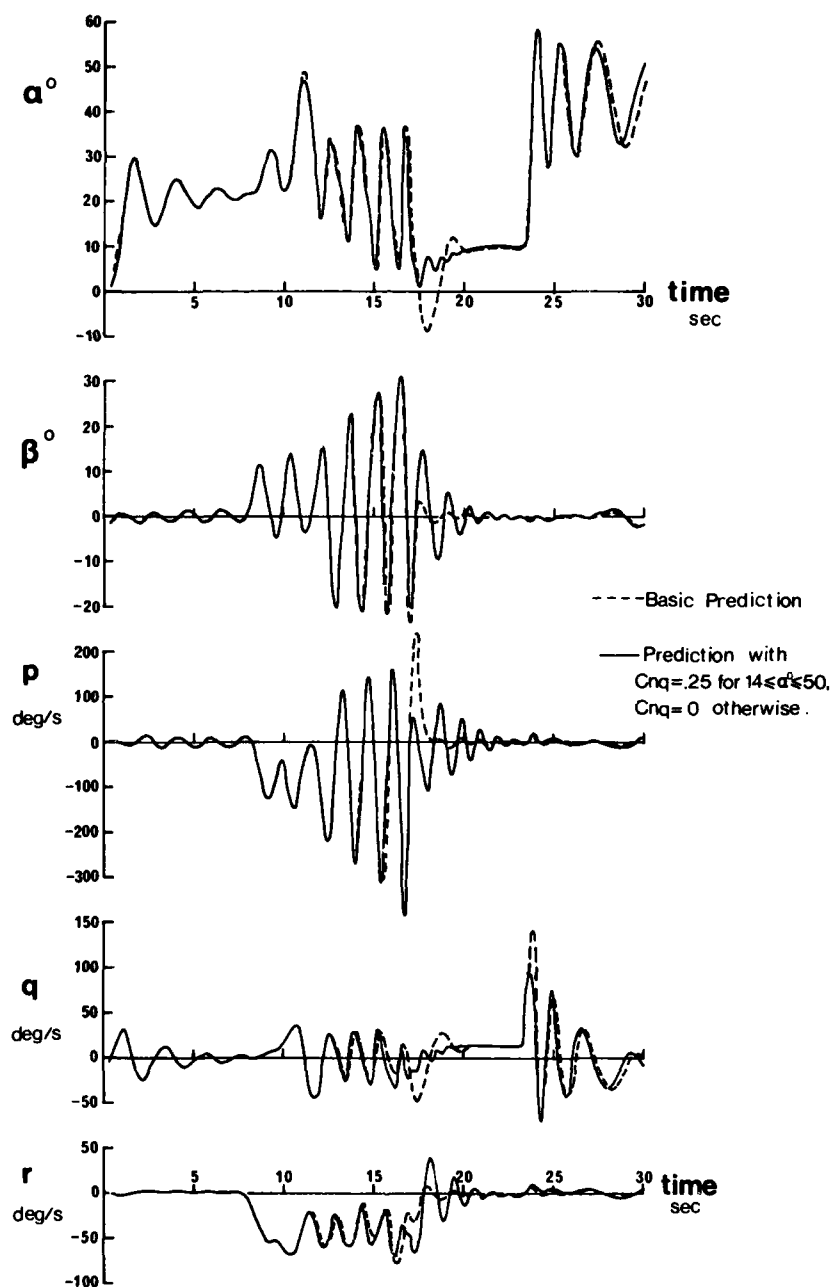


Fig 24 Effect of a cross-coupling yawing moment due to rate of pitch on the predicted motion for drop 6

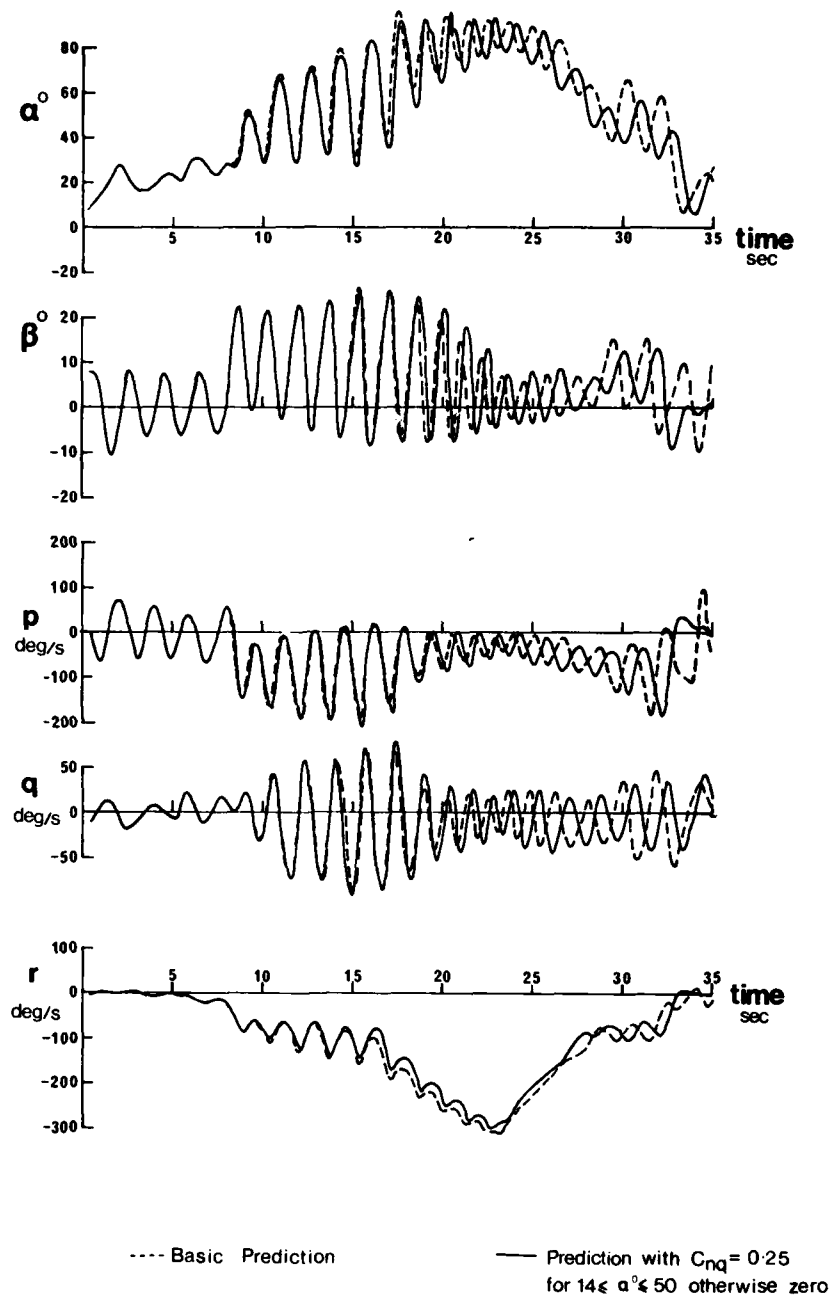


Fig 25 Effect of a cross-coupling yawing moment due to rate of pitch on the predicted motion for drop 7

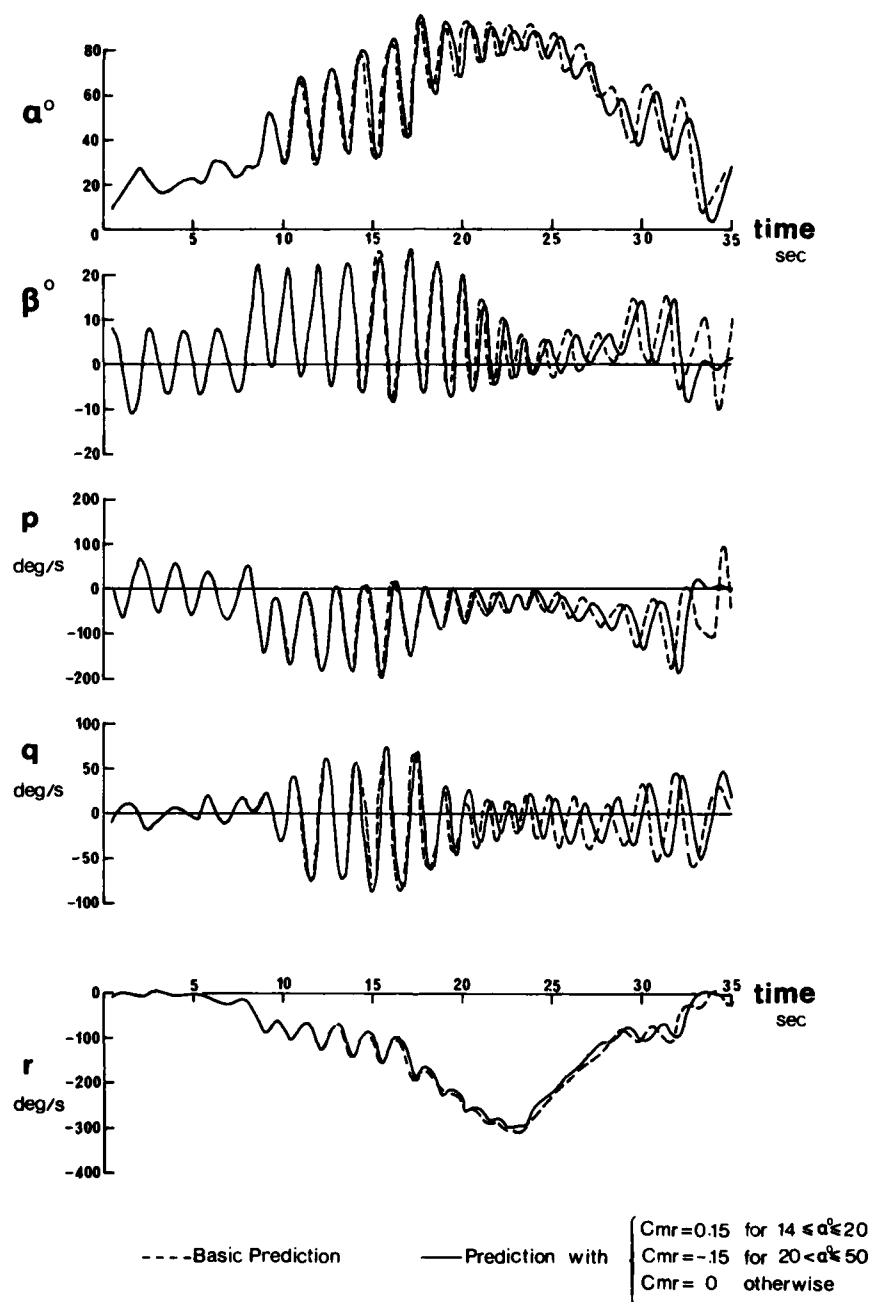
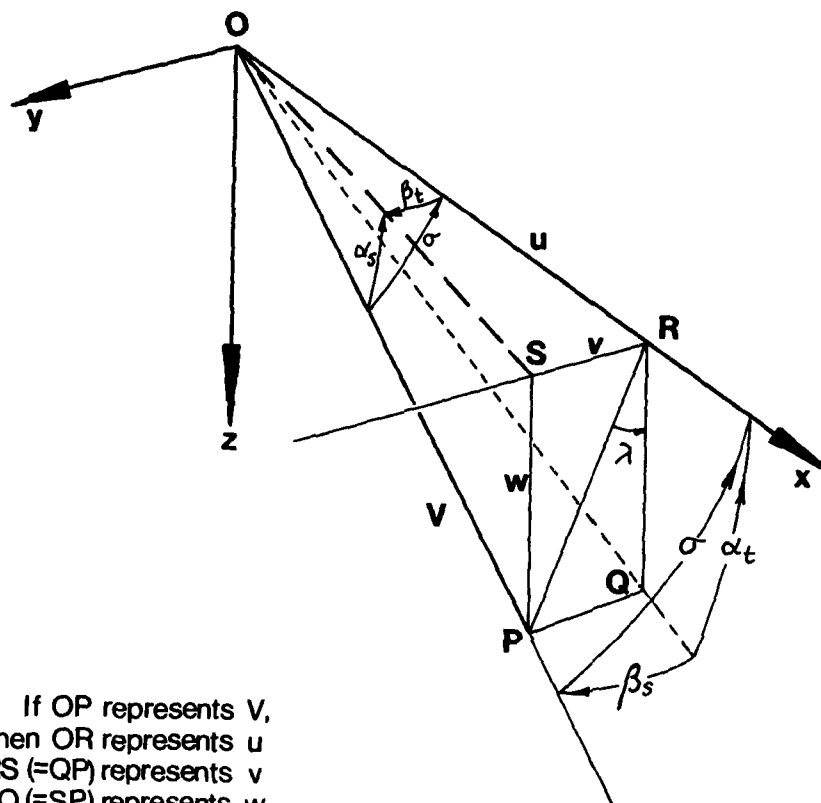


Fig 26 Effect of a cross-coupling pitching moment due to rate of yaw on the predicted motion for drop 7



If OP represents V ,
 then OR represents u
 $RS (=QP)$ represents v
 $RQ (=SP)$ represents w .

$$\begin{aligned} \cos \sigma &= u/V; & \tan \lambda &= v/w; \\ \sin \beta_s &= v/V; & \tan \alpha_t &= w/u; \\ \sin \alpha_s &= w/V; & \tan \beta_t &= v/u. \end{aligned}$$

If instead OP represents ω (angular velocity)
 then OR represents p
 $RS (=QP)$ represents q
 $RQ (=SP)$ represents r

In place of α_t the angle QOR is α_ω
 β_s " " POQ is β_ω .

Fig 27 Definitions of angles of incidence and angles defining direction of axis of rotation

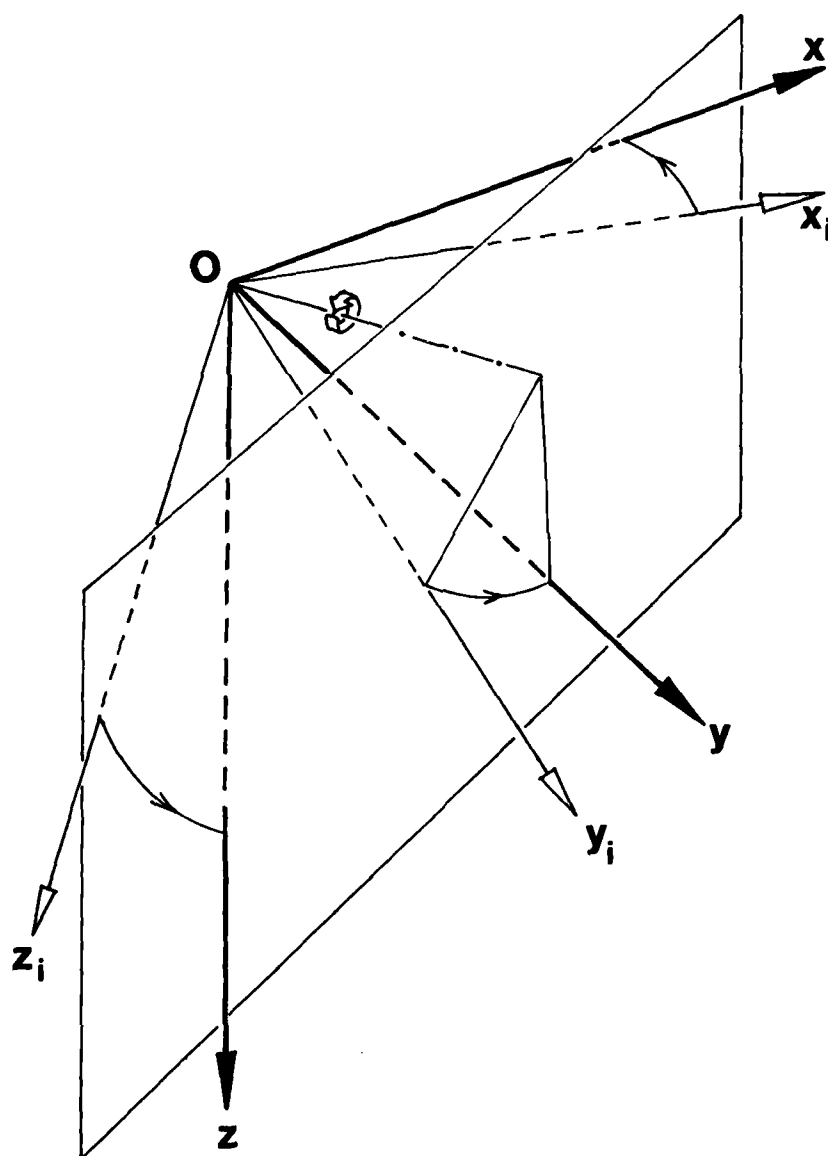


Fig 28 Illustration of invariance of direction cosines of a line through the origin following rotation of axes about it

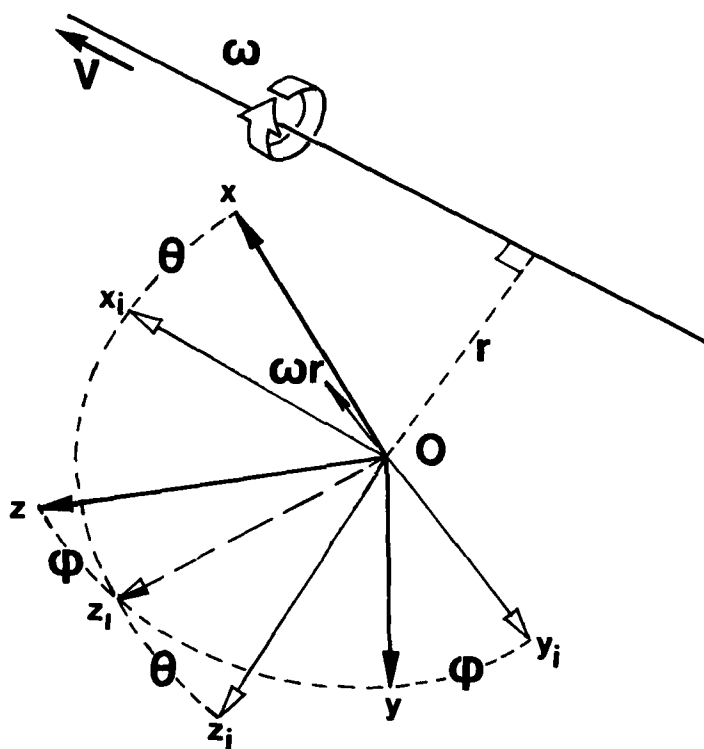


Fig 30 Rotational motion about an axis, parallel to the direction of V but offset from the origin

Appendix 1

ROTATION ABOUT A LINE OUT OF THE PLANE OF SYMMETRY OF THE MODEL
AND STARTING FROM AN ASYMMETRIC ATTITUDE

Definitions of angles used in the following analysis are given in Fig 27. Those defining the direction of the relative stream in the body axis system are the well-known pairs of the angles of incidence, of which the most commonly used are the angle of attack (α_t) and the angle of sideslip (β_s). It is, in the present context of large angles, necessary to make the distinction between these and the pair α_s, β_t .

In an analogous manner we may introduce angles which define the direction of the angular velocity vector in the body axes, such that α_ω corresponds to α_t and β_ω to β_s .

When rotation of the body axis-system occurs around the line defined by α_ω and β_ω it is evident (see Fig 28) that the direction cosines of the line remains invariant with respect to the axis system. If $Ox_i y_i z_i$ represent the initial position of the body axes and $Oxyz$ the axes at time t , then, in either axes, the direction cosines of the angular velocity vector (axis of rotation) are

$$\cos \alpha_\omega \cos \beta_\omega, \quad \sin \beta_\omega, \quad \sin \alpha_\omega \cos \beta_\omega.$$

Rotation about the line so defined through an angle ωt brings the $Ox_i y_i z_i$ axes into coincidence with body system of axes, $Oxyz$, at time t . If we introduce the abbreviations,

$$s_1 = \sin \beta_\omega, \quad c_1 = \cos \beta_\omega$$

$$s_2 = \sin \alpha_\omega, \quad c_2 = \cos \alpha_\omega$$

and

$$S = \sin \omega t, \quad C = \cos \omega t,$$

the transformation matrix associated with this rotation is

$$S_\omega = \begin{bmatrix} C + c_2^2 c_1^2 (1 - C) & c_2 s_1 c_1 (1 - C) + s_2 c_1 S & c_2 s_2 c_1^2 (1 - C) - s_1 S \\ c_2 s_1 c_1 (1 - C) - s_2 c_1 S & C + s_1^2 (1 - C) & c_2 c_1 S + s_2 s_1 c_1 (1 - C) \\ s_1 S + c_2 s_2 c_1^2 (1 - C) & s_2 s_1 c_1 (1 - C) - c_2 c_1 S & C + s_2^2 c_1^2 (1 - C) \end{bmatrix}.$$

If α_e, β_e represent the initial values of α_t, β_s then the components of the relative velocity V in the axis system $Ox_i y_i z_i$ are

$$V \cos \alpha_e \cos \beta_e, \quad V \sin \beta_e, \quad V \sin \alpha_e \cos \beta_e.$$

Thus in the body system of axes at time t , $Oxyz$, the components of V are u, v, w where,

$$\frac{1}{V} \begin{bmatrix} u \\ v \\ w \end{bmatrix} = S_\omega \begin{bmatrix} \cos \alpha_e \cos \beta_e \\ \sin \beta_e \\ \sin \alpha_e \cos \beta_e \end{bmatrix}. \quad (A1-1)$$

Evaluation of the individual components yields the following relationships,

$$\begin{aligned} \frac{u}{V} &= \{C + c_2^2 c_1^2 (1 - C)\} \cos \alpha_e \cos \beta_e + \{c_2 s_1 c_1 (1 - C) + s_2 c_1 S\} \sin \beta_e + \{c_2 s_2 c_1^2 (1 - C) - s_1 S\} \sin \alpha_e \cos \beta_e \\ &= \cos \alpha_\omega \cos \beta_\omega \{ \cos \beta_\omega \cos \beta_e \cos(\alpha_\omega - \alpha_e) + \sin \beta_\omega \sin \beta_e \} \\ &\quad + \cos \omega t \left[\cos \beta_e \{ \cos \alpha_e - \cos^2 \beta_\omega \cos \alpha_\omega \cos(\alpha_\omega - \alpha_e) \} - \sin \beta_e \sin \beta_\omega \cos \beta_\omega \cos \alpha_\omega \right] \\ &\quad + \sin \omega t \left[\sin \beta_e \cos \beta_\omega \sin \alpha_\omega - \cos \beta_e \sin \alpha_e \sin \beta_\omega \right], \end{aligned} \quad (A1-2)$$

$$\begin{aligned}
\frac{v}{V} &= \{c_2 s_1 c_1 (1 - C) - s_2 c_1 S\} \cos \alpha_e \cos \beta_e + \{C + s_1^2 (1 - C)\} \sin \beta_e + \{c_2 c_1 S + s_2 s_1 c_1 (1 - C)\} \sin \alpha_e \cos \beta_e \\
&= \sin \beta_\omega \{ \cos \beta_e \cos \beta_\omega \cos(\alpha_\omega - \alpha_e) + \sin \beta_e \sin \beta_\omega \} \\
&\quad + \cos \omega t \cos \beta_\omega \{ \sin \beta_e \cos \beta_\omega - \cos \beta_e \sin \beta_\omega \cos(\alpha_\omega - \alpha_e) \} - \sin \omega t \cos \beta_e \cos \beta_\omega \sin(\alpha_\omega - \alpha_e), \\
&\quad \dots (A1-3)
\end{aligned}$$

$$\begin{aligned}
\frac{w}{V} &= \{s_1 S + c_2 s_2 c_1^2 (1 - C)\} \cos \alpha_e \cos \beta_e + \{s_2 s_1 c_1 (1 - C) - c_2 c_1 S\} \sin \beta_e + \{C + s_2^2 c_1^2 (1 - C)\} \sin \alpha_e \cos \beta_e \\
&= \sin \alpha_\omega \cos \beta_\omega \{ \cos \beta_e \cos \beta_\omega \cos(\alpha_\omega - \alpha_e) + \sin \beta_e \sin \beta_\omega \} \\
&\quad + \cos \omega t \{ \cos \beta_e (\sin \alpha_e - \sin \alpha_\omega \cos^2 \beta_\omega \cos(\alpha_\omega - \alpha_e)) - \sin \beta_e \sin \alpha_\omega \sin \beta_\omega \cos \beta_\omega \} \\
&\quad + \sin \omega t \{ \cos \beta_e \cos \alpha_e \sin \beta_\omega - \sin \beta_e \cos \alpha_\omega \cos \beta_\omega \}.
\end{aligned} \quad (A1-4)$$

However, by definition, the various angles of incidence are related to u , v and w , as follows,

$$\frac{1}{V} \begin{bmatrix} u \\ v \\ w \end{bmatrix} = \begin{bmatrix} \cos \sigma \\ \sin \beta_s \\ \sin \alpha_s \end{bmatrix} = \begin{bmatrix} \cos \sigma \\ \sin \lambda \sin \sigma \\ \cos \lambda \sin \sigma \end{bmatrix} = \begin{bmatrix} \cos \alpha_t \cos \beta_s \\ \sin \beta_s \\ \sin \alpha_t \cos \beta_s \end{bmatrix}. \quad (A1-5)$$

As previously mentioned the most commonly adopted pair is the last and these are given by,

$$\begin{aligned}
\frac{v}{V} &= \sin \beta_s = \sin \beta_\omega \{ \cos \beta_e \cos \beta_\omega \cos(\alpha_\omega - \alpha_e) + \sin \beta_e \sin \beta_\omega \} \\
&\quad + \cos \omega t \cos \beta_\omega \{ \sin \beta_e \cos \beta_\omega - \cos \beta_e \sin \beta_\omega \cos(\alpha_\omega - \alpha_e) \} \\
&\quad - \sin \omega t \cos \beta_e \cos \beta_\omega \sin(\alpha_\omega - \alpha_e)
\end{aligned} \quad (A1-6)$$

and

$$\frac{w}{u} = \tan \alpha_t = \frac{W_1 + W_2 \cos \omega t + W_3 \sin \omega t}{U_1 + U_2 \cos \omega t + U_3 \sin \omega t}. \quad (A1-7)$$

$$\begin{aligned}
\text{where } W_1 &= \sin \alpha_\omega \cos \beta_\omega \{ \cos \beta_e \cos \beta_\omega \cos(\alpha_\omega - \alpha_e) + \sin \beta_e \sin \beta_\omega \}, \\
W_2 &= \cos \beta_e \{ \sin \alpha_e - \sin \alpha_\omega \cos^2 \beta_\omega \cos(\alpha_\omega - \alpha_e) \} - \sin \beta_e \sin \alpha_\omega \sin \beta_\omega \cos \beta_\omega, \\
W_3 &= \cos \beta_e \cos \alpha_e \sin \beta_\omega - \sin \beta_e \cos \alpha_\omega \cos \beta_\omega, \\
\text{and } U_1 &= \cos \alpha_\omega \cos \beta_\omega \{ \cos \beta_e \cos \beta_\omega \cos(\alpha_\omega - \alpha_e) + \sin \beta_e \sin \beta_\omega \}, \\
U_2 &= \cos \beta_e \{ \cos \alpha_e - \cos \alpha_\omega \cos^2 \beta_\omega \cos(\alpha_\omega - \alpha_e) \} - \sin \beta_e \cos \alpha_\omega \sin \beta_\omega \cos \beta_\omega, \\
U_3 &= \sin \beta_e \sin \alpha_\omega \cos \beta_\omega - \cos \beta_e \sin \alpha_e \sin \beta_\omega.
\end{aligned}$$

In the special case when the initial attitude is symmetrical and rotation takes place about a line in the plane of symmetry the expressions simplify considerably since $\beta_e = 0$, $\beta_\omega = 0$. We then have,

$$\sin \beta_s = - \sin \omega t \sin(\alpha_\omega - \alpha_e) \quad (A1-8)$$

$$\begin{aligned}
\tan \alpha_t &= \frac{\sin \alpha_\omega \cos(\alpha_\omega - \alpha_e) + \cos \omega t \{ \sin \alpha_e - \sin \alpha_\omega \cos(\alpha_\omega - \alpha_e) \}}{\cos \alpha_\omega \cos(\alpha_\omega - \alpha_e) + \cos \omega t \{ \cos \alpha_e - \cos \alpha_\omega \cos(\alpha_\omega - \alpha_e) \}} \\
&= \frac{\sin \alpha_\omega \cos(\alpha_\omega - \alpha_e) - \cos \omega t \cos \alpha_\omega \sin(\alpha_\omega - \alpha_e)}{\cos \alpha_\omega \cos(\alpha_\omega - \alpha_e) + \cos \omega t \sin \alpha_\omega \sin(\alpha_\omega - \alpha_e)}.
\end{aligned} \quad (A1-9)$$

The latter result is that which is obtained by direct analysis of this special case.

It is possible, of course, to derive these relationships by trigonometric argument. This can be illustrated by considering the special case, $\beta_\omega = 0$, $\beta_e = 0$, *ab initio*.

Suppose the aircraft model is placed in a symmetrical condition with respect to the airflow or the tunnel axis, that is, the axis Ox_1 makes an angle α_e , say, with $V(OP)$ and β_e is zero, see Fig 29.

Now let rotation at a rate ω take place about another line OM in the plane of symmetry Ox_1z_1 such that $X_1\hat{O}M = \alpha_\omega$. After a time t the plane Ox_1z_1 (that is, the plane X_1MO) takes up the position Oxz (or XMO).

If Q is the foot of the perpendicular from P on to MX, PQ is parallel to the y-axis, so that if OP represents V then PQ represents $-v$. Hence at time t the sideslip angle is given by the relationship,

$$\sin \beta = \frac{v}{V} = -\frac{MP}{OP} \sin \omega t = -\sin(\alpha_\omega - \alpha_e) \sin \omega t.$$

The calculation of the corresponding angle of attack is somewhat more complicated. It is the angle α in the triangle MOX, in which $MOX = \alpha_\omega$, being invariant for the specified rotation.

$$\begin{aligned} \text{Now} \quad ON &= V \cos(\alpha_\omega - \alpha_e) \\ MS &= V \cos(\alpha_\omega - \alpha_e) \sin \alpha_\omega \\ OS &= V \cos(\alpha_\omega - \alpha_e) \cos \alpha_\omega \end{aligned}$$

and since

$$QR = MS - QM \cos \alpha_\omega$$

and

$$OR = OS + SR$$

where we may replace MQ by

$$MP \cos \omega t = V \sin(\alpha_\omega - \alpha_e) \cos \omega t$$

and SR by

$$MQ \sin \alpha_\omega = V \sin(\alpha_\omega - \alpha_e) \sin \alpha_\omega \cos \omega t,$$

we finally have

$$\begin{aligned} QR &= V \left\{ \cos(\alpha_\omega - \alpha_e) \sin \alpha_\omega - \cos \omega t \cos \alpha_\omega \sin(\alpha_\omega - \alpha_e) \right\} \\ \text{and} \\ OR &= V \left\{ \cos \alpha_\omega \cos(\alpha_\omega - \alpha_e) + \cos \omega t \sin \alpha_\omega \sin(\alpha_\omega - \alpha_e) \right\}. \end{aligned}$$

Thus

$$\tan \alpha = \frac{QR}{OR} = \frac{\sin \alpha_\omega \cos(\alpha_\omega - \alpha_e) - \cos \omega t \cos \alpha_\omega \sin(\alpha_\omega - \alpha_e)}{\cos \alpha_\omega \cos(\alpha_\omega - \alpha_e) + \cos \omega t \sin \alpha_\omega \sin(\alpha_\omega - \alpha_e)}.$$

These results, in which the suffices s and t have been dropped, are in accord with those previously obtained.

The relationship between attitude and incidence angles

Means have to be provided to enable the model attitude to be adjusted so that the direction of the relative wind and the axis of rotation correspond to the two pairs of angles introduced in the above analysis, namely, α_e, β_e and $\alpha_\omega, \beta_\omega$ in the initial condition. To accomplish this, four attitude angles are required and it is expected that, as in the case of merely putting the model at incidence to the flow, when two attitude angles only are required, the attitude changes are effected by rotation of the apparatus about two axes in succession.

In the interest of simplicity and clarity the effects of elastic deflection and misalignment of the tunnel flow with its axis are ignored in the analysis which follows. The second pair of attitude angles sets the model at the desired incidence to the angular velocity vector (axis of rotation), whilst the combined effect of the two pairs of attitude angles is to put the model at the desired angles of incidence to the relative velocity. Expressed mathematically this statement is

$$\begin{bmatrix} p \\ q \\ r \end{bmatrix} = \omega \begin{bmatrix} \cos \alpha_\omega \cos \beta_\omega \\ \sin \beta_\omega \\ \sin \alpha_\omega \cos \beta_\omega \end{bmatrix} = S_2 \begin{bmatrix} \omega \\ 0 \\ 0 \end{bmatrix} \quad (A1-10)$$

and

$$\begin{bmatrix} u \\ v \\ w \end{bmatrix} = V \begin{bmatrix} \cos \alpha_e \cos \beta_e \\ \sin \beta_e \\ \sin \alpha_e \cos \beta_e \end{bmatrix} = S_2 S_1 \begin{bmatrix} V \\ 0 \\ 0 \end{bmatrix} \quad (A1-11)$$

where S_1 denotes the transformation matrix associated with the first pair of attitude angles and S_2 that associated with the second pair of attitude angles. The forms of S_1 and S_2 vary according to the nature of the tunnel rig. Two common types are a yaw/pitch (ψ, θ) rig and a pitch/roll (θ, ϕ) rig and the relationships between attitude angles and initial incidence angles for these are given below.

ψ, θ rig

Suppose ψ and θ represent attitude-deviation angles with respect to a datum position in which the body, x-axis and the axis of rotation lie along the tunnel axis.

For the two rotations represented by ψ_1 and θ_1 the transformation matrix is

$$S_1 = \begin{bmatrix} \cos \theta_1 \cos \psi_1 & \cos \theta_1 \sin \psi_1 & -\sin \theta_1 \\ -\sin \psi_1 & \cos \psi_1 & 0 \\ \sin \theta_1 \cos \psi_1 & \sin \theta_1 \sin \psi_1 & \cos \theta_1 \end{bmatrix}.$$

Similarly

$$S_2 = \begin{bmatrix} \cos \theta_2 \cos \psi_2 & \cos \theta_2 \sin \psi_2 & -\sin \theta_2 \\ -\sin \psi_2 & \cos \psi_2 & 0 \\ \sin \theta_2 \cos \psi_2 & \sin \theta_2 \sin \psi_2 & \cos \theta_2 \end{bmatrix}.$$

If the product

$$S = S_2 S_1 = \begin{bmatrix} l_1 & l_2 & l_3 \\ m_1 & m_2 & m_3 \\ n_1 & n_2 & n_3 \end{bmatrix} \quad \text{say,}$$

then in this case,

$$l_1 = \cos \theta_2 \cos \psi_2 \cos \theta_1 \cos \psi_1 - \cos \theta_2 \sin \psi_2 \sin \psi_1 - \sin \theta_2 \sin \theta_1 \cos \psi_1$$

$$m_1 = -\sin \psi_2 \cos \theta_1 \cos \psi_1 - \cos \psi_2 \sin \psi_1$$

$$n_1 = \sin \theta_2 \cos \psi_2 \cos \theta_1 \cos \psi_1 - \sin \theta_2 \sin \psi_2 \sin \psi_1 + \cos \theta_2 \sin \theta_1 \cos \psi_1.$$

From the equations for p, q, r we have,

$$\left. \begin{aligned} \cos \theta_2 \cos \psi_2 &= \cos \alpha_\omega \cos \beta_\omega, \\ -\sin \psi_2 &= \sin \beta_\omega, \\ \sin \theta_2 \cos \psi_2 &= \sin \alpha_\omega \sin \beta_\omega. \end{aligned} \right\} \quad (A1-12)$$

From the equations for u, v, w we have,

$$\left. \begin{aligned} l_1 &= \cos \alpha_e \cos \beta_e, \\ m_1 &= \sin \beta_e, \\ n_1 &= \sin \alpha_e \sin \beta_e. \end{aligned} \right\} \quad (A1-13)$$

By combination of the expressions for l_1, m_1, n_1 the following relationship can be deduced,

$$\left. \begin{aligned} -\sin \psi_1 &= (l_1 \cos \theta_2 + n_1 \sin \theta_2) \sin \psi_2 + m_1 \cos \psi_2, \\ \cos \theta_1 \cos \psi_1 &= (l_1 \cos \theta_2 + n_1 \sin \theta_2) \cos \psi_2 - m_1 \sin \psi_2. \end{aligned} \right\} \quad (A1-14)$$

With $\alpha_\omega, \beta_\omega$ specified equations (A1-12) yield the values of ψ_2, θ_2 and with α_e, β_e , and hence ℓ_1, m_1, n_1 specified, equations (A1-14) yield the first pair of attitude angles.

θ, ϕ rig

As there is little likelihood of confusion the altitude angles in this case are written as θ_1, ϕ_1 θ_2, ϕ_2 with transformation matrices as follows,

$$S_1 = \begin{bmatrix} \cos \theta_1 & 0 & -\sin \theta_1 \\ \sin \phi_1 \sin \theta_1 & \cos \phi_1 & \sin \phi_1 \cos \theta_1 \\ \cos \phi_1 \sin \theta_1 & -\sin \phi_1 & \cos \phi_1 \cos \theta_1 \end{bmatrix}$$

and

$$S_2 = \begin{bmatrix} \cos \theta_2 & 0 & -\sin \theta_2 \\ \sin \phi_2 \sin \theta_2 & \cos \phi_2 & \sin \phi_2 \cos \theta_2 \\ \cos \phi_2 \sin \theta_2 & -\sin \phi_2 & \cos \phi_2 \cos \theta_2 \end{bmatrix}.$$

Again writing the product as

$$S = S_2 S_1 = \begin{bmatrix} \ell_1 & \ell_2 & \ell_3 \\ m_1 & m_2 & m_3 \\ n_1 & n_2 & n_3 \end{bmatrix}$$

we have, in this case,

$$\begin{aligned} \ell_1 &= \cos \theta_2 \cos \theta_1 - \cos \phi_1 \sin \theta_2 \sin \theta_1, \\ m_1 &= \sin \phi_2 \sin \theta_2 \cos \theta_1 + \cos \phi_2 \sin \phi_1 \sin \theta_1 + \sin \phi_2 \cos \theta_2 \cos \phi_1 \sin \theta_1, \\ n_1 &= \cos \phi_2 \sin \theta_2 \cos \theta_1 - \sin \phi_2 \sin \phi_1 \sin \theta_1 + \cos \phi_2 \cos \theta_2 \cos \phi_1 \sin \theta_1. \end{aligned}$$

The second pair of attitude angles are determined by the relationships,

$$\left. \begin{aligned} \cos \theta_2 &= \cos \alpha_\omega \cos \beta_\omega, \\ \sin \phi_2 \sin \theta_2 &= \sin \beta_\omega, \\ \cos \phi_2 \sin \theta_2 &= \sin \alpha_\omega \cos \beta_\omega, \end{aligned} \right\} \quad (A1-15)$$

whilst the first pair is obtained from the equations

$$\left. \begin{aligned} \ell_1 &= \cos \alpha_e \cos \beta_e, \\ m_1 &= \sin \beta_e, \\ n_1 &= \sin \alpha_e \cos \beta_e. \end{aligned} \right\} \quad (A1-16)$$

From relationships between ℓ_1, m_1, n_1 and the attitude angles we have,

$$\left. \begin{aligned} \cos \theta_1 &= \ell_1 \cos \theta_2 + (m_1 \sin \phi_2 + n_1 \cos \phi_2) \sin \theta_2 \\ \cos \phi_1 \sin \theta_1 &= -\ell_1 \sin \theta_2 + (m_1 \sin \phi_2 + n_1 \cos \phi_2) \cos \theta_2 \end{aligned} \right\} \quad (A1-17)$$

The above equations enable $\theta_2, \phi_2, \theta_1$ and ϕ_1 to be calculated once $\alpha_e, \beta_e, \alpha_\omega$ and β_ω are specified.

Special Cases

The variation of α and β for a rotary motion about a line through the origin of body system of axes and starting from a symmetrical condition has already been discussed as a special case of the results of equations (A1-6 and 7). For this set-up the attitude angles for the apparatus are particularly simple and readily follow by setting $\beta_e = 0$ and $\beta_\omega = 0$ in the equations for ψ, θ and ϕ . They turn out, as must be the case, to be

where S_1 denotes the transformation matrix associated with the first pair of attitude angles and S_2 that associated with the second pair of attitude angles. The forms of S_1 and S_2 vary according to the nature of the tunnel rig. Two common types are a yaw/pitch (ψ, θ) rig and a pitch/roll (θ, ψ) rig and the relationships between attitude angles and initial incidence angles for these are given below.

ψ, θ rig

Suppose ψ and θ represent attitude-deviation angles with respect to a datum position in which the body, x-axis and the axis of rotation lie along the tunnel axis.

For the two rotations represented by ψ_1 and θ_1 the transformation matrix is

$$S_1 = \begin{bmatrix} \cos \theta_1 \cos \psi_1 & \cos \theta_1 \sin \psi_1 & -\sin \theta_1 \\ -\sin \psi_1 & \cos \psi_1 & 0 \\ \sin \theta_1 \cos \psi_1 & \sin \theta_1 \sin \psi_1 & \cos \theta_1 \end{bmatrix}.$$

Similarly

$$S_2 = \begin{bmatrix} \cos \theta_2 \cos \psi_2 & \cos \theta_2 \sin \psi_2 & -\sin \theta_2 \\ -\sin \psi_2 & \cos \psi_2 & 0 \\ \sin \theta_2 \cos \psi_2 & \sin \theta_2 \sin \psi_2 & \cos \theta_2 \end{bmatrix}.$$

If the product

$$S = S_2 S_1 = \begin{bmatrix} l_1 & l_2 & l_3 \\ m_1 & m_2 & m_3 \\ n_1 & n_2 & n_3 \end{bmatrix} \quad \text{say,}$$

then in this case,

$$l_1 = \cos \theta_2 \cos \psi_2 \cos \theta_1 \cos \psi_1 - \cos \theta_2 \sin \psi_2 \sin \psi_1 - \sin \theta_2 \sin \theta_1 \cos \psi_1$$

$$m_1 = -\sin \psi_2 \cos \theta_1 \cos \psi_1 - \cos \psi_2 \sin \psi_1$$

$$n_1 = \sin \theta_2 \cos \psi_2 \cos \theta_1 \cos \psi_1 - \sin \theta_2 \sin \psi_2 \sin \psi_1 + \cos \theta_2 \sin \theta_1 \cos \psi_1.$$

From the equations for p, q, r we have,

$$\left. \begin{aligned} \cos \theta_2 \cos \psi_2 &= \cos \alpha_\omega \cos \beta_\omega, \\ -\sin \psi_2 &= \sin \beta_\omega, \\ \sin \theta_2 \cos \psi_2 &= \sin \alpha_\omega \sin \beta_\omega. \end{aligned} \right\} \quad (A1-12)$$

From the equations for u, v, w we have,

$$\left. \begin{aligned} l_1 &= \cos \alpha_e \cos \beta_e, \\ m_1 &= \sin \beta_e, \\ n_1 &= \sin \alpha_e \sin \beta_e. \end{aligned} \right\} \quad (A1-13)$$

By combination of the expressions for l_1, m_1, n_1 the following relationship can be deduced,

$$\left. \begin{aligned} -\sin \psi_1 &= (l_1 \cos \theta_2 + n_1 \sin \theta_2) \sin \psi_2 + m_1 \cos \psi_2, \\ \cos \theta_1 \cos \psi_1 &= (l_1 \cos \theta_2 + n_1 \sin \theta_2) \cos \psi_2 - m_1 \sin \psi_2. \end{aligned} \right\} \quad (A1-14)$$

With $\alpha_\omega, \beta_\omega$ specified equations (A1-12) yield the values of ψ_2, θ_2 and with α_e, β_e , and hence ℓ_1, m_1, n_1 specified, equations (A1-14) yield the first pair of attitude angles.

θ, ϕ rig

As there is little likelihood of confusion the attitude angles in this case are written as $\theta_1, \phi_1, \theta_2, \phi_2$ with transformation matrices as follows,

$$S_1 = \begin{bmatrix} \cos \theta_1 & 0 & -\sin \theta_1 \\ \sin \phi_1 \sin \theta_1 & \cos \phi_1 & \sin \phi_1 \cos \theta_1 \\ \cos \phi_1 \sin \theta_1 & -\sin \phi_1 & \cos \phi_1 \cos \theta_1 \end{bmatrix}$$

and

$$S_2 = \begin{bmatrix} \cos \theta_2 & 0 & -\sin \theta_2 \\ \sin \phi_2 \sin \theta_2 & \cos \phi_2 & \sin \phi_2 \cos \theta_2 \\ \cos \phi_2 \sin \theta_2 & -\sin \phi_2 & \cos \phi_2 \cos \theta_2 \end{bmatrix}.$$

Again writing the product as

$$S = S_2 S_1 = \begin{bmatrix} \ell_1 & \ell_2 & \ell_3 \\ m_1 & m_2 & m_3 \\ n_1 & n_2 & n_3 \end{bmatrix}$$

we have, in this case,

$$\begin{aligned} \ell_1 &= \cos \theta_2 \cos \theta_1 - \cos \phi_1 \sin \theta_2 \sin \theta_1, \\ m_1 &= \sin \phi_2 \sin \theta_2 \cos \theta_1 + \cos \phi_2 \sin \phi_1 \sin \theta_1 + \sin \phi_2 \cos \theta_2 \cos \phi_1 \sin \theta_1, \\ n_1 &= \cos \phi_2 \sin \theta_2 \cos \theta_1 - \sin \phi_2 \sin \phi_1 \sin \theta_1 + \cos \phi_2 \cos \theta_2 \cos \phi_1 \sin \theta_1. \end{aligned}$$

The second pair of attitude angles are determined by the relationships,

$$\left. \begin{aligned} \cos \theta_2 &= \cos \alpha_\omega \cos \beta_\omega, \\ \sin \phi_2 \sin \theta_2 &= \sin \beta_\omega, \\ \cos \phi_2 \sin \theta_2 &= \sin \alpha_\omega \cos \beta_\omega, \end{aligned} \right\} \quad (A1-15)$$

whilst the first pair is obtained from the equations

$$\left. \begin{aligned} \ell_1 &= \cos \alpha_e \cos \beta_e, \\ m_1 &= \sin \beta_e, \\ n_1 &= \sin \alpha_e \cos \beta_e. \end{aligned} \right\} \quad (A1-16)$$

From relationships between ℓ_1, m_1, n_1 and the attitude angles we have,

$$\begin{aligned} \cos \theta_1 &= \ell_1 \cos \theta_2 + (m_1 \sin \phi_2 + n_1 \cos \phi_2) \sin \theta_2 \\ \cos \phi_1 \sin \theta_1 &= -\ell_1 \sin \theta_2 + (m_1 \sin \phi_2 + n_1 \cos \phi_2) \cos \theta_2. \end{aligned} \quad (A1-17)$$

The above equations enable $\theta_2, \phi_2, \theta_1$ and ϕ_1 to be calculated once $\alpha_e, \beta_e, \alpha_\omega$ and β_ω are specified.

Special Cases

The variation of α and β for a rotary motion about a line through the origin of body system of axes and starting from a symmetrical condition has already been discussed as a special case of the results of equations (A1-6 and 7). For this set-up the attitude angles for the apparatus are particularly simple and readily follow by setting $\beta_e = 0$ and $\beta_\omega = 0$ in the equations for ψ, θ and ϕ . They turn out, as must be the case, to be

and $\psi_2 = 0$, $\theta_2 = \alpha_\omega$ for the ψ, θ rig
 $\theta_2 = \alpha_\omega$, $\psi_2 = 0$ for the ψ, θ rig,

whilst ψ_1 and ϕ_1 respectively are zero and $\theta_1 = \alpha_\omega - \alpha_e$ in both cases.

Further special cases may be deduced.

Rotation about the tunnel axis or relative wind

When $\alpha_\omega = \alpha_e$ and $\beta_\omega = \beta_e$ there result the following,

$$\sin \beta = \sin \beta_e \quad \text{or} \quad \beta = \beta_e$$

$$\tan \alpha = \tan \alpha_e \quad \text{or} \quad \alpha = \alpha_e.$$

In other words such a motion causes no change in the angles of incidence. This is a special case of the general result illustrated by Fig 28.

Furthermore only one pair of attitude angles is necessary and these are given by

$$\cos \sigma_e = \cos \alpha_e \cos \beta_e = \cos \theta_2,$$

$$\sin \beta_e = \sin \phi_2 \sin \theta_2,$$

$$\sin \alpha_e = \sin \alpha_e \cos \beta_e = \cos \phi_2 \sin \theta_2,$$

which imply that

$$\sigma_e = |\theta_2|$$

and $\tan \lambda_e = \tan \phi_2$ or $\lambda_e = \phi_2$ for positive θ_2 ,
 $= \phi_2 + \pi$ for negative θ_2 .

Rotation about the body x-axis

Here $\alpha_\omega = 0$, $\beta_\omega = 0$ so that

$$\sin \beta = \cos \omega t \sin \beta_e + \sin \omega t \sin \alpha_e \cos \beta_e,$$

$$\cos \sigma = \cos \alpha \cos \beta = -\cos \alpha_e \cos \beta_e,$$

and

$$\sin \alpha \cos \beta = \cos \omega t \sin \alpha_e \cos \beta_e - \sin \omega t \sin \beta_e.$$

The attitude angles, of which again only one pair remains, we may denote by ψ_e, θ_e and θ_e, ϕ_e according to the arrangement used.

For the ψ, θ rig,

$$\cos \theta_e \cos \psi_e = \cos \alpha_e \cos \beta_e,$$

$$-\sin \psi_e = \sin \beta_e,$$

$$\sin \theta_e \cos \psi_e = \sin \alpha_e \cos \beta_e.$$

Hence,

$$\tan \theta_e = \tan \alpha_e \quad \text{and} \quad \psi_e = -\beta_e.$$

Expressed in terms of ψ_e and θ_e the angles of incidence at time t are given by.

$$\cos \sigma = \cos \alpha \cos \beta = \cos \theta_e \cos \psi_e,$$

$$\sin \lambda \sin \sigma = \sin \beta = \sin \omega t \cos \theta_e \cos \psi_e - \cos \omega t \sin \psi_e,$$

$$\cos \lambda \sin \sigma = \sin \alpha \cos \beta = \cos \omega t \sin \theta_e \cos \psi_e + \sin \omega t \sin \psi_e.$$

On setting $\psi_e = 0 = -\beta_e$, these last equations become

$$\cos \alpha \cos \beta = \cos \theta_e ,$$

$$\sin \beta = \sin \omega t \sin \theta_e ,$$

$$\sin \alpha \cos \beta = \cos \omega t \sin \theta_e .$$

For the θ, ϕ rig,

$$\cos \theta_e = \cos \alpha_e \cos \beta_e = \cos \sigma_e ,$$

$$\sin \phi_e \sin \theta_e = \sin \beta_e = \sin \lambda_e \sin \sigma_e ,$$

$$\cos \phi_e \sin \theta_e = \sin \alpha_e \cos \beta_e = \cos \lambda_e \sin \sigma_e .$$

Hence in terms of ϕ_e, θ_e the angles of incidence at time t are given by,

$$\cos \sigma = \cos \alpha \cos \beta = \cos \theta_e ,$$

$$\sin \lambda \sin \sigma = \sin \beta = \sin(\omega t + \phi_e) \sin \theta_e ,$$

$$\cos \lambda \sin \sigma = \sin \alpha \cos \beta = \cos(\omega t + \phi_e) \sin \theta_e .$$

On setting $\phi_e = 0$ or $\beta_e = 0, \lambda_e = 0$, these last equations become

$$\cos \alpha \cos \beta = \cos \theta_e ,$$

$$\sin \beta = \sin \omega t \sin \theta_e ,$$

$$\sin \alpha \cos \beta = \cos \omega t \sin \theta_e .$$

These are the same as those derived above for zero initial sideslip, which is to be expected as the two set-ups are identical in this limiting case.

The conditions governing rotation about the body x-axis are readily derived from first principles using the relationships between p, q, r and ϕ, θ, ψ .

Appendix 2

ROTATION ABOUT THE TUNNEL AXIS WITH THE CENTRE OF GRAVITY OF THE MODEL OFFSET BY A RADIUS, r

Consider a rotational motion about the axis of the tunnel with the model set at incidence to the flow and with its centre of gravity at a distance, r , from the axis of rotation. When the radius, r , of the equivalent helical path is properly adjusted to the model dimensions, such a motion reproduces the flow conditions of the steady spin. In this type of motion the angles of attack and sideslip vary with the rate of rotation, ω and the radius of the simulated spin. The relationship appropriate to a θ , ϕ rig are derived below.

In the axis system designated $Ox_0y_0z_0$ (see Fig 30) the components of the velocity of O are V , $-\omega r$, 0 . For a θ , ϕ rig the required attitude to the flow is arrived at by a rotation to an angle, θ_e , say, about the y_0 -axis followed by a rotation about the x_1 -axis through an angle, ϕ_e , say. The attitude of the axes $Oxyz$ defines that of model and the transformation matrix for the pair of axis systems, $Oxyz$ and $Ox_0y_0z_0$ is

$$S = \begin{bmatrix} \cos \theta_e & 0 & -\sin \theta_e \\ \sin \phi_e \sin \theta_e & \cos \phi_e & \sin \phi_e \cos \theta_e \\ \cos \phi_e \sin \theta_e & \sin \phi_e & \cos \phi_e \cos \theta_e \end{bmatrix} \quad (A2-1)$$

Hence the velocity components, u , v , w along the Ox , Oy and Oz axis respectively are given by the equation,

$$\begin{bmatrix} u \\ v \\ w \end{bmatrix} = V_R \begin{bmatrix} \cos \alpha \cos \beta \\ \sin \beta \\ \sin \alpha \cos \beta \end{bmatrix} = S \begin{bmatrix} V \\ -\omega r \\ 0 \end{bmatrix} \quad (A2-2)$$

where V_R is the resultant of V and $-\omega r$.

The relationships between α , β and θ_e , ϕ_e follow, they are given by,

$$\left. \begin{aligned} V_R \cos \alpha \cos \beta &= V \cos \theta_e \\ V_R \sin \beta &= V \sin \phi_e \sin \theta_e - \omega r \cos \phi_e \\ V_R \sin \alpha \cos \beta &= V \cos \phi_e \sin \theta_e + \omega r \sin \phi_e \end{aligned} \right\} \quad (A2-3)$$

With the introduction of a helical angle parameter defined $\lambda_\omega = \frac{\omega r}{V_R}$, these equations can be expressed in the form,

$$\left. \begin{aligned} \tan \alpha &= \cos \phi_e \tan \theta_e + \lambda_\omega \sin \phi_e \\ (1 + \lambda_\omega^2)^{1/2} \sin \beta &= \sin \phi_e \sin \theta_e - \lambda_\omega \cos \phi_e \end{aligned} \right\} \quad (A2-4)$$

These equations show that for a given ω and r the angles of incidence differ somewhat from those for either zero ω or r , which are the same, but are constant during the motion.

In the rotational motion considered here the angular velocity components with respect to the body system of axes, $Oxyz$, are given by,

$$\begin{bmatrix} p \\ q \\ r \end{bmatrix} = \omega \begin{bmatrix} \cos \theta_e \\ \sin \phi_e \sin \theta_e \\ \cos \phi_e \sin \theta_e \end{bmatrix} \quad (A2-5)$$

Examination of equations (A2-4) and (A2-5) shows that arbitrary angles of attack and a small range of sideslip angles may be obtained for zero rate of pitch ($q = 0$) by choosing $\phi_e = 0$. A choice of $\phi_e = 90^\circ$ sets a severe limit on the angle of attack to be achieved, whilst a single degree-of-freedom motion is only possible by setting θ_e either zero or a right angle, which in turn sets restrictions on the angles of attack and sideslip that can be achieved. The motion cannot be used to obtain isolated rotary derivatives at arbitrary angles of incidence. It can, however, be used to check on the validity of superimposing of angle-of-incidence effects and angular velocity effects by virtue of the fact the equation (A2-4) holds for $\lambda_\omega = 0$ and the angle of attack and sideslip can be varied from their values for $\lambda_\omega = 0$ by setting non-zero values of λ_ω ($r \neq 0$).

Appendix 3

The equations of motion, in a form suitable for analysis of large departures from a datum flight condition, can be written¹,

$$\left. \begin{aligned} \dot{u} + qw - rv - g_x &= \frac{QS}{m} C_X \\ \dot{v} + ru - pw - g_y &= \frac{QS}{m} C_Y \\ \dot{w} + pv - qu - g_z &= \frac{QS}{m} C_Z \\ \dot{p} + e_x(\dot{r} + pq) + b_x qr &= \frac{QS \ell_2}{I_x} C_\ell \\ \dot{q} + e_y(r^2 - p^2) + b_y rp &= \frac{QS \ell_1}{I_y} C_m \\ \dot{r} + e_z(\dot{p} - qr) + b_z pq &= \frac{QS \ell_2}{I_y} C_n \end{aligned} \right\} \quad (A3-1)$$

where ℓ_1 and ℓ_2 are representative length in longitudinal and lateral motions and $Q = \frac{1}{2} \rho V^2$.

With the use of the following relationships,

$$\left. \begin{aligned} V^2 &= u^2 + v^2 + w^2 \\ u &= V \cos \alpha \cos \beta \\ v &= V \sin \beta \\ w &= V \sin \alpha \cos \beta \end{aligned} \right\} \quad (A3-2)$$

where α is written in place of α_t and β in place of β_s , the equation (A3-1) can be rewritten thus,

$$\left. \begin{aligned} \dot{V} &= (g_x \cos \alpha + g_z \sin \alpha) \cos \beta + g_y \sin \beta + \frac{QS}{m} \left\{ (C_X \cos \alpha + C_Z \sin \alpha) \cos \beta + C_Y \sin \beta \right\} \\ \dot{\alpha} &= q - (p \cos \alpha + r \sin \alpha) \tan \beta + (g_z \cos \alpha - g_x \sin \alpha) \frac{\sec \beta}{V} + \frac{QS}{mV} \sec \beta \left\{ C_Z \cos \alpha - C_X \sin \alpha \right\} \\ \dot{\beta} &= p \sin \alpha - r \cos \alpha - \left\{ (g_x \cos \alpha + g_z \sin \alpha) \sin \beta - g_y \cos \beta \right\} \frac{1}{V} \\ &\quad - \frac{QS}{mV} \left\{ (C_X \cos \alpha + C_Z \sin \alpha) \sin \beta + C_Y \cos \beta \right\} \\ (1 - e_x e_z) \dot{p} &= e_x (b_z - 1) pq - (b_x + e_x e_z) qr + \frac{QS \ell_2}{I_x} (C_\ell - e_z C_n) \\ \dot{q} &= -b_y rp - e_y (r^2 - p^2) + \frac{QS \ell_1}{I_y} C_m \\ (1 - e_x e_z) \dot{r} &= - (b_z - e_x e_z) pq + e_z (1 + b_x) qr + \frac{QS \ell_2}{I_z} (C_n - e_x C_\ell) \end{aligned} \right\} \quad (A3-3)$$

LINEAR OR NON-LINEAR ANALYSIS METHODS: WHEN AND HOW?

by

Jan Roskam
Ackers Professor of Aerospace Engineering
The University of Kansas
Lawrence, Kansas 66045
U. S. A.

1. INTRODUCTION

Whenever dynamically or aerodynamically induced non-linear behavior in the control or gust response of an airplane is suspected, the following questions arise:

1. Are linear analysis methods for predicting stability behavior still valid? If not, what to do?
2. Are linear time response methods for predicting responses to control and gust inputs still valid? If not, what to do?

To address question 1 it is shown in Section 2 that the direct method of Lyapunov can be used to predict under what conditions of motion and input disturbances the answer is either yes or no.

To address question 2, it is shown in Section 3 by means of several examples that large differences can exist between roll and heading responses predicted from conventional linear methods and from "complete" non-linear methods. The causes of this non-linear behavior are identified and a simple three-step criterion for its early detection is suggested in Section 4.

If the answer to question 1 is no, an energy based criterion for determining the stability behavior is suggested in Section 5.

In section 6 examples of energy-time-histories are shown, to identify specific stability derivatives which can be major causes of non-linear behavior. A discussion is presented on the relative importance of the conventional stability derivatives and of specific non-linear dynamic terms in the equations of motion in inducing non-linear behavior.

2. ON THE VALIDITY OF LINEAR STABILITY THEORY

Before discussing criteria for the validity of the linear theory it is well to review some fundamental aspects of the linear theory of airplane stability. This will serve to establish clearly where its weakness originates. It should be mentioned at this point that the linear theory is thoroughly dealt with in references 1, 2 and 3.

The linear theory (also called small-disturbance theory) starts by writing all motion variables as the sum of some steady-state value and a small-disturbance value. The equations of motion are then linearized. This is done by assuming that terms containing products of small disturbances can be neglected. Next, the assumption is made that all coefficients in the resulting linear differential equations are constants. The stability behavior of these equations is then obtained from the roots of the characteristic equation (i.e. eigen-values of the system matrix).

Evidently, the validity of small-disturbance theory hinges on the accuracy of the assumptions made in deriving the characteristic equation.

The first assumption is that as a result of considering small disturbances it is permissible to neglect terms containing products of these disturbances. It is intuitively acceptable that this is reasonable for infinitesimally small disturbances. In such a limiting case the linear theory can always be expected to yield valid results. To the airplane designer this knowledge is of little value, since stability must be ensured in an environment of finite (and sometimes quite large) disturbances. The problem is therefore to define a domain of initial disturbances within which small-disturbance theory correctly predicts the stability behavior of the airplane.

Therefore, the first objective will be to show that such a domain can be constructed through the application of Lyapunov stability theory. A brief summary of those aspects of the Lyapunov theory needed here is given in Appendix A.

To apply Lyapunov stability theory the equations of motion of the airplane are written as first-order differential equations. The following form is used:

$$\{\dot{x}\} = [A] \{x\} + \{g(x)\} \quad (1)$$

In this expression $\{x\}$ represents the column matrix whose components are the dependent variables of the problem, for example:

$$\{x\}^T = \{u, v, w, p, q, r, \psi, \theta, \phi\}.$$

These components define completely the state of motion (flight) under consideration. The matrix $[A]$ multiplied into $\{x\}$ yields the linear parts of the equations while the matrix $\{g(x)\}$ symbolizes the nonlinear parts. Table 1 shows one possible form for equation 1. A derivation leading to the form of equation 2 (Table 1) is given in References 1 and 4.

It is shown in reference 5, that for linear equations of motion with constant coefficients it is always possible to construct a Lyapunov function V . Construction of this function V can be carried out as follows. Assume:

$$V = 1/2 \sum_{s,r} B_{sr} x_s x_r, \text{ with: } [B^T] = [B] \quad (3)$$

If V is to be a Lyapunov function for the linear part of equations 1 or 2, then it must satisfy:

$$\begin{aligned} \frac{dV}{dt} &= \sum_s \frac{\partial V}{\partial x_s} \dot{x}_s \\ &= \sum_s \frac{\partial V}{\partial x_s} (a_{s1}x_1 + \dots + a_{sn}x_n) = C \end{aligned} \quad (4)$$

where C is any negative definite form. It is convenient to select:

$$C = -(x_1^2 + \dots + x_n^2) \quad (5)$$

The coefficients a_{si} are the elements of $[A]$ in equations 1 or 2. It turns out that $[B]$ will be positive definite if and only if the eigen-values of $[A]$ have negative real parts. A unique solution for $[B]$ can always be found according to reference 5.

The function V obtained in this manner is a Lyapunov function for the linear equations. It is also a Lyapunov function for the nonlinear equations in some small neighborhood of the origin $\{x(0)\} = \{0\}$ if it satisfies theorem 1 (Appendix A) in the sense that for the complete equations:

$$\frac{dV}{dt} = \sum_s \frac{\partial V}{\partial x_s} \dot{x}_s \leq 0 \quad (6)$$

It is emphasized that even though V has been derived for the linear equations, \dot{x}_s in inequality (6) must be computed for the nonlinear set. So, in (6):

$$\{\dot{x}_s\} = [A] \{x_s\} + \{g(x_s)\} \quad (7)$$

By checking inequality (6) systematically for combinations of values of initial disturbances (arbitrarily selected), a domain of initial disturbances can be identified within which the linear approximation is valid.

The domain of small disturbances found in this manner guarantees the validity of small-disturbance theory for disturbances inside the domain. Outside the domain there still exists a possibility that small-disturbance theory applies. Because this method of constructing the domain will at least verify whether or not the size of the domain is large enough to be practical, the last fact is not considered a serious disadvantage. Malkin and Chetayev have discussed the problem of enlarging the domain of initial disturbances in references 5 and 6.

A useful observation is the following. It is possible to include in the non-linear part $\{g(x)\}$ of equation (1) expressions representing non-linearities in the aerodynamic forces and moments. In this manner the effect of aerodynamic non-linearities on the size of the domain of initial disturbances can also be determined.

If it turns out that the domain of validity for the linear equations is too small from a practical viewpoint then attention can be focussed on methods to determine the stability behavior outside. One such approach is suggested in Section 4.

3. ON THE VALIDITY OF LINEAR RESPONSE THEORY

It was shown in Section 2 that it is possible to construct a domain of validity for the linear equations of motion with regard to the prediction of stability. For disturbances within this region of validity the linear theory correctly predicts the stability character of the non-linear equations. This does not imply, however, that the linear equations will correctly predict the response of the airplane to such disturbances.

To illustrate the differences between responses predicted from linear and non-linear equations several examples are presented. Response calculations were made for two high-speed airplane configurations A and B. The geometric, inertial, and linearized aerodynamic characteristics of these airplanes are summarized in Appendix B. In addition, a brief mission summary is given for each configuration.

Dutch roll characteristics of these configurations are presented in the conventional manner in Table II. These data were prepared to indicate that configurations A and B are realistic according to conventional handling qualities theory.

For expedience, only responses to lateral control pulses of the form $\delta_s(t) = \delta_s\{u(t-1) - u(t-2)\}$ were computed. The constant δ_s indicates the degrees of surface deflection. The effect of longitudinal disturbances on the responses to lateral control was studied by a longitudinal control input of the form $\delta_E(t) = \pm \delta_E\{u(t-1) - u(t-4)\}$. Positive as well as negative control deflections were used because of expected asymmetric behavior. The aerodynamic characteristics of configurations A and B were assumed to be linear. The magnitudes of disturbances used are in accordance with this assumption.

Response Results for Airplane A

For configuration A, Figures 1, 2 and 3 show the results for three flight conditions. In all cases the configuration shown is called basic, indicating that no stability augmentation was used in the calculations. It may be seen that even though the lateral control responses are modified in the presence of longitudinal disturbances, the effects are not of such magnitude to invalidate the linear equations of motion.

Response Results for Airplane B

Considerable departure from linear theory is shown in Figure 4 for configuration B. Here, response to a purely lateral control disturbance of the basic airplane is normal. The same response under influence of longitudinal disturbances is seen to be quite different, however.

Non-linear behavior is generally typified by the fact that the superposition principle is not applicable. An example of this is provided by the responses in Figure 5. That damping augmentation has a significant effect on the non-linear behavior of this configuration may be seen from Figure 6. It must be concluded from these results that situations occur where the linear equations of motion, even for small disturbances, cannot be used to predict responses. Whenever such situations occur, it can be expected that conventional handling qualities and control synthesis theory will yield invalid results. Because the analysis of the non-linear equations of motion involves a considerable amount of computer work, it is important to be able to predict the occurrence of such non-linear response behavior. Section 5 formulates a proposed criterion for diagnosing such non-linear behavior.

4. ON A CRITERION TO PREDICT THE OCCURRENCE OF NON-LINEAR RESPONSE BEHAVIOR

It is interesting to observe from equation (2) that pitch rate couples into the lateral-directional modes through several terms. To determine the severity of this coupling it is possible to postulate a case where the pitch rate is kept steady. In that case the equations can still be linearized. By inspection of equation (2) it is seen that the effect of steady pitch rate on the lateral directional dynamics can be simulated by the following substitutions:

$$\begin{aligned} C_{l_p} &= + C_{l_p} + \frac{4I_{xz_s} Q_0}{\rho S U_0 b^2} & C_{l_r} &= + C_{l_r} - \frac{4(I_{zz_s} - I_{yy_s}) Q_0}{\rho S U_0 b^2} \\ C_{n_p} &= + C_{n_p} - \frac{4(I_{yy_s} - I_{xx_s}) Q_0}{\rho S U_0 b^2} & C_{n_r} &= + C_{n_r} - \frac{4I_{xz_s} Q_0}{\rho S U_0 b^2} \end{aligned} \quad (8)$$

Abzug (reference 7) showed that the dutch roll damping ratio can be adversely affected by high positive steady pitch rates, but that for practical purposes the effect is not important. The effect of both positive and negative pitch rate on dutch roll damping ratio and frequency for airplane configurations A and B is shown in Table II. It is seen that unstable dutch roll occurs even for small positive pitch rates. These results indicate that negative pitch rates can lead to divergences in the rolling and spiral modes. It is realized that steady pitch rate coupling as such will rarely occur in flight, because it is difficult to maintain steady pitch rates for an appreciable

length of time. However, the severity of the effect of Q_0 on dutch roll damping is indicative of failure of the linear theory to correctly predict airplane response to lateral disturbances in the presence of longitudinal disturbances. It was suspected that two other factors are important in early identification of the occurrence of non-linear response behavior: ϕ/β and $\phi_{\max, \beta}$. Table II summarizes the effects of Q -coupling, ϕ/β and $\phi_{\max, \beta}$. The parameter $\phi_{\max, \beta}$ is explained in Appendix C.

On the basis of the evidence of Table II and the response results discussed in Section 3, the following criterion is proposed to indicate whether or not the linear equations of motion can be expected to predict lateral response properly.

Criterion

If $|\phi/\beta| < 3.0$ and $\phi_{\max, \beta} < .11$ while steady pitch-rate-coupling is insignificant in the range of pitch-rate disturbances applicable to the given configuration, then it can be expected that the linear theory will correctly predict the response of the rigid airplane to small lateral disturbances.

From the limited amount of evidence presented in substantiation of this criterion, it will be clear that more research is needed for its proper establishment.

If it turns out that the linear equations cannot be used, then numerical integration methods must be employed to solve the non-linear equation of motion. This was done to obtain the non-linear time histories presented in Section 3.

Numerical solutions to the complete non-linear airplane equations of motion are being used more and more in engineering development (i.e. research and development flight simulations). A need is foreseen to determine what is meant by stability in such cases. Looking at time history traces of state variables is not a satisfactory way to determine whether or not a motion is stable. Section 6 suggests a method to determine stability behavior of motions obtained from non-linear equations.

5. ON A METHOD TO DETERMINE STABILITY BEHAVIOR OF THE NON-LINEAR EQUATIONS OF MOTION

For many years, stability has been associated with energy concepts. For example, in the analysis of stability of static equilibria in elastic systems the principle of minimum potential energy plays a fundamental role. Chetayev showed (reference 8) that for conservative dynamical systems with or without dissipative forces (provided the latter can be written as quadratic forms in the velocities) the total energy can be used as a Lyapunov function. From the total energy used as a Lyapunov function it is possible to determine the stability behavior in the sense of theorems 1 and 2 of Appendix A.

The airplane forms a non-linear system with non-conservative forces. The "dissipative" forces here can also add energy to the system. For these reasons it has not been found possible to apply conventional energy methods or to construct a Lyapunov function.

Asymptotic stability of the undisturbed motion implies that all disturbed phase variables vanish after some time. Weak stability implies that all phase variables remain inside some region around the origin. From a handling qualities viewpoint, it is desirable to have those phase variables designated as velocities vanish such that: $\lim_{t \rightarrow \infty} T(t) = 0$, where T is the kinetic energy of the disturbed motion variables. Because it is clearly impractical to observe a numerically obtained solution over an infinite time interval (as required by conventional stability definitions) it is necessary to determine the stability by observation of the motion during a limited time interval. Using the definition of stability in a limited time interval due to Lebedev (reference 9) it follows by interpreting T as a positive definite function that in the time interval $t_1 < t < t_3$ the condition for stability is:

$$T(t) < T(t_1) \quad (9)$$

A consequence of (9) is that both motions in Figure 7 must be called stable. This conclusion is acceptable for $T_1(t)$, but not always for $T_2(t)$.

This undesirable consequence can be eliminated by adding to inequality (9) a condition based on a time integral of kinetic energy.

A simple application of the energy-time integral to linear lateral equations of motion can be made in cases where the energy participation of the rolling convergence and spiral divergence modes (or lateral phugoid) is negligible compared with that of the dutch roll mode. In that case the motion is periodic with frequency ω_d . It is then possible to formulate a dynamic stability requirement by:

$$F = \frac{\int_{t_2}^{t_3} T(\tau) d\tau}{\int_{t_1}^{t_2} T(\tau) d\tau} < 1 \quad \text{for} \quad t_2 - t_1 = t_3 - t_2 = \frac{2\pi}{\omega_d} \quad (10)$$

The general solutions for β , ϕ and ψ can usually be written as:

$$\begin{aligned} \beta &= C_{1\beta} e^{\lambda_1 t} + C_{2\beta} e^{\lambda_2 t} + C_{3\beta} e^{n_3 t} \cos(\omega_3 t + a_1) \\ \phi &= C_{1\phi} e^{\lambda_1 t} + C_{2\phi} e^{\lambda_2 t} + C_{3\phi} e^{n_3 t} \cos(\omega_3 t + a_2) \\ \psi &= C_{1\psi} e^{\lambda_1 t} + C_{2\psi} e^{\lambda_2 t} + C_{3\psi} e^{n_3 t} \cos(\omega_3 t + a_3) \end{aligned} \quad (11)$$

Neglecting the first two modes, it is possible to show that:

$$F = e^{-4\pi n_3/\omega_3} = e^{-4\pi \xi_d/\sqrt{1-\xi_d^2}} \quad (12)$$

Since for stable dutch roll $0 < \xi_d < 1$ is necessary and sufficient, it follows that (10) is indeed a necessary and sufficient stability criterion under the imposed restrictions.

It is suggested that F as defined in (10) but with redefined limits, can be used as a practical stability criterion for the complete nonlinear equations of motion, especially in cases where stability is to be viewed inside a limited time interval. According to such a criterion, a motion would be called stable inside a time interval $t_1 < t < t_3$ if:

$$T(t) < T(t_1) \quad \text{and} \quad F = \frac{\int_{t_2}^{t_3} T(\tau) d\tau}{\int_{t_1}^{t_2} T(\tau) d\tau} < 1 \quad \text{with} \quad t_2 = \frac{t_1 + t_3}{2} \quad (13)$$

It is observed that in the case of the airplane, t_1 must be selected at the instant corresponding to a maximum of T , since otherwise (9) and (13) are violated right away, even for a perfectly stable airplane. The reason for this is that for arbitrary initial disturbances $\dot{T}(t=0) > 0$ is possible. This depends entirely on the character of the "kinetic energy generating terms" in the equations of motion. Examples of such behavior are given in Figures 9, 10 and 11.

The selection of t_3 is arbitrary. However, t_3 will in general be selected as the end of the time interval during which the motion is being observed.

It is realized that criterion (13) is more realistic for airplane applications than (9). It is also more restrictive. In the limiting case $t_3 \rightarrow \infty$, both conditions are necessary but not sufficient equivalents of the Lyapunov definition for stability (definition 2, Appendix A).

When the non-linear equations of motion are solved with a digital computer, the kinetic energy can be computed as a function of time. Therefore, it is possible to keep track of both conditions (9) and (13) and obtain a continuous history of the stability character of the motion. In this manner, a numerical procedure for the practical determination of stability of non-linear equations of motion is obtained.

Finally, it is suggested that F as defined in (13) can be used as a handling qualities parameter for the non-linear equations of motion. To verify this will require further research.

6. SOME INTERPRETATIONS OF ENERGY-TIME HISTORIES

To study the time history of energy participation of separate force and moment terms during rigid airplane motions requires the computation of energy contributions of individual terms in the equations of motion. These energy contributions can be found by multiplying each equation by its characteristic velocity and by a subsequent integration:

$$\begin{aligned}
\int_{t_1}^{t_2} F_z W dt &= \int_{t_1}^{t_2} (m\dot{W}W + mPVW - mQUW) dt \\
\int_{t_1}^{t_2} MQ dt &= \int_{t_1}^{t_2} (B\dot{Q}Q + RP(A - C)Q + E(P^2 - R^2)Q) dt \\
\int_{t_1}^{t_2} YV dt &= \int_{t_1}^{t_2} (m\dot{V}V + mRUV - mPWV) dt \\
\int_{t_1}^{t_2} LP dt &= \int_{t_1}^{t_2} (A\dot{P}P - ERP + QR(C - B)P - EP^2Q) dt \\
\int_{t_1}^{t_2} NR dt &= \int_{t_1}^{t_2} (-E\dot{P}R + CR\dot{R} + PQ(B - A)R + EQR^2) dt
\end{aligned} \tag{14}$$

It is noticed that several terms on the right-hand side of equations (14) integrate into kinetic energy expressions. After completing the integrations, adding the equations and rearranging, it is not surprising that a statement of energy balance is recovered:

$$\begin{aligned}
\left\{ \frac{1}{2} m\dot{W}^2 + \frac{1}{2} m\dot{V}^2 + \frac{1}{2} B\dot{Q}^2 + \frac{1}{2} A\dot{P}^2 + \frac{1}{2} C\dot{R}^2 - EPR \right\} \Big|_{t_1}^{t_2} &= \int_{t_1}^{t_2} (F_z W + MQ + YV + LP + \\
+ NR) dt - m \int_{t_1}^{t_2} (PVW - QUW) dt - (A - C) \int_{t_1}^{t_2} RPQ dt + E \int_{t_1}^{t_2} P^2 Q dt + \\
- E \int_{t_1}^{t_2} (P^2 - R^2) Q dt - m \int_{t_1}^{t_2} (RUV - PWV) dt - (C - B) \int_{t_1}^{t_2} QRP dt - E \int_{t_1}^{t_2} R^2 Q dt + \\
- (B - A) \int_{t_1}^{t_2} PQR dt
\end{aligned} \tag{15}$$

It may be of interest to refer the interested reader to reference 4 where it is shown that a connection exists between the derivation of the equations of motion based on Hamilton's Principle and the statement of energy balance as expressed by equation (15).

For the numerical evaluation of the energy contribution of each term in equation (15), a subroutine was added to the programs used for the numerical integration of the linear and non-linear equations of motion in Section 3. Before discussing the energy-time histories of individual terms during a typical disturbed motion of a rigid airplane the following basic discussion on the energy behavior of the aerodynamic forces and moments is given. The discussion is restricted to the linearized lateral equations of motion.

The total aerodynamic energy added to the airplane or extracted from it during a certain time interval may be written as:

$$E_{AER.} = EY + EL + EN \tag{16}$$

where

$$\begin{aligned}
EY &= \bar{q}_1 S U_o \int_{t_1}^{t_2} \left\{ C_{y_\beta} \beta + C_{y_p} \frac{\dot{\beta} b}{2U_o} + C_{y_r} \frac{\dot{\beta} b}{2U_o} \right\} \beta dt \\
EL &= \bar{q}_1 S b \int_{t_1}^{t_2} \left\{ C_{\ell_\beta} \beta + C_{\ell_p} \frac{\dot{\beta} b}{2U_o} + C_{\ell_r} \frac{\dot{\beta} b}{2U_o} \right\} \dot{\beta} dt \\
EN &= \bar{q}_1 S b \int_{t_1}^{t_2} \left\{ C_{n_\beta} \beta + C_{n_p} \frac{\dot{\beta} b}{2U_o} + C_{n_r} \frac{\dot{\beta} b}{2U_o} \right\} \dot{\beta} dt
\end{aligned} \tag{17}$$

A certain asymmetry is noticed in these equations. There appear to be one displacement variable (β) and two velocity variables ($\dot{\phi}$) and ($\dot{\psi}$) in the equations. That this is actually not the case can be seen by recognizing that $\beta \approx \dot{y}/U_0$ in the linear approximation. This not only makes equations (15) more symmetric, but also leads to the interpretation of the β -derivatives as a particular form of rate derivatives. According to this viewpoint, then, all derivatives in equations (17) are either positive or negative damping derivatives or both. As a consequence, three pure damping derivatives occur in the equations: $C_{y\beta}$, $C_{\dot{\phi}_p}$, and $C_{\dot{\psi}_r}$. Terms corresponding to these derivatives always dissipate energy. The other derivatives can either dissipate or add energy. This is mathematically evident because the sign of cross products of β , $\dot{\phi}$, and $\dot{\psi}$ can vary.

Some interesting aspects of energy-time histories for individual terms in the equations of motion are now discussed. It will be evident from the discussion that these energy-time histories can be used to identify terms responsible for undesirable motion effects. The energy-time histories are presented first for the linearized lateral equations of motion.

As a typical example of the energy transfer that take place during a dutch roll type of motion, Figures 8 through 11 are presented. In this example, airplane A is disturbed by a rudder pulse of the form:

$$\delta_R = 5 \{u(t-1) - u(t-2)\} \quad (18)$$

A striking fact noticed from Figure 8 is that the motions take place with energy levels of lateral translational energy considerably above those of the rotational energy. Although there is an alternating trade between translational and rotational energy, the latter remains a magnitude lower. The reason for this is that the aerodynamic derivatives $C_{\dot{\phi}_\beta}$ and $C_{\dot{\psi}_\beta}$, which are the main energy transferring agents (see Figures 10 and 11), are normally balanced in such a way that only relatively little energy can be transferred.

The energy-time histories of Figures 9 through 11 also bring out the following. The effect of the derivatives C_{y_p} and C_{y_r} on the motion to energy dissipation is small: it is almost two magnitudes below the level of translational energy shown in Figure 8.

From Figure 11 it is seen that in this flight condition the positive damping effect of $C_{\dot{\psi}_r}$ is practically cancelled by the negative damping effect of $C_{\dot{\psi}_p}$. It is also seen that $C_{\dot{\psi}_\beta}$ acts as a spring term: it alternately dissipates and adds energy. This conforms with the conventional interpretation of $C_{\dot{\psi}_\beta}$ as an aerodynamic spring.

For the L-equation Figure 10 indicates that $C_{\dot{\phi}_r}$ is not important whereas $C_{\dot{\phi}_p}$ continually dissipates energy. The unfavorable effect of $C_{\dot{\phi}_\beta}$ is evident in that it adds more energy than it dissipates.

Of course, all these facts can be obtained from conventional methods of analysis of the linear equations of motion. It is felt, however, that the energy-time histories given here provide an extra insight which cannot be obtained otherwise. This is particularly valuable in application to the non-linear equations of motion. In such an application the energy-time relations allow the identification of important non-linear terms.

Figures 12 and 13 present typical examples of energy-time behavior obtained for the non-linear lateral equations of motion of airplane B. This configuration was selected because of its marked non-linear behavior. Figure 12 shows the differences that exist between the energy-time relations as calculated from the linear and from the non-linear equations of motion. These results again emphasize the importance of the non-linear terms in the case of airplane B. Figure 13 demonstrates the fact that not all non-linear terms are important. It is seen that the non-linear terms in the Y- and N-equations are more important than those in the L-equation.

The examples of Figures 12 and 13 show that energy-time plots can be used to identify important non-linear effects. Even though no non-linear aerodynamic terms were included in the present study, it is clear that the importance of such effects in small-disturbance maneuvers can be determined in the same manner. In practical applications, the amount of work involved in preparing these time histories can be eliminated by the use of automatic plotting routines.

7. CONCLUSIONS

Methods have been suggested for:

1. predicting the magnitude of initial disturbances within which linear stability theory is valid;

2. predicting under what circumstances linear response theory is no longer valid;
3. determining the stability behavior of non-linear airplane equations of motion, during response calculations; and
4. identifying terms in the equations of motion which contribute to significant non-linear behavior.

Example applications are given for two hypothetical airplane configurations.

8. REFERENCES

1. Roskam, J., Flight Dynamics of Rigid and Elastic Airplanes, Parts I and II, Fourth Printing, 1976, Roskam Aviation and Engineering Corporation, 519 Boulder, Lawrence, Kansas, 66044.
2. McRuer, D., I. Ashkenas, and D. Graham, Aircraft Dynamics and Automatic Control, Princeton University Press, Princeton, New Jersey, 1973.
3. Etkin, B., Dynamics of Atmospheric Flight, John Wiley & Sons, Inc., New York, 1972.
4. Roskam, J., On Some Linear and Non-linear Stability and Response Characteristics of Rigid Airplanes and a Mass Method to Integrate Non-linear Differential Equations, Ph.D. Dissertation, 1965, University of Washington, Seattle.
5. Malkin, I. G., "Theory of Stability of Motion," United States Atomic Energy Commission, AEC-tr-3352.
6. Chetayev, N. G., "On the Stability of Rough Systems," Prikladnaja Matematika i Mekhanika, Vol. 24, 1960, pp. 20-22.
7. Abzug, M. J., "Effects of Certain Steady Motions on Small-Disturbance Airplane Dynamics," Journal of the Aeronautical Sciences, Vol. 21, No. 11, November 1954, pp. 749-752, 762.
8. Chetayev, N. G., The Stability of Motion, Pergamon Press, New York, 1961.
9. Hahn, W., Theory and Application of Lyapunov's Direct Method, Prentice Hall Inc., Englewood Cliffs, New Jersey, 1963.

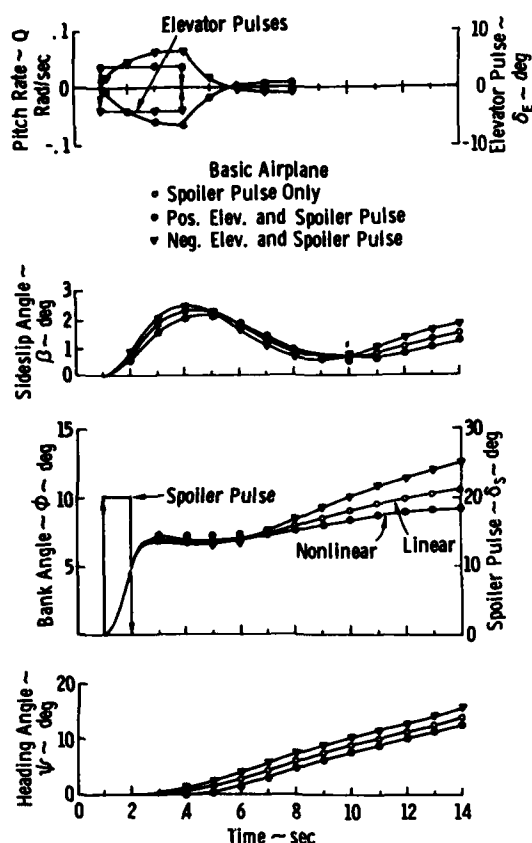


Figure 1. Linear and Non-Linear Lateral Responses for Airplane A (M = .19, Sea Level)

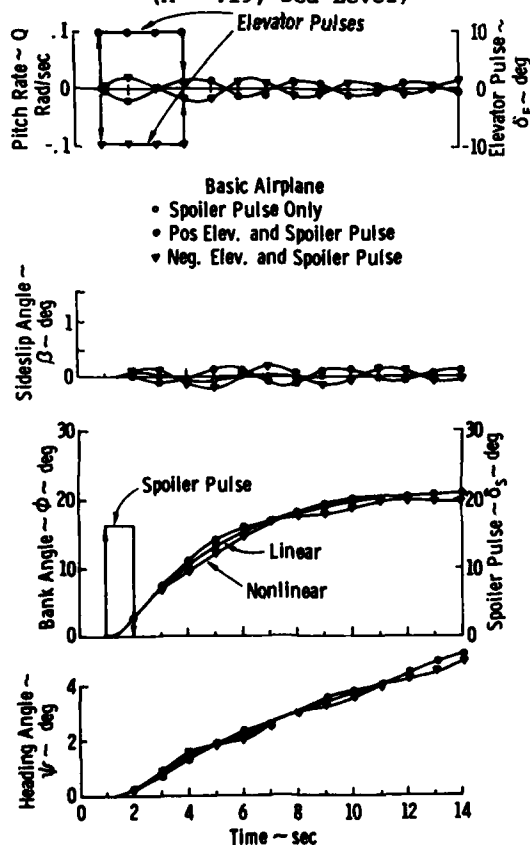


Figure 3. Linear and Non-Linear Lateral Responses for Airplane A (M = 2.7, 68,500 ft.)

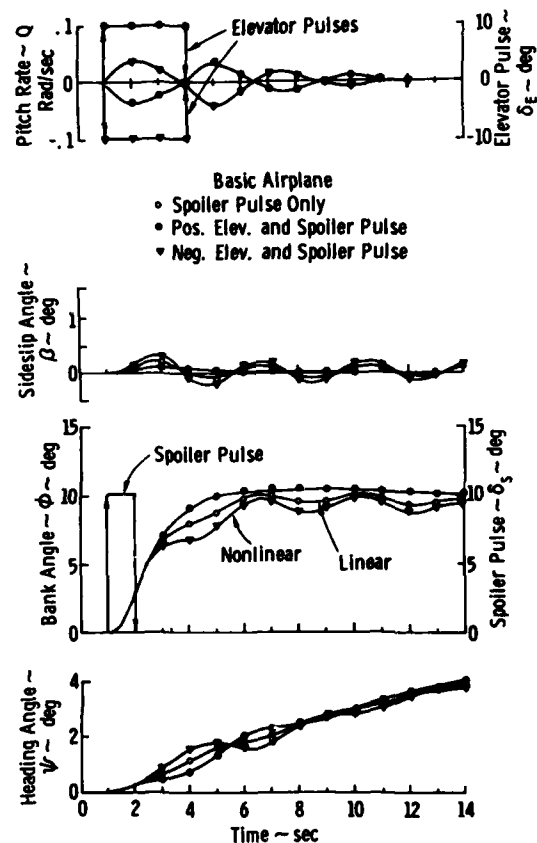


Figure 2. Linear and Non-Linear Lateral Responses for Airplane A (M = 1.2, 40,000 ft.)

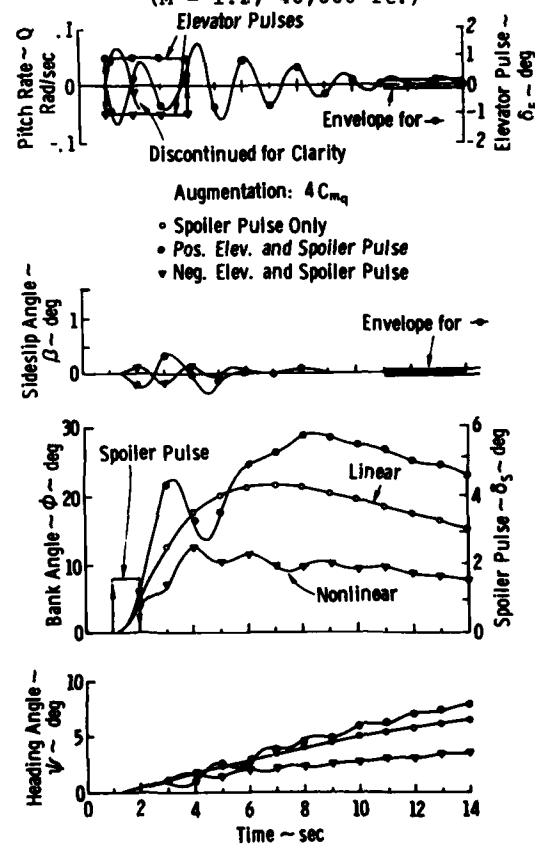


Figure 4. Example of Non-Linear Response for Airplane B (M = 2.0, 40,000 ft.)

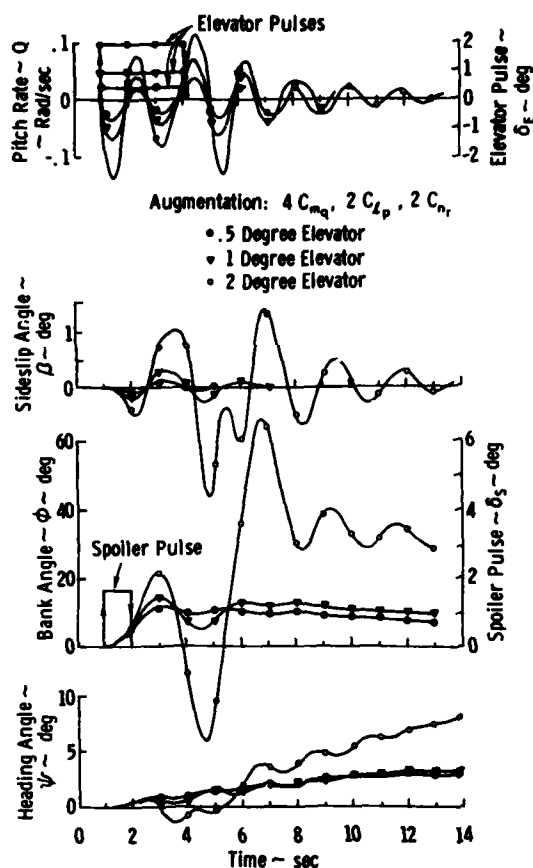


Figure 5. Non-Linear Lateral Responses under Different Longitudinal Disturbance for Airplane B (M = 2.0, 40,000 ft.)

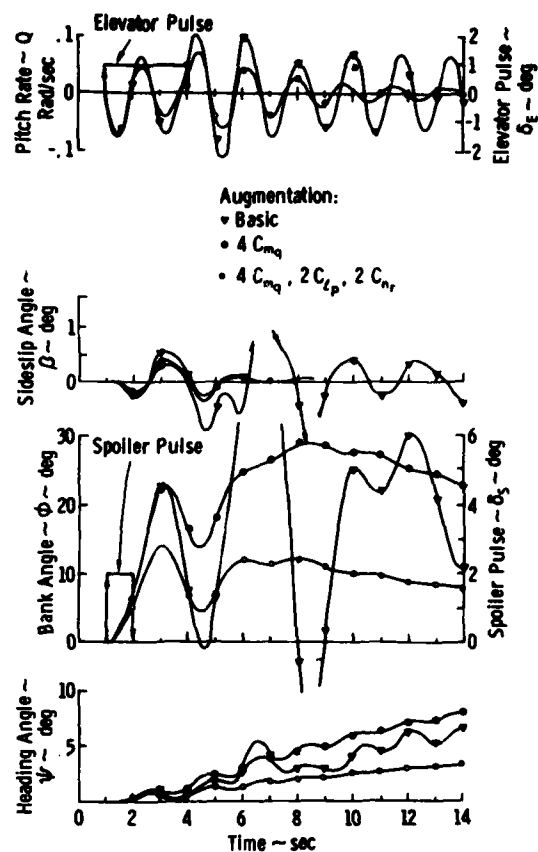


Figure 6. Effect of Damping Augmentation on Non-Linear Lateral Response for Airplane B (M = 2.0, 40,000 ft.)

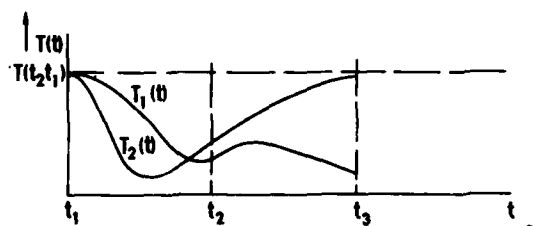


Figure 7. Examples of Kinetic Energy Time Histories

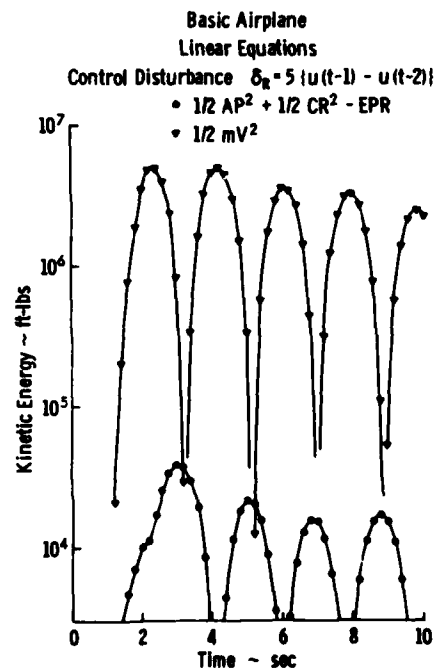


Figure 8. Time History of Kinetic Energy for Airplane A (M = 1.2, 40,000 ft.)

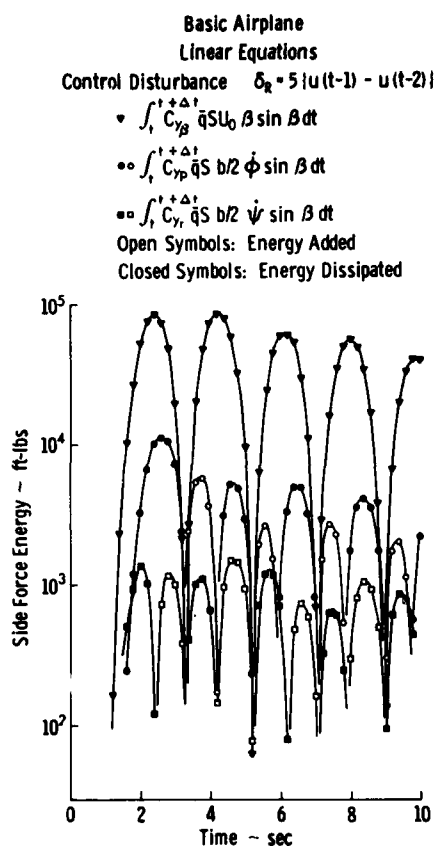


Figure 9. Time History of Aerodynamic Side Force Energy Participation for Airplane A ($M = 1.2$, 40,000 ft.)

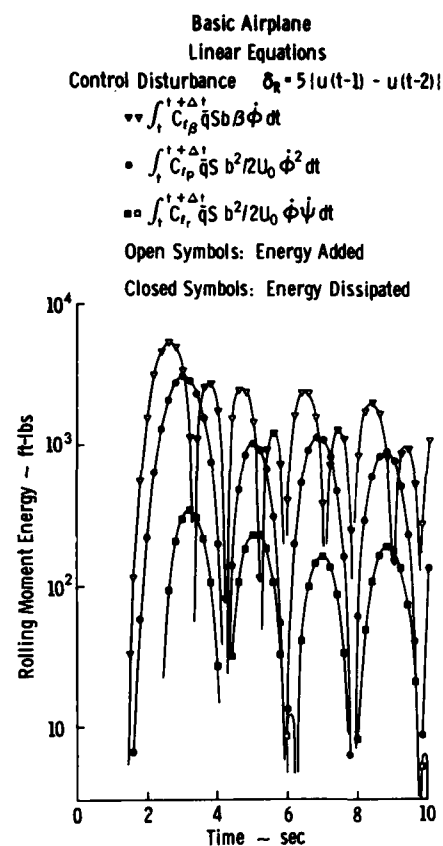


Figure 10. Time History of Aerodynamic Rolling Moment Energy Participation for Airplane A ($M = 1.2$, 40,000 ft.)

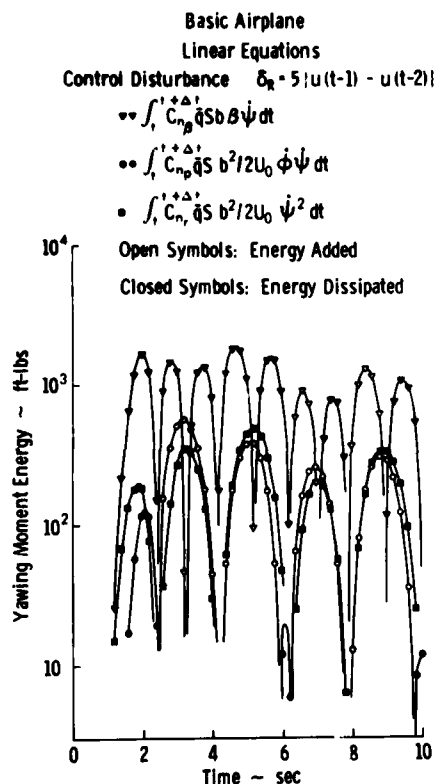


Figure 11. Time History of Aerodynamic Yawing Moment Energy Participation for Airplane A ($M = 1.2$, 40,000 ft.)

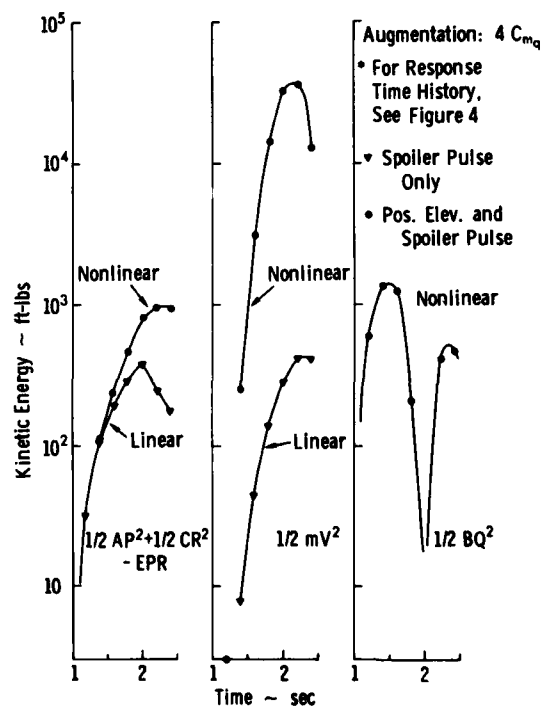


Figure 12. Time History of Kinetic Energy for Linear and Non-Linear Response, Airplane B ($M = 2.0$, 40,000 ft.)

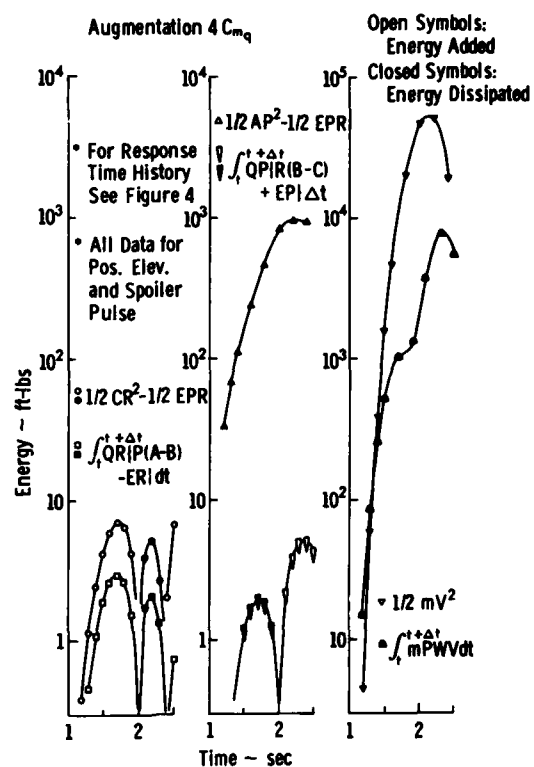


Figure 13. Time History of Energy Participation of Some Non-Linear Terms, Airplane B (M = 2.0, 40,000 ft.)

Table I. Non-Linear Airplane Equations of Motion

u	X_u	0	$X_u \frac{1}{U_0}$	0	0	0	0	$-g \cos \theta_0$	0	u	$U - U_0$
v	0	Y_v	$Y_v + (R_0 Y_v - \dot{Y}_v) \frac{1}{U_0}$	Y_v	0	$Y_v \cdot U_0$	$g \sin \theta_0$	0	$g \cos \theta_0 \cos \phi_0$	v	$W - g \sin \theta_0 \sin \phi_0 + g \cos \theta_0 \sin \phi_0 \left(\frac{\phi^2}{2} + \frac{\phi^2}{2} \right) + \frac{Y_v}{U_0} - \frac{Y_v}{U_0}$
w	$\frac{L_v}{1+L_v}$	$\frac{Q_v}{1+L_v}$	$\left(\frac{L_v \sin \theta_0}{\cos \theta_0} + L_v + \frac{Q_v}{\cos \theta_0} \right) \frac{1}{1+L_v}$	0	$\frac{U_0 \cdot L_v}{1+L_v}$	0	0	$\frac{g \sin \theta_0}{1+L_v}$	$\frac{g \cos \theta_0 \sin \phi_0}{1+L_v}$	w	$W - g \sin \theta_0 \sin \phi_0 + g \cos \theta_0 \sin \phi_0 \left(\frac{\phi^2}{2} + \frac{\phi^2}{2} \right) + \frac{L_v}{2 \cos \theta_0} \frac{D_v}{U_0} w^2$
p	0	$\frac{L_p + N_p A_1}{1 - A_1 B_1}$	$\frac{X_p + Y_p A_1}{1 - A_1 B_1}$	$\frac{L_p + N_p A_1 + Q_p A_1 (1 - E_1)}{1 - A_1 B_1}$	$\frac{-R_p (C_1 + A_1 B_1) + \dot{R}_p A_1 (1 - E_1)}{1 - A_1 B_1}$	$\frac{L_p + N_p A_1 + Q_p (C_1 + A_1 B_1)}{1 - A_1 B_1}$	0	0	0	p	$(1 - A_1 B_1)^{-1} (-\dot{p} R_p C_1 + A_1 B_1 \dot{p} + p R_p A_1 (1 - E_1) + \frac{p}{U_0} (L_p + N_p) (1 - p A_1) + \frac{p}{U_0} (L_p + N_p) R_p A_1 - p \dot{p} + \frac{p}{U_0} (A_1 L_v - N_p))$
q	M_q	$\frac{-P M_q}{1+L_v}$	$M_q - \frac{M_q}{1+L_v} \left(\frac{L_v \sin \theta_0}{\cos \theta_0} + L_v + \frac{Q_v}{\cos \theta_0} \right)$	$-R_q D_1 - 2 \dot{R}_q \dot{X}_1$	$M_q + \frac{M_q (U_0 - L_v)}{1+L_v}$	$-R_q B_1 + 2 \dot{R}_q \dot{X}_1$	0	$\frac{g \sin \theta_0 M_q}{1+L_v}$	$\frac{g \cos \theta_0 \sin \phi_0 M_q}{1+L_v}$	q	$q R_q + (r^2 - p^2) E_1 + M_q (1 + L_v)^{-1} (-\dot{p} - g \sin \theta_0 \sin \phi_0 + g \cos \theta_0 \sin \phi_0 \left(\frac{\phi^2}{2} + \frac{\phi^2}{2} \right) + \frac{L_v}{2 \cos \theta_0} \frac{D_v}{U_0} w^2$
r	0	$\frac{N_r + L_r B_1}{1 - A_1 B_1}$	$\frac{Y_r + X_r B_1}{1 - A_1 B_1}$	$\frac{N_r + L_r B_1 + Q_r (A_1 B_1 - E_1)}{1 - A_1 B_1}$	$\frac{R_r (A_1 B_1 - E_1) - \dot{R}_r B_1 (1 + C_1)}{1 - A_1 B_1}$	$\frac{N_r + L_r B_1 + Q_r B_1 (1 + C_1)}{1 - A_1 B_1}$	0	0	0	r	$(1 - A_1 B_1)^{-1} (-\dot{p} R_r C_1 + C_1 \dot{p} + p R_r A_1 B_1 - E_1) + \frac{p}{U_0} (L_r + N_r) R_r - \dot{p} R_r + \frac{p}{U_0} (L_r + N_r) B_1 + \frac{p}{U_0} (L_r - B_1 N_r)$

Notes:

- Symbolically: $\{x\} = \{A\} \{x\} + \{g\} x$ with: $\{x\}^T = u, v, w, p, q, r$
- Non-linear aerodynamic effects not symbolized in $\{g\}$
- $X_u = (R_0 Y_u - \dot{Y}_u) \frac{1}{U_0}$
- $Y_v = (R_0 Y_v + N_p) \frac{1}{U_0} + \dot{Y}_v \frac{1}{U_0}$
- For symbol definitions see list of symbols in references 1 and 4

Table II. Dynamic Stability Characteristics for Airplanes A and B According to Linear Theory

	DUTCH ROLL		DUTCH ROLL		DUTCH ROLL		ϕ/β	ϕ_{max}
	Pitch Rate = 0 RPS ϵ_D	ω_D (RPS)	Pitch Rate = .1 RPS ϵ_D	ω_D (RPS)	Pitch Rate = .1 RPS ϵ_D	ω_D (RPS)		
AIRPLANE A								
M = .10, Sea Level	.07	.25	.03	.26	.14	.23	.16	.01
M = 1.2, 40,000 ft	.09	.27	.02	.27	.09	.26	2.80	.11
M = 2.7, 60,500 ft	.09	.24	.01	.24	.16	.24	2.70	.10
AIRPLANE B								
M = 2.0, 40,000 ft	.09	.43	.11	.47	.30	.45	15.4	.67

APPENDIX A

SUMMARY OF CONCEPTS FROM LYAPUNOV'S STABILITY THEORY

In stating stability characteristics of differential equations without actually solving them the direct method of Lyapunov has been found very useful. Because this method and its applications are generally not familiar to airplane stability analysts, it was felt that a summary of definitions and theorem used in Section 2 would be helpful. All proofs have been omitted since these can be found in the literature (references 5, 8 and 9).

Consider the system of differential equations for an undisturbed motion:

$$\dot{y} = f(y, t) \quad (A1)$$

where y stands for a column vector whose components are the dependent variables of the problem. If $v = v(t)$ is the solution of (A1), it is called the solution of the undisturbed motion. Introducing $x = y - v$, the differential equation of the disturbed motion is obtained as:

$$\dot{x} = f(x + v, t) - f(v, t) \quad (A2)$$

The solution $x = 0$ corresponds to the equilibrium state of the motion i.e. the undisturbed motion itself. This is also expressed by saying that the origin ($x = 0$) is a singularity of the system (A2). The following definitions and theorems make statements about this equilibrium. For convenience, equation (A2) is written as:

$$\dot{x} = f(x, t) \quad \text{and} \quad x(t = t_0) = x_0 \quad (A3)$$

Definition 1. The equilibrium of Equation (A3) is called weakly stable if for each number $\epsilon > 0$ a number $\delta(\epsilon, t_0)$ with $\delta > 0$ can be found such that $|x(t = t_0)| < \delta$ implies that $|x(t, x_0, t_0)| < \epsilon$ for all $t \geq t_0$.

Definition 2. The equilibrium of equation (A3) is called asymptotically stable if a number $\delta(t_0)$ can be found such that $|x(t_0)| < \delta(t_0)$ implies that $\lim_{t \rightarrow \infty} x(t, x_0, t_0) = 0$.

The preceding definitions of stability can also be formulated in the following manner.

Definition 3. The equilibrium of equation (A3) is called weakly stable if for each number $H > 0$ a number γ can be found such that $\int_{t_0}^{\infty} x_s^2(t = t_0) \leq \gamma$ implies that $\int_{t_0}^{\infty} x_s^2(t, x_0, t_0) < H$ for all $t > t_0$.

Definition 4. The equilibrium of equation (A3) is called stable if it is both weakly stable and asymptotically stable.

It may be noticed that definition 4 implies that in such a case for each number $\eta > 0$ a number $\tau(\eta)$ exists such that $|x(t_0)| < \delta(t_0)$ implies that:

$$|x(t, x_0, t_0)| < \eta(t > t_0 + \tau) \quad (A4)$$

Definition 5. If inequality (A4) holds for all points x_0 from which motions originate, the equilibrium of equation (A3) is called stable in the large.

It is observed that linear differential equations with constant coefficients are always stable in the large.

Definition 6. If the equilibrium of equation (A3) is neither weakly stable nor asymptotically stable, it is called unstable.

Many variations on definitions 1 through 6 can be found in the literature. For the purposes of this paper, the above definitions are sufficient.

Before starting the major stability theorems used in this paper, the following definitions are required.

Definition 7. A function $V(x, t)$ is called positive definite if $V(0) = 0$ and if in a spherical neighborhood of the origin $V(x, t) \geq 0$. If $V(0) = 0$ and $V(x, t) > 0$ for $x \neq 0$, the function is called positive sign definite.

The definitions for negative definite and negative sign definite are obvious.

The following theorems are all due to Lyapunov.

Theorem 1. The equilibrium of equation (A3) is weakly stable if there exists a positive sign definite function $V(x, t)$ such that the total derivative dV/dt for equation (A3) is not positive.

Theorem 2. The equilibrium of equation (A3) is stable if there exists a positive sign definite function $V(x, t)$ such that the total derivative dV/dt for equation (A3) is negative sign definite.

Functions $V(x, t)$ for which theorems 1 or 2 are satisfied are called Lyapunov functions.

Consider the set of linear differential equations with constant coefficients:

$$\{\dot{x}\} = [A]\{x\} \quad (A5)$$

Theorem 3. The equilibrium of equations (A5) is stable if all eigen-values of the matrix A have negative real parts.

Theorem 4. The equilibrium of equations (A5) is unstable if at least one eigen-value of the matrix A has a positive real part.

Definition 8. The differential equations (A5) are said to have significant behavior if either theorem 3 or theorem 4 is satisfied.

Definition 9. The differential equations (A5) are said to be critical if they do not have significant behavior.

Consider next a modified form of (A5):

$$\{\dot{x}\} = [A]\{x\} + g\{x\} \quad (A6)$$

where $g(x)$ may contain non-linear combinations of the components of $\{x\}$. Equations (A5) are called the differential equations of the first approximation of (A6). For sufficiently small disturbances the following theorem applies.

Theorem 5. If the stability behavior of the differential equations of the first approximation (A5) is significant, then the equilibrium of the complete differential equations (A6) has the same behavior as the equilibrium of the equations of the first approximation.

If the equations (A5) are critical, then the stability behavior of (A6) can be found only from the complete equations.

APPENDIX B

SUMMARY OF AIRPLANE CHARACTERISTICS

To provide example airplanes for calculations of stability and response characteristics three high-speed airplane configurations were selected. The airplanes are identified as A and B. The flight conditions used in the calculations are identified in Table B-1. The geometric, inertial, and aerodynamic characteristics for these flight conditions are presented in Table B-2.

A brief mission summary for each configuration is given below.

Airplane A. This is a hypothetical large variable-sweep transport configuration. With the wings swept at 74° the airplane has a cruise Mach number of 2.7. Normal landings are carried out with the wings swept at 20°.

Airplane B. This configuration is representative of a hypothetical high performance swept-wing fighter, designed to fly at supersonic speed at sea level as well as at high altitude. This explains the very low ratio of rolling inertia to yawing inertia.

Table B-1. Flight Conditions for Configurations A and B

CONFIGURATION	FLIGHT CONDITION	ALTITUDE	MACH NUMBER	Λ_{LE}
A	1	Sea level	.19	20°
	2	68,500 ft	2.50	74°
	3	40,000 ft	1.20	65°
B	1	40,000 ft	2.0	79°

Table B-2. Geometric, Inertial and Aerodynamic Characteristics of Airplanes A and B

AIRPLANE	A1	A2	A3	B	AIRPLANE	A1	A2	A3	B
GEOMETRIC DATA					LONGITUDINAL AERODYNAMIC DATA, CONT.				
W (lbs)	240000	240000	400000	55000	$C_{L_{\alpha}}$ deg ⁻¹	.0525	.00019	.0006	.01
S (m ²)	4684	4684	4684	627	$C_{m_{\alpha}}$ deg ⁻¹	-.0105	-.00022	-.00068	-.0085
c (ft)	64.52	64.52	64.52	25.4	L/D	8.0	8.0	6.5	6.0
b (ft)	86.35	86.35	86.35	29	LATERAL AERODYNAMIC DATA				
I_{xx} - Slug ft ²	2.25×10^5	1.07×10^5	2.62×10^5	3.1×10^4	$C_{Y_{\beta}}$ rad ⁻¹	-.808	.52	-.6917	.79
I_{yy} - Slug ft ²	9.25×10^4	10.1×10^4	13.85×10^4	58.5×10^4	$C_{Y_{\dot{\beta}}}$ rad ⁻¹	.780	.730	.506	0
I_{zz} - Slug ft ²	11.11×10^4	10.81×10^4	15.7×10^4	58.5×10^4	$C_{Y_{\dot{\beta}}}$ rad ⁻¹	.098	.260	.353	0
I_{xy} - Slug ft ²	2.6×10^5	2.2×10^5	3.8×10^5	1.97×10^5	$C_{Y_{\alpha}}$ deg ⁻¹	.00237	.00028	.00053	.0004
A_{LE} (deg)	20	74	65	75	$C_{Y_{\dot{\alpha}}}$ rad ⁻¹	-.0566	.0280	.1184	.172
FLIGHT CONDITION					$C_{Y_{\ddot{\beta}}}$ rad ⁻¹	1.340	-.0750	.201	.130
h (ft)	Sea	68500	40000	40000	$C_{Y_{\ddot{\alpha}}}$ rad ⁻¹	.685	.064	.1099	.155
ρ (slug ft ⁻³)	.002378	.00048	.000565	.000565	$C_{Y_{\alpha\alpha}}$ deg ⁻²	.00183	.000035	.0002	.0002
σ	1.0	0.6233	.24617	.24617	$C_{Y_{\alpha\dot{\beta}}}$ deg ⁻¹ rad ⁻¹	-.000068	.000071	.000011	.00002
M	.19	2.7	1.2	2.0	$C_{Y_{\beta\dot{\beta}}}$ rad ⁻¹	.156	.099	.2153	.2
q_c (psf)	53.6	435	395	1095	$C_{Y_{\beta\alpha}}$ rad ⁻¹ deg ⁻¹	-.171	.086	.1785	.1
LONGITUDINAL AERODYNAMIC DATA					$C_{Y_{\dot{\alpha}\dot{\beta}}}$ rad ⁻¹	-.542	.39	-.4902	.62
C_{L_0}	.752	-.0591	.007	.022	$C_{Y_{\alpha\dot{\alpha}}}$ deg ⁻¹	.00161	.0003	.00099	.0014
$C_{L_{\dot{\alpha}}}$ rad ⁻¹	3.6	1.49	2.01	1.94	$C_{Y_{\alpha\ddot{\alpha}}}$ deg ⁻¹ rad ⁻¹	.000015	.000011	.000053	.00002
$C_{L_{\ddot{\alpha}}}$ rad ⁻²	0	0	0	0					
$C_{L_{\beta}}$ rad ⁻¹	0	0	0	0					
C_{m_0}	0	.0267	.0216	0					
$C_{m_{\dot{\alpha}}}$ rad ⁻¹	-.198	-.179	-.2005	-.417					
$C_{m_{\ddot{\alpha}}}$ rad ⁻²	0	0	-.65	0					
$C_{m_{\beta}}$ rad ⁻¹	-1.41	-.81	-1.41	-1.0					

APPENDIX C

EXPLANATION OF LATERAL RESPONSE PARAMETER $\phi_{\max, \beta}$

The parameter $\phi_{\max, \beta}$ represents the first bank angle extremum for an airplane subjected to a sinusoidal sideslip disturbance. Values for $\phi_{\max, \beta}$ follow from the single-degree-of-freedom equation:

$$\ddot{\phi} - L_p \dot{\phi} = L_\beta \sin \omega_d t \quad \phi(0) = \dot{\phi}(0) = 0 \quad (C1)$$

The time t^* for which the first ϕ -extremum occurs is calculated from the transcendental equation:

$$e^{L_p t^*} + \frac{1}{\omega_d} \sqrt{L_p^2 + \omega_d^2} \cos(\omega_d t^* - \psi) = 0 \quad (C2)$$

where $\psi = -\frac{\pi}{2} + \arctan \frac{-\omega_d}{L_p}$.

The value $\phi_{\max, \beta}$ is found from:

$$\phi_{\max, \beta} = \frac{\omega_d L_\beta}{57.3} \left\{ \frac{-1}{L_p \omega_d} - \frac{\cos(\omega_d t^* - \psi)}{\omega_d L_p \sqrt{L_p^2 + \omega_d^2}} + \frac{\sin(\omega_d t^* - \psi)}{\omega_d^2 \sqrt{L_p^2 + \omega_d^2}} \right\} \left(\frac{\text{RAD}}{\text{DEG}} \right) \quad (C3)$$

AIRCRAFT STABILITY CHARACTERISTICS AT HIGH ANGLES OF ATTACK

by

Juri Kalviste

Northrop Corporation, Aircraft Group

3901 West Broadway

Hawthorne, California 90250

U. S. A.

SUMMARY

At low to moderate angle of attack flight conditions the aircraft stability characteristics can be described in terms of longitudinal and lateral/directional modes of motion. At high angle-of-attack flight conditions the two modes are strongly coupled and this requires complete six-degree-of-freedom motion analysis. This paper reports on an analysis technique where six-degree-of-freedom equations are partitioned into rotational and translational equations of motion retaining all the cross coupling between the longitudinal and lateral directional modes of motion. The aircraft stability is characterized in terms of aircraft rotational motion due to static aerodynamic coefficients. A new dynamic stability axes system is defined. Stability parameters are defined about the dynamic stability axes system. A new set of stability criteria is defined in terms of the new dynamic stability derivatives. The new stability criteria are an extension of the classical stability parameter $C_{n\beta}$. The new criteria predict instability which correlates with com-

plete six-degree-of-freedom analysis where the classical parameter fails to predict instability. The analysis takes into account nonlinear aerodynamics and nonzero moments at zero sideslip condition. The definition of the Lateral Control Departure Parameter (LCDP) is extended for nonlinear aerodynamics and defined in terms of angle of attack and sideslip. The new criteria have been validated with complete six-degree-of-freedom perturbation equation stability analysis, nonlinear time history simulation, and flight test results.

LIST OF SYMBOLS

A. Aircraft motion, position, and attitude

V_T	Total velocity
U, V, W	Components of V_T along aircraft x, y, z body axes
α, β	Angle of attack and sideslip, same symbol is used for total angles or perturbation angles about α_0 and β_0 .
P, Q, R	Roll, pitch, and yaw rates about aircraft body axes
θ	Pitch angle about aircraft y-axis
ϕ	Roll angle about aircraft x-axis
μ	Bank angle about velocity vector
h	Altitude
δ_i	Control surface deflection, i = A = aileron, R = rudder, H = horizontal tail

B. Aerodynamics

L, D, Y	Aerodynamic lift, drag, and side force divided by mass, $\frac{\bar{q}S}{m}C_L, \frac{\bar{q}S}{m}C_D, \frac{\bar{q}S}{m}C_Y$
\mathcal{L}, M, N	Aerodynamic moment about aircraft x, y, z axes divided by moment of inertia, $\frac{\bar{q}Sb}{I_{xx}}C_l, \frac{\bar{q}Sb}{I_{yy}}C_m, \frac{\bar{q}Sb}{I_{zz}}C_n$
C_L, C_D, C_Y	Lift, drag, and side force coefficients
C_l, C_m, C_n	Roll, pitch, yaw, moment coefficients
DYN	Subscript, refers to dynamic stability axes
COP	Subscript, refers to coupled parameters
K	Coupling parameter
F_j	$\partial F / \partial j, F = \mathcal{L}, C_l, C_{l,DYN}, \text{ etc.}, j = \alpha, \beta, \delta$

C. Aircraft parameters

m	Mass of aircraft
I_{xx}, I_{yy}, I_{zz}	Moment of inertia about aircraft x, y, z body axes
I_{xy}, I_{xz}, I_{yz}	Cross moment of inertias

b	Wing span
\bar{c}	Mean aerodynamic chord
S	Wing reference area

D. Miscellaneous definitions

A, B	Polynomial coefficients
R, I	Real and imaginary part of complex number
ω, ζ	Natural frequency and damping
C_1, C_2	Roots of polynomial
D, d	Sign of polynomial discriminant
X, Y	Nondimensional form of polynomial coefficients
ω_ϕ	Roll rate to aileron transfer function numerator natural frequency
ω_D	Dutch roll frequency
σ, ω	Real and imaginary part of complex number
g	Acceleration due to gravity
S	Laplace transform operator
SP	Subscript, pitch short period
\cdot	Dot over symbol indicates differentiation with respect to time

1. INTRODUCTION

The stability analysis of an aircraft involves the complete six-degree-of-freedom equations of motion. At some flight conditions the equations can be partitioned into longitudinal and lateral/directional mode of motion and the stability analysis can be performed on the uncoupled modes. This is usually true at low to moderate angle-of-attack flight conditions. At these conditions the aerodynamics can be represented with linear derivatives and the kinematic coupling terms are small.

Another mode of motion that has been analyzed extensively is the developed spin mode, where the aircraft motion is predominately characterized by the dynamics of the body.

This paper reports on the stability characteristics of the aircraft in the "transition mode" where the aerodynamics cannot be represented by linear derivatives, the aerodynamic and kinematic coupling between the longitudinal mode and lateral/directional mode is large, and the motion is predominately controlled by aerodynamic moments.

2. EQUATIONS OF MOTION

The motion of an aircraft can be described by a set of six nonlinear second order differential equations representing the rotational and translational accelerations of the aircraft. The six equations can be expanded to twelve nonlinear first order differential equations: six acceleration equations and six velocity equations. For stability analysis the flat nonrotating earth assumption can be made and the twelve equations can be reduced to nine equations by eliminating the two horizontal velocity equations and the rate of change of heading angle equation. The nine equations are shown in Figure 1. The first five equations represent the aircraft rotational motion and the last four equations represent aircraft translational motion. The translational acceleration equations have been written in spherical coordinates ($\dot{\alpha}, \dot{\beta}, \dot{V}_T$) instead of in terms of accelerations along the aircraft body axes ($\dot{U}, \dot{V}, \dot{W}$). This is done because aerodynamic moments and forces are defined in terms of α, β , and Mach number instead of in terms of velocity components along body axes: U, V , and W . The rotational accelerations due to the aerodynamic moments ($\dot{\mathcal{L}}, \dot{M}, \dot{N}$) and the linear accelerations due to the aerodynamics forces ($\dot{L}, \dot{D}, \dot{Y}$) can be described in terms of the nine state variables, their rates and aircraft characteristics. The moments and forces due to thrust are included in the aerodynamic terms to simplify the notation.

The stability characteristics of an aircraft can be determined from the solution of the nine differential equations. This can be accomplished by perturbation analysis techniques or the time history solution of the complete equations. In either case it is difficult to isolate parameters which cause instability. At low to moderate angle-of-attack flight conditions, the equations can be separated into the longitudinal ($\dot{Q}, \dot{\theta}, \dot{\alpha}, \dot{V}_T$) and lateral/directional ($\dot{P}, \dot{R}, \dot{\phi}, \dot{\beta}$) modes of motion. This is the conventional way of aircraft stability analysis. The reduced equations allow identification of parameters which cause instability. At high angle-of-attack flight conditions, the coupling between the two modes is strong; therefore, the uncoupled mode stability analysis cannot be used.

Another way to analyze aircraft stability is to partition the six-degree-of-freedom equations into rotational and translational equations of motion. Rotational acceleration causes a change in aircraft attitude and the translational acceleration causes a change in direction of flight. For conventional aircraft the direction of flight is changed by rotating the aircraft, this causes a change in direction and magnitude of forces on the aircraft which causes a change in direction of flight. To accomplish this the aircraft must have rotational stability.

The aerodynamic forces and moments are a function of aircraft attitude relative to the direction of flight (α and β) and aircraft rotational rates (P, Q, R). The aircraft is defined as rotationally stable if small disturbance in α or β

about a trimmed condition causes a moment in a direction to reduce the disturbance and the moment due to the rates is in the direction to reduce the rates. The translational stability of an aircraft is a function of α and β , aircraft rates, and also aircraft attitude relative to the gravity vector. As an example, an aircraft flying straight and level with negative M_a and positive L_a is statically stable. A positive change in α causes a negative pitching moment to reduce α and positive force to change direction of flight to reduce α . In a 360-degree roll at constant α the aircraft is rotationally stable but translationally unstable when roll angle is between 90 degrees and 270 degrees. At these conditions an increase in α causes a force to increase α at a faster rate. Therefore, for an aircraft to be stable at any attitude requires the aircraft to have rotational stability.

The rotational stability was defined in terms of moments due to attitude (α and β) and rates P , Q , R . A necessary but not sufficient condition for stability is that the aircraft has position stability (moments due to attitude). A positionally unstable aircraft cannot be stabilized with stabilizing moments due to aircraft rates. They can only slow down the instability if they are stable or speed up the instability if they are unstable. The important parameters for aircraft stability are the aerodynamic moments due to the attitude of the aircraft relative to the velocity vector. This paper describes the analysis of aircraft dynamic stability and controllability due to static aerodynamic coefficients.

3. DYNAMIC STABILITY AXES

The aircraft rotational acceleration equations due to static aerodynamic moments about the principal body axes of the aircraft and zero rotational rates are:

$$\dot{P} = \mathcal{L}(\alpha, \beta, \delta) = (\bar{q} S b / I_{xx}) C_l(\alpha, \beta, \delta) \quad (10)$$

$$\dot{Q} = M(\alpha, \beta, \delta) = (\bar{q} S c / I_{yy}) C_m(\alpha, \beta, \delta) \quad (11)$$

$$\dot{R} = N(\alpha, \beta, \delta) = (\bar{q} S b / I_{zz}) C_n(\alpha, \beta, \delta) \quad (12)$$

The aerodynamic moments are functions of α , β and general control surface deflection (δ), where δ can represent aileron (δ_A), rudder (δ_R), or any other control surface. If the aerodynamic moments are defined about a body axis other than principal axis, the moments can be converted into principal axis by proper transformations. (Ref. 1)

The change in α and β due to rotation of the aircraft relative to the velocity vector is (from Eq. 6 and 7 in Figure 1):

$$\dot{\alpha} = Q - (P \cos \alpha + R \sin \alpha) \tan \beta \quad (13)$$

$$\dot{\beta} = P \sin \alpha - R \cos \alpha \quad (14)$$

Eq. (10-14) define the rotational motion of the aircraft relative to the velocity vector due to static aerodynamic moments. The rotational acceleration equations are written about the body axes while the rotation velocity equations are written about a coordinate system which is a function of α and β . For stability analysis it is desirable to define both sets of equations about the same coordinate system.

The orientation of the aircraft relative to the velocity vector can be defined by a system of three angles. Two angles have been defined already as sideslip (β) and angle of attack (α). The third angle will be defined as bank angle (μ), which is the rotation about the velocity vector. The term "bank angle (μ)" is used to indicate rotation about the velocity vector while the term "roll angle (ϕ)" is used to indicate rotation about aircraft x-axis. The bank angle can be defined in terms of rotation of the aircraft lift vector since the lift vector is perpendicular to the velocity vector and defined in the x-z plane of the aircraft. Bank angle is equal to zero when the aircraft x-z plane is vertical. The sequence of rotation from the velocity vector to the aircraft coordinates is (μ , β , α). The rates of change of these angles are not orthogonal. This axis system is defined as the dynamic stability axes.

The relationships of the angular rates in the new axis system and the aircraft axis system are (using equations from Ref. 1, page 23, CASE 5):

$$P = \dot{\mu} \cos \alpha \cos \beta + \dot{\beta} \sin \alpha \quad (15)$$

$$Q = \dot{\mu} \sin \beta + \dot{\alpha} \quad (16)$$

$$R = \dot{\mu} \sin \alpha \cos \beta - \dot{\beta} \cos \alpha \quad (17)$$

$$\dot{\mu} = (P \cos \alpha + R \sin \alpha) \sec \beta \quad (18)$$

$$\dot{\alpha} = Q - (P \cos \alpha + R \sin \alpha) \tan \beta \quad (19)$$

$$\dot{\beta} = P \sin \alpha - R \cos \alpha \quad (20)$$

When α and β are zero the two axis systems are superimposed and $P = \dot{\mu}$, $Q = \dot{\alpha}$, $R = -\dot{\beta}$. The ($\dot{\mu}$, $\dot{\alpha}$, $\dot{\beta}$) equations are functions of aircraft rotational rates only since the direction of the velocity vector is assumed to be constant.

Eq. (18-20) transform the body axis rates to dynamic stability axis rates. The same transformation is used to convert body axis accelerations to dynamic stability axis accelerations.

$$\ddot{\mu} = (\dot{P} \cos \alpha + \dot{R} \sin \alpha) \sec \beta \quad (21)$$

$$\ddot{\alpha} = \dot{Q} - (\dot{P} \cos \alpha + \dot{R} \sin \alpha) \tan \beta \quad (22)$$

$$\ddot{\beta} = \dot{P} \sin \alpha - \dot{R} \cos \alpha \quad (23)$$

New dimensional stability parameters will be defined by replacing (\dot{P} , \dot{Q} , \dot{R}) with Eq. (10-12).

$$\ddot{u} = \mathcal{L}_{DYN} = (\mathcal{L} \cos \alpha + N \sin \alpha) \sec \beta \quad (24)$$

$$\ddot{\alpha} = M_{DYN} = M - (\mathcal{L} \cos \alpha + N \sin \alpha) \tan \beta \quad (25)$$

$$\ddot{\beta} = -N_{DYN} = -(N \cos \alpha - \mathcal{L} \sin \alpha) \quad (26)$$

\mathcal{L}_{DYN} is the rolling acceleration about the velocity vector, M_{DYN} is the pitching acceleration which causes a change in α and $-N_{DYN}$ is the yawing acceleration which causes a change in β . The subscript (DYN) is used to indicate that the motion is about the new dynamic stability axes and also relates to the previously defined departure parameter $C_{n\beta DYN}$ (Ref. 2, 3, 4). At zero angle of attack and sideslip condition $\mathcal{L}_{DYN} = \mathcal{L}$, $M_{DYN} = M$, and $N_{DYN} = N$.

The new dimensional parameters are nondimensionalized by the same parameters as in Eq. (10-12).

$$C_{lDYN} = \left(C_l \cos \alpha + \frac{I_{xx}}{I_{zz}} C_n \sin \alpha \right) \sec \beta \quad (27)$$

$$C_{mDYN} = C_m - \frac{b}{c} \left(\frac{I_{yy}}{I_{zz}} C_n \sin \alpha + \frac{I_{yy}}{I_{xx}} C_l \cos \alpha \right) \tan \beta \quad (28)$$

$$C_{nDYN} = C_n \cos \alpha - \frac{I_{zz}}{I_{xx}} C_l \sin \alpha \quad (29)$$

At zero α and β , $C_{lDYN} = C_l$, $C_{mDYN} = C_m$, and $C_{nDYN} = C_n$. The aerodynamic moment coefficients (C_l , C_m , C_n) are functions of α and β ; therefore, the aerodynamic coefficients in the dynamic stability axis system are also functions of α and β and they also include the kinematic coupling between the two coordinate systems.

The new nondimensional coefficients are defined about the same axis system used to define α and β . Therefore, the uncoupled (between α and β motion) stability criteria is $\partial C_{mDYN} / \partial \alpha < 0$ and $\partial C_{nDYN} / \partial \beta > 0$.

The new nondimensional coefficients have been computed for two different aircraft configurations. Aircraft configuration A is the A-7 aircraft using the aerodynamic data from Ref. 5. The data are symmetric about zero sideslip angle and the pitching moment is a function of angle of attack and elevator position only (no sideslip variation). Aircraft configuration B is a fighter aircraft with a long slender nose. The nose generates asymmetric moments at high angle of attack and nonzero moments at zero sideslip (see Ref. 6 and 7, for example). The aero data are well-defined with wind tunnel tests at small α and β increments and the data has been correlated with flight test results. All three moments are functions of α and β .

Figures 2, 3, and 4 show C_{lDYN} , C_{mDYN} , and C_{nDYN} , respectively, for aircraft Configuration A. The data is given for an α range from 0° to 90° and β range from -20° to $+20^\circ$.

Since the data are a function of two variables the data are presented as contour lines of C_{lDYN} , C_{mDYN} , and C_{nDYN} . Referring to Figure 2, at low angle of attack the rolling moment at constant β increases with increasing α and then decreases as α increases from 10° to 23° . At higher α rolling moment hold fairly constant with α . Figure 3 shows the dynamic stability axis pitching moment variation with α and β . Trim α at zero β is 25° . The pitching moment is stable (increasing α causes a moment to decrease α) except local instability at low α and large β . Since the body axis pitching moment data was a function of α only the variation of C_{mDYN} with β is due to the kinematic coupling.

Figure 4 shows the dynamic stability axis yawing moments variation with α and β . At low and high α the aircraft has positive sideslip stability; that is, increasing β caused a yawing moment to decrease β . In the α range of 20° to 30° the aircraft has negative (unstable) sideslip stability; increasing β causes a moment to further increase β . There is also a local instability around $\alpha = 35^\circ$ and $\beta = 10^\circ$.

Figures 5, 6, and 7 show the parameters for aircraft configuration B. As can be seen the data is not symmetric about zero sideslip. At high angle of attack the rolling and yawing moment is not zero at zero sideslip. There is a large variation of pitching moment with sideslip. This is due to both aerodynamic and kinematic coupling. The pitching moment (Figure 6) is stable around trim α of 27° and small sideslips. At lower or higher α and large β , there are regions of local instability. The yawing moment (Figure 7) is stable at all α except around $\alpha = 24^\circ$. At high α the zero yawing moment is not at zero sideslip. This causes the aircraft to depart from zero sideslip as α is increasing. At moderate angle of attack ($\alpha = 15-20^\circ$) the sideslip for zero yawing moment (Figure 7) and zero rolling moment (Figure 5) are approximately the same; therefore, the aircraft will not roll as sideslip is building up. At higher angle of attack the sideslip for trim yawing and rolling moment are different; therefore, the aircraft will tend to generate a rolling moment as it is trimming in sideslip.

The dynamic stability axis aerodynamic moment plots of Figures 2 through 7 include the aerodynamic and kinematic coupling between the longitudinal (α variation) and the lateral/directional (β variation) modes. These coupling effects are static terms. Another mode of coupling is the dynamic coupling. Dynamic coupling involves the motion of the aircraft. The coupling terms are the change in M_{DYN} or (C_{mDYN}) with β and a change in N_{DYN} (or C_{nDYN}) with α . The dynamic coupling is zero if the C_{mDYN} contour lines (Figure 3 and 6) are horizontal and the C_{nDYN} contour lines (Figures 4 and 7) are vertical. The effect of this dynamic coupling on aircraft stability will be analyzed by perturbation techniques.

4. STABILITY ANALYSIS

The aircraft rotational equations of motion due to static aerodynamic coefficients are given by Eq. (24-26). Since the aerodynamics are functions of α and β only (not $\dot{\alpha}$) the $\ddot{\alpha}$ and $\ddot{\beta}$ equations will be used for stability analysis.

$$\ddot{\alpha} = M_{DYN} \quad (30)$$

$$\ddot{\beta} = -N_{\text{DYN}} \quad (31)$$

Taking partial derivatives of the aerodynamics and using Laplace transform gives:

$$(S^2 - M_{\alpha\text{DYN}})\alpha - (M_{\beta\text{DYN}})\beta = 0 \quad (32)$$

$$(S^2 + N_{\beta\text{DYN}})\beta + (N_{\alpha\text{DYN}})\alpha = 0 \quad (33)$$

where

$$M_{\alpha\text{DYN}} = M_{\alpha} - (\mathcal{L}_{\alpha} \cos \alpha_0 + N_{\alpha} \sin \alpha_0) \tan \beta_0 \quad (34)$$

$$M_{\beta\text{DYN}} = M_{\beta} - (\mathcal{L}_{\beta} \cos \alpha_0 + N_{\beta} \sin \alpha_0) \tan \beta_0 \quad (35)$$

$$N_{\alpha\text{DYN}} = N_{\alpha} \cos \alpha_0 - \mathcal{L}_{\alpha} \sin \alpha_0 \quad (36)$$

$$N_{\beta\text{DYN}} = N_{\beta} \cos \alpha_0 - \mathcal{L}_{\beta} \sin \alpha_0 \quad (37)$$

The dynamic derivatives are computed from Eq. (25 and 26) at constant value of α_0 and β_0 and trimmed (zero) value of \mathcal{L} , M , and N . The α and β without subscript are perturbation values.

The derivative $N_{\beta\text{DYN}}$ is the presently used lateral/directional departure parameter (Ref. 2). The aerodynamic derivatives are computed by taking the local slope at the specified α_0 and β_0 .

The stability is determined from the characteristics polynomial of Eq. (32 and 33).

$$S^4 + AS^2 + B = 0 \quad (38)$$

$$A = N_{\beta\text{DYN}} - M_{\alpha\text{DYN}} \quad (39)$$

$$B = N_{\alpha\text{DYN}} M_{\beta\text{DYN}} - N_{\beta\text{DYN}} M_{\alpha\text{DYN}} \quad (40)$$

If the product $(N_{\alpha\text{DYN}})(M_{\beta\text{DYN}})$ is zero then the longitudinal mode $(M_{\alpha\text{DYN}})$ and the lateral/directional mode $(N_{\beta\text{DYN}})$ are uncoupled. In this case:

$$S^4 + AS^2 + B = (S^2 + N_{\beta\text{DYN}})(S^2 - M_{\alpha\text{DYN}}) \quad (41)$$

$N_{\beta\text{DYN}}$ is the Dutch roll frequency squared and $-M_{\alpha\text{DYN}}$ is the pitch short period frequency squared

The general solution of Eq. (38) has two forms:

If $(A^2 - 4B) > 0$

$$S^4 + AS^2 + B = (S^2 + C_1)(S^2 + C_2) \quad (42)$$

$$C_1, C_2 = \frac{1}{2} \left(A \pm \sqrt{A^2 - 4B} \right) \quad (43)$$

If C is positive the roots are $(S \pm j\omega)$ and the equation is stable. Roots on the imaginary axis are considered stable since this analysis does not include damping terms. Stabilizing damping terms would move the roots from the imaginary axis to the left half plane. If C is negative the roots are $(S \pm \sigma)$ and the equation is unstable. One root is in the right half plane which is unstable.

If $(A^2 - 4B) < 0$ the equation is unstable:

$$S^4 + AS^2 + B = (S \pm R \pm jI) = S^2 \pm 2\zeta\omega S + \omega^2 \quad (44)$$

$$\omega = \sqrt[4]{B}, \quad \zeta = \pm \sqrt{\frac{1}{2} \left(1 - \frac{A}{2\sqrt{B}} \right)} \quad (45)$$

$$R = \sqrt{\frac{1}{2} \left(\sqrt{B} - \frac{1}{2}A \right)}, \quad I = \sqrt{\frac{1}{2} \left(\sqrt{B} + \frac{1}{2}A \right)} \quad (46)$$

The solution has two pairs of complex roots; two of them are in the right half plane and unstable. This is a new mode of motion where the pitch short period and Dutch roll are coupled to form a new oscillatory mode of instability.

The effect of this coupling between the longitudinal and lateral/directional mode is shown with the aid of a root locus plot in Figure 8. Three cases are shown. The first case shows both uncoupled pitch short period and Dutch roll modes stable. The second case shows one mode unstable and the third case shows both modes unstable. For all three cases the positive coupling term $(N_{\alpha\text{DYN}} M_{\beta\text{DYN}})$ has a stabilizing effect for small values but can drive the aircraft unstable for large values. Negative coupling is always destabilizing. A positive value of the coupling term in effect means "negative feedback" since a positive value of $N_{\alpha\text{DYN}}$ causes a negative β change for a positive α change.

The characteristics polynomial can be written in terms of two new coupled parameters similar to Eq. (41) for the uncoupled case. (If $A^2 - 4B$ is positive

$$S^4 + AS^2 + B = (S^2 + N_{\beta\text{COP}})(S^2 - M_{\alpha\text{COP}}) \quad (47)$$

where

$$N_{\beta\text{COP}} = \frac{1}{2} \left(A + D \sqrt{A^2 - 4B} \right) \quad (48)$$

$$M_{\alpha \text{COP}} = \frac{1}{2} \left(-A + D \sqrt{A^2 - 4B} \right) \quad (49)$$

$$D = \text{sign} \left(N_{\beta \text{DYN}} + M_{\alpha \text{DYN}} \right) \quad (50)$$

$N_{\beta \text{COP}}$ is the coupled Dutch roll mode frequency squared and $-M_{\alpha \text{COP}}$ is the coupled pitch short period frequency squared. The aircraft is stable if $N_{\beta \text{COP}} \geq 0$ and $M_{\alpha \text{COP}} \leq 0$.

For the unstable case, $(A^2 - 4B) < 0$, the new coupled parameters are defined as:

$$N_{\beta \text{COP}} = -M_{\alpha \text{COP}} = \sqrt{B} \quad (51)$$

The conditions of stability have been defined above in terms of dimensional stability parameters. The nondimensional form of the uncoupled dynamic parameters is:

$$C_{m_{\alpha \text{DYN}}} = C_{m_{\alpha}} - \frac{b}{\bar{c}} \left(\frac{I_{yy}}{I_{zz}} C_{n_{\alpha}} \sin \alpha_0 + \frac{I_{yy}}{I_{xx}} C_{l_{\alpha}} \cos \alpha_0 \right) \tan \beta_0 \quad (52)$$

$$C_{m_{\beta \text{DYN}}} = C_{m_{\beta}} - \frac{b}{\bar{c}} \left(\frac{I_{yy}}{I_{zz}} C_{n_{\beta}} \sin \alpha_0 + \frac{I_{yy}}{I_{xx}} C_{l_{\beta}} \cos \alpha_0 \right) \tan \beta_0 \quad (53)$$

$$C_{n_{\alpha \text{DYN}}} = C_{n_{\alpha}} \cos \alpha_0 - \frac{I_{zz}}{I_{xx}} C_{l_{\alpha}} \sin \alpha_0 \quad (54)$$

$$C_{n_{\beta \text{DYN}}} = C_{n_{\beta}} \cos \alpha_0 - \frac{I_{zz}}{I_{xx}} C_{l_{\beta}} \sin \alpha_0 \quad (55)$$

The nondimensional form of the characteristic polynomial coefficients is:

$$X = \frac{b}{I_{zz}} C_{n_{\beta \text{DYN}}} - \frac{\bar{c}}{I_{yy}} C_{m_{\alpha \text{DYN}}} \quad (56)$$

$$Y = \frac{\bar{c} b}{I_{yy} I_{zz}} \left(C_{n_{\alpha \text{DYN}}} C_{m_{\beta \text{DYN}}} - C_{n_{\beta \text{DYN}}} C_{m_{\alpha \text{DYN}}} \right) \quad (57)$$

Defining the nondimensional coupling parameter,

$$K = \text{sign} (X^2 - 4Y) \frac{I_{zz}}{b} \sqrt{|X^2 - 4Y|} \quad (58)$$

If K is positive

$$C_{n_{\beta \text{COP}}} = \frac{I_{zz}}{2b} \left(X + d \sqrt{X^2 - 4Y} \right) \quad (59)$$

$$C_{m_{\alpha \text{COP}}} = \frac{I_{yy}}{2\bar{c}} \left(-X + d \sqrt{X^2 - 4Y} \right) \quad (60)$$

$$d = \text{sign} \left(\frac{b}{I_{zz}} C_{n_{\beta \text{DYN}}} + \frac{\bar{c}}{I_{yy}} C_{m_{\alpha \text{DYN}}} \right) \quad (61)$$

If K is negative

$$C_{n_{\beta \text{COP}}} = \frac{I_{zz}}{b} \sqrt{Y} \quad (62)$$

$$C_{m_{\alpha \text{COP}}} = \frac{-I_{yy}}{\bar{c}} \sqrt{Y} \quad (63)$$

The new stability criteria in terms of nondimensional stability parameters are:

$$\underline{K \geq 0 \text{ and } C_{n_{\beta \text{COP}}} \geq 0, C_{m_{\alpha \text{COP}}} \leq 0}$$

All three conditions must be satisfied for stability.

5. APPLICATION OF NEW CRITERIA

The aircraft short period stability is computed by the use of the new criteria and is compared to the stability characteristics computed by the complete six degree of freedom equations (Fig. 1) or compared to time history traces. Three cases are computed for two aircraft configurations as shown in Table 1. The first two cases are for aircraft configuration B. The third case is for an F-4 configuration using the aerodynamic data from Ref. 5, page 41. The stability parameters are computed in the dimensional form so that the parameters can be compared directly with the frequency and damping as computed from the complete six degree of freedom equations. The table shows the angle of attack and sideslip, body axis derivatives, dynamic stability axis parameters, the coupled parameters, frequency and damping computed from the uncoupled parameters, coupled parameters, and complete six degree of freedom equations of motion.

For all three cases the existing criterion ($N_{\beta DYN} > 0$, $M_{\alpha} < 0$) predicts stability while the new criterion ($A^2 - 4B) > 0$, $N_{\beta COP} > 0$, $M_{\alpha COP} < 0$) predicts instability. CASE 1 and 3 have an oscillatory instability, $(A^2 - 4B) < 0$. Case 2 has lateral/directional divergence, $N_{\beta COP} < 0$. For CASE 1 the uncoupled pitch short period frequency at zero sideslip computed from M_{α} is stable. At non-zero sideslip the uncoupled pitch short period frequency computed from $M_{\alpha DYN}$ is unstable ($S \pm 1.21$). The coupled parameters predict oscillatory instability and the results agree well with the frequency and damping computed from the six degree of freedom equations. For CASE 2 the instability predicted by $N_{\beta COP}$ being negative agrees with the six degree of freedom results. For CASE 3 the instability is exhibited in Ref. 5 by a time history trace for a rudder impulse showing unstable coupled angle of attack and sideslip oscillations.

The new nondimensional stability parameters (Eq. 58-63) can be computed for the complete angle of attack and sideslip range of interest to define regions of stability and instability as a function of α and β . Figure 9 shows the stability boundaries for the aircraft configuration B. Three types of instability are shown (by shaded regions); the coupled oscillatory instability and the coupled longitudinal and coupled lateral/directional divergences. The stability calculations are based on the local derivatives of the aerodynamic coefficients at the specified α and β . If an aircraft is trimmed in a region of instability it will diverge from that value of α and β . If the unstable region is small it can diverge into a stable region. For large regions of instability the divergence can cause the aircraft rates to build up into a developed spin.

In maneuvering flight, if the angle of attack and sideslip pass through an unstable region, it does not necessarily mean that the aircraft will depart. If the trim α ($\dot{\alpha} = 0$) and trim β ($\dot{\beta} = 0$) are also in the unstable region the aircraft will have a tendency to depart. The $\ddot{\alpha}$ and $\ddot{\beta}$ are made up of two parts. One is due to the static aerodynamic moments, $C_{m DYN}$ and $C_{n DYN}$ as shown in Figures 6 and 7. The other term is due to the dynamic aerodynamic moments (function of P, Q, R) and due to inertial coupling. The effect of unstable regions on aircraft motion will be illustrated with a computer time history trajectory which simulates a flight time history of aircraft configuration B.

The trajectory is a pitch stick snap. The horizontal tail was commanded from the initial value of 2.7 degrees to -18.4 degrees for 3.5 seconds and then commanded back to 2.7 degrees. This caused the aircraft to pitch up, develop a sideslip, and then depart in angle of attack. The (α, β) trajectory is shown in two parts in Figure 10 and 11. Figure 10 shows the (α, β) trajectory for the first 4.0 seconds when δ_H is equal to -18.4 degrees. The figure also shows the static α and β trim curves ($C_{m DYN} = 0$, $C_{n DYN} = 0$) and the regions of instability for $\delta_H = -18.4$ degrees. Figure 11 shows the (α, β) trajectory for 3.5 sec to 7.0 sec when $\delta_H = 2.7$ degrees and also the trim curves and stability plots for $\delta_H = 2.7$ degrees. The aircraft trims at negative angle of attack at zero sideslip for $\delta_H = 2.7$ degrees; therefore, the $C_{m DYN} = -0.1$ curve is also shown.

Initially the aircraft overshoots the trim α of 27 degrees and pitches up to 52 degrees of α (Figure 10). The sideslip starts building up at $\alpha = 30^\circ$ due to nonzero moments at zero sideslip and oscillates about $C_{n DYN} = 0$ curve.

The angle of attack is recovering from the overshoot but then becomes unstable when δ_H is changed to 2.7 deg (Figure 11). In this case the (α, β) trajectory and the dynamic trim are in the unstable region and the aircraft diverges in angle of attack. The sideslip oscillations are building up in magnitude due to coupling from the longitudinal axis and low lateral/directional damping.

6. LATERAL CONTROL DEPARTURE PARAMETER

Another parameter that is used for predicting departure and spin susceptibility is the Lateral Control Departure Parameter (LCDP). This is usually defined for aileron control as:

$$LCDP = C_{n\beta} - C_{l\beta} \frac{C_{n\delta_A}}{C_{l\delta_A}} \quad (64)$$

For stability the parameter should be positive. The parameter is defined in terms of static stability and control derivatives. The parameter can be derived from the lateral/directional rotational equations of motion due to static moments only.

$$\dot{P} = \mathcal{L}_{\beta} \beta + \mathcal{L}_{\delta_A} \delta_A \quad (65)$$

$$\dot{R} = N_{\beta} \beta + N_{\delta_A} \delta_A \quad (66)$$

$$\dot{\beta} = P \sin \alpha - R \cos \alpha \quad (67)$$

The perturbation equation transfer function of roll rate due to aileron is:

$$\begin{aligned} \frac{P}{\delta_A} &= \frac{\mathcal{L}_{\delta_A} \left[S^2 + \left(N_{\beta} - \mathcal{L}_{\beta} \frac{N_{\delta_A}}{\mathcal{L}_{\delta_A}} \right) \cos \alpha \right]}{S \left[S^2 + \left(N_{\beta} \cos \alpha - \mathcal{L}_{\beta} \sin \alpha \right) \right]} \\ &= \frac{\mathcal{L}_{\delta_A} (S^2 + \omega_{\phi}^2)}{S (S^2 + \omega_D^2)} \end{aligned} \quad (68)$$

where

$$\begin{aligned}\omega_{\phi}^2 &= \frac{\bar{q} s b}{I_{zz}} \left(C_{n\beta} - C_{l\beta} \frac{C_{n\delta_A}}{C_{l\delta_A}} \right) \cos \alpha_0 \\ &= \frac{\bar{q} s b}{I_{zz}} (\text{LCDP}) \cos \alpha_0\end{aligned}\quad (69)$$

$$\begin{aligned}\omega_D^2 &= \frac{\bar{q} s b}{I_{zz}} \left(C_{n\beta} \cos \alpha_0 - \frac{I_{zz}}{I_{xx}} C_{l\beta} \sin \alpha_0 \right) \\ &= \frac{\bar{q} s b}{I_{zz}} C_{n\beta \text{ DYN}}\end{aligned}\quad (70)$$

The parameter, $\omega_{\phi}^2 / \omega_D^2 = (\text{LCDP}) \cos \alpha_0 / C_{n\beta \text{ DYN}}$ can be used to define lateral maneuvering performance:

$$\begin{aligned}\frac{\omega_{\phi}^2}{\omega_D^2} &> 1, \text{ proverse } \beta \\ &< 1, \text{ adverse } \beta \\ &< 0, \text{ roll reversal}\end{aligned}\quad (71)$$

This is illustrated by a simple example in Figure 12. The figure shows the variation of \dot{P} and $\ddot{\beta}$ as a function of β for ten degree aileron deflections and three value of N_{δ_A} . For $N_{\delta_A} = +0.1$ (Figure 12a) LCDP is positive, the sideslip trim ($\ddot{\beta} = 0$) is at negative sideslip, and roll acceleration (\dot{P}) is positive and greater than at zero sideslip. This corresponds to proverse sideslip (negative sideslip for positive roll rate). For $N_{\delta_A} = 0$ (Figure 12b) LCDP is positive, the sideslip trim is at positive sideslip, and the roll acceleration is positive but less than at zero sideslip. This corresponds to adverse sideslip condition and some loss of roll power due to sideslip buildup. For $N_{\delta_A} = -0.02$ (Figure 12c) LCDP is negative, the sideslip trim is at positive sideslip, and the roll acceleration is negative. This corresponds to roll reversal due to sideslip buildup.

This example used linear aerodynamics, showing the sideslip trim and the value of body axis rolling acceleration at trim sideslip. Similar plots can be made for nonlinear aerodynamics and plotting the rolling acceleration about velocity vector. At high angle of attack, the rolling acceleration about the velocity vector is more important than rolling acceleration about the body axis. Figure 13 shows the contour plot of rolling moment for aircraft configuration A with ten degree aileron deflection. This is based on the same aerodynamic data used in Figure 2. The sideslip trim curve ($C_{n\text{DYN}} = 0$) is also plotted in the Figure. At low α ($\alpha < 2^\circ$) the airplane trims with negative sideslip (proverse β). At higher α the sideslip trim is adverse. At $\alpha < 17.5^\circ$ the roll acceleration is positive at trim sideslip. This corresponds to positive LCDP. At $\alpha > 17.5^\circ$ roll acceleration is negative at trim sideslip, corresponding to roll reversal and negative LCDP.

Figure 14 shows the stability plot for the aircraft configuration A with ten degree aileron deflection.

The trim sideslip curve goes through three regions of instability. The first two regions ($\alpha = 3^\circ$ to 6° and $\alpha = 15^\circ$) of instability are small and the aircraft will trim into a stable region. At $\alpha = 17.5^\circ$ the sideslip trim curve enters the coupled lateral/directional instability region and stays in that region. That would cause the aircraft to depart into a spin. The angle of attack for instability occurs at a lower value ($\alpha = 17.5^\circ$) than is predicted by the existing criteria of $C_{n\beta \text{ DYN}} < 0$ which occurs at $\alpha = 20^\circ$ (from Figure 4). This agrees with the time history shown in Ref. 5.

For this aircraft the rotational instability and roll reversal occur at about the same angle of attack. This is not necessarily true for all aircraft. The rotational stability is dependent on the angle of attack and sideslip derivatives while roll reversal also depends on the control derivatives. The LCDP gives an indication of the aircraft lateral control performance but is not a good indicator of aircraft stability.

Three parameters can be defined to characterize the aircraft lateral stability and control performance. The first parameter is the rolling moment about the velocity vector at zero sideslip. This gives an indication of maximum roll performance for a coordinated ($\beta = 0$) roll. The second parameter is the rolling moment about the velocity vector at trim sideslip ($C_{n\text{DYN}} = 0$). This shows the loss (or gain) in roll performance due to adverse (or proverse) sideslip buildup. The third parameter is the value of trim sideslip and the stability about this value of sideslip. The stability should be computed at the trim sideslip instead of zero sideslip condition.

The three parameters are plotted in Figure 15 for the aircraft configuration as shown in Figures 13 and 14. The rolling moment at zero sideslip decreases with angle of attack. This is the maximum rolling moment for a coordinated roll maneuver. The rolling moment at trim sideslip reverses at $\alpha = 17.5$ degrees. The roll reversal is due to sideslip buildup. The sideslip trace shows regions of instability computed at the value of sideslip and angle of attack. The aircraft will tend to depart at α greater than 17.5 degrees.

7. CONCLUDING REMARKS

The present paper has given a brief description of aircraft rotational stability analysis. The presently used departure criterion has been extended to include the coupling between the longitudinal and lateral/direction modes of motion and has also been applied to nonlinear aerodynamics. A new way of presenting the stability characteristics of an aircraft has been developed. The stability plots show the stability characteristics throughout the angle of attack and sideslip range of the aircraft.

This type of analysis is made feasible by the use of high speed digital computers and automatic plotting capability. The aerodynamic data is defined as a function of α and β in a tabulated form. The computer is used to perform nonlinear interpolation of functions of two variables with continuous first derivatives through the (α, β) range. Iteration procedure is used to compute the contour lines.

8. REFERENCES

1. Thelander, J. A., "Aircraft Motion Analysis," Technical Documentary Report FDL-TDR-64-70, March 1965.
2. Weissman, R., "Status of Design Criteria for Predicting Departure Characteristics and Spin Susceptibility," AIAA Mechanics and Control of Flight Conference, Anaheim, California, 5-9 August 1974.
3. Greer, H. Douglas, "Summary of Directional Divergence Characteristics of Several High-Performance Aircraft Configurations," NASA Technical Note, NASA TN D-6993, November 1972.
4. Moul, M. T. and Paulson, S. W., "Dynamic Lateral Behavior of High Performance Aircraft," RM L58E16, August 1958, NACA.
5. Johnston, D. E.; Ashkenas, I. L.; and Hogge, J. R., "Investigation of Flying Qualities of Military Aircraft at High Angles of Attack," Technical Report AFFDL-TR-74-61, June 1974.
6. Chambers, J. R.; Anglin, E. L.; Bowman, J. S., Jr., "Effects of a Pointed Nose on Spin Characteristics of a Fighter Airplane Model Including Correlation with Theoretical Calculations," NASA Technical Note NASA TN D-5921, Sept. 1970.
7. Titiriga, A., Jr.; Ackerman, J. S.; Skow, A. M., "Design Technology for Departure Resistance of Fighter Aircraft," AGARD Conference on Stall/Spin Problems of Military Aircraft, AGARD-CP-199, November 1975.

TABLE 1. PREDICTION OF INSTABILITY BY NEW COUPLED PARAMETERS

		CASE 1	CASE 2	CASE 3
1	α_o	28.5	23.5	20.0
	β_o	7.5	-1.0	1.0
2	L_α	-23.52	-29.87	3.28
	N_α	2.94	-0.08	-0.505
	M_α	-1.07	-3.72	-2.83
	L_β	-6.94	0	0.191
	N_β	-0.21	1.15	0.32
	M_β	1.10	-0.80	-1.62
3	$N_{\alpha DYN}$	13.81	11.84	-1.596
	$M_{\alpha DYN}$	1.47	-4.20	-2.881
	$N_{\beta DYN}$	3.13	1.05	0.2354
	$M_{\beta DYN}$	1.91	-0.80	-1.635
4	$M_{\alpha COP}$	-4.67	-6.08	-1.813
	$N_{\beta COP}$	4.67	-0.82	1.813
	(A^2-4B)	-84.35	47.81	-3.439
5 UNCOUPLED	$\omega_{SP} \approx \sqrt{-M_\alpha} (\beta_o = 0)$	1.03	1.93	1.682
	$\omega_{SP} = \sqrt{-M_{\alpha DYN}}$	(S \pm 1.21)	2.05	1.697
	$\omega_D = \sqrt{N_{\beta DYN}}$	0.78	1.03	0.485
6 COUPLED	$\omega_{SP COP} = \sqrt{-M_{\alpha COP}}$	2.16	2.46	1.346
	$\zeta_{SP COP}$	0.64	0	0.265
	$\omega_{D COP} = \sqrt{N_{\beta COP}}$	2.16	(S + 0.91)	1.346
	$\zeta_{D COP}$	<u>-0.64</u>	<u>(S - 0.91)</u>	<u>-0.265</u>
7 EXACT BY 6 DOF	ω_{SP}	2.22	2.46	
	ζ_{SP}	0.69	0.04	
	ω_D	2.10	(S + 1.01)	
	ζ_D	<u>-0.60</u>	<u>(S - 0.91)</u>	

$$\dot{P} = \frac{1}{I_{xx}} \left[(\dot{Q} - PR) I_{xy} + (\dot{R} + PQ) I_{xz} + QR (I_{yy} - I_{zz}) + (Q^2 - R^2) I_{yz} \right] + \mathcal{L} \quad (1)$$

$$\dot{Q} = \frac{1}{I_{yy}} \left[(\dot{R} - PQ) I_{yz} + (\dot{P} + QR) I_{xy} + PR (I_{zz} - I_{xx}) + (R^2 - P^2) I_{xz} \right] + M \quad (2)$$

$$\dot{R} = \frac{1}{I_{zz}} \left[(\dot{P} - QR) I_{xz} + (\dot{Q} + PR) I_{yz} + PQ (I_{xx} - I_{yy}) + (P^2 - Q^2) I_{xy} \right] + N \quad (3)$$

$$\dot{\phi} = P + (Q \sin \phi + R \cos \phi) \tan \theta \quad (4)$$

$$\dot{\theta} = Q \cos \phi - R \sin \phi \quad (5)$$

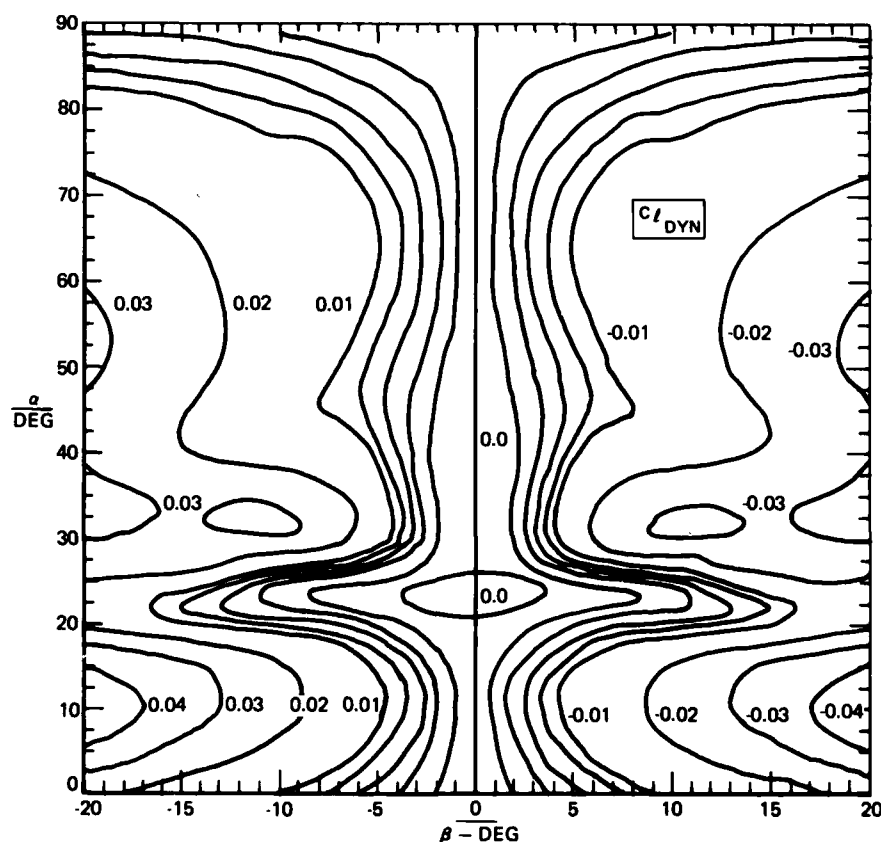
$$\begin{aligned} \dot{\alpha} = & Q - (P \cos \alpha + R \sin \alpha) \tan \beta - \frac{L}{V_T \cos \beta} \\ & + \frac{g}{V_T \cos \beta} (\cos \alpha \cos \theta \cos \phi + \sin \alpha \sin \theta) \end{aligned} \quad (6)$$

$$\begin{aligned} \dot{\beta} = & P \sin \alpha - R \cos \alpha + \frac{1}{V_T} (Y \cos \beta + D \sin \beta) \\ & + \frac{g}{V_T} [\sin \beta (\cos \alpha \sin \theta - \sin \alpha \cos \theta \cos \phi) + \cos \beta \cos \theta \sin \phi] \end{aligned} \quad (7)$$

$$\dot{V}_T = (Y \sin \beta - D \cos \beta) + g [\sin \beta \cos \theta \sin \phi + \cos \beta (\sin \alpha \cos \theta \cos \phi - \cos \alpha \sin \theta)] \quad (8)$$

$$\dot{h} = V_T [\cos \beta (\cos \alpha \sin \theta - \sin \alpha \cos \theta \cos \phi) - \sin \beta \cos \theta \sin \phi] \quad (9)$$

FIGURE 1. AIRCRAFT SIX-DEGREE-OF-FREEDOM EQUATIONS OF MOTION FOR STABILITY ANALYSIS

FIGURE 2. DYNAMIC STABILITY AXIS ROLLING MOMENT COEFFICIENT, $C_{l_{DYN}}$, FOR AIRCRAFT CONFIGURATION A, $\delta_H = -20^\circ$

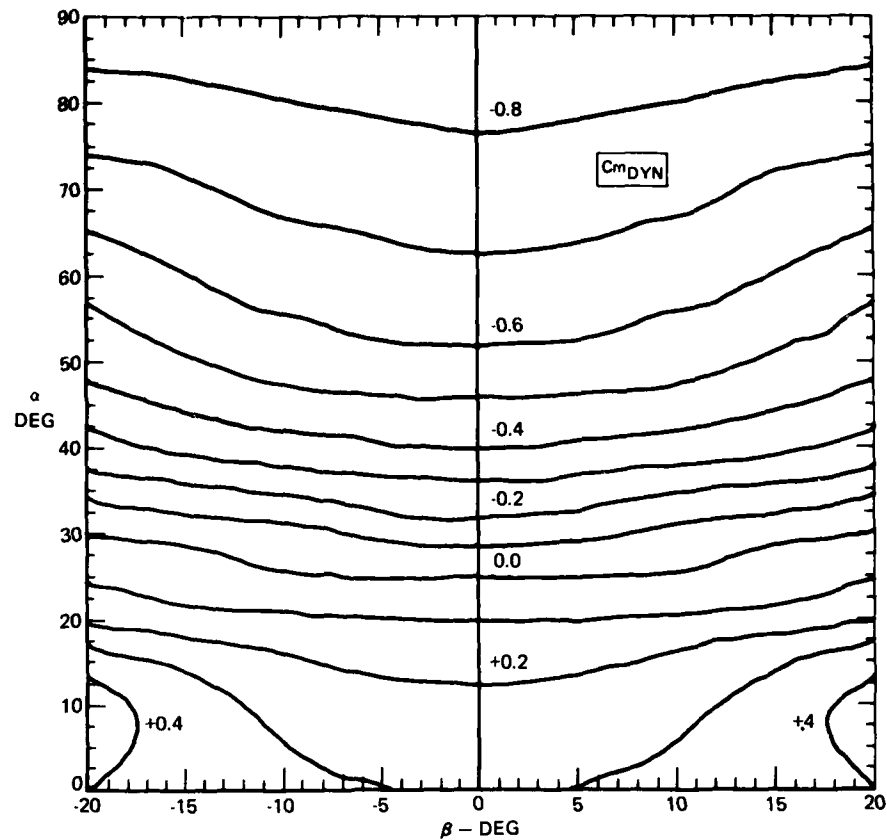


FIGURE 3. DYNAMIC STABILITY AXIS PITCHING MOMENT COEFFICIENT, C_{m_DYN} FOR AIRCRAFT CONFIGURATION A, $\delta_H = -20^\circ$

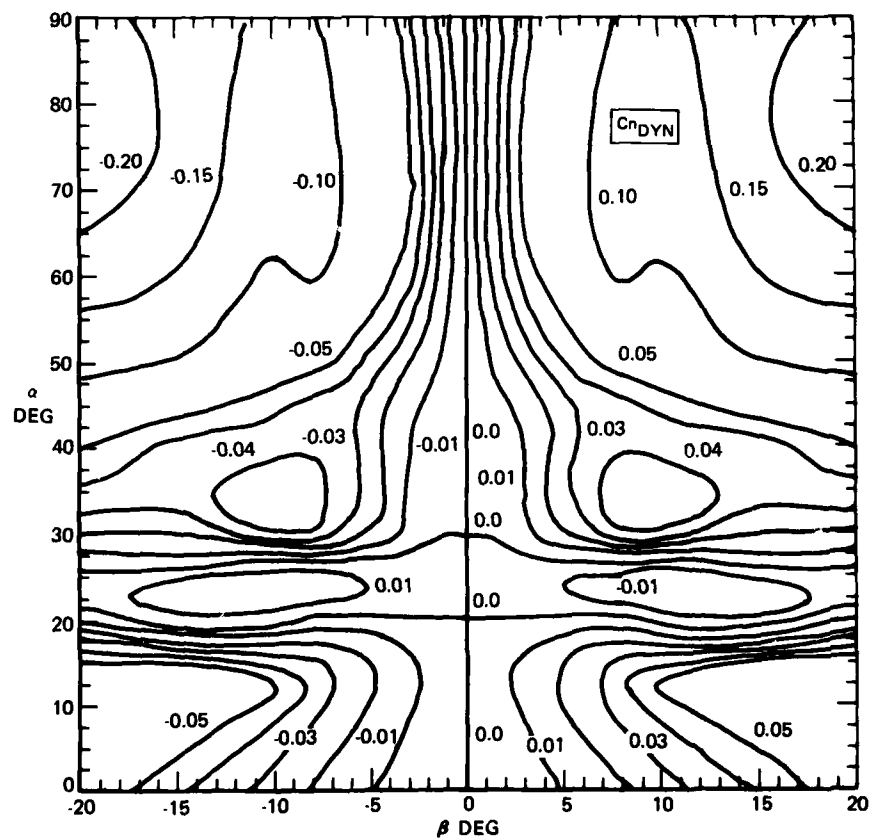


FIGURE 4. DYNAMIC STABILITY AXIS YAWING MOMENT COEFFICIENT, C_{n_DYN} FOR AIRCRAFT CONFIGURATION A, $\delta_H = -20^\circ$

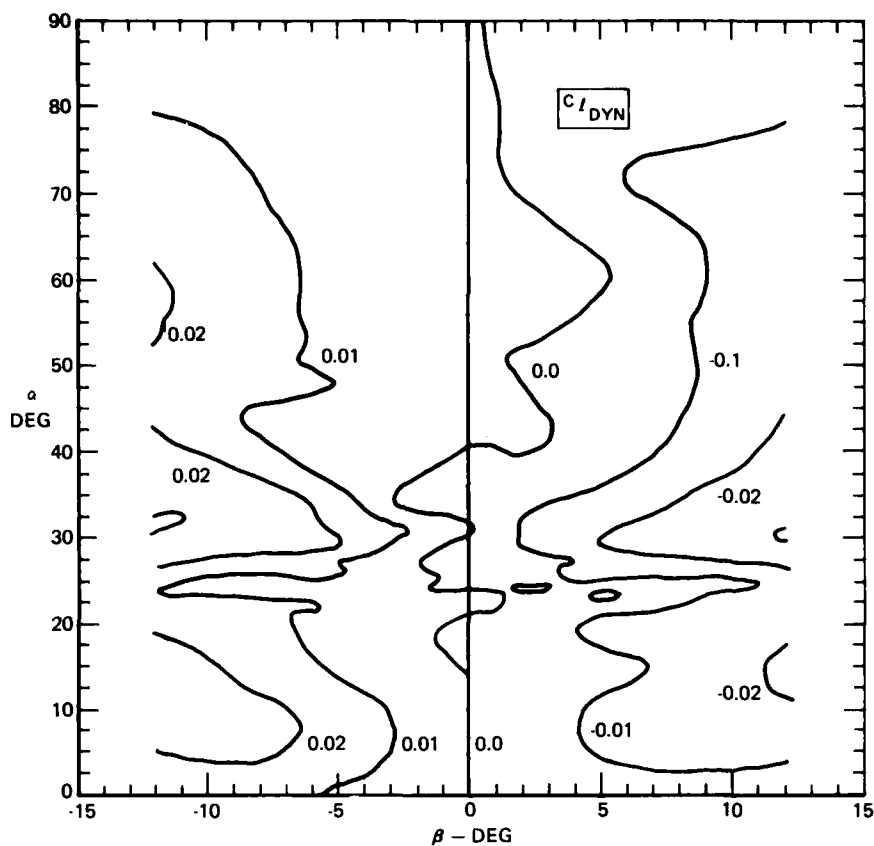


FIGURE 5. DYNAMIC STABILITY AXIS ROLLING MOMENT COEFFICIENT, $C_{l_{DYN}}$, FOR AIRCRAFT CONFIGURATION B, $\delta_H = -18.4^\circ$

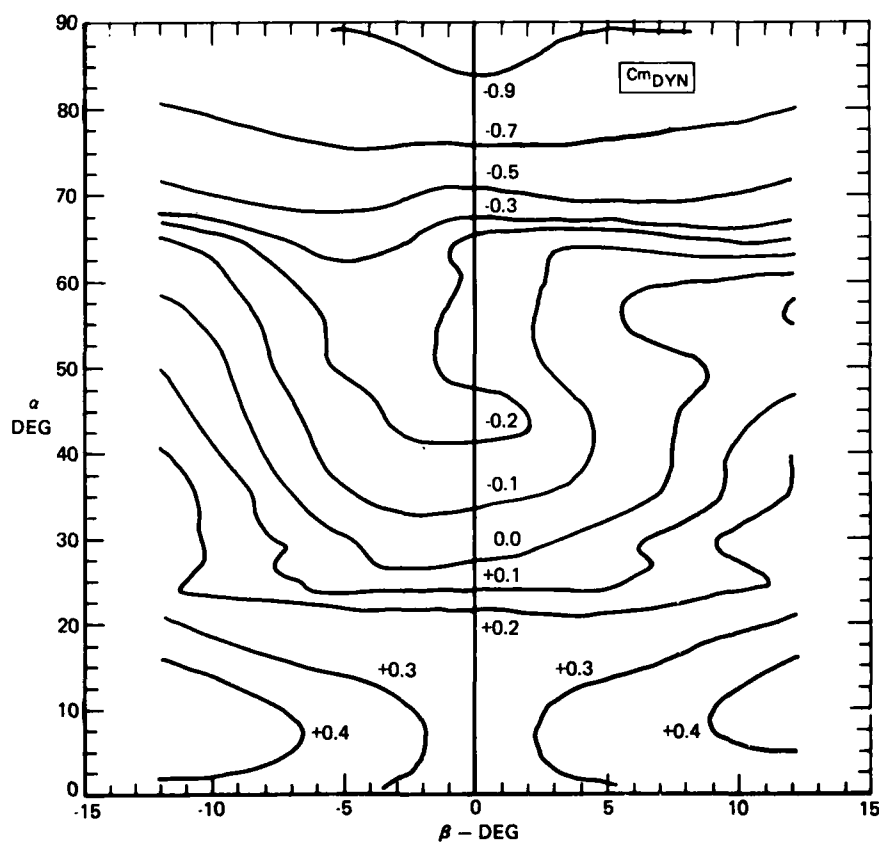


FIGURE 6. DYNAMIC STABILITY AXIS PITCHING MOMENT COEFFICIENT, $C_{m_{DYN}}$, FOR AIRCRAFT CONFIGURATION B, $\delta_H = -18.4^\circ$

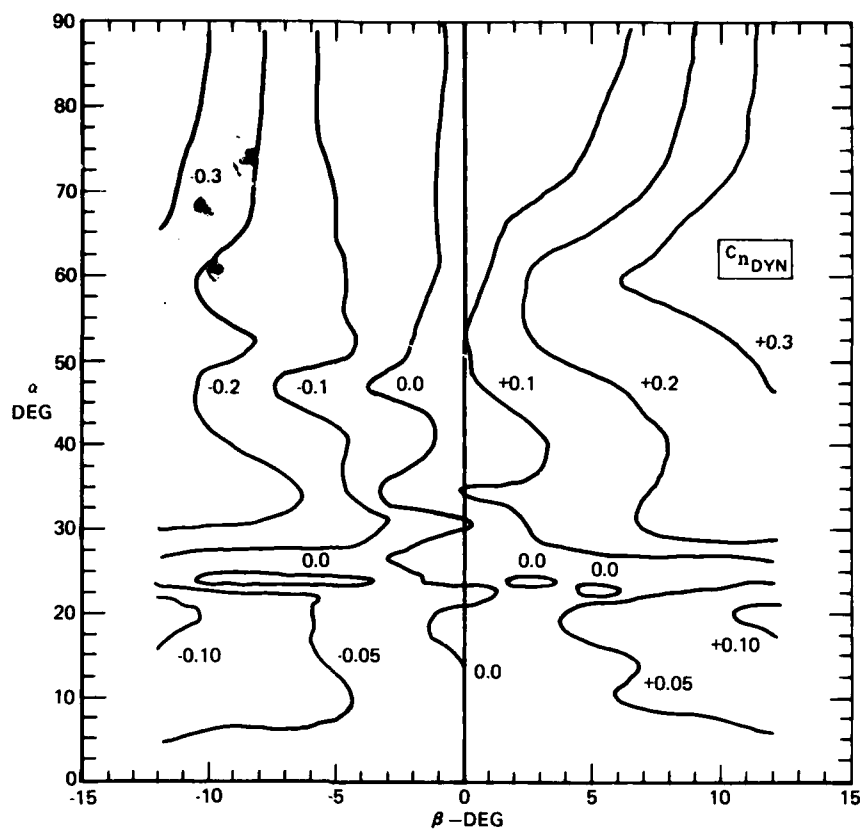
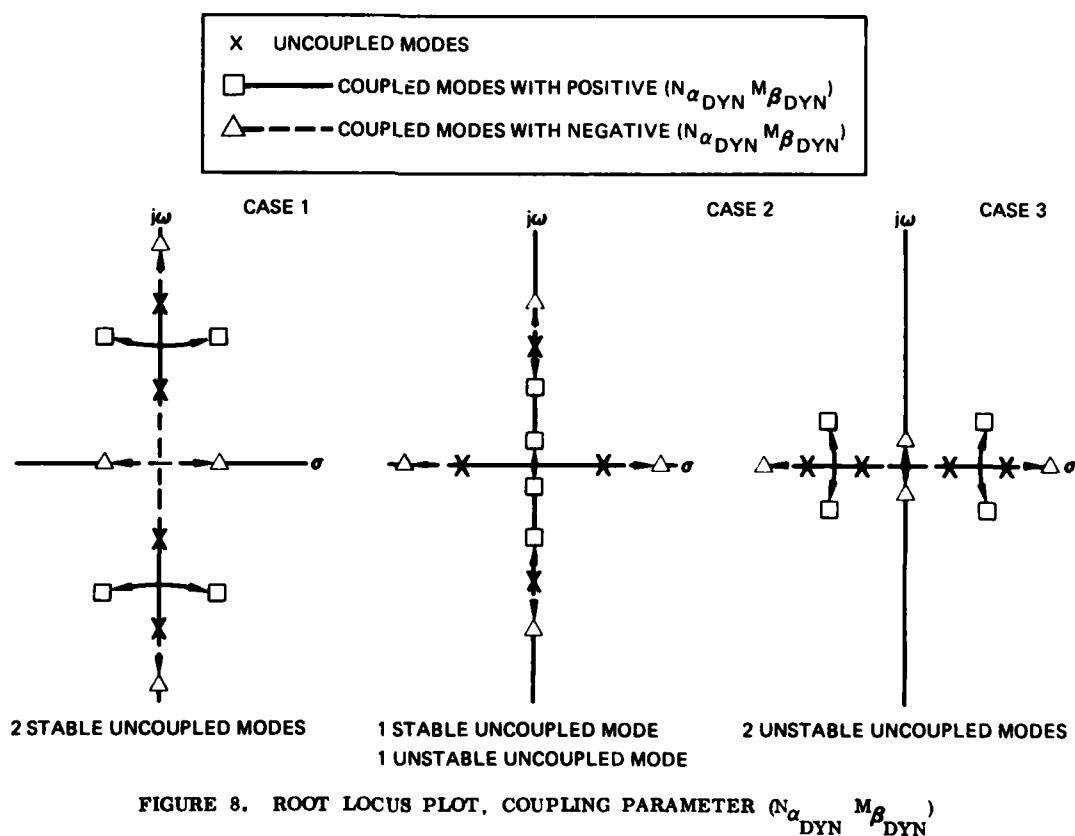


FIGURE 7. DYNAMIC STABILITY AXIS YAWING MOMENT COEFFICIENT, $C_{n_{DYN}}$, FOR AIRCRAFT CONFIGURATION B, $\delta_H = -18.4^\circ$



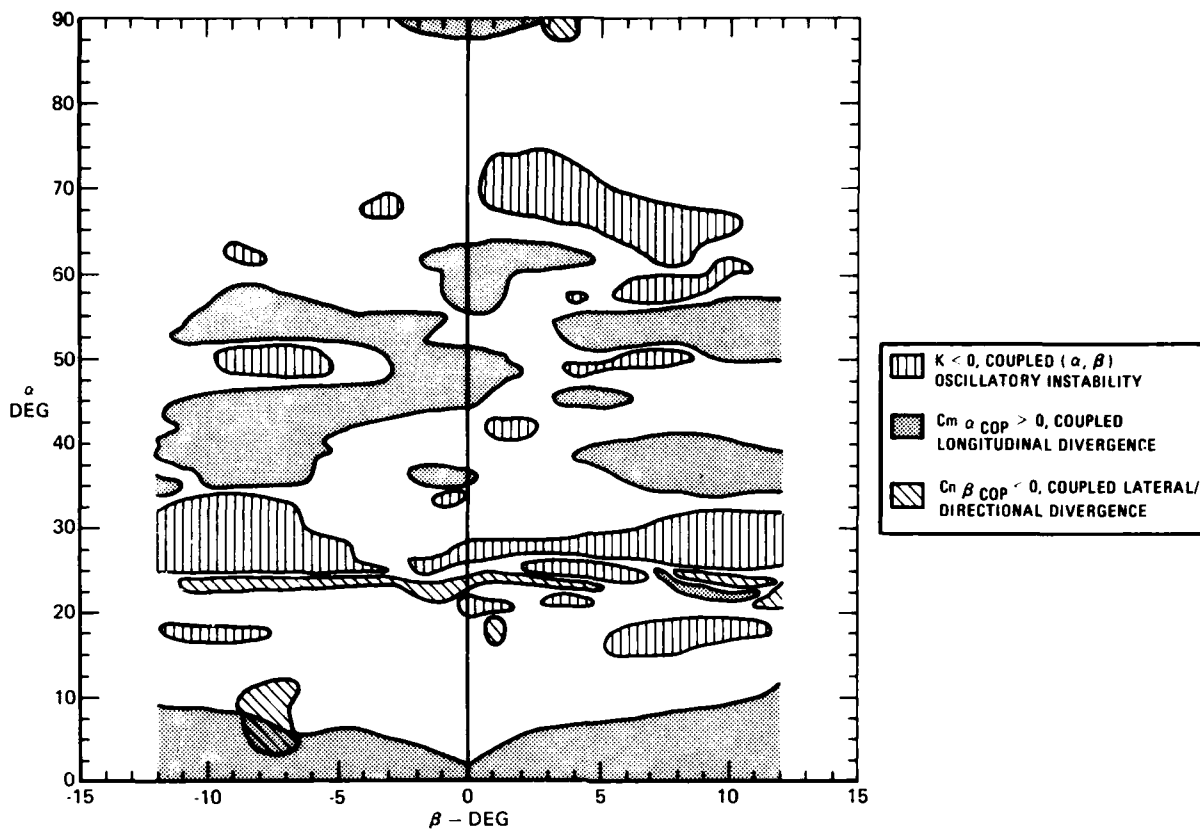


FIGURE 9. STABILITY PLOT FOR AIRCRAFT CONFIGURATION B, $\delta_H = -18.4^\circ$

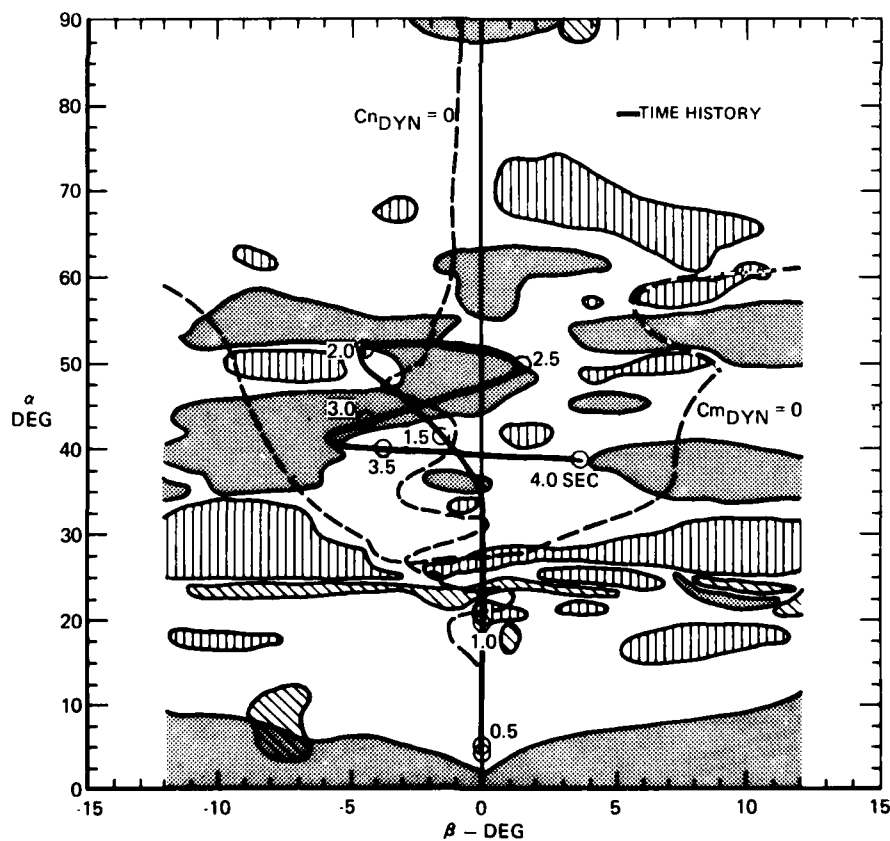


FIGURE 10. α, β TIME HISTORY FOR AIRCRAFT CONFIGURATION B, $\delta_H = -18.4^\circ$, TIME = 0 TO 4 SEC.

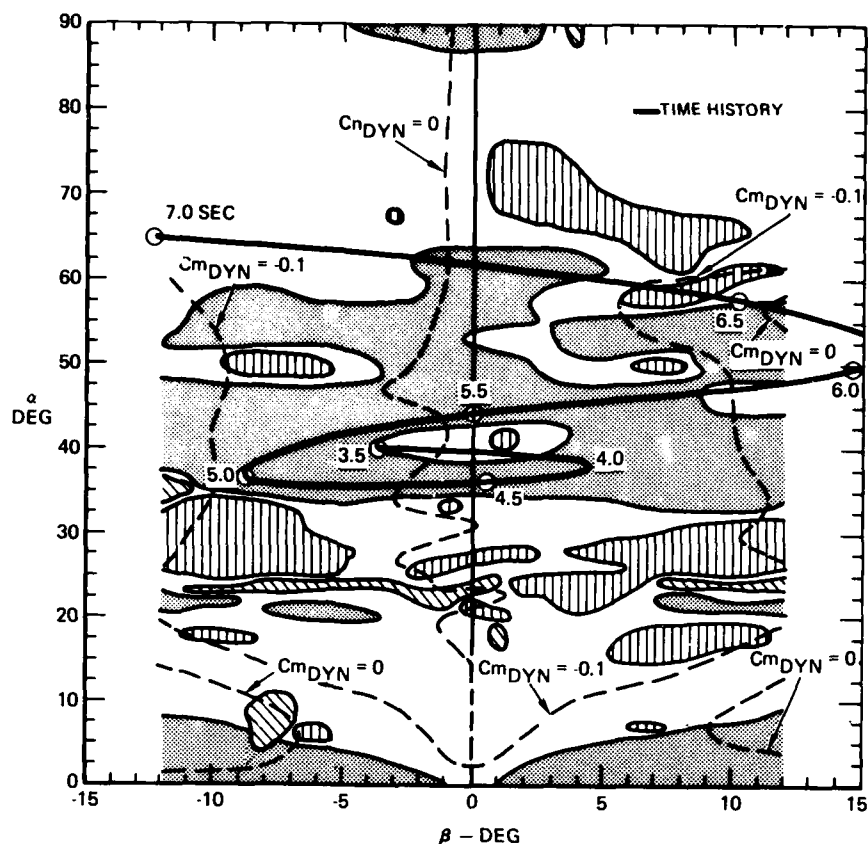


FIGURE 11. α, β TIME HISTORY FOR AIRCRAFT CONFIGURATION B,
 $\delta_H = 2.7^\circ$, TIME = 3.5 TO 7.0 SEC.

$L_\beta = -3.0$	$\alpha = 15^\circ$	$\dot{\rho} = L_\beta \beta + L_{\delta_A} \delta_A$
$N_\beta = 2.0$	$\delta_A = 10^\circ$	$\dot{r} = N_\beta \beta + N_{\delta_A} \delta_A$
$L_{\delta_A} = 0.1$	$\omega_D^2 = 2.7$	$\ddot{\beta} = \dot{\rho} \sin \alpha - \dot{r} \cos \alpha$

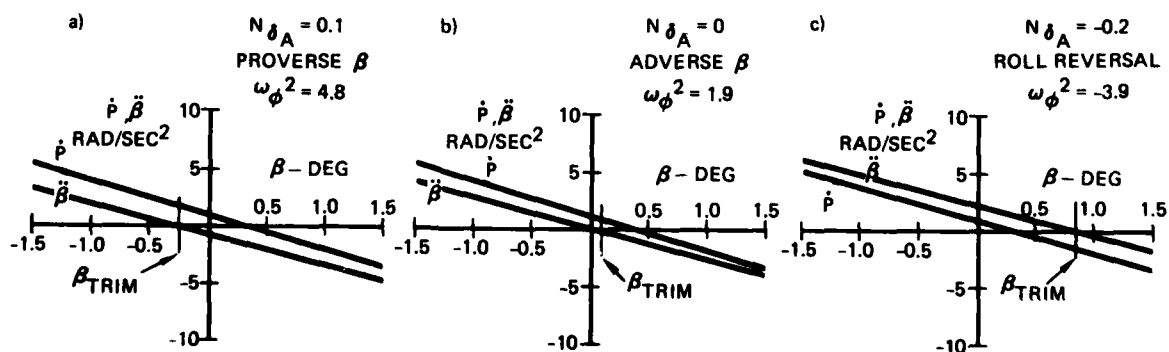


FIGURE 12. EFFECT OF N_{δ_A} ON SIDESLIP TRIM

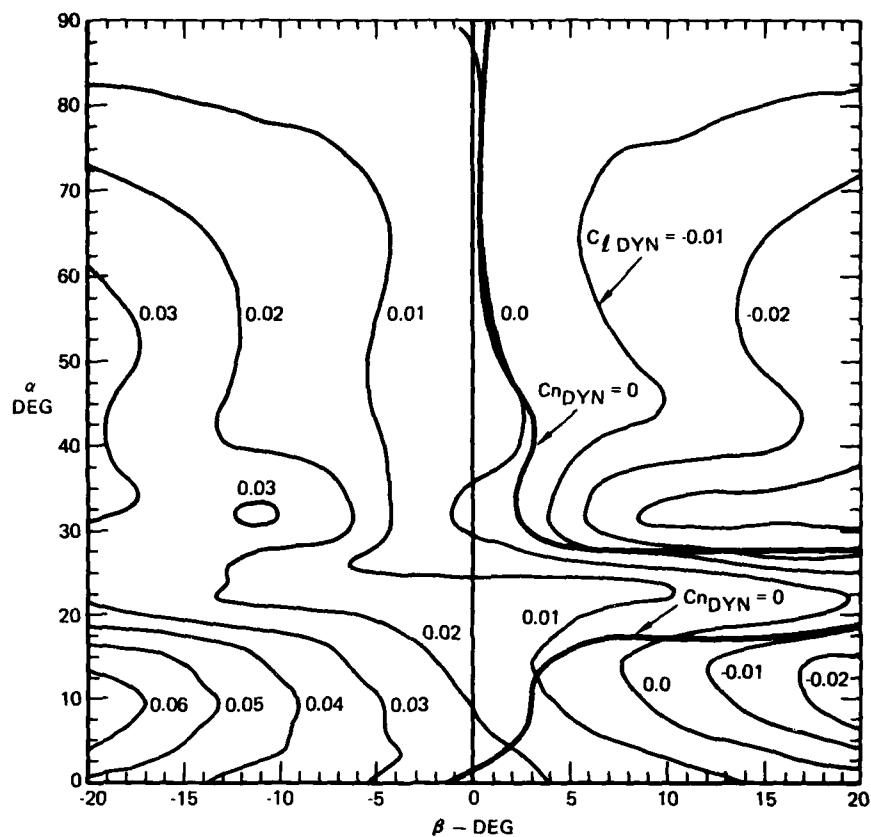


FIGURE 13. ROLLING MOMENT AND SIDESLIP TRIM FOR $\delta_A = 10^\circ$, AIRCRAFT CONFIGURATION A, $\delta_H = -20^\circ$

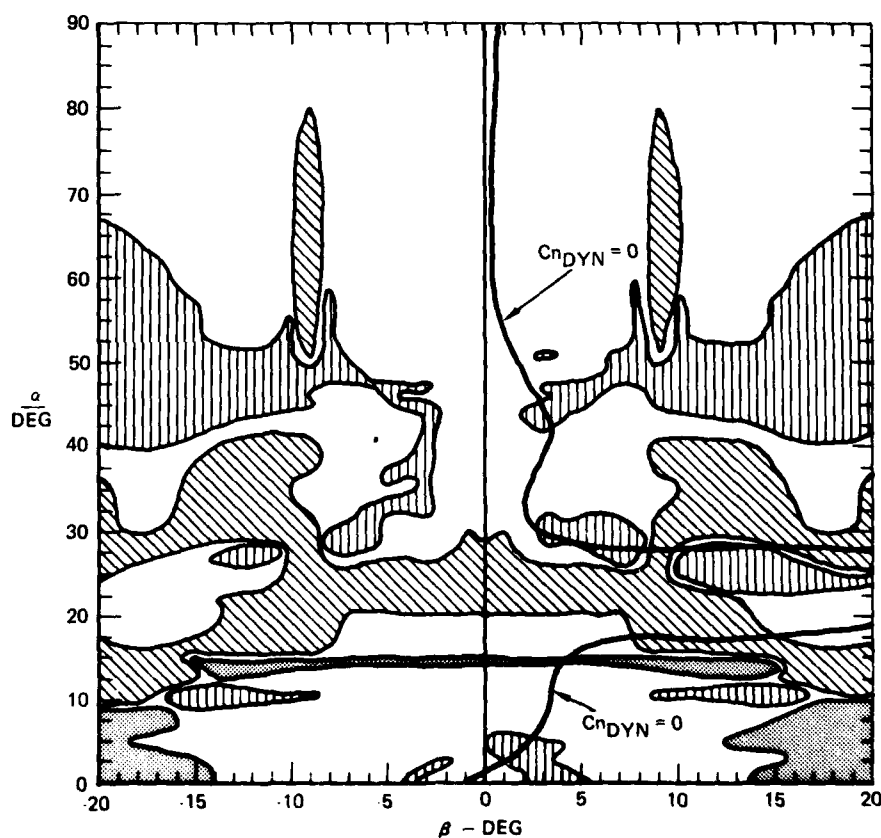


FIGURE 14. STABILITY PLOT AND SIDESLIP TRIM FOR $\delta_A = 10^\circ$, AIRCRAFT CONFIGURATION A, $\delta_H = -20^\circ$

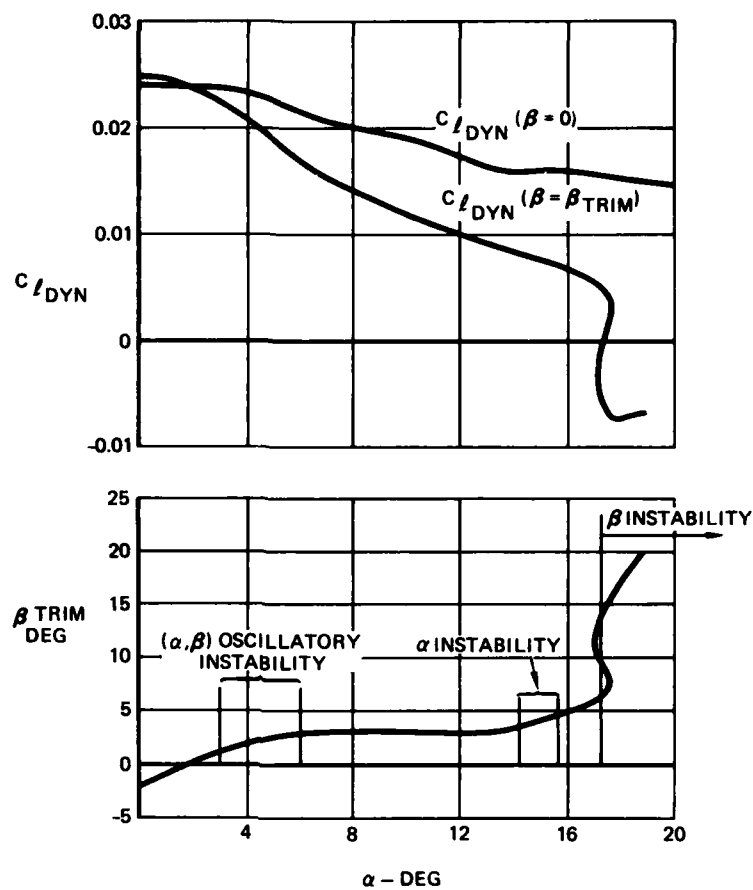


FIGURE 15. LATERAL STABILITY AND PERFORMANCE
PARAMETERS FOR AIRCRAFT CONFIGURATION A,
 $\delta_H = -20^\circ$, $\delta_A = -10^\circ$

EXPRESSION DES FORCES AERODYNAMIQUES NON-LINEAIRES EN DYNAMIQUE DU VOL.

par Michel SCHERER

Office National d'Etudes et Recherches Aérospatiales
92320 CHATILLON F R A N C E

RESUME

Une partie de plus en plus importante des informations nécessaires aux études de dynamique du vol se situe, à l'heure actuelle, dans le domaine non-linéaire intervenant dans le vol à grande incidence. La question est donc posée de trouver des modes de représentation du torseur aérodynamique convenant à l'application des méthodes d'analyse non-linéaire devenues classiques. L'objet de la présente note est de montrer des exemples de représentation proposés par différents auteurs dans des études de dynamique du vol effectuées pendant ces dernières années.

NON-LINEAR FORMULATION OF THE AERODYNAMIC FORCES FOR FLIGHT DYNAMIC STUDIES.

SUMMARY

An ever greater part of the information necessary in flight dynamics studies lies nowadays in the non-linear domain involved in flight at high angle of attack. Thus, the question is raised to find means for representing aerodynamic data, adequate for the application of now conventional non linear analysis methods.

The purpose of the paper is to present examples of formulation proposed by various authors in flight dynamics studies in the last few years.

1.- INTRODUCTION.

Dans cette communication sont présentées quelques remarques sur les approximations théoriques permettant d'exprimer les forces aérodynamiques non-linéaires dans les calculs de dynamique du vol.

Le but recherché est d'informer les expérimentateurs de soufflerie, généralement peu familiarisés avec ces questions, sur les méthodes de calcul conduisant à ces approximations. Ces remarques, inspirées de trois exemples publiés au cours de ces dix dernières années, ne font appel qu'à des notions mathématiques élémentaires sans prétendre à la rigueur.

Des développements des travaux mentionnés ici sont d'ailleurs présentés par leurs auteurs à cette même réunion AGARD [1] , [2] .

Les études théoriques de mécanique non-linéaire sont très anciennes; elles remontent à la fin du XIX^e siècle avec les travaux de Henri POINCARÉ, mais leur application sur une grande échelle aux techniques de l'ingénieur n'a pratiquement commencé qu'en 1950, à l'époque de la mise en service des premiers calculateurs numériques modernes. Les premières applications ont concerné l'électrotechnique, l'électronique et les asservissements.

Elles ont donné lieu à de nombreux travaux théoriques dont l'ensemble constitue...

à l'heure actuelle une technique de traitement des informations non-linéaires. Des ouvrages didactiques font le point sur les différentes méthodes, souvent d'un haut niveau mathématique; ils représentent pour l'ingénieur des guides pratiques qui l'orienteront dans le choix de la méthode la mieux adaptée à la question à traiter. Deux de ces ouvrages peuvent servir à l'initiation, l'un en anglais de W. CUNNINGHAM, paru en 1958, [3], et l'autre en français de J.C. GILLE, P. DECAULNE & M. PELEGRIN, [4], dont la troisième édition est parue en 1975.

Dans le domaine aérospatial, les méthodes non-linéaires sont appliquées depuis plus de vingt ans déjà à la dynamique du vol des engins.

Toutefois, ces premières applications pouvaient être effectuées avec les informations obtenues sur maquette fixe, ou sur maquette mobile dans le domaine linéaire, comme par exemple, lorsqu'il s'agissait de traiter les non-linéarités dues:

- aux couplages par inertie proportionnels aux carrés, ou aux produits deux à deux des composantes de la vitesse angulaire sur les axes liés à l'engin,
- ou bien à la variation rapide de la masse volumique de l'air au cours du vol ascendant des fusées-sondes, alors que les coefficients aérodynamiques peuvent être considérés constants, [5] et figure 1.

Ces questions de dynamique du vol n'entrent pas dans le cadre de l'aérodynamique non-linéaire; elles ne sont évoquées ici que pour mémoire.

Par contre, au cours de ces dernières années, le besoin s'est fait sentir d'entreprendre des études de dynamique du vol relevant effectivement de l'aérodynamique non-linéaire, principalement à la suite de l'extension aux incidences élevées des régimes de vol non marginaux des avions, comme le montre une étude récente d'ORLIK-RÜCKENANN [6].

On peut citer comme exemples de non-linéarités d'origine aérodynamique:

- un décollement localisé de l'écoulement sur certains engins lancés à des incidences situées à l'intérieur d'un petit angle centré sur l'incidence nulle.
- l'échappement des tourbillons en cornet sur l'extrados des ailes lancées, auquel correspond une évolution non-linéaire du gradient de portance et du moment de tangage en fonction de l'incidence.
- aux incidences plus élevées, les décollements observés sur les ailes des avions qui intéressent des zones plus ou moins étendues et s'établissent de façon plus ou moins brutale. Dans les intervalles d'incidence où ces décollements se produisent, des phénomènes d'hystérésis se manifestent par des retards au décollement quand l'incidence croît et des retards au recollement quand elle décroît. En outre, lorsque le décollement se produit au cours d'une manœuvre à facteur de charge élevé, avec braquage de la gouverne de gauchissement, il est généralement dissymétrique et peut être cause d'un départ en vrille.

Les exemples d'aérodynamique non-linéaire discutés dans cette note se présentent de la façon suivante:

- le premier donne l'expression du moment de tangage déduit des informations relevées en soufflerie sur un engin de révolution à jupe tronconique en oscillations de tangage autour de l'incidence nulle, d'après des méthodes établies par X. VAUCHERET. Ce mouvement est à un seul degré de liberté.
- le modèle mathématique du moment aérodynamique, proposé par C.H. MURPHY et J.W. BRADLEY pour figurer dans l'équation du mouvement "conique" d'une maquette d'engin lancé symétrique observé au tunnel de tir, est pris comme second exemple.

Ce mouvement est à deux degrés de liberté, compte tenu des hypothèses du calcul:

- a) la trajectoire est rectiligne et parcourue à vitesse constante,
- b) le moment dû à la rotation propre de l'engin autour de son axe de symétrie est négligeable.

- le troisième exemple est un rappel des hypothèses et des conclusions de l'analyse de M. TOBAK et L.B. SCHIFF, sur l'expression du torseur aérodynamique d'un avion en régime de vrille établie, considéré comme un cycle limite. L'expression de ce torseur permet de compléter par les termes aérodynamiques la première approximation de la solution génératrice, figurée par un mouvement de Poincaré, proposée par C. LA BURTHE. Un tel mouvement, en principe à 6 degrés de liberté, peut cependant être étudié sans trop de difficulté grâce aux hypothèses admises.

Par ailleurs, dans l'ensemble de cet exposé, un effort a été fait pour tenter d'uniformiser les notations, en se conformant aux recommandations de l'I S O sur la Mécanique du vol [11] adoptées par plusieurs nations européennes. La correspondance avec les notations utilisées par les auteurs cités en référence est indiquée. La généralisation de l'utilisation de ces notations devrait faciliter la lecture des documents sur la dynamique du vol et éviter des erreurs d'interprétation.

2.- EXPRESSION DU MOMENT DE TANGAGE NON LINEAIRE D'UN CORPS DE RENTREE DE REVOLUTION A JOUE TRONCONIQUE D'APRES X. VAUCHERET [7].

Il est souvent observé que les oscillations libres de tangage des maquettes de ces engins, essayées en soufflerie dans des écoulements supersonique et hypersonique, ont tendance à se stabiliser vers un "cycle limite" à amplitude et fréquence constantes, lorsque l'incidence moyenne est voisine de l'incidence nulle.

De plus cette tendance persiste quelles que soient les conditions initiales, par exemple que la valeur initiale de l'amplitude soit supérieure ou inférieure à celle du cycle limite, fig.2-4.

Un tel comportement ne pouvait être représenté par une équation linéaire.

X. VAUCHERET a exprimé le moment de tangage suivant deux schémas comportant:

- le premier, des non-linéarités discontinues à des valeurs discrètes de l'élongation
- le second, une évolution continue de la discontinuité en fonction de l'élongation.

Notations.

Θ	élongation de l'assiette longitudinale ($\Theta=0$, correspond à la position horizontale de l'axe x),
Θ_m	valeur moyenne de l'élongation,
I_y	moment d'inertie autour de l'axe d'oscillation y,
S	surface de référence,
l	corde de référence,
ρ	masse volumique de l'air,
M	moment de tangage autour de l'axe y,
α	angle d'incidence,
$C_{m\alpha}$	coefficient de la dérivée de rappel en tangage

$$C_{m\dot{\alpha}} + C_{m\ddot{\alpha}} \quad \text{coefficient d'amortissement de tangage:}$$

$$\frac{\rho}{2} V^2 S l C_{m\dot{\alpha}} = \partial M / \partial \dot{\alpha} l$$

$$\frac{\rho}{2} V^2 S l C_{m\ddot{\alpha}} = \partial M / \partial \ddot{\alpha} l$$

Nota. Les symboles précédents sont conformes aux recommandations de l' I S O .

$(\dot{}), (\ddot{})$	dérivées première et seconde par rapport au temps,
k_0	pente changée de signe de AC et FE, $(dM/d\Theta)$ fig. 2-2,
k_1	pente changée de signe de CD et BF,
k_Θ	rigidité angulaire de l'articulation élastique,
c_e	amortissement de structure de l'articulation élastique,
c	amortissement total (structure et aérodynamique)
ζ	coefficient d'amortissement réduit $\zeta = c / 2I_y \omega_0$
ω_0	pulsation propre du système linéaire $(\omega_0^2 = k_0 / I_y)$.

2.1- Première méthode de X. VAUCHERET. [7.1] Non linéarités discontinues.

Les non-linéarités sont figurées par quatre discontinuités de la pente du moment de rappel en fonction de l'élongation, disposées symétriquement par rapport à l'origine. Elles sont visibles sur la figure 2-2 aux points BD et CF.

Un cycle complet d'oscillation est représenté sur cette figure, à la partie supérieure l'évolution du moment de rappel en fonction de l'élongation, et à la partie inférieure l'évolution de l'élongation en fonction du temps. Il est à remarquer que la courbe représentant l'ensemble des cycles en fonction du temps, contient toutes les informations nécessaires au traitement qui donne l'expression du moment aérodynamique de tangage.

A l'origine des temps, le point figuratif (M, Θ) se trouve en A, d'abscisse Θ_A , d'ordonnée M_A ; la vitesse $\dot{\Theta}_A$ est nulle et,

$$\Theta_A > 0 \quad M_A < 0 \quad \dot{\Theta}_A = 0$$

Sous l'effet du moment M_A , le mouvement prend naissance avec,

$$\dot{\Theta}_A < 0$$

et le point figuratif décrit le segment de droite A B C de pente $-k_0$. Au point C, il part suivant C D de pente plus élevée $-k_1$, jusqu'en D. A partir de ce point, il suit le segment D E de même pente que A C. La vitesse s'annule en E,

$$\dot{\Theta}_E = 0, \quad \Theta_E < 0, \quad M_E > 0,$$

puis le point figuratif suit la ligne brisée E D F, F B et B G. En G la vitesse est nulle ($\dot{\Theta}_G = 0$) et un cycle complet a été parcouru.

Les valeurs absolues de $\Theta_A, \Theta_E, \Theta_G$ peuvent être constantes, croissantes ou décroissantes, suivant les conditions d'essai.

La droite A B C coupe l'axe des abscisses en un point d'abscisse $-\Theta_0$ et la droite symétrique E D F le coupe au point symétrique Θ_0 .

En outre, il est admis que la somme des amortissements de structure de l'articulation et de l'aérodynamique est exprimée par un coefficient réduit $\zeta > 0$; ce signe correspond à un amortissement effectif, conformément à l'usage habituel en mécanique des oscillations. De même k_0 et k_1 positifs correspondent à des rappels effectifs, ce qui est le cas de l'exemple représenté sur la figure 2-2.

Le sens de parcours de la boucle d'hystérésis, formée par le quadrilatère B C D F, indique que la maquette reçoit de l'écoulement, à chaque cycle, une énergie W qui s'exprime par l'intégrale:

$$\int_C M d\Theta = W,$$

dans laquelle le contour C est figuré par B C D F.

W est absorbée en totalité ou en partie par les amortissements de structure de l'articulation et de l'aérodynamique. Si l'énergie nécessaire à la compensation de ces amortissements est supérieure à W, l'amplitude décroît et inversement. Lorsqu'il y a égalité, on peut observer un cycle limite, sous la forme d'une oscillation entretenue, si les conditions nécessaires à la stabilité de ce cycle limite sont remplies. Dans le cas contraire, l'oscillation peut disparaître complètement ou diverger.

Les discontinuités sont nettement visibles à la partie supérieure de la figure 2-2 mais il est pratiquement impossible de les distinguer à la partie inférieure, par suite des évolutions continues de l'élongation Θ et de sa vitesse $\dot{\Theta}$.

Elles peuvent être observées dans le plan de phase, sur lequel sont portées, suivant l'abscisse x, l'élongation Θ et suivant l'ordonnée, sa vitesse $\dot{\Theta}$, écrite sous forme réduite $\dot{\Theta}/\omega_0$. La courbe $y(x)$ est ainsi représentée dans un espace métrique.

Le tracé de cette courbe, nécessite la connaissance des solutions des équations du mouvement. Ces équations se présentent sous la forme des 4 équations linéaires suivantes:

$$\begin{aligned} (1) \quad I_y \ddot{\Theta} + k_0 \Theta &= -c \dot{\Theta} - k_0 \Theta_0 \\ (2) \quad I_y \ddot{\Theta} + k_1 \Theta &= -c \dot{\Theta} - k_1 \Theta_1 \\ (3) \quad I_y \ddot{\Theta} + k_0 \Theta &= -c \dot{\Theta} + k_0 \Theta_0 \\ (4) \quad I_y \ddot{\Theta} + k_1 \Theta &= -c \dot{\Theta} + k_1 \Theta_1 \end{aligned}$$

dans lesquelles $k_0, k_1, \Theta_0, \Theta_1$ sont les constantes à déterminer par le traitement des informations.

Nota.- Les équations (1) à (4) peuvent s'écrire sous une forme condensée:

$$(1bis) \quad I_y \ddot{\Theta} + K_j \Theta = -c \dot{\Theta} + \eta k_j \Theta_j \quad \text{avec } j = 0 \text{ ou } 1 \text{ et } \eta = \text{sign} \dot{\Theta}.$$

Les emplacements des points figuratifs dans le cycle, la répartition des équations sont indiqués dans le tableau présenté § 2.1.2, après quelques indications sur les solutions des équations et sur les courbes $y(x)$, figures 2-2, 2-3, 2-4, dans le plan de phase. Les solutions des équations linéaires sont classiques, elles ont pour expressions pour l'équation (1), au cours du passage de A à C au début du cycle:

$$(1a) \quad \Theta \approx (\Theta_A + \Theta_0) e^{-\zeta \omega_0 t} \cos \omega_0 t - \Theta_0,$$

et dans la dernière partie du cycle, entre B et G:

$$(1b) \quad \Theta \approx (\Theta_A + \Theta_0) e^{-\zeta \omega_0 t} \cos(\omega_0 t + 2\varphi) - \Theta_0,$$

Pour l'équation (3), suivant D E F :

$$(1c) \quad \Theta \approx (\Theta_A + \Theta_0) e^{-\zeta \omega t} \cos(\omega_0 t + \varphi) + \Theta_0, \quad \text{avec } \omega = \omega_0 \sqrt{1 - \zeta^2} \approx \omega_0.$$

A remarquer les sauts de phase entre les solutions (1a) et (1b), de la première équation d'une part, entre les solutions de la première et de la troisième équation d'autre part. Les solutions des équations (2) et (4) ont la même forme.

Le calcul de $y(x)$ et de $\frac{dy}{dx}$ est immédiat, entre A et C :

$$y(x) = \frac{\dot{\Theta}}{\omega_0} = -(\Theta_A + \Theta_0)(\sin \omega_0 t + \zeta \cos \omega_0 t) e^{-\zeta \omega_0 t},$$

et

$$\frac{dy}{dx} = \frac{dy}{dt} \frac{dt}{dx} = \frac{(1 - \zeta^2) \cos \omega_0 t - 2\zeta \sin \omega_0 t}{\cos \omega_0 t + \sin \omega_0 t},$$

et des expressions de même forme pour le reste du cycle.

2.1.1.- ζ étant généralement petit ($\zeta < 0,02$), il est commode de le supposer nul dans le raisonnement. Sous cette hypothèse, la courbe du plan de phase $y(x)$ correspondant à un cycle, se compose de 6 arcs de cercles, centrés sur l'axe des abscisses, dont les abscisses et les rayons ont pour valeurs:

$-\theta_0$	entre A et C et celle du rayon	$\theta_A + \theta_0$
$-\theta_1$	entre C et D et d°	$\theta_C + \theta_1$
θ_0	entre D et F et d°	$ \theta_D + \theta_0$
θ_1	entre F et B et d°	$\theta_F + \theta_1$
$-\theta_0$	entre B et G et d°	$\theta_G + \theta_0$

L'examen de la courbe $y(x)$ conduit aux remarques suivantes:

- a) la faible valeur des arcs C D et F B correspond à la faible valeur des fractions de période qu'ils représentent, qui apparaissent nettement à la partie inférieure de la figure 2-2. Il est donc possible de considérer confondus, les couples de points, C D d'une part et F B d'autre part.
- b) l'abscisse du point (CD) sensiblement égale à $-\theta_1$ est négative, par conséquent les grandeurs des deux amplitudes successives, écrites aux équations (1a) et (1c) sont dans l'ordre:

$$\theta_A + \theta_0 < |\theta_D| + \theta_0 \quad \text{d'où} \quad \theta_A < |\theta_D|$$

et de même au point (BF):

$$|\theta_F| < \theta_0 \quad \text{et finalement} \quad \theta_A < \theta_0$$

par conséquent, le mouvement diverge si la boucle d'hystérésis est décrite dans le sens des aiguilles d'une montre et si l'amortissement est nul.

- c) en ces points, on observe les sauts de phase ψ exprimés dans les relations (1b) et (1c) ci-dessus; en effet, c'est en ces points que se raccordent les arcs de cercle de centre $-\theta_0$ et $+\theta_0$. Compte tenu de la faible valeur de ces angles de saut, la relation suivante en donne une bonne approximation:

$$\psi = \frac{4\theta_0}{\theta_A + |\theta_D|} \left(1 - \frac{2\theta_0}{\theta_A + |\theta_D|}\right).$$

Ces sauts de phase entraînent des écarts entre les périodes mesurées T_N et la période propre de l'équation linéaire (1), soit: $T_0 = 2\pi/\omega_0$.

Dans les cas représentés sur les figures 2-2 à 2-4, ψ est positif et $T_N < T_0$.

Cet écart entraîne la relation:

$$\frac{T_N}{T_0} = \frac{2\pi - 2\psi}{2\pi} = 1 - \frac{\psi}{\pi}$$

2. 1. 2. - Les considérations précédentes peuvent être résumées dans le tableau suivant, dans lequel il est tenu compte d'un amortissement de coefficient ζ :

point figuratif	A	C	D	E	F	B	G
temps	$\frac{\zeta \neq 0}{\omega_0}$	t_0	$t_0 + \delta t$	$\frac{1}{2}T_N$	$\frac{1}{2}T_N + t_1$	$\frac{1}{2}T_N + t_1 + \delta t$	T_N
équation	(1)	(2)	(3)	(4)	(1)		
$\frac{dy}{dx}$	$-\infty+$	\nearrow	$-\infty+$	\nearrow	$-\infty+$	\nearrow	$-\infty+$
$\omega_0 t$	$-\zeta \neq 0$	SAUT DE PHASE DE $\frac{\pi}{2} - \eta_0$		$(\pi - \psi)$	SAUT DE PHASE DE $\frac{\pi}{2} - \eta_0$		$2(\pi - \psi)$
argument du cosinus	$\omega_0 t$	$\frac{\pi}{2} + \eta_1$		$\omega_0 t + \psi$	$\frac{\pi}{2} + \eta_1$		$\omega_0 t + 2\psi$

L'analyse de VAUCHERRET conduit à deux relations approchées, fonctions de l'amplitude:

- la décroissance d'amplitude par cycle,

$$(a) \quad \Theta_A - \Theta_E = [\Theta_A + \Theta_E] \left[\pi \left(1 - \zeta \frac{1}{2} \right) - 2\zeta \Theta_0 (4 - \pi) - 8\bar{\omega} \frac{\Theta_0^2}{\Theta_A + \Theta_E} \right]$$

le dernier terme de cette expression, qui représente la boucle d'hystérésis, est proportionnel à la surface de cette boucle, car:

$$\bar{\omega} \frac{\Theta_0^2}{\Theta_A + \Theta_E} = \frac{k_1}{k_1 - k_0} \frac{\Theta_A \Theta_E}{\Theta_A + \Theta_E} = \frac{\Theta_A \Theta_E}{2} \frac{\Theta_0}{\Theta_A + \Theta_E} \quad \text{ce qui définit } \bar{\omega}.$$

- le rapport de la fréquence propre de l'oscillation linéaire, f_0 , à celle mesurée sur le cycle de rang N , f_N , a pour expression:

$$(b) \quad \frac{f_N}{f_0} = \frac{f_0}{f_N} = 1 - \frac{4}{\pi} \frac{\Theta_0}{\Theta_A + \Theta_E} \left[1 + \zeta \frac{1}{2} - \frac{2\Theta_0}{\Theta_A + \Theta_E} \right]$$

étant donné la faible valeur de ζ , cette relation montre que l'évolution de la fréquence en fonction de l'amplitude ne dépend pratiquement que de Θ_0 , qui caractérise l'écart entre les deux droites A C et E F. Elle ne dépend pas de la surface de la boucle d'hystérésis, car $\bar{\omega}$ ne figure pas dans cette relation.

Les deux relations (a) et (b) écrites ci-dessus, peuvent être retrouvées aisément en utilisant la courbe du plan de phase.

2.1.3.- Calcul des constantes ζ , Θ_0 , $\bar{\omega}$ et ω_0 .

La relation (a) est l'équation d'une hyperbole de coordonnées:

$$\begin{aligned} X &= \Theta_A + \Theta_E \\ Y &= \Theta_A - \Theta_E \end{aligned}$$

soit:

$$XY - \pi \zeta X^2 + 1,7168 \zeta \Theta_0 X + 8\bar{\omega} \Theta_0^2 = 0$$

Si l'amplitude de départ des oscillations est importante (par exemple 6 degrés sur la figure 2.1), un grand nombre de couples de valeurs distinctes de X Y est disponible. Les coefficients $\pi \zeta$, $\zeta \Theta_0$ et $8\bar{\omega} \Theta_0^2$ pourraient être déterminés par une méthode de moindres carrés. Mais l'expérience montre que les résultats ainsi obtenus sont peu satisfaisants, et qu'il est préférable de procéder en deux étapes. La première consiste à appliquer la méthode des moindres carrés à la détermination des coefficients de l'asymptote d'équation:

$$Y = \pi \zeta X - 1,7168 \zeta \Theta_0$$

dont la pente ne dépend que de ζ et l'intersection avec l'axe X , de Θ_0 .

Les valeurs ainsi obtenues, portées dans l'équation de l'hyperbole, donneront $\bar{\omega}$.

De même, portées dans la relation b), elles donneront f_0 , donc ω_0 .

2.1.4.- Cas du cycle limite.

a) examen des conditions d'existence.

Le cycle-limite est caractérisé par $\Theta_A = \Theta_E = \Theta_L$, voir la courbe en traits pleins de la figure 2-4.

Les amplitudes instantanées des sinusoides amorties aux points C et D, sensiblement confondus, s'expriment par les relations,

$$(1) \quad \begin{aligned} R_0 &= (\Theta_L + \Theta_0) e^{-\zeta(\frac{\pi}{2} - \eta_0)} \\ R_1 &= (\Theta_L + \Theta_0) e^{-\zeta(\frac{\pi}{2} - \eta_1)}, \end{aligned}$$

le rapport R_0/R_1 est lié au saut de phase φ et aux angles η_0 et η_1 par :

$$(2) \quad \begin{aligned} \varphi &= 2 \frac{\Theta_0}{\Theta_L} \left(1 + \zeta \frac{\pi}{2} - \frac{\Theta_0}{\Theta_L} \right) \\ &= \eta_0 + \eta_1 \end{aligned}$$

et par conséquent, d'après (1) et (2) :

$$(3) \quad \frac{R_0}{R_1} = \frac{\cos \eta_1}{\cos \eta_0} = k = e^{-\zeta(\pi - \varphi)}$$

d'où :

$$(4) \quad k \cos \eta_0 - \cos(\varphi - \eta_0) = 0$$

à $\frac{\Theta_0}{\Theta_L}$ et ζ donnés, les constantes φ , k , η_0 , η_1 , peuvent être calculées successivement φ d'après (2), k d'après (3), η_0 d'après (4), puis η_1 d'après (2).

Les relations (1) donnent ensuite R_0 et R_1 .

Pour que le cycle limite existe, il faut en outre que, dans le triangle de côtés R_0 , R_1 , $2\Theta_0$, l'angle compris entre R_0 et R_1 ait la valeur de φ calculée. Cette condition, compte tenu de (3), s'exprime par :

$$(5) \quad 1 + \frac{1}{k^2} - \frac{2}{k} \cos \varphi = \frac{4\Theta_0^2}{R_0^2}$$

Un exemple de cycle limite est donné figure 2-4.

b) Calcul des constantes ζ et W en fonction de f_L et x_L .

La fréquence f_L et l'amplitude x_L du cycle limite sont mesurées en essai. Les relations écrites de (1) à (5) ci-dessus, auxquelles il convient d'ajouter :

$$(6) \quad \frac{f_0}{f_L} = 1 - \frac{2}{\pi} \frac{\Theta_0}{\Theta_L + \Theta_0} \left(1 + \zeta \frac{\pi}{2} - \frac{\Theta_0}{\Theta_L} \right)$$

représentent 7 équations à 7 inconnues, qui sont :

$$\Theta_0, \eta_0, \eta_1, R_0, R_1, \zeta, f_0.$$

Leur solution peut être recherchée par itérations successives en prenant, par exemple, comme valeurs initiales, celles de Θ_0 et ζ déduites du traitement effectué sur la partie décroissante de l'oscillation. W est directement liée à l'abscisse du point CD figure 2-4.

2.1.5.- Calcul des coefficients aérodynamiques $C_{m\alpha}$, C_{mq} et $C_{m\dot{\alpha}}$.

- Des oscillations en absence d'écoulement, dont l'équation du mouvement a la même forme que celle du mouvement dans l'écoulement, permettent de déterminer les constantes de la maquette et de la suspension, d'après :

$$k_\theta = I_y \omega_{os}^2 \quad \text{et} \quad c_s = 2\zeta_s \omega_{os} I_y$$

et s'il y a lieu Θ_{00} et Θ_{10} ; ω_{00} est la pulsation propre de l'oscillation .

- Les coefficients aérodynamiques C_{mq} , $C_{mq} + C_{m\dot{q}}$ sont obtenus à partir des constantes déduites des résultats d'essai d'après :

- a) dans les intervalles d'élongation parcourus avec la pente- k_0 , suivant ABC et EDF :

$$C_{m\ddot{q}0} = -(k_0 - k_{\Theta}) / \frac{1}{2} \rho V^2 S l \quad \text{avec} \quad k_0 = \omega_0^2 I_y ,$$

- b) dans les intervalles d'élongation parcourus avec la pente- k_1 , suivant CD et FB :

$$C_{m\ddot{q}1} = -(k_1 - k_{\Theta}) / \frac{1}{2} \rho V^2 S l ,$$

et à toutes les valeurs de l'élongation :

$$C_{mq} + C_{m\dot{q}} = -2(\zeta - \zeta_{\frac{\omega_0}{\omega_{00}}}) \omega_0^2 I_y / \frac{1}{2} \rho S l^3$$

Des valeurs numériques sont présentées dans la référence [7.1] on y remarquera la faible valeur de ζ , de l'ordre de 5.10^{-3} à 10^{-2} .

Remarque. La courbe représentative du moment des forces d'inertie, $-I\ddot{\Theta}$, en fonction de l'élongation est confondue avec celle du moment de rappel, M , quand l'amortissement est nul. Les deux courbes sont légèrement différentes dans le cas contraire, $\zeta \neq 0$. En effet le point figuratif de $-I\ddot{\Theta}$ ne suit pas le même trajet dans les deux sens, comme le montre la figure 2-4. Cependant, les écarts indiqués sur cette figure correspondent à une valeur de ζ beaucoup plus importante que celles rencontrées dans la pratique.

2.2- Deuxième méthode [7.2&3] . Non linéarités continues.

Dans la publication citée en référence, VAUCHERET examine la présence simultanée de non linéarités continues du coefficient de la vitesse et de celui de l'élongation. Pour simplifier le présent exposé, ces non linéarités sont examinées isolément dans les cas les plus simples.

2.2.1.- Non-linéarité sur le terme de rappel et amortissement nul.

L'équation du mouvement dans un des cas les plus simples, a pour expression :

$$\ddot{\Theta} + \omega_0^2 (1 + a\Theta^2) \Theta = 0.$$

C'est une équation de DUFFING, dont le moment de rappel, du troisième degré en Θ se présente comme le montre la figure 2-5. Au second ordre près, la solution de cette équation est de la forme :

$$\Theta = \Theta_A \cos \omega_1 t \quad \text{avec} \quad \omega_1 = \omega_0 / (1 - \frac{3}{8} a \Theta_A^2)$$

la valeur de la fréquence dépend de la valeur de l'amplitude qui reste constante au cours de l'oscillation ; suivant le signe de a , la fréquence augmentera ou diminuera avec l'amplitude. a et ω_0 sont des constantes.

Le moment de rappel présente une analogie avec celui décrit au paragraphe 2.1, mais dans le cas présent les déplacements des points Θ_0 se font de façon différente. Au lieu de ne mettre qu'une faible fraction de la période pour passer de la position fixe Θ_0 à la position fixe $-\Theta_0$, ainsi que pour le retour en sens inverse, le point correspondant Θ_{0m} se déplace maintenant de façon continue pendant toute la durée de la période.

Au cours d'un cycle Θ varie entre Θ_A et $-\Theta_A$; Θ_{OM} , point de rencontre avec l'axe des Θ de la tangente en M à la courbe $M(\Theta)$, se déplace de $-\Theta_{OA}$ à $+\Theta_{OA}$ d'après la relation :

$$\Theta_{OM} = 2a\Theta_M^3 / (1 + 3a\Theta_M^2).$$

La courbe de phase est représentée, sans tenir compte des harmoniques supérieures, avec une bonne approximation par la circonférence correspondant à l'oscillation fondamentale de pulsation ω_1 .

2.2.2.- Non linéarité de vitesse et moment de rappel linéaire.

L'équation de VAN der POL:

$$\ddot{\Theta} + 2\zeta\omega_0(1 + b\Theta^2)\dot{\Theta} + \omega_0^2\Theta = 0$$

représente un exemple simple de non-linéarité de cette espèce.

Si l'amplitude initiale est choisie égale à :

$$\Theta_A = 2/\sqrt{-b},$$

ce qui implique $b < 0$, la solution est périodique et a pour expression approchée:

$$\Theta = \Theta_A(\cos\omega_0 t - \frac{3\zeta}{4}\sin\omega_0 t) + \frac{\zeta}{4}\sin 3\omega_0 t, \quad \text{car } \omega = \frac{\omega_0}{1 + \zeta^2/4} \approx \omega_0.$$

Cette solution correspond à un cycle limite. En effet, si l'amplitude a une valeur différente de:

$$\Theta_A = 2/\sqrt{-b},$$

elle a tendance à s'en rapprocher.

La vitesse angulaire de tangage a pour expression:

$$\frac{\dot{\Theta}}{\Theta_A\omega_0} = -\sin\omega_0 t - \frac{3\zeta}{4}(\cos\omega_0 t - \sin 3\omega_0 t),$$

La représentation dans le plan de phase est donnée figure 2-6, sur laquelle la circonférence représentant l'oscillation linéaire a également été tracée.

Lorsque les conditions du cycle-limite sont satisfaites, le coefficient d'amortissement linéaire réduit est négatif ($\zeta < 0$), le coefficient d'amortissement:

$$M_{\dot{\Theta}} = \zeta \left[1 - \left(\frac{2\Theta}{\Theta_A} \right)^2 \right] \quad \text{avec } \Theta_A = \frac{2}{\sqrt{-b}},$$

est négatif aux faibles valeurs de l'élongation et positif aux valeurs plus élevées, suivant:

- a) $\Theta < \frac{\Theta_A}{2} \longrightarrow M_{\dot{\Theta}} < 0,$
- b) $\Theta = \frac{\Theta_A}{2} \longrightarrow M_{\dot{\Theta}} = 0,$
- c) $\Theta > \frac{\Theta_A}{2} \longrightarrow M_{\dot{\Theta}} > 0.$

La maquette reçoit de l'énergie de l'écoulement dans le cas a) et restitue cette énergie à l'écoulement quand c) est vérifié.

La figure 2-6, montre que dans le premier quart de période, pour une valeur donnée de l'élongation, la valeur absolue de la vitesse angulaire réduite $\dot{\Theta}/\omega_0$ est plus faible que celle de l'équation linéaire et que le contraire existe dans le second quart; de sorte que le moment d'amortissement moyen au cours d'une période est nul.

2.2.3.- Cas général. Non linéarités continues de vitesse et de rappel.

L'équation du mouvement étudié par VAUCHERET s'écrit :

$$\ddot{\Theta} + \omega_0^2 \Theta + \varepsilon F(\Theta, \dot{\Theta}) = 0,$$

$F(\Theta, \dot{\Theta})$ a la dimension de $\ddot{\Theta}$, ε est un scalaire tel que : $\varepsilon \ll 1$

F peut s'exprimer par des polynômes en $\Theta, \dot{\Theta}$, écrits le plus souvent sous la forme :

$$F = \left(\sum_n a_n \Theta^n \right) \dot{\Theta} + \left(\sum_p b_p \dot{\Theta}^p \right) \Theta.$$

La solution de cette équation a pour expression :

$$\Theta = \Theta_A(t) \cos \omega_0 t + \Phi(t).$$

Compte tenu de la valeur de ε , $\Theta_A(t)$ et $\Phi(t)$ peuvent être écrits sous la forme :

$$\Theta_A(t) = \Theta_A + \Delta\Theta(t) \quad \text{et} \quad \omega_0 t + \Phi(t) = \left\{ \left[\omega_0 + \frac{\Delta\omega(t)}{t} \right] t + \Phi_0 \right\},$$

Θ_A , ω_0 et Φ_0 sont des constantes de l'oscillation et les expressions $\Delta[\]$ sont des accroissements dont les grandeurs restent modérées par rapport aux constantes. Il est montré dans la référence [7.3], que la non-linéarité du coefficient de Θ influence uniquement la fréquence et que la non-linéarité du coefficient de $\dot{\Theta}$ influence uniquement l'amplitude des oscillations.

Le calcul des expressions des coefficients de F à partir des variations de fréquence et d'amplitude est indiqué dans la même référence, qui donne également les expressions des coefficients aérodynamiques non-linéaires $C_{m\dot{\alpha}}$ et $C_{mq} + C_{m\ddot{\alpha}}$.

3.- EXPRESSION DU MOMENT AERODYNAMIQUE SUR UN ENGIN EN MOUVEMENT "CONIQUE".

d'après MURPHY et BRADLEY [8].

Ce mouvement, observé au tunnel de tir sur des maquettes d'engins élanés de révolution, se présente sous la forme d'une rotation uniforme autour du vecteur vitesse, dont la direction et la grandeur restent constantes. L'angle entre l'axe de symétrie de l'engin et la direction de la vitesse est important; il n'est jamais inférieur à une vingtaine de degrés.

Un vecteur vitesse constant implique des équations du mouvement limitées aux équations du moment cinétique. En outre, elles se réduisent à deux équations seulement, car la forme particulière de l'engin rend négligeables les moments autour de l'axe de symétrie. La rotation propre autour de cet axe sera donc négligée, dans l'analyse qui suit elle sera supposée nulle.

Il reste donc deux équations qui expriment l'équilibre autour du centre de gravité G de l'engin, des moments décomposés suivant deux axes rectangulaires liés à l'engin, fig.3-1 et perpendiculaires entre eux, soit :

- l'axe de tangage Gy perpendiculaire au plan formé par l'axe de symétrie Gx et le vecteur vitesse \vec{V} , porté par l'axe Gx_A ,
- l'axe de lacet Gz contenu dans le plan Gxx_A .

Ce mouvement, à deux degrés de liberté, dépend de deux variables qui peuvent être représentées par l'angle d'incidence ($\alpha = Gx_A, Gx$) et la vitesse angulaire de rotation suivant Gx_A , soit p_A .

Il y a lieu de noter, qu'au cours du mouvement, l'angle de dérapiage β reste constamment nul.

MURPHY et BRADLEY étudient le mouvement libre de l'engin, puis le mouvement entre-tenu par un moment de tangage dû à une légère dissymétrie. Leur analyse est basée sur l'hypothèse que l'engin est dynamiquement instable aux faibles valeurs absolues de l'angle d'incidence, instabilité qui s'exprime par des valeurs négatives du coefficient d'amortissement réduit ζ et par des valeurs positives des dérivées de stabilité par rapport aux vitesses angulaires telles que C_{mq} et C_{nr} .

Le présent paragraphe est consacré au rappel de leur mise en équation dans le cas du mouvement libre et à la présentation de quelques remarques sur la stabilité de ce mouvement.

Notations particulières à la référence [8].

Gxyz	axes liés à l'engin, Gx axe de symétrie,
Gx $\tilde{y}\tilde{z}$	axes aérobalistiques, appelés aussi axes sans roulis (non-rolling axes) ils sont animés d'une vitesse de roulis $-\dot{p}$ par rapport aux axes Gxyz.
$\tilde{\zeta}$	affixe de la projection de la vitesse réduite \tilde{w}/V dans le plan $\tilde{y}\tilde{z}$, (complex-yaw).
δ	module de $\tilde{\zeta}$ ($\delta = \sin\alpha$),
θ	angle d'incidence, entre Gx et \tilde{w} , argument de $\tilde{\zeta}$, $[\tilde{\zeta} = (\tilde{w} + i\tilde{w})/V = \delta e^{i\theta}]$
C_M	coefficient sans dimension du moment autour de l'axe Gy.
s	longueur réduite de trajectoire, ($s = Vt/\ell$)
ω_0	pulsation de l'équation de Van der Pol.

Coefficients des dérivées aérodynamiques de stabilité.

C_M	coefficient de la dérivée du moment statique de tangage ($\frac{\partial C_M}{\partial \alpha}$),
d_0	coefficient du terme <u>linéaire</u> des dérivées d'amortissement. ce coefficient à la même valeur en tangage et en lacet.
ad_2	coefficient du terme en δ^2 du coefficient d'amortissement de tangage,
d_2	coefficient du terme en δ^2 du coefficient d'amortissement de lacet.

Indices supérieurs.

$\dot{(\)}$, $\ddot{(\)}$	dérivées première et seconde par rapport au temps,
$(\)'$, $(\)''$	dérivées première et seconde par rapport à s.

Notations conformes aux recommandations ISO.

p, q, r	composantes de la vitesse angulaire sur les axes Gxyz liés à l'engin.
p_a	composante de la vitesse angulaire sur Gx _a , support du vecteur-vitesse.
p^*, q^*, r^*	formes réduites des grandeurs précédentes ($p^* = p\ell/V$ etc.)
Φ	angle de gîte
$\dot{\Phi}$	vitesse angulaire correspondante

Nota.- Les opérateurs $(\)'$ et $(\)^*$ sont identiques, en effet:

$$\frac{d}{ds} = \frac{d(\)}{dt} \frac{dt}{ds} = \frac{d(\)}{dt} \frac{\ell}{V}$$

il en résulte que :

$$(\)' = (\)^*_{\frac{\ell}{V}} = (\)^*$$

et de même :

$$(\quad)' = (\quad)\frac{\ell^2}{V^2} = (\quad)''$$

La correspondance entre les variables de la référence [8] et celles recommandées par l'ISO est rappelée ci-dessous.

variables ISO	variables [8]	correspondance
α	δ	$\sin \alpha = \delta$
p_a^*	θ'	$p_a^* \cos \alpha = \theta' + \dot{\phi} = \dot{p}^*$
$p^* = p_a^* \cos \alpha$		
$q = \dot{\alpha}$	δ'	$q^* \cos \alpha = \delta'$
$r = p_a^* \sin \alpha$		$r^* \cos \alpha = \theta \delta$
\dot{p}^*		$\dot{p}^* = \theta''$
\dot{q}^*		$\dot{q}^* \cos \alpha = \delta''$
\dot{r}^*		$\dot{r}^* \cos \alpha = \theta'' \delta + \theta' \delta'$

L'affixe dans les axes $\tilde{y} \tilde{z}$, de la projection sur z du vecteur unité de x_a , et ses dérivées ont pour expressions :

$$\tilde{\xi} = \delta e^{i\theta}, \quad \tilde{\xi}' = (\delta' + i\theta'\delta)e^{i\theta}, \quad \tilde{\xi}'' = [\delta'' - \theta'^2\delta + i(2\theta'\delta' + \theta''\delta)]e^{i\theta},$$

Les équations générales du moment cinétique ont pour expression vectorielle:

$$\left[\frac{d}{dt} + \Omega_e \wedge \right] (I\Omega) = (\text{moment aéro.}) \quad \text{avec} \quad (I) = \begin{bmatrix} I_x & 0 & 0 \\ 0 & I_y & 0 \\ 0 & 0 & I_z \end{bmatrix}$$

et étant donné la forme de l'engin:

$$I_y = I_z = I \quad \text{et} \quad \frac{I_x}{I} \ll 1.$$

$[\Omega]$ est le vecteur rotation de l'engin,

$[\Omega_e]$ le vecteur rotation d'entraînement, soit :

$$[\Omega] = [p_a \cos \alpha + \dot{\phi} \quad \dot{\alpha} \quad p_a \sin \alpha]^T \quad (\text{T symbole de transposition})$$

$$[\Omega_e] = [p_a \cos \alpha \quad \dot{\alpha} \quad p_a \sin \alpha]^T$$

Dans la suite $[\Omega_e] = [\Omega]$ car, par hypothèse $\dot{\phi} = 0$. Dans le cas particulier examiné ici l'équation de roulis peut être négligée. Les équations du moment cinétique sont limitées aux équations de tangage et de lacet, qui ont pour expression matricielle:

$$\begin{bmatrix} p_a \sin \alpha & \frac{d}{dt} & -p_a \cos \alpha \\ -\dot{\alpha} & p_a \cos \alpha & \frac{d}{dt} \end{bmatrix} \begin{bmatrix} \frac{I_x}{I} p_a \cos \alpha \\ \dot{\alpha} \\ p_a \sin \alpha \end{bmatrix} = \begin{bmatrix} M/I \\ N/I \end{bmatrix}$$

et avec les variables de la référence [8] :

$$\begin{bmatrix} \frac{\dot{\theta}\delta}{\cos \alpha} & \frac{d}{dt} & -\dot{\theta} \\ -\frac{\dot{\theta}}{\cos \alpha} & \dot{\theta} & \frac{d}{dt} \end{bmatrix} \begin{bmatrix} \frac{I_x}{I} \dot{\theta} \\ \dot{\theta} \\ \dot{\theta}\delta/\cos \alpha \end{bmatrix} = \begin{bmatrix} M/I \\ N/I \end{bmatrix}$$

et sous forme développée avec les variables sans dimension:

$$\delta'' - \theta'^2 \delta \left(1 - \frac{I_x}{I}\right) - \frac{M \ell^2}{I V^2} \cos \alpha = 0$$

$$\theta'' \delta + 2\theta' \delta' \left(1 - \frac{I_x}{2I}\right) - \frac{N \ell^2}{I V^2} \cos \alpha = 0$$

après avoir posé: $1 - \frac{I_x}{I} \approx 1 - \frac{I_x}{2I} \approx 1$,

les deux équations peuvent être remplacées par une seule équation à termes complexes

$$\ddot{\zeta} - \frac{\rho S \ell^3}{2I} (C_m + iC_n) e^{i\theta} \cos \alpha = 0.$$

avec,

$$\begin{aligned} C_m &= C_{m\alpha} \alpha + (C_{mq} + C_{m\dot{\alpha}}) q^* \\ C_n &= C_{nr} r^* \end{aligned}$$

On remarque l'absence de terme en β et $\dot{\beta}$, due à la forme particulière de l'engin et à $\dot{\phi} = 0$.

En remplaçant q^* et r^* , par les variables de la référence [8], (voir le tableau ci-dessus) on obtient d'une part, la correspondance :

$$\boxed{C_{m\alpha} = C_{M\alpha}} \quad \text{et} \quad \boxed{\begin{aligned} C_{mq} + C_{m\dot{\alpha}} &= -[d_0 + d_2(1+a)\delta^2] \\ C_{nr} &= -[d_0 + d_2\delta^2] \end{aligned}}$$

et d'autre part:

$$(C_m + iC_n) e^{i\theta} \cos \alpha = (C_{M\alpha} - d_2 a \delta \delta') \tilde{\xi} - (d_0 + d_2 \delta^2) \tilde{\xi}',$$

et compte tenu des relations suivantes, utilisées dans [8]:

$$\frac{1}{2} \frac{\rho S \ell^3}{I} C_M = M, \quad \frac{1}{2} \frac{\rho S \ell^3}{I} d_0 = H_0, \quad \frac{1}{2} \frac{\rho S \ell^3}{I} d_2 = H_2,$$

on retrouve, dans le cas $\dot{\phi} = 0$, l'équation de Van der Pol à variable complexe présentée dans [8]:

$$(1) \quad \ddot{\tilde{\xi}} + (H_0 + H_2 \delta^2) \tilde{\xi}' - (M - H_2 a \delta \delta') \tilde{\xi} = 0$$

En séparant les parties réelles et imaginaires, on obtient :

$$(2) \quad \begin{aligned} \delta'' + \frac{1}{2} \frac{\rho S \ell^3}{I} [d_0 + d_2(1+a)\delta^2] \delta' - \left(\frac{1}{2} \frac{\rho S \ell^3}{I} C_{m\alpha} + p^{*2} \right) \delta &= 0. \\ p^{*'} \delta + 2p^* \delta' + \frac{1}{2} \frac{\rho S \ell^3}{I} (d_0 + d_2 \delta^2) p^* \delta' &= 0. \end{aligned}$$

Les équations (2) admettent deux solutions particulières:

1) une oscillation plane autour d'un axe fixe, caractérisée par la rotation:

$$p = 0, \quad q = \dot{\alpha} \neq 0, \quad r = 0.$$

$p = 0$ vérifie la seconde équation (2) quelle que soit la valeur de δ .

La première équation (2) est une équation de Van der POL à variable réelle δ ; la fréquence et l'amplitude du cycle-limite défini par cette équation ont pour valeurs:

$$f_L = \frac{1}{2\pi} \sqrt{-\frac{1}{2} \rho S V^2 \ell C_{m\alpha} / I}, \quad \alpha_L = \pm \left| \text{Arc sin } \sqrt{-d_0 / d_2(1+a)} \right|.$$

2) un mouvement "conique" caractérisé par :

- une rotation constante dirigée suivant le vecteur vitesse, soit

$$p_{ac} \quad (p_0 = \text{constante}, \quad q_0 = 0, \quad r_0 = \text{constante}),$$

- un angle d'incidence constant α_0 ($\sin \alpha_0 = \delta_0$, $\delta'_0 = 0$).

La seconde équation de (2) donne la valeur de α_0 ,

$$\alpha_0 = \text{Arc sin } \sqrt{-d_0 / d_2},$$

La première équation de (2) donne la valeur de p_{ac} ,

$$p_{ac} = \frac{1}{\cos \alpha_0} \sqrt{-\frac{1}{2} \rho S V^2 \ell C_{m\alpha} / I}.$$

Le mouvement résultant peut être une combinaison de ces deux mouvements.

La stabilité de ces mouvements est étudiée par la méthode des petites perturbations, qui consiste à donner de petits accroissements aux valeurs de régime des variables. On obtient ainsi un système d'équations linéaires, dont la stabilité est étudiée de façon classique. Le cas du mouvement conique est donné ici à titre d'exemple.

Soient les accroissements:

$$\Delta\delta = \delta - \delta_c, \quad \Delta\delta' = \delta', \quad \Delta\delta'' = \delta''; \quad \Delta p^* = p^* - p_c^* \quad \Delta p^{*'} = p^{*'},$$

$$\text{avec } \delta_c^2 = -d_0/d_2, \quad \text{d'après la seconde équation de (2).}$$

Les équations de stabilité déduites de (2) s'écrivent:

$$(3) \quad \begin{cases} \Delta\delta'' + ad_2 \delta_c^2 H \Delta\delta' - 2p_c^* \delta_c \Delta p^* = 0 \\ 2p_c^* \Delta\delta' + 2d_2 p_c^* \delta_c^2 H \Delta\delta + \delta_c \Delta p^{*'} = 0. \end{cases}$$

dans lesquelles on a posé :

$$H = \frac{1}{4} \rho S \ell^3 / I,$$

Le système (3) est linéaire en $\Delta\delta$ et Δp^* ; son équation caractéristique s'écrit:

$$\begin{vmatrix} \lambda^2 + ad_2 \delta_c^2 H \lambda & -2p_c^* \delta_c \\ 2p_c^* \lambda + 2d_2 p_c^* \delta_c^2 H & \delta_c \lambda \end{vmatrix} = 0$$

et en développant :

$$(4) \quad \delta_c (\lambda^3 + ad_2 \delta_c^2 H \lambda^2 + 4p_c^{*2} \lambda + 4d_2 p_c^{*2} \delta_c^2 H) = 0$$

L'expérience montre que l'on obtient une bonne approximation de l'une des racines de (4) par :

$$\lambda_1 \approx -d_2 H \delta_c^2,$$

L'équation peut alors s'écrire sous la forme approchée,

$$(4bis) \quad \delta_c [\lambda^2 + (a-1)d_2 \delta_c^2 H \lambda + 4p_c^{*2}] (\lambda + d_2 H \delta_c^2) = 0,$$

ce qui revient à considérer :

$$\frac{a-1}{4p_c^{*2}} d_2 \delta_c^2 H \approx 0$$

La condition nécessaire à la stabilité du mouvement, indiquée dans (8) :

$$a > 1,$$

qui rend positif le terme en λ^2 de (4) est mise en évidence dans (4bis).

Cette condition peut également s'exprimer par :

$$\left| \frac{\partial (C_{mq} + C_{m\dot{\alpha}})}{\partial \delta^2} \right| > 2 \left| \frac{\partial C_{nr}}{\partial \delta^2} \right|.$$

4.- EXPRESSION DU TORSEUR AERODYNAMIQUE SUR UN AVION EN RÉGIME DE VRILLE ÉTABLIE CONSIDÉRÉ COMME UN CYCLE LIMITE. d'après TOBAK et SCHIFF [9].

L'étude de la vrille d'un avion est très complexe, car ce mouvement est à six degrés de liberté et les équations du mouvement comprennent des termes non-linéaires d'inertie et d'aérodynamique.

Il ne semble pas qu'il existe, à l'heure actuelle, une méthode de détermination systématique des termes aérodynamiques non-linéaires. Les méthodes de calcul de dynamique de la vrille sont purement numériques. Elles utilisent les résultats obtenus en vol, sur maquette libre en soufflerie verticale, et récemment les résultats obtenus avec les montages en rotation uniforme en soufflerie. Les valeurs des termes aérodynamiques sont calculées par différence sur les réponses de l'avion ou de la maquette, dont la masse et le tenseur d'inertie sont connus. Les travaux de TOBAK et SCHIFF, entrepris depuis de nombreuses années, représentent une tentative intéressante pour guider le choix d'un modèle mathématique non-linéaire.

La cause essentielle de la vrille est la tendance à l'autorotation provoquée, à incidence élevée, par des décollements dissymétriques sur l'aile. Il est donc admissible, dans une première phase de l'étude de supposer la trajectoire rectiligne parcourue à vitesse constante. La présente étude est ainsi ramenée à une étude analogue à celle du paragraphe précédent, mais il faudra, cette fois, tenir compte de l'équation de roulis. Le mouvement considéré est donc à trois degrés de liberté et l'on peut prendre comme paramètres variables, fonctions du temps, les angles d'incidence α , de dérapage β et le vecteur rotation $\vec{\Omega}$, qui n'est pas généralement confondu avec le vecteur vitesse. Or, $\vec{\Omega}$ est fonction de ses 3 composantes p, q, r , sur les axes-avion $Gxyz$, et il semblerait à première vue que le mouvement dépende de cinq paramètres. Il n'en est rien, car la trajectoire étant rectiligne, la direction de l'accélération du centre de gravité reste fixe, ce qui se traduit par les deux premières relations suivantes:

$$\begin{bmatrix} \dot{\alpha} \\ \dot{\beta} \\ p_a \end{bmatrix} = [MP] \begin{bmatrix} p \\ q \\ r \end{bmatrix} \quad \text{avec } [MP] = \begin{bmatrix} -\cos\alpha \tan\beta & 1 & -\sin\alpha \tan\beta \\ \sin\alpha & 0 & -\cos\alpha \\ \cos\alpha \cos\beta & \sin\beta & \sin\alpha \cos\beta \end{bmatrix}$$

p_a , dans la troisième relation, est la projection de $\vec{\Omega}$ sur la direction de la vitesse. $\vec{\Omega}$ peut donc être défini indifféremment par $[p \ q \ r]^T$ ou par $[\dot{\alpha} \ \dot{\beta} \ p_a]^T$.

- l'autorotation est proche, comme l'a montré LA BURTHE [10], d'un mouvement de Poincaré auquel est adjoint un torseur aérodynamique de faible grandeur par rapport à celle du torseur des forces d'inertie.

Pour une vitesse V_0 donnée, les conditions d'existence d'un régime d'autorotation et, par conséquent, les valeurs des paramètres $\alpha, \beta, \dot{\alpha}, \dot{\beta}, p_a$ sont complètement définies par les équations du moment cinétique. Elles sont composées généralement de la somme d'un terme constant et d'un terme fonction du temps, soit,

$$\alpha_0 + \Delta\alpha(t), \quad \beta_0 + \Delta\beta(t), \quad p_{a0} + \Delta p_a(t).$$

- en régime de vrille, deux paramètres supplémentaires viennent s'ajouter à ceux qui caractérisent l'autorotation: le rayon de vrille et le cap relatif.

Le cap relatif est l'angle entre le rayon de vrille et la projection de l'axe longitudinal avion Gx sur le plan perpendiculaire à l'axe de vrille, soit χ cet angle.

Le rayon de vrille R est presque toujours petit par rapport aux dimensions de l'avion il ne représente généralement qu'une faible fraction de la longueur de référence.

Il en résulte que les équations du moment cinétique de l'autorotation et de la vrille sont pratiquement les mêmes: la vitesse angulaire p_a reste inchangée et les différences entre les valeurs des angles d'incidence et de dérapage en autorotation et en vrille sont très petites.

Les caractéristiques de la vrille peuvent être exprimées sous la forme du vecteur d'état :

$$[E] = [\alpha \ \beta \ p_a \ V_0 \ R \ \chi]^T,$$

dont les composantes sont généralement fonction du temps.

TOBAK et SCHIFFR, en partant d'observations expérimentales, proposent de représenter le torseur aérodynamique par des coefficients sans dimension, écrits dans des axes liés à l'avion, de la forme:

$$[C_K(t)] = [C_K(\alpha_0, \beta_0, p_{a0})] + [C_{K\alpha} \ C_{K\beta} \ C_{Kp} \ C_{Kq} \ C_{Kr}] [\Delta E],$$

dans cette expression,

$[C_k(t)]$ est un vecteur dont les k composantes sont fonction du temps; k représente les six symboles X, Y, Z, ℓ, m, n .

Les termes du second membre représentent:

$[C_k(\alpha_0, \beta_0, p_{a0})]$ un vecteur constant,

$[\Delta E] = [\Delta \alpha \Delta \beta \Delta p \Delta q \Delta r]^T$ un vecteur à cinq composantes fonction du temps, expressions des elongations et des vitesses angulaires d'une oscillation.

$[C_{k\alpha} C_{k\beta} C_{kp} C_{kq} C_{kr}]$ une matrice de k lignes et cinq colonnes dont les éléments sont les dérivées partielles de $[C_k]$ par rapport aux composantes de $[\Delta E]$.

L'existence de cette matrice implique que $[C_k(\alpha_0, \beta_0, p_{a0})]$ soit continu et dérivable par rapport aux éléments de $[\Delta E]$. Dans le cas où ces éléments sont des quantités petites du premier ordre et si $[C_k(t)]$ ne contient pas de terme explicite en t , c'est-à-dire si:

$$\frac{\partial}{\partial t} [C_k(t)] = 0,$$

la matrice $[C_{k\alpha} \dots C_{kr}]$ ne contient que des termes indépendants du temps, et $[C_k(t)]$ ne dépend du temps que par l'intermédiaire de $[\Delta E]$.

Le deuxième terme du second membre peut également s'exprimer par:

$$[C_{k\alpha} C_{k\beta} \dot{\alpha}_0 \dot{\beta}_0 C_{kp} \dot{p}_0 C_{kr}] [\Delta E']$$

avec,

$$[\Delta E'] = [\Delta \alpha \Delta \beta \Delta \dot{\alpha} \Delta \dot{\beta} \Delta p_a]^T$$

Les deux vecteurs $[\Delta E]$ et $[\Delta E']$ sont liés par la relation suivante, qui tient compte de l'expression de la matrice $[MP]$ et de son accroissement $\Delta[MP]$ à la suite de l'accroissement $[\Delta E]$, soit:

$$\begin{bmatrix} \Delta \alpha \\ \Delta \beta \\ \Delta \dot{\alpha} \\ \Delta \dot{\beta} \\ \Delta p_a \end{bmatrix} = \begin{bmatrix} 1 & 0 & 0 & 0 & 0 \\ 0 & 1 & 0 & 0 & 0 \\ 0 & -p_0 \cos \alpha_0 + r_0 \sin \alpha_0 \cos^2 \beta_0 & -\cos \alpha_0 \tan \beta_0 & 1 & -\sin \alpha_0 \tan \beta_0 \\ p_0 \cos \alpha_0 + r_0 \sin \alpha_0 & 0 & \sin \alpha_0 & 0 & -\cos \alpha_0 \\ 0 & 0 & \cos \alpha_0 \cos \beta_0 & \sin \beta_0 & \sin \alpha_0 \cos \beta_0 \end{bmatrix} \begin{bmatrix} \Delta \alpha \\ \Delta \beta \\ \Delta p \\ \Delta q \\ \Delta r \end{bmatrix}$$

La matrice $[C_{k\alpha} \dots C_{kpa}]$ est donc, dans le cadre des hypothèses admises, indépendante au temps et la connaissance de l'une des deux matrices facteur de $[\Delta E]$ ou $[\Delta E']$ suffit à définir l'autre.

Par ailleurs, il faut remarquer que sur les cinq grandeurs $\alpha_0, \beta_0, p_0, q_0, r_0$ trois d'entre elles seulement sont indépendantes, car elles sont reliées par:

$$\begin{bmatrix} p_0 \\ q_0 \\ r_0 \end{bmatrix} = p_{a0} \begin{bmatrix} \cos \alpha_0 \cos \beta_0 \\ \sin \beta_0 \\ \sin \alpha_0 \cos \beta_0 \end{bmatrix}$$

La présente analyse permet de tirer des conclusions applicables aux expériences de vrille et plus particulièrement aux mesures dynamométriques obtenues avec les balances en rotation uniforme d'axe parallèle à la direction de l'écoulement.

ainsi le vecteur $[C_k(\alpha_0, \beta_0, p_{a0})]$ peut être déterminé en recherchant les vecteurs $[\alpha_0 \beta_0 p_{a0}]^T$ définissant des régimes d'autorotation, exprimés par $C_{\ell a} = 0$, qui caractérise un moment nul autour de l'axe x_a .

De plus, si l'on impose un petit accroissement à un vecteur $[\alpha_0 \ \beta_0 \ p_{ao}]^T$ qui définit un régime d'autorotation donné, et si le vecteur $[C_k]$ est continu et dérivable, les mesures permettront de déterminer les trois premières colonnes de la matrice des dérivées partielles $[C_{k\alpha} \ C_{k\beta} \ C_{kp_a}]$. Les matrices correspondant à différents régimes d'autorotation ne sont pas a priori identiques entre elles, car $[C_k]$ ne varie pas nécessairement de façon linéaire en fonction de $[\alpha_0 \ \beta_0 \ p_{ao}]^T$.

Par ailleurs l'étude de la vrille nécessite aussi la connaissance des dérivées $C_{k\dot{\alpha}}$ et $C_{k\dot{\beta}}$; un moyen d'obtenir ces coefficients, proposé par TOBAK, consisterait à effectuer les mesures avec l'axe de rotation incliné sur la direction de l'écoulement. Les composantes de $\vec{\Omega}$ sur les axes-avion restent constantes pendant ce mouvement, alors que α et β varient périodiquement à chaque tour.

Cependant dans la pratique, les hypothèses restrictives émises par TOBAK et SCHIFF, qui sont vérifiées dans les cas de vrilles dites "peu agitées", ne sont plus admissibles lorsqu'il s'agit des vrilles des avions de combat modernes. Cette observation est mise en évidence sur la figure 4, tirée de la référence [10] qui reproduit les réponses des gyromètres obtenues au cours d'une évolution en vrille d'un tel avion. Elles montrent la présence d'oscillations, en assiette longitudinale et en angle de gîte, d'amplitude supérieure à ± 40 degrés. Le modèle quasi-linéaire qui vient d'être exposé ne suffit donc pas à leur étude, pour laquelle il conviendrait d'utiliser les méthodes non-linéaires présentées aux paragraphes 2 et 3, adaptées aux équations du mouvement dont les coefficients sont des matrices et les variables des vecteurs.

Les notations de ce paragraphe sont conformes aux recommandations I S O. La correspondance avec les notations de TOBAK et SCHIFF est indiquée en annexe.

5. - CONCLUSION.

Les quelques applications des méthodes de mécanique non-linéaire, publiées par différents auteurs au cours de ces dernières années, qui viennent d'être exposées, couvrent un vaste domaine aérodynamique allant des oscillations de tangage à un seul degré de liberté à des mouvements à six degrés de liberté aussi complexes que celui de la vrille.

Les hypothèses et les raisonnements suivis par les auteurs pour établir les expressions des torseurs aérodynamiques non-linéaires ont été rappelés de façon schématisée et simplifiée. Il a été montré comment ils expriment des non-linéarités discontinues des termes de rappel aérodynamique, qui traduisent des phénomènes d'hystérésis, et des non-linéarités continues des termes d'amortissement aérodynamique, causes d'instabilité dynamique par divergence ou tendance vers des cycles-limites.

Cependant, pour donner une vue d'ensemble des modes d'expression non linéaire, il faudrait compléter le présent exposé, limité aux mouvements "libres", par une représentation analogue des mouvements "forcés", dont on trouve de nombreux exemples dans l'aérodynamique des pales d'hélicoptère, des gouvernes d'avion et d'engin.

En outre, les applications pratiques de ces considérations théoriques au traitement des informations, recueillies en vol et en soufflerie, nécessiteraient au préalable la mise au point de méthodes permettant de caractériser de façon systématique la nature des non-linéarités présentes dans ces informations.

REFERENCES

- 1 X. VAUCHERET - Détermination des non-linéarités de stabilité dynamique.
Meeting AGARD FDP Dynamic Stability Parameters Athènes Mai 1978.
- 2 M. TOBAK & L.B.SCHIFF- The Role of Time History Effect in the Formulation of the
Aerodynamics of Aircraft Dynamics .
Meeting AGARD FDP Dynamic Stability Parameters Athènes Mai 1978.
- 3 W. CUNNINGHAM -Introduction to Nonlinear Analysis McGRAW-HILL, New-York 1958.
- 4 J. CH. GILLE P. DECAULNE M. PELEGRIEN - Systèmes asservis non-linéaires
Dunod Automatique Paris 1975.
- 5 M. BISMUT - La dynamique du vol ascendant des fusées sondes.
Progress in Aerospace Sciences N°12 p. 359 - 432 Pergamon Press 1972
et T.P. ONERA N° 1056 1972 .
- 6 K.J. ORLIK-RÜCKEMANN - 1) Survey of Needs and Capabilities for Wind Tunnel
Testing of Dynamic Stability of Aircraft at High Angles of Attack.
NASA C.R. II4583 1973 .
2) Dynamic Stability Testing of Aircraft Needs Versus
Capabilities. ICIASF Record p. 8-22. Ottawa 1975, and Progress in
Aerospace Sciences Vol. 16 N° 4 p.431-447 Pergamon Press 1975.
- 7 X. VAUCHERET - 1) Dépouillement d'oscillations libres d'un corps de rentrée
présentant un cycle limite.
La Recherche Aéronautique p.21 à 32 N° 104 1965.
2) Oscillations auto-entretenues d'un corps de rentrée .
La Recherche Aéronautique p. 25 à 32. 1- 1971.
et T.P.ONERA N° 917 1971.
3) Calcul des fonctions non linéaires de stabilité dynamique
d'un corps de rentrée de révolution .
La Recherche Aéronautique p. 155 à 159 3 - 1973.
et T.P.ONERA N° 1262 1973.
- 8 CH.H.MURPHY & J.W.BRADLEY - Non Linear Limit Motions of a Slightly Asymmetric
Re-entry Vehicle. AIAA Journal p.851 à 857 Vol. 13 July 1975.
- 9 M.TOBAC & L.B.SCHIFF- On the Formulation of the Aerodynamic Characteristics in
Aircraft Dynamics. Lecture Series 80 Aircraft Stability and Control
V.K.I. Rhodes St Genese Belgique Mai 1975.
- 10 C. LA BURTHE - Une nouvelle analyse de la vrille basée sur l'expérience française
sur les avions de combat. AGARD C.P. 199 p.15A-1 à 15A-9 1975.
et T.P. ONERA N° 143 1975.
- 11 Recommandations ISO - Symboles de la Mécanique du Vol.R 1151-1969,
R 1152-1974 R 1153-1972 etc. Publiées en versions anglaise et française.

Annexe

CORRESPONDANCE ENTRE LES SYMBOLES DE LA REFERENCE 9 & LES SYMBOLES
CONFORMES AUX RECOMMANDATIONS I S O.

SYMBOLES		
Référence [9] TOBAK & SCHIFF	I S O	
\hat{C}_k	C_k	coefficient sans dimension d'une composante du torseur aérodynamique sur les axes du trièdre avion; k désigne les symboles X Y Z l m n.
$x_B y_B z_B$	$x y z$	trièdre avion.
$x_B y z$	-----	trièdre "aérodynamique" dans lequel l'axe normal z est dans le plan défini par x_B et le vecteur vitesse-air. <u>à ne pas confondre avec le trièdre aérodynamique I S O rappelé à l'alinéa suivant.</u>
-----	$x_a y_a z_a$	trièdre aérodynamique dans lequel l'axe x est dirigé suivant le vecteur vitesse-air, l'axe z_a est situé dans le plan de symétrie et l'axe y_a normal au plan formé par les deux autres.
$\hat{\alpha}$	w/V	vitesse normale réduite. $\hat{\alpha} = \sin \alpha \cos \beta$.
$\hat{\beta}$	v/V	vitesse transversale réduite. $\hat{\beta} = \sin \beta$.
γ	u/V	vitesse axiale réduite. $\gamma = \cos \sigma = \cos \alpha \cos \beta$.
σ		angle du vecteur vitesse-air avec l'axe longitudinal avion x (angle xOx_a).
δ		projection du vecteur unitaire de la vitesse air sur le plan normal à l'axe longitudinal avion. $\delta = \sin \sigma = \sqrt{\sin^2 \beta + \cos^2 \beta \sin^2 \alpha}$
ϵ		$\epsilon = \delta / \gamma = \tan \sigma$.

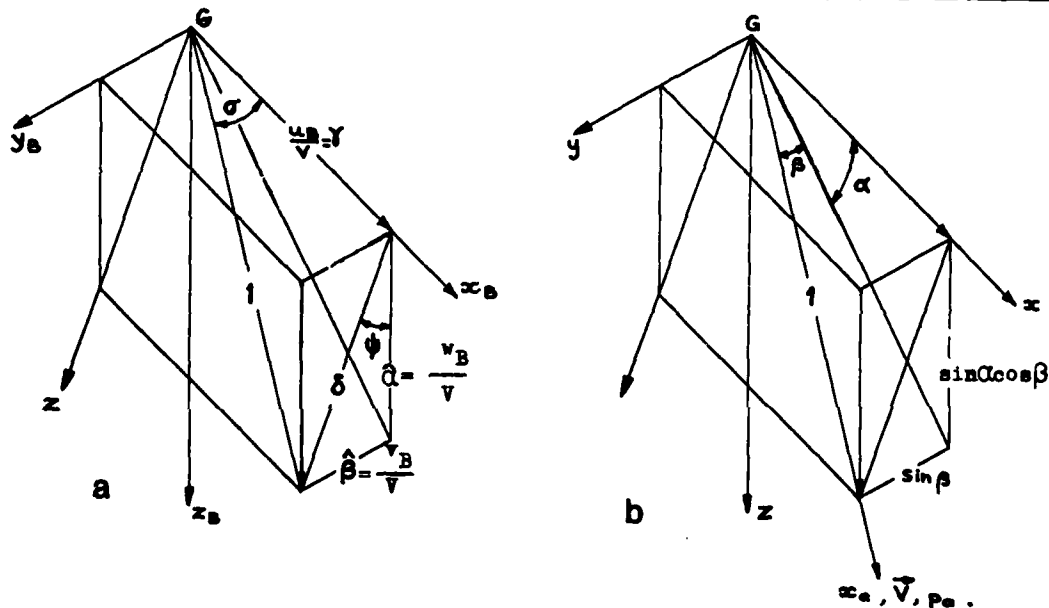


Fig. A

Correspondance entre les notations de TOBAK et SCHIFF (a) et celles des recommandations ISO (b).

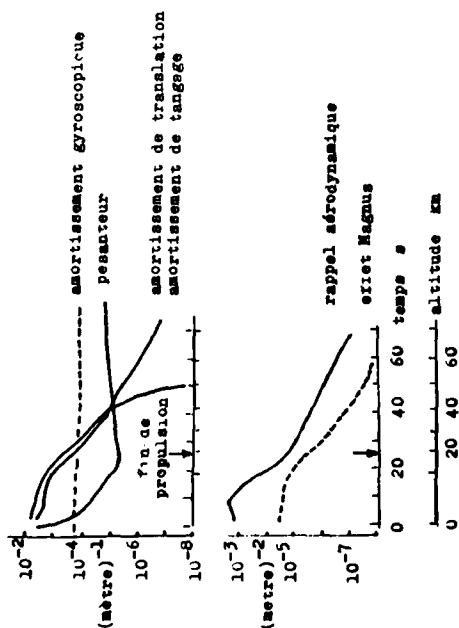


Fig. 1 Dérivées de stabilité d'une fusée sonde fonctions de l'altitude -
Origine référence [5] page 375.

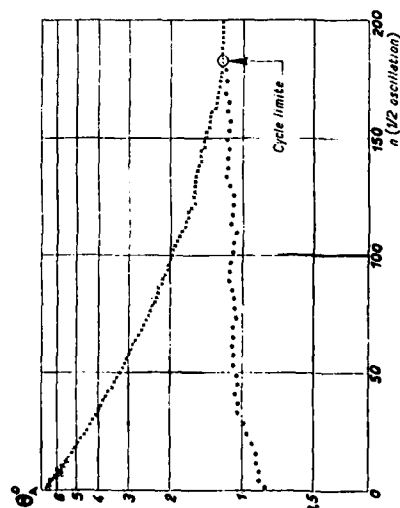


Fig. 2-1 Oscillations libres de tangage d'un corps de révolution à
jupe tronconique. Amplitude fonction du nombre de cycles. Origine
référence [7-1]

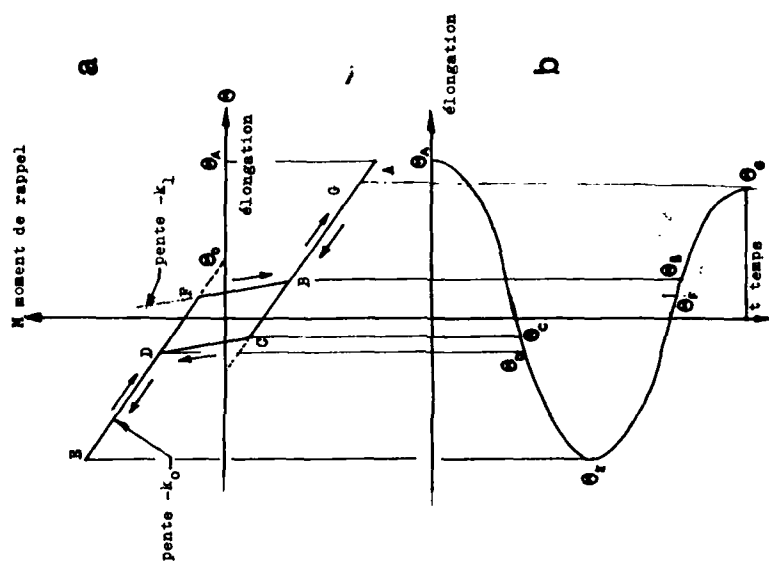


Fig. 2-2 a) Moment de rappel fonction de l'élongation
- discontinuités de pente avec hystérésis -
b) Elongation fonction du temps, d'après [7-1]

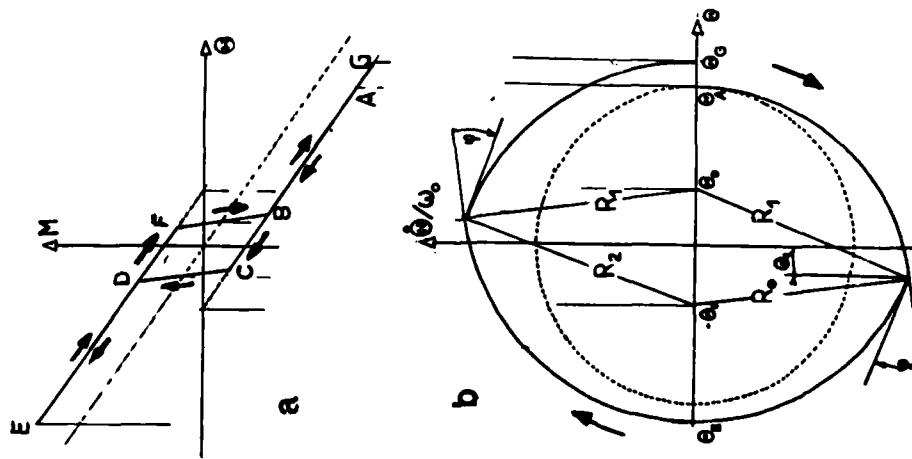
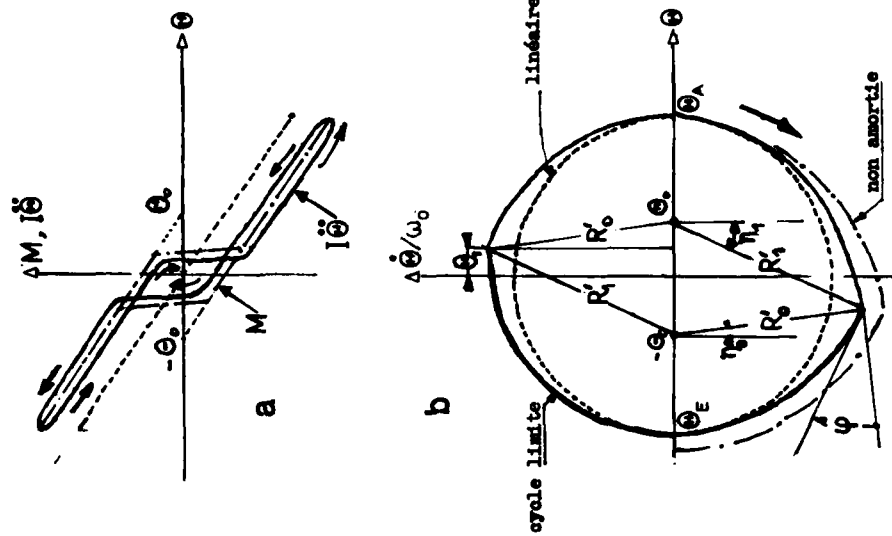


Figure 2-3

Oscillation non amortie ($\zeta = 0$) avec moment de rappel discontinu présentant de l'hystérésis.

- a) M , moment de rappel en fonction de l'élongation identique à figure 2-2
 b) Courbes du plan de phase : 1 - cas linéaire ; 2 - cas non linéaire discontinu ($\theta_0/\theta_A \geq 0,2$, sauts de phase φ), hystérésis ($\theta_1 \neq 0$).



Cycle limite de l'oscillation amortie ($\zeta > 0$) avec moment de rappel discontinu et hystérésis.

- a) Moment de rappel $M = -I\omega_j^2(\theta + \eta\theta_j)$ et moment des forces d'inertie $I\ddot{\theta} = -2\zeta\omega_j\dot{\theta}_j + M$ ($j = 0$ et $1, \eta = \text{sig}(\dot{\theta})$).
 b) Courbes du plan de phase, cas linéaire, non linéaire non amorti et amorti avec cycle limite ($\theta_A = |\theta_j|, \theta_0/\theta_A = 0,2$).

Figure 2-4

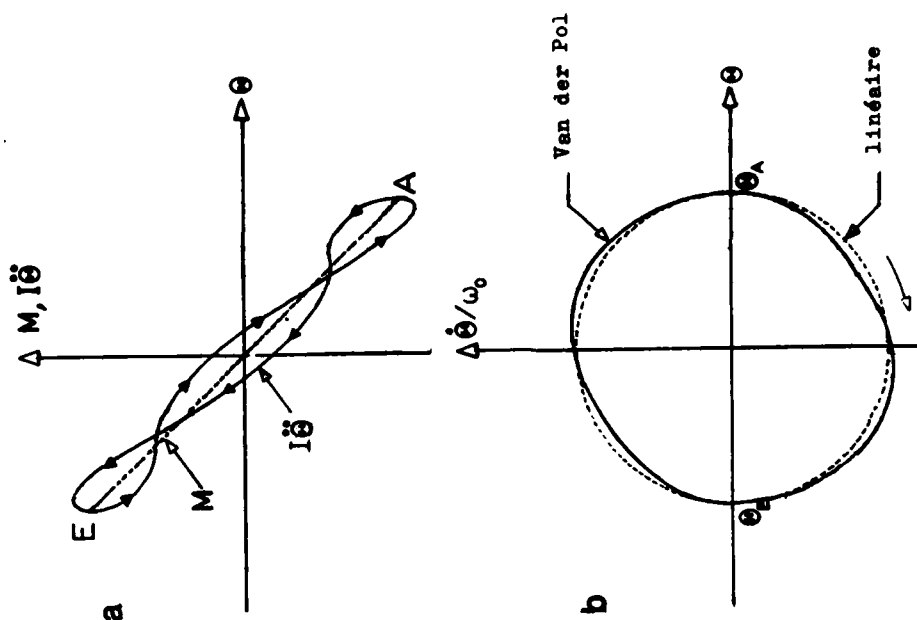


Figure 2-6

Cycle limite de l'oscillation régie par une équation de Van der Pol, $\theta_A = |\theta|$, amortissement $\zeta = -0,1$.
 a) Moment de rappel, $M = -I\omega_0^2 \theta$ et moment des forces d'inertie $I\ddot{\theta} = -2\zeta I\omega_0 \dot{\theta} - 4\theta^2/\theta_A^2 \dot{\theta} + M$
 b) Courbes du plan de phase, cas linéaire et cycle limite de Van der Pol.

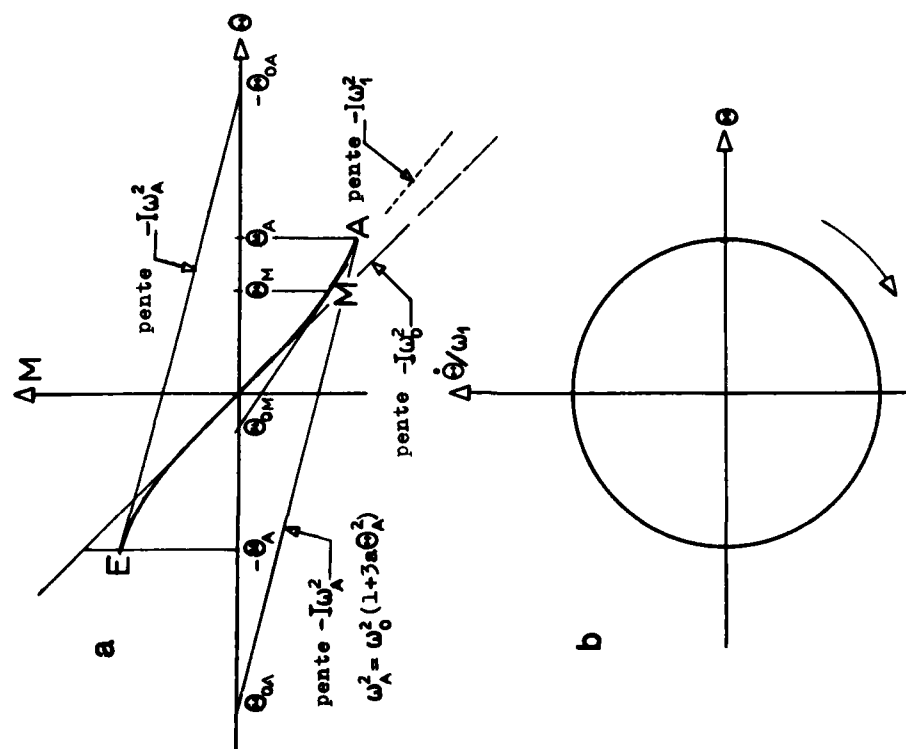


Figure 2-5

Oscillation non amortie ($\zeta = 0$) avec moment de rappel M non linéaire continu.
 a) $M = -I\omega_0^2 (\theta + a\theta^3)$, DUFFING type doux $a < 0$, sans hystérésis $\theta_1 = 0$;
 b) courbe du plan de phase, cas approximation linéaire.
 pulsation $\omega_1^2 = \omega_0^2 / (1 - \frac{3}{8}a\theta_A^2)$.

NONLINEAR OSCILLATIONS AT HIGH INCIDENCE

by

G. D. Padfield
Structures Department,
Royal Aircraft Establishment
Bedford, Bedfordshire, UK

SUMMARY

Of great importance in the study of aircraft motion is the derivation of simple functional relationships between the basic aerodynamic coefficients and the motion characteristics. Such relationships can lead to a better understanding of the underlying mechanisms producing the motion. When a flight behaviour prediction demands the use of nonlinear governing equations then the amplitude of the motion will appear as an additional parameter. Nonlinear problems in flight mechanics are not generally amenable to exact analytic techniques and there is therefore a requirement for the development of rational approximations. To some extent the perturbation method can meet these requirements and the paper outlines an approximate scheme for stability problems where the linear theory predicts that an aircraft is flying close to a stability boundary. The method of multiple scales is used to predict the transient oscillatory growth to a limit cycle condition. For the case of slender aircraft at high angles of incidence it is shown by example what effects can be expected on the lateral motions. Within the framework of the perturbation analysis it is shown how damping moments may be synthesised from response measurements.

LIST OF SYMBOLS

A	state matrix (Eq.1)	s	wing semi-span
A_0	amplitude function (Eq.46)	t	time (Eq.1)
B_{11}, B_{22}	sub-matrices (Fig 3)	v	sideslip velocity (Eq.A1)
C	transformation matrix	\underline{x}	state vector (Eq.1)
E, K	complete elliptic integrals (Eq.51)	y	displacement variable (Eq.38)
G, H	amplitude functions (Eq.40)	\underline{y}	transformed state vector
S	wing area	$\underline{y}_1, \underline{y}_2$	sub-vectors of \underline{y} (Eq.3)
U	eigenvector matrix (Eq.A7)	\underline{y}_{20}	periodic form of \underline{y}_2 (Eq.8)
R_2	nonlinear coefficient (Eq.28)	y_3, y_4	critical mode variables (Eq.25)
Y_{20}	principal matrix solution (Eq.19)	\underline{z}_2	equivalent to \underline{y}_2
a_0	amplitude (Eq.21)	\underline{z}_{2i}	i th order approximation for \underline{z}_2 (Eq.14)
$a_1, b_1, c_1, d_1, \dots$	coefficients in lateral equations of motion (Eq.A2, A5)	Δ	linear coefficient (Eq.29)
b_3, c_3, d_3		γ	$\frac{\partial v_2}{\partial n_{v_2}}$
$c(y)$	stiffness function (Eq.38)	γ_m	stiffness parameter (Eq.50)
c_1, c_3	stiffness coefficients (Eq.44)	ϵ	a small parameter (Eq.1)
e_x, e_z	$i_{xz}/i_{xx}, i_{xz}/i_{zz}$	η	periodic time scale (Eq.12)
\underline{g}	nonlinear vector function (Eq.1)	λ_1, λ_2	noncritical eigenvalues (Eq.5)
$h(y, \dot{y})$	damping function (Eq.38)	μ	damping (Eq.27)
h_0, h_2	damping coefficients (Eq.45)	μ_0	argument of elliptic functions (Eq.47)
$\underline{h}_1, \underline{h}_2$	noncritical and critical vector functions (Eq.3)	μ_2	relative density = $M/\rho S$
h_{21}, h_{22}	components of \underline{h}_2 (Eq.21)	v	system parameter (Eq.1)
i_{xx}, i_{zz}, i_{xz}	inertias normalised by $M s^2$	σ	sideslip function (Eq.30)
k	normalising coefficient (Eq.A6)	σ_0, σ_L	initial and limit value of σ (Eq.32, 34)
k_2	nonlinear damping parameter (Eq.50)	τ	slow time scale (Eq.13)
$\ell_v(v), n_v(v)$	rolling and yawing moment coefficients (Eq.23)	x, ψ	transient response functions (Eq.34)
ℓ_p, n_r etc	nondimensional aerodynamic derivatives (Eq.A2)	ψ_m	damping decrement function (Eq.49)
		ω_0, ω_1	critical frequency and correction (Eq.6, 12)

1. INTRODUCTION

The dynamic behaviour of a rigid aeroplane in flight is characterised by the interaction of the resultant aerodynamic, gravitational and inertial forces and moments acting on and about the vehicle's centre of gravity. A mathematical representation of these contributions can be linearised about a reference condition and the nature of free or stimulated small motion relative to this reference condition

determined by solving the linearised equations of motion. The results of the linear model will continue to provide the bulk of the information required on an aircraft's stability and control characteristics. However, there are a number of flight situations where the linear analysis fails to predict or explain aircraft behaviour because the linearisation is not appropriate. Such motions, including the stall, spin and spin entry, wing rocking and roll coupling, can generally be associated with the applied forces and moments involving a nonlinear dependence on the motion they generate and hence can only be fully explained by solving the resultant nonlinear equations of motion.

Now the nonlinear problems of flight mechanics are not generally amenable to exact analytic techniques and there is a requirement for the development of sound approximations that can be justified for a number of reasons. One important reason is that the range of validity of a linear theory can be readily established if a nonlinear theory is also available. Another is that an analytic approximation is more suitable for a parametric study of a problem than is a purely numerical solution. An analytic technique, which has probably found more application in the physical sciences than any other, is the small parameter perturbation method. The expansion scheme involved is based on an order of magnitude analysis and thus has an intrinsically rational flavour and allows improvements to be made systematically by including higher order successive approximations. The method is well suited to problems in which the nonlinearities are small so that the nonlinear problem can be treated as a perturbation of a linear problem.

This paper is concerned with the application of perturbation methods to stability problems where the linear theory predicts that the aircraft is flying close to a stability boundary where the stability characteristics are determined by the nonlinearities. The method is illustrated by the effect of aerodynamic nonlinearity on the sideslip oscillations of slender configurations at high incidence. Within the framework of the perturbation analysis it is also shown how damping moments may be estimated from response measurements on wind tunnel models.

2. MATHEMATICAL STATEMENT OF THE PROBLEM

The class of problems to be discussed are distinguished by the following characteristics.

A nonlinear autonomous system, the solution of which depends on parameters v and ϵ , is described by the matrix differential equation

$$\frac{dx}{dt} - A(v)x = \epsilon g(x, v; \epsilon) \quad (1)$$

where $x(t, v; \epsilon)$ is an n -vector containing the components of the state of the system, $A(v)$ is an $(n \times n)$ matrix and $g(x, v; \epsilon)$ is a nonlinear function of $x(t, v; \epsilon)$, continuous and analytic in x and satisfying the condition

$$\lim_{x \rightarrow 0} \frac{|g|}{|x|} = 0 \quad (2)$$

ϵ is a small parameter not necessarily having physical significance. For the application to lateral dynamics later in the paper, the vector x contains sideslip velocity, rates of roll and yaw and roll attitude. The matrix A contains the linear aerodynamic derivatives and v may be interpreted as angle of attack; the vector function g contains the nonlinear terms. Suppose that at some value of v , say v_f , the unique linear part of Eq.(1) when $\epsilon = 0$ exhibits a periodic solution, $x_f(t, v_f; 0)$. At this condition $A(v_f)$ is referred to as being critical. It is then appropriate to ask the following questions for $\epsilon \neq 0$.

- Q1 For small values of ϵ are there any periodic solutions of Eq.(1) that bifurcate or branch off the linear solution x_f and if so how do we approach determining these solution curves and ones nearby?
- Q2 How is the geometry of the state space modified close to the equilibrium point $x(t, v; \epsilon) = 0$?

As will be shown the answer to Q2 is closely connected with the stability characteristics of the periodic solutions of Eq.(1) when $\epsilon \neq 0$. Using a perturbation method we can develop quantitative answers to these questions in an approximate form.

The condition that $A(v)$ is critical is crucial to the resolution of these questions. Any attempt to generate an approximate solution of Eq.(1) at $v = v_f$ via a straightforward asymptotic expansion in powers of ϵ will fail due to the presence of secular terms in the higher order approximations. These unbounded terms can be corrected for in the search for *periodic* solutions by noting that the frequency of the solution depends on the amplitude and thus requires an asymptotic expansion itself. It is in the elimination of the secular terms that we obtain the conditions necessary for periodic solutions to exist. Before proceeding to answer Q1 and Q2 in detail it is pertinent to pose a further question at this stage.

- Q3 Can we continue a solution, obtained for $\epsilon \neq 0$ as a function of v for small variations in about $v = v_f$ so as to include the regions in which the linear approximation predicts asymptotic stability and instability.

The answer to this question would indicate whether the instability is mild (stability boundary safe) or catastrophic (stability boundary dangerous) and will be sought after by transforming Eq.(1) into an equivalent system.

With regard to the stability properties of Eq.(1) it is known that at the critical condition the terms in $g(x, v; \epsilon)$ become important. Assuming that we can expand $g(x)$ as a Taylor series in x about $x = 0$, then a useful definition of stability in critical cases relates to the stability in the N th approximation. Here, N is the degree to which terms in $g(x)$ have been retained. Much of the work on the stability of these critical cases has been formulated by Malkin¹, and the theorems developed are applicable

to systems in which the stability properties in the N th approximation can be determined from the stability properties of a reduced form of Eq.(1) in which only the critical variables appear.

The analysis will be developed for a fourth order system with matrix $A(v)$ having distinct eigenvalues. By a suitable transformation of co-ordinates, $\underline{x} = C\underline{y}$, Eq.(1) can always be written in the decomposed form.

$$\frac{d\underline{y}_1}{dt} - B_{11}\underline{y}_1 = \epsilon \underline{h}_1(\underline{y}_1, \underline{y}_2; \epsilon) \quad (3)$$

$$\frac{d\underline{y}_2}{dt} - B_{22}\underline{y}_2 = \epsilon \underline{h}_2(\underline{y}_1, \underline{y}_2; \epsilon) \quad (4)$$

where $\underline{y}_1(t; \epsilon)$ and $\underline{y}_2(t; \epsilon)$ are the two-dimensional sub-vectors of $\underline{y}(t; \epsilon)$ composed of the non-critical and critical variables respectively, such that,

$$B_{11} = \begin{bmatrix} 0 & 1 \\ -\lambda_1 \lambda_2 & \lambda_1 + \lambda_2 \end{bmatrix} \quad (5)$$

$$B_{22} = \begin{bmatrix} 0 & 1 \\ -\omega_0^2 & 0 \end{bmatrix} \quad (6)$$

Here λ_1 and λ_2 are the eigenvalues of A with negative real parts and $\pm i\omega_0$ are the purely imaginary eigenvalues of A when $v = v_f$. It is assumed at the outset that $\operatorname{Re}(\lambda_1)$ and $\operatorname{Re}(\lambda_2)$ are negative so that, when $\epsilon = 0$, the equilibrium of Eq.(1) is asymptotically stable in the first approximation. The periodic solutions of Eq.(3) and Eq.(4) when $\epsilon = 0$ are therefore restricted to the sub-vector $\underline{y}_2(t; 0)$ i.e.

$$\underline{y}_1(t) = 0 \quad (7)$$

$$\underline{y}_2(t) = \underline{y}_{20}(t) \quad (8)$$

When $\epsilon \neq 0$, a family of periodic solutions bifurcate off the zeroth order solution given by Eqs.(7) and (8) and we need to determine the particular member of \underline{y}_{20} , i.e. the associated amplitude and frequency, appropriate to the function $\underline{h}_2(0, \underline{y}_2; \epsilon)$. Hence, for small ϵ , the problem reduces to one in two dimensions. For this approximation to be valid it is perhaps clear that there should be more restrictive conditions on the non-critical vector \underline{h}_1 . In Ref 1, it is shown that the abbreviated system given by Eq.(4) with $\underline{y}_1(t)$ set to zero will reproduce the stability nature of the equilibrium of the complete system in the N th approximation if the resolution of the function $\underline{h}_1(0, \underline{y}_2; \epsilon)$ begins with terms of order greater than N . If this is not the case then a suitable transformation of \underline{y}_1 should be devised to eliminate terms in \underline{y}_2 of order $\leq N$.

With the above condition assumed to hold, the reduced system takes the form,

$$\frac{d\underline{y}_2}{dt} - B_{22}\underline{y}_2 = \epsilon \underline{h}_2(0, \underline{y}_2; 0) \quad (9)$$

It has already been noted that a straightforward expansion of $\underline{y}_2(t; \epsilon)$ in powers of ϵ would lead to nonuniformities in the higher order expansions due to the presence of secular terms. These nonuniformities can be eliminated for periodic solutions by expanding the unknown frequency in powers of ϵ and this is conveniently achieved by introducing a new time scale for which the period is 2π . Expanding Eq.(9) in powers of ϵ and equating like orders of ϵ leads to a system of perturbation equations. The amplitude and frequency correction for the m th order approximation can then be obtained by eliminating the secular or resonance terms in the $(m+1)$ th order equation.

The above procedure will yield a family of limit cycles in the restricted phase plane and will go a long way in providing answers to our previous questions Q1 and Q2. We would like to go one step further here and determine the behaviour of nearby trajectories or the actual transient growth or decay to or from the limit cycle. In tackling this initial value problem we employ a technique known as the method of multiple scales. The rationale of the method is discussed in Ref 2 but the important assumption we make for the present problem is that for slowly varying oscillations the amplitude and frequency depend explicitly on the slow time ϵt . By imbedding the scale ϵt in the problem of determining periodic solutions it will be possible to approximate the slow transient response.

We therefore re-define the function $\underline{y}_2(t; \epsilon)$ as a function of two time scales η and τ ,

$$\underline{y}_2(t; \epsilon) \equiv \underline{z}_2(\eta, \tau; \epsilon) \quad (10)$$

so that

$$\frac{d}{dt} = \frac{d\eta}{dt} \left(\frac{\partial}{\partial \eta} \right) + \epsilon \frac{\partial}{\partial \tau} + O(\epsilon^2) \quad (11)$$

where we write

$$\frac{d\eta}{dt} = \omega_0(\tau) + \epsilon \omega_1(\tau) + O(\epsilon^2) \quad (12)$$

and

$$\tau = \epsilon t + O(\epsilon^2) \quad (13)$$

In Eq.(10) the variables η and τ are to be regarded formally as independent so that Eq.(11) becomes a partial differential operator. We are now in a position to expand the new function $z_2(\eta, \tau; \epsilon)$ as an asymptotic expansion in powers of ϵ , i.e.

$$z_2 \equiv z_2(\eta, \tau; \epsilon) = z_{20}(\eta, \tau) + \epsilon z_{21}(\eta, \tau) + O(\epsilon^2). \quad (14)$$

Substituting Eq.(14) into Eq.(9), using Eqs.(11) and (12), and equating equal powers of ϵ we obtain the zeroth and first order perturbation equations

$$O(1) \quad \frac{\partial z_{20}}{\partial \eta} - B_{22}^* z_{20} = 0 \quad (15)$$

$$O(\epsilon) \quad \frac{\partial z_{21}}{\partial \eta} - B_{22}^* z_{21} = -\frac{1}{\omega_0} \left\{ \omega_1 \frac{\partial z_{20}}{\partial \eta} + \frac{\partial z_{20}}{\partial \tau} - h_2(0, z_{20}; 0) \right\} \quad (16)$$

where

$$B_{22}^* = \begin{bmatrix} 0 & \frac{1}{\omega_0} \\ -\omega_0 & 0 \end{bmatrix}. \quad (17)$$

The zeroth order approximation is given by

$$z_{20}(\eta, \tau) = Y_{20}(\eta) a_{20}(\tau) \quad (18)$$

where the principal matrix solution $Y_{20}(\eta)$ is given by

$$Y_{20}(\eta) = \begin{bmatrix} \cos \eta & \sin \eta \\ -\omega_0 \sin \eta & \omega_0 \cos \eta \end{bmatrix}. \quad (19)$$

Without loss of generality we can set the second component in a_{20} to zero and denote the first element by $a_0(\tau)$. Invoking the periodicity condition for Eq.(16), i.e. that the right side should contain no resonance terms, leads to the bifurcation equations for determining $a_0(\tau)$ and $\omega_1(\tau)$. The periodicity condition requires that the right side of Eq.(16) be orthogonal to the two periodic solutions of the adjoint homogeneous form of Eq.(16), i.e.

$$\int_0^{2\pi} Y_{20}^{-1}(\eta) \left\{ \omega_1 \frac{\partial z_{20}}{\partial \eta} + \frac{\partial z_{20}}{\partial \tau} - h_2(0, z_{20}; 0) \right\} d\eta = 0. \quad (20)$$

If we denote the upper and lower components of h_2 by h_{21} and h_{22} respectively then, after some reduction, the bifurcation equations take the scalar form

$$\frac{da_0}{d\tau} = -\frac{1}{2\pi\omega_0} \int_0^{2\pi} (h_{22} \sin \eta - \omega_0 h_{21} \cos \eta) d\eta \quad (21)$$

$$\omega_1(\tau) = -\frac{1}{2\pi\omega_0 a_0} \int_0^{2\pi} (h_{22} \cos \eta + \omega_0 h_{21} \sin \eta) d\eta. \quad (22)$$

3. THE PHYSICAL PROBLEM - NONLINEAR SIDESLIP OSCILLATIONS AT HIGH INCIDENCE

A feature of the lateral motion of inertially slender aircraft is the possible marked reduction in the damping of the oscillatory mode that occurs as the flight angle of incidence is increased. At high enough incidence this mode can become dynamically unstable and we can expect that, in the vicinity of this critical condition, large excursions in the mode can take place. Generally speaking, we would like to know whether the stability boundary is safe, in the sense that motions will be self limiting, or dangerous where the instability persists with growing amplitude. We also require to know how stable is flight at angles of incidence lower than the critical value since a large enough disturbance may cause a divergent motion to develop. A linear theory is clearly inadequate in this respect and hence we need to consider any nonlinear effects that exist.

Results of the linear theory do, however, shed light on the basic small perturbation motions as shown in Figs 1 to 4. The basic data for these configurations is given in Table 1. The two aircraft considered are slender deltas and both exhibit an oscillatory instability at high incidence. The instabilities are somewhat different in origin however with the BAC 221 exhibiting a bursting of the concentrated vortex flow over the leeward wing surface along with a change in sign of n_v within the incidence range considered. The HP 115 characteristics, on the other hand, can be attributed to a uniform degradation, with angle of incidence, of the damping in the mainly rolling oscillation. Both of these oscillatory modes involve a substantial amount of sideslip motion and it is to be expected that any nonlinearity of the rolling and yawing moments with sideslip will have a significant effect on the oscillations. Data sources for these aircraft^{3,4} reveal such nonlinearities and these can probably be attributed to the changing strength and positions of the vortices over the wing and those springing from the forebody.

To simplify the analysis we shall neglect additional nonlinearities present either of aerodynamic (incidence angle and roll rate) or kinematic (roll angle) origins and assume that the rolling and yawing moments are asymmetric functions of sideslip velocity. Hence, a cubic variation takes the form

$$C_n(v) = (n_{v_0} + n_{v_2} v^2) v \quad (23)$$

$$C_\ell(v) = (\ell_{v_0} + \ell_{v_2} v^2) v \quad (24)$$

Including these terms in the lateral equations of motion as described in Appendix 1 and applying the reducing transformation leads to a critical mode (at $\omega = \omega_f$) described by Eq.(9) where, in terms of the critical variables, we have

$$y_3 = -\omega_0^2 v, \quad y_4 = -\omega_0^2 v \quad (25)$$

To investigate the behaviour of trajectories close to the stability boundary we will assume that the eigenvalue pair λ_3, λ_4 have a small real part μ of $O(\epsilon)$, corresponding to the computed linear damping when $\alpha \neq \alpha_f$. Combining this term with the nonlinearities, the right hand side of Eq.(9) takes the form

$$h_2(0, y_2; 0) = \begin{bmatrix} 0 \\ 2\mu y_4 \end{bmatrix} + \begin{bmatrix} -(\lambda_1 + \lambda_2) \\ \omega_0^2 - \lambda_1 \lambda_2 \end{bmatrix} \left(\frac{3c_3 y_3^2 y_4 + 6b_3 y_3 y_4^2 + (d_3 - 3\omega_0^2 b_3) y_3^3}{\omega_0^4 (\omega_0^2 (\lambda_1 + \lambda_2)^2 + (\omega_0^2 - \lambda_1 \lambda_2)^2)} y_3 \right) \quad (26)$$

The transient characteristic is defined by Eq.(21) which takes the expanded form

$$\frac{da_0}{dt} = \frac{1}{2} \left\{ 2\mu - \frac{3}{4} \frac{R_2}{\Delta \omega_0} a_0^2 \right\} a_0 \quad (27)$$

where

$$R_2 = - \left((\lambda_1 + \lambda_2) \omega_0^2 b_3 - (\lambda_1 \lambda_2 - \omega_0^2) c_3 - (\lambda_1 + \lambda_2) d_3 \right) \quad (28)$$

and

$$\Delta = \omega_0^2 (\lambda_1 + \lambda_2)^2 + (\omega_0^2 - \lambda_1 \lambda_2)^2 \quad (29)$$

The solution to Eq.(27) is readily obtained and it is useful to express the result for the sideslip envelope, $v_e(\tau)$, using Eq.(25). We define new variables σ and γ as

$$\sigma = \frac{3}{4} n_{v_2} v_e^2; \quad \gamma = \ell_{v_2} / n_{v_2} \quad (30)$$

Equation (28) may then be written in the concise form

$$R_2 = (\ell_1 + \ell_2 \gamma) n_{v_2} \quad (31)$$

where ℓ_1 and ℓ_2 are functions of the eigenvalues.

The solution for Eq.(27) can be written in terms of σ as

$$(\sigma/\sigma_L) = \frac{(\sigma_0/\sigma_L) e^{2\mu\tau}}{(1 - (\sigma_0/\sigma_L)(1 - e^{2\mu\tau}))} \quad (32)$$

Or, more simply, in the form

$$\psi = \chi / (1 + \chi) \quad (33)$$

where

$$\psi = (\sigma/\sigma_L) \quad \text{and} \quad \chi = \frac{(\sigma_0/\sigma_L) e^{2\mu\tau}}{1 - (\sigma_0/\sigma_L)} \quad (34)$$

σ_0 is the initial and σ_L the limit cycle value of σ given by

$$\sigma_L = 2\mu \Delta / \ell_1 + \ell_2 \gamma \quad (35)$$

The function defined by Eq.(33) tells the whole story for the isolated critical mode and is shown plotted in Fig 5. It can be seen that there exist six possible envelopes illustrated by the sketches A to F. The parameter ranges appropriate to these sketches are shown in Table 2.

To summarise the table we note that limit cycles are possible above (A,F) and below (E,B) the critical condition whereas for the other two ranges (C,D) limit cycles are absent. The effect of the nonlinear moment terms can be stabilising or destabilising depending on the damping μ .

For the two slender configurations referred to earlier the effects are somewhat different. Figs 6 and 7 illustrate the limit cycle amplitude variation with angle of incidence for the HP 115 and BAC 221 respectively. In general limit cycles above the critical incidence are stable while those below the critical incidence are unstable since the stability characteristics of the equilibrium or trim state away from critical are not affected by the nonlinearities. The stability boundary is safe if the motion is limited above the critical incidence and dangerous if limit cycles exist below the critical incidence. Table 3 summarises the situation for the two aircraft.

We can see from Table 3 that, generally speaking, the parameter λ_{v_2} has an opposite effect for the two aircraft. For example, when $n_{v_2} > 0$, a positive λ_{v_2} can be described as stabilising for the HP 115 and destabilising for the BAC 221. The situation is reversed for $n_{v_2} < 0$. Referring back to Figs 3 and 4 we can see that for the HP 115 the mode that becomes unstable is the classical rolling oscillation whereas for the BAC 221 a mode that has formed from the union of the more conventional spiral and roll subsidence eventually goes unstable. For more conventional configurations a large negative λ_v improves spiral stability but is detrimental to Dutch roll damping. It is, perhaps, too simple-minded to extrapolate the result to the new situation but the analogy is apparent. The curious situation above is further reflected in the linear theory through the variation of the oscillatory stability boundary with λ_v and n_v , shown in Fig 8. For the HP 115 the decreasing damping, rotating the boundary to the right, and the increasing negative λ_v gave rise to the crossing. For the BAC 221 the opposite occurs but it is the large change in n_v that has the main effect.

The connection between the Routhian variation and the nonlinear results is more than qualitative. If one had started with the fourth order, nonlinear equation in sideslip velocity, assumed a periodic solution, and carried out a harmonic balance the result obtained would read³

$$a_1 \left(b_1 + \frac{3}{4} b_3 v_L^2 \right) \left(c_1 + \frac{3}{4} c_3 v_L^2 \right) - \left(c_1 + \frac{3}{4} c_3 v_L^2 \right)^2 - a_1^2 \left(d_1 + \frac{3}{4} d_3 v_L^2 \right) = 0 \quad (36)$$

The result given by Eq.(34) can be shown to be formed from the $O(\epsilon)$ terms in Eq.(36) and the implication is that the limit cycle amplitude can be obtained by measuring the distance that the point (λ_v, n_v) is offset from the appropriate Routhian boundary. In order to obtain the full result given by Eq.(36) it would be necessary to include the coupling effects of the non-critical mode given by Eq.(3). The procedure is discussed in detail in Ref 1 and involves introducing a transformation in Eq.(3) of the form

$$y_1 = u + f_1(y_2) \quad (37)$$

Substituting Eq.(37) into Eq.(3) and collecting forms of equal order in y_2 the function $f_1(y_2)$ can be built up. For the present problem f_1 begins with terms of third order and hence when these are included in the critical mode, Eq.(4), the additional terms begin with fifth order forms. These terms will affect the stability characteristics of the critical mode when the lower order nonlinearities vanish on the stability boundary ($R_2 = 0$) and in this case the present approximation breaks down.

Restricting the nonlinearity to a single variable, the sideslip velocity, has resulted in a great simplification of the problem and allowed the companion form solution to be developed. In practice a departing aircraft will develop large excursions in incidence as well as sideslip and the motion can build up to the point where inertial and aerodynamic nonlinearities due to high angular rates are significant. For the initial phase of such departures when the flight speed changes are small it is probably sufficient to include the coupling from the short period longitudinal mode. The non-critical system will then be of fourth order and the reduction transformation referred to above will inevitably be cumbersome. A numerical treatment of this aspect would be time saving and the method of solution would still be more suitable for parametric studies than a wholly numerical method.

Having approximately defined the critical mode for a particular configuration an oscillation rig that produced a similar motion, could be constructed for testing a model in a wind tunnel. Estimates of the damping close to the critical condition could then be made and we now outline a method for achieving their estimation.

4. DAMPING ESTIMATES FOR SINGLE MODE MOTION

In this section a method is proposed whereby the damping coefficients, appropriate to a mathematical model of the motion of a wind tunnel model, can be estimated from measurements of the logarithmic decrement of the oscillation records. This is achieved by matching the measurements to an approximate functional relationship between the damping decrement and the oscillation amplitude envelope which is derived, in turn, from an approximate analytic solution of the describing equation. The method is described in detail in Ref 6 and a similar technique is developed by Rasmussen⁷.

We assume that the adopted mathematical model can be described by the differential equation

$$\ddot{y} + c(y) + \epsilon h(y, \dot{y}; \epsilon) = 0 \quad (38)$$

$c(y)$ is a general nonlinear function of y and $h(y, \dot{y}; \epsilon)$, the damping function, which could include higher derivatives with respect to time t . When $\epsilon = 0$, we assume that Eq.(38) admits a known periodic solution. Using the two time scale method to expand y as an asymptotic series in ϵ we find that the bifurcation equation for the zeroth order approximation can be written in the form

$$\frac{\partial G(A_0)}{\partial \tau} + H(A_0) = 0 \quad (39)$$

where

$$G(A_0) = \int_0^{T_{11}} \omega_0 \left(\frac{\partial y_0}{\partial \eta} \right)^2 d\eta$$

$$H(A_0) = \int_0^{T_{11}} h \left(y_0, \omega_0 \frac{\partial y_0}{\partial \eta}; 0 \right) \frac{\partial y_0}{\partial \eta} d\eta \quad (40)$$

and

$$\frac{d\eta}{dt} = \omega_0 + \epsilon \omega_1, \quad \tau = \epsilon t. \quad (41)$$

$A_0(\tau)$ is the amplitude function defining the envelope of the oscillation, T_{11} is the period in η and $y_0(\eta, \tau)$ is the zeroth order approximation to Eq.(38), satisfying the equation

$$\omega_0^2 \frac{\partial^2 y_0}{\partial \eta^2} + c(y_0) = 0. \quad (42)$$

From Eq.(39) we can derive an $O(\epsilon)$ approximation for the damping decrement between adjacent maxima, y_n and y_{n+1} . After some reduction Eq.(39) can be written as

$$\log_e \left| \frac{y_{n+1}}{y_n} \right| c(y_m) y_m = -\epsilon H(y_m) \quad (43)$$

where $y_m^2 = (y_{n+1}^2 + y_n^2)/2$.

Eq.(43) can be used, in conjunction with a least squares method, to estimate the form of the damping function. A good illustration is provided by the example where $c(y)$ is a strongly nonlinear cubic function and $h(y, \dot{y})$ is a quadratic amplitude dependent damping function.

$$c(y) = c_1 y + c_3 y^3 \quad (44)$$

$$h(y, \dot{y}) = (h_0 + h_2 y^2) \dot{y}. \quad (45)$$

The exact solution for the zeroth order approximation, Eq.(42), can be written in terms of Jacobian elliptic functions. For the case of a hardening restoring force ($c_1 > 0, c_3 > 0$) we have that

$$y_0(\eta, \tau) = A_0(\tau) C_n(\eta, \mu_0(\tau)) \quad (46)$$

with

$$\omega_0^2 = c_1 + c_3 A_0^2; \quad \mu_0^2 = \frac{\frac{1}{2} c_3 A_0^2}{c_1 + c_3 A_0^2}. \quad (47)$$

The asymptotic approximation for the logarithmic decrement can be written as

$$2 \log_e \left| \frac{y_{n+1}}{y_n} \right| \frac{c_1^{\frac{1}{2}}}{\pi} = -\epsilon h_0 \psi_m + O(\epsilon^2) \quad (48)$$

where

$$\psi_m = \frac{8(1 + \gamma_m)^{\frac{1}{2}}}{3\gamma_m \pi} \left\{ L_0 + \frac{8}{5} k_2 (1 + \gamma_m) L_2 \right\} \quad (49)$$

$$\gamma_m = \frac{c_3}{c_1} y_m^2, \quad k_2 = \frac{h_2}{4h_0} \left| \frac{c_1}{c_3} \right| \quad (50)$$

and

$$L_0 = (2\mu_0^2 - 1)E(\mu_0) + (1 - \mu_0^2)K(\mu_0)$$

$$L_2 = (1 - \mu_0^2)(\mu_0^2 - 2)K(\mu_0) + 2(\mu_0^4 + 1 - \mu_0^2)E(\mu_0). \quad (51)$$

$K(\mu_0)$ and $E(\mu_0)$ are complete elliptic integrals of the first and second kind respectively. The function ψ_m is shown plotted against $\gamma_m^{\frac{1}{2}}$ in Fig 9. The occurrence of a zero damping decrement implies the existence of a periodic approximate solution and this can be interpreted here as a limit cycle oscillation. A similar set of curves can be obtained for the two other cases, ($c_1 > 0, c_3 < 0$) and ($c_1 < 0, c_3 > 0$) and are shown in Figs 10 to 12 along with typical phase plane portraits⁶. Least squares estimates of the damping coefficients can be obtained from the measurements of the damping decrement using Eq.(48). Results obtained from measurements of numerically integrated equations of this form are accurate to within a few percent⁶; typical results are shown in Table 4 and Fig 13.

5. GENERAL DISCUSSION AND CONCLUSIONS

Approximations have been developed for free aircraft motion when nonlinear effects are present and when the aircraft is flying close to a stability boundary. The analysis is based on the behaviour of the isolated critical mode. Results for the lateral motion of slender aircraft with nonlinear aerodynamic

moments have revealed an interesting situation where limit cycles are possible above and below the critical incidence. Aircraft motions can therefore be 'practically' stable when the linear theory predicts instability and 'practically' unstable when stability is predicted. For the two aircraft considered the nonlinear rolling moment was seen to produce opposite effects. It could be speculated that the two distinct types of behaviour represent the limiting cases when vortex breakdown is present, as for the BAC 221, or absent as for the HP 115. In flight it was found that the BAC 221 became unstable at a lower angle of incidence than the natural critical value when the pilot constrained bank angle with aileron. The instability took the form of a divergence and occurred when the LCDP vanished⁸. The present technique can also be applied to this situation with the critical mode having zero frequency on the divergence boundary.

The most important feature inherent in the perturbation method is the assumption of small damping in the critical mode. For larger values of the damping the accuracy can be improved by including higher order approximations but these should not destroy the basic stability characteristic predicted by the zeroth order approximation if the conditions on the non-critical mode are met. The analysis becomes very lengthy and it may be more appropriate for flight situations well away from a stability boundary to resort to the less analytic averaging methods such as the algorithm proposed recently by Simpson⁹.

The technique proposed in section 4 synthesises weak nonlinear damping moments from oscillatory tests of single mode motion. The method can cope with strong nonlinear static moments and is therefore well suited to large amplitude tests. Oscillations based on Jacobian elliptic functions show encouraging results.

6. REFERENCES

- 1 I.G. Malkin, Theory of stability of motion. United States Atomic Energy Commission (translation series). AEC - TR 3352
- 2 A.H. Nayfeh, Perturbation methods. John Wiley (1973)
- 3 P.L. Bisgood, R.L. Poulter, Flight measurements of the lateral stability and control characteristics of a slender wing research aircraft (HP 115) and comparison with wind tunnel results. RAE Technical Report 72186 (1972)
- 4 D.M. Holford, Aerodynamic data for the BAC 221 up to a Mach number of 0.955 as measured in wind tunnel tests. ARC CP No.1230 (1972)
- 5 A. Jean Ross, L.J. Beecham, An approximate analysis of the nonlinear lateral motion of a slender aircraft (HP 115) at low speeds. ARC R & M No.3674 (1971)
- 6 G.D. Padfield, The application of perturbation methods to nonlinear problems in flight mechanics. PhD Thesis. Cranfield Institute of Technology (1976)
- 7 M.L. Rasmussen, On the damping decrement for nonlinear oscillations. Int J Nonlinear Mechanics, Vol 12, pp 81-90 (1977)
- 8 R.D. Milne, G.D. Padfield, The strongly controlled aircraft. Aeronautical Quarterly, pp 146-168, May 1971
- 9 A. Simpson, An algorithm for autonomous nonlinear dynamical equations. Aeronautical Quarterly, pp 211-234, August 1977.

7. ACKNOWLEDGMENTS

The present work was carried out while the author was working in the Aerodynamics Division at Cranfield Institute of Technology where the financial support was provided by the Science Research Council. For countless fruitful discussions on nonlinear problems the author is grateful to Professor Maurice Rasmussen of the University of Oklahoma.

Copyright
©

Controller HMSO London
1978

Table 1
BASIC AIRCRAFT DATA

Relative density	HP 115	BAC 221
μ_2	20.0	83.27
i_{xx}	0.109	0.106
i_{zz}	1.27	0.634
i_{xz}	0.0806	0.0
s	3.05 m	3.84 m
S	40.18 m ²	45.5 m ²

Table 2
PARAMETER RANGES FOR THE ENVELOPES A-F IN FIG 5

$\mu < 0$	$(\sigma_0/\sigma_L) > 0$,	(a) $(\sigma_0/\sigma_L) < 1$	E
		(b) $(\sigma_0/\sigma_L) > 1$	B
$\mu < 0$	$(\sigma_0/\sigma_L) < 0$		C
$\mu > 0$	$(\sigma_0/\sigma_L) > 0$,	(a) $(\sigma_0/\sigma_L) < 1$	F
		(b) $(\sigma_0/\sigma_L) > 1$	A
$\mu > 0$	$(\sigma_0/\sigma_L) < 0$		D

Table 3

	HP 115	BAC 221
Stability boundary safe	$n_{v_2} > 0$ $\ell_{v_2} > 0$	$n_{v_2} > 0$ $\ell_{v_2} < 0$
	limited $\ell_{v_2} < 0$	limited $\ell_{v_2} > 0$
	$n_{v_2} < 0$ most $\ell_{v_2} > 0$	$n_{v_2} < 0$ most $\ell_{v_2} < 0$
Stability boundary dangerous	$n_{v_2} > 0$ most $\ell_{v_2} < 0$	$n_{v_2} > 0$ most $\ell_{v_2} > 0$
	$n_{v_2} < 0$ $\ell_{v_2} < 0$	$n_{v_2} < 0$ $\ell_{v_2} > 0$
	limited $\ell_{v_2} > 0$	limited $\ell_{v_2} < 0$

Table 4
(a) PARAMETER VALUES FOR OSCILLATORY
SOLUTIONS OF (38)

Case	(i)	(ii)	(iii)	(iv)
c_1	1.0	1.0	-1.0	-1.0
c_3	10.0	-2.0	10.0	2.0
h_0	-0.5	-0.5	-0.5	-0.5
h_2	2.0	6.0	2.0	2.0
ϵ	1.0	1.0	1.0	1.0

(b) LEAST SQUARES ESTIMATES OF
DAMPING PARAMETERS h_0, h_2

Case	(i)	(ii)	(iii)	(iv)
h_0	-0.513	-0.499	-0.504	-0.49
h_2	2.035	6.063	2.03	2.09

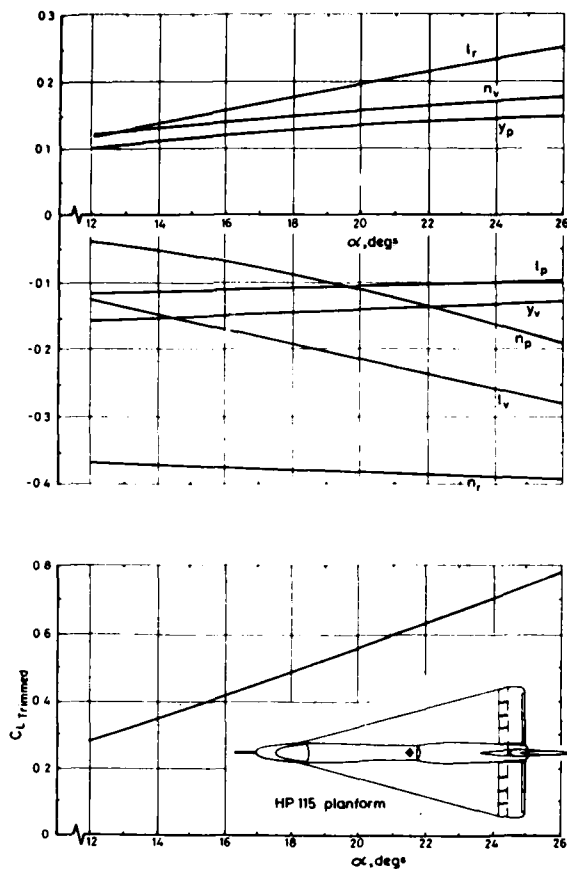


Fig 1 Aerodynamic data for HP 115

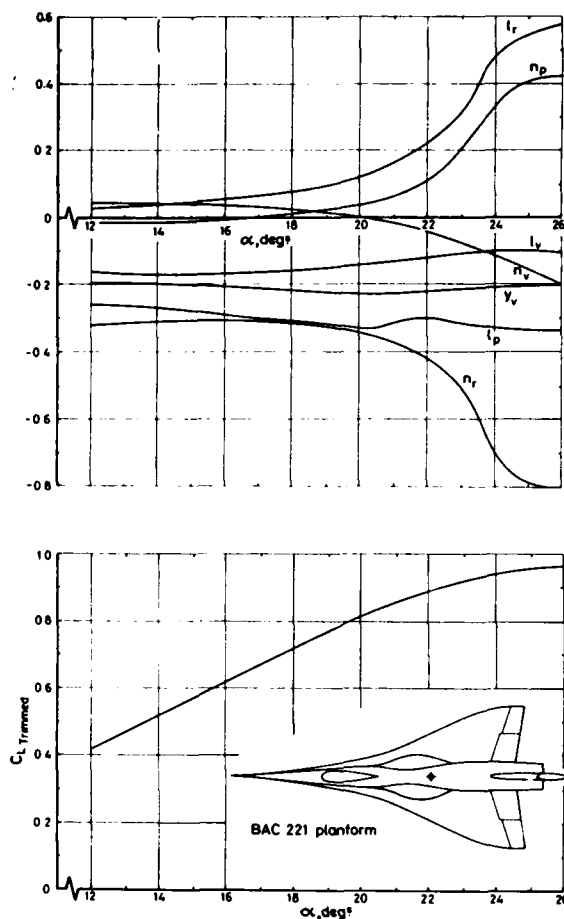


Fig 2 Aerodynamic data for BAC 221

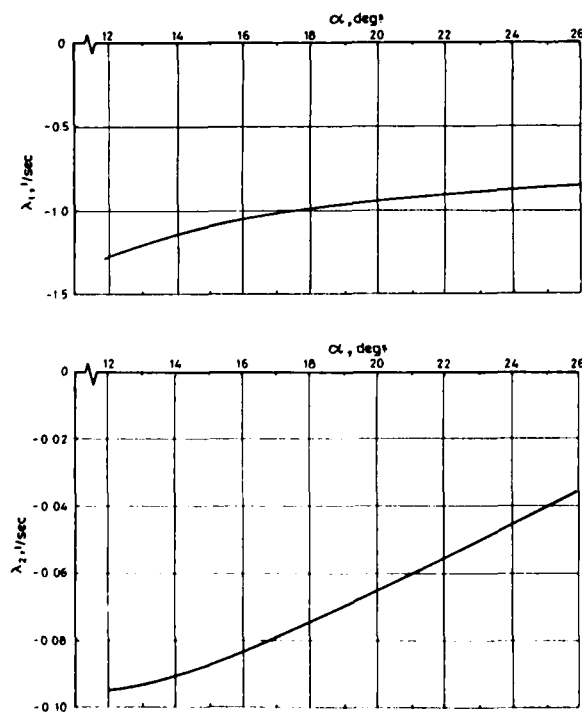


Fig 3 Eigenvalues for HP 115

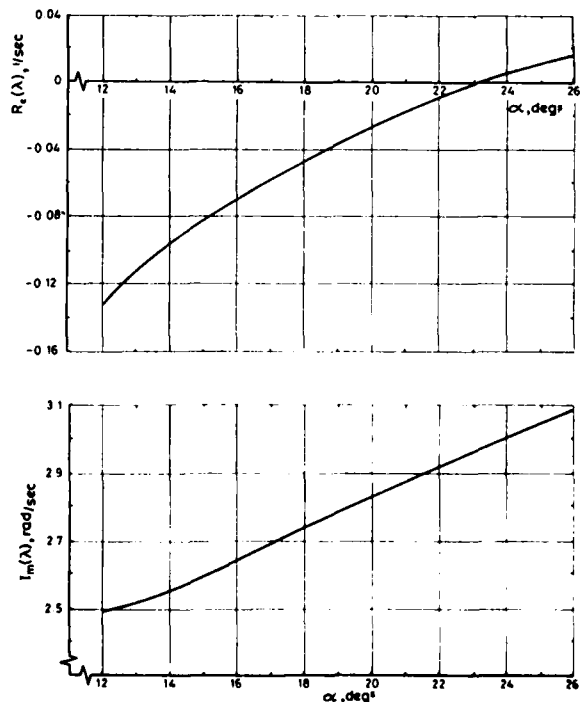


Fig 3 (cont) Eigenvalues for HP 115

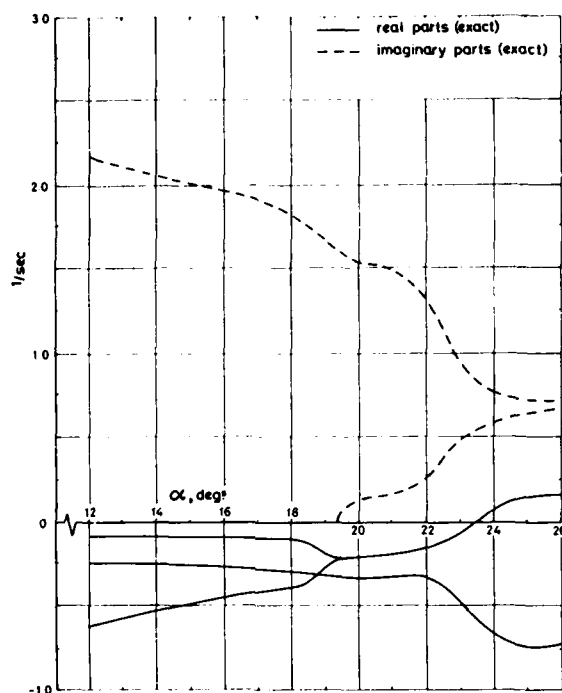


Fig 4 Eigenvalues for BAC 221

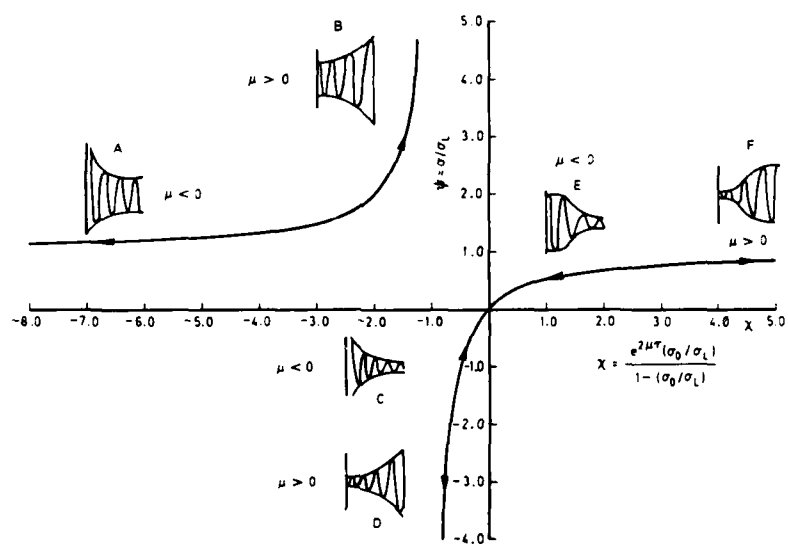


Fig 5 Transient growth characteristics for the critical mode

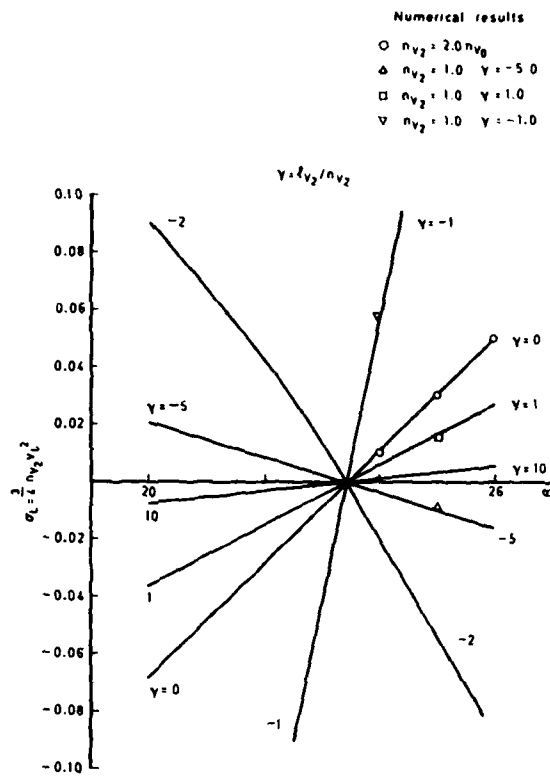


Fig 6 Sideslip limit cycles for HP 115

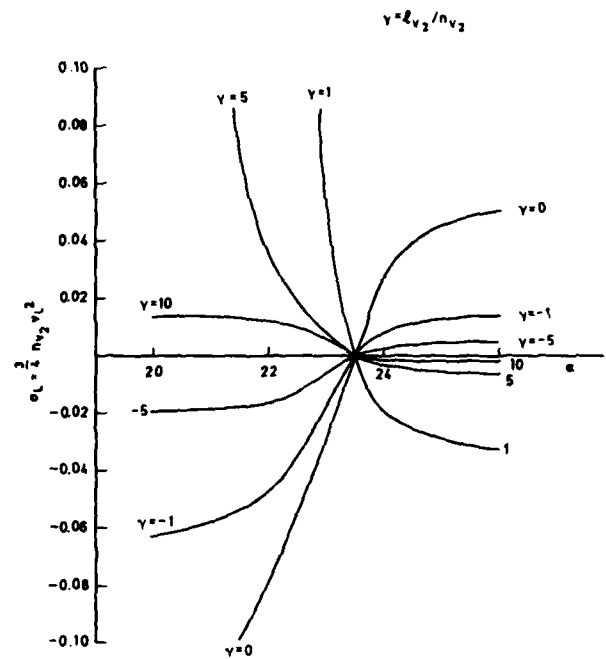


Fig 7 Sideslip limit cycles for BAC 221

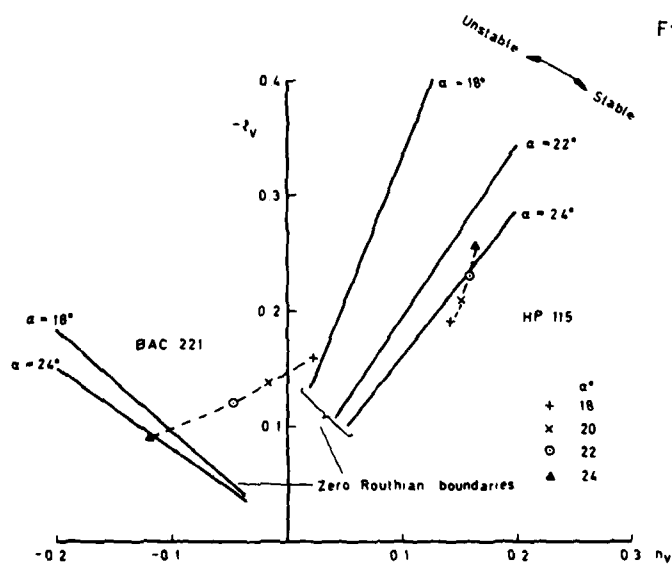


Fig 8 The sideslip derivative loci crossing the oscillatory stability boundary

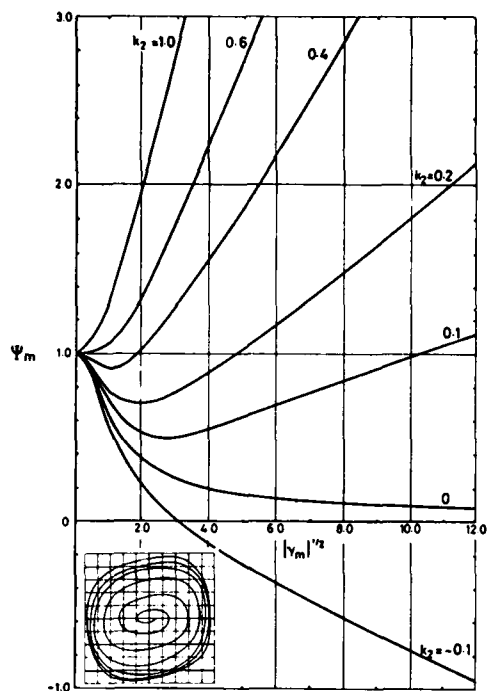


Fig 9 Approximate variation of logarithmic decrement with amplitude for the case $c_1 > 0$; $c_3 > 0$

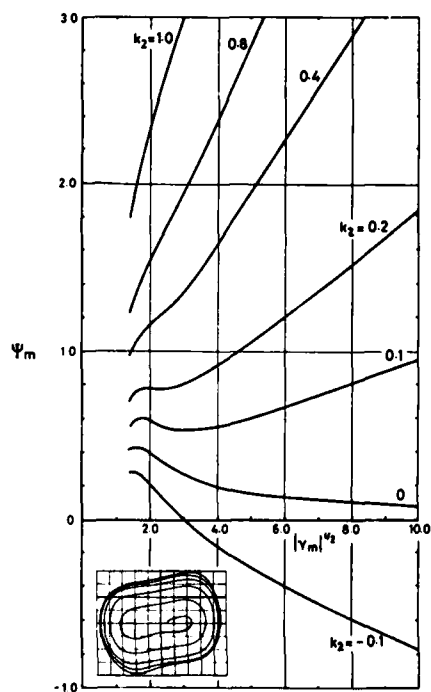


Fig 11 Approximate logarithmic decrement for the case $c_1 \leq 0$, $c_3 \geq 0$, $\gamma \leq -2$

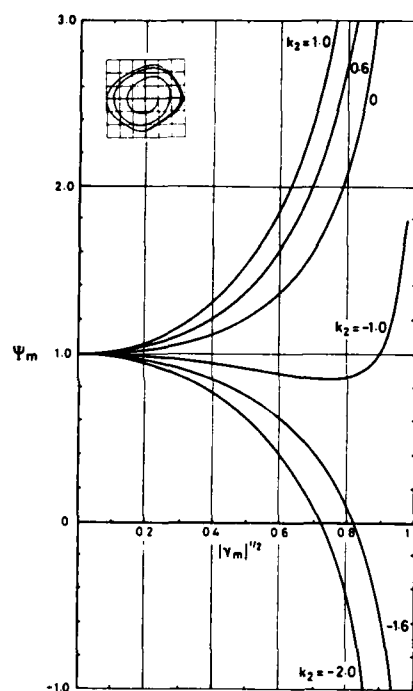


Fig 10 Approximate logarithmic decrement for the case $c_1 \geq 0$, $c_3 \leq 0$, $-1 \leq \gamma \leq 0$

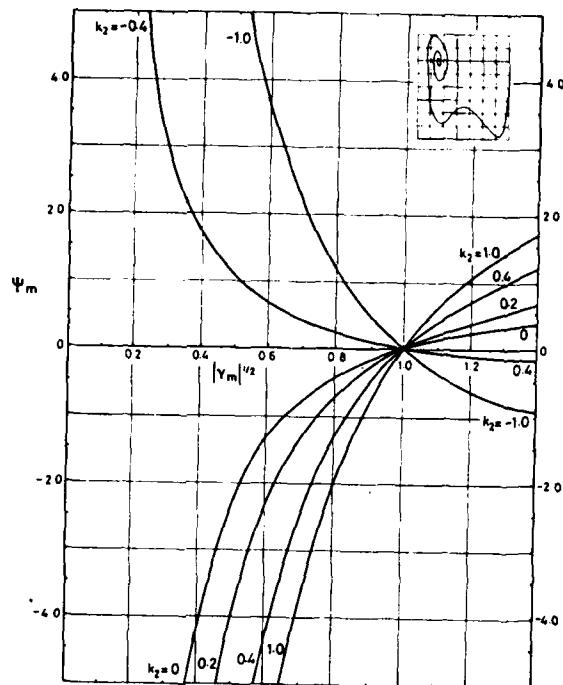
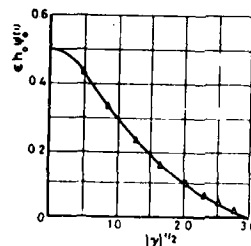
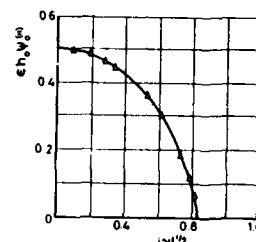


Fig 12 Approximate logarithmic decrement for the case $c_1 \leq 0$, $c_3 \geq 0$, $-2 \leq \gamma \leq 0$

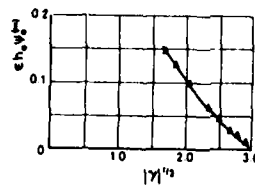


Case (i)

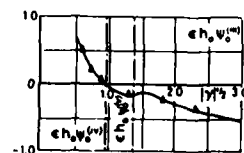


Case (ii)

— first order approximations
 A measurements of $2 \log_e \left| \frac{\gamma_{n+1}}{\gamma_n} \right| \left| \frac{c_1}{\pi} \right|^{1/2}$



Case (iii)



Case (iv)

Fig 13 Comparison of measured logarithmic decrement and least squares approximation for cases (i) to (iv) (Figs 9 to 12 Table 4) respectively

Appendix 1

LATERAL EQUATION OF MOTION

The normalised lateral equations of motion of an aircraft in terms of the sideslip velocity and its derivatives can be written in the companion matrix form as

$$\frac{dx}{dt} - Ax = g(x) \quad (A-1)$$

where $x = \{v, \dot{v}, \ddot{v}, \ddot{v}\}$.

The matrix A takes the form

$$A = \begin{bmatrix} 0 & 1 & 0 & 0 \\ 0 & 0 & 1 & 0 \\ 0 & 0 & 0 & 1 \\ -d_1 & -c_1 & -b_1 & -a_1 \end{bmatrix}$$

$$\text{where} \quad a_1 = -y'_v - \dot{y}'_p - n'_r \quad (A-2a)$$

$$b_1 = \ell'_p y'_v + \ell'_p n'_r + y'_v n'_r - \ell'_r n'_p - \ell'_v (y'_p + w_0) - n'_v (y'_r - u_0) \quad (A-2b)$$

$$c_1 = y'_v (\ell'_r n'_p - n'_r \ell'_p) + (y'_p + w_0) (\ell'_v n'_r - \ell'_r n'_v) + (y'_r - u_0) (\ell'_p n'_v - n'_p \ell'_v) - g_1 (\ell'_v n'_v + n'_v \tan \theta_0) \quad (A-2c)$$

$$d_1 = -g_1 (n'_v (\ell'_r - \ell'_p \tan \theta_0) - \ell'_v (n'_r - n'_p \tan \theta_0)) \quad (A-2d)$$

With the nonlinearity defined by Eqs. (23) and (24) the vector $g(x)$ takes the form

$$g(x) = \{0, 0, 0, g_4(x)\} \quad (A-3)$$

$$\text{where} \quad g_4(x) = -3b_3(2v\dot{v}^2 + v^2\ddot{v}) - 3c_3v^2\dot{v} - d_3v^3 \quad (A-4)$$

with

$$b_3 = -\ell'_v (y'_p + w_0) - n'_v (y'_r - u_0) \quad (A-5a)$$

$$c_3 = \ell'_v [n'_r (y'_p + w_0) - n'_p (y'_r - u_0) - g_1] + n'_v [\ell'_p (y'_r - u_0) - \ell'_r (y'_p + w_0) - g_1 \tan \theta_0] \quad (A-5b)$$

$$d_3 = -g_1 (n'_v (\ell'_r - \ell'_p \tan \theta_0) - \ell'_v (n'_r - n'_p \tan \theta_0)) \quad (A-5c)$$

The particular normalising scheme adopted will not affect the analysis of the paper and hence all dressings are omitted. The primed concise derivatives include the product of inertia terms and therefore take the form

$$n'_v = k \frac{n_v + e_x \ell_v}{i_{zz}(1 - e_x e_z)}, \quad n'_p = k \frac{n_p + e_x \ell_p}{i_{zz}(1 - e_x e_z)}, \quad n'_r = k \frac{n_r + e_x \ell_r}{i_{zz}(1 - e_x e_z)} \quad (A-6a)$$

$$\ell'_v = k \frac{\ell_v + e_z n_v}{i_{xx}(1 - e_x e_z)}, \quad \ell'_p = k \frac{\ell_p + e_z n_p}{i_{xx}(1 - e_x e_z)}, \quad \ell'_r = k \frac{\ell_r + e_z n_r}{i_{xx}(1 - e_x e_z)} \quad (A-6b)$$

where k is a constant appropriate to the particular normalising scheme used.

For a companion matrix the transformation required to separate Eq. (A-1) into two levels of its natural modes takes a relatively simple form.

Let U be the matrix of eigenvectors of A so that

$$U = \begin{bmatrix} U_{11} & U_{12} \\ U_{21} & U_{22} \end{bmatrix} \equiv \begin{bmatrix} 1 & 1 & 1 & 1 \\ \lambda_1 & \lambda_2 & \lambda_3 & \lambda_4 \\ 2 & 2 & 2 & 2 \\ 1 & 1 & 1 & 1 \\ \lambda_1 & \lambda_2 & \lambda_3 & \lambda_4 \end{bmatrix} \quad (A-7)$$

The required similarity transformation can be written as

$$\underline{x} = \begin{bmatrix} I & U_{12}U_{22}^{-1} \\ U_{21}U_{11}^{-1} & I \end{bmatrix} \underline{y} = C \underline{y} \quad (A-8)$$

At the critical condition when $\lambda_1 \lambda_2 = i\omega_0$ the sub matrices B_{11}, B_{22} take the form given in Eqs. (5) and (6) and we also have that

$$U_{12}U_{22}^{-1} = \begin{bmatrix} -\frac{1}{2} & 0 \\ \omega_0 & \end{bmatrix}; \quad U_{21}U_{11}^{-1} = \begin{bmatrix} -\lambda_1\lambda_2 & \lambda_1 + \lambda_2 \\ -\lambda_1\lambda_2(\lambda_1 + \lambda_2), (\lambda_1 + \lambda_2)^2 - \lambda_1\lambda_2 \end{bmatrix} \quad (A-9)$$

The nonlinear vector has to be pre-multiplied by the inverse of C but the only relevant terms are those in the final column and those pre-multiplying the nonlinear terms in the critical mode are given by the last two entries. At the critical condition these reduce to

$$C_{34}^{-1} = \frac{-\omega_0^2(\lambda_1 + \lambda_2)}{\omega_0^2(\lambda_1 + \lambda_2)^2 + (\omega_0^2 - \lambda_1\lambda_2)^2}, \quad C_{44}^{-1} = \frac{(\omega_0^2 - \lambda_1\lambda_2)^2}{\omega_0^2(\lambda_1 + \lambda_2)^2 + (\omega_0^2 - \lambda_1\lambda_2)^2} \quad (A-10)$$

THE DYNAMIC STABILITY IN FLIGHT OF SPINNING BLUNT BODY PROJECTILES

P C Parks
Department of Mathematics and Ballistics,
Royal Military College of Science,
Shrivenham,
Swindon SN6 8LA
England.

SUMMARY

Blunt projectiles fired from rifled guns are used for a number of specialised rôles, military and civilian. Such projectiles have a pitching moment which is a highly non-linear function of incidence. For very small angles of incidence the pitching moment is a restoring one, but for larger angles the moment changes sign and an unspun projectile would then tumble. Spin stabilisation appears to be the solution but the precessional motion in flight can result in quite large angles of incidence building up during flight, with additional drag and drift. This paper investigates the precessional motion for a particular cylindrical projectile. A solution is proposed involving an optimum rounding of the leading edge of the projectile: this alters the pitching moment characteristics and also reduces drag.

NOTATION

A	Moment of inertia of projectile about its axis of symmetry
B	Moment of inertia in pitch projectile
c	Aerodynamic damping coefficient
$G_{2,3}$	Aerodynamic moments in pitch and yaw
g	Acceleration due to gravity
k	Local slope of moment curve versus incidence
M(.)	Aerodynamic pitching moment about projectile centre of gravity
O	Origin of yaw and pitch diagram in Figs 4 and 6
n	Projectile spin rate about its axis of symmetry
o	Suffix to denote equilibrium point values
P, Q, R	Equilibrium points shown in Fig 4
p)	
q)	Angular velocities about projectile axis of symmetry and in pitch and yaw
r)	
V	Forward velocity of projectile
α	Angle of incidence
δ	Yaw angle) shown in Fig 3
θ	Pitch angle)
λ	Root of characteristic equation for stability
ω	Frequency in rad s ⁻¹

1. INTRODUCTION

Blunt body projectiles are used for a number of military and civilian purposes, ranging from anti-tank missiles to non-lethal anti-riot projectiles used by the police. The pitching moment of such projectiles is a highly non-linear function of incidence. In Fig 1 the pitching moment of a circular cylinder, representing a projectile of the latter type, is plotted from wind-tunnel tests made on a scaled-up model.

The pitching moment changes sign at an incidence of $\pm 4^\circ$ and so that unspun projectile flying end-on would experience a restoring or stabilising moment for small angular perturbations of less than 4° , but would become unstable and "tumble" for any larger disturbances. Cylindrical projectiles of the type shown in Fig 1 have been observed sometimes to fly end-on and sometimes to tumble when fired from a smooth bored gun.

To prevent tumbling a natural and well-known solution applied to pointed projectiles such as conventional bullets or shells which have pitching moments which are destabilising for all angles of incidence, is spin stabilisation. However when projectiles of the type shown in Fig 1 are fired from rifled guns although tumbling has been prevented quite large angles of incidence are seen to build up in flight.

This paper examines the precessional motion in pitch and yaw about the flight path of the projectile shown in Fig 1. Now any spinning projectile has to precess in flight in order for its axis of symmetry to follow the flight trajectory which is curved under the influence of gravity. Under the conventional stability theory for artillery shells the shell settles down at a small incidence in yaw - the "equilibrium yaw". This yaw angle provides an aerodynamic moment in yaw which achieves the appropriate precession in the pitch plane necessary to follow the curved flight path. For a conventional shell depicted in Fig 2 the equilibrium yaw, δ , is to the right of the flight path as shown and the lift produced causes a deviation of the shell to the right known as "drift".

Now for the conventional shell there is only one equilibrium yaw angle which provides the correct precessional moment: for the projectile and conditions shown in Fig 1 there are three such angles, as indicated on Fig 1. This leads to a more complicated regime of precessional motions in pitch and yaw which are described in the following section.

ADDITIONAL DATA:

Mass 0.132 kg, Diameter 3.7 cm, Length 10 cm,
 Moments of inertia $A = 0.23 \times 10^{-4} \text{ kg m}^2$,
 $B = 1.21 \times 10^{-4} \text{ kg m}^2$,
 Spin $n = 817 \text{ rad s}^{-1}$, Drag coefficient $C_D = 0.76$,
 Initial velocity 80 ms^{-1} , Initial angle of
 departure 10° , Nominal trajectory: Range 145m,
 Time of flight 2.5s, Vortex height 7.7m, Initial
 angular velocity of tangent 6.92 deg s^{-1} , final
 angular velocity 12.00 deg s^{-1} , final velocity
 46 ms^{-1}

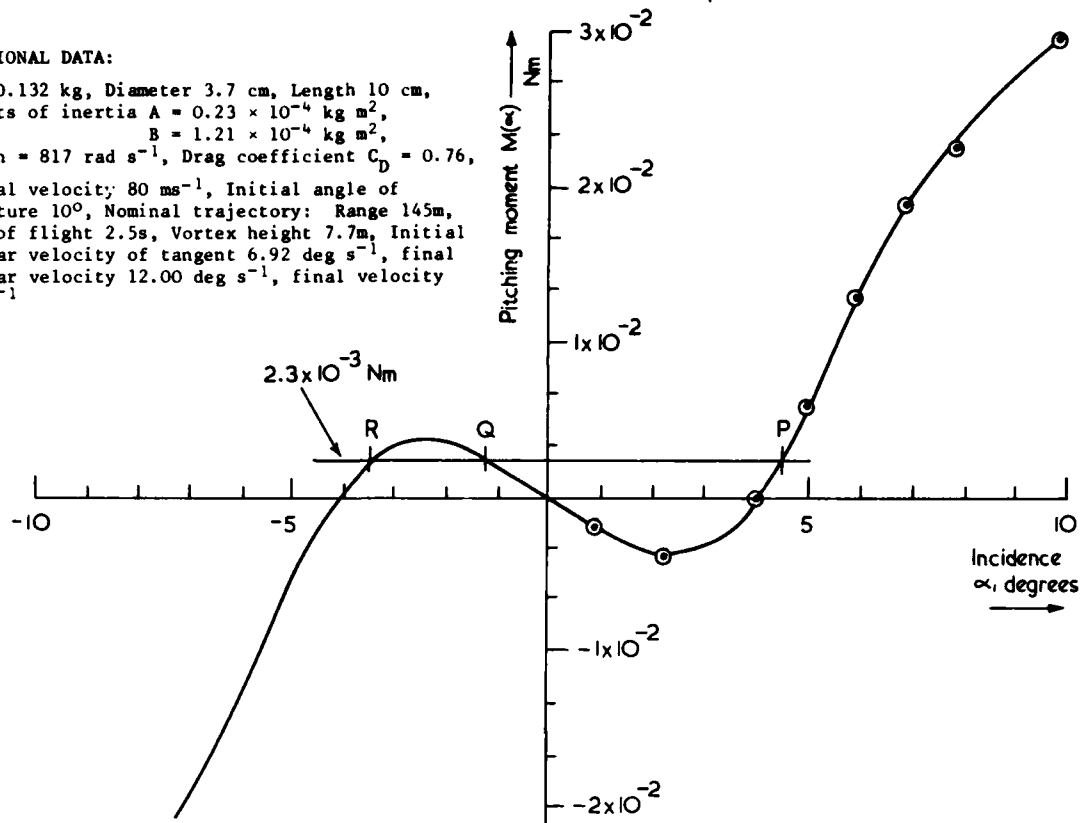
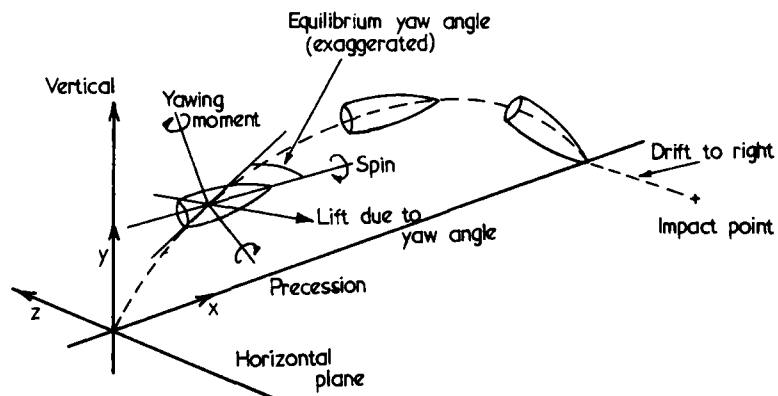
Fig 1. Pitching moment of cylinder about CG, $V = 80 \text{ ms}^{-1}$ 

Fig 2. Equilibrium yaw angle for conventional spinning shell

2. PRECESSIONAL MOTIONS IN PITCH AND YAW

In the following analysis we shall make a number of simplifying assumptions. We shall neglect Magnus forces and moments on the spinning projectile and we shall assume the moment due to incidence on the spinning body is the same as that on an unspun body as measured in the wind tunnel tests on which Fig 1 is based.

The equations of motion are

$$B\dot{q} + Apr = G_2 \quad (2.1)$$

$$B\dot{r} - Apq = G_3$$

We shall at first neglect the angular acceleration terms in \dot{q} and \dot{r} and we shall put $p = n$, the spin of the projectile which we assume to be constant.

The aerodynamic moments G_2 and G_3 may be written as

$$G_2 = M(\alpha) \frac{\theta}{\alpha}, \quad G_3 = M(\alpha) \frac{\delta}{\alpha} \quad (2.2)$$

where δ and θ are the small angular deviations in yaw and pitch respectively of the axis of symmetry from the flight path, and $\alpha = \sqrt{\delta^2 + \theta^2}$ (see Fig 3). The angular velocities q and r are referred to fixed axes in space so that

$$\begin{aligned} q &= \dot{\theta} - (g/V) \\ r &= \dot{\delta} \end{aligned} \quad (2.3)$$

since the tangent to the flight path is turning at an approximate rate g/V for fairly flat flight paths. (The precise rate is $g \cos \psi / V$ where ψ is the inclination of flight path to the horizontal. We assume that $|\psi| < 10^\circ$, say, for flight paths of interest).

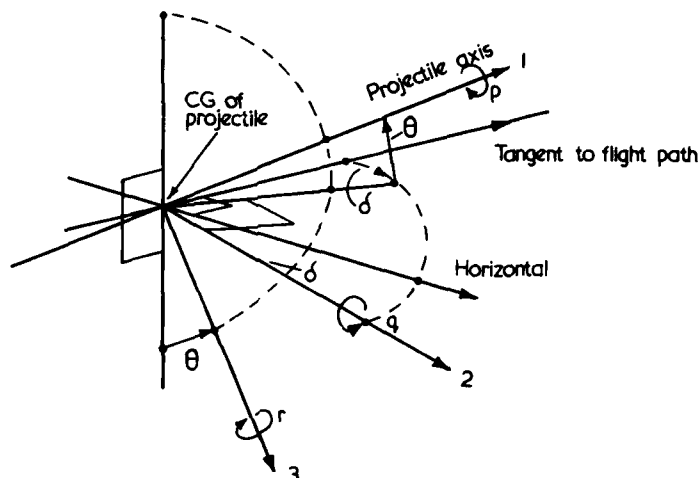


Fig 3. Definition of angles δ , θ , axes and angular velocities

We have therefore the simplified non-linear differential equations for δ and θ

$$\begin{aligned} A n \dot{\delta} &= M(\alpha) \frac{\theta}{\alpha} \\ - A n \dot{\theta} &= M(\alpha) \frac{\delta}{\alpha} - \frac{Ang}{V} \end{aligned} \quad (2.4)$$

where $\alpha = \sqrt{\delta^2 + \theta^2}$ and $M(\alpha)$ is given in Fig 1.

We shall assume temporarily that V is constant and examine the behaviour of the coupled equations (2.4) in the state plane of δ and θ .

We seek first equilibrium points for equations (2.4) in the (δ, θ) plane. These are situated where the right hand sides of (2.4) are simultaneously zero. From the first equation we have $\theta = 0$ and in the second equation we then have $\alpha = \delta$ and we seek solutions of

$$M(\alpha) = Ang/V \quad (2.5)$$

Now for the values of A , n and V given in Fig 1 there are three values of δ satisfying equation (2.5), giving rise to the three equilibrium points P, Q, R shown in Fig 4.

The character of the motion in the vicinity of these equilibrium points is of interest and to investigate these motions we linearise about a particular equilibrium point $(\delta_0, 0)$ by putting

$$\begin{aligned} \delta &= \delta_0 + \delta' \\ \theta &= \theta' \end{aligned} \quad (2.6)$$

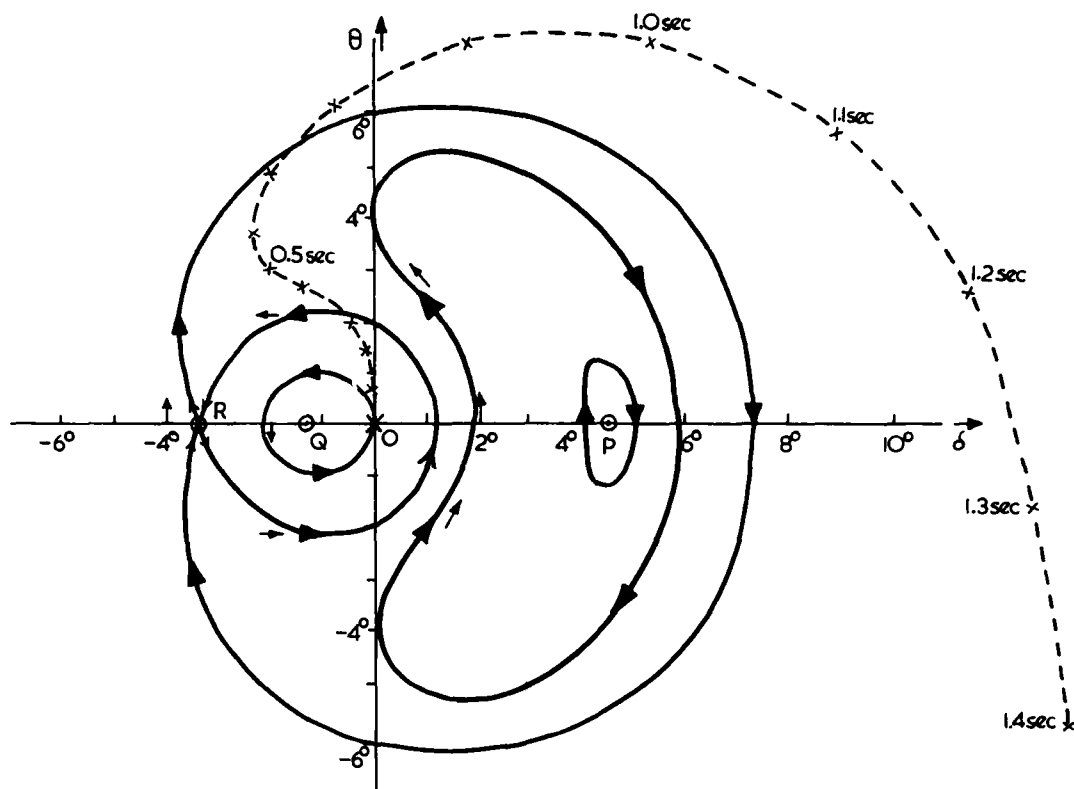
Now $\alpha = \sqrt{(\delta_0 + \delta')^2 + \theta'^2} = \delta_0 \left(1 + \frac{\delta'}{\delta_0}\right)$ to first order, and so equations (2.4) become

$$A n \dot{\delta}' = (M_0 + k \delta') \frac{\theta'}{\delta_0 + \delta'} = M_0 \frac{\theta'}{\delta_0} \quad (2.7)$$

$$\text{and} \quad - A n \dot{\theta}' = (M_0 + k \delta') \frac{(\delta_0 + \delta')}{(\delta_0 + \delta')} - \frac{Ang}{V} = k \delta'$$

since $M_0 = Ang/V$. Here k is the slope of the $M(\alpha)$ curve at $\alpha = \delta_0$.

Eliminating θ' between the two equations in (2.7) we obtain

Fig 4. Trajectories of motions on δ, θ plane

$$A^2 n^2 \ddot{\delta} = - \frac{M_0 k}{\delta_0} \delta \quad (2.8)$$

Thus the equilibrium point will be a stable centre if $\frac{M_0 k}{\delta_0} > 0$ and will be an unstable saddlepoint if $\frac{M_0 k}{\delta_0} < 0$.

For the point P on Fig 4 $M_0 > 0$, $\delta_0 > 0$ and $k > 0$ and so P is a stable centre. Trajectories surrounding P are ellipses described in a clockwise direction as time increases. The major axis is parallel to the θ axis and the major and minor axes for the particular example of Fig 1 are in the ratio of 1.62 to 1. The frequency ω of the simple harmonic motions in δ and θ are given by

$$\omega^2 = \frac{1}{An} \frac{M_0 k}{\delta_0}$$

which gives a value of ω of 28.5 rad s^{-1} or 0.85 Hz .

For the point Q, $M_0 > 0$, $\delta_0 < 0$ and $k < 0$ and so Q is also a stable centre. Q is surrounded by elliptical trajectories described counter-clockwise as time increases. In the particular example these ellipses are almost circular and the frequency of the simple harmonic motions happens to be 0.85 Hz also.

For the point R, $M_0 > 0$, $\delta_0 < 0$ and $k < 0$ and so R is an unstable saddlepoint. We can deduce the directions of the separatrices at R which are straight lines through R with slopes $\pm \tan^{-1} \frac{-k\delta_0}{M_0}$, or $\pm 62.3^\circ$ for the given example.

Elsewhere in the (δ, θ) it is possible to calculate the local slopes of the trajectories from the equations (2.4) since these slopes are given by $\dot{\theta}/\dot{\delta}$ and from (2.4)

$$\frac{\dot{\theta}}{\dot{\delta}} = - \frac{\delta}{\theta} + \frac{An \alpha}{VM(\alpha)\theta} \quad (2.9)$$

where $\alpha = \sqrt{\delta^2 + \theta^2}$. The circle $\delta^2 + \theta^2 = 16$ (where δ and θ are measured here in degrees) is an isocline on which the slope of trajectories is infinite since $M(\alpha) = 0$ on this circle. From these local slopes the general form of the trajectories may be deduced as shown in Fig 4, where the arrows denote the direction

of increasing time.

At the time of firing $\delta = \theta = 0$ and so the axis of an undisturbed projectile would precess about the equilibrium point Q in an approximately circular counter-clockwise orbit as shown passing through O on Fig 4. A gust or other disturbance, for example reverse flow conditions just after ejection from the gun, could cause a jump on to a larger orbit around P described in a clockwise direction and involving larger angles of incidence and increased drag and drift.

3. FURTHER CONSIDERATIONS

The neglect of the acceleration terms $B\dot{q}$ and $B\dot{r}$ in (2.1) does not greatly influence the situation as depicted in Fig 4. If these terms are included then the trajectory starting at O becomes the rosette motion sketched in Fig 5. For the numerical example of Fig 1 there is a high frequency nutation of 24.7 Hz at an amplitude which is about 1/30 of the precessional motion at a frequency of about 0.85 Hz shown in Fig 4. Moreover these high frequency nutations are damped out by aerodynamic damping.

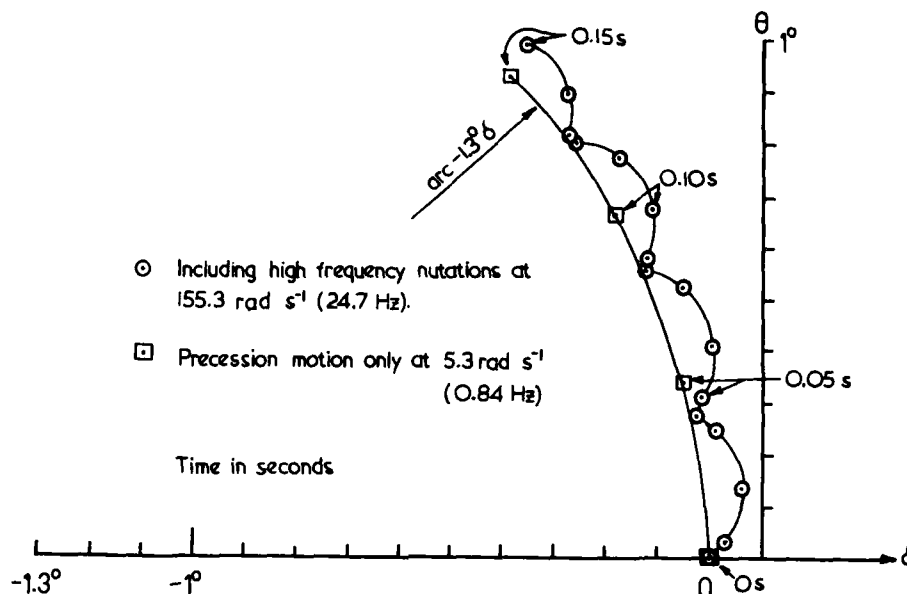


Fig 5. Rosette motion from origin of δ, θ plane

Aerodynamic damping, which may be introduced by adding terms such as $-c\dot{\theta}$ and $-c\dot{\delta}$ ($c > 0$) to the right-hand sides of (2.4), leads to a modified stability criterion for the modified form of equations (2.7). The characteristic equation will be

$$(A^2 n^2 + c^2) \lambda^2 - \lambda c \left(k + \frac{M_0}{\delta_0} \right) + \frac{k M_0}{\delta_0} = 0 \quad (3.1)$$

where we have sought solutions of the form $\delta' = a e^{\lambda t}$, $\theta' = b e^{\lambda t}$. For stability of (3.1) we require

$$\frac{k M_0}{\delta_0} > 0 \quad \text{and} \quad \left(k + \frac{M_0}{\delta_0} \right) < 0.$$

Thus the equilibrium point P ($M_0 > 0$, $\delta_0 > 0$, $k > 0$) becomes an unstable focus for small c , Q ($M_0 > 0$, $\delta_0 < 0$, $k < 0$) becomes a stable focus and R remains as an unstable saddlepoint. The new form of the trajectory diagram is shown in Fig 6. Many trajectories end up by spiralling into Q but a few can spiral outwards in a growing clockwise motion.

The effect of aerodynamic damping on precessional and nutational motions does not seem to be widely known and can be tabulated below:

	Precessional (low frequency) motions	Nutational (high frequency) motions
Aerodynamically stable projectile ($k < 0$)	Stabilising	Stabilising
Aerodynamically unstable projectile ($k > 0$)	Destabilising	Stabilising

Table: Effect of aerodynamic pitch damping on stability of precessional and nutational motions of a spinning shell.

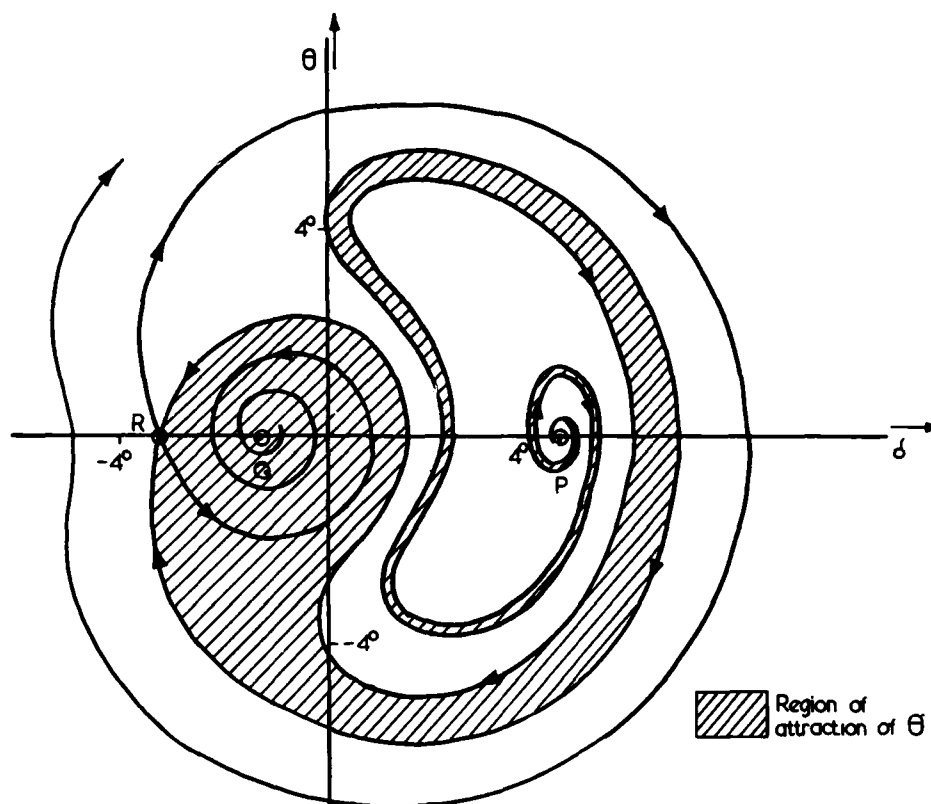


Fig 6. Modification of δ , θ motions of Fig 4 due to damping

A more drastic modification of the behaviour of the projectile from that shown by the trajectories in Figs 4 or 6 is however caused by the fact that V in equations (2.4) is not constant. This will affect the term $M(\alpha)$ which depends on V^2 as well as the term Ang/V .

A step-by-step calculation allowing for these effects gives rise to a trajectory originating from 0 and plotted in Fig 4 as a curve of dashes. After about 1s angles of incidence of 10° or more have built up on a trajectory which is spiralling outwards with greatly increased drag and drift. This is an unsatisfactory result. A more precise computer calculation of this motion is shown in Fig 9.

4. IMPROVEMENTS IN THE BALLISTIC PERFORMANCE

The difficulties described above are really brought about by the low aerodynamic moments available from the moment curve shown in Fig 1. A distinct improvement in performance is possible if the leading edge of the projectile can be rounded in the manner shown in Fig 7. First, the drag coefficient C_D is dramatically reduced as the ratio radius of rounding/projectile diameter exceeds about 0.15, as shown in Fig 7. (See also [1]). Secondly, the pitching moment curve is "straightened out" from the form shown in Fig 1 to that shown in Fig 3. There is now only one equilibrium point with $\delta = 0.3^\circ$, $\theta = 0$ as shown in Fig 8. With aerodynamic damping this is an unstable focus but the instability will be a mild one and so the angles of incidence in flight will be very much smaller than those shown in Fig 4.

5. CONCLUSIONS

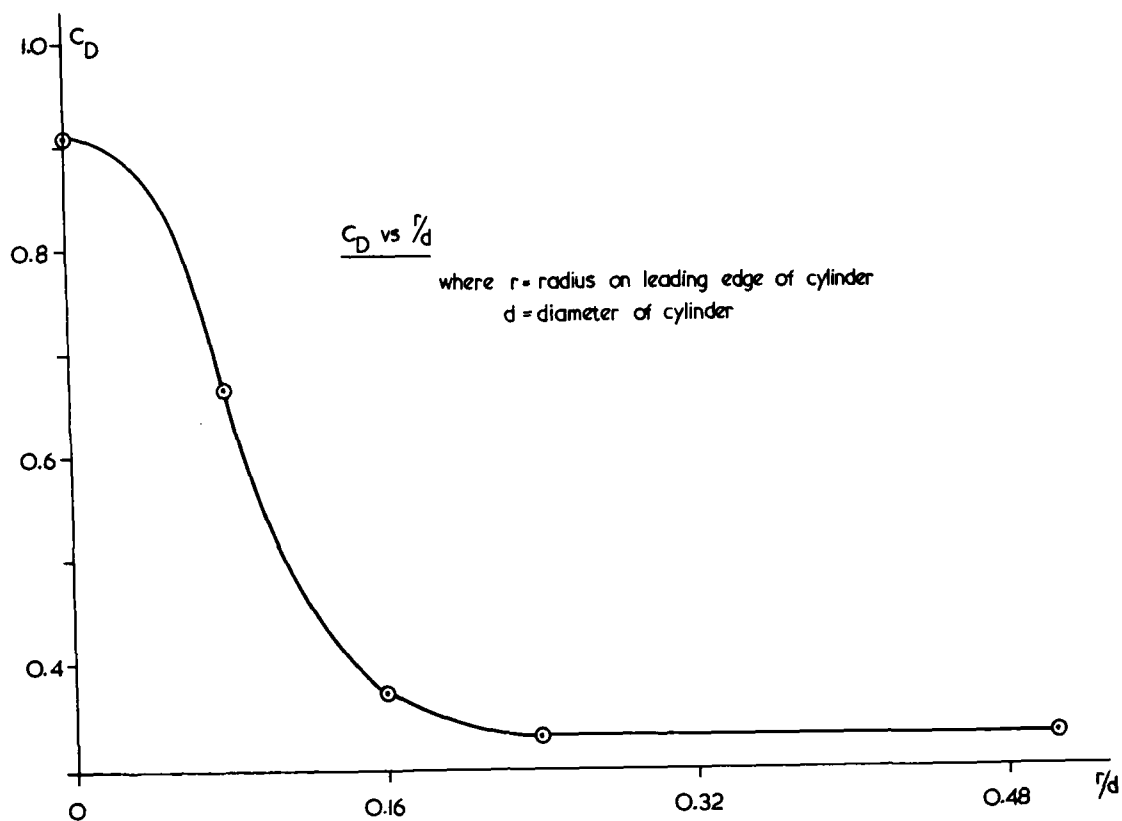
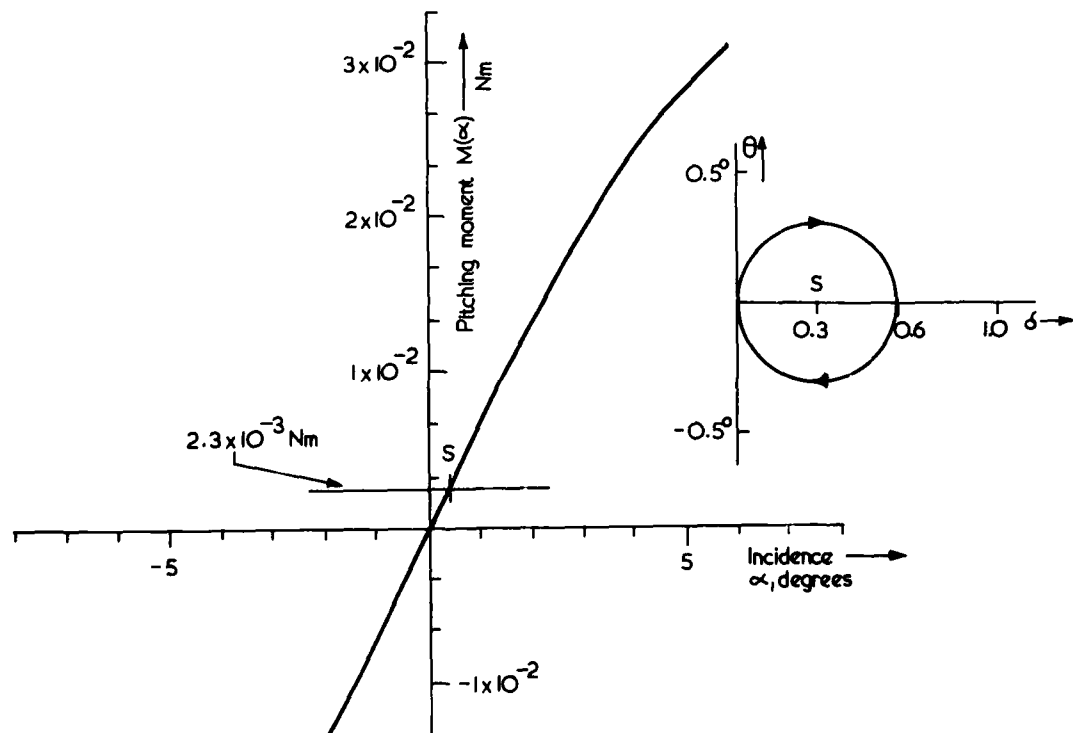
Precessional motions of spinning blunt projectiles with highly non-linear pitching moment characteristics have been analysed and proposals for improving their performance in flight by rounding the leading edge have been put forward. Further wind-tunnel and ballistic range tests on such modified projectiles are in hand.

6. ACKNOWLEDGEMENTS

Some of this work is supported by the UK Ministry of Defence Chemical Defence Establishment under a research contract. The author wishes to thank Mr F P Watkins of CDE and his colleagues, Mr A K Weaver, Dr L Pennelegion, Mr P J Richards and Mr S G Clements for comments on various aspects of this paper and for their supporting experimental work.

7. REFERENCE

1. S F Hoerner, Fluid-Dynamic Drag, S F Hoerner, POB 342, Brick Town, New Jersey 08723, USA, 1965.

Fig 7. Effect of leading edge radius on C_D Fig 8. Pitching moment of cylinder with leading edge radius of 9 mm (radius/diameter = 9/37) and corresponding (δ, θ) trajectory from origin

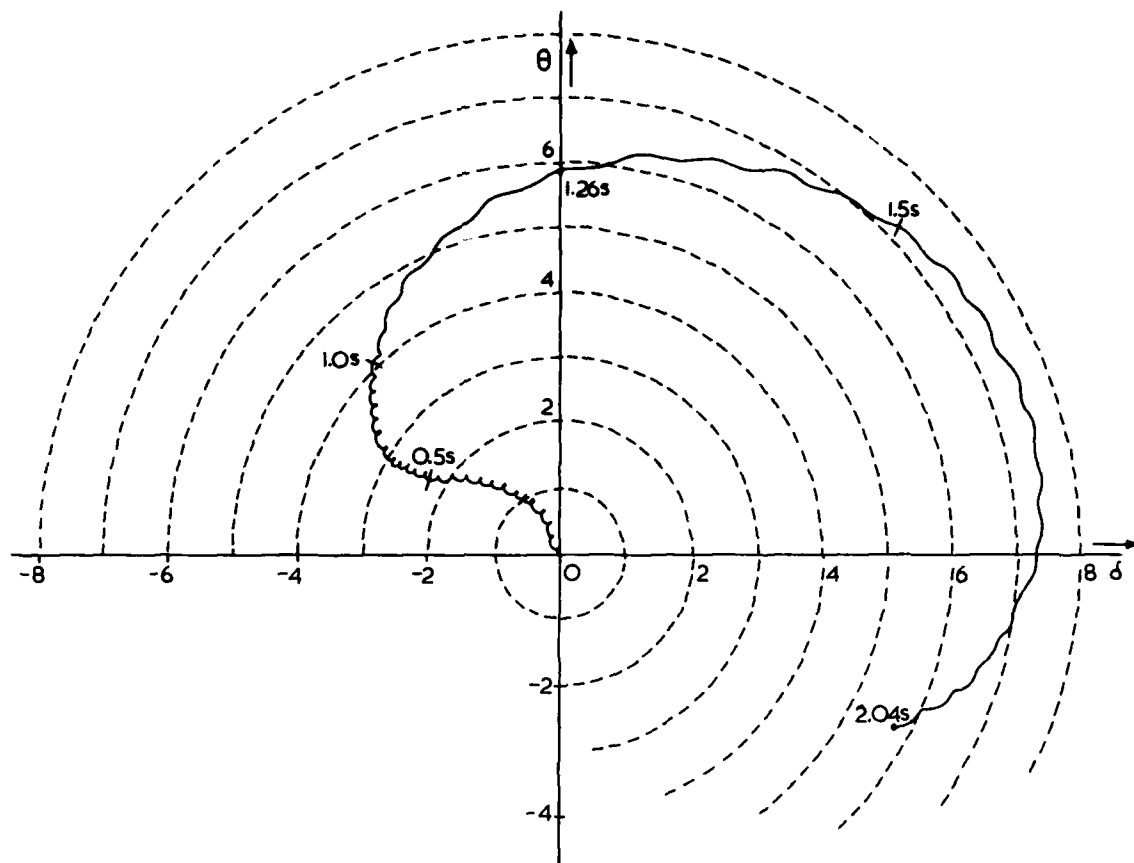


Fig 9. Computer calculation of δ , θ motion for nominal trajectory shown on Fig 1.

RESULTS OF PILOTED SIMULATOR STUDIES OF FIGHTER AIRCRAFT AT HIGH ANGLES OF ATTACK

Joseph R. Chambers, William P. Gilbert,
and Luat T. Nguyen
Aeronautical Engineers
NASA Langley Research Center
Hampton, Virginia 23665
U.S.A.

SUMMARY

Recent interest in close-in air-to-air combat and the maneuverability demanded by this tactical philosophy have resulted in increased emphasis on providing good handling characteristics for fighter aircraft at high angles of attack. In the past decade, the use of advanced piloted simulators has been extensively evaluated in the U.S. as a means of predicting, evaluating, and analyzing these characteristics. The paper discusses the experience gained at the NASA Langley Research Center during the application of simulator techniques to high angle of attack flight conditions for several current fighters. The discussion includes (1) the simulator hardware, (2) requirements for static and dynamic aerodynamic data inputs, (3) evaluation procedures, (4) correlation with flight, and (5) the effects of dynamic stability parameters.

Accurate and valid simulation of maneuvering flight at high angles of attack requires extensive aerodynamic data due to the extremely nonlinear and configuration-dependent aerodynamic characteristics produced by flow separation and the strong vortex flows encountered at such flight conditions. These data requirements, together with the mathematical model required to simulate current flight control systems, are best met with real-time digital simulation techniques which utilize 360° real-world visual displays to provide a realistic piloting task and environment.

Results obtained with the simulator technique have correlated well with flight test experience, resulting in early identification of potential problems, identification of critical flight conditions, and solutions to various deficiencies in stability and control characteristics. With regard to dynamic stability parameters, the results indicate that certain parameters - particularly damping in roll - can have a large influence on the flying qualities and tactical effectiveness of fighters at high angles of attack.

As a result of the demonstrated value of the simulator technique, piloted simulation now plays a major role in the design and development process for high-performance military aircraft.

SYMBOLS

b	Wing span, m (ft)	V	Free-stream velocity, m/sec (ft/sec)
C_L	Lift coefficient	α	Angle of attack, deg
$C_{l\beta}$	Effective dihedral derivative	β	Angle of sideslip, deg
$C_{l_p} + C_{l\beta} \sin \alpha$	Damping-in roll parameter	δ_h	Horizontal tail deflection
C_n	Yawing-moment coefficient	Ω	Spin rate, rad/sec
$C_{n\beta}$	Directional stability derivative	$\sigma_{a_{wt}}$	rms buffet acceleration at wing tip, g
$C_{n_r} - C_{n\beta} \cos \alpha$	Damping-in-yaw parameter		

INTRODUCTION

Recent military experience has shown that close-in air-to-air combat often occurs and that the strenuous maneuvers utilized during such engagements require that fighter aircraft be capable of controlled flight at high angles of attack near maximum lift. This experience has also shown that fighter configurations not designed for flight at high angles of attack may exhibit severe degradations in stability and control characteristics in this flight condition which make them extremely susceptible to inadvertent loss of control, departures, and spins from which recovery may be difficult or impossible. In recognition of the importance of good flying qualities at high angles of attack, an effort has been underway in the U.S. for about a decade to develop and accelerate the technology required to design highly maneuverable, spin-resistant fighter airplanes.

As a result of its unique testing techniques and experience in stall/spin technology, the Langley Research Center of the National Aeronautics and Space Administration has been extremely active in this national research effort. At Langley, these studies include a wide matrix of testing and analysis techniques, as illustrated in figure 1. Stall and departure characteristics are evaluated during wind-tunnel free-flight model tests in the Langley full-scale wind tunnel; developed spin and spin-recovery characteristics are studied during tests in the Langley spin tunnel, and spin entry characteristics are studied with unpowered radio-controlled drop models. These models are also used in static and dynamic wind-tunnel force tests to determine their aerodynamic characteristics; and the data are used as inputs to theoretical analyses which are conducted to develop mathematical models to describe airplane motions at high angles of attack. Although the model tests provide much information on high angle of attack characteristics, they have several critical shortcomings. For example, the inputs of the human pilot have been minimized or entirely eliminated. Thus, they do not allow for a quantitative pilot evaluation of the flying qualities of the full-scale airplane. In addition, the use of unpowered models and space constraints within the wind tunnels do not permit an evaluation of the spin susceptibility of airplanes during representative air combat maneuvers. Finally, the effects of sophisticated flight control systems are not evaluated because of space limitations within the models. With the advent of real-time digital simulation techniques and air combat simulators, Langley has incorporated the use of piloted simulation into its high angle of attack/stall/spin research program to provide the foregoing data.

The use of piloted simulation at Langley to investigate high angle of attack characteristics has evolved from the initial use of a simple, single-cockpit with a limited visual display (ref. 1), to the present Differential Maneuvering Simulator (DMS) which will be described later. Early simulation efforts with the simple hardware identified several important factors to be encountered in this application of simulator technology. Results of the studies indicated that in order to obtain a realistic evaluation of the departure and spin susceptibility of an airplane design, the simulation must present the pilot with a realistic air combat maneuvering environment. In particular, he should not be presented with a task based on instruments; or he will quickly recognize an impending loss-of-control situation, reduce angle of attack, and provide an overly optimistic result. The task should therefore require him to be almost constantly looking outside of the cockpit to acquire and maneuver against an adversary. In addition, there must be provided a good simulation of the cockpit environment in terms of pilot visibility, the display of flight instruments, and the use of a realistic force-feel system for the pilot stick and rudder pedals. As Langley's stall/spin simulation work progressed, it was found necessary to employ the DMS to more completely meet the above mentioned requirements and to cover additional needs for improved hardware and software.

The general objectives of the stall/departure simulation research today are to comprehensively evaluate high-angle-of-attack stability and control characteristics during realistic maneuvering tasks and to define automatic control concepts which provide improved flying qualities and resistance to loss-of-control during high-angle-of-attack maneuvering. More specifically, for a given airplane configuration, the objectives are (1) to determine the controllability and departure resistance during 1-g stalls and accelerated stalls, (2) to determine departure susceptibility during demanding air combat maneuvers, (3) to identify maneuvers or flight conditions which might overpower the departure-resistant characteristics provided by the airframe and control system, and (4) to determine the effects of any proposed airframe modifications on departure resistance.

This paper will discuss the experience gained at Langley during recent applications of the DMS to several current fighter configurations; including descriptions of the simulator hardware, aerodynamic data inputs, procedures employed, and correlation of results with flight test experience. In view of the theme of this symposium, an effort is also made to point out the relative importance of dynamic stability parameters on high angle of attack characteristics as observed during the studies.

DESCRIPTION OF SIMULATOR HARDWARE

The Langley DMS is a fixed-base simulator which has the capability of simultaneously simulating two airplanes as they maneuver with respect to one another, including a full-wide-angle visual display for each pilot. A sketch of the general arrangement of the DMS hardware and control console is shown in figure 2. Two 12.2-m diameter projection spheres each enclose a cockpit, an airplane-image projection system, and a sky-Earth-Sun projection system.

A control console located between the spheres is used for interfacing the hardware and the computer, and it includes critical parameters used in monitoring of the hardware operation. Each pilot is provided a projected image of his opponent's airplane, with the relative range and attitude of the target shown by use of a television system controlled by the computer program.

A photograph of one of the cockpits and the target visual display during a simulated engagement is shown in figure 3. A cockpit and an instrument display representative of current fighter aircraft equipment are utilized, and a fixed gunsight is used for tracking. Each cockpit is located to position the pilot's eyes near the center of the sphere, which results in a field of view representative of that obtained in current fighter airplanes. The cockpits are equipped with a conventional center stick, rudder pedals, and a throttle. A hydraulic force-feel system provides desired stick and pedal force and dynamic characteristics. Although the cockpits are not provided with attitude motion, each cockpit incorporates a buffet system capable of providing programmable rms buffet accelerations as high as 0.5g with up to three primary structural frequencies simulated.

The visual display in each sphere consists of a target image projected on a sky-Earth scene. The sky-Earth scene is generated by two point-light sources projecting through two hemispherical transparencies (one transparency of blue sky and clouds and the other of desert terrain features), and the scene provides a well-defined horizon for reference purposes. Spatial attitude motions are simulated; however, no provision is made to simulate translational motions with respect to the sky-Earth scene (such as altitude variation). A flashing light located in the cockpit behind the pilot is used as a cue when an altitude of less than 1425 m is reached. The target-image generation system uses an airplane model mounted in a four-axis gimbal system and a television camera with a zoom lens to provide an image of the target projector within the sphere. The system can provide a simulated range between airplanes from 90 m to 13,700 m with a 10-to-1 brightness contrast between the target and the sky-Earth background at minimum range.

Additional special features of the DMS hardware include dimming of the visual display as a function of exposure time at high normal acceleration to simulate blackout, use of an inflatable anti-g garment for simulation of normal-acceleration loads, and use of sound cues to simulate wind, engine, and weapons noise as well as artificial stall warning systems.

The simulation is operated with real-time digital simulation techniques and a CYBER 175 computer. The motions of the evaluation airplane are calculated by using equations of motion with a fixed-interval (1/32 sec) numerical integration technique. The equations describing the flight control system and engine dynamics are also programmed in the digital computer and integrated numerically.

The features of the DMS facility of particular significance to the high-angle-of-attack regime are summarized in figure 4. Additional information and details regarding the DMS are presented in reference 2.

AERODYNAMIC DATA REQUIREMENTS

The application of a piloted simulator to studies of the high angle of attack/stall/spin area is, of course, dependent on the development of a valid mathematical model which generates accurate flight motions and handling qualities. The most important, and most difficult input required in the development of the math model is a representation of the aerodynamic behavior of the airplane. Wind-tunnel and flight-test results have shown that aerodynamic characteristics at high angles of attack are unusually complex, involving nonlinear, configuration-dependent phenomena produced by flow separation and the strong vortex flows associated with such flight conditions. The aerodynamic input data used in the DMS studies have been generated by static and dynamic wind-tunnel tests at Langley and at the Ames Research Center of NASA; and in wind tunnels of the aircraft industry. Some illustrations of the complex and unconventional nature of static and dynamic aerodynamic characteristics exhibited by current fighter configurations are presented in figures 5 and 6.

Representative variations of static wind-tunnel data are illustrated by the directional stability and control characteristics shown in figure 5. The data presented in the upper left of the figure show two aerodynamic phenomena produced by fighter aircraft with long, pointed noses. The first phenomenon consists of marked nonlinearity of C_n with angle of sideslip. In the example shown, the nonlinear variation was a result of airflow separation on a long, pointed fuselage which resulted in a high degree of static directional stability for a limited range of sideslip. At higher values of sideslip, the stabilizing flow condition was eliminated, and the configuration was extremely unstable. The second high angle of attack aerodynamic phenomenon illustrated by these data is the existence of a large out-of-trim or asymmetric value of yawing moment at $\beta = 0^\circ$. The asymmetric moment, which was caused by asymmetric vortex shedding from the pointed nose, was several times larger than the corrective yawing moments produced by rudder deflection. Such asymmetries have been identified as the cause of several out-of-control conditions exhibited by some current fighters. Wind-tunnel tests indicate that the angle of attack for onset of such asymmetries and the relative magnitude of the asymmetries are dependent on the physical features of the nose including fineness ratio, cross-sectional shape, and nose tip angle.

Data presented at the upper right of figure 5 illustrate that the conventional directional stability $C_{n\beta}$ (based on measurements of C_n at $\beta = \pm 5^\circ$) can exhibit large, rapid changes over a relatively small range of angle of attack, and data at the lower middle of figure 5 show that control deflections about one airplane axis (in this case deflection of an all-moveable horizontal tail) can affect stability about other axes. Such results are, of course related to the large aerodynamic interference effects which can exist between airframe components at high angles of attack.

Analysis of flight characteristics of fighter aircraft has indicated that variations in static data such as those presented in figure 5 can have a predominate effect at high angles of attack, and that the representation of such phenomena is absolutely essential to the development of a valid simulation. Experiences with data for several current fighters also indicate that the phenomena at high angles of attack, where there is extensive separated flow, are relatively insensitive to variations in Reynolds number.

Unfortunately, there has been a tendency of aerodynamicists to overlook potential nonlinear and unconventional behavior of dynamic aerodynamic stability parameters; and in many erroneous studies of flight motions the dynamic stability derivatives have been estimated using classical estimation techniques and used as single-valued functions over the range of angle of attack. Wind-tunnel and flight results indicate that, to the contrary, the dynamic derivatives are subject to nonlinear, unconventional effects similar to those previously discussed for static derivatives. Dynamic wind-tunnel test techniques such as forced-oscillation tests (ref. 3) and rotary-spin tests (ref. 4) have been extremely informative regarding the behavior of dynamic aerodynamic characteristics of fighters at high angles of attack and such tests have proven to be the most accurate prediction method for recent fighter designs. Some of the more important trends of dynamic data noted are illustrated in figure 6.

The data for the damping-in-yaw parameter $C_{nr} - C_{n\dot{\beta}} \cos \alpha$ shown at the left of figure 6 show that, as was the case for static directional stability, large variations in damping may occur over a small range of angle of attack, and that extremely large unstable values of damping may be encountered at high angles of attack. As discussed in reference 5, this result is also associated with aerodynamic characteristics produced by long, pointed fuselage forebodies.

Flow separation on highly-swept wings can result in large effects of motion variables (such as frequency and amplitude) during oscillatory motions as illustrated by the results of forced-oscillation tests shown at the upper right of figure 6. The large effect of amplitude of the oscillatory motion on the damping-in-roll parameter $C_{lp} + C_{l\dot{\beta}} \sin \alpha$ would obviously be expected to be of great importance to the behavior of high performance aircraft during rolling motions at high angles of attack.

Finally, wind-tunnel results using rotary-spin balance techniques have indicated that the usefulness of data obtained from forced-oscillation tests may be severely limited due to nonlinear variations of moments with angular rates, as illustrated for C_n at the lower right of figure 6. Indeed, the classical stability

derivative concept becomes questionable if such nonlinearities exist. These nonlinearities are especially prevalent at higher angles of attack associated with spinning, and they represent a major obstacle to the theoretical analysis of complex spin motions.

No discussion of dynamic aerodynamic data requirements would be complete without reference to the representation of the so-called " $\dot{\beta}$ " derivatives (ref. 6). It is relatively well known that the physical constraints of forced-oscillation tests conducted in conventional wind tunnels result in the measurement of dynamic stability parameters (such as $C_{N\dot{\beta}} - C_{N\dot{\beta}} \cos \alpha$) which are combinations of pure rate derivatives and derivatives due to rate-of-change-of sideslip, or $\dot{\beta}$. Except for the use of special wind-tunnels with curved flows or linear oscillation rigs, it appears that separation of the terms is impossible. In the simulator work described in this paper, the dynamic parameters were arbitrarily assumed to be due to pure angular rate only. That is, the parameter $C_{N\dot{\beta}} - C_{N\dot{\beta}} \cos \alpha$ was used in the equations of motion as $C_{N\dot{\beta}}$. Although technically incorrect, the results obtained from simulation have agreed quite well with flight test results for the high α simulations; evidently because either the effect of the $\dot{\beta}$ derivatives was negligible, or because the aircraft motions closely resembled those of the wind tunnel test model. At the present time, exploratory studies are being conducted in a wind tunnel with yawing and rolling flow to further investigate $\dot{\beta}$ derivatives for current fighters.

EVALUATION PROCEDURES

The evaluation procedures that are currently used in stall/departure simulations at Langley have evolved as experience was gained during individual simulation programs. The procedures that have been found most effective reflect considerable care in both the selection of the evaluation maneuvers to be performed on the simulator and in the specification of the ground rules for the pilot to follow in executing the maneuvers and tasks assigned to him. All of the evaluations are performed using a NASA research test pilot who is familiar with air combat maneuvers employed with current fighter airplanes; however, military and contractor test pilots, and fleet pilots often fly the simulation during the course of a study to obtain information prior to airplane test flights, and in some cases, to validate the simulation.

Experience with the simulation of fighter stall/departure characteristics has shown that mild, well-defined evaluation maneuvers can produce misleading results inasmuch as a configuration that behaves fairly well in such slow maneuvers may be violently uncontrollable in the complex and pressing environment of high-g, air combat maneuvering (ACM); therefore, the tasks used should vary considerably in complexity and difficulty. Finally, for purposes of evaluation in comparing the performance of the airplane with modifications, the tasks used must be repeatable. The following evaluation procedures are used to account for the foregoing considerations. In order to force the evaluation pilot to fly the simulated airplane at high angles of attack, the target airplane is programmed to have the same thrust and performance characteristics as the evaluation airplane; however, the target is given idealized high-angle-of-attack stability and control characteristics. When faced with such an adversary, the evaluation pilot must force his airplane to the limit of performance and controllability. The superior target airplane is flown by the evaluation pilot through a series of ACM tasks of varying levels of difficulty while the target motions are simultaneously recorded on magnetic tape for playback later to drive the target model as a tracking task for the evaluation airplane. In this manner, repeatable tasks, ranging from simple tracking tasks to complex, high-g ACM tasks are developed for use in the evaluation.

Normally the simulation evaluation of a particular configuration is conducted in two fairly distinct phases. The first phase of the study involves pilot familiarization with the simulated airplane, evaluation of the "open-loop" departure/spin resistance characteristics of the airplane, and development of the air combat maneuvering (ACM) tasks for use in the second phase of the study. The second phase of the study involves having the pilot(s) fly the simulated airplane (with various control system and airframe configurations) against the various taped ACM tasks. Some of the various maneuvers and tasks that are employed during the simulation evaluation of an airplane configuration are listed in figure 7. During the first phase of a study, the pilot looks for flight conditions or maneuvers in which the simulated airplane exhibits degraded stability and control characteristics. This involves an evaluation of the stall, departure, and spin resistance characteristics. Flights involve both slow and rapid (accelerated) entries into the stall/post-stall angle of attack region and the assessment of applying various control inputs, individually and in combination.

A further assessment of departure/spin resistance is made using several specific maneuvers for stall entry: (1) an aerodynamically-coupled entry, (2) an inertially-coupled entry and (3) a vertical stall entry. Although such maneuvers may not be frequently encountered in air combat, they are usually critical at high angles of attack and should therefore be considered for highly maneuverable fighter airplanes. The aerodynamically-coupled entry consists of the pilot pulling the airplane into a low-speed, high-angle-of-attack condition in a turn and then rapidly reversing the bank angle. The bank-angle change kinematically translates angle of attack into sideslip and a large sideslip excursion will result serving as a critical test of the stability provided by the airframe and flight control system. A condition such as this might occur in combat if the pilot attempted a rapid heading change at very low airspeeds during a near-vertical maneuver. In the inertially-coupled entry, the pilot applies full back stick while rolling rapidly from a moderate angle of attack condition (a roll and pull maneuver). The combined large roll and yaw rates often cause sufficient inertial coupling into the pitch axis to drive the airplane to large angles of attack. The last maneuver, a vertical entry, is accomplished by flying the airplane into a near vertical climb, allowing the airspeed to drop to near zero, and then pushing the nose over to cause a rapid increase in angle of attack. In this case, large excursions in angle of attack will develop and an airplane pitch control system designed to limit angle of attack will be severely tested due to low dynamic pressure and the consequent lack of longitudinal control power.

Several tasks which differ in difficulty and complexity are used to evaluate the airplane during high-angle-of-attack tracking. These tasks are: (1) a steady windup turn with gradually increasing angle of attack up to the maximum trim angle of attack, (2) a bank-to-bank task (or horizontal S) to evaluate rapid rolls and target acquisition, and (3) a complex, vigorous ACM task to evaluate the susceptibility of the simulated airplane to high angle of attack handling qualities problems during aggressive maneuvering.

The rationale behind including the mild tasks, such as the windup turn, and the severe maneuvering tasks is that handling qualities deficiencies that may be manageable for the pilot in a mind, slowly-changing task can become completely unmanageable in a pressing, rapidly changing task where the pilot has insufficient time to compensate for airplane handling deficiencies. The intent is then to find any such situations and attempt to develop airframe or control system improvements to alleviate the deficiencies if possible.

CORRELATION WITH FLIGHT

During the high angle of attack simulations conducted to date on the DMS, seven different airplane configurations have been studied; five of these are depicted in photographs shown in figure 8. Each of these configurations exhibited unique aerodynamic stability and control characteristics at high angles of attack. Also, each of the configurations incorporated significantly different automatic control law concepts, particularly relative to the control system characteristics at high angles of attack. Control system complexities ranged from the simple, limited-authority, rate damper concepts employed in the F-5E to the full-authority, fly-by-wire, maneuver-demand control system and angle of attack-limiter concept used by the YF-16 configuration. The simulations have therefore covered a broad range of aerodynamic and automatic control concepts, many of which have been found to be quite effective in preventing loss-of-control during high angle of attack maneuvering. Some results of these studies are reported in references 7 to 9.

Most of the simulations were conducted early in the airplane development programs for the specific aircraft, and results were obtained prior to actual flight tests. In each case, military and industry test pilots were able to experience invaluable exposure to the anticipated high-angle-of-attack characteristics of the aircraft before entering into flight tests to determine spin susceptibility.

An important measure of the value of results produced from piloted simulations is whether or not problems and solutions identified in simulation have also been verified in full scale flight testing. It is not the intent of this paper to present a comprehensive set of detailed simulation results for comparison with flight tests but rather to point out the problem areas where application of the simulation techniques described herein have proven successful and predicted characteristics in general agreement with flight test experience. This correlation covers two areas: the correlation between high angle of attack problems experienced during simulation and flight tests; and the effectiveness of solutions to these problems. Some of the specific areas of correlation are indicated in figure 9.

The general problems identified during simulation and the critical maneuvers identified for each configuration studied on the DMS to date have been found to correlate extremely well with flight test results. This correlation covers such areas as the decrease in tracking capability of a configuration due to wing rock, inertially-coupled departures, and loss-of-control from such problems as excessive adverse yaw generated by roll control surfaces. Airframe and automatic control concepts developed in simulation for improving high angle of attack characteristics have also proven out in flight tests. For example, the development of a lateral-stick-to-rudder interconnect concept to alleviate roll-reversals due to adverse yaw at high angles of attack was one such successful project.

Another area of correlation between simulation and flight is that of piloting problems peculiar to flight at high angles of attack encountered during the development of advanced high angle of attack control concepts. One control concept (known as stability-axis rolling) is that of rolling the airplane about the flight path at high angles of attack to minimize sideslip excursions. However, in causing the aircraft to roll about the velocity vector, the control system both yaws and rolls the airplane in response to a pilot roll control input. It was found that pilots used to rolling about the airplane longitudinal body axis were very disconcerted by the substantial initial yawing motion which they observed in response to what they thought was a pure roll control input. It was found, both in simulation and in flight, that the concept was totally acceptable after the pilots adapted to this new control concept.

INFLUENCE OF DYNAMIC STABILITY PARAMETERS

As might be expected from knowledge of the configuration-dependent nature of high angle of attack stability and control characteristics, the relative importance of aerodynamic dynamic stability parameters has varied considerably. For example, in some of the simulator studies, virtually all of the major factors affecting high angle of attack handling characteristics were related to static aerodynamic phenomena, and the effects of the dynamic parameters were essentially negligible. On the other hand, several configurations have indicated a susceptibility to handling deficiencies related to the dynamic parameters.

One specific maneuver limitation resulting from dynamic aerodynamic phenomena is wing rock, which is characterized by uncommanded limit-cycle roll oscillations at high angles of attack. The motions tend to be periodic in nature, and the roll amplitudes reached during the rolling motions may reach large magnitudes, resulting in a serious degradation in tracking capability. A flight test time history of a current fighter configuration encountering wing rock during a tracking-task is presented in figure 10. The pilot initiated the maneuver by banking the aircraft into a left turn and increasing g loading by pulling back on the control stick while avoiding intentional lateral stick inputs. As angle of attack increased, the airplane suddenly exhibited large-amplitude wing rock which completely negated the tracking capability of the pilot. In order to regain tracking, the pilot reduced angle of attack and had to reacquire his target.

The seriousness of the degradation in tracking which may be experienced due to wing rock is illustrated in figure 11. Data are presented which indicate representative values of C_L for onset of buffet and wing rock for a recent fighter configuration. Data are also presented indicating the relative magnitude of normal accelerometer readings of buffet as measured at a wing tip station. As shown at the right side of figure 11, the effect of buffet on miss distance during tracking was noticeable, although relatively small. However, when the aircraft encountered wing rock, the tracking error became very large, and the pilot was only able to track for brief periods of time.

Recent experience with fighter configurations exhibiting wing rock indicates that the phenomenon may also have large effects on the performance of flight control systems designed to enhance high angle of attack handling characteristics. For example, the implementation of an aileron-to-rudder interconnect concept may result in aggravation and excitation of the wing rock as a result of sideslip generated by rudder inputs at high angles of attack. In one case, a fighter configuration had been modified to incorporate a stability augmentation system designed to alleviate wing rock tendency which was easily aggravated by the pilot during precise, closed-loop tracking tasks. Unfortunately, the control system modification not only failed to suppress the wing rock problem but inadvertently seriously degraded the airplane departure/spin resistance. After sufficient piloted simulation study and correlation with flight tests, an improved automatic stability and control augmentation system was designed which successfully suppressed the airplane wing rock tendency while providing a high level of departure and spin resistance.

Considerable research has been conducted in the U.S. and England on the identification and aerodynamic causes of wing rock. Wind-tunnel tests and flight studies at subsonic and transonic speeds have indicated several potential causes of wing rock, as indicated in figure 12. At the present time, additional research is believed to be needed to verify that aerodynamic hysteresis is a major factor causing wing rock; but there is little doubt that aerodynamic nonlinearities, shock-induced separation at transonic speeds, and loss of roll damping near wing stall are major factors.

At subsonic speeds, it appears that the major factor producing wing rock is loss of roll damping. Some results of wind-tunnel forced-oscillation tests of a current fighter with wing rock are presented in figure 13. The data show that the magnitude of $C_{lp} + C_{l\dot{\beta}} \sin \alpha$ decreased markedly at angles of attack near wing stall, resulting in a loss of roll damping near $\alpha = 12^\circ$. The magnitude of $C_{l\dot{\beta}}$, however, remained large near $\alpha = 12^\circ$. As a result of these aerodynamic trends, the aircraft exhibited wing rock in the angle of attack region indicated.

Although the foregoing loss of roll damping can be identified as a cause of wing rock, the mathematical modelling of such aerodynamic behavior normally requires additional data for valid simulation of fighters at high angles of attack. In particular, wind-tunnel studies have shown that the effects of frequency and amplitude of the oscillatory motion experienced during wing rock can have very large effects on the magnitude of damping in roll. For example, shown in figure 14 are results of forced oscillation tests over a range of reduced frequency and oscillation amplitude for a fighter configuration at $\alpha = 30^\circ$. The large effects of frequency and amplitude would be expected to be extremely important in the calculation and theoretical analysis of wing rock. It has been necessary in most simulator studies at Langley to obtain similar data for valid simulation results, and it is extremely important to recognize the existence of such effects in any theoretical or simulator study of high angle of attack flight dynamics.

With the necessary supporting forced-oscillation test results, it has been possible to obtain simulator results which are in relatively good agreement with flight test results. For example, shown in figure 15 are time histories which indicate the correlation of wing-rock motions obtained for a recent fighter.

CONCLUDING REMARKS

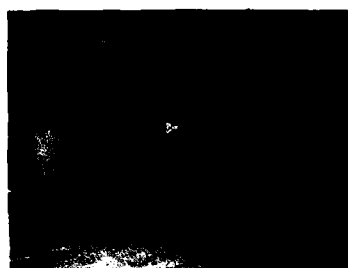
The NASA-Langley high angle of attack/stall/spin research program on military configurations has resulted in a considerable amount of experience in conducting piloted simulations to study the high angle of attack characteristics of current fighter configurations. Piloted simulation has proven to be an extremely valuable research tool for the analysis of these characteristics, and it will continue to be used to explore the behavior of advanced aerodynamic configurations and to develop automatic control concepts to provide improved high angle of attack characteristics for both current and advanced high-performance airplane configurations. The value of fixed-base piloted simulation as a tool for studying airplane characteristics has been recognized and utilized by most military airplane manufacturers in the U.S., and they are now placing emphasis on conducting such simulations during the airplane development cycle.

REFERENCES

1. Moore, Frederick L.; Anglin, Ernie L.; Adams, Mary S.; Deal, Perry L.; and Person, Lee H., Jr.: Utilization of a Fixed-Base Simulator to Study the Stall and Spin Characteristics of a Fighter Airplane. NASA TN D-6117, 1971.
2. Ashworth, B.R.; and Kahlbaum, William M., Jr.: Description and Performance of the Langley Differential Maneuvering Simulator. NASA TN D-7304, 1973.
3. Grafton, Sue B.; and Anglin, Ernie L.: Dynamic Stability Derivatives at Angles of Attack from -5° to 90° for a Variable-Sweep Fighter Configuration with Twin Vertical Tails. NASA TN D-6909, 1972.
4. Chambers, Joseph R.; Bowman, James S.; and Malcolm, Gerald N.: Stall/Spin Test Techniques Used by NASA. Paper presented at the AGARD Flight Mechanics Panel Specialist's Meeting on Stall/Spin Problems of Military Aircraft, Brussels, Belgium, Nov. 18-21, 1975.
5. Chambers, Joseph R.; Gilbert, William P.; and Grafton, Sue B.: Results of Recent NASA Studies on Spin Resistance. Paper presented at AGARD Flight Mechanics Panel Specialist's Meeting on Stall/Spin Problems of Military Aircraft, Brussels, Belgium, Nov. 18-21, 1975.
6. Lee, Paul L., Jr.; Graham, A. Bruce; and Chambers, J. R.: Summary of Information on Low-Speed Aerodynamic Derivatives Due to Rate of Change of Sideslip $\dot{\beta}$. NASA TN D-7972, 1975.
7. Lee, Paul L., Jr.; Gilbert, William P.; Nguyen, Luat T.; and VanGunst, Roger W.: Simulator Study of Applications of Stall and Spin Prevention Concepts to a Variable-Sweep Fighter Airplane. NASA TM X-2928, 1975.

8. Gilbert, William P.; Nguyen, Luat T.; and VanGunst, Roger W.: Simulator Study of the Effectiveness of an Automatic Control System Designed to Improve the High-Angle-of-Attack Characteristics of a Fighter Airplane. NASA TND-8176, 1976.

9. Nguyen, Luat T.; Gilbert, William P.; and VanGunst, Roger W.: Simulator Study of the Departure Resistance of a Lightweight Fighter Airplane with Twin Vertical Tails. NASA TM X-3510, 1977.



STALL AND DEPARTURE



DEVELOPED SPIN AND RECOVERY



SPIN ENTRY



AERODYNAMICS
AND THEORETICAL ANALYSIS



SPIN SUSCEPTIBILITY

Figure 1.- Scope of stall/spin research test techniques used by NASA-Langley.

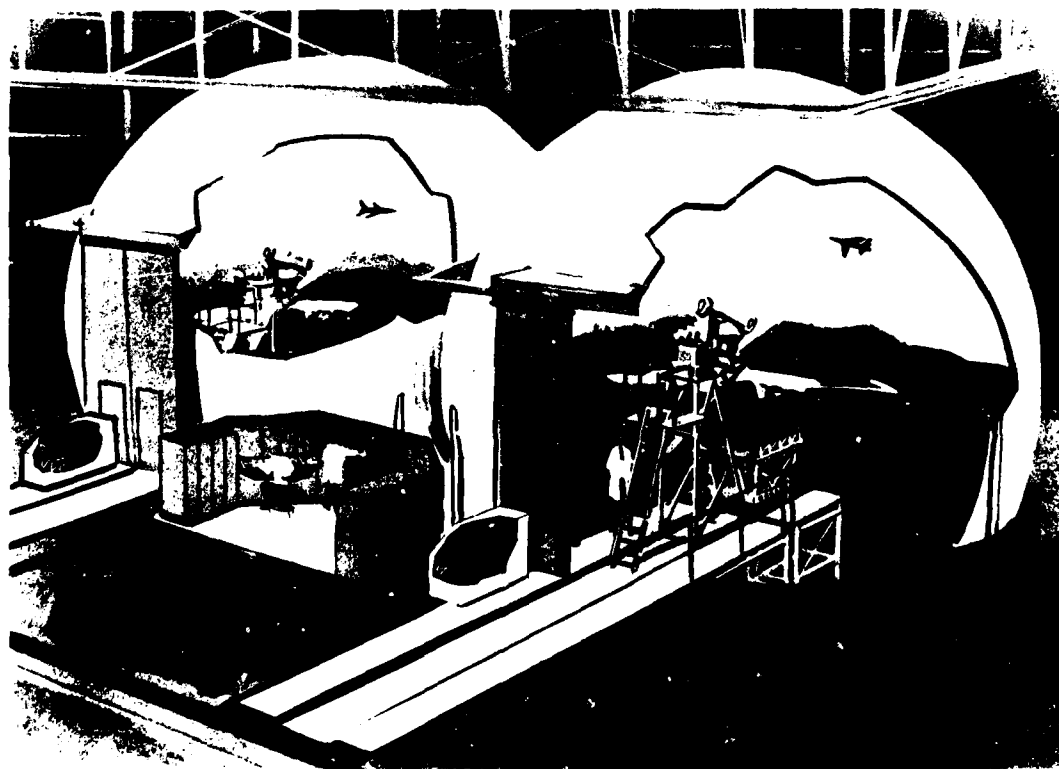


Figure 2.- Sketch of the Langley Differential Maneuvering Simulator (DMS).



Figure 3.- Visual display during simulated engagement.

- REALISTIC COCKPIT/VISUAL REPRESENTATION
 - STICK FORCE/FEEL
 - BUFFET
 - G SIMULATION (BLACKOUT AND G-SUIT)
- REALISTIC EVALUATION TASKS
 - TAPED, REPEATABLE TRACKING TASKS
 - ONE-ON-ONE MANEUVERS
- COMPREHENSIVE DATA PACKAGE

Figure 4.- Features of the Differential Maneuvering Simulator (DMS).

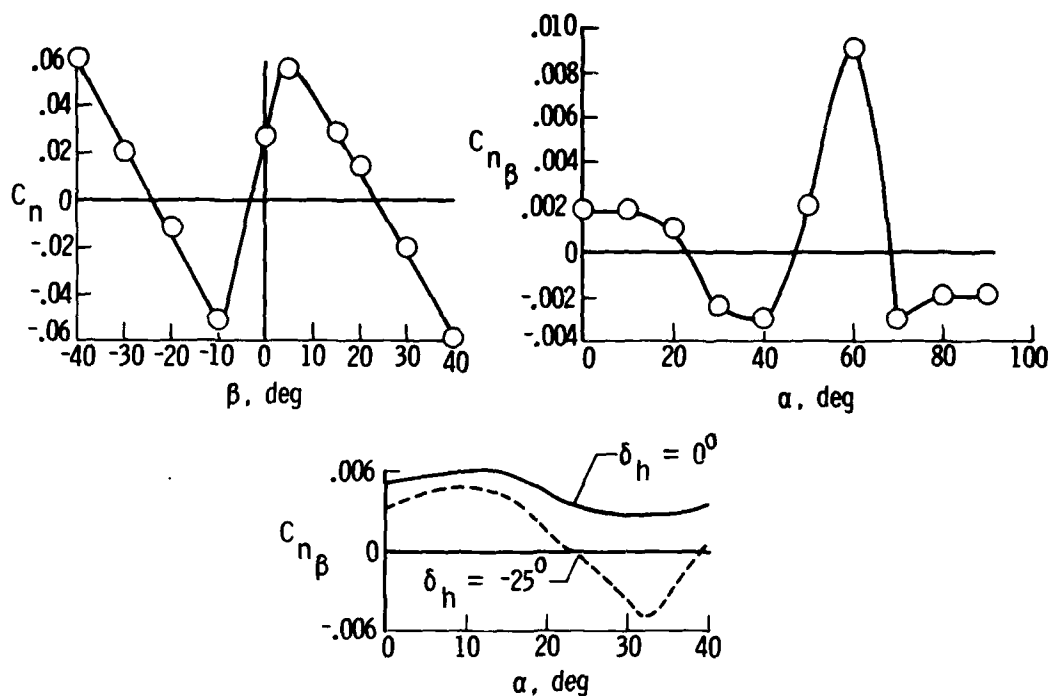


Figure 5.- Typical variations of static aerodynamic data at high angles of attack.

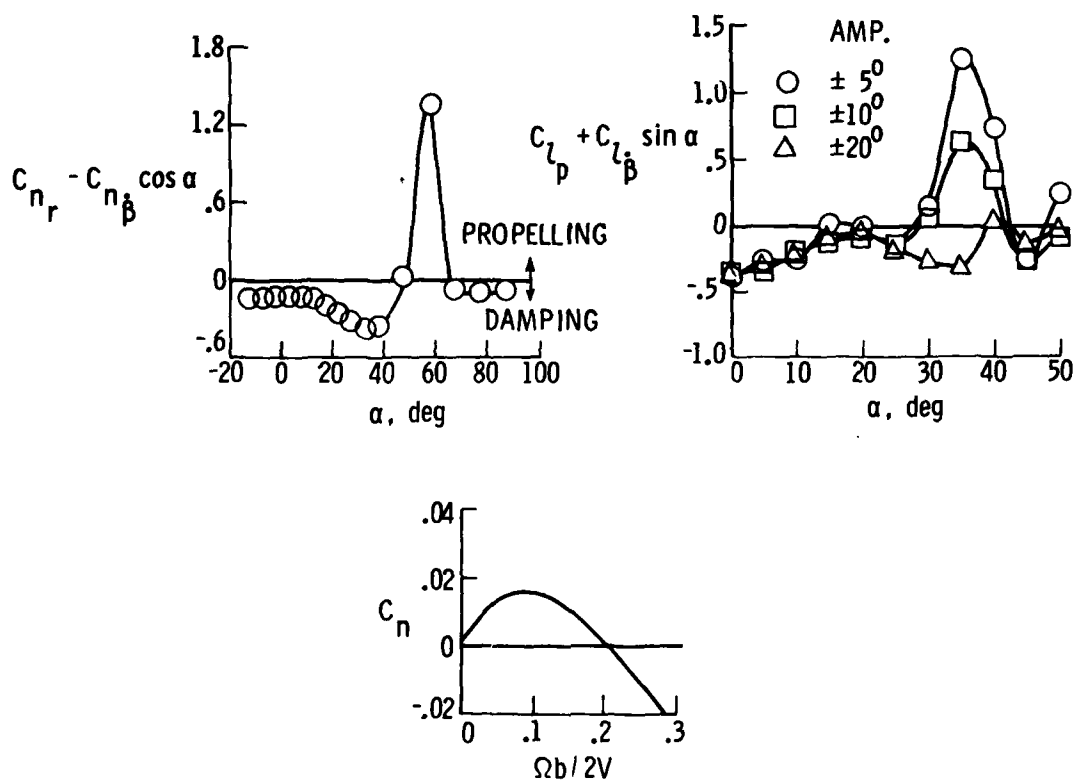


Figure 6.- Typical variations of dynamic aerodynamic data at high angles of attack.

- STALL ENTRIES - IG AND ACCELERATED
 - SYMMETRIC AND WINDUP TURNS
 - ADVERSE CONTROLS
 - MANEUVER CONTROLS
- SPECIAL ENTRY MANEUVERS
 - AERODYNAMICALLY COUPLED
 - INERTIALLY COUPLED
 - VERTICAL
- REPEATABLE TRACKING TASKS
 - STEADY TURNS
 - BANK-TO-BANK REVERSALS
 - COMPLEX ACM

Figure 7.- Simulation evaluation maneuvers.



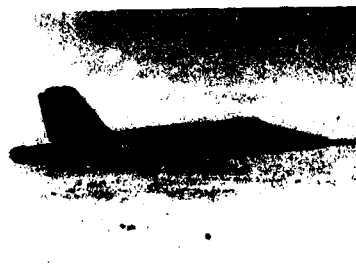
F-14



F-5E



B-1



YF-17



YF-16

Figure 8.- Configurations studied at high angles of attack in DMS.

- PROBLEMS

NOSE SLICE
WING ROCK
ADVERSE YAW
COUPLING
PITCH UP
CRITICAL FLIGHT CONDITIONS

- SOLUTIONS

CONTROL INTERCONNECTS
AIRFRAME MODS
MANEUVER LIMITING

Figure 9.- Areas of correlation between results obtained in simulation and flight.

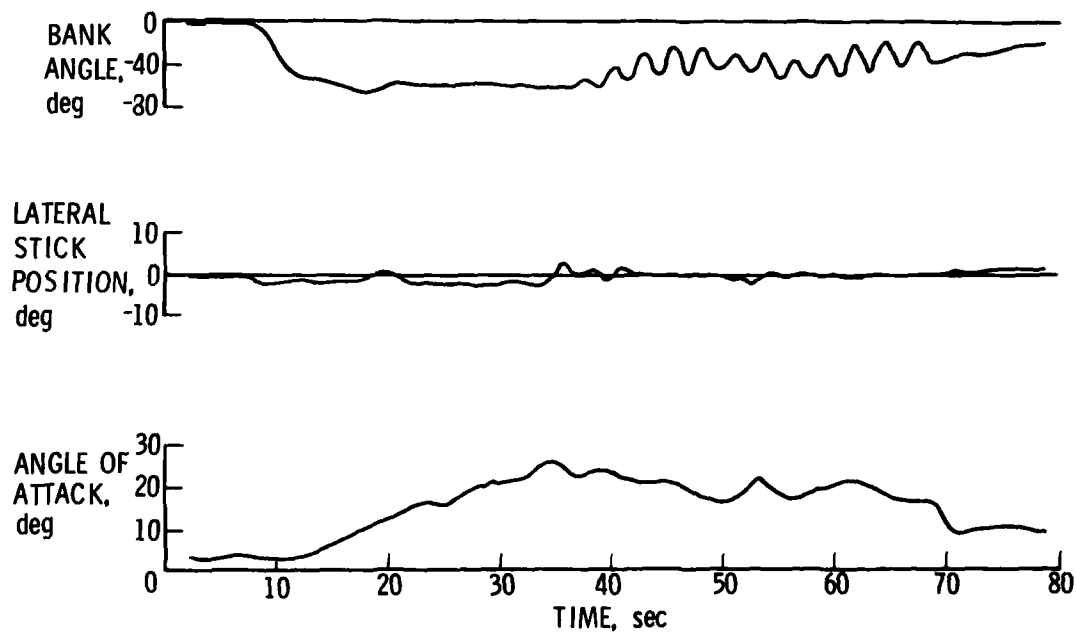


Figure 10.- Flight record of fighter encountering wing rock.

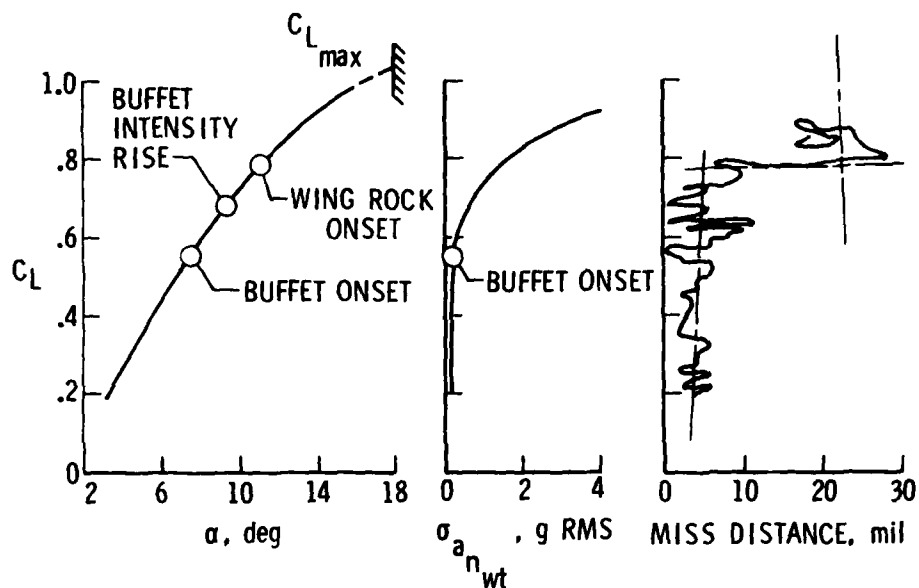


Figure 11.- Effects of buffet and wing rock on tracking accuracy.

- AERO HYSTERESIS
- STATIC AERO NONLINEARITIES
- SHOCK-INDUCED SEPARATION
- LOSS OF ROLL DAMPING

Figure 12.- Some potential aerodynamic causes of wing rock.

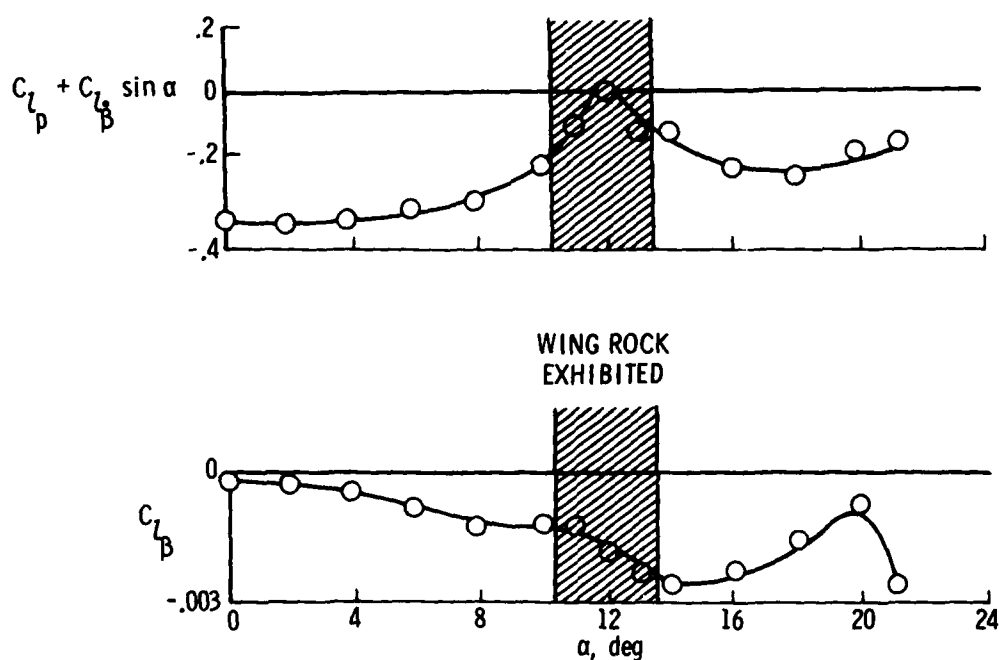


Figure 13.- Static and dynamic lateral aerodynamic characteristics for fighter with wing rock.

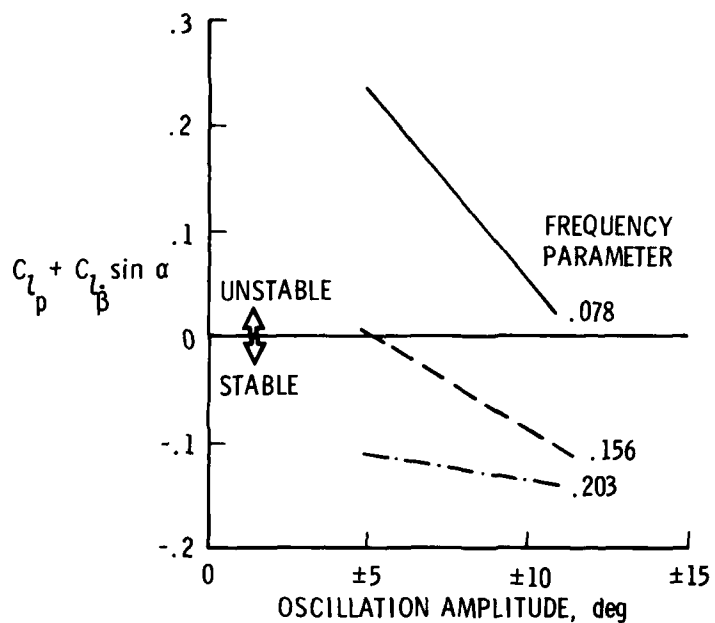


Figure 14.- Variation of damping-in-roll parameter with frequency and amplitude of oscillation. $\alpha = 30^\circ$.

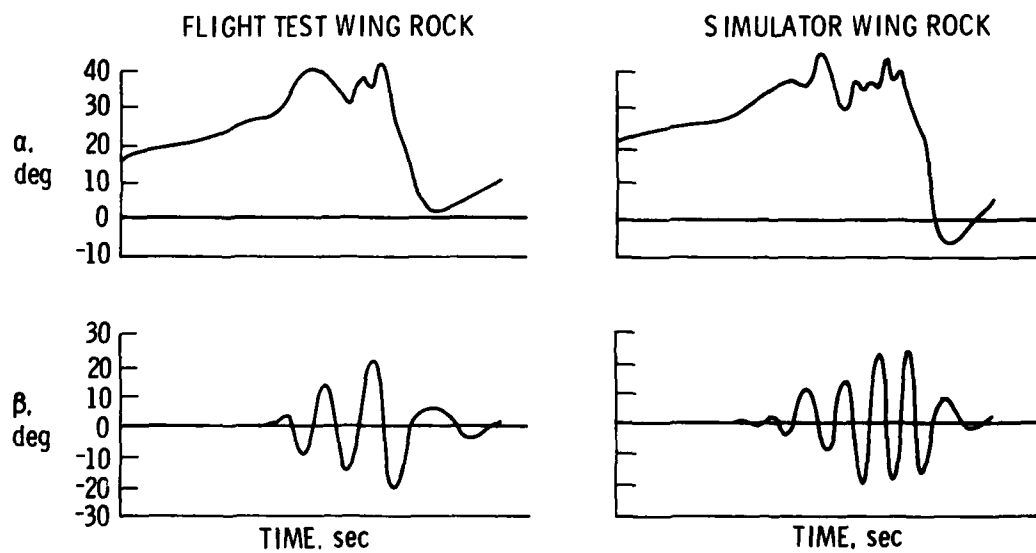


Figure 15.- Correlation of wing-rock motions experienced in flight and simulation.

SENSITIVITY OF AIRCRAFT MOTION TO AERODYNAMIC CROSS-COUPLING AT HIGH ANGLES OF ATTACK

by

W. H. Curry

Member of Technical Staff

Sandia Laboratories

Albuquerque, NM 87115 USA

and

K. J. Orlik-Rickemann

Head, Unsteady Aerodynamics Laboratory

National Aeronautical Establishment

Ottawa, Ontario K1A 0R6, Canada

SUMMARY

In order to ascertain whether the inclusion in the equations of motion of certain aerodynamic cross-coupling terms may be important for correct prediction of the motion of an aircraft at high angles of attack, a study was undertaken in which the sensitivity of the motion time histories to these various terms was examined using a six-degree-of-freedom simulation on a hybrid computer. Both straight and turning flight conditions were included, and to simplify the problem, the equations were formulated for the constant-thrust, stick-fixed condition. The aerodynamic cross-coupling derivatives were considered both as constants and as locally linearized functions of angle of attack. The effects of varying certain derivatives from an assumed nominal set on the response of the aircraft to an initial perturbation are presented graphically. This limited study indicates that the dynamic cross-coupling moment derivatives due to pitching have a marked effect, while those due to yawing are relatively unimportant.

NOMENCLATURE

a	acceleration
b	wing span
\bar{c}	wing mean aerodynamic chord
C_L	$L/(\bar{q}Sb)$
C_m	$M/(\bar{q}S\bar{c})$
C_n	$N/(\bar{q}Sb)$
C_x, C_y, C_z	(aerodynamic force components)/ $\bar{q}S$
F	force
g	acceleration of gravity
h	altitude
I	moment or product of inertia
L	aerodynamic rolling moment
m	mass
M	aerodynamic pitching moment
N	aerodynamic yawing moment
n	aircraft load factor
p	angular velocity about roll axis
q	angular velocity about pitch axis
\bar{q}	dynamic pressure
r	angular velocity about yaw axis
S	gross wing area
T	thrust
t	time
u, v, w	velocity components in x, y and z directions, respectively
V	freestream velocity
X, Y, Z	earth fixed orthogonal axes with origin at origin of flight and with Z-axis pointing down
x, y, z	orthogonal system of body axes with origin at the aircraft CG and with x-axis pointing forward
α	angle of attack
$\Delta\alpha$	difference between α and α_T
β	angle of sideslip
ϕ	aircraft bank angle
ϕ_A	aerodynamic roll angle
γ_H, γ_V	horizontal and vertical flight path angles, respectively
δ	$\arctan(\tan \alpha_0 \cos \beta_0)$
ψ, θ, ϕ	Euler angular rotations in yaw, pitch, and roll, respectively

Subscripts:

o	refers to value at time zero
T	refers to trimmed flight condition
x, y, z	refer to x, y or z body axis
$\alpha, \beta, \dot{\alpha}, \dot{\beta}, p, q, r$	denote derivative (of a moment) with respect to α, β , etc.

Superscripts:

A dot indicates time derivative

Traditional Moment Derivatives:

$$C_{L\beta} = \partial C_L / \partial \beta$$

$$C_{m\alpha} = \partial C_m / \partial \alpha$$

$$C_{n\beta} = \partial C_n / \partial \beta$$

$$C_{L\dot{\beta}} = \partial C_L / \partial (\dot{\beta}b/2V)$$

$$C_{m\dot{\alpha}} = \partial C_m / \partial (\dot{\alpha}\bar{c}/2V)$$

$$C_{n\dot{\beta}} = \partial C_n / \partial (\dot{\beta}b/2V)$$

$$C_{Lp} = \partial C_L / \partial (pb/2V)$$

$$C_{mq} = \partial C_m / \partial (q\bar{c}/2V)$$

$$C_{np} = \partial C_n / \partial (pb/2V)$$

$$C_{Lr} = \partial C_L / \partial (rb/2V)$$

$$C_{nr} = \partial C_n / \partial (rb/2V)$$

Cross-Coupling Moment Derivatives:

$$C_{L\alpha} = \partial C_L / \partial \alpha$$

$$C_{m\beta} = \partial C_m / \partial \beta$$

$$C_{n\alpha} = \partial C_n / \partial \alpha$$

$$C_{L\dot{\alpha}} = \partial C_L / \partial (\dot{\alpha}\bar{c}/2V)$$

$$C_{m\dot{\beta}} = \partial C_m / \partial (\dot{\beta}b/2V)$$

$$C_{n\dot{\alpha}} = \partial C_n / \partial (\dot{\alpha}\bar{c}/2V)$$

$$C_{Lq} = \partial C_L / \partial (q\bar{c}/2V)$$

$$C_{mp} = \partial C_m / \partial (pb/2V)$$

$$C_{nq} = \partial C_n / \partial (q\bar{c}/2V)$$

$$C_{mr} = \partial C_m / \partial (rb/2V)$$

Corresponding force derivatives are defined in a similar fashion. All derivatives are referenced to a system of body axes. The "rotary" derivatives are those with respect to p, q, r ; and the "acceleration" derivatives are those with respect to $\dot{\alpha}$ and $\dot{\beta}$. This is in agreement with recent terminology as explained, for example, in Ref. 1.

1. INTRODUCTION

Modern military aircraft are designed to maneuver at relatively high angles of attack and therefore are subjected to conditions where the flow becomes highly asymmetric. It has been realized for some time (e.g., Ref. 2) that under such circumstances, the aerodynamic cross-coupling between the longitudinal and the lateral degrees of freedom may become important. More recently (Ref. 3), in a joint program between the National Aeronautics and Space Administration (NASA) in the USA, the National Aeronautical Establishment (NAE) in Canada, static and dynamic cross-coupling derivatives due to pitching and yawing have actually been measured in a wind tunnel, and some dynamic cross-coupling terms were found to be of the same order of magnitude as the well-established damping terms in the equations of motion. In these tests, cross-coupling derivatives were measured for a range of angles of attack up to 40 degrees, and considerable variations of the various derivatives with angle of attack were observed. It was found that the derivatives at high angles of attack were sometimes many times larger than at low angles of attack and that in certain narrow ranges of angles of attack a very rapid variation in a derivative could occur.

In order to ascertain whether the inclusion in the Newtonian equations of motion of certain aerodynamic cross-coupling terms may be important for correct prediction of the motion of an aircraft, a study was required where the sensitivity of the predicted motion time histories to these various terms could be examined. Such a study was undertaken as a joint project between the Sandia Laboratories in the USA, and the NAE. An earlier sensitivity study with similar objectives was described in Ref. 4 but, because of the approach used and the cross-coupling data employed (which were based on preliminary findings of the present second author and were later found to be far too small), the results of that study are believed to be incorrect and should be disregarded.

In the present investigation, a hybrid computer was utilized for the six-degree-of-freedom flight simulations required to evaluate the effects of the aerodynamic cross-coupling derivatives. The aircraft chosen for the investigation was hypothetical, but possessed physical characteristics representative of contemporary high performance configurations. Flight conditions were a straight course and a 2 g coordinated turn at constant altitude with a trim angle of attack of 0.576 rad (33 deg). This paper describes the approach used to implement the simulation, includes pertinent motion histories, and comments on the effects of the various aerodynamic derivatives.

2. AIRCRAFT CHARACTERISTICS

The representative military aircraft defined for this investigation had physical characteristics as follows:

b	11.89 m	(39 ft)
\bar{c}	4.88 m	(16 ft)
I_X	366.10 kg m ²	(27000 slug ft ²)
I_Y	162700 kg m ²	(120000 slug ft ²)
I_Z	183000 kg m ²	(135000 slug ft ²)
I_{XZ}	6780 kg m ²	(5000 slug ft ²)
mass	17510 kg	(1200 slugs)
S	164.6 m	(540 ft ²)

For the specified trim angle of attack of 0.576 rad (33 deg) and trim angle of sideslip of zero, the basic force coefficients were given the following values:

$$C_x = -0.04$$

$$C_y = 0$$

$$C_z = -0.841$$

A nominal set of aerodynamic derivatives (per radian) was designated as shown below.

$$C_{l_\alpha} = 0$$

$$C_{m_\alpha} = -0.6$$

$$C_{n_\alpha} = 0.05$$

$$C_{l_\beta} = -0.2$$

$$C_{m_\beta} = -0.1$$

$$C_{n_\beta} = 0.25$$

$$C_{l_p} = -0.3$$

$$C_{m_p} = 0$$

$$C_{n_p} = 0.2$$

$$C_{l_q} = 0.5-30\Delta\alpha$$

$$C_{m_q} = -7-120\Delta\alpha$$

$$C_{n_q} = 0.5-60\Delta\alpha$$

$$C_{l_{\dot{\alpha}}} = 0.5-30\Delta\alpha$$

$$C_{m_{\dot{\alpha}}} = -7-120\Delta\alpha$$

$$C_{n_{\dot{\alpha}}} = 0.5-60\Delta\alpha$$

$$C_{l_r} = 0.25$$

$$C_{m_r} = 0.1-25\Delta\alpha$$

$$C_{n_r} = -0.15-6\Delta\alpha$$

$$C_{l_{\dot{\beta}}} = -0.3$$

$$C_{m_{\dot{\beta}}} = -0.1-25\Delta\alpha$$

$$C_{n_{\dot{\beta}}} = 0.2-6\Delta\alpha$$

$$C_{y_\beta} = -0.8$$

$$C_{z_\alpha} = -2$$

$$C_{z_q} = -13$$

$$C_{z_{\dot{\alpha}}} = -13$$

The traditional derivatives were primarily based on various low speed NASA experiments (Refs. 5,6) on a representative aircraft configuration. The cross-coupling derivatives were based on data (Refs. 3,7) which were obtained on a simplified aircraft configuration at a higher speed. Since no other applicable data on aerodynamic cross-coupling is known to exist, this inconsistency had to be accepted. The derivative C_{m_p} and all dynamic force derivatives with the exception of C_{z_q} and $C_{z_{\dot{\alpha}}}$ were assumed to be zero, partly to simplify the analysis and partly because their values, in most cases, were unknown. All purely rotary derivatives (such as C_{m_q} , C_{n_q} , etc.) and all acceleration derivatives (such as $C_{m_{\dot{\alpha}}}$, $C_{n_{\dot{\alpha}}}$, etc.) were assigned nominal values in such a way that their combined values (that is $C_{m_q} + C_{m_{\dot{\alpha}}}$, etc.) for

oscillation around a fixed body axis agreed with the measured ones. In most cases it was assumed that each part contributed equally to the combined value. Certain derivatives were locally linearized around the designated trim angle of attack of 0.576 rad (33 deg) where many significant changes in these derivatives occurred. The nominal slopes selected corresponded approximately to the largest slopes measured for a given derivative (Ref. 7). In this study, the range of $\Delta\alpha$ for the nominal slopes was limited to about ± 0.05 rad (± 3 deg). When performing simulations with constant coefficients, the above set of derivatives was used with $\Delta\alpha$ terms excluded. When performing simulations with locally linearized derivatives zeroed or doubled, both the constant and slope terms were zeroed or doubled.

3. INITIAL CONDITIONS

Effects of the aerodynamic cross-coupling derivatives were investigated for straight, level flight ($n = 1$), and for steady 2 g turning flight ($n = 2$). The sequence of equations used to determine nominal values of parameters for these conditions was as follows:

$$\bar{q}_0 = mg / [-C_z(\sin \alpha_0 \tan \alpha_0 + \cos \alpha_0)S] \quad (1)$$

$$T = (-C_z \tan \alpha_0 - C_x) \bar{q}_0 S \quad (2)$$

$$\rho_0 = 0.002377 e^{-(h_0/33300)} \quad (3)$$

$$V_0 = (2 \bar{q}_0 / \rho_0)^{1/2} \quad (4)$$

$$\phi_0 = \arccos(1/n) \quad (5)$$

$$\theta_0 = \arcsin(\sin \phi_0 \sin \beta_0 + \cos \phi_0 \sin \delta \cos \beta_0) \quad (6)$$

$$\psi_0 = \arcsin[(\sin \phi_0 \sin \delta \cos \beta_0 - \cos \phi_0 \sin \beta_0) / \cos \theta_0] \quad (7)$$

$$\phi_0 = \arcsin[(\sin \phi_0 \cos \beta_0 - \cos \phi_0 \sin \delta \sin \beta_0) / \cos \theta_0] \quad (8)$$

$$\dot{\psi}_0 = g \sin \phi_0 / [(\cos \phi_0 \cos \alpha_0 + \tan \theta_0 \sin \alpha_0) V_0] \quad (9)$$

$$p_o = -\dot{\psi}_o \sin \theta_o \quad (10)$$

$$q_o = \dot{\psi}_o \cos \theta_o \sin \phi_o \quad (11)$$

$$r_o = \dot{\psi}_o \cos \theta_o \cos \phi_o \quad (12)$$

$$C_{z_T} = C_{z_c} - C_{z_q} (q_o \bar{c} / 2V_o) \quad (13)$$

$$C_{l_T} = -C_{l_p} (p_o b / 2V_o) - C_{l_q} (q_o \bar{c} / 2V_o) - C_{l_r} (r_o b / 2V_o) \quad (14)$$

$$C_{m_T} = -C_{m_q} (q_o \bar{c} / 2V_o) - C_{m_r} (r_o b / 2V_o) \quad (15)$$

$$C_{n_T} = -C_{n_p} (p_o b / 2V_o) - C_{n_r} (r_o b / 2V_o) - C_{n_q} (q_o \bar{c} / 2V_o) \quad (16)$$

For the trim angle of attack of 0.576 rad (33 deg), and for an altitude of 9960 m (32670 ft), consistent with assumed values of V_o and \bar{q}_o , calculations using Eqs. (1)-(16) yield the following set of parameter values for unperturbed straight and 2 g turning flight:

Parameter	Straight, Level Flight ($n = 1$)	Coordinated 2 g Turn ($n = 2$)	Units
\bar{q}_o	3414 (71.3)	6828 (142.6)	Pa (lbs/ft ²)
T	100400 (22570)	200800 (45140)	N (lbs)
ρ_o	0.4593 (0.000891)	0.4593 (0.000891)	kg/m ³ (slugs/ft ³)
V_o	121.9 (400.0)	172.4 (565.7)	m/s (ft/sec)
$\dot{\psi}_o$	0	1.047 (60.0)	rad (deg)
θ_o	0.576 (33.0)	0.2758 (15.80)	rad (deg)
ψ_o	0	0.5123 (29.35)	rad (deg)
ϕ_o	0	1.1199 (64.17)	rad (deg)
$\dot{\psi}_o$	0	0.09851 (5.644)	rad/sec (deg/sec)
p_o	0	-0.02683 (1.537)	rad/sec (deg/sec)
q_o	0	0.08531 (4.888)	rad/sec (deg/sec)
r_o	0	0.04131 (2.367)	rad/sec (deg/sec)
C_{z_T}	-0.841	-0.825316	
C_{l_T}	0	-0.001237	
C_{m_T}	0	0.008303	
C_{n_T}	0	-0.000205	

It will be noted that the thrust-to-weight ratio for the steady 2 g turn is 1.17 which is borderline for current aircraft designs.

Perturbations to the nominally steady flight condition were introduced by initializing the simulations with an angle of attack or sideslip different from the trimmed value by 0.05 rad (3 deg). Eqs. (5)-(8) were used to calculate the new initial values for the Euler angles.

4. SIMULATION MODELING

The set of equations used to model the aircraft flight simulation on the hybrid computer is as follows (e.g., see Ref. 8):

a) Motion Equations

$$\dot{u} = \Sigma F_x / m - q w + r v \quad (17)$$

$$\dot{v} = \Sigma F_y / m - r u + p w \quad (18)$$

$$\dot{w} = \Sigma F_z / m - pv + qu \quad (19)$$

$$\dot{p} = [\Sigma L - (I_z - I_y)qr + I_{xz}(\dot{r} + pq)] / I_x \quad (20)$$

$$\dot{q} = [\Sigma M - (I_x - I_z)rp + I_{xz}(r^2 - p^2)] / I_y \quad (21)$$

$$\dot{r} = [\Sigma N - (I_y - I_x)pq + I_{xz}(\dot{p} - qr)] / I_z \quad (22)$$

b) Loading Equations

$$\Sigma F_x = T - mg \sin \theta + C_x \bar{q} S \quad (23)$$

$$\Sigma F_y = mg \cos \theta \sin \phi + C_y \bar{q} S \quad (24)$$

$$\Sigma F_z = mg \cos \theta \cos \phi + [C_{z_T} + C_{z_\alpha}(\alpha - \alpha_T) + C_{z_q}(\dot{q}\bar{c}/2V) + C_{z_{\dot{\alpha}}}(\dot{\alpha}\bar{c}/2V)]\bar{q} S \quad (25)$$

$$\begin{aligned} \Sigma L = [C_{L_T} + C_{L_\alpha}(\alpha - \alpha_T) + C_{L_\beta} \beta + C_{L_p}(pb/2V) + C_{L_q}(q\bar{c}/2V) \\ + C_{L_{\dot{\alpha}}}(\dot{\alpha}\bar{c}/2V) + C_{L_r}(rb/2V) + C_{L_{\dot{\beta}}}(\dot{\beta}b/2V)]\bar{q} S b \end{aligned} \quad (26)$$

$$\begin{aligned} \Sigma M = [C_{m_T} + C_{m_\alpha}(\alpha - \alpha_T) + C_{m_\beta} \beta + C_{m_p}(pb/2V) + C_{m_q}(q\bar{c}/2V) \\ + C_{m_{\dot{\alpha}}}(\dot{\alpha}\bar{c}/2V) + C_{m_r}(rb/2V) + C_{m_{\dot{\beta}}}(\dot{\beta}b/2V)]\bar{q} S \bar{c} \end{aligned} \quad (27)$$

$$\begin{aligned} \Sigma N = [C_{n_T} + C_{n_\beta} \beta + C_{n_\alpha}(\alpha - \alpha_T) + C_{n_p}(pb/2V) + C_{n_r}(rb/2V) \\ + C_{n_{\dot{\beta}}}(\dot{\beta}b/2V) + C_{n_q}(q\bar{c}/2V) + C_{n_{\dot{\alpha}}}(\dot{\alpha}\bar{c}/2V)]\bar{q} S b \end{aligned} \quad (28)$$

c) Auxiliary Equations

$$\dot{X} = u \cos \psi \cos \theta + v (\cos \psi \sin \theta \sin \phi - \sin \psi \cos \phi) + w (\cos \psi \sin \theta \cos \phi + \sin \psi \sin \phi) \quad (29)$$

$$\dot{Y} = u \sin \psi \cos \theta + v (\sin \psi \sin \theta \sin \phi + \cos \psi \cos \phi) + w (\sin \psi \sin \theta \cos \phi - \cos \psi \sin \phi) \quad (30)$$

$$\dot{Z} = -u \sin \theta + v \cos \theta \sin \phi + w \cos \theta \cos \phi \quad (31)$$

$$\alpha = \arctan (w/u) \quad (32)$$

$$\beta = \arctan (v/u) \quad (33)$$

$$\dot{\alpha} = (u\dot{w} - \dot{u}w)/(u^2 + w^2) \quad (34)$$

$$\dot{\beta} = (u\dot{v} - \dot{u}v)/(u^2 + v^2) \quad (35)$$

$$\phi_A = \arctan (v/w) \quad (36)$$

$$\gamma_H = \arctan (\dot{Y}/\dot{X}) \quad (37)$$

$$\gamma_V = \arctan [-\dot{Z}/(\dot{X}^2 + \dot{Y}^2)^{1/2}] \quad (38)$$

$$V = (u^2 + v^2 + w^2)^{1/2} \quad (39)$$

The flight simulation was programmed for the AD/5-PDP11/45 analog-digital equipment described in Ref. 9. The hybrid rather than an all-digital computer was used because an existing program could be easily modified for this particular problem, and because of the quick turn-around time between successive simulations. The problem was partitioned such that the inertial equations (17-22) and the coordinate transformation equations (29-31) were solved on the analog computer, and the force and moment equations (23-28) and the auxiliary equations (32-39) were solved on the digital computer. Frame time, i.e., time between consecutive analog samples, was 0.02 seconds which provided a minimum of about 60 updates per cycle for any variable. Analog samples were phase-shifted to correct for error introduced by digital lag by applying the second-order correction method described in Ref. 10. The flight simulation was programmed to run in real time. Run duration was 8 seconds, and only a few minutes were required between runs to change parameters and reinitialize. Parameter changes were made through the VTO5 CRT keyboard of the PDP11/45; results were recorded on a Tektronix 4015-1 display terminal and 4631 hard copy unit.

5. PROCEDURE

The approach used to define the series of simulation involved specifying either straight flight or turning flight and either the set of aerodynamic derivatives with all values constant or the set with some values locally linearized. These respective sets of derivatives were considered "nominal" when studying the sensitivity of individual derivatives. The procedure was first to run with the nominal

set of derivatives and with no perturbation to the motion in order to verify that the specified flight condition was being achieved. Next, with no changes to the derivatives, a run was made with the initial angle of attack or sideslip different from the trimmed value by 0.05 rad (3 deg). The angle that was selected depended upon the derivative(s) to be studied; e.g., if the derivative were $C_{n\dot{q}}$, the perturbation would be in α , and attention would be focused on aircraft response in β . Next, the derivative(s) to be studied would be zeroed or doubled, appropriate changes made to the trim moments (ref. Eqs. 14-16), and another run made to verify the desired flight condition. Finally, with this last set of derivatives, a run was made with the appropriate perturbation. Results obtained would be compared with the nominal case.

For each simulation, time histories were obtained for the following variables: $p, q, r, X, Y, Z, \psi, \theta, \phi, \gamma_H, \gamma_V, \bar{q}, a_x, a_y, a_z, \phi_A, \alpha, \beta, \dot{\alpha}, \dot{\beta}$. All data were recorded in graphical form by hard copy of the traces on the display terminal. Only four signals could be multiplexed, so several repeat runs were necessary to acquire the full complement of data.

Early in the investigation an attempt was made to curve-fit p, q, r histories in order to obtain quantitative information on damping ratio and frequency. To do this, an existing curve-fit program was modified for use on the PDP11/45 digital computer in the hybrid system. It soon became apparent that the time variation of any angular rate or displacement ($p, q, r, \alpha, \beta, \phi_A$, etc.) was too complex for the simple algorithm used; namely:

$$A = A_1 e^{A_2 t} \cos(A_3 t + A_4) + A_5 + A_6 t + A_7 t^2 \quad (40)$$

where A_3 represents frequency and A_2 is the negative product of frequency and damping ratio. Since elaborate curve-fitting techniques would have required considerably more effort, nothing further was done in this area.

6. RESULTS

a) Relative Magnitudes of Cross-Coupling Moments

Pertinent results of the investigation are summarized in Figs. 1-11. However, before examining these in detail, it is instructive to make a simple mathematical calculation for the case of 2 g steady turning flight with the nominal set of constant coefficients. This exercise is similar to that performed in Ref. 3. From Eq. (26), and the appropriate constants, it follows that:

$$L_q/L_p = (C_{l\dot{q}}/C_{l\dot{p}}) (q/p) (\bar{c}/b) = (0.5/-0.3) (0.0853/-0.0268) (16/39) = 2.2$$

Similarly, from Eqs. (27) - (28):

$$M_r/M_q = 0.02 \text{ and } N_q/N_r = -2.8$$

This shows that the absolute values of the rolling and yawing moments L_q and N_q present as a consequence of aerodynamic cross-coupling are larger than their well established damping counterparts L_p and N_r , and that the pitching moment M_r present as a consequence of aerodynamic cross-coupling is very small compared with M_q .

b) Effects of $C_{m\dot{r}}$ and $C_{m\dot{\beta}}$

The expectation that there would be no significant effect of aerodynamic cross-coupling on aircraft response in pitch was confirmed early in the investigation. When given a perturbation in β , only small oscillation was observed in $\alpha, \dot{\alpha}$, and q . The only figure included that contains data in this regard is the last one, Fig. 11c. This figure contains q and α histories for the β -perturbed turning flight with locally linearized coefficients. Since all coefficients are included, the effect due to the static derivative $C_{m\beta}$ is also present. It can be seen that the total effect of $C_{m\dot{r}}$, $C_{m\dot{\beta}}$, and $C_{m\beta}$ is small. Other simulations were run to study sensitivity of these derivatives by respectively zeroing and doubling them. Again, no significant effects were observed.

c) Effects of $C_{l\dot{q}}, C_{l\dot{\alpha}}, C_{n\dot{q}}$, and $C_{n\dot{\alpha}}$

Aircraft motion in roll and yaw, however, was noticeably affected by aerodynamic cross-coupling. Sensitivity of the motion to $C_{l\dot{q}}, C_{l\dot{\alpha}}, C_{n\dot{q}}$, and $C_{n\dot{\alpha}}$ is summarized in Figs. 1-6. Results are presented as time histories of ϕ_A or β depending on the derivative, and as time histories of γ_H or γ_V depending on the flight condition. Histories of ϕ_A and β are presented only for the first four seconds of the eight second simulation because of their small variations thereafter. Histories of γ_H and γ_V , however, are presented only for the last four seconds because of their increasing variation with time. Results are shown for both constant and locally linearized coefficients, and for both positive and negative perturbances in angle of attack. When examining these figures it must be remembered that for all cases designated "nominal", all derivatives are included at their nominal values. If the eight cross-coupling derivatives $C_{l\dot{q}}, C_{l\dot{\alpha}}, C_{m\dot{r}}, C_{m\dot{\beta}}, C_{n\dot{q}}, C_{n\dot{\alpha}}, C_{m\beta}$, and $C_{n\alpha}$ were simultaneously deleted, the variables ϕ_A, β , and γ_V would remain essentially zero; so would also the variable γ_H for straight flight. The cases designated "nominal" therefore show the combined influence of all cross-coupling derivatives. Most noticeable effect of the combined set was on the vertical component of flight path angle for turning

flight. Referring to Fig. 2d, it can be seen that after 8 seconds γ_V has reached a value of about -0.38 rad (22 deg); the altitude lost was about 183 m (600 ft).

The sensitivity of the motion to C_{L_q} and $C_{L_{\dot{\alpha}}}$ is shown in Figs. 1, 2, and 5. In Figs. 1 and 2, the results are shown for both derivatives zeroed and doubled, respectively, and in Fig. 5, for one derivative zeroed while the other is doubled, and vice versa. It is apparent from these figures that the motion is noticeably sensitive to C_{L_q} and $C_{L_{\dot{\alpha}}}$. The extent of sensitivity is dependent upon flight condition, nature of coefficients, and direction of perturbation. With constant coefficients, negative perturbations yield approximately the inverse of results obtained with positive perturbations; but as may be expected, this was not the case with locally linearized coefficients. Also, with constant coefficients, the amplitude of ϕ_A and deviations in γ_H and γ_V were approximately the same between straight and turning flight (even though dynamic pressure was different by a factor of two). Again, this was not the case with locally linearized coefficients. Most significant effects were obtained with the locally linearized coefficients and a negative perturbation in angle of attack for the case of turning flight (ref. Fig. 2d). When both coefficients were doubled, ϕ_A reached a value almost as great in magnitude as the initial perturbation in α , and γ_V at 8 seconds was projected to be about 0.62 rad (35 deg) with related altitude loss in the neighborhood of 300 m (1000 ft). Also, when the coefficients were zeroed, ϕ_A was reduced in amplitude but was of opposite sign, and γ_V and altitude loss were considerably reduced. When one coefficient was zeroed and the other doubled, noticeable changes in ϕ_A and γ_V were again observed at least for the turning flight condition (ref. Fig. 5). This emphasizes the importance of treating C_{L_q} and $C_{L_{\dot{\alpha}}}$ separately and not arbitrarily considering them of equal magnitude.

Results for C_{n_q} and C_{n_r} are shown in Figs. 3, 4, and 6. The general pattern is similar to that for C_{L_q} and $C_{L_{\dot{\alpha}}}$ with ϕ_A replaced by β . Amplitudes in β are about half those observed in ϕ_A , but flight path angles are of comparable magnitudes. Again, the most significant effects were obtained with turning flight, locally linearized coefficients, and negative perturbation (ref. Fig. 4d).

It may be observed that similar changes in the cross-coupling derivatives C_{L_q} , $C_{L_{\dot{\alpha}}}$ and C_{n_q} , $C_{n_{\dot{\alpha}}}$ produce excursions of opposite directions in ϕ_A and β , and of the same direction in γ_H and γ_V . These effects represent the normal response with conventional axes systems when the derivatives are of the same algebraic sign, which is the present situation.

d) Effects of C_{L_r} , $C_{L_{\dot{\beta}}}$, C_{n_r} , and $C_{n_{\dot{\beta}}}$

At this point in the investigation it was considered desirable to assess the sensitivity of the motion to the traditional derivatives C_{n_r} , $C_{n_{\dot{\beta}}}$, C_{L_r} , and $C_{L_{\dot{\beta}}}$ under the same conditions where most significant effects were obtained with the cross-coupling derivatives. The results are shown in Figs. 7 and 8. It is interesting to note that compared with the corresponding cross-coupling effects (ref. Figs. 2d and 4d, resp.) the effects of the derivatives C_{L_r} and $C_{L_{\dot{\beta}}}$ are not markedly greater as far as ϕ_A is concerned, and considerably smaller as far as γ_V is concerned; and the effects of the well-established derivatives C_{n_r} and $C_{n_{\dot{\beta}}}$ are considerably smaller both on β and γ_V .

e) Effects of $C_{m_{\dot{\beta}}}$ and $C_{n_{\dot{\alpha}}}$

Finally, the sensitivity of motion to the static cross-coupling derivatives $C_{m_{\dot{\beta}}}$ and $C_{n_{\dot{\alpha}}}$ was examined under these same conditions. Effects of $C_{m_{\dot{\beta}}}$ on α and γ_V were very small. Effects of $C_{n_{\dot{\alpha}}}$, shown in Fig. 9, were only moderate.

f) Angular rates

The last two figures (Figs. 10 and 11) are included to show angular rates obtained for perturbed straight and turning flight with the nominal set of locally linearized coefficients. These data are intended to complement the "nominal" results shown in the previous figures. Particular attention should be given Fig. 11b which shows the rate data for the case where most significant aerodynamic cross coupling effects were encountered. It can be seen that the direction of the initial perturbation was such as to maximize the combined contributions due to q and $\dot{\alpha}$.

7. CONCLUDING REMARKS

The importance of including aerodynamic cross-coupling terms in the equations of motion of a modern fighter aircraft flying at high angles of attack was examined in a six-degree-of-freedom computer study for both straight and 2g turning flight. It was found that

- (1) some dynamic cross-coupling moment derivatives had as large an effect on the predicted motion time histories as some of the well-established traditional dynamic derivatives. The most important of these cross-coupling derivatives were the derivatives of the rolling and yawing moments due to pitching (C_{L_q} , $C_{L_{\dot{\alpha}}}$, C_{n_q} , and $C_{n_{\dot{\alpha}}}$). This finding was in agreement with the results of a simple assessment of the magnitude of certain terms in the equations of motion;
- (2) particularly large effects were observed when the local nonlinearities with angle of attack were taken into account by substituting locally linearized values of certain derivatives for the conventionally used constant coefficients. In some cases this could result in deflections

in roll of the same magnitude as the initial perturbation in pitch, and in an altitude loss of as much as 300 m (1000 ft) during the first eight seconds following the initial perturbation;

- (3) when the derivatives were represented by constant coefficients, the effects of the dynamic cross-coupling derivatives were quite comparable for both the straight and the turning flight investigated; when locally linearized coefficients were used, the effects were noticeably larger for the turning flight. In this latter case the sign of the initial perturbation played a dominant role in the subsequent time histories;
- (4) for turning flight, when investigating separately the sensitivity of relevant time histories to various combinations of the purely rotary and acceleration derivatives, the effect of C_{lq} on the deflection in roll was found to be much larger than that of $C_{l\dot{\alpha}}$, whereas, when examining the effect of yawing motion derivatives on the angle of sideslip, $C_{n\dot{\alpha}}$ was found to be more important than C_{nq} . In both cases, however, it was obvious that using simply a sum of these effects (as is the current practice) or arbitrarily considering them equal in magnitude, may lead to significant errors;
- (5) derivatives of the pitching moment due to yawing, $C_{m\dot{\beta}}$ and $C_{m\dot{\alpha}}$, were found to be of drastically less importance than the derivatives discussed above. This also agrees with the results of a simple order-of-magnitude analysis. It should be noted, however, that these cross-coupling terms have to be compared with the usually very large damping-in-pitch term. If a situation could arise where for a high angle of attack the damping in pitch was relatively small, a much larger effect of $C_{m\dot{\beta}}$ and $C_{m\dot{\alpha}}$ could be expected.
- (6) the effect of the dynamic cross-coupling terms due to pitching was in the present analysis much larger than the effect of some static cross-coupling terms, such as $C_{m\beta}$ and $C_{n\alpha}$. It should be kept in mind, however, that this depends very much on the magnitude of these static terms, which in turn is a very strong function of the position of the center of gravity of the aircraft. The present finding, therefore, should not automatically be generalized.
- (7) cross coupling derivatives due to pitching caused noticeable changes in the rates of roll, yaw, and sideslip following an initial perturbation in angle of attack; these rates remained essentially constant when the cross-coupling terms were not included.

Although the nominal set of derivatives employed in this study was, of necessity, based on data obtained for two different configurations flying at different speeds, it is believed that the magnitude of the derivatives as well as of their rate of change with angle of attack is probably quite representative of a present-day fighter aircraft flying at a high enough angle of attack to cause asymmetric flow conditions. It would be of interest, of course, to confirm this by obtaining a complete set of derivatives for one and the same configuration at a suitably-chosen flight condition. In the meantime, however, the conclusions of the present investigation support the contention that at high angles of attack some of the dynamic cross-coupling and acceleration derivatives may be of similar importance as some of the traditional dynamic derivatives and should therefore be given the same careful attention. Also, it appears that significant nonlinearities in the various derivatives should be taken into account.

8. Acknowledgements

The authors wish to thank M. D. Bennett of the Sandia Laboratories for the many extremely helpful technical discussions throughout the course of this work. This project was jointly supported by the United States Department of Energy and the National Research Council of Canada.

9. References

1. Orlik-Rückemann, K. J., "Techniques for Dynamic Stability Testing in Wind Tunnels," Proceedings of the AGARD Symposium on Dynamic Stability Parameters, Athens, Greece, May 22-24, 1978.
2. Orlik-Rückemann, K. J., "Dynamic Stability of Aircraft - Needs versus Capabilities," Proceedings of the International Congress on Instrumentation in Aerospace Simulation Facilities, Pasadena, CA, 1973.
3. Orlik-Rückemann, K. J., "Aerodynamic Coupling Between Lateral and Longitudinal Degrees of Freedom," *AIAA Journal*, Vol. 15, No. 12, pp. 1792-1799, December 1977. Also presented as Paper 77-4, AIAA Aerospace Sciences Meeting, Los Angeles, CA, 1977.
4. Butler, R. W., "Aircraft Motion Sensitivity to Cross and Cross-Coupling Damping Derivatives," AEDC-TR-76-138, November 1976.
5. Grafton, S. D. and Liddey, C. E., "Dynamic Stability Derivatives of a Twin Jet Fighter Model at Angles of Attack from -10 to 110 Degrees," NASA TN D6091, January 1971.
6. Coe, P. L., Jr., Graham, A. B., and Chambers, J. R., "Summary of Information on Low Speed Lateral Directional Derivatives Due to Rate of Change of Sideslip $\dot{\beta}$," NASA TN D7972, September 1975.

7. Orlik-Rückemann, K. J., Hanff, E. S., and LaBerge, J. G., "Direct and Cross-Coupling Subsonic Moment Derivatives due to Oscillatory Pitching and Yawing of an Aircraft-Like Model at Angles of Attack Up to 40° in Ames' 6' x 6' Wind Tunnel," NRC NAE LTR-UA-38, November 1976.
8. Etkin, B., Dynamics of Atmospheric Flight, John Wiley & Sons, Inc., New York 1972.
9. Curry, W. H., and Nielson, J. M., "Sandia Laboratories Hybrid Computer and Motion Simulator Facilities," Sandia Laboratories Report SAND76-0091, June 1976.
10. Curry, W. H., "An Evaluation of a Correction Method for Digital Computer Lag in Hybrid Systems," Proceedings of the Summer Computer Simulation Conference, Chicago, IL, 1977.

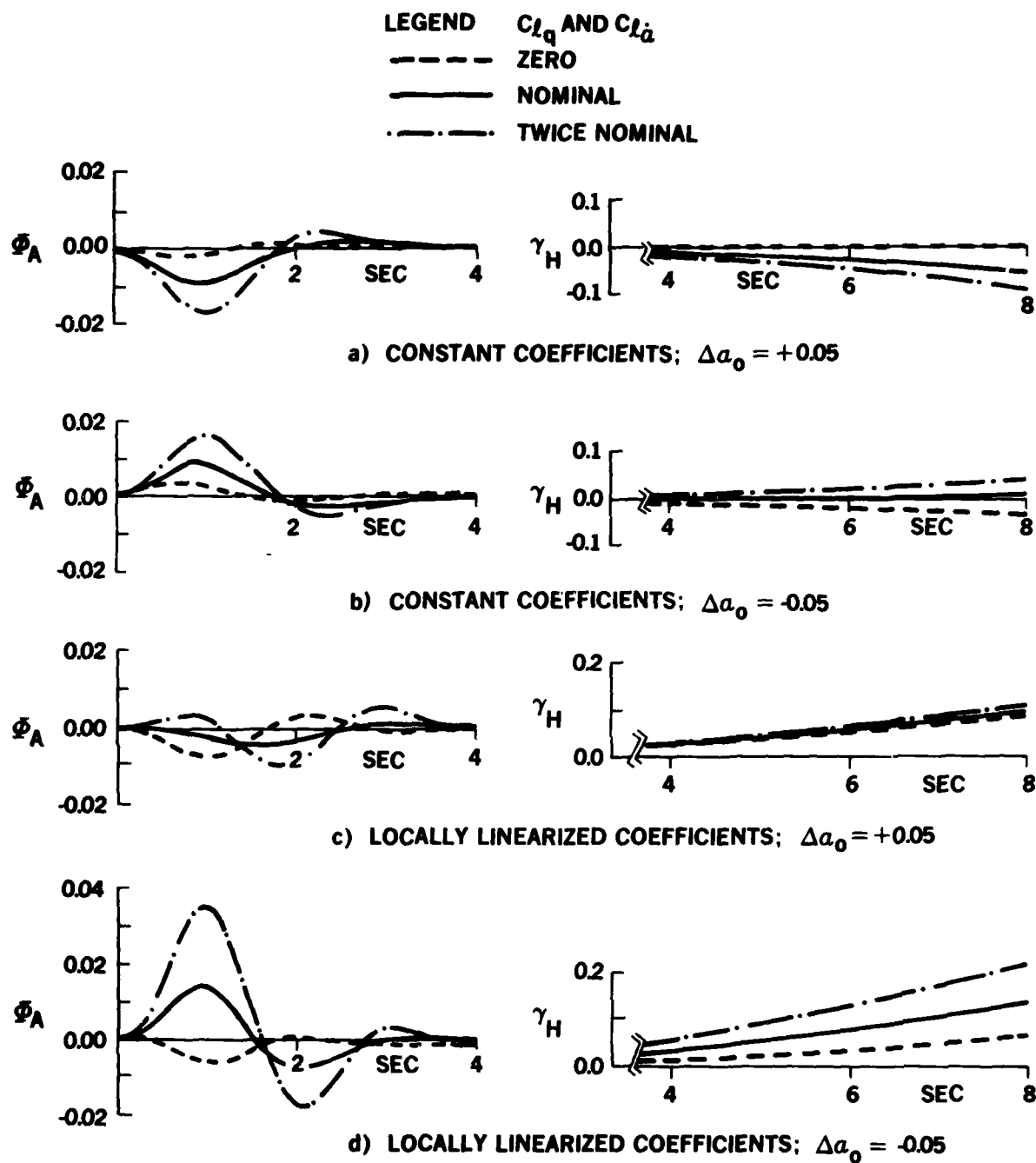


FIG. 1. EFFECTS OF C_{l_q} AND $C_{l_{\dot{\alpha}}}$ FOR STRAIGHT FLIGHT

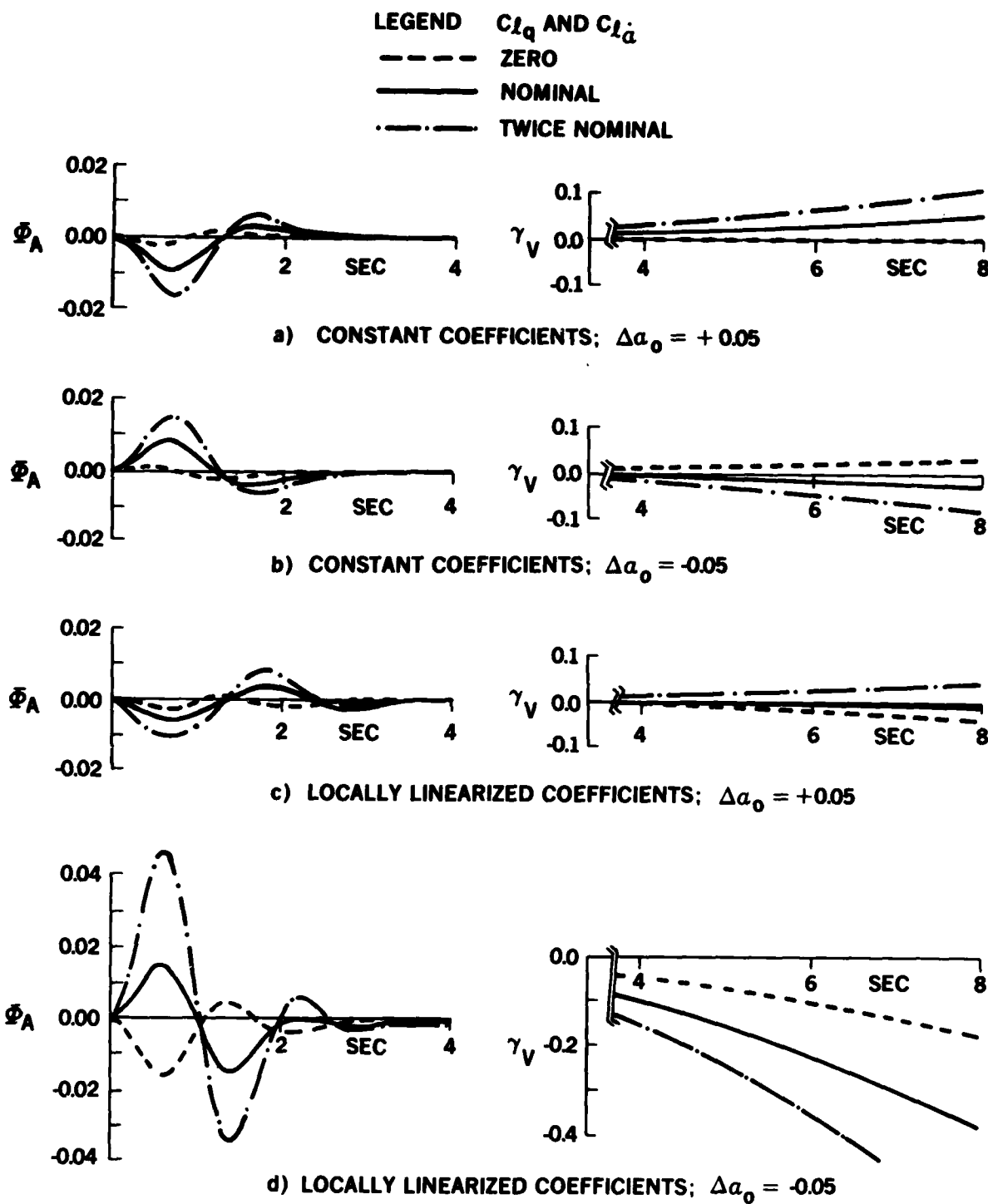


FIG. 2. EFFECTS OF C_{l_q} AND $C_{l_{\dot{\alpha}}}$ FOR 2g TURNING FLIGHT

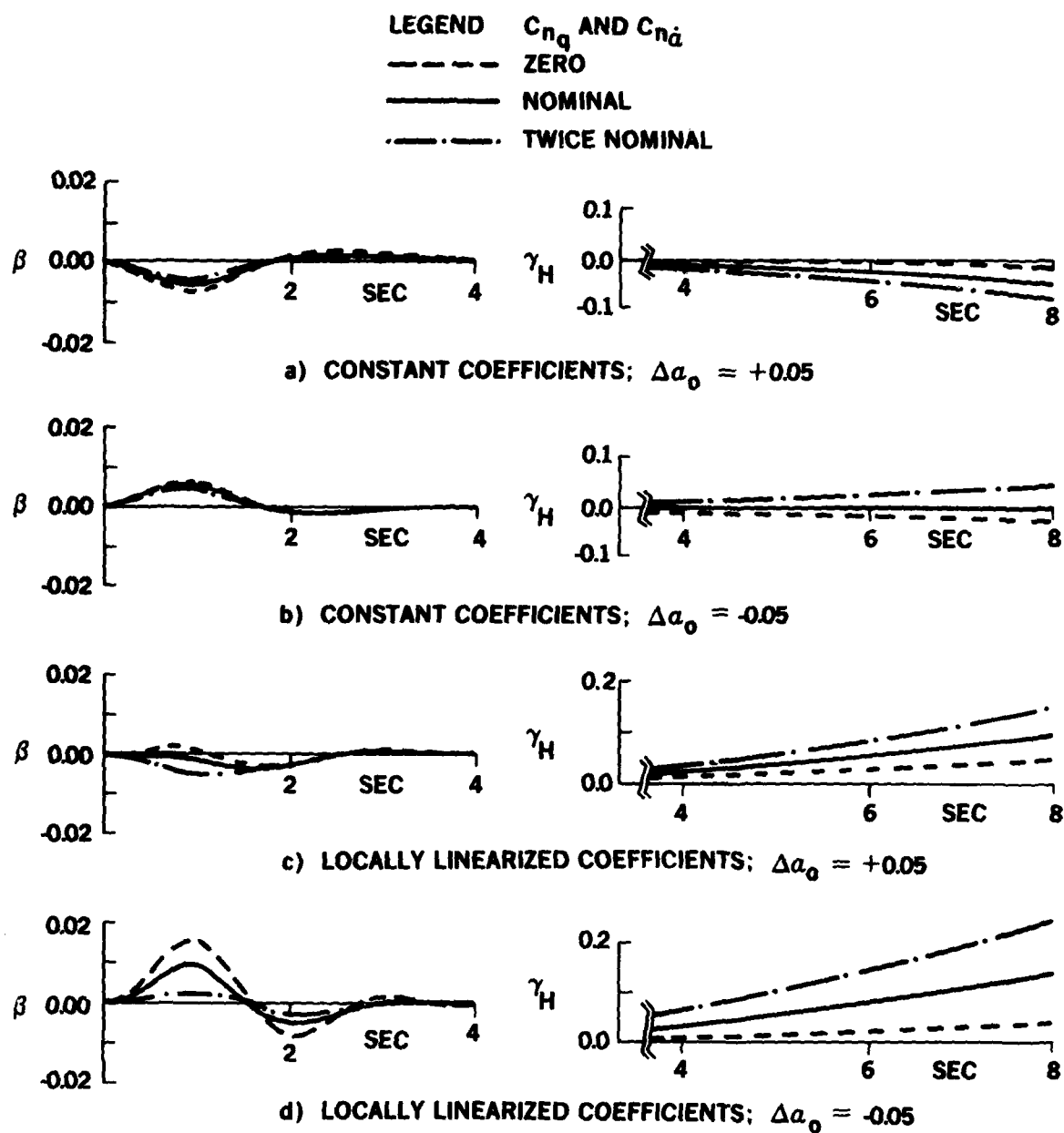


FIG. 3. EFFECTS OF C_{n_q} AND $C_{n_{\dot{a}}}$ FOR STRAIGHT FLIGHT

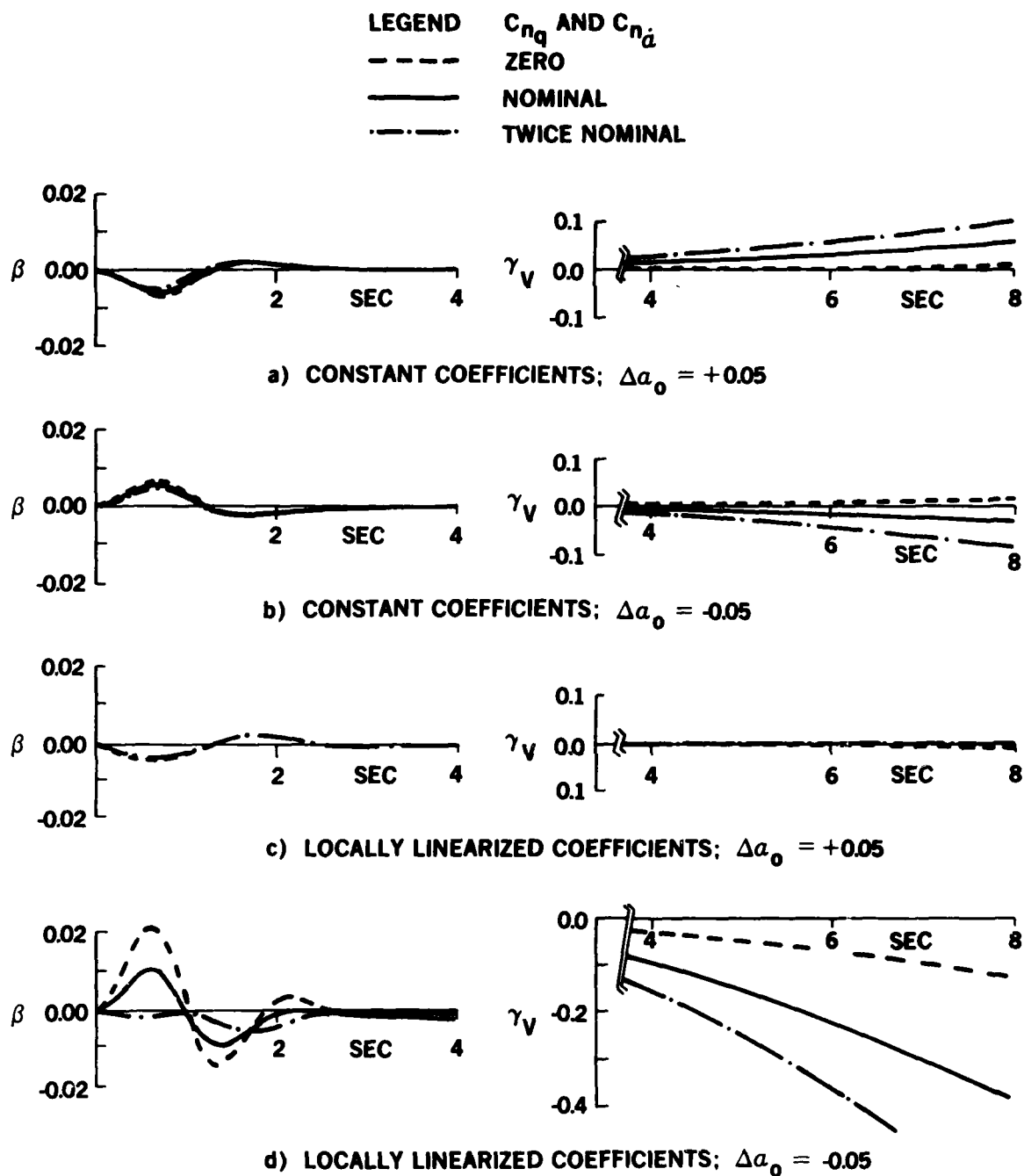


FIG. 4. EFFECTS OF C_{nq} AND $C_{n\dot{\alpha}}$ FOR 2g TURNING FLIGHT

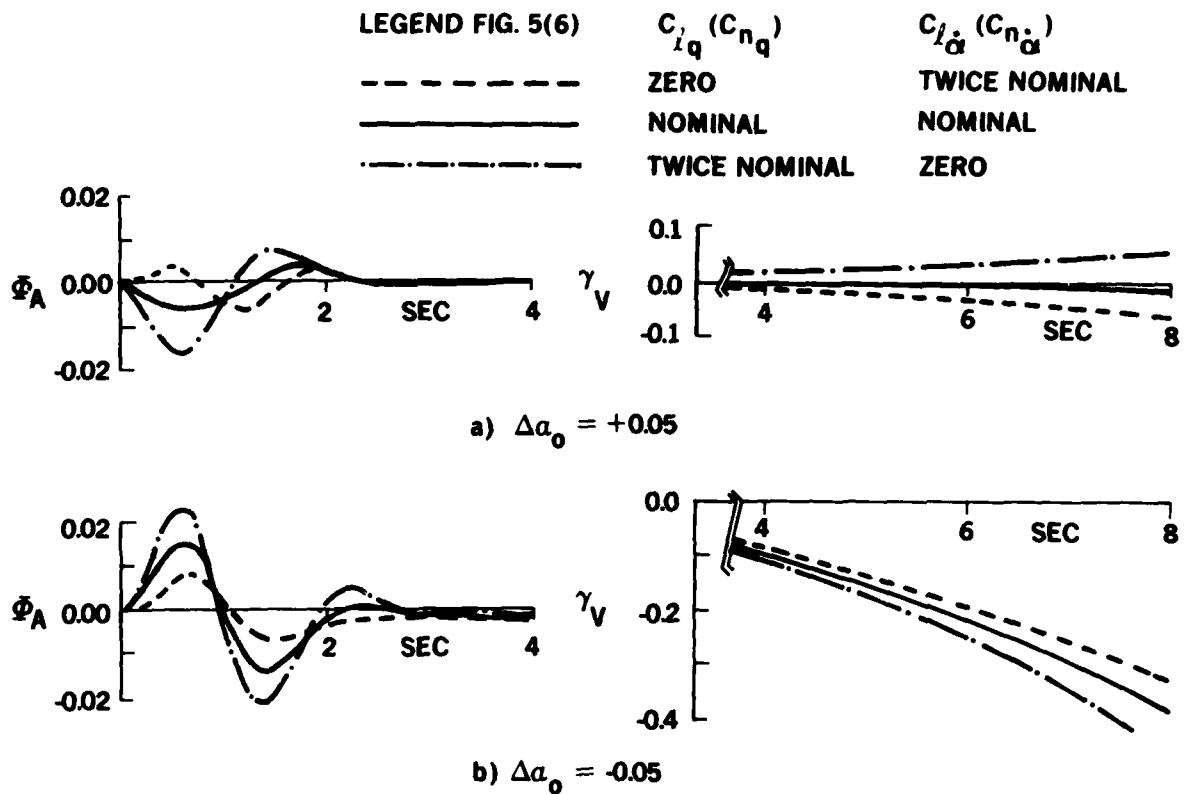


FIG. 5. FURTHER EFFECTS OF C_{l_q} AND $C_{l_{\dot{\alpha}}}$ FOR CASE WITH LOCALLY LINEARIZED COEFFICIENTS AND 2g TURNING FLIGHT

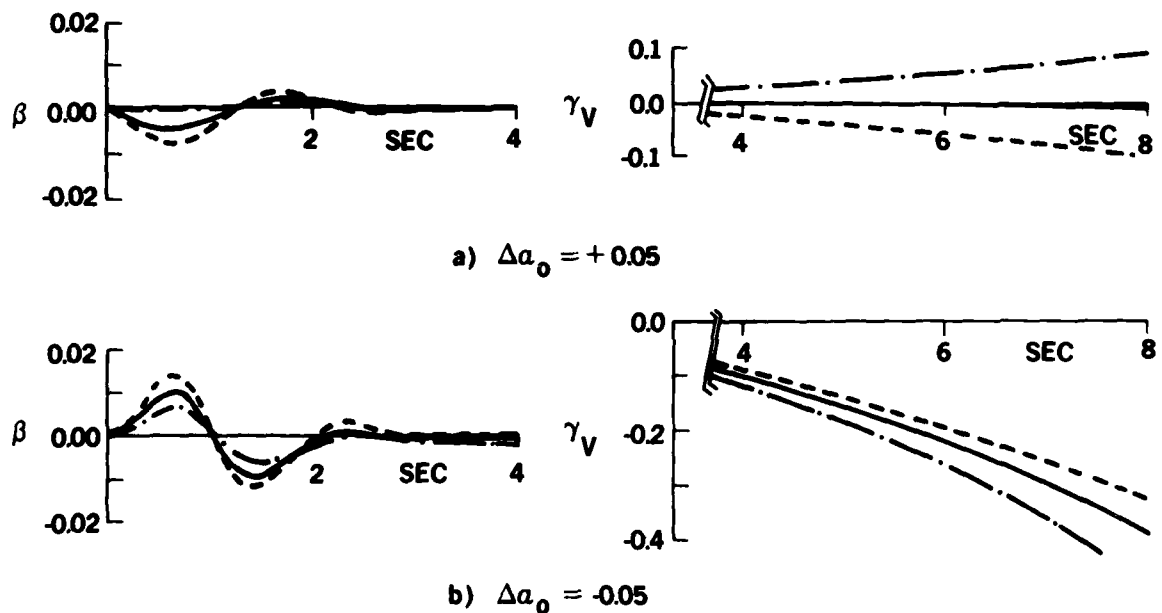
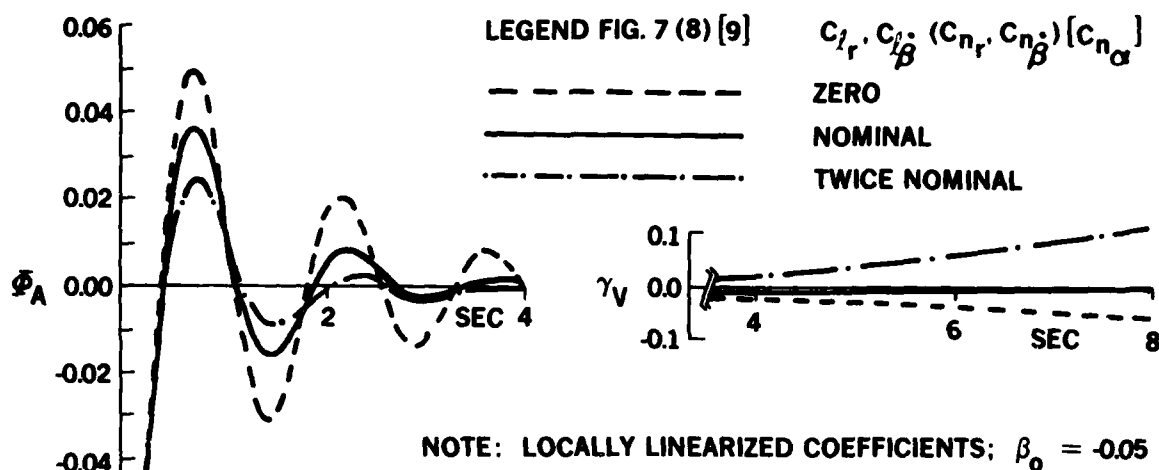
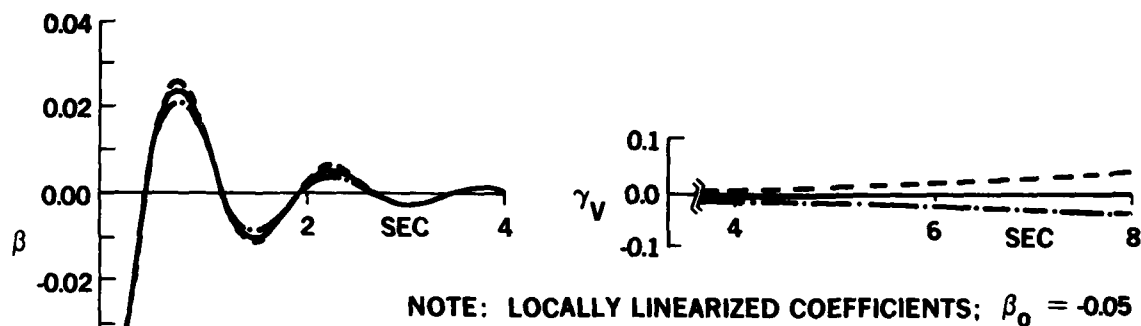
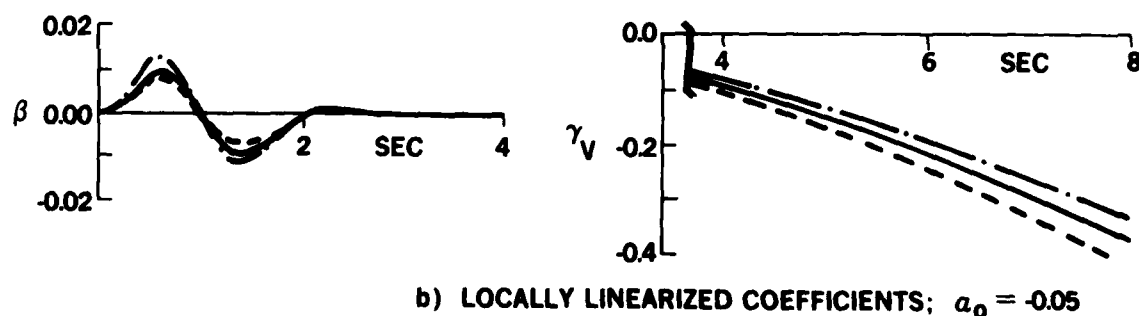
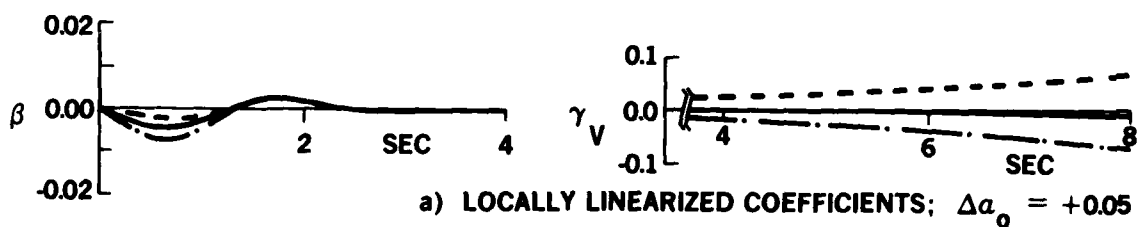
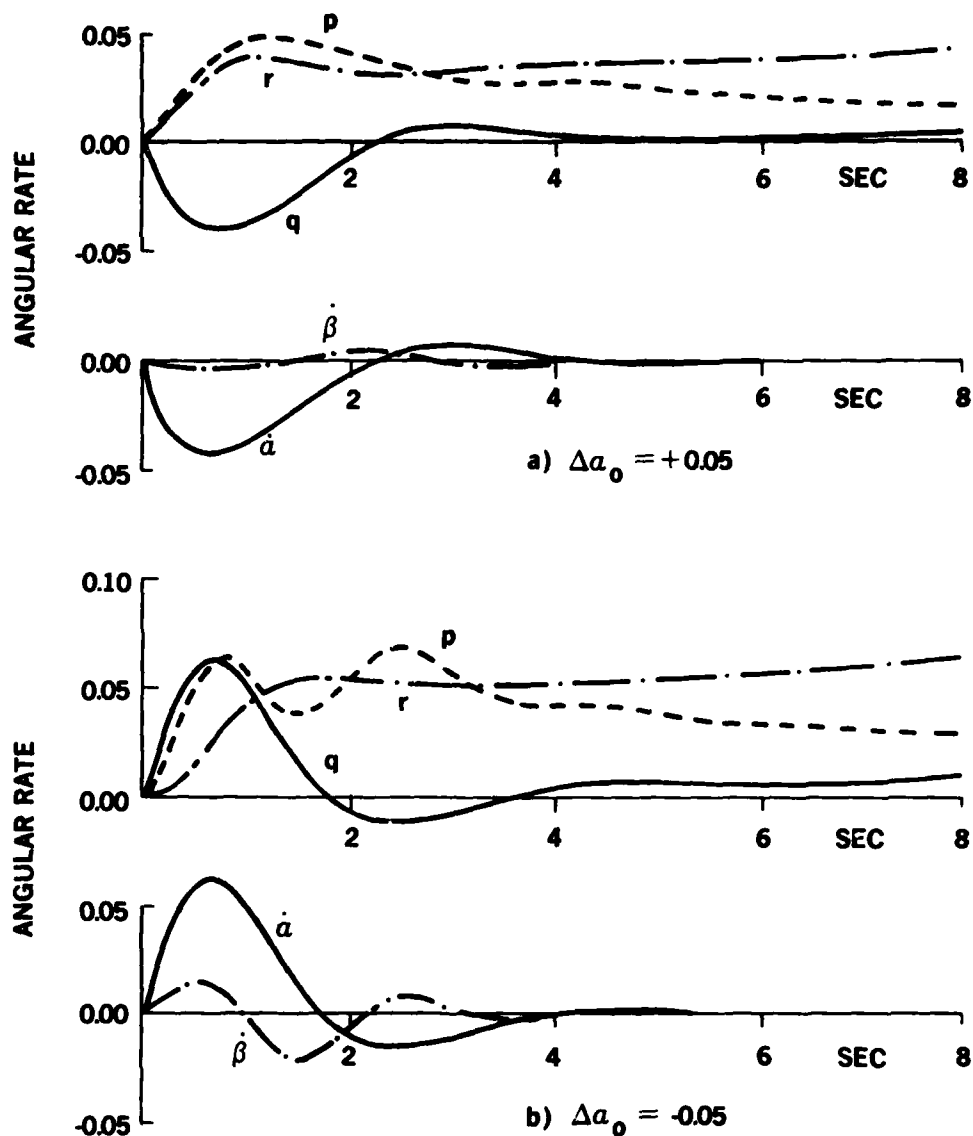


FIG. 6. FURTHER EFFECTS OF C_{n_q} AND $C_{n_{\dot{\alpha}}}$ FOR CASE WITH LOCALLY LINEARIZED COEFFICIENTS AND 2g TURNING FLIGHT

FIG. 7. EFFECTS OF C_{l_r} AND $C_{l_{\dot{\beta}}}$ FOR 2g TURNING FLIGHTFIG. 8. EFFECTS OF C_{n_r} AND $C_{n_{\dot{\beta}}}$ FOR 2g TURNING FLIGHTFIG. 9. EFFECTS OF $C_{n_{\alpha}}$ FOR 2g TURNING FLIGHT



NOTE: WITH ALL AERODYNAMIC CROSS COUPLING DERIVATIVES EQUAL TO ZERO, THE RATES p , r , AND $\dot{\beta}$ REMAIN ESSENTIALLY ZERO WHEN PERTURBED IN a

FIG. 10. ANGULAR RATES FOR NOMINAL CASE WITH LOCALLY LINEARIZED COEFFICIENTS FOR STRAIGHT FLIGHT

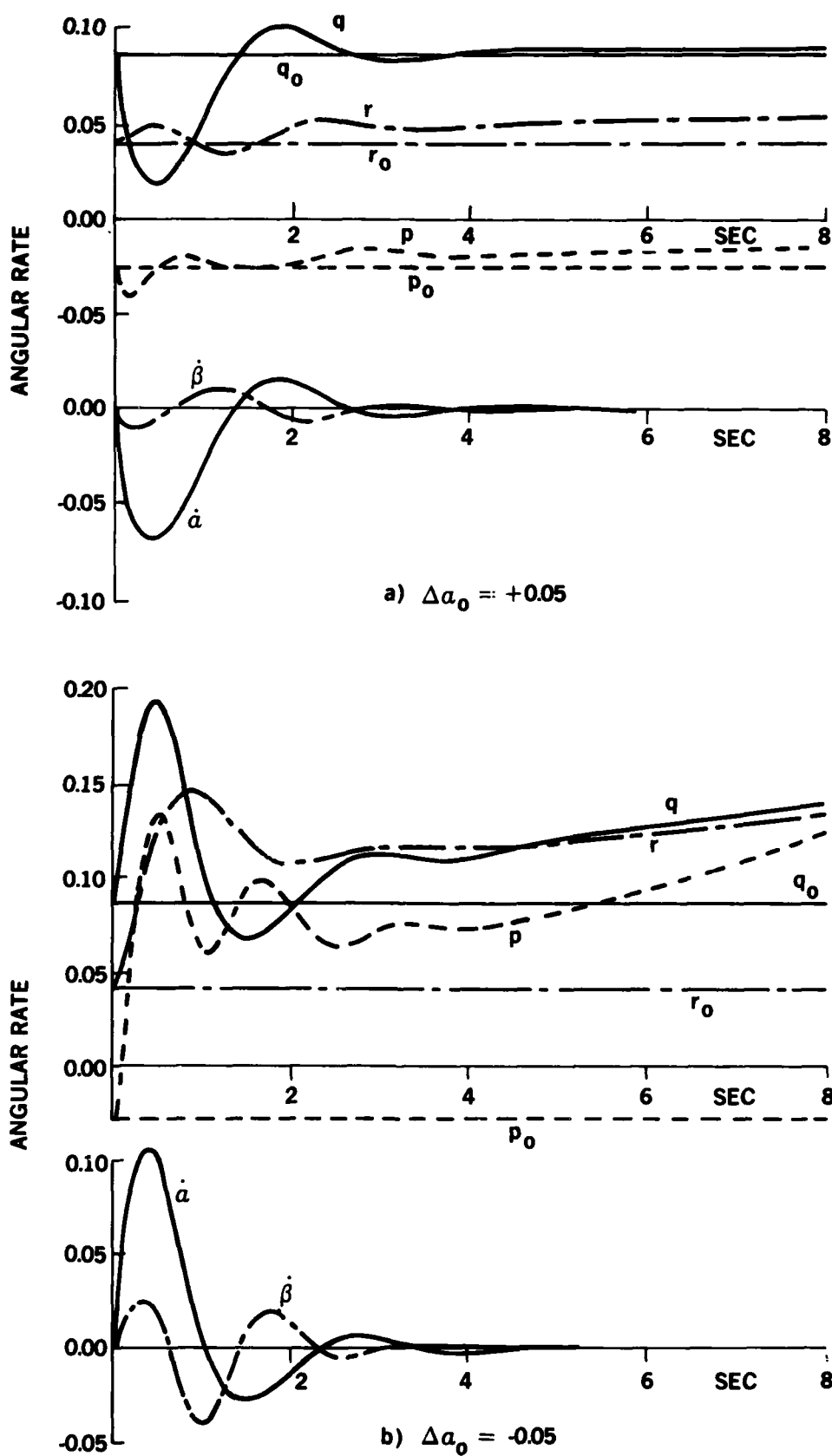
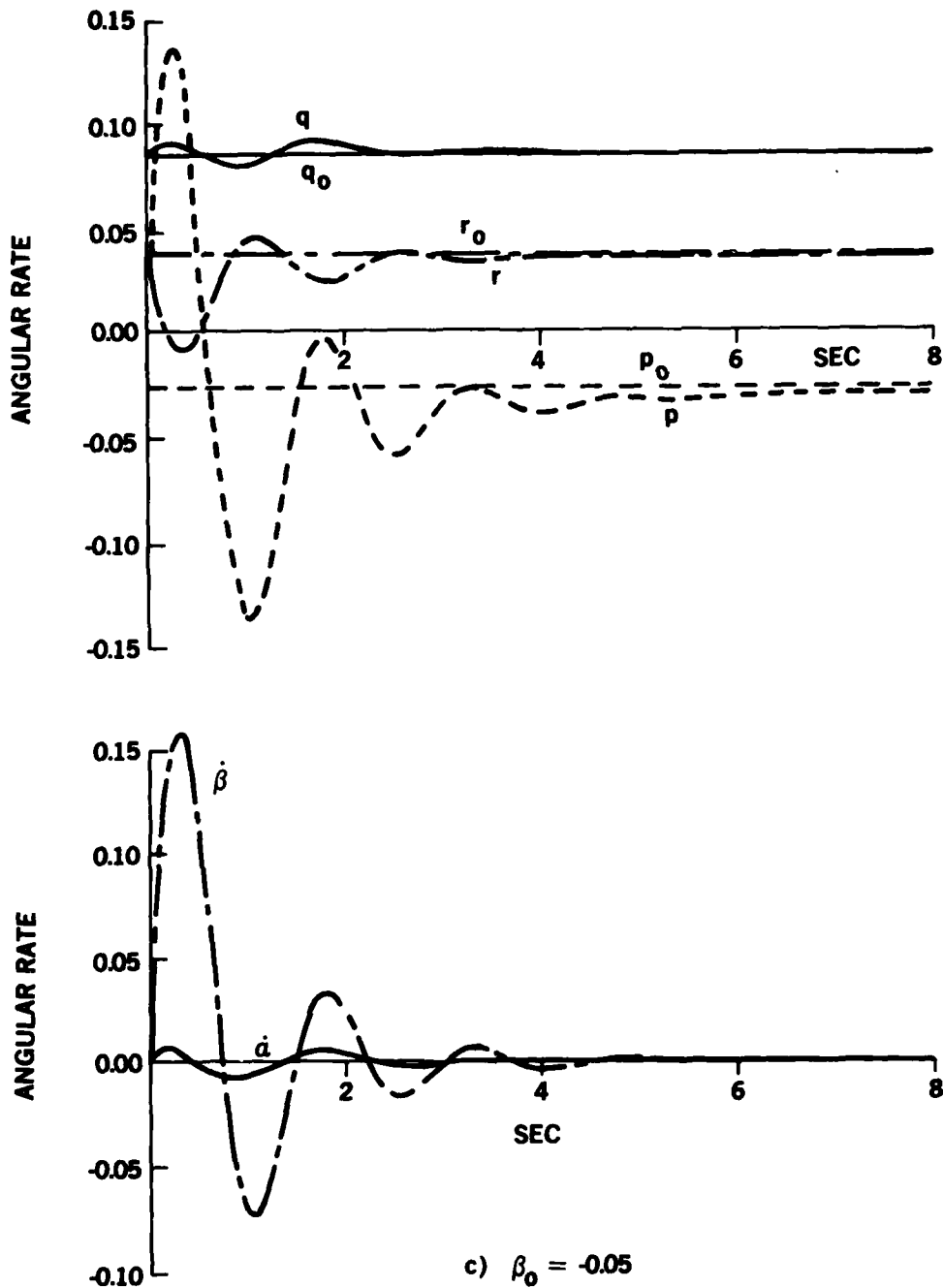


FIG 11. ANGULAR RATES FOR NOMINAL CASE WITH LOCALLY LINEARIZED COEFFICIENTS FOR $2g$ TURNING FLIGHT



NOTE 1: ANGULAR RATES FOR THE UNPERTURBED CASE REMAIN CONSTANT AND ARE DENOTED BY p_0, q_0, r_0 .

NOTE 2: WITH ALL AERODYNAMIC CROSS COUPLING DERIVATIVES EQUAL TO ZERO, THE RATES p, r , AND β REMAIN ESSENTIALLY CONSTANT WHEN PERTURBED IN α ; SIMILARLY THE RATES q AND $\dot{\alpha}$ REMAIN ESSENTIALLY CONSTANT WHEN PERTURBED IN β

FIG 11. (CONCLUDED)

AIRCRAFT MOTION SENSITIVITY TO VARIATIONS IN DYNAMIC STABILITY PARAMETERS*

by
R. W. Butler and T. F. Langham
ARO, Inc.
AEDC Division
A Sverdrup Corporation Company
Propulsion Wind Tunnel Facility
Arnold Air Force Station, Tennessee

SUMMARY

A 6-DOF nonlinear and 5-DOF linearized dynamic sensitivity study has been conducted on a fighter/bomber and attack type aircraft. The dynamic derivatives investigated in the study were C_{ℓ_q} , C_{n_q} , C_{m_r} , $C_{\ell_{\dot{\beta}}}$, and $C_{n_{\dot{\beta}}}$. The cross-coupling derivatives C_{ℓ_q} and C_{n_q} are shown to have significant effects on the aircraft motion in 1 "g" flight and 3 "g" turning flight while the derivative C_{m_r} shows little effect in the same regime. The acceleration derivatives $C_{n_{\dot{\beta}}}$ and $C_{\ell_{\dot{\beta}}}$ each have a significant influence on the aircraft motion in 1 "g" flight. The analysis also documents the interactive nature of the dynamic derivatives in the aircraft equations of motion.

NOMENCLATURE

a, b, c	Identified in Fig. 9	p, q, r	Total roll, pitch, and yaw rates about aircraft body axis, deg/sec
F_x, F_y, F_z	Aerodynamic forces along A/C X, Y, Z body axis, lb	$\dot{p}, \dot{q}, \dot{r}$	Total roll, pitch, and yaw accelerations about aircraft body axis, deg/sec ²
g	Acceleration due to gravity, ft/sec ²	u, v, w	Velocity components along aircraft body axes system, ft/sec
L, M, N	Aerodynamic moments about A/C X, Y, Z body axis, ft lb	$\ddot{u}, \ddot{v}, \ddot{w}$	Acceleration components along aircraft body axis system, ft/sec ²
I_x, I_y, I_z	Moments of inertia, body axis, slug-ft ²	V_{∞}	Aircraft total velocity, $\sqrt{u^2 + v^2 + w^2}$, ft/sec
I_{xz}	Product of inertia, body axis, slug-ft ²	α	Aircraft angle of attack, deg
L_p	Dimensional stability derivative, $(1/I_x)(\partial L/\partial p)$	β	Aircraft angle of sideslip, deg
L_q	Dimensional stability derivative, $(1/I_x)(\partial L/\partial q)$	$\dot{\beta}$	Rate of change of angle of sideslip, deg/sec
L_r	Dimensional stability derivative, $(1/I_x)(\partial L/\partial r)$	θ	Aircraft angle of pitch, deg
M_p	Dimensional stability derivative, $(1/I_y)(\partial M/\partial p)$	ϕ	Aircraft angle of yaw, deg
M_q	Dimensional stability derivative, $(1/I_y)(\partial M/\partial q)$	ζ	Damping ratio
M_r	Dimensional stability derivative, $(1/I_y)(\partial M/\partial r)$	ω_d	Actual frequency, rad/sec
N_r	Dimensional stability derivative, $(1/I_z)(\partial N/\partial r)$	ω_n	Natural frequency, rad/sec
N_q	Dimensional stability derivative, $(1/I_z)(\partial N/\partial q)$	δ_R	Aircraft rudder deflection, deg
N_p	Dimensional stability derivative, $(1/I_z)(\partial N/\partial p)$	δ_H	Aircraft horizontal stabilizer deflection, deg
		Subscript	
		0	Initial condition, time = 0

INTRODUCTION

The simulation of aircraft motion through analytical techniques has become a very important tool in the development, testing and operational phases of modern fighter aircraft programs. Pilot-in-the-loop fixed-base simulators, which in the past have been used primarily for pilot training and proficiency checks, are now being applied to the development and testing phases of new fighter aircraft. Aircraft subsystems such as automatic departure prevention systems, stall inhibitors, spin-prevention concepts, etc. (Refs. 1 through 4) are continually being evaluated in motion simulators such as the NASA Langley Differential Maneuvering Simulator (Ref. 5).

*The research reported herein was performed by the Arnold Engineering Development Center, Air Force Systems Command. Work and analysis for this research was done by personnel of ARO, Inc., a Sverdrup Corporation Company, operating contractor of AEDC. Further reproduction is authorized to satisfy needs of the U. S. Government.

The confidence level in simulated aircraft motion is high when operating in the low angle of attack unstalled flight regime. As the angle of attack increases to the extremes of the aircraft operating envelope, the confidence level diminishes correspondingly. This is unfortunate since most of the aircraft handling quality problems of greatest interest for simulator evaluation occur at high AOA. This degradation in confidence, resulting from poor "before the fact" simulation, is not due to an inadequacy in the aircraft equations of motion at high AOA but results from improper or inadequate definition of the aircraft aerodynamics in this regime. The poor definition of the aircraft dynamic characteristics at high AOA is believed to be a major factor in this deficiency.

The classical method of modeling the aircraft dynamic characteristics in motion simulation utilizes the direct damping derivatives ($C_{m_q}, C_{n_r}, C_{l_p}$, etc.) and cross derivatives (C_{n_p}, C_{l_r}). This method has proven to be accurate in low AOA flight where aircraft aerodynamics are linear and cross-coupling and acceleration derivatives are small. As AOA increases and associated nonlinear flow resulting from separation and asymmetric vortex shedding occur, the heretofore secondary cross-coupling ($C_{n_q}, C_{l_q}, C_{m_p}$) and acceleration ($C_{n_{\dot{\beta}}}, C_{l_{\dot{\beta}}}$) derivatives become large. Orlik-Rückemann, Hanff, and Laberge at NAE (Ref. 6) have shown experimentally, with an aircraft type model, that the magnitude of the cross-coupling rate derivatives in combination with acceleration derivatives at high AOA approach those of the direct damping derivatives. Likewise NASA Langley through the use of a curved flow tunnel (Ref. 7) has shown the $\dot{\beta}$ acceleration derivatives to be the predominate terms at high AOA in the classical $C_{n_r} + C_{n_{\dot{\beta}}}$ and $C_{l_r} + C_{l_{\dot{\beta}}}$ combinations measured in forced oscillation experiments.

Since the representative magnitudes of the cross-coupling and $\dot{\beta}$ acceleration derivatives have been documented, the question arises as to their importance in aircraft flight mechanics. This study addresses the question by investigating the motion sensitivity of a fighter/bomber and attack type aircraft to variations in the cross-coupling C_{m_r}, C_{l_q} , and C_{n_q} and acceleration $C_{n_{\dot{\beta}}}, C_{l_{\dot{\beta}}}$ derivatives in a high angle of attack operational environment. The cross-coupling derivative C_{m_p} was not addressed in this investigation because no experimental data were available for defining its relative magnitude.

Method of Analysis

Two different aircraft were utilized in the motion sensitivity study, a fighter/bomber type configuration, Fig. 1, and an attack configuration, Fig. 2. The primary analysis centers around the fighter/bomber aircraft with the attack aircraft being utilized to ascertain and document configuration dependency. Both a 6-DOF nonlinear motion program and a 5-DOF linearized stability program are used in the analysis. The 6-DOF program was formulated by North American Rockwell (Ref. 8) using a fourth-order Runge-Kutta integration algorithm with a fixed integration size. The program input and aerodynamic modules have since been modified for adaptation to the cross-coupling and acceleration dynamic derivatives. The 6-DOF equations of motion describing the aircraft motion are rigid-body equations referenced to a body-fixed axis system in the aircraft. The basic equations are as follows:

$$F_x = m(\dot{u} - rv + qw + g \sin \theta) \quad (1)$$

$$F_y = m(\dot{v} - pw + ru - g \cos \theta \sin \phi) \quad (2)$$

$$F_z = m(\dot{w} - qu + pv - g \cos \theta \cos \phi) \quad (3)$$

$$L = \dot{p}I_x - qr(I_y - I_z) - (\dot{r} + pq)I_{xz} \quad (4)$$

$$M = \dot{q}I_y - pr(I_z - I_x) - (r^2 - p^2)I_{xz} \quad (5)$$

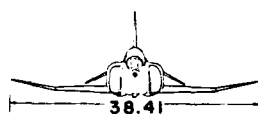
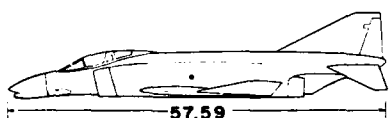
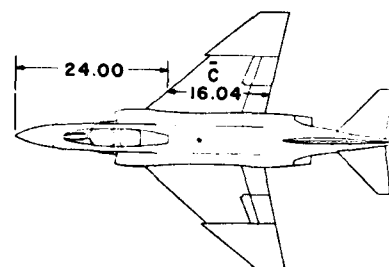
$$N = \dot{r}I_z - pq(I_x - I_y) - (\dot{p} - qr)I_{xz} \quad (6)$$

The left side of each equation represents the static and dynamic aerodynamic forces and moments acting on the aircraft. The cross-coupling and acceleration derivatives investigated are incorporated in the moment terms L, M, and N. The moment equations are defined as follows:

$$(\text{Roll}) \quad L = \left(\frac{\partial L}{\partial \alpha}\right)\alpha + \left(\frac{\partial L}{\partial \beta}\right)\beta + \left(\frac{\partial L}{\partial \dot{\beta}}\right)\dot{\beta} + \left(\frac{\partial L}{\partial \delta_R}\right)\delta_R + \left(\frac{\partial L}{\partial p}\right)p + \left(\frac{\partial L}{\partial r}\right)r + \left(\frac{\partial L}{\partial q}\right)q \quad (7)$$

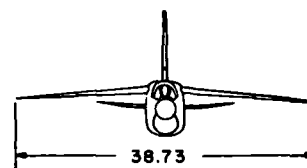
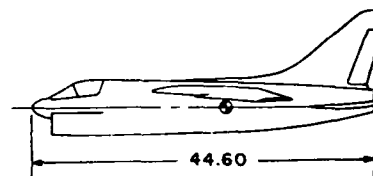
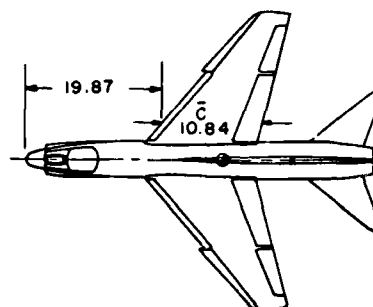
$$(\text{Pitch}) \quad M = \left(\frac{\partial M}{\partial \alpha}\right)\alpha + \left(\frac{\partial M}{\partial \beta}\right)\beta + \left(\frac{\partial M}{\partial \delta_H}\right)\delta_H + \left(\frac{\partial M}{\partial q}\right)q + \left(\frac{\partial M}{\partial r}\right)r \quad (8)$$

$$(\text{Yaw}) \quad N = \left(\frac{\partial N}{\partial \alpha}\right)\alpha + \left(\frac{\partial N}{\partial \beta}\right)\beta + \left(\frac{\partial N}{\partial \dot{\beta}}\right)\dot{\beta} + \left(\frac{\partial N}{\partial \delta_R}\right)\delta_R + \left(\frac{\partial N}{\partial r}\right)r + \left(\frac{\partial N}{\partial p}\right)p + \left(\frac{\partial N}{\partial q}\right)q \quad (9)$$



DIMENSIONS IN FEET

Fig. 1 Three-View Sketch of the Fighter/Bomber Type Aircraft



DIMENSIONS IN FEET

Fig. 2 Three-View Sketch of the Attack Type Aircraft

Using the 6-DOF program, the fighter bomber aircraft was trimmed at a high angle of attack in 1 "g" flight. At this trimmed flight condition, either a rudder or elevator doublet was executed to excite the appropriate derivative. For example, a rudder doublet would be used to perturbate the C_{m_r} derivative and likewise an elevator doublet for exciting the C_{ℓ_q} derivative. Initially, each derivative was isolated and varied individually by forcing all other cross-coupling and acceleration derivatives to be zero. Although this method of derivative variation provided the isolation needed for investigating a single derivative, it is far removed from actual flight where all derivatives vary simultaneously.

To supplement the 6-DOF analysis with a more quantitative method of determining derivative significance, a 5-DOF linearized program was utilized. The 5-DOF program was built around the above equations of motion in their linearized form, the velocity was assumed to remain constant therefore the F_v equation was omitted. The equations of motion in their linearized form for turning flight with initial pitch attitude and roll rate assumed to be small are defined as follows:

$$F_y = m \left(\dot{\beta} + r \cos \alpha_0 - p \sin \alpha_0 - \phi \frac{g \cos \phi}{V_\infty} \right) \quad (10)$$

$$F_z = m \left(\alpha - q + \phi \frac{g \sin \phi_0}{\phi_0} \right) \quad (11)$$

$$L = \dot{p} I_x + q_0 r (I_z - I_y) + r_0 q (I_z - I_y) - (\dot{r} + q_0 p) I_{x_z} \quad (12)$$

$$M = \dot{q} I_y + r_0 p (I_x - I_z) - 2 r_0 r I_{x_z} \quad (13)$$

$$N = \dot{r} I_z + p q_0 (I_y - I_x) - (\dot{p}_0 - q_0 r - q r_0) I_{x_z} \quad (14)$$

With the linearized equations, changes in frequency and damping of the predominate aircraft modes of motion with variations in derivatives could be ascertained. This quantitative measure of effectiveness coupled with a factorial analysis permitted a more thorough investigation of derivative significance when acting alone and in combination with other cross-coupling derivatives.

The ranges over which the dynamic derivatives are varied in this study correspond to approximate maximum and minimum experimental values obtained from recent wind tunnel testing. The cross-coupling derivatives $C_{\ell q}$, C_{nq} , and C_{mr} were obtained from the program outlined in Ref. 6 using an aircraft type model. The $\dot{\beta}$ acceleration derivatives $C_{n\dot{\beta}}$ and $C_{\ell\dot{\beta}}$ were obtained (Ref. 7) with a fighter/bomber aircraft configuration similar to the one used in this investigation. The ranges over which the derivatives are varied in the study are presented in Fig. 3.

MAGNITUDES PER RADIAN	CROSS-COUPLING DERIVATIVES			ACCELERATION DERIVATIVES	
	$C_{\ell q}$	C_{nq}	C_{mr}	$C_{n\dot{\beta}}$	$C_{\ell\dot{\beta}}$
MAXIMUM	+2	+2	+1	+1	0
MINIMUM	-2	-2	-1	0	-1

Fig. 3 Derivative Ranges Obtained from Wind Tunnel Testing

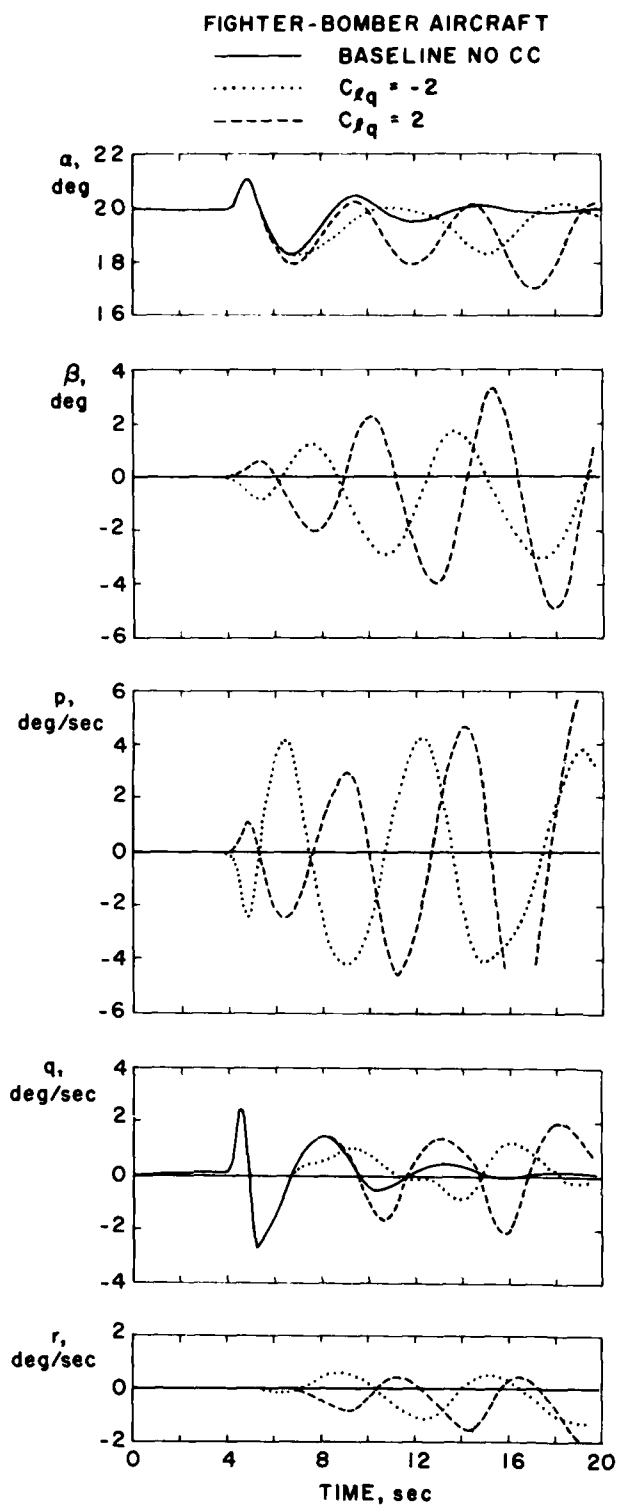
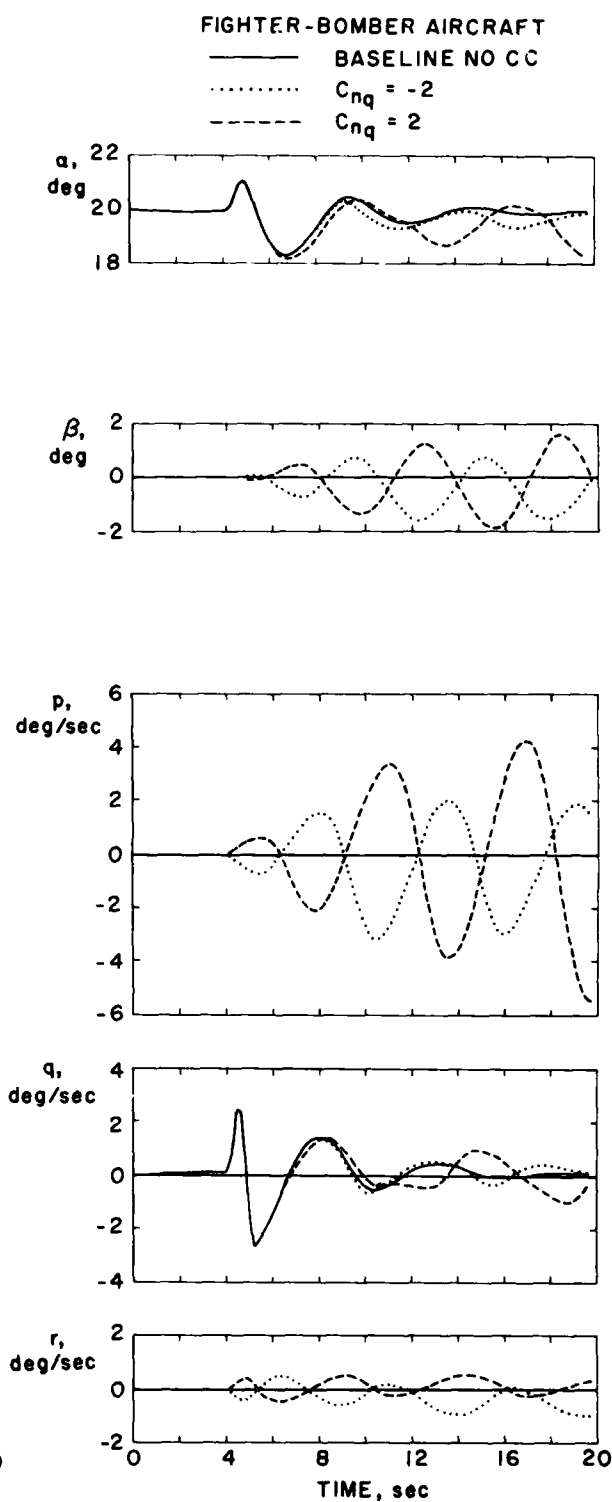
$C_{\ell q}$ and C_{nq} Derivative Evaluation

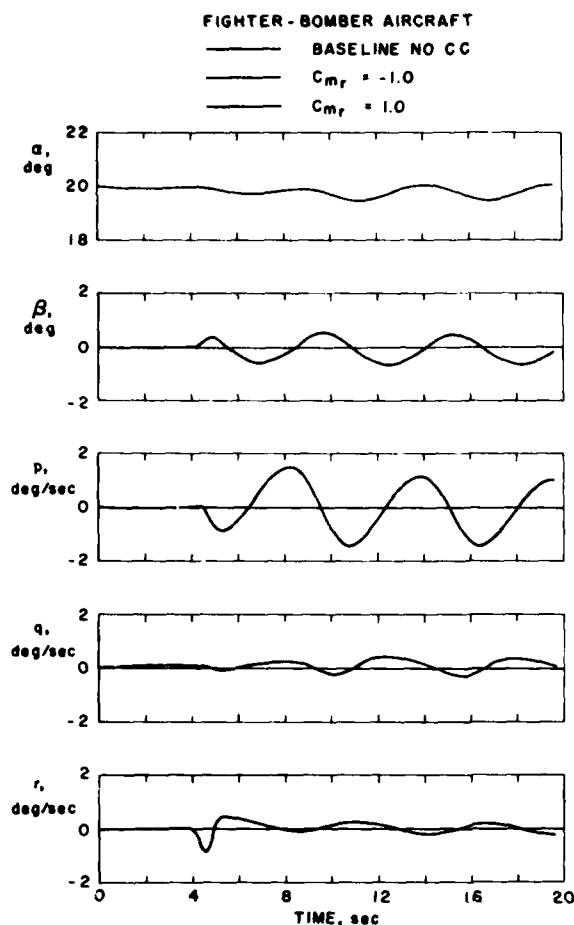
Coupled motion between the aircraft longitudinal and lateral/directional modes of motion may result from either aircraft aerodynamic or inertia characteristics. The cross-coupling derivatives $C_{\ell q}$ and C_{nq} represent a means of obtaining aerodynamic coupling between modes. Time history motion plots given in Figs. 4 and 5 present the effectiveness of the above derivatives in producing aerodynamic coupling. For these figures, the fighter/bomber aircraft is initially trimmed in 1 "g" flight for an angle of attack of 20 deg at an altitude of 30,000 ft (9144m). At a time of 4 sec, an elevator doublet is executed perturbing the aircraft q (pitch) rate. For the baseline motion case, no perturbation in p (roll) and r (yaw) rate occur from the q motion. This results from the fact that no aerodynamic coupling terms exist in the baseline case and inertia coupling is minimized because of the near zero p and r rates associated with 1 "g" trimmed flight.

When the cross-coupling derivatives $C_{\ell q}$ and C_{nq} are included in the baseline cases of Figs. 4 and 5, respectively, the motion no longer remains planar. In each figure, cross-coupling derivative values of ± 2 per radian exhibit a strong influence on coupling the motion between the aircrafts modes. Both roll and yaw motion of the aircraft are driven by longitudinal q rates in combination with the derivatives. As expected, the motion resulting from derivative values of +2 and -2 are near mirror images in the β , p , and r plots. The divergence from symmetry as time progresses can be attributed to the asymmetry of the static data matrix as a function of β used in the 6-DOF motion program. Assuming the C_{nq} and $C_{\ell q}$ derivatives to be of the magnitude approaching those used in Figs. 4 and 5, the resulting perturbations in p and r are considered to be significant in A/C motion simulation.

C_{mr} Derivative Evaluation

To investigate the importance of the cross-coupling derivative C_{mr} in motion simulation, some baseline motion must be generated with a realistic yaw rate r . The 1 "g" trimmed flight of Figs. 4 and 5 meets this requirement if a rudder doublet is substituted for the elevator doublet. Figure 6 presents the resulting motion for the rudder doublet executed at 4 sec while in 1 "g" trimmed flight. The q perturbations shown are a result of inertia coupling as may be seen in Eq. 5 (6-DOF equations of motion). Also shown in Fig. 6 is the negligible effect of the C_{mr} derivative variation of ± 1 on the aircraft motion with all other cross-coupling derivatives zero. Although the r rate perturbation from the rudder doublet is of lesser magnitude than the q rate, perturbations occurring from the elevator doublet, Figs. 4 and 5, it appears that the C_{mr} derivative should have at least a fraction of the motion coupling effect as that of the previous $C_{\ell q}$ and C_{nq} derivatives.

Fig. 4 C_{lq} Variation, Elevator DoubletFig. 5 C_{nq} Variation, Elevator Doublet

Fig. 6 C_{m_r} Variation, Rudder Doublet

The absence of aerodynamic coupling due to the C_{m_r} derivative variation can be explained by reviewing the aircraft equations of motion in their linearized form. Consider the rotational equations of motion \dot{p} , \dot{q} , and \dot{r} (Eqs. 12, 13, and 14) with the assumption that the I_{xz} terms are zero and that $I_y = I_z$ which is approximate for modern fighter aircraft with small wings and high density fuselages. Then

$$\dot{L} = \dot{p}I_x \quad (15)$$

$$\dot{M} = \dot{q}I_y + r_O p(I_x - I_z) \quad (16)$$

$$\dot{N} = \dot{r}I_z + p q_O (I_y - I_x) \quad (17)$$

If only the dynamic dimensional derivatives are considered as external forces, the equations become

$$\dot{p} - L_p p - L_q q - L_r r = 0 \quad (18)$$

$$\dot{q} - M_q q - M_r r - (M_p - A)p = 0 \quad (19)$$

$$\dot{r} - N_r r - N_q q - (N_p - B)p = 0 \quad (20)$$

where

$$A = r_O (I_z - I_x) / I_y$$

$$B = q_O (I_x - I_y) / I_z$$

Now by assuming an exponential solution

($p = \tilde{p}e^{st}$, $q = \tilde{q}e^{st}$, $r = \tilde{r}e^{st}$ for the linear differential equations, a set of homogeneous algebraic equations may be obtained which have the following characteristic equation:

$$\begin{aligned} (S - L_p)(S - M_q)(S - N_r) - (S - L_p)N_q M_r - (S - N_r)(M_p - A)L_q \\ - (S - M_q)(N_p - B)L_r - (N_p - B)M_r L_q - (M_p - A)N_q L_r = 0 \end{aligned} \quad (21)$$

Although this equation is a simplified example of a 6-DOF nonlinear system, it does point out the degree of interaction which occurs between the stability derivatives. For the case in question, the C_{m_r} (M_r) variation, it is apparent that zero values of the cross-coupling derivatives C_{n_q} (N_q) and C_{l_q} (L_q) eliminate any effect of the C_{m_r} derivative on the aircraft motion.

From the above discussion, giving the C_{n_q} and C_{l_q} derivatives a nominal value of +2 per radian should allow the C_{m_r} derivative to have an effect on the time history motion. As observed in Fig. 7, the motion resulting from the rudder doublet with C_{m_r} values of ± 1 exhibits differences in the longitudinal plane (α and q) which did not occur in the C_{m_r} variation of Fig. 6. These differences continue to be small and would most likely be neglected when conducting motion simulation studies. From this example, it is apparent that when conducting dynamic sensitivity studies of this nature, all direct, cross, and cross-coupling derivatives should be included in the study model at some nominal value before making individual derivative variations.

FIGHTER-BOMBER AIRCRAFT

— BASELINE CC IN
 - - - $C_{m_r} = -1$

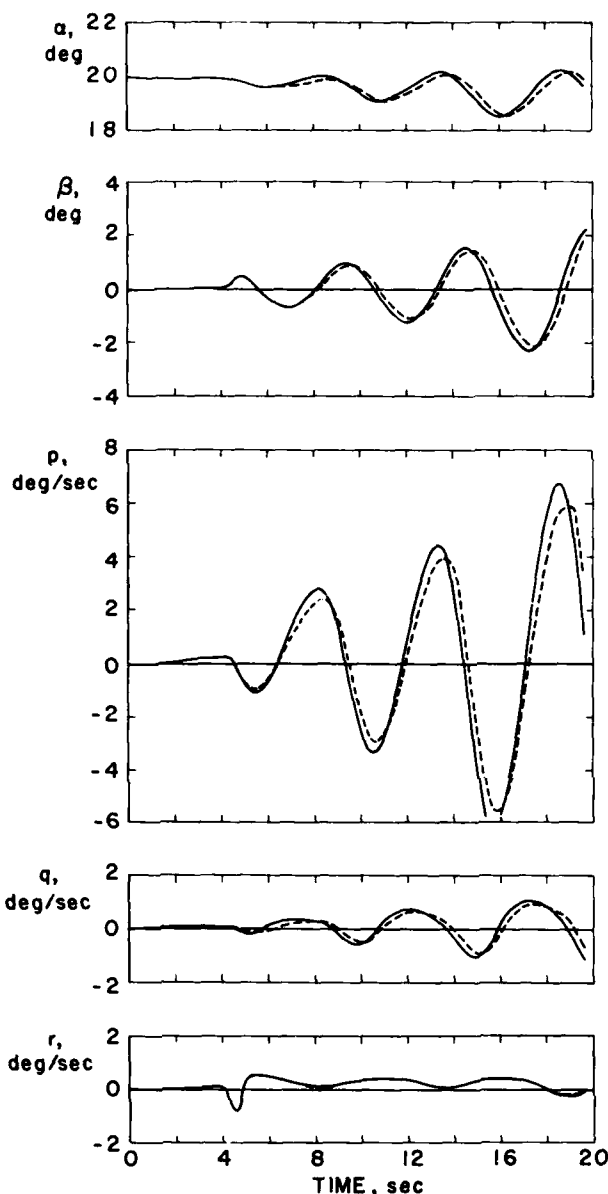


Fig. 7 C_{m_r} Variation with $C_{n_q} = 2.0$ and $C_{l_q} = 2.0$, Rudder Doublet

$C_{n_{\dot{\beta}}}$ and $C_{l_{\dot{\beta}}}$ Derivative Evaluation

Recent work in a curved flow wind tunnel (Ref. 7) on a modern fighter/bomber aircraft has resulted in the separation of the acceleration derivatives $C_{n_{\dot{\beta}}}$ and $C_{l_{\dot{\beta}}}$ from the classical $C_{n_r} + C_{n_{\dot{\beta}}}$ and $C_{l_r} + C_{l_{\dot{\beta}}}$ combinations obtained from forced oscillation testing. The derivatives were shown to possess values ranging from zero to +1 for $C_{n_{\dot{\beta}}}$ and -1 for $C_{l_{\dot{\beta}}}$ at angles of attack near 20 deg. Figure 8 presents a comparison of the baseline rudder doublet previously used (Fig. 6) with the same maneuver involving $C_{n_{\dot{\beta}}}$ and $C_{l_{\dot{\beta}}}$ included individually. As expected from the sign of the derivatives, a damping in the lateral direction planes of motion occurs. The magnitude of the damping indicates gross errors may be occurring in motion simulation at high angles of attack when the rate and acceleration derivatives are not separated and varied individually.

FIGHTER-BOMBER AIRCRAFT

— BASELINE NO CC
 $C_{l_{\dot{\beta}}} = -1.0$
 - - - $C_{n_{\dot{\beta}}} = 1.0$

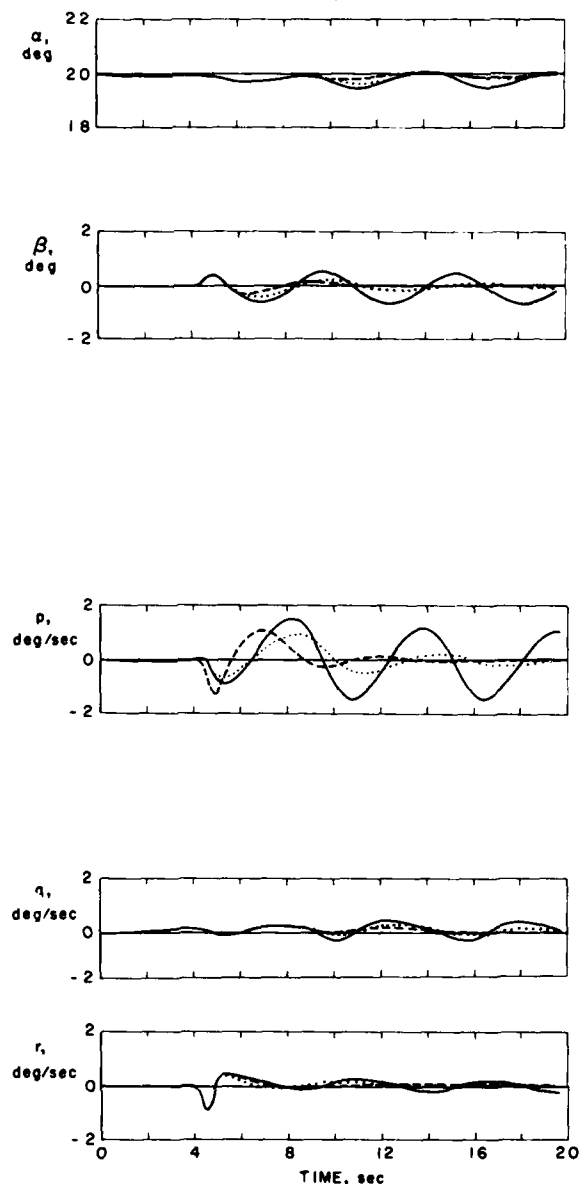


Fig. 8 $C_{n_{\dot{\beta}}}$ and $C_{l_{\dot{\beta}}}$ Variation, Rudder Doublet

Quantitative Derivative Evaluation

In the previous 6-DOF analysis it was shown that the dynamic derivatives in the equations of motion are highly interactive. When conducting a sensitivity study under these conditions, it becomes difficult to draw generalized conclusions of the importance of specific derivatives. Since in actual flight all dynamic derivatives are continually changing simultaneously as a function of aircraft aerodynamics, it becomes necessary when conducting sensitivity studies to look at many combinations of derivatives.

One approach for obtaining a more generalized picture than that presented with the 6-DOF analysis is to apply statistical techniques to the sensitivity study. Using a factorial design concept (Refs. 9 and 10), a statistical technique, each derivative under study may be evaluated for several values of each of the other derivatives. That is, each derivative effect is dependent upon the level of the other derivatives. Conducting the study in this manner helps to account for the interaction effects.

Some "measure of effectiveness" must be established for evaluating the results. The independent variables, derivatives in this case, are varied over two ranges, high and low, and the resulting effect on aircraft motion is reflected in the "measure of effectiveness." For this study, the change in frequency ($\Delta\omega_d$) and damping ($\Delta\zeta\omega_n$) of the predominate air-

craft modes of motion will be used as the measure of effectiveness. The high and low ranges of derivative variation will correspond to the maximum and minimum values in Fig. 3. Ideally, all aircraft dynamic derivatives should be included in this experiment with both low and high values. An experiment of this size would constitute 2^n combinations where n is the number of derivatives included. The subject study was limited to a variation of the cross-coupling derivatives C_{lq} , C_{nq} , and C_{mq} in the factorial design. Therefore, the com-

binations will be 2^3 . Figure 9 presents the combination of derivatives to be used in the experiment. As an example, a conventional sensitivity study may evaluate changes in aircraft frequency and damping characteristics when C_{mr} is varied from -1 to 1 at fixed levels of C_{nq} and C_{lq} . To account for interactions, C_{mr} should be varied at all combined levels of C_{nq} and C_{lq} . An algebraic expression based on Fig. 9 for achieving this goal is given below where A is the average change in frequency or damping which occurs with the derivation variation.

$$A(C_{mr}) = [|a - 1| + |ab - b| + |ac - c| + |abc - bc|] / 4 \quad (22)$$

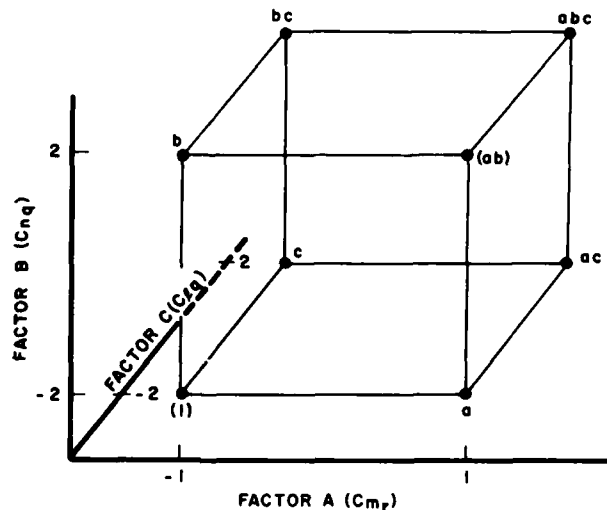


Fig. 9 2^3 Factorial Design Experiment

A 5-DOF linearized program based on the equations (10-14) was utilized to obtain changes in frequency and damping characteristics of the aircraft roll, dutch roll, spiral and short period modes of motion with derivative variation. These quantitative parameters (frequency and damping) were in turn used in Eq. 22 of the factorial design experiment. The factorial evaluation was conducted using the two aircraft previously mentioned. The second aircraft (attack aircraft) was included in this portion of the investigation to give an indication if the study results were configuration dependent. The 5-DOF analysis was conducted in trimmed 3 "g" turning flight at an altitude of 30,000 ft (9144 m). The fighter/bomber and attack aircraft trimmed angles of attack were 20 and 15 deg, respectively.

Results of the factorial design experiment are shown in Figs. 10, 11, 12, and 13 for the dutch roll, spiral, roll, and short period modes, respectively, of each aircraft. The plots give the average change in damping ($\Delta\zeta_{\omega_n}$) and frequency ($\Delta\omega_d$), which occur when

varying a derivative from its high to low value. The average changes include interactions as calculated by Eq. 22. Also included in Figs. 10 through 13 are frequency and damping changes for the dynamic cross derivatives $C_{\ell r}$ and $C_{n p}$. Since these derivatives are gen-

erally considered important in aircraft motion analysis, they are used here as benchmarks for ascertaining the importance of the cross-coupling derivatives. The frequency and damping changes presented for $C_{\ell r}$ and $C_{n p}$ variations do not include interactions as

described in the above factorial experiment. The values (high and low) over which the $C_{\ell r}$ and $C_{n p}$ derivatives are varied were obtained from experimental testing (Ref. 11)

of a fighter/bomber configuration. It should be noted that the magnitude of the $C_{\ell r}$ and $C_{n p}$ derivative variation is 1/2 to 1/4 that of the cross-coupling derivatives.

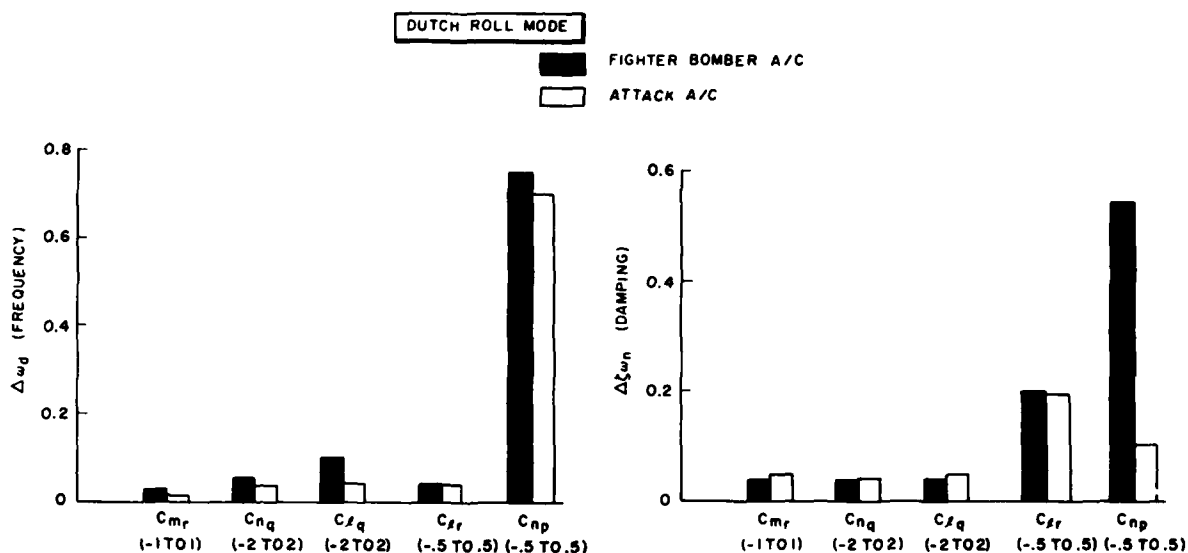


Fig. 10 Dutch Roll Mode, Linearized Analysis

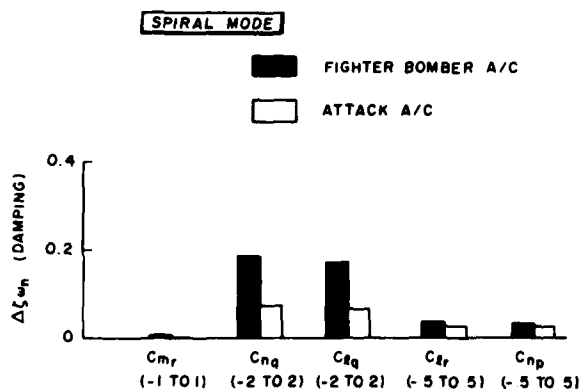


Fig. 11 Spiral Mode, Linearized Analysis

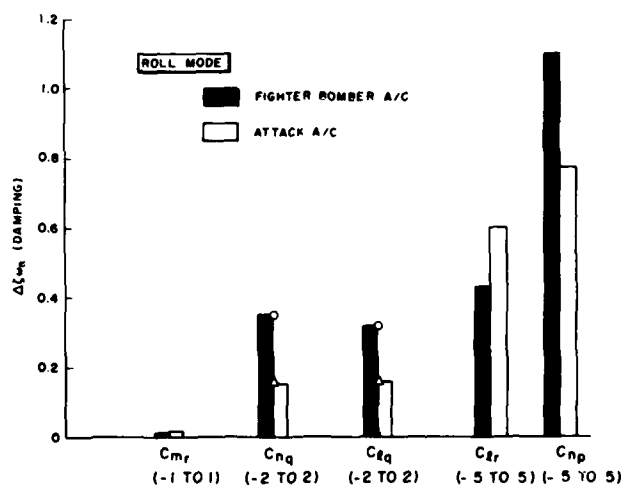


Fig. 12 Roll Mode, Linearized Analysis

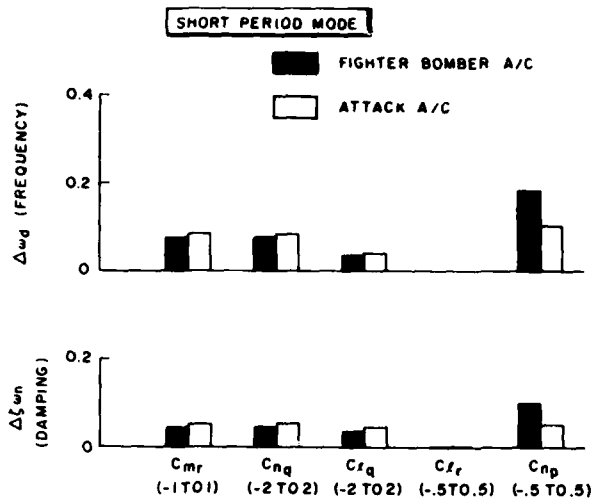


Fig. 13 Short Period Mode, Linearized Analysis

Changes in the aircraft lateral/directional modes of motion are presented in Figs. 10, 11, and 12. In these figures, the C_{m_r} derivative has little effect on the aircraft dutch roll, spiral and roll modes of motion. This result is not unexpected since the C_{m_r}

derivative should have its greatest effect on the longitudinal modes. The C_{n_q} and C_{l_q} derivatives have varying effects on the aircraft lateral/directional modes. The dutch roll mode damping and frequency are virtually insensitive to the derivative variations, as seen in Fig. 10. Although these derivatives may not appreciably alter the dutch roll mode frequency and damping, they have shown (Figs. 4 and 5) to be capable of exciting a dutch roll type motion with the proper "q" driving rate. The C_{n_q} and C_{l_q} derivative variations do have a measurable effect on the aircraft lateral/directional roll and spiral modes of motion. In the spiral mode, changes in the aircraft damping parameter $\zeta\omega_n$ with C_{n_q} and C_{l_q} variations

exceed those experienced with cross-derivative variations C_{n_p} and C_{l_r} . But it must be remembered that the ranges over which the two sets of derivatives are varied are different. It should be noted that additional solutions, not included in this paper, verified that if the derivatives C_{n_q} and C_{l_q} were of the same magnitude as the cross derivatives C_{l_r} and C_{n_p} , their effect on the roll and spiral motion becomes insignificant.

The C_{m_r} derivative which should have had the greatest effect on the short period mode exhibited the same negligible effect as encountered in the 6-DOF analysis.

The quantitative analysis verifies the preliminary conclusions arrived at the 6-DOF analysis, primarily that C_{l_q} and C_{n_q} may be important in aircraft motion analysis if they possess magnitudes approximately four times that of maximum values used in this study for the cross derivatives C_{l_r} and C_{n_p} , but that the C_{m_r} derivative appears to be insignificant. The 5-DOF analysis also indicates that the general conclusions are not highly configuration dependent.

CONCLUSIONS

As a result of this analysis, the following observations and conclusions are offered:

1. The cross-coupling derivatives C_{l_q} and C_{n_q} are important in aircraft motion if they are of a magnitude of approximately four times that of the maximum values of the cross derivatives C_{l_r} and C_{n_p} used in the subject investigation.
2. The cross-coupling derivative C_{m_r} appears to be insignificant in aircraft motion.
3. Acceleration derivatives C_{n_β} and C_{l_β} have a strong effect on the damping characteristics of an aircraft lateral/directional motion and therefore should be included in motion simulation separated from their rate counter parts C_{n_r} and C_{l_r} .
4. Interactions between dynamic derivatives should be considered when conducting dynamic sensitivity studies.

REFERENCES

1. Chen, Robert T. N., Newell, Fred D., and Schelhorn, Arno E. "Development and Evaluations of an Automatic Departure Prevention System and Stall Inhibitor for Fighter Aircraft." AFFDL-TR-73-29, U. S. Air Force, April 1973.
2. Gilbert, William P., Nguyen, Luat T., and Van Gunst, Roger W. "Simulator Study of Applications of Automatic Departure- and Spin-Prevention Concepts to a Variable-Sweep Fighter Aircraft." NASA TM X-2928, 1973.
3. Moore, Frederick L., Anglin, Ernie L., Adams, Mary S., Deal, Perry L., and Person, Lee H. "Utilization of a Fixed-Base Simulation to Study the Stall and Spin Characteristics of Fighter Airplanes." NASA TN-D-6117, 1971.
4. Gilbert, William P., Nguyen, Luat T., Van Gunst, Rober W. "Simulator Study of the Effectiveness of an Automatic Control System Designed to Improve the High Angle of Attack Characteristics of a Fighter Airplane." NASA TN D-8176, 1976.
5. Ashworth, B. R and Kahlbaum, William M., Jr. "Description and Performance of the Langley Differential Maneuvering Simulator." NASA TN-D-7304, 1973.
6. Orlik-Ruckemann, K. J., Hanff, E. S., Laberge, J. G. "Direct and Cross-Coupling Subsonic Moment Derivatives Due to Oscillatory Pitching and Yawing of an Aircraft-Like Model of Angles of Attack up to 40° in Ames 6 x 6 Wind Tunnel." NAE LTR-UA-38, 1976.
7. Coe, Paul L., Graham, Bruce, H., Chambers, Joseph R. "Summary of Information on Low-Speed Lateral-Directional Derivatives Due to Rate of Change of Sideslip β ." NASA TN-D-7972.
8. North American Rockwell: "Digital Simulation User's Manual, NR70H-232-2, June 1970.
9. Thomas, Jerry. "Application of Statistical Techniques to Model Sensitivity Testing." Army Concepts Analysis Agency, AD/A-005-032, 1974.
10. Hicks, Charles, R. "Fundamental Concepts in the Design of Experiment.." Holt, Rinehart and Winston, Inc. 1974.
11. Grafton, Sub, B., Libbey, Charles E. "Dynamic Stability Derivatives of a Twin-Jet Fighter Model for Angles of Attack from -10° to 110°." NASA TN-D-6091, 1971.

IDENTIFICATION OF KEY MANEUVER-LIMITING FACTORS IN HIGH-ANGLE-OF-ATTACK FLIGHT

Donald E. Johnston
Systems Technology, Inc.
3700 South Hawthorne Boulevard
Hawthorne, California, U.S.A.

ABSTRACT

New results of a current analytic and simulation investigation of maneuver-limiting (e.g., loss of control) factors in fighter aircraft at high angle of attack are reported. Two goals of the program are to identify the key parameters which result in high-angle-of-attack maneuver-limiting phenomena such as wing rock, nose slice, and rolling divergence and to demonstrate the influence of these key parameters in controlling the nature of the maneuver-limiting phenomena. This analysis and simulation have centered on unsymmetric flight.

It is shown that lateral-longitudinal coupling due to nonlinear aerodynamic $C_{l\dot{\alpha}}$ interaction produces terms and influences which can severely limit the applicability of analytical methods employing frozen point aerodynamic coefficients and linearized, small perturbation equations of motion. It is shown that linearized 7 or 11 degree-of-freedom analytical approaches can predict a divergent dutch roll; whereas 11 degree-of-freedom simulation with nonlinear aerodynamic coefficients as $f(\alpha, \beta)$ shows a constant amplitude (limit-cycle-like) lateral oscillation. The constant amplitude wing rock is accompanied by a constant amplitude longitudinal oscillation having twice the wing rock frequency which is unpredicted by conventional linear analysis techniques. However, it also is shown that linear analysis techniques can provide much insight into the nature and cause of wing rock, nose slice, and other forms of departure.

INTRODUCTION

In recent years many high-performance swept-wing aircraft have been lost in high α maneuvering due to stall-departure incidents. Departure is defined as uncommanded and/or uncontrollable motion of the aircraft, Ref. 1, and may be manifested as wing rock, nose slice, pitch-up, etc. Wing rock is generally described as a predominantly rolling motion of significant amplitude. Nose slice is represented as a large rapid yaw generally followed by rapid roll. Pitch-up may or may not accompany either of these lateral-directional phenomena. Some aircraft primarily exhibit wing rock (Ref. 2), some only nose slice (Ref. 3), and some transition from wing rock to nose slice as α increases (Ref. 1).

Considerable research, Refs. 4-7, has been conducted into possible causal factors for such departures. Analysis has generally centered around open-loop criteria ($C_{n\dot{\alpha}_{dyn}}$ and LCDP, the lateral control divergence parameter, Ref. 4) in symmetric, uncoupled lateral-longitudinal flight. The success of these parameters in predicting or providing insight to departure often leaves much to be desired.

This paper presents a somewhat different view of the role played by $C_{n\dot{\alpha}_{dyn}}$ in defining departure and identifies other aerodynamic coefficients which also play key roles. The analysis is then extended into development of, and possible physical explanation for, open- and closed-loop parameters which arise in unsymmetric ($\beta \neq 0$) flight and appear to underlie certain characteristics of wing rock, pitch-up, and nose slice. The analysis is based on a nonlinear six-degree-of-freedom digital model which incorporates aerodynamic coefficients as functions of α and β .

The F-4 aircraft has been selected as the principal example partially because it exhibits both wing rock and nose slice but mainly due to the extensive data base on this aircraft. In fact, it is probably one of the most completely analyzed and tested aircraft in existence. Figure 1 presents motion traces from a flight in which the pilot was intent upon obtaining departure and spin entry. These reflect an oscillatory sideslip divergence beginning at approximately 20 deg α . As α is steadily increased the sideslip oscillation increases in amplitude until at about 25 deg α a lateral excursion is obtained which immediately leads to a spin entry. Computer-generated images (Fig. 2) constructed from aircraft attitude measurements show the departure to be predominantly in yaw (nose slice). Figure 3 presents motion traces from another situation in which the task was to obtain and demonstrate wing rock. The α is increased until wing rock onset and then maintained relatively constant to allow the oscillation to build. The lateral stick is then centered but the yaw damper is functioning. In this case the oscillation does not continue to build but reaches a constant amplitude. An oscillation at twice the wing rock frequency also develops in the α trace. The latter effect has been observed to accompany wing rock in a number of aircraft.

SYMMETRIC FLIGHT ANALYSIS

The classic divergence criteria are defined by Moul and Paulson, Ref. 4, to be

$$C_{n\dot{\alpha}_{dyn}} = C_{n\dot{\alpha}} \cos \alpha_0 - \frac{I_z}{I_x} C_{l\dot{\alpha}} \sin \alpha_0$$

and

$$LCDP = C_{n\dot{\alpha}} - \frac{C_{n\dot{\beta}_a}}{C_{l\dot{\beta}_a}} C_{l\dot{\alpha}}$$

where all coefficients are in aircraft body centerline axis and negative values of the criteria predict directional divergence and roll reversal, respectively. If the aircraft principal axis is close to the centerline, these same criteria are expressed in primed body axis dimensional derivative form:

$$N'_{P_{\text{dyn}}} = N'_P \cos \alpha_0 - L'_P \sin \alpha_0 = N'_{P_{\text{stability}}}$$

and

$$LCDP = N'_P \frac{N'_{\delta a}}{L'_{\delta a}} L'_P$$

These two parameters evaluated for a symmetric ($\beta = 0$) aircraft configuration and a range approximating that of Fig. 1 are plotted in Fig. 4. The criteria predict a directional divergence for $\alpha > 22.5$ deg and establish $\alpha \approx 18$ as the α at which sideslip due to adverse "aileron" yaw becomes so severe as to produce roll reversal. Hence, the latter is an indication of the region in which rudder maneuvering and unsymmetric, $\beta \neq 0$, flight may predominate.

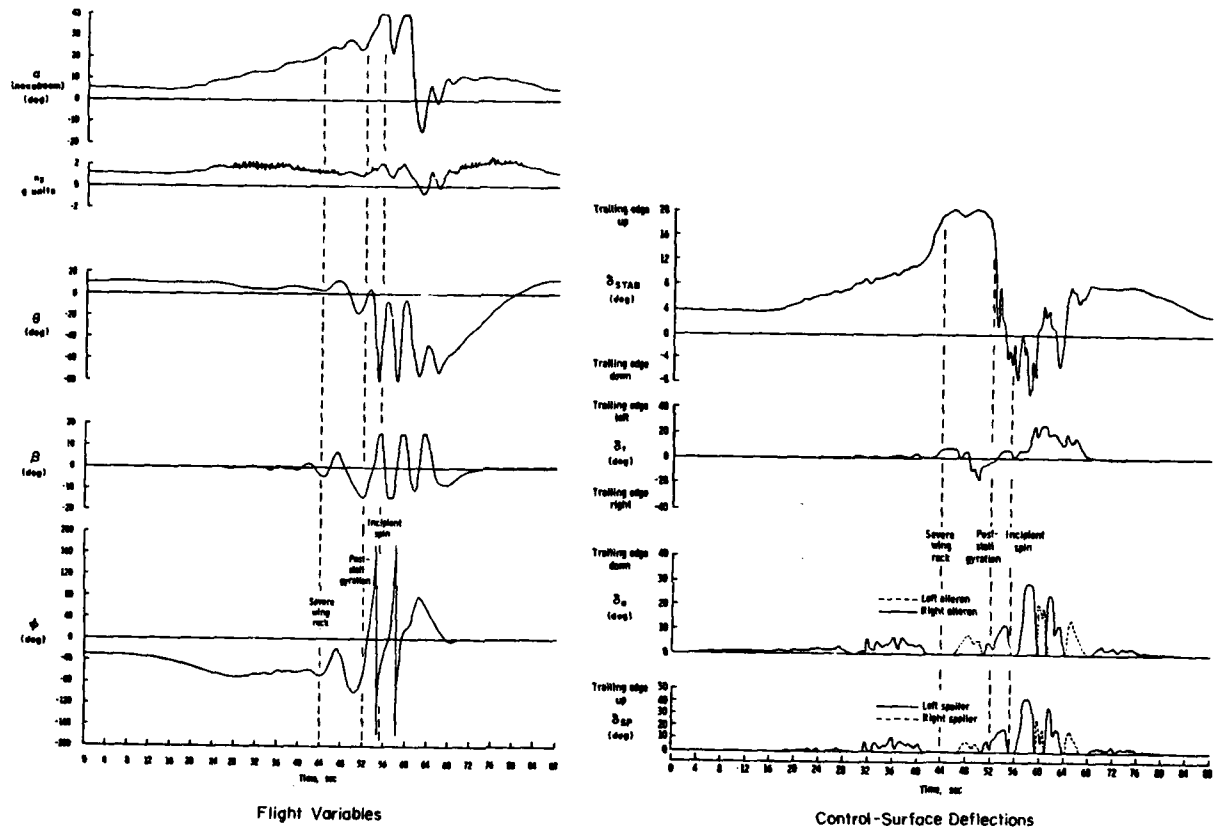


Figure 1. Typical Roll Departure/Spin Entry

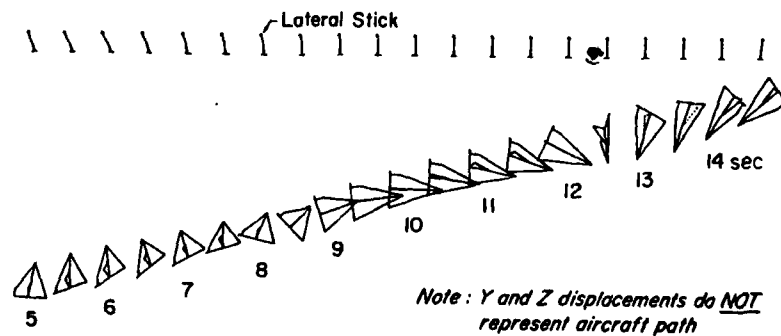


Figure 2. Aircraft Attitude During Departure and Spin Entry

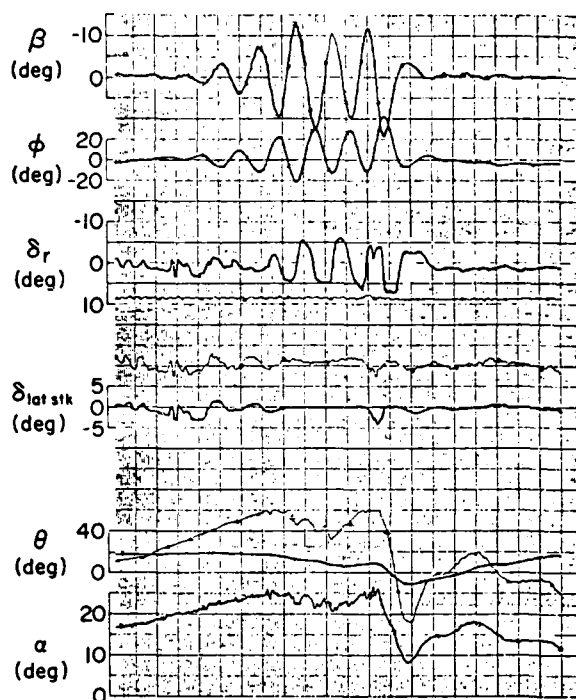


Figure 3. Pull-up and Steady Wing Rock

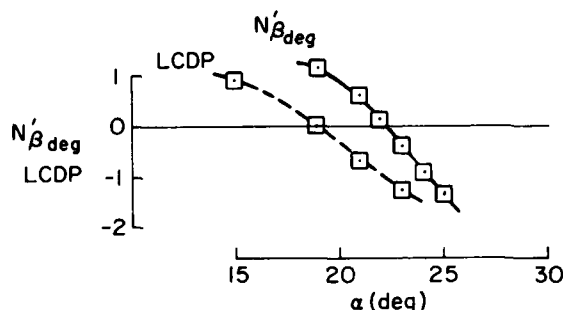
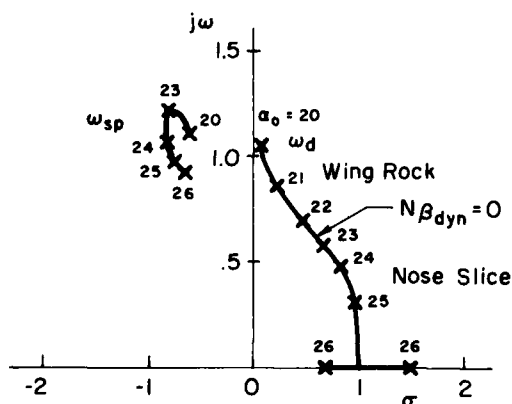


Figure 4. Divergence Criteria Predictions for the F-4

Figure 5. Lateral/longitudinal Root Migration With α

On the surface, both criteria appear to fit well with the flight traces of Figs. 1 and 3. That is, lateral stick (aileron) excites sideslip and the aircraft does indeed become divergent at $\alpha \approx 23$ deg. However, these criteria do not signal the onset of self-sustaining wing rock or provide indications of its severity.

Dutch roll and short-period roots obtained from conventional $p = 0$, frozen point six-degree-of-freedom (DOF) perturbation equations are plotted in Fig. 5 for the same α range. The dutch roll (ω_d) is increasingly divergent for $\alpha > 20$ deg, while the short-period (ω_{sp}) is stable and relatively unchanged with α . Also identified in Fig. 5 are the α ranges in which test pilot commentary, Ref. 1, indicates wing rock and nose slice predominate.

The migration of roots in Fig. 5 and pilot commentary appear to be quite consistent with the flight traces of Fig. 1. As noted by others, Ref. 8, wing rock develops from the dutch roll mode and is identified with a region in which $N'_\beta \ll 1$ and $1/p/L$ is small. Any disturbance or control input which produces sideslip then sets off a lowly damped or divergent rolling-sideslipping dutch roll oscillation. Because $N'_\beta \ll 1$, the instantaneous roll axis for sideslip is very near the aircraft centerline axis and the motion is viewed by the pilot as wing rock.

As α is increased, $N'_{\beta_{dyn}}$ approaches zero because N'_β and $N'_\beta \cos \alpha$ increase negatively. Thus the instantaneous roll axis for sideslip steadily rotates downward toward the flight path axis, and the resulting motion of the aircraft nose appears to the pilot to be predominantly yaw — or nose slice. Thus $N'_{\beta_{dyn}} < 0$ is adequate for predicting a tendency toward nose slice and the general α region in which it might be expected.

There is one problem in that the root locations of Fig. 5 obtained from linearized, frozen point analytic techniques are not in agreement with the flight traces of Fig. 3. As noted previously, the latter indicates a constant amplitude wing rock in the region of 21-23 deg α and a small pitch oscillation having twice the frequency of the wing rock, whereas the former indicates the two modes to be about the same frequency and the wing rock to be rapidly divergent. However, the nonlinear, 6 DOF mathematical model produced the time responses as shown in Fig. 6 when trimmed for level, symmetric flight in the region of 21-22 deg α . The complete nonlinear model lateral response emulates the actual aircraft rather than the unbounded divergent motion predicted by the frozen point small perturbation linear mathematical model. Furthermore, the nonlinear model longitudinal response exhibits a continuous oscillation with frequency twice that of the dutch roll instead of the predicted well-damped short-period mode having about the same frequency as the dutch roll. Thus the Fig. 6 traces agree quite well with the flight traces of Fig. 3.

It is clear then that the response of the unrestrained six-degree-of-freedom model having aerodynamic coefficients as a function of α and β produces aircraft motion in good agreement with the actual aircraft. However, frozen point, symmetric flight, small-perturbation theory transfer functions obtained from the same mathematical model do not predict these aircraft responses. Such shortcomings of linear analysis techniques for high α flight situations have been noted by others, Refs. 10 and 11. Ross, Ref. 11, obtained constant amplitude wing rock accompanied by small

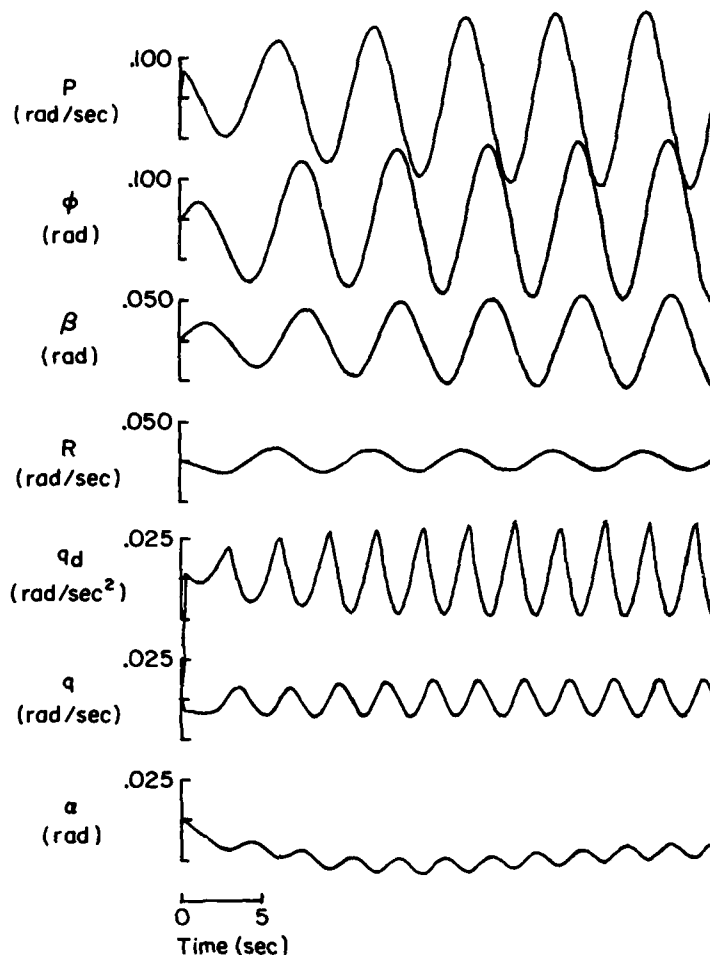


Figure 6. Open-Loop Nonlinear Airframe Response to Pulse Aileron; $\alpha_0 = 21$ deg; $\beta_0 = 0$ deg

amplitude longitudinal oscillations. The latter were dismissed as of little concern because they are of small amplitude and caused by the lateral motion. Rather, attention was focused on developing a nonlinear analytic model to predict the constant amplitude of the lateral oscillation. The model so developed emphasized nonlinear yawing moments of the form $C_n = n_1\beta + n_3\beta^3$ and was partially successful in that it predicted a limit cycle but the amplitude of oscillation was about 40-50 percent greater than actually obtained in full 6 DOF nonlinear simulation. This discrepancy was not explained by Ross but may well have been due to the longitudinal motions which were not considered.

If one were to observe only the pitch rate or angle-of-attack traces of Fig. 6 it might be difficult to deduce the potential source of the longitudinal oscillation. The pitch acceleration trace, however, reflects a rectification or folding phenomenon with the sharp cusps coinciding with zero crossings in the sideslip trace. This provides a strong clue that the source of coupling might be an aerodynamic cross derivative, $C_{m\beta}$. To test this theory the variation in pitching moment with sideslip was set to zero and the nonlinear 6 DOF model no longer exhibited the double frequency pitch oscillation and, more important, the lateral-directional oscillation diverged in amplitude as predicted by the linearized frozen point math model. In fact, the amplitude of wing rock oscillation was found to be inversely proportional to $C_{m\beta}$.

An additional test was performed with the nonlinear 6 DOF model containing $C_{m\beta}$ coupling. A pitch attitude to elevator control loop was closed to approximate pilot control of aircraft attitude. The feedback gain was selected to produce a closed-loop pitch response natural frequency twice that of the wing rock. The resulting vehicle motion is shown in Fig. 7. As one might expect, the pitch loop closure reinforces the basic aircraft coupling and causes the pitch oscillation to grow in amplitude. This in turn causes the lateral-directional oscillation to diverge. Neither result is predicted by conventional linear systems analysis techniques. The potential catastrophic results of such an unpredicted event in actual flight are self evident.

As a final check on the influence of $C_{m\beta}$ lateral-longitudinal coupling the sign of this coefficient was reversed (made positive) and the same trim condition established. With positive $C_{m\beta}$ the aircraft pitched up at each sideslip excursion, became more divergent laterally, and rapidly departed.

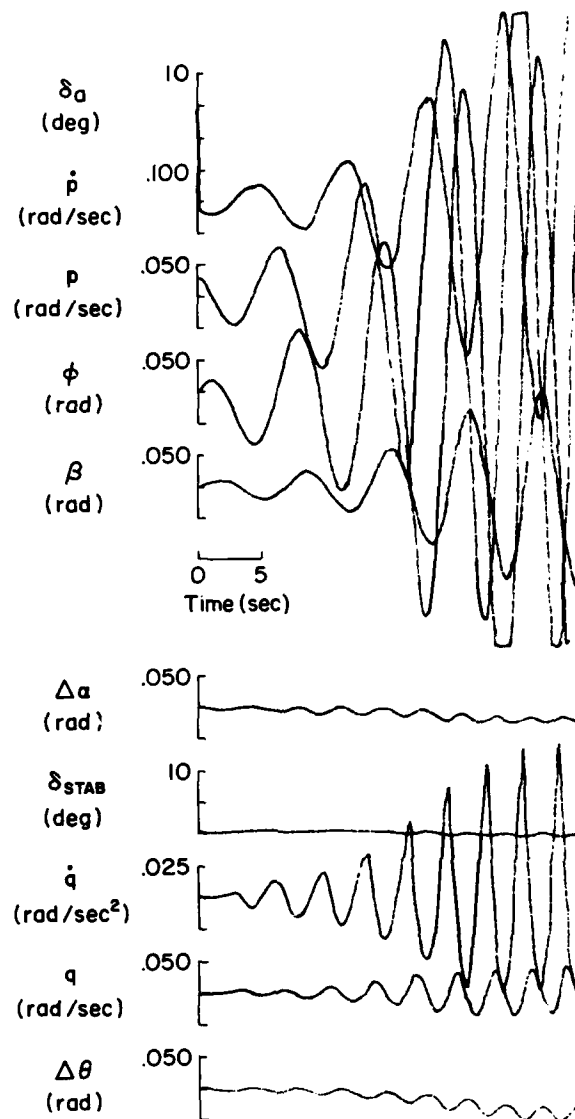


Figure 7. Destabilizing Influence of Pitch Attitude Loop Closure at the Coupled Pitch Frequency; $\alpha_0 = 21$ deg; $\beta_0 = 0$ deg

Quite obviously, the discrepancy between frozen point, linearized analysis and unfrozen, coupled airframe responses needs to be resolved. Either nonlinear analytic techniques need to be developed or new ways of applying and interpreting linear analysis must be derived. One such approach is to employ unsymmetric ($\beta \neq 0$) trim conditions.

UNSYMMETRIC FLIGHT ANALYSIS

The purpose of this analysis is twofold: to show the influence of steady β on key F-4 open- and closed-loop stability factors; and to show the usefulness and limitations of linear analysis techniques in coping with asymmetric flight. Asymmetric flight can arise from a number of situations, e.g., inadequate trimming of aircraft asymmetries (construction tolerances, asymmetric stores), rudder maneuvering, uncoordinated turns, departure onset, etc.

For this analysis the digitally simulated nonlinear 6 DOF aircraft was trimmed to 1 g flight over a range of α and β conditions. Perturbation aerodynamic coefficients were obtained from partial derivative expansion and the equivalent dimensional stability derivatives and transfer functions calculated. Figure 8 presents the nine-by-nine matrix (three body axis angular rates, three velocity vector axis forces, three Euler angle attitudes) obtained. The major derivatives are identified in literal form and, for comparison, are evaluated at $\alpha_0 = 21$ deg and $\beta_0 = 1.5$ deg. Very small off-diagonal terms have been deleted for simplicity. The major aerodynamic coupling is seen to be provided by the terms within the heavy borderlines: $L_{\dot{\alpha}}$, $N_{\dot{\alpha}}$, and $M_{\dot{\beta}}$. Note that even at this relatively small sideslip angle (1.5 deg) the magnitude of these coupling derivatives approaches or exceeds those of the conventional derivatives.

Figure 8. Matrix for Coupled Equations with $f_0 \neq 0$

Figure 9 presents the dutch roll and short-period root locations for the range of α and β investigated. This plot indicates the F-4 exhibits an exchange of energy between lateral and longitudinal modes as sideslip increases. The dutch roll becomes more divergent (as actually demonstrated in asymmetric flight testing, Ref. 1), and the short-period becomes more heavily damped. These root migrations are in close agreement with the literal, approximate factor analytical technique developed by Hamel, Ref. 12, for determining the influence of \dot{L}_{α} , N_{α} , and M_{β} on the 5 DOF airframe characteristic roots.

Open-loop time traces for the nonlinear 6 DOF airframe at $\alpha_0 = 21$ deg and $\beta_0 = 1.5$ deg are shown in Fig. 10. As predicted from the Fig. 9 migration, the lateral-directional responses are seen to be more divergent than those of Fig. 6 (where $\beta_0 = 0$) until zero β crossings are encountered. The yaw traces then become quite nonlinear. However, the longitudinal traces come as a complete surprise. The root location of Fig. 9 indicates any short-period disturbance should rapidly damp to zero, yet the longitudinal time traces reflect an instability of the same frequency and divergence rate as the lateral-directional motions until zero β crossings are encountered. The latter again indicate the strong influence of sideslip in forcing pitch motions.

Clearly, a simple analytic technique is needed to provide insights to the coupled airframe responses not afforded by the preceding linear analysis techniques. Attention was turned to the time vector and force moment polygon methods, Ref. 9. Time vectors for the $\alpha_0 = 21$ deg, $\beta_0 = 1.5$ deg dutch roll and short-period modes are shown in Fig. 11. The model composition of the dutch roll is seen to be dominated by roll and to have comparable magnitudes of r , q , α , θ , and β . The acute angle between the roll and yaw attitude and rate vectors indicates a mild divergence. This is consistent with the nonlinear airframe time traces of Fig. 10 until zero β crossings occur. Due to the proximity of the two modal frequencies, the short period also has about the same initial magnitude and motion composition as the dutch roll but with slightly different phasing. Here the obtuse angle between pitch attitude and rate vectors indicates large modal damping. The interpretation is that the initial short-period and dutch roll modal responses are so similar that they cannot be identified individually. The short period rapidly decays and all subsequent lateral and longitudinal motion is due solely to the dutch roll. Thus the time vector approach appears applicable in gaining insight to coupled lateral-longitudinal response provided no zero β crossings are involved.

Vector polygons are shown in Fig. 12 for the force and moment equations as constructed from dutch roll mode time vectors and their appropriate aerodynamic and kinematic multipliers. The key equations are \dot{p} , \dot{r} , and \dot{q} where the influence of the coupling derivatives \dot{L}_{α} , N_{α} , and M_{β} , respectively, may be observed. For example, in the \dot{p} equation, the \dot{L}_{α} term is phased, along with a large component of the $L_{\dot{r}}$ vector, to oppose the basic roll damping, $L_{\dot{p}}$. These aerodynamic terms therefore

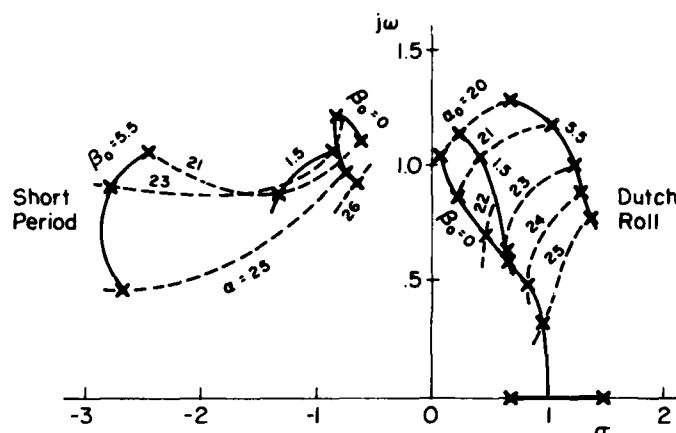


Figure 9. 6 DOF Linearized Equation; Lateral/Longitudinal Root Migration with α and β

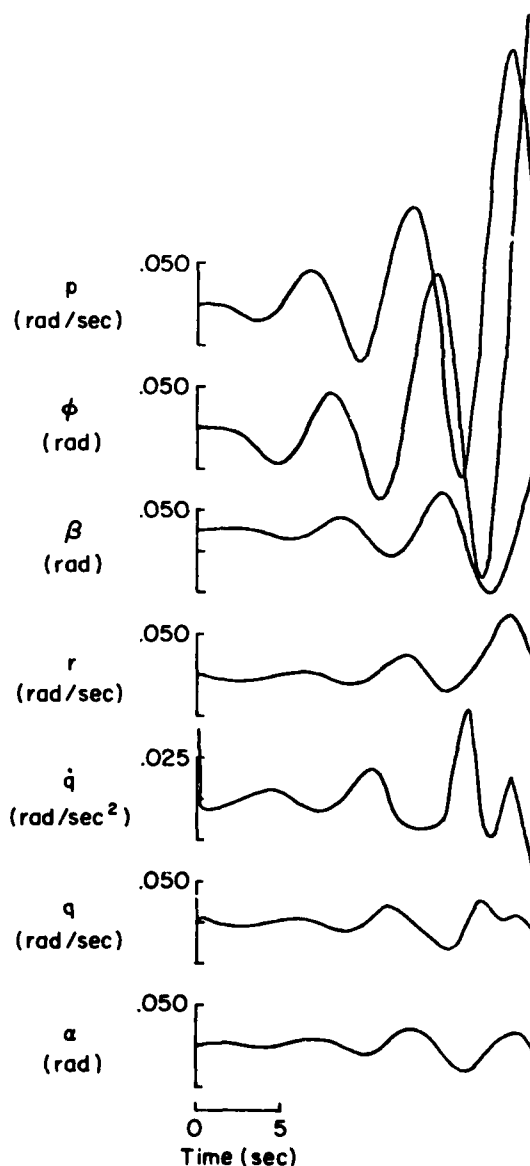


Figure 10. Open-loop Nonlinear Airframe Response to Elevator Pulse; $\alpha_0 = 21$ deg; $\beta_0 = 1.5$ deg

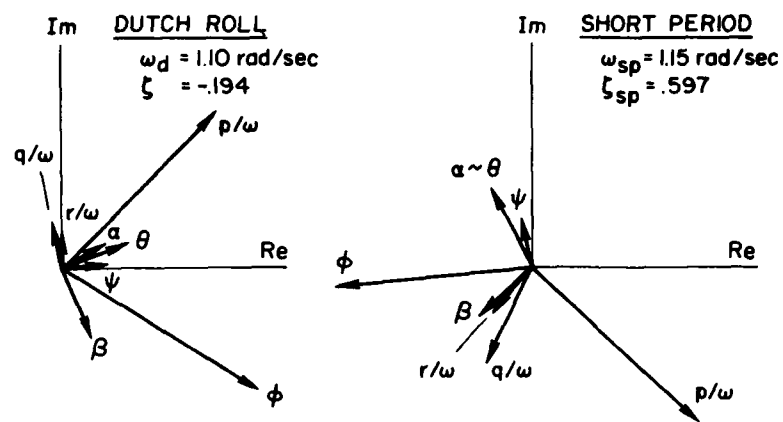
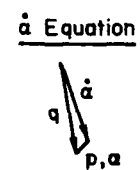
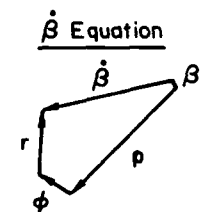
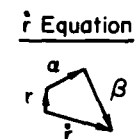
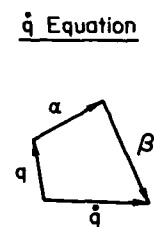
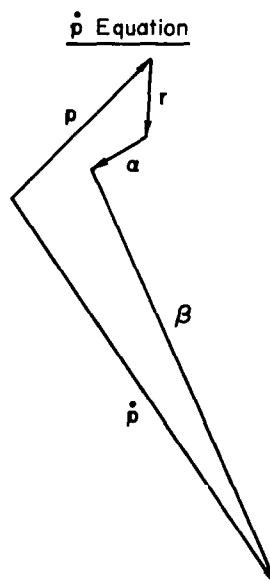
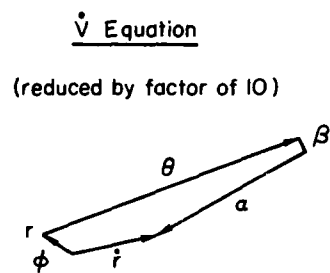


Figure 11. Eigenvectors

Figure 12. Vector Polygons; $\alpha_0 = 21 \text{ deg}$, $\beta_0 = 1.5 \text{ deg}$

reduce the effective roll damping and should thereby cause the dutch roll root to move further into the right half plane as shown in Fig. 9. The $N_{\dot{\alpha}}$ contribution to the \dot{r} equation augments the $N_{\dot{r}}$ damping; however, yaw motion in the dutch roll is so small that this coupling appears to have minimal effect at this flight condition.

The most interesting vector diagram is that for the \dot{q} equation. Here the $M_{\dot{\beta}}$ vector is larger than and phased almost 180 degrees to the $M_{\dot{q}}$ vector. Hence the $M_{\dot{\beta}}$ contribution overpowers the basic airframe longitudinal damping, $M_{\dot{q}}$, and forces transfer of the dutch roll mode into longitudinal responses.

A plot of pitching moment coefficient versus sideslip at several angles of attack for the F-4 aircraft is shown in Fig. 13. This indicates the pitch moment with sideslip is essentially symmetric about the $\beta = 0$ line and, indeed, our model was made precisely so. The slope $\partial C_m / \partial \beta$ is particularly steep in the region around 20 deg α with sideslip of either sign producing nose-down pitch. This then is the final clue to the limit-cycle-like oscillation of Fig. 6. Any symmetric oscillation about $\beta = 0$ produces pitch-down moments on each β excursion and, for a set trim elevator deflection, reduces the trim α and increases dutch roll stability. A possible accompanying, stabilizing influence is the energy expenditure required to overcome aircraft pitch inertia and force the oscillation at double the aircraft natural frequency.

Thus, the application of time vector and vector polygon techniques to frozen point, unsymmetric flight conditions provides insight to cause-effect relations not afforded by more commonly employed linear analysis methods. The vector techniques also help identify flight regions and conditions where nonlinear analysis and simulation must be relied upon if precise stability modeling is required.

CLOSED-LOOP DEPARTURE CRITERIA

As shown previously, for the F-4 when $N_{\dot{\alpha}} = 0$ the open-loop aircraft becomes sufficiently unstable directionally that it will depart. The resulting motion may be a nose slice or, depending upon the aircraft motion and control inputs immediately preceding the departure, may be a rolling departure.

A closed-loop parameter was discovered during investigation of the A-7 (Ref. 13) which produces nose slice departure at α less than predicted by $N_{\dot{\alpha}}$. This parameter, $1/T_{\theta 3}$, is a non-minimum phase zero in the elevator to pitch attitude numerator that arises only in unsymmetric flight. It attracts a denominator pole upon closure of the loop and results in a nose slice divergence. The divergence rate is determined by how far the non-minimum phase zero lies in the right half s-plane.

A single-loop system survey, Ref. 9, for elevator control of pitch attitude with the 6 DOF coupled A-7 airframe in asymmetric flight is shown in Fig. 14. The transfer function is shown in the upper left. The root locus in the top right of the figure reflects root migrations for a pure gain closure. Note that the roots starting at ω_{SR} rapidly move to the real axis and then split into two real roots — one moves towards $1/T_{\theta 2}$, the other moves towards $1/T_{\theta 3}$. The rapidity of the movement of these closed-loop poles towards the zeros is demonstrated by a Bode-siggy plot in the bottom half of Fig. 14. The heavy solid and dashed lines of the Bode correspond to the path of the closed-loop roots along the real (σ) axis in the root locus above. As the loop gain is increased, the complex poles emanating from ω_{SR} meet the real axis at the apex of the solid curve in the Bode-siggy plot. Further increase in gain moves one closed-loop root to a lower frequency or towards the origin, while the other root moves to higher frequency and, at very high gain, asymptotically approaches $1/T_{\theta 2}$. The root that goes toward the origin passes into the right-half-plane as shown in the root locus. This is represented in the Bode-siggy by the dashed line which reflects the mirror image of the closed-loop pole asymptotically approaching the $1/T_{\theta 3}$ zero at -0.3 rad. If the pilot is to achieve effective control of pitch attitude, he must close the loop so the gain line lies below the low-frequency asymptote of the Bode plot, thereby intersecting the dashed locus corresponding to a closed-loop pole in the right-half-plane. If the pilot closes the loop so that unity gain "crossover" is achieved in the region of 1-3 rad/sec, which covers the range of usual "loose" to "tight" piloted pitch attitude control, it may be seen that the closed-loop poles will lie very close to the open-loop zeros. For example, a unity DC gain provides a crossover between 1.5 and 2.5 rad/sec and closed-loop roots at -0.28 and $+0.66$ rad/sec. The resulting first-order divergence has a time constant of about 3.6 sec.

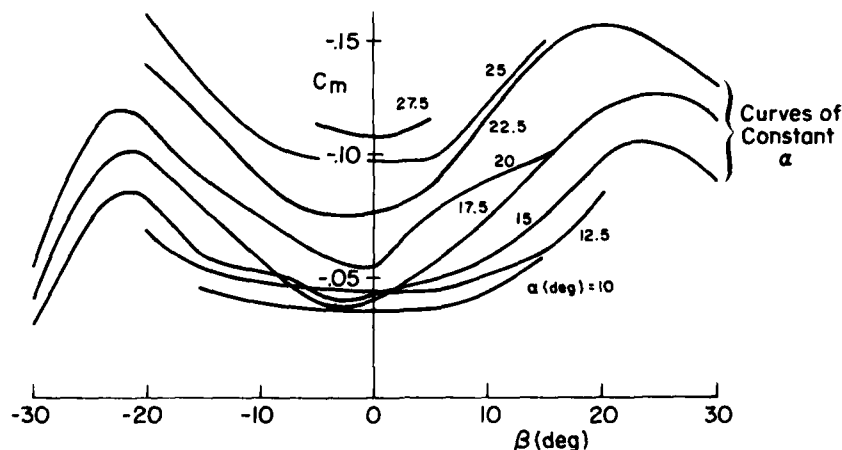


Figure 13. C_m Versus β From F-4 Lookup Tables

Shields, Ref. 3, and Bell and Ethridge, Ref. 14, indicate that A-7 departure recovery is best accomplished by neutralizing the cockpit controls or, preferably, "letting go" of the stick. In Fig. 14 this opens the loop and returns the aircraft roots to the stable open-loop pole position and the aircraft then should recover by itself.

The difference in A-7 open- and closed-loop responses may be observed from time traces of a 6 DOF digital simulation using nonlinear aerodynamics. Figure 15 shows open-loop lateral and longitudinal time traces for the A-7 initially trimmed at 17.3 deg α_0 and 0 deg β_0 and with a ramp δ_e input of 1.2 deg/sec. There is no indication of instability at 19 deg α . An aileron doublet is introduced to provide some excitation of the lateral modes, and it is several seconds before a slow directional divergence starts at approximately 21 deg α (9 sec). It then couples with p (and α) to form a divergent lateral oscillation with a period of approximately 11 sec. This is shown, Ref. 13, to be an unstable lateral-phugoid mode. It should be noted that for symmetric flight $N_{\dot{\beta}dyn}$ goes to zero at $\alpha = 21$ deg.

Figure 16 shows the system response when the pitch attitude loop is closed with unity gain (as in Fig. 14) and a step θ_0 of 0.57 deg is introduced. The aircraft is initially trimmed for steady flight at $\alpha = 19$ deg, $r = 6$ deg, and $\varphi = 5$ deg. A first-order nose slice divergence is seen to start immediately even though $N_{\dot{\beta}dyn} = 0$ does not occur until $\alpha = 22.5$ deg at $\beta = 6$ deg. The divergence time constant of 3.6 sec for the r , φ , θ , and α traces is consistent with the closed-loop right-half-plane root location predicted in Fig. 14. By the time 24 deg α is reached the aircraft has long since departed.

The origin of $1/T_{\theta 3}$ was traced, Ref. 13, to the aerodynamic coupling terms $\dot{\alpha}'_a$ and N'_a that arise in asymmetric flight. It was also confirmed by the Ref. 13 piloted simulation that variation in $\dot{\alpha}'_a$ and N'_a controls location of $1/T_{\theta 3}$ and the severity of the aircraft closed-loop control nose slice departure. Further support comes from recent analysis and simulation of additional aircraft as summarized in Table 1. Since it is indeed common for the pilot to be exerting closed-loop pitch control in high α flight, it appears $1/T_{\theta 3}$ and/or its underlying parameters ($\dot{\alpha}'_a$ and N'_a) are worthy of consideration to avoid surprise departures at angles of attack well below that for $N_{\dot{\beta}dyn} = 0$.

CONCLUSIONS

The discussion has demonstrated that the more common frequency domain linear analysis techniques applied to symmetric, frozen point airframe models may produce totally misleading or erroneous answers if the aircraft exhibits significant coupling due to sideslip. These same analytic techniques provide valid predictions in cases where C_m , C_l , C_n are $f(\alpha, \beta)$ providing the frozen point model represents asymmetric trim conditions and the analytic results are not applied to β excursions through zero.

The time vector and force and moment equation polygon linear analysis technique provides considerable insight to the nature of coupled lateral-longitudinal motions and to cause-effect relationships. Thus, they serve as a powerful adjunct to conventional lateral approximate factors in identifying aerodynamic or flight control means of combating undesirable vehicle characteristics.

The coupling derivative $\dot{\alpha}'_a$ causes a significant decrease in the F-4 high α roll damping and hence increases its tendency to wing rock. The constant amplitude, limit-cycle-like characteristic of the F-4 wing rock is principally due to negative $M_{\dot{\beta}}$ coupling. This coupling term is also the source of the high-frequency pitch oscillation that accompanies F-4 wing rock, and any aircraft exhibiting $M_{\dot{\beta}} \neq 0$ in a region of significant wing rock may have a propensity to longitudinal pilot-induced oscillation (PIO).

The cross-coupling derivatives $\dot{\alpha}'_a$ and N'_a together give rise to a non-minimum phase zero in the pitch attitude control numerator and can cause closed-loop nose slice departure at angles of attack considerably less than predicted by the open-loop parameter, $N_{\dot{\beta}dyn}$.

Continued application of these techniques is needed to increase understanding and interpretation of the results and confidence in their usefulness.

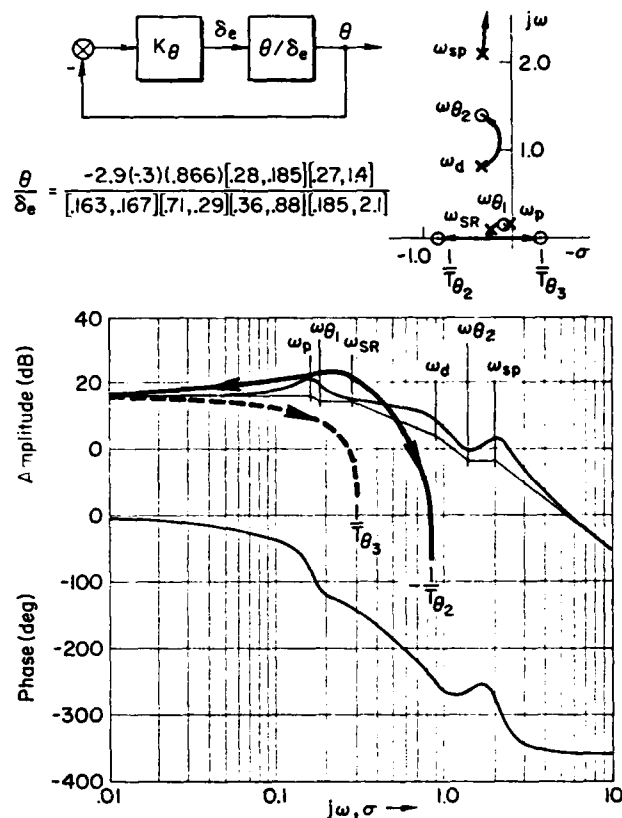
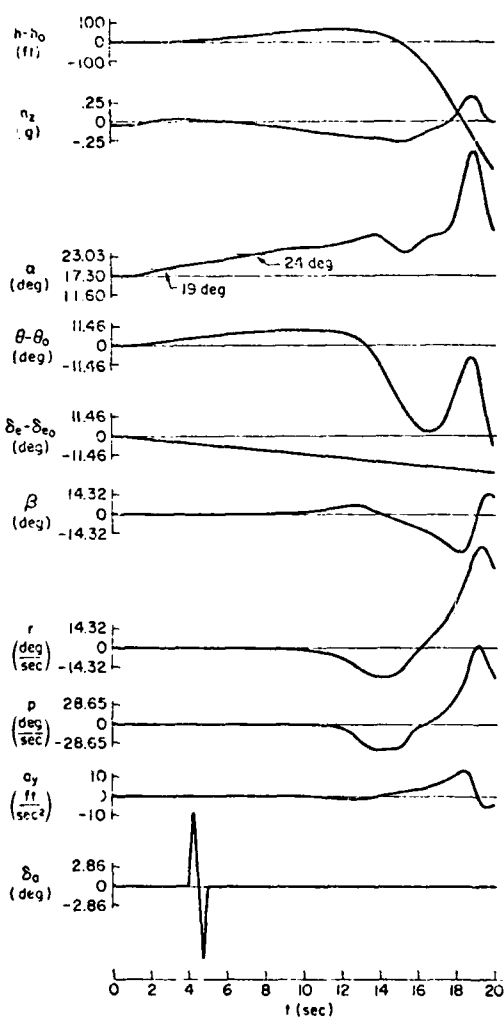
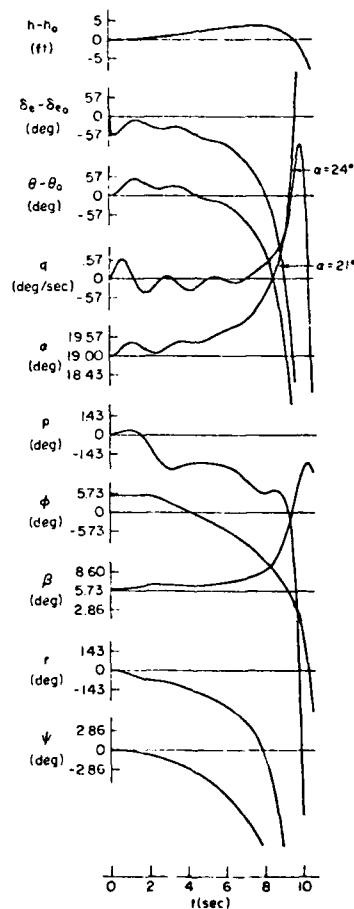


Figure 14. Pitch Attitude Closure Survey, $\alpha_0 = 19.8$ deg, $\beta_0 = 6$ deg

TABLE 1. RELATIONSHIP BETWEEN SIDESLIP, PITCH ATTITUDE ZERO, AND CLOSED-LOOP DEPARTURE CHARACTERISTICS

AIRCRAFT	α_0	β_0	$1/T\theta_3$	NOSE SLICE CHARACTERISTIC
A	21	1.5	+0.233	None
	21	5.5	-0.6	Severe
B	19	0	-0.013	None
	19	6.	-0.45	Moderate
C	21	1.5	-0.01	None
	21	5.5	-0.18	No apparent nose slice

Figure 15. Open-Loop Six-Degrees-of-Freedom Simulation Response to Ramp δ_e Figure 16. Closed-Loop Digital Simulation Response to Step θ_c ; $\alpha_0 = 18.8$ deg; $\beta_0 = 6$ deg

REFERENCES

1. Rutan, E. L., McElroy, C. E., and Gentry, J. R., Stall Near Stall Investigation of the F-4E Aircraft, FTC-TR-70-30, Aug. 1970.
2. Titiriga, A., Jr., J. S. Ackerman, and A. M. Skow, "Design Technology for Departure Resistance of Fighter Aircraft," Stall/Spin Problems of Military Aircraft, AGARD Conference Proceedings No. 199, June 1971, pp. 5-1 through 5-14.
3. Shields, M. E., Shaw, A. W., and Louthan, J. D., "VAC Experience in the Stall/Post-Stall and Spin Flight Regimes," Proceedings of the Stall/Post-Stall Spin Symposium, Wright-Patterson AFB, Dec. 1971, pp. I-1 through I-3.
4. Moul, M. T., and Paulson, J. W., Dynamic Lateral Behavior of High-Performance Aircraft, NASA RM 159E1-6, Aug. 1972.
5. Chambers, J. R., and E. I. Anglin, Analysis of Lateral-Directional Stability Characteristics of a Twin-Jet Fighter Airplane at High Angles of Attack, NASA TN D-5351, Aug. 1969.
6. Weissman, R., "Development of Design Criteria For Predicting Departure Characteristics and Spin Susceptibility of Fighter Type Aircraft," AIAA Paper No. 7-984, Sept. 1971.
7. Greer, H. D., Summary of Directional Divergence Characteristics of Several High Performance Aircraft Configurations, NASA TN D-6993, Nov. 1971.
8. Ross, A. Jean, "Flying Aeroplanes in Buffet," Aeronautical Journal, Vol. 81, No. 802, Oct. 1977.
9. McRuer, D. T., Ashkenas, I. L., and Graham, D., Aircraft Dynamics and Automatic Control, Princeton University Press, 1973.
10. Porter, R. F., and Loomis, J. P., "Examination of an Aerodynamic Coupling Phenomenon," Journal of Aircraft, Vol. 2, No. 2, Nov.-Dec. 1965, pp. 553-556.
11. Ross, A. Jean, "Investigation of Nonlinear Motion Experienced on a Slender-Wing Research Aircraft," Journal of Aircraft, Vol. 9, No. 9, Sept. 1972.
12. Hamel, P., "A System Analysis View of Aerodynamic Coupling," J. Aircraft, Vol. 7, No. 6, Nov.-Dec. 1970, pp. 567-569.
13. Johnston, Donald E., Irving L. Ashkenas, and Jeffrey R. Hogge, Investigation of Flying Qualities of Military Aircraft at High Angles of Attack. Vol. I: Technical Results and Vol. II: Appendices, AFFDL-TR-74-51, June 1974.
14. Bell, M. A., and Etheridge, J. D., A-7 Accelerated Stall Departure Study, LTV/Vought, Rept. 2-53310 IR-5598, Apr. 1971.

ACKNOWLEDGMENT

Research sponsored by the USAF Flight Dynamics Laboratory, Wright-Patterson AFB, Ohio, under Contracts F33615-73-C-3101 and F33615-76-C-3072.

GUST-VEHICLE PARAMETER IDENTIFICATION BY DYNAMIC SIMULATION IN WIND-TUNNELS

by

B. Krag

Institut für Flugmechanik
Deutsche Forschungs- und Versuchsanstalt
für Luft- und Raumfahrt e.V. (DFVLR)
Braunschweig-Flughafen

Introduction

Advanced small transport aircraft powered by turbo-prop powerplants normally fly in the atmospheric regions where the most turbulence is encountered. These aircraft also have wings with a high aspect ratio, which results in poor ride quality when the aircraft flies through turbulence. This is the reason why the application of gust alleviation systems for these aircraft is most promising. The proper design of gust alleviation systems presupposes exact knowledge of the dynamic and instationary aerodynamic effects, which are especially pronounced with high aspect ratio wings. This year the DFVLR Institut für Flugmechanik and the IMFL will start a joint research program to develop methods for identifying the instationary transient phenomena. For this purpose, different experimental methods will be used, which complement each other in many ways. The IMFL uses their catapult free flight installation and the DFVLR uses dynamic derivative balances and their equipment for dynamic simulation in wind-tunnels. The same model will be used at both institutes so that the results can be easily compared. The results will show which approach is best suited to solve particular problems. This paper will give a description of the DFVLR installation for dynamic simulation in wind-tunnels. Also described will be the application of this installation in the above mentioned research program and its capability and limitation.

Description

Fig. 1: The installation for dynamic simulation in wind-tunnels uses a remotely controlled wind-tunnel model. The model flies in a special suspension frame which allows freedom of motion in pitch, yaw, roll, and heave. This is sufficient for the simulation of the short period longitudinal motion of conventional aircraft. The model has scaled inertial properties which give it a dynamic response similar to the original aircraft. The experimental installation includes a gust generator and a measurement van which houses the model control devices, the measurement data processor, and various monitoring devices.

Fig. 2: The model is a replica of a small transport aircraft powered by turbo-prop. The model is constructed completely from carbon fiber reinforced material, which results in a low weight, rigid structure. All control surfaces are driven by electric torque-motors. The model is equipped with rate gyros, accelerometers, pressure transducers, and angle of attack probes. All deflections can be measured using built-in potentiometers. Power, control signals, and measured data flow to and from the model via an umbilical cable.

Fig. 3: The advantage of this type of simulation is the good observability of all state variables and all disturbances which act on the model. The testing time can be as long as necessary to perform a detailed measurement of all important parameters.

Fig. 4: All standard test routines for dynamic response evaluation, such as harmonic, impulse, and stochastic excitations, can be performed. Either the gust generator and/or the control surfaces can be used to excite the model, as shown in figure 4. The response can be evaluated using time histories, frequency response measurements, or power spectra analysis.

Fig. 5: One of the main features of this installation is the gust generator. The two gust generator flaps are driven by an electrohydraulic actuator. This device allows a deflection of the airstream within the testsection of up to 10 degrees. The gust generator can generate winds in the frequency range from zero to fifteen Hertz. It is possible to generate various types of gust profiles, such as impulses, harmonic oscillating, or stochastic. As indicated in figure 5, the complex aerodynamic processes, which strongly influence the propagation of the gust field, have to be carefully considered when using the gust generator at high frequencies.

Fig. 6: The properties of the gust generator allow the simulation of a scaled down stochastic gust field with a Dryden- or v. Karman characteristic. There is a strong correlation between the measured power spectrum of the gust angle of attack and the shaping filter output. This correlation can be maintained to a frequency of 8 Hertz. Above this frequency, the natural turbulence of the wind-tunnel dominates. These stochastic gust fields are used to test and evaluate gust alleviation systems for small transport aircraft.

Fig. 7: Figure 7 shows these signals, shaping-filter output, gust generator flap deflection, and the gust angle of attack, in the time domain. The bottom three signals show good correlation. The instationary effects are small in amplitude and only appear at higher frequencies. There, the natural turbulence of the wind-tunnel predominates, and the instationary effects cannot be identified in the a_g -plot.

Fig. 8: For the identification of the instationary transient effects the application of the maximum likelihood method is suggested. Good identification of these effects depends on a correct mathematical model of the aircraft motion, including the instationary aerodynamics. Further it depends on the shape of the input signals. The shape has to be optimised so that the desired phenomena are present with a measurable amplitude. The important instationary effects are the lift-lag, as described by Wagner's and Küssner's function, and the deadtimes required by the downwash or the gust to travel from the wing to the elevator. The lift lags are approximated by linear transfer functions of low order. The order of these approximations of Wagner's and Küssner's function depends on the upper frequency at which the model can be excited. The validity of these approximation is therefore limited. In order to keep the number of variables to be identified as low as possible, the deadtimes do not appear explicitly in the mathematical model. They are included within the wing and elevator angles of attack, which are used as system input signals. Further, all control surface deflections are also used as system input signals. Because the gust angle of attack can be measured at all locations along the aircraft, the angles of attack at the wing and the elevator can be computed quite accurately. The identification, which is currently in progress, will show the feasibility of this approach. If it fails to give good results, the number of variables will have to be increased to include an approximation of the deadtime, and the angles of attack will have to be treated as a state variable.

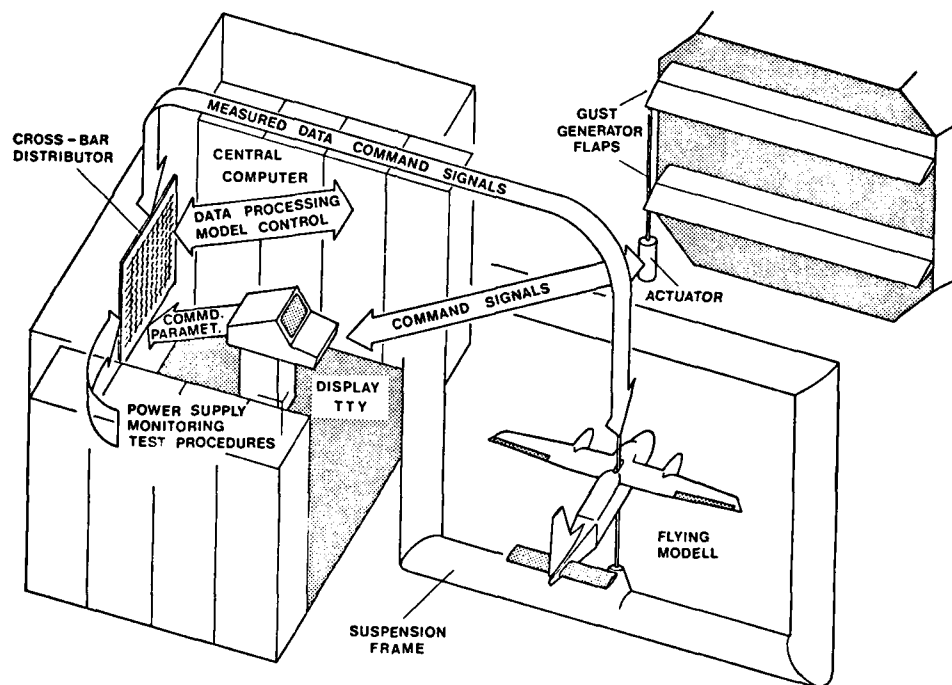


Fig. 1 Arrangement of the installation for dynamic simulation in wind-tunnels

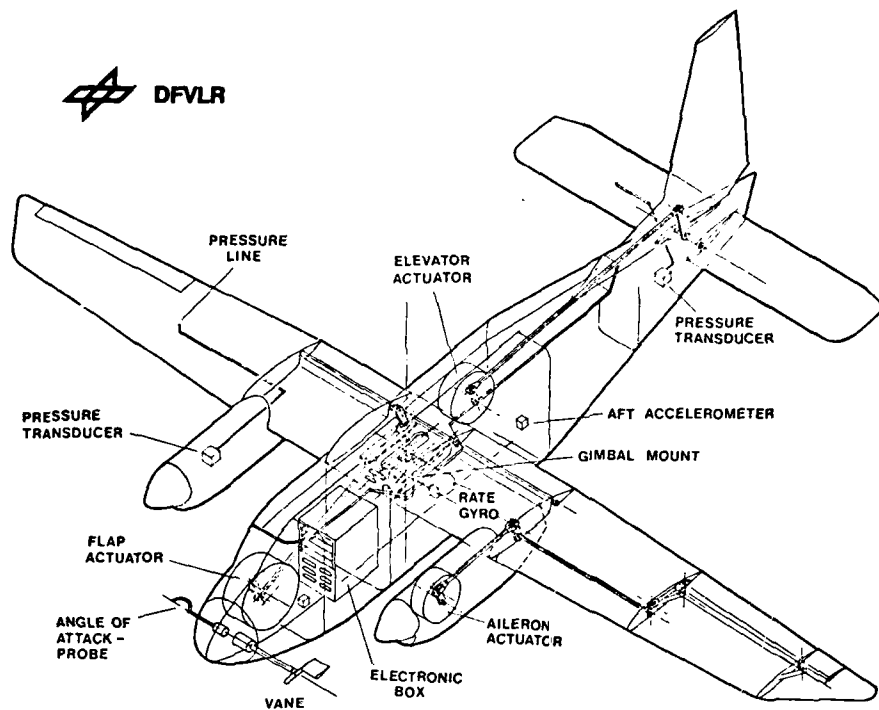


Fig. 2 Remotely controlled wind-tunnel model of the DFVLR

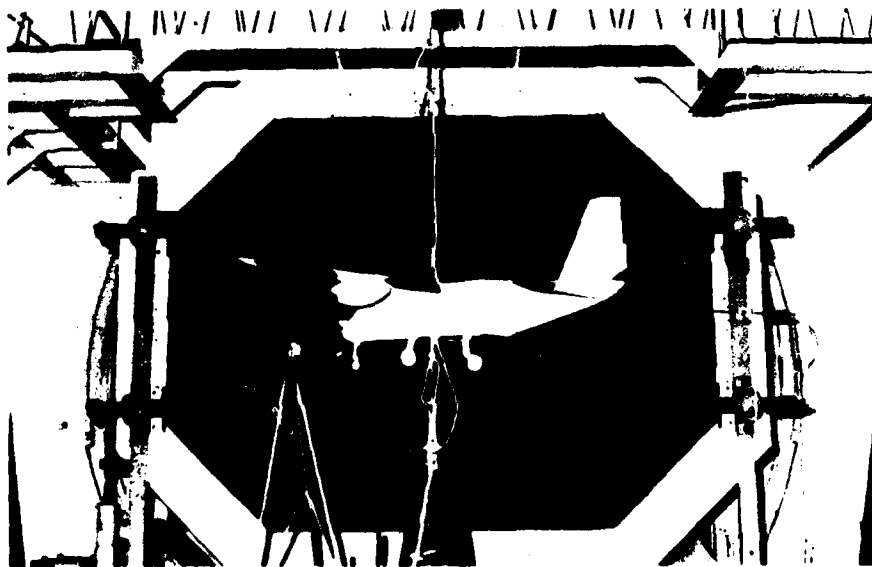


Fig. 3 Wind-tunnel model in flying position

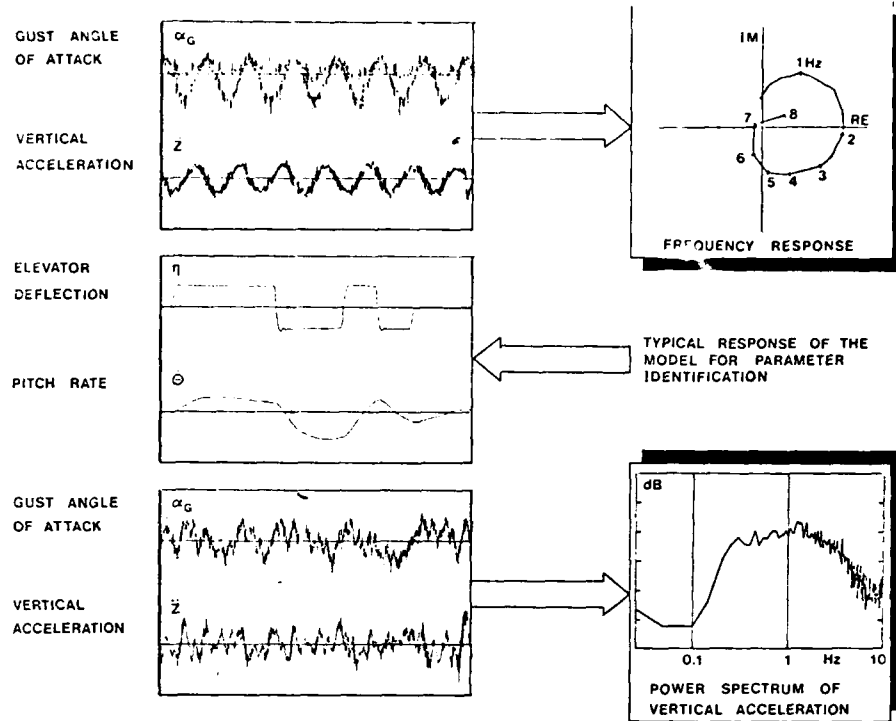


Fig. 4 Typical input-output relationships measured from dynamic response tests

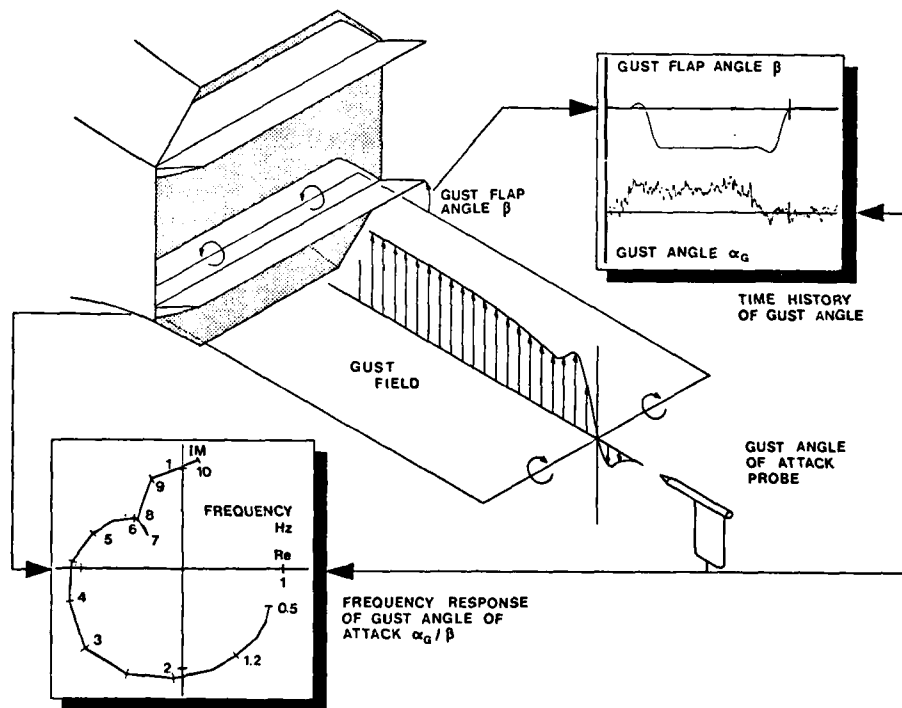


Fig. 5 Aerodynamic properties of the artificial gust field

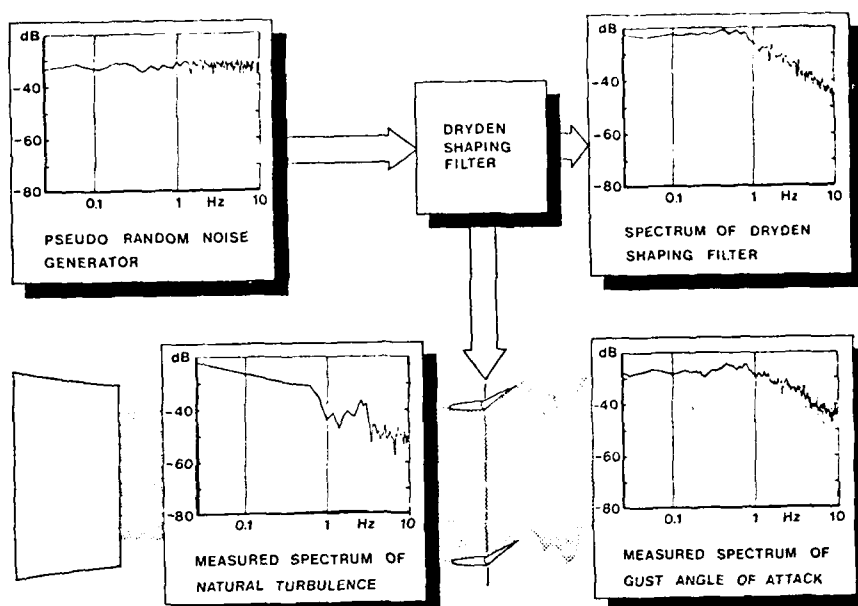


Fig. 6 Generation of a scaled down gust field with a Dryden characteristic

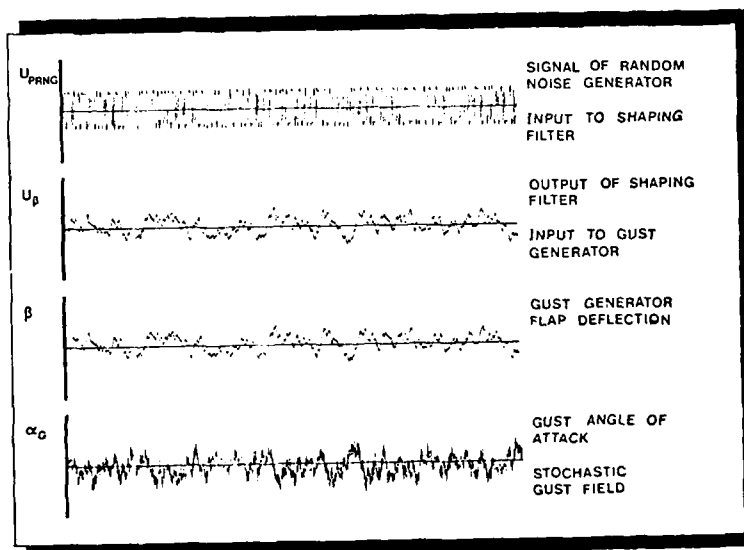


Fig. 7 Correlation between gust generator signal and measured gust angle of attack

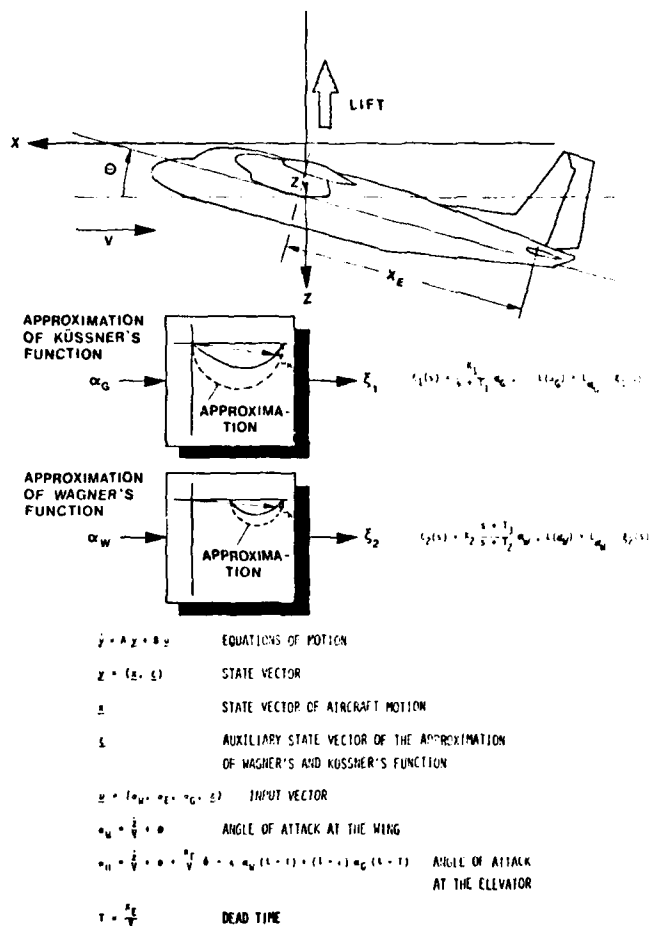


Fig. 8 System equation of motion and approximation of instationary aerodynamic effects

ROUND TABLE DISCUSSION

Chairman: Dr. Orlik-Rückemann

Ladies and Gentlemen, this is the final session of this meeting, namely, the Round Table Discussion. Before I forget to mention it later, this part of our meeting will be recorded; so the comments made here at the round table as well as the questions, comments and remarks from the floor will all be put on tape. Therefore, I would be grateful if everybody would identify himself before he starts speaking. Also, I am quite certain that by now you probably recognize some of us here. Just to make sure, I will reintroduce the panel to you. On your left, we have Dr. Ken Iliff from NASA Dryden; then we have Mr. Beaumont Thomas from RAE. My name is Kazik Orlik-Rückemann from NAE. On my left you have Mr. Andrew Titirega from Northrop, and finally, Mr. Joseph Chambers from NASA Langley.

All of us have presented invited papers at this symposium, and each has appeared in a different session, so that between the five of us we cover all the five sessions of the symposium. Now each of us will speak for a few minutes, covering some salient points of the topic of each particular session, but not necessarily going over all the papers. After each such set of introductory remarks, we will have a general discussion from the floor, with the participation, of course, of the members of the panel. We will allow about one hour for this exercise, after which time, I understand, buses will take us all to the Acropolis.

With your permission I will lead off this affair, since I was the invited speaker at the first session. You will recall that the first session dealt with the subject of Wind Tunnel Techniques. In my opening paper on Monday morning, I listed a fairly large number of wind tunnel techniques for dynamic stability experiments. The question, of course, immediately arises as to which of these techniques are the most important ones. The question also arises, on what grounds we should base such a possible assessment. When thinking about this last night, I thought about three important criteria which may be considered in this connection. One is that the measurement of any particular parameter should be independent of the mathematical modelling which involves all the other parameters as well. I will explain this in a moment. The second is that the accuracy of measurements should be acceptable. The third is that the technique itself should be applicable to experiments at much higher Reynolds numbers than it is currently done.

If I may elaborate on the first point, this criterion really says that the experiment should be based on a direct relation between the stability parameter to be determined and the physical quantity which is being measured. Any other approach, such as solving a system of equations of motion for a certain number of stability parameters, is an indirect approach, and if we go through such an exercise, it appears that the results would always be dependent on the mathematical modelling. That is, on the system of equations which has been used. If you then later change the system of equations, probably some of your results actually become invalid.

The second criterion has to do with accuracy and you may notice that I used the expression "an acceptable accuracy", rather than "as high as possible" or anything like that. I would like to make a strong point about this. A lot of people who are not working in our field may expect that we will be delivering to them dynamic stability derivatives which are accurate within 1 or 2%. Partly, this is very difficult to do, as I am sure many of you realize. More importantly, there is no need of doing this, because most often, although there may be exceptions, in the general case we are not really interested in variations smaller than maybe 20% to 50%. Certainly anything less than 20% would, in general, be inconsequential as far as a study of the behavior of the motion of an aircraft is concerned. Fortunately, the conditions to get this acceptable accuracy are similar to those stated in my first criterion, i.e., both these requirements are best fulfilled if you have a direct relation between the derivative to be measured and the quantity which you are actually obtaining experimentally. This is very fortunate.

The third question has to do with Reynolds number simulation, and of course, this is a standard problem in any aerodynamic testing. As you know, most of our aerodynamic experiments are always carried out at too low Reynolds numbers. We are currently engaged in many countries of the world in providing facilities which will improve this situation. Many of the dynamic stability apparatuses which I described in my opening paper are completely unsuitable for taking very high loads. Only certain classes of those techniques can be actually operated so that very large normal loads of the order of several thousand pounds or so can be accommodated. So this is the third criterion. Maybe I can very quickly add that, for the moment, we are not really sure how dependent are the stability derivatives on the Reynolds number. Of course, as Prof. Bogdonoff inquired before, at high angles of attack with all the separated flows, shedded vortices and so on, there is probably a strong dependence. However, this still remains to be proven and the possibility should not be completely eliminated that, after accumulating a certain amount of data in this area, we may decide that certain phenomena are less critical than others when the Reynolds number is concerned, so that experiments could actually be performed in lower Reynolds number facilities, which is much less expensive. However, the first thing to do is to check it in as high a Reynolds number environment as we can to find out what the situation really is.

Regarding the questions that I posed initially, what techniques would be considered most important on the basis of these three criteria, it seems to me that the techniques involving forced oscillation, steady roll and rotary balances are the ones which are the most promising at the present time. When I say forced oscillation, I refer, of course, to a very broad category of techniques. It includes oscillation in both the angular and the translational degrees of motion. It includes also oscillation involving motion around a fixed axis as well as the snaking motion or porpoising motion as the gentleman from Greece suggested here two days ago. All those techniques are covered by the word "forced oscillation", so it is really not just one apparatus or one type of approach.

There are many other things which I would like to say, but I think I will leave this to the open discussion. I would like to close my remarks by recognizing the large number of topics which were only very slightly touched upon during this meeting. The reason for this is partly because there was no time, but even more importantly, because so far we don't really know enough about these things to present a paper on the subject. I would like to list some of those topics to you. The first one is of very large importance; the question of static and dynamic sting interference. Dr. Ericsson has already touched on this. By static sting interference I mean the very fact that the sting is there which, for instance, promotes transition near the base. The second, the dynamic sting interference, is the term which I use for taking into account the fact that the sting itself vibrates or oscillates. This changes your motion and can also introduce significant disturbances to the flow around the model you are studying, especially at low speeds. Another topic is wind tunnel interference. We have wind tunnel interference not too badly in hand for low-speed steady experiments. However, for oscillatory work at high angles of

attack and especially in high transonic and subsonic ranges, there is simply nothing we know about this as far as I am concerned. If anybody thinks otherwise, I would be happy to hear about it. Yet another topic relates to the question of the desirable amplitude of oscillation. There is a whole range of problems involving the choice whether you should test at a small amplitude or at a large amplitude. Ultimately, of course, the answer rests with what kind of motion you are trying to simulate, and probably both kinds of testing are in some cases justified. For the moment, most of the testing which we are all doing employs the small amplitude approach, because this is a simpler way to do such tests. Prof. Bogdonoff has already mentioned the fourth of the topics, which I have on my list here, and that is the effect of wind tunnel flow unsteadiness. This is an important parameter even for steady experiments, and it goes without saying that it could modify significantly any dynamic results you would be obtaining from oscillatory tests. This has hardly been looked into, and I am sure that we will find that our answers may be considerably modified by this parameter. I certainly would like to encourage some work along those lines.

Then we have the problem that in many cases when we develop an oscillatory test technique or any other dynamic test technique, we really don't know any answers. We may be measuring certain quantities for the first time, and we have nothing to compare with. We have no expectations as to what will materialize as the result of such an experiment. Here, I can encourage everybody who does this type of testing to build some kind of a dynamic calibrator, such as was described by Dr. Han during the meeting. In this way you can at least be assured that what you are getting in the way of in-phase and out-of-phase moments or forces is actually correctly measured and correctly interpreted in your data reduction.

Then there are many other considerations such as detail construction problems: how to construct the model, how to construct the apparatus. You are all familiar with the difficulties to construct even static balances for very high loads. Well, these difficulties are amplified many times when you try to construct a dynamic balance for very high loads, partly because the sting has to be much more slender to provide some space for the model to oscillate in. Then we have questions regarding more advanced instrumentation systems, more efficient data reduction programs, etc. I am just listing all this to give you some ideas. Maybe somebody wants to address some of these topics. I would be very glad if he did. With this, I would like to close my remarks, and I would like to ask for comments from the floor. Identify yourself, please, as this is being recorded.

Mr. Antonatos

You listed the various topics, but you never used the word aeroelastic. I think that for the dynamic simulators it is important these days for certain aircraft to consider the aeroelastic effects as they affect the stability derivatives.

Dr. Orlik-Rückemann

I could not agree more. That is one of the many things I did not list. We are still very far from measuring the dynamic stability on aeroelastic models, and in fact, I can see considerable difficulties in doing this. For every conceivable flight condition, the model would deflect slightly differently and so you would have to simulate or duplicate the flight condition and the aeroelasticity built into your full-scale aircraft for a particular flight condition. For any other flight condition you may end up having to test another model. Unless, of course, you try to build a few models with different aeroelastic characteristics, and if so, one of them should be a completely rigid model. On the basis of this, one could try to obtain some general guidelines as to how aeroelasticity affects the final results.

Dr. Ericsson

I would like to respond to Antonatos' question. In our work for the NASA Marshall Space Flight Center, on the Apollo vehicles and now on the space shuttle, we found that you can use static experimental data and dynamic rigid body data to firm up the theoretical model between the static and dynamic data that permits you, with the structural information, to predict the aeroelastic characteristics of rather complicated vehicles. It is very much more difficult to dynamically simulate an elastic vehicle in a wind tunnel than a rigid one. So, there is a lot of hope in this respect that it will be possible, with good rigid body dynamic systematic data, to check out the theoretical model that will give you the assurance that you can predict the aeroelastic characteristics.

Dr. Orlik-Rückemann

You are really basing this on the work you did for Marshall, you said, so this would have to do with the long missile-type bodies?

Dr. Ericsson

Or, the recent work discussed on the space shuttle orbit just presented, which was exactly the same thing. No, I am sorry, that was rigid body dynamics. We did the same thing for the elastic characteristics for the piggy back, for instance, the orbiter on top of the 747, and also for the ascent configuration. We haven't had, in those cases for the space shuttle, any data to compare with the aeroelastic predictions. With the standup vehicle, the Saturn-Apollo, we did, and could show good agreement.

Dr. Orlik-Rückemann

So you are optimistic that the aeroelastic effects can be corrected for?

Dr. Ericsson

Yes, and I think this is very important because of the Reynolds number effect on flow separation. You can go up to the high Reynolds number in the dynamic rigid body test, whereas, you would have a hard time very often to have the dynamic simulation under those loading conditions, and also to have the instrumentation in the elastic case to get the information needed.

Mr. Butler

I somewhat disagree with your comment that flight mechanics engineers should be satisfied with derivatives from say 20 to 50% accuracy bands. This may hold true for the cross-coupling derivatives or cross derivatives, but you take the direct derivatives for a specific maneuver and a specific derivative and the case I am thinking of would be, say, an aircraft in wingrock at high angle of attack. You take the direct derivative C_{lp} and you change that derivative by 20% and you get drastic changes in the character of the maneuver. So that may hold true for some of the derivatives and a large part of the

flight regime, but it doesn't cover the whole thing by a long shot.

Mr. Thomas

I would concur with what you have just said and add to it that in these days of control systems, the derivatives for the controls should be known to the same sort of accuracy as the stiffness derivatives.

Dr. Orlik-Rückemann

You have some actual cases where a 20% change in damping-in roll would affect significantly the time-history of the flight?

Mr. Butler

Yes. I guess that is what I am saying. If you let me pick a particular so-called maneuver, a particular derivative, I would pick a wingrock, the C_{lp} derivative. I can show you drastic changes in the wingrock motion with a 20% change in this derivative.

Dr. Orlik-Rückemann

O.K. I stand corrected. But, I would tend to consider this as an exception that confirms the rule.

Mr. Antonatos

All I was going to comment on was, whether we are talking about aircraft with real flexible wings or in particular a vehicle that has a rather thick, possibly more rigid wing. I think that the answers could be quite different.

Dr. Orlik-Rückemann

Alright, any more comments regarding wind tunnel testing techniques?

Mr. Thomas

I think you are kidding yourself a bit when you think that you can do your wind tunnel tests completely devoid of a mathematical model. You must have some mathematical model in mind in order to define what you are measuring. Otherwise you just execute any motion you like and come up with something for the forces and moments without any means of interpretation.

Dr. Orlik-Rückemann

Yes, but I didn't say that. I said that the measurement of a particular derivative should not be dependent on the mathematical modelling involved with the other derivatives. For that particular derivative that you are measuring, you must know what you are doing. But I don't want to measure a C_{nr} , for instance, and make the answer dependent on what else I have in all the other equations of motion, because then my answer obviously depends on the entire system of equations. If I change one term of it, I will get another answer.

Mr. Thomas

It is a fine idea, but I don't know how long you will be able to keep on going that way.

Dr. Orlik-Rückemann

Using direct methods of measurement, you can do that. We are not solving any equations of motion at all in our work.

Mr. Curry

I guess it is not clear to me what level of accuracy is required for the dynamic derivatives, considering the capabilities of control systems. Can someone comment on this?

Mr. Thomas

Recently in the context of a discussion of the relative importance presently of different derivatives, we drew up a chart and decided that perhaps damping derivatives were going down in importance as, in fact, control derivatives were going up. In other words, apart perhaps from situations such as, for example, C_{lp} being nearly zero, you would not need to know the derivative (C_{lp} in this instance) that accurately if you were making things good by use of a control system. The derivatives for the appropriate control by means of which the stability deficiency was being corrected would have to be known to the sort of accuracy that one previously needed for C_{lp} , when the latter directly governs the Dutch roll damping.

Dr. Orlik-Rückemann

You are talking about dynamic hinge-moment derivatives?

Mr. Thomas

Primarily I meant that the rolling moment and yawing moment derivatives for the lateral control, say, would assume an increased importance. In the full dynamics of the aircraft dynamic hinge-moment derivatives would also be involved.

Col. Jeglum

I would like to put a few comments in here, and it is nothing anybody here does not know, but it has to do with how accurate the stability derivatives have to be. It seems to me that we have been talking about control-configured vehicles, we had an excellent paper on that. I think that we all realize that we can do some rather magnificent things with controlled configurations, lateral translation, direct lift, etc. We have been talking about high angle of attack and in general sort of alluding to tasks. From my point of view, I think what I would like to say is that really the accuracy of the stability derivatives, the accuracies that we require, depend entirely on the task that we are going to assign that airplane to do. It seems to me that what we are talking about is task orientation. In other words, the way that I would like to approach this ideally is to define a task that is to be accomplished. For instance, if in a bombing task, we find that we can use side translation to increase accuracy, that

is the objective. The objective is to give ourselves enough translation that we can achieve this increased accuracy, but it seems to me that there is another very important part of this problem that establishes requirements like alpha, G, Mach number, whatever we have. It establishes a performance level with respect to flying qualities now, not conventional performance, but the flying qualities achievement that we want from the vehicle. At that point, we get in the game as flight mechanists, if you will, as flight mechanics people. We have to then establish that capability by either control system, aerodynamic design or whatever we have got. At that point, the thing that we haven't heard a lot about here, we really have to optimize the pilot's capability to do that. In other words, anything that we give him which puts him at x-1, which exceeds his capability to do, is not a worthwhile task to talk about. Consequently, having achieved that task, then we get into what my business is, i.e., development. And that is to ensure that we achieve goals, to confirm those limits that we think we have, to confirm the possibility to do it finally. The accuracy that we demand at every step along the way is strictly dependent on what you want to do with it in the final analysis.

Dr. Orlik-Rückemann

Thank you very much. Now we will pass on to the next topic, and I would like to ask Ken Iliff to make his comments.

Dr. Iliff

It doesn't seem particularly fair to me to ask someone who was in a session to summarize what he thinks was important in that session, because there is a temptation to outline his own paper. Therefore, I will try not to be very specific. I will try to outline just briefly what we covered and address some questions as Dr. Orlik-Rückemann asked. I will then try to give some final thoughts.

The session I participated in was called Flight Test Techniques. I think that the presentations demonstrated that satisfying broad criteria is no longer adequate to ensure that the aircraft has been satisfactorily tested. The satisfactory completion of flight test programs now requires estimation of a large number of unknown coefficients and demonstration that the aircraft satisfies some very complex criteria. A vast amount of the experience has been gained already in estimating the stability and control derivatives (these are the linearized versions) from a great variety of aircraft. Yesterday's presentations showed that more complex problems are now being investigated by many different techniques. A complete presentation of all the flight test techniques and problems being pursued would, of course, not be possible in a reasonable amount of time. A fairly representative sample was presented during the session.

Some of the papers dealt with specific problems of testing new or modified aircraft configurations. These tests are viewed by some as the ultimate confirmation of both analytical and wind tunnel test techniques. The other papers were primarily concerned with improving the ability to provide satisfactory estimates of unknown coefficients for very complex systems or analyzing data that does not lend itself to routine analysis. The current techniques appear adequate to solve the standard problems facing flight data analysts. In other words, solving the problems that we have been working on for the past ten years. The definition of satisfactory models for the more complex phenomena, many of which have been discussed at length in this conference, remains a significant problem. The long-range goal of the flight test analyst, I would say, is to obtain flight data with sufficient information to validate the models supplied by the analytical experts and wind tunnel experts, some of whom have made presentations here. The complete definition of the aircraft mathematical model will always depend on analytical or wind tunnel tests. The flight test aircraft will at best be able to validate the predictions where the aircraft can supply sufficient data for a thorough analysis at some points in the flight envelope. Then, on the basis of this validation at these points, the prediction can be relied on to describe the vehicle throughout the rest of the flight regime. In order to make this possible, better and more frequent communication must take place between the experts supplying the models and the predictions and the specialists conducting the aircraft flight test. This should result in the most meaningful problems being investigated in earnest.

In the meantime, the flight data analyst may need to resort to ad hoc techniques of modeling and identification. You may disagree with using ad hoc techniques, and by ad hoc techniques I mean power series expansions generated in order to make the data fit better, but people are using them already, and I think you can rest assured that they will continue to use them. I have some criteria that I like to follow when complicating a model without phenomenological basis. When I am reading literature with results that are obtained from flight test, I have six criteria that I like to apply to an analysis to see if I believe that the analysis is particularly meaningful or if I think the analysis was done simply in order to improve agreement between computed data and the measured data from flight.

1. The higher order statistics of the estimated coefficients of the solution (e.g., f-tests and Cramer-Rao bounds) must indicate that the estimates are valid.
2. The quality of the fit must be good, and even small discrepancies must be explained, since these discrepancies can result in serious misinterpretations of non-linear systems.
3. The simplest model that adequately fits the data should be chosen. A more complex model cannot be justified.
4. A consistent trend must result for each estimated coefficient as each independent variable is changed.
5. A plausible physical explanation for each resulting model should be found.
6. The most important task, in my mind, is the evaluation of the resulting mathematical model and coefficients with a completely independent set of data.

In conclusion, I have a question that I would like to ask. Perhaps some of you will have some ideas on this subject. The question is, are the non-linear methods being used for dynamic flight maneuver analysis being applied with sufficient emphasis to dynamic wind tunnel tests? These techniques appear to me to be natural candidates for the problems I have heard discussed here, like sorting out aerodynamic effects and tunnel turbulence effects. This may aid in comparing dynamic and static tests of the same wind tunnel model and help get around some of the Reynolds number questions that are being raised. The wind tunnel tests should make application of these techniques as they are more controlled experiments than flight tests.

Mr. Thomas

On this question of the motions in wind tunnels, I think the motions that I outlined in my talk are precisely those to which I would imagine you would apply more or less the same processes as you do to the flight data, with some differences, perhaps. We might even draw you on the question of how you

would, in fact analyze the information from such tests. In other words, if I take one or more of the coefficients as a function of two or three of the variables, and I wish to retain it in that form and not begin to develop it in a polynomial, can you think of any means of analyzing in that form?

Dr. Iliff

My response to that would be that I believe in most cases the dynamic testing can be a more controlled experiment, so I would try to vary the state variables one at a time. Then I would vary a combination of parameters to validate the analysis of varying them one at a time.

Mr. Thomas

Precisely, if you will recall, there was a progression in motion complexity for each test and one underlay the other in that it already gives one piece of information.

Dr. Orlik-Rückemann

It appears to me that what you call a controlled condition of a wind tunnel test also means that if your wind tunnel test is of the direct type, that I have been describing, then you really get this particular parameter independently of any other considerations, so this is what you may need. Then you can start putting it together. Of course, you may very correctly point out that this parameter may change in the presence of motion in other degrees of freedom at the same time. No solution is ideal, but I think that we should try to build it up from individual blocks, so to speak.

Dr. Iliff

I was just proposing an independent way of avoiding some of these very complex wind tunnel rigs that are being designed. You are trying to obtain the effect of varying one parameter at a time in the tunnel, however, these techniques that we have used in flight tests are able to determine the effect of varying several things at a time.

Mr. Rynaski

I would like to say a word about modelling. Modelling, I think, has much to do with the task or the reason for the model. For instance, the person involved in performance is not necessarily too concerned with rotary derivatives and a person who is involved in flutter testing may have requirements for an entirely different type of model. So, it is not necessarily always true that the identification need reproduce all the motions that you see, or it need not match the time history data exactly, as long as you are able to describe where the differences come from, so that your model depends on task or the particular purpose that you have in mind for using it or generating the model in the first place.

Dr. Orlik-Rückemann

This confirms that if we have a kind of a building-block type of a system, superposing different extra conditions, this will be really most amenable to application to all possible tasks or situations.

Dr. Green

I would like to pick up the point that possible better parameter identification might enable you to do some unscrambling of the low Reynolds number problems that you are faced with. This is, after all, a meeting of the Fluid Dynamics Panel, and I think that before we finally leave the question of tunnel testing and the low Reynolds number problems, I would like to suggest that there hasn't been in this meeting enough emphasis on what exactly are the natures of the flows that are producing these non-linear effects. I would like to plead in future for these experiments to be more concerned with identifying the particular flow characteristics that are producing the non-linearities, because it is primarily by understanding the flow that you will get an understanding of whether it is Reynolds number sensitive or not. We should note that in the aerodynamic design field, quite good advances are being made in flow field calculation methods and in allowing for viscous effects and calculating boundary layer development and predicting where separation may occur even in difficult situations. These techniques are by no means perfected yet, but nevertheless, if you are going to make an assessment of whether or not the flow you are dealing with is going to be Reynolds number sensitive or not, they should be able to help in indicating what kind of separation is occurring and where it is coming from.

Dr. Orlik-Rückemann

I would like to assure you, and I think that I can speak for everybody here, that the point you are making is fully recognized. It is just that at this meeting, there have not been enough papers presented on the aerodynamic aspects of these effects. Of course, one of the reasons may again be that we haven't yet got too many experiments or analytical methods which we could use to explain this fully. However, several speakers have at least alluded to some activities which are now being performed. There are flow visualization tests which Mr. Titiriga has described; although they were in a water tunnel, they still give us a handle on the mechanism of the flow. There are pressure tests on oscillating models which Mr. Malcolm was describing, and so we are going in this direction, but this takes time. The whole business of cross-coupling was not even known two years ago, at least when it comes to aerodynamic dynamic cross coupling. Give us time.

Mr. Titiriga

One of the problems is the only good flow visualization techniques we have right now are techniques that are performed at low Reynolds number. So far, we haven't found out how to get good flow visualization in that big wind tunnel in the sky. There are very few techniques that I know of that can give you adequate visualization. Some of the best visualization we have gotten is from vapor in the air by accident; having chase planes photograph an airplane at high angles of attack and because of the moisture content of the air, we see some vortices, but some of the planned techniques just don't work.

Dr. Orlik-Rückemann

The next presentation or comment will be by Mr. Titiriga, who will address the subject of Analytical Techniques.

Mr. Titiriga

Many achievements have been recorded here in the field of high angle of attack analytical techniques. To name a few of them we have extended some of our analytical methods to include separated flow effects, unsteady effects and some vortex induced aerodynamic effects. We have also defined some criteria and levels of parameters which have improved the departure predictions. We have identified some coupled parameters in defined regions of instability. Although we have made some significant progress, we still have some formidable tasks facing us in the future. The gambit of new aircraft designs includes fore-bodies of various fineness ratios with round as well as elliptic cross-sections. We have single and two vertical tails, we have lift generated by several techniques from conventional wing circulation to lift generated by strong vortex systems originating from leading edge extensions or engine inlets and to lift augmentation provided by blended body concepts. Designs incorporate variable camber, either leading edge alone or in combination with trailing edge devices. With all these design trends, it is rather hard to say what we should be doing here in the future. However, I believe that the future analytical studies should be directed towards uncovering the tools necessary to allow the engineer to successfully design these highly maneuverable airplanes within the time and the money constraints of the program. To do this we have to identify the tools using dedicated research programs to uncover the aerodynamic mechanisms that are instrumental in providing spin resistance using data of existent departure resistant aircraft.

This should be accomplished by a correlation of the analytical, experimental and flight test data. From these correlations the overall minimum degree of analytical and experimental data sophistication required to adequately predict departure and spin characteristics should be identified. In addition, within the various analytical and experimental techniques it must be determined how much sophistication is necessary. In other words, for the analytical prediction parameters and the methodologies we are developing right now, what are the threshold values or the critical combination of these values required to prevent departures? Is the requirement for sophistication of data highly configuration dependent? We have vast amounts of analytical, experimental and flight test data available on a number of aircraft. Because of the many constraints, individual contractors seldom have the opportunity to fully correlate the data. Even if it is correlated it is only one segment of the total problem. All this data must be brought together, analyzed and conclusions obtained. Individual successes with correlation between certain parameters and flight test results indicates available data may produce other pertinent relationships if the data were analyzed across the board instead of aircraft by aircraft.

Unidentified Comment

I would like to suggest that for our predictions to be meaningful the question of modelling the propulsive forces will have to take on a stronger role. Prof. Bogdonoff did mention this, and I think that in the current state of development, the problem is being treated properly. But, as we learn more about the unpowered characteristics, we will then want to compare them with the powered characteristics from flight. Some of the differences between the two will probably be related to propulsive effects, particularly for configurations which have thrust off the axis and for configurations in which the propulsive flow can alter the fluid dynamics of the wing or control surfaces, such as jets impinging upon control surfaces or affecting flow on wings. So, as the technology develops, Dr. Orlik-Rückemann says that we have been in the business a short time, and this is understandable, but as we get further along we will have to keep in mind that some of the effects we are looking at, will be highly interactive with the propulsion systems.

Dr. Ericsson

I would like to comment on the topic which was covered by Mr. Titiriga. In your speech you had several examples of the drastic effects of asymmetric vortex shedding. In that regard a simple analysis sometimes can help out. I can reveal the experience we had in our missile business. It became important that our missile would be able to make a sharp pull-up maneuver for range safety reasons, and that put our missile in the high angle of attack region where these asymmetric vortices would occur. We started looking at wind tunnel data, and as you know, it is a jungle. You can't get any data to establish what is the maximum side load or side moment you could experience, because anything will change the wind tunnel data: paint on the model, rolling it, anything. What we ended up doing was to try to estimate the highest possible side load that we could get. We simply made the assumption that the side load to normal force ratio could never exceed the transient condition you have for a cylinder normal to the flow where you have the instantaneous lift to drag ratio. In doing that, we bounded all the existing data in the literature on these side-force-to-normal-force ratios. The article will appear in the coming issue of the Journal of Spacecraft. It was a very simple analysis to get the answer to the question that was needed by the end of the week for a flight go or no-go decision. It so happened that the control capability was there, so it was yes.

Mr. Titiriga

I am not sure about using that kind of analysis. Would it be very conservative? In other words, if you may not be really seeing those loads, I am sure it would influence the structural design of the airplane. In other words, you might get loads that never are going to be seen and over design the structure.

Dr. Ericsson

This was for ogive cylinder bodies. On an airplane you have more complications due to the downstream surfaces. In this case it is simply the side load generated on the forebody that causes the problem.

Mr. Titiriga

We did have problems with repeatability. I think that I mentioned that. We would go into the wind tunnel, and one time we would have a very low value of this yawing moment and another time a high value. Well, it just turned out it was a high value on the airplane.

Dr. Ericsson

Yes. It turns out that you probably never get the maximum value in the wind tunnel, because

then you really would have to test all possible roll positions and also in different wind tunnels.

Unidentified Comment

I would like to support the plea for correlation of different configurations but for a different reason. The designer just can't afford to wait for all these research problems to be carried out. Could I take this a little further and maybe propose configuration studies, rather than correlation of existing configurations? I am particularly concerned about the control of the aircraft and the way in which the separated flow and vortex flow affect the tail surfaces.

Mr. Titiriga

If I understand you correctly, you said that you would support the correlation of configurations, but more than just on existing aircraft, on other configurations, for different reasons, i.e., to help the designer? The reason I mention that was that there are data on existing airplanes that have been correlated within the existing configuration, but that configuration was not compared to the other configurations. I think that we have to do an across the board correlation here to come up with configuration effects. We can see at some point in the papers that were presented here that in some cases people were saying that they didn't have a configuration effect and in other cases it was a strong configuration effect. I think that they are both right. It depends on what you are looking at.

Dr. Orlik-Rückemann

Let us move on then. If I may ask Mr. Thomas to comment on Motion Analysis and Non-linear Formulations, please.

Mr. Thomas

I am going to be very brief. We start from the concept that this session shows you could have, as one speaker earlier said, different models to fit different circumstances. That is, from very complex ones to simple ones. The first paper by Tobak showed how to extend the model to include hysteresis effects. Now, I recall in the discussion subsequently, that somebody said that he had nothing to say because it had all gone over his head. This work can at first sight seem like a complicated means of proving what some may consider as obvious, but I feel very reassured by the fact that the answer comes out as one would have expected on an intuitive basis. This is often the way that science proceeds. One does things intuitively and then is able to prove everything in a rigorous mathematical way. The other papers addressed themselves to questions of where the linear model is adequate, where it is not and how far you can push the linear model. We were shown that we could extend the well-known criteria for departure to include certain terms of a coupling nature. I think that this is a fairly significant development. Finally, we had two papers which showed that in the particular problems considered, very simplified models including only non-linearities of a very particular and restricted nature were sufficient to answer the problem in those special cases. It was a demonstration that the complexity of the model should match the problems that you are trying to answer.

Dr. Orlik-Rückemann

Are there any comments from the floor? Obviously, everybody agrees. In that case we will move on to Mr. Chambers who will comment on Sensitivity and Simulator Study session.

Mr. Chambers

Having a graphics department available, I decided to summarize my comments via slides, so it will be easier for you, rather than hearing me read a presentation. I have tried to reiterate the recent accomplishments that have taken place in the area of sensitivity studies and simulator activity. You have heard about these during the session today, and I extend my congratulations to the speakers for some very interesting papers. I have decided not to spend too much time on the highlights that they have discussed today, but rather to talk about what I view as future research requirements, particularly as they relate to dynamic stability of aircraft at high angles of attack. Forgive me if I expand my comments from sensitivity and simulator studies to other areas as well. I would like to bring to the attention of the panel some very interesting areas of needed research.

The first research requirement is the rather obvious need for sensitivity studies of configurations. In discussing aerodynamics at high angles of attack, we are talking about aerodynamic phenomena which are very configuration dependent, down to very small details on each airplane. This simply once again points out that we need to keep in mind that today's solution may not apply to tomorrow's airplane. Just to emphasize that a little, some of the fighter aircraft that are being looked at around the world today, involve rather drastic changes in configuration from today's airplanes. We can rest assured that these aircraft will show us new aerodynamic phenomena, requiring new solutions both from an airframe point of view and also from a control system point of view.

I would also like to plead that sensitivity studies be done for complete configurations, with a complete set of aerodynamic data - as complete as we can measure with our limited wind tunnel techniques of today. I think that today we know very little about the effect of such things as non-zero sideslip on some of the very important dynamic parameters, and in aircraft motions experienced at high angles of attack these may play very important roles in flight dynamics.

The third requirement is the need for probably the most important input into this problem, aerodynamic data at high Mach number and Reynolds number. Personally, I am very excited about the possibilities that are offered by the marriage of cryogenic and magnetic suspension techniques to offer us the capability of obtaining this type of data at high angles of attack. I think a very significant opportunity exists there. In that same area of aerodynamic data there is an extreme need for estimation methods for use by aircraft designers today. Unfortunately, with the demise of interest in dynamic stability back during the 1950's, there has been very little basic research done with a viewpoint towards supplying the designer with the information he needs to estimate some of these derivatives.

Another important area is the status of theory to predict high angle of attack motions. This is my personal viewpoint of how we stand today in being able to predict aircraft motions at high angles of attack. As you can see, in the normal flight range and in the immediate post-stall range, our experience has been that the conventional approach is adequate. By that I mean static and forced oscillation aerodynamic data measured at the highest possible Mach and Reynolds number have been sufficient inputs for the calculations. At the other extreme, in the areas of very smooth steady spins, our experience has been that rotary spin type balance data is mandatory, and such data are quite adequate to predict

equilibrium spin conditions. The largest problem we face at the current time is that in between regions, which I have labelled oscillatory spin or post-stall gyrations, which involve steady coning motions with oscillations superimposed.

It may be of interest to the group as a whole that, with regard to simulator studies, our experiences at Langley have shown that certain aircraft control systems at high angles of attack can produce very disconcerting motion cues to the pilot, which don't show up with fixed base simulation. For example, if you as an aerodynamicist cause the aircraft to roll about the stability or wind axis at high angles of attack, the pilot senses this up in the cockpit as a yawing departure, although you have minimized sideslip by implementing that control feature. It is very disconcerting to him, and it is very apparent to him in a moving base simulator. As our computer storage banks grow, I think that we will see more and more application of simulation to investigate areas of hazardous flight conditions, particularly the high angle of attack condition. Concluding in the area of simulation, I think that the obvious application of such simulators to pilot training is a very interesting one, and is being explored by the US Navy and Air Force at this time.

I would like to make one last comment. This is a personal philosophy or concern, I might add, which has to do with the relationship between our current interest in high angle of attack flight dynamics and the relative interest in dynamic stability derivatives. I think it is interesting to note that a majority of the papers in this symposium dealt with high angle of attack flight conditions. Following the Korean war, in the U.S., there wasn't much interest expressed in high angle of attack flight conditions, because we were going to build stand-off missile launchers, which would not require much maneuverability or flight at high angles of attack. As a result there was an almost immediate degradation in our research on dynamic stability parameters, because the available estimation procedures worked quite well in the conventional flight envelope. We within NASA, therefore, lost several unique facilities and the work was stopped. It wasn't until the advent of the Viet Nam war and the recognition that fighters were to be flown at high angles of attack, that there was a sudden interest in dynamic stability back in the U.S. My personal concern is that we are faced with the situation today, wherein several current fighters, as a direct result of research and development in the area, have demonstrated outstanding high angle of attack characteristics; and there is a complacency at the current time among some military planners with regard to the need for such maneuverability in the future or interest in the high angle of attack area. I would like to point out to this group, that the relative interest in dynamic stability goes along with that interest in high angle of attack, and I certainly would hope that with the recognition of the unique new configurations that are coming forward, that certainly there should be no lessening of this emphasis in this area.

Dr. Orlik-Rückemann

Thank you Mr. Chambers. Comments from the floor please?

Unidentified Comment

I would like to make a general comment if I may, that has nothing to do with Mr. Chambers presentation. I have heard nothing in this conference about ground effects on stability derivatives. I was wondering whether anyone on the panel would care to discuss this in terms of its importance and the relative state of the art.

Mr. Titiriga

You must be referring to take-off data.

Unidentified Comment

No, I am referring both to take-off and landing data, such as the Concorde which, I understand, exhibits ground effect characteristics. I was wondering whether they are of any importance or whether they have any effect on the stability derivatives and what they are. Are investigations going on in this area?

Dr. Orlik-Rückemann

I think that nobody has really done this type of investigation, maybe something at NASA Ames in the 40' x 80' tunnel?

Mr. Titiriga

I think that we have to ask the NASA people.

Mr. Thomas

I don't know of any work going on in this area, I agree with you that there are lots of things that we don't know about ground effects. Fortunately, it isn't one of the problems on combat aircraft, but on transport aircraft it is very important. I was talking earlier in this meeting with M. Charon from Lille and it seemed to me that their setup there was an ideal one for studying ground effects using parameter identification techniques.

Dr. Orlik-Rückemann

O.K. We will take two more comments.

M. Charon

Nous avons à l'Institut de Mécanique des Fluides de Lille une installation qui permet effectivement d'étudier les effets de sol. Vous avez entendu la deuxième présentation qui était faite par M. Verbrugge. Il s'agissait de maquettes catapultées qui permettent donc d'étudier l'effet de sol dans des conditions réelles de vol. Seulement, ce que nous n'avons pas encore fait jusqu'à présent, c'est une étude complète pour déterminer les dérivées en effet de sol. Nous avons fait des études simplement qualitatives pour voir comment se comportaient certains appareils lors d'atterrissages.

Dr. Orlik-Rückemann

You are optimistic then, that it is possible to obtain derivatives with your technique?

M. Charon

Oui, absolument.

Mr. Chaszeyka

Somebody in the audience mentioned earlier in these Round Table Discussions that aircraft ground effects were not included in the agenda for this symposium, and that apparently little, if any, attention is being given that subject anywhere. I wish to mention that the McDonnell Douglas Research Laboratories, under the auspices of the Office of Naval Research, is conducting numerical investigations in which a finite-difference scheme for the calculation of the flowfields associated with two three-dimensional, incompressible, turbulent impinging jet configurations in ground effect is to be developed. The results of this program could be useful in potential flow paneling methods used to predict suckdown-induced forces on complete VTOL aircraft configurations. The relationship to Harrier-type aircraft is apparent.

The Fluid Dynamics Panel should be aware that there is a dearth of information on VTOL flight dynamics from hover through transition to wing-borne flight. From the user's point of view major issues in aerodynamics are the handling qualities and dynamics of VSTOL aircraft. Scientific investigations in those areas should be encouraged.

Dr. Orlik-Rückemann

Well, this will then conclude our round table discussion. I would just like to add some comments of my own on the general meeting. I proposed this meeting about two years ago, and at that time some fears were expressed that the topic may simply not be important or significant enough and that the level of activity was not high enough to warrant such a meeting. Fortunately, we went ahead with it anyhow, and I think that the very good response to our call for papers, the number and the quality of the contributions that we have had here, and the general turnout which even surpassed my optimistic expectations, all seem to indicate that the symposium has really fulfilled a real need.

Personally, and I think several people will join me in this, I think that one of the most important things that we have accomplished was to bring together people who were pursuers of the different disciplines involved here. That is, wind tunnel people, flight test people, analytical people and flight mechanics people. There are very few meetings where this type of get together takes place. Direct contact and direct communications between all four groups will allow us to gradually achieve some kind of understanding of the problems which are facing us today. As far as the meeting itself, it appears from the lively discussion that it was probably not altogether bad. We have introduced a few new ideas for the Fluid Dynamics Panel. We had a workshop session for instance, that we didn't try before as far as I know. This was a nice safety valve for last minute information and nice propaganda talks like Prof. Bogdonoff's. We also tried to select some of the speakers by inviting quite a large number of papers, large by comparison with other meetings organized by the Fluid Dynamics Panel.

We will probably analyze all those facts later on in the business meeting of the Panel, but so far it appears that the whole thing has worked fairly well. My only regret is that we did not have enough time to discuss all the problems at a somewhat more leisurely pace. This is certainly something that we are going to try to improve upon. With this I would like to turn the meeting over to the Chairman of the Fluid Dynamics Panel, Mr. Jones.

Mr. Jones

I am sure you appreciate the success of a meeting such as this depends on the attention and the efforts of a number of people, and I would like to give a little recognition to some of those people. First of all, to our hosts from Greece, General Trakakis, who is the Deputy Chief of Staff of the Air Force, Brigadier General Achtidas, who is the National Delegate to AGARD and who was our host at the reception on Monday evening, for making available to us these fine facilities for the meeting. To Colonel Iosifides, who is the National Coordinator for Greece for AGARD activities and to Captain Panaras who is the Fluid Dynamic Panel member and the coordinator for this meeting; we thank them for their efforts in providing all the arrangements for the meeting.

Some recognition is due to the chairman, Dr. Orlik-Rückemann and his program committee for providing such an excellent meeting. I would like to thank the speakers for putting together such fine papers as we have had here. There are a number of others also involved. As you can tell from some of the comments, one of the most difficult tasks is the translation. With the large number of speakers, each very interested in his subject, it is a difficult job to follow the rapid speech, and I want to thank the interpreters for an excellent job.

The AGARD staff worked very hard to put this meeting together and I would like to recognize the retiring Panel Executive, Mr. Michael Fischer, who worked very hard on this one and on others during the past years. We are going to miss him in the future. I also would like to thank those of you who attended and who contributed to the discussion which made the meeting a success. I now declare the meeting adjourned.

REPORT DOCUMENTATION PAGE			
1. Recipient's Reference	2. Originator's Reference	3. Further Reference	4. Security Classification of Document
	AGARD-CP-235	ISBN 92-835-0223-X	UNCLASSIFIED
5. Originator	Advisory Group for Aerospace Research and Development North Atlantic Treaty Organization 7 rue Ancelle, 92200 Neuilly sur Seine, France		
6. Title	DYNAMIC STABILITY PARAMETERS		
7. Presented at	the Fluid Dynamics Panel Symposium held in Athens, Greece, 22-24 May 1978.		
8. Author(s)/Editor(s)	Various		9. Date November 1978
10. Author's/Editor's Address	Various		11. Pages 636
12. Distribution Statement	This document is distributed in accordance with AGARD policies and regulations, which are outlined on the Outside Back Covers of all AGARD publications.		
13. Keywords/Descriptors	<div style="display: flex; justify-content: space-between;"> <div> Aerodynamic stability Dynamic response Dynamic structural analysis </div> <div> Wind tunnel tests Flight characteristics Unsteady flow </div> </div>		
14. Abstract	<p>↙ The Symposium discussed the specific needs for dynamic stability information of aerospace vehicles, the form in which it should be presented and the various means of obtaining it.</p> <p>The modern aerospace vehicle is often exposed to unsteady, irregular or asymmetrical flow fields that may have significant effects on its characteristics of motion. This is caused by the fact that the flight envelope of a present-day military aircraft or missile often encompasses flight at high angles of attack, flight at non-zero sideslip angles and the ability to perform translational maneuvers.</p> <p>The Symposium included reports on new developments in wind-tunnel, flight test, and analytical techniques; motion analysis and non-linear formulations; and sensitivity and simulator studies. Specialists discussed a broad spectrum of approaches to determination of dynamic stability parameters. ↗</p>		

<p>AGARD Conference Proceedings No.235 Advisory Group for Aerospace Research and Development, NATO DYNAMIC STABILITY PARAMETERS Published November 1978 636 pages</p> <p>The Symposium discussed the specific needs for dynamic stability information of aerospace vehicles, the form in which it should be presented and the various means of obtaining it.</p> <p>The modern aerospace vehicle is often exposed to unsteady, irregular or asymmetrical flow fields that may have significant effects on its characteristics of motion. This is caused by the fact that the flight envelope of a</p> <p>P.T.O.</p>	<p>AGARD-CP-235</p> <p>Aerodynamic stability Dynamic response Dynamic structural analysis Wind tunnel tests Flight characteristics Unsteady flow</p>	<p>AGARD Conference Proceedings No.235 Advisory Group for Aerospace Research and Development, NATO DYNAMIC STABILITY PARAMETERS Published November 1978 636 pages</p> <p>The Symposium discussed the specific needs for dynamic stability information of aerospace vehicles, the form in which it should be presented and the various means of obtaining it.</p> <p>The modern aerospace vehicle is often exposed to unsteady, irregular or asymmetrical flow fields that may have significant effects on its characteristics of motion. This is caused by the fact that the flight envelope of a</p> <p>P.T.O.</p>	<p>AGARD-CP-235</p> <p>Aerodynamic stability Dynamic response Dynamic structural analysis Wind tunnel tests Flight characteristics Unsteady flow</p>
<p>AGARD Conference Proceedings No.235 Advisory Group for Aerospace Research and Development, NATO DYNAMIC STABILITY PARAMETERS Published November 1978 636 pages</p> <p>The Symposium discussed the specific needs for dynamic stability information of aerospace vehicles, the form in which it should be presented and the various means of obtaining it.</p> <p>The modern aerospace vehicle is often exposed to unsteady, irregular or asymmetrical flow fields that may have significant effects on its characteristics of motion. This is caused by the fact that the flight envelope of a</p> <p>P.T.O.</p>	<p>AGARD-CP235</p> <p>Aerodynamic stability Dynamic response Dynamic structural anal analysis Wind tunnel tests Flight characteristics Unsteady flow</p>	<p>AGARD Conference Proceedings No.235 Advisory Group for Aerospace Research and Development, NATO DYNAMIC STABILITY PARAMETERS Published November 1978 636 pages</p> <p>The Symposium discussed the specific needs for dynamic stability information of aerospace vehicles, the form in which it should be presented and the various means of obtaining it.</p> <p>The modern aerospace vehicle is often exposed to unsteady, irregular or asymmetrical flow fields that may have significant effects on its characteristics of motion. This is caused by the fact that the flight envelope of a</p> <p>P.T.O.</p>	<p>AGARD-CP-235</p> <p>Aerodynamic stability Dynamic response Dynamic structural analysis Wind tunnel tests Flight characteristics Unsteady flow</p>

<p>present-day military aircraft or missile often encompasses flight at high angles of attack, flight at non-zero sideslip angles and the ability to perform translational maneuvers.</p> <p>The Symposium included reports on new developments in wind-tunnel, flight test, and analytical techniques; motion analysis and non-linear formulations; and sensitivity and simulator studies. Specialists discussed a broad spectrum of approaches to determination of dynamic stability parameters.</p> <p>Papers presented and discussions held at the Fluid Dynamics Panel Symposium held in Athens, Greece, 22–24 May 1978.</p> <p>ISBN 92-835-0223-X</p>	<p>present-day military aircraft or missile often encompasses flight at high angles of attack, flight at non-zero sideslip angles and the ability to perform translational maneuvers.</p> <p>The Symposium included reports on new developments in wind-tunnel, flight test, and analytical techniques; motion analysis and non-linear formulations; and sensitivity and simulator studies. Specialists discussed a broad spectrum of approaches to determination of dynamic stability parameters.</p> <p>Papers presented and discussions held at the Fluid Dynamics Panel Symposium held in Athens, Greece, 22–24 May 1978.</p> <p>ISBN 92-835-0223-X</p>
<p>present-day military aircraft or missile often encompasses flight at high angles of attack, flight at non-zero sideslip angles and the ability to perform translational maneuvers.</p> <p>The Symposium included reports on new developments in wind-tunnel, flight test, and analytical techniques; motion analysis and non-linear formulations; and sensitivity and simulator studies. Specialists discussed a broad spectrum of approaches to determination of dynamic stability parameters.</p> <p>Papers presented and discussions held at the Fluid Dynamics Panel Symposium held in Athens, Greece, 22–24 May 1978.</p> <p>ISBN 92-835-0223-X</p>	<p>present-day military aircraft or missile often encompasses flight at high angles of attack, flight at non-zero sideslip angles and the ability to perform translational maneuvers.</p> <p>The Symposium included reports on new developments in wind-tunnel, flight test, and analytical techniques; motion analysis and non-linear formulations; and sensitivity and simulator studies. Specialists discussed a broad spectrum of approaches to determination of dynamic stability parameters.</p> <p>Papers presented and discussions held at the Fluid Dynamics Panel Symposium held in Athens, Greece, 22–24 May 1978.</p> <p>ISBN 92-835-0223-X</p>